

EARTHQUAKE RESISTANCE OF COMPOSITE BEAM-COLUMNS

A thesis submitted for the degree of Doctor of Philosophy
in the Faculty of Engineering of the University of London

by

Ahmed Youssef Elghazouli BSc, MSc, DIC

Civil Engineering Department

Imperial College of Science, Technology and Medicine

University of London

December 1991



To my parents

ABSTRACT

This thesis deals with the behaviour of partially-encased composite steel/concrete beam-columns subjected to cyclic and earthquake loading conditions, including experimental testing, analytical studies and design considerations.

Design codes from different countries are examined and a quantitative comparison of the provisions is undertaken.

A new on-line computer-controlled experimental facility, developed for testing of structural members and assemblies under earthquake loads, is described. The theory and implementation details are presented as well as a number of verification tests carried out to demonstrate the accuracy and reliability of the system.

Experiments on twelve composite members, tested under cyclic and pseudo-dynamic loading, are reported. The set-up, instrumentation, control and model manufacture are presented, and a full description of the experimental results is given. Within the testing programme, a novel configuration of composite beam-columns, designed to provide improved seismic performance, was developed. Using this new configuration, the ductility and energy dissipation capacity is shown to be substantially enhanced as compared to conventional members.

Analytical work was performed using advanced nonlinear dynamic analysis procedures and constitutive material models, including a new simplified cyclic model developed to account for local flange buckling. A parametric study, conducted to examine the effect of salient parameters on the behaviour, is presented.

Based on the results of the experimental and analytical investigations, methods for ductility-based design are proposed in line with modern code recommendations for earthquake resistance.

ACKNOWLEDGEMENTS

I would like to express my sincere gratitude to my supervisor Dr Amr Elnashai for his constant encouragement and unfailing technical and moral support. His clear guidance and constructive suggestions have been invaluable throughout the duration of my studies.

I am also indebted to Professor P. J. Dowling, Head of the Civil Engineering Department, who first gave me the chance to pursue studies at Imperial College, and willingly gave advice on a subject which he pioneered. His encouragement has been a great asset.

I consider it a privilege to have worked within the Engineering Seismology and Earthquake Engineering Section, and to have been instructed by Professor N. N. Ambraseys, Head of Section.

The financial support of the Arab British Foundation Scholarship and the Overseas Research Scholarship are gratefully acknowledged. Financial support for the experimental work was provided by the Science and Engineering Research Council.

I am grateful to Professor K. Takanashi of the Institute of Industrial Science, University of Tokyo, for partial funding of the experimental programme and for many useful discussions on pseudo-dynamic testing.

I would like to thank Dr Bassam Izzuddin for his valuable advice in the development of the analytical models incorporated in the computer program ADAPTIC, and for many useful suggestions and discussions. Thanks are also due to Dr Kypros Pilakoutas and Dr Julian Bommer for their assistance and support, and to Panos Madas and Ashraf El-Mesallamy for their help and co-operation.

The expert technical support of the staff in the structures laboratories is gratefully acknowledged, especially, but not exclusively, that of Mr Jack Neale, Mr Tony Boxall, Mr Peter Jellis and Mr George Scopes.

The advice of Mr Clive Hargreaves in using the dynamic testing equipment and of Dr Robert Wing in the selection of hardware for the on-line computer-controlled facility is appreciated.

Last but by no means least, I thank all the researchers of the ESEE and Structures sections for providing a pleasant and intellectual working environment.

This thesis is dedicated to my parents who provided me with tremendous support, care and encouragement.

TABLE OF CONTENTS

| | Page |
|---|-------------|
| ABSTRACT | 3 |
| ACKNOWLEDGEMENTS | 4 |
| TABLE OF CONTENTS | 6 |
| NOTATION | 12 |
| | |
| 1 INTRODUCTION | 17 |
| 1.1 Preamble | 17 |
| 1.1.1 General | 17 |
| 1.1.2 Types of composite members | 17 |
| 1.1.2 Earthquake-resistant design | 18 |
| 1.2 Scope and Organisation of the Present Work | 19 |
| | |
| 2 COMPOSITE BEAM-COLUMNS, A LITERATURE REVIEW | 21 |
| 2.1 Introduction | 21 |
| 2.2 Behaviour of Encased Beam-Columns under Static Loading | 21 |
| 2.2.1 Axially loaded columns | 21 |
| 2.2.2 Beam-column behaviour | 22 |
| 2.3 Behaviour under Cyclic and Dynamic Loading | 24 |
| 2.3.1 Members failing in flexure | 24 |
| 2.3.2 Members failing in shear | 26 |
| 2.4 Bond between Embedded Steel Shapes and Concrete | 27 |
| 2.5 Effects of Long-Term Loading | 28 |
| 2.6 Effects of Elevated Temperatures | 29 |
| 2.7 Commentary | 31 |
| | |
| 3 ASSESSMENT OF DESIGN GUIDANCE FOR COMPOSITE BEAM-COLUMNS | 39 |
| 3.1 Introduction | 39 |
| 3.2 Design Codes, a Brief Description | 40 |
| 3.2.1 AIJ standards | 40 |

| | | |
|----------|--|-----------|
| 3.2.2 | BS 5400 Part 5 | 41 |
| 3.2.3 | ACI-318-83 | 42 |
| 3.2.4 | AISC-LRFD-1986 | 42 |
| 3.2.5 | Eurocode 4 and DIN 18806 | 42 |
| 3.2.6 | Australian and East European standards | 43 |
| 3.3 | Code Differences | 43 |
| 3.3.1 | Design basis | 43 |
| 3.3.1.1 | Origin of method | 43 |
| 3.3.1.2 | Loading and resistance | 43 |
| 3.3.2 | Concrete strength | 44 |
| 3.3.3 | Interaction curves | 44 |
| 3.3.4 | Equivalent stiffness | 45 |
| 3.3.5 | Slenderness considerations | 46 |
| 3.3.6 | Minimum eccentricities | 47 |
| 3.3.7 | Shear transfer | 47 |
| 3.3.8 | Material properties | 49 |
| 3.3.9 | Dimensional limitations | 49 |
| 3.3.9.1 | Steel wall thickness | 49 |
| 3.3.9.2 | Steel and concrete contributions | 49 |
| 3.3.9.3 | Slenderness and section dimensions | 49 |
| 3.3.9.4 | Reinforcement details | 51 |
| 3.4 | Comparative Resistances | 52 |
| 3.4.1 | General | 52 |
| 3.4.2 | Equivalent stiffness | 53 |
| 3.4.3 | Comparison of axial capacities | 54 |
| 3.4.3.1 | Unfactored axial capacity | 54 |
| 3.4.3.2 | Factored axial capacity | 55 |
| 3.4.4 | Combined flexure and axial compression | 55 |
| 3.4.4.1 | Unfactored capacity | 55 |
| 3.4.4.2 | Factored capacity | 56 |
| 3.5 | Commentary | 57 |
| 4 | ON-LINE COMPUTER-CONTROLLED TESTING | 65 |
| 4.1 | Introduction | 65 |
| 4.2 | The Pseudo-Dynamic Testing Method | 66 |
| 4.2.1 | Theoretical basis | 66 |
| 4.2.2 | Numerical schemes | 67 |

| | | |
|----------|--|------------|
| 4.2.3 | Comparison with other testing procedures | 70 |
| 4.2.4 | Sources of on-line test errors | 73 |
| 4.2.4.1 | Discrete parameter models | 73 |
| 4.2.4.2 | Geometric effects | 74 |
| 4.2.4.3 | Strain-rate effects | 74 |
| 4.2.4.4 | Energy dissipation | 75 |
| 4.3 | Implementation Details | 78 |
| 4.3.1 | System description | 78 |
| 4.3.2 | Data conversion | 78 |
| 4.3.3 | Signal conditioning | 80 |
| 4.3.4 | Measurement transducers | 81 |
| 4.3.5 | Electro-hydraulic equipment | 82 |
| 4.3.6 | Software layout | 83 |
| 4.4 | Verification Tests | 84 |
| 4.4.1 | Specimen details | 84 |
| 4.4.2 | Experimental set-up and instrumentation | 85 |
| 4.4.4 | Elastic free vibration response | 87 |
| 4.4.5 | Elastic seismic test | 88 |
| 4.4.6 | Inelastic tests | 89 |
| 4.4.7 | Experimental error evaluation | 90 |
| 4.5 | Commentary | 92 |
| 5 | EXPERIMENTAL METHODOLOGY | 119 |
| 5.1 | Introduction | 119 |
| 5.2 | Experimental Set-up | 120 |
| 5.2.1 | Self-reacting test frame | 120 |
| 5.2.2 | Beam-column test-rig | 122 |
| 5.3 | Description of Models | 123 |
| 5.3.1 | Specimen Details | 123 |
| 5.3.2 | Material properties | 124 |
| 5.3.2.1 | Steel sections | 124 |
| 5.3.2.2 | Reinforcing bars | 125 |
| 5.3.2.3 | Concrete | 126 |
| 5.4 | Instrumentation and Control | 128 |
| 5.4.1 | Bending tests | 128 |
| 5.4.2 | Beam-column tests | 129 |
| 5.5 | Analysis of Measurements | 129 |

| | | |
|---------|--|-----|
| 5.6 | Loading Regime | 131 |
| 5.6.1 | Axial loads | 131 |
| 5.6.2 | Cyclic tests | 132 |
| 5.6.3 | Pseudo-dynamic tests | 134 |
| 5.6.3.1 | Tests on models EM03 and IC03 | 134 |
| 5.6.3.2 | Tests on models EM05, IC05 and IC06 | 135 |
| | | |
| 6 | EXPERIMENTAL RESULTS | 157 |
| 6.1 | Introduction | 157 |
| 6.2 | Cyclic Loading Tests | 158 |
| 6.2.1 | Model EM01 | 158 |
| 6.2.2 | Model IC01 | 158 |
| 6.2.3 | Model EM02 | 159 |
| 6.2.4 | Model IC02 | 159 |
| 6.2.5 | Model EM04 | 160 |
| 6.2.6 | Model IC04 | 160 |
| 6.2.7 | Model IC07 | 161 |
| 6.3 | Pseudo-Dynamic Tests | 162 |
| 6.3.1 | Model EM03 | 162 |
| 6.3.2 | Model IC03 | 162 |
| 6.3.3 | Model EM05 | 163 |
| 6.3.4 | Model IC05 | 163 |
| 6.3.5 | Model IC06 | 164 |
| 6.4 | Discussion of Strain Gauge Results | 164 |
| 6.4.1 | General | 164 |
| 6.4.2 | Extreme fibre strains in the plastic hinge region | 165 |
| 6.4.3 | Extreme fibre strains outside the plastic hinge region | 167 |
| 6.4.4 | Strains in vertical reinforcement | 167 |
| 6.4.5 | Strains in lateral reinforcement | 168 |
| | | |
| 7 | ANALYSIS OF COMPOSITE BEAM-COLUMNS | 201 |
| 7.1 | Introduction | 201 |
| 7.2 | The Nonlinear Dynamic Analysis Program 'ADAPTIC' | 202 |
| 7.2.1 | General description | 202 |
| 7.2.2 | The elasto-plastic cubic element | 203 |
| 7.3 | Existing Material Models | 204 |

| | | |
|----------|---|------------|
| 7.3.1 | Models for mild steel | 204 |
| 7.3.1.1 | Bilinear model | 205 |
| 7.3.1.2 | Multi-surface model | 206 |
| 7.3.2 | Constitutive relationships for concrete | 207 |
| 7.3.2.1 | Monotonic model | 208 |
| 7.3.2.2 | Concrete confinement | 208 |
| 7.3.2.3 | Cyclic loading model | 209 |
| 7.4 | Confinement in Encased Sections | 210 |
| 7.5 | Local Flange Buckling | 213 |
| 7.5.1 | General | 213 |
| 7.5.1.1 | Elastic buckling | 213 |
| 7.5.1.2 | Inelastic buckling | 214 |
| 7.5.1.3 | Post-buckling strength | 216 |
| 7.5.1.4 | Cyclic models for frame analysis | 218 |
| 7.5.2 | The Proposed model | 219 |
| 7.5.2.1 | Determination of buckling strain | 219 |
| 7.5.2.2 | Post buckling relationship | 220 |
| 7.5.2.3 | Description of the cyclic model | 221 |
| 7.5.2.4 | Implementation of the model | 223 |
| 7.5.2.5 | Verification | 224 |
| 7.6 | Comparison with Experimental Results | 225 |
| 7.6.1 | General | 225 |
| 7.6.2 | Tests by Ballio et al | 226 |
| 7.6.3 | Cyclic tests on beam-columns | 227 |
| 7.6.4 | Pseudo-dynamic tests | 228 |
| 7.6.5 | Commentary | 230 |
| 8 | ANALYTICAL PARAMETRIC STUDY | 260 |
| 8.1 | Introduction | 260 |
| 8.2 | Preliminaries | 261 |
| 8.2.1 | Geometry and loading | 261 |
| 8.2.2 | Definition of yield | 262 |
| 8.2.3 | Failure criteria | 264 |
| 8.3 | Presentation of Results | 265 |
| 8.3.1 | Capacity | 265 |
| 8.3.2 | Neutral axis depth | 265 |
| 8.3.3 | Ductility | 265 |

| | | |
|---------|---|-----|
| 8.3.4 | Plastic hinge length | 266 |
| 8.4 | Strain Hardening Study | 266 |
| 8.5 | Yield Stress of Steel | 267 |
| 8.6 | Concrete Confinement | 268 |
| 8.7 | Member Slenderness | 269 |
| 8.8 | Flange Slenderness | 270 |
| | | |
| 9 | DISCUSSION AND DESIGN IMPLICATIONS | 296 |
| 9.1 | Introduction | 296 |
| 9.2 | Stiffness Characteristics | 296 |
| 9.3 | Capacity | 299 |
| 9.3.1 | Yield moment | 299 |
| 9.3.2 | Ultimate moment | 301 |
| 9.4 | Plastic Hinge Length | 302 |
| 9.5 | Ductility | 304 |
| 9.5.1 | Ductility of the experimental models | 304 |
| 9.5.2 | Parameters influencing ductility | 305 |
| 9.5.3 | Relationship between curvature and rotational ductilities | 306 |
| 9.5.4 | Design for ductility | 308 |
| 9.5.4.1 | Steel and composite structures in EC8 | 308 |
| 9.5.4.2 | Assessment of local ductility | 310 |
| 9.6 | Slenderness Considerations | 312 |
| 9.7 | Energy Dissipation | 313 |
| | | |
| 10 | CLOSURE | 322 |
| 10.1 | Summary and Conclusions | 322 |
| 10.2 | Suggestions for Future Research | 327 |
| | | |
| | REFERENCES | 329 |
| | | |
| | APPENDIX A : STRAIN GAUGE RESULTS | 340 |

NOTATION

General Rules

- All notations are defined when they first appear. Notations from other work are defined only in the text.
- Equations are identified by the numbers in parentheses, located on the right-most margin and composed of up to three entries (e.g. 7.1.a) where the first entry indicates the chapter in which the equation appears.

Symbols

| | |
|-------------|--|
| A_c | area of concrete |
| A_{cc} | area of confined concrete |
| A_e | area of effectively confined concrete |
| A_g | gross cross-sectional area |
| A_r | area of longitudinal reinforcing bars |
| A_s | area of steel section |
| B | overall width of the section |
| b | half flange width |
| b/t | flange slenderness |
| B_c | overall breadth of composite section |
| b_c | breadth of concrete section |
| b_f | overall breadth of steel flange |
| b_s | breadth of steel section |
| C | viscous damping matrix |
| c | damping coefficient of a single degree of freedom system |
| $C_{1,2,3}$ | factors to account for confined concrete strength |
| C_m | factor relating actual moment diagram to an equivalent uniform diagram |
| D | depth of cross-section |
| D_c | overall depth of composite section in direction of bending |
| d_c | depth of effectively confined concrete area |
| D_ϕ | curvature ductility |
| d_p | depth of confinement parabola |
| D_s | overall dimension of steel tube |

| | |
|--------------------|---|
| d_w | depth of web |
| E | modulus of elasticity of steel |
| E_c | modulus of elasticity of concrete |
| E_s | secant modulus |
| E_{st1}, E_{st2} | strain hardening moduli |
| E_t | tangent modulus |
| F | actuator force |
| \mathbf{F} | external force vector (italics, Chapter 4) |
| f'_1 | effective lateral confining pressure |
| f'_{cc} | compressive strength of confined concrete |
| f | external force |
| f_1 | lateral confining pressure |
| f_c | compressive concrete stress |
| f_{co} | compressive strength of unconfined concrete |
| f_{cu} | concrete cube strength |
| f_{cyl} | concrete cylinder strength |
| F_r | friction force |
| F_y | yield force |
| H | horizontal force |
| h_c | height of concrete section |
| h_s | height of steel section |
| I | second moment of area |
| i | integration step |
| i | monitoring area |
| j | number of monitoring points in flange |
| K | stiffness |
| \mathbf{K} | stiffness matrix (italics, Chapter 4) |
| k | buckling coefficient |
| k | stiffness of a single degree of freedom system (italics, Chapter 4) |
| $K_{cracked}$ | cracked stiffness |
| k_σ | confinement factor |
| $K_{uncracked}$ | uncracked stiffness |
| L, L_1 | length of cantilever member |
| L_2 | length of loading beam |
| L_b | buckling length |
| L_e | equivalent length |
| L_{ey} | major axis equivalent length |
| L_{ez} | minor axis equivalent length |

| | |
|-------------|--|
| M | mass matrix (<i>italics</i> , Chapter 4) |
| M | moment |
| m | mass of a single degree of freedom system (<i>italics</i> , Chapters 4 and 5) |
| M_p | flexural plastic capacity |
| M_u | ultimate moment |
| M_{ult} | ultimate moment capacity |
| M_y | yield moment |
| N | axial load |
| N_p | axial plastic capacity |
| N_{pc} | squash load of concrete section |
| N_{ps} | squash load of steel section |
| P | axial load |
| P_E | Euler buckling load |
| P_u | ultimate weld resistance |
| P_y | yield resistance of weld |
| Q | component of force |
| R | reaction at support |
| R | structural restoring force vector (<i>italics</i> , Chapter 4) |
| r_{comp} | radius of gyration of composite section |
| R_s | strength reduction factor |
| r_{steel} | radius of gyration of steel section |
| R_ψ | rotational ductility |
| s | spacing of bars |
| s' | clear spacing of lateral bars |
| s_{pc} | factor to account for concrete strain limit |
| T | structural period of vibration |
| t | steel wall thickness |
| t | time (<i>italics</i> , Chapter 4) |
| t_f | thickness of steel flange |
| t_{pl} | steel plate thickness |
| t_w | thickness of web |
| U | displacement vector |
| u, u | displacement |
| \ddot{u} | acceleration |
| \ddot{U} | acceleration vector |
| \bar{u} | displacement amplitude |
| \dot{u} | velocity |
| \dot{U} | velocity vector |

| | |
|----------------|---|
| W | normal force, weight |
| w | unit weight of concrete |
| X_1 to X_6 | displacements |
| x_i | distance from flange monitoring point, i , to centre of web |

Greek Symbols

| | |
|---|---|
| α | centre of yield surface |
| α_c | confinement effectiveness coefficient |
| α^0 | centre of yield surface at start of increment |
| β | slope angle |
| δ | lateral displacement |
| δ | logarithmic decrement (<i>italics</i> , Chapter 4) |
| δ_m | moment magnification factor |
| δ_o | actuator displacement |
| Δt | time step |
| δ_y | yield displacement |
| ε | strain |
| ε_b | strain at onset of local buckling |
| ε_{bp} | critical strain for steel plate at onset of local buckling |
| ε_c | longitudinal compressive concrete strain |
| ε_{cc} | critical strain of confined concrete |
| ε_{cr} | critical buckling strain |
| $\varepsilon_k, \varepsilon_m, \varepsilon_r$ | strains determining the post-buckling cyclic constitutive relationships |
| ε_o | critical strain of unconfined concrete |
| ε^0 | strain at start of increment |
| ε_s | strain corresponding to zero stress |
| ε_u | ultimate strain |
| ε_y | yield strain |
| ϕ_f | coefficient of dynamic friction (<i>italics</i> , Chapter 4) |
| ϕ_p | plastic curvature |
| ϕ_s | capacity reduction factor |
| ϕ_u | curvature at ultimate |
| ϕ_y | curvature at yield |
| γ | stress reduction factor |
| λ_s | non-dimensional slenderness parameter |
| λ_p | plate slenderness parameter |
| μ | strain hardening parameter |

| | |
|--------------------------------|--|
| ν | Poisson's ratio |
| ν_s | factor of safety |
| θ | slope angle |
| ρ_c | concrete contribution factor |
| ρ_s | steel contribution factor |
| σ | stress |
| σ_b | stress at onset of local buckling |
| σ_{cr} | critical buckling stress |
| $\sigma_k, \sigma_m, \sigma_r$ | stresses determining the post-buckling cyclic constitutive relationships |
| σ^0 | stress at start of increment |
| σ_u | ultimate stress |
| σ_y | yield stress |
| τ | normalised plastic hinge length |
| τ_s | shear stress |
| ω | natural circular frequency |
| ξ | normalised neutral axis depth |
| ξ | viscous damping ratio (<i>italics</i> , Chapter 4) |
| ψ | deflection angle |
| ψ_p | plastic deflection angle |
| ψ_u | deflection angle at ultimate |
| ψ_y | deflection angle at yield |

CHAPTER 1

1. INTRODUCTION

1.1 PREAMBLE

1.1.1 General

Over the years, use of composites to achieve objectives beyond the capabilities of the constituent materials has been rapidly gaining ground. Whereas reinforced concrete can be considered as a composite material, the more conventional definition of composite steel/concrete structures uses steel sections in conjunction with concrete. Such systems ideally combine the advantages of both components. In this context, composite beam-columns offer an attractive solution to problems such as local and overall buckling for steel members, and deterioration and shear failure for conventional reinforced concrete members. Consequently, this form of structural member exhibits excellent earthquake-resistant properties, demonstrated in high stiffness, strength, ductility and energy absorption capacity.

Whereas the favourable behaviour of composite members under earthquake loading has been realised by Japanese researchers for many years, previous European research was confined mainly to static loading applications. Only recently has the engineering community in Europe taken an interest in the subject, partly as a result of the introduction of the new Eurocode (EC8, 1988), 'Structures in Seismic Regions'.

1.1.2 Types of Composite Members

Composite steel/concrete sections may be broadly classified as either hollow sections filled with concrete or steel sections encased in concrete. In concrete-filled members, there is a mutual enhancement of ductility as the tube provides confinement for the concrete which in turn prevents the inward buckling of the steel tube thus delaying outward buckling. Concrete-encased steel sections offer high strength and ductility, while enhancing the steel section buckling strength and fire performance. Partially-encased members, used in European practice, exhibit additional structural and

constructional advantages such as simple beam-to-column connections, impact resistance, and reduced or omitted shuttering.

Due to its high strength and ductility, the use of encased members has significantly increased. In Japan, steel-reinforced concrete structures, termed (SRC), have been in common use for multi-storey buildings after showing superior earthquake-resistant qualities during major earthquakes, particularly when compared to reinforced concrete members.

1.1.3 Earthquake-Resistant Design

Economical Design of structures to resist strong earthquakes mandates the use of structural components responding well into the inelastic range. During a severe event, a structure should be able to sustain large deformations without collapse, and be capable of dissipating substantial energy through inelastic deformations of its structural members.

By appropriate use of the ductility and energy absorption capability of a structure, it is possible to reduce the cost significantly without compromising safety. Moreover, in 'Capacity Design', key members are dimensioned to develop a carefully chosen ductile failure mode, and to demonstrate plastic deformational capability sufficient for the development of the full capacity of the whole structural system. Components other than the key members are henceforth designed to resist forces consistent with the ultimate capacity of the key members. It is therefore imperative that the full deformational and strength capacities of members are accurately evaluated and assessed, through realistic seismic testing techniques and reliable analytical investigations, to provide a safe and economical structure.

Whilst the work on the steel and reinforced concrete parts in Eurocode 8 are nearing completion, there is a dearth of information on composite structures. Therefore, a number of design philosophies utilizing either reinforced concrete or steel concepts are being adopted, missing to capitalize on the synergy resulting from the combination of the two materials.

The present work was initiated to study the behaviour of partially-encased composite beam-columns, typically used in Europe for static design, subjected to cyclic and earthquake loading. This was motivated by the success of composite beam-columns in dealing with fire resistance problems coupled with a recognised need for seismic design criteria for composite construction, to be included in Eurocode 8.

1.2 SCOPE AND ORGANISATION OF THE PRESENT WORK

The purpose of this work is to investigate the behaviour of partially-encased members under seismic loading conditions. This includes experimental and analytical examination, introduction of improved detailing practices and suggestions for the design process.

Available work on testing and analysis of encased composite beam-columns subjected to monotonic and cyclic loading is reviewed in Chapter 2. Emphasis is given to investigations of particular relevance to the present research.

A survey of existing design regulations dealing with composite beam-columns is undertaken in Chapter 3. The current state of design provisions from different countries is first briefly described. This is followed by a general comparison of code recommendations in terms of design basis, slenderness considerations, material properties and dimensional limitations. A quantitative assessment of capacity calculation for a specific cross-section under axial loading and combined axial loading and flexure is presented for a wide range of slenderness ratios.

A new on-line computer-controlled testing facility is described in Chapter 4. The system was developed to provide a verifiably accurate and realistic testing procedure. This is needed for accurate evaluation of full deformational and strength capacities of structural members. The accuracy and stability of the system was investigated by testing two steel members under impulse and earthquake excitations in the linear and the nonlinear domains, and compared with analytical simulations. The results demonstrated the reliability and high precision of the developed set-up.

In Chapter 5, a new configuration of partially-encased member is introduced. Two unconventional features are incorporated to provide improved performance for earthquake-resistance. The first is variable pitch confining stirrups, with a reduced pitch in the potential plastic hinge zone. The second is the provision of additional transverse bars intended to inhibit local buckling at large displacements, and to increase the interaction between the two materials. Two cross-section details were tested. The first is typical of European practice, whilst the second is the new modified configuration. Details of the experimental investigation are given. This includes the design and description of test-rigs, instrumentation of the specimens, control of the tests, details of model manufacture, properties of materials and the choice of loading.

Description of seven cyclic tests and five pseudo-dynamic experiments is given in Chapter 6. Details of loading procedures, test progression and immediate observations are presented. Strain gauge results are given in Appendix A. Main results are shown and discussions relevant to subsequent parts of the thesis are introduced. It is demonstrated that, in comparison with the conventional European members, the modified section shows a significant improvement in ductility under cyclic and transient loading.

The existing advanced nonlinear analysis program, ADAPTIC, used for conducting the analytical part of this work is briefly described in Chapter 7. A discussion of confinement effects in concrete is presented. Also, a simple model to account for local flange buckling is proposed. Analytical simulations are compared with some of the experimental results to verify the accuracy of the analytical model.

In Chapter 8, an analytical parametric study is undertaken to quantify the capacity and ductility of partially encased members. The choice of parameters and range of variation is followed by a presentation and brief discussion of all the results.

A general discussion of experimental and analytical results is presented in Chapter 9. Stiffness characteristics, capacity, ductility and energy dissipation capacity of partially encased members are addressed. The relationship between curvature and rotational ductility and the extent of the plastic hinge zone are examined. Recommendations of modern seismic codes in Europe are assessed and compared with the results. Finally, suggested methods for ductility-based design are outlined.

In the final chapter, general conclusions from the present study are drawn alongside with recommendations for further research and developments in the subject.

CHAPTER 2

2. COMPOSITE BEAM-COLUMNS, A LITERATURE REVIEW

2.1 INTRODUCTION

In the context of assessing the benefits of using composite beam-columns for earthquake-resistant design, this chapter presents a brief review of available research on testing and analysis of composite members. Particular emphasis is given to encased members subjected to cyclic loading. Also, separate short sections focus on bond between steel sections and concrete and the effect of elevated temperatures on composite sections. A more detailed review including the behaviour of beam-to-column connections was carried out by the author (Elghazouli, 1988). Governing factors in testing and analysis were highlighted, and areas worthy of further analytical and experimental research were identified in the above-mentioned reference.

2.2 BEHAVIOUR UNDER STATIC LOADING

2.2.1 Axially Loaded Columns

Concrete encased steel columns have been in use since about 1910 as a means of fire protection. However, experiments carried out by early investigators, such as Burr (1912) and Faber (1956) demonstrated that the concrete added significantly to the load carrying capacity of the steel column.

Stevens (1965) tested a large number of axially loaded columns varying the slenderness ratio, reinforcement and concrete strength, and concluded that the axial load capacity of a short column can be safely calculated as the sum of the individual strengths of steel and concrete sections. Early investigations in Japan, reviewed by Wakabayashi (1987), converged to the same result and the strength of the axially loaded short column was also predicted by the sum of strengths of steel and concrete; but a reduction factor was applied to the compressive strength of concrete to account for the strain limit of the material.

On the other hand, slender columns fail by buckling along their lengths. Consequently, the load carried by such a column depends not only on the material strength but also on the slenderness. The early British Standards, BS 449 (1959), allowed for an increase in the radius of gyration of the steel column to take account of the concrete encasement in a method referred to as 'the Cased-Strut' method. However, tests carried out by Jones and Rizk (1963) and Stevens (1965) showed that the method was grossly over conservative and inaccurate because of the inadequacy of the simple method to account for the large number of relevant parameters. Moreover, the method was empirically based on very few experimental results. Research on improved design methods has been undertaken by several researchers such as Basu and Sommerville (1969) and Viridi and Dowling (1976a). Use was made of the European buckling curves of steel sections, and a nondimensional slenderness parameter. Also simplified concrete stress-strain relationships were assumed. Analytical treatment of the inelastic composite column stability was undertaken by Bondale (1962, 1966) in which the application of the tangent modulus approach gave good correlation with test results.

It should be noted that most of the information was derived from tests on pin-ended composite columns, and the effective length method was proposed for different boundary conditions. Moreover, full interaction between steel and concrete provided by bond was assumed up to collapse which was shown in all tests to be a valid assumption.

2.2.2 Beam-Column Behaviour

Experimental studies on encased columns loaded eccentrically about one axis have been reported by Bondale (1962, 1966), Jones and Rizk (1963), Stevens (1965), Procter (1967), Roderick and Rogers (1969), and Bridge and Roderick (1978). Stevens and Procter employed a linear interaction between the axial load and bending moment to obtain the theoretical capacity. However, it was later known that the linear interaction gives conservative strength for columns of small slenderness and overestimates the strength in the range of large slenderness.

The accurate estimation of the strength of an encased column can be performed by von Karman's method primarily developed for steel columns. In this method, the equilibrium between internal resistance and external load is satisfied at every cross section along the length of the column. Another simple, and usually adequately accurate method, assumes the deflected shape of the column as a part of a cosine curve and considers equilibrium at mid-height only. These methods were employed by Bondale (1966) and Basu (1967).

The former constructed axial load-moment interaction diagrams for columns of small slenderness.

For design purposes, the column behaviour can be described in terms of interaction curves showing the change in ultimate load with increasing moment. For the case of short columns, the interaction diagram can be simply obtained by studying the equilibrium of the fully plastic cross section, represented by rectangular stress blocks. By varying the position of the plastic neutral axis, sets of moment and normal force values will be obtained to complete the interaction diagram. However, to take account of overall buckling in slender members, a series of inelastic analyses would be required in order to develop a similar interaction curve in which buckling is considered. Simplified methods have been developed to obtain the interaction curve of slender columns by making use of the slenderness parameters of the member, such as those proposed by Basu and Sommerville (1969) and Viridi and Dowling (1976a).

In Japan, Wakabayashi (1977) proposed the application of the 'superposed strength method' for the design of slender columns. In this method, the strength of a slender column is calculated by superimposing the interaction curves of a slender steel column and a slender reinforced concrete column. Other design methods were also proposed by Furlong (1967, 1979). A review of available design methods from different countries is given in Chapter 3 of this thesis.

Experimental investigations on the behaviour of pin-ended columns subjected to biaxial eccentricity was undertaken by Viridi and Dowling (1973, 1976b). The tests included a series of concrete encased H-sections with variable lengths and biaxial eccentricities. In parallel, two theoretical treatments were given. The first was a general method applicable to members subjected to any load combinations using the actual deflected shape. The second method assumed that the deflections followed a cosine curve, but was applicable only to members with symmetrical biaxial bending. Viridi and Dowling also showed that the interaction formula of Bresler (1960) used for reinforced concrete yielded consistently conservative values.

Other work on biaxial bending was also conducted by May and Johnson (1978) and by Roik and Bergmann (1984). The latter proposed a design formula for biaxially loaded encased columns based on the strength interaction under uniaxial bending. The load-deflection relationships of columns under biaxial bending was also investigated experimentally by Morino et al (1984, 1987).

2.3 BEHAVIOUR UNDER CYCLIC AND DYNAMIC LOADING

2.3.1 Members Failing in Flexure

In Japan, shear failures of reinforced concrete columns caused by the 1968 Tokachi-oki earthquake drew considerable attention to the favourable behaviour of encased columns. Wakabayashi and Minami (1980) conducted a series of experimental investigations on the ductility of encased beam-columns subjected to a constant axial thrust and a large number of lateral load cycles. The specimen and test-rig details are shown in Figure 2.1. The end surfaces of the specimen were maintained parallel to each other. The amplitude of horizontal deflection was stepwise increased by a unit amplitude of 0.005 radians in deflection angle after two cycles of loading at each amplitude.

The hysteretic load-deflection curves under different values of axial loads are shown in Figure 2.2. In the case of specimens which were not subjected to an axial force, the hysteresis loops were stable and had a spindle-shape with good energy absorption and ductility, and the degradation was very small. On the other hand, when the specimens were subjected to axial thrusts of 10% and 20% of the plastic capacity of the section, respectively, the length of the plateau, where the maximum capacity is maintained, became shorter as the axial force increased. Moreover, when the specimen was subjected to larger axial forces of 30%, 40% and 50% of the axial capacity, the ductility and stability of the loops deteriorated further and failure was brittle.

It was clearly observed in the latter investigation that large axial forces have a damaging effect on the ductility of members. Based on the results of the above-described investigation, Wakabayashi and Minami proposed a limiting value of axial thrust for columns failing in flexure under constant axial thrusts and cyclic lateral load, given by:

$$N_{cr} = (b_c D f_c + 2 A_s f_{sc}) / 3 \quad (2.1)$$

where, b_c is the width of the column, D is the depth of the column, A_s is the cross sectional area of encased steel, f_c is the compressive strength of concrete, and f_{sc} is the allowable compressive stress for steel under temporary loading.

Another set of experiments by Wakabayashi and Minami (1976) compared the hysteretic behaviour of encased columns failing in flexure with similar reinforced concrete and open-web encased members having the same moment capacity. It was observed that

owing to the effect of shear force, the battened type sections and the reinforced concrete sections showed the reversed S-shapes (pinched) with poor energy absorption, while the full-web encased columns showed spindle-shaped hysteresis loops and were much less affected by the applied shear force.

In general, the experimental investigations on the flexural behaviour of encased columns carried out in Japan clarified quantitatively the change in the deformation capacity of composite columns due to the magnitude of working axial thrusts. However, the effects of the ratio of the cross-sectional area of encased steel to that of reinforcing bars, width to thickness ratio of encased steel elements, and area and spacing of lateral ties, were not covered by these investigations.

Analytical work on composite members subjected to cyclic loading has been underway in Japan since 1974. Wakabayashi et al (1974) conducted a theoretical investigation on the behaviour of members failing in flexure, subjected to constant axial force and monotonically increasing or cyclic horizontal loading. The analysis of a member was carried out assuming plastic hinges in which the curvature is uniformly distributed and all the deformation is concentrated, while the rest of the member deforms only as a rigid body. The relationship between moment and curvature under constant axial force and monotonic or cyclic bending is computed by sub-dividing the cross-section into a number of strip elements. Based on the assumption that plane sections remain plane after deformation, and knowing the stress-strain relationships of both steel and concrete, the moment-curvature relationship can be obtained over the entire section.

The stress-strain relationship of steel was assumed as uniaxial piecewise-linear taking the Baushinger effect into consideration. Two different stress-strain relationships were adopted for confined concrete and covering concrete assuming uniaxial piecewise-linear functions, while neglecting the tensile strength. On the other hand, the relationship between deflection and curvature was computed by neglecting shear deformations. The deflection of the member was assumed to be equivalently lumped at the flexible ends of members, and thus the deflection-curvature relationship was obtained, and substituting in the moment-curvature relation, the force or moment-deflection relationship of the member could finally be computed. The theoretical results were compared with experimental investigations on members failing in flexure. Some comparisons are shown in Figure 2.3. General agreement was observed. Discrepancies were attributed to the inaccuracies in the steel and concrete models.

In Europe, Ballio et al (1987) conducted an investigation of the flexural behaviour of partially-encased members. The flange slenderness was varied but no axial loads were applied. Bare steel members were also tested for comparison. Minimal horizontal reinforcement was provided at a spacing of 150 mm. The specimens were subjected to lateral cyclic displacements of increasing amplitudes applied at the tip of the cantilever. The experimental results are shown in Figure 2.4 and 2.5 for the composite and steel members, respectively.

The analytical treatment was based on the same approach used by Wakabayashi et al. The member was assumed to be rigid with an elasto-plastic hinge at the end where all the deformation is concentrated. The cross-section was divided into strips, and the position of the neutral axis defined as a function of the rotation of the hinge which in turn is a function of the deflection at the tip of the cantilever. The value of the stress was then obtained from the material constitutive relationships for each strip assuming that plane sections remain plane. Finally, checking the longitudinal equilibrium of the cross section, the force and moment applied on the member were calculated.

The steel material model used was a bilinear cyclic model considering the Baushinger effect. The concrete constitutive model was a uniaxial cyclic relationship, neglecting tension and confinement. The analytical method accounted for local buckling through a simplified approach. The steel section was divided into small strips, for which the strain was continuously compared to a critical value. The area of the strip was set to zero if the critical strain was exceeded. The possibility of fracture in the section was also considered by an empirical formula whereby the area of the strip reduces in accordance to the number of strain cycles applied, assuming that fracture starts after four cycles. The analytical results, given in Figure 2.6, were shown to be in general agreement with the experimental results.

The above-mentioned investigation demonstrated the improved ductility and energy absorption capacity of partially encased members as compared to bare steel members. However, more experimental and analytical examination are needed to quantify the effect of different parameters such as flange slenderness, concrete confinement and magnitude of axial loads on the behaviour of such member under various loading conditions.

2.3.2 Members Failing in Shear

Behaviour of encased composite columns failing in shear has been investigated mainly in Japan, where the design for large lateral earthquake loads leads to stocky members. Early

investigations on the shear strength of encased columns with open web steel cores were conducted by Wakabayashi and Tsuboi (1957). Two types of failure occurred; the first was diagonal shear failure while the second was termed 'shear-bond failure'. The latter, which was critical in most cases, was a combination of bond failure at the surface of the steel flange and shear failure of concrete at the flange sides.

Tests on encased I-sections with full webs, open webs and battened open-webs subjected to combined compression and shear were carried out by Naka et al (1972). Two theoretical approaches were proposed. The first assumed that the bending moment and axial load was resisted by the flanges and that shear was resisted by the steel web. It was shown that this assumption was reasonable for open web sections connected by battens. The second approach was to assume that shear produces yielding in part of the web while the remaining parts carry the axial compression and bending moment. The correlation between the experimental and analytical results was reasonable except for cases of high axial thrusts. The behaviour of columns with solid webs showed the highest ductility, while those with batten plates showed very brittle behaviour similar to that of an ordinary reinforced concrete column.

Wakabayashi and Minami (1980) later conducted 43 full-scale column tests to obtain back-up data for the revision of the standards of the Architectural Institute of Japan (AIJ). The tests included encased beam-columns with various types of cross-sections under constant axial thrusts and alternating shear and bending. Most specimens failed in 'shear-bond' initiated by the direct shear failure of covering concrete in the outside of the tip of the flange, along the longitudinal direction of a member. As a result of this investigation, a semi-empirical 'superimposed strength formula' for the ultimate shear strength was proposed. For design, both diagonal shear failure and shear-bond failure should be prevented until members develop their full flexural capacity.

2.4 BOND BETWEEN EMBEDDED STEEL SHAPES AND CONCRETE

As mentioned before, the assumption of full interaction between steel and concrete was validated by most researchers. However, if the load is not transferred to both the concrete and the steel parts at the floor levels, the bond and stress transfer must be carefully studied.

In Japan, Wakabayashi and Tsuboi (1954) conducted pull-out tests using steel plates embedded in concrete and concluded that the bond strength ranged from 8% to 10% of

the compressive strength of concrete, which was less than half that for the case of embedded rebars. The standards of Japan thus specified the value of allowable bond stress to be one third that for rebars. In the USA, Roeder (1984) conducted a similar investigation, but varied the steel section, embedment length, tie reinforcements and concrete strength. The bond strength was estimated to be about 9% of the concrete compressive strength. However, it was shown to vary significantly with the surface condition of steel and concrete confinement. The stress distribution was also indicated to be variable along the length of the specimen. In cases of unloading and reloading, the bond strength was reduced by about 45% after initial slip.

It should be noted that pull-out tests have a highly strained centrally loaded steel section in relation to a totally unstrained concrete at the top of the specimen, which is not the case in most composite columns. In encased members, shear transfer between steel shapes and covering concrete is required to transmit flexural compression forces and to distribute column loads through floor reactions into both the steel and concrete parts of the cross-section. This transfer can occur either through direct bearing of concrete against reinforcement and other steel surfaces welded to the steel shape, or through the shear friction mechanism of concrete held tightly against the steel section by transverse ties.

Furlong (1984) also drew attention to the special problem of fully encased sections, where cracks at the flange tip are likely to develop, hence transverse ties or mechanical devices might be needed to retain the flange concrete cover as part of the cross-section. The provision of mechanical attachments on bearing surfaces welded to the outer face of the flange was recommended if the width to thickness ratio of the edge concrete exceeded a certain value. These cracks are usually critical when the concrete segment outside the flange is very thin. This might be caused by the residual tension stresses in concrete due to shrinkage during its hardening process which becomes very significant in the case of thin layers of concrete.

2.5 EFFECTS OF LONG-TERM LOADING

Early investigators proposed simplified methods to account for creep and shrinkage in composite columns for use in design. Basu and Sommerville (1969) suggested a scaling factor of up to 2 to be applied to the strains of the concrete stress-strain relationship. Using a factor of 2 in their computations, they developed a magnification factor for long-term loading which depended on the column slenderness ratio and the amount of concrete in the cross section, but independent of the ratio of end moments. Sharples (1970) later

suggested that the concrete strains should have been multiplied by a factor of 4. However, the latter did not propose a new magnification factor for long term loading.

The behaviour of encased columns under sustained load has been investigated both experimentally and analytically by Bridge (1979, 1987). The test series included columns of different lengths and eccentricities, while the cross-section consisted of two channels encased in plain concrete. Analytical procedures were developed enabling the prediction of long-term deformation within acceptable errors. The analysis was used to extend the results to determine full load-deflection-time relationships. On release of applied load, significant cracking was observed due to the recovery of elastic strains in steel. A design proposal to account for these effects was proposed. This study also indicated the need for minimum reinforcement in the concrete encasement.

Roik and Bergmann (1987) recently conducted long term loading tests on encased I-sections of variable length and end eccentricity. The results indicated a maximum reduction factor, caused by creep, of 80% of the capacity for long-term loading as compared to short-term loading.

The accurate estimation of long-term effects is complicated and tedious for design. Hence, simplified methods are used in codes of practice. A summary of these methods is given elsewhere (Elghazouli, 1988).

2.6 EFFECTS OF ELEVATED TEMPERATURES

Fire may break out in buildings and industrial units due to different causes including strong earthquakes. Good fire resistance of structural elements, especially vertical load-bearing members is necessary to preserve the integrity of a structure under severe fire conditions. The fire resistance of reinforced concrete structures, which is higher than that of bare steel structures, is explained by the low thermal conductivity of concrete, which is approximately one-tenth that of steel. It seems logical, therefore, to combine the advantages of both steel and concrete and at the same time develop a structural member which exhibits superior fire resistant qualities.

The temperature gradient over the cross-section of a composite member leads to different heating rates of its single components. In case of fire, differences in cross-section type involve differences in load bearing behaviour. Figure 2.7 shows the ultimate plastic load of the components of a composite member plotted against fire time as given by Schleich

et al (1984). External steel directly exposed to fire will lose its load bearing capacity very rapidly because of its high heating rate and consequently its high strength reduction. The load shed by external steel must then be carried by the concrete core. Conversely, in cross-sections with embedded steel profiles, the steel section is protected by concrete and loss of strength will proceed rather moderately.

Steel columns fully encased with concrete, historically used for fire protection, are now designed for both structural and fire protection purposes. Extensive experimental and theoretical investigations have been conducted to examine the fire resistance of these columns (Klingsh, 1975; Schleich, 1984). It was shown that as a consequence of the earlier heating of the reinforcing bars in comparison with the steel section, increase in the percentage of reinforcement in order to improve the load bearing capacity at normal temperatures might cause early failure of columns at elevated temperatures.

If the influence of the steel section prevails, the load bearing capacity is improved under fire conditions because of the considerably slower heating of the inner section. On the other hand, an increase in the flange cover increases the insulation and prolongs the time to failure. However, the increase in the profile cover means an increase in the load bearing share of concrete which is unfavourable. In general, with equal loading and equal failure time, the outer dimensions of the cross section can be considerably reduced if the reinforced concrete part is reduced and the steel profile becomes the predominant component of the cross section.

The partially encased section, shown in Figure 2.8, was introduced by 'ARBED' research centre in Luxembourg (Schleich, 1984). Although the outer faces of the steel flanges are visible and directly exposed to fire, it still offers very good fire resistant qualities in comparison with bare steel columns. This has been proven by recent experimental and analytical studies (Schleich et al, 1982; Shleich, 1988). The load bearing capacity of such columns at elevated temperatures can be estimated using a practical simplified method, where the section is analysed with a reduction in dimensions, as shown in Figure 2.9, depending on the exposure time. This implies that even if no fire retardants were applied to the external faces of the flanges, the reduced section can be designed to carry the static loads in case of fire. The full section, however, is utilized to resist other accidental loads such as wind or earthquake forces.

2.7 COMMENTARY

The above review has demonstrated the favourable behaviour of encased composite columns, mainly from Japanese research work, under repeated loading. Important parameters governing this behaviour were identified. Nevertheless, it was shown (Elghazouli, 1988) that although the forms of encased members and connections used in Japan were reliable for earthquake-resistance, they have clear deficiencies from constructional and economical viewpoints. In this respect, partially encased members offer advantages such as use of conventional steel beam-to-column connections, reduced or omitted shuttering and high impact resistance. Moreover, this type was shown to exhibit good fire resistant qualities.

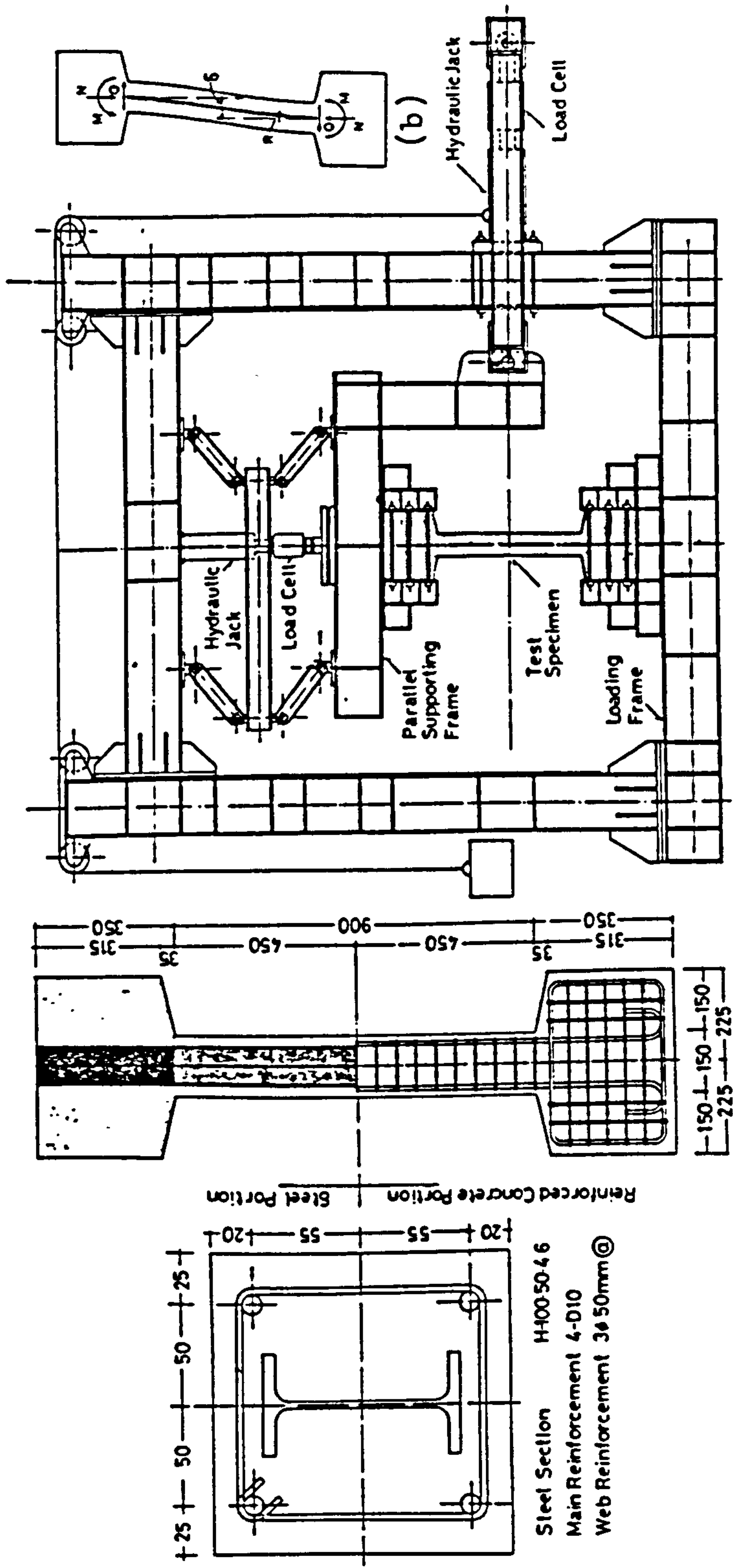


Fig. 2.1 Test set-up and specimen details (Wakabayashi and Minami, 1980)

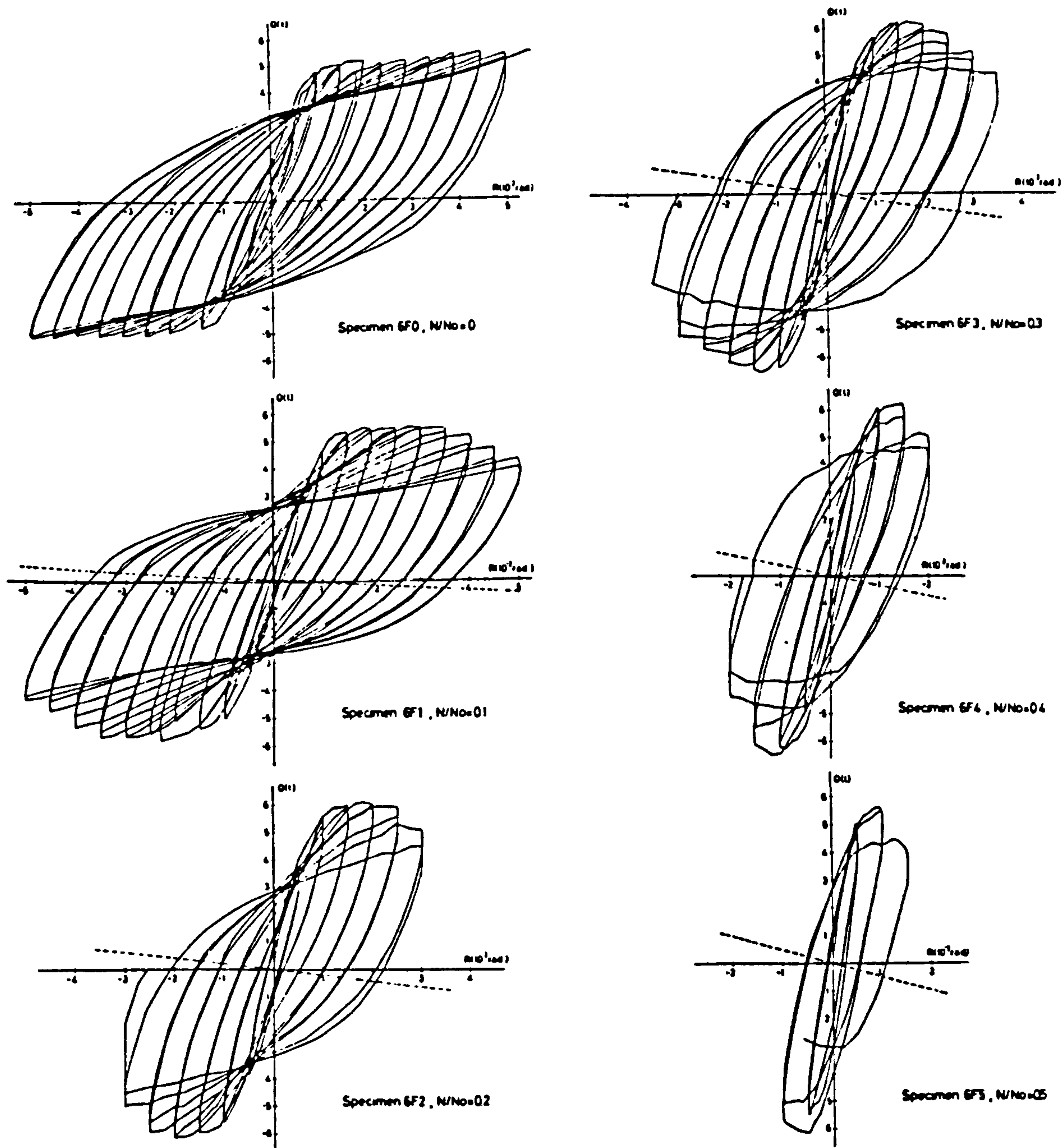
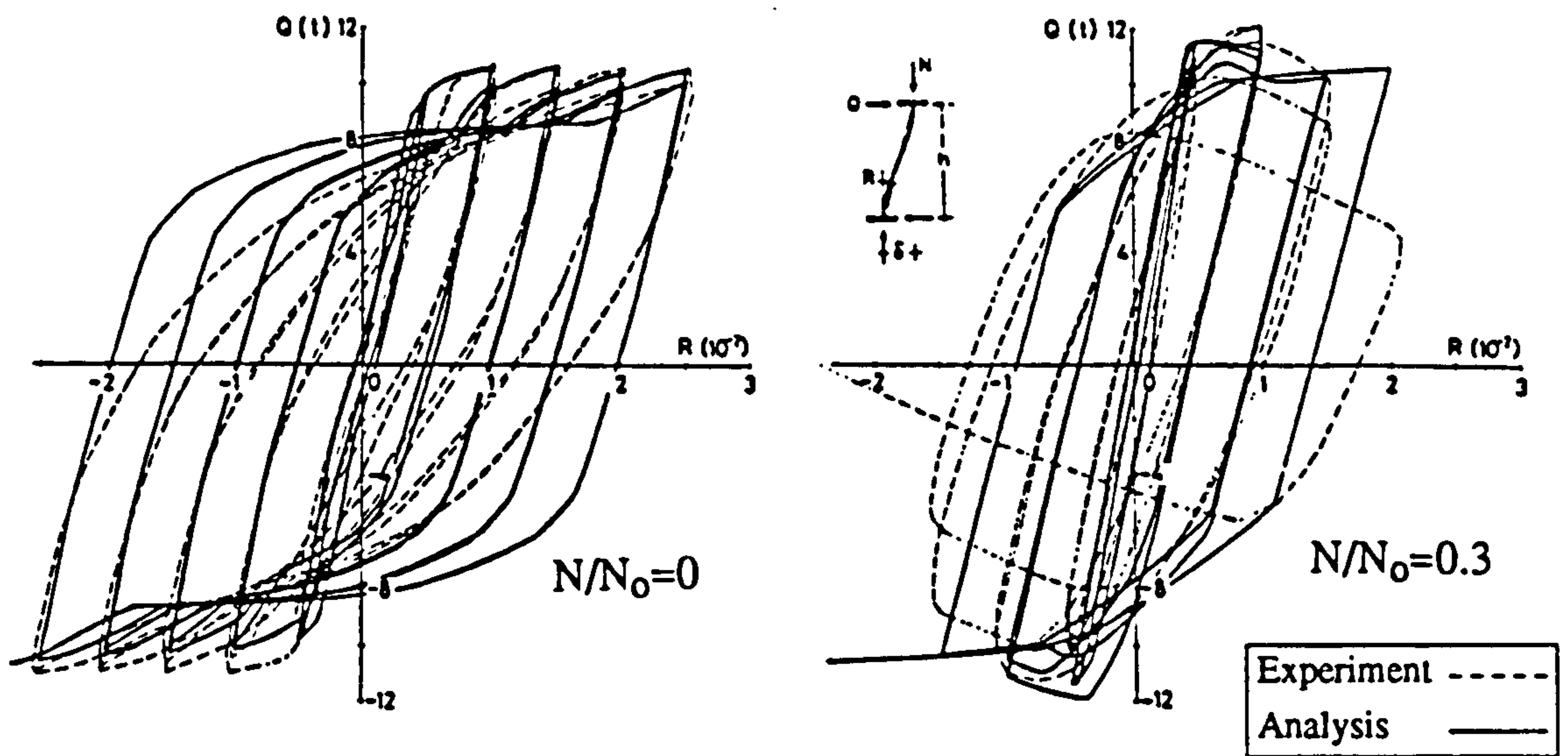
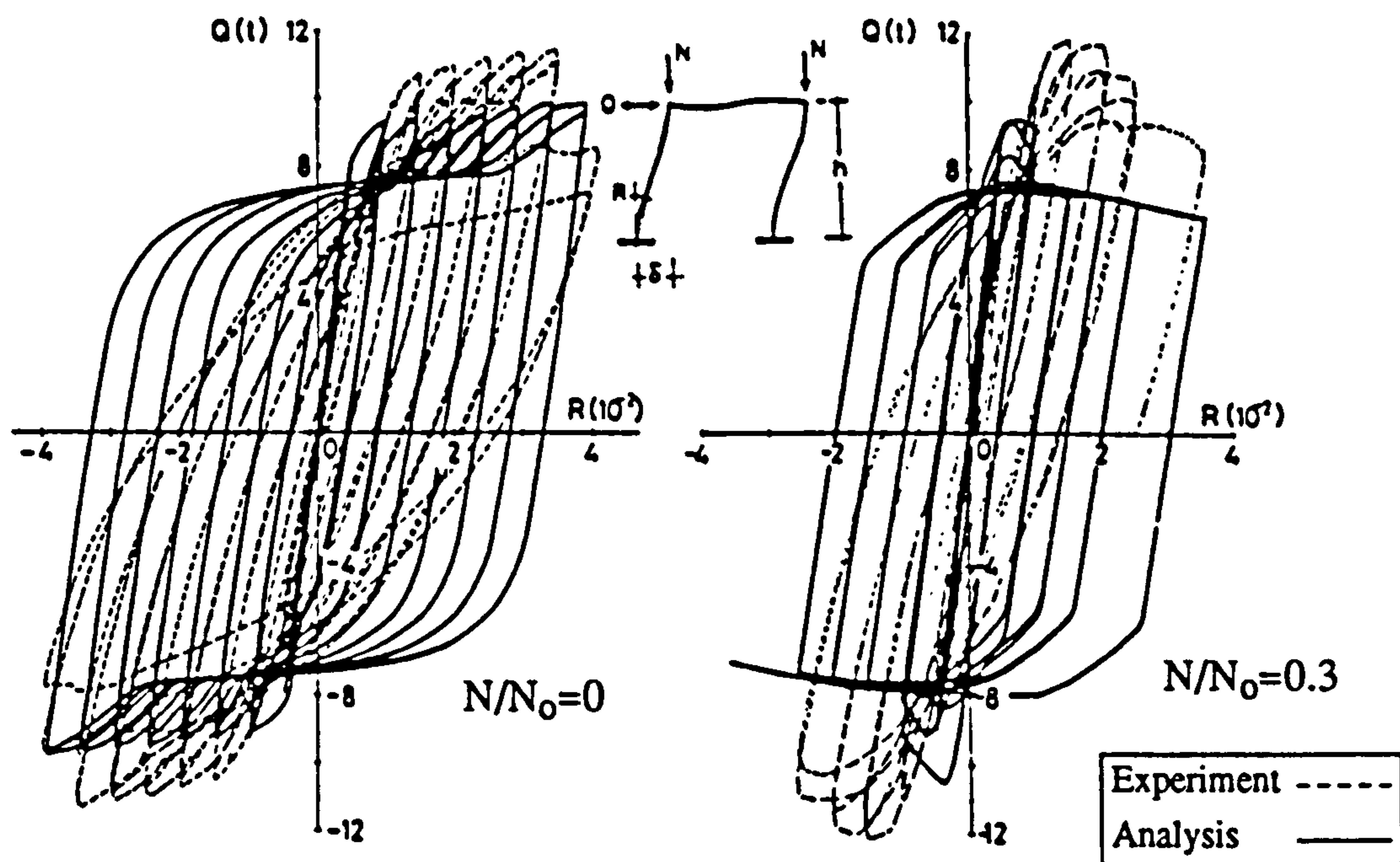


Fig. 2.2 Load-deflection relationships under different values of compressive axial loads (Wakabayashi and Minami, 1980)



Load-deflection curves of composite members



Load-deflection curves of composite frames

Fig. 2.3

Comparison of analytical and experimental results
(Wakabayashi et al, 1974)

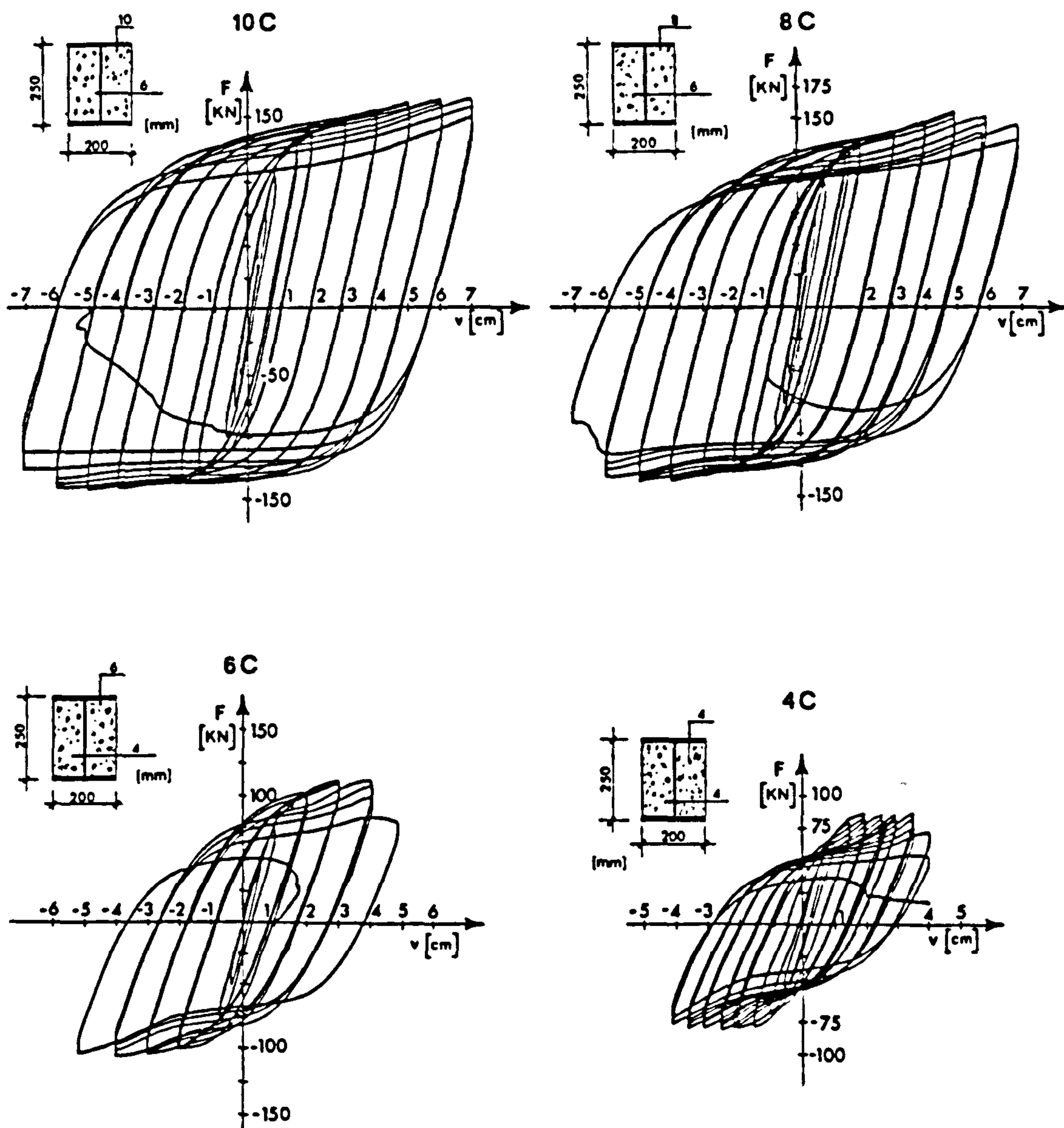


Fig. 2.4 Experimental load-deflection relationships of composite members (Ballio et al, 1987)

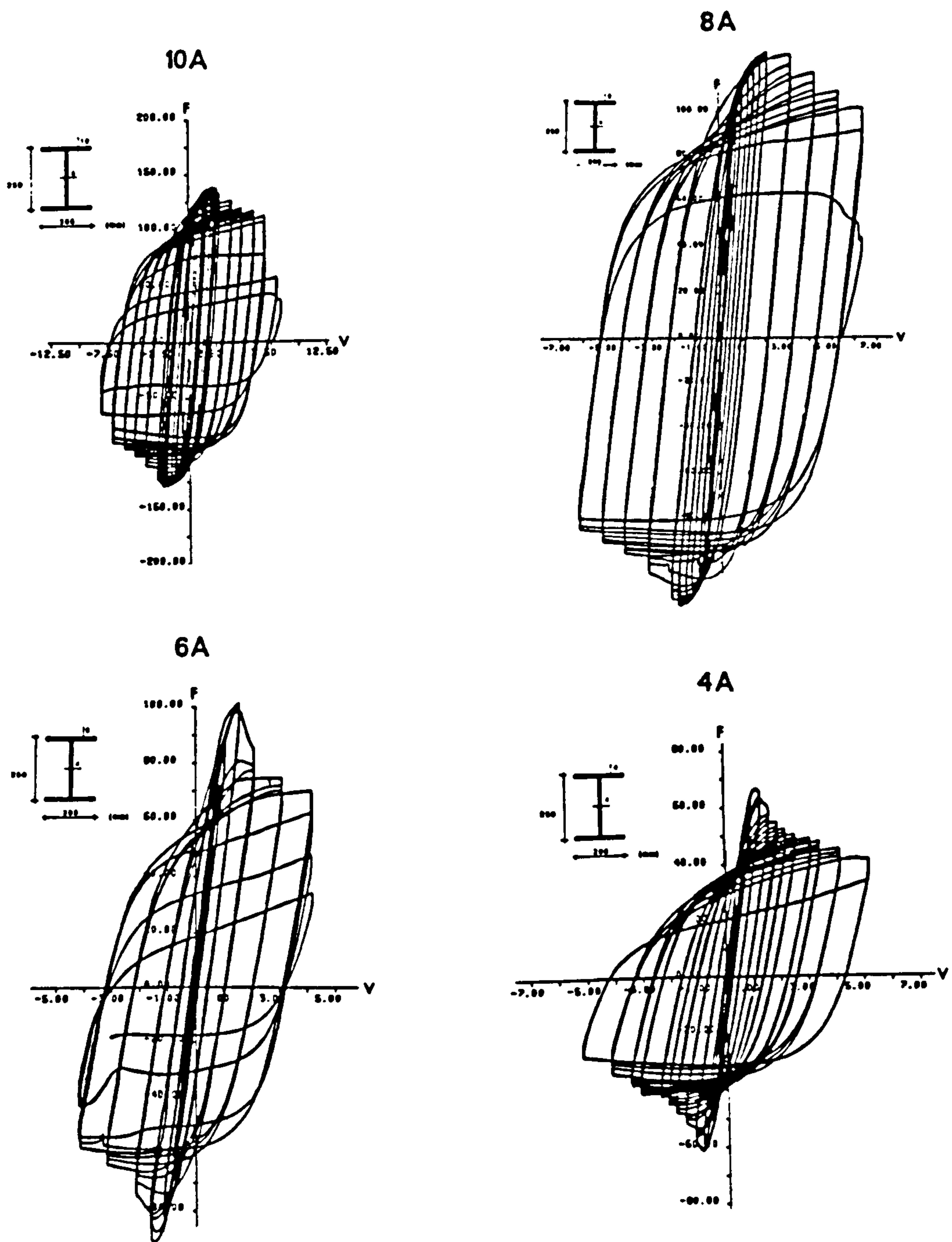


Fig. 2.5 Experimental load-deflection relationships of bare steel members (Ballio et al, 1987)

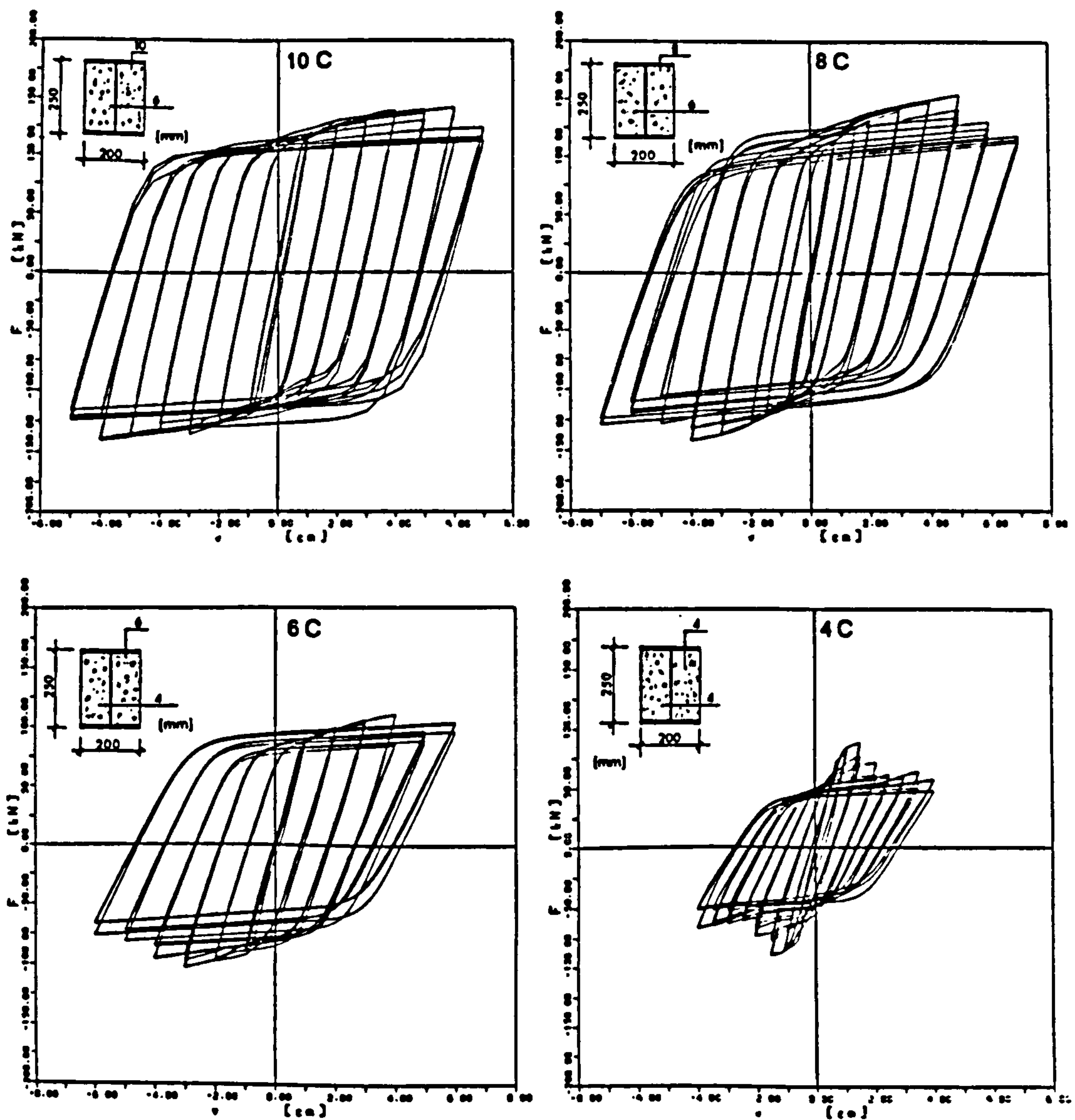


Fig. 2.6 Analytical load-deflection relationships of composite members (Ballio et al, 1987)

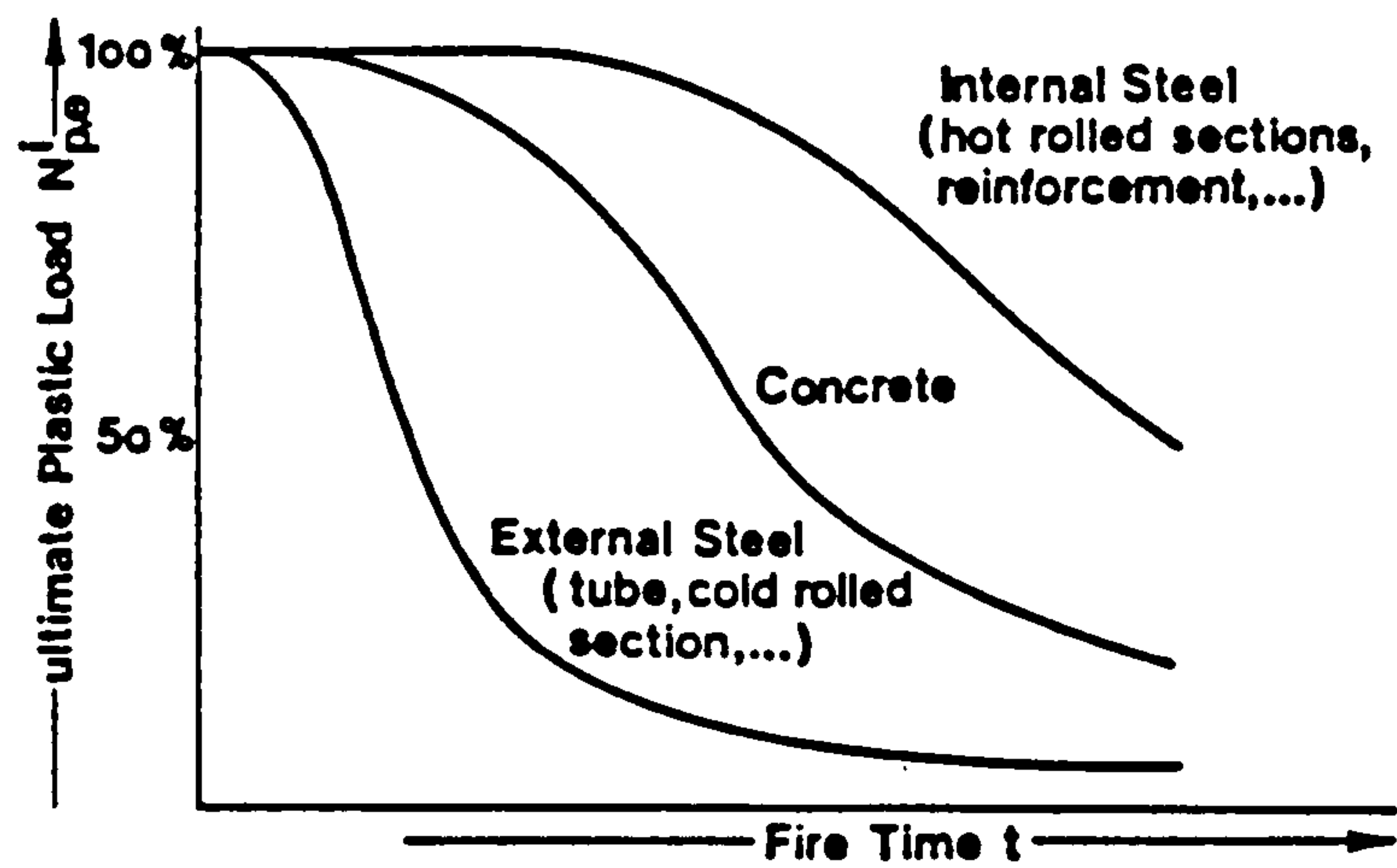


Fig. 2.7 Ultimate plastic load of the of cross-section components as a function of fire time (Schleich, 1984)

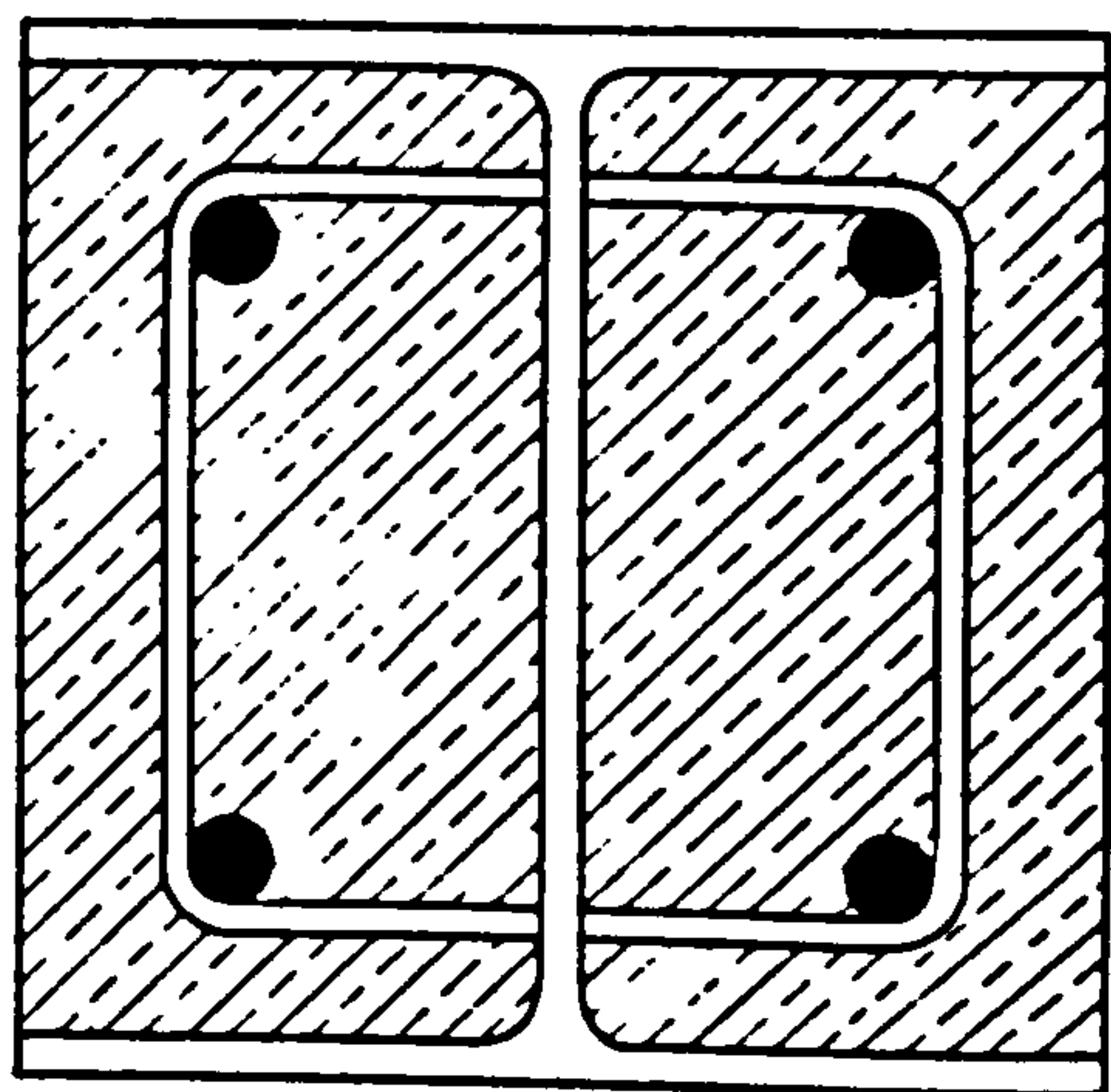


Fig. 2.8 Partially-encased composite section (Schleich et al, 1982)

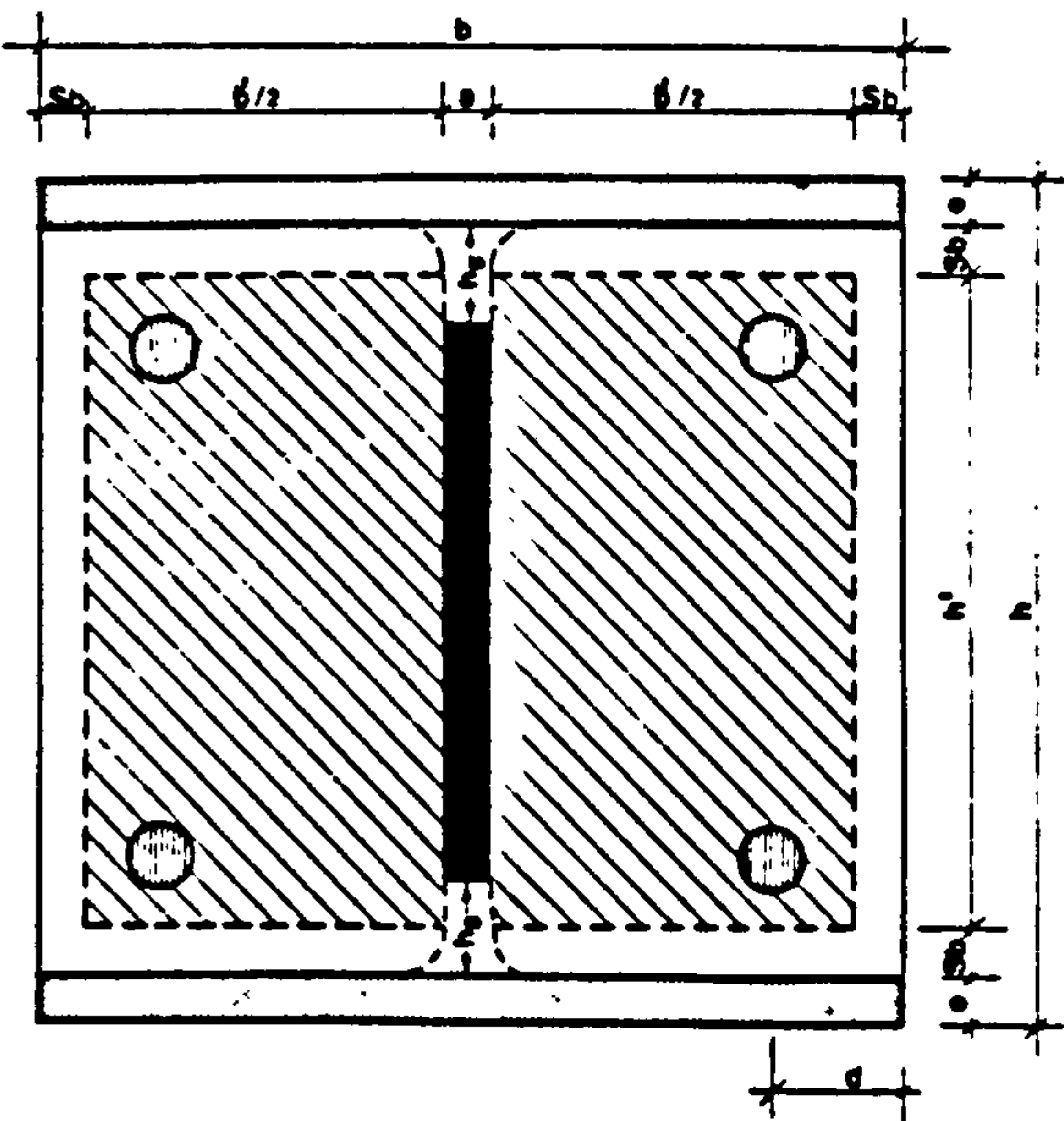


Fig. 2.9 Reduced composite cross-section (Schleich et al, 1982)

CHAPTER 3

3. ASSESSMENT OF DESIGN GUIDANCE FOR COMPOSITE BEAM-COLUMNS

3.1 INTRODUCTION

Different methods for the design of composite columns exist in codes of practice. A composite column may be treated in some methods as a steel column strengthened by concrete, whereas other methods may consider it as a reinforced concrete column with special reinforcement. Furthermore, the strength of a column may be evaluated as the sum of strengths of both components.

Existing code differences can be attributed to two main reasons: difference in design philosophy, and/or numerical quantification. Whereas the former covers fundamental considerations, such as stress distribution and slenderness, the latter is a consequence of the use of a specific experimental data base to arrive at actual design expressions. Even when two codes use the same philosophy and the same experimental results, some discrepancies are to be expected in estimating the final section properties for a given load, or the capacity of a pre-defined section. This may be due to the differences in safety factors, allowable material properties, limiting dimensions, consideration of long-term loading, etc. It is therefore not surprising that various codes would yield a wide range of designs for the same conditions.

Besides, for composite columns subjected to cyclic and earthquake loading, most codes are either silent on the matter or provide general recommendations for structural members without particular consideration to composite columns. This is also the case in Eurocode 8 (EC8, 1988), that has been recently drafted to cover the design of all types of structures in seismic regions. Earthquake-resistant structures are classified by the code into non-dissipative and dissipative. For non-dissipative structures, the design is based on elastic analysis without taking the nonlinear material behaviour or ductility into account. On the other hand, for dissipative structures, the deformation capacity is considered by scaling down the elastic design response spectrum by a behaviour factor 'q'. This factor depends only on the structural system according to the anticipated ductility. Apart from the uncertainties related to this factor, the same values for steel

structures have been proposed for composite structures. This proposal ignores the more favourable behaviour of composite members, mainly due to inadequate investigations. Furthermore, the code does not provide design guidance for composite columns, and the reader is referred to either steel and reinforced concrete column design, or to Eurocode 4. In other words, the earthquake engineer has the choice between either designing composite columns according to EC4, without due consideration for dynamic behaviour, or to use earthquake-resistant regulations for steel or concrete members.

In this chapter, the current state of design code provisions for composite steel/concrete columns from several countries is reviewed, with a view to arriving at unified design procedures under static loading conditions that would form a viable basis for earthquake-resistant design studies. A general comparison of code recommendations in terms of design basis, slenderness considerations, material properties and dimensional limitations is first presented, and the main differences are highlighted. This is followed by a quantitative assessment of capacity calculation for a specific cross-section under axial loading and flexure.

3.2 DESIGN CODES, A BRIEF DESCRIPTION

3.2.1 AIJ STANDARDS (Architectural Institute of Japan)

Composite construction, termed steel reinforced concrete (SRC) in Japan is in common use. This is attributed to its superior earthquake-resistant behaviour compared to reinforced concrete structures. Hence, extensive research has been undertaken by Japanese researchers during this century. Concrete-encased steel columns are frequently used for medium- to high-rise buildings. Concrete filled steel tubes are used for columns of subway stations and also in buildings.

The design is based on the allowable stress method. However, the ultimate strength of the member has to be evaluated for earthquake resistance (Wakabayashi, 1989). The cross-sectional strength is calculated by superimposing the strength of both the steel and reinforced concrete components. Full plastic distribution is used with a reduction factor in the concrete strength to account for the strain limit in concrete. This factor is assigned a different value for filled sections, where the concrete strength is enhanced by triaxial confinement. The method is applicable to asymmetrical sections and columns under biaxial bending.

As framed columns are usually stocky, because of the design for large lateral forces under earthquake loading, less attention has been given to slender columns. Beam-columns are similarly designed by the superposition of steel and reinforced concrete beam-columns. The Euler buckling load is used with a reduced concrete stiffness and factors of safety for both materials. Moment magnifiers are used for slenderness consideration in the reinforced concrete portion. The code also specifies minimum axial load eccentricities.

To achieve sufficient ductility, flexural failure should precede shear failure in a member. Moreover, the axial compression force and the width/thickness ratios of steel sections are limited to specified values. On the other hand, loads are transferred between steel and concrete by bond. If the bond strength is insufficient, direct bearing is used.

3.2.2 BS 5400 Part 5 (British Standards Institution)

Code provisions in BS 5400 (1979) are based on limit state design including loading factors and partial safety factors for materials. The ultimate moment is calculated from plastic stress distribution over the cross-section, and an approximation for the interaction curve for axial load and moment is used. Reduced concrete properties are used to account for the effects of creep and the use of uncracked concrete section in stiffness calculation. Minimum eccentricities due to construction tolerances are considered. In case of filled columns, an enhanced concrete strength due to triaxial confinement may be taken into account.

Slenderness effects are accounted for by the use of a non-dimensional slenderness parameter and the European buckling curves used for the design of steel columns. The choice of the appropriate curve depends on the geometry of the cross-section. The different curves reflect the effect of residual stresses and initial imperfections in the member. The uncracked concrete section is used in stiffness calculation. The use of the slenderness parameter is consistent with the design of steel columns since the method reduces to the bare steel column design when the concrete portion is removed. Consequently, the method is applicable to symmetric sections only, and is restricted to the range of sections catered for in the European buckling curves. For uniaxial bending, distinction is made for the presence, or lack of restraint in the direction orthogonal to the bending axis. Expressions are given for biaxial bending for filled circular hollow sections as well as encased sections.

3.2.3 ACI-318-83 (American Concrete Institute)

The building code of the American Concrete Institute uses the limit state design format with loading factors and capacity reduction factors (ACI-318-83, 1983). The strength of a composite column is computed as for reinforced concrete members. Failure is defined in terms of a 0.3% strain limit for any concrete fibre. This failure strain is used with a set of neutral axis locations to arrive at an interaction curve for thrust and moment. Slenderness effects are analysed in terms of moment magnifiers using a reduced Euler load. The expression for equivalent stiffness includes a creep factor and a cracked concrete stiffness is considered. Minimum eccentricities are specified to cover construction tolerances.

3.2.4 AISC-LRFD-1986 (American Institute of Steel Construction)

The Load and Resistance Factor Design (AISC-LRFD, 1986) also uses the limit state design with loading factors and capacity reduction factors. The design of composite columns is based on the design equations for steel columns. However, the slenderness and area parameters are modified for the presence of concrete. The code uses a simple interaction formula for uniaxial and biaxial bending and recognizes the confinement effect in filled columns. Moment magnifiers are specified to account for slenderness effects except for the case of axial loading only where a steel buckling curve is used, as no minimum eccentricities are specified. Load transfer should be provided by direct bearing at the connections.

3.2.5 Eurocode 4 and DIN 18806

Eurocode 4 (EC4, 1984) was drafted to cover the design of composite steel and concrete structures. Limit State design is applied with partial safety factors for materials. Three methods of design are available in the EC4 draft. The first two methods are derived from the West German practice, DIN 18806 (Roik and Bergmann, 1989), where slenderness effects are analyzed in term of bending moments as in reinforced concrete design. However, as opposed to moment magnification, an equivalent strength reduction is derived using the European Steel Buckling Curves in conjunction with the cross-sectional interaction curve. Full plastic distribution is used to obtain the axial to flexural strength interaction curve, whereas a simplified polygonal approximation is introduced in the second method. The third method is derived from the method in BS 5400 which is essentially a modified steel column design.

3.2.6 Australian and East European Standards (unpublished)

The Australian code provisions do not include design of composite columns. However, proposals for draft code provisions have been discussed (Bridge et al, 1987), where a limit state philosophy is adopted. Two methods are proposed; one relates to reinforced concrete column design, and the other is akin to steel codes, namely moment magnifier and strength reduction. Specifications in East Europe are currently under consideration (Lapos and Streleckij, 1989), where plastic design approach is allowed.

3.3 CODE DIFFERENCES

3.3.1 Design Basis

3.3.1.1 Origin of Method

This is largely dictated by whether steel designers were considering composite construction as an improvement over bare steel design, or concrete designers were attempting to achieve higher strength and confinement. In the former case, steel buckling curves were used, while in the latter reinforced concrete design methods were adopted.

The modified steel design methods are used in AISC-LRFD and BS 5400, both explicitly reducing to the bare steel section. The American Concrete Institute makes use of reinforced concrete column design, whereas EC4 and DIN use a combination of both approaches. Distinctly, the Japanese Code (AIJ) uses a superposition of the individually calculated capacities.

3.3.1.2 Loading and Resistance

Various codes use significantly different loading factors and combinations. On the other hand, capacity reduction is achieved through one of two approaches. Whereas the American codes (ACI and AISC) use capacity reduction factors ϕ_s (of 0.7 and 0.85 respectively), the European practice is to use partial safety factors on materials. Different values for the partial safety factor are given for concrete, steel and reinforcing bars (typically 1.5, 1.0-1.1 and 1.15, respectively).

In contrast to the above limit state-based codes, the Japanese code (AIJ) uses the allowable stress approach. However, owing to the severe earthquake loading in Japan, the ultimate strength has to be verified.

3.3.2 Concrete Strength

Table 3.1 gives a brief comparison of recommended values for concrete compressive strength.

TABLE 3.1
Specifications for Concrete Compressive Strength

| Code | Encased | Filled |
|---|---|--|
| AIJ (allowable strength) (ultimate strength) | $f_{cyl}(1-15_{spc})$ $f_{cyl} (0.85-2.5_{spc})$ | f_{cyl} $0.85 f_{cyl}$ |
| BS 5400 (axial compression) (bending) | $0.675 f_{cu}$ $0.6 f_{cu}$ | $0.675 f_{cu}(C_1)$ $0.6 f_{cu}(C_1)$ |
| EC4 | $0.85 f_{cyl}$ | $0.85 f_{cyl}(C_2)$ |
| DIN 18806 | $0.60 f_{cu}$ | $0.70 f_{cu}(C_3)$ |
| ACI 318-83 | $0.85 f_{cyl}$ | $0.85 f_{cyl}$ |
| AISC-LRFD | $0.60 f_{cyl}$ | $0.85 f_{cyl}$ |

It is noteworthy that some codes use cube while others use cylinder strength. Furthermore, there is some controversy on the effect of confinement on the crushing strength. For an assumed ratio of f_{cu}/f_{cyl} of 1.2, the range of compressive strength (normalized by f_{cyl}) is between 0.7 and 1.0, for unconfined concrete.

3.3.3 Interaction Curves

Discrepancies observed for minor and major axis bending interaction curves are discussed in detail in Section 3.4, and shown in Figures 3.3 to 3.12. Table 3.2, however, gives a general comparison.

TABLE 3.2
Basis of Interaction Diagrams

| Code | Specifications | |
|------------|--|---|
| AIJ | Plastic distribution (PD) | Reduced f_{cy1} |
| BS 5400 | PD for M_{ult} | Approximate surface |
| EC4, DIN | Full PD | Reduced moment capacity Simplified surface in method B |
| ACI 318-83 | Equilibrium and compatibility of strains | 0.3% concrete strain limit |
| AISC-LRFD | PD for M_{ult} | Approximate surface |

For members subjected to combined compression and biaxial bending, the design is based on different interaction formulae. In EC4 and DIN, the moment capacities of the two main axes are calculated separately and used to plot a linear interaction, and the imperfections have to be considered only for the more critical axis. BS 5400 uses a different interaction formula. Approximate methods are also given in ACI and AISC, and AIJ extends the superimposed strength methods to deal with biaxial bending.

As discussed in Section 3.4 below, there are large variations in capacity under combined axial loading and bending, depending on the code used. The comparison given hereafter does not consider biaxial bending cases, for which the differences are expected to be even larger.

3.3.4 Equivalent Stiffness

For slenderness considerations and deflection calculations, the equivalent stiffness (EI) is required. Various codes use different approaches to arrive at a value of modulus of elasticity for concrete (E_c) which takes account, directly or indirectly, of the cracked stiffness and creep. The recommended E_c values for the codes considered herein are presented in Table 3.3.

TABLE 3.3
Modulus of Elasticity of Concrete

| Code | E_c | Comments |
|-----------|---|--|
| BS 5400 | $450F_{cu}$ | Low, to account for use of uncracked section and creep |
| EC4 | $600F_{cyl}$ (to be multiplied by a creep factor) | Same as above, but creep accounted for in expression |
| ACI | $57,000(f_{cyl})^{1/2}$ in psi | Higher, as a cracked section is used, with a creep factor |
| AISC-LRFD | $w^{1.5}(f_{cyl})^{1/2}$ | High as a cracked section is used (w=unit weight of concrete in lb/ft ³ and f_{cyl} in ksi) |

The expression for the equivalent (EI) may or may not use a creep coefficient, depending on the code.

3.3.5 Slenderness Considerations

The effect of slenderness is accounted for in one of two ways, strength reduction or moment magnification.

TABLE 3.4
Slenderness Considerations

| Code | Specifications | |
|-------------------|---|--|
| AIJ | Strength reduction | $R_s=(1-v_sP/P_E)$ where v_s =factor of safety |
| BS 5400, DIN, EC4 | Strength reduction | European steel buckling curves |
| ACI 318-83 | Moment magnification Minimum eccentricity | $\delta_m=C_m/(1-P/\phi_sP_E)$ |
| AISC-LRFD | Moment magnification for compression and bending Critical load for axial compression | $\delta_m=C_m/(1-P/\phi_sP_E)$ $r_{comp}=r_{steel}$ (not less than 0.3 of depth) |

European codes (BS 5400, DIN and EC4) use a strength reduction, so does the AIJ code. Alternatively, ACI uses a moment magnification factor as well as the definition of a minimum eccentricity, as discussed below. The AISC recommendations use a moment magnifier for bending with axial load, and a critical load for pure compression, with no minimum eccentricity. Table 3.4 gives a comparison of the specifications.

3.3.6 Minimum Eccentricities

Recommended values of minimum eccentricity are given in Table 3.5.

TABLE 3.5
Minimum Eccentricities

| Code | Minimum Eccentricity | |
|------------|------------------------------|---|
| AIJ | $5\%D_c$ | (for the concrete portion design) |
| BS 5400 | $3\%B_c$ | (in bridges, would be 4% in buildings) (axial load limited to 85% of the short column minor axis capacity) |
| EC4 | None | (in methods A and B, 4% in method C) |
| DIN 18806 | None | |
| ACI 318-83 | $(0.6+0.03D_c)$ in inches | (axial load limited to 85% of the plastic capacity) |
| AISC-LRFD | None | |

It is noteworthy that limiting the axial capacity to a percentage of the flexural plastic capacity imposes a further limitation on the minimum eccentricity. Hence, values quoted above may not be strictly comparable in some cases.

3.3.7 Shear Transfer

All codes assume full interaction between steel and concrete, but some impose restrictions on the shear stress at the steel/concrete interface. It is customary to use direct bearing, or provide shear connectors, if and where the specified limiting shear stress is exceeded. Table 3.6 lists the various approaches and values adopted by design codes. Furthermore, design of shear connectors, if required, is given in detail in most codes.

TABLE 3.6
Specifications for Shear Transfer

| Code | Specifications |
|--------------|---|
| AIJ | Detailed design for encased sections Direct bearing for filled sections if bond is insufficient |
| BS 5400, EC4 | Connectors provided if $\tau_s > 0.6 \text{ N/mm}^2$ for encased or 0.4 N/mm^2 for filled |
| DIN 18806 | Connectors provided if $\tau_s > 0.55$ to 0.80 N/mm^2 for encased, reduced by 30% for filled (for $f_{cu} = 25$ to 55 N/mm^2) |
| ACI 318-83 | Direct bearing at connections Concrete strength for bearing = $1.7(0.7^a)(f_{cyl})$ |
| AISC-LRFD | Direct bearing at connections Concrete strength for bearing = $1.7(0.6^a)(f_{cyl})$ |

^a *Capacity reduction factor (resistance factor) for bearing*

3.3.8 Material Properties

Limits on the extreme values of concrete crushing and steel yield strength are given in most codes, as shown in Table 3.7. Lower bound limits for concrete strength are considered to eliminate concrete of unreliable quality. The upper limits for steel yield stress are considered to ensure that concrete remains stable until steel reaches yield. If these limits are not satisfied, the concept of adding the axial capacities of both components might be invalidated. In this case, a modification in existing code regulations must be considered before new forms of high strength steel are confidently used in composite columns, as discussed later in Chapter 8.

TABLE 3.7
Limits on Material Properties

| Code | Concrete strength (N/mm ²) | Steel yield (N/mm ²) |
|------------|---|--|
| AIJ | $f_{cyl} \geq 15$ $f_{cyl} \geq 18$ (with re-bars) | $\sigma_y \leq 360$ (for $t_p < 40\text{mm}$) $\sigma_y \leq 340$ (for $t_p > 40\text{mm}$) |
| BS 5400 | $f_{cu} \geq 20$ (for encased) $f_{cu} \geq 25$ (for filled) | |
| EC4 | $f_{cyl} \geq 20$ | $f_y \leq 450$ (350 in method C) |
| DIN 18806 | $f_{cu} \geq 25$ | |
| ACI 318-83 | $f_{cyl} \geq 17$ | $\sigma_y \leq 330$ |
| AISC-LRFD | $20 \leq f_{cyl} \leq 50$ | $\sigma_y \leq 365$ |

3.3.9 Dimensional Limitations

3.3.9.1 Steel wall thickness

Expressions given for steel wall thickness, shown in Table 3.8, reduce to the same values in North American and Western European codes. However, only EC4 and DIN include values for partially encased sections. On the other hand, AIJ is the only code that considers limits for fully encased sections due to the design for severe earthquake loads.

3.3.9.2 Steel and concrete contributions

Limits on concrete contribution to the plastic axial capacity are included in Western European codes. North American and Japanese codes define direct limitations on the steel or concrete area. These differences are summarized in Table 3.9.

3.3.9.3 Slenderness and section dimensions

Limits on slenderness, which correspond to the range of available experimental data, are included in some codes as shown in Table 3.10.

TABLE 3.8
Steel Wall Thickness

| Code | Specifications |
|--------------------------------------|---|
| AIJ | $t/D_s \geq ((\sigma_y)^{1/2}/240)/1.5$ for circular hollow sections of outer diameter D_s $t/D_s \geq ((\sigma_y)^{1/2}/74)/1.5$ for rectangular sections of outer dimension D_s $t/b_f \geq ((\sigma_y)^{1/2}/24)/1.5$ for flanges of encased sections, of overall breadth b_f $t/d_w \geq ((\sigma_y)^{1/2}/74)/2.0$ for webs of encased sections, of depth d_w σ_y in t/cm^2 |
| BS 5400, ACI 318-83, AISC-LRFD | $t \geq D_s(\sigma_y/8E_s)^{1/2}$ for circular hollow sections of outer diameter D_s $t \geq D_s(\sigma_y/3E_s)^{1/2}$ for rectangular sections of outer dimension D_s |
| DIN 18806 | $D_s/t \leq 51$ (St 37) 42 (St 52) for rectangular hollow sections of greater overall dimension D_s $D_s/t \leq 84$ (St 37) 68 (St 52) for circular hollow sections of greater overall dimension D_s $b_f/t_f \leq 44$ (St 37) 36 (St 52) for partially encased I-sections , where t_f and b_f are the thickness and overall breadth of flange |
| EC4 | $D_s/t \leq 52\varepsilon$ for rectangular hollow sections of greater overall dimension D_s $D_s/t \leq 85\varepsilon$ for circular hollow sections of greater overall dimension D_s $b_f/t_f \leq 44\varepsilon$ for partially encased I-sections , where t_f and b_f are the thickness and overall breadth of flange $\varepsilon = (235/\sigma_y)^{1/2}$ (σ_y in N/mm^2) |

TABLE 3.9
Steel and Concrete Contributions

| Code | Specifications | |
|-----------|---|--|
| AIJ | $A_s/A_g \geq 0.8\%$ | |
| BS 5400 | $0.15 < \rho_c < 0.80$ (for encased) $0.10 < \rho_c < 0.80$ (for filled) | $(\rho_c = N_{pc}/N_p)$ |
| DIN 18806 | $0.20 < \rho_s < 0.90$ | $(\rho_s = N_{ps}/N_p)$ $(\rho_s = 1 - \rho_c$ if reinforcement is disregarded) |
| ACI | $A_r/A_c \geq 3\%$ $A_r/A_c \leq 0.08$ (for filled) $0.01 \leq A_r/A_g \leq 0.08$ (for encased) | |
| AISC-LRFD | $A_s/A_g \geq 0.04$ | |

TABLE 3.10
Slenderness Ranges

| Code | Specifications |
|----------|--|
| BS 5400 | $L_e/B_c \leq 30$ (encased) $L_e/B_c \leq 55$ (circular filled) $L_e/B_c \leq 60$ (rectangular filled) |
| EC4, DIN | $\lambda_s \leq 2.0$ (comparable to BS 5400) |

3.3.9.4 Reinforcement Details

For practical considerations and for insuring sufficient concrete confinement, several codes include limitations on detailing of reinforcement bars in encased columns as shown in Table 3.11.

TABLE 3.11
Reinforcement Detailing

| Code | Specifications |
|------------|--|
| BS 5400 | Stirrups spacing ≤ 200 mm, with 4 corner longitudinal bars Cover to surface of steel shape ≥ 50 mm |
| ACI 318-83 | Stirrups spacing $\leq B_c/2$ ≤ 16 Longitudinal bar diameter ≤ 48 stirrup diameter Stirrup diameter $\geq B_c/50$ |
| AISC-LRFD | Stirrups spacing $\leq 2B_c/3$ Stirrup area ≥ 0.007 of the spacing in inches (similar to ACI in the practical range of columns) |

3.4 COMPARATIVE RESISTANCES

3.4.1 General

Comparison between the resistances given by the methods in Eurocode 4 and the British Standard BS 5400 (Smith and Johnson, 1986) was extended to cover the two North American codes AISC-LRFD-1986 and ACI 318-83. The Japanese standard was not included as the method is based on allowable stress design and hence would give resistances that cannot be compared directly, unless loading factors were considered. Only method A of EC4 was included in the comparison, as method B is an approximation for A, and method C is a simplification of the method in BS 5400. Dedicated computer programs were developed for each code to obtain accurate evaluation of the capacities.

The cross-section considered is an Encased Universal Column 356 x 368 x 129 with h_s/h_c and b_s/b_c ratios of 0.74 and 0.75, respectively. A comparison using a partially-encased section was not possible as this type is explicitly considered in one code only. A pin-ended column, with a range of slenderness from zero to 30 is covered. The slenderness is represented in terms of equivalent length divided by relevant section dimension, as each code would yield a different value for the radius of gyration of the composite section. The steel is of 340 N/mm² yield strength and the casing is of Grade 35 cylinder strength. For the bridge code BS 5400, the partial safety factor for steel and

the minimum eccentricity were modified to 1.0 and 0.04, respectively. These modifications would be required to use the code for building design. The Grade 35 cylinder strength was assumed equivalent to Grade 40 cube strength in lieu of ISO 3893 recommendations. For the methods of ACI 318-83 and EC4 the maximum live load was assumed equal to the maximum dead load in the calculation of the effective stiffness. The value of modulus of elasticity for concrete was estimated in accordance with the requirements given in each code. For the methods of ACI and AISC the moment magnification required for slenderness considerations was equivalently included as a reduction in the moment capacity.

In Figures 3.1 to 3.12, the resistances given by the different methods are shown with the values of N_p and M_p calculated according to EC4. The loading factors were not included in the comparison because of the different load combinations given in each code, and only the factors on the resistance side were considered.

In the following quantitative comparison, the code is interpreted from the latest available version, as would be the case in design office practice. The possibility of inadvertently misinterpreting certain clauses exists. However, this may highlight an inherent ambiguity in the code presentation. Finally, numbers appearing in parentheses indicate the clause number in the code under consideration.

3.4.2 Equivalent Stiffness

As mentioned in Section 3.3.4, above, the equivalent stiffness of the composite section is required mainly for slenderness considerations and also in deflection calculations. Table 3.12 gives a comparison of the values for concrete modulus of elasticity and equivalent stiffness (EI) for the section under consideration, as calculated from each code. The values presented are normalized to that of EC4.

The stiffness estimated by the two North American codes is much lower than that calculated from the Western European codes as a cracked concrete section is considered. This is not adequately compensated by the lower E_c used in EC4 and BS 5400. The difference is more pronounced in the minor axis direction where the concrete has a higher contribution to the total stiffness.

TABLE 3.12
Comparison of Normalized Equivalent Stiffness

| Code | E_c | Equivalent (EI) Major axis | Equivalent (EI) Minor Axis | Comments |
|------------|-------|-------------------------------|-------------------------------|--|
| EC4 | 1.00 | 1.00 | 1.00 | uncracked concrete section creep factor included in E_c |
| BS 5400 | 1.14 | 1.06 | 1.10 | uncracked concrete section no explicit creep factor (reduced E_c) |
| ACI | 1.79 | 0.68 | 0.43 | 1/5 of concrete stiffness creep factor included in (EI) |
| AISC | 1.60 | 0.71 | 0.52 | 1/5 of concrete stiffness no explicit creep factor (reduced f_{cy1}) |

All values are normalized to that of EC4

3.4.3 Comparison of Axial Capacities

3.4.3.1 Unfactored Axial Capacity

The unfactored axial capacities of the four methods are shown in Figure 3.1 normalized to that of EC4. Slenderness is represented in terms of the ratio of the pin-ended column length to the cross-sectional dimension in the direction of minor axis bending. The use of radius of gyration was avoided as its value is dissimilar in different codes.

For very low slenderness ratios, BS 5400 gives the lowest capacity, 19% less than EC4 and about 4% less than ACI and AISC. This is attributed to: (1) the reduced concrete strength of $0.6 f_{cu}$ (0.45 factored) (11.1.4) to take account of creep which is not included in the equivalent stiffness, and (2) the minimum eccentricity requirement for short columns calculated from the limitation on axial capacity (0.85 the minor axis axial capacity) (11.3.2.1). The ACI code gives values which are 15% less than EC4 as a result of the limitation of 0.85 of the axial plastic capacity, in accordance with the minimum eccentricity requirement (10.3.5.1). For AISC, the values are 16% less than EC4 because of the reduced concrete strength of $0.6 f_{cy1}$ in encased columns (I2.2).

For higher slenderness ratios, the difference between EC4 and BS 5400 is reduced because the value of equivalent stiffness is lower as it takes account of creep (4.8.6).

However, the minimum eccentricity requirement of 0.04 in BS 5400 causes a reduction in capacity in the range of slenderness used in practice. The capacities of ACI are in agreement with other codes, but decrease at high slenderness due to the following: (1) use of cracked section of concrete, (2) creep factor included in the expression for equivalent stiffness (10.14) and (3) the minimum eccentricity requirement accompanied by a moment magnification factor (10.11.15). Although the AISC code uses the radius of gyration of the steel section only, this is limited to 0.3 of the overall section dimension (I2.2), which is the governing case for the minor axis for the current example. At a slenderness of 30, the ACI code gives a capacity 48% less than AISC and about 41% less than EC4 and BS 5400.

3.4.3.2 Factored Axial Capacity

Figure 3.2 shows the axial capacities given by the different codes, including the capacity factors in ACI and AISC and the partial safety factors in EC4 and BS 5400. The values are normalized by that of the factored capacity of EC4. The same general observations are made as for the case of factored axial capacity, for all codes but ACI. This is a consequence of the equivalence of the partial safety factors used by EC4 and the resistance reduction factor used in AISC. In contrast, ACI curve drop substantially, as a consequence of the inclusion of a reduction factor of 0.7 (as opposed to 0.85 for AISC). This situation is aggravated for higher slenderness, admittedly above the practical limits, where the discrepancy between ACI and all the other codes is in the range of 65%.

3.4.4 Combined Flexure and Axial Compression

3.4.4.1 Unfactored Capacity

Figures 3.3 and 3.5 show the unfactored major and minor interaction curves for short columns. N_p and M_p are the plastic capacities calculated according to EC4.

ACI considers a full interaction curve calculated from conditions of equilibrium and compatibility of strains with a strain limit in concrete of 0.3%. On the other hand, in EC4 the resistance may be calculated from first principles using appropriate stress-strain curves. Alternatively, the Eurocode considers a full interaction curve but with full plastic distribution using rectangular stress blocks, which leads to an overestimate of the ultimate resistance. However, the moment capacity in EC4 is accompanied by a reduction to 90% of the moment capacity (4.8.8) to account for two assumptions: (1) use of

uncracked stiffness for concrete and (2) use of rectangular stress blocks without due consideration to concrete strain restrictions.

For major axis bending at zero axial force, EC4 converges to 0.9 instead of unity because of the above mentioned reduction in moment capacity (which overcompensates for the plastic distribution in this case). The capacities of BS 5400 and AISC are almost the same (about 98% of the plastic capacity of EC4) because both codes use plastic distribution for determining the pure bending capacity. In this case, the capacities of BS 5400 and AISC are similar to that given by ACI because in the major direction at this position of the neutral axis, most of the steel would have yielded, and hence, the plastic distribution does not significantly overestimate the strength. It is also obvious that the difference in concrete strength is not significant in pure bending in the major axis direction because the main contribution to the strength is due to the steel section.

Similarly, for minor axis bending at zero axial force, EC4 gives a value of 0.9, as a result of the reduction factor. However, other codes show slightly larger differences than in the major axis case, as the concrete strength and the use of plastic distribution assume a more prominent role, because of the geometry of the cross-section.

With regard to the shape of the interaction curve, EC4 is comparable to ACI by virtue of the 90% reduction, which compensates for the overestimation in strength. BS 5400 and AISC use approximate interaction curves which are very simple to construct but with some sacrifice of strength. In BS 5400 no account is taken of the increasing moment capacity at low axial loads because its availability depends on the loading history of the column. Owing to the use of simplified interaction curves, BS 5400 gives resistances 14% and 11% less than EC4 and ACI for major and minor axis bending, respectively. For AISC, this drop in strength is as high as 32% and 36%, respectively.

3.4.4.2 Factored Capacity

The factored resistances for major and minor axis bending were calculated for columns of slenderness zero, 12, 20 and 30. Figures 3.4, 3.7, 3.8 and 3.9 show the interaction curves for major axis bending at a slenderness of zero, 12, 20 and 30 respectively, and Figures 7.6, 7.10, 7.11 and 7.12 show the corresponding comparisons for minor axis bending. The moment magnification used in ACI and AISC was considered by an equivalent strength reduction.

At low levels of compression the resistance factor specified by ACI may be increased linearly to reach 0.9 at zero axial force (9.3.2.2). For AISC, when the axial force is less than 0.3 of the factored nominal axial capacity, the nominal flexural strength is determined by straight line transition between the nominal flexural strength evaluated from the plastic distribution on the composite cross section at 0.3 and the flexural strength at zero axial load (I4). This explains the two resistances that appear in the figures at low values of axial force for ACI and AISC. Comparison between the unfactored and factored resistances for major and minor axis at zero slenderness shows that the capacity factors are, in general, more conservative (especially the 0.7 factor given by ACI, as it is based on reinforced concrete design).

For major axis bending, at a slenderness of zero, EC4 and BS 5400 are generally in good agreement, where BS 5400 gives values within 5% difference. ACI and AISC give values up to 20% and 32%, respectively, less than EC4, except at low values of axial loads and at high axial loads where the minimum eccentricities affect the resistance. At slendernesses of 12 and 20 the methods of ACI and BS show a much better agreement but are about 25% less than EC4, whereas AISC generally gives resistances up to 36% less than EC4, except at very low and very high levels of compression. As the slenderness increases to 30, the resistances given by EC4 and BS are similar within a discrepancy of 10%, whereas ACI and AISC are about 33% less than EC4, except at extreme values of axial compression.

For minor axis bending at zero slenderness, BS, ACI and AISC are up to 9%, 18% and 33% less than EC4, except at extreme values of axial force. At slenderness of 12, ACI, BS and AISC show very good agreement except at extreme values of normal force, but are up to 24% less than EC4. At slendernesses of 20 and 30, the agreement between AISC and BS is still observed and the discrepancy with EC4 decreases to a maximum of about 12%. Also, ACI shows very low resistances of up to 40% less than EC4 at slenderness of 30, except at extreme values of axial forces where the discrepancy increases because of the minimum eccentricity requirement. This low resistance is due to the low value of stiffness, which is less than half that given by other codes.

3.5 COMMENTARY

The comparative study, presented in section 3.4 above, highlights the large discrepancies between various design codes. These variations exist in terms of philosophy and geometric and strength parameters, even when the same design philosophy is adopted.

As shown in Figures 3.1 to 3.12, a design which conforms to one code may be more than 60% unconservative according to a different code, notwithstanding that both utilize the same general principles. This is particularly true for slenderness ratios other than the middle range.

As mentioned before, in addition to the differences in capacity calculated from different codes, composite members subjected to earthquake loading are not given particular consideration. Instead, most codes concentrate on the estimation of seismic forces, and in almost all cases with the exception of the Japanese code, a composite member is treated basically as a steel or a reinforced concrete member.

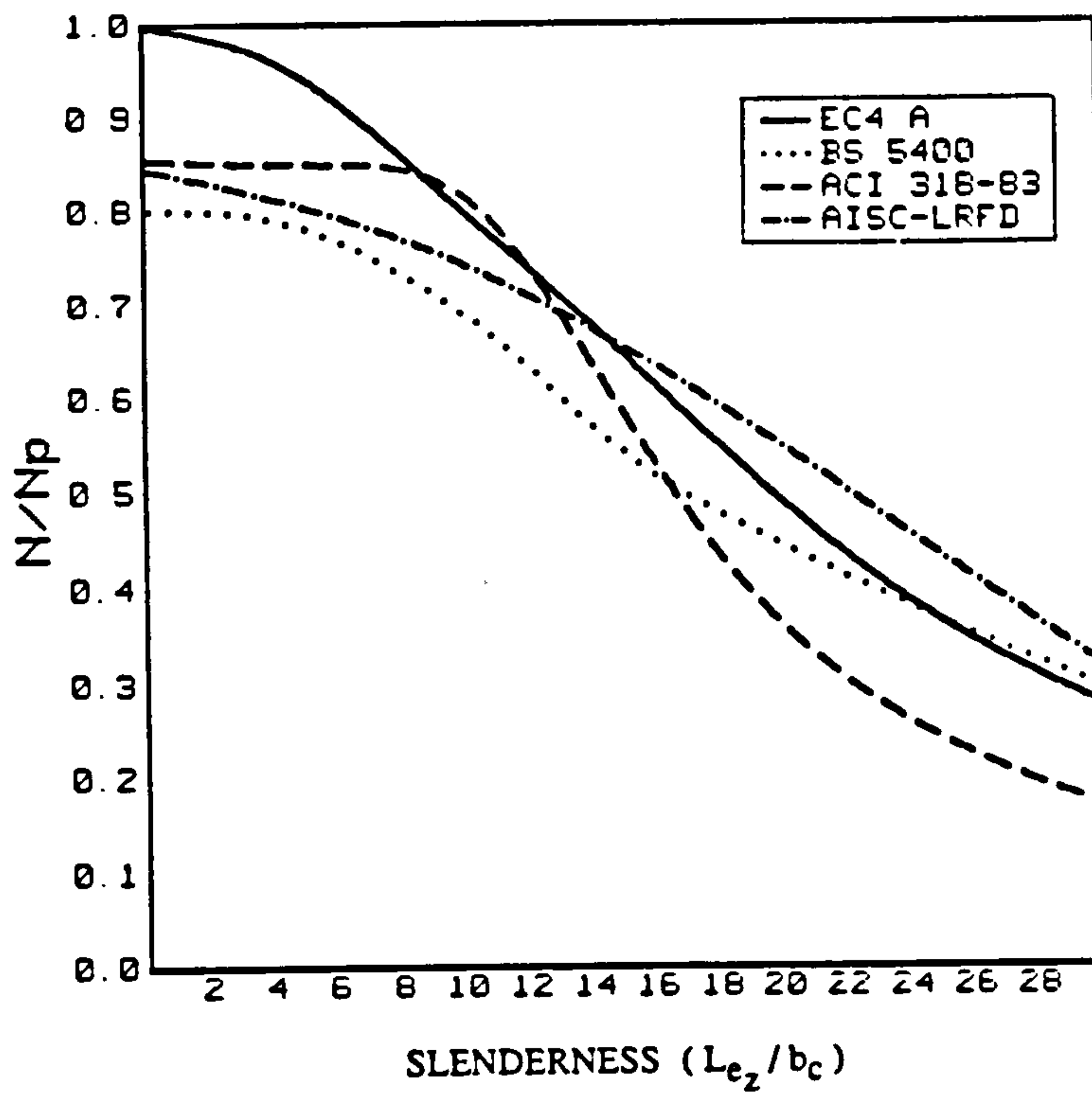


Fig. 3.1 Unfactored axial capacity

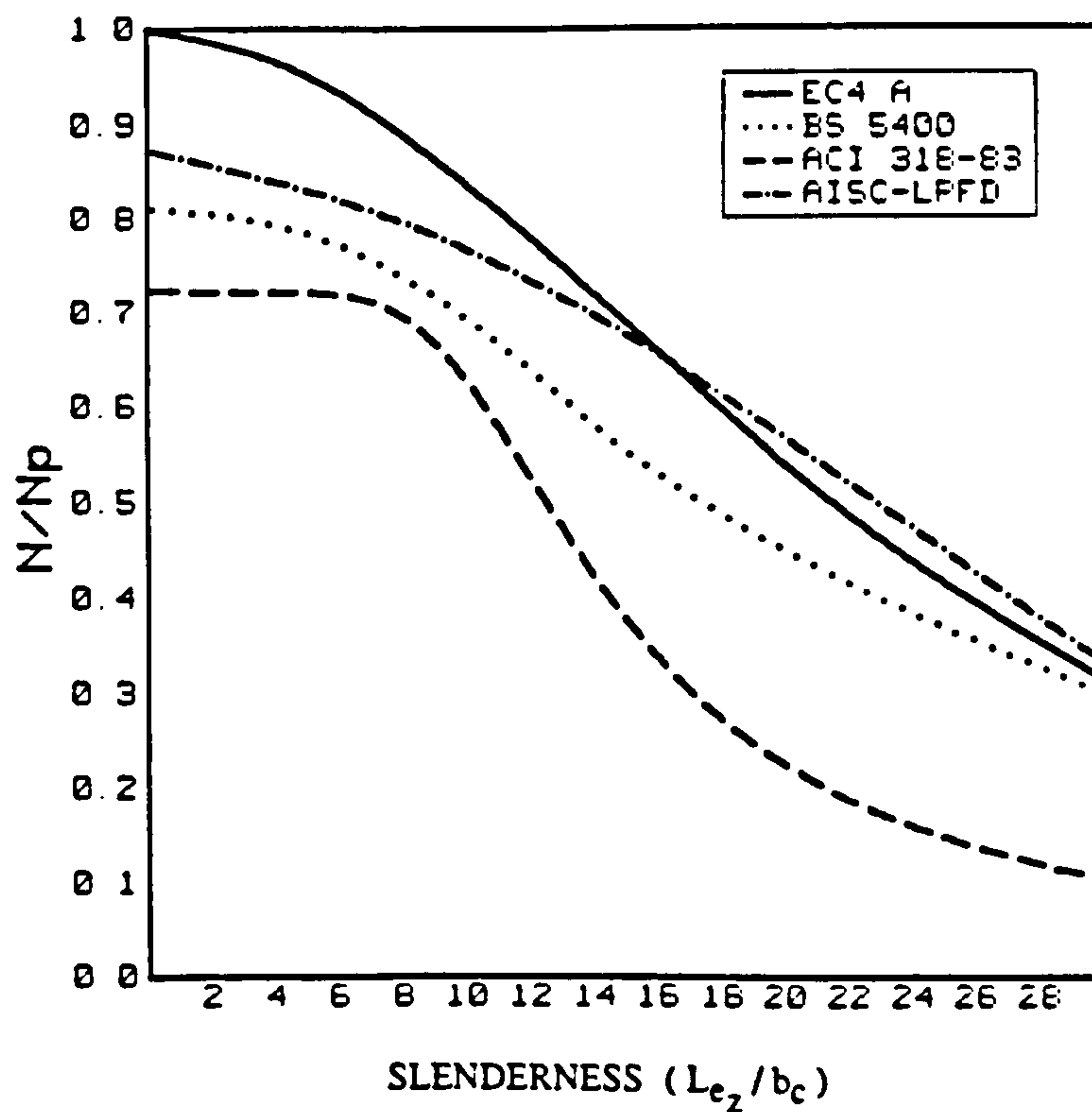


Fig. 3.2 Factored axial capacity

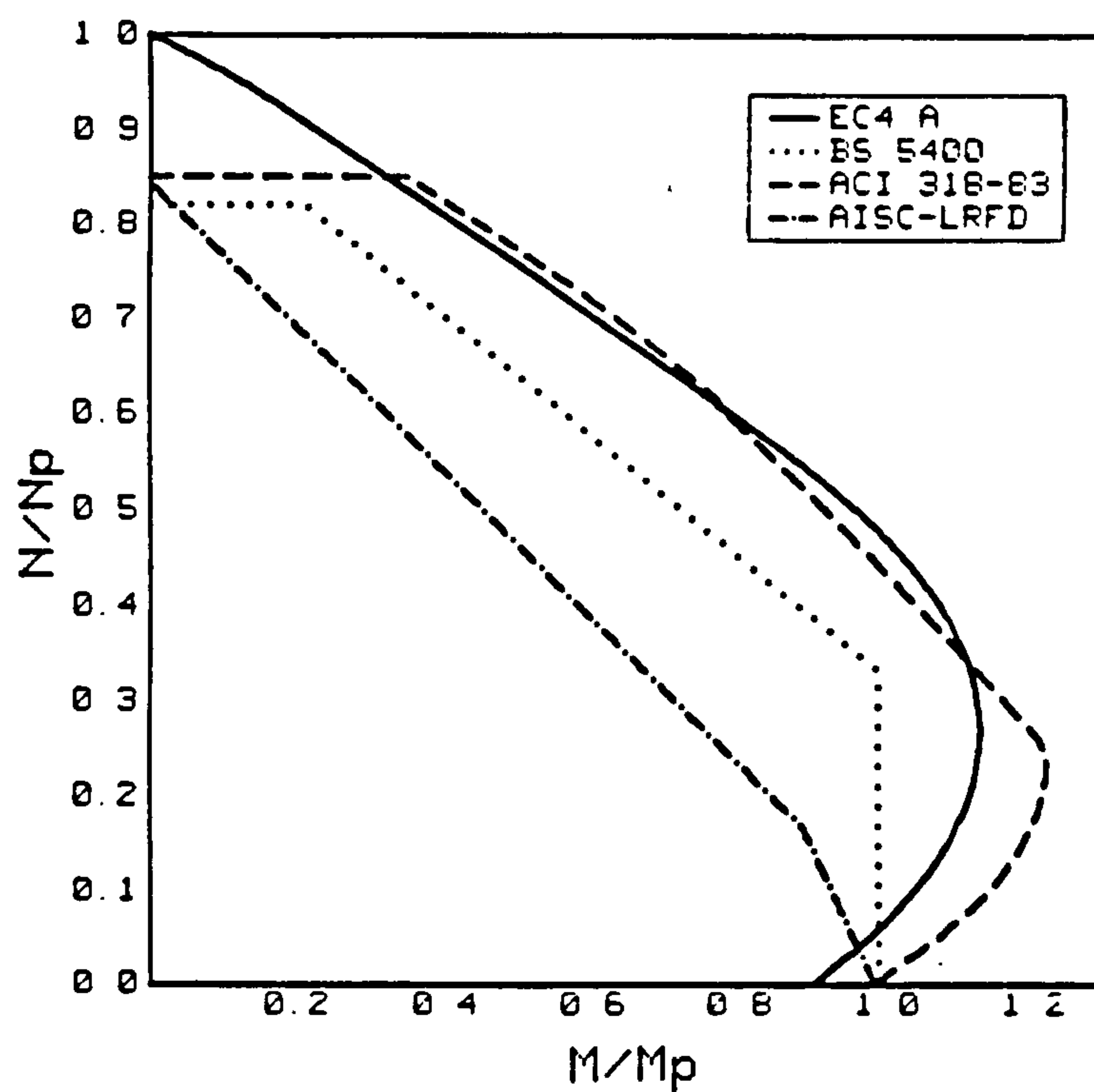


Fig. 3.3 Major axis bending (unfactored); $L_{ey}/h_c = 0$

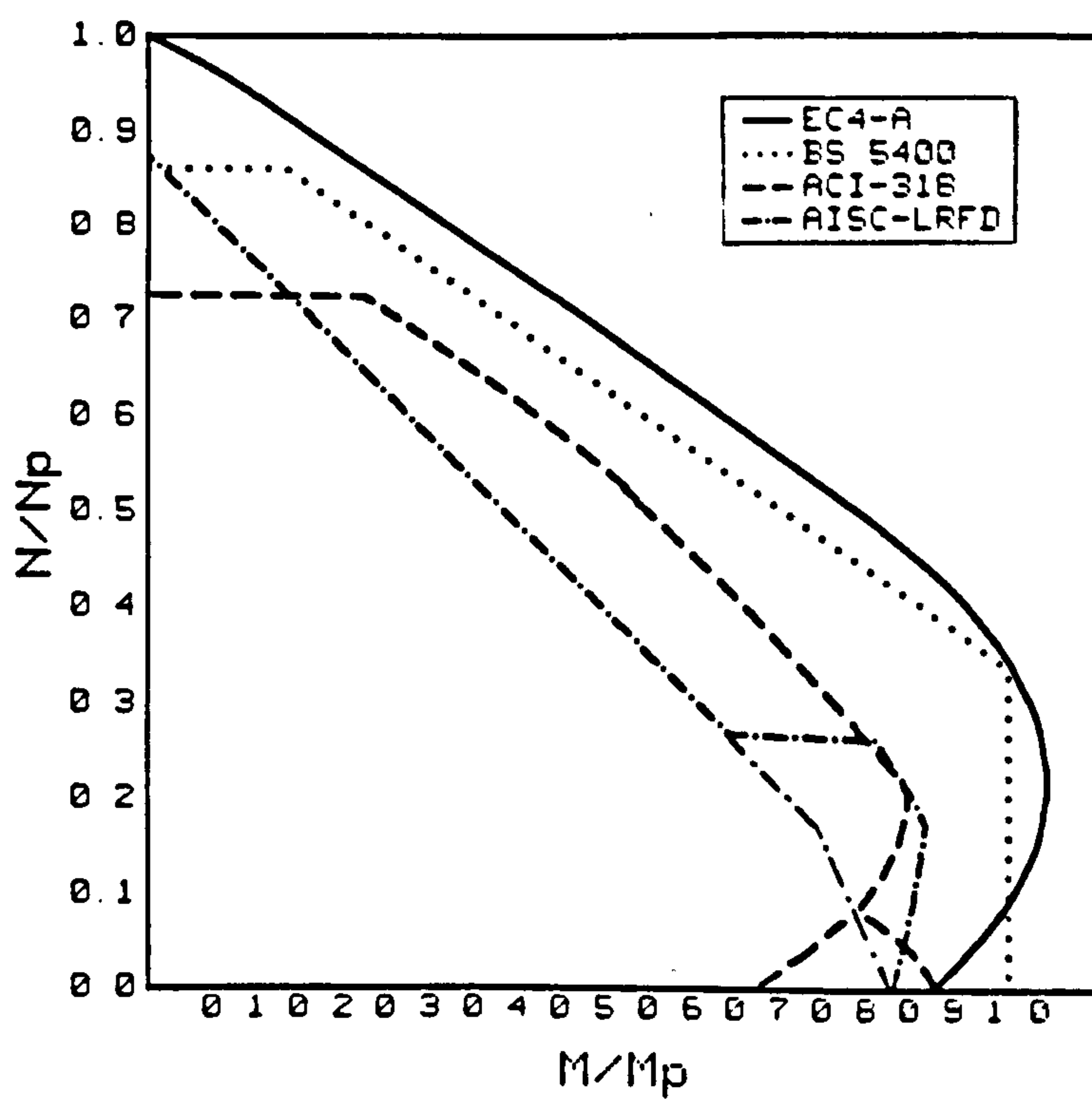


Fig. 3.4 Major axis bending; $L_{ey}/h_c = 0$

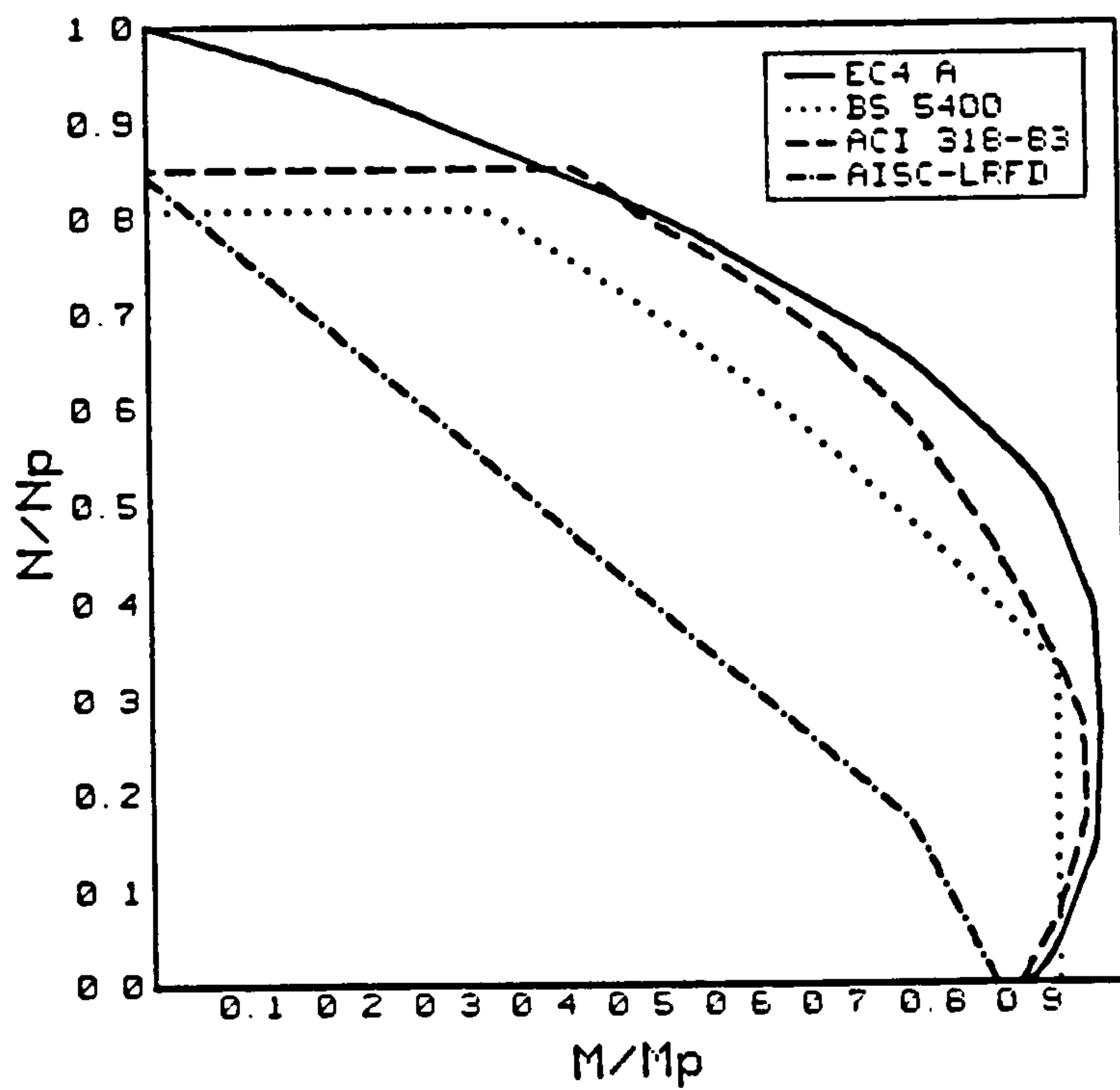


Fig. 3.5 Minor axis bending (unfactored); $L_{ez}/b_c = 0$

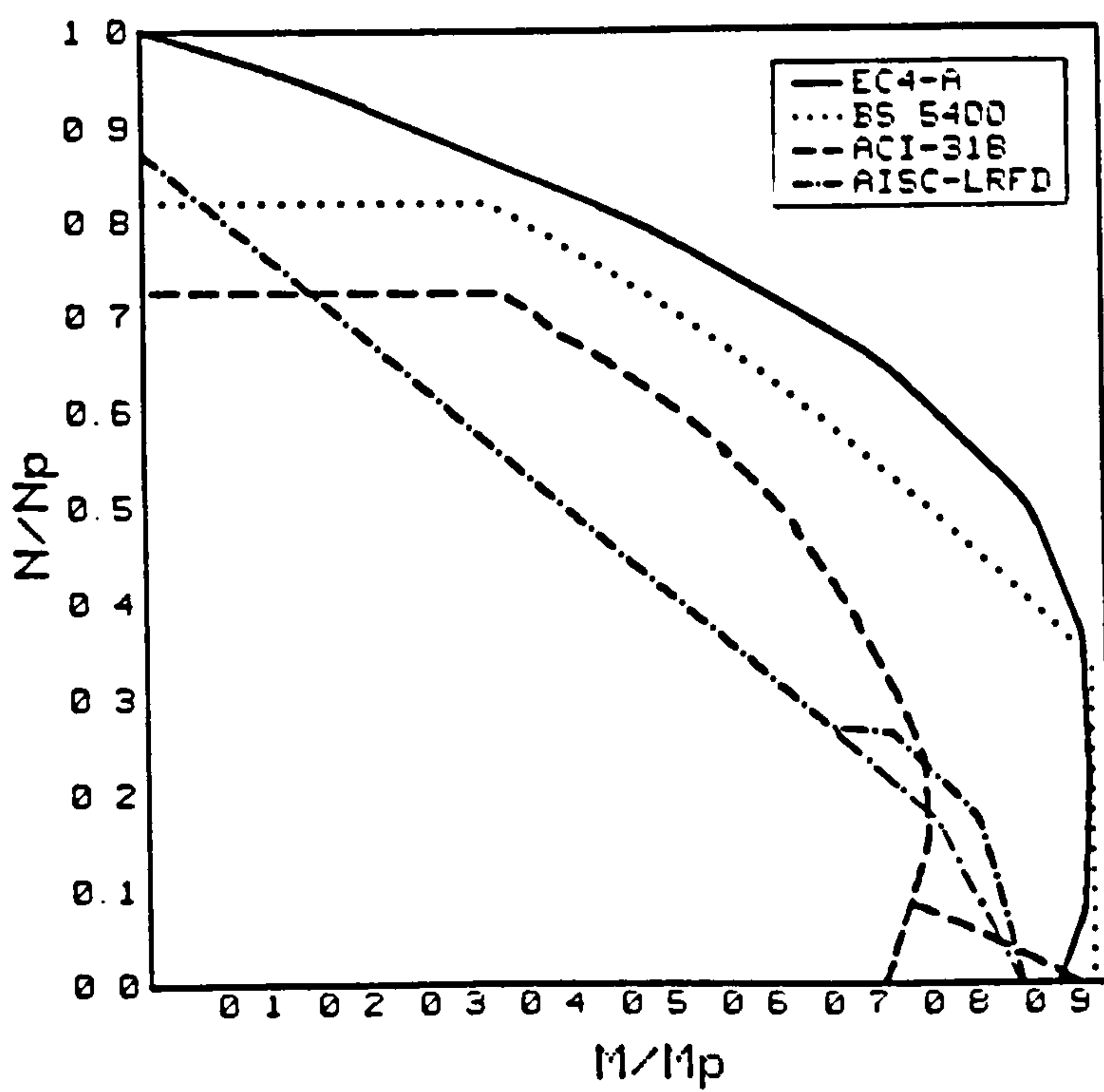


Fig.3.6 Minor axis bending; $L_{ez}/b_c = 0$

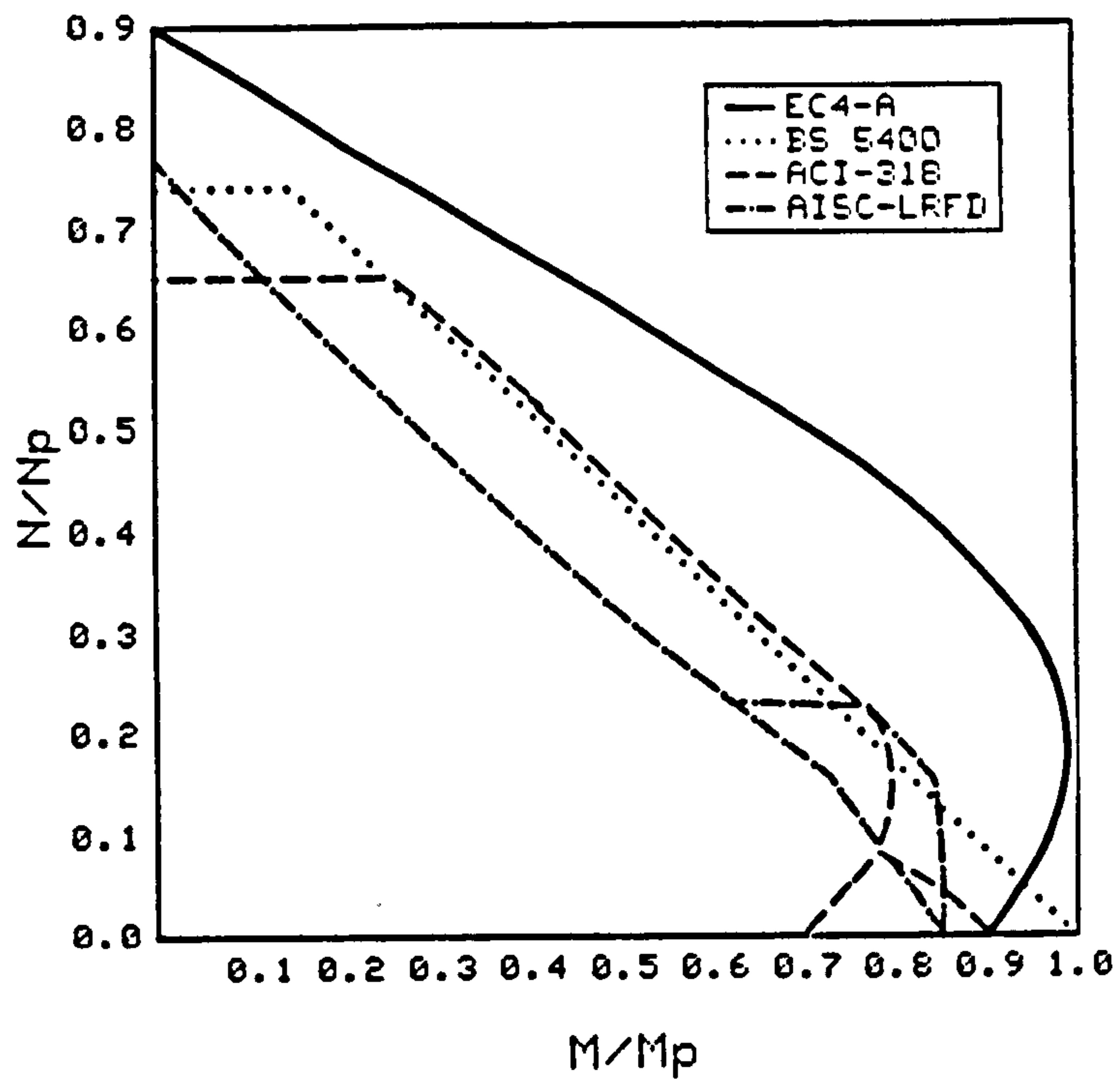


Fig. 3.7 Major axis bending; $L_{ey}/h_c = 12$

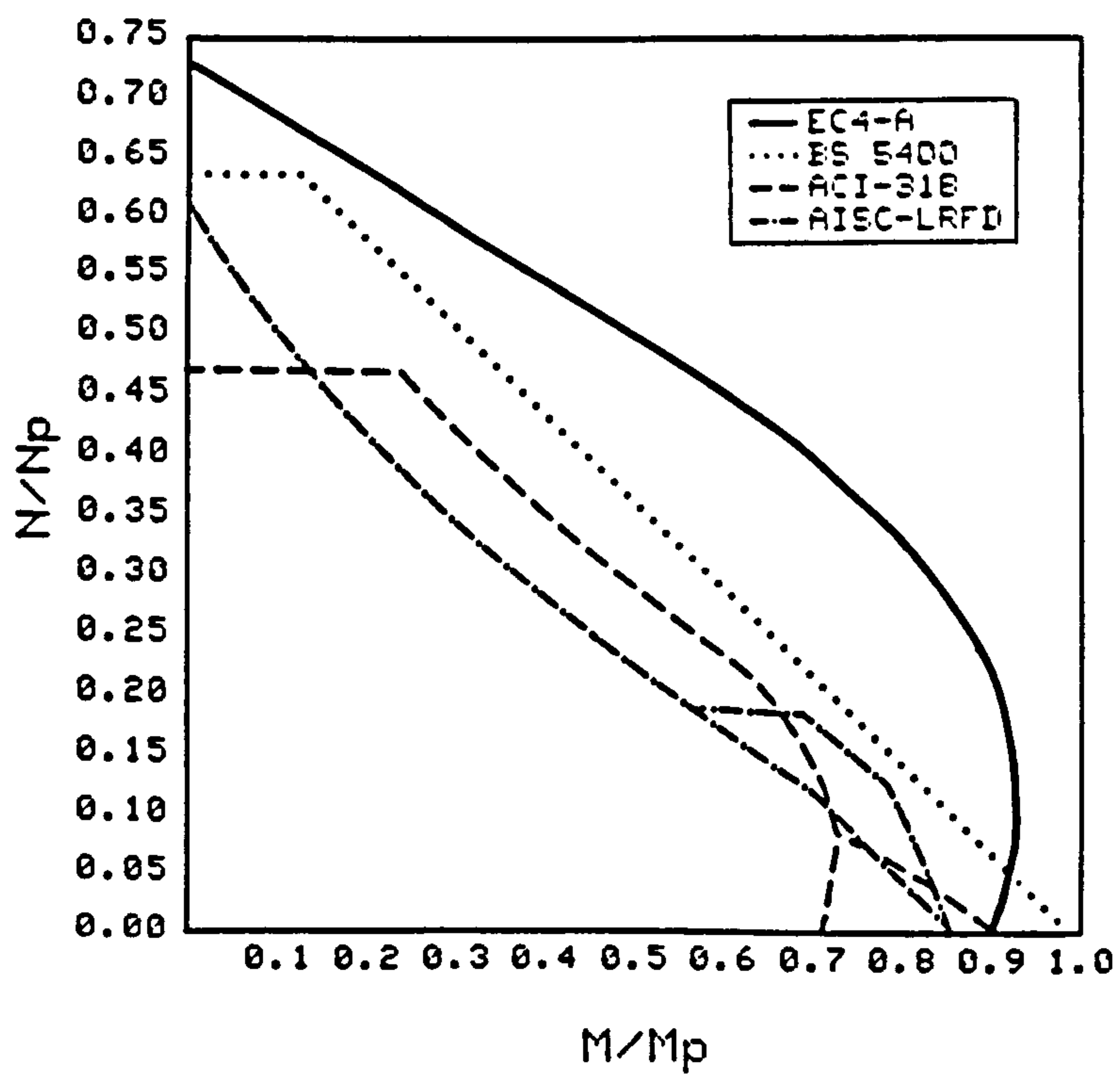


Fig. 3.8 Major axis bending; $L_{ey}/h_c = 20$

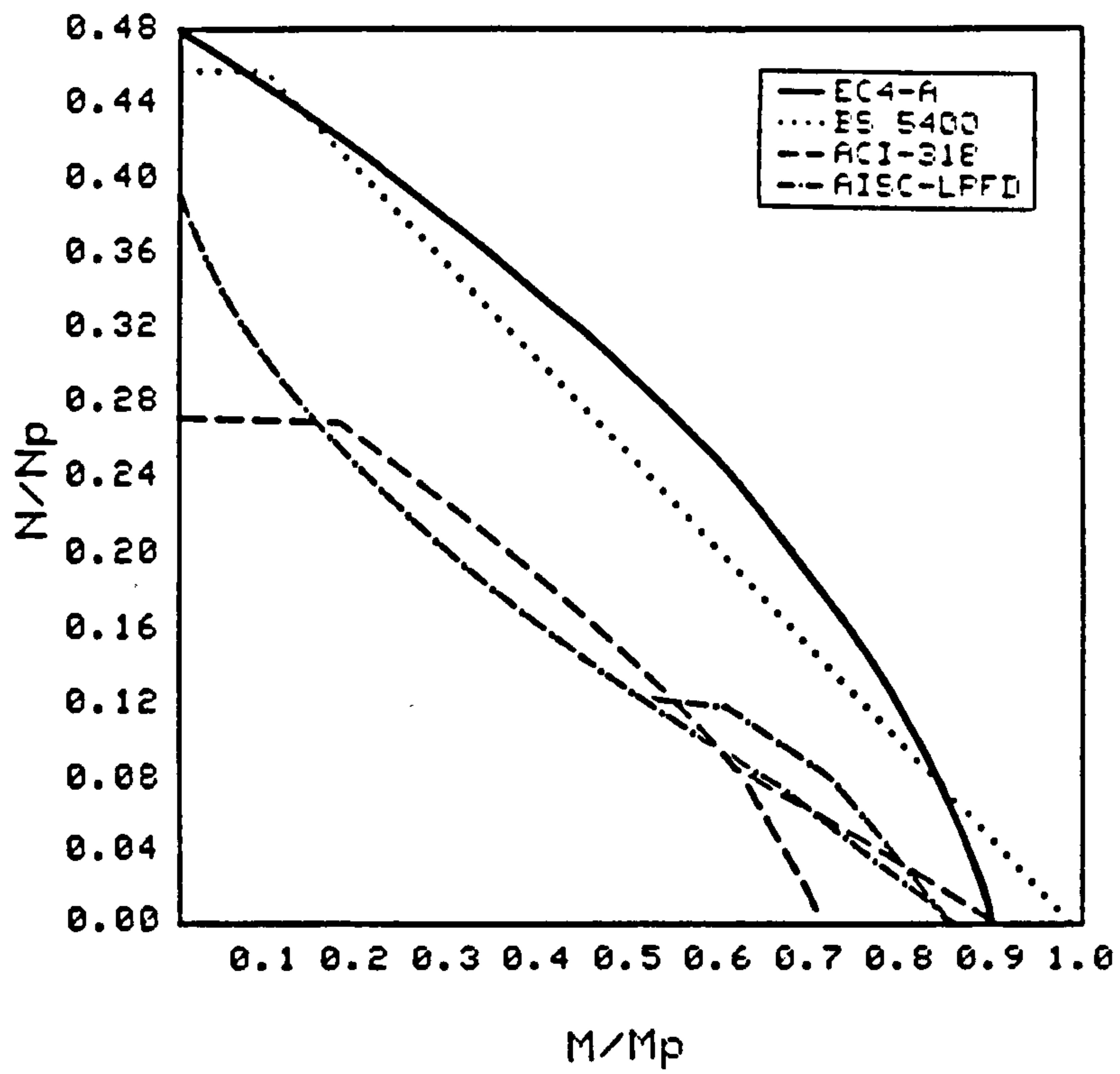


Fig. 3.9 Major axis bending; $L_{ez}/b_c = 30$

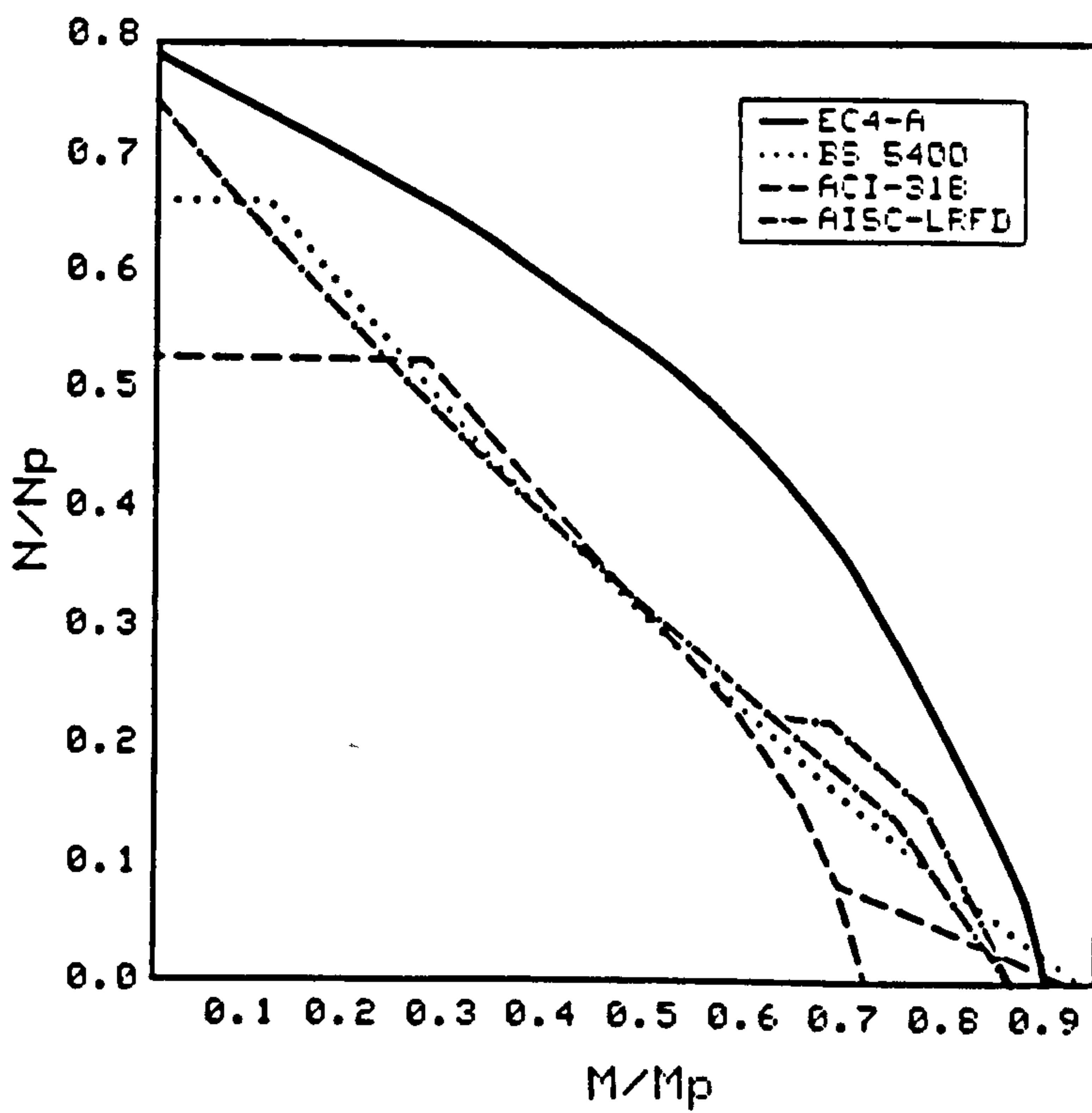


Fig. 3.10 Minor axis bending; $L_{ez}/b_c = 12$

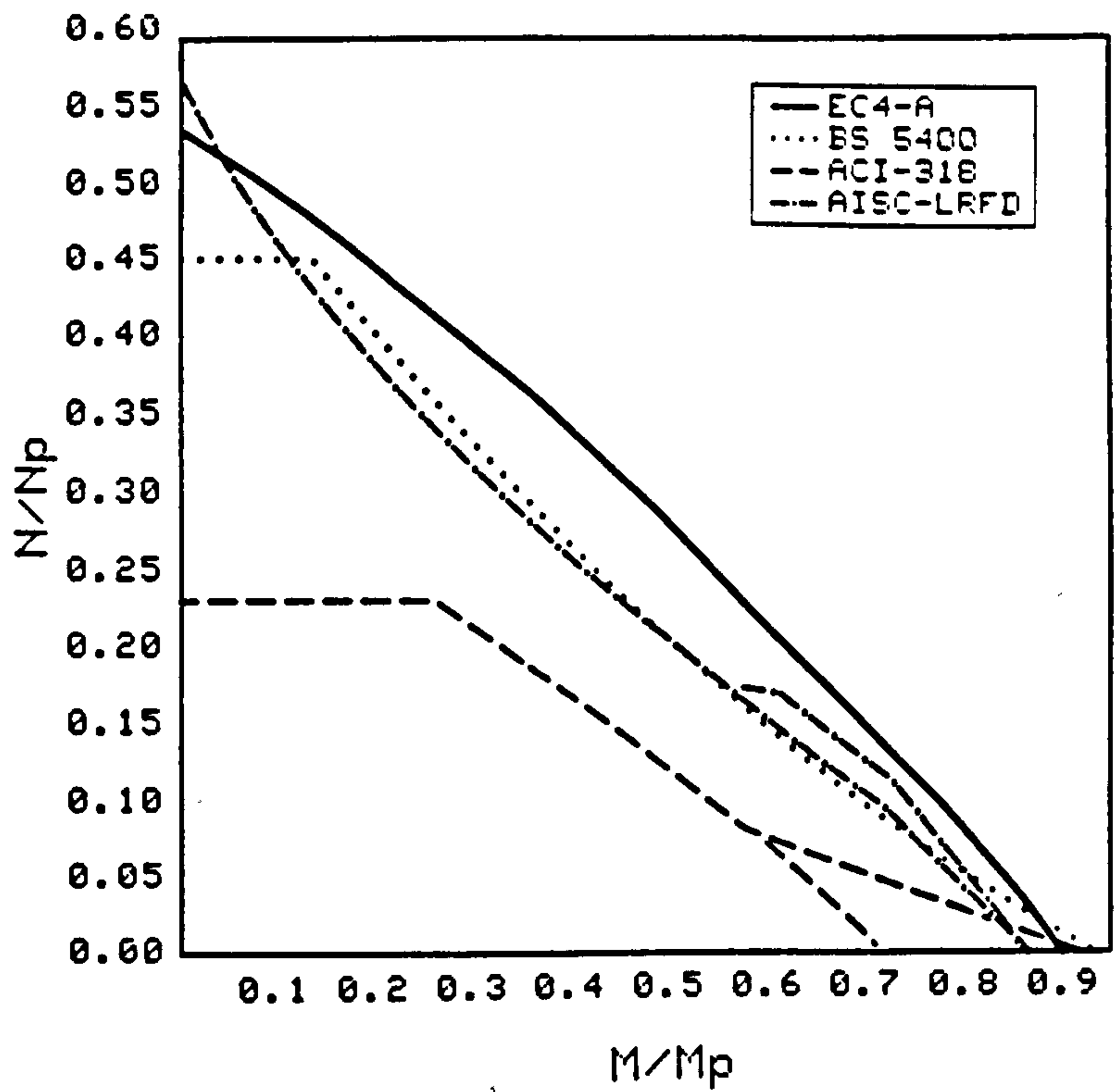


Fig. 3.11 Minor axis bending; $L_{ez}/b_c = 20$

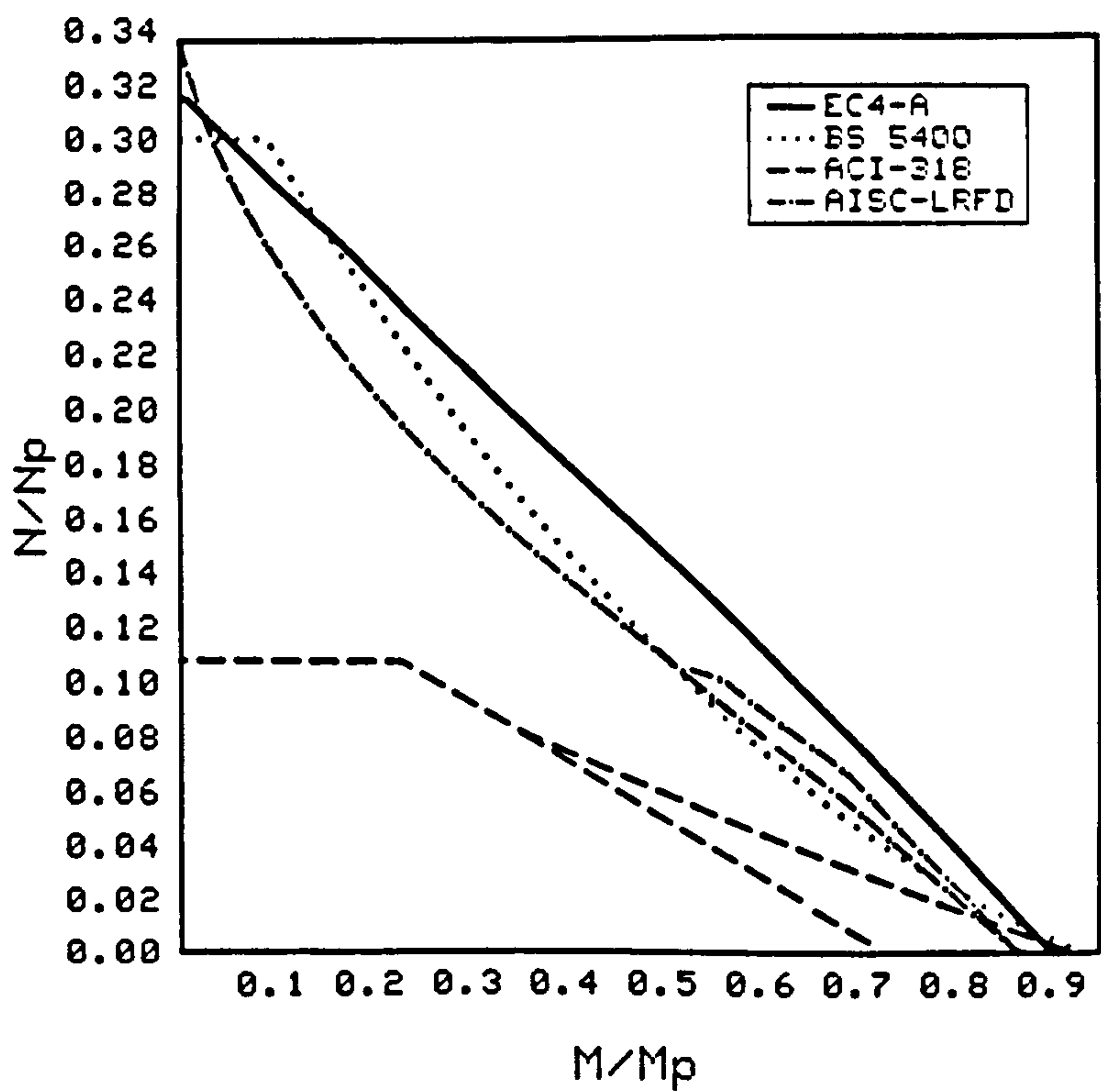


Fig. 3.12 Minor axis bending; $L_{ez}/b_c = 30$

CHAPTER 4

4. ON-LINE COMPUTER-CONTROLLED TESTING

4.1 INTRODUCTION

Although powerful and advanced computing methods to predict the nonlinear behaviour of structures are available, the confidence that can be placed in analytical methods is hampered by the uncertainties related to nonlinear modelling of materials and structural components. Consequently, experimental testing remains the most reliable method to understand and evaluate the inelastic structural behaviour, and to verify and calibrate existing analytical procedures as well as to develop new models.

An investigation of a structural component should start by evaluating the properties of the materials in use. This information is utilized to develop mathematical models for predicting the behaviour of members or assemblies, the actual response of which is then evaluated and/or verified through simple cyclic tests. Finally, the predictions must be compared with the observed behaviour during a real earthquake or a realistic seismic test. Utilization of either monotonic or cyclic testing only may lead to unsafe or over-conservative estimates of deformation capability. Since earthquake loading imposes a number of inelastic excursions of variable amplitude on the structure, testing under variable amplitude dynamic loading is the only technique that will furnish reliable and accurate information.

An on-line computer-controlled dynamic testing method was introduced by Takanashi and his co-workers in Japan (Takanashi, 1975). This technique, also known as pseudo-dynamic testing, offers an attractive alternative to shake-table testing. The pseudo-dynamic test method has the potential for combining the versatility and economy of quasi-static testing with the realism of shake-table testing. Whereas researchers in Japan (Takanashi et al, 1980; Takanashi and Ohi, 1984; Yamouchi et al, 1984; Yamazaki et al; 1984; Takanashi and Nakashima 1986) and the USA (Mahin and Shing, 1984; Shing et al, 1984; Hanson and McClamroch, 1984; Aktan, 1986; Shing and Mahin, 1988; Mahin et al 1989) have been utilising and developing this powerful testing technique during the last decade, only recently has this procedure been introduced in Europe at Imperial

College (Elnashai, Elghazouli and Dowling, 1990), whilst other facilities in Europe are following suit.

After introducing the theoretical and practical particulars of pseudo-dynamic testing, this chapter describes a new facility developed at Imperial College. The implementation details are presented as well as the results of verification tests carried out to demonstrate the accuracy and reliability of the system.

4.2 THE PSEUDO-DYNAMIC TESTING METHOD

4.2.1 Theoretical Basis

Pseudo-dynamic testing is an on-line computer-controlled technique that combines physical measurements and numerical analysis to simulate the dynamic behaviour of structural systems. The method uses similar equipment to quasi-static tests. However, it differs from conventional methods in that the displacement history imposed on a specimen is determined by an on-line computer. This displacement is based on the measured characteristics of the specimen and a specified excitation record. Displacements, imposed on the specimen quasi-statically, closely resemble those that would be developed if the specimen was tested dynamically. To achieve this, a test structure is first idealised as a discrete parameter system, the inertial and viscous damping characteristics of which are analytically prescribed. The displacement response of the structure to a predefined excitation is then evaluated by solving the governing equations of motion using reliable numerical integration algorithms. The computed displacement response is imposed on the specimen by hydraulic actuators. Based on the measured restoring force characteristics of the structure from the previous steps and the prescribed inertial and damping values, the displacement for the next time increment is calculated. A simplified diagram of the procedure is given in Figure 4.1.

The method, therefore, utilises the same numerical approaches used in nonlinear dynamic analysis, except that the nonlinear stiffness is based on direct experimental feedback rather than on idealised mathematical models. In general, one can obtain very reliable results by using high performance equipment alongside appropriate instrumentation and numerical techniques. However, the problems related to the fundamental principles of the pseudo-dynamic method have to be clearly understood by the user. It must be realised that the structural discretisation and numerical integration techniques used in pseudo-dynamic testing only provide an approximate solution for the dynamic response of a test

structure. The accuracy of these results depends largely on the determination of realistic discrete-parameter models and the use of reliable numerical methods. In order to ensure accurate numerical results, the stability and accuracy of the step-by-step integration method should be fully understood, especially with regard to the selection of appropriate integration time intervals. Additionally, viscous damping, strain-rate effects and the performance of loading-apparatus may all affect the results of pseudo-dynamic tests. These problems need to be identified and carefully examined in planning a test and before the method can be applied with confidence.

4.2.2 Numerical Schemes

In pseudo-dynamic testing, a structure is idealised as a discrete parameter system for which the equations of motion can be represented in matrix form as:

$$M\ddot{U} + C\dot{U} + R = F(t) \quad (4.1)$$

where M and C are the mass and viscous damping matrices, respectively; R is the structural restoring force vector; $F(t)$ is the external load vector; \dot{U} and \ddot{U} are the velocity and acceleration vectors, respectively. For linear dynamic response the restoring force can be represented as KU , where K is the stiffness matrix and U is the displacement vector.

Equation 4.1 can be conveniently solved under any arbitrary external excitation by direct step-by-step integration, where equilibrium is sought at discrete time intervals Δt apart. In the solution, the time span under consideration is sub-divided into n equal time intervals Δt and the integration scheme employed establishes an approximate solution at times $0, \Delta t, 2\Delta t, 3\Delta t, \dots, t, t+\Delta t, \dots, n\Delta t$, assuming that the solution in each step is a function of that in the previous step or steps. In the discretised form, equation 4.1, can now be presented at any step i as:

$$M\ddot{U}_i + C\dot{U}_i + R_i = F(i\Delta t) \quad (4.2)$$

Direct integration schemes can generally be classified into explicit and implicit methods. An integration method is considered to be explicit if equilibrium conditions are applied at the current step, i.e. at time t , where the displacement solution in each step is assumed to be a function of previous steps only. Otherwise, the method is considered to be implicit.

Substantial work has been carried-out by other researchers (Shing and Mahin, 1984; Thewalt and Mahin, 1987; Tsutsumi and Higashiura, 1988) to study the application of the different direct integration algorithms to pseudo-dynamic testing. An assessment of these methods is beyond the scope of this thesis. For brevity, only the basic scheme commonly used in pseudo-dynamic testing and implemented in this set-up is described hereafter.

In the Central Difference method, which is an explicit scheme, a parabolic variation of acceleration is assumed. The velocity and acceleration are assumed to be represented by the following difference equations:

$$\dot{U}_i = \frac{U_{i+1} - U_{i-1}}{2 \Delta t} \quad (4.3)$$

$$\ddot{U}_i = \frac{U_{i+1} - 2U_i + U_{i-1}}{\Delta t^2} \quad (4.4)$$

The displacement solution for a step $i+1$, i.e. at time $t+\Delta t$, is obtained by substituting these equations into the equilibrium equation, 4.2, at time t , resulting in equation 4.5 given below.

$$U_{i+1} = \left[M + \frac{\Delta t}{2} C \right]^{-1} \left[\Delta t^2 (F_i - R_i) + \left\{ \frac{\Delta t}{2} C - M \right\} U_{i-1} + 2 M U_i \right] \quad (4.5)$$

where $F_i = F(i \Delta t)$

The application of this method to pseudo-dynamic testing is described diagrammatically in Figure 4.2. The mass and viscous damping are analytically prescribed, whilst the actual restoring forces are measured from the specimen and used by the computer to calculate the displacements for the next increment. Those displacements are then applied on the test structure by the actuators. Consequently, the stiffness properties need not be idealised since they are directly measured during the test.

It should be noted that, unlike implicit methods such as Wilson and Newmark Methods, the Central Difference does not require a factorisation of the effective stiffness matrix in the step-by-step solution. For this reason, explicit methods are more commonly used in on-line testing. In contrast, implicit methods that require the determination of the structural tangent stiffness have been avoided since reliable estimates of the nonlinear

stiffness during the test are very difficult or impossible. Furthermore, the solution of nonlinear differential equations by an implicit method usually requires iterative corrections, which are normally unsuitable for inelastic testing since the restoring forces are generally path dependent.

On the other hand, the stability and accuracy of an integration scheme have to be considered. A stable method is defined as one by which the numerical solution of a free-vibration response will not grow without bound for any arbitrary initial conditions. If a method is stable and if the numerical solution will approach the exact solution as Δt tends to zero, then the method is convergent. This is a necessary condition for obtaining reliable solutions. Consider ω to be the fundamental natural circular frequency of the analysed system; whereas many implicit methods are stable for any value of $\omega\Delta t$, i.e. unconditionally stable, explicit methods are generally conditionally stable. In that case, numerical solutions become unstable when $\omega\Delta t$ exceeds a certain critical value, Δt_{cr} . It can be shown (Bathe, 1982) that this value for the Central Difference method is given as:

$$\Delta t_{cr} = \frac{T_n}{\pi} \quad (4.6)$$

where T_n is the smallest period of vibration of a system with n degrees of freedom. This limitation does not represent a practical problem except in multi-degree of freedom system with a considerable number of freedoms, where the magnitude of Δt is severely restrained by the stability condition on the highest frequency mode of the structure. In this respect, the stability limit of Δt applies for the highest existing mode, even if this mode is beyond the modes of interest, and is not needed for accuracy. At this stage, the pseudo-dynamic procedure becomes more time intensive, because of the increase in the number of steps, making the test more susceptible to experimental error propagation from test equipment, and more pronounced effect from strain aging or relaxation.

For nonlinear systems the time step should also be small enough to trace the inelastic response of the test structure with the discretised displacement increments. In general, a time step of $T_y/20$ should be sufficient, where y is the highest frequency mode of interest.

Disregarding the energy effects, the stability and accuracy characteristics of the explicit schemes for linear systems are locally valid for nonlinear systems by virtue of the fact that a nonlinear system can always be considered as a piecewise linear system in which the tangent stiffness is changing. Hence changing the natural period which is inversely proportional to the square root of the tangent stiffness. This implies that Δt selected for a

linear system will remain conservative if the system becomes nonlinear and if the nonlinearity is of the softening type, as long as the nonlinear behaviour can be accurately traced by the time step selected. This is due to the decrease in the effective $\Delta t/T$ as the system becomes less stiff. In this respect, the opposite will be true for a hardening system.

Since only a limited number of structural degrees of freedom are generally involved in a pseudo-dynamic test, the stability criterion imposed by an explicit integration method will not usually affect the efficiency of the test. Besides, explicit methods are usually as accurate as implicit ones. It was even shown (Thewalt and Mahin, 1987) that unconditionally stable implicit methods can become unstable when applied to nonlinear systems with large time steps. Also, the iterative corrections or tangent modulus assumptions may often cause erroneous energy effects. Hence, explicit methods may be finally more favoured for nonlinear systems.

4.2.3 Comparison with other Testing Procedures

Tests can be broadly classified as representing either dynamic or quasi-static loading conditions. In dynamic excitations, such as natural earthquakes or shake-table tests, the forces developed in a structure are due to its inertia, while in quasi-static tests, inertia forces are simulated by actuators moving at variable loading rates.

Shake-table testing is one of the most reliable and realistic experimental methods for evaluating the inelastic seismic performance in structural engineering. Excluding the difficulty to account for soil-structure interaction, shake-tables allow the test structure to be subjected to the same earthquake forces in the laboratory as they would experience in situ. Nevertheless, in addition to problems such as table-structure interaction for heavy specimens and the high cost of shake-tables, the main disadvantage in research is that a shake-table test does not allow for detailed observation of structural behaviour during the experiment. Moreover, the size and weight of the specimen is often restricted by the payload.

Dynamic tests into the inelastic range can also be performed using mechanical exciters, pulse generators or blast-induced ground motions. Nevertheless, it is difficult to reflect the inelastic seismic response through the mechanical exciters as it is sensitive to the history of inertia forces. Also, blast-induced ground motion is a high cost experiment and is normally limited to special problems involving soil-structure interaction.

In quasi-static tests, structural systems are subjected to a prescribed deformation or load history. These tests utilise conventional equipment and allow for detailed observation of structural behaviour during the experiment. Such an investigation can be particularly valuable in assessing the effect of different details on the inelastic behaviour of structural components, and in studying the basic mechanisms that affect the inelastic behaviour of a structural member or assembly by altering the pattern or rate of applied deformations. However, it is not possible to directly relate the energy dissipation capacity with that required for earthquake resistance. Consequently, questions arise as to whether the test structure is under or over-tested.

Forced vibration tests are similar to quasi-static tests in that dynamic actuators are used to apply forces at specific nodal points. However, in this case, the equivalent loads are applied dynamically in real time. Although this method is more realistic than quasi-static testing, it requires special data acquisition systems and, more importantly, as in shake table tests, does not allow for detailed observation of the of structural behaviour during the experiment.

On the other hand, pseudo-dynamic testing combines most advantages of both shake-table and quasi-static testing. The procedure is superior to quasi-static testing since the nonlinear structural characteristics are based on instantaneous experimental feedback rather than on hypothetical mathematical models. The method is also as realistic as shake-table testing where discretisation of the model is feasible. Furthermore, it exhibits various advantages over shake-tables, such as: (i) versatility, since it allows for detailed observation of the specimen during the test, (ii) possibility of testing full and large scale models thus eliminating the problems involved with dynamic similitude, (iii) actual masses need not be provided since it is modelled numerically, (iv) much lower cost of equipment, installation and operation , (v) elimination of problems arising from shake-table interaction for heavy specimens and (vi) improved actuator control and data acquisition reliability due to relatively slow rate of loading. However, shake table testing might be favoured in cases where strain-rate effects are significant and/or in distributed parameter systems. A brief comparison between the different inelastic testing procedures is presented in Table 4.1.

TABLE 4.1

Seismic Performance Tests

| Shake Table | Pseudo-Dynamic | Forced Vibration | Quasi-static |
|--|--|--|---|
| Most realistic method; allows the specimen to be subjected to the same seismic forces in the laboratory; forces developed are due to the inertia | Load application is realistic; however, the stability and accuracy of the numerical algorithm must be carefully studied | Load application is realistic | Load application is not realistic |
| Real time only for full scale testing | Actual testing time is longer | Real time only for full scale testing | Static loading |
| No assumptions on inertia, damping or stiffness properties are required | Stiffness characteristics are realistically accounted for, while mass and viscous damping are analytically prescribed | No assumptions on inertia, damping or stiffness properties are required | Based on idealised mathematical models |
| Strain-rate effects are incorporated | Strain-rates are not incorporated | Strain-rates are incorporated | Strain-rates are not incorporated |
| Distributed mass systems may be tested | Most suitable for discrete-parameter systems since equivalent loads are applied | Most suitable for discrete-parameter systems since equivalent loads are applied | Most suitable for discrete-parameter systems since equivalent loads are applied |
| Size, mass and strength are limited, often making reduced scale models necessary, thus raising the problems of dynamic and material similitude | Full and large scale testing is possible; also a mass may not be needed in most cases. | Full and large scale testing is possible | Full and large scale testing is possible |
| Fast test; does not allow for detailed observation of structural behaviour during the test | Relatively slow, allowing for detailed observation of structural behaviour during the test; the test can also be paused at any time if necessary | Fast test; does not allow for detailed observation of structural behaviour during the test | Allows for detailed observation |
| Problems may arise due to table-structure interaction for heavy specimens, or actuators not following accurately the input signals | Accurate application of input signals is possible because of the relatively slower rate of loading | Actuators may not accurately follow the input signals | High accuracy is possible because of the slow rate of loading |
| High speed data acquisition systems are required | High speed data acquisition systems are not essential | High speed data acquisition systems are required. | Data collection is usually very slow |
| High cost of installation and operation | Relatively lower cost of installation and operation | Relatively lower cost compared to shake table | Much lower cost |

4.2.4 Sources of On-line Test Errors

As pointed out before, errors may be introduced in a pseudo-dynamic test from a number of sources. Figure 4.3 summarizes possible sources of error. The accuracy and stability of the numerical schemes used in step-by-step integration must be understood, as discussed in section 4.2.2. Also, experimental feedback errors are introduced into the computation. Although the experimental errors in each step are relatively small, significant cumulative errors from a large number of steps may occur in a subsequent stage of the test. A description of the hardware used in the procedure is presented in section 4.3, together with an account of the accuracy and reliability of each component.

On the other hand, a number of errors may arise from the idealisation of a structure to a simplified form suitable for pseudo-dynamic testing. The reliability of the experiment depends largely on the viability of this idealised model. The inertial and viscous damping properties are analytically modelled, where the mass is concentrated discretely at a limited number of degrees of freedom. The dynamic characteristics of a discrete model might not accurately resemble those of a continuous structure which has a uniformly distributed mass, since the higher mode effects may be lost and lower frequencies may be distorted. The exact damping characteristics are difficult to model. Geometric effects may influence the accuracy of the results. Besides, because of the comparatively slow rate of loading, strain-rate effects may influence the inelastic structural response. The significance of these sources of errors in a pseudo-dynamic test is discussed hereafter.

4.2.4.1 Discrete Parameter Models

Pseudo-dynamic testing involves the discretisation of the structure. The stiffness properties of a structure are directly measured during a test in the form of restoring forces at specified degrees of freedom. The mass matrix has to be constructed using analytical assumptions. The mass matrix of a structure is usually assembled from the mass matrices of the elements by the direct stiffness method. Customarily, element mass matrices are constructed either by simple lumping of element masses at nodal points, or by employing displacement shape functions of elements. The consistent mass matrix formed by the latter method incorporates the rotational as well as the translational inertia of an element, and cross-coupling of inertia effects at different degrees of freedom exists.

The lumped mass matrix is based on the assumption that the total mass of an element is concentrated at its two ends, hence the inertial effects are not coupled. Therefore, the consistent mass formulation is more accurate than the lumped mass one, especially in

distributed-mass systems, if similar number of nodal points are selected in both cases. This is because of the larger number of degrees of freedom considered at each nodal point in a consistent mass model.

In general, the lumped mass concept is the more practical choice for pseudo-dynamic testing, since the rotational inertia considered in a consistent mass approach not only requires a greater computational effort, but also imposes loading and instrumentation difficulties on pseudo-dynamic experiments. Moreover, although the accuracy of a discrete parameter model can be improved by increasing the degrees of freedom, a small number usually offers sufficient accuracy if the structure has a large portion of its mass concentrated at several points.

4.2.4.2 Geometric Effects

As pointed out before, actual masses need not be installed in a pseudo-dynamic test as the inertial forces are modelled analytically. It may, however, be desirable in these tests to approximate the geometric stiffness effects of the missing mass (i.e. P- Δ effect). A simple linear correction can be achieved by supplying a geometric stiffness matrix to correct the measured force vector in terms of the current displacement. This approach is appropriate only if the proper stress states caused by gravity loads are not significant. Otherwise, actuators applying equivalent gravity loads should be used in the absence of masses to ensure accurate representation of stress conditions.

4.2.4.3 Strain-Rate Effects

The nonlinear properties of structural materials are often dependent on the rate of loading. Therefore, the inelastic behaviour in a pseudo-dynamic test may differ from that in an actual dynamic response. This difference, however, vary depending on the material used. The yield strength generally increase with the increase in strain-rates. Consequently, if the material is strain-rate-sensitive, a test specimen will usually display a lower strength in a pseudo-dynamic test.

For mild steel, whereas the elastic properties are not affected by the strain-rate, the yield stress shows a gradual increase with the increase in strain-rate (Manjoine, 1944; Hanson, 1966; Chang and Lee, 1987). The ultimate stress, however, shows less increase with strain-rate and may in fact coincide with the yield stress at very high strain-rates in the order of 100/sec. Considering that the maximum strain rate exhibited in seismic events is about 0.1/sec, yield strength will be no more than 30% different from that in monotonic

static loading carried-out at strain rates of about 10^{-5} /sec. However, pseudo-dynamic tests are conducted at a rate approximately between 10^{-2} /sec to 10^{-3} /sec, which compared with 0.1/sec, will cause about 15% to 17% difference in yield strength.

The above-mentioned results are based on monotonic tests. The strain-rate effects are reduced significantly for cyclic loading, depending on the frequency of the structure, the frequency of loading and the properties of material. This is because the maximum strain rates usually occur at very small strain levels, where the deformation is mainly elastic. To illustrate this point, consider that the variation of strain in a structural member during seismic response is approximately represented as a sinusoidal function, which is governed by the fundamental structural period and the yield strain and ductility of the material. In this case, the rate of change in strain will be at its peaks when the response is at its lowest levels. Consequently, the highest strain rates often occur when they have the least effect. This has been confirmed by other researchers (Shing and Mahin, 1988), where it has been shown that the strain-rate effect on yield strength of steel structures in pseudo-dynamic testing is usually less than 5%, and is generally considered to be insignificant.

Although less investigations are available with regards to the strain-rate effect of pseudo-dynamic tests on concrete structures, it generally follows the same pattern as in steel structures (Mahin and Bertero, 1972). Again, the yield stress increases with the increase in strain-rate. An increase in strain rate from 10^{-3} /sec to 0.1/sec is reported to cause a 20% increase in the yield strength. Also, crack propagation and patterns may be affected by a significant difference in strain-rate. It is, however, to be noted that the above comments pertain to tests on members or sub-assemblages. For redundant structures, strain-rate effects may have an influence on the sequence of plastic hinge formation, hence the overall response.

The previously-mentioned investigations also report that force relaxation, sometimes called strain history, will have a negligible effect on the behaviour of structural members. This was later confirmed by the tests conducted at Imperial College. In general, a pseudo-dynamic test should be executed at a reasonable rate. It should not be very slow to avoid significant strain-rate effects, neither should it be very fast, to avoid the inclusion of actuator inertial effects into the restoring force measurements.

4.2.4.4 Energy Dissipation

Several energy dissipating mechanisms such as viscous damping, friction (Coulomb) damping and hysteretic damping may exist in a real dynamic system. The characteristics

of each of these damping mechanisms for a simple single degree of freedom system are discussed hereafter.

Viscous damping, which is proportional to velocity, can be represented by a dash-pot model, as shown in Figure 4.4.a. The equation of motion including viscous damping is:

$$m\ddot{u} + c\dot{u} + ku = f(t) \quad (4.7)$$

where m , c and k are the mass, damping coefficient and stiffness of a single degree of freedom system. The magnitude of viscous damping in an analytical model is usually specified in terms of the damping ratio ξ which is equal to $c/(2m\omega)$. If damping is less than the critical, i.e., $\xi < 1$, the free vibration amplitude has a logarithmic decay given by:

$$\bar{u}_{n+1} = \bar{u}_1 e^{-2\pi\xi n} \quad (4.8)$$

in which \bar{u}_1 is the response amplitude at time t_1 and \bar{u}_{n+1} is the amplitude after n cycles. This logarithmic decay can also be represented in terms of the logarithmic decrement, δ , which is approximately equal to $2\pi\xi$. The exact relation between ξ and δ is given as:

$$\xi = \frac{\delta / 2\pi}{1 + (\delta^2 / 4\pi^2)} \quad (4.9)$$

The logarithmic decrement can be estimated from the free vibration response as follows:

$$\delta = \frac{\ln \bar{u}_n}{\ln \bar{u}_{n+1}} \quad (4.10)$$

in which \bar{u}_n and \bar{u}_{n+1} are any two consecutive displacement amplitudes. Equation 4.8 and 4.10 are identical, but presented in a different form.

Coulomb damping, on the other hand, is caused by friction. The frictional force F_f is of constant magnitude and is opposite to the direction of motion. It depends only on the coefficient of dynamic friction of the contact surface ϕ_f , and the normal force applied to this surface W . The equation of motion is, therefore, given as

$$m\ddot{u} + F_f \text{sign}(\dot{u}) + ku = f(t) \quad (4.11)$$

where F_r is the product of W and ϕ_f , and $\text{sign}(\dot{u})$ is the sign of the velocity at any time t . Unlike viscous damping, the decay of free vibration amplitude due to friction damping is linear as shown in Figure 4.4.b, such that:

$$\bar{u}_{n+1} = \bar{u}_n - 4 F_r / k \quad (4.12)$$

This implies that friction damping becomes insignificant as the displacement response amplitude increases, or if the stiffness of the system is relatively high.

Another important form of energy dissipation developed from the inelastic behaviour of structural materials is hysteretic damping. In this case, the energy dissipated in one cycle of loading is equivalent to the area enclosed by the load-displacement loop, as shown in Figure 4.4.c.

In practice, damping in structural dynamics applications is commonly considered in the form of an equivalent viscous damping ratio, ξ_{eq} , because of its convenience in analytical studies. This is adequate only if the effects of friction and hysteretic damping are relatively small.

By measuring the actual restoring forces in the test structure, friction and hysteretic damping are included in a pseudo-dynamic test. Viscous damping, however, has to be analytically prescribed. An adequate estimate of viscous damping can be obtained by comparing the pseudo-dynamic free vibration response without viscous damping with the actual free-vibration response of the structure. The difference between the equivalent viscous damping measured in both gives an approximate value of viscous damping to be included in the on-line test.

Although the viscous damping changes as the structure behaves inelastically, the energy dissipation becomes almost totally dominated by hysteretic damping. Therefore the effect of changes in viscous damping in the inelastic range is very small. Furthermore, since equivalent structural dampings measured from most vibration tests vary between 1 and 3%, a small discrepancy in a prescribed damping value will have no effect on the inelastic response. This has been confirmed by previous researchers such as Shing and Mahin (1984).

In this context, it should be noted that frictional forces arising from the loading and support assembly may, sometimes, be unrealistically high causing a considerable viscous

damping estimate, as discussed in Section 4.4. These are negligible if the frictional forces are small with respect to the stiffness of the structure.

It is clear from the above that although accurate damping values are difficult to measure, the most important form of damping in inelastic tests, hysteretic damping, is implicitly accounted for in a pseudo-dynamic test. Also, reasonably accurate viscous damping values can be assigned to the test rendering it even more reliable.

4.3 IMPLEMENTATION DETAILS

4.3.1 System Description

Figure 4.5 shows the basic components of the pseudo-dynamic set-up as implemented at Imperial College. As mentioned before, the nature of the procedure makes it very sensitive to experimental errors since feedback errors are introduced into numerical computation during the test. Due to the error accumulation in the subsequent steps, a test can be rendered unreliable even though the experimental errors introduced in each step are relatively small. For this reason, every single element of the experimental loop should be carefully studied to achieve the highest possible accuracy and reliability from the system. Hereafter, the fundamental operation and performance of the different components of the pseudo-dynamic closed loop control are briefly described together with their main sources of error.

4.3.2 Data Conversion

Most transducers and testing equipment are analogue in nature, accepting or giving out a voltage signal or a direct current (DC). The computer processor, however, requires the information in digital form. To digitise the analogue signal, an analogue to digital (A/D) converter or, conversely, a digital to analogue (D/A) converter, is required. Although all signals are assumed to be changing with time, analogue signals have information contained in their incremental variation in amplitude, while digital signals are represented by only two possible values, high or low, or in other words true or false (on or off; 1 or 0). Figure 4.6 shows typical analogue and digital signals.

The A/D converter is the component that changes the analogue signal into a digital code pattern representing this input value. Each digital line carries only one bit of data. At each signal sampling instant, a code pattern is produced, as shown in Figure 4.7 for a 4-bit

converter. A converter is normally categorised by the number of bits that form the output code. This represents the smallest input signal change that can be detected by the converter and is called its resolution. The full scale range of the signal is discretised into the maximum number of digital combinations, which is 2^n , where n is the number of bits. In this set-up, 12-bit A/D converters are used. Therefore, for an output of +/- 10 volts, the available resolution would be 0.004883 volts. This means that a signal, such as a displacement increment, less than this value would be lost in the conversion. Consequently, to maximise the dynamic range which in turn increases the attainable resolution, the different equipment should be calibrated (evaluation of relationships between voltage and displacement or force units) as close as possible to the maximum values expected during a test.

Additionally, the accuracy of the converter is also important and must not be confused with its resolution. A converter of high resolution does not necessarily mean that it is very accurate. Converters may have offset errors, thus may output a non-zero digital code for zero input. Furthermore, code changes may not take place at equal increments of the analogue voltage. This causes differential nonlinearity, which is normally defined in terms of the least significant bit (LSB) size. Generally, a converter of 0.5 to 1.0 LSB accuracy would be acceptable.

Another parameter that needs consideration is the speed of conversion. In practice, conversion takes a finite amount of time for completion, during which the output cannot be updated. Hence, in an A/D converter there is a maximum rate at which analogue information can be digitised. Based on current technology, a rough guide to A/D conversion speed (Cooling, 1986) is given in Table 4.2 below.

TABLE 4.2
Speed of A/D Converters

| A/C Category | Very Slow | Slow | Medium Speed | Fast | Very Fast |
|--------------------|-----------|---------|--------------|-----------|------------|
| Conversion Time | 100 ms | 1 ms | 50 us | 1 us | 50 ns |
| Sampling Frequency | 10 Hz | 1000 Hz | 20 KHz | 1,000 KHz | 20,000 KHz |

The converters used in this set-up have a speed of 32 KHz. In other words, the conversion time for a signal update is 31.25 micro-second, i.e. it can sample the changing signal up to 32,000 times in every second. This high speed is particularly useful in sampling several values at any given time, hence allowing for software filtering of the signal.

In contrast, the D/A converter is responsible for transmitting displacement commands from the computer to the servo-controllers. The performance characteristics of D/A converters are very similar to A/D converters. Hence, the resolution is again specified by the number of bits. The D/A converters employed in this study are of 16-bit resolution. However, this can be altered between 12 and 16-bit through software control according to the specific test requirements. This means that, in theory, a signal change as small as 0.0003 volts can be produced in the conversion process. Nevertheless, this voltage resolution is not expected from other components such as the servo-controllers and measurement transducers.

4.3.3 Signal Conditioning

Most signals entering a data acquisition system will include unwanted noise. Whether this noise is troublesome depends upon the signal-to-noise ratio and the specific set-up. For pseudo-dynamic testing, it is desirable to minimise noise to achieve high accuracy and avoid accumulation of error through different time steps.

Digital signals are relatively immune to noise because of their discrete and high level nature. In contrast, analogue signals are directly influenced by comparatively low disturbances. Electric noise can be reduced significantly by adopting proper wiring techniques such as shielding of cables, wire twisting, use of minimum cable length, differential signalling and grounding. Nevertheless, in some cases it is difficult to avoid noise completely. In this set-up, a slight oscillation in the acquired data, especially in the force readings, was observed, which is attributed mainly to dynamic effects from the electro-hydraulic system. For these reasons, filtering was employed to ensure reliable closed loop control.

Although filtering can be achieved by computer averaging of a series of incoming signals, this is most effective only in reducing random or non-periodic noise sources. Consequently, low-pass analogue filters were used to attenuate frequencies above a corner frequency of 2 to 5 Hz, depending on the speed of testing. Figure 4.8 shows a typical transfer function for such a low-pass filter. The pseudo-dynamic test was always

performed at a slow rate and the actual data was, therefore, not disturbed by the filtering process.

Other important signal conditioning operations such as amplification, current to voltage conversion, voltage scaling, surge protection etc., are provided by manufacturers for different components of the set-up. Also, the converters are provided with several gain choices under software control. Programmable gain amplifiers (PGA) help in achieving improved converter performance for low level signals.

4.3.4 Measurement Transducers

The reliability of the test depends largely on the accuracy in imposing the computed displacements and measuring the corresponding restoring forces developed in the structure. This can be achieved by using high performance transducers, which are electronic devices capable of relating displacement or force changes to voltage signals. An ideal transducer would give a linear correlation between the physical measurement and the analogous voltage.

In the closed loop, the calculated displacements are sent out from the D/A converters to the servo-controller, which then moves the specimen until the target and feed-back signal are identical. It is, therefore, imperative that displacement transducers have minimal nonlinearities and are able to detect small variations in displacement. Also, proper calibration of the device should be carried out. The LVDTs (Linear Variable Displacement Transducers) used in this particular set-up have an accuracy of 0.5% (i.e. linear within 0.5% of total travel), the attained resolution is 0.05% of range (5 milli-volts in a 10 volts signal), and their total travel is ± 125 mm. Additionally, great care should be given to the positioning of transducers in order to measure the actual specimen displacement. In particular, errors arising from the flexibility of the actuator support must be avoided, and the significance of inaccuracies due to the change in geometry at large deformation must also be evaluated.

Force transducers, which are standard strain gauge based load cells, are positioned between the actuator and the specimen. The load cells used at Imperial College are the Instron 2518 Series Fatigue Resistant devices, mounted directly on the actuators' pistons, measuring dynamic loads with a linearity of $\pm 0.4\%$ of reading. Again, errors in restoring force measurement may arise from nonlinearities or miscalibration of load cells, misalignment of actuators, significant frictional forces in actuator joints and attachments, or from geometric effects at large displacement positions.

4.3.5 Electro-Hydraulic Equipment

The Electro-Hydraulic control system is responsible for imposing the correct displacements on the test specimen. The basic components of the Instron system, used in this set-up, is presented in a simplified block diagram form in Figure 4.9.

A servo-valve is a device which is part electro-mechanical and part hydro-mechanical. It directs oil flow to either end of a double acting actuator in proportion to the magnitude and direction of an electrical signal. The amplitude and frequency achieved by the actuator are limited by the maximum flow of the servo-valve or power pack, whichever is smaller. More flow is needed the larger the actuator amplitude and the higher the operating frequency. Also, the actuator stroke affects the performance because the oil in the actuator piston is compressible and some of the flow is used in pressurising this oil. The flow rate is normally specified in litres per minute. The two power packs at Imperial College have a capacity of 460 litres/minute each. However, since the pseudo-dynamic tests were conducted at a rate less than 5Hz, a servo-valve of 96 litres/minute flow rate was sufficient to achieve the full static capacity of the actuator at a maximum amplitude of ± 120 mm.

The actuator is described by its force capacity and its total stroke. The static force capacity is the product of the supply pressure and the actuator piston area. The operational system pressure used in this set-up is 3000 psi. In a simplified form the oil column inside the actuator compartment can be considered as an axial spring. In this case, the stiffness is directly proportional to the piston area and the bulk modulus of the hydraulic fluid, and inversely proportional to the total stroke. This stiffness can also be affected by any leakage across the actuator piston.

An integral component of the loop is the servo-controller. The main task of the controller is to compare the command signal voltage with the displacement transducer voltage output signal. The difference, the servo error signal, is then amplified by the loop gain producing a current used to drive the servo-valve. This causes the actuator to move in order to reduce the error. In effect, the gain setting controls the displacement error necessary to move the actuator at a specified velocity, or, in practical terms, it controls how closely the response follows the command signal. Best performance is achieved with the highest possible loop gain setting consistent with a stable output wave form.

The controller gain is critical for the accuracy of the displacement closed loop. As shown in Figure 4.10, if the controller gain is set too high, oscillatory behaviour will be exhibited with large overshoots and even instability. On the other hand, if the gain is set too low, a very sluggish performance will be obtained. In a pseudo-dynamic test, either of the above is desirable since significant error accumulation can occur as a result of the consistent introduction of erroneous measurements to the computer. Instead, an optimal gain should be sought, such that the actuator response will faithfully follow the command signal. It is advisable to adjust the loop gain before each test. This can be done by observing a rectangular waveform on an oscilloscope until the best optimal shape is achieved.

Extensive experimental studies on the Electro-Hydraulic equipment performance have been carried out by several researchers (McClamroch et al, 1981; Thewalt and Mahin, 1987). Also manufacturers guides provide ample information on the theory and details of such systems.

4.3.6 Software Layout

A flowchart of the developed pseudo-dynamic testing program is shown in Figure 4.11. This section will not describe in detail the secondary tasks needed in pseudo-dynamic testing such as direct data acquisition, on-line graphics and calibration routines, which are basic utility programs available in most laboratories. It will rather focus on the main control loop of the program.

The procedure starts with checking different components of the set-up. Error messages are returned in case of a faulty unit. This is followed by input of user-defined initial parameters which include the number of degrees of freedom, number of data channels, excitation record file name, masses, time increment and viscous damping. The displacement ramp speed, and the ramp shape, either linear or haver-siner, can also be predefined by the user. The calibration factors for all instruments are specified, together with the data limits for the control channels. A linear displacement amplitude level must also be selected if automatic estimation of the initial stiffness is required. A choice is available for updating graphics and data storage within, or outside the ramp generation.

During any intermediate step 'i', the control loop starts by reading the data from all channels through the A/D converters, from which the force vector is extracted and its limits are checked. After reading the excitation vector at the current step, the control displacements for the following step are computed. The displacement ramps are then generated and sent to the D/A converters. There are two options concerning the updating

of graphical display and storage of data from all channels. If the first option is chosen, these operations will be performed before the ramp generation and just after reading the data channels. Alternatively, they can be performed during the generation of the ramp, while the program is polling the hardware for the ramp completion. The latter option is preferable, especially if the number of data channels is large, since it reduces the hold periods between actuator movements, which may cause force relaxation.

The procedure can be paused at any step and the user has the choice of either aborting or resuming the test. The data from the last time increment may either be saved or discarded. The program also includes a routine for unloading the test specimen after the end of execution. In general, the completion of the control loop for any time step can be performed in less than one second. However, as mentioned before, the test should not be very slow to avoid force relaxation and strain aging, and not very fast to ensure the exclusion of inertia forces from heavy attachments such as the load cell. Assuming a time step of 0.02 sec, the above-described set-up can be used to conduct the test as fast as 60 times the real time without sacrificing the accuracy and reliability of the system.

4.4 VERIFICATION TESTS

In order to verify the reliability and stability of the developed system, a number of pseudo-dynamic tests were conducted on two steel cantilevers. This section describes details relevant only to the verification tests. General details of hardware and software will only compliment the information given in Section 4.3.

4.4.1 Specimen Details

Two steel cantilevers, V1 and V2, were used in the tests, representing single degree of freedom systems. Universal Column section 152x152x23 was used for both specimens. The heights of V1 and V2 were 1.08 and 0.95 metres, respectively, measured from the point of load application to the base of the column. An inertial mass of 32,000 Kilograms, concentrated at the tip of the cantilever was assumed in the on-line test and in the analysis. Based on the column stiffness and the prescribed mass, the natural periods were 0.43 and 0.39 seconds, respectively. Therefore, a time step of 0.02 seconds was chosen, and was used in the central difference method, to achieve both the stability requirement and the accuracy for the linear and nonlinear ranges. Table 4.3 summarises the details of the specimens.

TABLE 4.3
Specimen Details

| Specimen Reference | V1 | V2 |
|--|---------------|---------------|
| Section Type | UC 152x152x23 | UC 152x152x23 |
| Flange Width x Thickness (mm) | 152.5x6.8 | 141.4x6.07 |
| Web Depth x Thickness (mm) | 152.5x6.8 | 141.4x6.07 |
| Height L (m) | 1.08 | 0.95 |
| Stiffness $\{3EI/L^3\}$ (KN/m) | 6832.40 | 8305.80 |
| Yield Stress (N/mm ²) | 302.54 | 301.20 |
| Ultimate Stress (N/mm ²) | 445.38 | 448.32 |
| Young's Modulus E (N/mm ²) | 206,000 | 206,000 |
| Strain Hardening (%) | 1.46 | 1.48 |
| Assumed Lumped Mass m (kg) | 32,000 | 32,000 |
| Period T (sec) | 0.43 | 0.39 |

4.4.2 Experimental Set-up and Instrumentation

The self-reacting test-rig shown in Figure 4.12 was modified and used for the verification tests. A more detailed description of this testing frame is given in Chapter 5. The specimen is welded to top and bottom plates. The bottom plate is prestressed to the base plate of the test-frame by high tensile 40 mm diameter bolts to ensure total fixity. The actuator base is again firmly stressed to the reaction frame, through several plates and box sections, by 16 high strength 24 mm diameter bolts. Two low friction Instron swivel joints were used for connecting the actuator to both the reaction frame and the specimen to allow free in-plane movement. Top springs were installed to counteract the weight of the actuator. The stiffness of the springs was carefully chosen and tested so that it serves this purpose only without creating an undesirable constraint on the loading set-up. Besides, careful consideration was given to the rigidity of the test-rig as compared to the column stiffness in order to achieve accurate deflection measurements. For this purpose, a series of detailed elastic analysis of the arrangement including the loading frame was conducted and confirmed the adequacy of the design.

Plate 4.1 shows a general view of the testing set-up. An IBM/AT/286/10MHz computer with a hard disk of 40 MByte storage capacity was used for control, data acquisition and

storage. The A/D and D/A conversion boards were installed inside the computer, and operated by direct memory access (DMA). Since the boards engaged part of the actual random access memory (RAM) of the computer during the test, maximum speed and efficiency was achieved. The 12-bit A/D converters used can read up to 32 channels at a sampling speed of 32KHz. The computed displacements were converted to analogue signals by a 2 channel D/A converter of 16-bit resolution and a speed of 32KHz. Low pass filters were used to attenuate the acquired data sharply above 3 Hz to remove high frequency systematic noise that was observed especially on the force readings. This did not influence the actual data as the tests were performed at a relatively slower rate.

The performance of the electro-hydraulic equipment was carefully examined. An Instron 3375 hydraulic actuator of 113 KN static capacity (100 KN dynamic capacity) and +/- 125 mm stroke was used in the tests. A Moog servo-valve of 96 litres/minute flow rate was installed. The power pack was set to supply oil at a rate of 230 litres/minute, with a low start-up pressure of 100 psi and a high working pressure of 3000 psi. The Instron 2180 series mini-controller was used under displacement control. Limits on displacement and force readings were properly adjusted in each test. The feed-back restoring force was measured by an Instron 2518 load cell mounted on the actuator piston. The displacements measured by the internal transducer of the actuator were used in the control loop. However, they were also continuously compared to the readings of an external LVDT monitoring the structural displacements at the top of the column. Most components operated in the +/- 10 volts range, which was set to represent the maximum readings expected in each particular test in order to achieve the best possible accuracy from the available resolution.

The pause between displacement increments was suitably adjusted with the sampling speed in order to achieve two purposes. Firstly, the acquisition must be fast enough in order to pick up the actual force values before relaxation takes place. Secondly, it must not be very small to make sure that the actuator has converged to the correct command signal. In all tests a step including the ramp and hold period was completed in less than 1.5 seconds, of which the hold period is about 0.5 seconds. In inelastic tests, it is generally advisable to take a reading of all channels immediately after the completion, and a second sample after the usual wait period. If the force magnitude increases across the step, and the immediate reading has a larger magnitude than the reading after the pause, then the immediate reading is used for dynamic calculations, otherwise the second reading should be used.

Throughout the tests, the data was displayed on-line through the computer screen and digital plotters. The screen output was divided into several windows, showing on-line updated graphics of the displacement history, force-displacement relationship, and digital values of step number, computed displacement, measured displacement and restoring force. Plate 4.2 shows an example for this graphical display during an on-line test. The software also allows the user to pause or abort the test at any intermediate step. This facilitates close observation of the test progression.

4.4.3 Test Procedure

A series of four pseudo-dynamic tests were carried-out, as given in Table 4.4. An impulse excitation was first applied simulating a free-vibration response in order to determine the mechanical energy dissipation in the testing system.

TABLE 4.4
Testing Sequence

| Test Number | Specimen Reference | Excitation History | Test Designation |
|-------------|--------------------|--------------------------|------------------------|
| PSD1 | V1 | Acceleration Impulse | Elastic-Free Vibration |
| PSD2 | V1 | Scaled El Centro (8%) | Transient-Elastic |
| PSD3 | V1 | Scaled El Centro (36%) | Transient-Inelastic |
| PSD4 | V2 | Full-scale Spitak (100%) | Transient-Inelastic |

Linear elastic response under earthquake excitation was then investigated. This was followed by two seismic tests in the inelastic range. The results were compared with numerical analysis. The details of these tests are presented and discussed hereafter.

4.4.4 Elastic Free Vibration Response

Figure 4.13 shows the short duration impulse applied to specimen V1. The free vibration response attained in the pseudo-dynamic test is shown in Figure 4.14. The decay observed is ascribed to the damping in the system. The pseudo-dynamic test had a friction damping related to the actuator connections and swivel joints rather than viscous damping and friction occurring in actual dynamic tests. This explains the shape of the hysteresis loops shown in Figure 4.15. As discussed in section 4.2, friction damping

has a linear decay as opposed to a logarithmic decay for viscous damping. An approximate linear envelope can be fitted in Figure 4.14 from which an estimate for the magnitude of the friction force can be obtained. In order to compensate for this effect, a numerical correction can be employed to remove the hysteretic shape shown in Figure 4.15. Alternatively, if the friction is within acceptable low levels, an equivalent viscous damping value can be chosen, and used in the analysis for realistic comparison with test results. If this equivalent value is lower than the expected viscous damping in an actual dynamic test, then the difference should be used in the pseudo-dynamic algorithm.

As mentioned before, the decay of the free vibration response is associated with friction rather than viscous damping. Consequently, it is expected that a choice of equivalent viscous damping for analytical comparisons will largely depend on the average amplitude dominating the response. To obtain a wider data base for investigating this relation, a number of additional free-vibration pseudo-dynamic tests under impulse excitations were carried out on specimen V1. The tests are identical to that presented above and follow exactly the same response patterns, but cover broader displacement amplitude levels. For each of these tests, the logarithmic decrement and the corresponding critical damping ratio was calculated for each two consecutive displacement amplitudes for both positive and negative peaks. The cumulative results are presented in Figure 4.16, which shows the relationship between the displacement amplitude and the equivalent critical damping ratio. This relationship was then used for comparing the results of the elastic seismic test with numerical analysis, as discussed below.

4.4.5 Elastic Seismic Test

The elastic response obtained from pseudo-dynamic testing with zero damping subjected to a 8% scaled El Centro S-E component acceleration time history is shown in Figures 4.17 and 4.18 (the unscaled El Centro record is shown in Figure 4.19). In order to verify the accuracy of the results, a comparison was undertaken with analytical predictions using the computer program ADAPTIC (Izzuddin and Elnashai, 1989). For the amplitudes considered, a value of equivalent viscous damping obtained directly from Figure 4.16 would be 1.1%. This value was then used in the numerical simulation which matched very closely the pseudo-dynamic response, as shown in Figure 4.17. Nevertheless, slight discrepancies are observed in the response at small amplitudes, as expected, where the actual damping would be slightly higher than the prescribed value. This comparison demonstrates the accuracy of the pseudo-dynamic procedure used, since the method is very sensitive in the elastic range due to the significance of viscous and Coulomb damping.

Although considerable friction damping was observed in elastic tests, viscous and friction damping become insignificant as the specimen deforms inelastically. Besides, as pointed out before in section 4.2, the significance of friction damping depends upon the relative magnitude of the ratio between the friction force and the stiffness with respect to the displacement amplitudes under consideration. Consequently, if the frictional force and the stiffness remain constant, the influence of friction damping becomes less significant as the displacement amplitude increases. In other words, the influence of friction damping is generally negligible if the system is relatively stiff or if considerable inelastic deformations occur.

4.4.6 Inelastic Tests

As discussed before, the results of the pseudo-dynamic tests in the inelastic range should be more accurate than in the elastic range. In inelastic tests the effect of Coulomb and viscous damping diminishes and the energy dissipation characteristics becomes dominated by hysteretic damping, which is directly accounted for in any pseudo-dynamic test. Consequently, after achieving very accurate results in the elastic tests, even better results are to be expected in the inelastic tests

The inelastic pseudo-dynamic response of specimen V1 under a 36% scaled El Centro S-E record is shown in Figures 4.20 and 4.21, and the analytical force-displacement relationship is shown in Figure 4.22. The second specimen V2 was tested under the horizontal component of the Spitak (Armenia, USSR) earthquake of 7 December 1988, obtained from Gukasyan station. The acceleration record is given in Figure 4.23. Figures 4.24, 4.25 and 4.26 show the experimental and analytical response under the Armenian earthquake. In this respect, use was made of the adaptive dynamic analysis code, ADAPTIC (Izzuddin and Elnashai, 1989), incorporating large displacements and material nonlinearities. The details of this computer program are presented in Chapter 7 of this thesis.

Figures 4.20 and 4.24 show the comparison between the pseudo-dynamic response and the analytical simulation. Since cyclic material testing required for the evaluation of the multi-surface plasticity model parameters has not been undertaken, the values given by Mizuno et al (1987) were used, normalized to the experimental monotonic virgin curve obtained from a coupon test. Nevertheless, the analytical and experimental results are still in very good agreement. The experimental and analytical shapes and amplitudes are

almost identical, with a slight shift attributable to inaccuracies in the analytical model parameters.

4.4.7 Experimental Error Evaluation

Detailed studies concerning the experimental and analytical error propagation in pseudo-dynamic testing are available in the literature (Shing and Mahin, 1983; Shirai et al, 1988; Nakashima and Kato, 1988). Only the main experimental error sources that were identified in this particular set-up are described in this section.

Experimental errors occur from the following three main sources:

- a. Displacement control errors, introduced by an inaccurate application of displacement from the controller-actuator closed-loop system, flexibility of specimens supports or from the resolution limits of the A/D converters.
- b. Displacement measurement errors, caused by imprecise measurement of response displacement by the transducer, electrical noises, flexibility of supports, conversion resolution limits or from geometric effects.
- c. Force measurement errors, caused by relatively high friction existing in the test set-up, by erroneous measurement of restoring forces from the load cell, or again by geometric effects.

These errors amount to the total displacement and force feedback errors which can be introduced into numerical computation used in pseudo-dynamic testing. It is important to note that the displacement feedback errors are contributed to by the displacement control errors and the displacement measurement errors. Force feedback errors, however, are contributed to by both the force measurement errors and the displacement control errors.

In the verification tests described above, the computed displacements were always used in the numerical algorithm instead of the measured ones for calculating the displacements for subsequent steps. This has ensured the avoidance of the cumulative growth of displacement feedback errors throughout the test. Nevertheless, force feedback errors are always introduced into the numerical computation. Therefore, the cumulative growth of force feedback errors is unavoidable, but has to be limited to a minimum. Although cumulative growth of displacement feedback errors can be completely avoided, force feedback errors depend largely on the magnitude of displacement control errors at each step. Consequently, in addition to minimizing the force measurement errors, the

displacement control errors have to be also reduced to small values in order to mitigate the cumulative growth in force feedback errors.

The most reliable approach to examine the accuracy of a pseudo-dynamic set-up is certainly to compare the results of preliminary linear elastic tests with exact numerical simulation. In this case the accuracy of all components is checked and verified. By using properly calibrated, and correctly positioned load-cells of high resolution and linearity, force measurement errors can be almost totally eliminated. Displacement control errors are easy to check in trial tests, by observing the difference between the computed and measured displacements, which includes both control and measurement displacement errors. In such a manner, any inherent displacement control errors or instability sources can be easily identified.

To further demonstrate the accuracy of the system, both the measured and computed displacement extracted from some of the verification test results are compared hereafter. Figures 4.27, 4.28 and 4.29 show the relationship between the computed and measured displacement in the tests. It is evident that the relationship is linear. To quantify the errors, Figure 4.30, 4.31 and 4.32 shows the error history for tests PSD1, PSD2 and PSD3, respectively. Figures 4.33, 4.34 and 4.35 show the relationship between the computed displacements and the displacement feedback errors for the same tests. It is clear that the errors are very close to that forced by the conversion limits and resolution of transducers and controllers. In other words, very high performance is achieved from the controller-actuator system, and the displacements imposed by the actuator faithfully follow the command signals.

Figures 4.36, 4.37 and 4.38 depict the relationship between the absolute computed displacement and the relative displacement feedback error, i.e. absolute error divided by the absolute computed displacement. It is evident that the relative error is significantly reduced as the displacement amplitudes increase. This is true for both the elastic and inelastic ranges. Therefore, because of the latter, coupled with the insignificance of viscous and friction damping in the inelastic range, inelastic testing should always be more accurate than elastic testing, as far as experimental error propagation is concerned.

As pointed-out before, force feedback errors are the main source for cumulative error growth. Force feedback errors can be either of systematic or random nature. Systematic errors often result from improper performance or inaccuracy of experimental equipment. Random errors can occur from many sources that are not easy to identify or interpret, but their cumulative growth can be reduced by using a smaller Δt . However, systematic

errors can cause significant cumulative error growth even when the feedback errors are relatively small, introducing either considerable damping in the response or instability.

In general, the rate of cumulative error growth with the number of integration time steps depends on the value of $\Delta t/T$ (Shing and Mahin, 1983). The larger $\Delta t/T$ is, the faster will be the error growth. Consequently, the higher frequencies of a multi-degree of freedom system are more susceptible to error propagation than the lower frequencies. In other words, error propagation becomes more severe in systems having wider frequency bands.

4.5 COMMENTARY

This chapter has described the details of the new pseudo-dynamic testing facility developed at Imperial College. It was demonstrated that reliable results can be obtained by means of accurate instrumentation and appropriate testing conditions, as well as using suitable numerical integration methods. Experimental results are very sensitive to feedback errors, especially systematic errors. Fortunately, this type of error can be eliminated or significantly reduced by using proper experimental techniques. Also, other sources of error such as strain-rate effect, damping, discretization of masses and geometric effects must be carefully studied before a pseudo-dynamic test is conducted.

The discrepancy between the computed and measured displacement is a very good indication of the magnitude of displacement control errors, and in turn of the force feedback errors, provided that reasonably accurate force measurements are ensured. This discrepancy can always be monitored during preliminary tests, and usually any unacceptable control errors or instability can be identified before a major experiment is carried-out. Nevertheless, to examine the accuracy of the integrated system it is always recommended to conduct linear elastic tests before testing in the inelastic range, which should then be compared with exact (in a numerical analysis context) analytical simulations. Considerable discrepancy indicates the presence of experimental errors, which should be reduced by suitable modification of testing equipment and techniques. As far as the experimental accuracy is concerned, the larger the inelastic displacement is, the more accurate will be the pseudo-dynamic test results.

Considerable work has recently been undertaken to further improve the accuracy and efficiency of pseudo-dynamic testing, especially in its application to multi-degree of freedom systems. This includes rapid testing techniques to overcome strain rate effects

(Thewalt and Mahin, 1988), improved experimental equipment through the use of digital instrumentation (Mahin et al, 1989) and electro-mechanical actuators (Ohi and Takanashi, 1988), and the application of unconditionally stable numerical algorithms (Mahin et al, 1989). Also, several investigations were carried-out to study the employment of substructuring techniques (Iemura et al, 1988; Nakashima et al, 1988), whereby part of a structure is tested pseudo-dynamically and the other portion is modelled analytically. Using this technique, the effects of soil-structure interaction can also be analytically modelled and included in the testing.

Having established confidence in the procedure and equipment, Chapters 5 and 6 describe the utilization of the system in testing composite steel/concrete specimens. Present work at Imperial College is directed towards the implementation of substructuring techniques in pseudo-dynamic testing, and the application of the new system in testing and analysis of multi-degree of freedom structures.

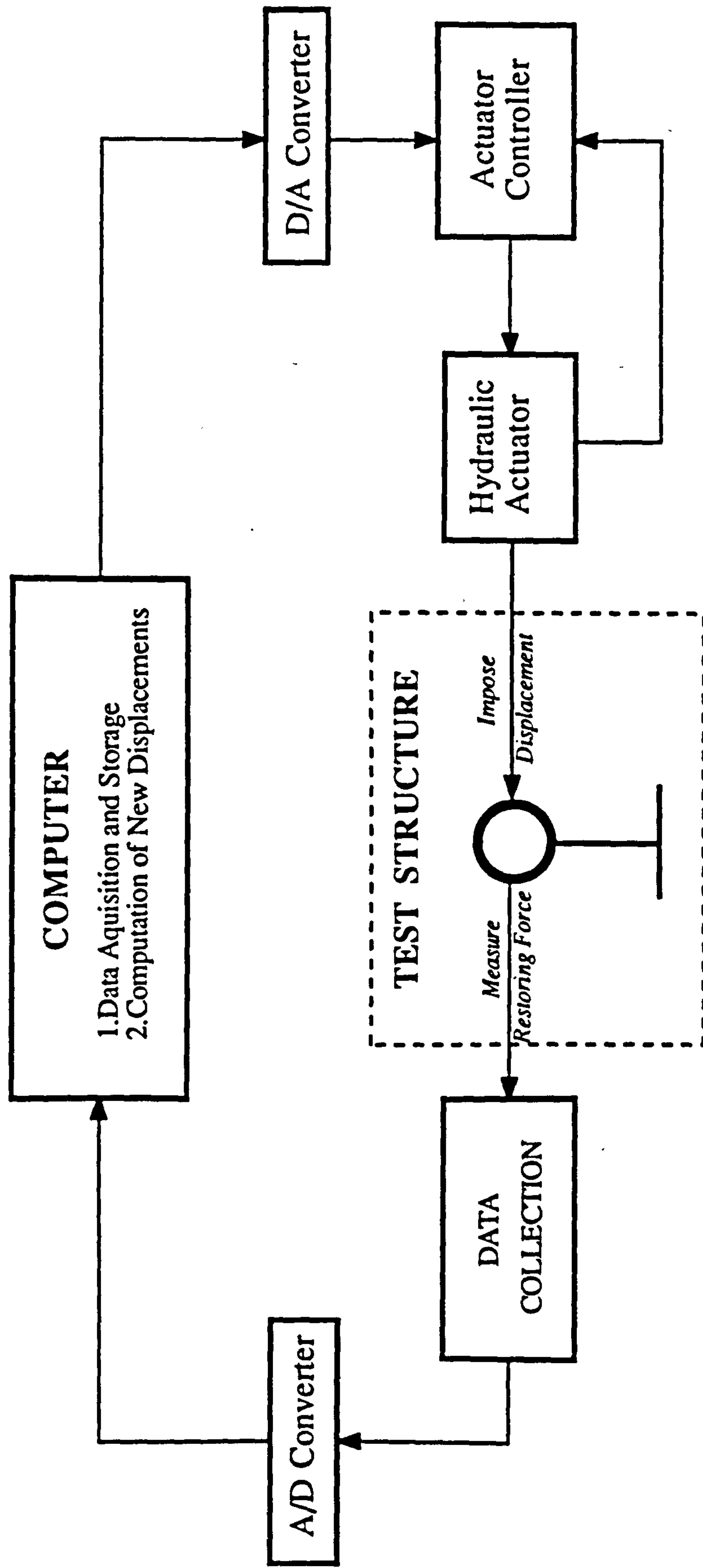


Fig. 4.1 Simplified diagram of Pseudo-dynamic test procedure

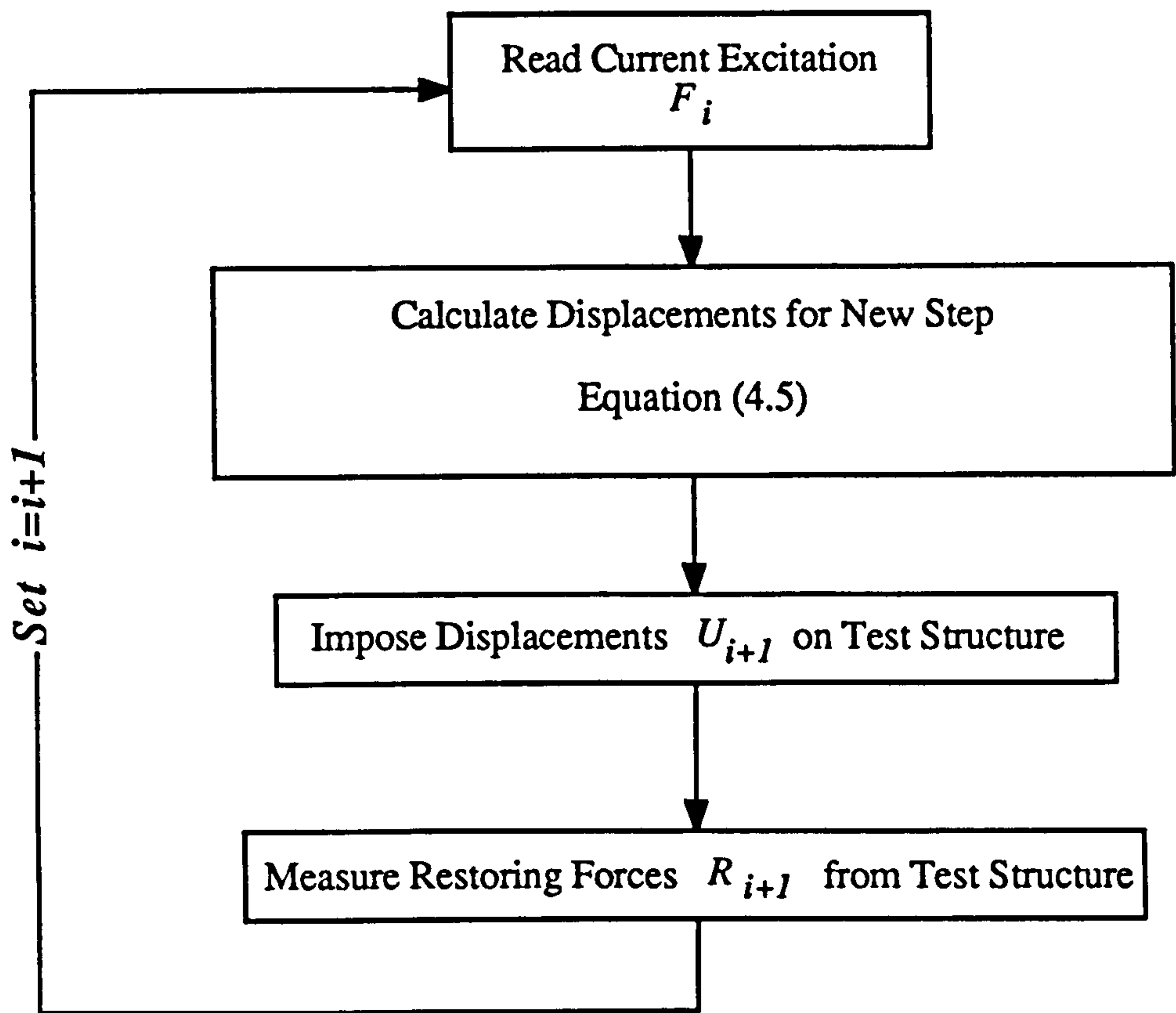


Fig. 4.2 Application of Central Difference scheme to pseudo-dynamic testing

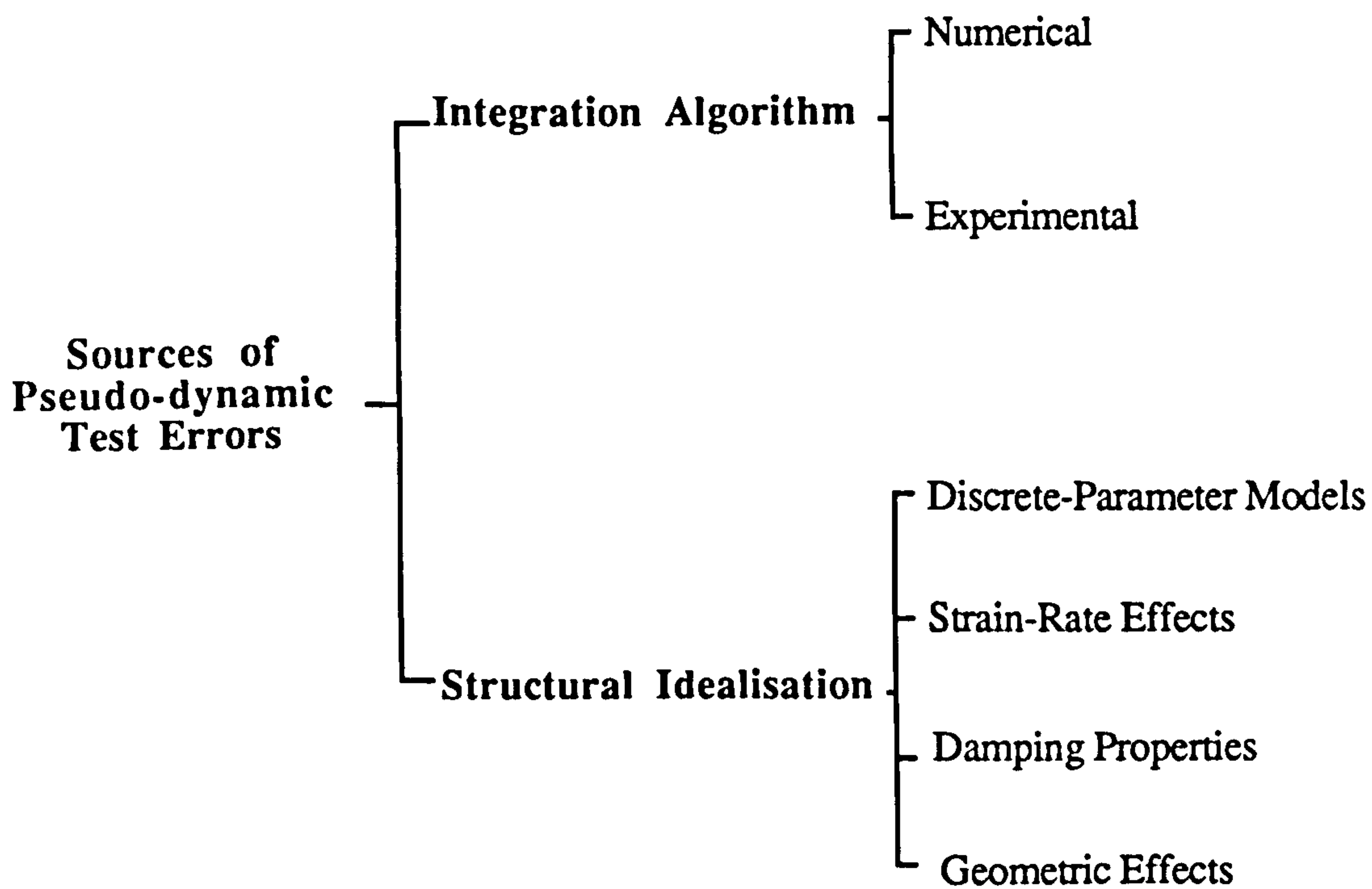
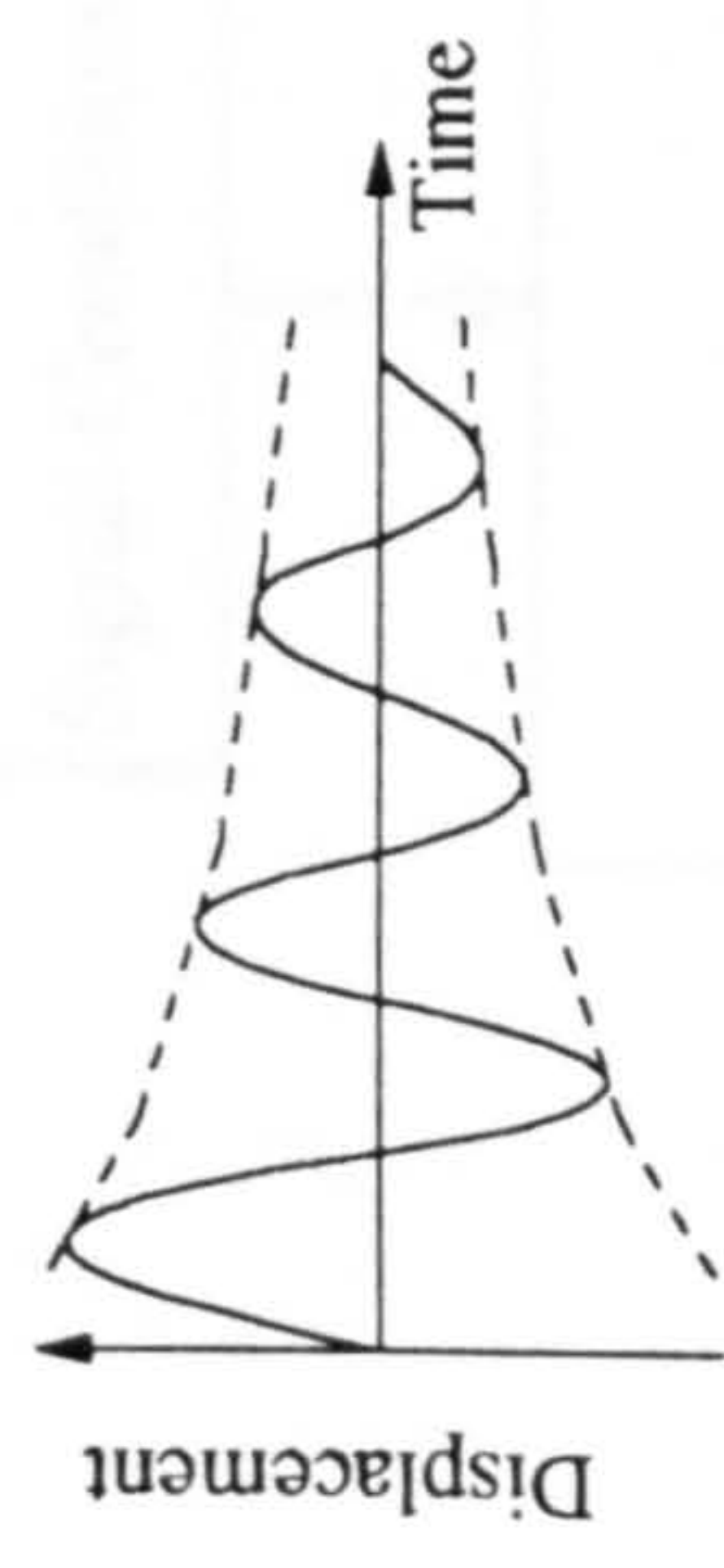
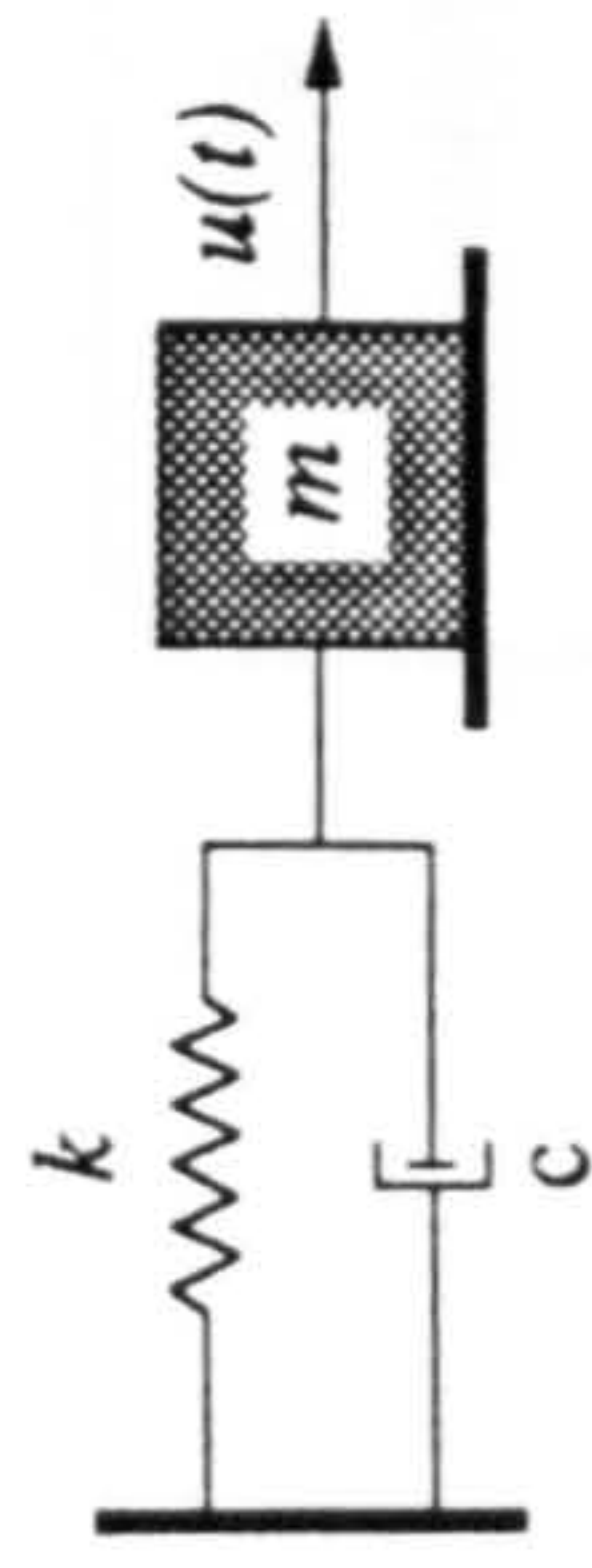
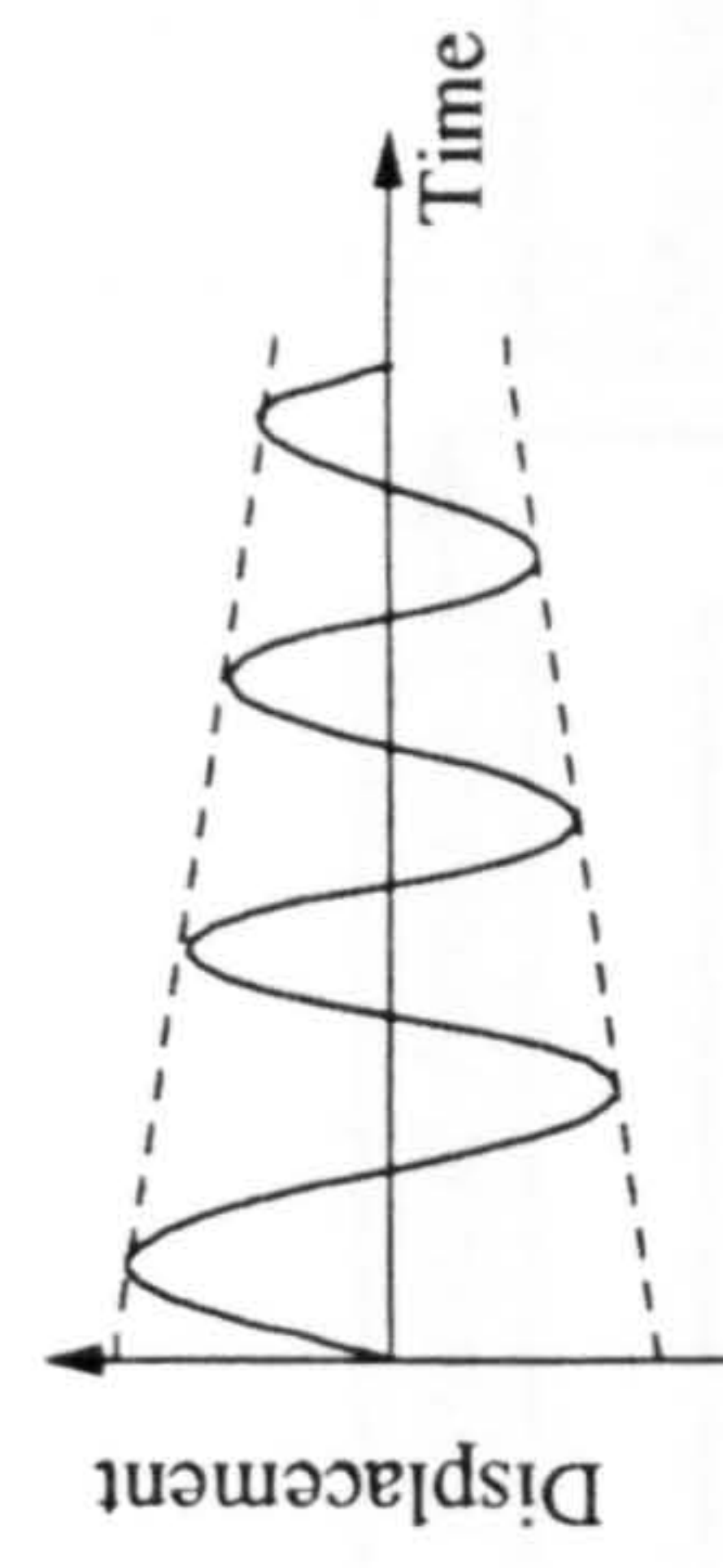
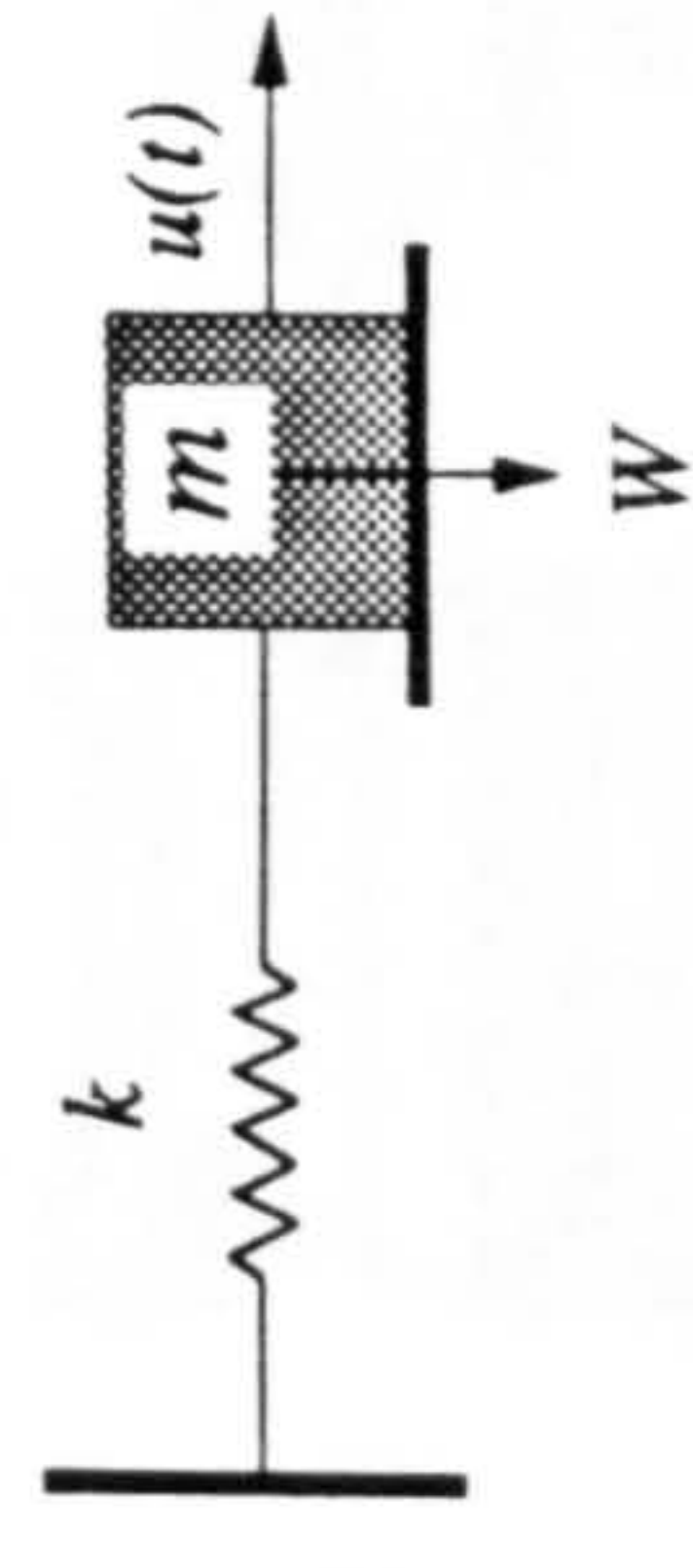


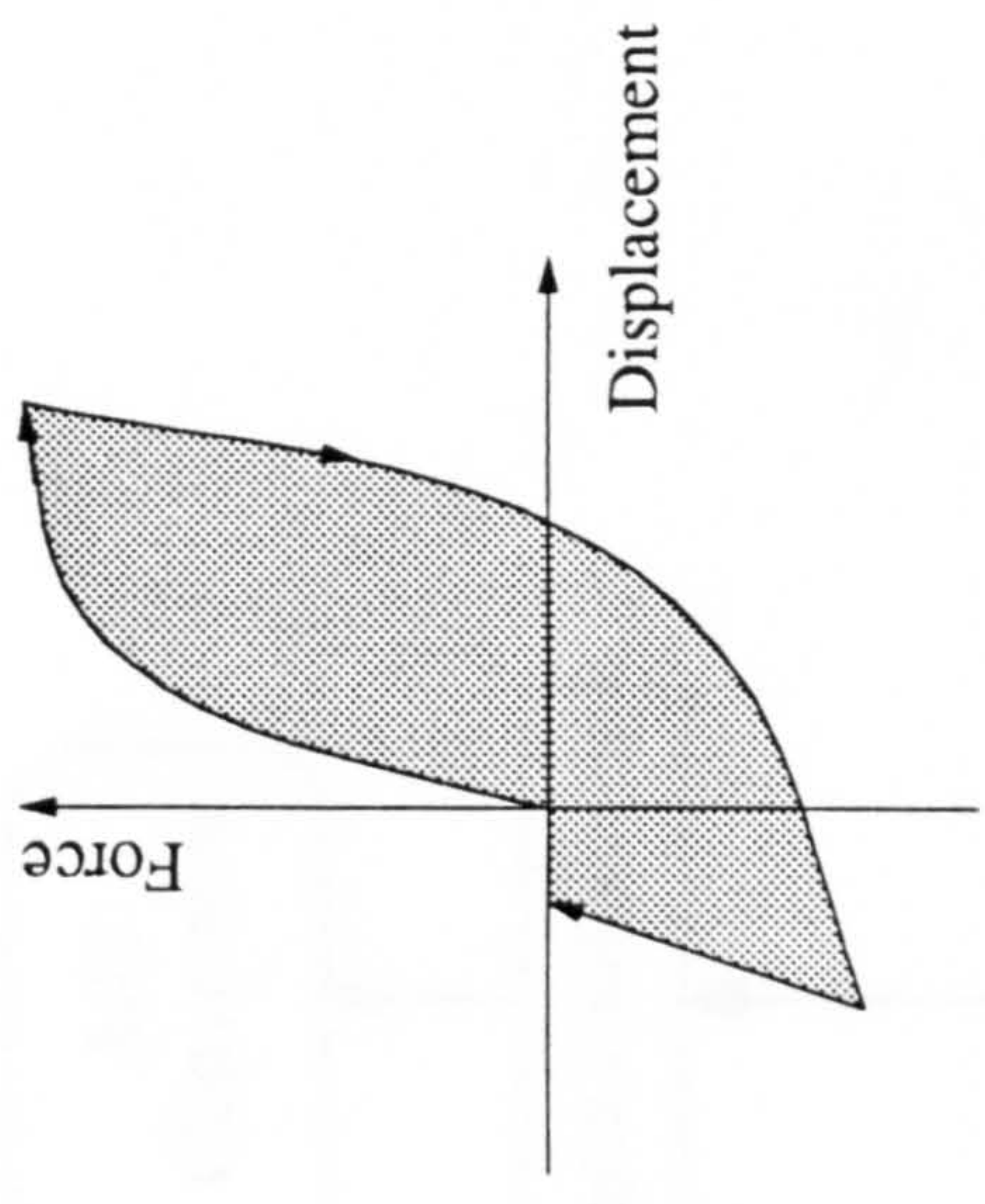
Fig. 4.3 Sources of pseudo-dynamic test errors



(a) Viscous Damping



(b) Friction Damping



(c) Hysteretic Damping

Fig. 4.4 Types of damping

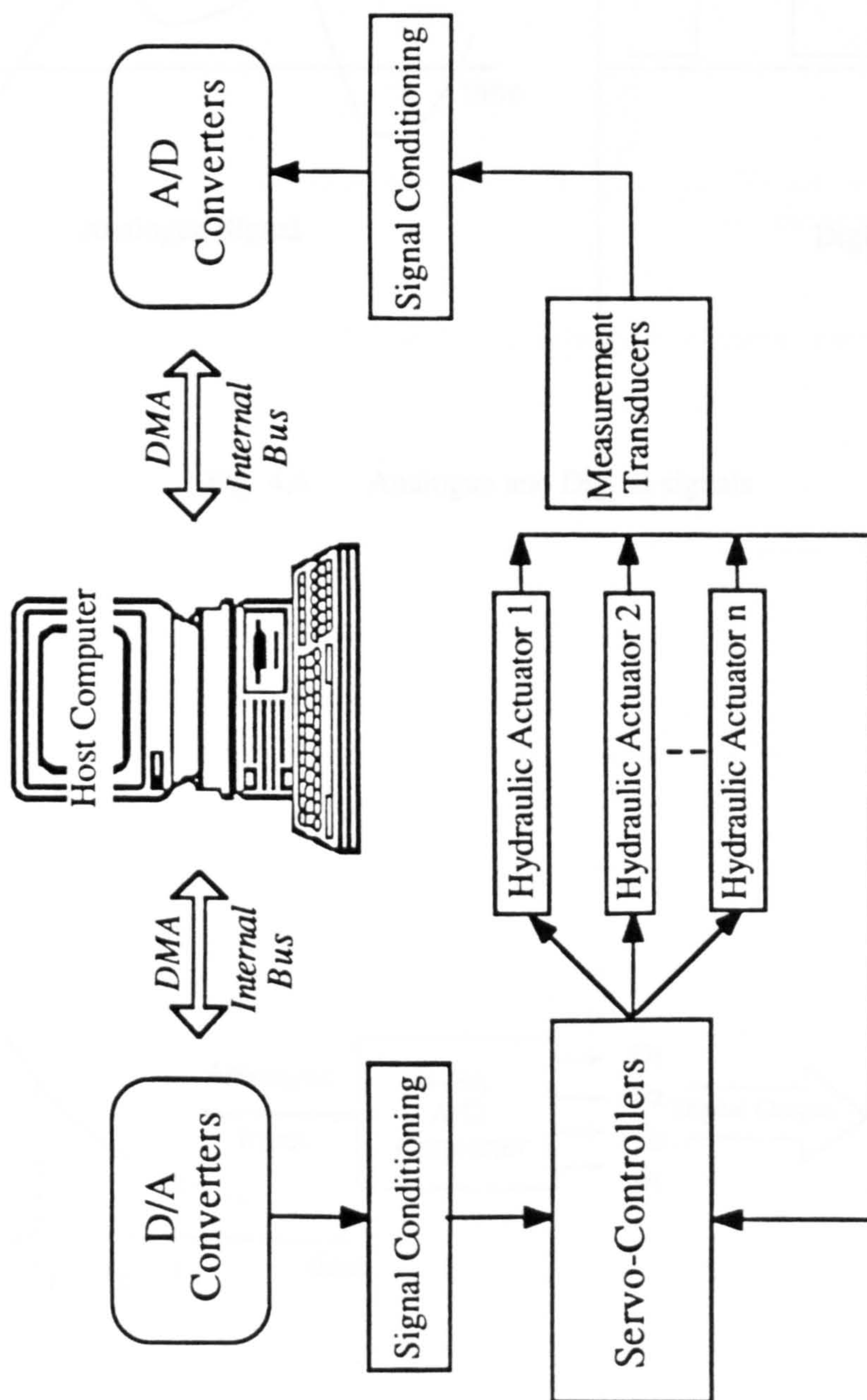


Fig. 4.5 Implementation of pseudo-dynamic testing

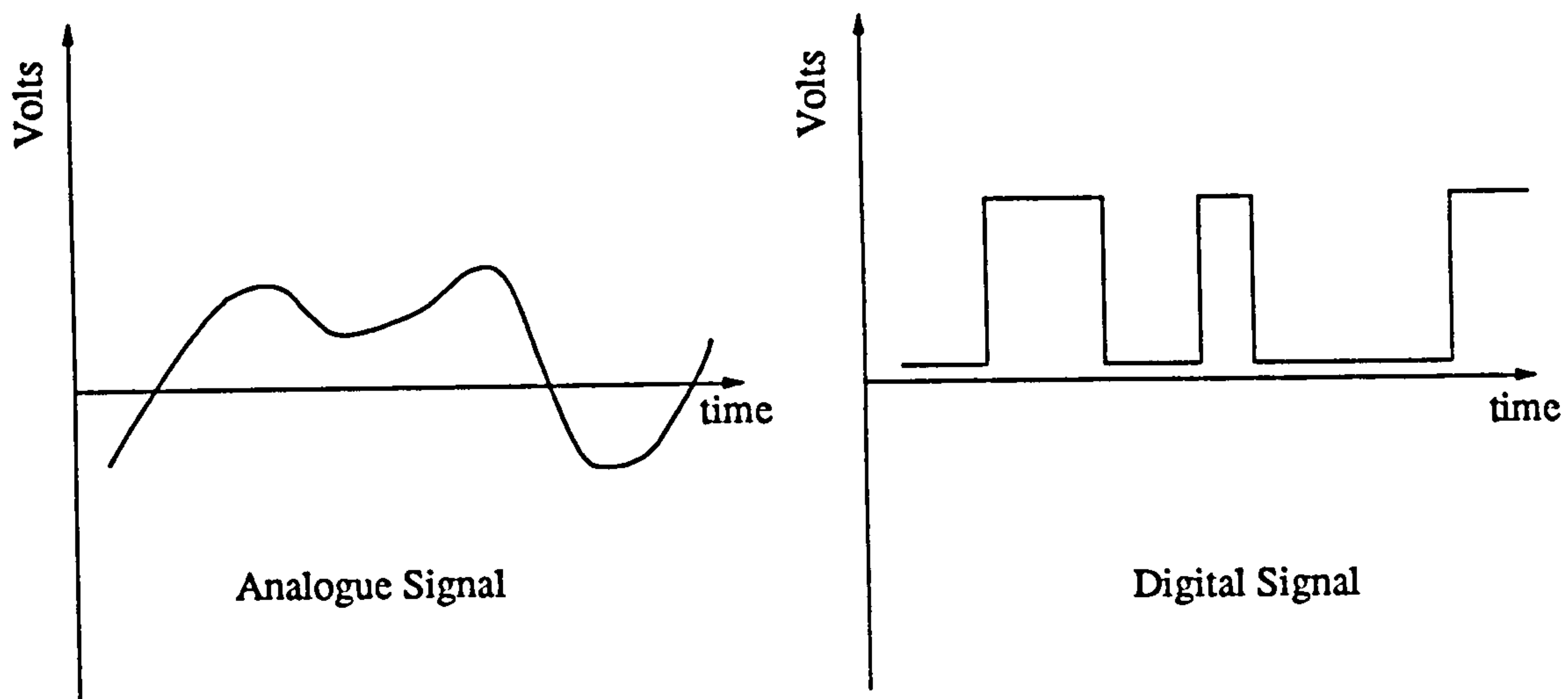


Fig. 4.6 Analogue and Digital signals

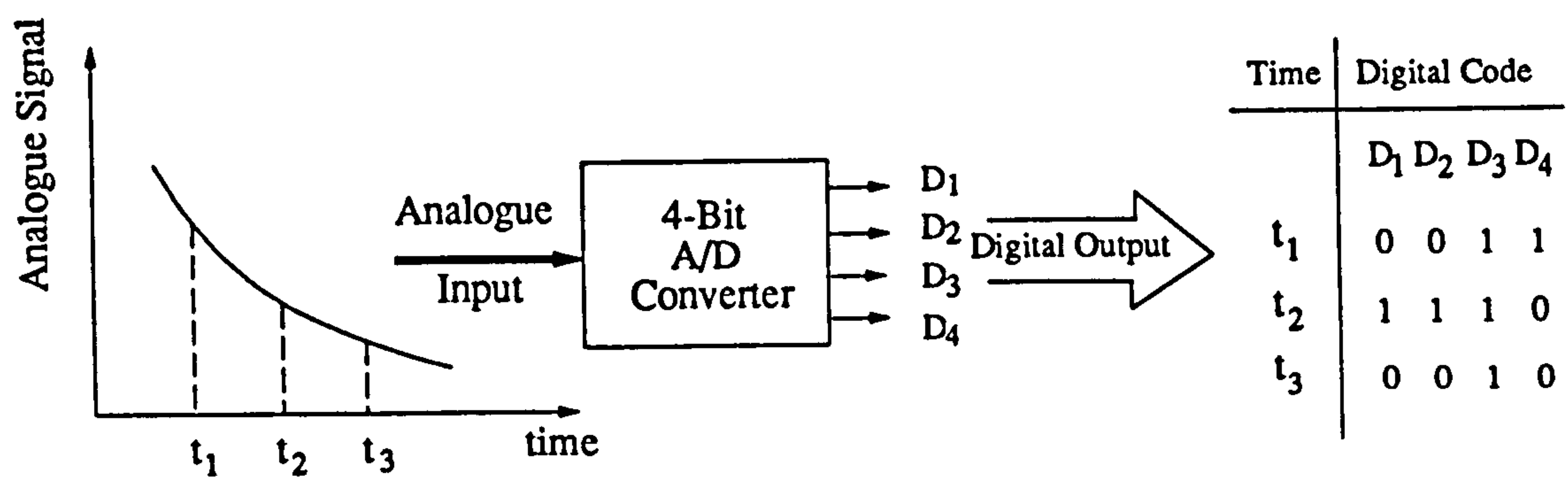


Fig. 4.7 Analogue to Digital conversion

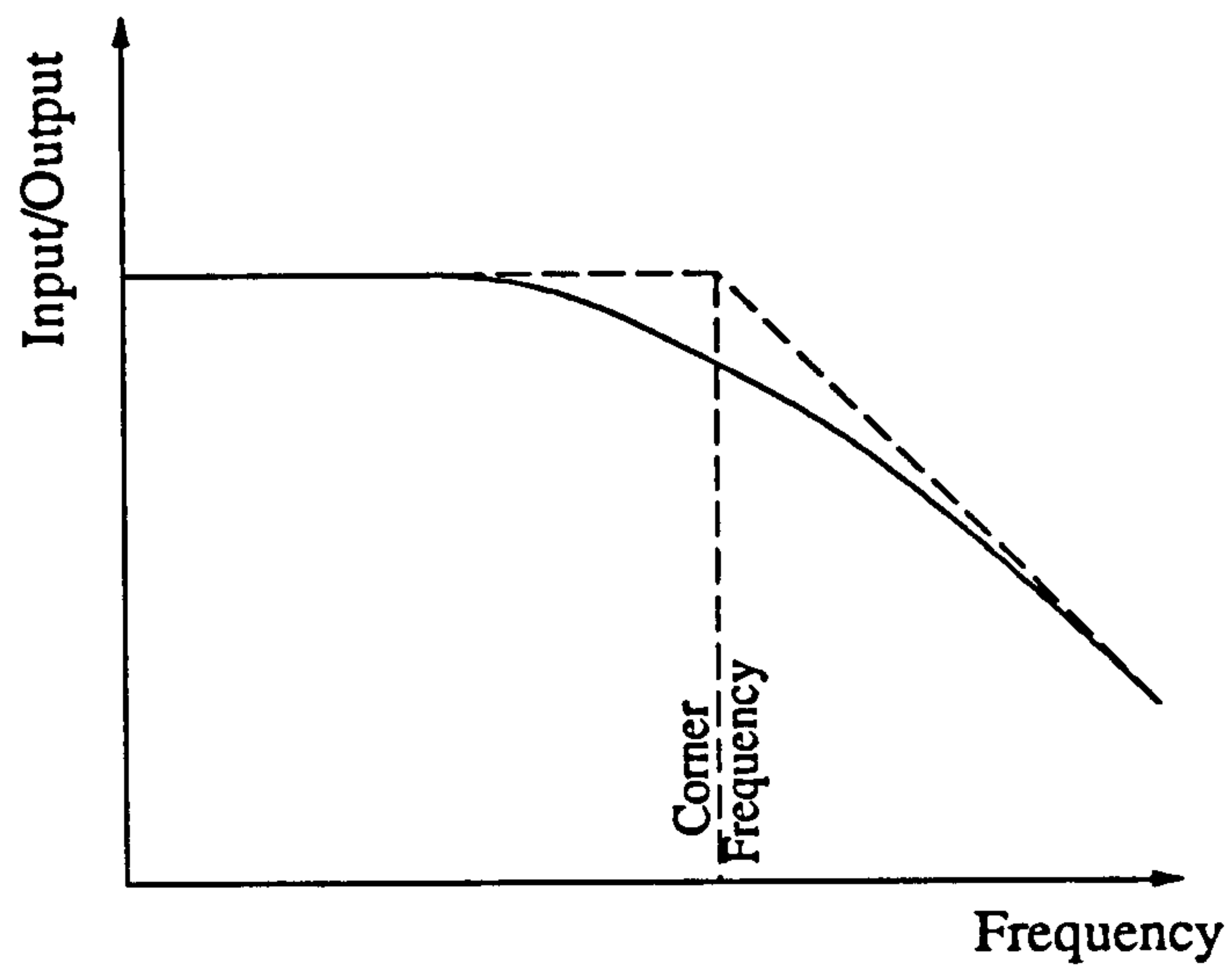


Fig. 4.8 Amplitude vs frequency plot for a low-pass filter

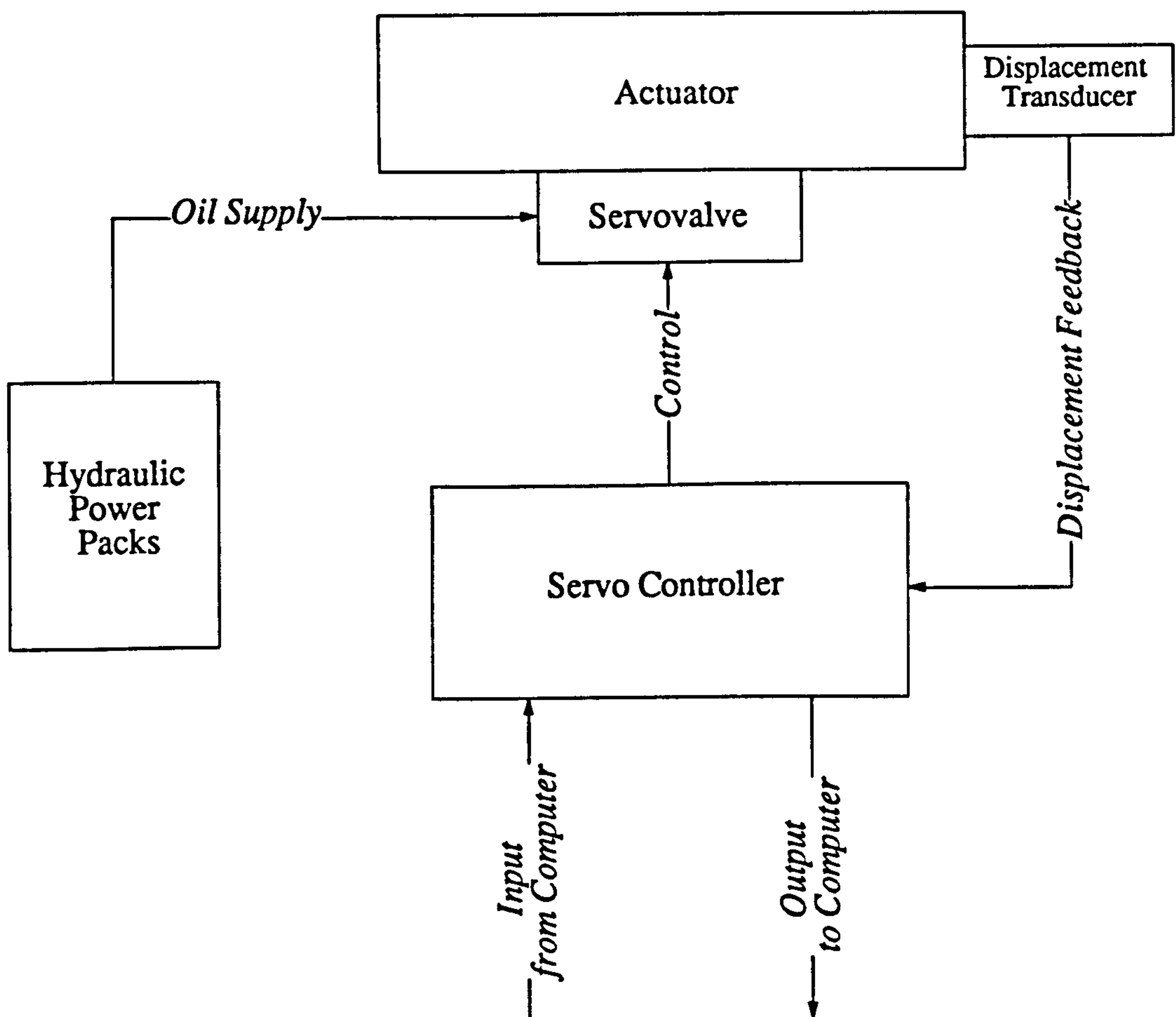


Fig. 4.9 Block diagram of Electro-Hydraulic control system

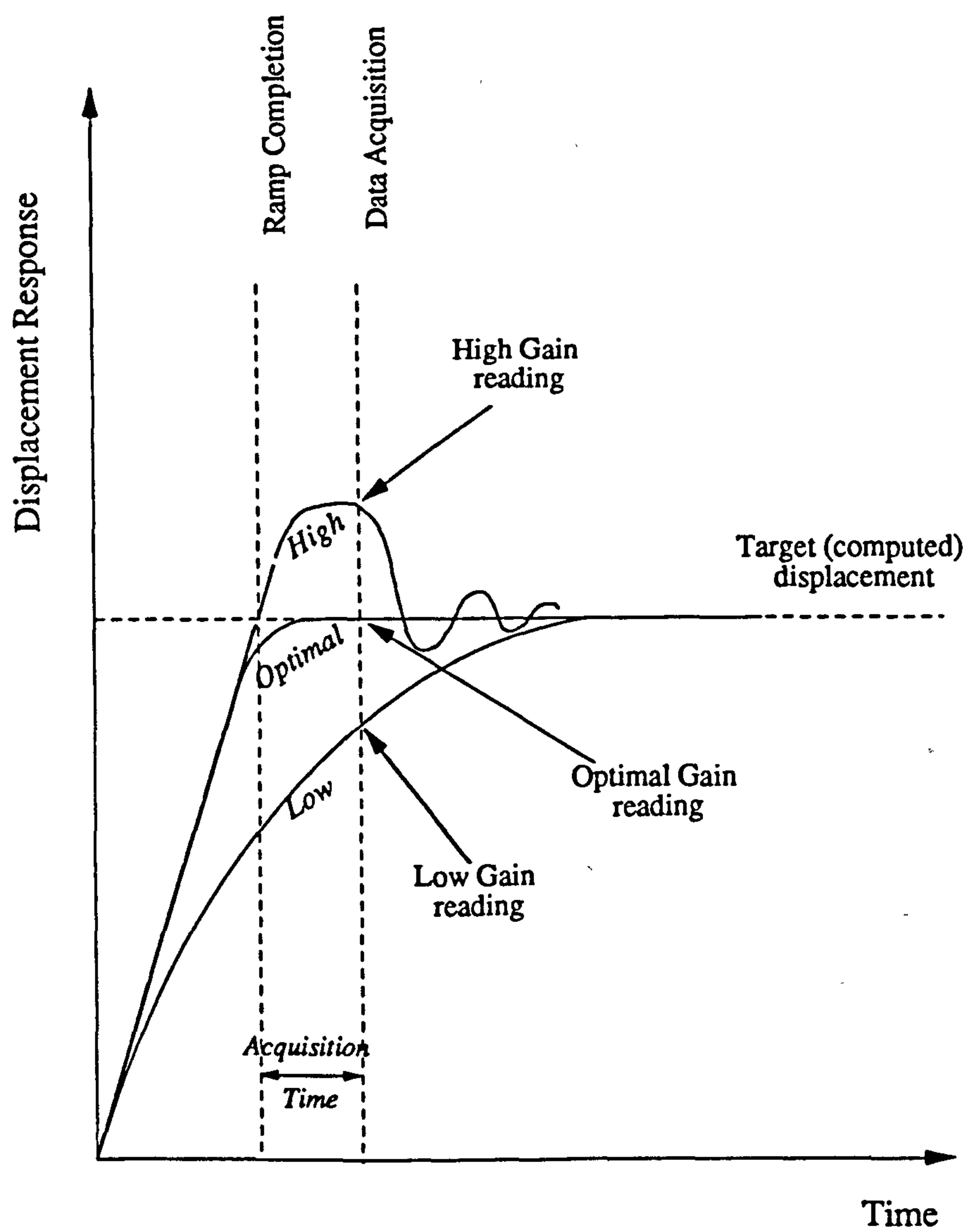


Fig. 4.10 Actuator response for different gain settings

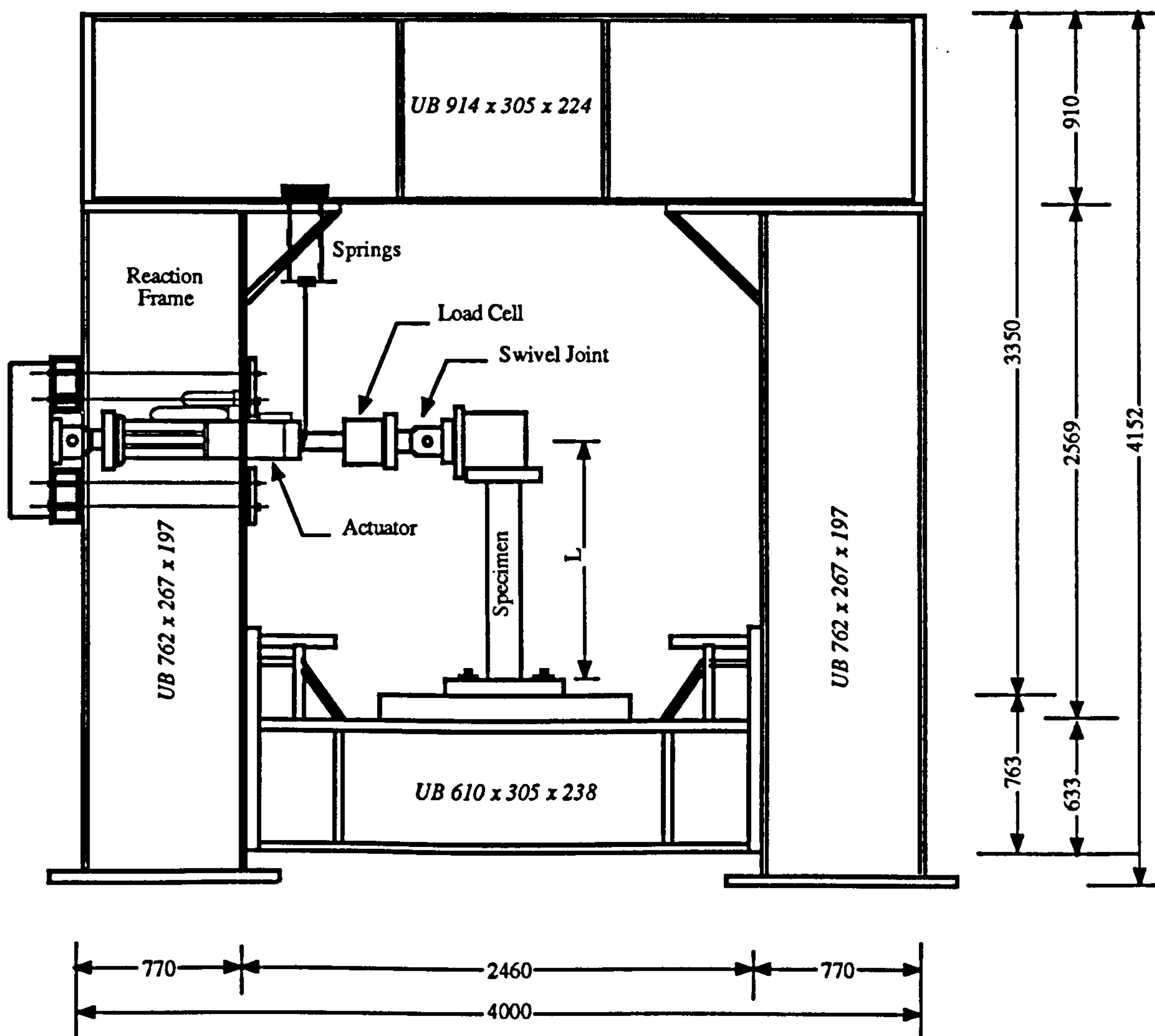


Fig. 4.12 Test-rig assembly (dimensions in mm)

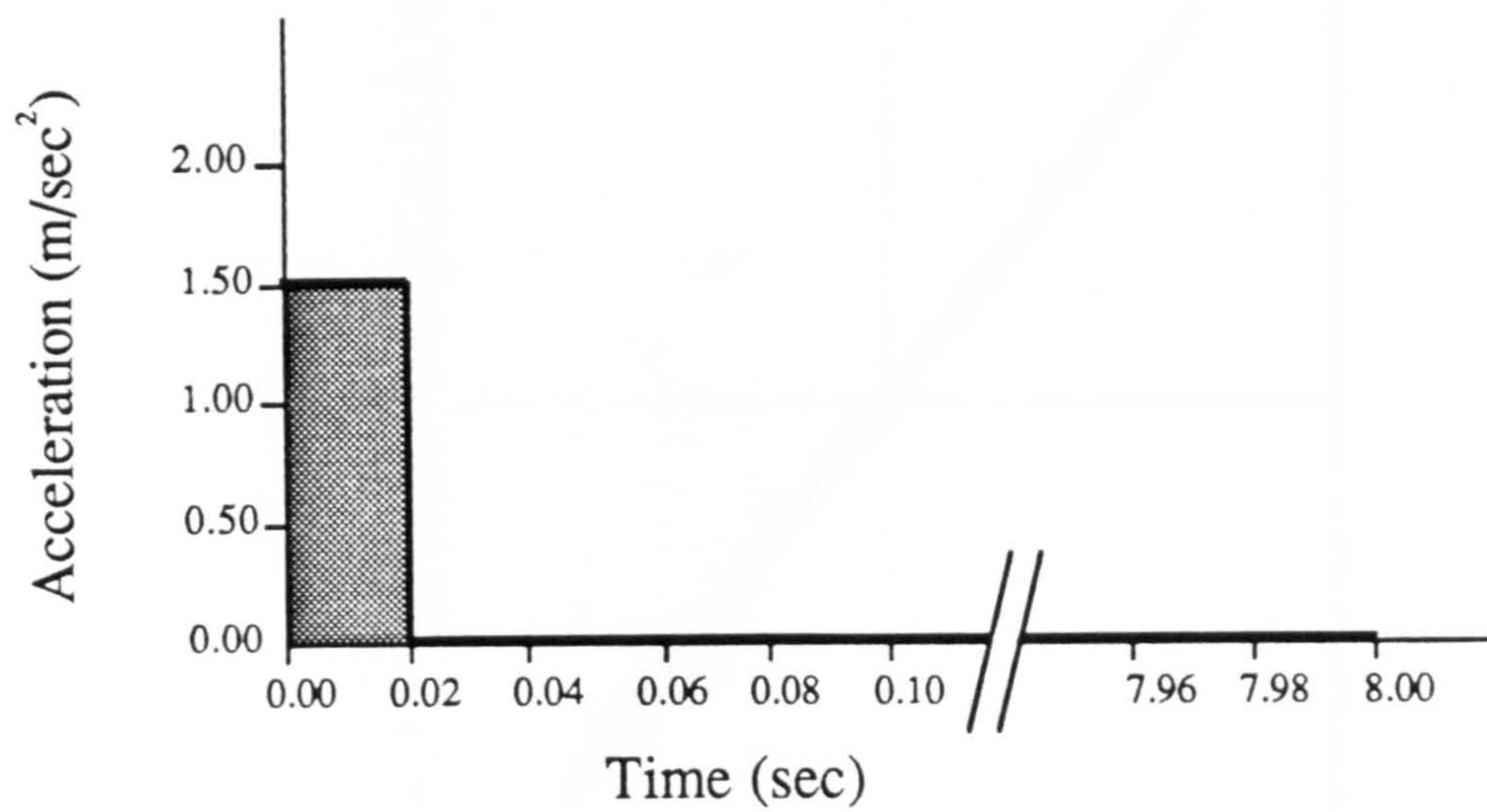


Fig. 4.13 Impulse excitation

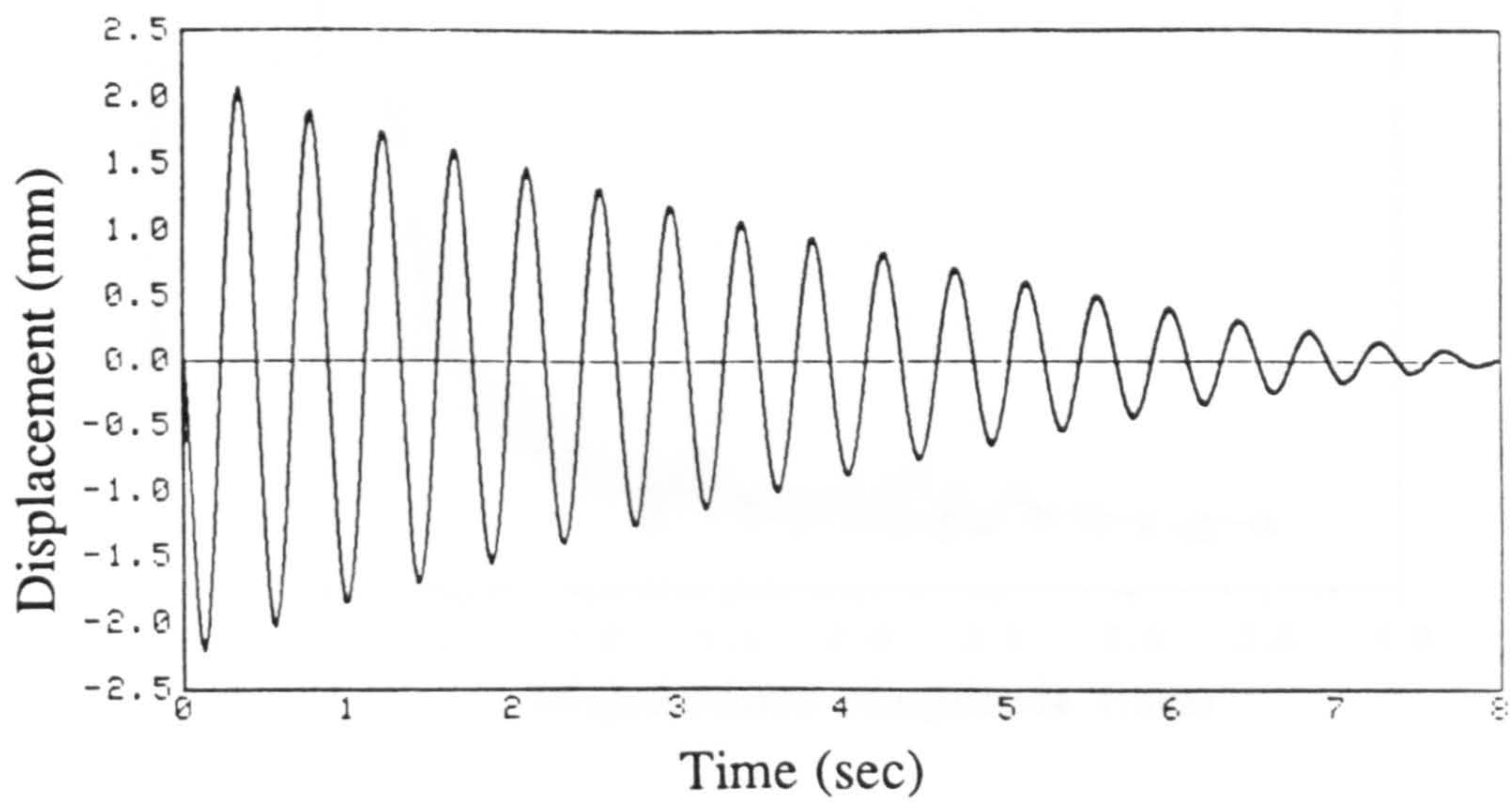


Fig. 4.14 Free vibration response of PSD1

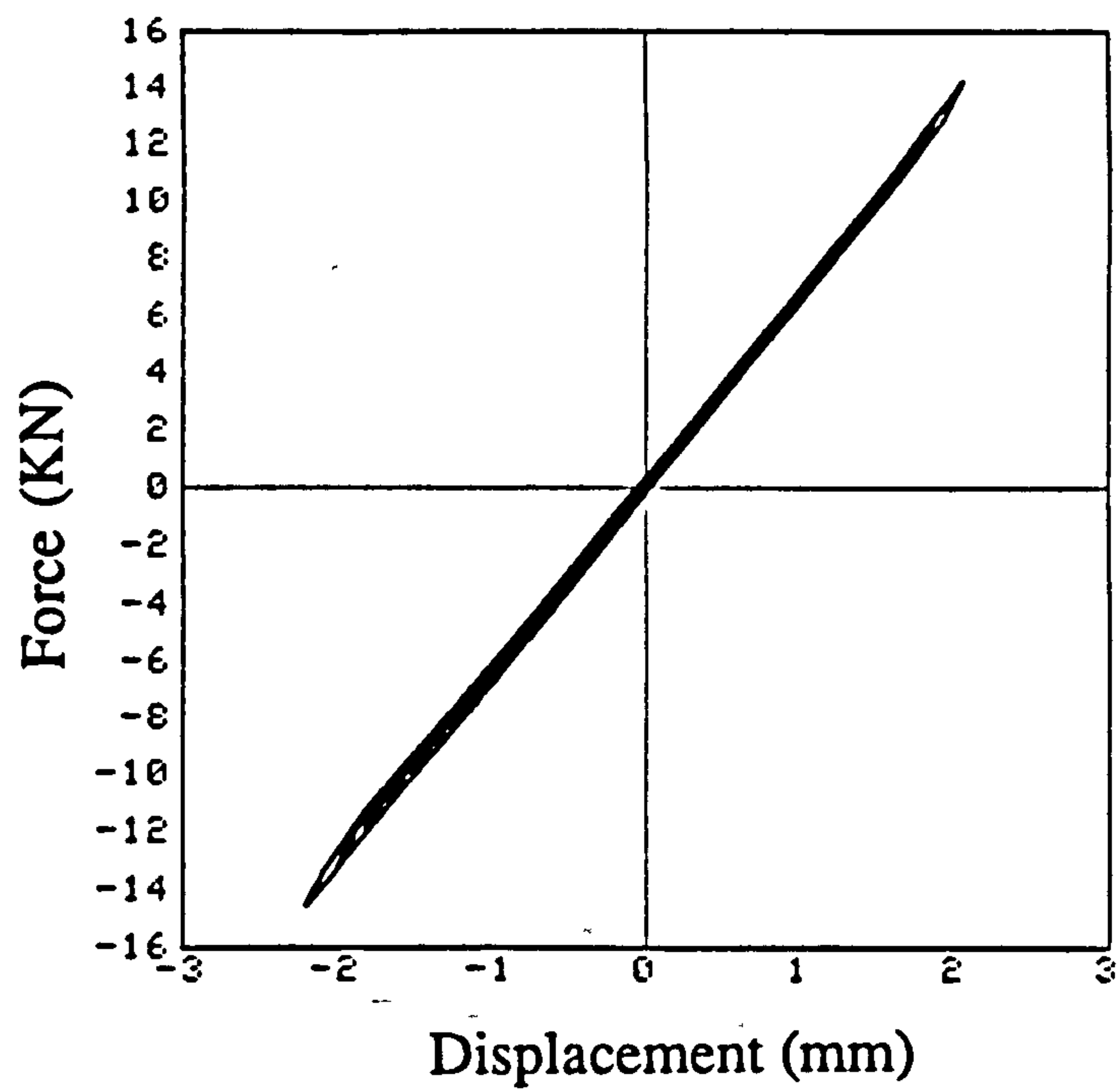


Fig. 4.15 Force-displacement Relationship for PSD1

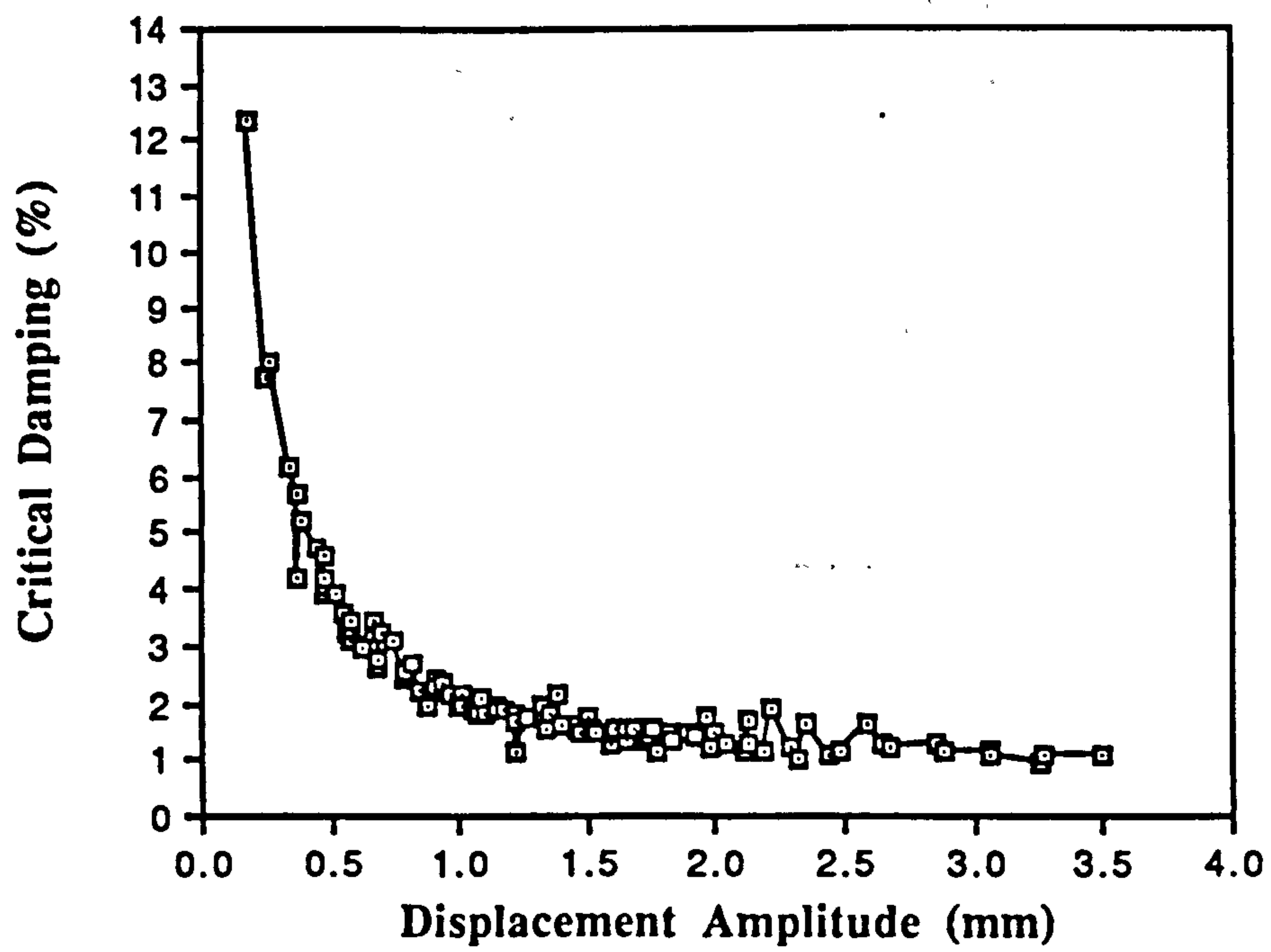


Fig. 4.16 Damping versus displacement level

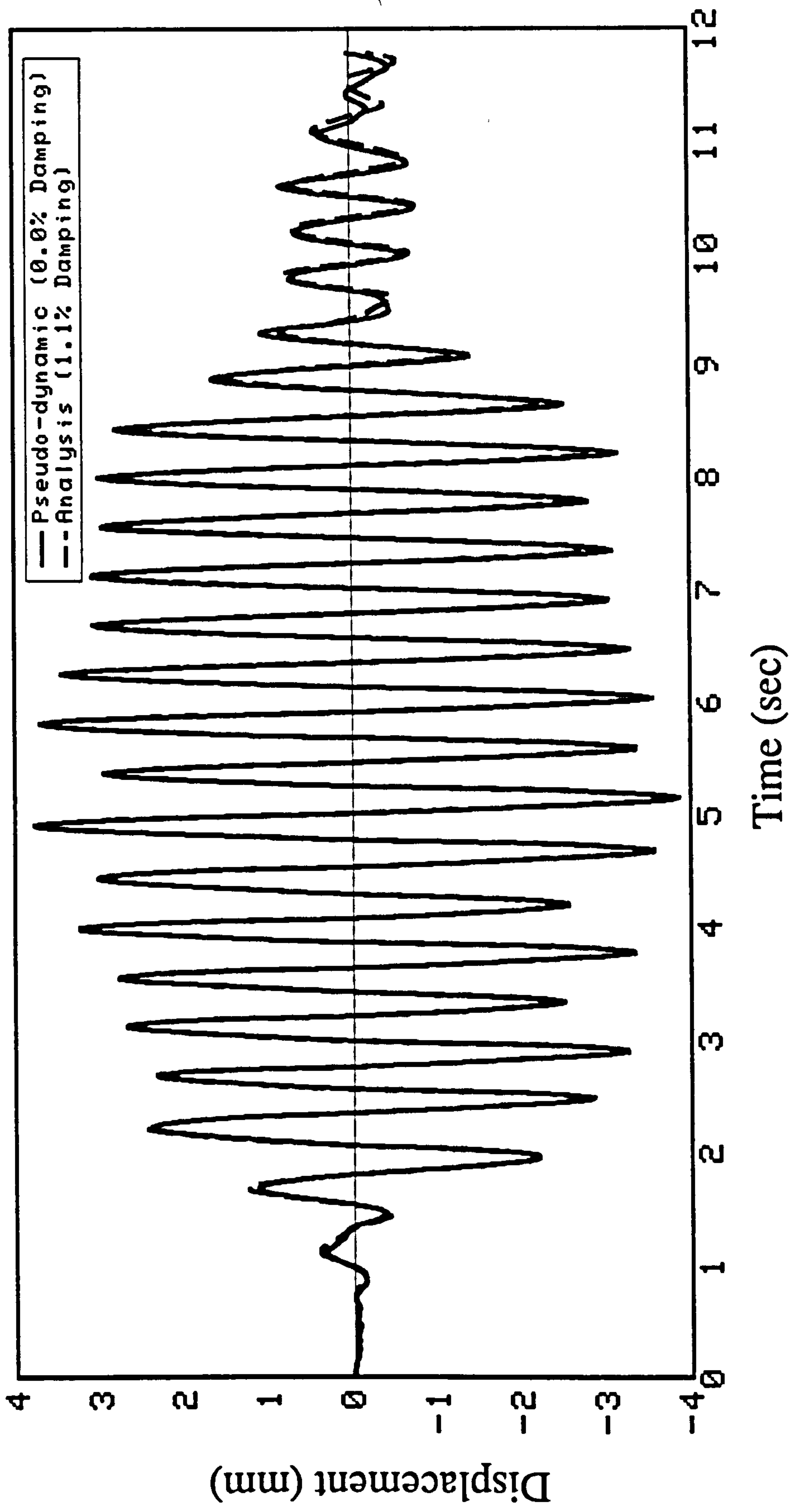


Fig. 4.17 Elastic displacement response for test PSD2

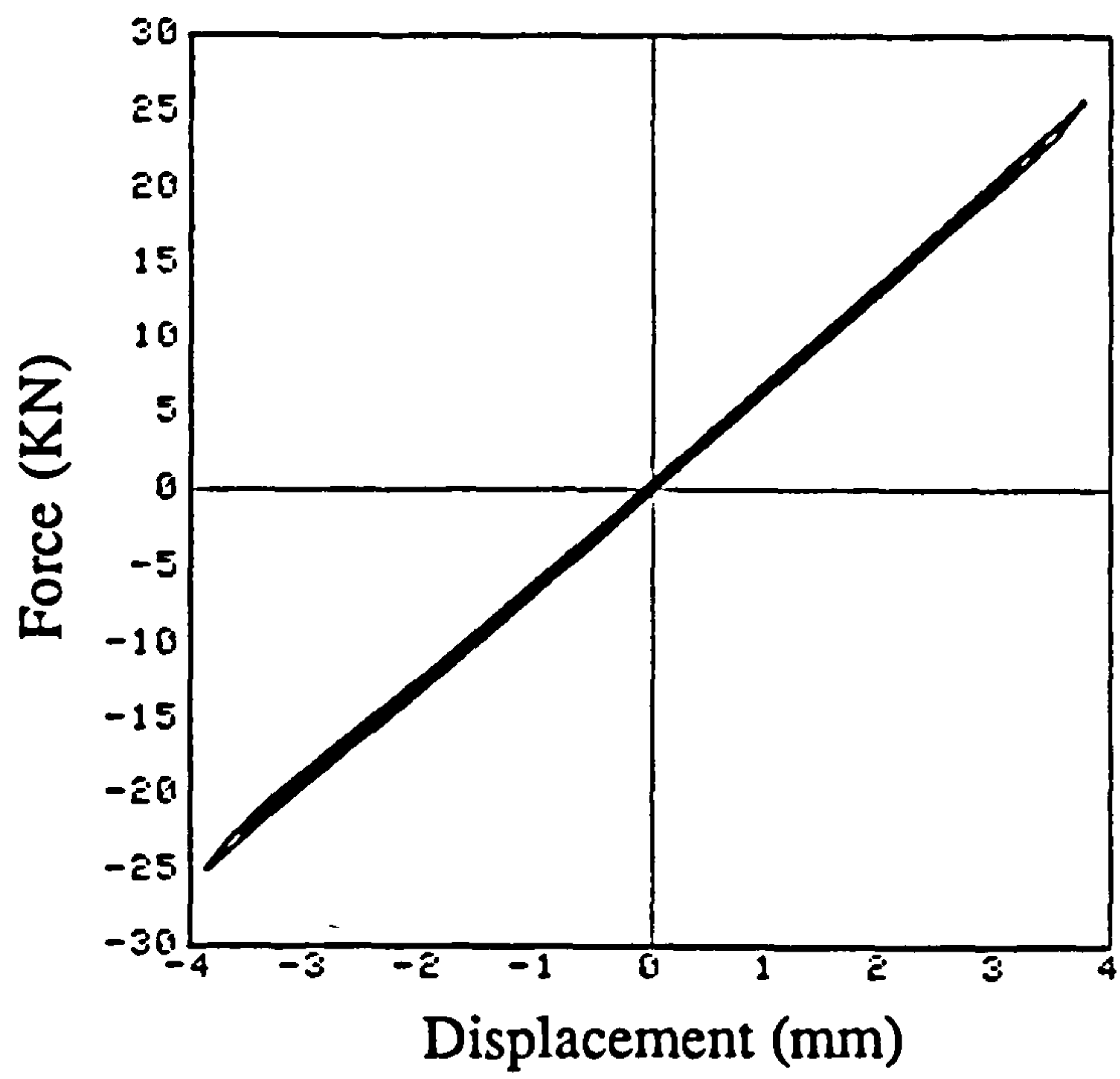


Fig. 4.18 Force-displacement relationship for test PSD2

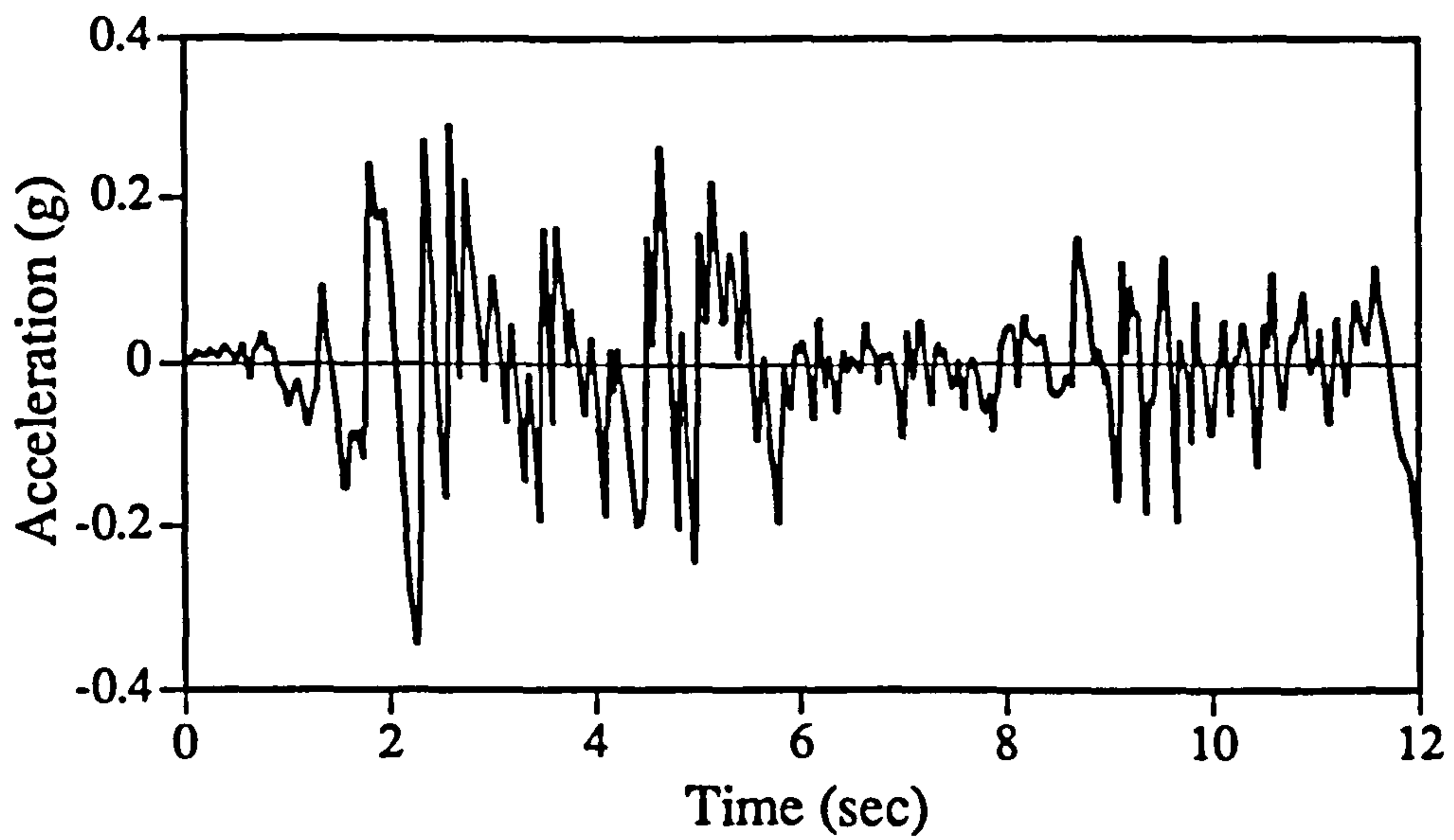


Fig. 4.19 El Centro acceleration time history record

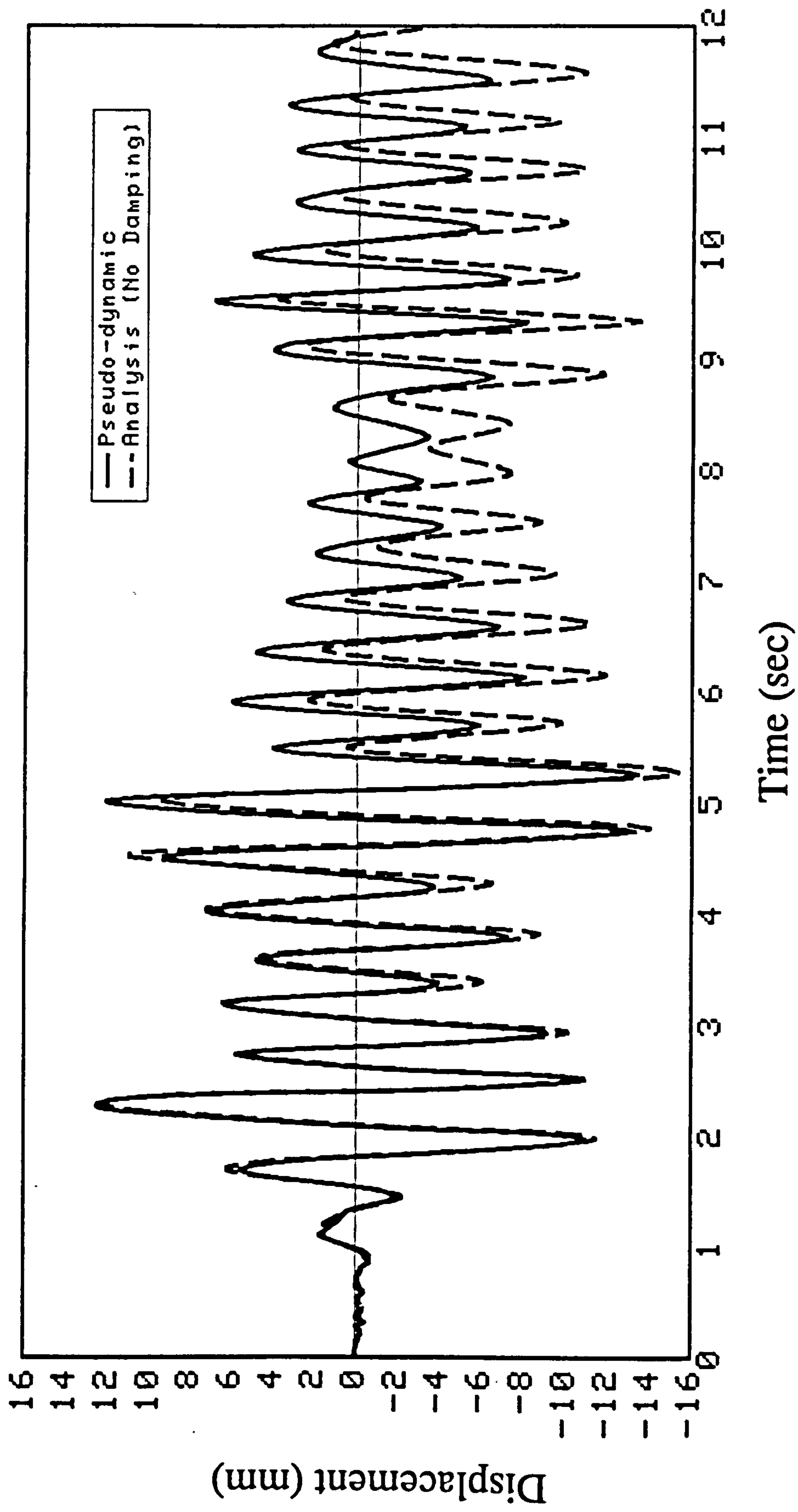


Fig. 4.20 Inelastic displacement response for PSD3

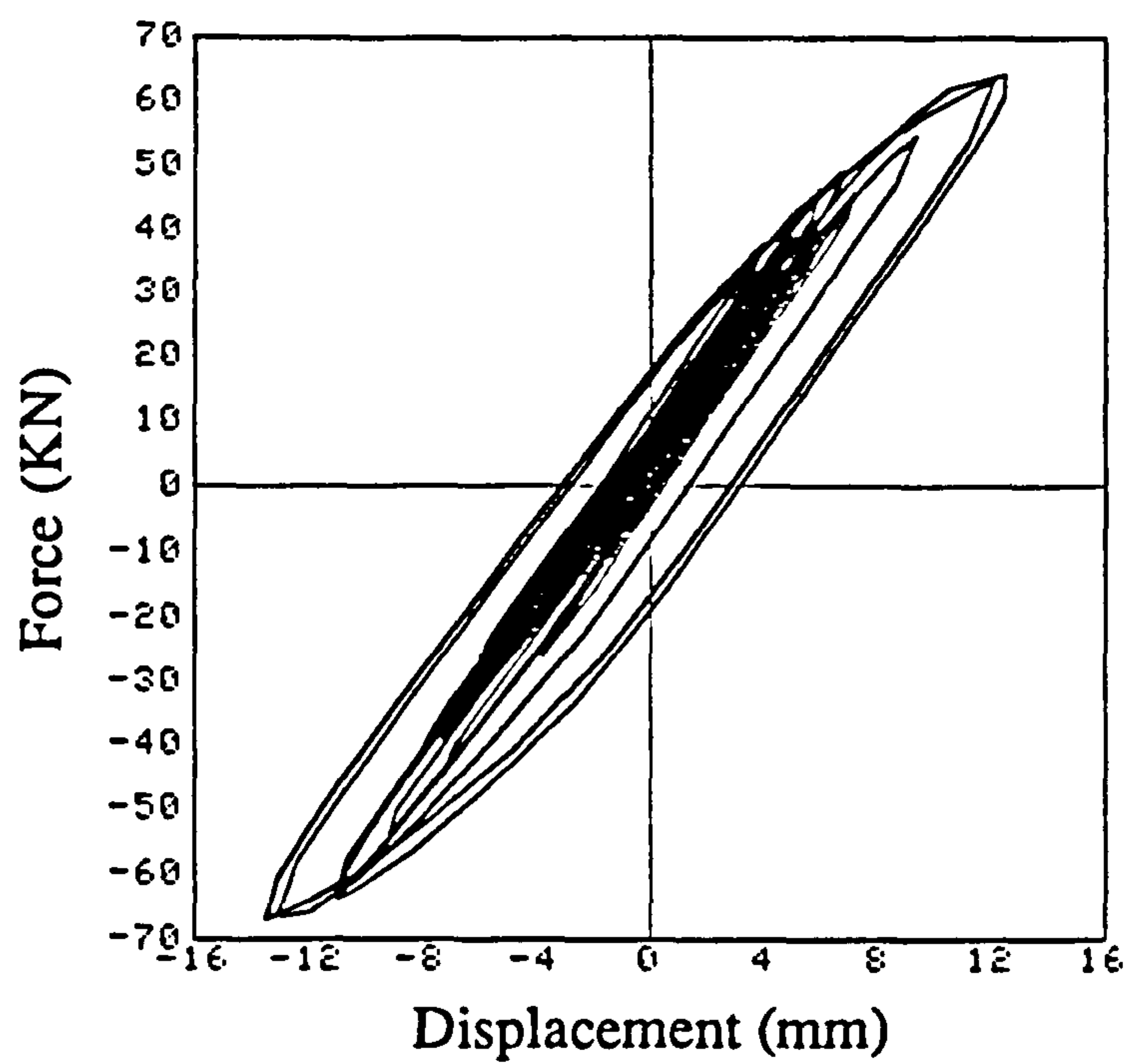


Fig.4.21 Experimental force-displacement relationship for PSD3

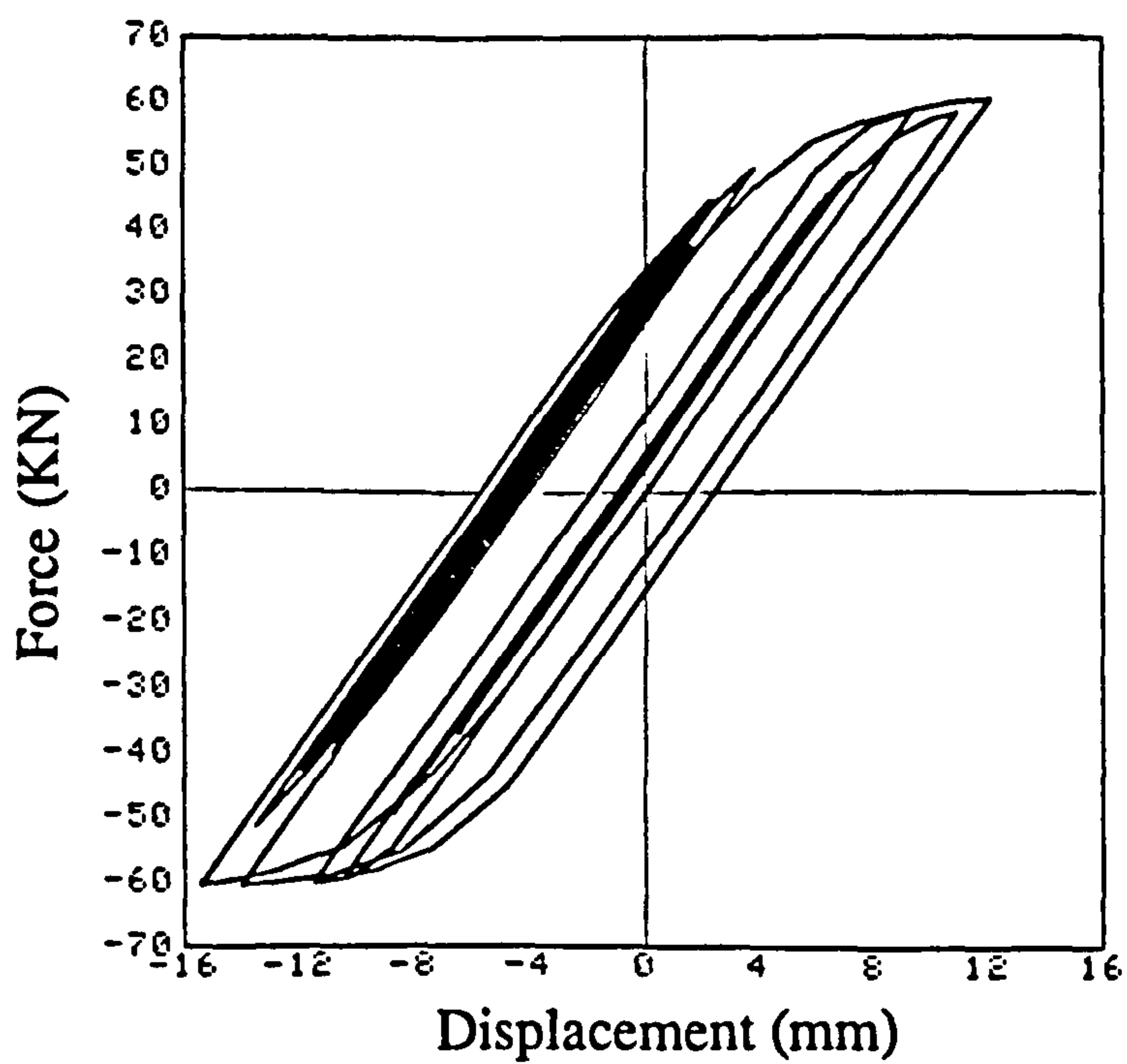


Fig. 4.22 Analytical force-displacement relationship for PSD3

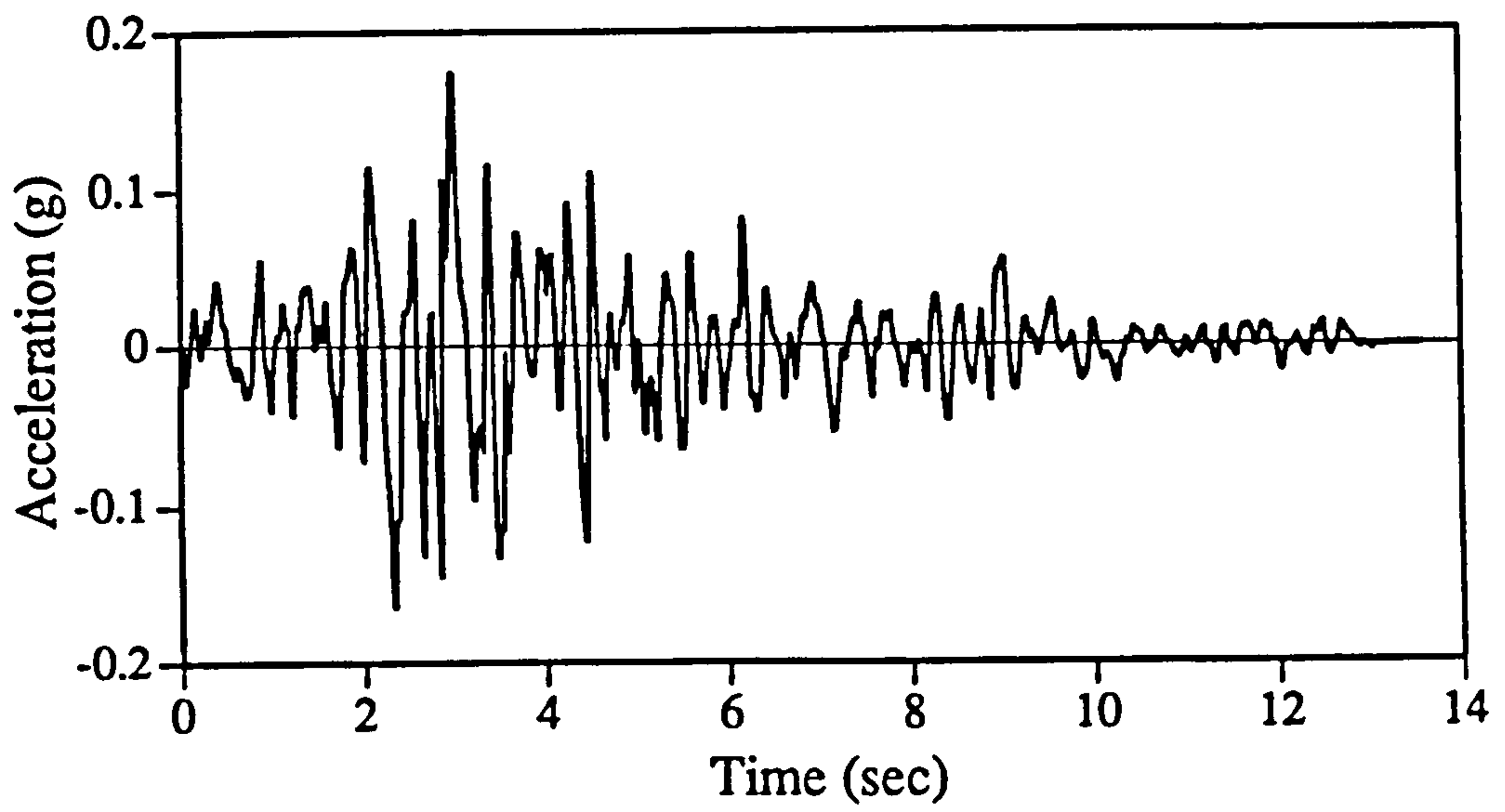


Fig. 4.23 Spitak acceleration time history record

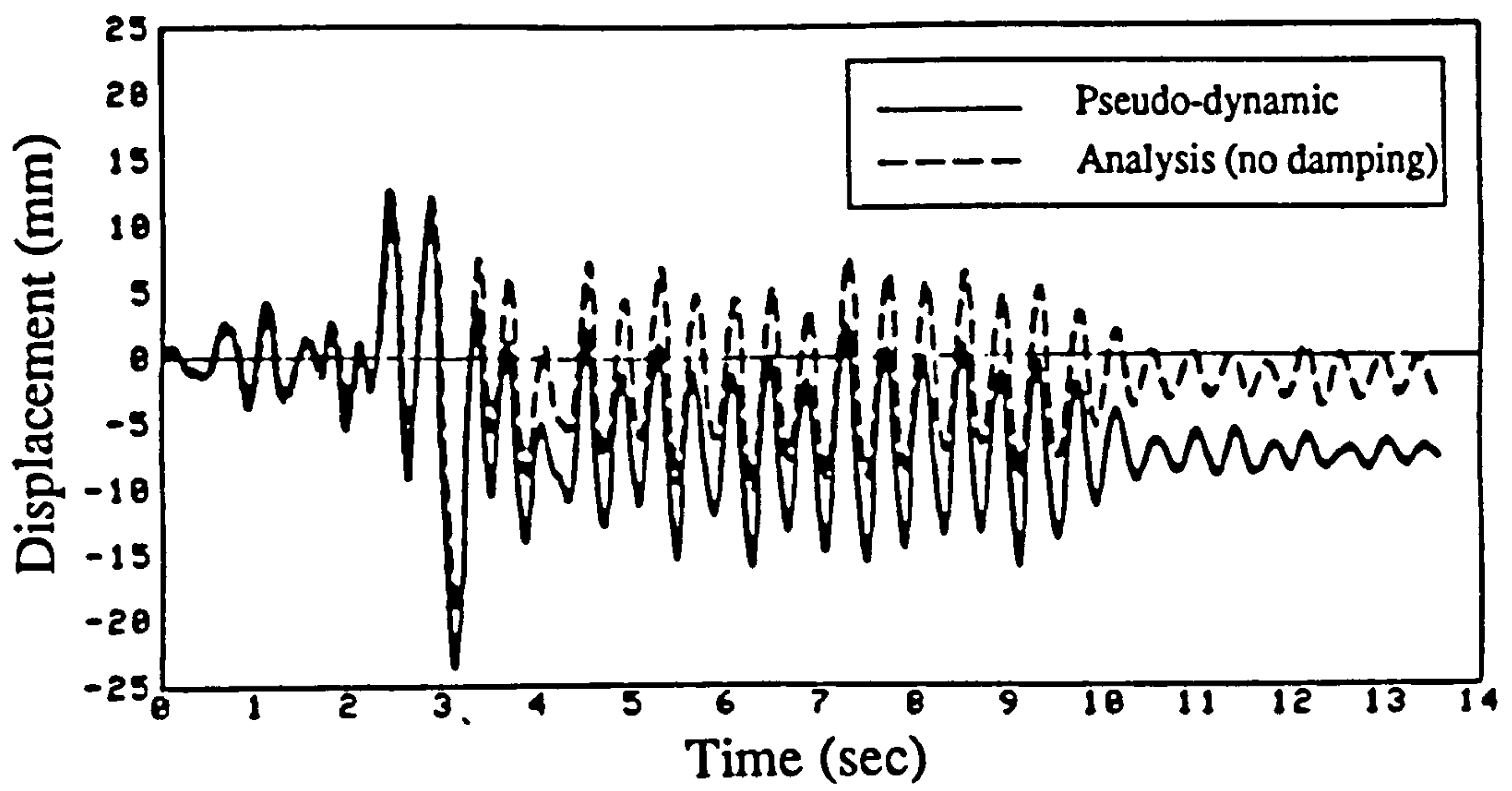


Fig. 4.24 Inelastic displacement response for PSD4

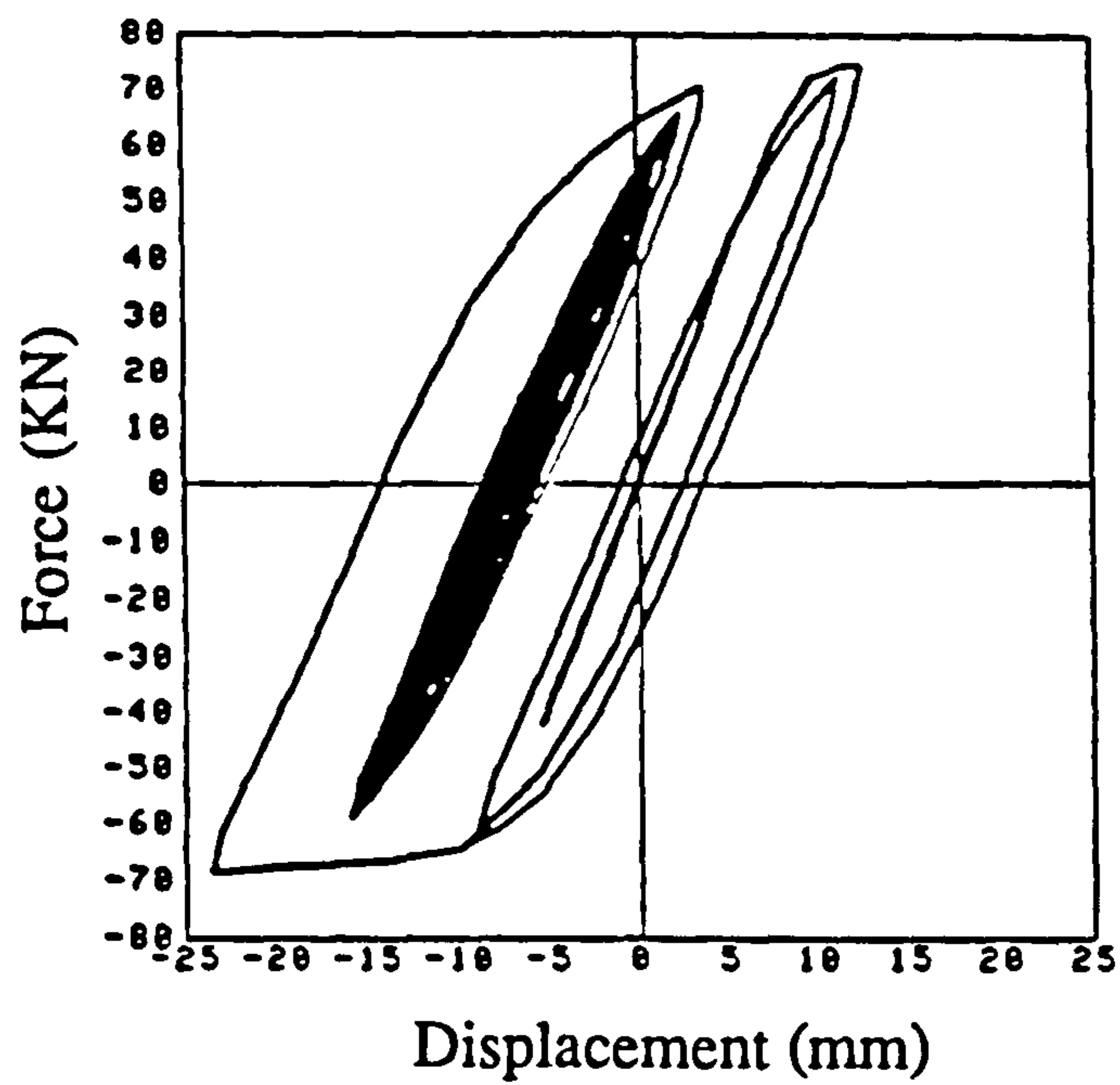


Fig. 4.25 Experimental force-displacement relationship for PSD4

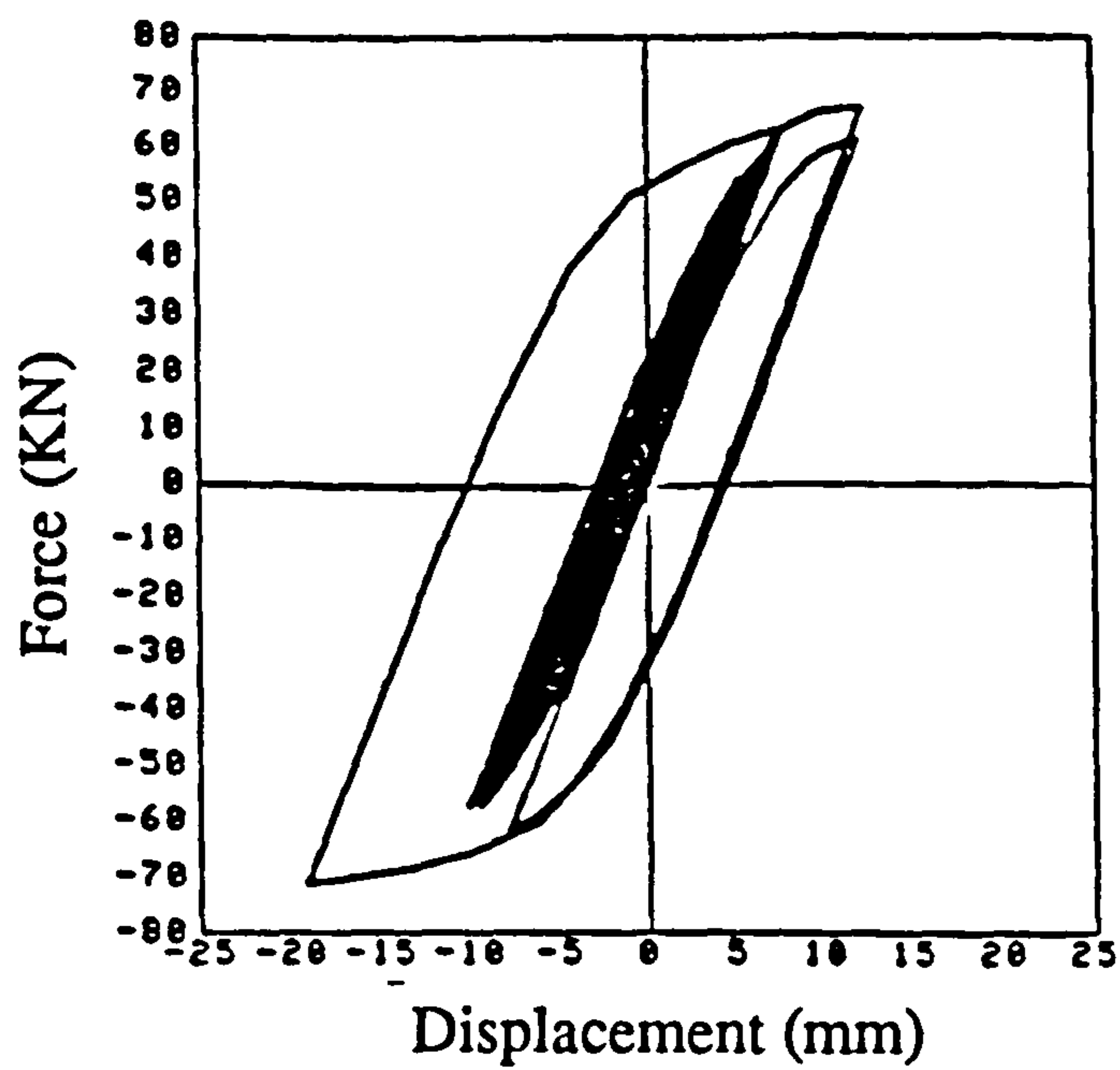


Fig. 4.26 Analytical force-displacement relationship for PSD4

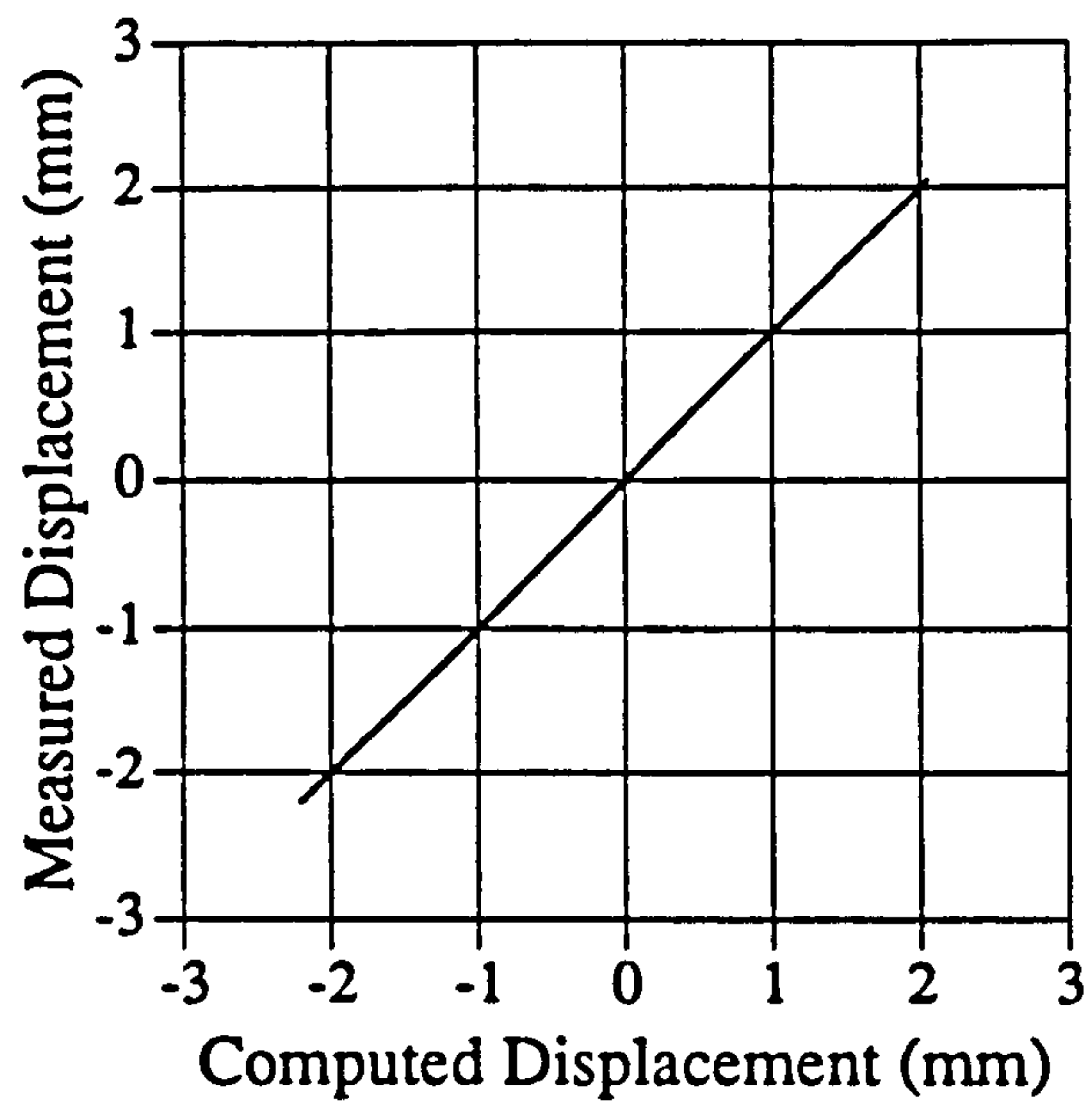


Fig. 4.27 Computed vs measured displacements for PSD1

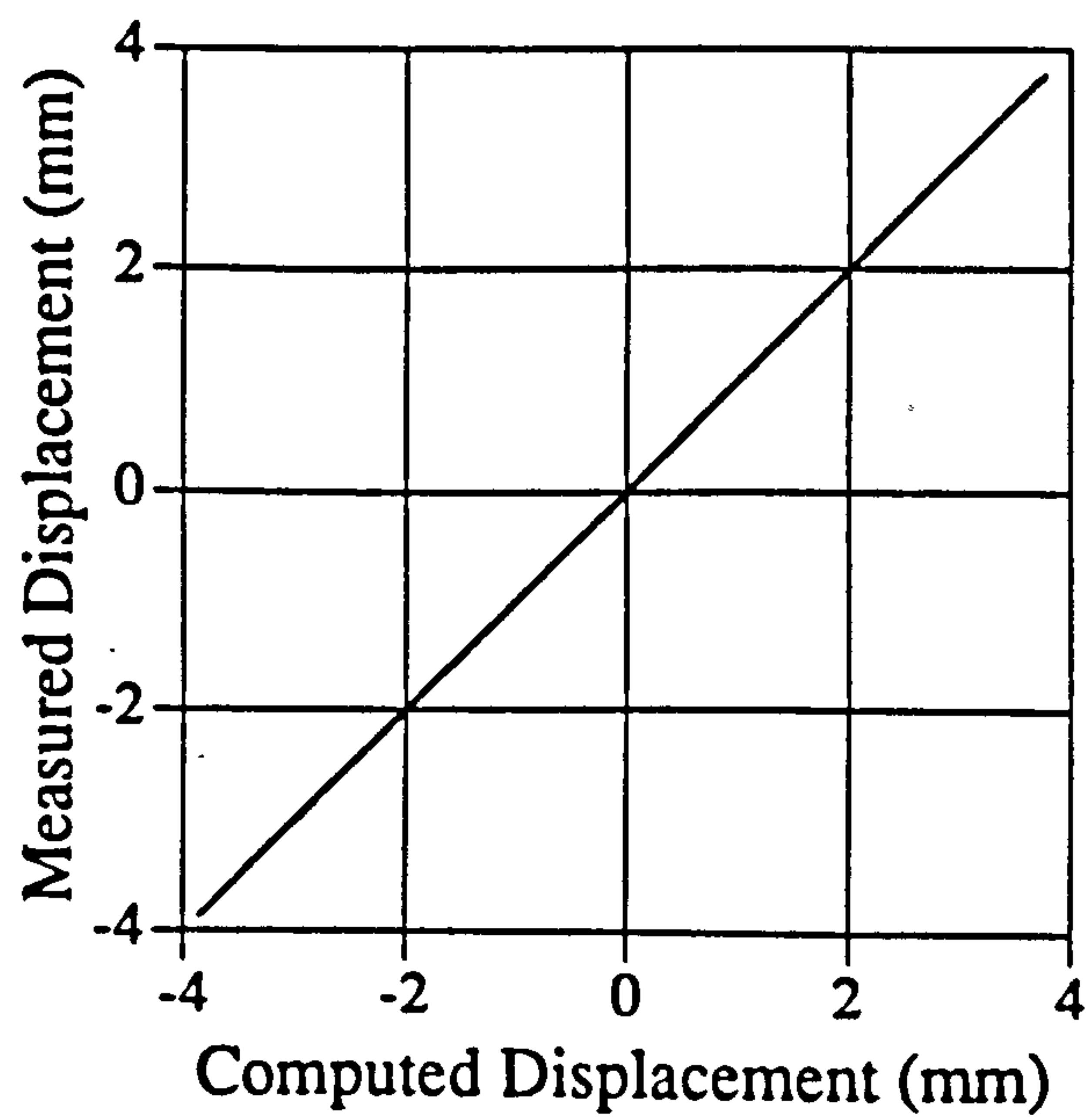


Fig. 4.28 Computed vs measured displacements for PSD2

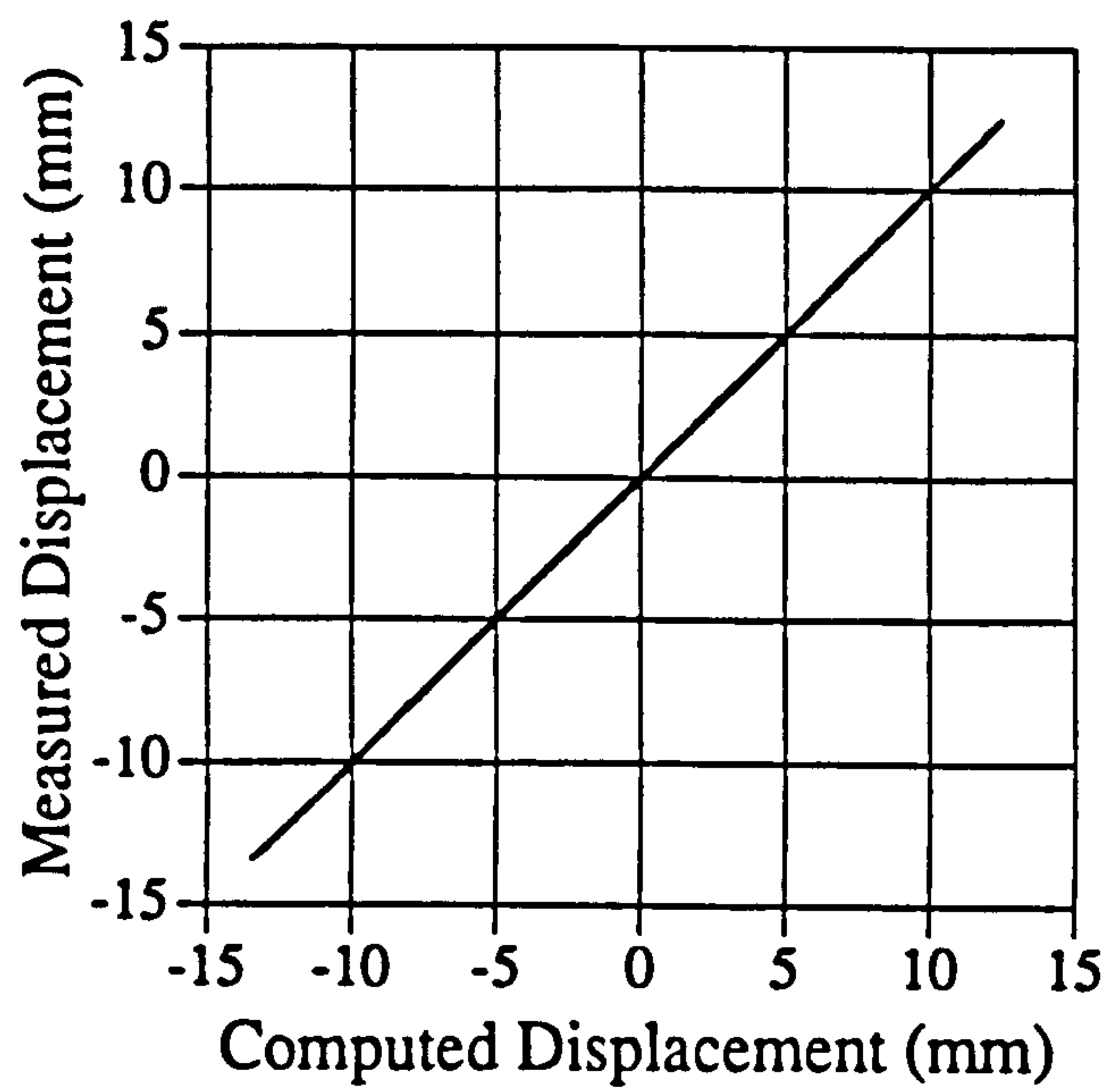


Fig. 4.29 Computed vs measured displacements for PSD3

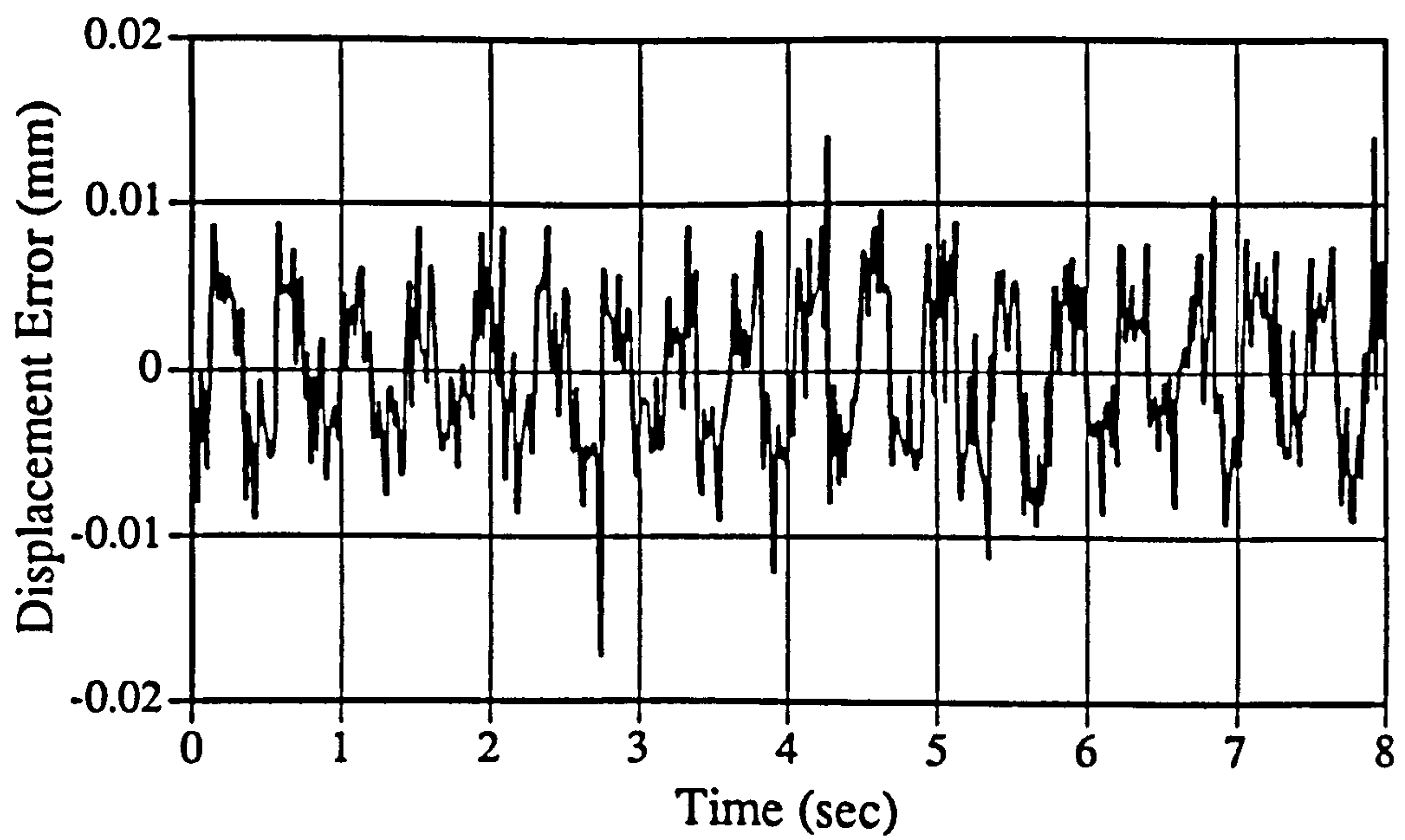


Fig. 4.30 Error history for PSD1

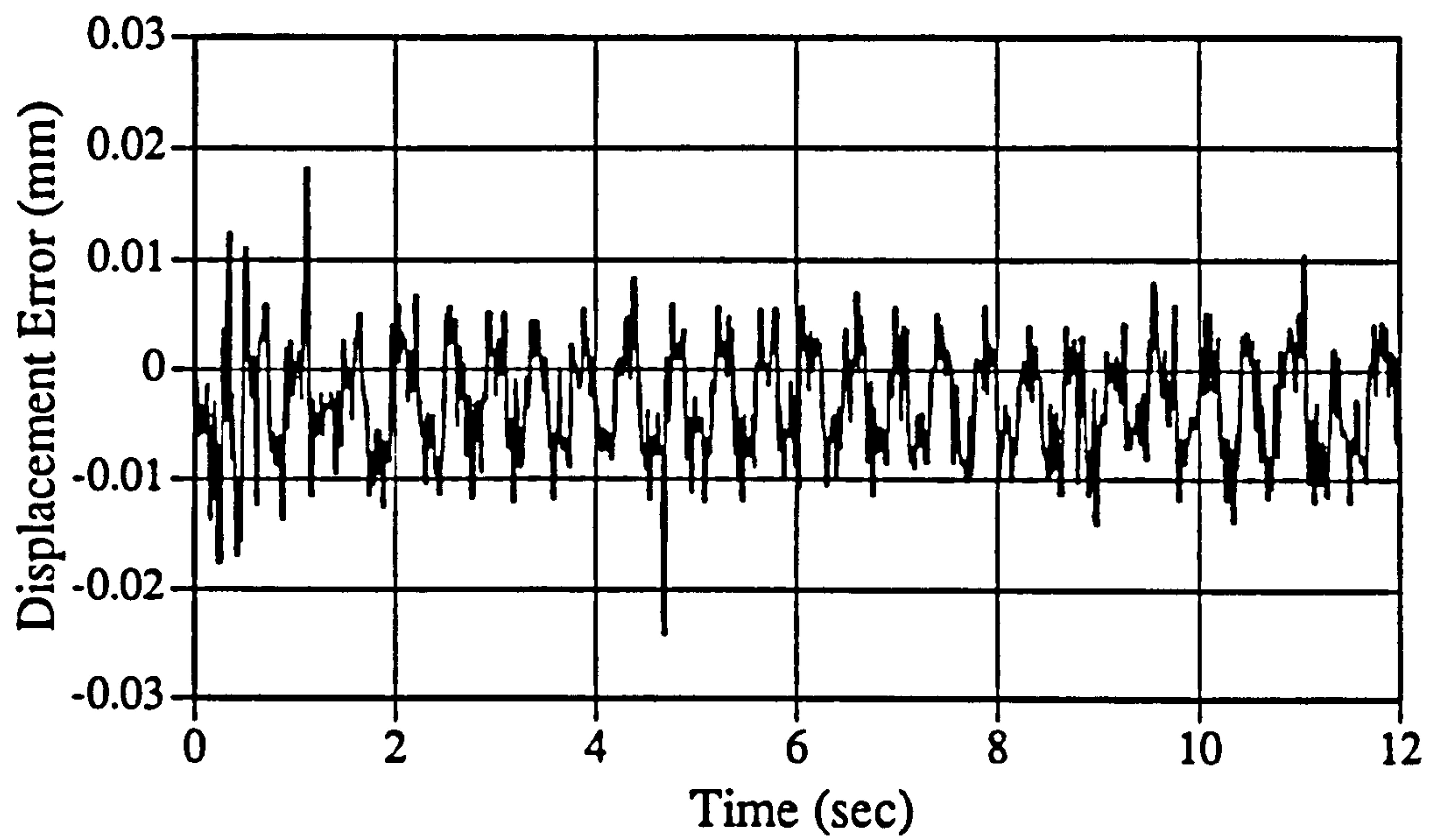


Fig. 4.31 Error history for PSD2

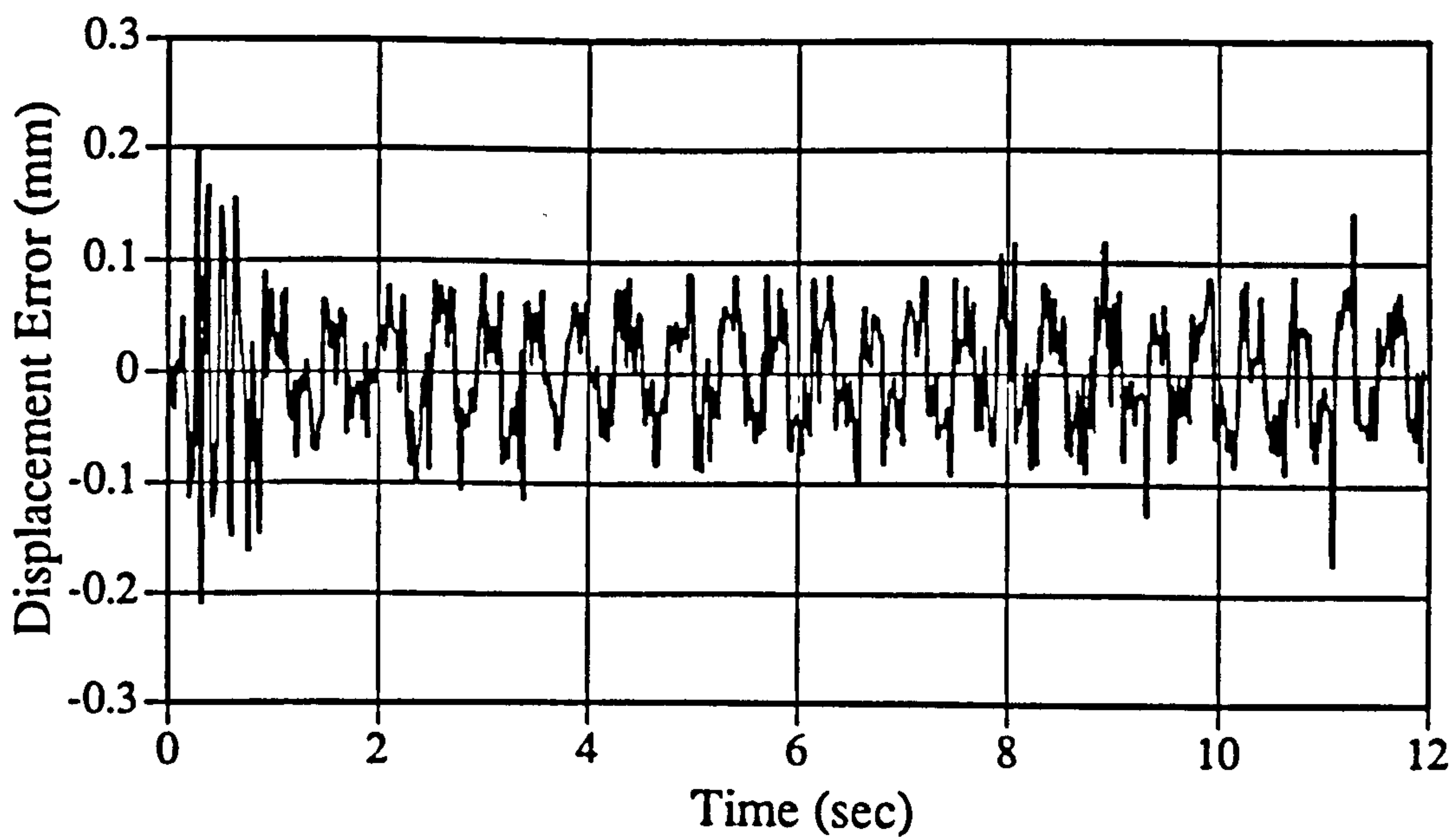


Fig. 4.32 Error history for PSD3

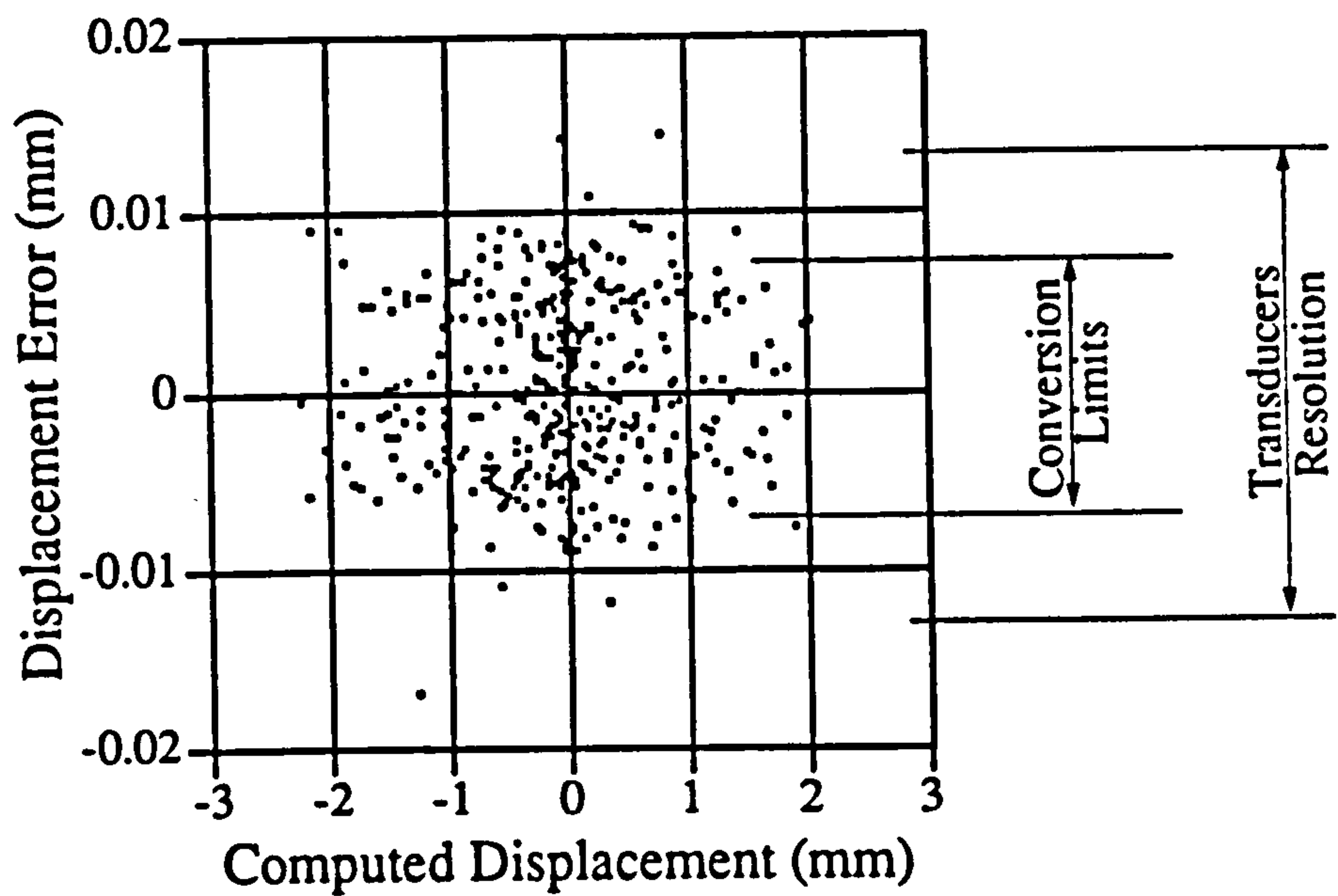


Fig. 4.33 Computed displacement vs displacement error for PSD1

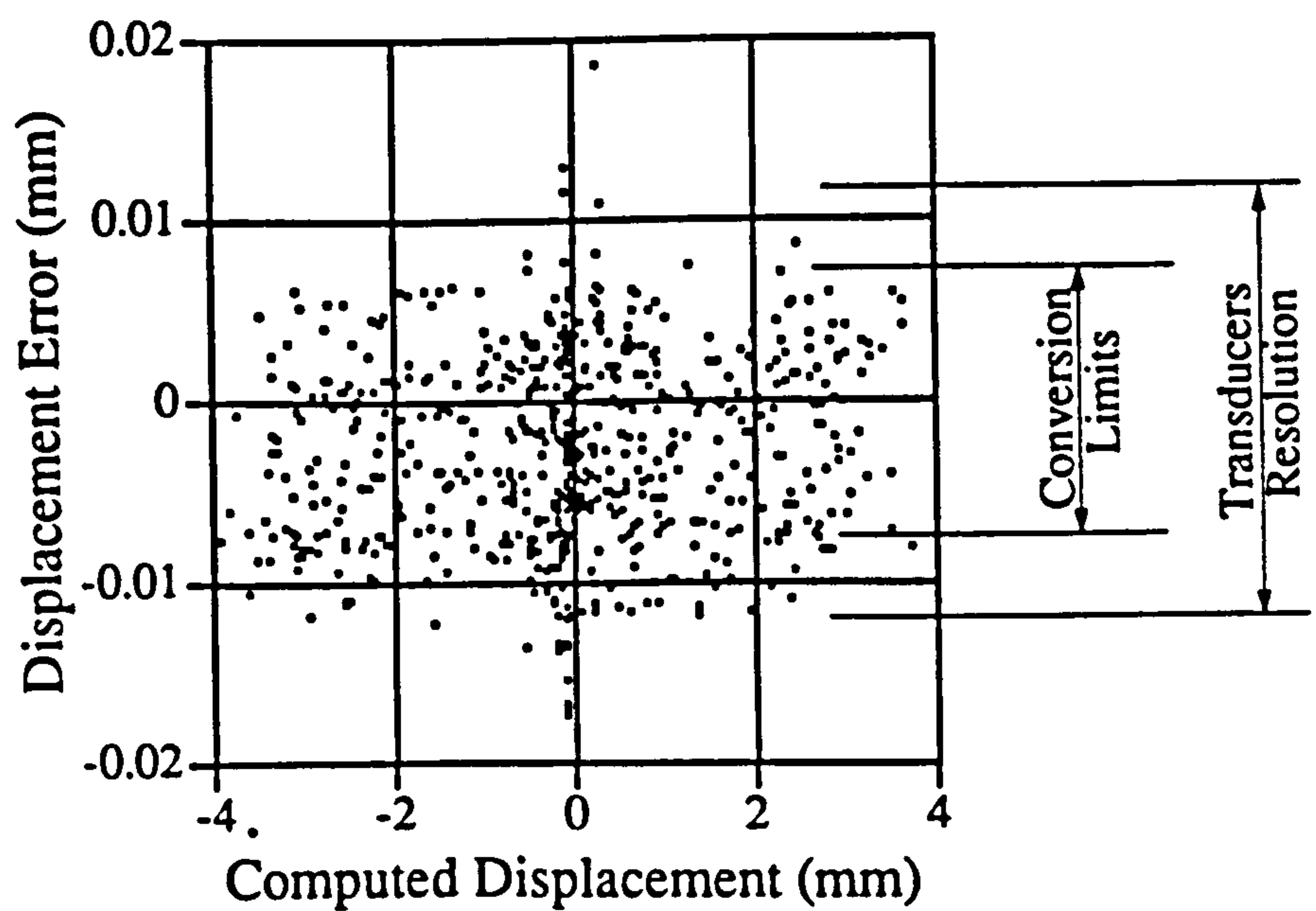


Fig. 4.34 Computed displacement vs displacement error for PSD2

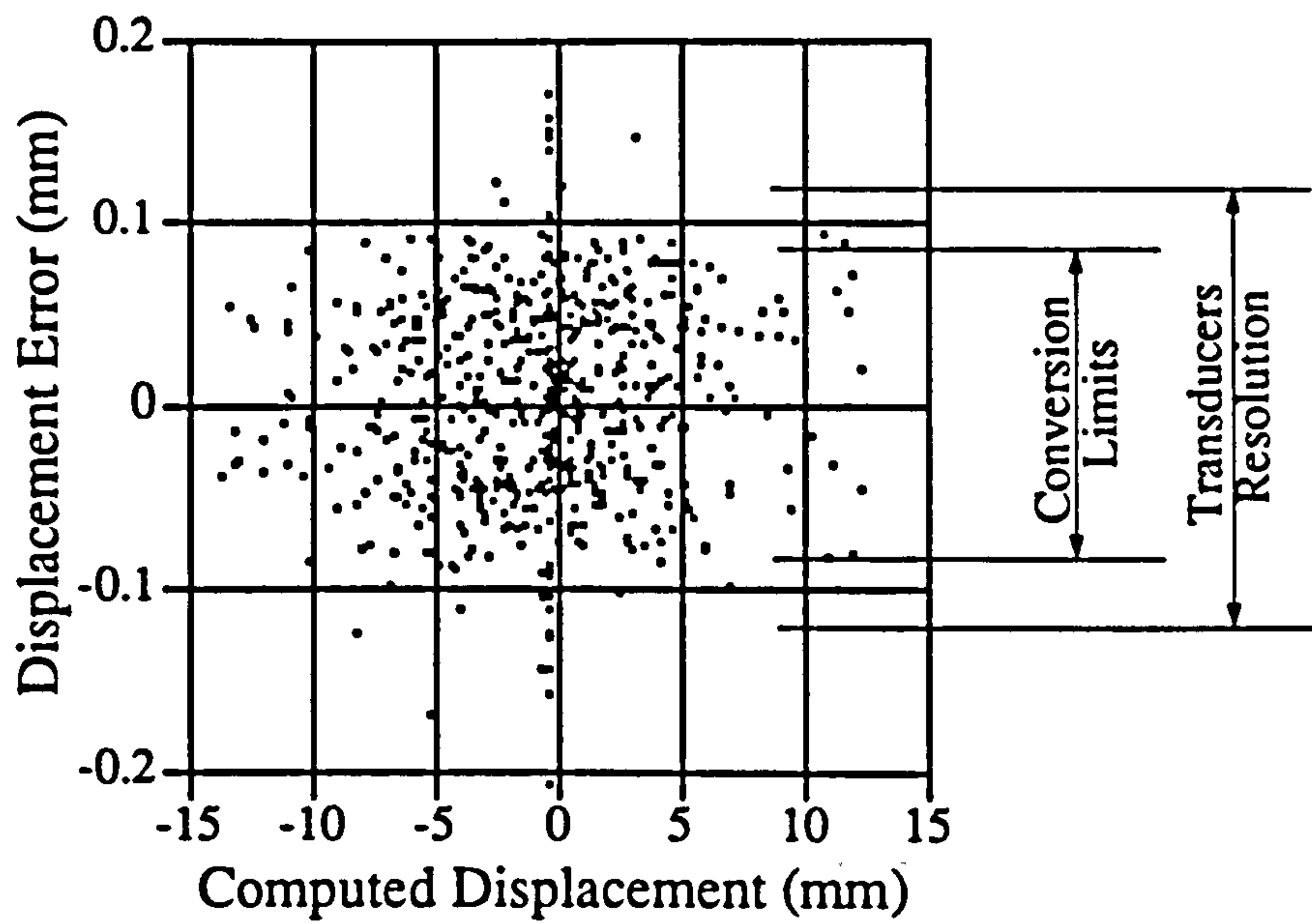


Fig. 4.35 Computed displacement vs displacement error for PSD3

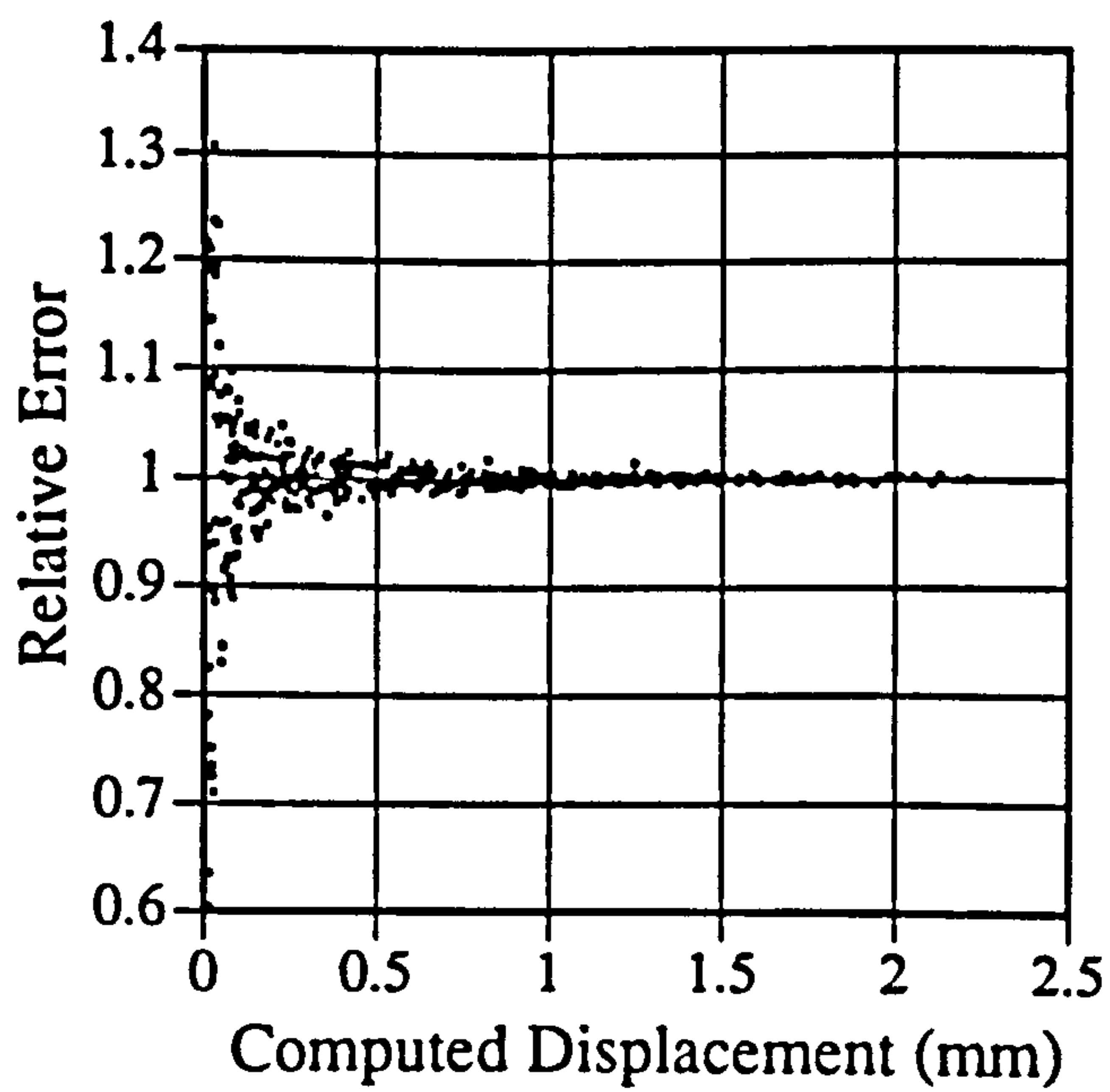


Fig. 4.36 Computed displacement vs relative error for PSD1

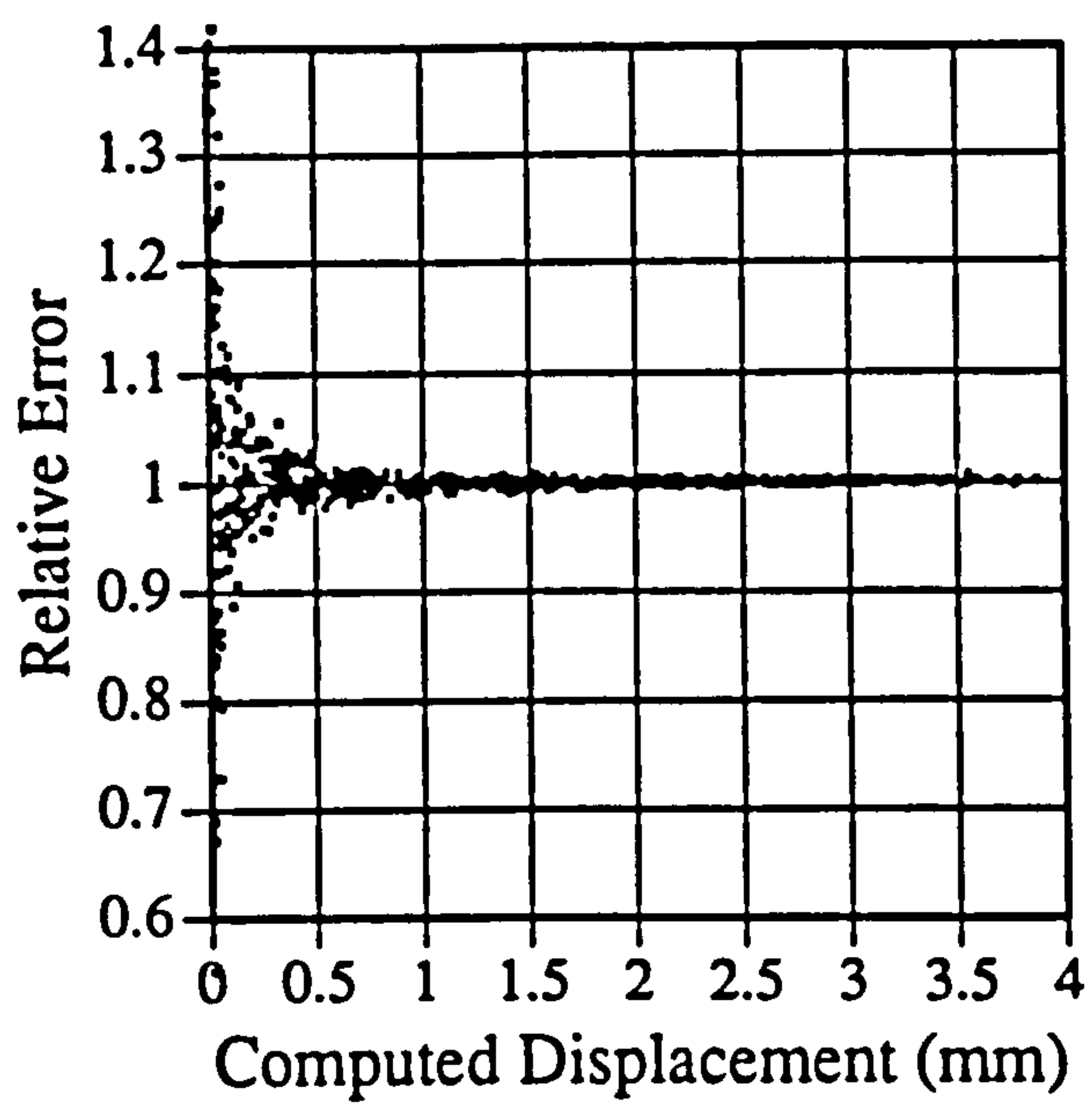


Fig. 4.37 Computed displacement vs relative error for PSD2

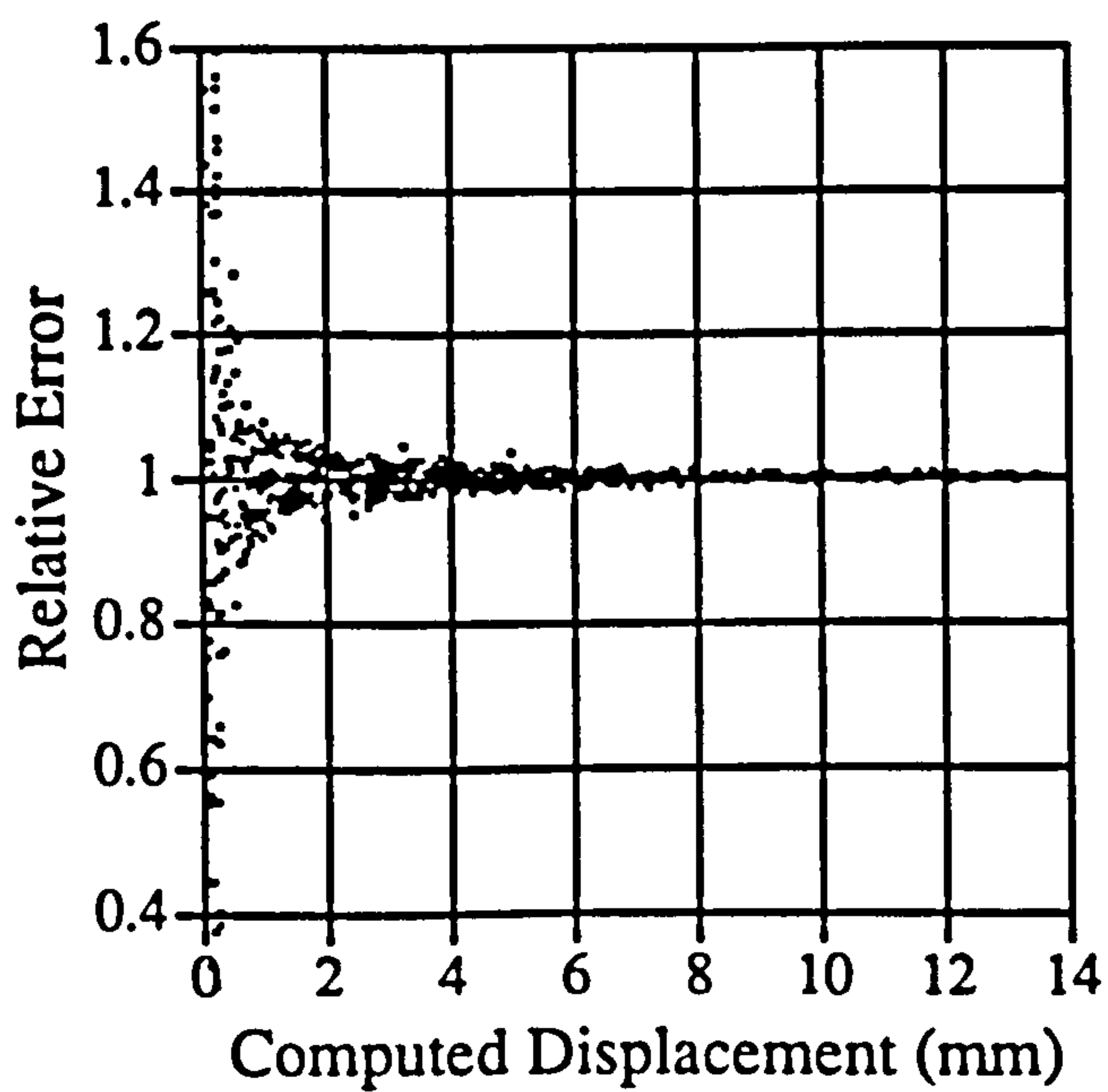


Fig. 4.38 Displacement vs relative error for PSD3

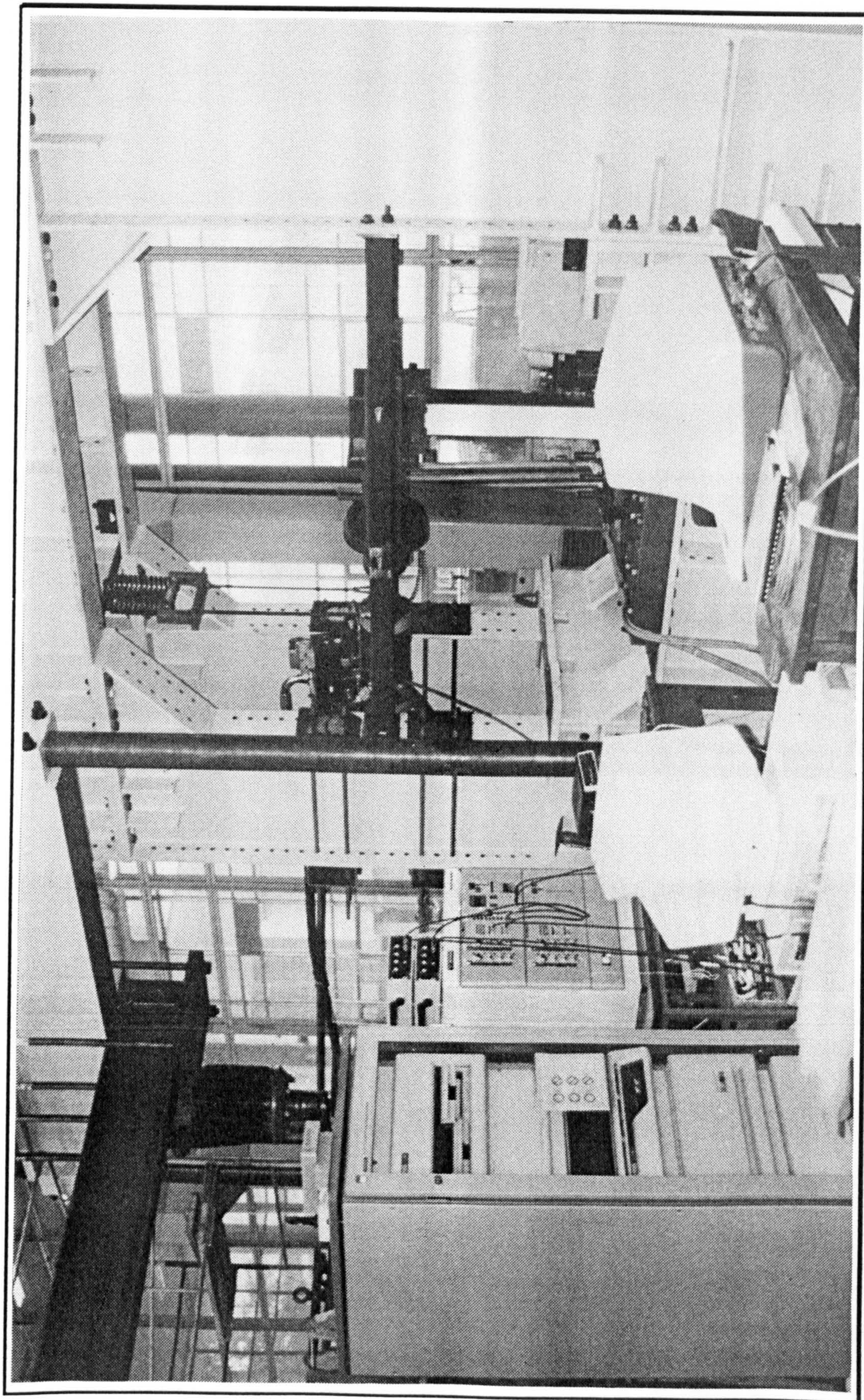


Plate 4.1 General view of testing assembly

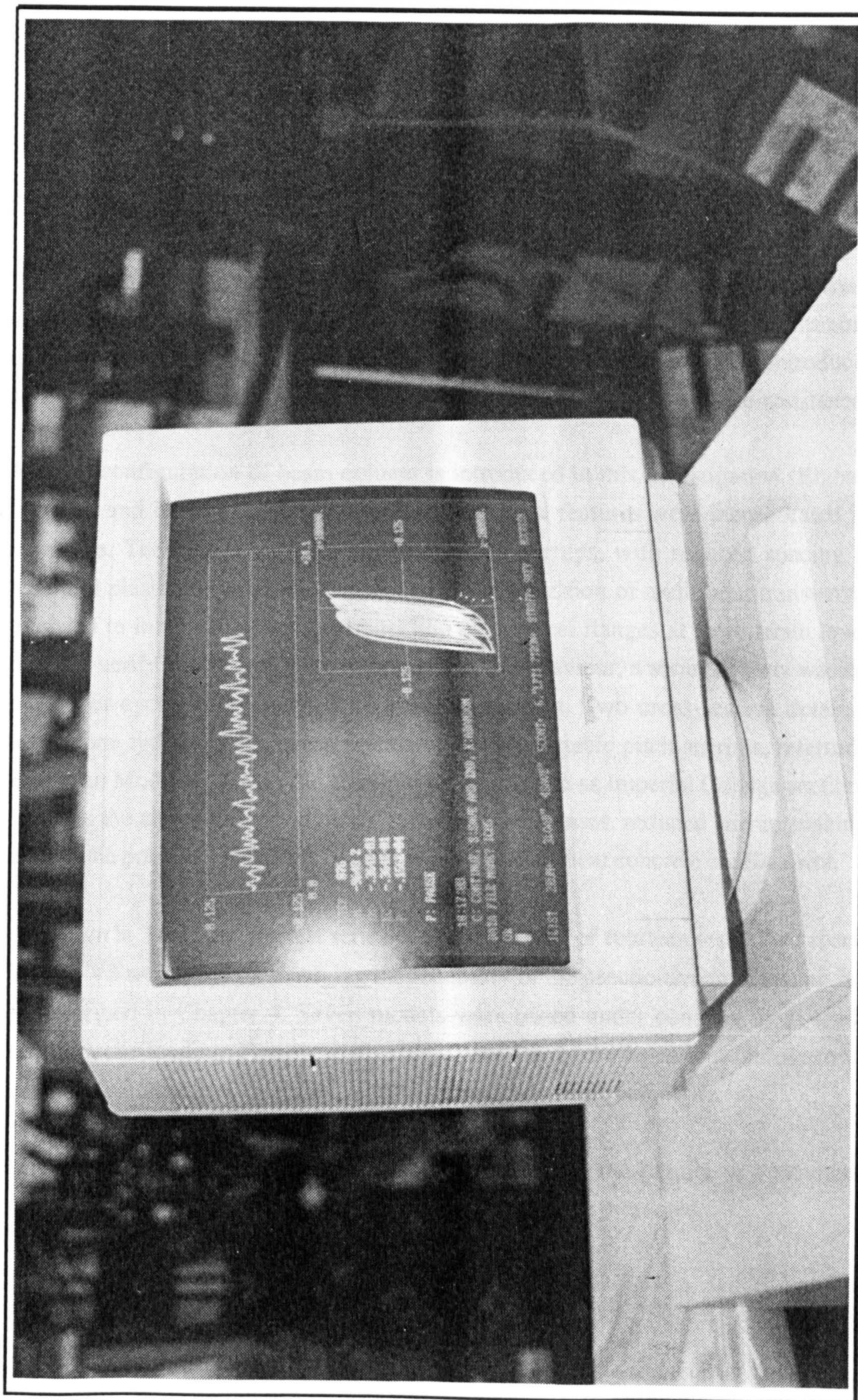


Plate 4.2 On-line graphical display during a pseudo-dynamic test

5. EXPERIMENTAL METHODOLOGY

5.1 INTRODUCTION

The experimental scheme was set out to satisfy two main objectives. Firstly, to understand the behaviour of conventional forms of partially-encased beam-columns under cyclic and earthquake loads. The other primary objective was to introduce new configurations designed to provide improved performance for earthquake-resistance.

A novel configuration of beam-column is introduced in this investigation (Elghazouli, Elnashai and Dowling, 1991). Two unconventional features were incorporated in this new type. The first is variable pitch confining stirrups, with reduced spacing in the potential plastic hinge zone. The second is the provision of additional transverse bars intended to inhibit or delay local buckling of the steel flanges at large strain levels. In order to verify and quantify the improvement in behaviour, a series of tests was carried out under cyclic and earthquake loading conditions. Two cross-section details were tested, one typical of European practice but with variable pitch stirrups, referred to as European Modified (EM). The second type, referred to as Imperial College section (IC), includes the above-described modifications. In both cases, reduced stirrup spacing was used in the potential plastic hinge zone to provide sufficient concrete confinement.

As shown in Table 5.1, the test series comprised a total of fourteen tests. Two specimens V1 and V2 were used for verifying the reliability of the pseudo-dynamic testing facility, as described in Chapter 4. Seven models were tested under constant axial loads and lateral cyclic loading. Finally, to investigate and verify the behaviour under earthquake loading, five models were tested using the pseudo-dynamic technique.

In this chapter, the experimental set-up is described, the details of specimens and materials are given and the general loading procedures are presented.

TABLE 5.1
Summary of Experimental Programme

| Model Reference | Testing Technique |
|-----------------|-------------------|
| V1 | Pseudo-dynamic |
| V2 | Pseudo-dynamic |
| EM01 | Cyclic |
| IC01 | Cyclic |
| EM02 | Cyclic |
| IC02 | Cyclic |
| EM03 | Pseudo-dynamic |
| IC03 | Pseudo-dynamic |
| EM04 | Cyclic |
| IC04 | Cyclic |
| EM05 | Pseudo-dynamic |
| IC05 | Pseudo-dynamic |
| IC06 | Pseudo-dynamic |
| IC07 | Cyclic |

5.2 EXPERIMENTAL SET-UP

The cyclic and pseudo-dynamic tests were divided into two groups. The first group of tests were conducted at Imperial College. This comprised bending tests on models V1, V2, EM05, IC04, IC05, IC06 and IC07. The second group of tests were carried out at the Institute of Industrial Science (IIS), University of Tokyo. In the latter group, which included specimens EM01, EM02, EM03, IC01, IC02 and IC03, all models were subjected to moderate or high axial loads in addition to the lateral loads. The details of both test-rigs are described hereafter.

5.2.1 Self-Reacting Testing Frame

Figure 5.1 shows the details of the test-rig. The different parts of the assembly were adequately prestressed to form a self-reacting frame. The rig was then modified to accommodate the horizontal actuator and a rigid base for the specimens. Also, out-of-plane supports for the specimens were added.

In this set-up, the models were tested as vertical cantilevers. The specimen was welded to top and bottom plates of size 300x250x40 and 550x250x70 mm, respectively. To ensure total fixity, the bottom plate was prestressed to a 130 mm base plate using high tensile 40 mm diameter bolts, which was stressed-up to a load of 60 tonnes each. A base plate of dimensions 1200x1200x130 mm were stressed to the frame using 44 bolts of 24 mm diameter.

In both the cyclic and pseudo-dynamic tests, displacements were applied at the top of the specimens using a double-acting hydraulic actuator. The actuator had a static capacity of ± 113 KN, and a maximum stroke of ± 125 mm. The base of the actuator was firmly connected to the reaction frame. The back of the actuator was stressed to two base plates of dimensions 710x460x70 mm, each. The base plates were stressed to 10 tonnes each by 4 bolts of 40 mm diameter to two box sections, which in turn transfer the load to the main reaction frame. The box sections were stressed to both sides of the frame section through long high strength bolts of 24 mm diameter, and end plates at the internal face of the frame. The lateral force in both direction of loading was, therefore, always reacting against the full section of the reaction frame rather than against the flanges. The two box sections, 250x250x10 mm, were provided with stiffening tubes at the location of bolts to avoid local buckling at these points.

Two low friction Instron swivel joints were used to connect the actuator to both the reaction frame and the specimen to allow free in-plane movement. The load cell was mounted on the actuator piston. A rigid box was used to transfer the load from the horizontal actuator to the vertical specimen. It was not possible to use the swivel joint for this purpose as its rotation is limited to $\pm 90^\circ$. To counter-act the weight of the actuator, it was connected to the top beam of the frame by vertical springs. The stiffness and capacity of the springs were carefully chosen and tested so that they serve the intended purpose only without creating an undesirable constraint on the loading set-up.

In order to prevent excessive out-of-plane deformations, a simple system was provided to limit side movements of the specimens. Two 'cam followers' were fixed to each side of the rigid box on top of the specimen. The rollers were designed to slide against side plates which are fixed to horizontal beams and connected to both ends of the test-rig. The clearance between the rollers and the side plates was adjusted prior to each test, and was always kept smaller than 3.0 mm.

Careful consideration was given to the rigidity of the test-rig in order to achieve accurate deflection measurements. For this purpose, a series of detailed elastic analyses of the

arrangement including the loading frame was conducted and confirmed the adequacy of the design. The maximum deflection in the frame was expected to be less than 0.2 mm at peak loads. This was later confirmed in the verification tests. The internal transducer of the actuator was used for deflection measurements. However, the readings were continuously compared with the displacements obtained from an external transducer monitoring the structural displacements at the top of the specimen, which vindicated the accuracy of the measurements.

The details of the electro-hydraulic equipment and the computer-controlled procedure are as described in Chapter 4. The same electronic and hydraulic equipment were used. The details of the pseudo-dynamic procedure are also described in Chapter 4. However, a different program was developed for the computer-controlled cycling loading. The details of this program are presented in section 5.4.

5.2.2 Beam-Column Test-Rig

The second group of tests were carried-out using the testing assembly developed at IIS and shown in Figure 5.2. Displacements were applied at the intermediate point joining a relatively stiff steel beam on one side and the test specimen on the other side, as shown in the simplified layout in Figure 5.3. The relationship between the different control parameters is described in detail in section 5.5. In effect, the specimen was tested as a vertical cantilever under lateral horizontal displacements and vertical load of constant magnitude.

The specimen was welded to bottom and top plates of dimensions 360x280x30 mm and 360x360x20 mm, respectively. The steel loading beam was also welded to two similar plates. The bottom plate of the specimen, which represents the base of the cantilever, was rigidly connected to the base of the steel beam, using twelve 24 mm diameter bolts. The other side of the specimen, which represents the tip of the cantilever, was fixed to a hinge connected to two top and two bottom hinges. As a result, horizontal and rotational movement were allowed, whereas vertical movement was prevented. An actuator of 1000 KN capacity applied the constant load on the specimen and reacted against a reinforced concrete reaction wall. The other side of the steel loading beam was connected to a hinge allowing rotational movement only. The pin was rigidly fixed to a stiff steel section transferring the load to the base of the rig.

A double-acting hydraulic actuator of 200 KN capacity applied the displacements at the intermediate point. The actuator was connected to two hinges to allow in-plane

movement. A load cell was also placed after the piston to measure the applied load. The distance between the two pins was more than two metres. Consequently, the change in applied load due to a slight horizontal movement of the intermediate point was negligible. The base of the actuator reacted against a stiff steel beam.

A separate trussed steel frame was installed to act as a reference for mounting displacement transducers in order to achieve accurate deflection measurements. A detailed investigation of the control and accuracy of this set-up was undertaken and is presented in section 5.5.

5.3 DESCRIPTION OF MODELS

5.3.1 Specimen Details

The details of all models are shown in Figures 5.4 to 5.8, and summarized in Table 5.2. Models EM01 to EM05 and IC01 to IC05 represent one of two cross section details considered. The additional bars were welded to the inside of both flanges, and hence act as connectors for improved interaction. In both cases, reduced stirrup spacing was used in the potential plastic hinge zone to provide sufficient concrete confinement.

As pointed out before, one of the main objectives of this test series was to compare the behaviour of IC models to that of the corresponding EM models. Consequently, each two comparable specimens, (i.e. EM01 and IC01, EM02 and IC02, up to EM05 and IC05), were manufactured from identical materials and dimensions. This allowed direct comparison between each pair of EM and IC models subjected to the same loading regime and the same constant axial load.

The last two models IC06 and IC07 included only the straight stirrups throughout the height to compare the behaviour with that of other configurations. Again, the stirrups were arranged such that the spacing in the potential plastic hinge zone was half that elsewhere. All models, including IC06 and IC07 were tested under strong-axis bending

The dimensions of the sections were chosen to be similar to that used in European sections. Models EM04, EM05, and IC04 to IC07 were manufactured from rolled sections, whereas models EM01 to EM03, and IC01 to IC03 were formed by welding steel plates. The difference in reinforcement cover was due to the difference in the size of aggregates used in some of the models. Also, the change in the height of the models was

introduced due to experimental constraints in the two test-rigs used. These variations were allowed as they had no bearing on the main objectives and conclusions of the test series.

TABLE 5.2
Specimen Details

| Model Reference | Section Type | Height L (mm) | $b_f \times t_f$ (mm) | $d_w \times t_w$ (mm) | Figure Number |
|-----------------|---------------|---------------|-----------------------|-----------------------|---------------|
| EM01 | H 150x150x6 | 1200 | 150.0x6.0 | 138.0x6.0 | 5.4 |
| IC01 | H 150x150x6 | 1200 | 150.0x6.0 | 138.0x6.0 | 5.5 |
| EM02 | H 150x150x6 | 1200 | 150.0x6.0 | 138.0x6.0 | 5.4 |
| IC02 | H 150x150x6 | 1200 | 150.0x6.0 | 138.0x6.0 | 5.5 |
| EM03 | H 150x150x6 | 1200 | 150.0x6.0 | 138.0x6.0 | 5.4 |
| IC03 | H 150x150x6 | 1200 | 150.0x6.0 | 138.0x6.0 | 5.5 |
| EM04 | UC 152x152x23 | 1030 | 152.4x6.8 | 141.4x6.1 | 5.6 |
| IC04 | UC 152x152x23 | 1030 | 152.4x6.8 | 141.4x6.1 | 5.7 |
| EM05 | UC 152x152x23 | 1030 | 152.4x6.8 | 141.4x6.1 | 5.6 |
| IC05 | UC 152x152x23 | 1030 | 152.4x6.8 | 141.4x6.1 | 5.7 |
| IC06 | UC 152x152x23 | 1030 | 152.4x6.8 | 141.4x6.1 | 5.8 |
| IC07 | UC 152x152x23 | 1030 | 152.4x6.8 | 141.4x6.1 | 5.8 |

5.3.2 Material Properties

5.3.2.1 Steel Sections

Coupon tests were conducted on the steel sections used. In the case of rolled sections, specimens from both the flange and the web were tested. The strength obtained is given in Table 5.3, and a typical stress-strain curve is shown in Figure 5.9. In all cases, the values presented are the average of at least three tests. In the coupon tests, both stress-strain curves and load-displacement curves were plotted. The stress-strain curves were limited to a specific strain limit, whereas the load-displacement curve represented the full relationship up to fracture.

TABLE 5.3
Properties of Steel Sections

| Model Reference | EM01, IC01, EM02, IC02, EM03, IC03 | | EM04, IC04, EM05, IC05, IC06, IC07, | |
|---------------------------------|--|---------|---|---------|
| | Flange | Web | Flange | Web |
| σ_y (N/mm ²) | 274 | 274 | 289 | 282 |
| σ_u (N/mm ²) | 419 | 419 | 459 | 458 |
| E (N/mm ²) | 190,000 | 190,000 | 206,000 | 206,000 |
| E_{st1} (N/mm ²) | 3,700 | 3,700 | 4,160 | 4,400 |
| E_{st2} (N/mm ²) | 1,800 | 1,800 | 2,200 | 2,900 |
| ϵ_y (%) | 0.15 | 0.15 | 0.14 | 0.14 |
| ϵ_1 (%) | 2.20 | 2.20 | 1.50 | 0.60 |
| ϵ_m (%) | 24.40 | 24.40 | 26.50 | 25.00 |

5.3.2.2 Reinforcing Bars

Table 5.4 gives the strength of the reinforcement bars used in the models. The values represent the average of at least three tensile test results. The details of reinforcement are presented in section 5.2 above. In all models, deformed bars of diameter 8 or 10 mm, referred to as D8 or D10, were used, while plain bars of diameter 6 mm, referred to as R6, were used for the bent and straight stirrups.

Separate tests were undertaken to study the strength of the weld between the straight stirrups and the flanges in the IC models. The tests specimens simulated exactly the weld in the models, where 6 mm bars were welded to two steel plates. The length of the bar was identical to the distance between the two flanges. For models IC04 to IC07, the bars failed prior to the failure of the weld. In this case, fillet weld was placed around the 6 mm bars, and hence its resistance was higher than the reinforcement bar. However, in the other IC models, IC01 to IC03, the bars were butt-welded. The average result from three tests on this weld is shown in Figure 5.10. In this case, the weld showed lower resistance than the bars, and was, therefore, the limiting failure component of the straight bars.

TABLE 5.4
Properties of Reinforcing Bars

| Model Reference | | EM01, IC01 EM02, IC02 EM03, IC03 | EM04, IC04 EM05, IC05 IC06, IC07 |
|-----------------------|---------------------------------|--|--|
| Vertical Bars D10 | σ_y (N/mm ²) | 359 | -- |
| | σ_u (N/mm ²) | 502 | -- |
| Vertical Bars D8 | σ_y (N/mm ²) | -- | 487 |
| | σ_u (N/mm ²) | -- | 639 |
| Horizontal Bars D6 | σ_y (N/mm ²) | 520 | 347 |
| | σ_u (N/mm ²) | 562 | 454 |
| Weld Strength | P_y (KN) | 7.8 | 9.8 |
| | P_u (KN) | 10.8 | 12.8 |

In case of the IC models, the straight stirrups have to satisfy minimum requirements in order to inhibit local flange buckling at the level of the bars. An accurate assessment of such requirements would involve a detailed study including the effect of imperfections. Nevertheless, a conservative estimate may be obtained by considering the stability of the portion of the flange between the bars, assuming simply supported connections. Using this approach, it can be shown that the minimum required area of the bar would be equal to $(2 t_f b_f d_w \sigma_y) / (s E)$, where σ_y is the yield stress of the flange, s is the spacing of the bars and E is the modulus of elasticity of steel for the bars. This assessment is expected to be conservative provided that the weld satisfies the strength requirement of the bars. For the experimental models under consideration, the required diameter of the straight bars would be 4 mm. Consequently, 6 mm bars were used in all the IC models. This choice was later vindicated by the results of the experiments.

5.3.2.3 Concrete

Two concrete mixes were used. Models EM04, EM05, and IC04 to IC07 were cast from mix A, whilst models EM01, EM02, EM03, IC01, IC02 and IC03 were cast from mix B. Both mixes are shown in Table 5.5. The aggregate size of mix A was 10 mm, while that of mix B was 15 mm.

TABLE 5.5
Concrete Design Mixes

| Proportions by Weight | Mix A | Mix B |
|-----------------------|-------|-------|
| Cement | 1.00 | 1.00 |
| Aggregate | 3.15 | 3.14 |
| Coarse Sand | 2.00 | 1.94 |
| Fine Sand | 0.89 | 0.67 |
| Free Water | 0.74 | 0.61 |

In order to demonstrate the elimination of the need for form-work in the partially encased configuration, the sides of the specimens were cast three days apart. The resulting difference in compressive strength should reduce after 28 days, if the mix was very well controlled. However, significant differences were still observed at the day of testing. Nevertheless, these differences had no bearing on the results, since the models had the same strength distribution under strong axis bending.

TABLE 5.6
Concrete Compressive Strength

| Model | Mean | Cube | Strength (N/mm ²) | Mean | Cylinder | Strength (N/mm ²) |
|-----------|--------|--------|-------------------------------|--------|----------|-------------------------------|
| Reference | Side 1 | Side 2 | Average | Side 1 | Side 2 | Average |
| EM01 | -- | -- | -- | 42.4 | 35.2 | 38.8 |
| IC01 | -- | -- | -- | 42.4 | 35.2 | 38.8 |
| EM02 | -- | -- | -- | 42.4 | 35.2 | 38.8 |
| IC02 | -- | -- | -- | 42.4 | 35.2 | 38.8 |
| EM03 | -- | -- | -- | 42.4 | 35.2 | 38.8 |
| IC03 | -- | -- | -- | 42.4 | 35.2 | 38.8 |
| EM04 | 38.9 | 30.7 | 34.8 | 33.8 | 24.2 | 29.0 |
| IC04 | 38.9 | 30.7 | 34.8 | 33.8 | 24.2 | 29.0 |
| EM05 | 36.6 | 35.5 | 36.1 | 27.4 | 25.8 | 26.6 |
| IC05 | 36.6 | 35.5 | 36.1 | 27.4 | 25.8 | 26.6 |
| IC06 | 37.7 | 34.1 | 35.9 | -- | -- | -- |
| IC07 | 37.7 | 34.1 | 35.9 | -- | -- | -- |

Table 5.6 shows the concrete strengths obtained for all models at the day of testing. In most cases, the average of three cubes, of size 4x4 inches, or three cylinders, of size 4x10 inches, for each side of the model, was used to estimate the cube or cylinder strength of concrete. Additionally, one cube or cylinder was tested after one week to control the curing process. All models were cast horizontally. Pocker vibrators were used to compact the concrete. The specimens were trowel finished two hours after completion of casting and covered with wet hessian and nylon after about four hours. The models were turned the other side after three days of casting the first side.

5.4 INSTRUMENTATION AND CONTROL

5.4.1 Bending Tests

The control and data acquisition details used for these tests are as described in Chapter 4. The actuator transducer measured the horizontal displacement whilst the load cell mounted on the actuator piston measured the restoring force. The change in force at large displacements due to geometrical effects was found to be negligible. In several tests, vertical transducers were placed on top of the specimen to measure vertical extensions. The data acquisition system installed in the computer can handle up to 32 channels. In addition, a large 'Solatron' data logger, capable of scanning up to 1000 channels, was linked to the system.

Strain gauges were placed on the steel section and on the vertical and horizontal reinforcement. Most of the gauges were located in the expected plastic hinge zone. Nevertheless, other gauges were located to measure the deformation along the height of the members. The locations of the strain gauges are shown in the strain plots presented in Appendix A. The deformed bars were ground at the strain gauge locations. All gauges and wiring were adequately waterproofed. The manufacturers specifications state that reliable readings are expected under cyclic loading up to strains in the order of 30,000 microstrains.

The details of the pseudo-dynamic testing computer-controlled program are described in Chapter 4. Another program was developed for conducting computer-controlled cyclic tests. A simplified flow chart is shown in Figure 5.11. The program uses the same general utility routines developed for pseudo-dynamic testing. However, the main control loop is different; the user defines the required target displacement, which is then

divided into a number of sub-increments and applied gradually to the test specimen. The test progression is monitored by on-line graphical display and the user has the option of pausing or aborting the test at any intermediate stage.

5.4.2 Beam-Column Tests

For the set-up described in section 5.2.2, more measurements were needed for accurate control of the tests, as shown in Figure 5.12. The following control channels were required:

- Two load cells, for transverse and axial forces (1, 2)
- Two displacements X1 and X2, to calculate transverse control displacements (3, 4)
- Two displacements X3 and X4, to calculate accurately the tilt angle (5, 6)
- One displacement X5, for chord deformation (7)
- One displacement X6, for axial deformation (8)

The available self-contained data acquisition system offers a 32 channel logging facility, which gives 24 channels after the allocation of the control values given above. This was sufficient for the pseudo-dynamic tests. However, for the cyclic tests, a separate data logger was used to provide more data acquisition channels. In the pseudo-dynamic tests, 24 strain gauges were used. In the cyclic tests, 38 strain gauges were placed to obtain more accurate curvature distribution. The locations of the strain gauges are shown in the strain plots presented in Appendix A.

5.5 ANALYSIS OF MEASUREMENTS

For the set-up described in section 5.2.1, direct measurement of the cantilever displacement and force is straightforward. As mentioned before, the change in force values at large displacements due to geometric effects was found to be negligible; of the order of 0.1%.

To calculate the applied load and response displacement of the equivalent cantilever for the set-up described in section 5.2.2, the relationships between the control parameters, given in Figure 5.12(a), were considered. The ratio of inter-span applied load F to the reaction H is 0.625. To reduce the dependence of the control displacement on transducer readings, a simplified geometry transformation, shown in Figure 5.12(b), was utilized.

An analytical study of the errors involved in the simplified transformation was undertaken. The test rig was modelled in detail, including the specimen, the loading beam and the rigid members, as shown in Figure 5.13. The nonlinear program ADAPTIC (Izzuddin and Elnashai, 1989) was used for the analysis. The description of this program is given in Chapter 7. A summary of the analytical results is given in Table 5.7 for two levels of axial loading.

TABLE 5.7
Analytical Results

| Axial Load % | 15% | | | 30% | | |
|-----------------|---------|---------|---------|----------|---------|---------|
| δ_o (mm) | 20 | 50 | 100 | 20 | 50 | 100 |
| L_1 (mm) | 1200 | 1200 | 1200 | 1200 | 1200 | 1200 |
| N (KN) | 250 | 250 | 250 | 250 | 500 | 500 |
| F (KN) | 93.26 | 95.89 | 88.80 | 94.36 | 85.70 | 58.89 |
| β (deg.) | 0.456 | 1.301 | 2.723 | 0.447 | 1.293 | 2.720 |
| H (KN) | 58.283 | 59.916 | 55.494 | 58.980 | 53.568 | 36.826 |
| χ (mm) | 1199.86 | 1199.57 | 1198.88 | 1199.514 | 1199.21 | 1196.56 |
| δ (mm) | 29.55 | 77.22 | 156.84 | 29.35 | 77.05 | 156.67 |
| Q (KN) | 56.29 | 54.22 | 43.55 | 49.67 | 42.27 | 13.058 |
| R (KN) | 250.456 | 251.296 | 252.354 | 500.403 | 501.081 | 501.184 |

The results of this analytical investigation confirmed that the errors introduced in the simplified transformation are negligible, as shown in Table 5.8. The actuator displacement in this case was 100 mm and the axial load was 30% of the squash load. It is clear that the errors are insignificant. However, it is important to note that the angle of rotation used in the calculations was assumed to be exact (measured from X_3 and X_4). It is necessary to maintain good accuracy in the measurement of X_3 and X_4 , since an error of 10% in the angle would lead to an error of 3.8% and 3.6% in the control displacement and peak force, respectively.

As shown in Figure 5.14, depicting H/F vs δ_o for two levels of axial force, the ratio H/F changes slightly at the point of yield of the specimen. This is a consequence of the abrupt change in stiffness and its effect on the geometric relationships. However, it is noted that

corresponding to an applied actuator displacement of 150 mm, which is clearly excessive, the applied load ratio changes to 0.626, which is less than 0.2% in error. It is, therefore, reasonable to assume that the applied equivalent cantilever load will be a constant percentage, 62.5%, of the load corresponding to the control transverse displacement.

TABLE 5.8
Approximation Error in Geometry Transformation

| Parameter | Analytical | Approximation | Error % | Remarks |
|-----------------|------------|---------------|---------|----------|
| δ_o (mm) | 100 | 100 | -- | applied |
| L_1 (mm) | 1200 | 1200 | -- | -- |
| N (KN) | 500 | 500 | -- | applied |
| F (KN) | 58.890 | 58.890 | -- | measured |
| β (deg.) | 2.72 | 2.72 | -- | -- |
| H (KN) | 36.826 | 36.806 | 0.06 | -- |
| χ (mm) | 1196.56 | 1200 | 0.29 | -- |
| δ (mm) | 156.67 | 156.83 | 0.10 | control |
| Q (KN) | 13.058 | 13.038 | 0.15 | control |
| R (KN) | 501.184 | 501.183 | 0.00 | -- |

The data retrieved from the experimental results confirmed that the above assessment is accurate, and that the results obtained using the simplified geometry transformations are adequate.

5.6 LOADING REGIME

5.6.1 Axial Loads

As pointed out before, the tests were designed such that the vertical load applied at the top of an equivalent vertical cantilever model would remain vertical after the horizontal displacement is applied. Consequently, the term 'axial load' does not accurately represent the nature of this load. However, to avoid confusion with respect to the direction of the cantilever, this term will be used hereafter in the description of the tests. Although the

value of this vertical load varies slightly because of geometric effects, it was shown in the previous section that this change is insignificant.

Table 5.9 gives the value of the axial load applied in the tests. The load is given in KN and as an approximate percentage of the axial plastic capacity of the composite section. In calculating the squash load, the effect of concrete confinement in increasing the strength was not considered and approximate material properties were used.

TABLE 5.9
Applied Axial Loads

| Model Reference | Testing Technique | Axial Load (KN) | Axial Load (%) |
|-----------------|-------------------|-----------------|----------------|
| EM01 | Cyclic | 248 | 15% |
| IC01 | Cyclic | 248 | 15% |
| EM02 | Cyclic | 498 | 30% |
| IC02 | Cyclic | 498 | 30% |
| EM03 | Pseudo-dynamic | 498 | 30% |
| IC03 | Pseudo-dynamic | 498 | 30% |
| EM04 | Cyclic | -- | -- |
| IC04 | Cyclic | -- | -- |
| EM05 | Pseudo-dynamic | -- | -- |
| IC05 | Pseudo-dynamic | -- | -- |
| IC06 | Pseudo-dynamic | -- | -- |
| IC07 | Cyclic | -- | -- |

5.6.2 Cyclic Tests

The recommended testing procedure given by the European Convention for Constructional Steelwork (ECCS, 1986) was used to start with. The ECCS guidelines give a choice of two loading regimes, namely complete and short testing procedures. In the former, two monotonic tests are first conducted for the identification of the yield displacement in both directions. The third test is a cyclic test in which displacement cycles are applied at amplitudes defined in terms of the yield displacement as follows:

- One cycle at each of $\pm 0.25, 0.5, 0.75$ and 1.0 of the yield displacement.
- Three cycles at each of $\pm 2.0, 4.0, 6.0$ etc., of the yield displacement.

The procedure also allows for modification of the above regime and the number of cycles, depending on observation of the specimens under testing. In the absence of monotonic loading results, the test may proceed with the short regime. This is defined as the application of small amplitudes to ensure that four levels are reached prior to yield, followed by the remaining part of the complete testing procedure, as described above. In the current test series, the short procedure was adopted and the yield displacement used was estimated by analysis, pending the first test results. Thereafter, analytical predictions were calibrated and used to quantify the yield displacement for subsequent tests.

The ECCS document recognises several methods of defining the yield point. Some of these are shown in Figure 5.15, where F_y is the yield force and δ_y is the yield displacement. These methods are as follows:

- a. The value corresponding to first yield in any fibre, or in other words first deviation from linearity.
- b. The maximum reached load. This applies well in buckling problems, but may correspond to large deformation in flexural behaviour.
- c. The value corresponding to a certain deformation that would have been obtained in a purely elastic behaviour. Figure 5.15(c) gives an example with twice the elastic deformation. This definition applies well to flexural behaviour of beams and joints, but not to buckling problems.
- d. The intersection of the two tangents shown in Figure 5.15(d). This definition is recommended in the document since it can be used in most applications.

In other cases, the yield force can also be a reference load deduced from analysis. In this series of tests, the definition shown in Figure 5.15(d) was adopted. As mentioned previously, it was approximately estimated from analysis, and then adjusted after the first few tests.

The actual loading history used in each test is given in Chapter 6. In general, within the elastic range, one full cycle per amplitude was used. In the inelastic range, usually three cycles were applied. Two cycles, or even one cycle in a few cases, were applied when

little change was observed between the cycles or in the case of an already failed specimen.

5.6.3 Pseudo-dynamic Tests

All the models tested using the pseudo-dynamic technique were controlled as equivalent cantilevers, as shown in Figure 5.16. Several earthquake records obtained from the Imperial College Strong Motion Data Base (Ambraseys et al, 1989) were considered. The peak acceleration was scaled appropriately in conjunction with the choice of mass, as described in subsequent sections. Two earthquakes, El Centro (Imperial Valley, 19 May 1940, SE component) and Montenegro (Petrovac, 15 April 1979, NS component) were chosen, since both exhibit a number of large amplitude cycles. The acceleration time histories for the two earthquakes are given in Figures 5.17 and 5.18. The response spectra of the records for two values of damping are also shown in Figures 5.19 and 5.20.

In order to choose the appropriate parameters, a series of nonlinear analyses using ADAPTIC was undertaken. The details of this study are described in the following two sub-sections.

5.6.3.1 Tests on Models EM03 and IC03

In case of the pseudo-dynamic tests on models EM03 and IC03, there was a choice of either controlling the actuator displacement, assuming a simple beam, or the tip displacement, assuming an equivalent cantilever. This is of significance in the choice of mass, as discussed hereafter.

If a mass of 50,000 Kg is assumed at the mid-span loading point, and noting that the initial stiffness of the simple beam, obtained from the analysis, is approximately 14.2×10^6 N/m, the fundamental period of the simple beam is 0.37 seconds. This period coincides with maximum dynamic amplification in the El Centro record, giving a peak response acceleration of about 0.9 g, for 3% damping. For the Montenegro record, a slightly higher mass would have been needed. It is noted, however, that this treatment is based on the initial elastic stiffness and is likely to be different from the observed behaviour in the nonlinear range.

On the other hand, the stiffness of the equivalent cantilever is estimated to be about 4.7×10^6 N/m. For an assumed mass of 20,000 Kg at the tip of the cantilever, the period

becomes 0.41 seconds. This is acceptable provided that the applied force, given by the product of mass and peak acceleration, is sufficiently high. Otherwise, the acceleration should be scaled up, with no regard to dynamic similitude.

Analysis of the equivalent cantilever using the Montenegro earthquake indicated that the level of dynamic force is substantially higher than the capacity of the member, as shown in Figure 5.21. Consequently, the choice was narrowed down to the El Centro earthquake with appropriate scaling. Figures 5.22 (a), (b), (c) and (d) depict the analytical response under the latter record, scaled by a factor of 1.1, 1.3, 1.5 and 1.7, respectively. Considering that failure occurred for model EM02 at a cyclic displacement of 33 mm, and accounting for the severe reversal conditions in the cyclic test, the equivalent displacement was expected to be at about 40 to 45 mm. Therefore, to demonstrate the improvement in performance in the IC section, a response of about 60 mm in the largest early peak of El Centro record was sought. With reference to Figures 5.22(b) and (c), it was decided to interpolate between the two, and apply a scaling factor of 1.4, which allows for some error in the analytical results, with preference given to erring on the safe side.

Based on the estimated period of vibration of 0.41 seconds, a time step of 0.02 seconds is sufficient for the stability and accuracy of the central difference integration algorithm. Nevertheless, control of the test specimen as an equivalent cantilever requires a smaller time step, for accuracy. It was, therefore, decided to use a time step of 0.01, to be reduced to 0.005 seconds if necessary.

5.6.3.2 Tests on Models EM05, IC05 and IC06

Following the same basis as in the previous section, models EM05, IC05 and IC06 were subjected to an 8 seconds (5.5 to 13.5 seconds) acceleration time history of Montenegro earthquake. A mass of 30,000 Kg was assumed in the procedure, and a time step of 0.02 seconds was used. The earthquake record was first scaled down by 10%. This was followed by another 8 seconds of the unscaled acceleration time history, to examine the ultimate behaviour of the models.

TABLE 5.10
Summary of Pseudo-Dynamic Tests

| Model Reference | EM03 | IC03 | EM05 | IC05 | IC06 |
|-----------------------------|-------------------|-------------------|--------------------------|--------------------------|--------------------------|
| Inertial Mass m (Kg) | 20,000 | 20,000 | 30,000 | 30,000 | 30,000 |
| Period T (sec) | 0.41 | 0.41 | 0.39 | 0.39 | 0.39 |
| Earthquake Record | El Centro | El Centro | Montenegro | Montenegro | Montenegro |
| Peak Acceleration (g) | 0.34 g | 0.34 g | 0.45 g | 0.45 g | 0.45 g |
| Total Duration (sec) | 54.21 | 54.21 | 48.24 | 48.24 | 48.24 |
| Curtailed Duration (sec) | 8 sec (0 to 8) | 8 sec (0 to 8) | 2x8 sec (5.5 to 13.5) | 2x8 sec (5.5 to 13.5) | 2x8 sec (5.5 to 13.5) |
| Scaling Factor (%) | 140% | 140% | 90%, 100% | 90%, 100% | 90%, 100% |
| Time Step Δt (sec) | 0.01 | 0.01 | 0.02 | 0.02 | 0.02 |

Figures 5.23(a), (b) and (c) show the response predicted by analysis under the Montenegro earthquake using scaling factors of 0.9, 1.0 and 1.1, respectively. Based on an assessment of the cyclic loading tests, a scaling factor of 0.9 was first chosen. A further test was conducted using the unscaled record to examine the ultimate behaviour of model IC05. Using a mass of 30,000 Kg, and an estimated stiffness of about 7.8×10^6 N/m, the natural period is 0.39 second giving a time step of 0.02 seconds. The details of the pseudo-dynamic tests on all models are summarized in Table 5.10.

A detailed account of the loading regimes, experimental results and observations from all tests is presented in Chapter 6 of this thesis.

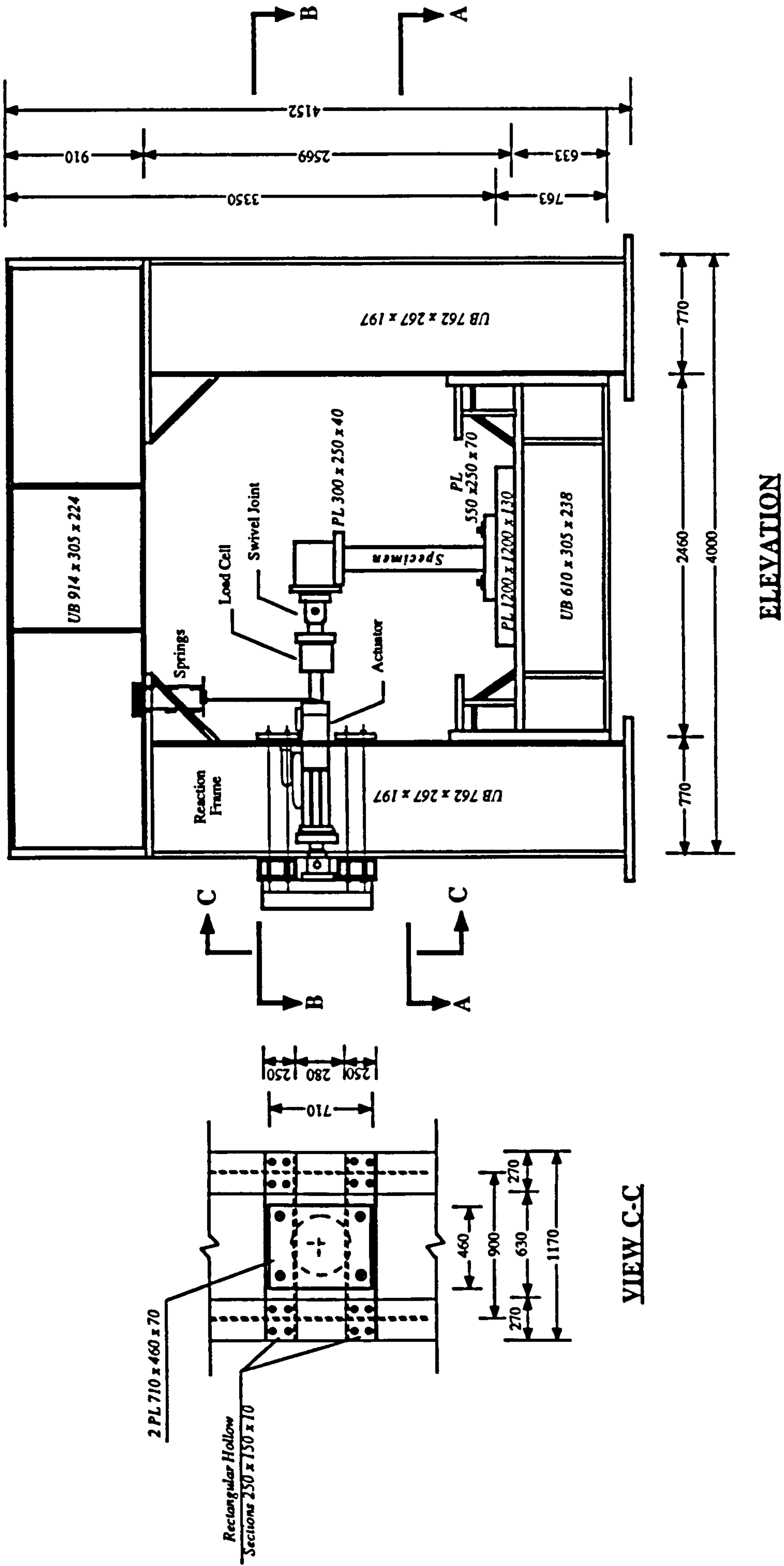


Fig. 5.1.a Self-reacting testing frame (dimensions in mm)

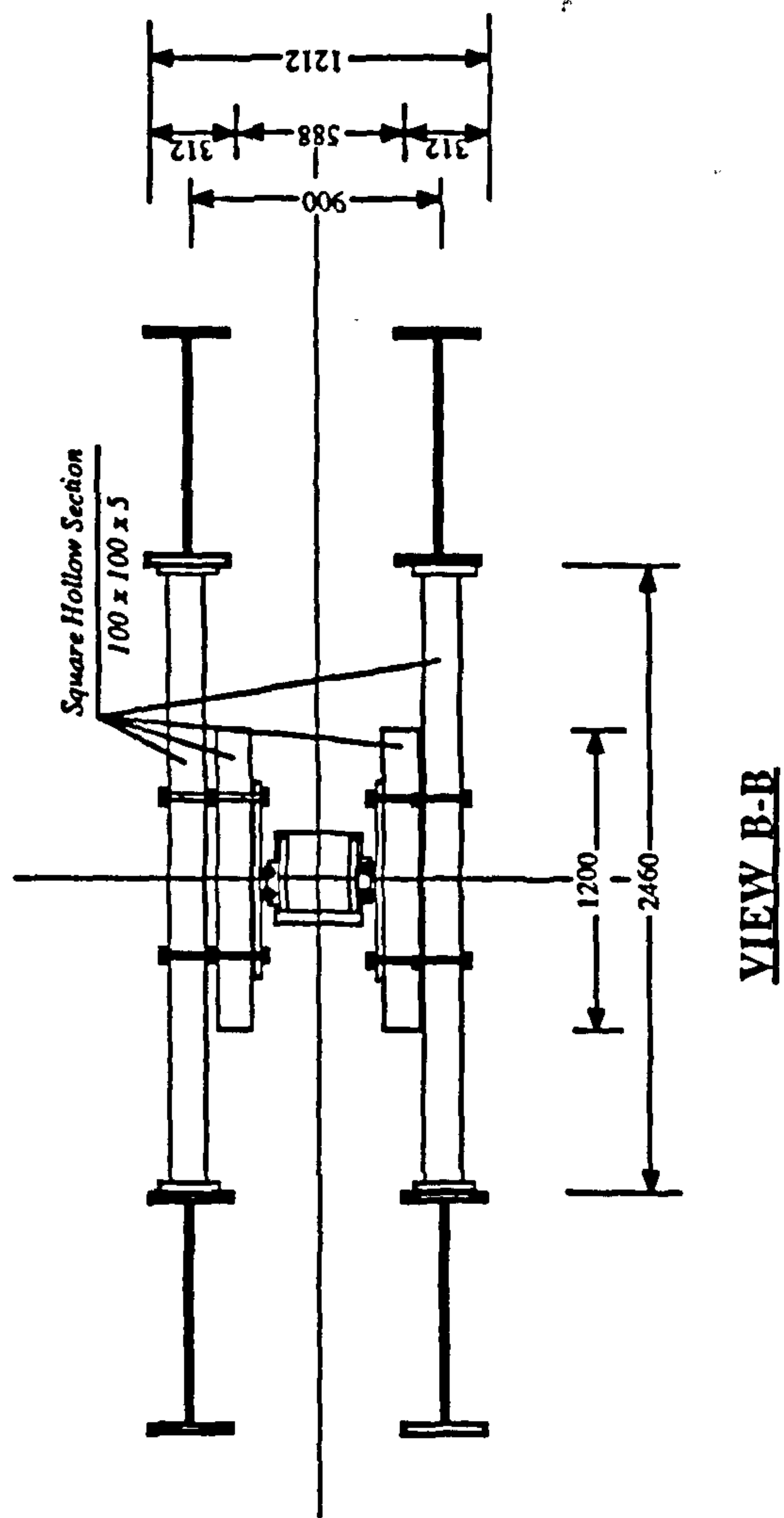
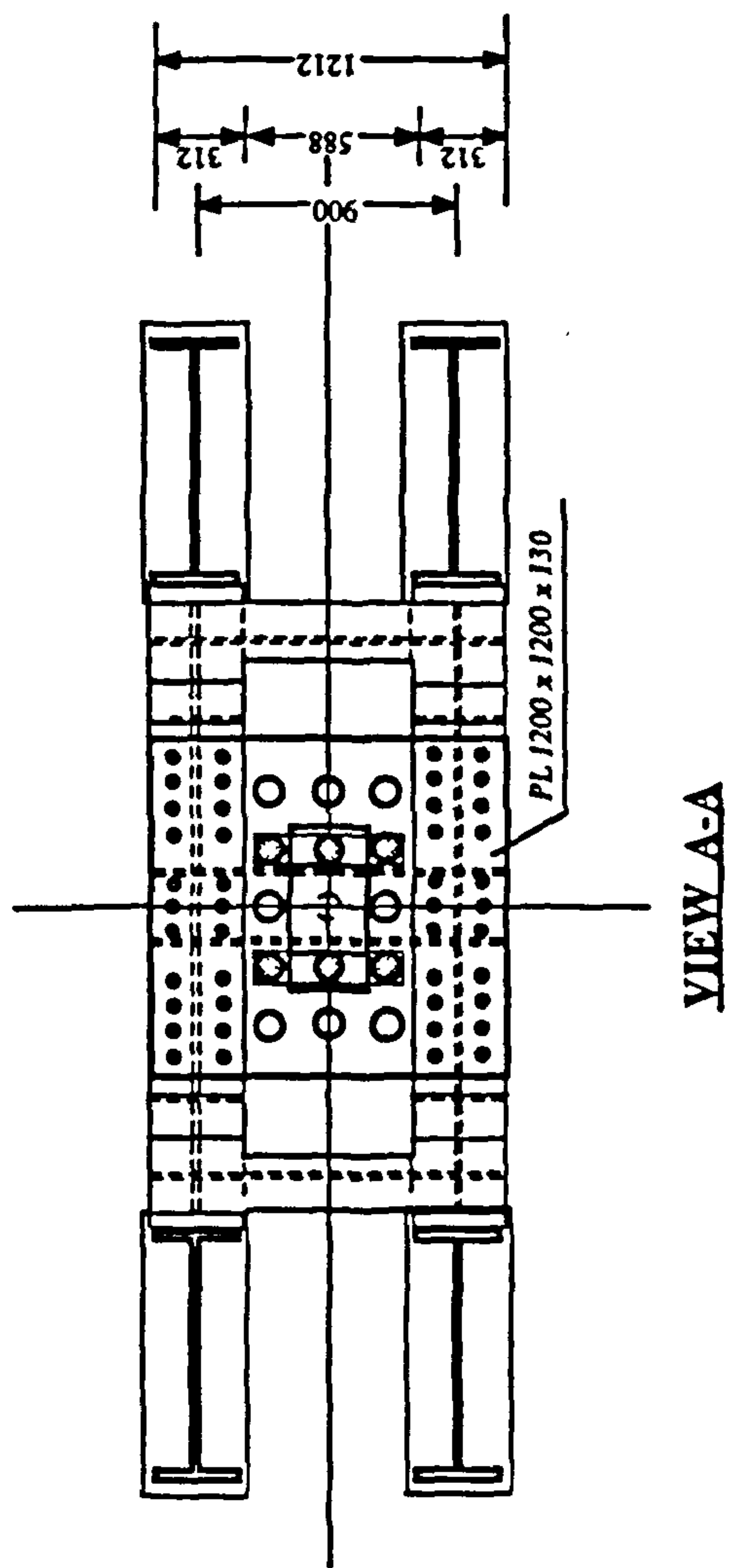


Fig. 5.1.b Self-reacting testing frame (continued) (dimensions in mm)

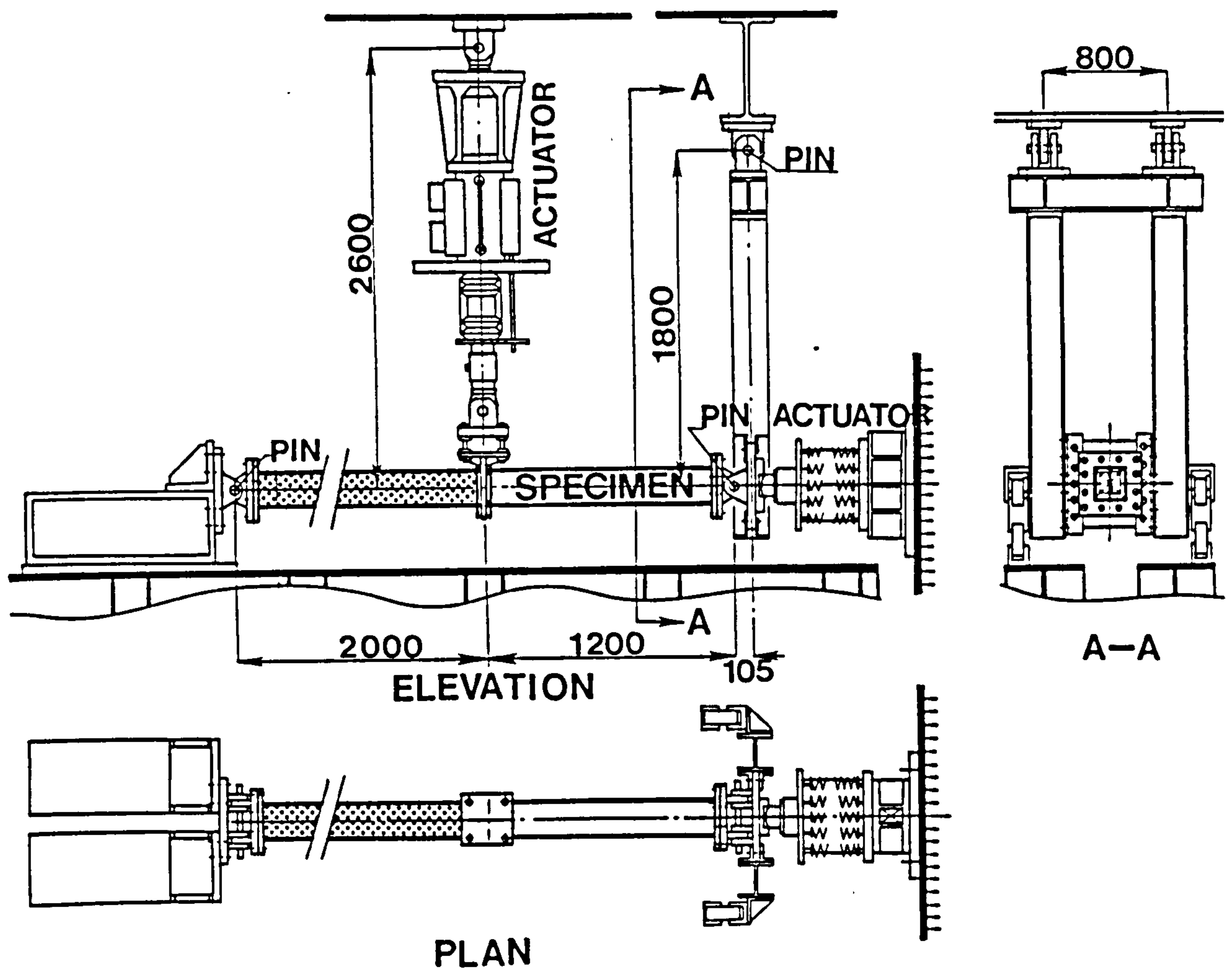


Fig. 5.2 Testing assembly (dimensions in mm)

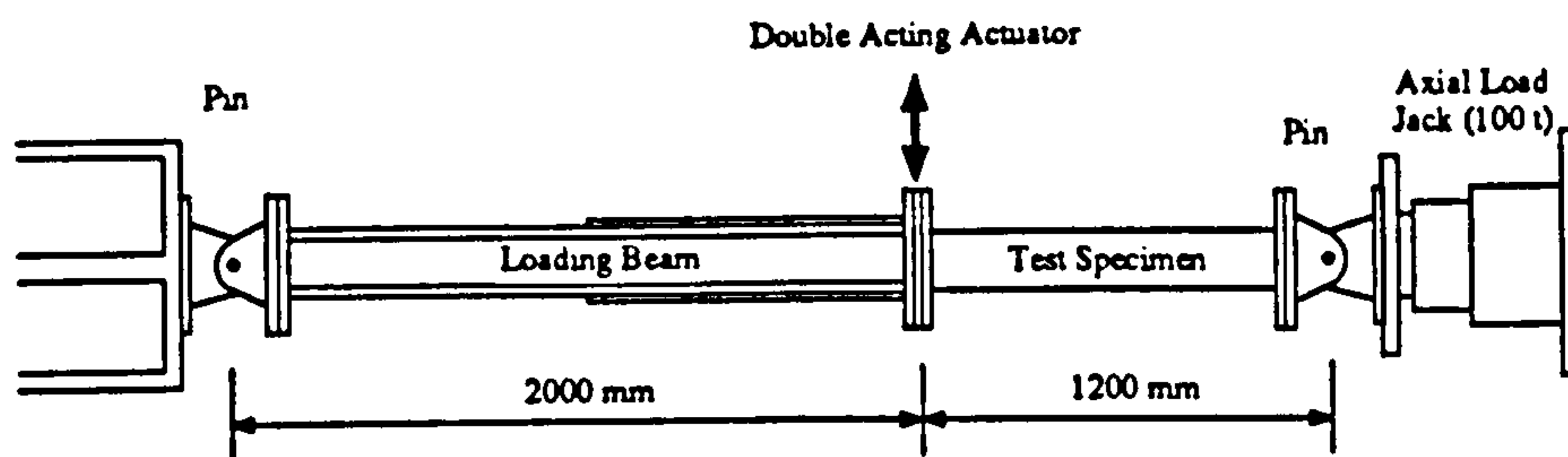
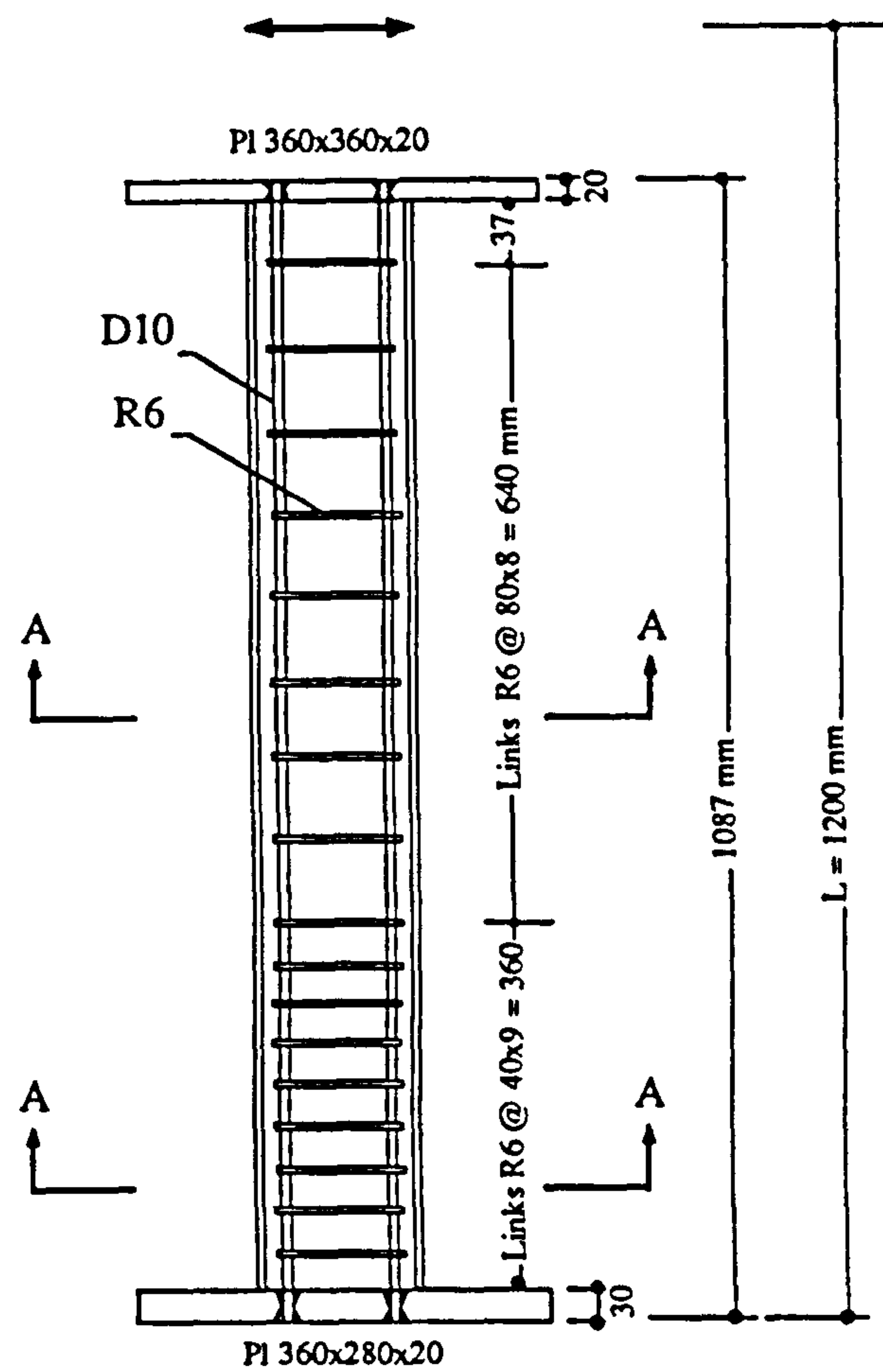
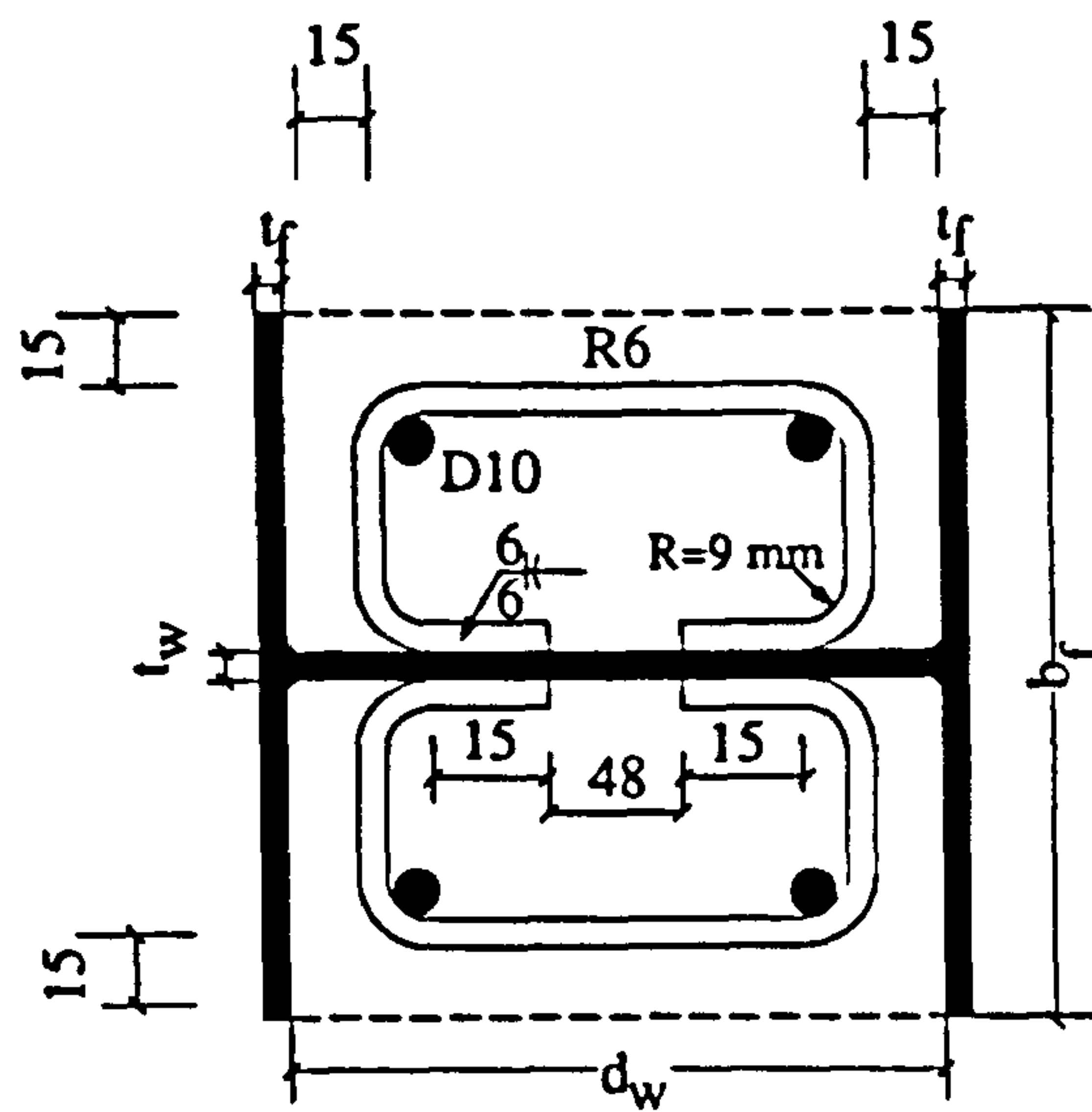


Fig. 5.3 Test layout (dimensions in mm)

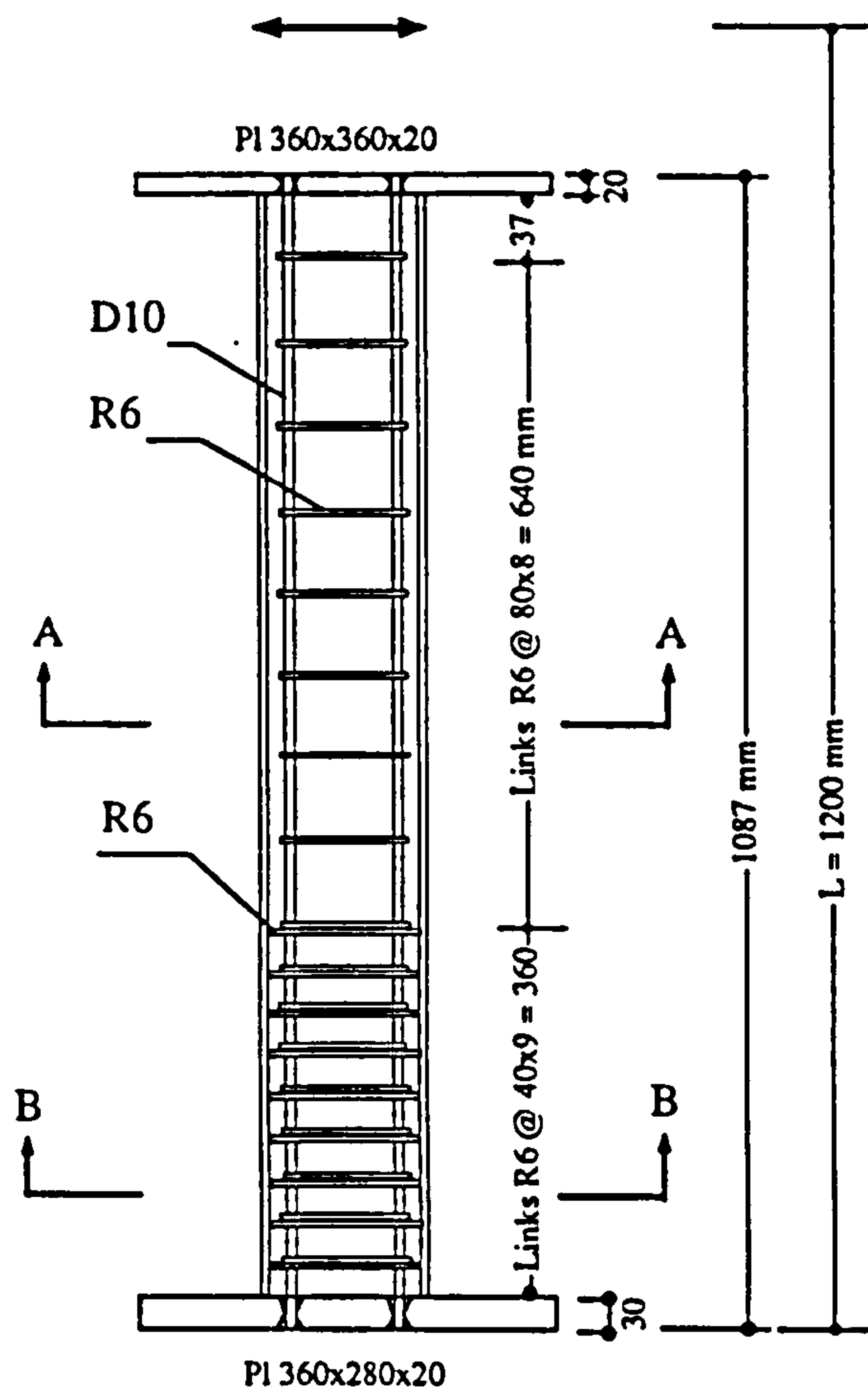


Elevation

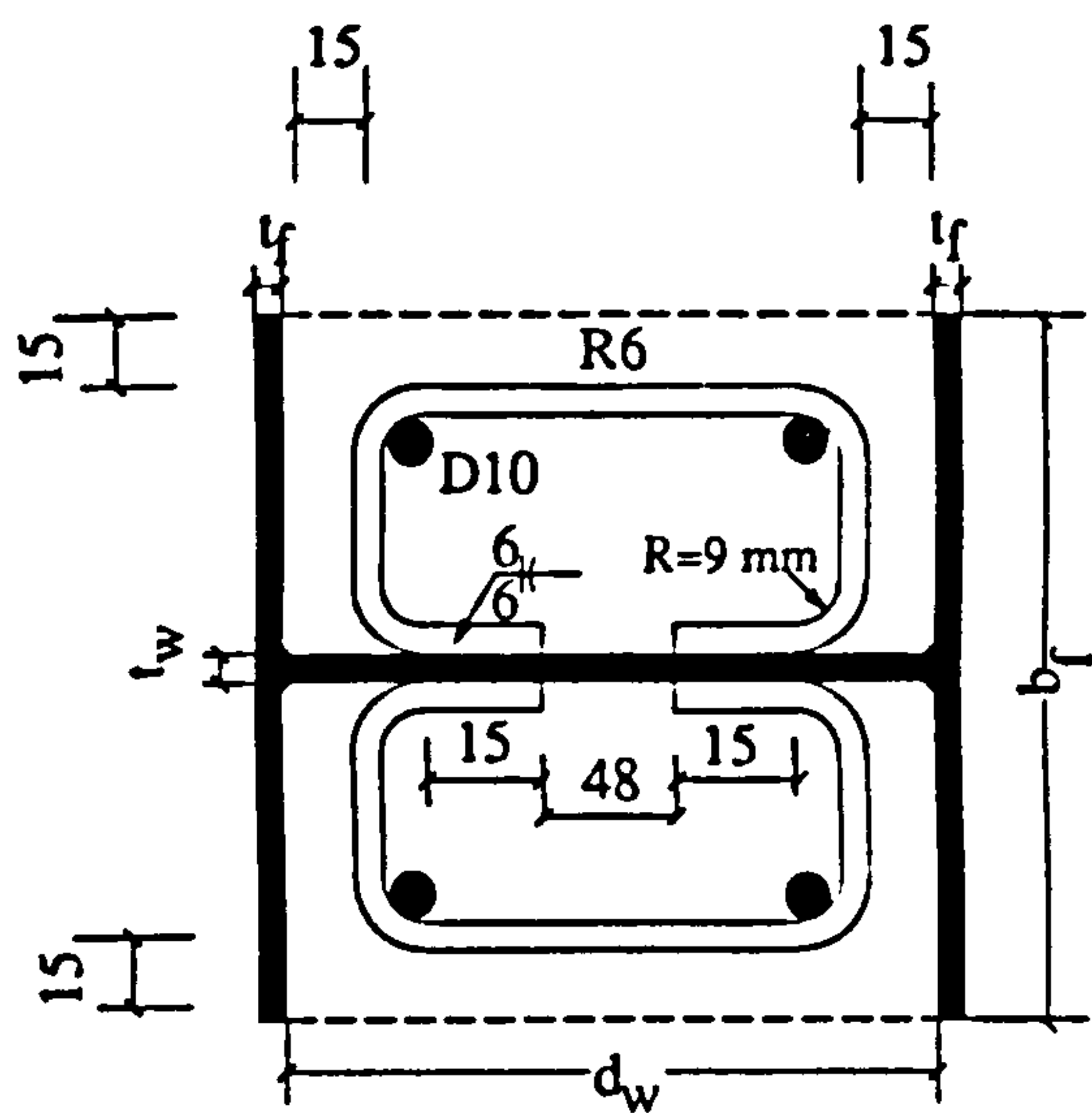


Section A-A

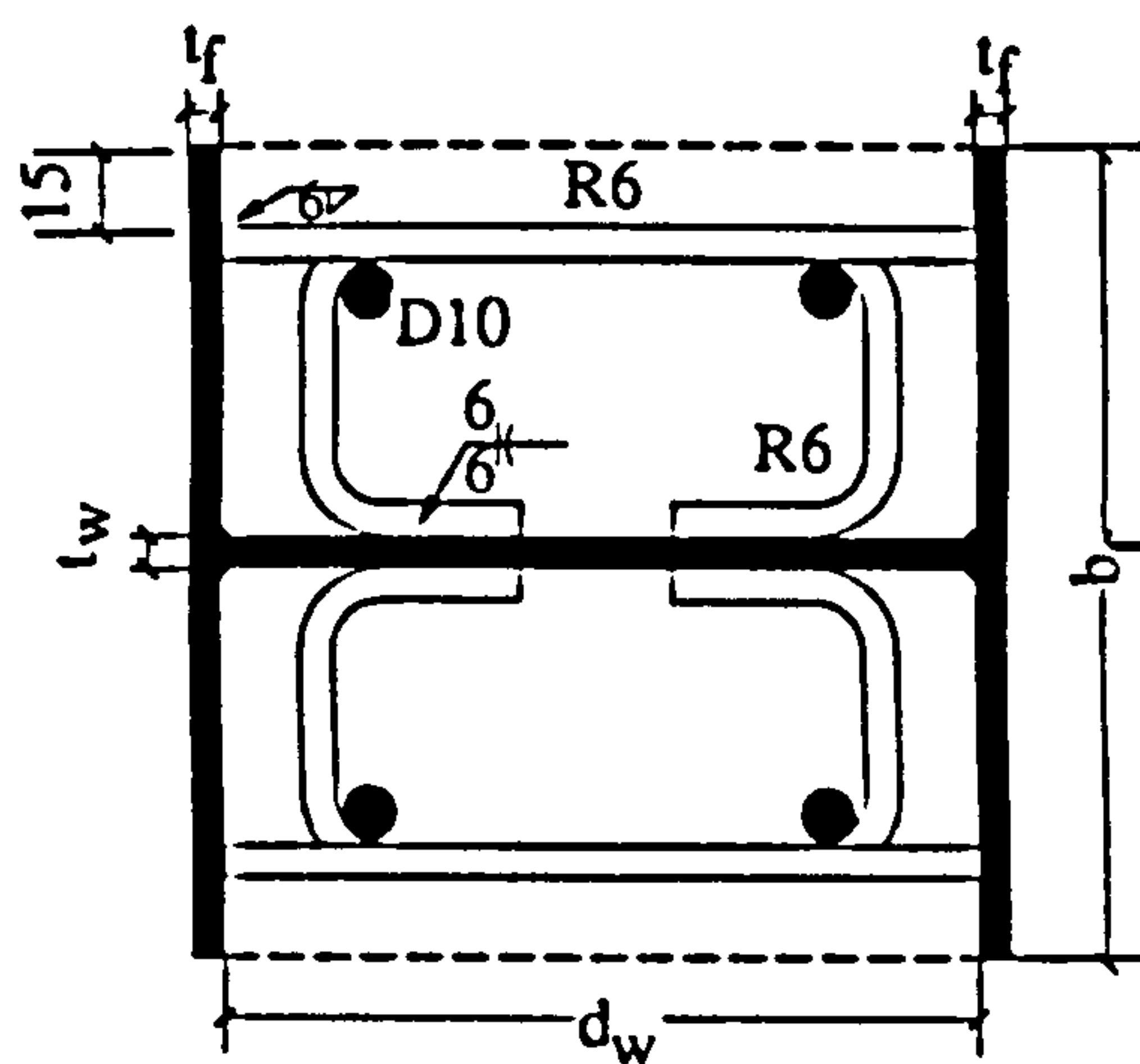
Fig. 5.4 Details of models EM01, EM02 and EM03 (dimensions in mm)



Elevation

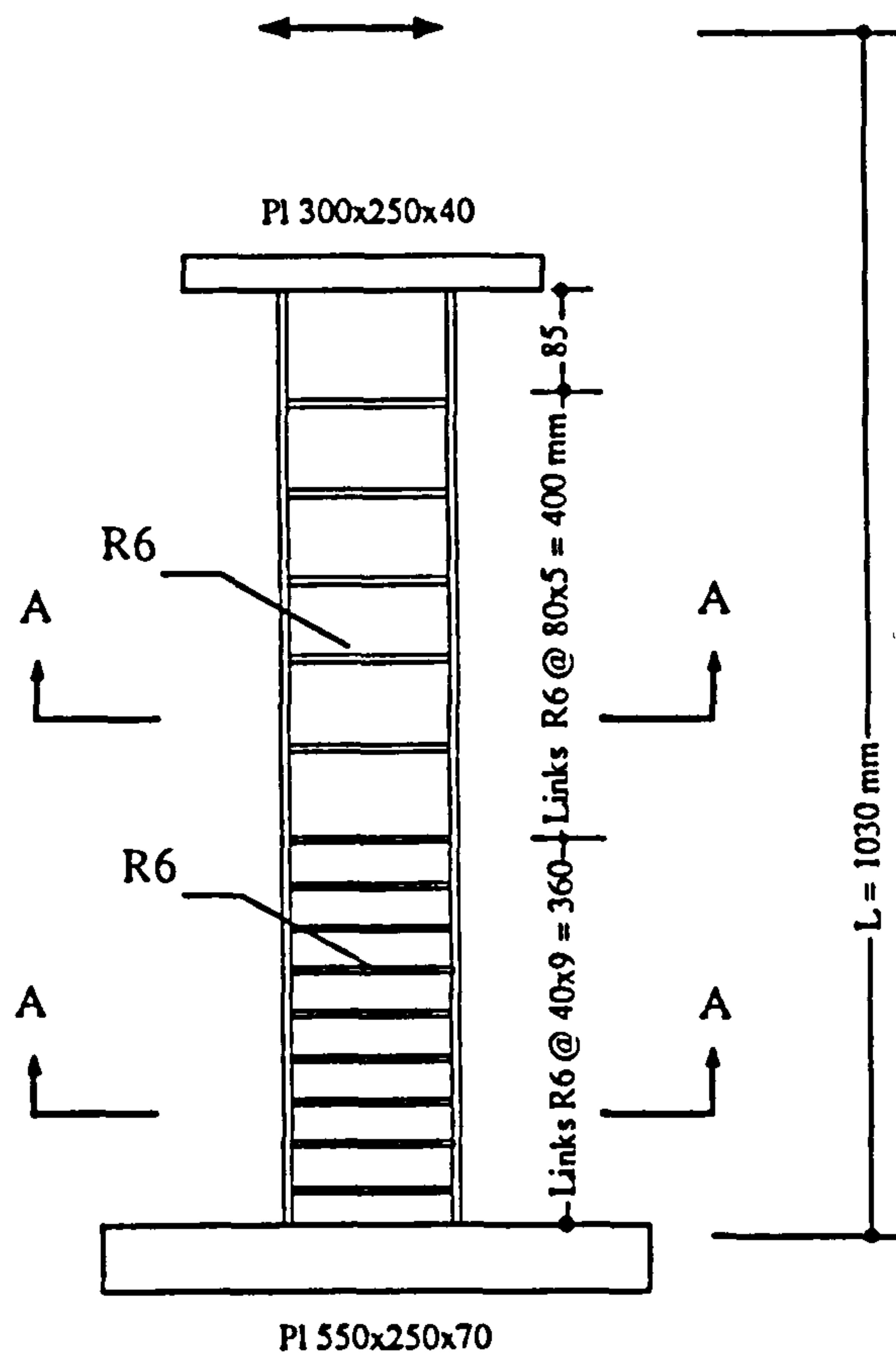


Section A-A

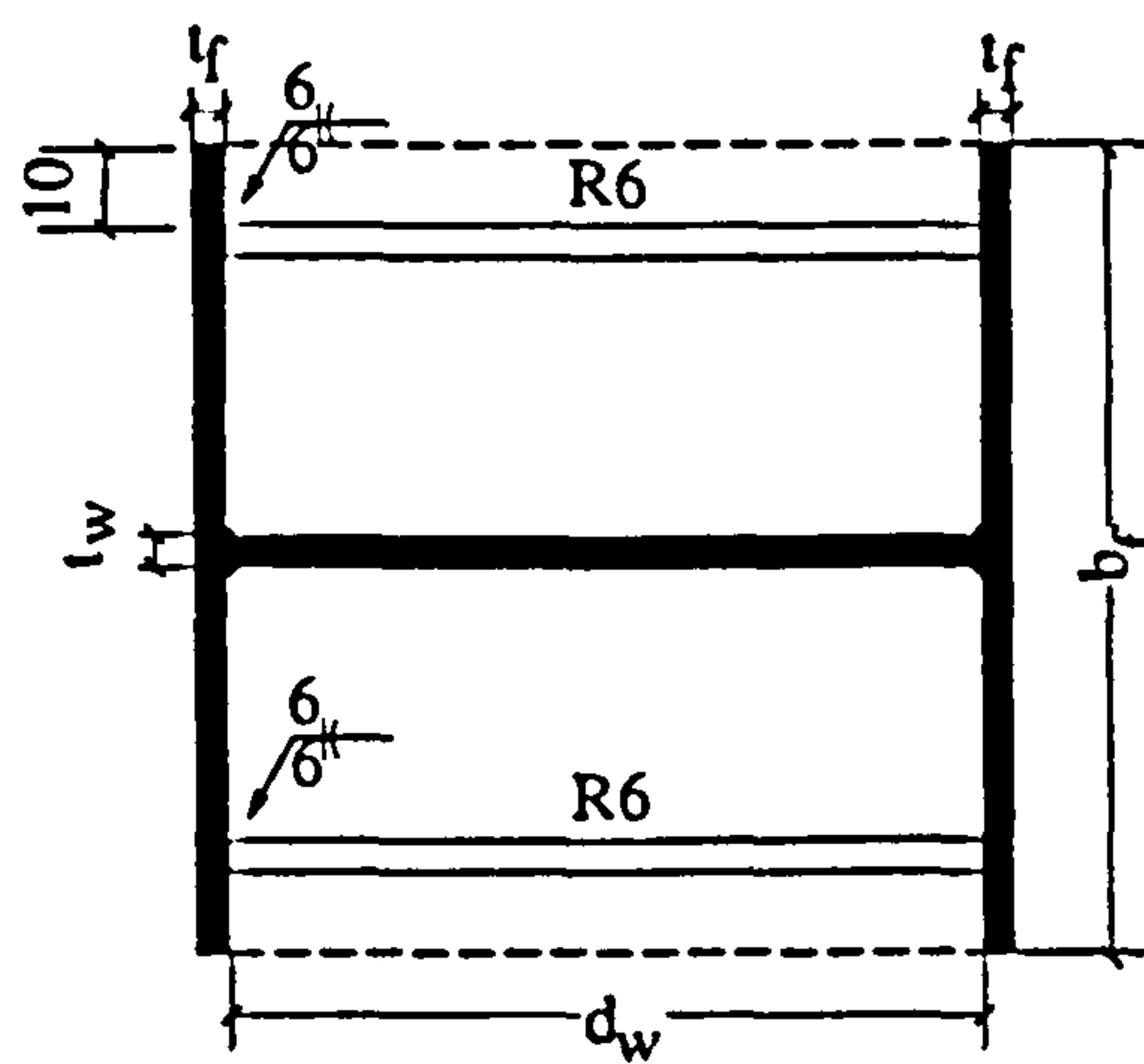


Section B-B

Fig. 5.5 Details of models IC01, IC02 and IC03 (*dimensions in mm*)

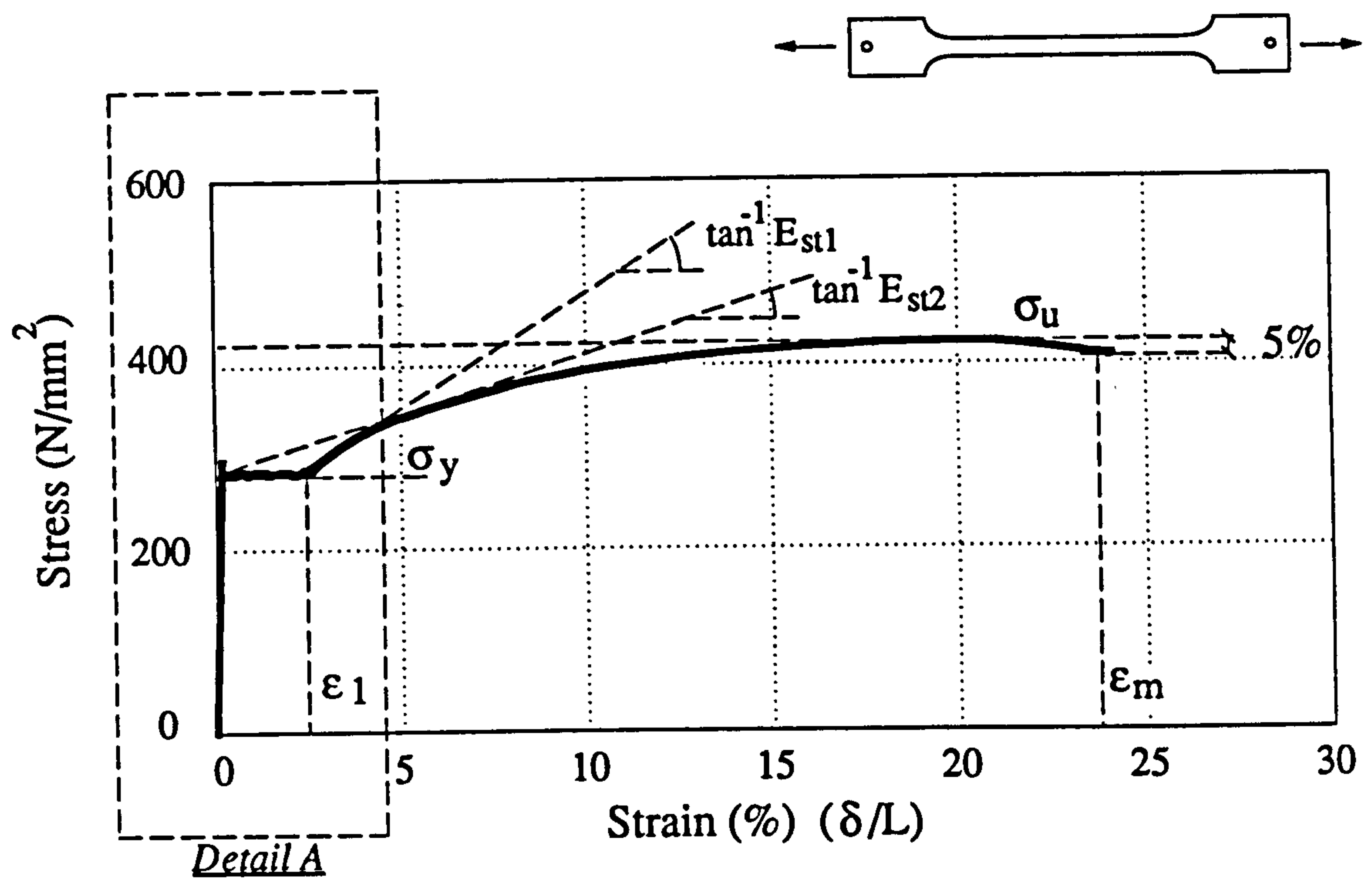


Elevation

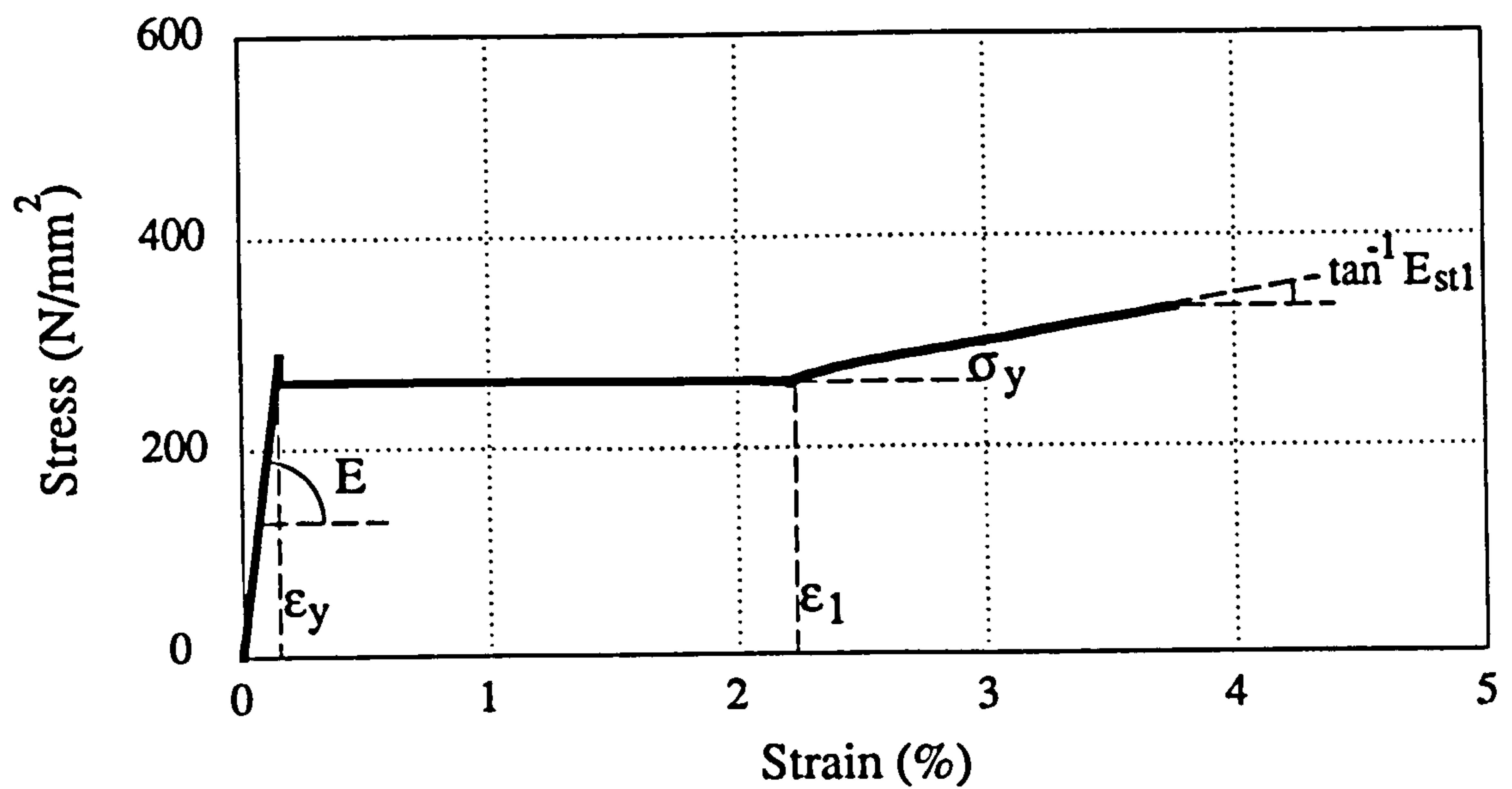


Section A-A

Fig. 5.8 Details of models IC06 and IC07 (dimensions in mm)

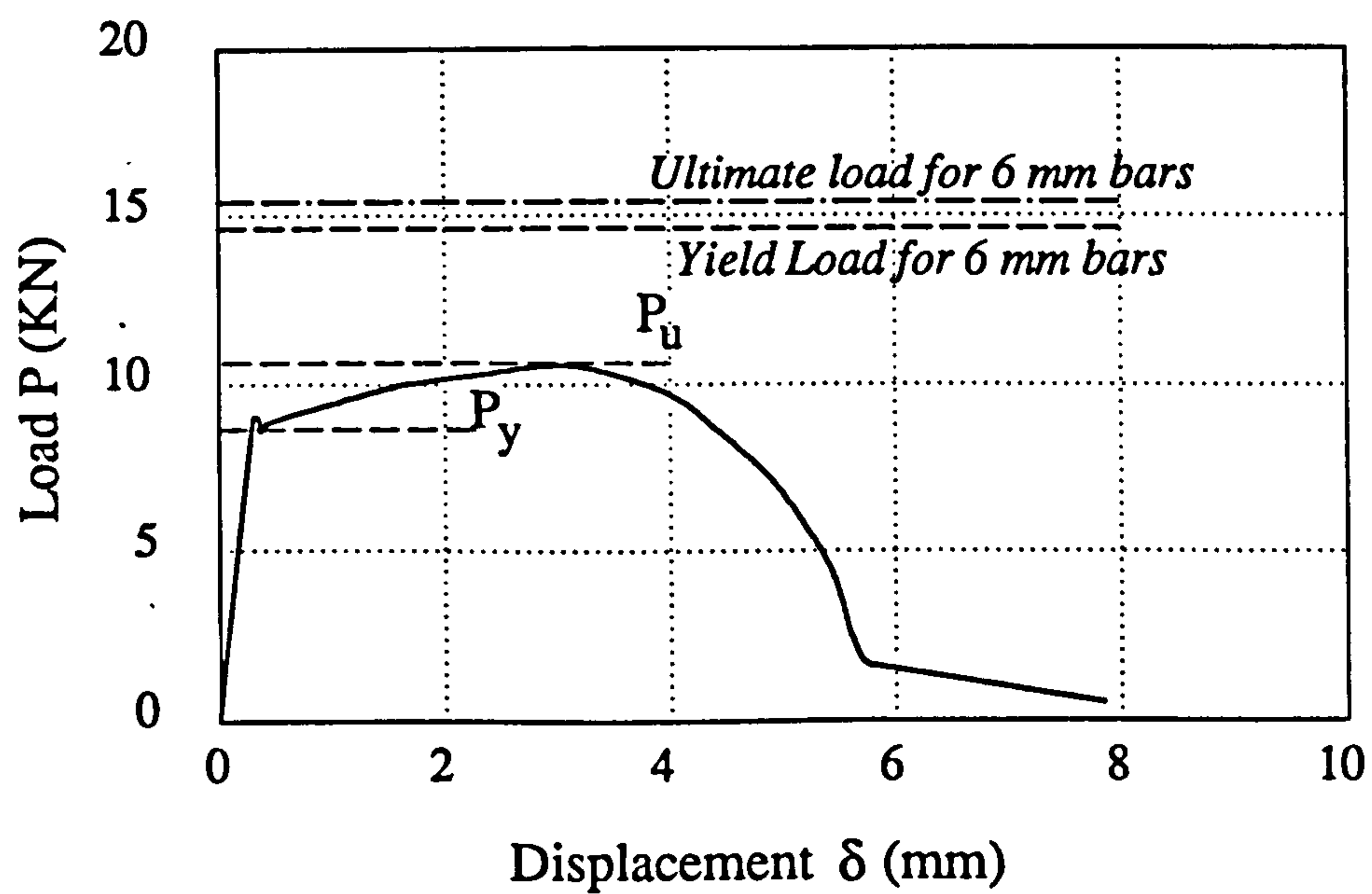
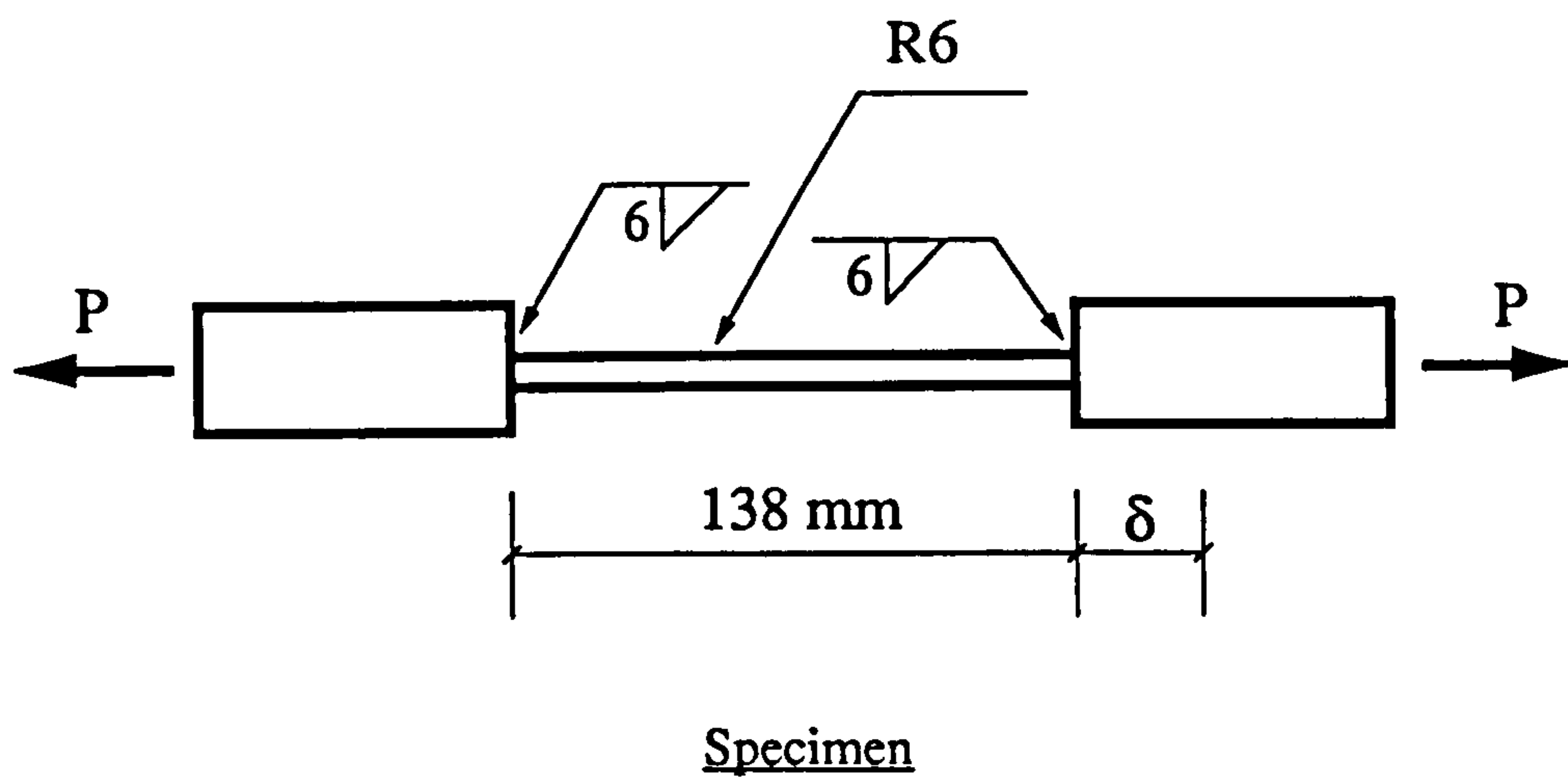


Stress versus strain relationship



Stress versus strain relationship (*Detail A*)

Fig. 5.9 Typical stress-strain relationship



Load versus displacement Relationship

Fig. 5.10 Strength of weld

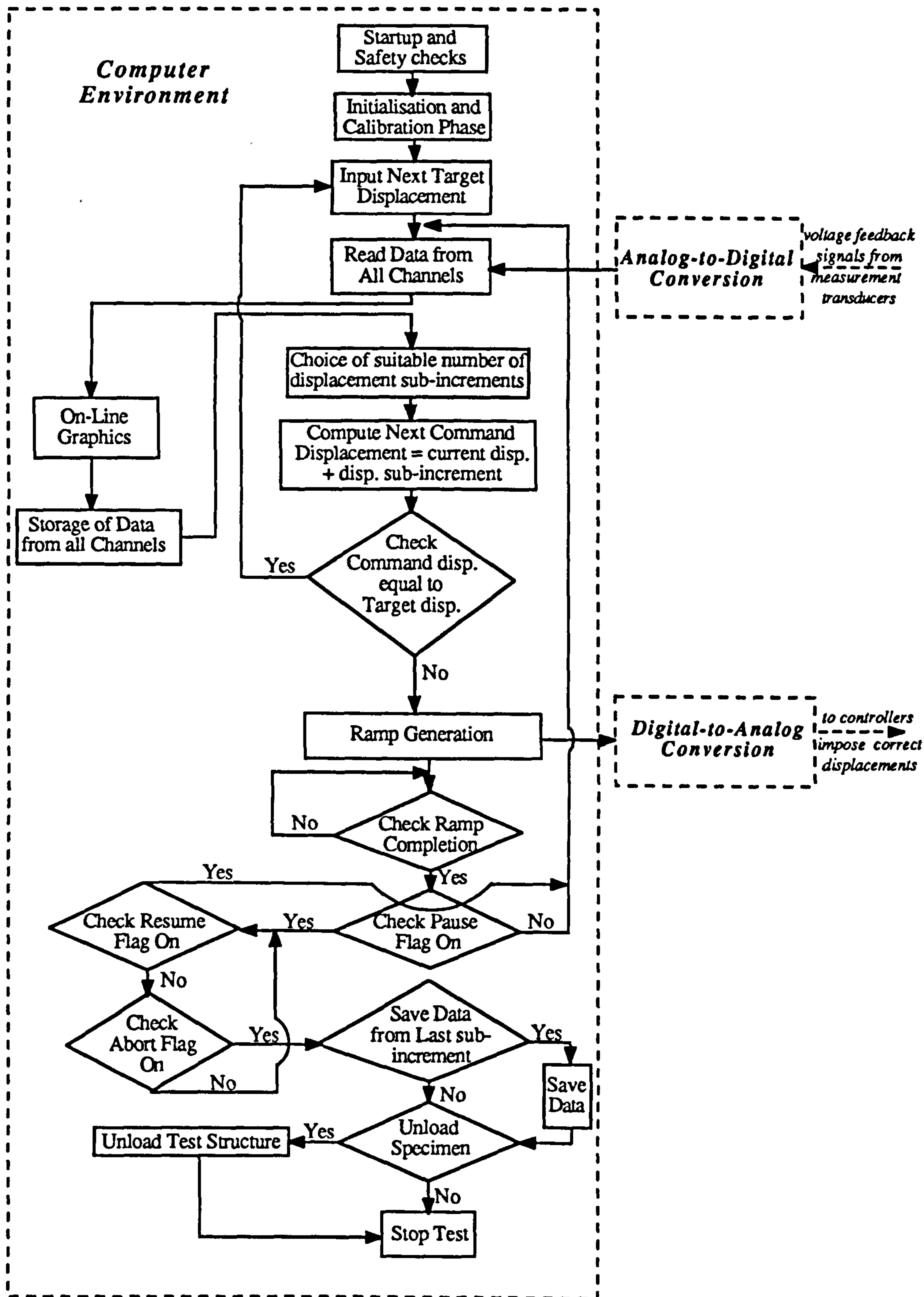
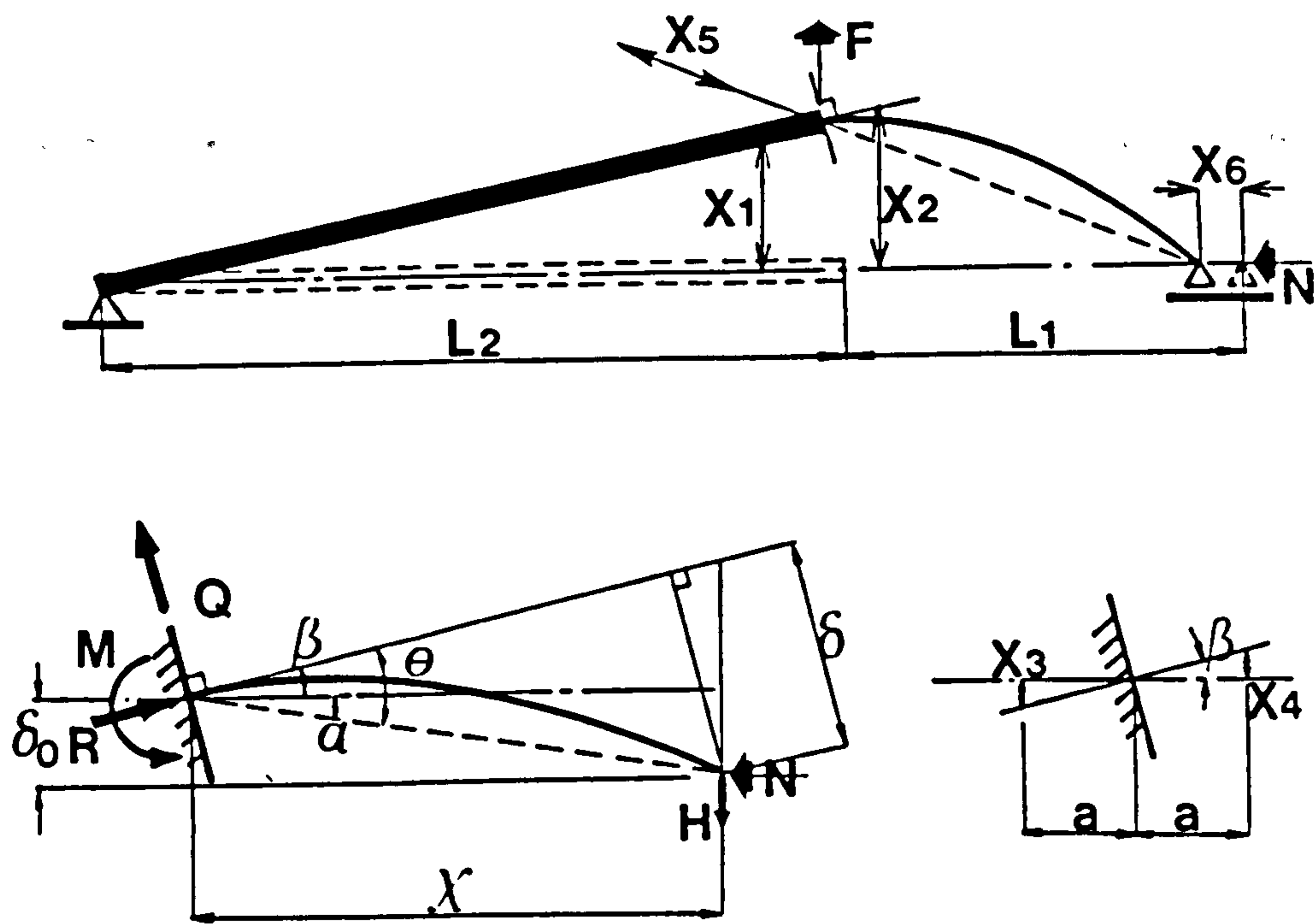


Fig. 5.11 Software layout of the cyclic loading program



$$\begin{aligned}
 M &= H \chi + N \delta_0 & \delta &= (\chi \tan \beta + \delta_0) \cos \beta \\
 \theta &= \alpha + \beta & \chi &= \sqrt{(L_1 - X_5)^2 + \delta_0^2} \\
 H &= [L_2 / (L_1 + L_2)] F & \delta_0 &= (X_1 + X_2) / 2 \\
 \alpha &= \tan^{-1} \left(\frac{\delta_0}{\chi} \right) & \beta &= \tan^{-1} \left(\frac{X_4 - X_3}{2a} \right) \\
 Q &= H \cos \beta - N \sin \beta & R &= H \sin \beta + N \cos \beta
 \end{aligned}$$

(a)

$$\begin{aligned}
 M &= H L_1 + N \delta_0 & \delta &= (L_1 \tan \beta + \delta_0) \cos \beta \\
 H &= [L_2 / (L_1 + L_2)] F & \delta_0 &= (X_1 + X_2) / 2 \\
 \beta &= \tan^{-1} \left(\frac{X_4 - X_3}{2a} \right) \\
 Q &= H \cos \beta - N \sin \beta & R &= H \sin \beta + N \cos \beta
 \end{aligned}$$

(b)

Fig. 5.12 Geometric relationships for testing assembly: (a) Detailed Geometry Transformation; (b) Simplified Geometry Transformation

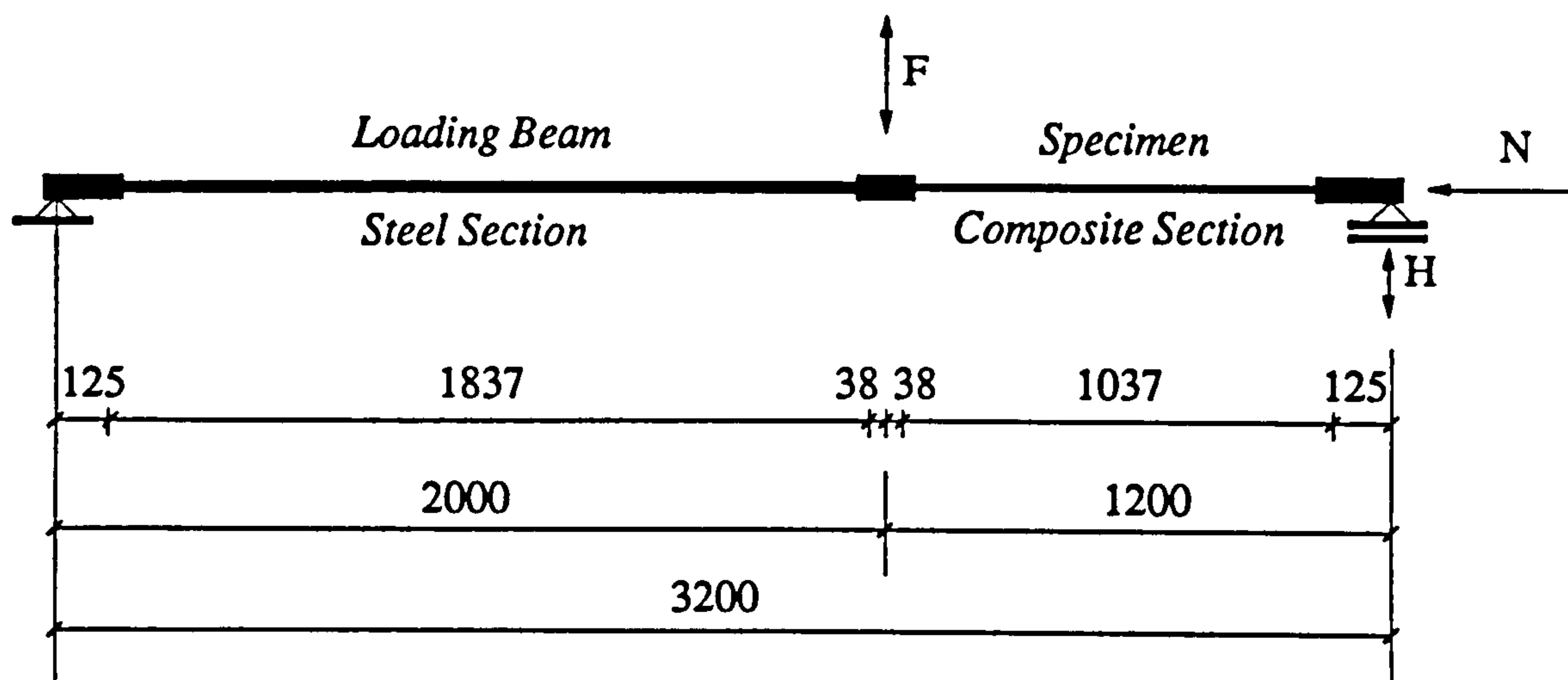


Fig. 5.13 Analytical model of the test-rig (*dimensions in mm*)

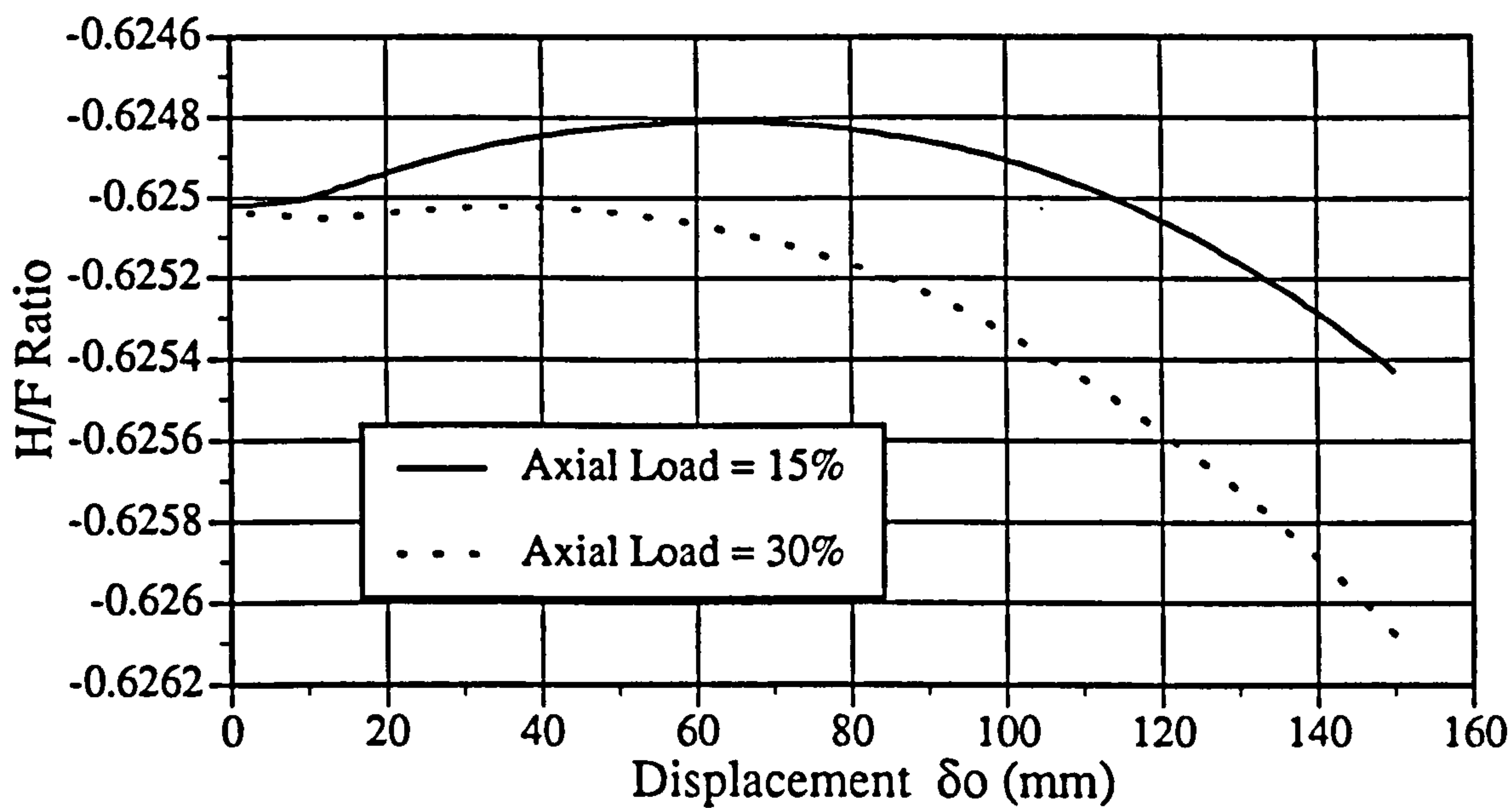


Fig. 5.14 Relationship between beam displacement and the ratio of applied load to reaction at roller support

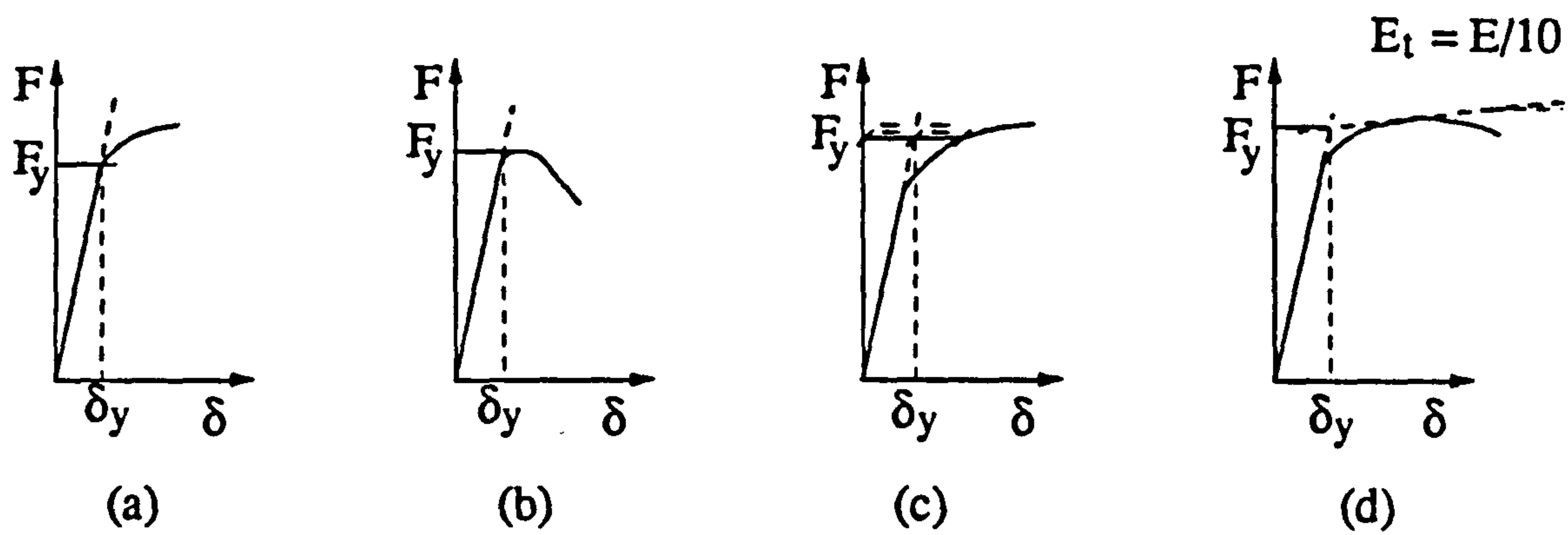


Fig. 5.15 Definition of yield point

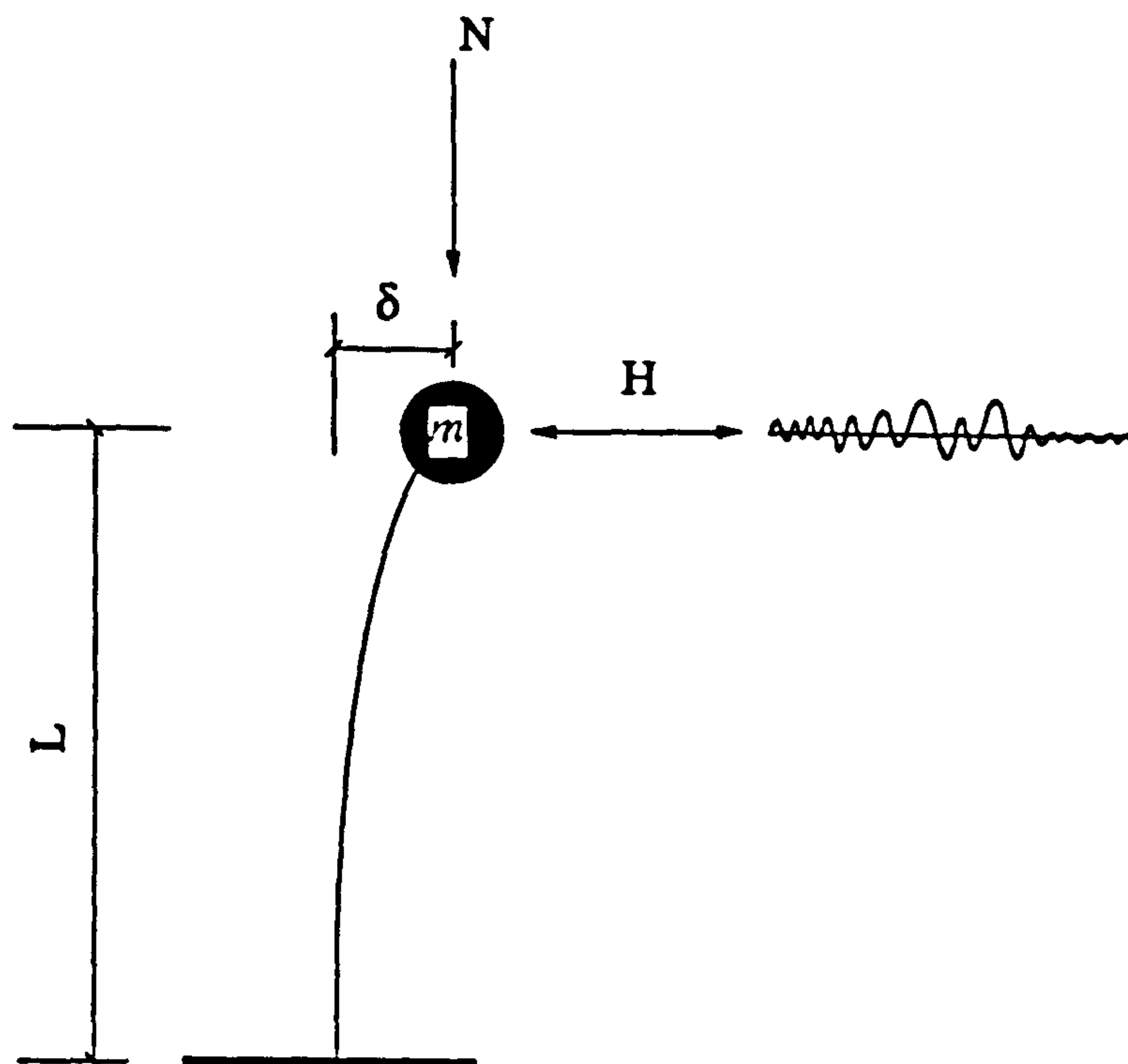


Fig. 5.16 Equivalent single degree of freedom system

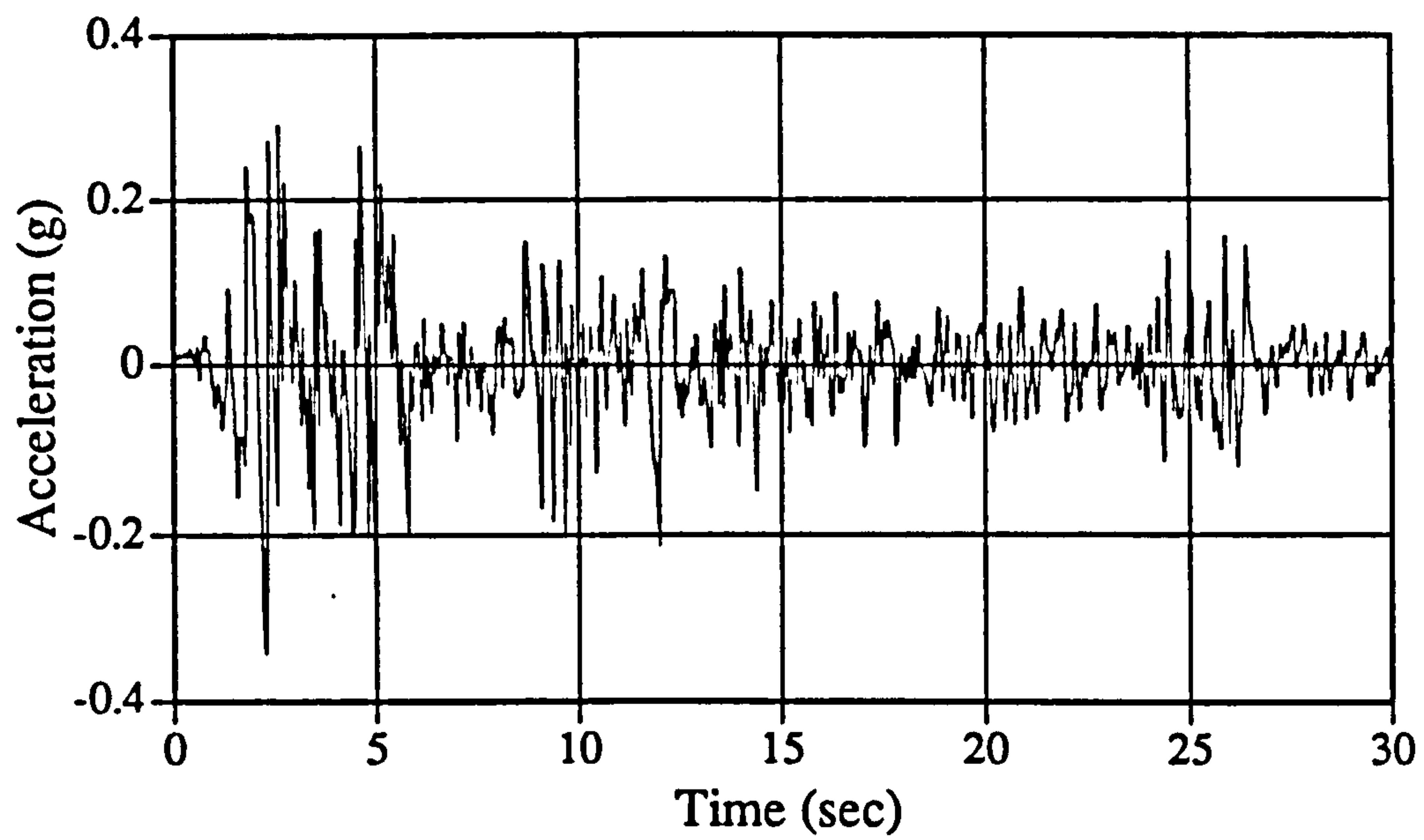


Fig. 5.17 Acceleration time history of El Centro earthquake

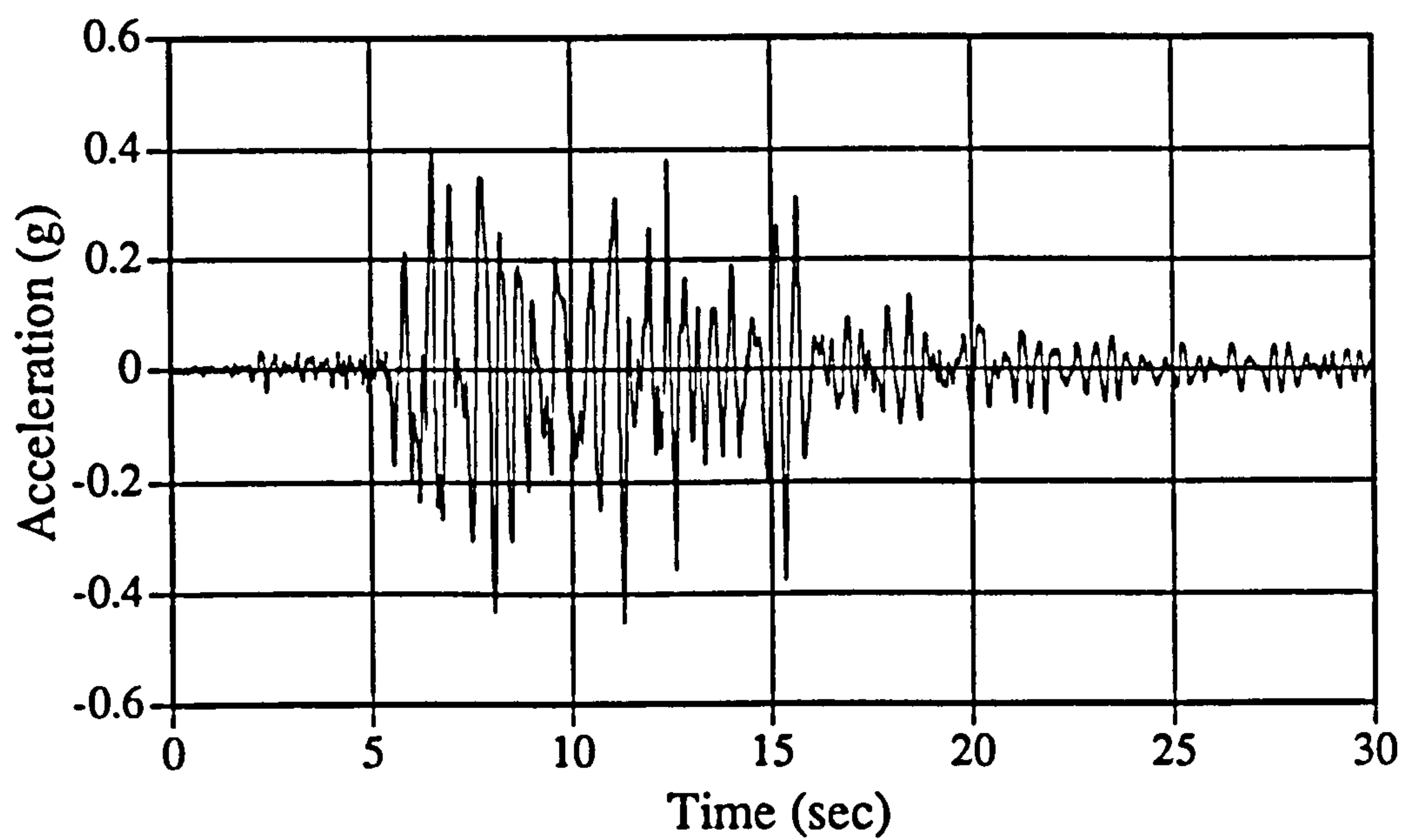


Fig. 5.18 Acceleration time history of Montenegro earthquake

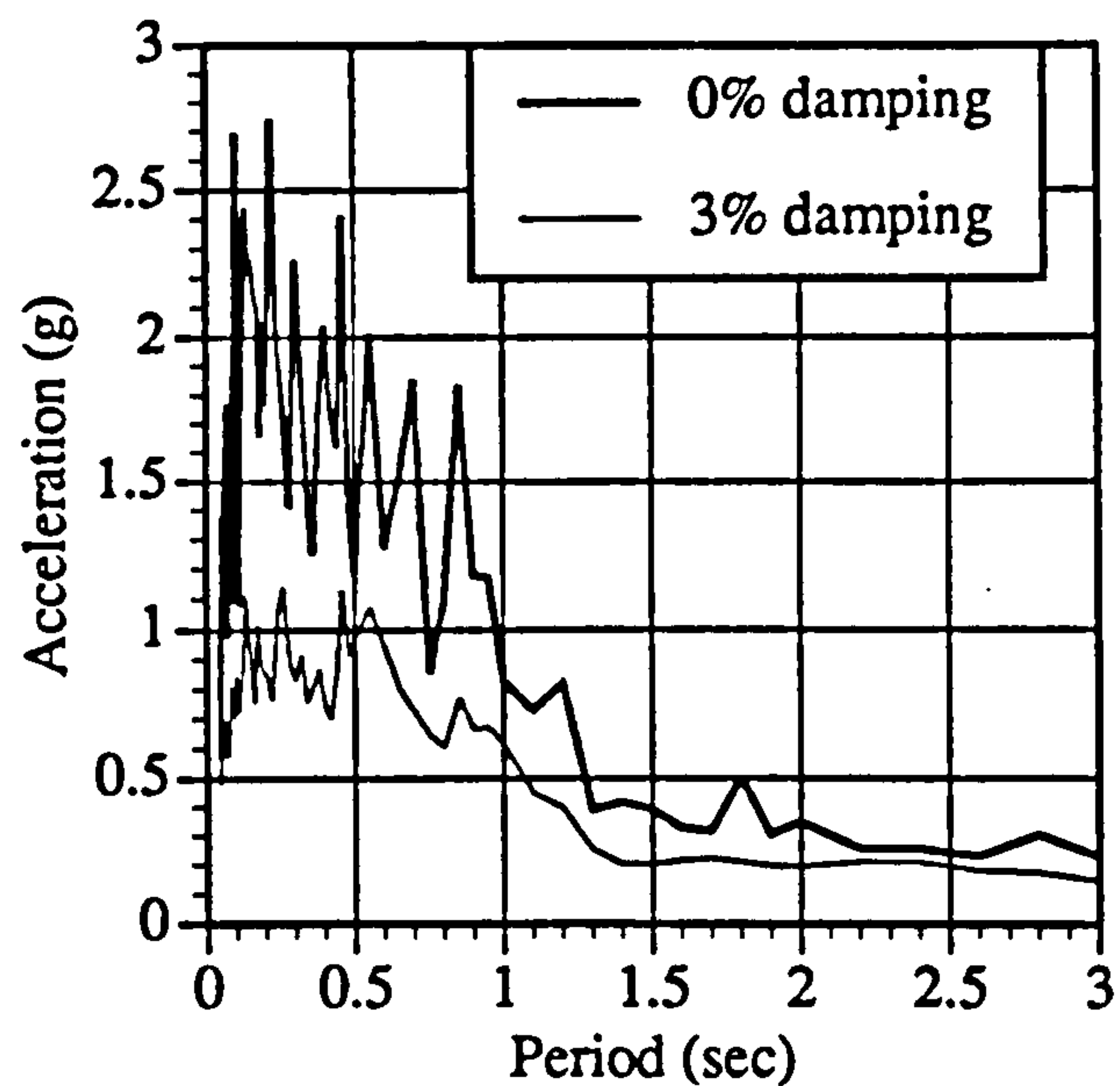


Fig. 5.19 Response spectrum of El Centro earthquake

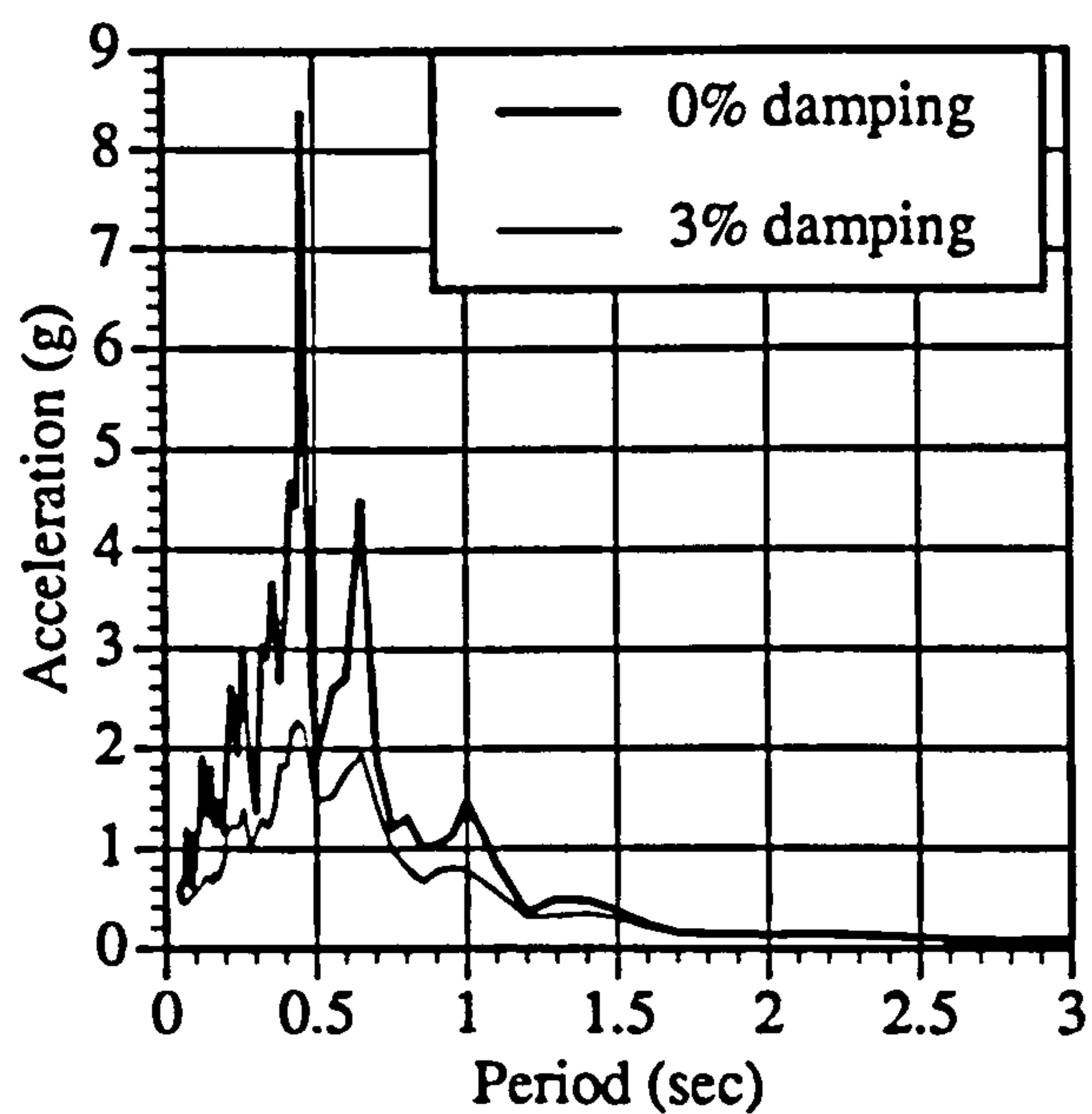


Fig. 5.20 Response spectrum of Montenegro earthquake

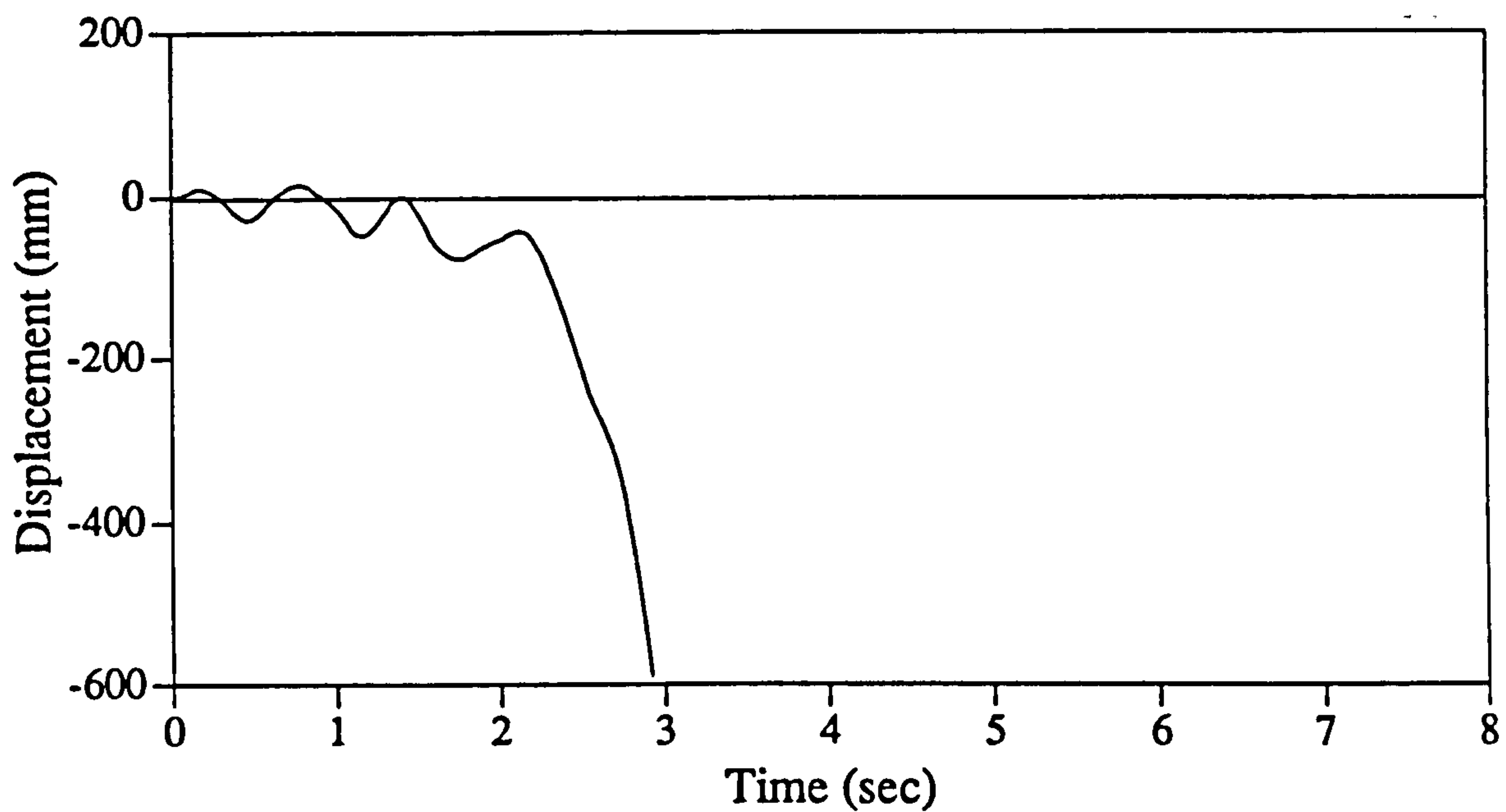


Fig. 5.21 Analytical response under full scale Montenegro earthquake

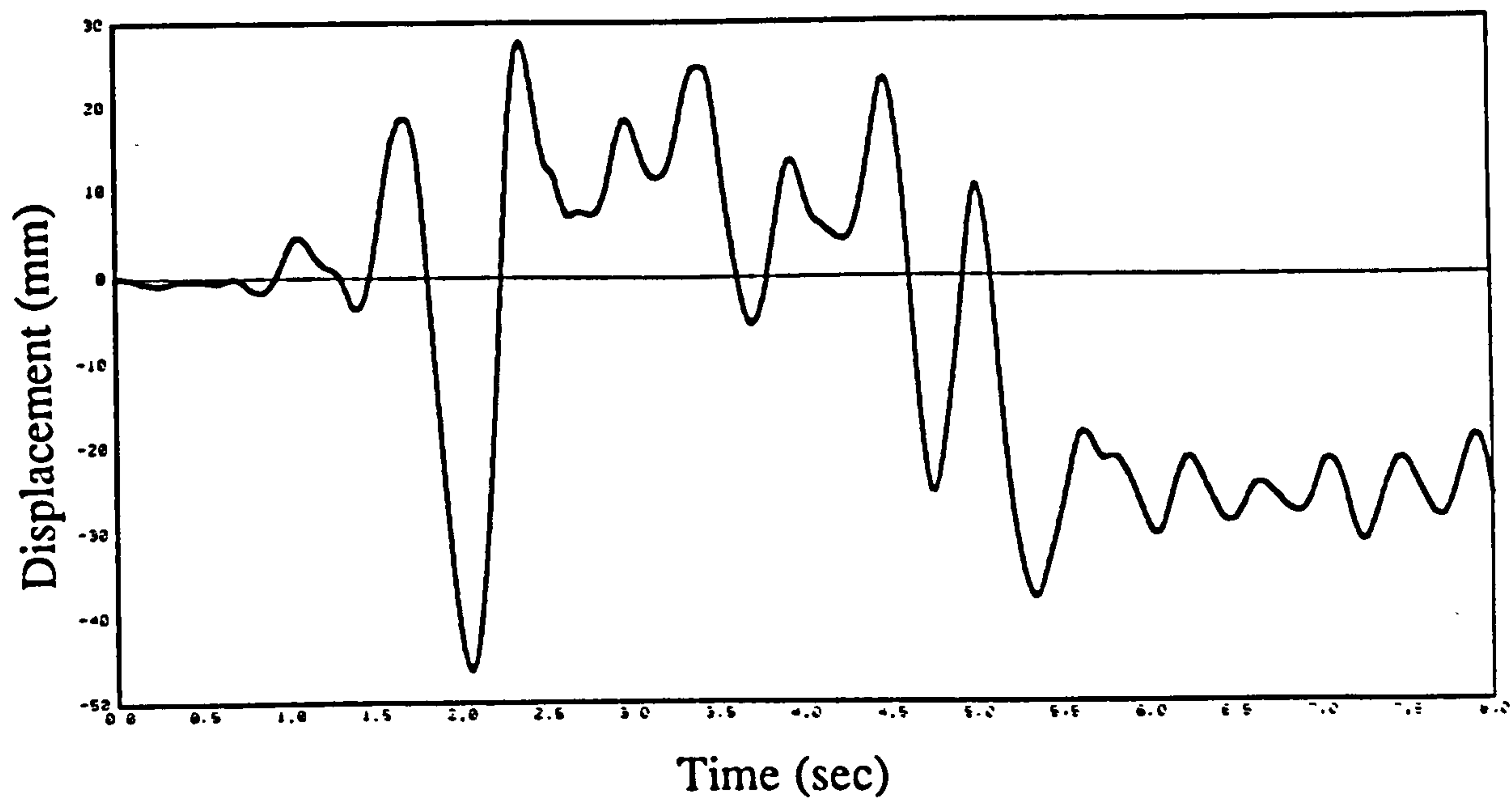


Fig. 5.22.a Analytical response under 110% El Centro earthquake

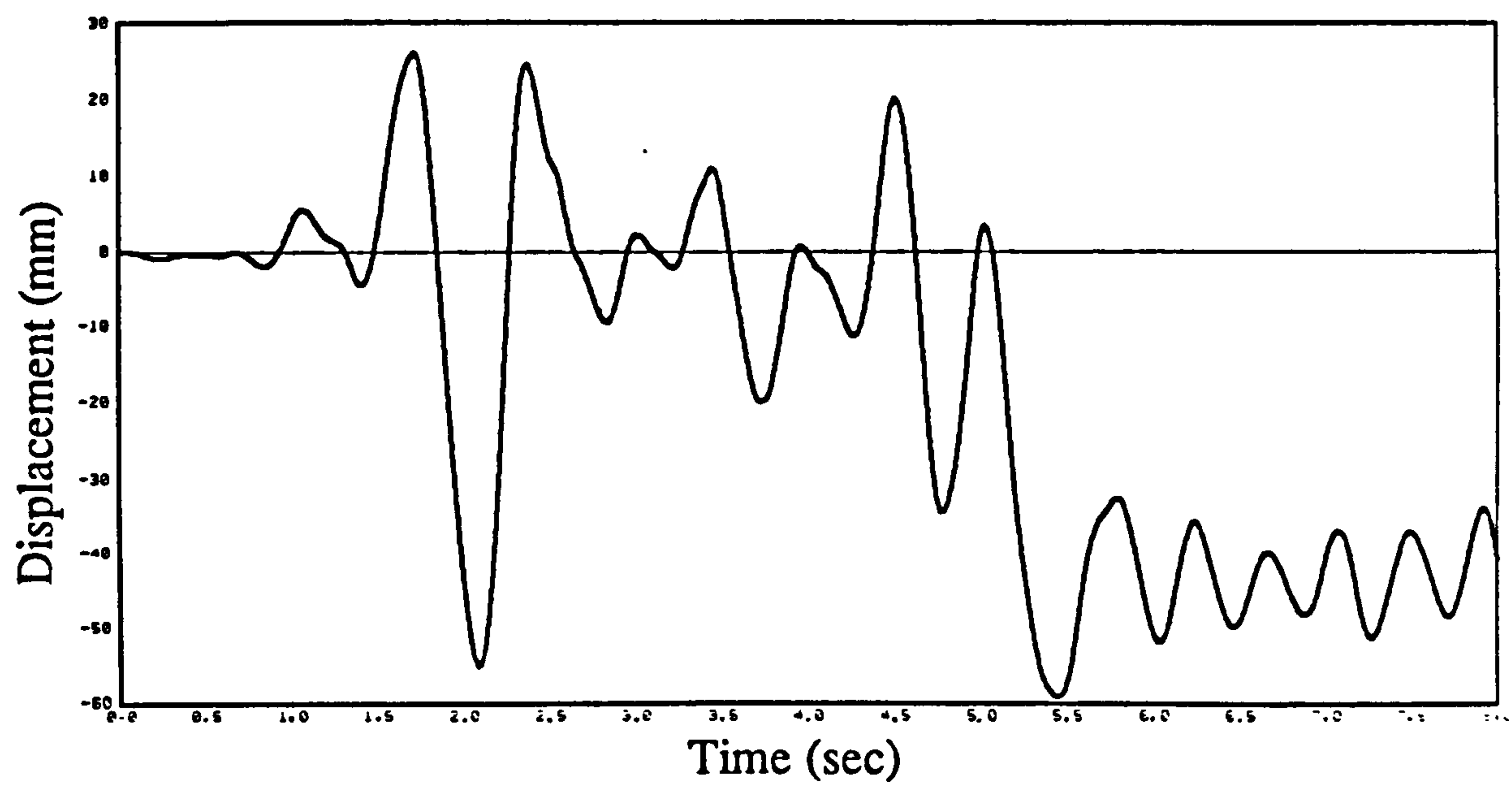


Fig. 5.22.b Analytical response under 130% El Centro earthquake

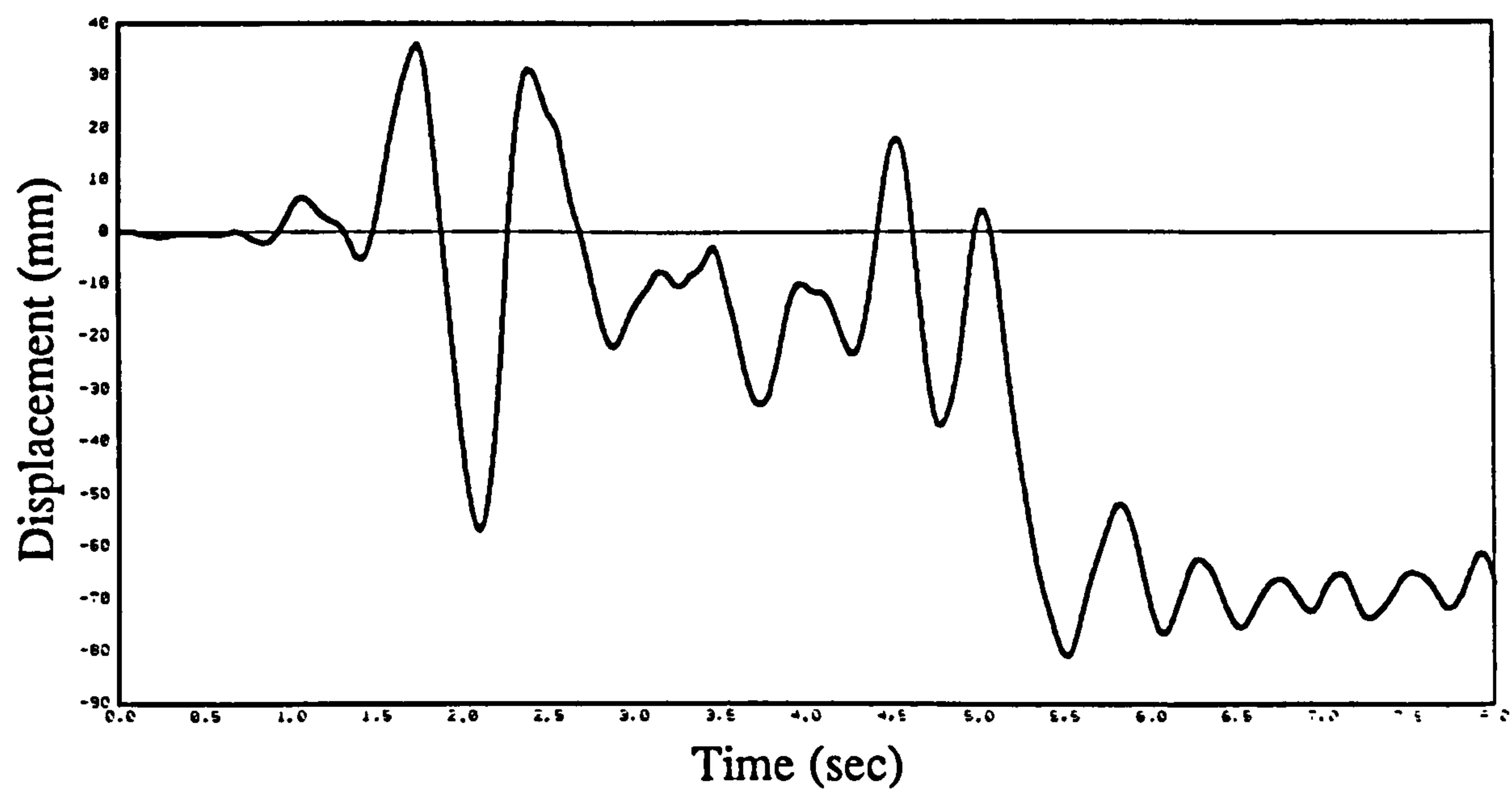


Fig. 5.22.c Analytical response under 150% El Centro earthquake

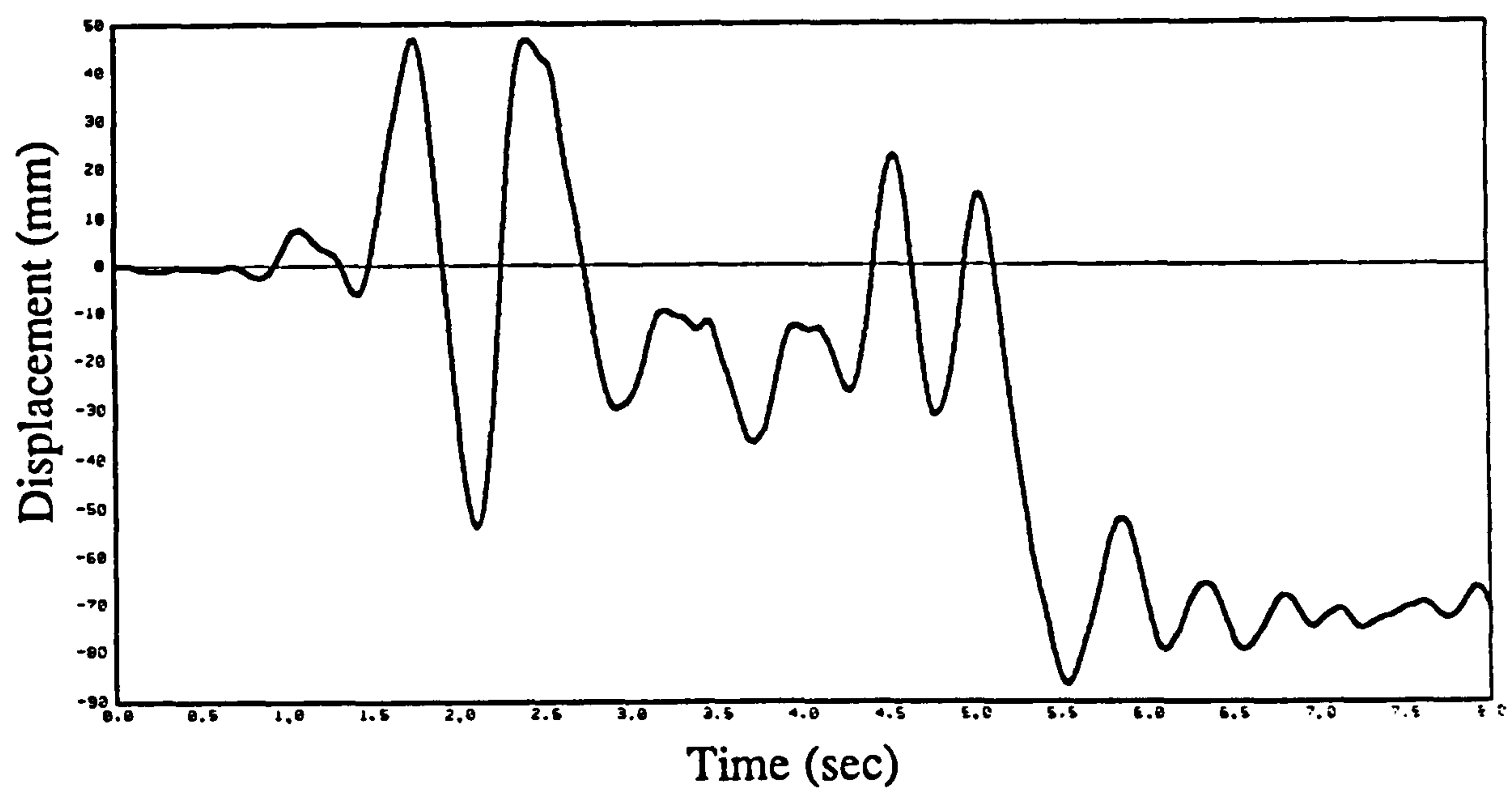


Fig. 5.22.d Analytical response under 170% El Centro earthquake

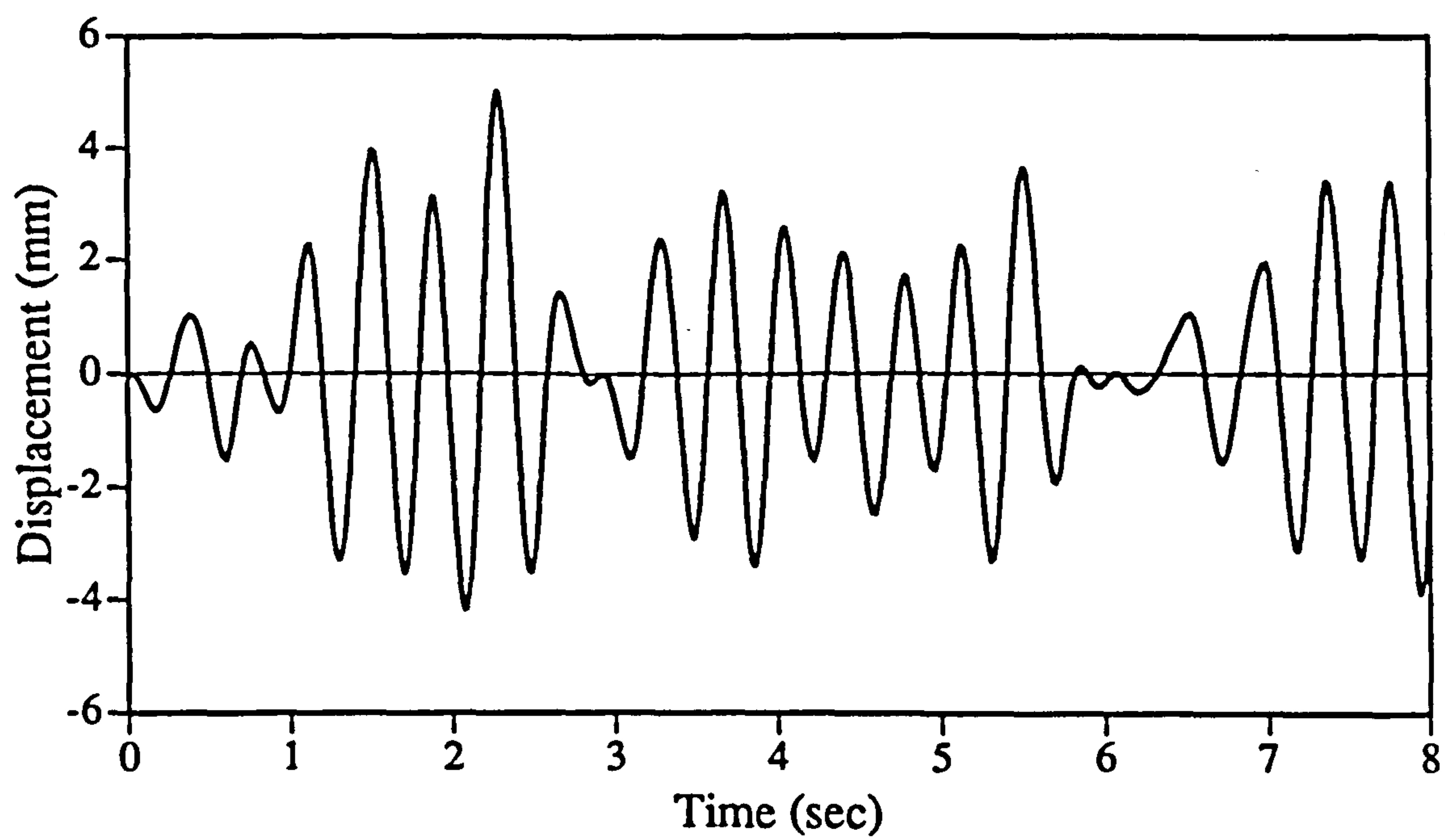


Fig. 5.23.a Analytical response under 90% Montenegro earthquake

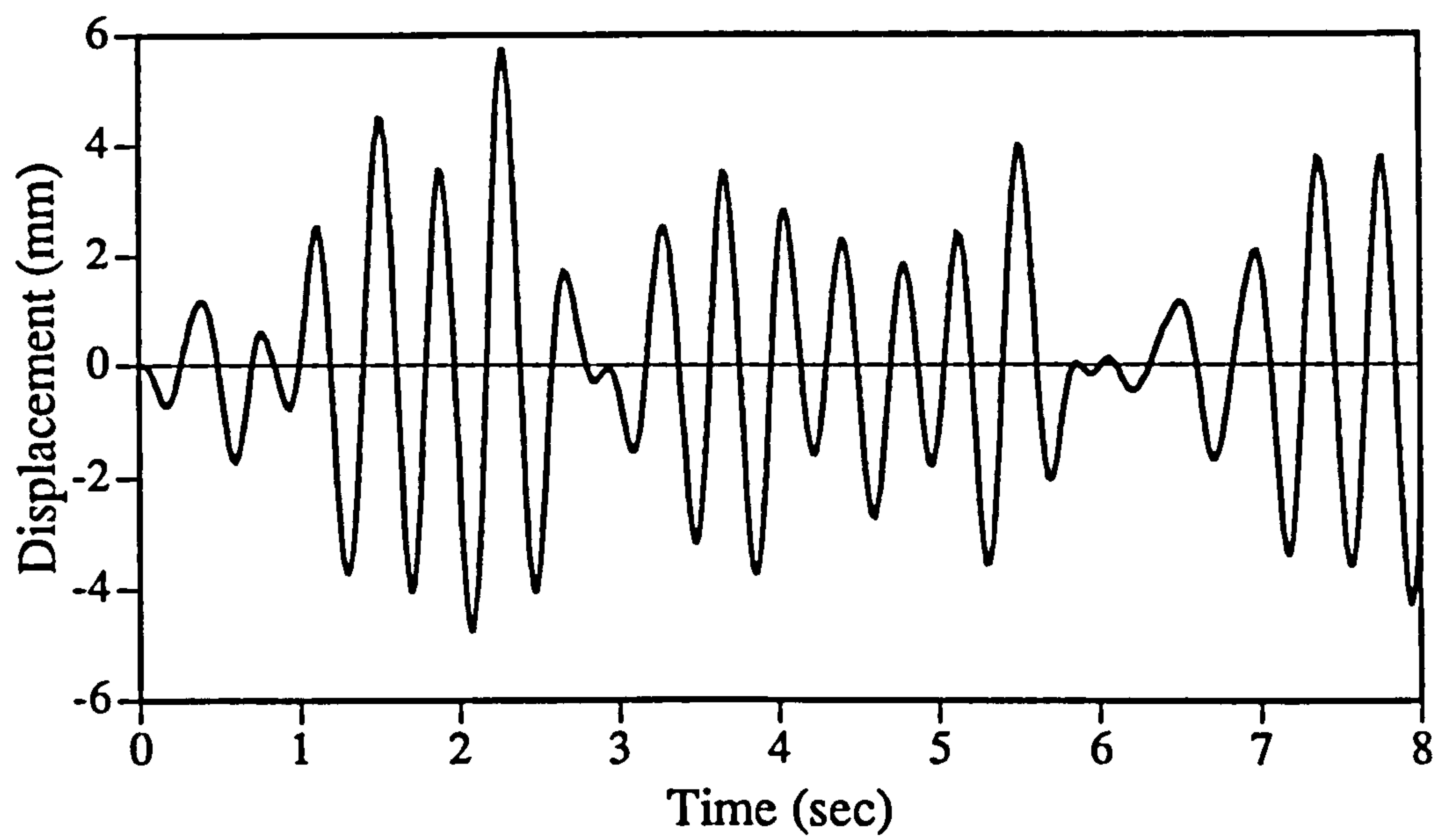


Fig.5.23.b Analytical response under full scale Montenegro earthquake

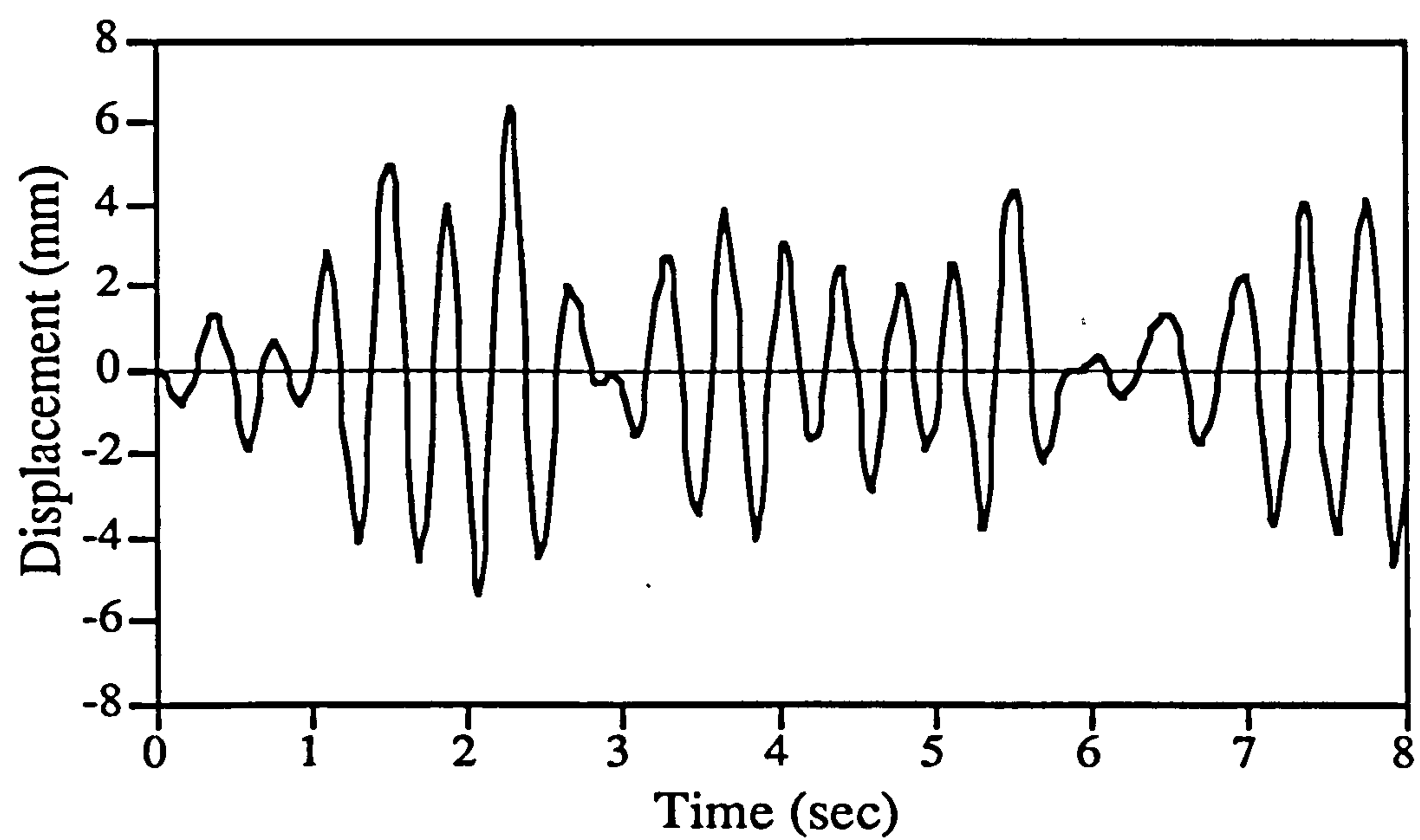


Fig. 5.23.c Analytical response under 110% Montenegro earthquake

CHAPTER 6

6. EXPERIMENTAL RESULTS

6.1 INTRODUCTION

In this chapter, the experimental results of the cyclic and pseudo-dynamic tests are presented. An account of the test progression is given and the immediate observations on the behaviour of the models are introduced. [The description of the models and the experimental set-up and procedure are given in Chapter 5]. A number of photographs are also shown to demonstrate certain behavioural patterns or failure mechanisms.

For compactness, selected strain gauge readings are given in Appendix A. It should be noted that the accuracy of strain gauge readings varied from one test to the other. A number of strain gauges failed after significant inelastic excursions. There are a number of reasons for strain gauge failures, such as breakage of bridge wires, loss of bond at high strains, gauge physical strain limits or workmanship defects. In cases where the gauges were clearly defective, the readings are not presented. However, in other cases, it was not easy to determine the exact point of gauge breakdown and hence, the full results are presented.

In the cyclic loading tests, the peak load values obtained in both directions were not identical, hence the peak loads referred to in the test description are the average of the positive and negative values. In all tests, the displacement values are given in mm, loads are given in KN and strains are shown in microstrains. The position of the strain gauge under consideration is shown in all figures of Appendix A.

The final section of this chapter includes a brief discussion of strain gauge results, in particular those pertinent to subsequent parts of the thesis. A general discussion of the experimental and analytical results and their implication on the design process is given in Chapter 9.

6.2 CYCLIC LOADING TESTS

6.2.1 Model EM01

The loading regime imposed on this model is shown in Figure 6.1, whilst Figure 6.2 gives the relationship between the lateral restoring force and the tip cantilever displacement. Selected strain gauge results are presented in Figures A.1 to A.27. The lateral restoring force is plotted versus the strain. However, for gauges 21 to 27, which were obtained on a data logger, the strains are presented against the intermediate beam displacement (X_2 in Figure 5.13).

Fine cracks were noticed in concrete in the tensile side almost from the first increment of loading. After the initial stiff response, the load-displacement curve deviated noticeably from linearity, at about 11 mm. The peak load of 59.4 KN was achieved at about 33 mm displacement, where the flanges started to buckle locally, as shown in Plate 6.1. At the onset of local buckling, concrete confinement was suddenly released, hence the concrete started disintegrating very soon after. In subsequent cycles, there was a gradual and continuing drop in capacity. At a displacement amplitude of 44 mm, large buckles appeared in the compression flange on both sides of the web, with a marked reduction in load-carrying capacity. A further cycle at 55 mm and another at 66 mm were applied, since this was the first test and it was interesting to assess the large displacement residual strength. Plate 6.2 shows the model at a displacement amplitude of 55 mm, where the concrete has disintegrated in the plastic hinge zone following local buckling.

6.2.2 Model IC01

The sequence of displacement cycles on this model is given in Figure 6.3. The load versus displacement relationship is shown in Figure 6.4. Strain gauge plots are presented in Figures A.28 to A.48.

The initial response up to a displacement of 33 mm was almost the same as for EM01, with a strength of 59.8 KN, only 0.7% higher than in EM01. The peak load, however, was reached at 44 mm, and was 60.3 KN. This load was sustained up to a displacement of 66 mm, where the measured force was 59.3 KN, only 0.9% below the peak load. At a displacement amplitude of 77 mm, the first sign of local buckling appeared in the compression flange between the welded bars, with an amplitude not exceeding 3 mm, and the load was 58.0 KN, 3.3% below the peak load. The behaviour remained relatively stable up to a displacement of 88 mm, with a load of 56.3 KN, only 5.9%

below the ultimate load, until failure of the weld between the flanges and the straight bars occurred, and a large local buckle developed at a displacement of 99 mm. At that instance the load dropped to 80% of the ultimate load.

The concrete cracking pattern was similar to that in EM01. Plate 6.3 and 6.4 show the model at displacement amplitudes of 11 and 22 mm, respectively. Although local buckling was delayed to a displacement of 88 mm, spalling of cover concrete started at a displacement of 44 mm. Plates 6.5, 6.6 and 6.7 show the model at displacements of 33, 44 and 55 mm, respectively. At displacement levels of 66 mm and 77 mm, deeper cracks were observed as shown in Plates 6.8 and 6.9. Again, concrete crushing occurred just after local buckling at a displacement of 99 mm, as shown in Plate 6.10.

6.2.3 Model EM02

The displacement cycles applied on this model are given in Figure 6.5; Figure 6.6 depicts the load-displacement curve. Strain gauge results are presented in Figure A.49 to A.75, where strains obtained on the logger are presented versus the beam displacement.

The results from the cyclic test on model EM02 followed similar behavioural patterns as for EM01, with a more pronounced second order effect. The measured capacity was 56.4 KN, corresponding to a displacement of 15 mm. At a displacement of 22 mm, the capacity dropped by only 3% to 55.2 KN. Local buckling started at a displacement of 30 mm, corresponding to a load of 50.2 KN. Thereafter, the strength progressively dropped as local buckling increased causing concrete crushing, aided by the high level of applied axial load. Plate 6.11 shows the model at a displacement of 33 mm where the initiation of local buckling caused sudden loss of lateral confinement and, consequently, crushing of concrete. At 44 mm displacement amplitude, the measured load was 39.2 KN or 69% of ultimate load and the concrete was severely damaged, as shown in Plate 6.12.

6.2.4 Model IC02

The displacement history is shown in Figure 6.7. The load versus displacement relationship is given in Figure 6.8. The strain gauge locations and results are presented in Figure A.76 to A.102. As in previous models, strains acquired on the logger are presented against the intermediate beam displacement.

In this test, the peak load measured 56.6 KN, only 0.4% higher than EM02, and was reached at a displacement of 22 mm. However, a reasonably stable load was sustained

up to a displacement of 44 mm, where a reduction of only 8% in load was observed, but with clear spalling and crushing of the cover concrete, mainly due to the co-existing high axial force. Plates 6.13 and 6.14 show the model at displacements of 33 and 44 mm, respectively. A reduction of load-carrying capacity of 12.3% was observed at a displacement amplitude of 55 mm, where a small local buckle started forming in the spacing between the straight lateral bars, as shown in Plate 6.15. At 66 mm, the straight bars snapped with an audible noise, and a large buckle immediately developed, followed by concrete crushing. The strength at this instance was 78% of the ultimate load. Plate 6.16 shows the plastic hinge zone at a displacement amplitude of 66 mm.

6.2.5 Model EM04

The displacement cycles applied on the model are shown in Figure 6.9. The relationship between the lateral restoring force and the horizontal displacement at the tip of the cantilever is presented in Figure 6.10. Strain gauge results for EM04 and IC04 were found to be erroneous in the inelastic range, and are not presented to avoid misinterpretation of the results.

The load-displacement relationship started deviating from linearity at about 10 mm. Concrete cracking followed similar patterns as described in previous models. The first sign of local buckling was observed at a displacement of approximately 45 mm. Plate 6.17 shows a close-up of the compression flange after the first cycle was applied at a displacement of 48 mm. In subsequent cycles, the concrete progressively disintegrated causing a considerable drop in load. Plate 6.18 shows the compression area after the third cycle at 48 mm was applied. It should be noted, however, that the large drop in load shown in Figure 6.10 was a consequence of both crushing of concrete and an observed local buckle in the web. This buckling mode occurred after the restraint provided by the concrete was released at the web-flange intersection.

6.2.6 Model IC04

The sequence of displacement cycles applied in the test is shown in Figure 6.11. The relationship between the restoring force and the applied displacement is shown in Figure 6.12. The behaviour was again very similar to that observed in previously-described IC models. However, the sustained load was monotonically increased due to steel strain hardening and the absence of second order effects. First deviation from linearity in the displacement versus load relationship was again observed at a displacement of about 10 mm. The crack pattern was also similar to that of other models, as shown in Plate 6.19 at

a displacement of 32 mm. The first sign of local buckling in the compression flange appeared in the spacing between the welded bars at a displacement of about 80 mm. Plate 6.20 shows the plastic hinge zone of the model at this instance.

In subsequent cycles, no degradation was observed with the exception of spalling of the cover concrete. The load carried by the model gradually increased up to about 102.0 KN at a displacement of 96 mm. At this stage, the test had to be terminated as the actuator limits were exceeded. However, the model was expected to sustain higher load and displacement levels as the flange buckling length was restricted to the spacing of the straight bars and the concrete confinement was not significantly reduced.

6.2.7 Model IC07

The lateral displacement history applied on this model is given in Figure 6.13. The relationship between the lateral load and the displacement is shown in Figure 6.14. Readings from a number of strain gauges are presented in Figures A.103 to A.108.

The model showed an initial stiff response up to a displacement of about 10 mm, where the load was approximately 74.0 KN. Fine flexural cracks were observed at early stages of the test at about 6 mm displacement. At a displacement of 16 mm, the cracks were well distributed over the height of the specimen with a spacing following the position of the lateral ties, as shown in Plate 6.21. At a displacement of 32 mm, concrete cracks in the plastic hinge increased in depth and spalling of concrete cover started. It was noted in this test that cracks were deeper and more extensive than in other IC models, as shown in Plate 6.22, due to the lower lateral confinement provided by the straight bars only.

Local flange buckling started in the space between the welded bars on the third cycle at a displacement of 64 mm, as shown in Plate 6.23. On reversing the direction of loading, a similar buckle appeared in the opposite side as shown in Plate 6.24. It was observed that the opposite flange recovered from local buckling completely under the effect of tensile stresses, which was a common observation in all cyclic tests. [This has implications on the analytical model proposed in Chapter 7].

Increasing the displacement afterwards caused an increased deterioration in concrete and twisting in the straight welded bars restricting the half wave length of local buckling. At a displacement of 96 mm, two of the straight bars failed with an audible noise, after which the concrete crushed and a drop of load from 98.0 KN to 82.0 KN was observed in the

two subsequent cycles at the same displacement level. Plate 6.25 and 6.26 show the plastic hinge area of the model after failure.

6.3 PSEUDO-DYNAMIC TESTS

6.3.1 Model EM03

As mentioned before, this model was tested under the first 8 seconds of El Centro record, and an axial load of 30% of the squash capacity. The acceleration input was scaled up to 140%, based on predictive analysis. The details of the record and the specimen are given in Chapter 5. The displacement response history obtained in the test is presented in Figure 6.15, whilst Figure 6.16 gives the measured load history. The relationship between the restoring force and the displacement of the equivalent cantilever is given in Figure 6.17. The strain gauge locations and results are presented in Figures A.109 to A.129.

The response displacement corresponding to the first significant peak of the record measured 19 mm, and the corresponding force was 57.0 KN. The major peak of the record, just after 2 seconds of the start of shaking, produced a displacement of 72 mm and large local buckling in the flange on either side of the web. At this instance, concrete crushing occurred as shown in Plate 6.27. Due to the loss of stiffness and the P- Δ effect, the specimen did not recover back to a near zero displacement position. The displacement continued increasing with a gradual increase in the local buckling half wave length and extensive concrete crushing, as shown in Plate 6.28. In the subsequent negative peak, the test-rig reached the limit of the actuator stroke of 150 mm, and the test was aborted.

6.3.2 Model IC03

The loading and test procedure were identical to that used for model EM03. The displacement and load response histories are given in Figures 6.18 and 6.19, respectively. Figure 6.20 depicts the load versus displacement relationship. The strain gauge locations and results are given in Figures A.130 to A.150.

As in model EM03, the displacement corresponding to the first significant peak was 19 mm. On the reverse peak, just after 2 seconds, the displacement was 62 mm. This did not, however, cause local flange buckling, hence the specimen continued to carry its full capacity. The test proceeded for the full 8 seconds, with intermittent breaks due to the

attainment of more than 90% of the actuator stroke, used as a safety limit by the system. At the tail of the record, a displacement close to 150 mm was measured, with no clear signs of buckling; only very small amplitude deformations were observed in the flange, none exceeding 2 mm, with disintegration of cover concrete, as shown in Plate 6.29. A general view of the test at the tail of the response is shown in Plate 6.30.

6.3.3 Model EM05

The specimen was first subjected to 90% of the 8 seconds acceleration time history of Montenegro earthquake. This was followed by another 8 seconds of the unscaled history. Details of the record and the specimen are given in Chapter 5. The displacement and load response histories are presented in Figures 6.21 and 6.22, respectively. The relationship between the lateral load and displacement is also given in Figure 6.23. Figures A.151 to A.156 present selected strain gauge results.

The first sign of local buckling in the compression flange appeared after 2.3 seconds, where the displacement was about 50 mm in the negative side. At the peak, 2.4 seconds from the start of the record, the displacement of EM05 was 78 mm, and local buckling clearly appeared on the compression flange, as shown in Plate 6.31. However, the model displayed stable behaviour up to about 10.4 seconds, where the deterioration in stiffness caused the displacements to increase beyond 120 mm, with only 7% drop in load, and deterioration of concrete as shown in Plate 6.32. The test had to be aborted at this stage as the actuator stroke limit was reached.

6.3.4 Model IC05

The loading and specimen details in this model were identical to that used in EM05. The displacement response is shown in Figure 6.24, whilst Figure 6.25 gives the load response history. The load versus displacement relationship is presented in Figure 6.26. Selected strain gauge results are given in Figure A.157 to A.162.

The behaviour followed that of EM05 up to 2.4 seconds where the peak displacement was 61 mm, with no sign of local buckling. The peak load was only 1.5% higher than in EM05. Following this, the specimen showed response qualitatively similar to EM05, but with comparatively lower displacement amplitudes. At 10.6 seconds from the start of loading, the displacement reached about 90 mm compared to 120 mm in EM05 with no sign of local buckling. Plate 6.33 shows a close-up of the model at the latter

displacement level. The specimen did not suffer from any noticeable deterioration up to the end of the excitation history.

6.3.5 Model IC06

This model was subjected to the same loading as in EM05 and IC05. As mentioned in Chapter 5, the only difference was the details of the stirrups in the plastic hinge zone, where only the straight bars were provided. The displacement and load histories as well as the displacement versus load relationships are presented in Figures 6.27, 6.28 and 6.29, respectively.

Although local buckling of compression flange was also prevented in this model, it seems that the stirrups were not as effective in providing lateral confinement as in IC05, since considerably higher displacement levels were obtained in the response. At the peak after 2.4 seconds, the displacement was 87 mm, compared to 61 mm in IC05, and the load was 9% lower than the case of IC05. As shown in Plate 6.34, the observed cracks were wider than that in IC05. After 10.6 seconds from the start of loading, the displacement approached the limits of the actuator stroke and the test was aborted.

6.4 DISCUSSION OF STRAIN GAUGE RESULTS

6.4.1 General

This section presents a brief discussion of the strain gauge results given in Appendix A. In particular, main characteristics addressed in subsequent chapters are pointed out and some observations are highlighted.

Most of the strain gauges were located in the expected plastic hinge region of the members. A considerable number of gauges were placed on the flanges, whilst few gauges were placed on the vertical and horizontal reinforcements. In some models, several strain gauges were distributed along the length of the member to obtain an estimate for the extent of the plastic hinge zone.

As mentioned before, interpretation of the strain gauge results of cyclic tests in the inelastic range must be carried out with care. Although most of the clearly defective results were eliminated, variation in the readings may arise from several inaccuracies from a number of experimental error sources.

6.4.2 Extreme Fibre Strains in the Plastic Hinge Region

In most of the models a large number of strain gauges were located at the flanges in the plastic hinge area. The main features of the force versus strain curves in the plastic hinge zone are summarised as follows:

- a. Before yielding, there is almost no energy dissipation. Loading and unloading in tension and compression occur at a constant gradient (slope of the load-strain relationship) which is slightly higher in compression than it is in tension.
- b. After yielding, the maximum plastic strains increase with the increase of applied displacements. The area within the loops increases considerably indicating substantial dissipation of energy.
- c. Initial unloading in tension and compression after yield also occur at a constant gradient, the latter being slightly higher. However, the gradient decreases on reloading.
- d. On reloading in tension, there is a gradual softening in the behaviour. The inclination of the load-strain plot decreases with the increase of applied displacements in the inelastic range.
- e. On reloading in compression, an initially low gradient increases gradually near the ultimate load due to closure of the concrete cracks.
- f. With progressive increase in the applied cyclic displacements, more plastic strains are accumulated. For models subjected to low axial loads up to 15% of the axial capacity, the plastic tensile strains increase progressively whereas the compressive strains stabilise at a certain maximum value and may even reduce in some cases. The opposite is observed for models subjected to compressive loads of 30% of the axial capacity where large compressive plastic strains are accumulated.

As shown in the description of the tests, significant degradation of the composite section in the plastic hinge zone follows the onset of local buckling of the compression flange. Table 6.1 depicts the values of the accumulated plastic strain in the compression flange at the initiation of local buckling as estimated from the different strain gauge readings. This is shown only for models where a sufficient number of strain gauges were located on the flanges in the plastic hinge region.

TABLE 6.1
Estimated Plastic Strain at Onset of Local Flange Buckling

| Model | EM01 | IC01 | EM02 | IC02 | EM03 | IC03 |
|------------|------|------|------|------|------|------|
| Gauge | G5 | G5 | G5 | G5 | G7 | G7 |
| Strain (%) | 1.43 | 3.19 | 1.14 | 2.38 | 0.72 | 3.19 |
| Gauge | G6 | G6 | G6 | G6 | G8 | G8 |
| Strain (%) | 1.71 | 3.14 | 1.33 | 2.71 | 0.86 | 3.14 |
| Gauge | G7 | G7 | G7 | G7 | G9 | G9 |
| Strain (%) | 1.57 | 3.19 | 1.28 | 2.57 | 0.76 | 3.19 |
| Gauge | G8 | G8 | G8 | G8 | -- | -- |
| Strain (%) | 1.14 | 3.05 | 1.09 | 2.67 | -- | -- |
| Gauge | G9 | G9 | G9 | G9 | -- | -- |
| Strain (%) | 1.52 | 2.95 | 0.91 | 2.57 | -- | -- |
| Gauge | G10 | G10 | G10 | G10 | -- | -- |
| Strain (%) | 1.14 | 2.67 | 0.91 | 2.05 | -- | -- |
| Gauge | G11 | -- | G11 | G11 | -- | G13 |
| Strain (%) | 1.43 | -- | 1.19 | 2.38 | -- | 2.76 |
| Gauge | G12 | G12 | G12 | G12 | -- | -- |
| Strain (%) | 1.57 | 3.42 | 1.05 | 2.76 | -- | -- |
| Gauge | G13 | -- | G13 | G13 | G14 | G14 |
| Strain (%) | 1.57 | -- | 1.43 | 2.95 | 0.68 | 3.05 |
| Gauge | G14 | G14 | G14 | G14 | -- | -- |
| Strain (%) | 1.19 | 2.95 | 1.08 | 2.71 | -- | -- |
| Gauge | G15 | G15 | G15 | G15 | -- | -- |
| Strain (%) | 1.57 | 2.81 | 1.05 | 2.57 | -- | -- |
| Gauge | G16 | G16 | G16 | G16 | -- | -- |
| Strain (%) | 1.62 | 2.95 | 1.19 | 2.71 | -- | -- |

The above table confirms the substantial increase in the plastic strain and, consequently, the ductility and energy dissipation capacity of the IC models as compared to the corresponding EM models before local buckling is initiated in the compression flange. Detailed discussion of the ductility of the members is given in Chapters 8 and 9 of this thesis.

6.4.3 Extreme Fibre Strains Outside the Plastic Hinge Region

In order to assess the extent of the plastic hinge zone strain gauges were placed in some models along the height of the member. As indicated in the results from gauges G4, G5 and G6 of EM05 and G3 and G6 of IC05, almost no energy is dissipated before yield of the extreme flange fibres. Due to concrete cracking, the slope of the force versus strain relationship is slightly lower in tension.

In model EM01, yielding in both directions is observed in gauges G23 and G24. At higher levels, G25 and G26 approach yield in the compression side only, whilst G27 show strain values well below the yield level. For model EM02, G23 and G24 exceed yield strains in compression but are lower than yield in tension, whereas yield is not observed in both directions in G25 and G27 located at higher levels. In the case of IC02, G23 and G24 show yielding in both tension and compression and indicate strain values well above compressive yield in G25 and G26.

Similarly, in the pseudo-dynamic tests, yield is reached in both directions in gauges G3 and G4 of EM03, whilst G1 and G2 exceed yield only in compression. In model IC03, strains well above yield are indicated by G1 and G2. Gauges G4, G5 and G6 in EM05 and G3 and G6 in IC05 show strain values close to yield in tension.

Further discussion of the length of the plastic hinge length is presented in Chapter 9 based on both the experimental results and analytical investigations.

6.4.4 Strains in Vertical Reinforcement

The gauges on the vertical reinforcement are subjected to less severe strain reversals than those placed on the flanges at the same level. Similar observations to those given in section 6.4.2 regarding the slope of the force versus strain relationship are also noticed for the vertical bars.

Comparison of the relative values of strain on the vertical bars with those on the extreme flange fibres at different stages of loading clearly validates the assumption of linear strain distribution within the section. For example, this is demonstrated in the strain values indicated by gauges G17 and G18 placed on the vertical reinforcement of IC01 as compared to those given by gauges G5 to G10 located on the extreme fibres of the flanges at the same level.

6.4.5 Strains in Lateral Reinforcement

In general, strain gauge readings of horizontal reinforcement showed low strain values particularly when low axial loads were applied. Yield strains were exceeded in G19 of EM01 only after local flange buckling, whilst other gauges in EM01 showed values below yield. In IC01, strains given by G19 reached yield in the last loading cycles. As for EM01, strains registered by gauge G19 of EM02 exceeded yield after local buckling of the flange was initiated. In model IC02, G19 and G20 indicate values well above yield at final stages of loading. Similar observations are also noted in models IC07, EM03 and IC03.

Further discussion of the experimental results is given in Chapter 9. Also, comparison of some of the experimental results with analytical simulations is presented in Chapter 7.

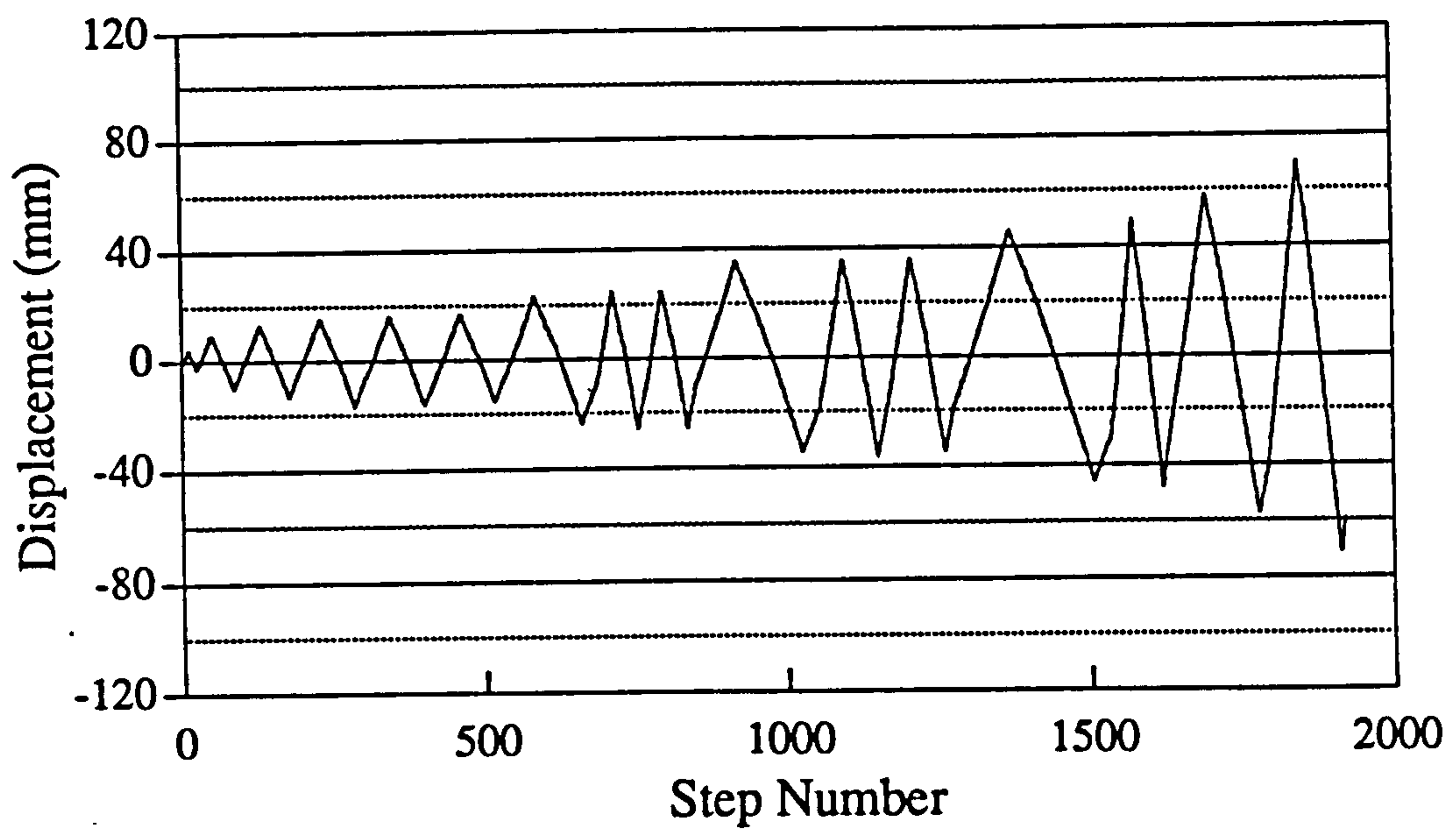


Fig. 6.1 Loading history for EM01

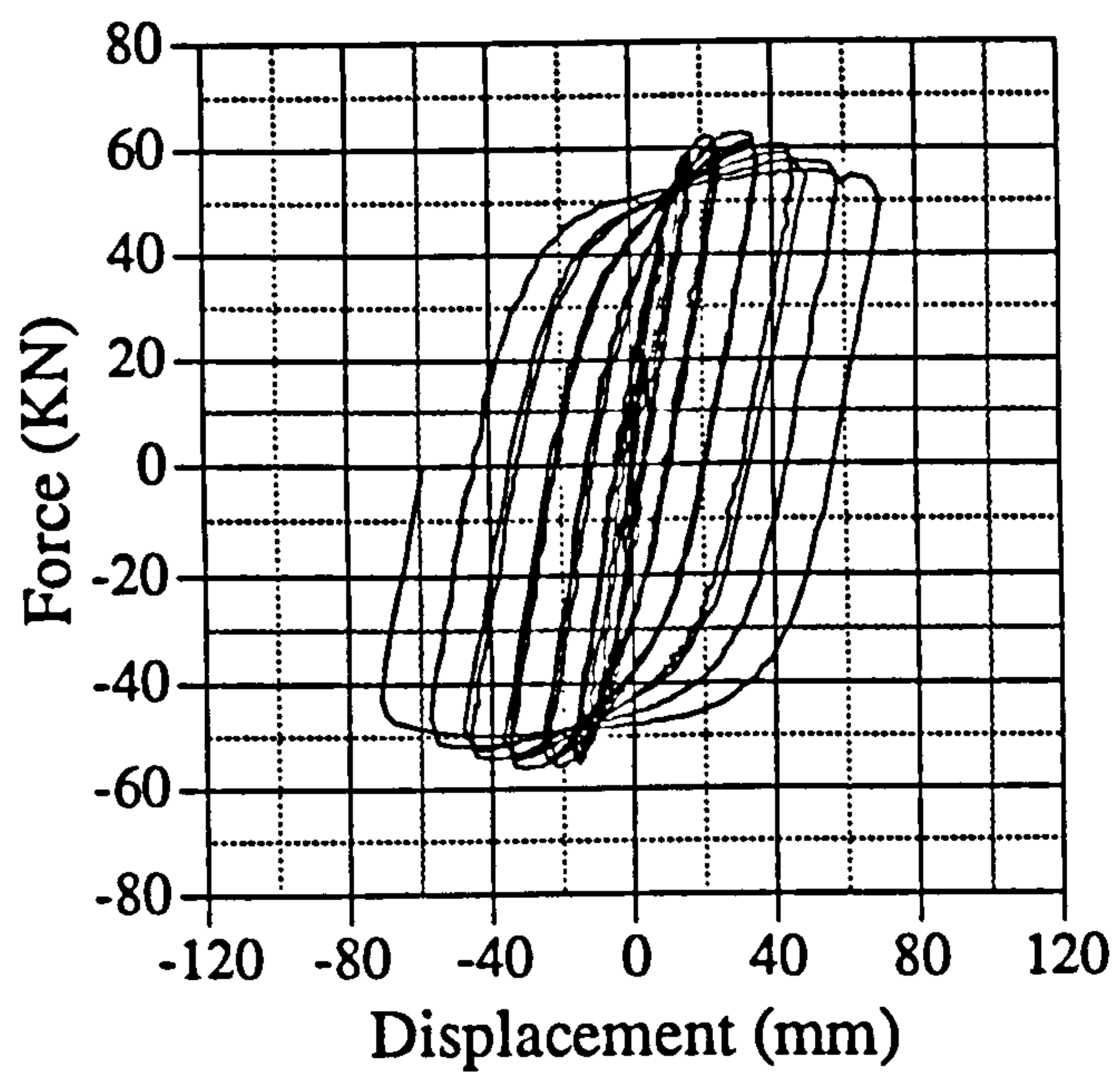


Fig. 6.2 Load versus displacement relationship for EM01

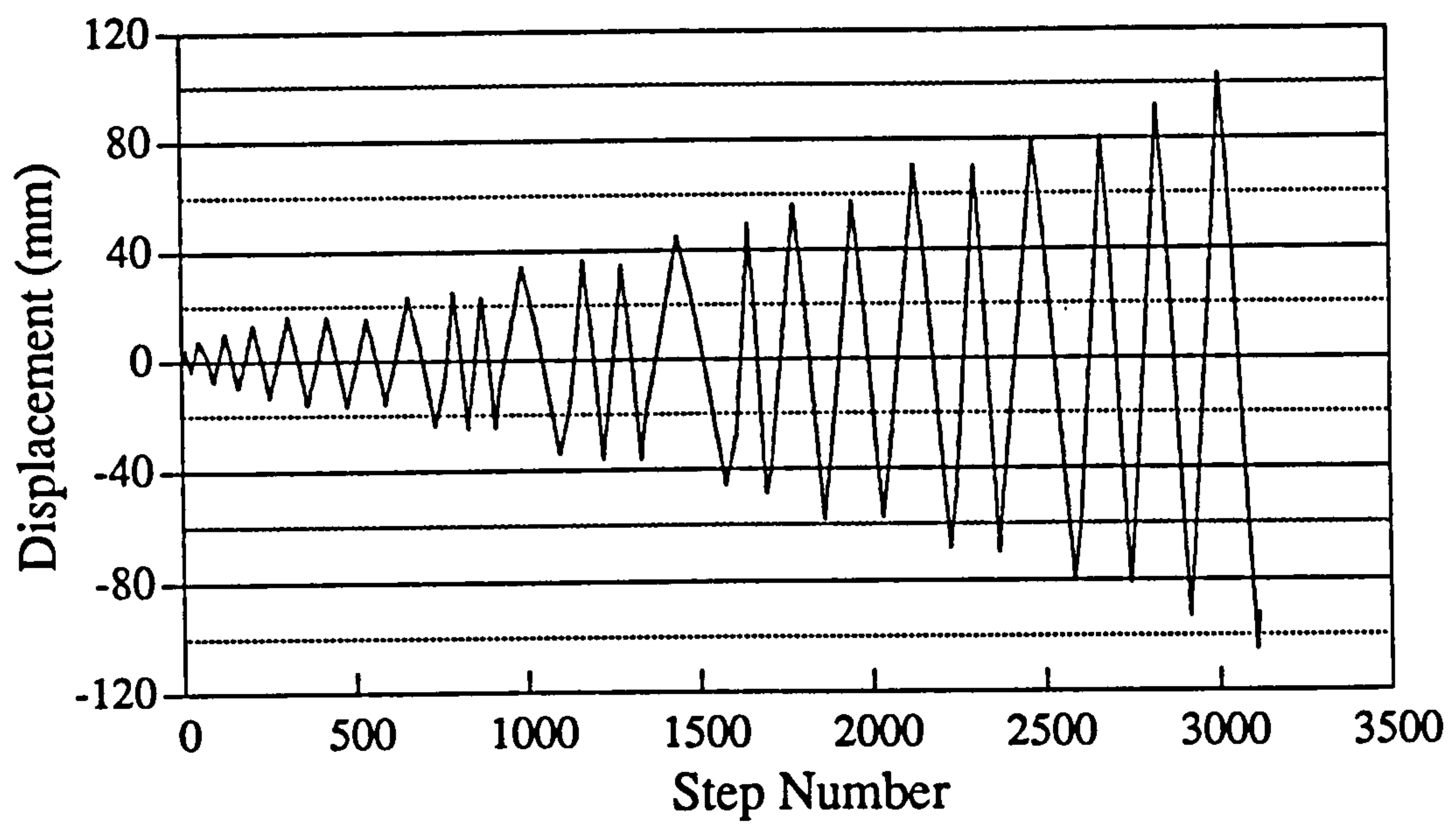


Fig. 6.3 Loading history for IC01

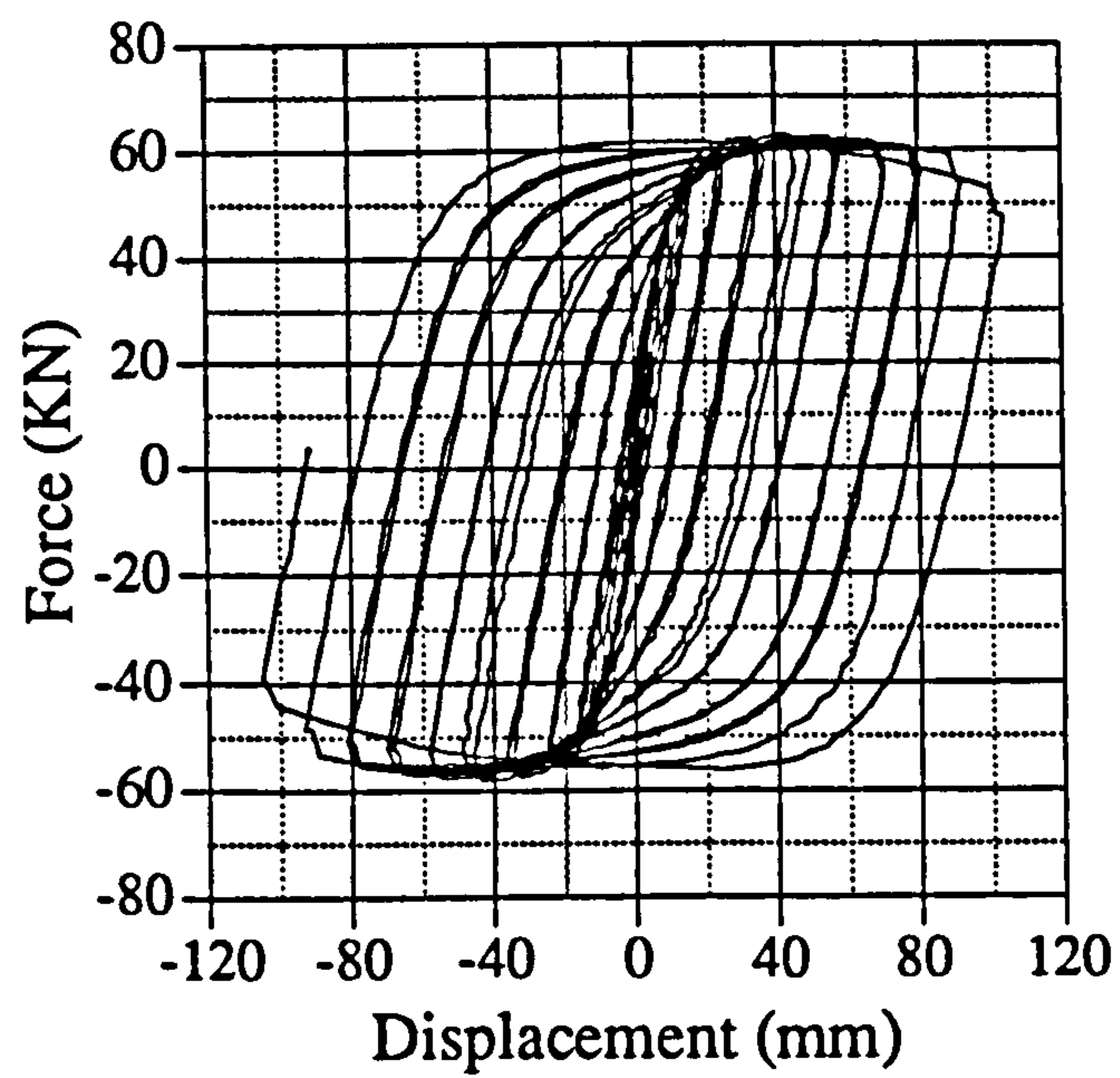


Fig. 6.4 Load versus displacement relationship for IC01

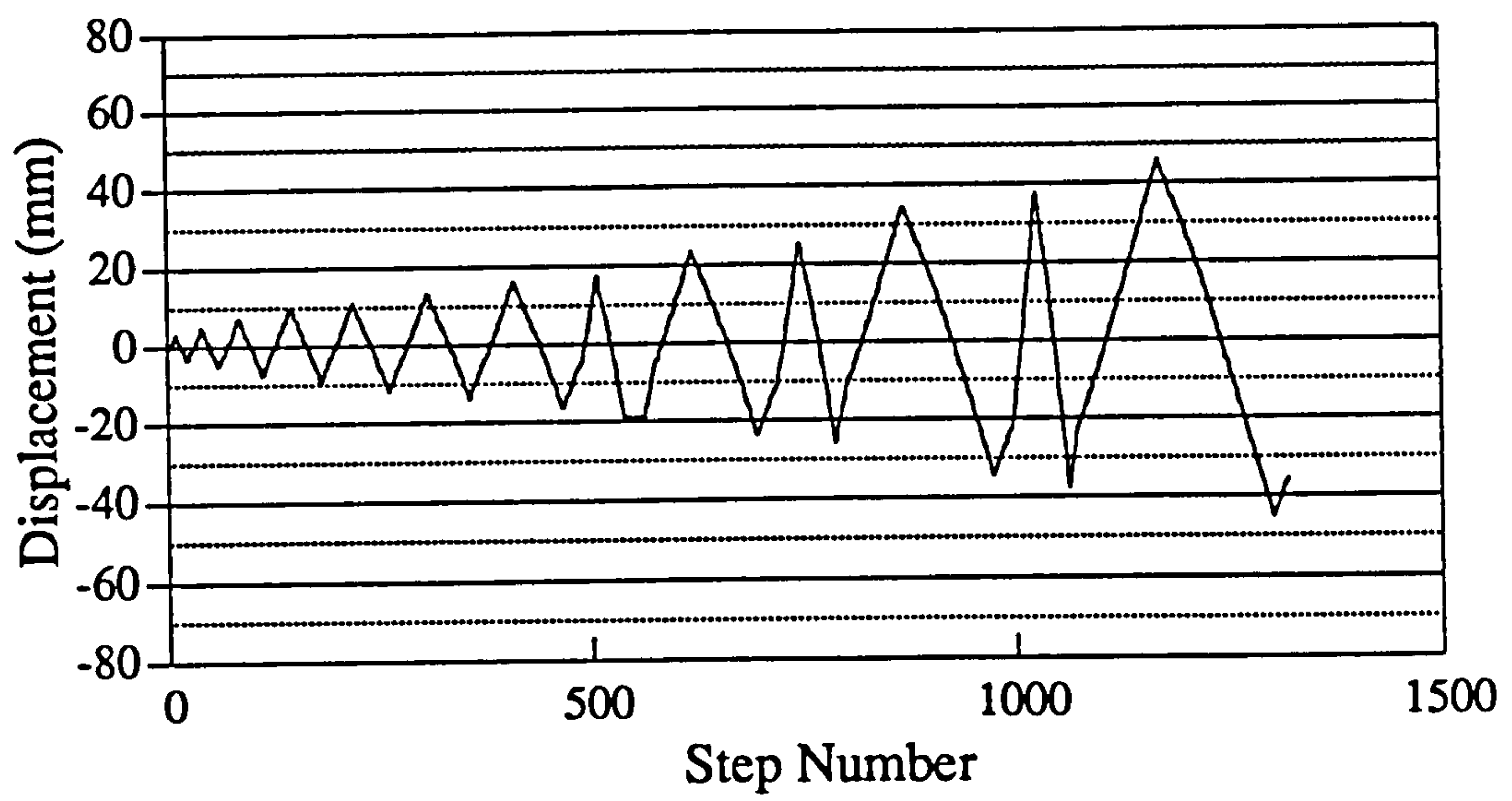


Fig. 6.5 Loading history for EM02

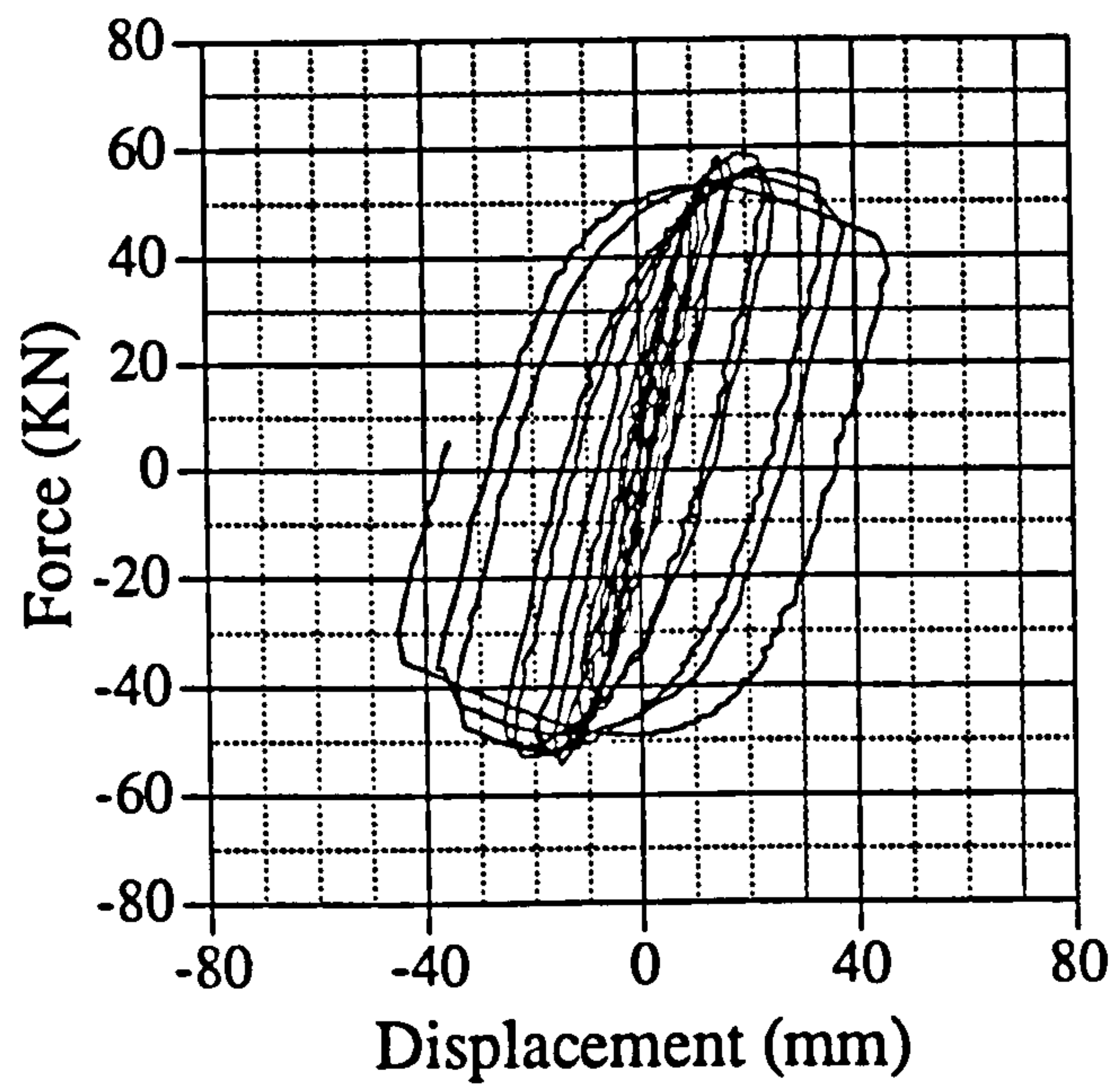


Fig. 6.6 Load versus displacement relationship for EM02

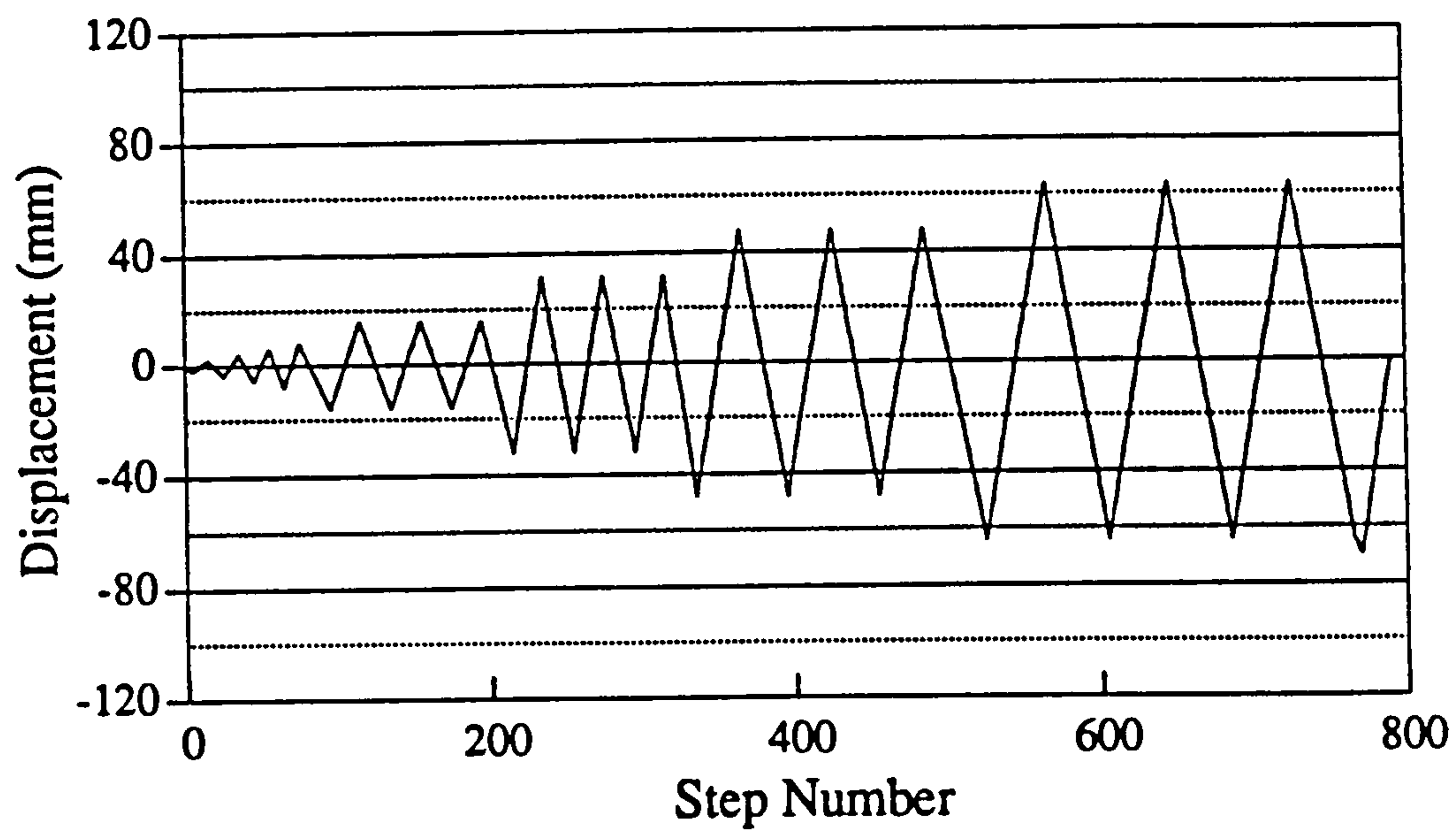


Fig. 6.9 Loading history for EM04

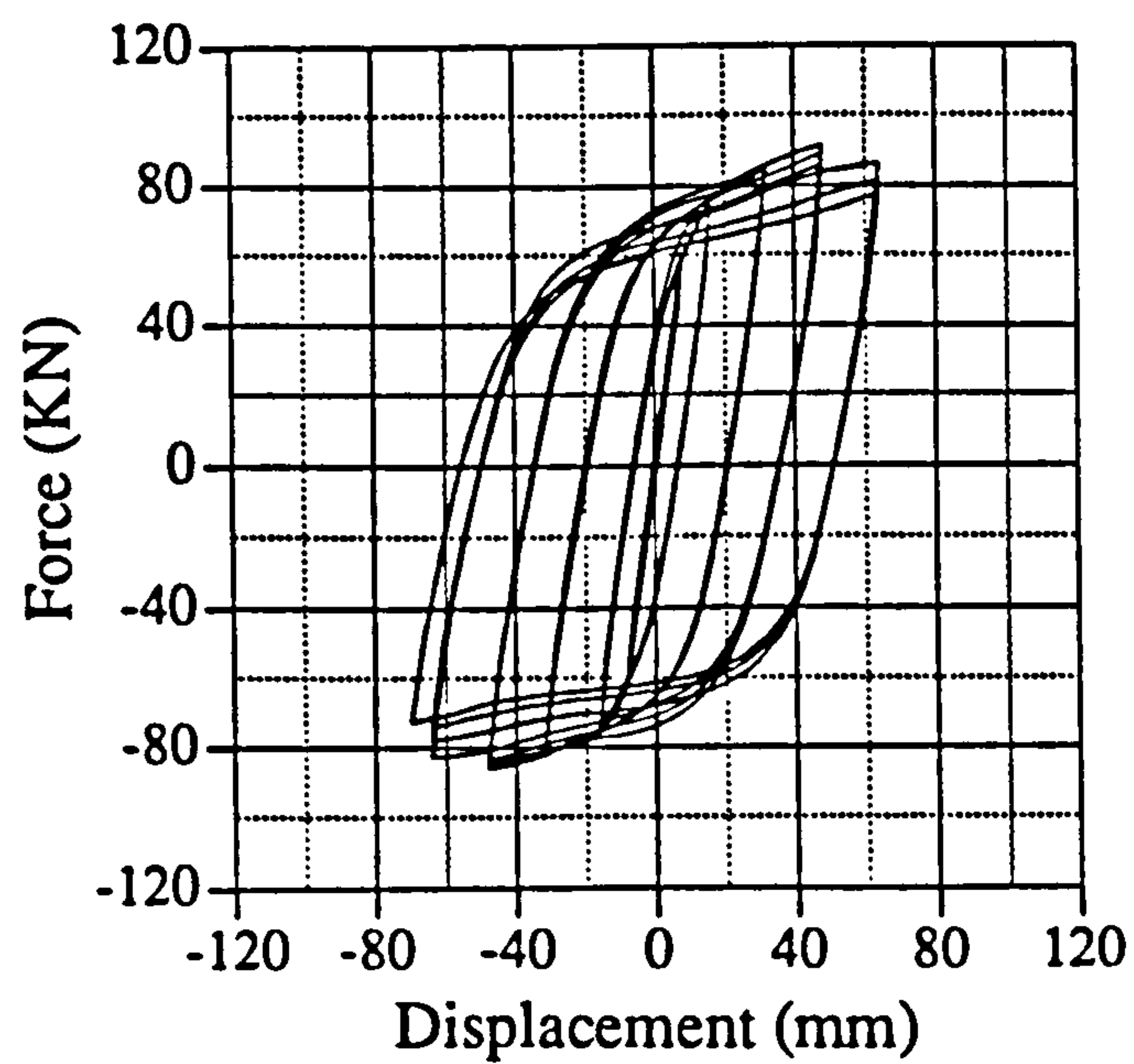


Fig. 6.10 Load versus displacement relationship for EM04

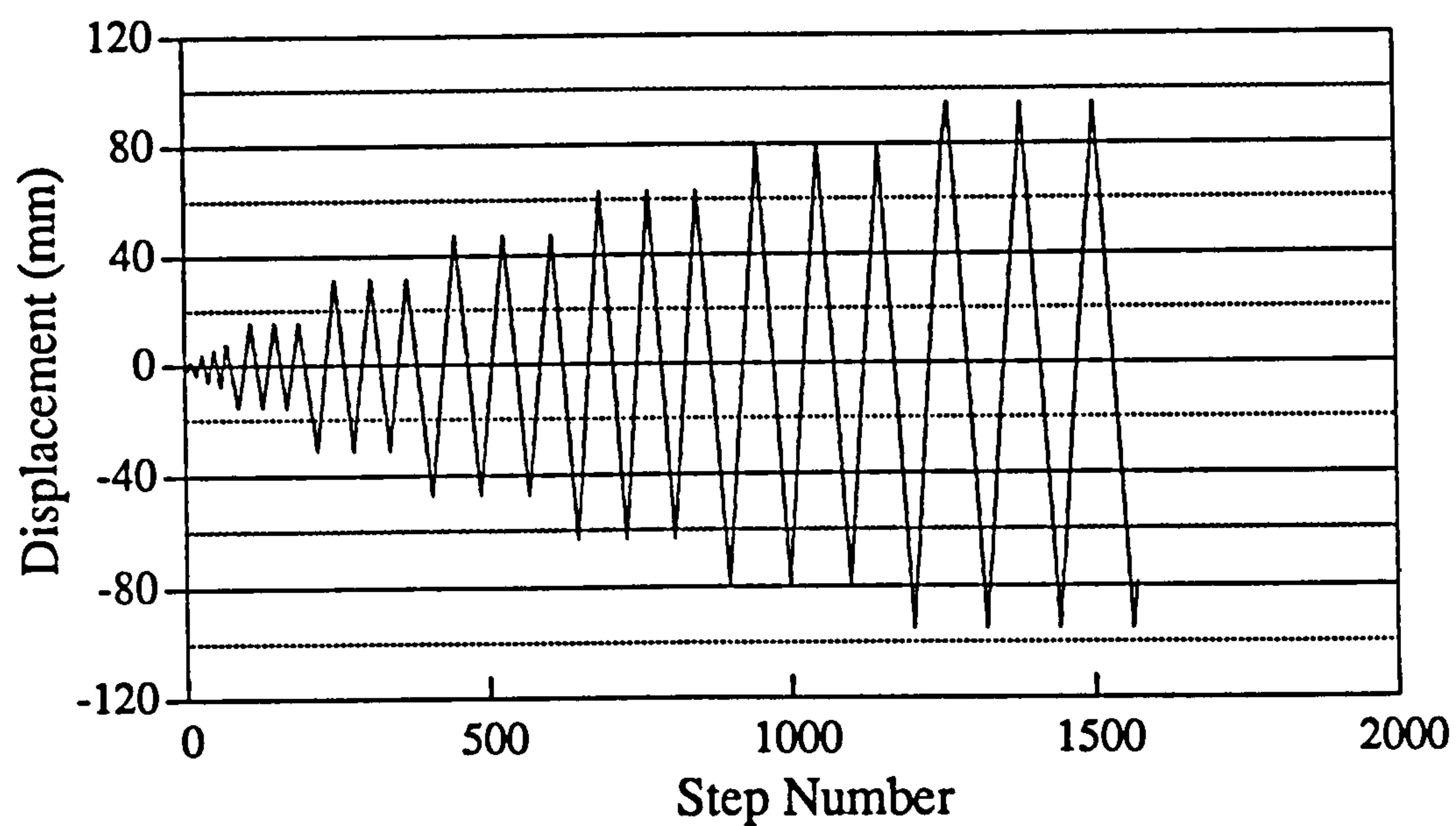


Fig. 6.11 Loading history for IC04

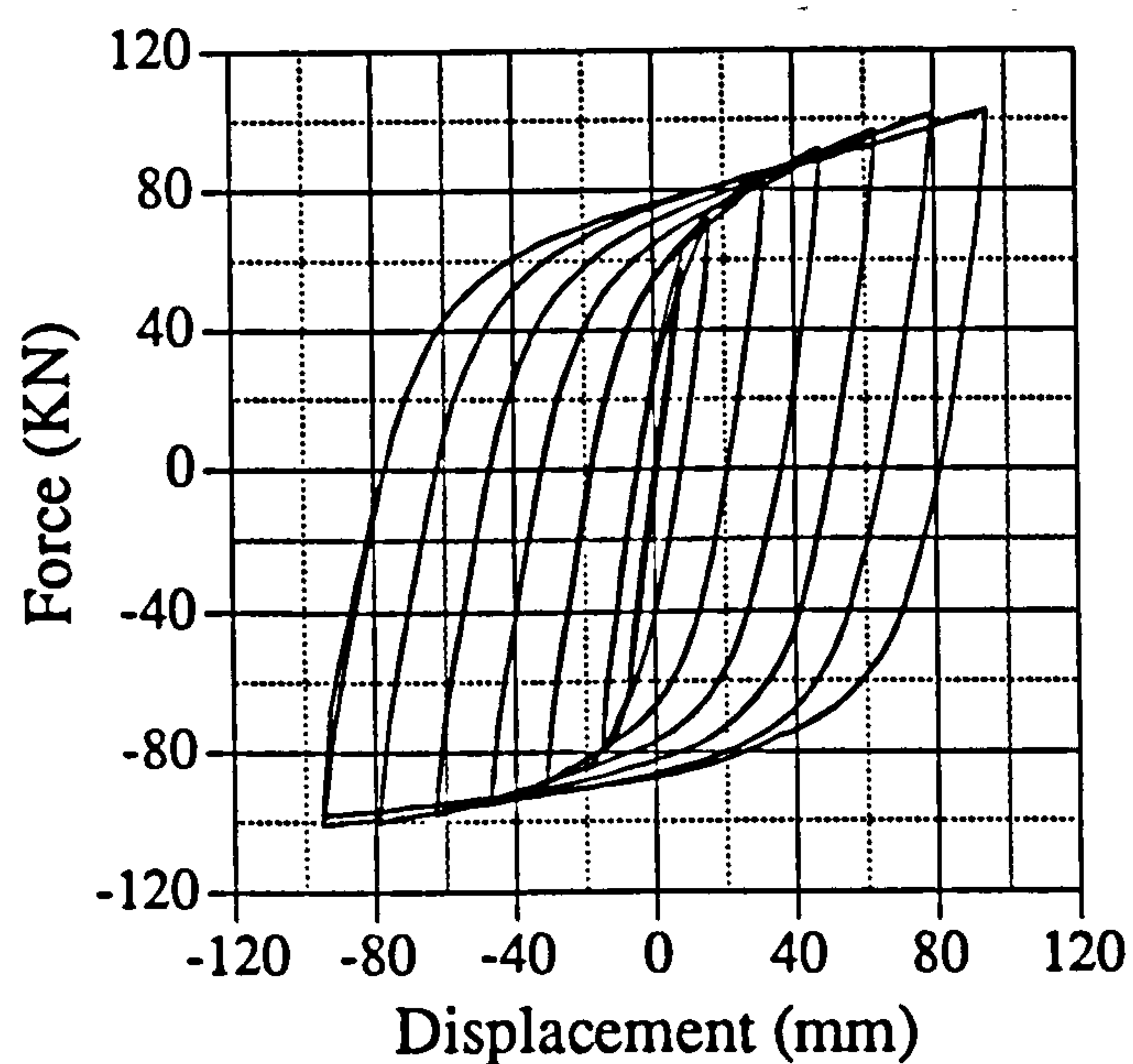


Fig. 6.12 Load versus displacement relationship for IC04

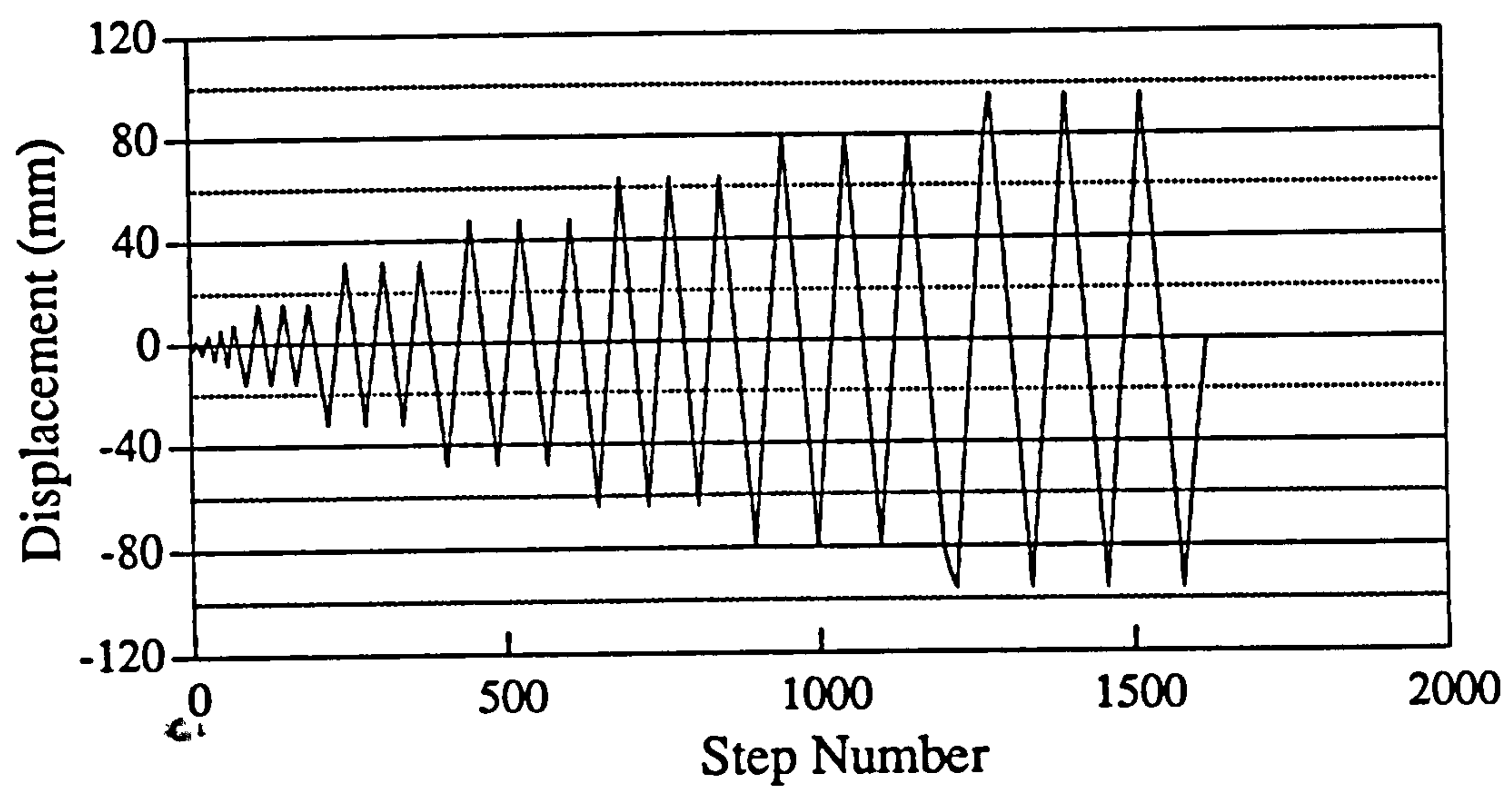


Fig. 6.13 Loading history for IC07

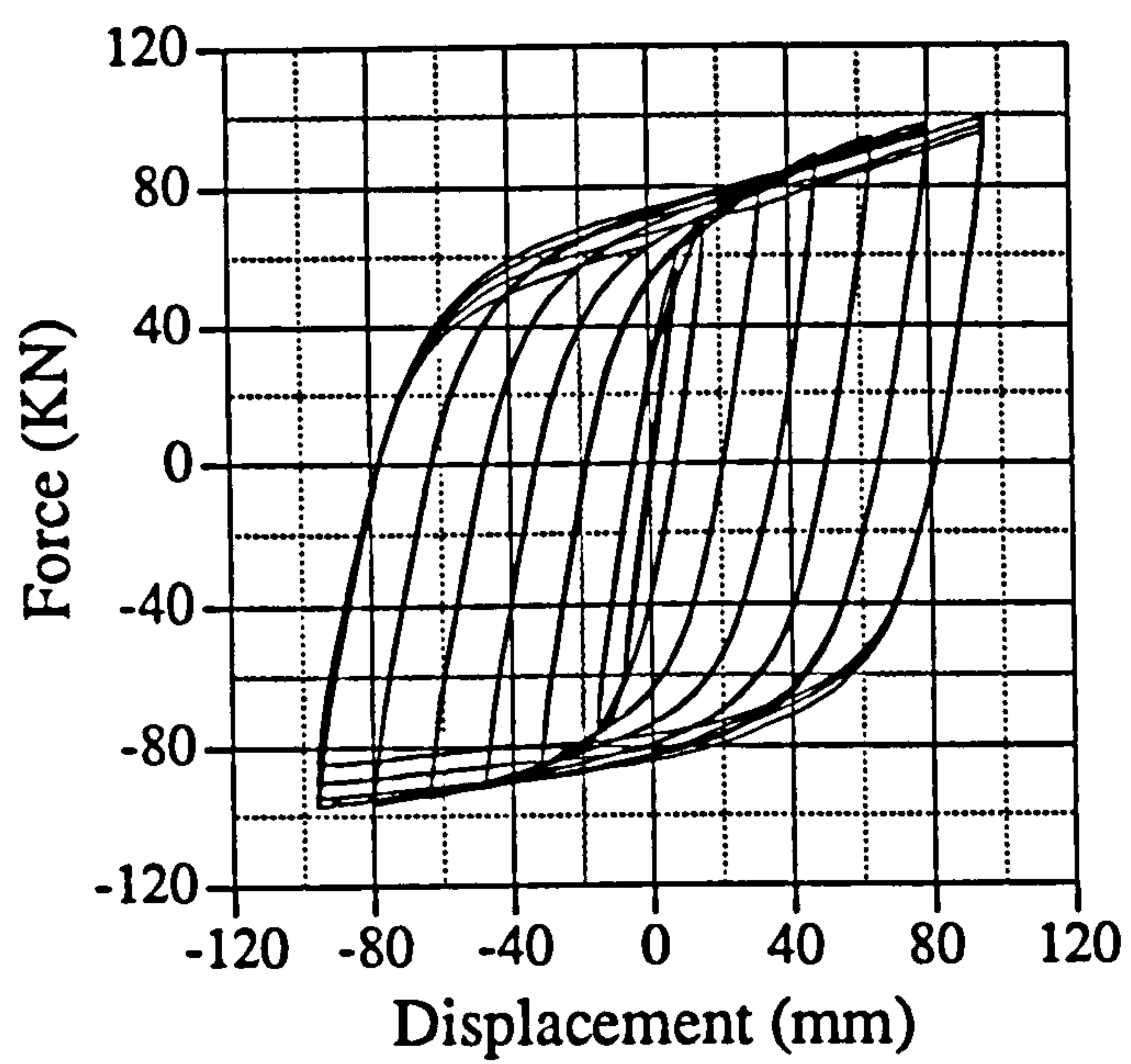


Fig. 6.14 Load versus displacement relationship for IC07

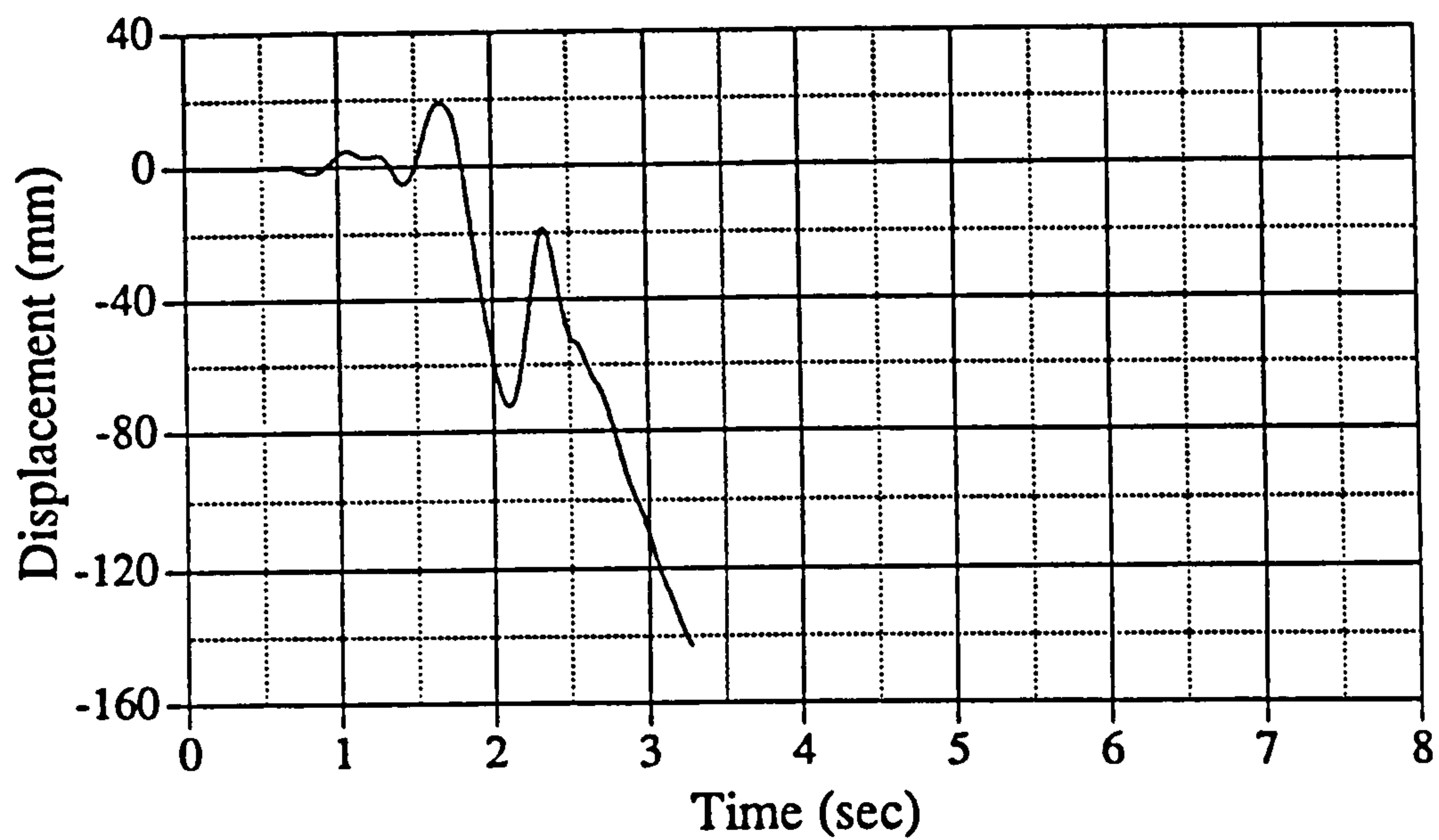


Fig. 6.15 Displacement response history for EM03

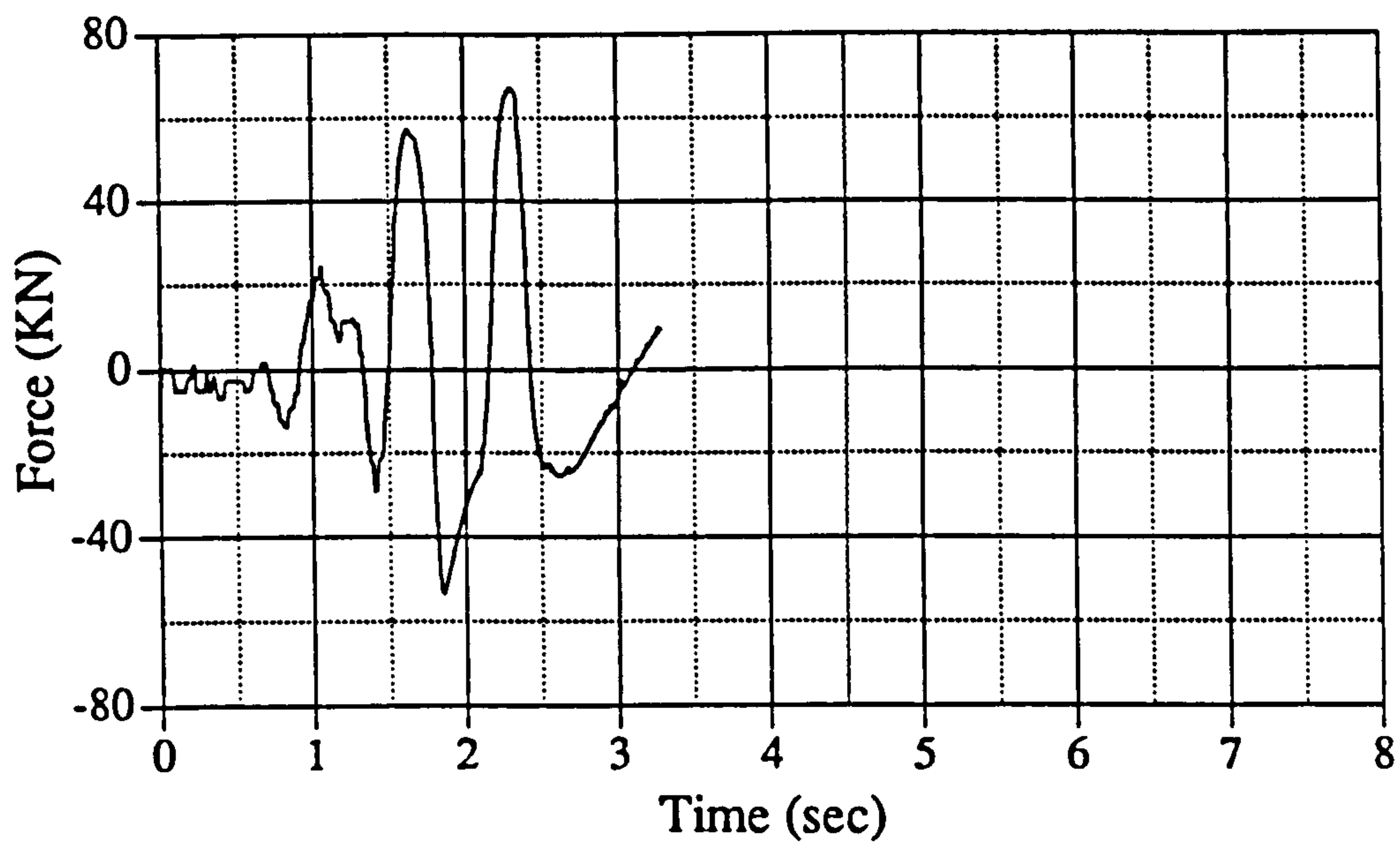


Fig. 6.16 Force response history for EM03

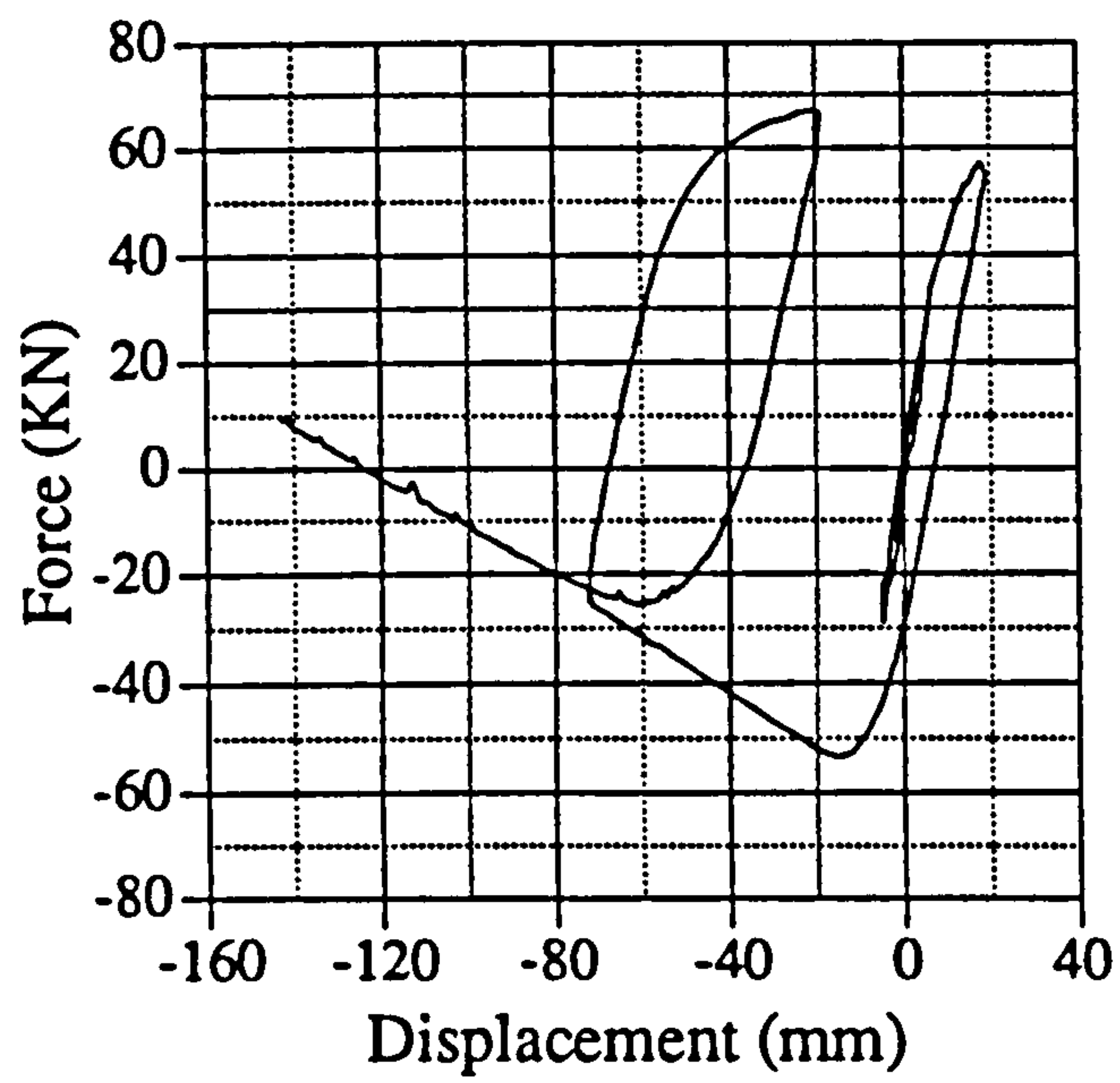


Fig. 6.17 Load versus displacement relationship for EM03

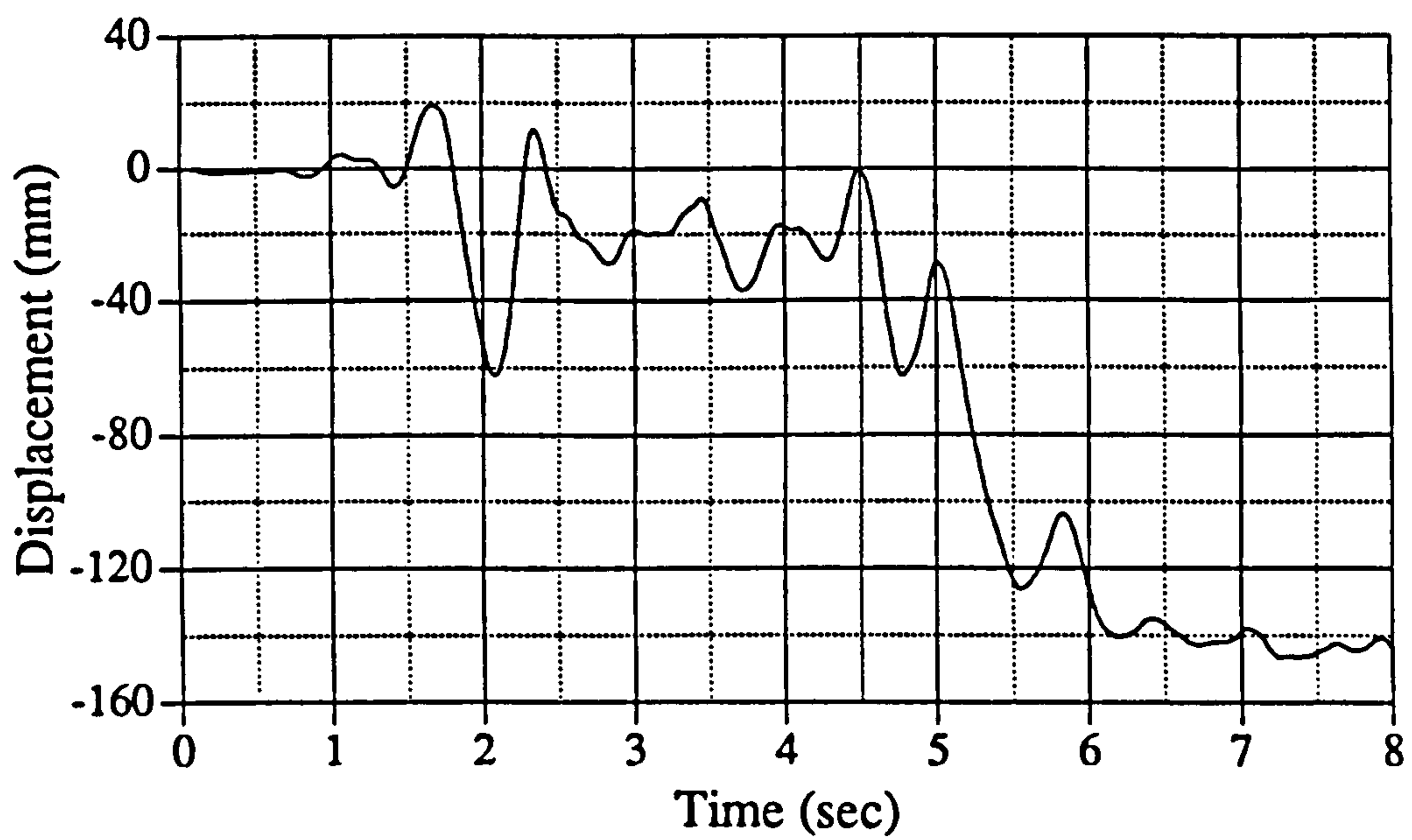


Fig. 6.18 Displacement response history for IC03

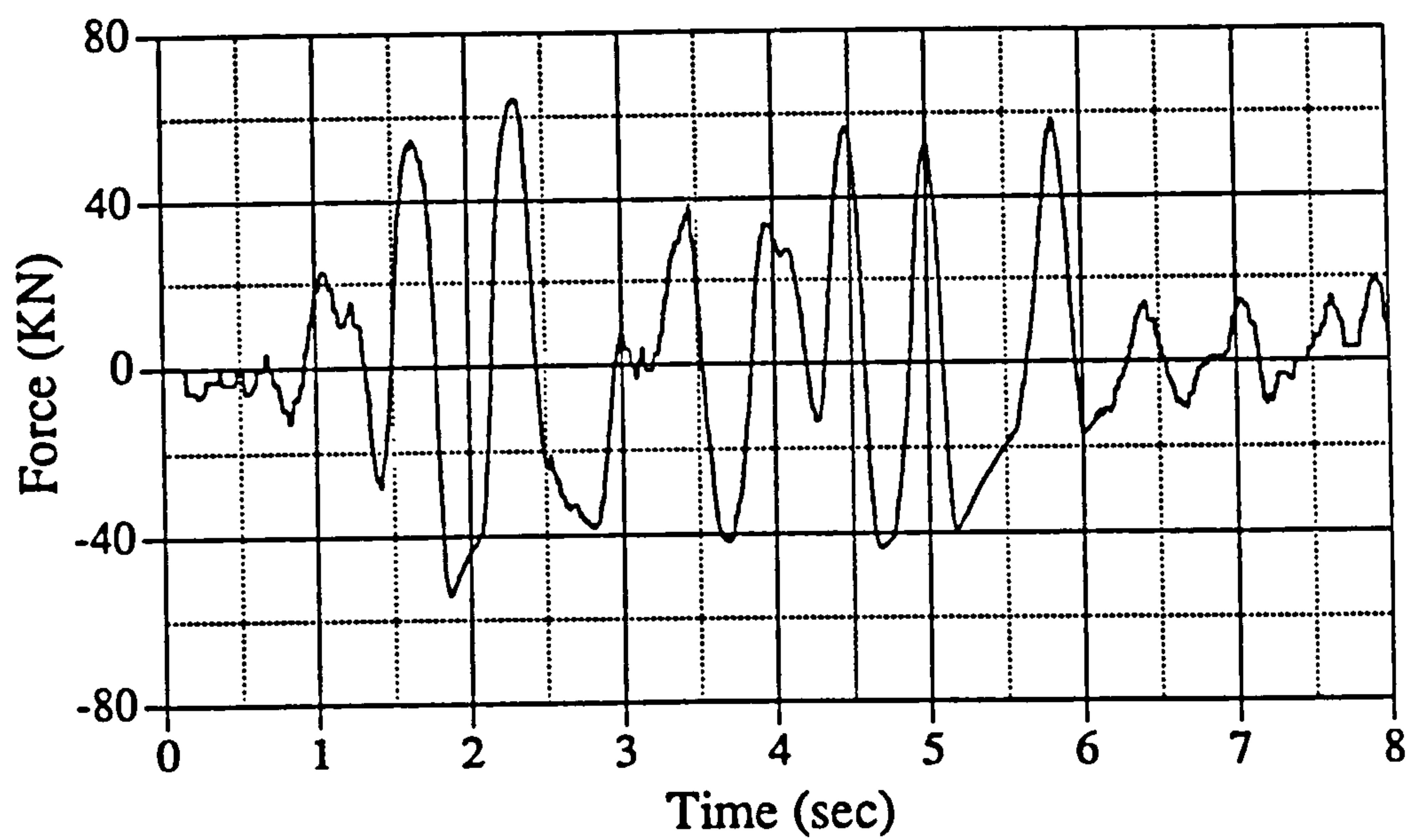


Fig. 6.19 Force response history for IC03

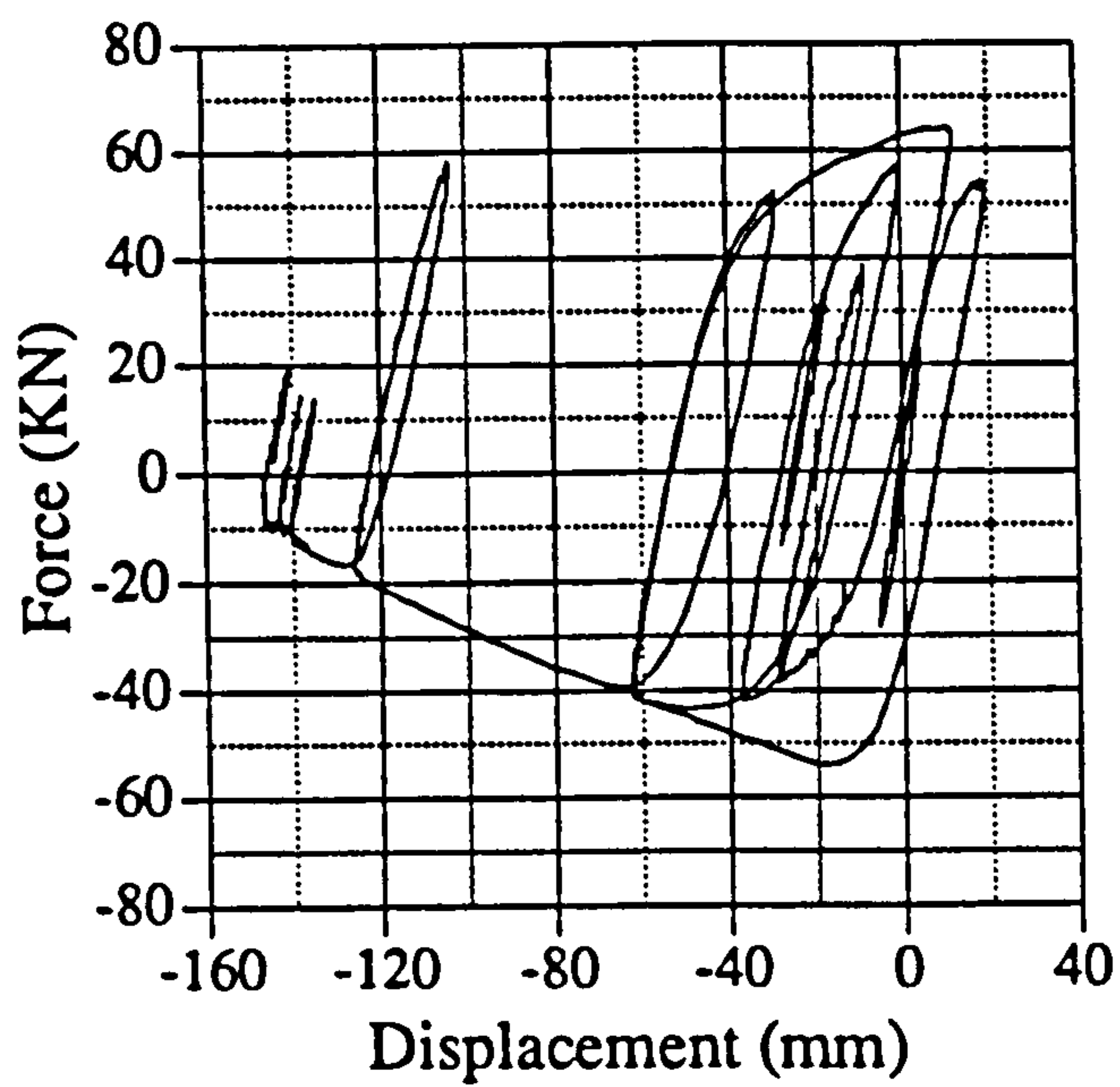


Fig. 6.20 Load versus displacement relationship for IC03

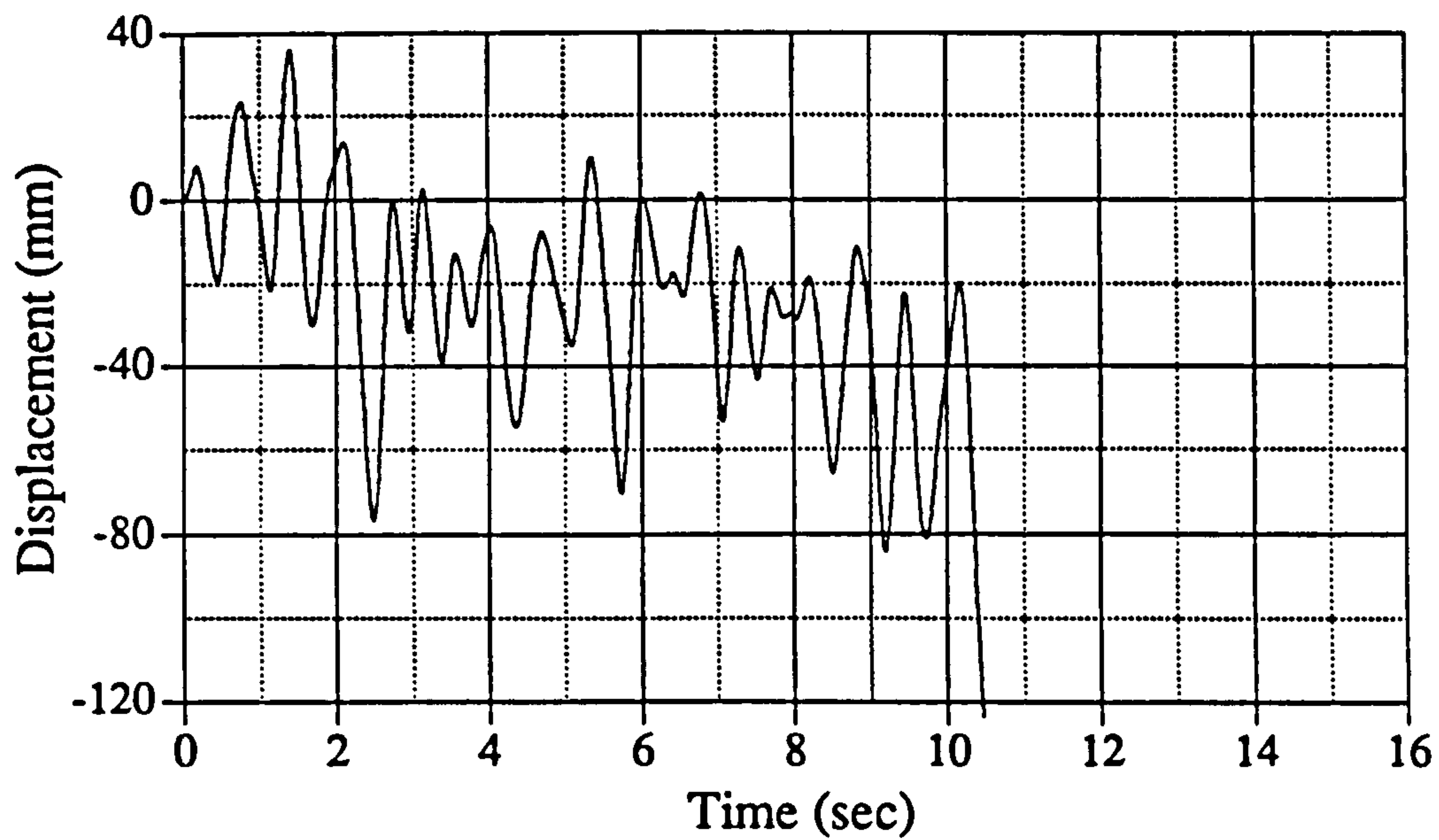


Fig. 6.21 Displacement response history for EM05

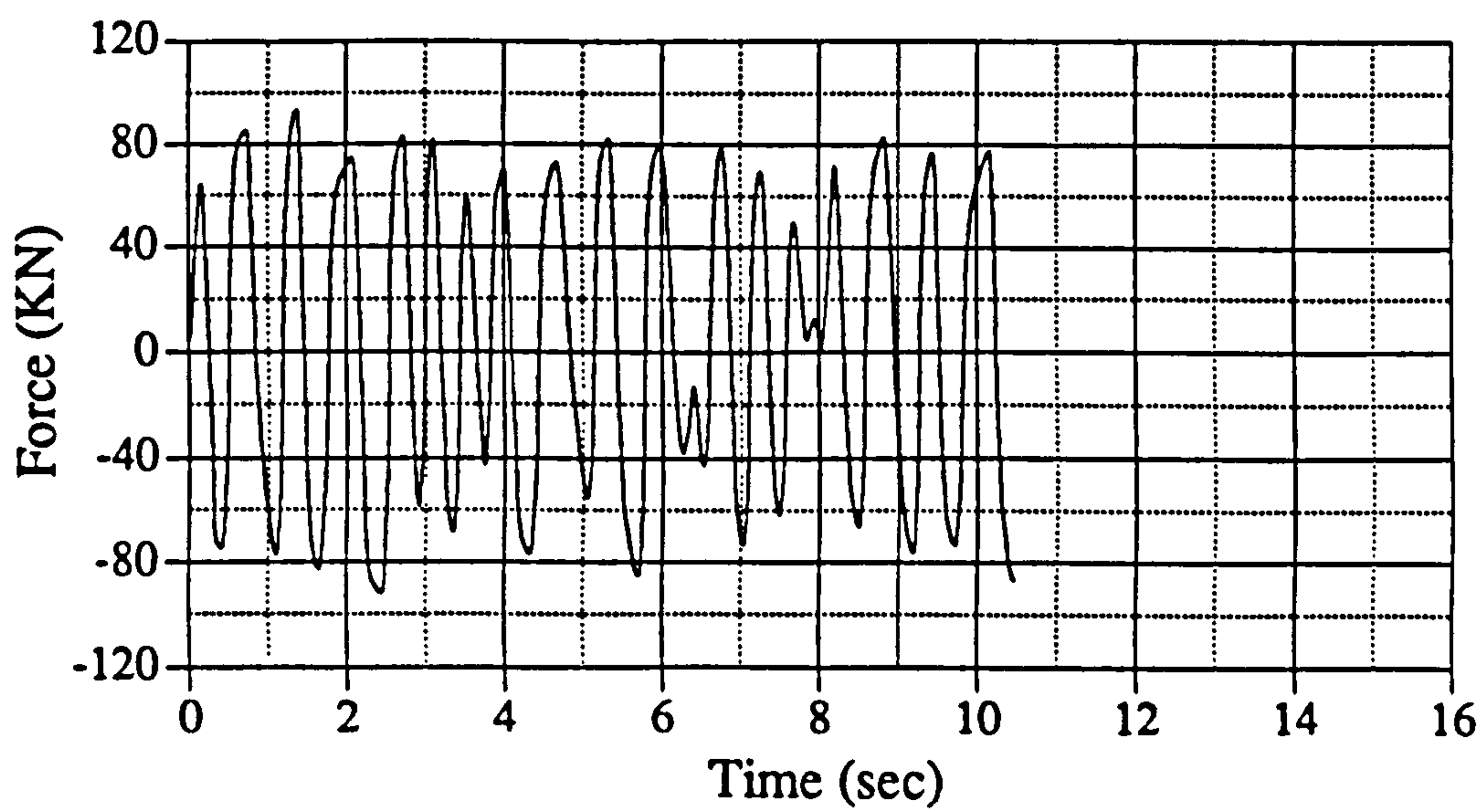


Fig. 6.22 Force response history for EM05

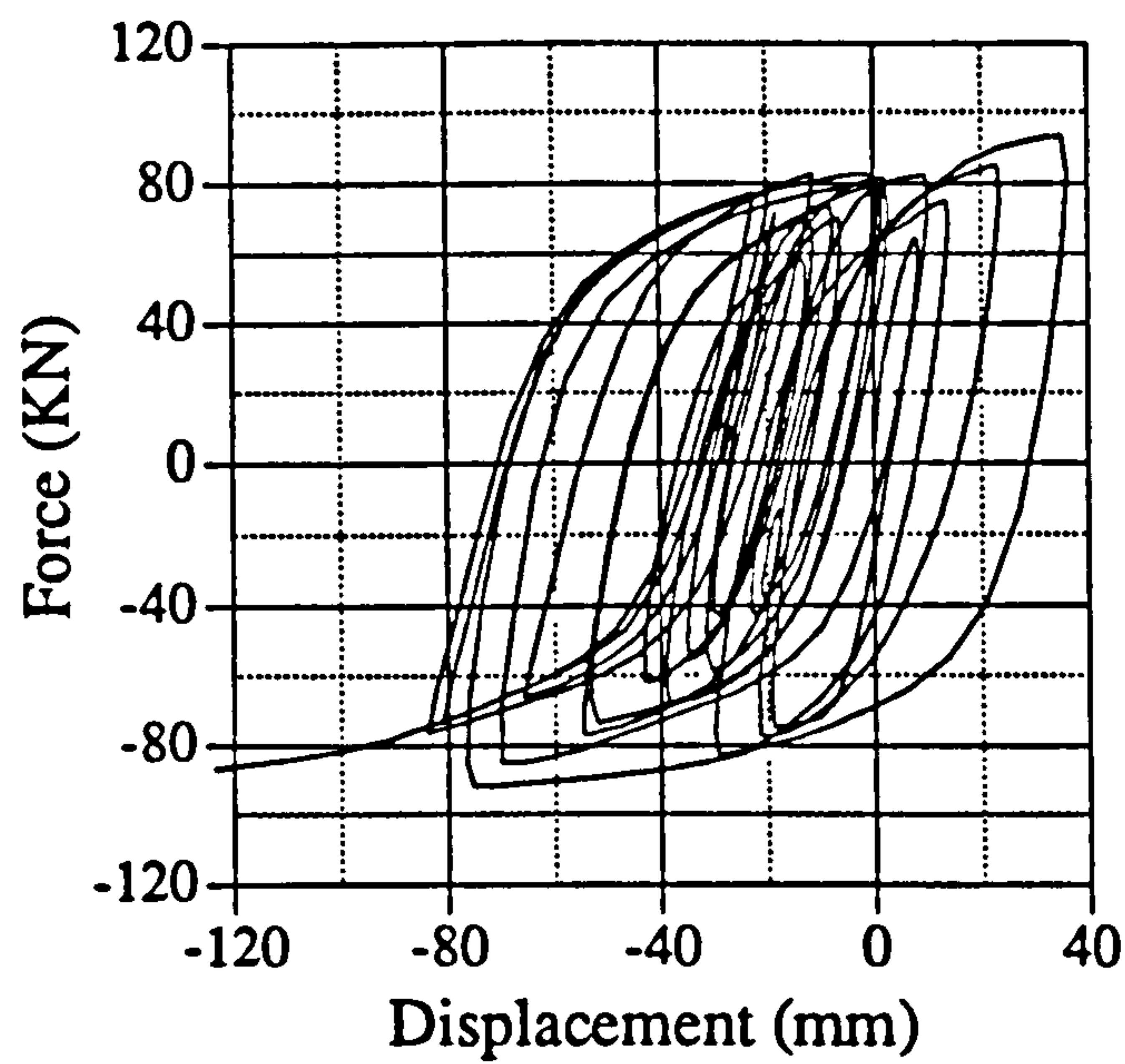


Fig. 6.23 Load versus displacement relationship for EM05

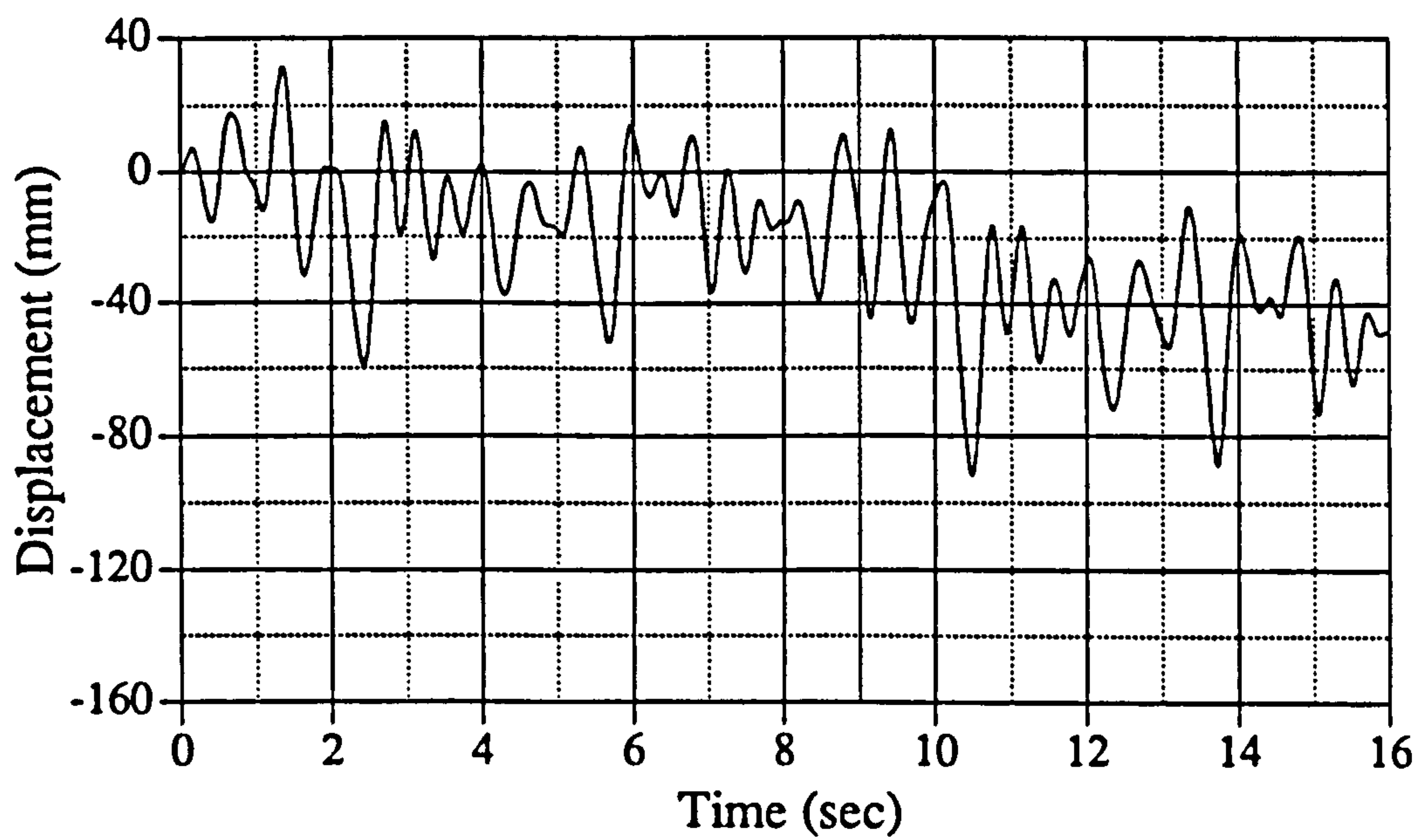


Fig. 6.24 Displacement response history for IC05

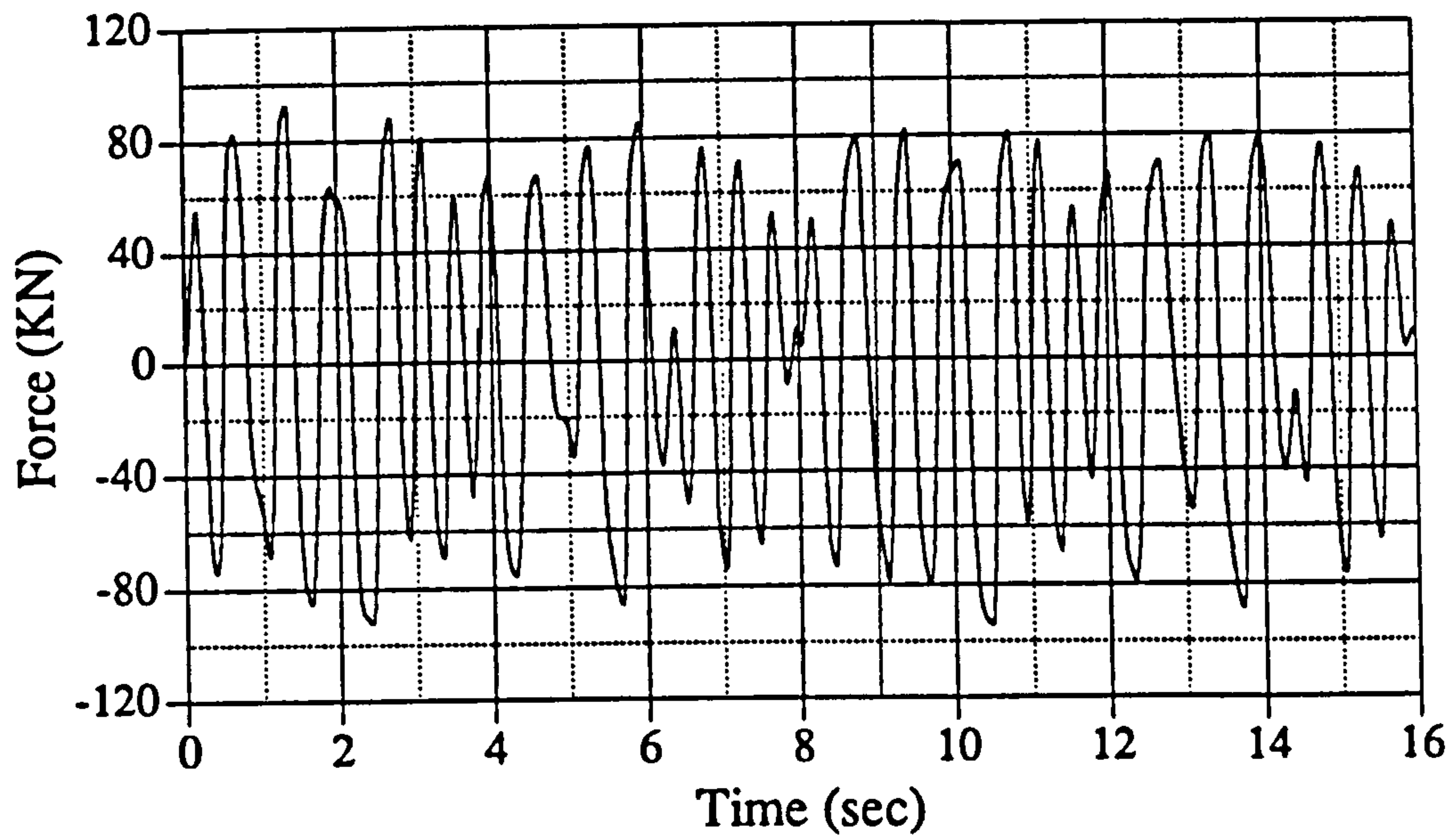


Fig. 6.25 Force response history for IC05

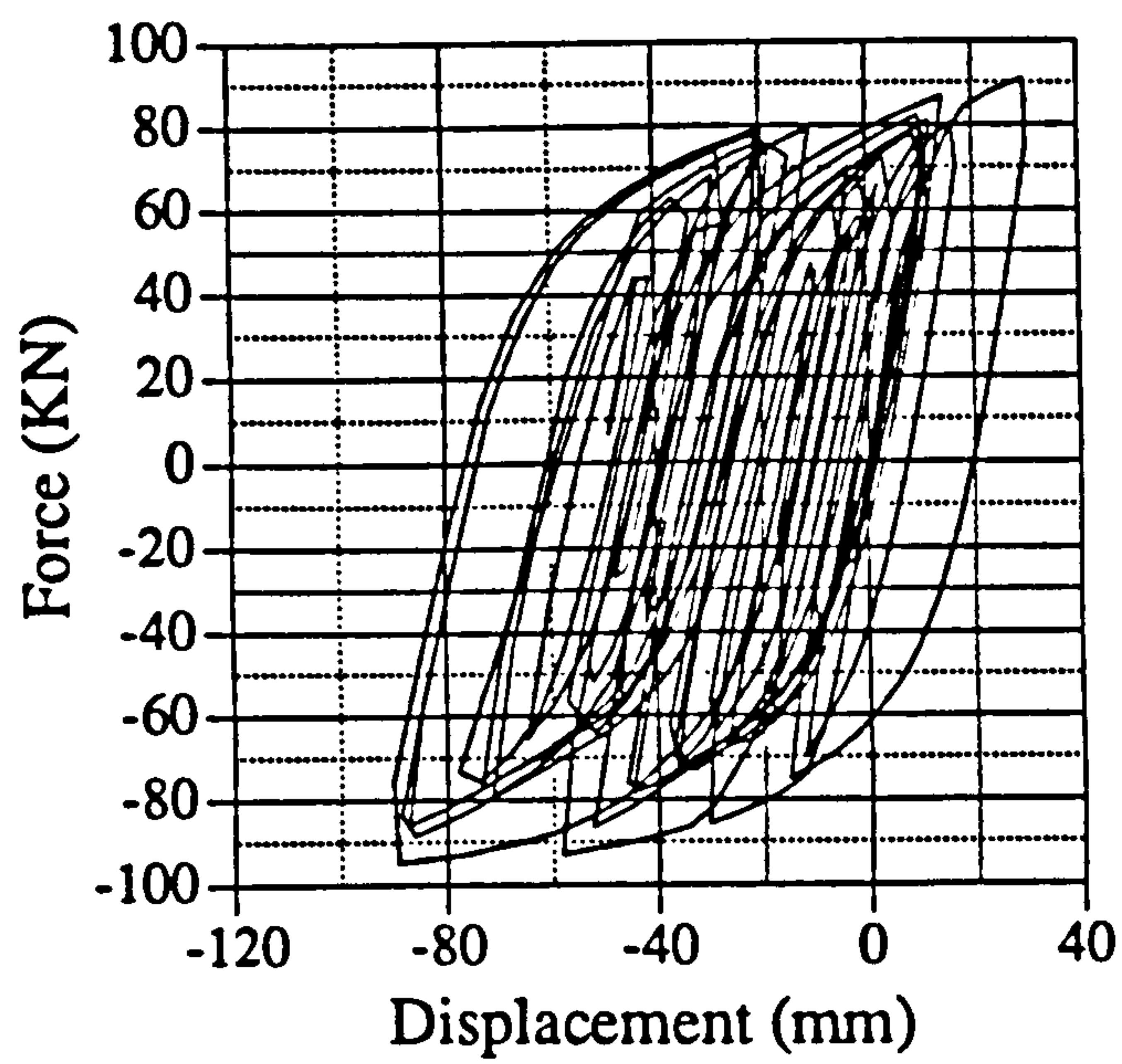


Fig. 6.26 Load versus displacement relationship for IC05

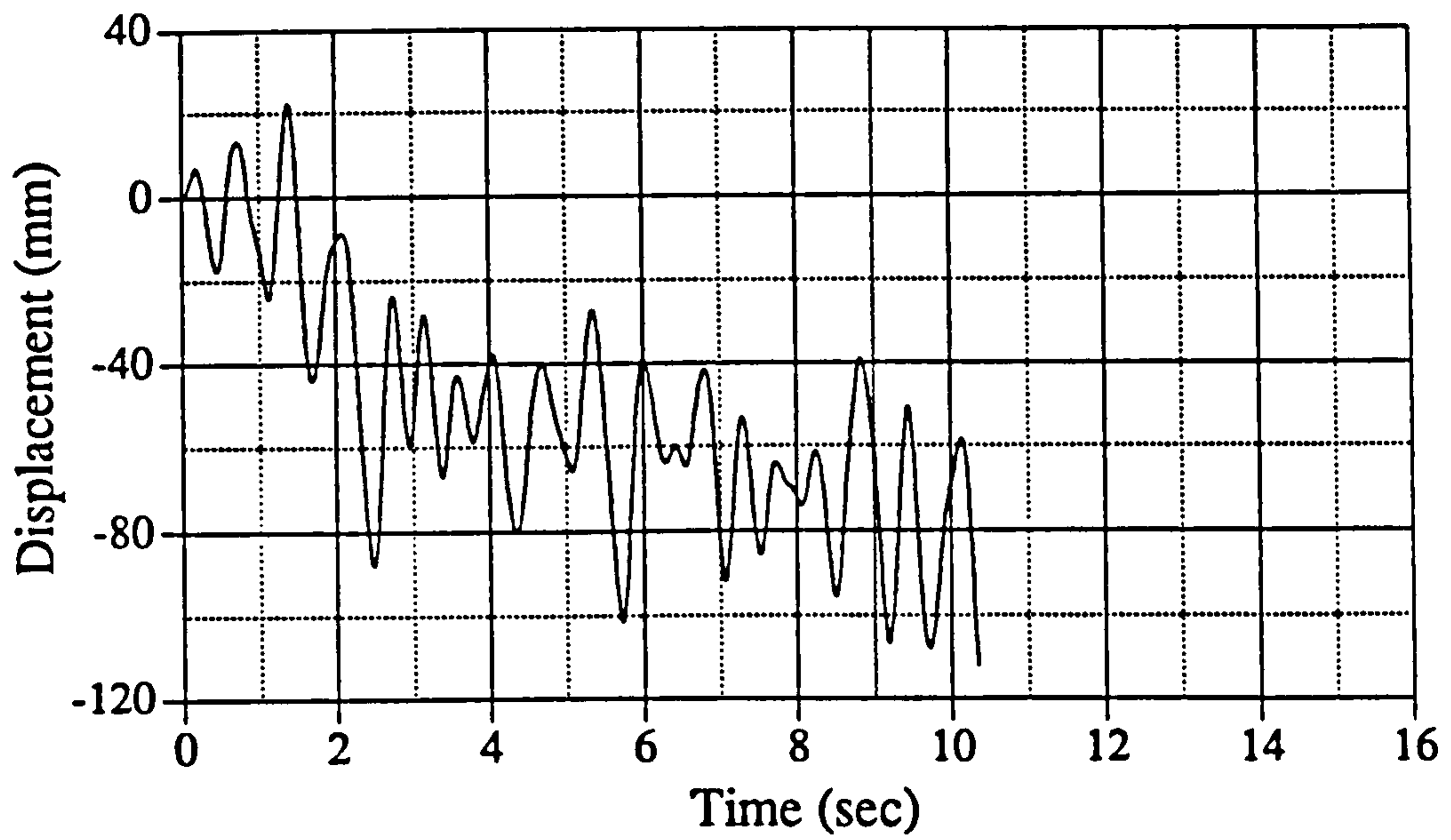


Fig. 6.27 Displacement response history for IC06

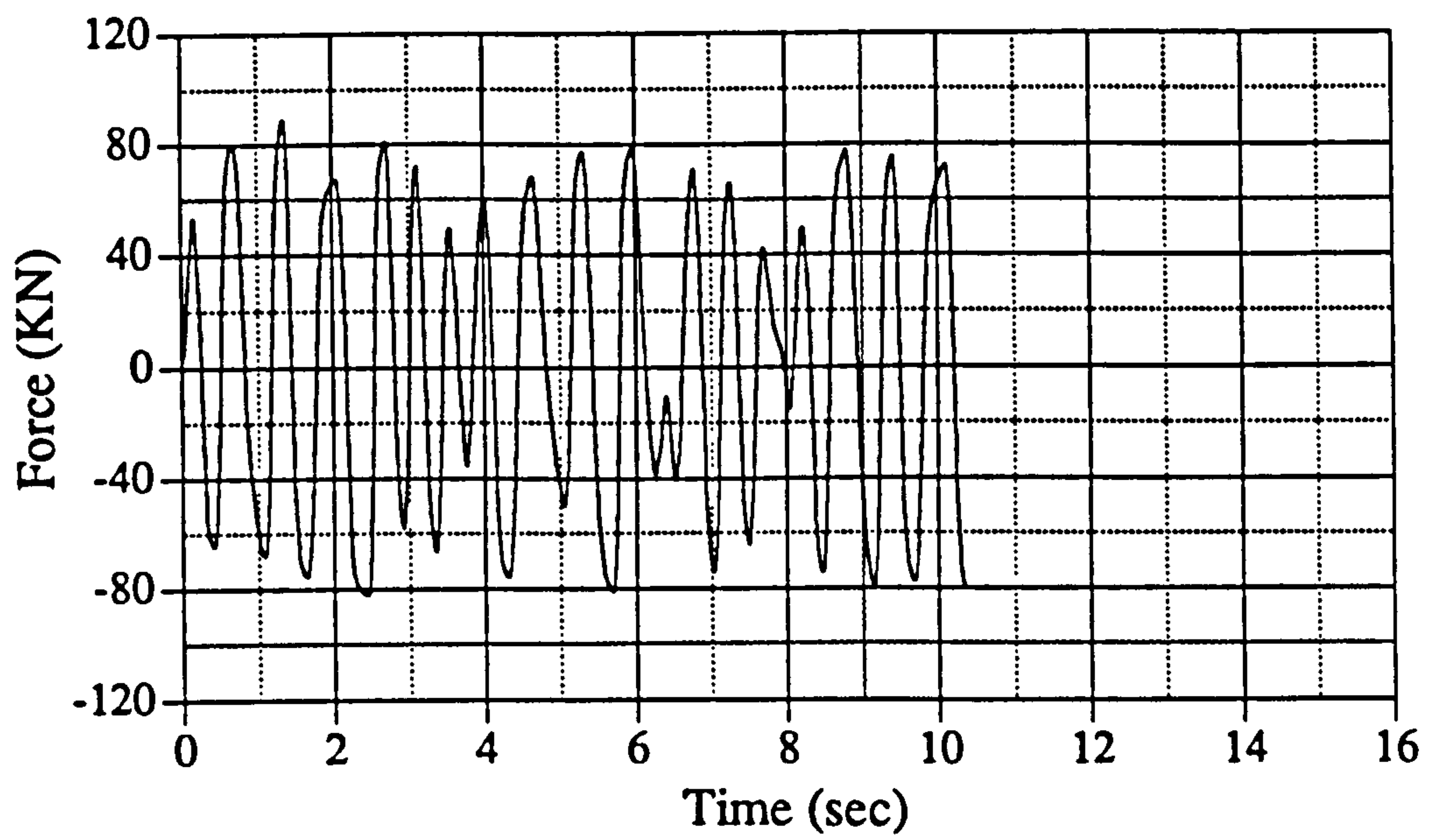


Fig. 6.28 Force response history for IC06

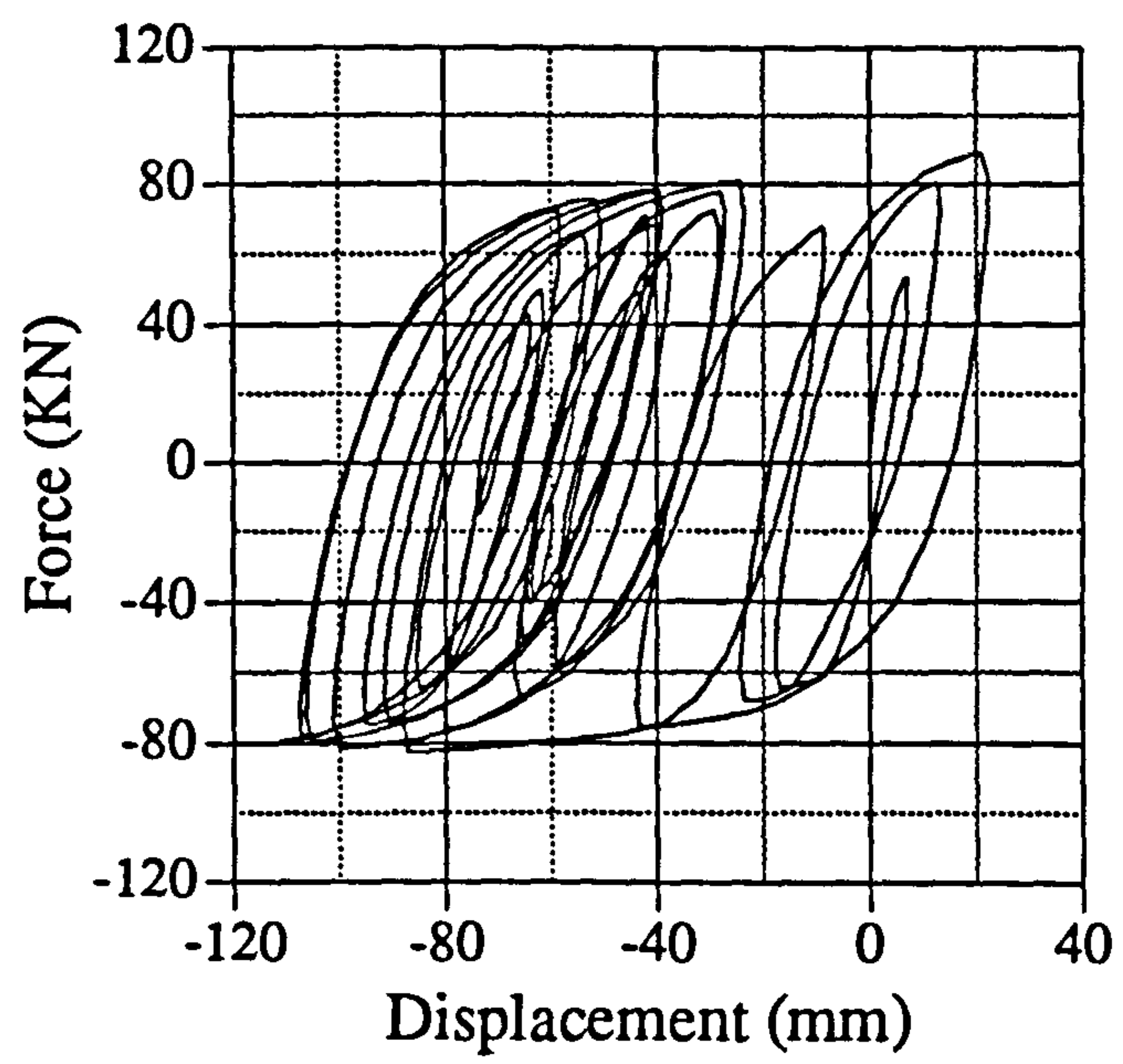


Fig. 6.29 Load versus displacement relationship for IC06

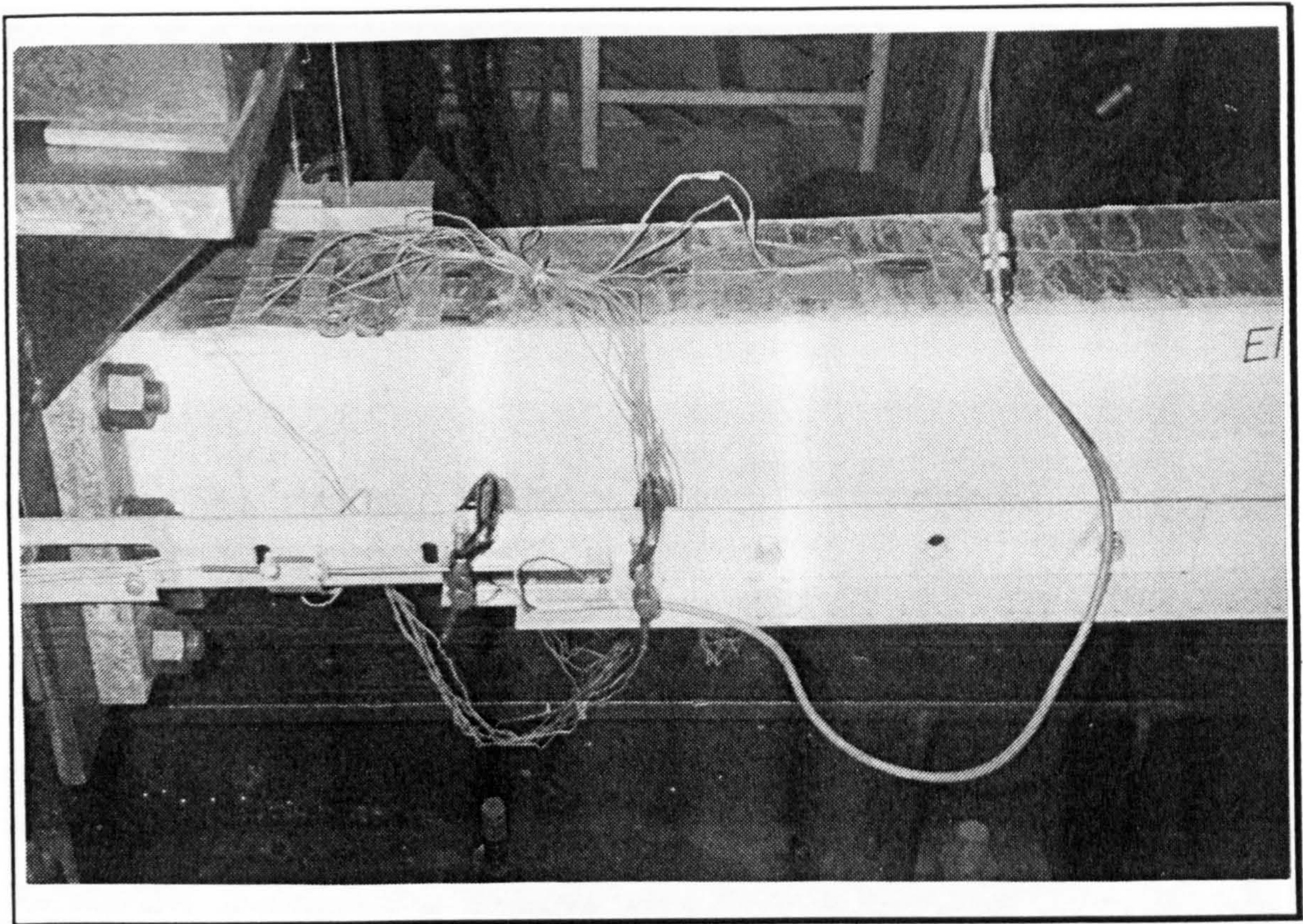


Plate 6.1 EM01 at 33 mm, onset of local buckling in compression flange

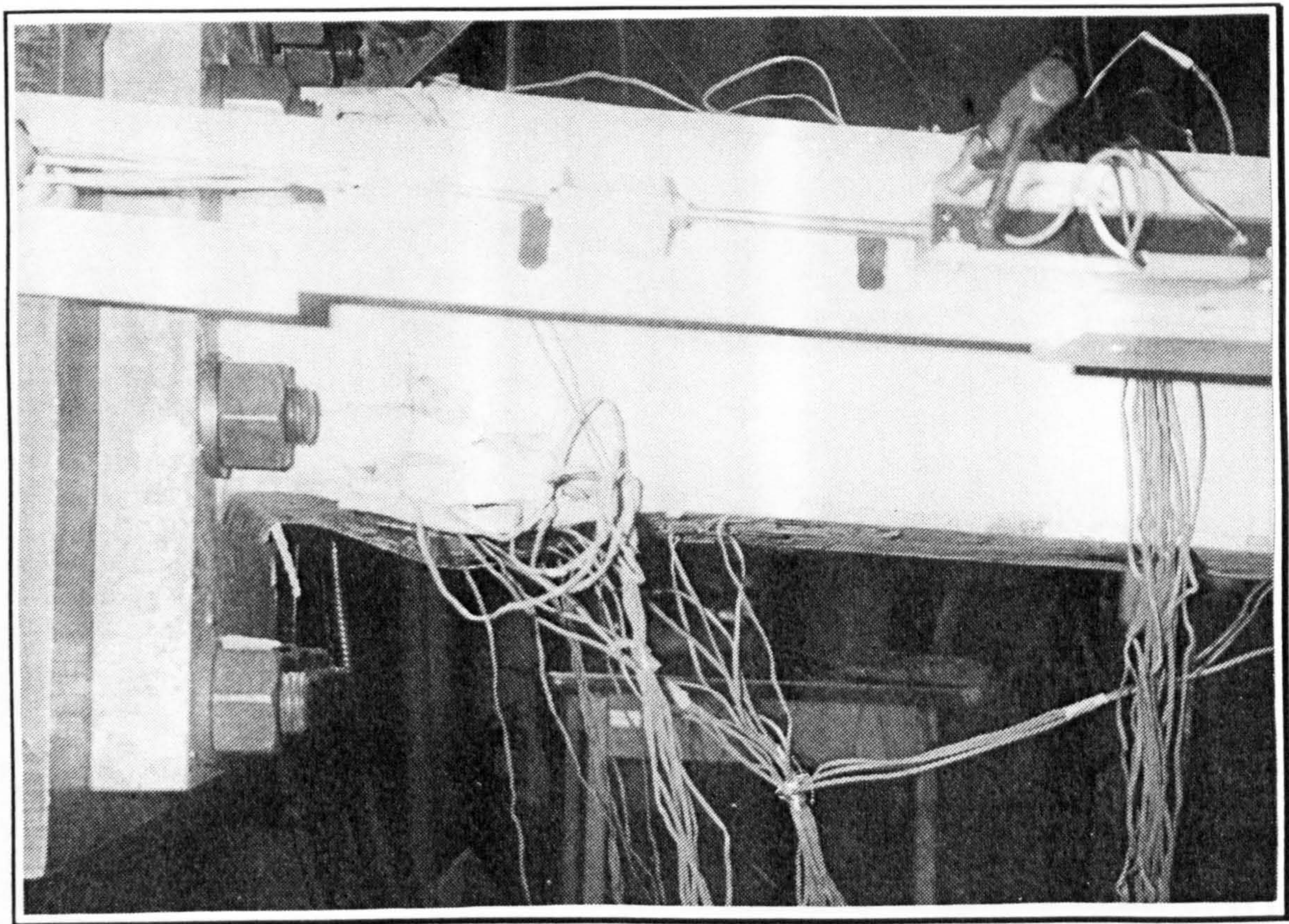


Plate 6.2 EM01 at 55 mm, crushing of concrete following local buckling

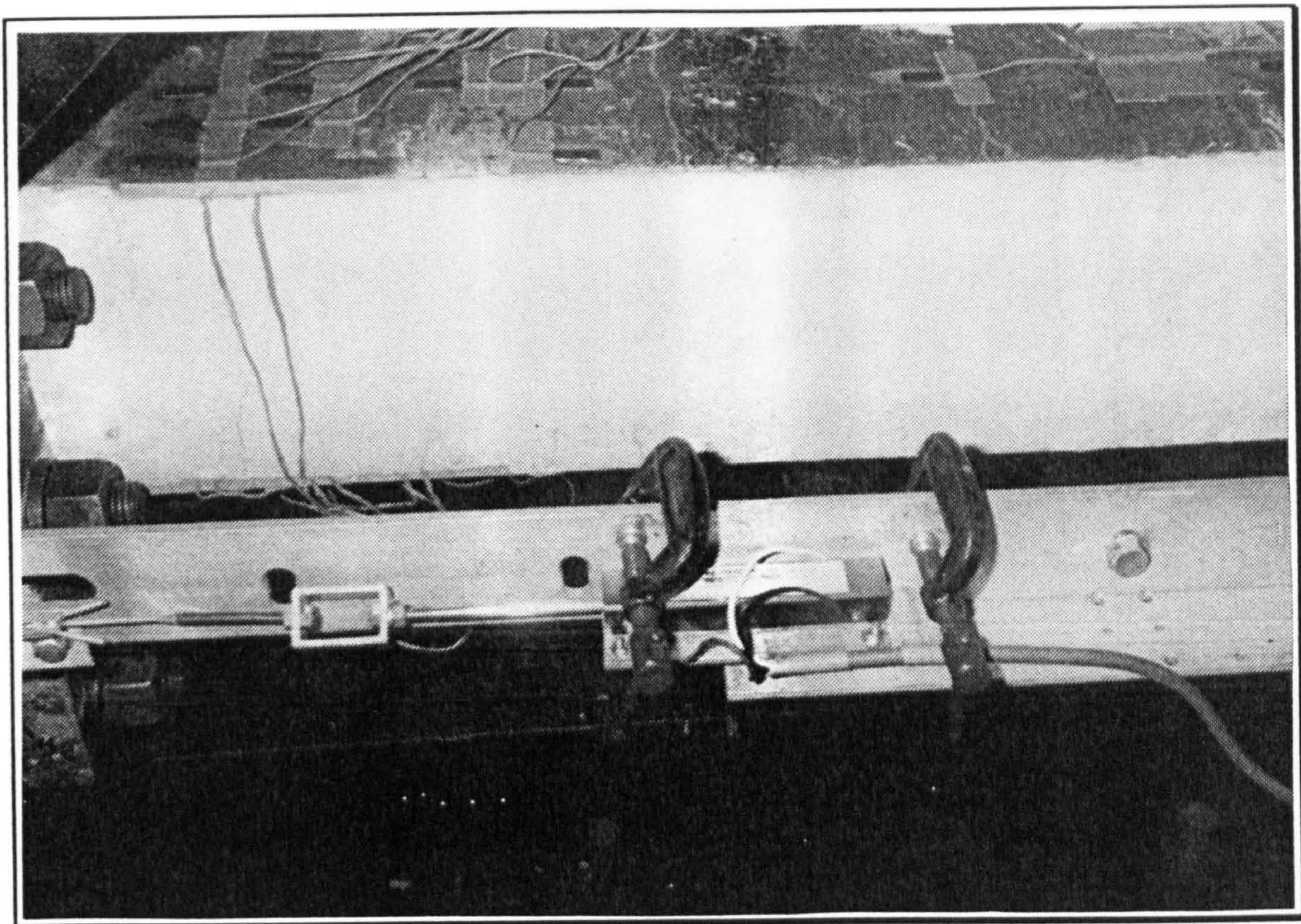


Plate 6.3 IC01 at a displacement amplitude of 11 mm

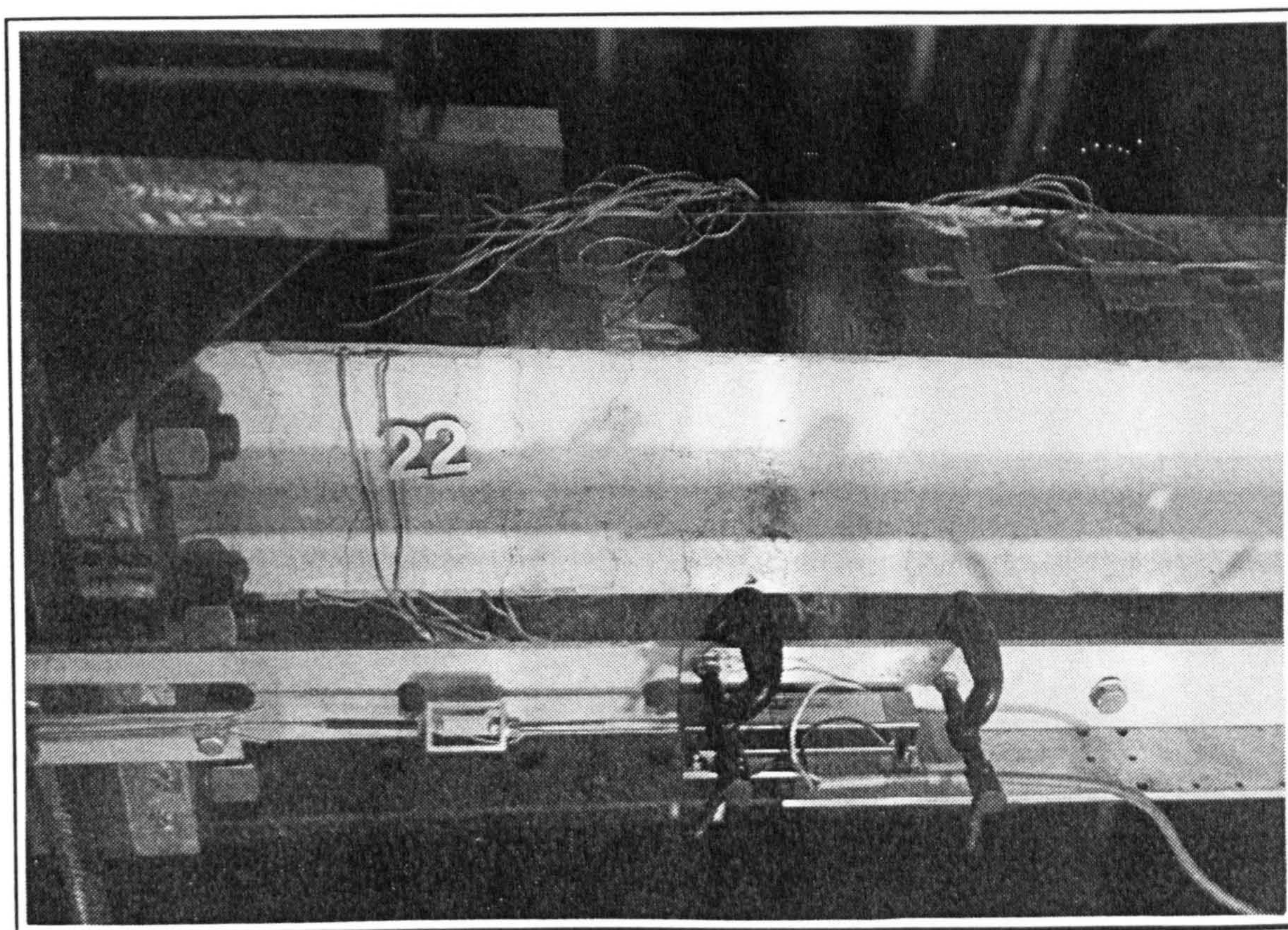


Plate 6.4 IC01 at 22 mm, distribution of flexural cracks along the length

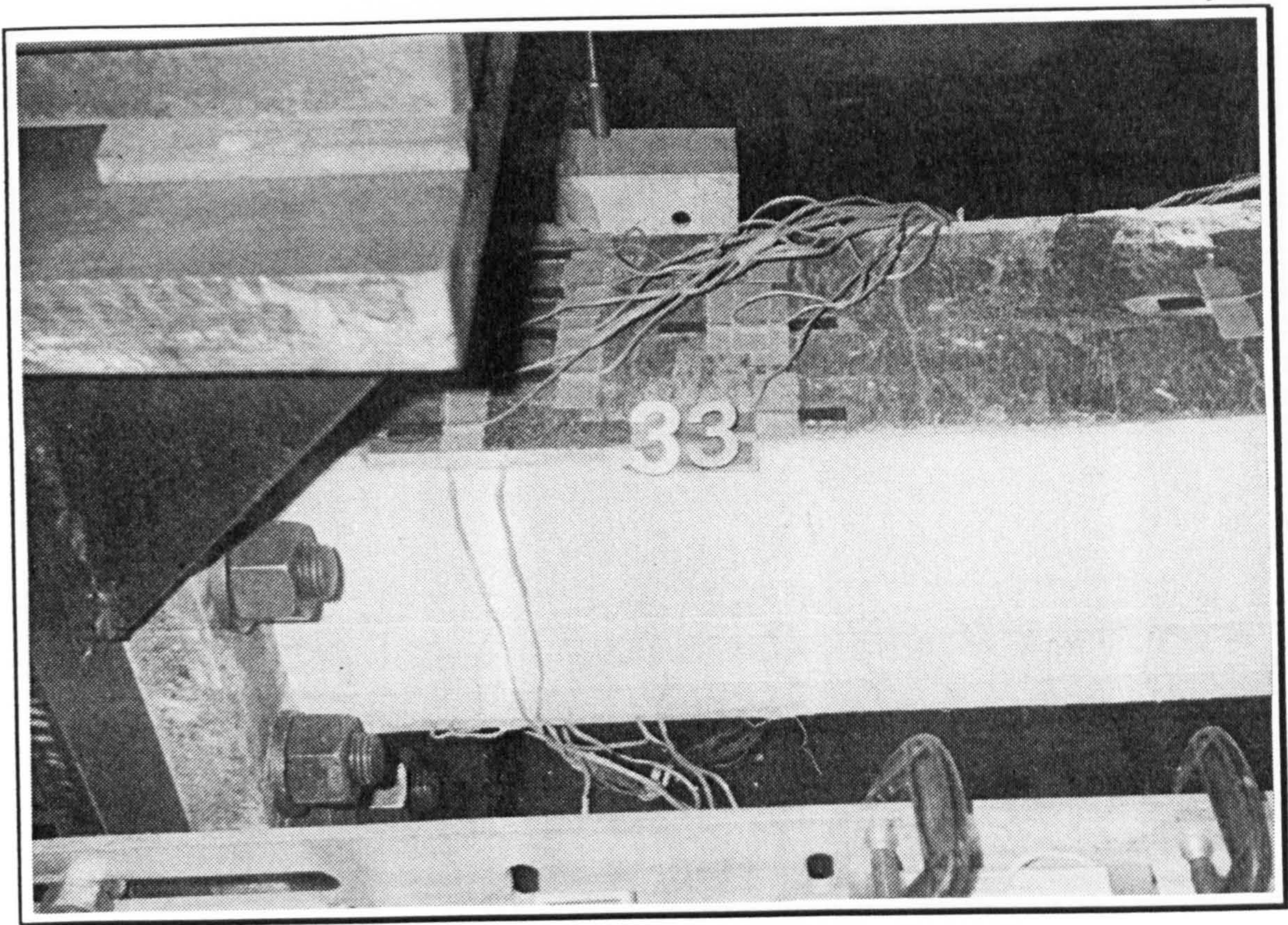


Plate 6.5 IC01 at a displacement amplitude of 33 mm

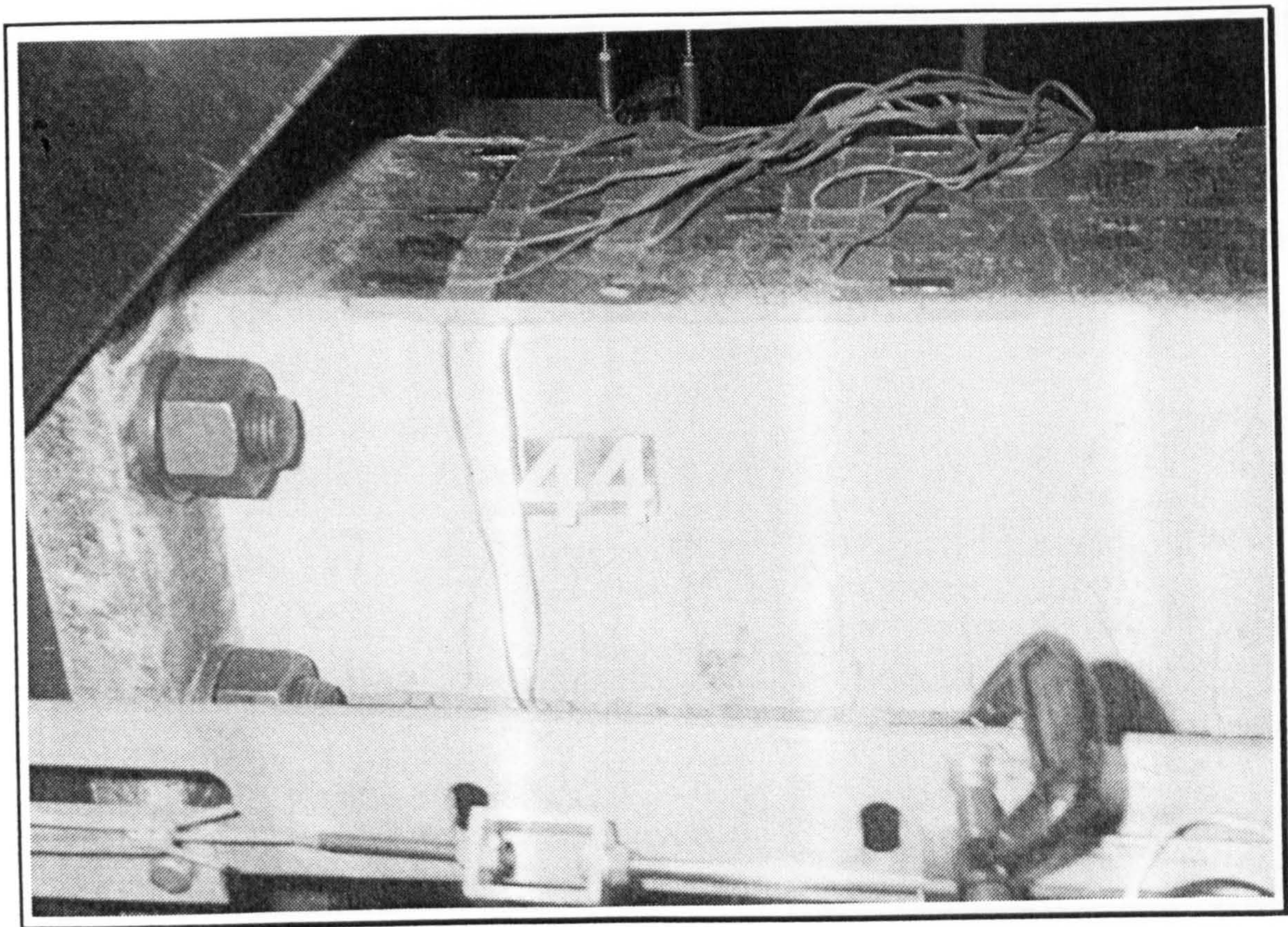


Plate 6.6 IC01 at a displacement amplitude of 44 mm

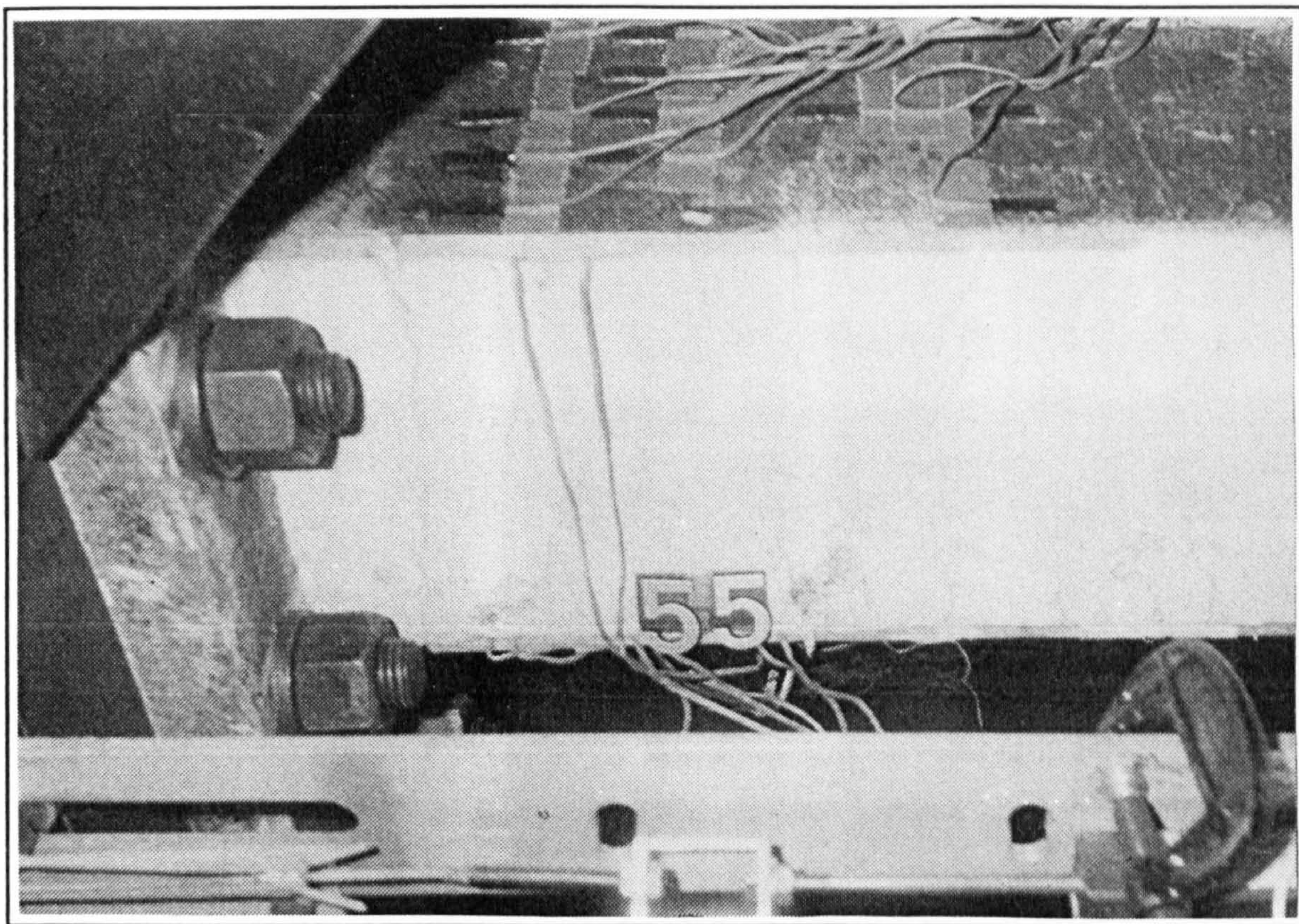


Plate 6.7 IC01 at a displacement amplitude of 55 mm

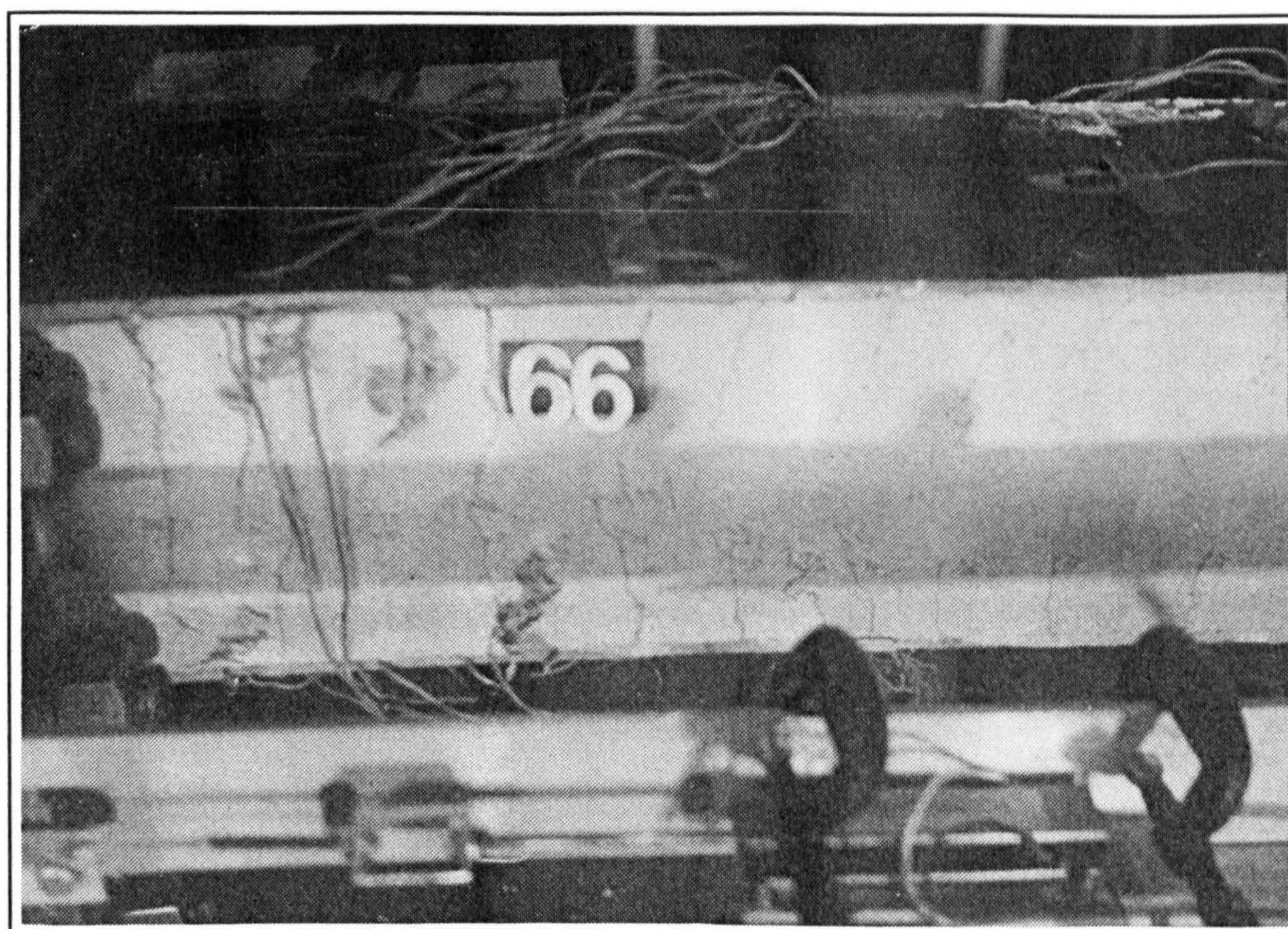


Plate 6.8 IC01 at 66 mm, deeper flexural cracks in the plastic hinge zone

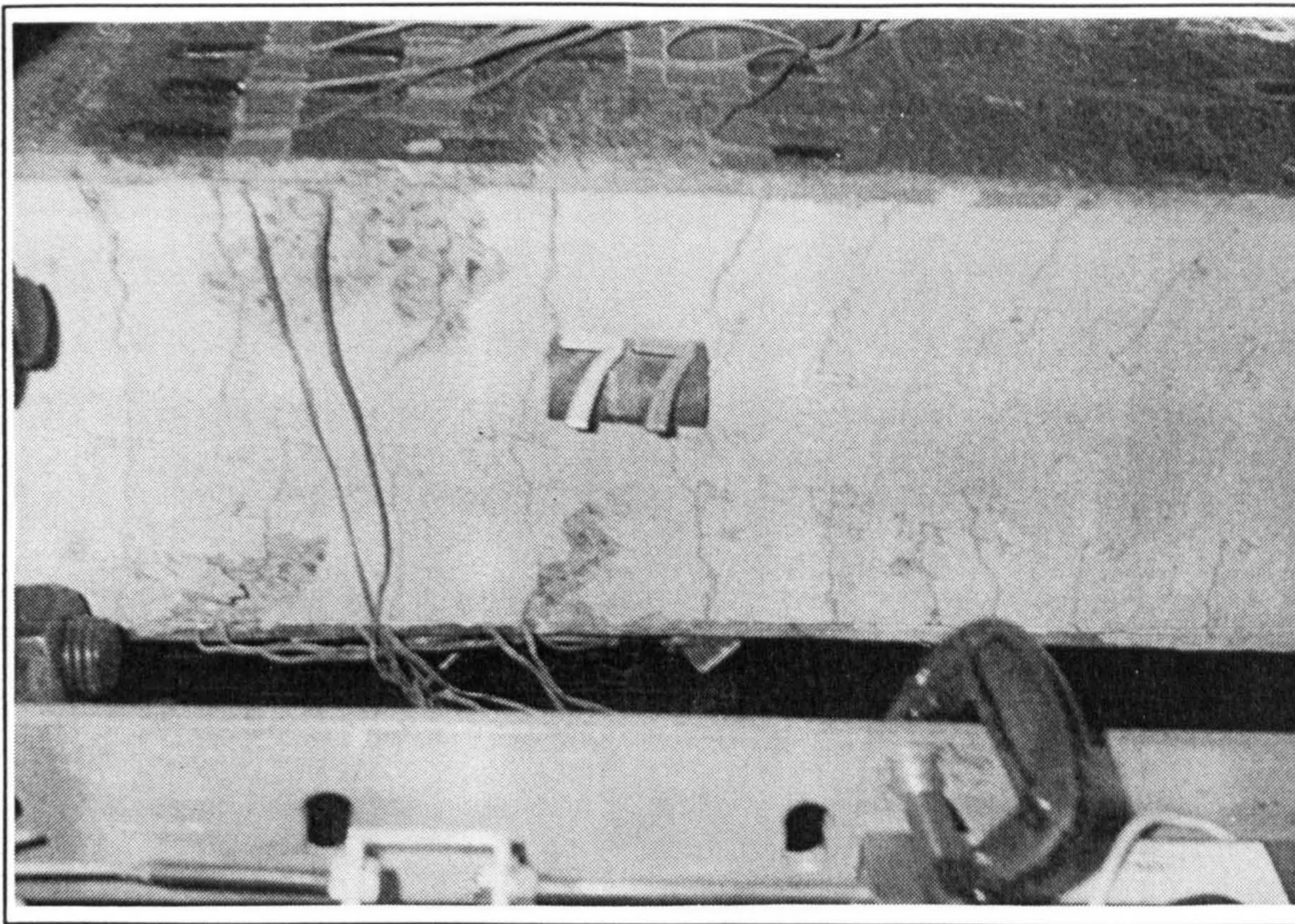


Plate 6.9 IC01 at 77 mm, concrete cracks and spalling of cover concrete

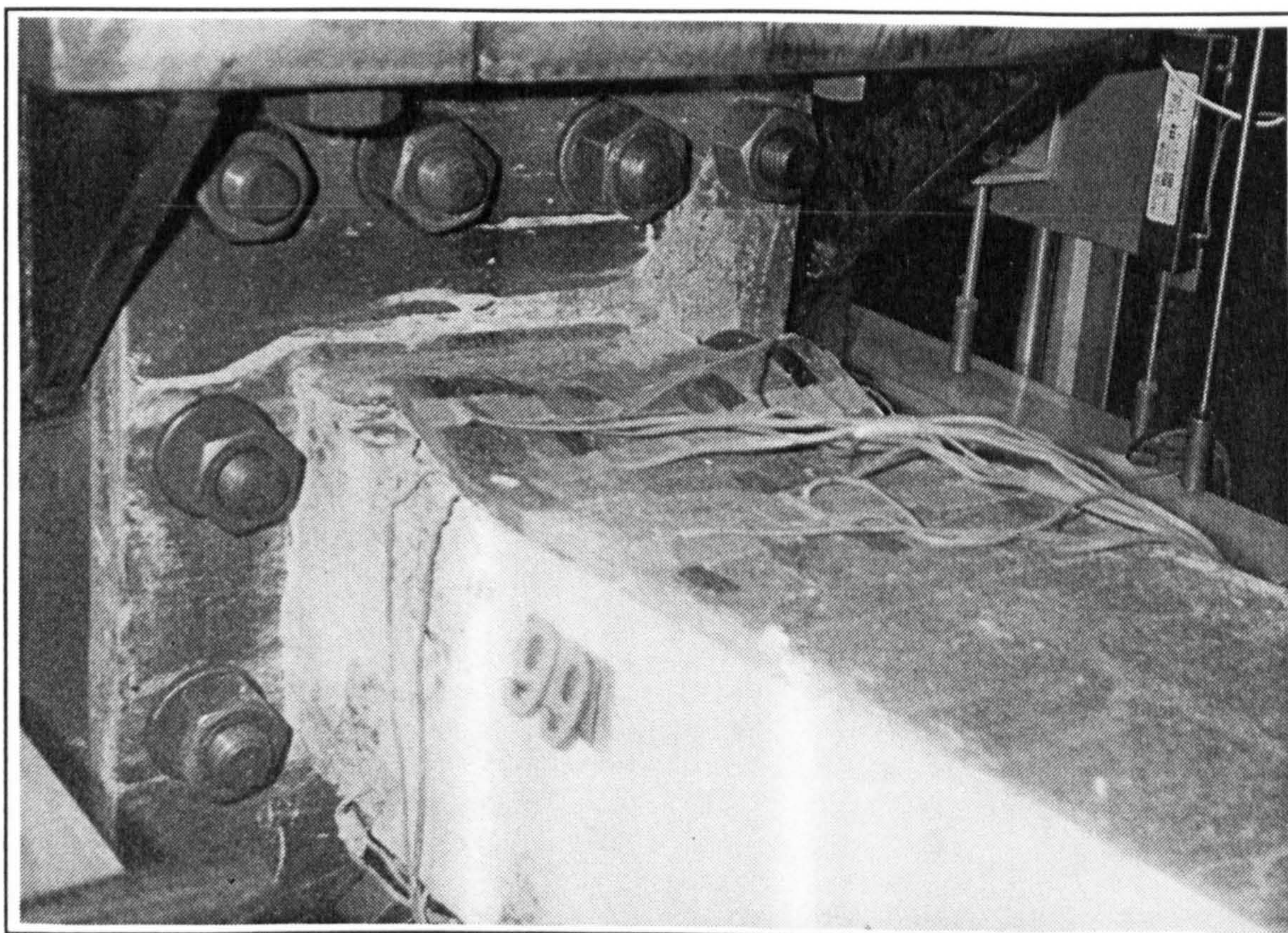


Plate 6.10 IC01 at 99 mm, local buckling in both sides of the compression flange

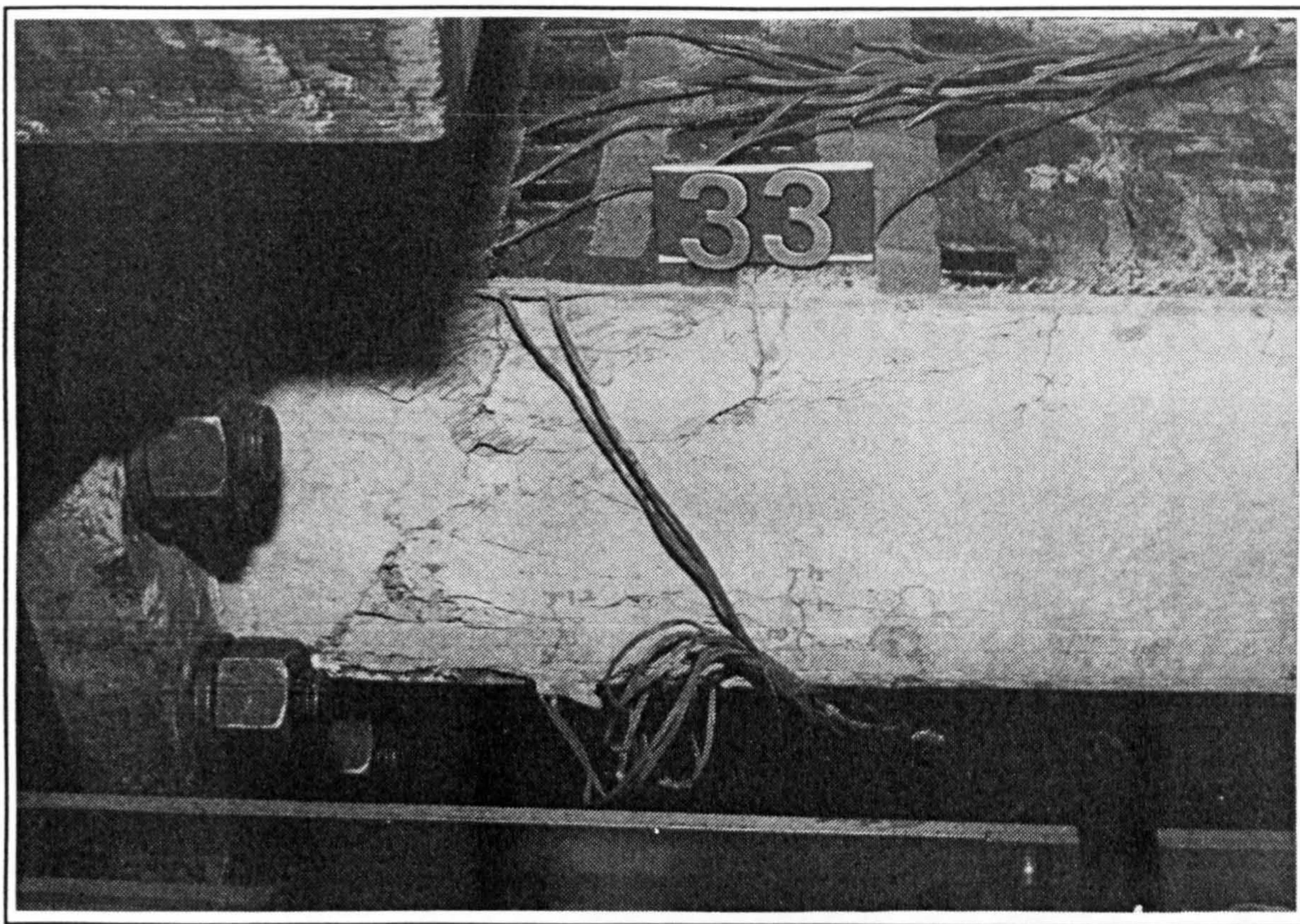


Plate 6.11 EM02 at 33 mm, plastic hinge zone following the onset of local buckling

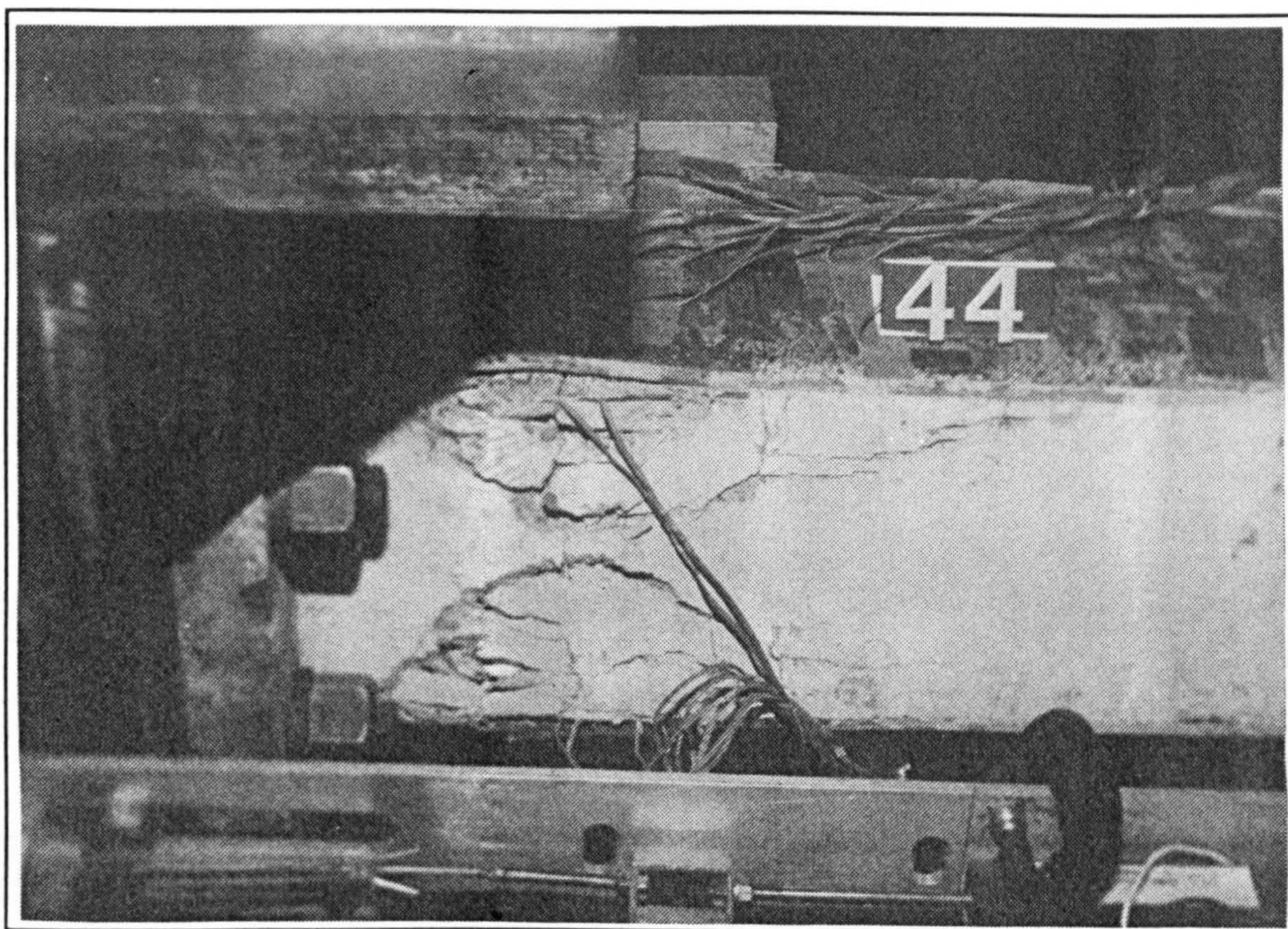


Plate 6.12 EM02 at 44 mm, crushing of concrete following local buckling

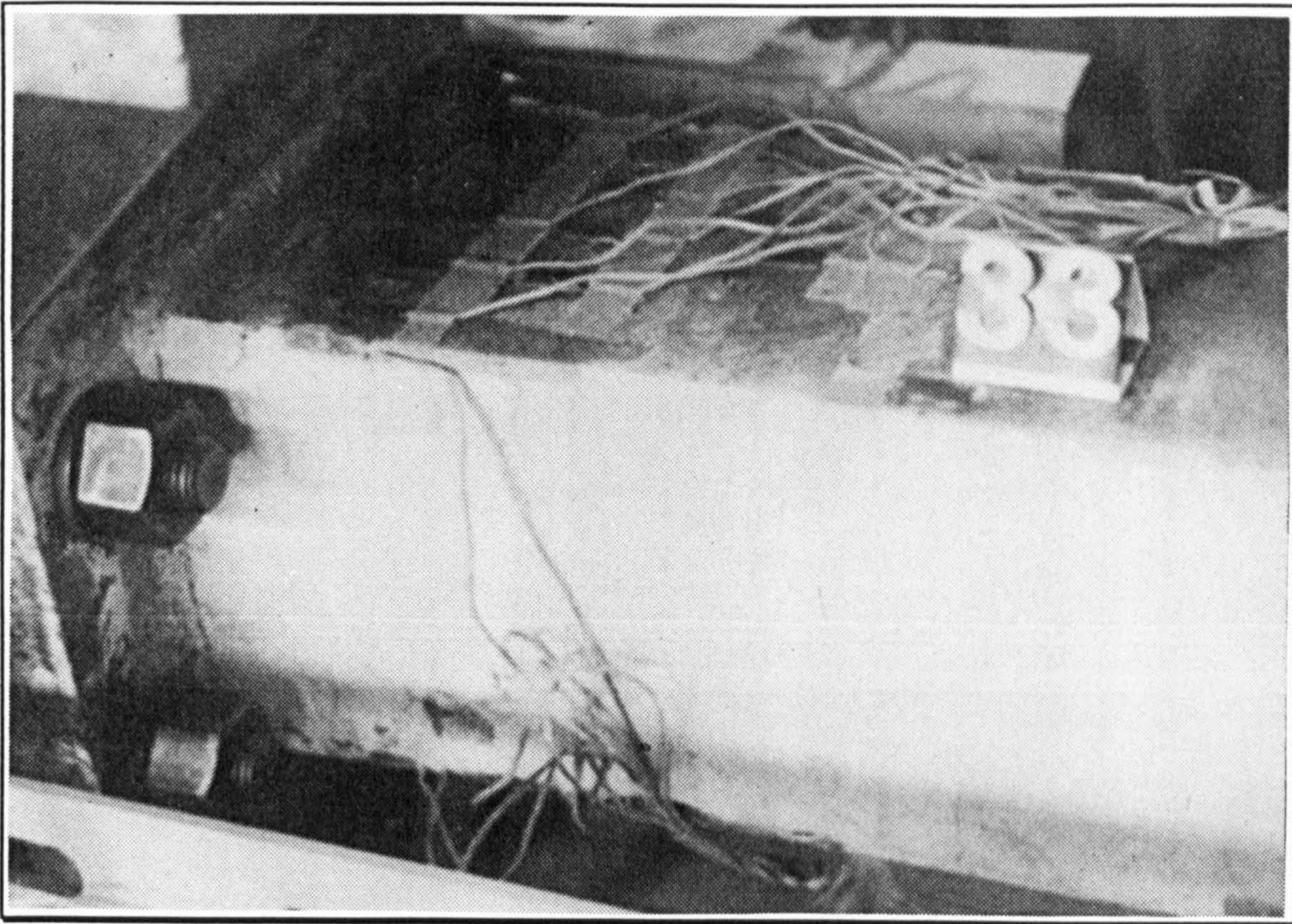


Plate 6.13 IC02 at a displacement amplitude of 33 mm

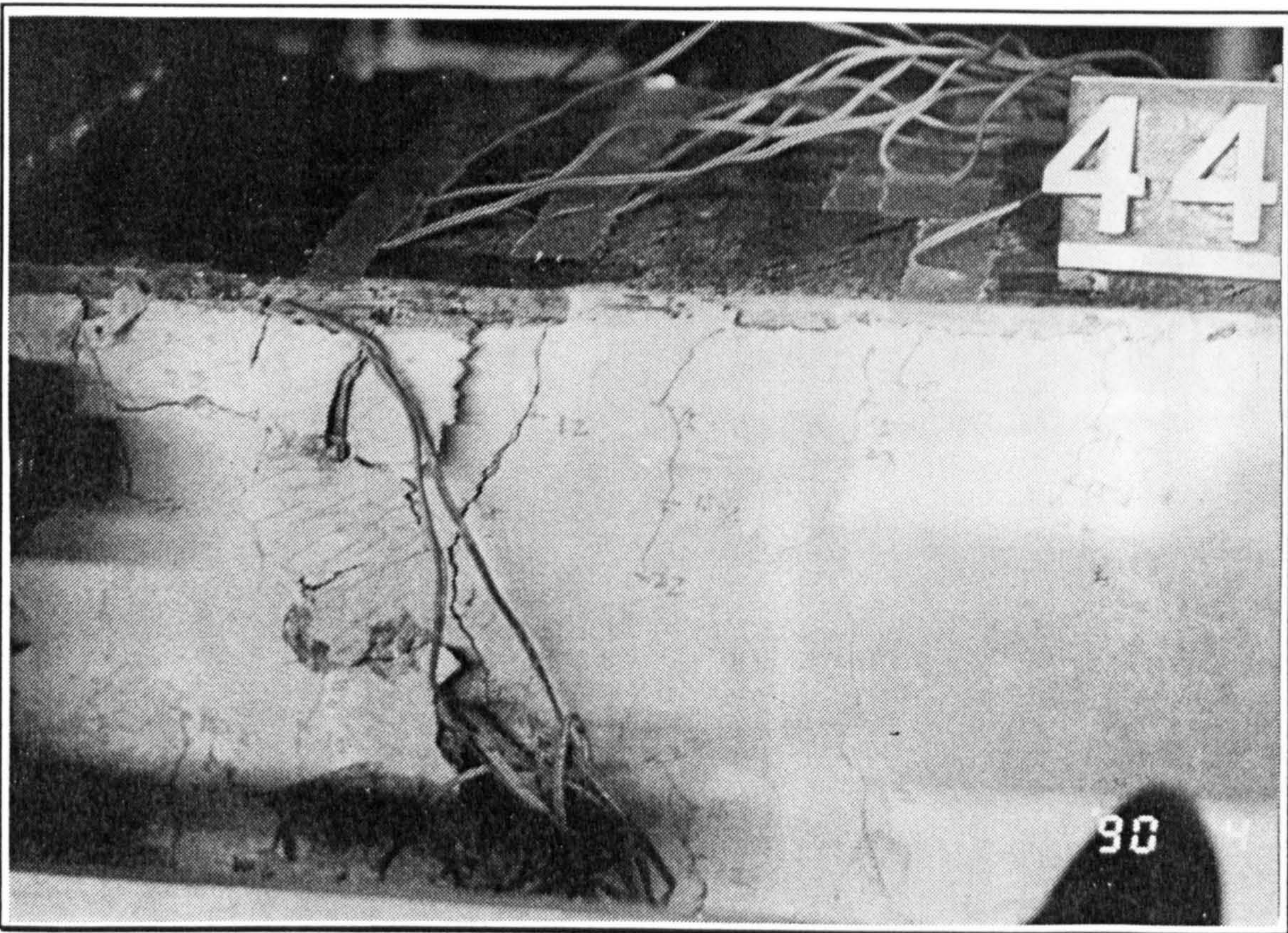


Plate 6.14 IC02 at 44 mm, cracking and spalling of cover concrete

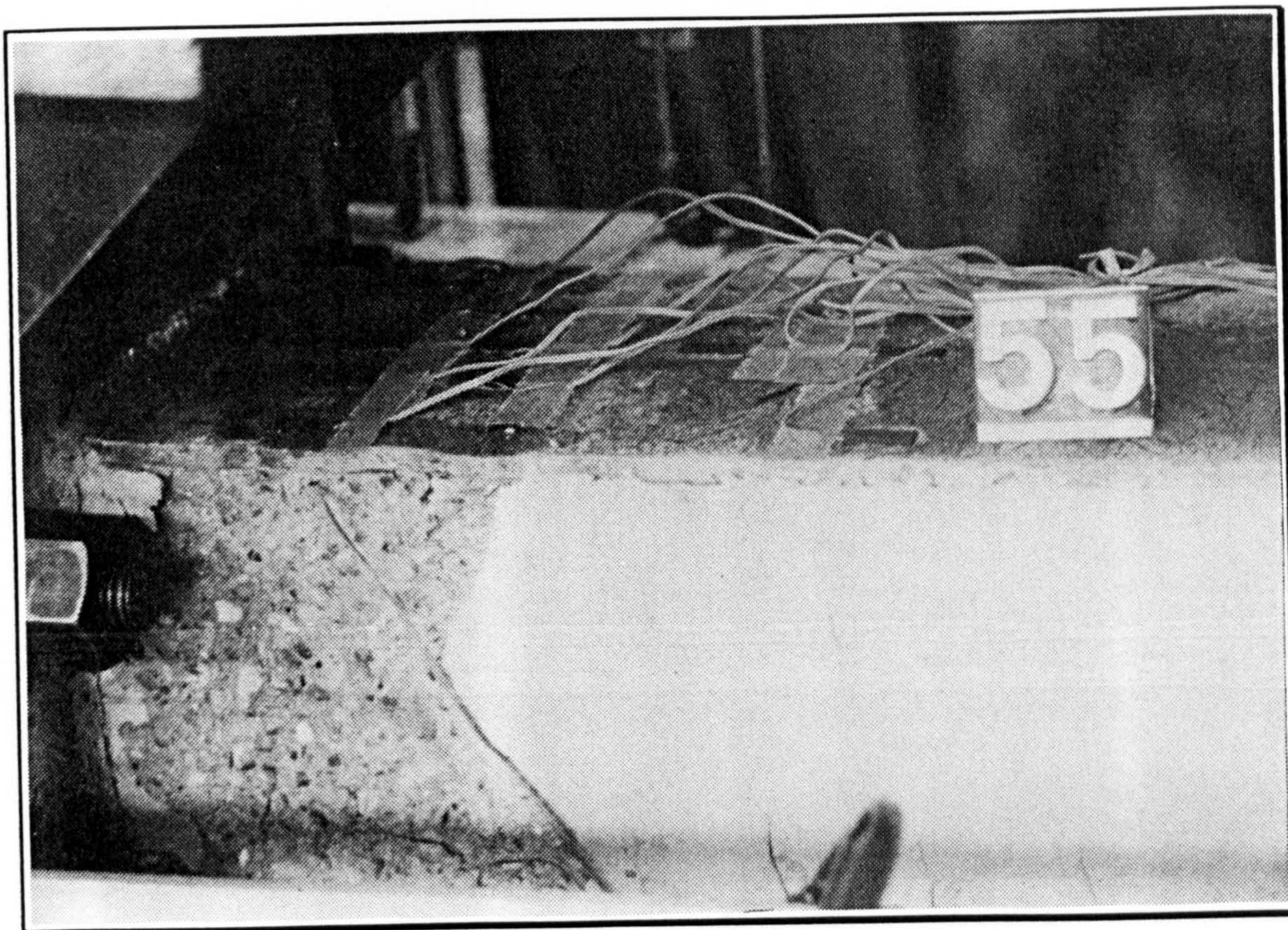


Plate 6.15 IC02 at 55 mm, onset of local flange buckling between the lateral ties

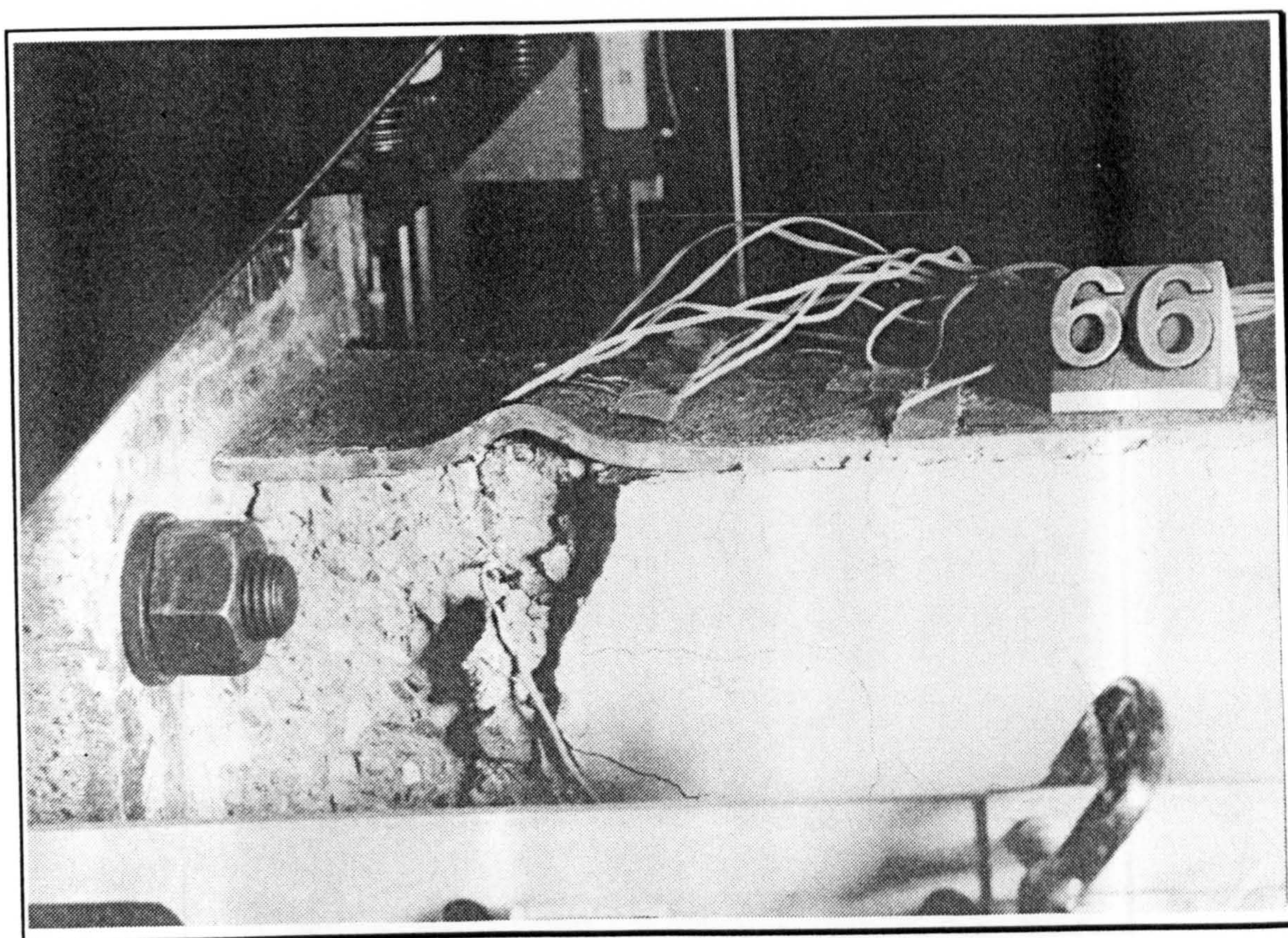


Plate 6.16 Plastic hinge zone of model IC02 at 66 mm

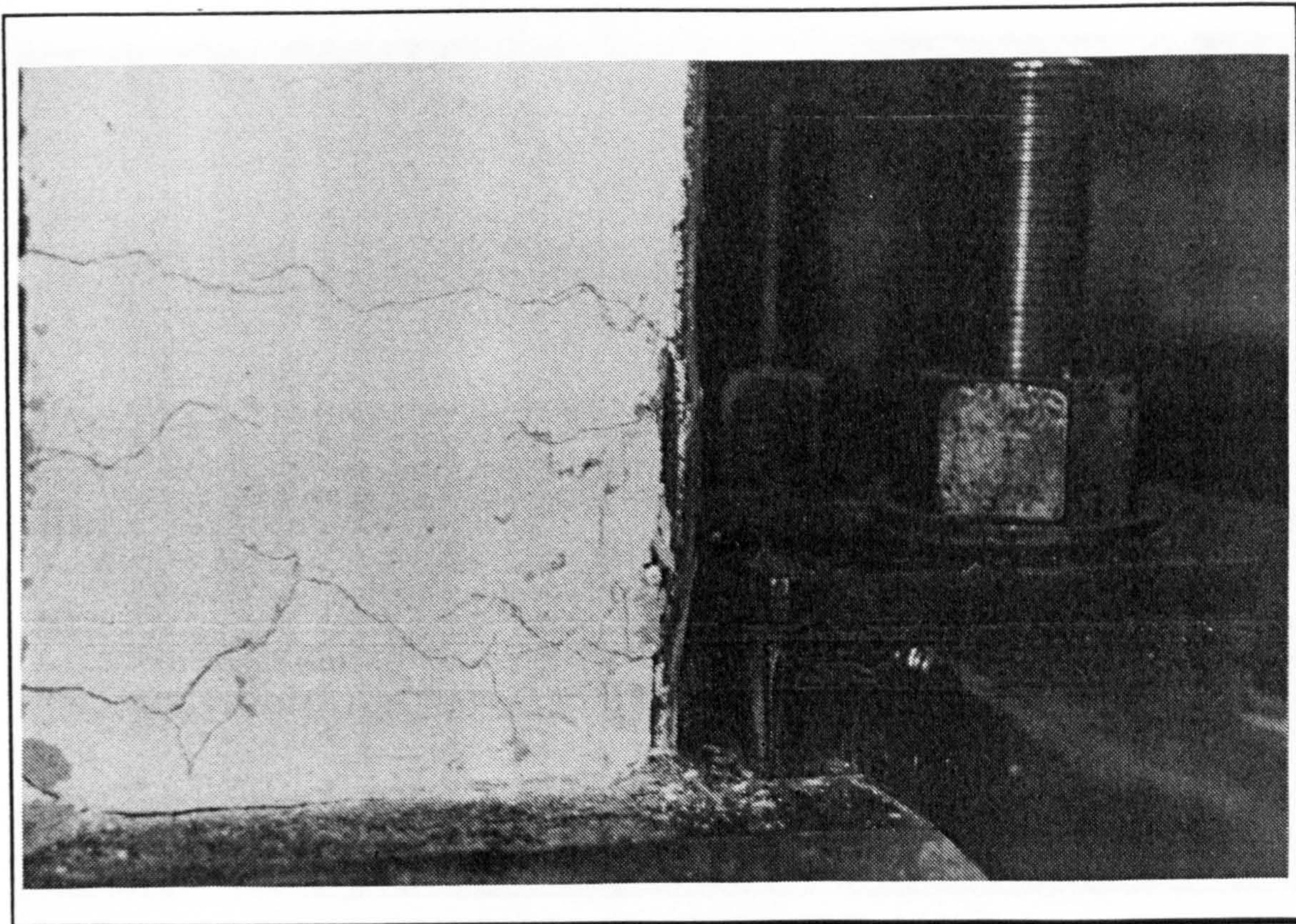


Plate 6.17 EM04 at 48 mm, onset of local buckling in compression flange

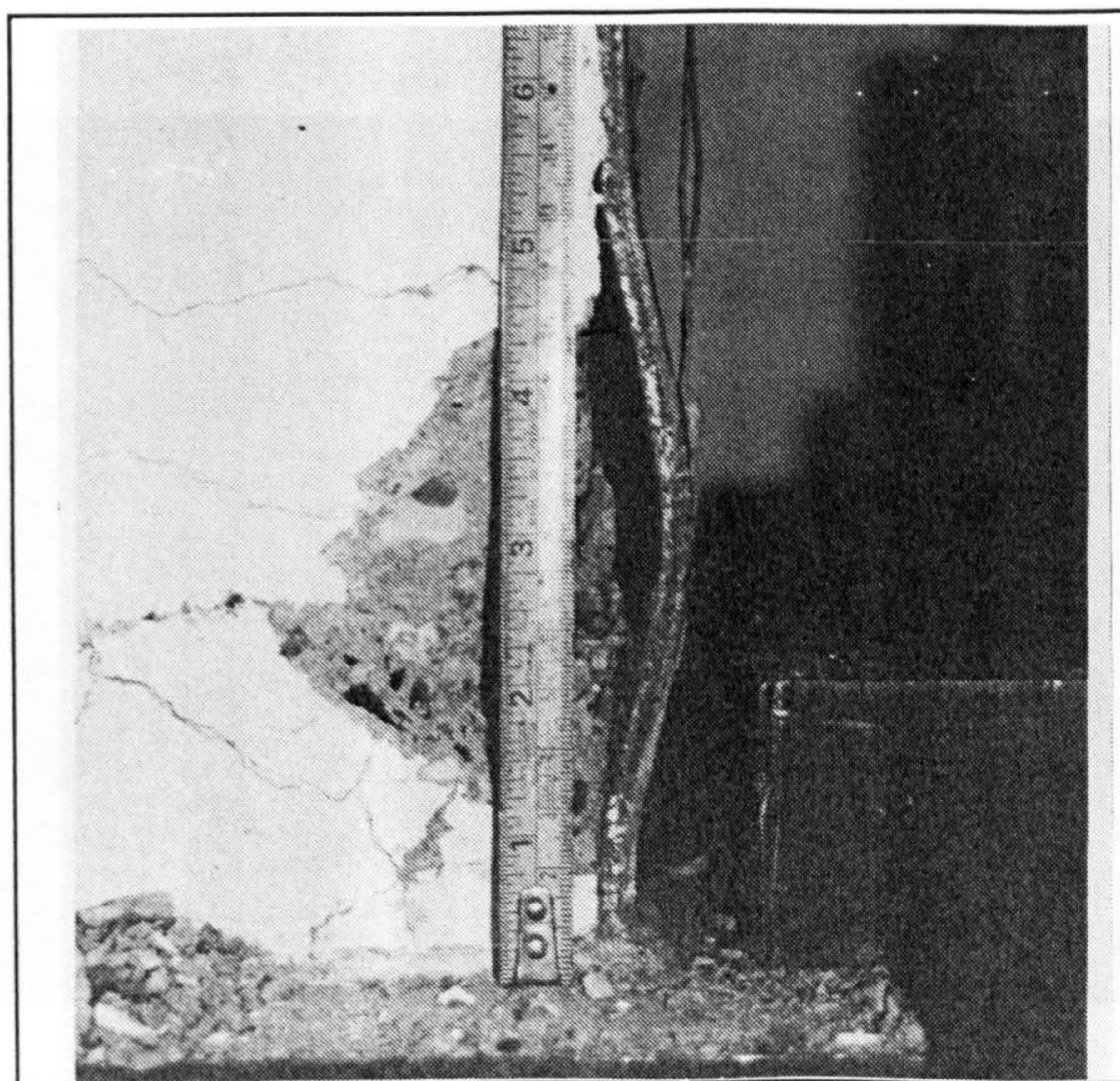


Plate 6.18 Compression area of plastic zone of EM04 after 3 cycles at 48 mm

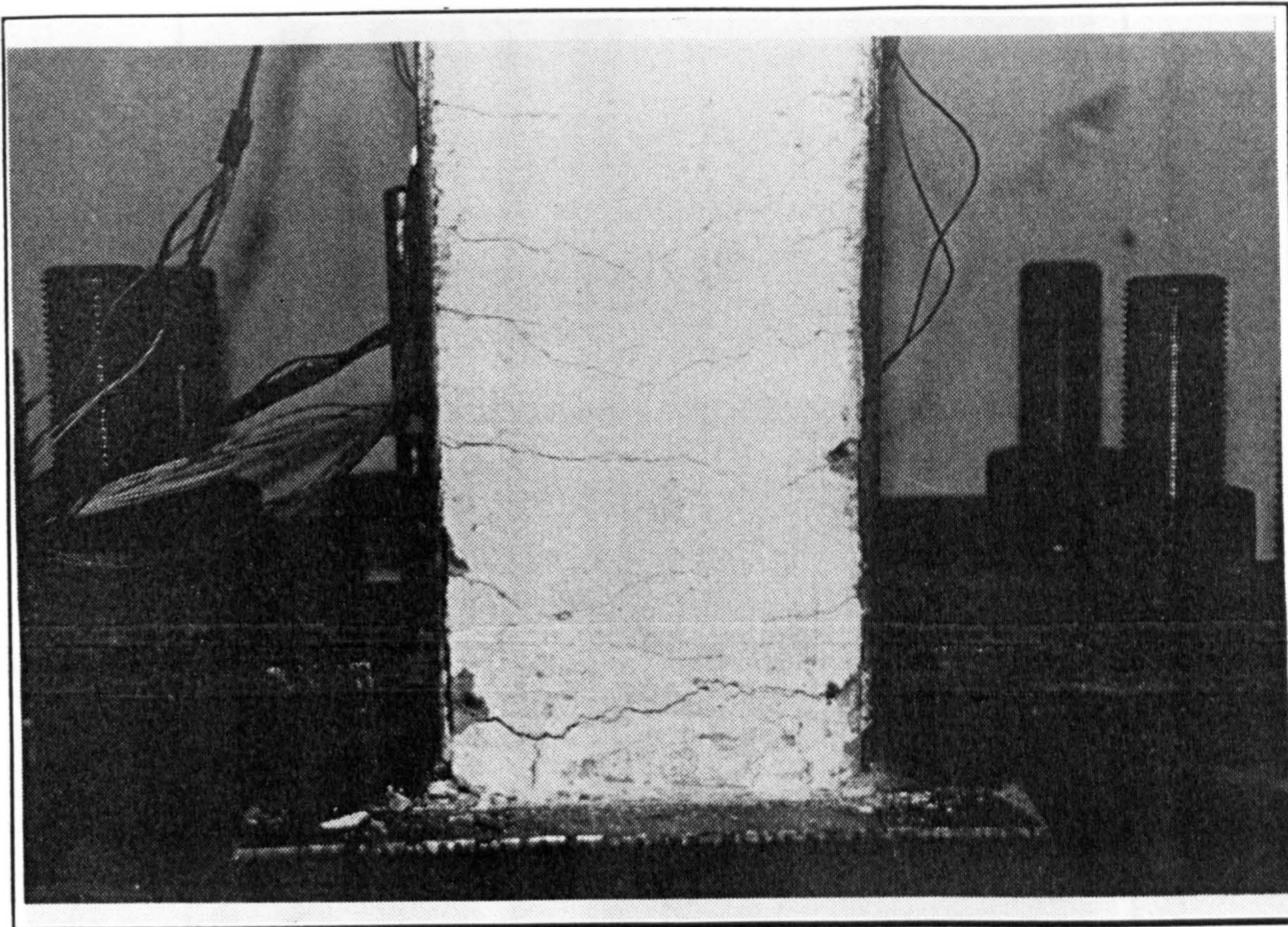


Plate 6.19 IC04 at 32 mm, distribution of flexural cracks

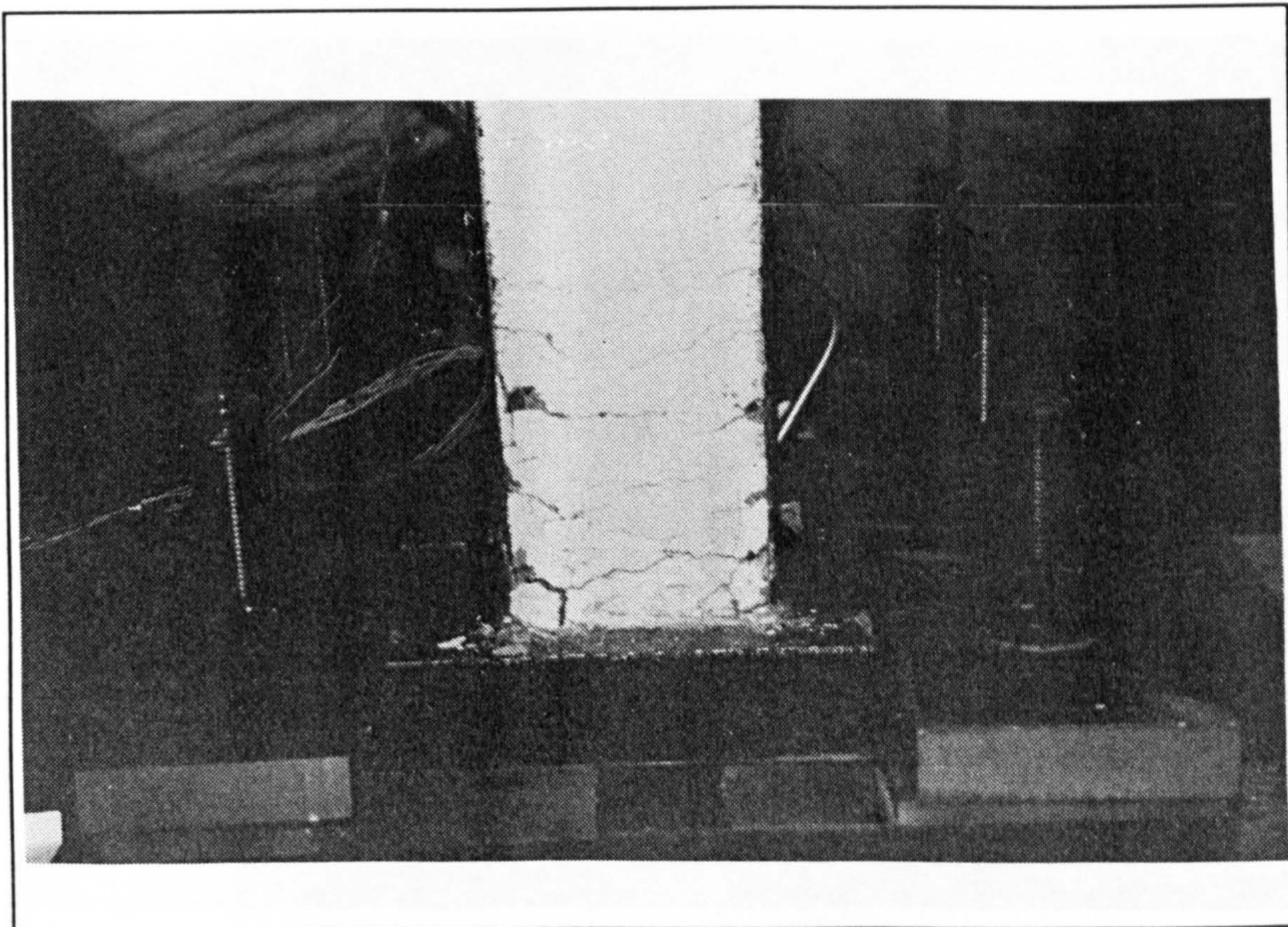


Plate 6.20 IC04 at 80 mm, onset of local flange buckling between the lateral bars

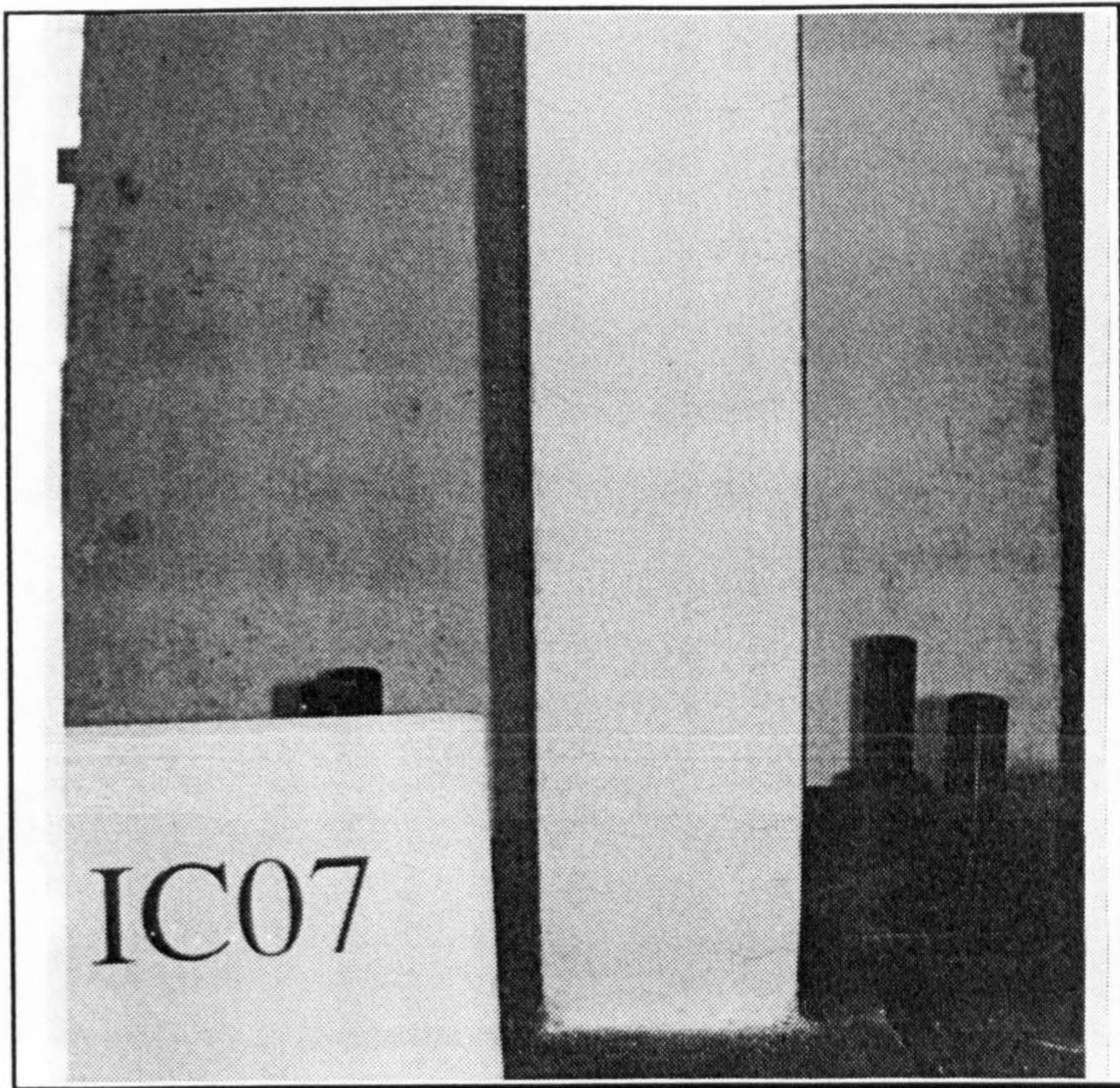


Plate 6.21 Model IC07 at a displacement amplitude of 16 mm

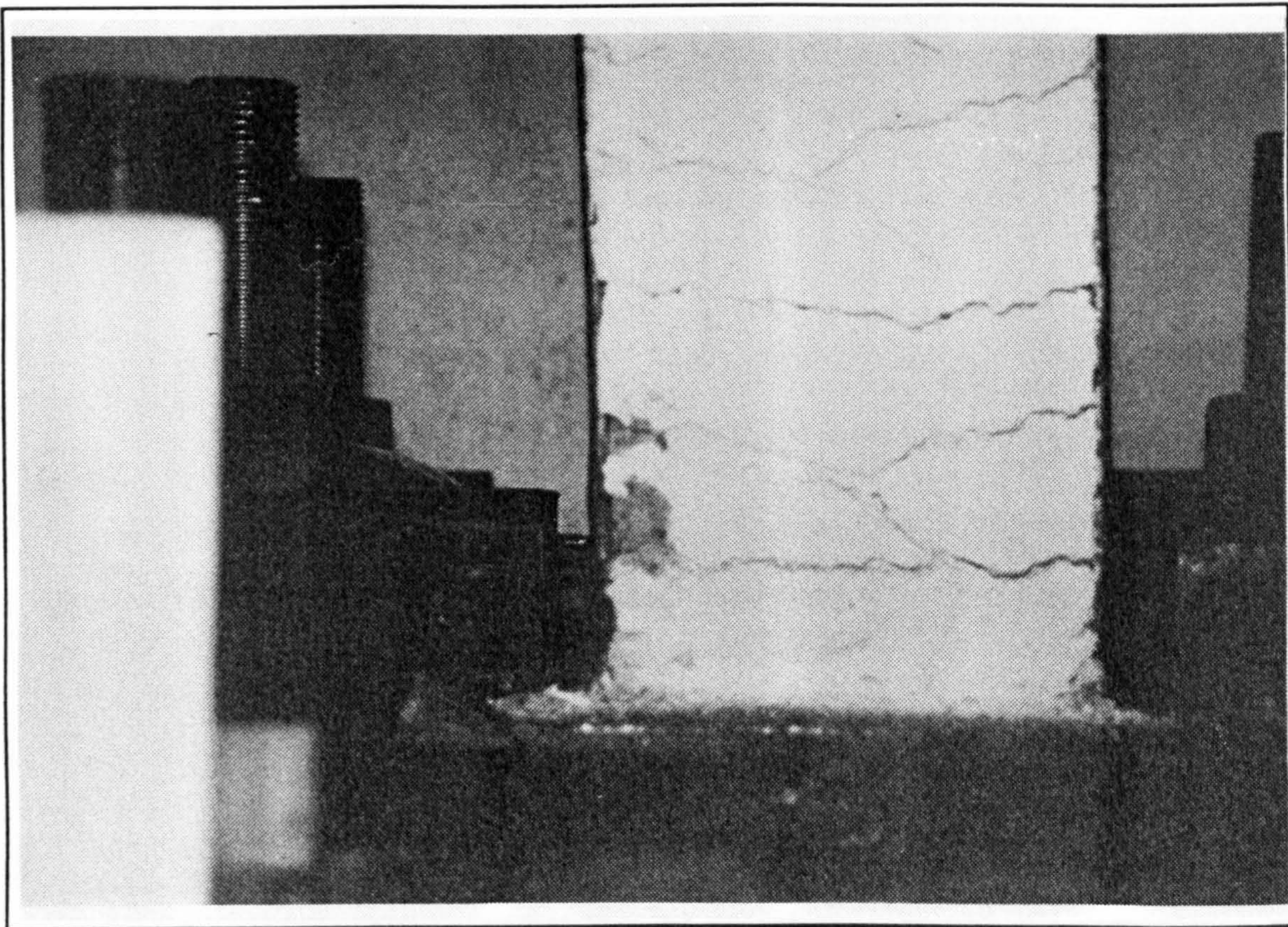


Plate 6.22 IC07 at 32 mm, deep flexural cracks in the plastic hinge zone



Plate 6.23 IC07 at 64 mm, local buckling in the compression flange

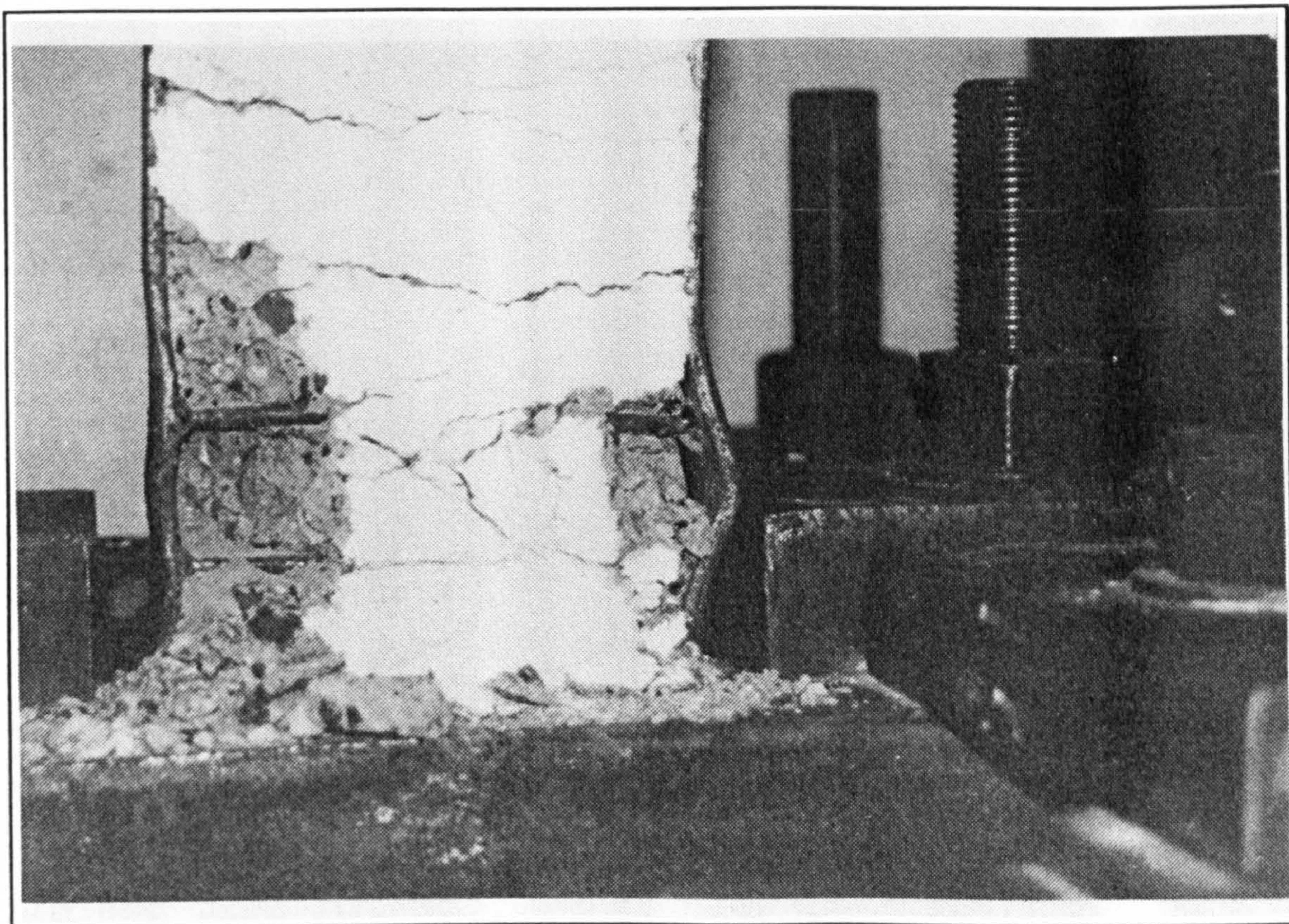


Plate 6.24 IC07 after three cycles at a displacement of 64 mm

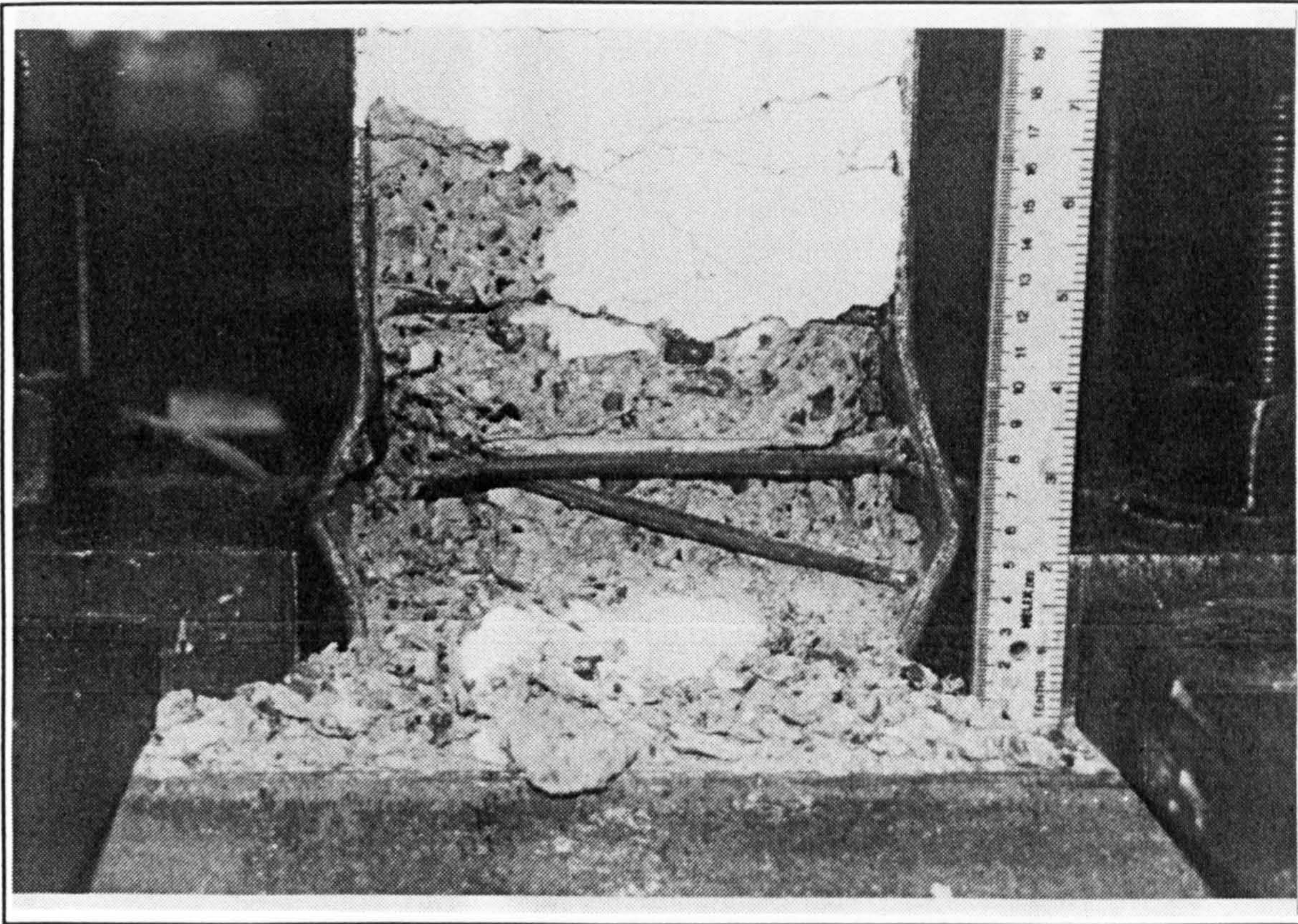


Plate 6.25 IC07 at 96 mm, failure of the straight bars following local buckling



Plate 6.26 Plastic hinge zone of IC07 at the end of the test

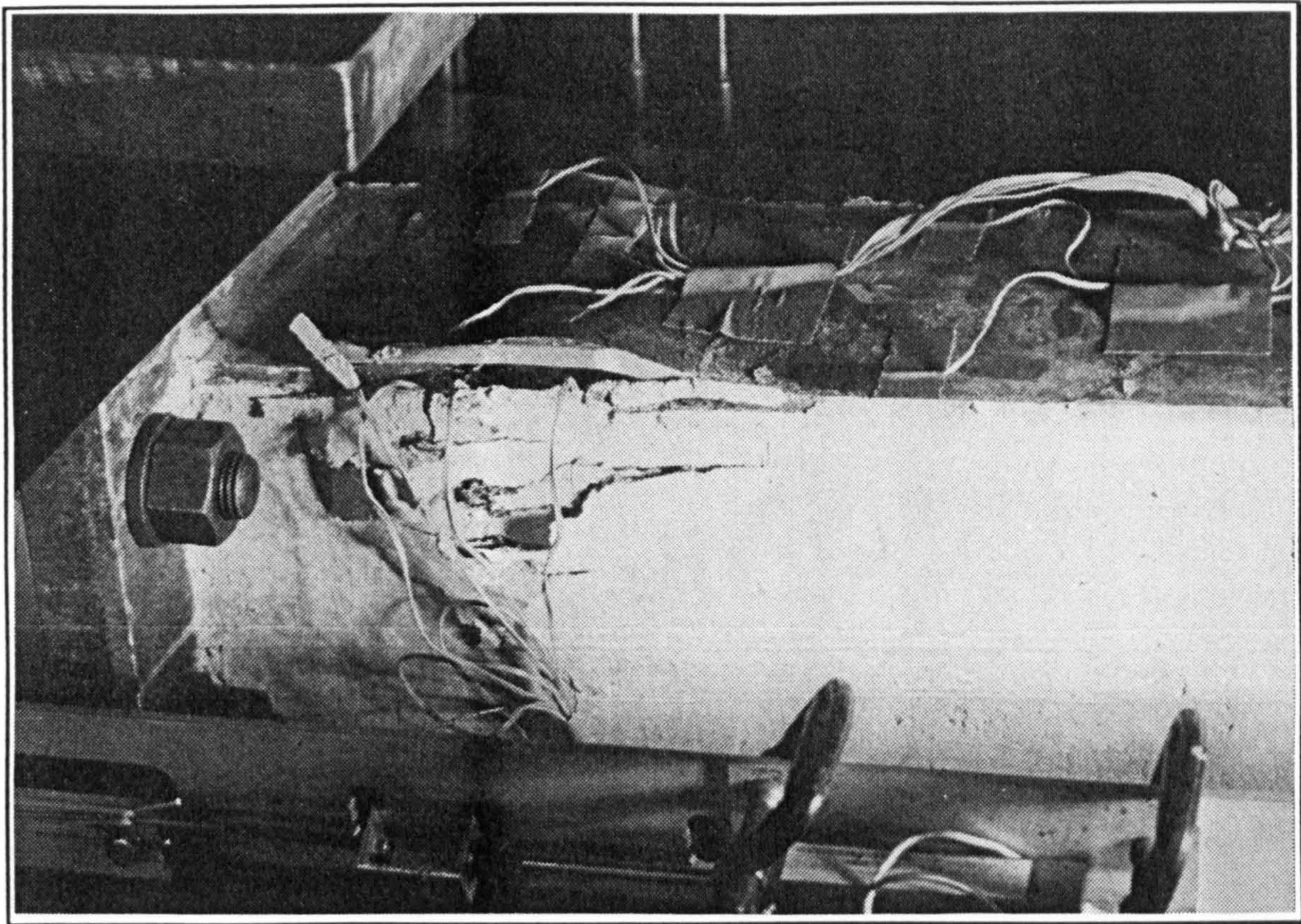


Plate 6.27 EM03 after 2.2 seconds, local flange buckling and concrete crushing

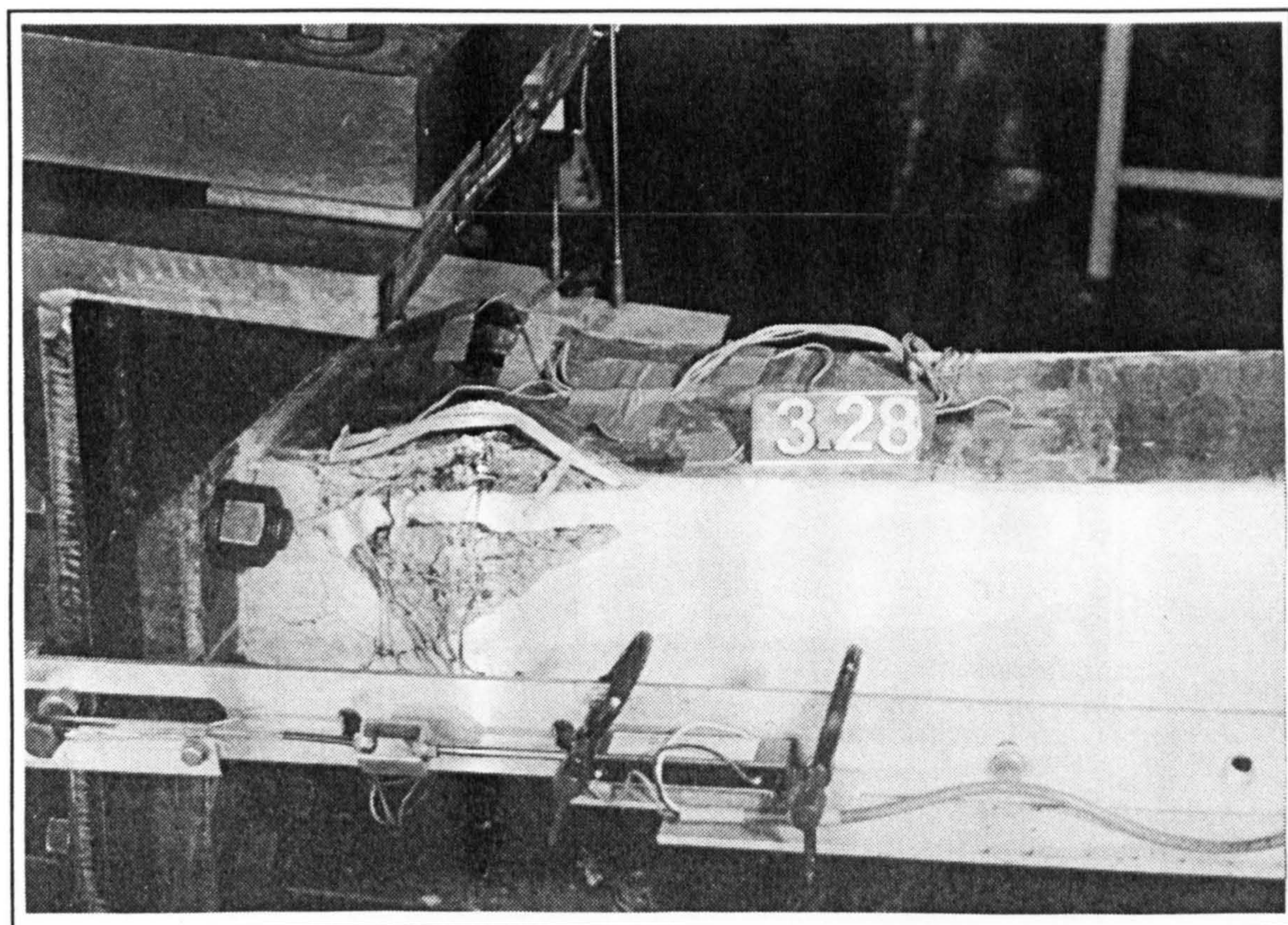


Plate 6.28 Plastic hinge zone of EM03 after 3.28 seconds of El Centro earthquake

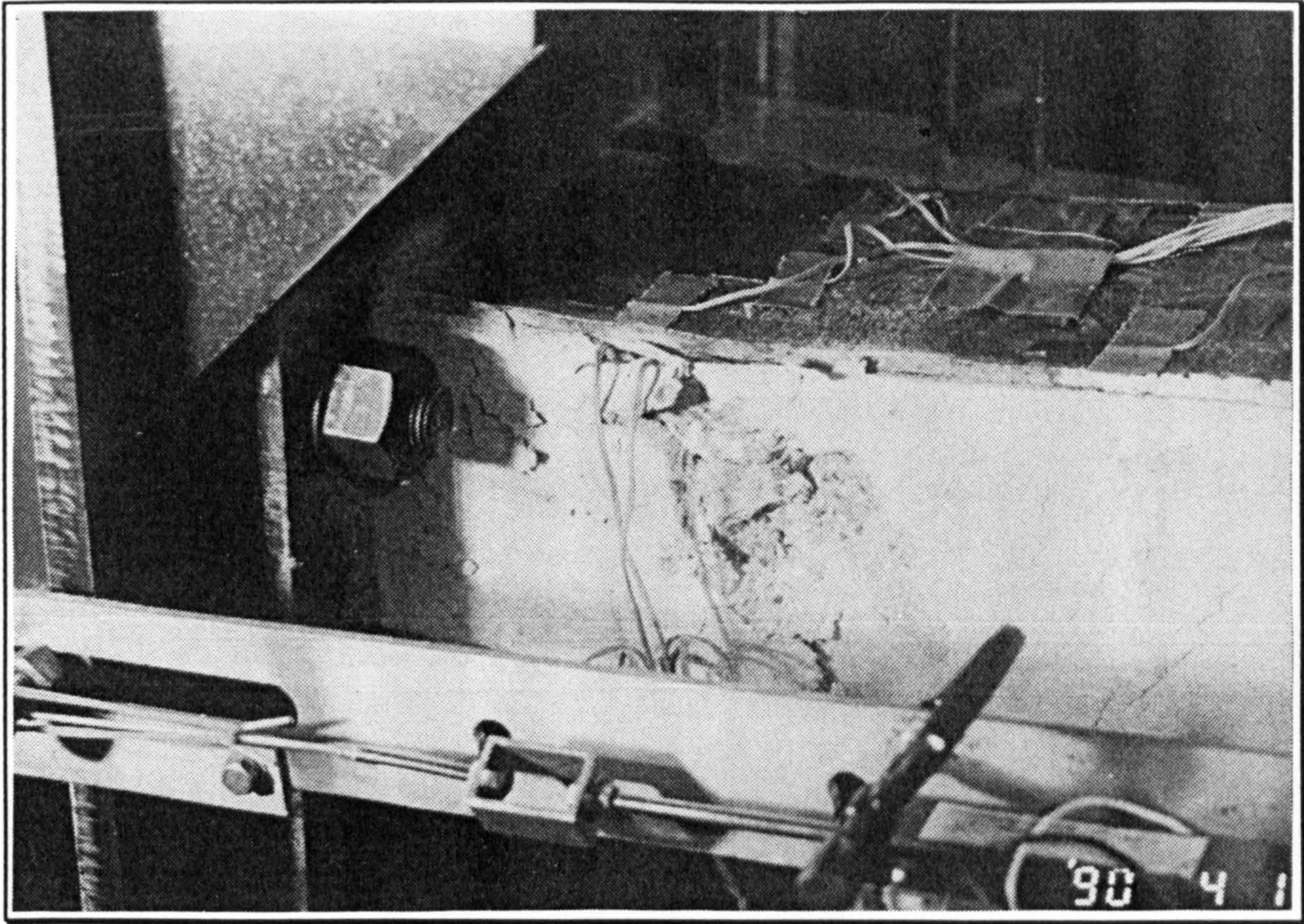


Plate 6.29 IC03 at the tail of the 8 seconds of El Centro earthquake

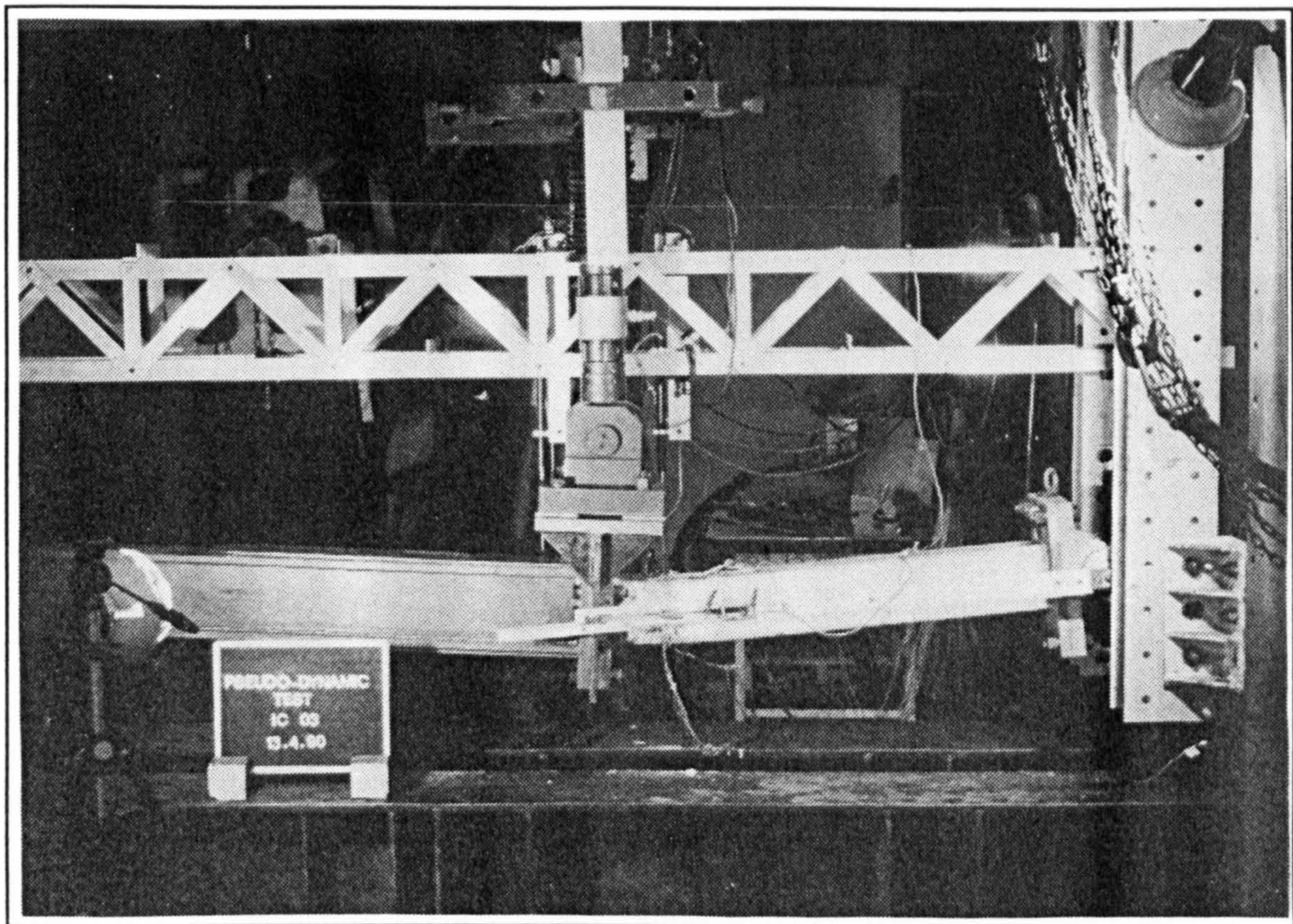


Plate 6.30 General view of model IC03 at a displacement of 140 mm



Plate 6.31 EM05 after 2.4 seconds, local buckling of compression flange



Plate 6.32 Plastic hinge zone of EM05 after 10.4 seconds of Montenegro earthquake



Plate 6.33 IC05 after 10.4 seconds of Montenegro earthquake



Plate 6.34 IC06 after 10.4 seconds from the start of the earthquake record

CHAPTER 7

7. ANALYSIS OF COMPOSITE BEAM-COLUMNS

7.1 INTRODUCTION

In the design of engineering structures subjected to severe loading scenarios, the nonlinear behaviour of structural members and assemblies must be clearly understood in order to achieve higher levels of design economy and structural reliability. Most codes of practice adopt a design philosophy by which the limit state is checked on the level of the individual components instead of that of the overall structure. This is usually achieved through the determination of the distribution of forces within the structure using simple analysis methods, such as linear elastic analysis. Using such philosophy, the effect of nonlinear behaviour on the distribution of forces within the structure is not accurately accounted for, especially if significant geometric and material nonlinearities are involved prior to the ultimate limit state. Also, this approach does not allow for redistribution of forces after the failure of individual members, and hence does not consider the structure reserve strength.

Although experimental work is essential in the understanding of the nonlinear behaviour of structures, as well as in the verification of analytical models, laboratory testing is time-consuming and capital-intensive. Consequently, accurate and efficient analytical tools are invaluable in enriching and directing experimental investigations. Appropriate analytical models can be employed in the design of testing schemes, as well as in achieving better understanding of complex structural behaviour. Furthermore, reliable analytical methods can provide an abundance of information through parametric studies on realistic engineering problems.

The rapid advancement of computers over the past three decades has paved the way for development and implementation of sophisticated nonlinear analysis methods. In particular, the finite element method is widely used because of its acceptable levels of accuracy and efficiency. Several formulation procedures have been applied within the finite element methods, and advanced nonlinear material models have been implemented. One of the advantages of the finite element method is its versatility in modelling the nonlinear behaviour of complex structural configurations. Moreover, its extension into

the domain of dynamic analysis is straightforward, where the effects of inertia and damping can be represented by equivalent nodal loads via the use of lumped or consistent mass and damping idealizations.

In this chapter, the advanced nonlinear dynamic frame analysis program 'ADAPTIC' developed at Imperial College by Izzuddin and Elnashai (1989), is briefly described, and the existing nonlinear cyclic models for concrete and steel materials used within the program are presented. Also, a simplified cyclic model to account for local flange buckling is proposed. Finally, analytical simulations are compared with some of the experimental results.

7.2 THE NONLINEAR DYNAMIC ANALYSIS PROGRAM 'ADAPTIC'

7.2.1 General Description

The computer program 'ADAPTIC' has been developed to provide an efficient tool for the nonlinear analysis of steel, reinforced concrete and composite frames. The program is capable of predicting the behaviour of two- and three-dimensional frames, taking into account geometric nonlinearities and the effect of material inelasticity. A variety of elements may be used ranging from the plastic hinge element to the elasto-plastic cubic formulation, accounting for the spread of plasticity across the section and along the member length. Static, dynamic and eigenvalue analysis are available. For static analysis, the program has built-in facilities to predict the post-ultimate response of frames subjected to proportional loading, and has an option for varying loads independently in the time domain. The formulations implemented in the program are beam-column finite elements accounting for large nodal displacements. The Eulerian axes system forms the basis of derivation, and exact relationships are used to establish transformations between chord and global systems.

Comprehensive dynamic analysis capabilities are available in ADAPTIC. Separate non-structural elements are used to calculate inertia and damping forces. Direct integration using the unconditionally stable Newmark method is used, with automatic time-step adjustment. The forcing function may be load or displacement time histories. Independent support motion is also possible, using displacements, velocities or accelerations. The solution procedure used is iterative and can be full or modified Newton-Raphson or a combination of both. Automatic switching from one strategy to the other is also included.

Several cross-section configurations can be analyzed, including rectangular solid sections, rectangular or circular tubes and I-sections. In addition, steel I-sections partially and fully encased with concrete were developed, to allow the modelling of composite frames. The cubic plastic element was chosen for the analysis of composite steel/concrete frames, and a cyclic constitutive relationship for concrete materials was also implemented by Madas and Elnashai (1989) for this purpose.

The accuracy of 'ADAPTIC' has been extensively verified elsewhere (Izzuddin and Elnashai, 1989; Madas and Elnashai, 1989; Elnashai et al, 1989; Izzuddin, 1990). Subsequent sections of this chapter will only give a brief description of the cubic plastic element and the nonlinear material models for steel and concrete.

7.2.2 The Elasto-Plastic Cubic Element

This element assumes a cubic shape function in the chord system, and monitors stresses and strains at various points across two Gaussian sections, allowing the spread of plasticity throughout the cross-section. Adequate measures are taken in the implementation to allow the use of any material law. The element is defined by two nodes, and the cross section is divided into a number of monitoring points. The stresses are calculated at each monitoring point and for the two Gaussian sections. The basic characteristic of the element is that it predicts member behaviour based on material stress-strain relationships and large displacements. The accuracy increases by using more elements in the plastic zones of the member and/or by increasing the number of monitoring points.

Three degrees of freedom are used in the 2D analysis, whereas six degrees of freedom are employed in the 3D formulation, as shown in Figure 7.1. The strain state within the cross-section is uniquely determined by the four generalized strains: centroidal axial strain, curvature strains about the two principal axes, and the rate of twist. The centroidal axial strain is assumed constant along the element length. Although in the presence of material plasticity this condition does not necessarily imply a constant axial force along the element length, the variation of the axial force is insignificant if the element is used to model short lengths of elasto-plastic members.

Since the relationship between the generalized stresses and strains cannot be established explicitly in the presence of material plasticity, the integration of the virtual work equation to obtain the element forces is performed numerically. Only two Gauss integration sections are employed along the length. The position of the Gauss sections, given in

Figure 7.2, is chosen such that the exact integration of the virtual work equation is obtained for the elastic element. Each Gauss section is divided into a number of areas across which strains and stresses are monitored. The effect of shear strains on material plasticity is neglected, and only direct strains are established at the monitoring points using an appropriate uniaxial stress-strain relationship.

To establish the global response of the cubic element, transformations from the chord to the global system are applied. In the calculation of direct stresses at the monitoring points, strains are considered incrementally from the last equilibrium state. This requires storage for material variables (stresses, strains, etc.) at the start of the load increment and for the current iteration, with the variables of the former being updated only after global equilibrium is achieved.

7.3 EXISTING MATERIAL MODELS

7.3.1 Models for Mild Steel

The evaluation of the response of an elasto-plastic cubic element requires the definition of a uniaxial stress-strain law for the constituent material. For structural steel, different models were developed to represent its cyclic behaviour. A review of the available relationships and their relative merits is given by Izzuddin (1990).

The uniaxial behaviour of mild steel in its virgin state is essentially linear elastic up to the point of yield. Under monotonic loading, the characteristic yield plateau is followed by a region of increased strength due to strain hardening, as shown in Figure 7.3. When subjected to constant strain amplitude cycling, steel exhibits a response which always converges to a stabilized saturation loop dependent only on the amplitude of cycling. The curve joining the tips of the stabilized cycles is known as the 'cyclic stress-strain curve', as shown in Figure 7.4.

Due to the difference in shape between the cyclic and virgin curves, the transient response under constant strain amplitude cycling is characterized by softening for small amplitudes and hardening for large amplitudes. Relaxation to zero mean-stress accompanies the process of cyclic softening or hardening if, during the transient response, the mean-stress attains a non-zero value, as demonstrated in Figure 7.5. Therefore, an accurate cyclic model for steel must exhibit the ability to represent the virgin response, the steady state cyclic response and the transient behaviour involving softening, hardening, and mean-

stress relaxation. Such a model must also be capable of representing random cycling without spurious prediction of the real response.

In this section, two cyclic models for mild steel implemented within the elasto-plastic cubic formulation in 'ADAPTIC' (Izzuddin, 1990), are briefly described. The first is the bilinear model with kinematic strain-hardening, while the second is the uniaxial case of the multi-surface model originally proposed by Popov and Petersson (1978). Although the former model is simple to implement and computationally more efficient, and its parameters can be more easily identified, the second model captures more realistically the behaviour of mild steel under elasto-plastic cycling.

7.3.1.1 Bilinear Model

In this model, the elastic range remains constant throughout the various loading stages, and the kinematic hardening rule for the yield surface is assumed to be a linear function of the increment of plastic strain, as shown in Figure 7.6.

The calculation of the current stress state is described in Figure 7.7, and can be expressed mathematically as:

$$\left. \begin{array}{l} \alpha = \alpha^0 \\ \sigma = \sigma^0 + E(\epsilon - \epsilon^0) \end{array} \right\} \text{ if } \left(\frac{\alpha^0 - \sigma_y - \sigma^0}{E} \right) \leq (\epsilon - \epsilon^0) \leq \left(\frac{\alpha^0 + \sigma_y - \sigma^0}{E} \right) \quad (7.1.a)$$

$$\left. \begin{array}{l} \alpha = \alpha^0 + \mu E \left(\epsilon - \epsilon^0 - \frac{\alpha^0 + \sigma_y - \sigma^0}{E} \right) \\ \sigma = \alpha + \sigma_y \end{array} \right\} \text{ if } (\epsilon - \epsilon^0) > \left(\frac{\alpha^0 + \sigma_y - \sigma^0}{E} \right) \quad (7.1.b)$$

$$\left. \begin{array}{l} \alpha = \alpha^0 + \mu E \left(\epsilon - \epsilon^0 - \frac{\alpha^0 - \sigma_y - \sigma^0}{E} \right) \\ \sigma = \alpha - \sigma_y \end{array} \right\} \text{ if } (\epsilon - \epsilon^0) < \left(\frac{\alpha^0 - \sigma_y - \sigma^0}{E} \right) \quad (7.1.c)$$

where, according to Figures 7.6 and 7.7,

- E elastic Young's modulus
- μ strain hardening parameter
- σ_y initial yield surface (radius of yield surface)

ϵ current strain
 σ current stress
 α current centre of elastic range (centre of yield surface)
 superscript (o): denotes values at the start of an increment

The tangent modulus, required for the element tangent stiffness calculation, is dependent on the current stress state and is given by:

$$\left. \begin{aligned} \frac{d\sigma}{d\epsilon} &= E && \text{if } (\alpha - \sigma_y) < \sigma < (\alpha + \sigma_y) \\ \frac{d\sigma}{d\epsilon} &= \mu E && \text{if } \left\{ \sigma = (\alpha - \sigma_y) \right\} \text{ or } \left\{ \sigma = (\alpha + \sigma_y) \right\} \end{aligned} \right\} \quad (7.2)$$

7.3.1.2 Multi-surface Model

The multi-surface steel model was used in the verification of pseudo-dynamic testing, described in section 4.4 of this thesis. In this model, a number of surfaces enclosing the yield surface are each associated with a value for the increment of plastic strain. The expansion/contraction (isotropic hardening) and translation (kinematic hardening) of these surfaces are governed by pre-specified hardening rules.

As suggested by Popov and Petersson, isotropic hardening of the loading surfaces is expressed as a function of accumulated plasticity. A weighting function dependent on the cumulative plastic strain is hence applied to the virgin and cyclic stress-strain curves to obtain the initial and current sizes of the loading surfaces, as shown in Figure 7.8. In ADAPTIC, each of these curves is represented by five cubic polynomials over five adjacent intervals and a straight line at the end (Izzuddin, 1990). Conditions of continuity of values and slopes are enforced at the common points to obtain the parameters of the cubic polynomial and the straight line.

The tangent modulus is required in the calculation of the element tangent stiffness matrix. If the current stress state is within the yield surface, the linear elastic modulus is used. Otherwise, the tangent modulus can be determined from the elastic and plastic moduli. This is established through considering that the infinitesimal increment of total strain is composed of elastic and plastic parts resulting in the same infinitesimal increment of stress when multiplied by their respective moduli.

7.3.2 Constitutive Relationships for Concrete

Many uniaxial models for concrete materials under monotonic and cyclic loading have been proposed. A review of the main models is given by Madas and Elnashai (1989). These uniaxial relationships consider one or more of the significant three-dimensional effects that influence the principal axial direction of loading. This includes the effect of triaxial confinement on the peak stress, the peak strain and the inclination of the post-peak stress-strain curve.

Although experimental and analytical work on the confinement of concrete has been carried out by many researchers, in most of these experiments active confining pressures were applied on plain concrete either hydrostatically or through loading platens. In reality, confinement in structural members is passive and is provided by transverse steel which, due to the elongation imposed on it by the expansion of concrete, induces compressive confining stresses in the concrete core. This also means that the degree of confinement is a function of the axial strain imposed. The effect of transverse steel in providing passive confinement has long been recognised, and several models have been presented based on reinforced concrete column experiments.

Less information is available on the cyclic behaviour of concrete. Variable loading can cause either fatigue effects, due to a large number of cycles of relatively low stress level or incremental deformations under a relatively small number of cycles of high stress. The latter arises from the fact that unloading in concrete follows a different path to loading. Such hysteretic behaviour and the characteristics of strength and stiffness have to be simulated realistically by an appropriate cyclic concrete model. Analytical models for cyclic loading are based on experimental results, observations, or allocated values to model parameters by means of calibration studies. Most available models consider that the stress-strain relationship for concrete under compressive load histories possess an envelope curve, which is unique and identical to the stress-strain curve obtained under constantly increasing load. If the stress is decreased, an unloading curve will be traced. Increasing the stress again forces the material along a reloading curve as shown in Figure 7.9.

In subsequent sections the uniaxial cyclic model implemented in 'ADAPTIC' by Madas and Elnashai (1989) is briefly described. It is based mainly on the model proposed by Mander et al (1988), with minor modifications.

7.3.2.1 Monotonic Model

The stress-strain relationship presented by Mander et al, has been proposed mainly for circular and rectangular concrete sections, under static and dynamic axial compressive loading. The concrete section may contain any general type of confining steel either spirals or circular hoops, or rectangular hoops with or without supplementary cross ties. For monotonic loading, the longitudinal compressive concrete stress, f_c , is given by:

$$f_c = \frac{f'_{cc} x r}{r - 1 + x^r}$$

in which :

$$x = \frac{\epsilon_c}{\epsilon_{cc}} \quad r = \frac{E_c}{E_c - E_{sec}} \quad E_{sec} = \frac{f'_{cc}}{\epsilon_{cc}} \quad E_c = 5000 \sqrt{f_{co}} \quad \text{in MPa} \quad (7.3)$$

where:

- f'_{cc} compressive strength of the confined concrete (defined in section 7.3.2.2)
- ϵ_c longitudinal compressive concrete strain
- ϵ_{co} critical strain of unconfined concrete
- f_{co} compressive strength of unconfined concrete
- E_c modulus of elasticity of concrete
- ϵ_{cc} critical strain of confined concrete (defined in section 7.3.2.2)

The monotonic stress-strain relationship is shown in Figure 7.10 for confined and unconfined concrete. Modelling of triaxial confinement effects is described in the following section.

7.3.2.2 Concrete Confinement

In the model suggested by Mander et al, the effect of confinement on the stress-strain relationship given in (7.3) is calculated taking into account the maximum transverse pressure from confining steel. This pressure can only be exerted effectively on the part of the concrete core where the confining stress has fully developed due to the arching action, as shown in Figure 7.11 for a reinforced concrete section. In Figure 7.11.b, it is clear that the area of effectively confined concrete, A_e , is smallest mid-way between the levels of transverse reinforcement. On the other hand, at the level of the stirrups, the confined area, A_{cc} , is largest. In order to account for the fact that $A_e < A_{cc}$, the effective lateral confining pressure is given by:

$$f'_1 = f_1 \alpha_c \quad (7.4)$$

where α_c is the confinement effectiveness coefficient given by:

$$\alpha_c = \frac{A_e}{A_{cc}} \quad (7.5)$$

and f_1 is the lateral confinement pressure from transverse reinforcement, assumed to be uniformly distributed over the surface of the concrete core. This pressure which is calculated from the 'free body diagram', corresponds to yielding of the confining steel, and is, therefore, dependent on the shape and distribution of transverse reinforcement in the cross-section.

The confined concrete compressive strength, f'_{cc} in (7.3) is calculated from f'_1 through a multi-axial failure criterion for concrete. From the results of triaxial models implemented in computer programs, curves giving the confined strength ratio, f'_{cc}/f_{co} , are obtained for any combination of equal or unequal confining pressures in both lateral directions. Also, Mander et al use equation (7.6) below to calculate the critical strain of confined concrete, ϵ_{cc} in (7.3), where ϵ_{co} is the critical strain of unconfined concrete.

$$\epsilon_{cc} = \epsilon_{co} \left\{ 1 + 5 \left(\frac{f'_{cc}}{f_{co}} - 1 \right) \right\} \quad (7.6)$$

The above relation is based on experimental results of concrete specimens subjected to active confinement. Further discussion related to confinement effects in encased sections is given in section 7.4 of this chapter.

7.3.2.3 Cyclic Loading Model

The cyclic model implemented within 'ADAPTIC' is shown diagrammatically in Figure 7.12. The monotonic stress-strain curve, presented in section 7.3.2.1, is assumed to envelope the cyclic loading response.

For the definition of the unloading curves, a plastic strain, ϵ_{pl} , must first be determined. This strain is based on the co-ordinates at the reversal point when unloading takes place from the envelope, as shown in Figure 7.12.a. The plastic strain lies on the unloading

secant slope which in turn is dependent on the strain at the intersection of the initial tangent and the plastic unloading secant slopes.

In the case of tensile unloading, deterioration in the tensile strength due to previous compressive strain histories is assumed, as shown in Figure 7.12.b. When the tensile strain at the tensile strength is exceeded, cracks open and the tensile strength is assumed to be zero for all subsequent increments of strain.

Figure 7.12.c shows a stress-strain curve including unloading and reloading branches. The co-ordinates of the point of reloading (ϵ_{ro} , f_{ro}) may be either at the unloading curve or at the cracked state. The reloading stress-strain curve is assumed to be a straight line between ϵ_{ro} and ϵ_{un} to a revised stress magnitude to account for cyclic degradation. Mander et al use a parabolic transition curve between the straight line and the monotonic stress-strain curve at the return co-ordinate point (ϵ_{re} , f_{re}), shown in Figure 7.12.c. However, since this transitional parabolic fit gives occasionally stresses that exceed the envelope curve, Madas and Elnashai assume a straight line passing through (ϵ_{un} , f_{new}), and having a reduced slope.

7.4 CONFINEMENT IN ENCASED SECTIONS

In order to utilize the concrete model described in section 7.3 in the analysis of composite members, concrete confinement zones were suggested by Madas and Elnashai (1989) for partially and fully encased sections, as shown in Figure 7.13. These were based on the approach proposed by Mirza (1989) for fully encased sections. Figure 7.13 also show the distribution of areas and monitoring points for the composite sections. The confinement zones were implemented in conjunction with the stress-strain relationships of Mander et al. The confinement factors, $k_{\sigma} = f'_{cc} / f_{co}$, used in (7.3) and (7.6), are user-defined for each confinement zone. The depth of the unconfined area and of the confinement parabola are also defined in the input.

Hereafter, the confinement factors for partially encased members is estimated according to three simplified approaches for symmetric reinforced concrete members. The first is the method used in Appendix A of Eurocode 8 (1988). The second is based on the equations given by Ahmad and Shah (1982). The relationship used by Mander et al (1988) is also considered. All three methods use the same approach for calculating a confinement effectiveness coefficient and a lateral confinement pressure as that described

by Mander et al. However, different simplified equations are given to translate these values into confinement factors for the case of equal lateral confinement pressures.

According to the EC8 approach, the confinement factor k_{σ} is given as:

$$\begin{aligned} k_{\sigma} &= 1.0 + 5.0 \alpha_c f_1/f_{co} && \text{for } f_1/f_{co} < 0.05 \\ \text{or} \\ k_{\sigma} &= 1.125 + 2.5 \alpha_c f_1/f_{co} && \text{for } f_1/f_{co} \geq 0.05 \end{aligned} \tag{7.7}$$

From the equations given by Ahmad and Shah, the confinement factor can be deduced as:

$$k_{\sigma} = 1.0 + 4.25 \alpha_c f_1 / f_{co} \tag{7.8}$$

The equation given by Mander et al is as follows:

$$k_{\sigma} = - 1.254 + 2.254 \sqrt{1 + 7.94 \alpha_c \frac{f_1}{f_{co}}} - 2 \alpha_c \frac{f_1}{f_{co}} \tag{7.9}$$

Table 7.1 compares the values of confinement factors obtained for the experimental models using the above three equations.

TABLE 7.1
Estimation of Confinement Factors

| Model Reference | α_c | f_1/f_{co} | from (7.7) | from (7.8) | from (7.9) |
|-----------------|------------|--------------|------------|------------|------------|
| EM01/2/3 | 0.71 | 0.49 | 1.99 | 2.48 | 2.42 |
| IC01/2/3 | 0.71 | 0.63 | 2.24 | 2.90 | 2.66 |
| EM04/5 | 0.68 | 0.65 | 2.23 | 2.88 | 2.65 |
| IC04/5 | 0.68 | 0.79 | 2.47 | 3.15 | 2.84 |
| IC06/7 | 0.51 | 0.65 | 1.95 | 2.41 | 2.38 |

In calculating the confinement effectiveness factor, the effective concrete areas were assumed as shown in Figure 7.14. The smaller lateral confining pressure from the two orthogonal directions was considered as representative of the behaviour. The depth of the parabola, d_p in Figure 7.14, was considered to be $0.25 d_c$, as suggested by Mirza

(1989), except for IC06 and IC07 for which d_p was assumed as $0.50 d_c$ to account for the lower confinement observed in the experiments.

A considerable difference, up to 30%, for the confinement factor is obtained from the three equations. Despite the differences in the results, it shows that confinement factors for well-confined members may easily exceed a value of 2.0. This is relatively high compared to a reinforced concrete section of the same dimensions and of similar reinforcement detailing, which would give a value of about 1.2. Nevertheless, it would be substantially lower than that obtained in a steel tube of similar plate dimensions, yielding a confinement factor higher than 6.0.

At this stage it is important to note that inspite of the elaborate calculations of available confinement models for reinforced concrete members, several assumptions remain to be of concern and can affect the accuracy of the results:

- a. The confined compressive strength is determined through the confining pressure at the yielding of the transverse reinforcement. Thus, it is assumed that yielding of the transverse steel occurs as soon as the compressive strength is reached, irrespective of the characteristics of the section.
- b. The critical strain of confined concrete is taken from experimental work on active confinement tests. Consequently, this strain corresponds to a constant confinement pressure, although in reality the concrete core is subjected to passive confinement.
- c. The effect of the strain gradient is not accounted for in these models. However, the compressed area of sections subjected to bending is loaded by varying strain and not constant as in columns under pure compression.

New uniaxial concrete models that account for variable passive confinement with the change in axial compressive strains have recently been proposed by Madas and Elnashai (1991).

From the above discussion, it is clear that an accurate estimate for the confinement factors in encased sections is difficult to obtain. Not only are all the available expressions based on investigations for reinforced concrete sections, but there are also inherent inaccuracies in these models. It seems, however, that amongst the available simplified expressions the approach given by EC8 results in a relatively conservative assessment of the confinement factors.

7.5 LOCAL FLANGE BUCKLING

Plated elements are susceptible to buckling out of their plane when subjected to compressive stresses. Local buckling might either reduce the ultimate strength of a section or diminish its rotational capacity in the inelastic range. This is largely dependent on the width/thickness (b/t) ratios of the components of the section. Since the ductility of partially encased members is adversely affected by inelastic local buckling of the steel flanges, this effect has to be considered in estimating the rotational capacities. This, however, is an involved problem that warrants a detailed study including the effect of imperfections and geometric nonlinearities and using detailed material plasticity formulations, which is beyond the scope of this thesis. Nevertheless, a simple yet sufficiently accurate approach is suggested in this section.

After briefly reviewing several methods dealing with local buckling from the literature, the proposed model is presented and its implementation within ADAPTIC is described. It should be noted that the review presented in subsequent sections is by no means an exhaustive survey but only serves to highlight certain points relevant to the approach used in this thesis.

7.5.1 General

7.5.1.1 Elastic Buckling

Critical buckling loads are obtained from the concept of bifurcation of an initially perfect structure. In practice, however, the response of a member is continuous due to the inevitable presence of initial imperfections and, often, residual stresses. Thus, the critical stress of a perfect structure must only be viewed as a useful index to the behaviour.

The elastic critical stress of a long segment is determined by the plate width/thickness ratio, by the restraint conditions along the longitudinal boundaries, and by the elastic material properties. The critical stress, σ_{cr} , is expressed as:

$$\sigma_{cr} = k \frac{\pi^2 E}{12(1 - \nu^2)(b/t)^2} \quad (7.10)$$

in which ν is Poisson's ratio, E is the modulus of elasticity, and k is a 'buckling coefficient' determined by a theoretical critical-load analysis. The value of k is a function of plate geometry and boundary conditions. Figure 7.15 shows the variation in k (for

structural steel) with the aspect ratio (a/b) for the three most used idealized edge conditions, i.e., clamped, simply supported, and free (Salmon and Johnson, 1980).

When the member cross-section is composed of various connected elements, a lower bound of the critical stress can be determined by assuming, for each plate element, a simple support condition for each edge attached to another plate element, or a free condition for any unattached edge. Also, when a plate element is relatively short in the direction of the compressive stress (i.e., $a/b \ll 1$), the critical stress may be conservatively estimated by assuming that a unit width of plate behaves like a column. More detailed information about k factors can be found in the literature (Salmon and Johnson, 1980; Timoshenko and Gere, 1963; Bleich, 1952).

7.5.1.2 Inelastic Buckling

Several theories have been proposed for cases of inelastic buckling of members. As reviewed by Timoshenko and Gere (1963) and Bleich (1952), for columns whose buckling stress is above the proportional limit of the material, two theories were first suggested namely the reduced modulus theory (double modulus theory) and the tangent modulus theory. In these methods, the equation for elastic buckling stress is used with a reduced modulus or the tangent modulus, respectively, instead of the modulus of elasticity. For plates, E_s/E was first suggested as a multiplier to the elastic critical stress, where E_s is the secant modulus. This was in good agreement with some test results on flange buckling of channel and Z-sections. However, general validity of this proposal was not accepted since it contradicted the theory of column buckling which is controlled by the tangent modulus.

Bleich (1952) generalized the expression for the elastic critical stress of a flat plate, under uniform compressive stress in both the elastic or inelastic range in the following manner:

$$\sigma_{cr} = k \frac{\pi^2 E \eta}{12(1 - \nu^2)(b/t)^2} \quad (7.11)$$

in which:

$$\eta = \sqrt{\frac{E_t}{E}}$$

This modification to adapt the elastic critical stress to a value higher than the proportional limit was a conservative, and rather arbitrary, approximation to the solution of a complex problem that involves a continuous updating of the constitutive relationships depending on the applied axial stress. According to Bleich (1952), Stowell's theory of plastic buckling indicated that in cases of plate buckling the effective modulus is in the vicinity of the secant modulus. The parameter η assumes a value of E_s/E in the case of a long hinged flange which buckles by twisting but is significantly smaller when the flange is clamped along one side or when the plate is supported along both unloaded edges. In these cases, η is a function of both E_s and E_t . Bleich showed that in most cases, the value of $\eta = (E_t/E)^{1/2}$, proposed for plates is very close to the values deduced from Stowell's theory. This value was shown to be generally more applicable since it is independent of the boundary conditions along the unloaded edges, and also since it furnishes limiting conservative values of the critical stress.

The appearance of the factor E_t/E , however, invalidates the basic assumptions of plastic analysis using structural steel elements. Nevertheless, since the mechanism of yield is discontinuous, and due to the existence of imperfections and residual stresses, steel elements do not buckle suddenly at yield and buckling strains well above the idealised yield strains are achieved. Haaijer and Thurlimann (1960) dealt with inelastic buckling of steel plates in more detail using different theories of plasticity. General expressions for the critical strains in the inelastic range were given for plates with different boundary conditions. Transition curves between Euler hyperbola and strain hardening were also suggested to account for the effect of residual stresses. The American Institute of Steel Construction provisions to prevent plate buckling (AISC-LRFD, 1986) adopt a similar procedure. To account for residual stresses, transition curves for columns and plates based on those proposed by Haaijer and Thurlimann are given.

Due to the complexity of the problem and its dependence on imperfections and residual stresses, many single plate and stub column tests under axial compression were conducted to investigate local instability of plate elements in the inelastic range. Fukumoto and Itoh (1984) carried-out a survey of available experimental reports. Figure 7.16 show the non-dimensional edge strain ϵ_{cr}/ϵ_y at the ultimate plate strength of the compression flange outstand of I-shaped sections, for different values of the plate slenderness parameter λ_p , defined as:

$$\lambda_p = \frac{b}{t} \sqrt{\frac{12(1-\nu^2)\sigma_y}{E\pi^2 k}} \quad (7.12)$$

Figure 7.17 shows the non-dimensional maximum stress, σ_{cr} , normalised by the actual yield stress from the tests for the I-section flanges. Reference curves for von Karman's relationship, $\sigma_{cr}/\sigma_y = 1/\lambda_p$, and Euler relationship, $\sigma_{cr}/\sigma_y = 1/\lambda_p^2$, are also shown in Figure 7.17. It is clear that strain hardening tends to increase the ultimate strength of flanges at λ_p of approximately 0.65, where the compressive stress starts to exceed the yield stress. The corresponding edge strain may reach the initial strain hardening at about 9 to 15 times the yield strain. For much smaller λ_p values, the critical stress increases into the strain hardening range and larger σ_{cr}/σ_y values are achieved.

Fukumoto and Itoh also obtained a simple relationship between ϵ_{cr}/ϵ_y and λ_p of the compression flange in the elasto-plastic and strain-hardening ranges, which represents approximately the mean of the experimental results in Figure 7.16. The relationship is given as:

$$\lambda_p = \frac{1}{\sqrt{1 + 0.5 \left(\frac{\epsilon_{cr}}{\epsilon_y} - 1 \right)}} \quad \text{for} \quad \lambda_p \leq 1.0 \quad (7.13)$$

In a recent investigation by Kato (1989), which formed the basis of the recommendations included in the new draft of the Japanese Standards (AIJ-LSD, 1990), an elaborate procedure for assessing the rotation capacity of steel H-section members based on susceptibility to local buckling was developed. The critical buckling stress was estimated from experimental results on stub columns. A linear regression relationship between the normalised critical stress and the flange and web slenderness parameters was used.

It is evident from the above discussion that accurate determination of the inelastic critical stress of plate elements requires detailed investigation of a number of inter-related factors affecting the behaviour. Nevertheless, a rational estimate can be obtained by combining fundamental plate buckling theories with results of experimental investigations.

7.5.1.3 Post-buckling Strength

Plates may continue to carry additional loads well after initial buckling. Post-buckling resistance is due to the redistribution of axial compressive stresses and, to a lesser extent, to the membrane tension and shear that accompany the out-of-plane bending of the plate in both the longitudinal and transverse directions. The longitudinal stresses tend to concentrate in the vicinity of the longitudinally supported edges, which are the stiffest parts of the buckled plate.

Morino et al (1986) suggested a simple approach by which an equivalent post-buckling stress-strain relationship can be obtained for the compression flange assuming a specific buckling mechanism as shown in Figure 7.18.a. The deformed portion is assumed to be simply supported along the edge lines OA and OB, and a plastic hinge line OC is formed. After buckling, the stress in the flange changes linearly from σ_y at the centre of the web to $\gamma\sigma_y$ at the flange tip, as shown in Figure 7.18.b. Considering a unit width from the flange tip which buckles under the compressive force $\gamma\sigma_y$, a mechanism shown in Figure 7.18.c is produced. The lateral deflection δ and the longitudinal shortening δ' occur and a plastic hinge forms at mid-height. Considering equilibrium and geometric relationships, and ignoring strain hardening, it was shown that the stress reduction factor, γ , can be written as:

$$\gamma = \frac{\sqrt{(L_b Z)^2 + t^2} - L_b Z}{t}$$

where

$$Z = \sqrt{1 - \left(1 - (\epsilon - \epsilon_{cr})^2\right)}$$
(7.14)

in which L_b is the buckling length shown in Figure 7.18, and $(\epsilon - \epsilon_{cr}) = \delta'/L_b$, where ϵ_{cr} is obtained from experimental results.

Consequently, the descending branch of the stress-strain relationship for the flange tip becomes:

$$\sigma_i = \gamma \sigma_y$$
(7.15)

The average stress acting on the compression flange can be obtained by substituting γ with $(\gamma+1)/2$ in (7.14) leading to a fictitious relationship for the descending branch of the stress-strain curve for the flange, given by:

$$\sigma = \sigma_y \frac{\sqrt{(L_b Z)^2 + t^2} - L_b Z + t}{2t}$$
(7.16)

The stress-strain relationship is shown schematically in Figure 7.19. Results obtained by Marino et al using this approach was shown to give good results in comparison with

more rigorous analytical procedures and experimental data of monotonic tests on fully encased composite members.

7.5.1.4 Cyclic Models for Frame Analysis

Detailed modelling of nonlinear inelastic cyclic behaviour of plates is now possible due to the rapid advancement of computers and the development of the finite element method including refined elements and elaborate plasticity formulations. Nevertheless, a more simple and efficient approach must be considered if inelastic local buckling is to be accounted for in a frame analysis program. If, in relatively short plates, the behaviour of a unit width of the plate is similar to that of a column, suitable approaches can be drawn from the cyclic behaviour of struts.

Ballio et al (1987) suggested a simple method to account for local buckling of bare and partially encased steel sections, that can be conveniently applied in frame analysis programs. In this approach, the cross-section is divided into a finite number of strips. If the compressive strain in any strip, i , exceeds a certain critical strain ϵ_{cr} , the area of the strip is reduced to zero for subsequent load cases. In order to extend the applicability of elastic buckling values in the inelastic range, the critical strain ϵ_{cr} , was obtained by dividing the elastic critical stress by the yield strain, ϵ_y , giving the following relationship:

$$\frac{\epsilon_{cr}}{\epsilon_y} = \frac{k\pi^2 E}{12\sigma_y(1 - \nu^2) \left(x_i / t\right)^2} \quad (7.17)$$

where x_i is the distance between the centroid of the strip, i , and the plate connection; t is the thickness of the plate; the value of k is assumed as: 1 for free plates (bare steel sections), 4 for the web of partially encased sections and 1.33 for the flanges of partially encased sections. Several considerations related to cyclic behaviour such as post-buckling strength in compression and recovery of tensile stresses after buckling were not accounted for in this approach.

7.5.2 The Proposed Model

The proposed model is intended to represent the basic phenomenon of local flange buckling through a simple and expedient approach that can be implemented within ADAPTIC. Therefore, a number of simplifications had to be included in order to establish the model within the existing structure of the main program, and without

impairing the efficiency of the analysis. In particular, two main improvements were sought over the approach used by Ballio et al (1987). The first is representing a more realistic cyclic behaviour in compression and the second is concerned with accounting for recovery of stresses in tension following local buckling.

7.5.2.1 Determination of Buckling Strain

In the case of partially encased sections, the concrete is assumed to provide the web with an effective rotational restraint and hence the flange outstand is considered to be fixed at its connection with the web. Consequently, with reference to Figure 7.15 and assuming that the value of the buckling coefficient, k , may be employed in both the elastic and the inelastic range, a value for k of 1.277 can be used. The validity of these assumptions was confirmed in the investigations of Ballio et al (1987) and experimental examination of axially loaded members carried out in ARBED research centre (Hahn and Jungbluth, 1983). The latter formed the basis for the b/t limitations proposed for partially encased sections in Eurocode 4 (EC4, 1984).

Figure 7.20 shows the relationship between the flange slenderness parameter, λ_p , and the normalised critical strain ϵ_{cr}/ϵ_y , as given by equations (7.13) and (7.18). The latter is obtained from (7.17) by replacing x_i with half the flange width, b , as follows:

$$\frac{\epsilon_{cr}}{\epsilon_y} = \frac{k\pi^2 E}{12\sigma_y(1-\nu^2)(b/t)^2} \quad (7.18)$$

The critical strains estimated from the strain gauge readings of some of the experimental results are also indicated in Figure 7.20. Whereas (7.13) is unconservative, it is clear that equation (7.18) provides a lower bound for the experimental results. It also lies well inside the experimental results presented in Figure 7.16. In addition, it has the advantage of being generally applicable in both the elastic and the inelastic domains. This relationship was, therefore, utilised in the proposed model.

According to Figure 7.15, the length of the buckling half wave length normalised by the flange outstand, i.e. a/b , would be 1.6. This seems to be in good agreement with the experimental observations from the EM models (Chapter 6), where the height of the local buckling region varied between 110 to 120 mm, i.e. a/b of 1.46 to 1.6. Whereas the length of the local buckling region has been studied experimentally and theoretically for steel members, there seems to be a lack of information related to this topic for the case of

partially encased members. In the absence of more accurate information, the value of 1.6 was considered to represent the length of the buckling region for the EM models.

In the IC models, the buckling length is readily determined by the spacing 's' of the local buckling inhibitors. From an assessment of the experimental results presented in Table 6.1, the following relationship is proposed for the value of the coefficient k:

$$k = \frac{3.03}{(s / b)} + 1.18(s / b) - 2.50 \quad (7.19)$$

The above relationship gives a value for k of 1.277 corresponding to s/b of 1.6 and approaches infinity as s/b tends to zero. The relationship in Figure 7.15 for elastic buckling was found to be unconservative compared to the experimental results. In contrast, equation (7.19) was calibrated to represent a lower bound of the experimental results. Figure 7.21 depicts the relationship between s/b and ϵ_{cr}/ϵ_y using equation (7.19) in conjunction with (7.18). The experimental results are also indicated in the figure. The critical strain is shown to be conservatively estimated using the above equations.

7.5.2.2 Post-buckling Relationship

The approach used by Morino et al (1986) was considered for representing the post-buckling relationship in compression because of its efficiency and simplicity. After careful examination of equations (7.14) and (7.16), several points are noteworthy. Firstly, the slope of the descending branch at the point of initiation of buckling is vertical, thus the tangent modulus of the relationship at that point is undefined. Also, the minimum value of the stress reduction, replacing L_b by s, is given as:

$$\gamma_{min} = \frac{\sqrt{s^2 + t^2} - s}{t} \quad (7.20)$$

This value is achieved when the strain ($\epsilon - \epsilon_{cr}$) is unity, after which the relationship becomes invalid due to the geometric constraint suggested in Figure 7.18. It is also clear that γ_{min} is not significantly affected by the value of s within its practical ranges. Therefore, γ_{min} is always close to zero, or in other words, the minimum value of σ/σ_y approaches a value of 0.50 at large strain levels.

In order to simplify the implementation of the model within ADAPTIC, it was decided to assign a stress-strain relationship for each monitoring area of the steel flange. The slopes of the descending branches were chosen in such a way that, for the case of zero strain

hardening, the average stress-strain relationship of the flange approaches that given by equation (7.16).

7.5.2.3 Description of the Cyclic Model

The proposed model is essentially an extension of the bilinear kinematic model presented in section 7.3.1.1. Before local buckling is initiated, the stress state is calculated according to (7.1), as shown in Figure 7.6.

For a compressive strain increment, the value of the strain, ϵ_s , at which the stress changes from positive to negative is updated. Local buckling is initiated if the current compressive strain at the monitoring point under consideration exceeds the buckling strain value, ϵ_b , given by:

$$\epsilon_b = \epsilon_s - \frac{k\pi^2}{12(1 - \nu^2) \left(x_i / t\right)^2} \quad (7.21)$$

where x_i is the distance from the monitoring point of the strip 'i' in the flange to the centre of the web and k is calculated from equation (7.19).

As shown in Figure 7.22, an increase in compressive strain beyond the buckling strain ϵ_b will cause a drop in stress below the compressive yield stress. The current stress in this case is calculated as:

$$\left. \begin{aligned} \sigma &= \sigma_b + \frac{\sigma_b(\epsilon_b - \epsilon)}{(\epsilon_k - \epsilon_b)} & \text{if } (\epsilon_b - \epsilon) \leq (\epsilon_b - \epsilon_k) \\ \sigma &= 0 & \text{if } (\epsilon_b - \epsilon) > (\epsilon_b - \epsilon_k) \end{aligned} \right\} \quad (7.22)$$

in which σ_b is the stress corresponding to ϵ_b , and ϵ_k is given by:

$$\epsilon_k = \epsilon_b + \left[\left(\frac{\epsilon_b}{\epsilon_{bp}} \right)^2 (\epsilon_b - \epsilon_{bp}) \right] \quad (7.23)$$

where ϵ_{bp} is the critical strain of the flange obtained by replacing x_i with half the flange width in equation (7.21).

The value of the current stress is set to zero if the compressive strain exceeds ϵ_k until this strain value is recovered in a tensile strain increment.

The cyclic behaviour of the strip following local buckling is based on the observed behaviour of steel axially loaded members (e.g. Popov and Maison, 1980; Ballio and Perotti, 1987). Figure 7.23 shows the different loading and unloading paths after the onset of initial local buckling. In a tensile strain increment after buckling, the stress path is determined by a straight line given as:

$$\sigma = \sigma_m + \frac{(\epsilon - \epsilon_m)(\sigma_r - \sigma_m)}{\epsilon_r - \epsilon_m} \quad \text{if} \quad (\epsilon - \epsilon_b) \leq (\epsilon_r - \epsilon_m) \quad (7.24)$$

in which ϵ_m and σ_m are the co-ordinates of the point of reloading in tension after buckling, and the point (ϵ_r, σ_r) , is given by:

$$\epsilon_r = \frac{\sigma_y(1 - \mu) + \epsilon_r E - \sigma_b}{E(1 - \mu)} \quad (7.25)$$

and,

$$\sigma_r = (\epsilon_r - \epsilon_b)E + \sigma_b \quad (7.26)$$

If the strain value of ϵ_r is exceeded, the current stress follows the envelope plastic path according to the bilinear kinematic hardening model:

$$\sigma = (\epsilon - \epsilon_r)\mu E + \sigma_r \quad (7.27)$$

Subsequent unloading and reloading follows the paths shown in case A and B of Figure 7.23, depending on whether the value of ϵ_r was exceeded. In each cycle, the co-ordinates of the intermediate unloading point (ϵ_m, σ_m) , the buckling point (ϵ_b, σ_b) and the tensile return point (ϵ_r, σ_r) are continuously updated. In a compressive strain increment after initial buckling, the buckling stress and strain are updated as a function of the previous intermediate unloading point through the following relationships:

$$\epsilon_b = \frac{(\sigma_m - \sigma^0) + E(\epsilon^0 - \mu\epsilon_m)}{E(1 - \mu)} \quad (7.28)$$

$$\sigma_b = \mu E(\epsilon_r - \epsilon_b) + \sigma_m \quad (7.29)$$

where ϵ^0 and σ^0 are the strain and stress values at the start of the compressive increment causing subsequent local buckling. The value of the return point when the new buckling strain is exceeded in compression is again updated using the updated buckling strain and stress from (7.28) and (7.29) and substituting in (7.25) and (7.26), respectively.

7.5.2.4 Implementation of the model

Two distinct sub-programs form the basic structure of 'ADAPTIC', as shown in Figure 7.24. The first, READ, is an interface which operates on the user data and stores the resulting information in a set of temporary files. These files are then accessed by the second sub-program, ANALYSE, which uses the stored information to perform the required analysis. ANALYSE is the main part of the program where the incremental analysis is performed. Within each load step, an iterative solution is performed until convergence is achieved. Element variables are then updated for the current load step, and numerical results are output before the next load step is applied.

The above-described local buckling model, was implemented within 'ADAPTIC'. A layout of the main subroutines used by the model is shown in Figure 7.25 and described hereafter:

- INMDL6 sets the initial values of model parameters for all the monitoring points.
- SCFRC6 adds the contribution of monitoring points belonging to this material model to the section forces.
- Within SCFRC6, the subroutine STMDL6 is called and the new nonlinear stress vector corresponding to a given strain vector is calculated for each monitoring point and for each Gauss section in the cubic elements.
- The subroutine ETMDL6 calculates the tangent modulus of the stress-strain relationship at both Gauss sections for all monitoring points.
- The tangent modulus is then communicated to SCSTF6 which adds the contribution of monitoring points to the section stiffness for the evaluation of the stiffness matrix.

- The values of all variables used by the model are updated through the subroutine UPMDL6 only after equilibrium is achieved.

7.5.2.5 Verification

Four simple examples are presented hereafter to verify the implementation of the local buckling model within ADAPTIC. A fictitious short member represented by one cubic element is loaded axially in order to examine the model on the entire flange level. The cross-section consists of two flanges, as shown in Figure 7.26. The results are presented in a non-dimensional form normalized by the appropriate yield values.

Figure 7.27 depicts the relationship between the axial displacement and the corresponding restoring force for the member under monotonic compressive loading. No strain hardening is considered. The relationship is shown for different numbers of monitoring points used to represent each flange. As indicated, the accuracy of the model depends on an appropriate choice of the number of monitoring points. The error in estimating the critical strain for different numbers of monitoring points per flange is given in Table 7.2 below.

TABLE 7.2
Effect of Number of Monitoring Points on Critical Strains

| Monitoring points | 2 | 4 | 5 | 10 | 14 | 20 | 50 |
|---------------------------------------|------|------|------|------|------|------|------|
| $\epsilon_{cr}/\epsilon_{cr(actual)}$ | 4.00 | 1.77 | 1.56 | 1.23 | 1.16 | 1.10 | 1.02 |

The ratio between the calculated and the actual critical strains can be estimated through the following relationship:

$$\frac{\epsilon_{cr}}{\epsilon_{cr(actual)}} = \left(\frac{1}{1 - \frac{1}{j}} \right)^2 \quad (7.30)$$

where j is the number of monitoring points per flange.

As shown in Figure 7.27, the post-buckling relationship is accurately predicted when 20 monitoring points are used. Sufficient accuracy is hence achieved if at least 20 divisions are used within each flange. This number is well below the recommended number of

monitoring points for use with the cubic element of ADAPTIC, even if the local buckling of the flange is not considered. Therefore, the model can be conveniently used without impairing the efficiency of the analysis.

The monotonic response in compression using different values of strain hardening is shown in Figure 7.28, using 30 monitoring points per flange. The behaviour under axial cyclic displacement is shown in Figures 7.29 and 7.30 for zero and 1% strain hardening ratios, respectively. Two cycles at each displacement level are applied. The model accounts for both the recovery of stresses in tension and the degradation in compression in subsequent cycling following the onset of local buckling.

7.6 COMPARISON WITH EXPERIMENTAL RESULTS

7.6.1 General

As mentioned before, the accuracy of ADAPTIC in representing the behaviour of composite members has been extensively studied elsewhere (Madas and Elnashai, 1989 and 1991). In this section, some of the experimental results are compared with analytical simulations using ADAPTIC including the new developments. In particular, specimens that were significantly affected by local flange buckling are considered. The comparison also includes two of the bending tests conducted by Ballio et al (1987). Finally, nonlinear dynamic analysis simulations are compared with the results of two pseudo-dynamic tests.

The finite element mesh employed is shown in Figure 7.31. Five cubic elements were used to represent the member, with a reduced length near the support. A further subdivision was not necessary, since a finer mesh did not affect the results significantly. The composite section was represented by 150 monitoring points. Average confinement factors were assigned to the partially and fully confined concrete as calculated from equation (7.7) and given in Table 7.1, whilst the cover concrete was assumed to be unconfined.

7.6.2 Tests by Ballio et al

Figures 7.32 and 7.33 show the comparison between the experimental results of two bending tests (6C and 8C) on partially encased cantilever members, conducted by Ballio et al (1987), and analytical results using ADAPTIC. Material properties and specimen dimensions reported by the investigators were used. A strain hardening parameter of

1.0% was assumed in the analysis of both models, and the average confinement factors were estimated as 1.30 and 1.35 for specimens 6C and 8C, respectively.

As shown in Figure 7.32, the comparison for specimen 6C indicates good correlation between the experimental results and the analysis. The initial stiffness is accurately predicted by the analytical results. Noticeable deviation from linearity occurs at approximately 10 mm in both the analysis and experiment. The analysis, however overestimates the yield capacity by about 7% since stress softening at low strain levels is not accounted for in the steel model. The behaviour up to the first cycle at 20 mm shows very good correlation between the experiment and analysis, both giving a capacity of approximately 100 KN. In the analysis, the onset of local buckling occurs following the first cycle at 20 mm. This seems to be conservative compared to the experimental results, for which the shape of the hysteretic loops indicates the initiation of local buckling after three cycles at 20 mm. The ultimate load at 30 mm is underestimated by about 10% in the analysis as a consequence of the early flange buckling and possible inaccuracy in representing the strain hardening of steel. Nevertheless, the shape of the loops following local buckling is very well predicted by the analytical model.

The comparison for specimen 8C is presented in Figure 7.33. Again, the yield load is slightly over-estimated by the analysis, whilst the ultimate load is about 13% lower than the experiment. Initial local buckling of the flange in the experiment seems to occur following the first cycle at 50 mm. This again is conservatively estimated by the analysis, in which the displacement corresponding to the onset of local buckling is approximately 40 mm. As for the case of specimen 6C, the final failure occurs due to weld failure caused by low cycle fatigue. However, prior to weld failure, the drop in the ultimate load, approximately 14 % in both models, corresponds to only 3% in the analysis. This is due to the sudden release of concrete confinement following local flange buckling in the experiments, an effect not accounted for in the analysis.

7.6.3 Cyclic Tests on Beam-Columns

Figure 7.34 presents the comparison of results for the cyclic test on model EM04, in which no axial load was applied. Similar observations to those mentioned in the previous section regarding the stiffness and the capacity are shown. Both the experiment and analysis indicate local flange buckling prior to the application of the displacement cycles at 48 mm. This explains the change in shape of the hysteretic curves of the second and third cycles at this level. The exact point of flange buckling is, however, conservatively estimated by the analysis to be approximately 37 mm compared to about 45 mm in the

experiment. The ultimate capacity is also under-estimated by about 10% in the analysis, which may be attributable to inaccuracies in the assigned confinement factor and the strain hardening parameter. In subsequent cycles, the degradation in the hysteretic behaviour is well represented by the analysis, in terms of both reduction in capacity and stiffness deterioration.

The experimental and analytical load-deflection relationships for IC07 are shown in Figure 7.35. Excellent correlation is observed in the stiffness, capacity and area enclosed by the hysteresis loops. The load at a displacement of 16 mm is only 3% over-estimated by the analysis, whilst the ultimate capacity is only 4% lower in the analysis. The stiffness deterioration on loading and unloading occurs rather sharply in the analysis as compared to the smooth transition observed in the experiment. This is due to the piecewise linear relationships assumed in the steel constitutive model. Nevertheless, the overall shape of the loops is accurately represented by the model. Local buckling, which occurs at 64 mm in the experiment, is observed in the analysis, as indicated by the similarities in the stiffness deterioration near the plastic load in subsequent cycles. However, as observed in other models, the drop in ultimate capacity at 96 mm due to release of confinement, especially after the failure of the welded bars, is not observed in the analysis.

Figures 7.36 and 7.37 depict the hysteretic curves of models EM02 and IC02, respectively. Both models were subjected to a high axial compressive load representing 30% of the squash capacity. In case of EM02, the analysis accurately predicts the ultimate load within an error margin of 4%. The onset of local buckling is also conservatively estimated by the analysis to occur at approximately 15 mm compared to a displacement exceeding 20 mm in the experiment and again the loss of confinement causes a larger drop in capacity in the experiment as compared to the analysis. The striking discrepancy, however, is in the shape of the hysteretic loops at displacements larger than 20 mm. The smooth decrease in stiffness starting at a load of approximately 40 KN in the experiment is represented by an abrupt drop in stiffness at about 35 KN in the analysis. Following a region of an almost horizontal stiffness, the analytical results indicate another rather abrupt increase of the stiffness. This is attributable to three main reasons:

- a. The concrete model assumes a perfect cracking mechanism, whereby cracks open when a specific strain is reached in a tensile strain increment after which the stress in concrete is neglected. If the latter plastic strain is recovered in a compressive strain increment, the stress in concrete is increased. This is not the case in experiments,

however, where such process occurs rather gradually due to imperfect closure of cracks.

- b. Following local buckling, recovery of flange stiffness in tensile strain increments is modelled by semi-empirical relationships which seem to represent the change in stiffness more abruptly compared to the experiment.
- c. The piecewise linear steel constitutive relationship does not accurately represent the smooth deterioration in stiffness as in the experimental behaviour.

It is interesting at this stage to discuss the results for IC02 shown in Figure 7.37. Similar to EM02, at displacements cycles of amplitude larger than 30 mm, a rather abrupt decrease in stiffness is indicated in the analysis at a load close to 40 kN. This is due to the previously-mentioned concrete modelling inaccuracies. This effect is also observed in models subjected to low axial loads, but it becomes more pronounced with the increase of axial load due to the increased contribution of concrete. However, since local buckling is delayed in this specimen, the shape of the hysteretic loops are closer to the experimental curves than for EM02. The displacement corresponding to the onset of local buckling is underestimated by the analysis to be about 49 mm compared to approximately 55 mm in the experiment. The capacity and second-order effects are accurately represented by the analysis for both EM02 and IC02.

7.6.4 Pseudo-Dynamic Tests

The experimental results and analytical simulations for models EM03 and IC03, tested using El Centro earthquake record, are given in Figures 7.38, 7.39 and 7.40. Both specimens were subjected to axial compressive loads representing 30% of the squash capacity.

Figure 7.38 shows the displacement response history obtained for both models from the experimental and analytical results. The correlation between the experimental and analytical displacement histories is presented in Figure 7.39. Finally, Figure 7.40 depicts the experimental and analytical load versus displacement relationships of both models. Excellent agreement is observed between the experimental and analytical results. Several points observed in the comparison are noteworthy:

- a. The behaviour up to about 1.8 seconds from the start of the record is almost identical in both EM03 and IC03, and is precisely predicted by the analysis. It should be noted

that the observed marginal discrepancy in the analytical results of EM03 and IC03 at 1.7 seconds (at a displacement of 20 mm in the positive direction, IC03 shows lower force and higher displacement compared to EM03), is due to slight inaccuracy in the mathematical relationships in the concrete model (Mander et al, 1988) which underestimates the concrete stress for higher confinements at low strain levels. This, however, has no bearing on the results.

- b. The onset of local buckling occurs after 1.8 seconds, as shown in the experimental load-deflection relationships, which is very accurately predicted by the analysis. This clearly indicates that the accuracy by which the onset of local buckling is estimated in the analysis is substantially improved when a small number of cycles is applied at low strain levels.
- c. Following local flange buckling, the behaviour is very well represented by the analysis. However, the displacements attained in the experiment are larger, which can be attributed to the lower confinement of concrete at this stage and possible inaccuracy in the post-local buckling representation of the analytical model.
- d. The response of IC03 is also very well predicted by the analysis, with a shift in the displacement response. Local flange buckling of IC03 is detected at large displacement level of 120 mm in the analysis compared to about 140 mm in the experiment.

In general, both the displacement response and the load-displacement indicate very good correlation between the pseudo-dynamic test results and the nonlinear dynamic analysis simulations.

7.6.5 Commentary

The above comparisons have demonstrated the overall accuracy of the analytical model in predicting the behaviour of composite members. However, it was shown that the accuracy of the local buckling model increases with the decrease of the number of loading cycles applied at low strain levels. Whereas conservative results are predicted when a large number of cycles close to the yield level is applied, the accuracy is substantially improved for monotonic or earthquake loading with a small number of cycles. This is a consequence of the inability of the simplified model to account for the effects of stress

softening. For more accuracy, other improvements are needed in the analytical models such as accounting for loss of confinement following local flange buckling, which would require coupling of the steel and concrete constitutive relationships.

The analytical tools described and validated in this chapter are used in Chapter 8 of the thesis in conducting parametric studies to examine the effect of different important parameters on the behaviour of partially encased members.

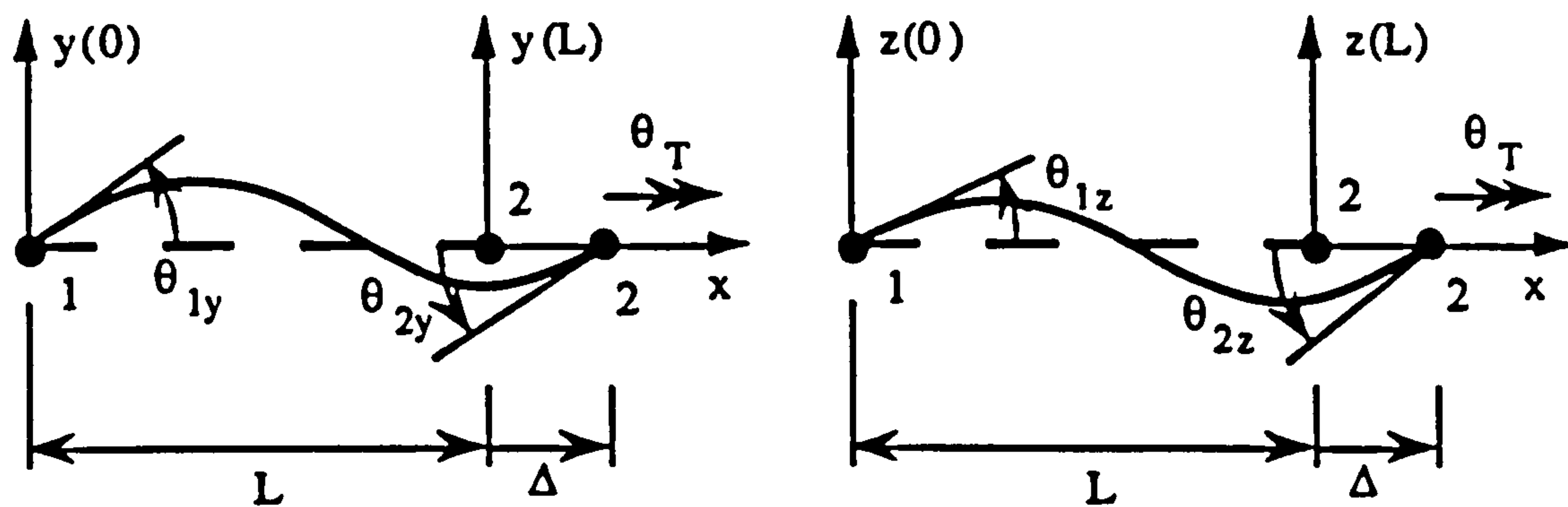


Fig. 7.1 Chord freedoms of the cubic formulation (Izzuddin, 1990)

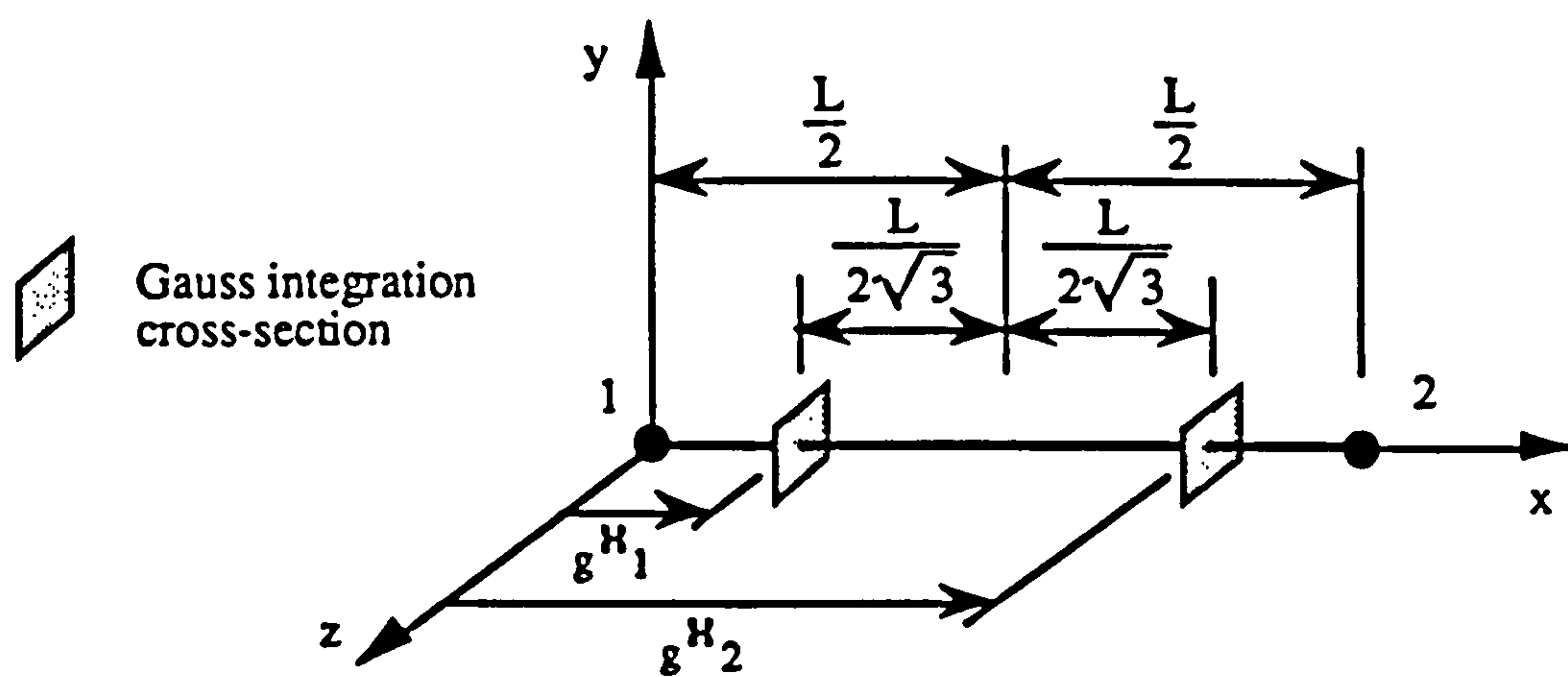


Fig. 7.2 **Location of the two Gauss Integration sections (Izzuddin, 1990)**

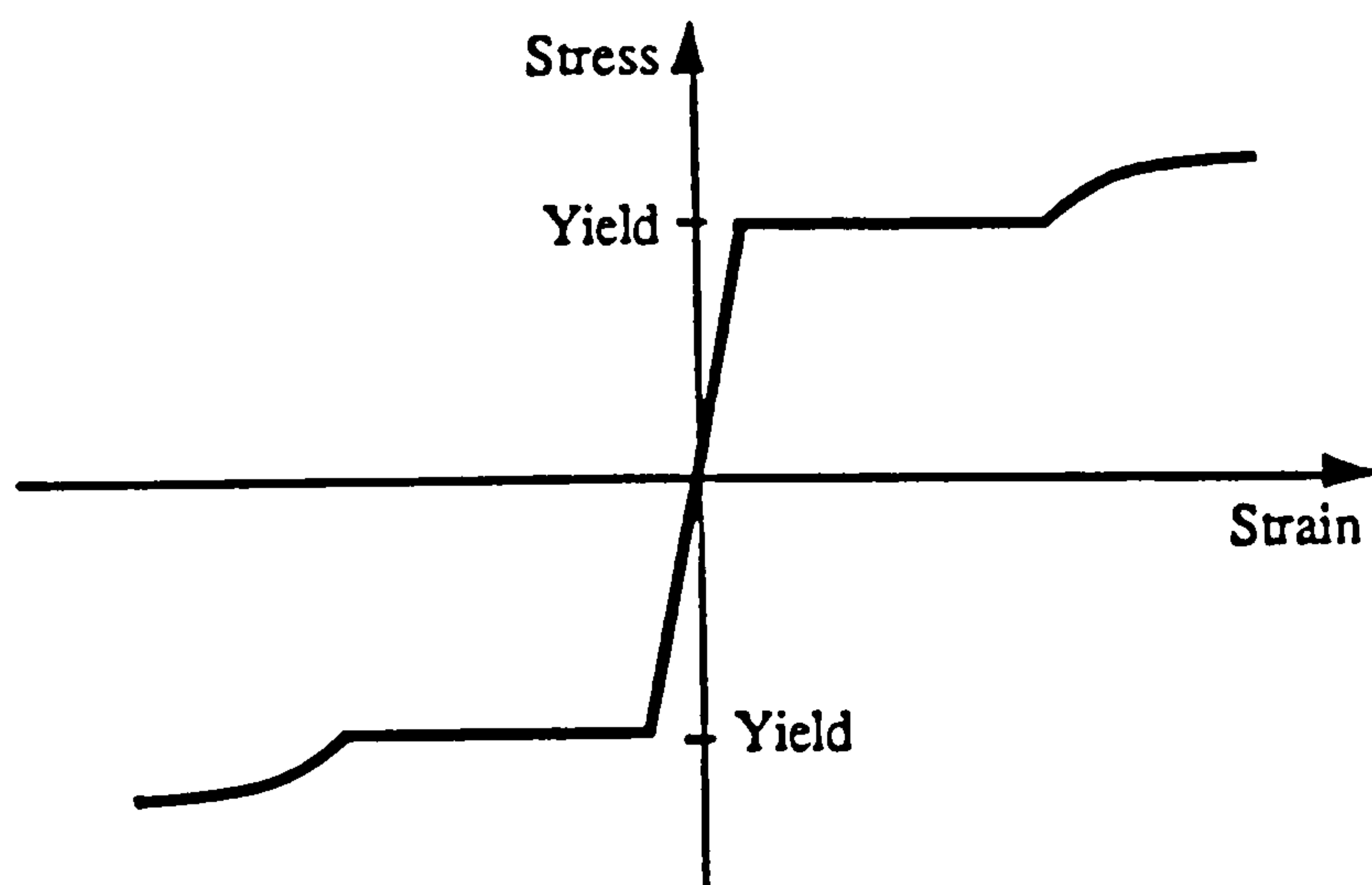


Fig. 7.3 Virgin monotonic response of mild steel (Izzuddin, 1990)

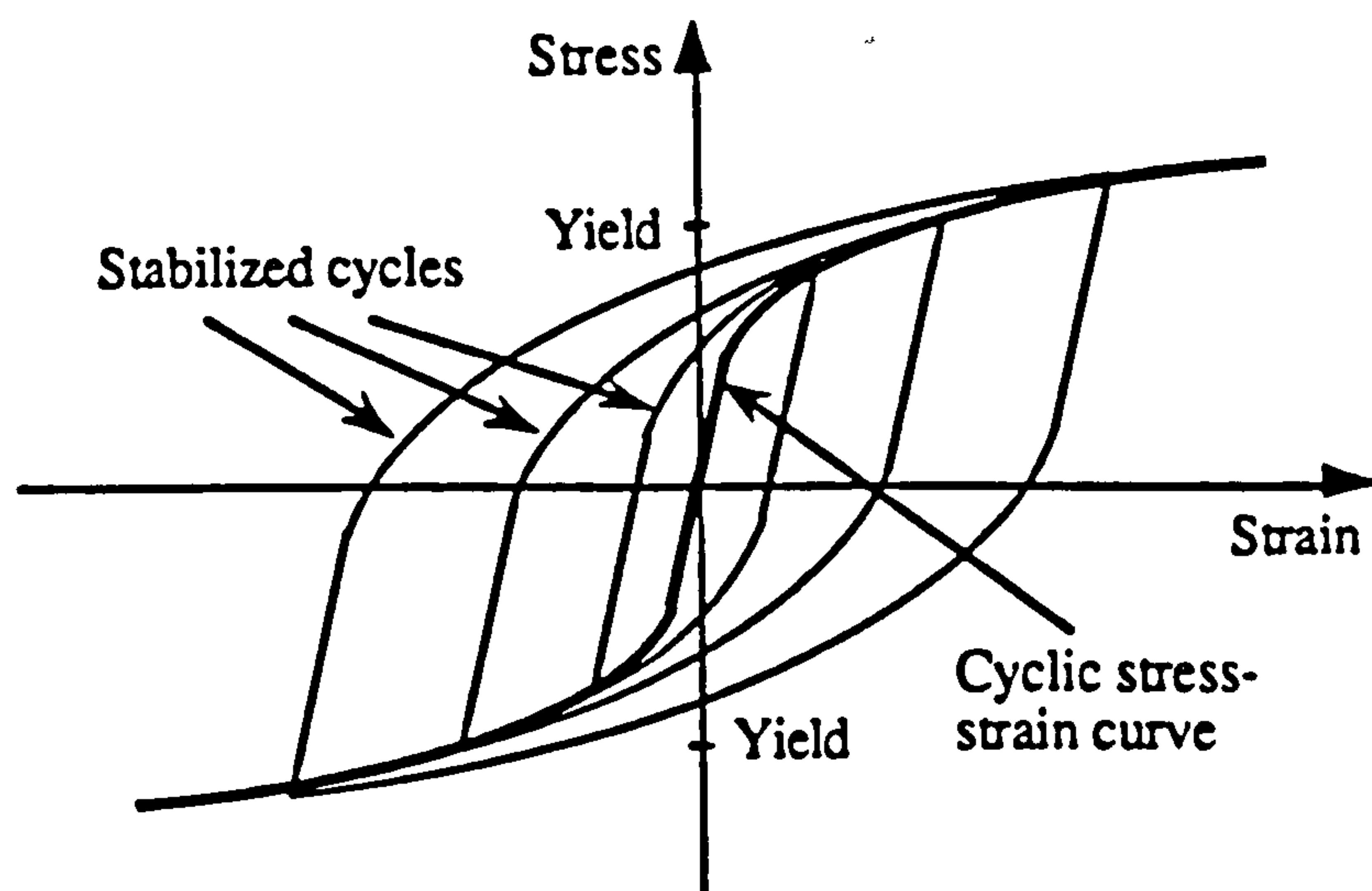
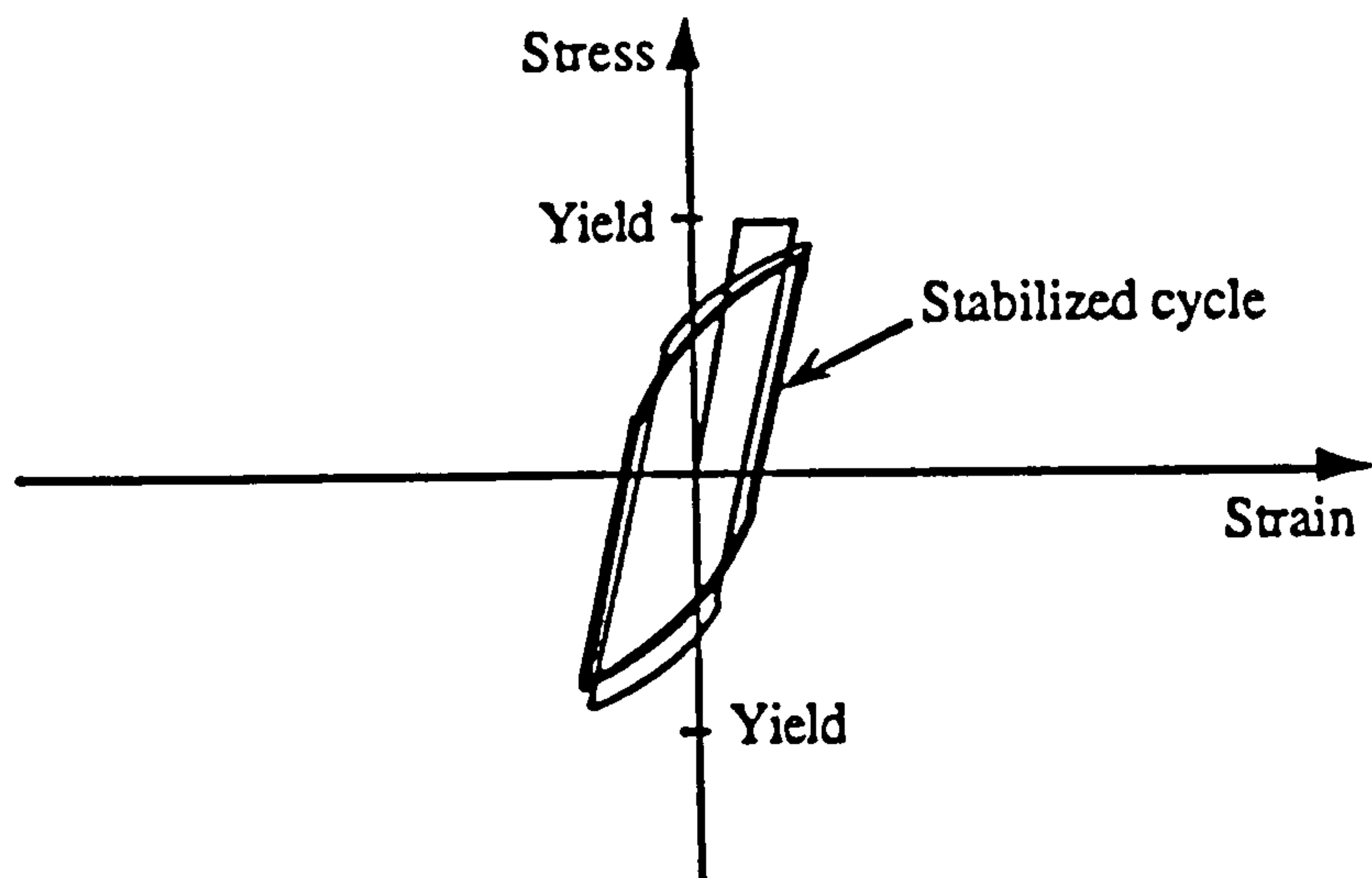
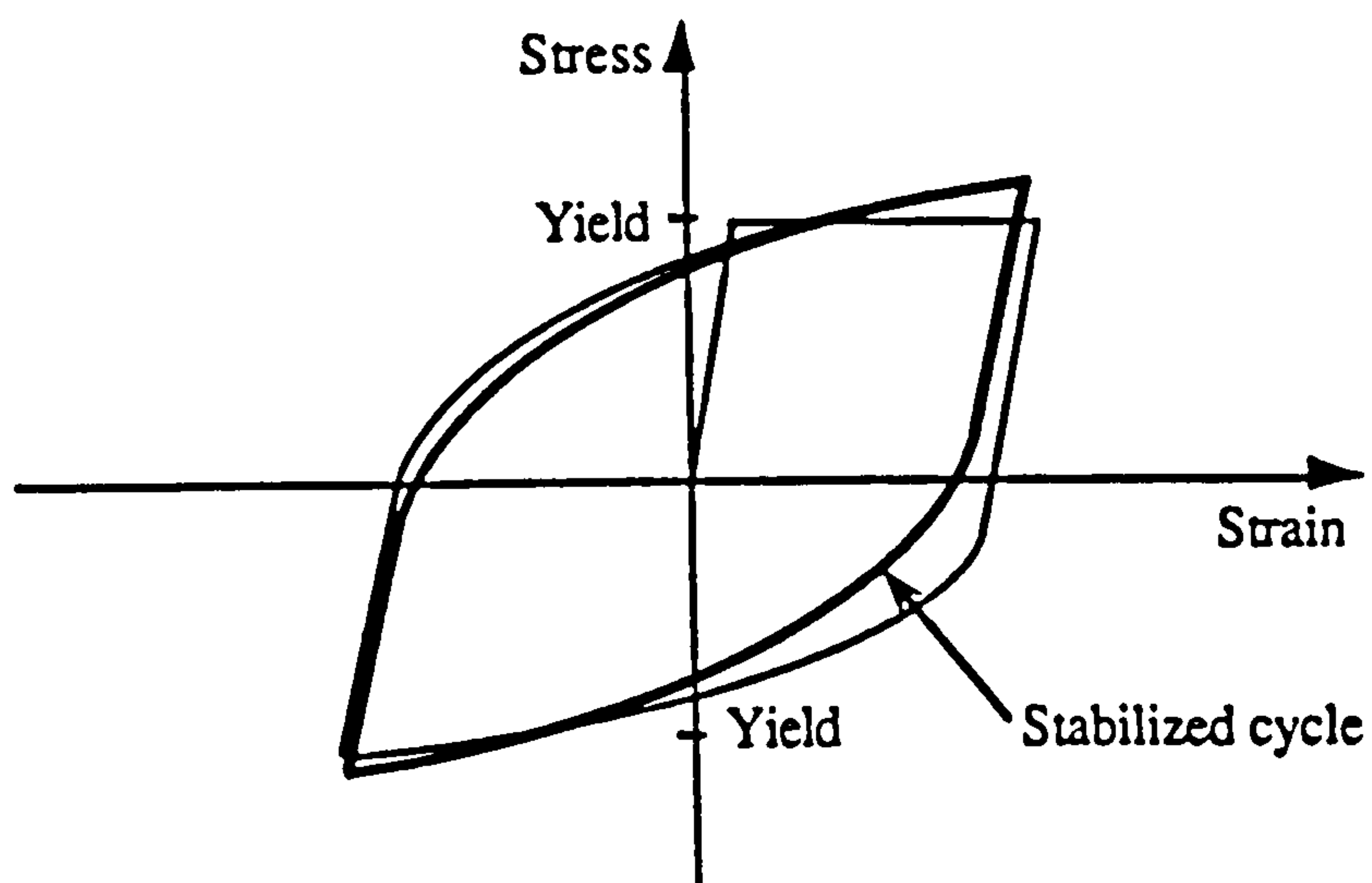


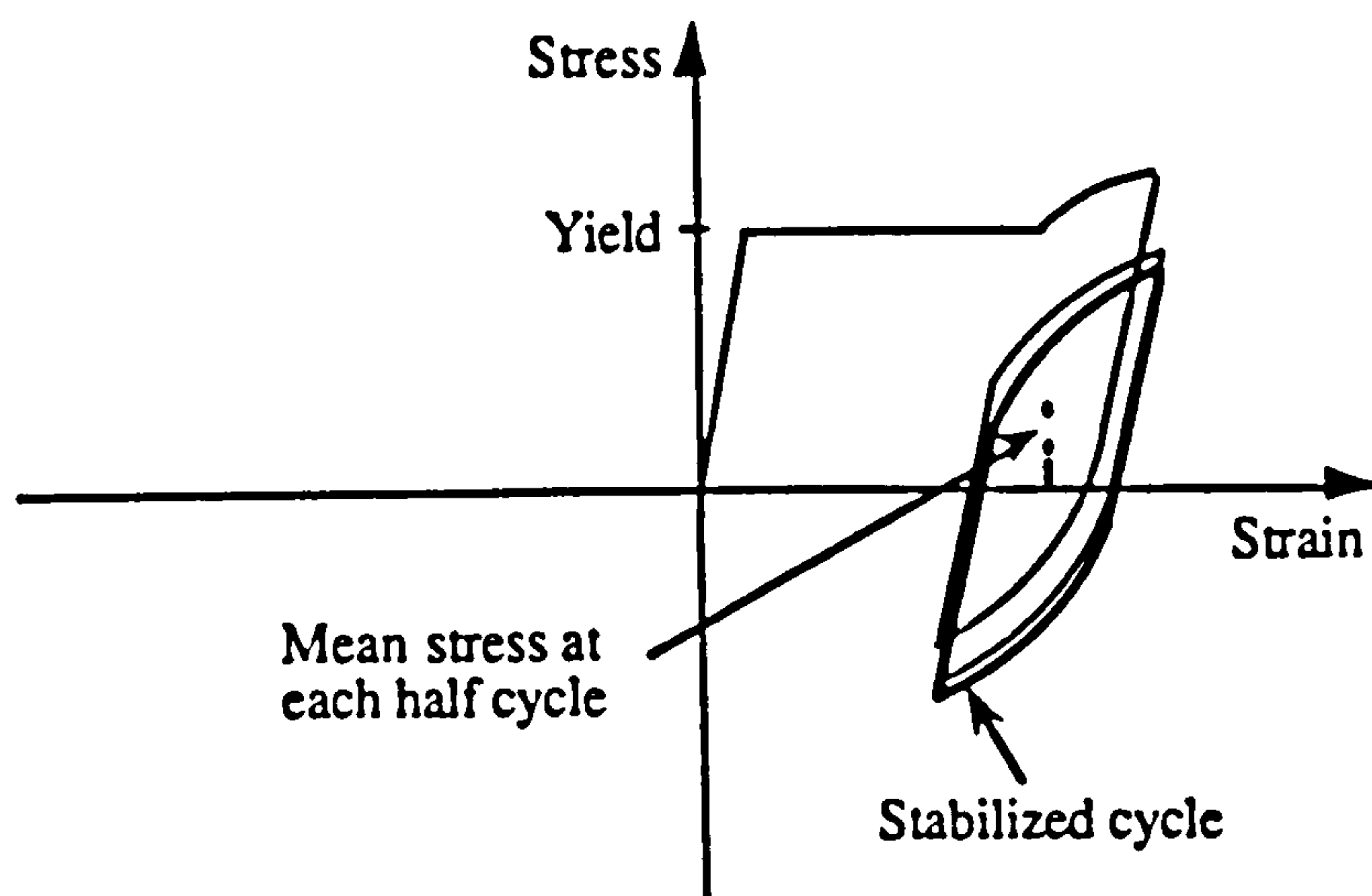
Fig. 7.4 Steady state cyclic response of mild steel (Izzuddin, 1990)



Softening under small strain amplitudes



Hardening under large strain amplitudes



Mean-stress relaxation

Fig. 7.5 Steady state cyclic response of mild steel (Izzuddin, 1990)

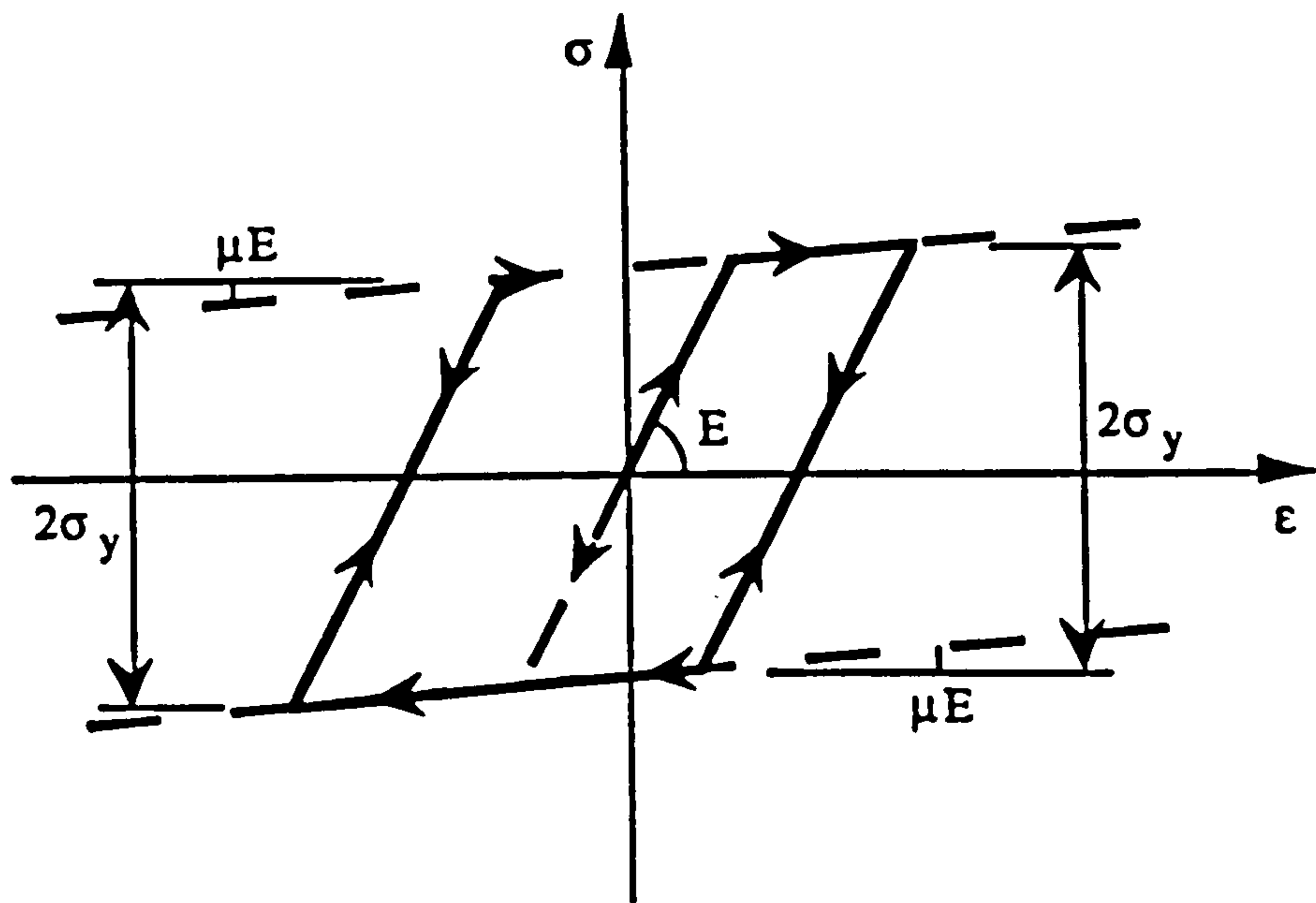


Fig. 7.6 Loading and unloading paths of bilinear kinematic model (Izzuddin, 1990)

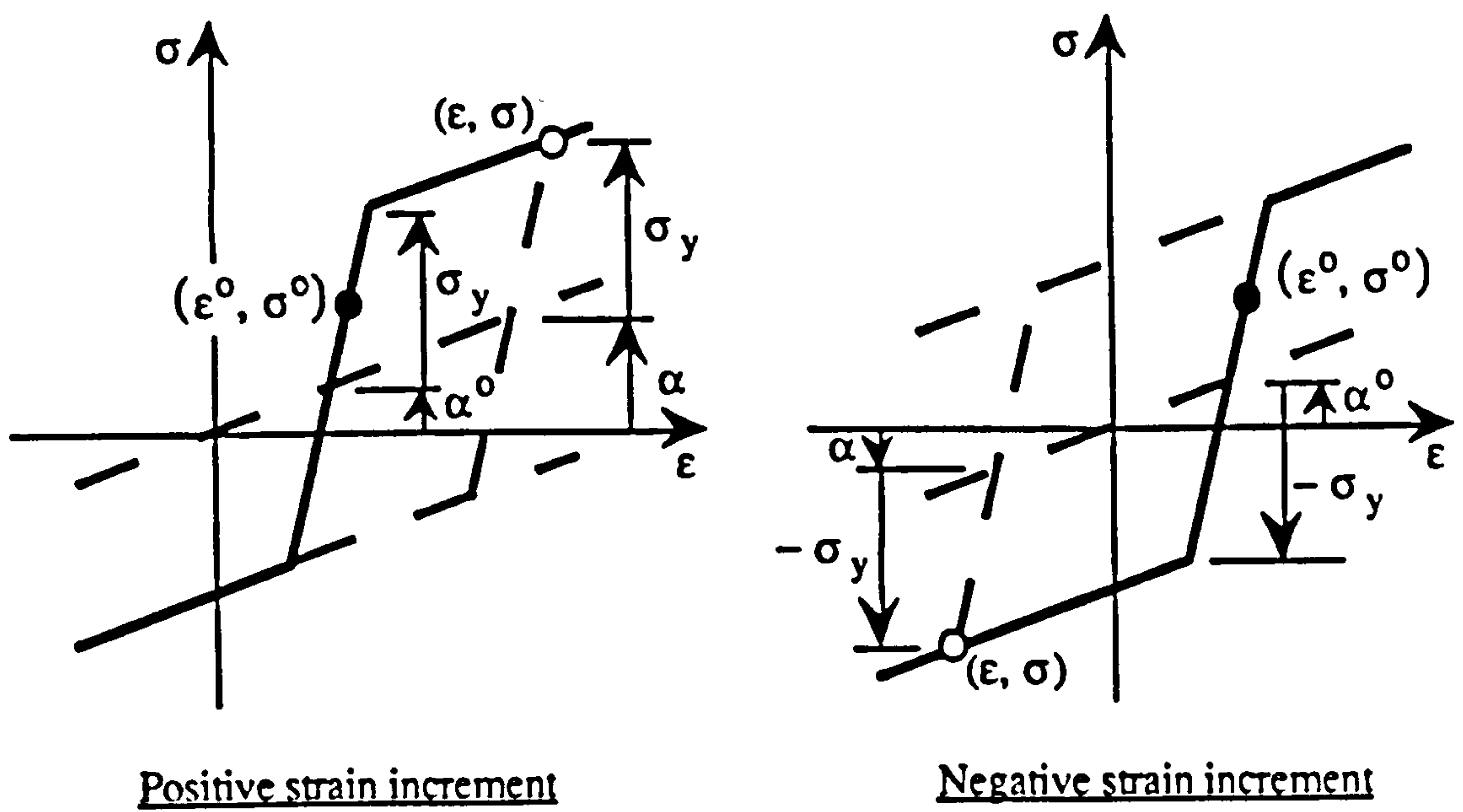
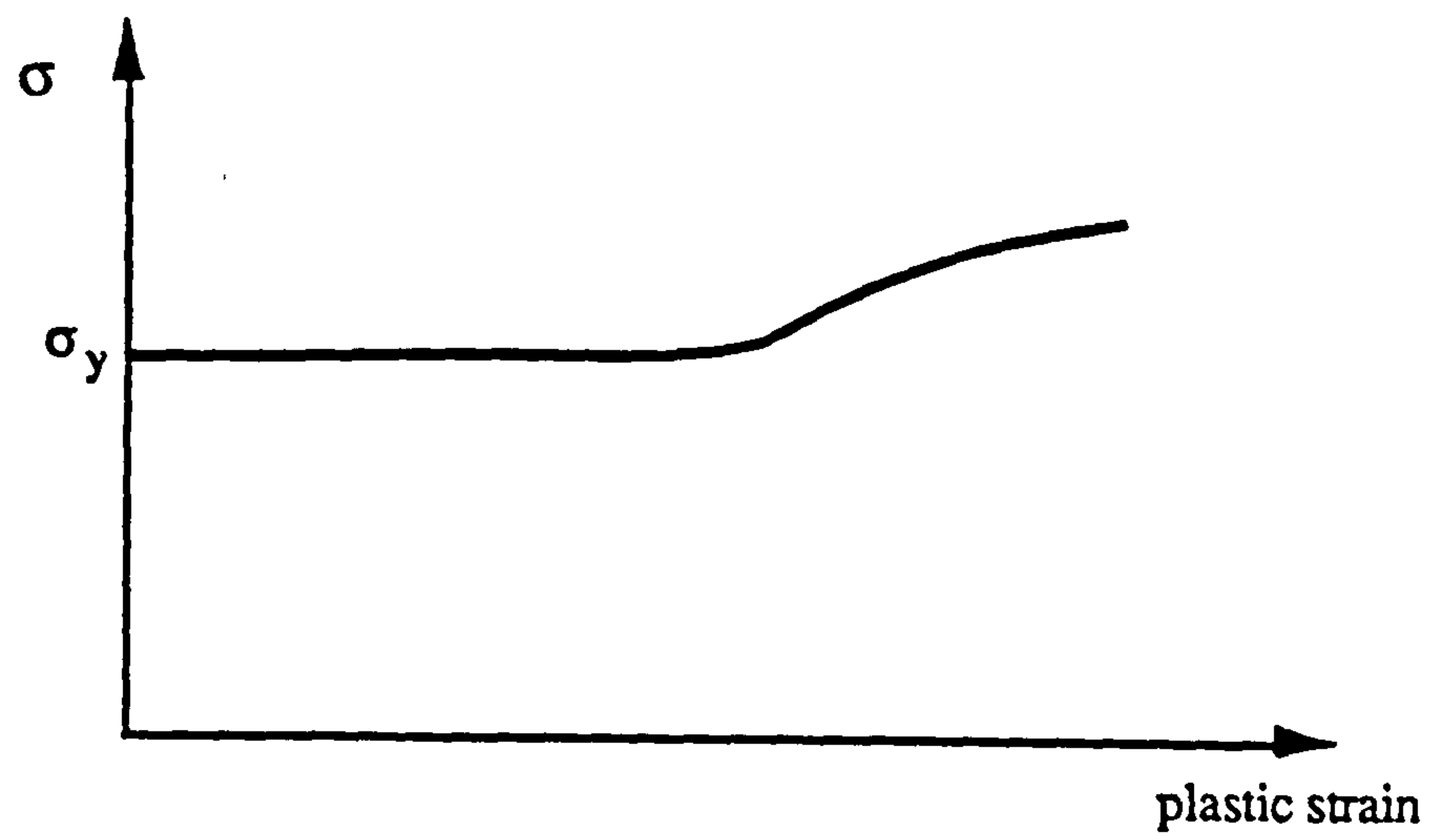


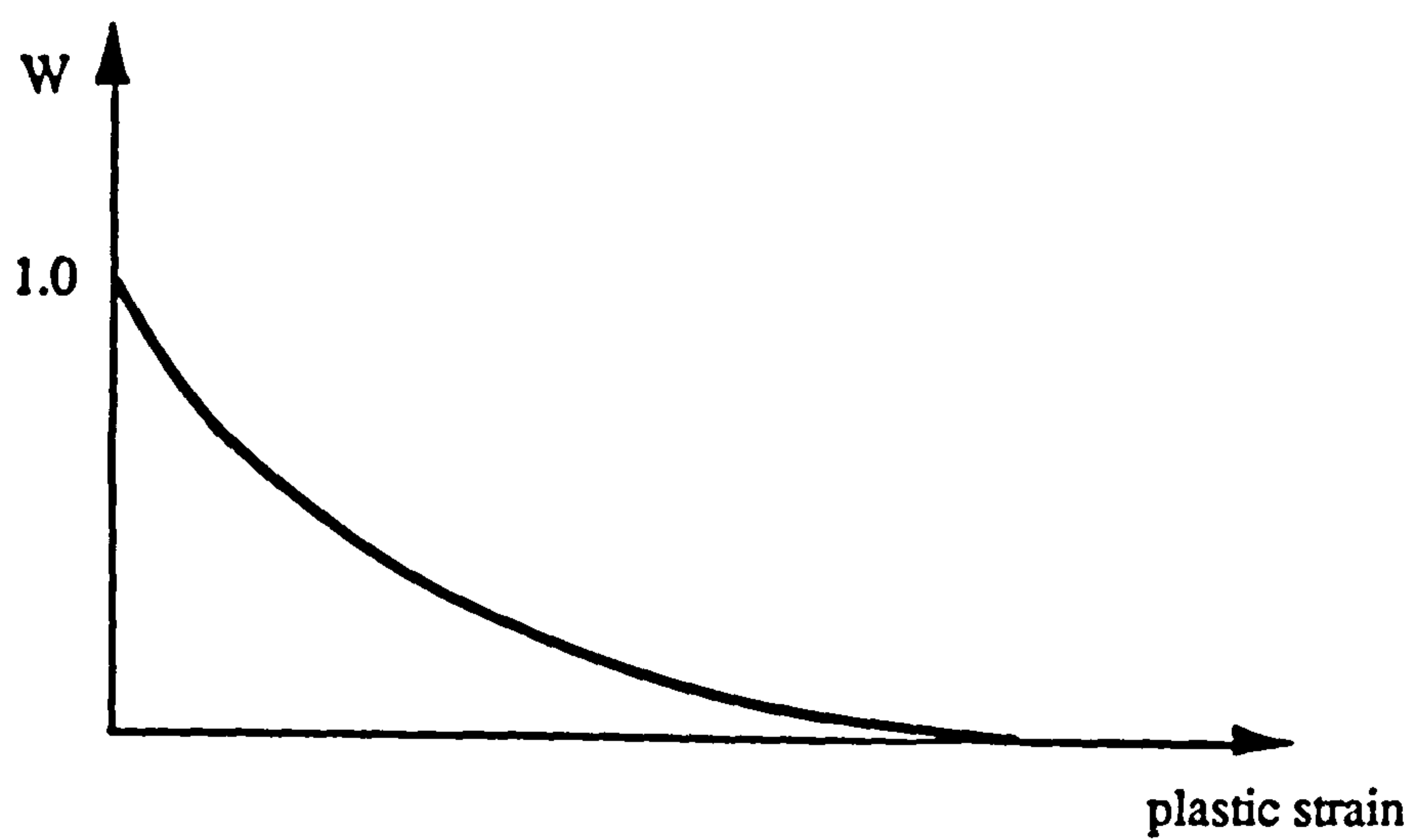
Fig. 7.7 Stress determination with the bilinear kinematic model (Izzuddin, 1990)



Virgin curve



Cyclic curve



Weighting function

Fig. 7.8 The basic curves for isotropic hardening determination (Izzuddin, 1990)

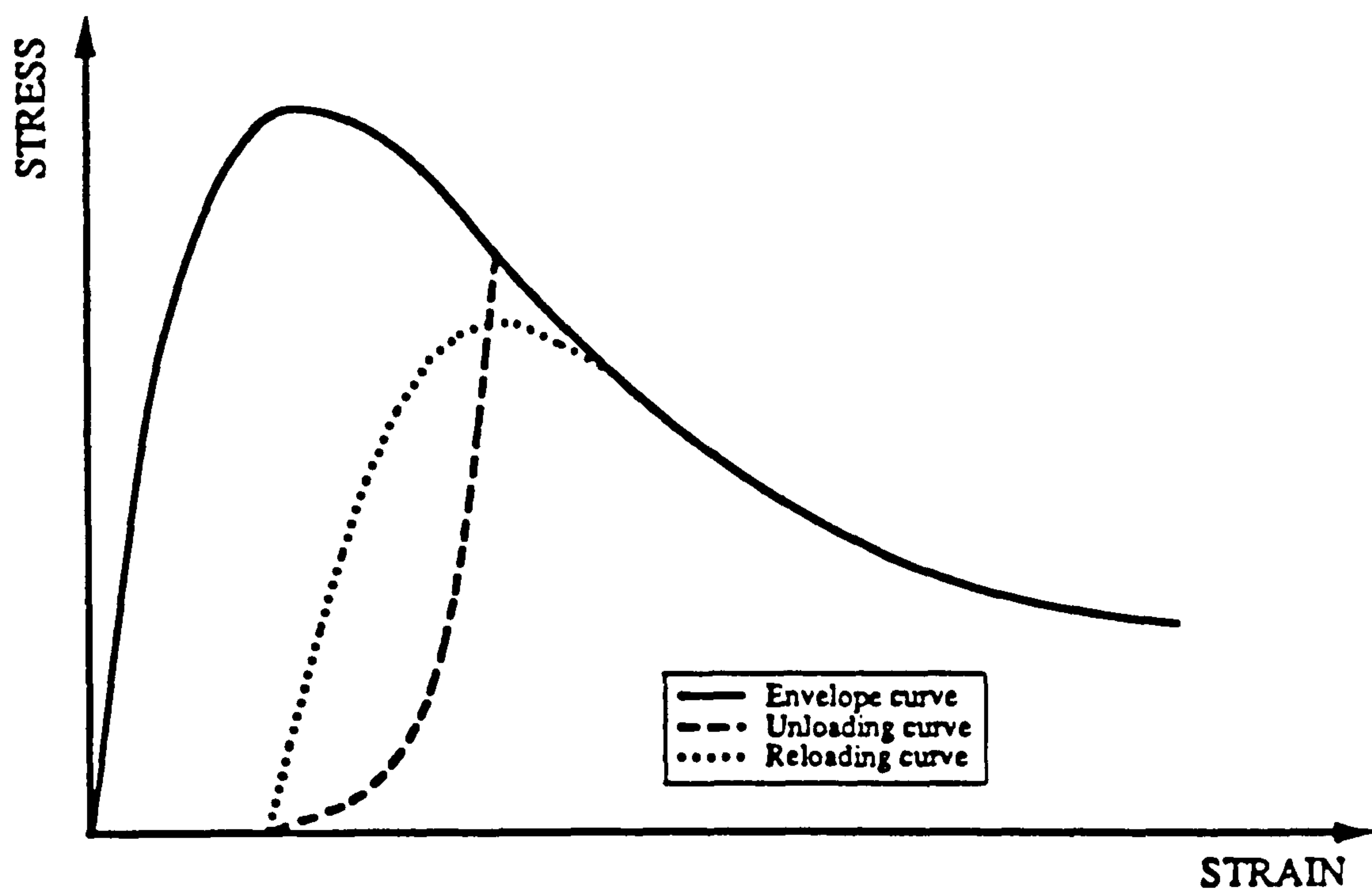


Fig. 7.9 Behaviour of concrete under cyclic loading (Madas and Elnashai, 1989)

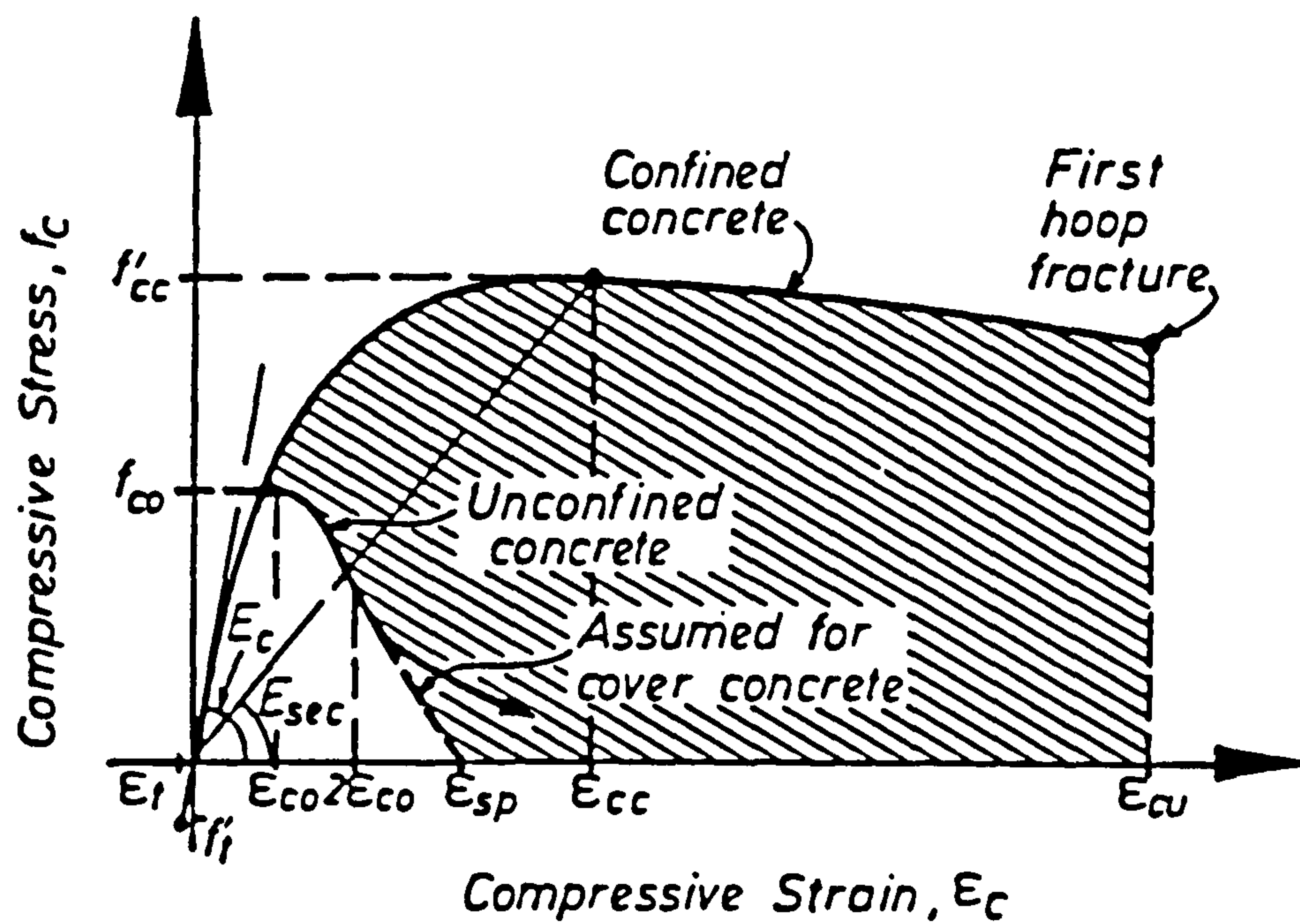


Fig. 7.10 Monotonic relationship proposed by Mander et al (1988)

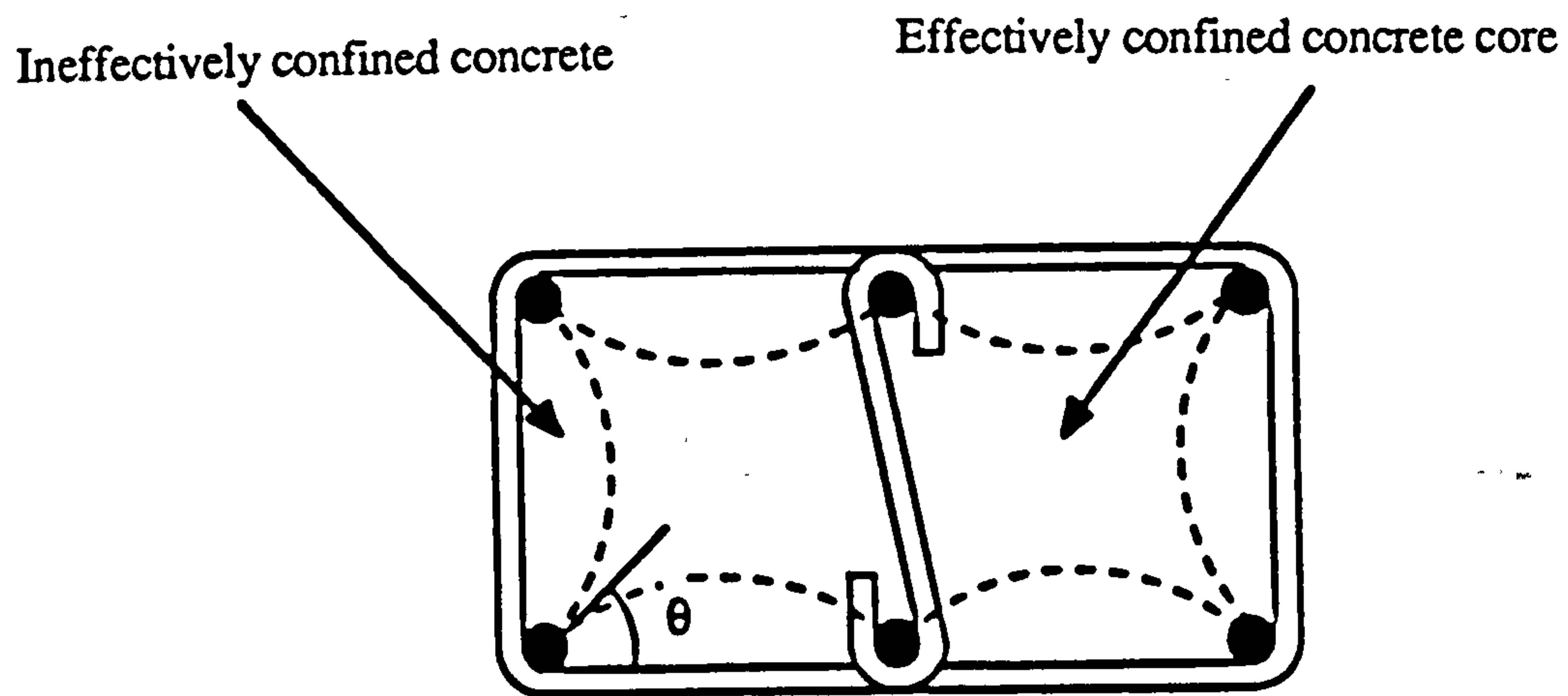


Fig. 7.11.a Effectively confined concrete core for a rectangular section (Mander et al 1988)

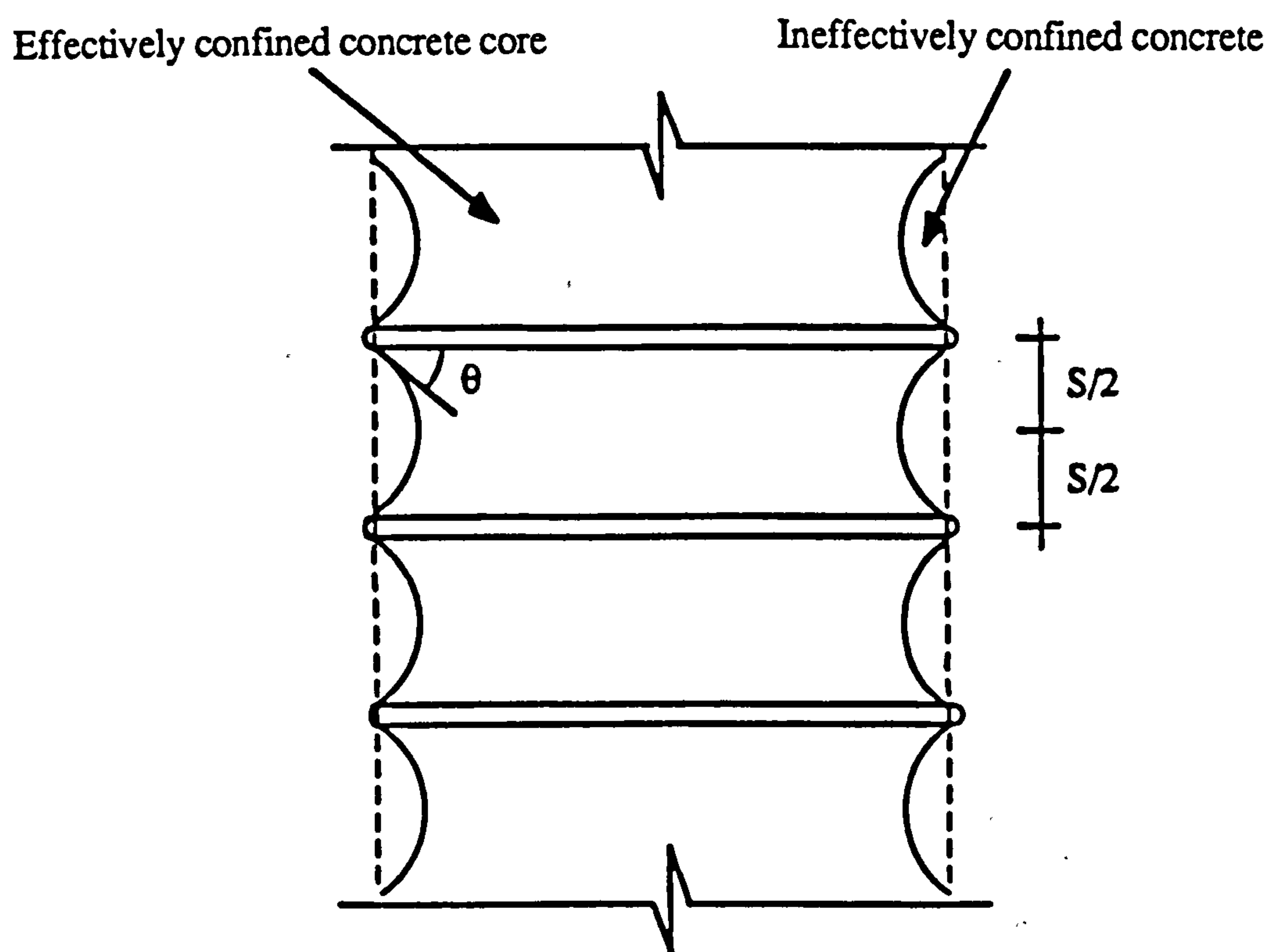


Fig. 7.11.b Confined concrete in the longitudinal direction (Mander et al 1988)

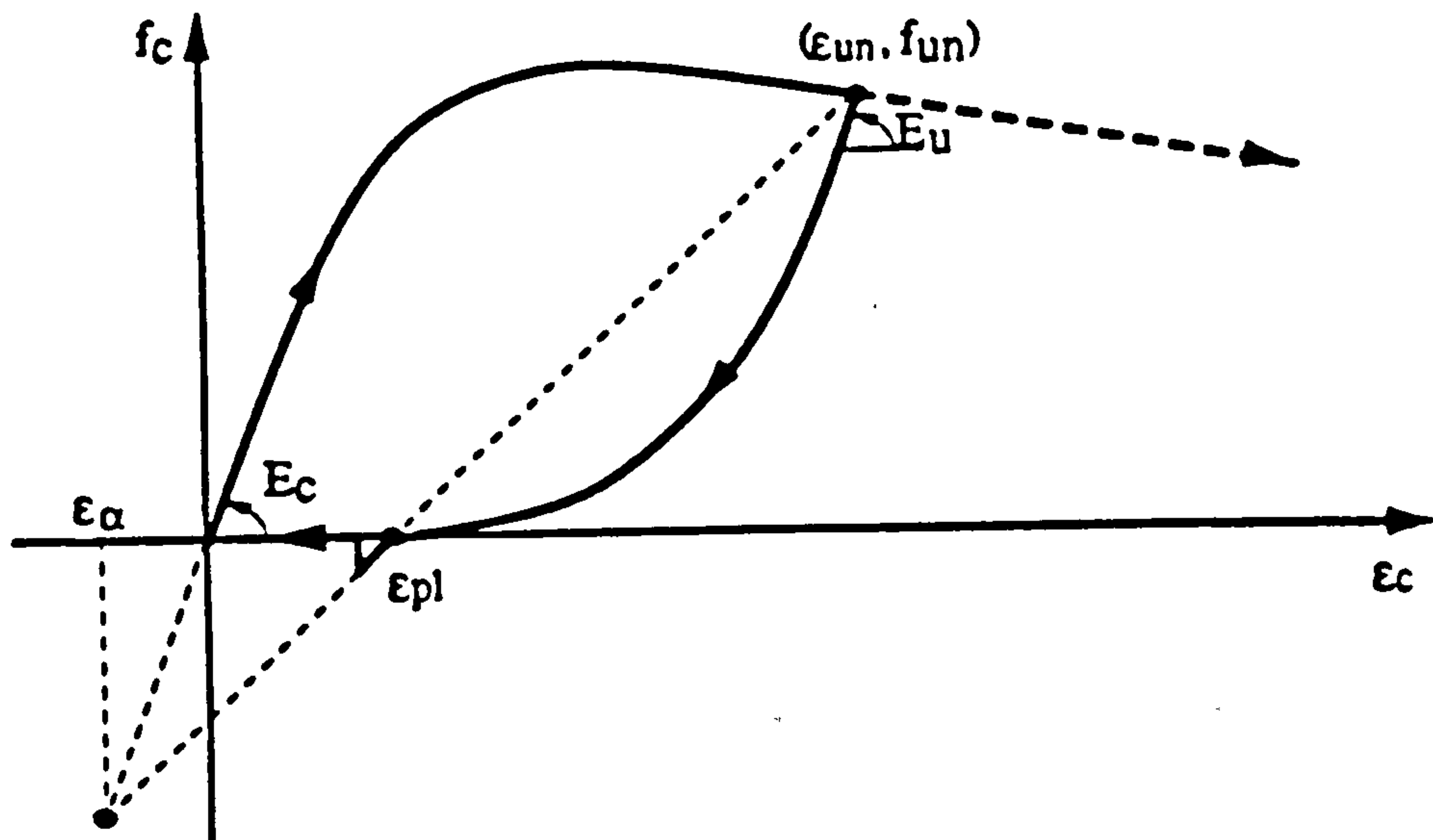


Fig. 7.12.a Stress-strain curve for unloading branch and determination of plastic strain (Madas and Elnashai, 1989)

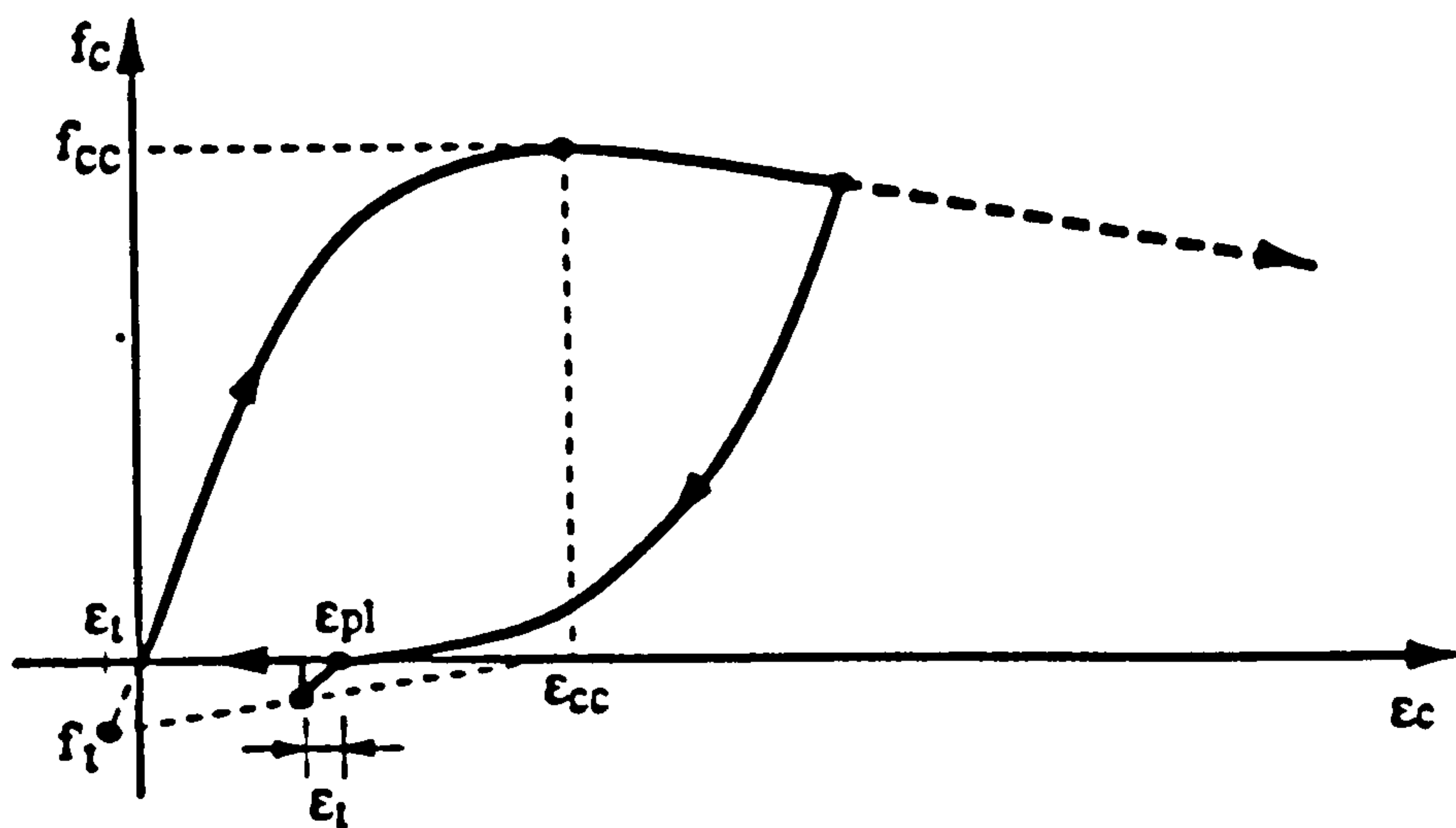


Fig. 7.12.b Assumed deterioration in tensile strength of concrete (Madas and Elnashai, 1989)

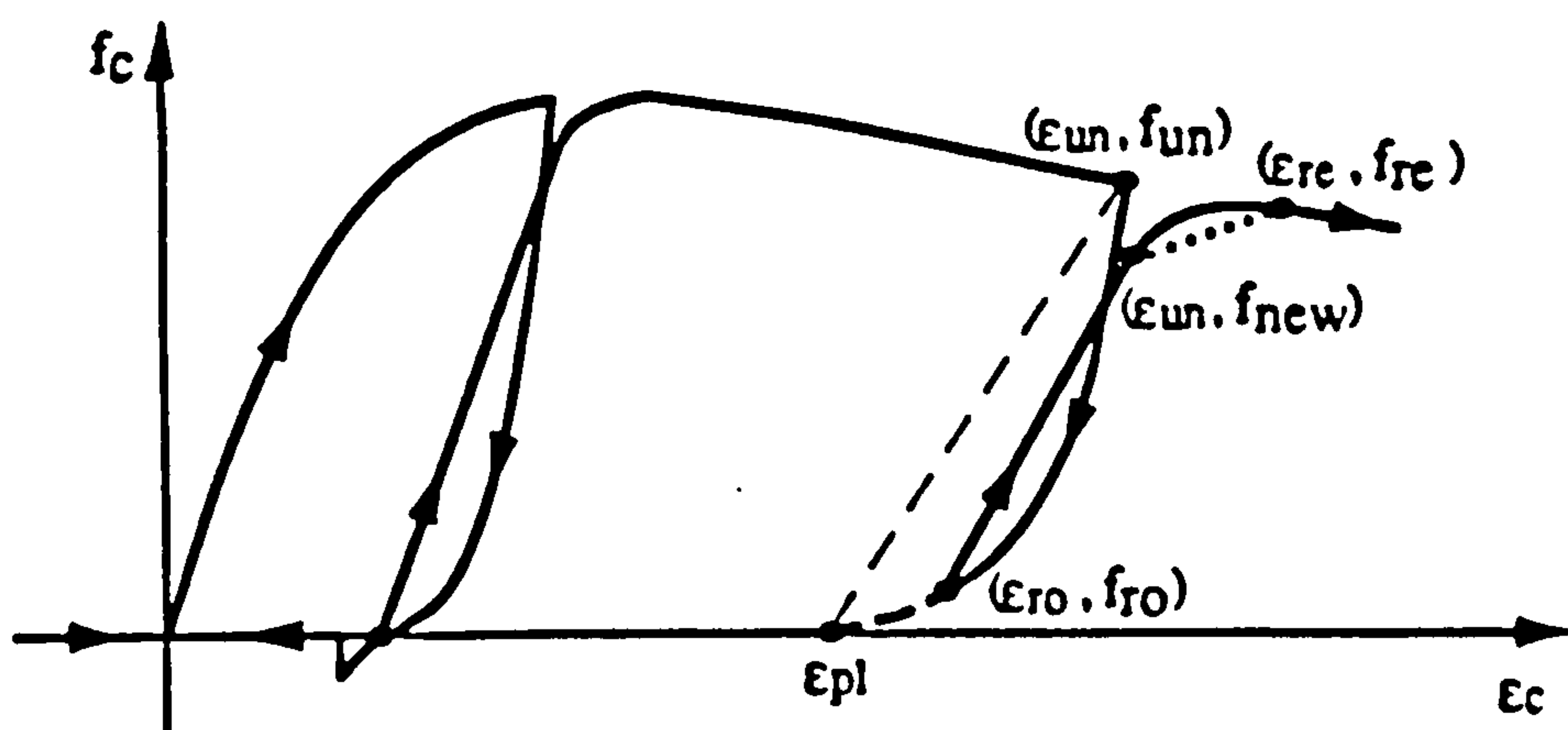


Fig. 7.12.c Stress-strain curves for reloading branch (Madas and Elnashai, 1989)

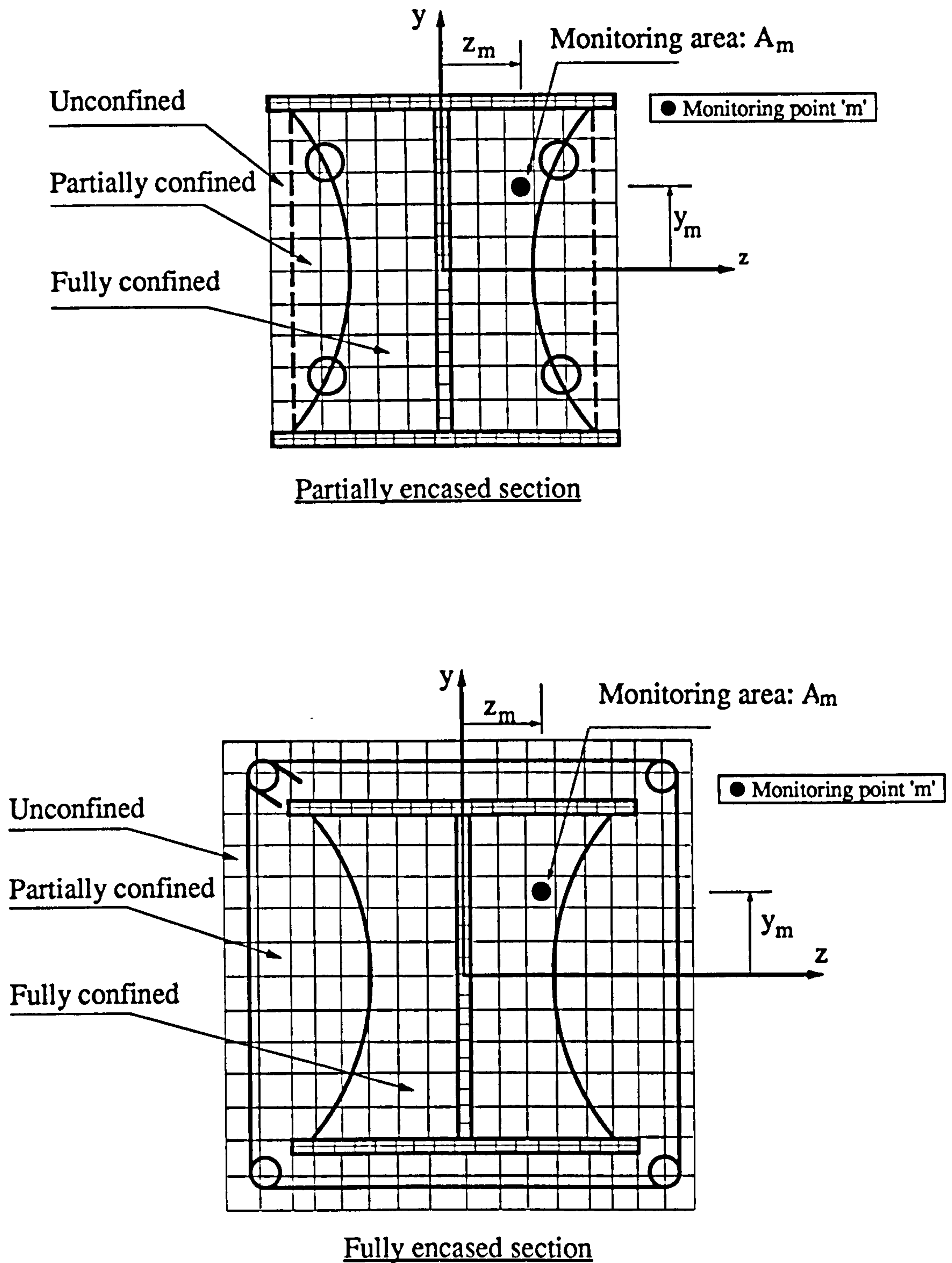


Fig. 7.13 Confinement zones and distribution of monitoring points for composite sections

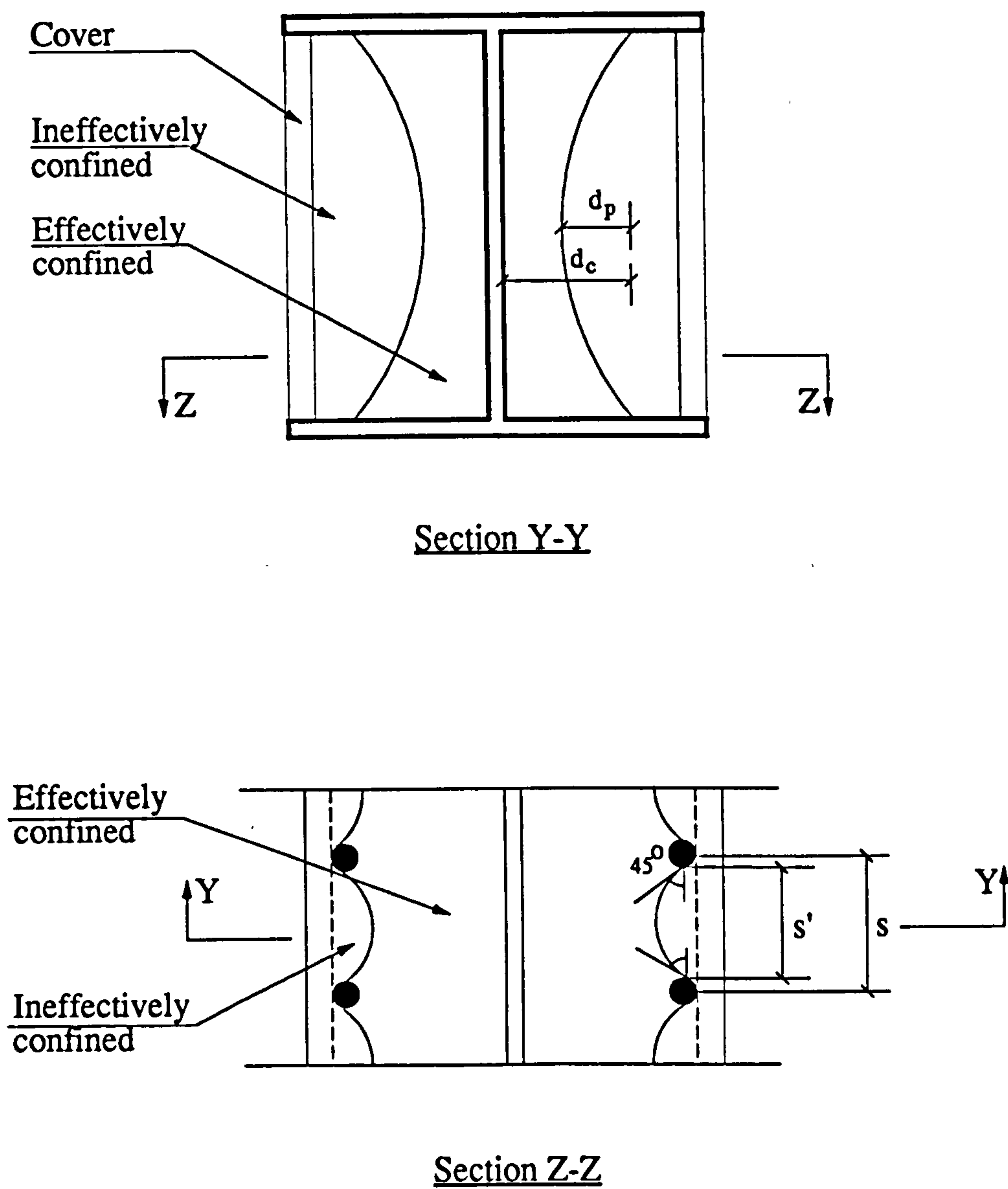


Fig. 7.14 Effectively confined core for partially encased members

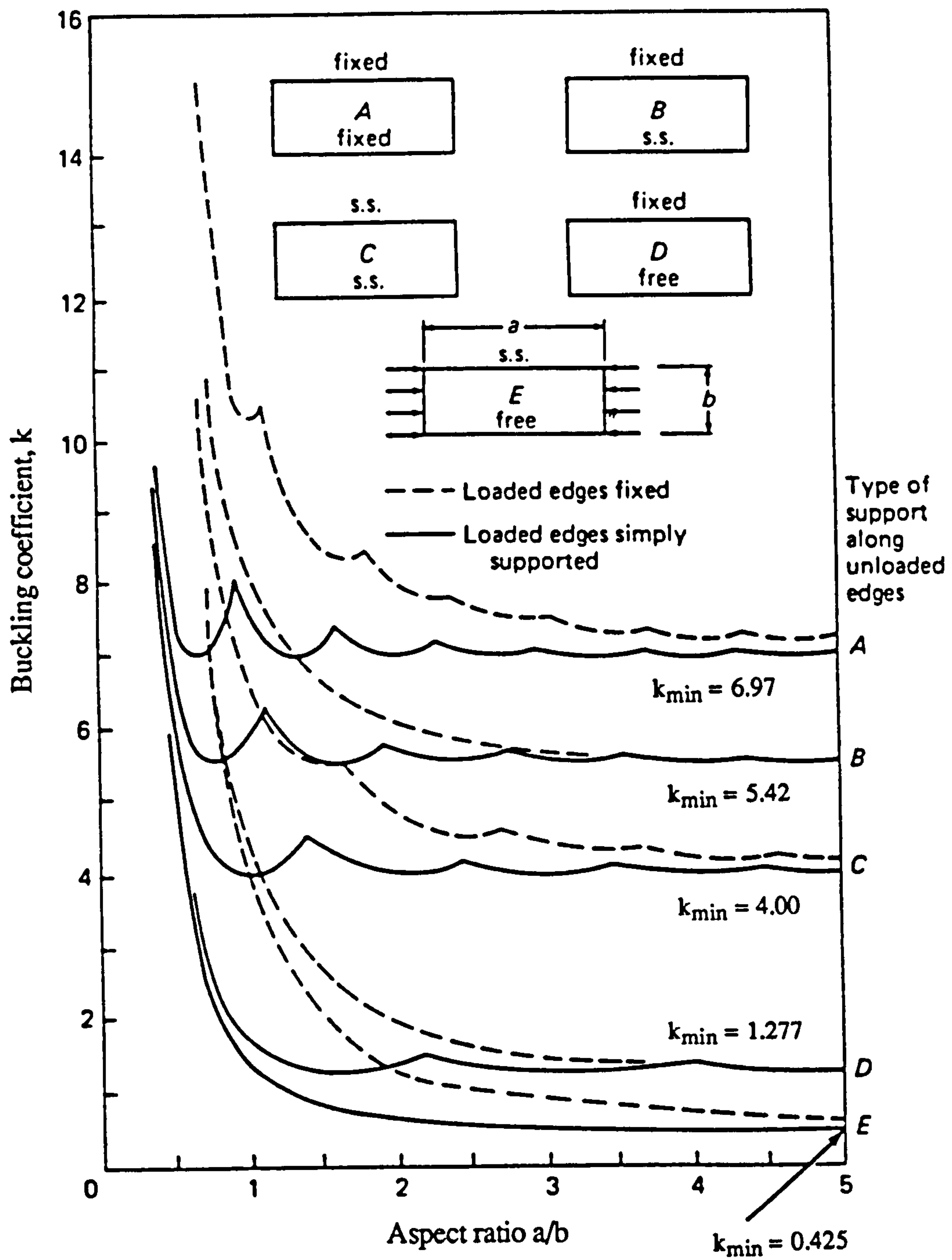


Fig. 7.15 Elastic buckling coefficients for compression in flat rectangular plates (Salmon and Johnson, 1980)

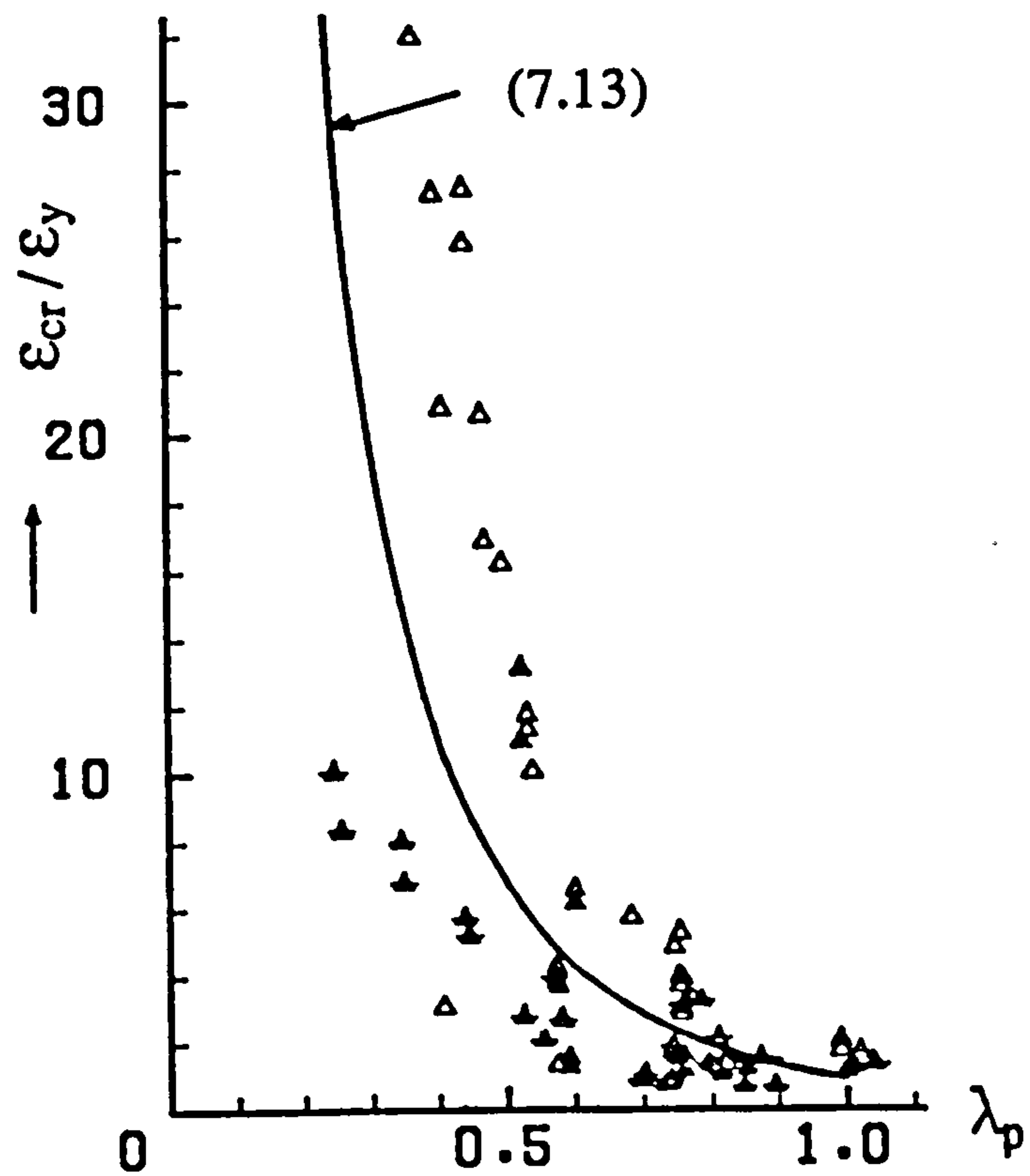


Fig. 7.16 Maximum non-dimensional edge strains at ultimate strength of flange outstands of I-shaped sections (Fukumoto and Itoh, 1984)

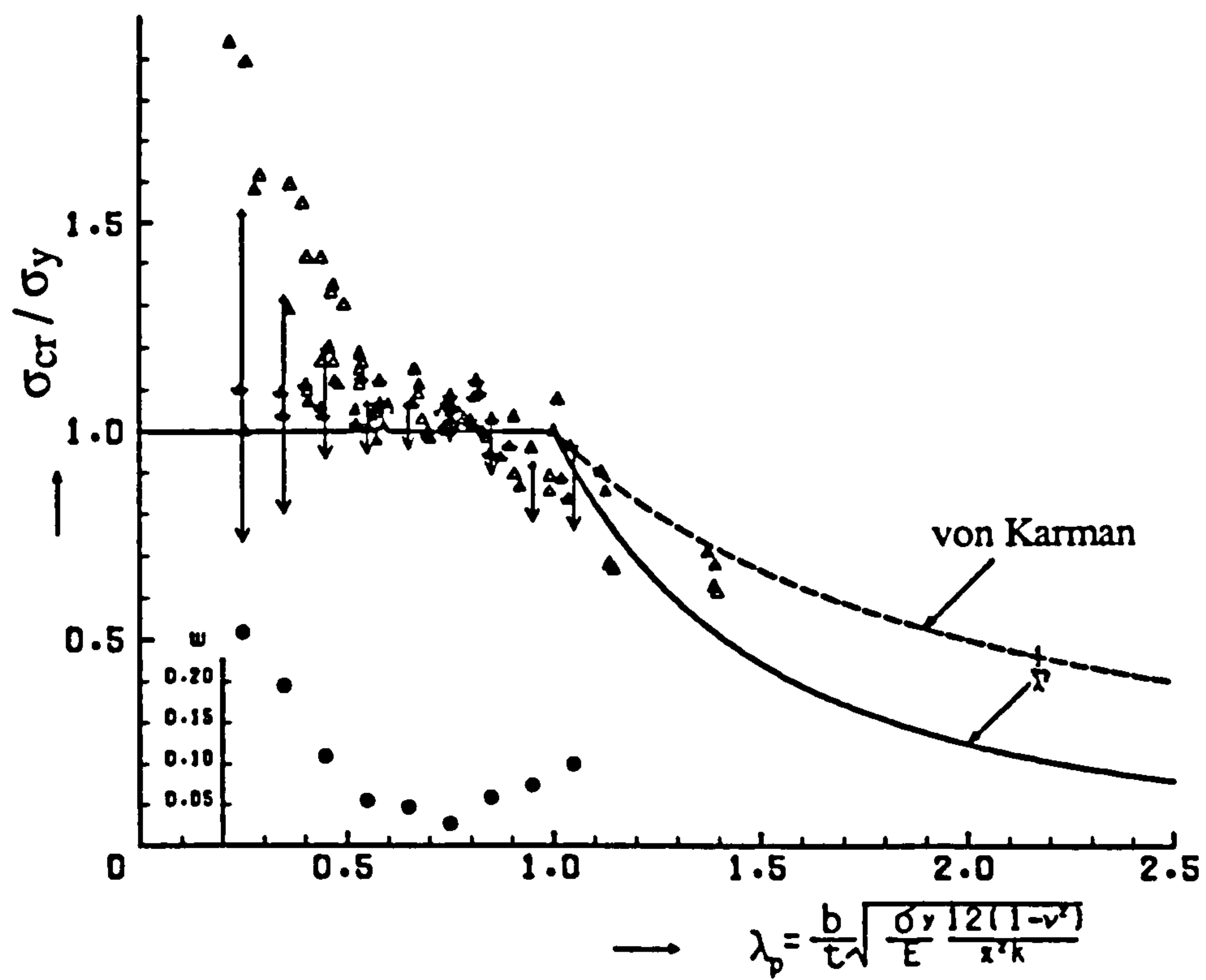


Fig. 7.17 Maximum non-dimensional stress for flange outstands (Fukumoto and Itoh, 1984)

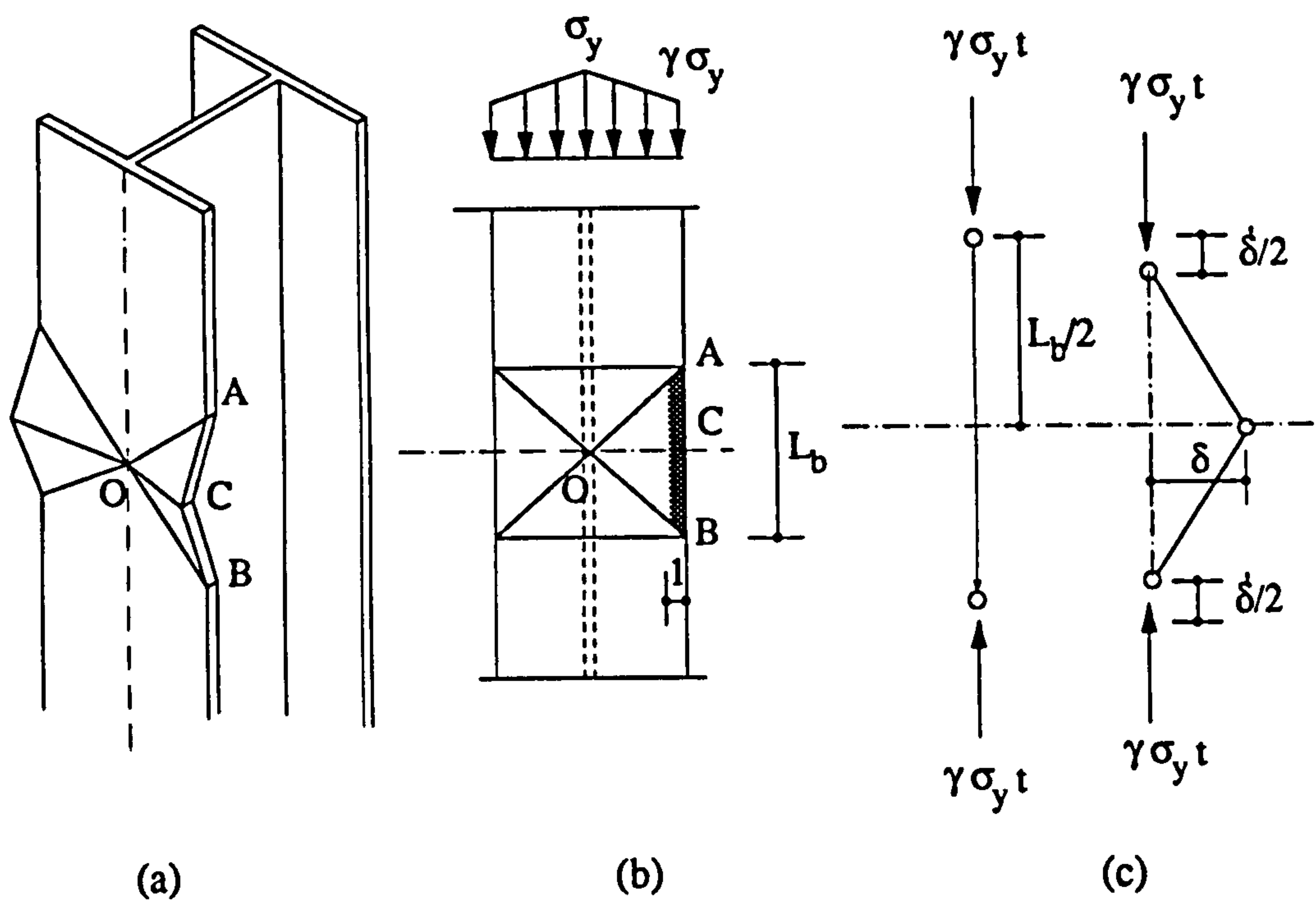


Fig. 7.18 Assumed mechanism of local flange buckling (Morino et al, 1986)

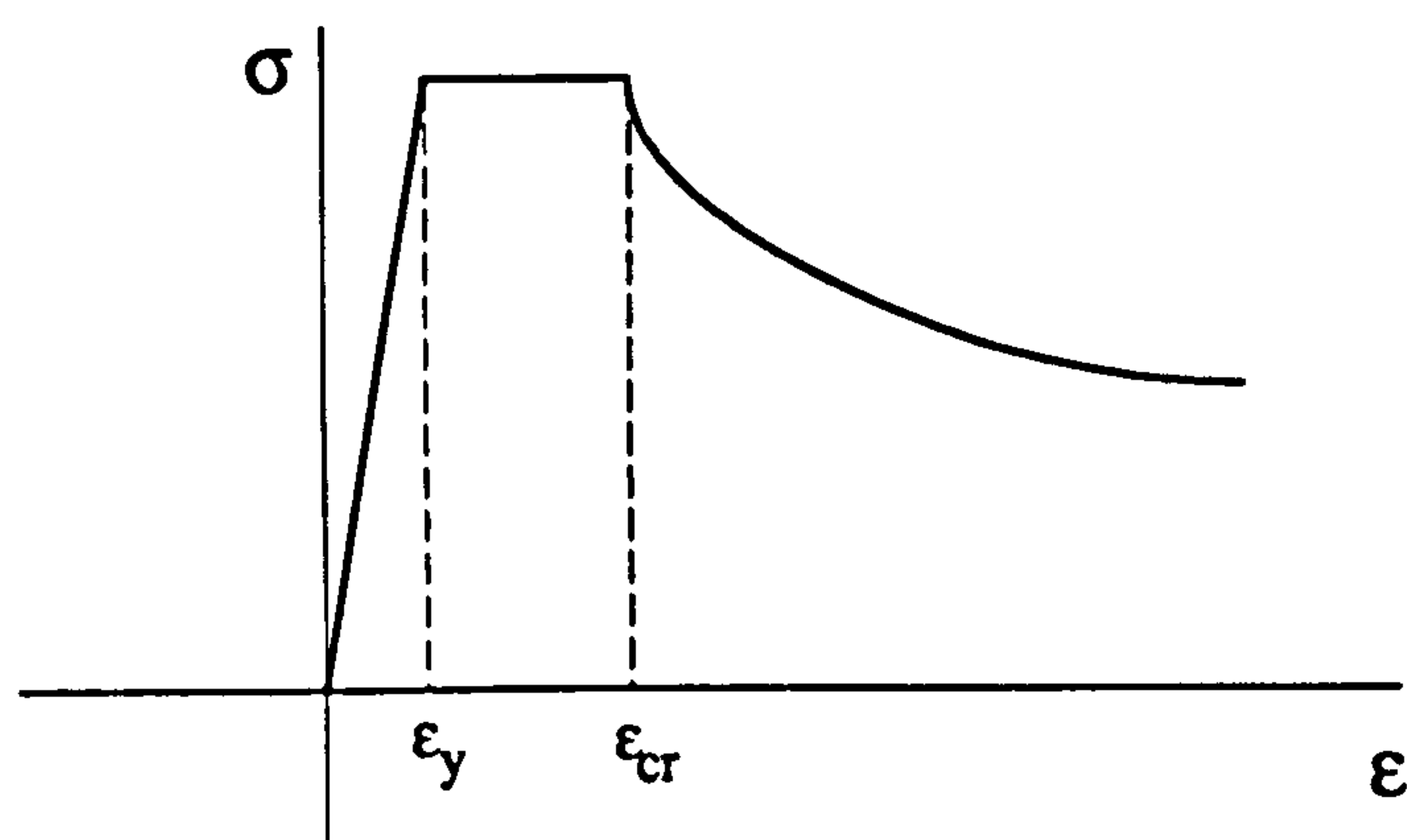


Fig. 7.19 Stress-strain relationship for flange including local buckling (Morino et al, 1986)

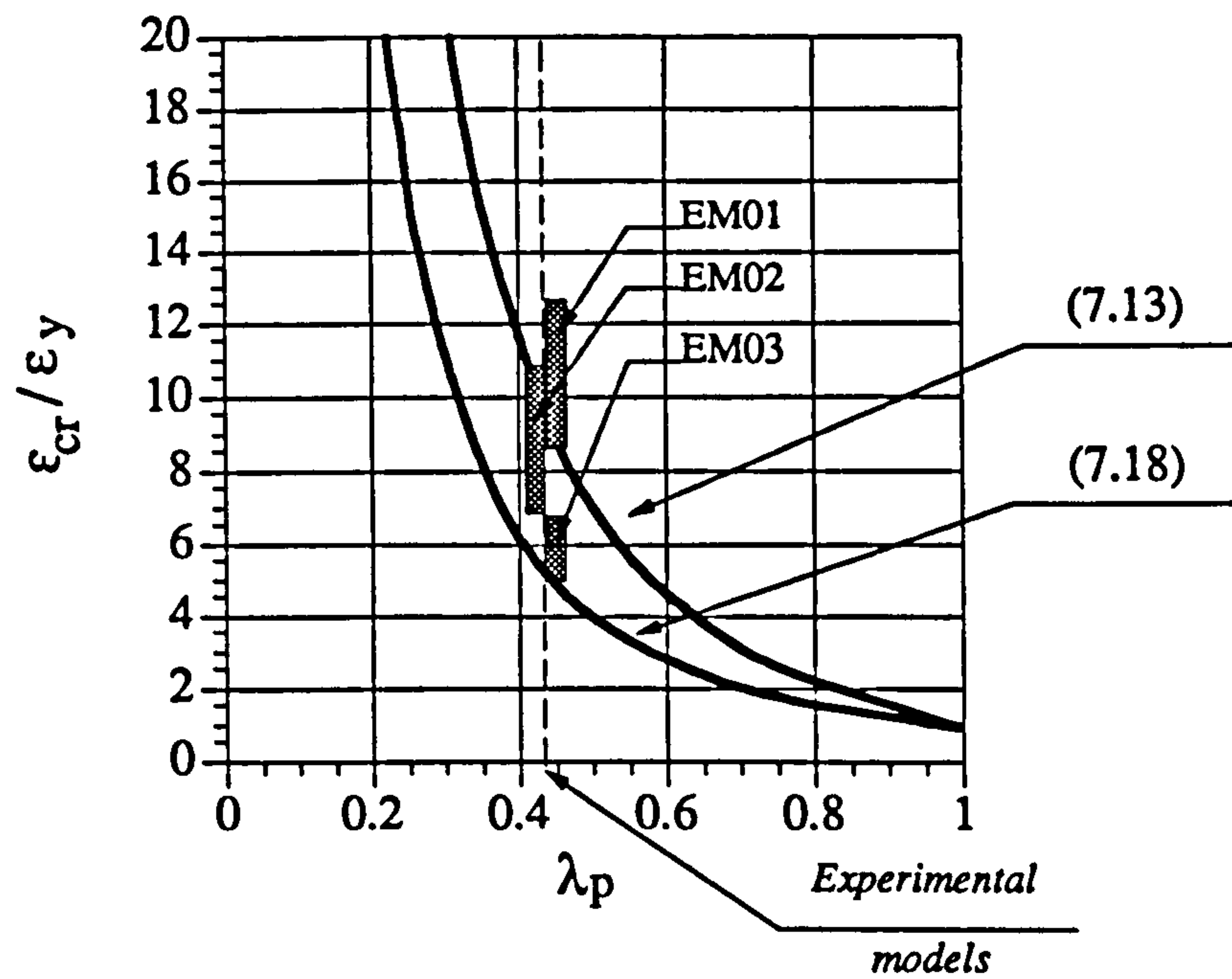


Fig. 7.20 Relationship between the normalised critical strain and slenderness

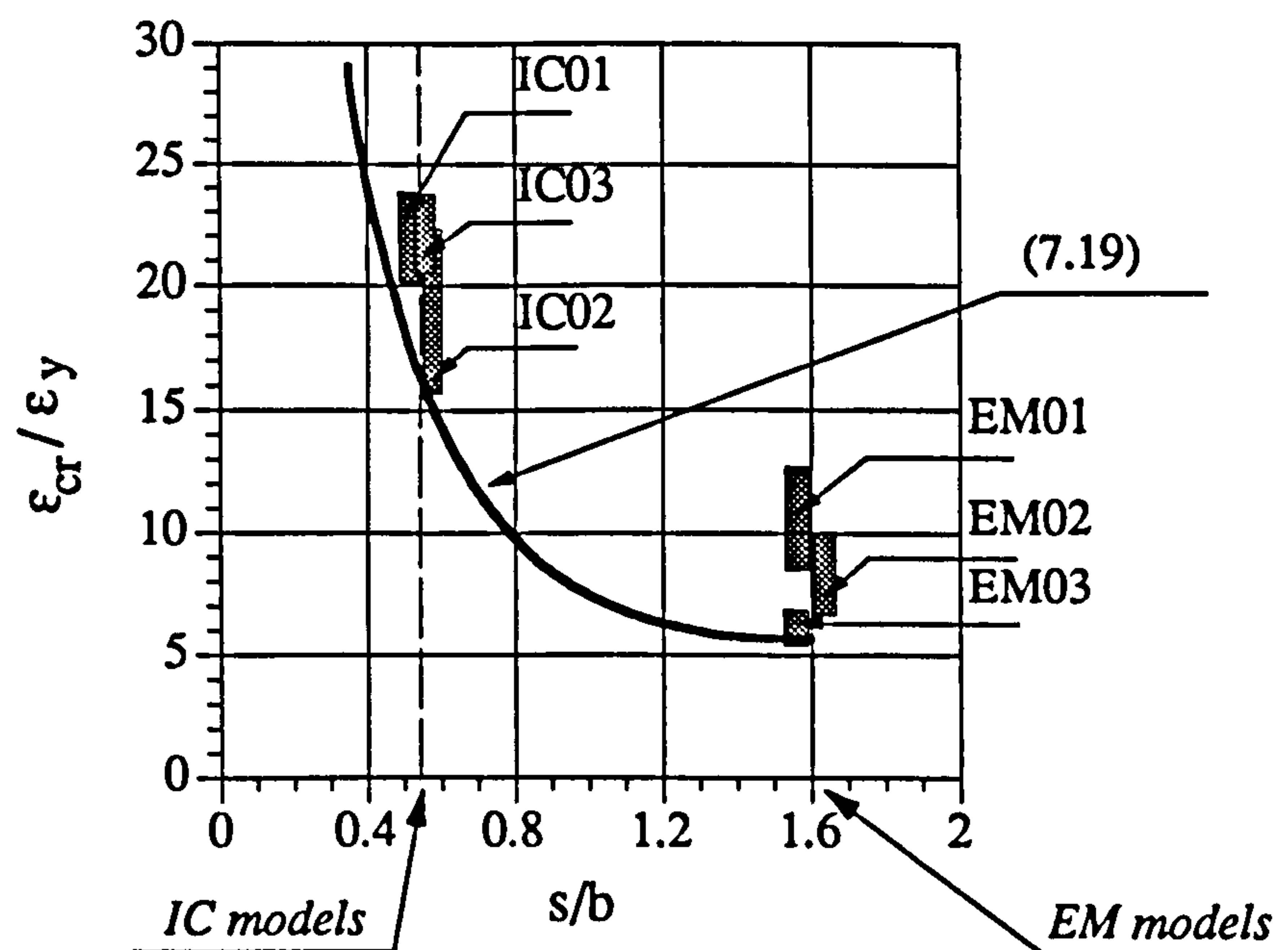
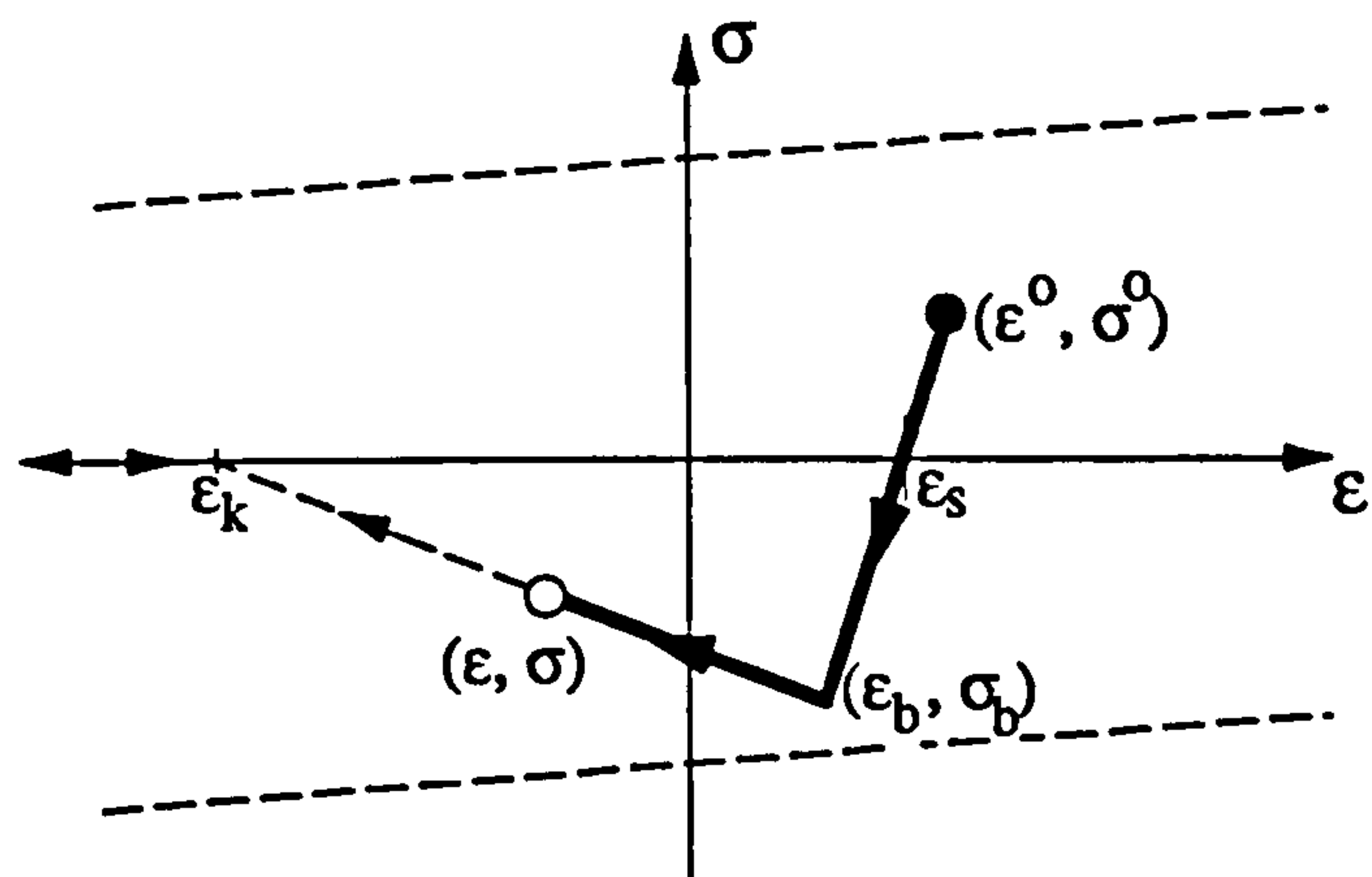
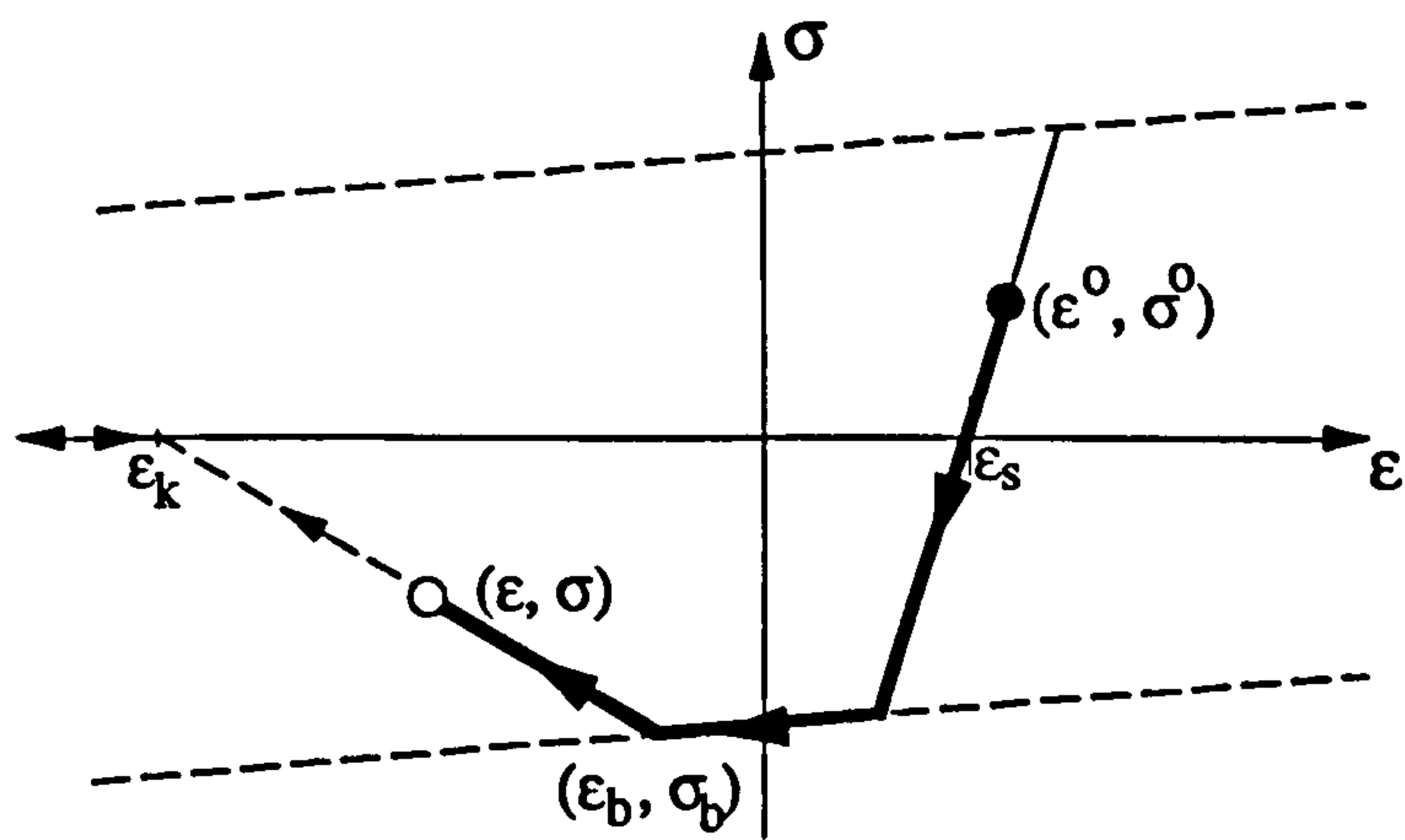


Fig. 7.21 Relationship between the normalised critical strain and the normalised spacing of the bars

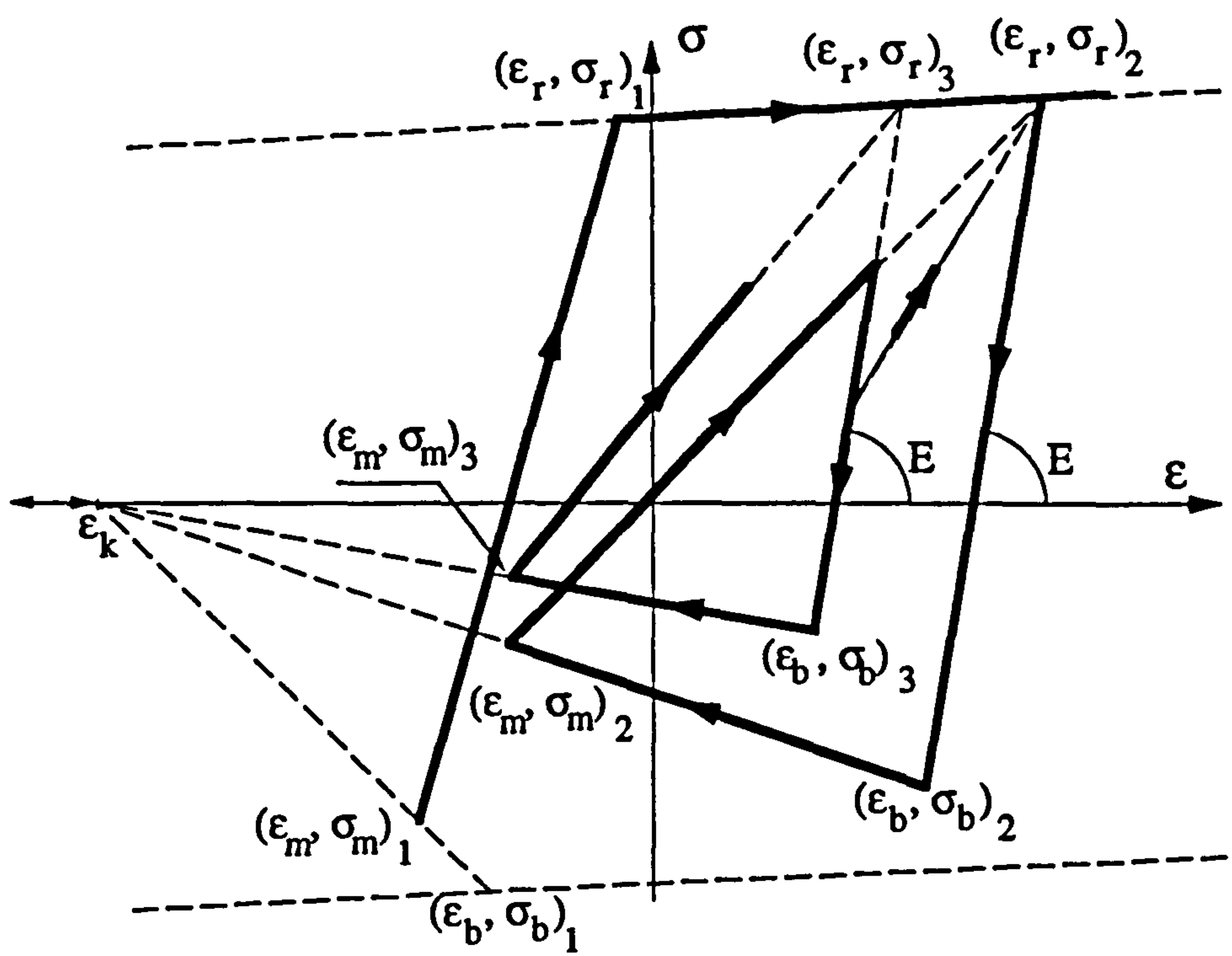


Initial elastic buckling

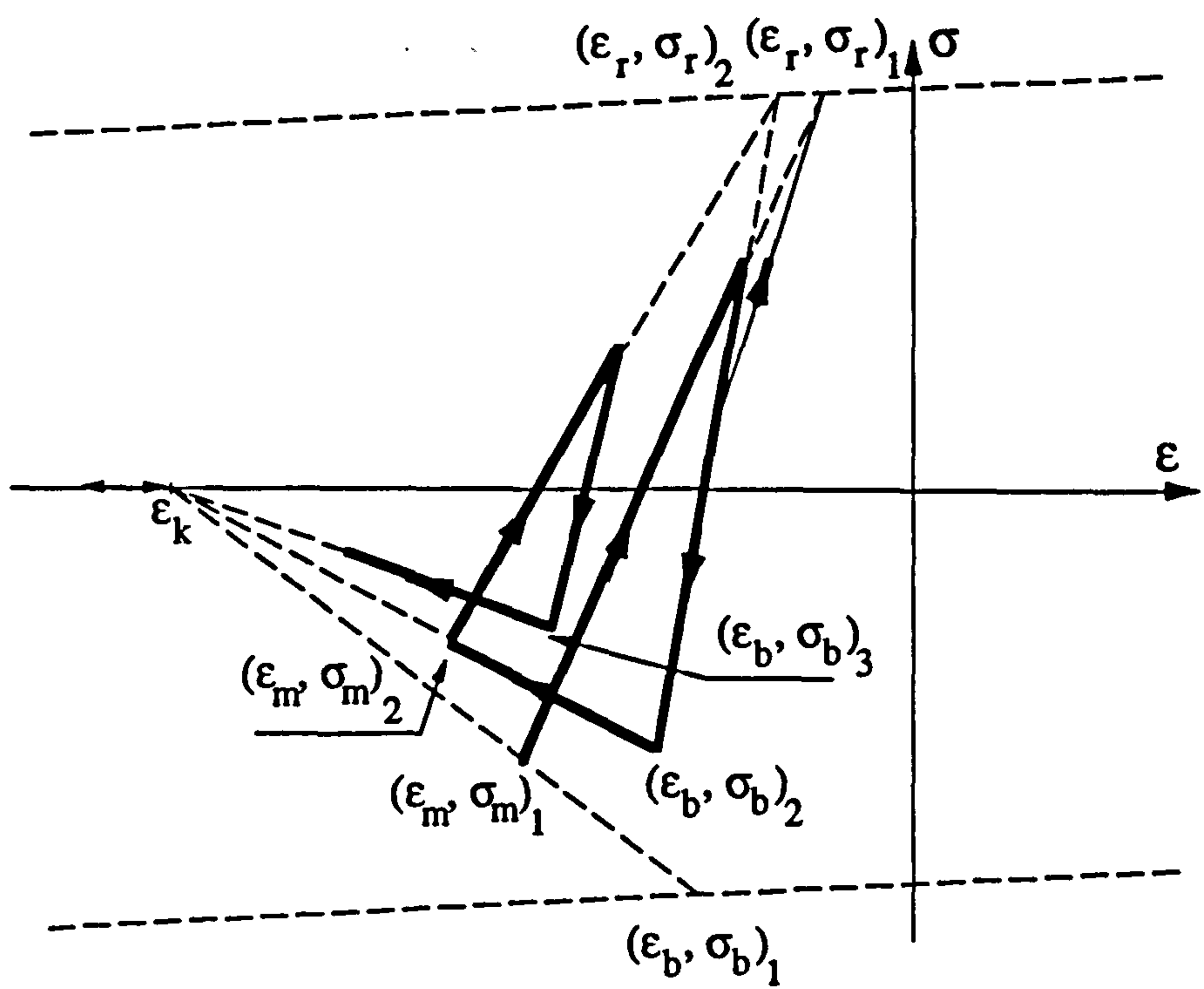


Initial inelastic buckling

Fig. 7.22 Stress determination following initial local buckling



Case A



Case B

Fig. 7.23 Loading and unloading paths following initial local buckling

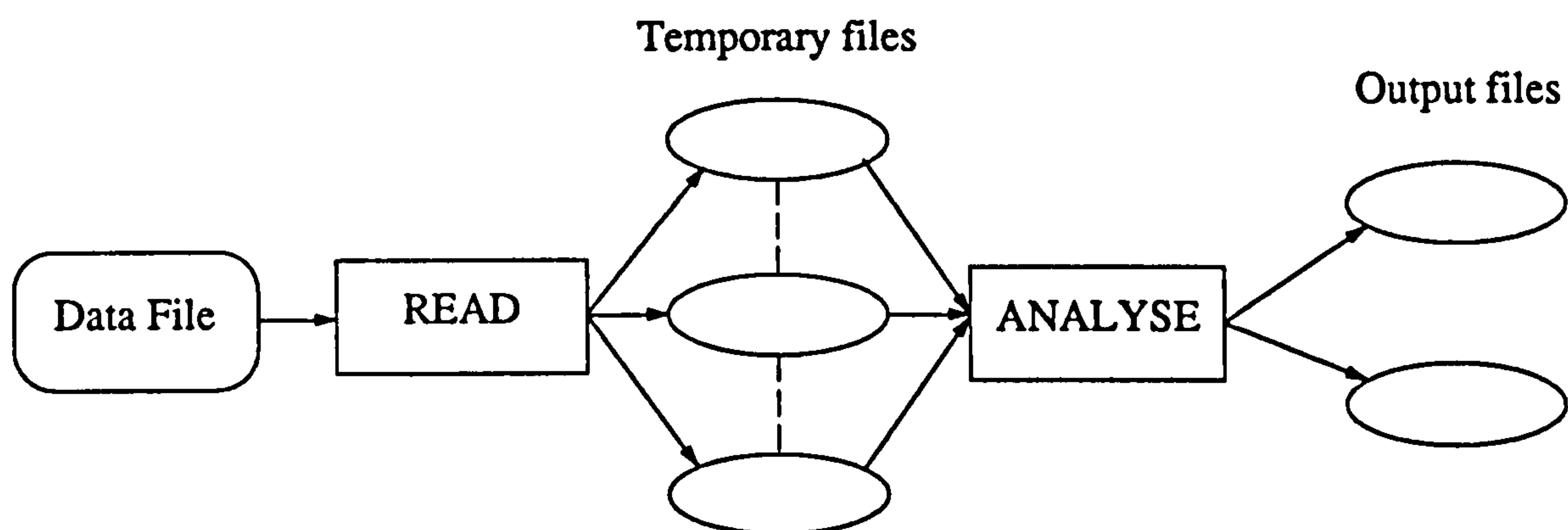


Fig. 7.24 Structure of 'ADAPTIC'

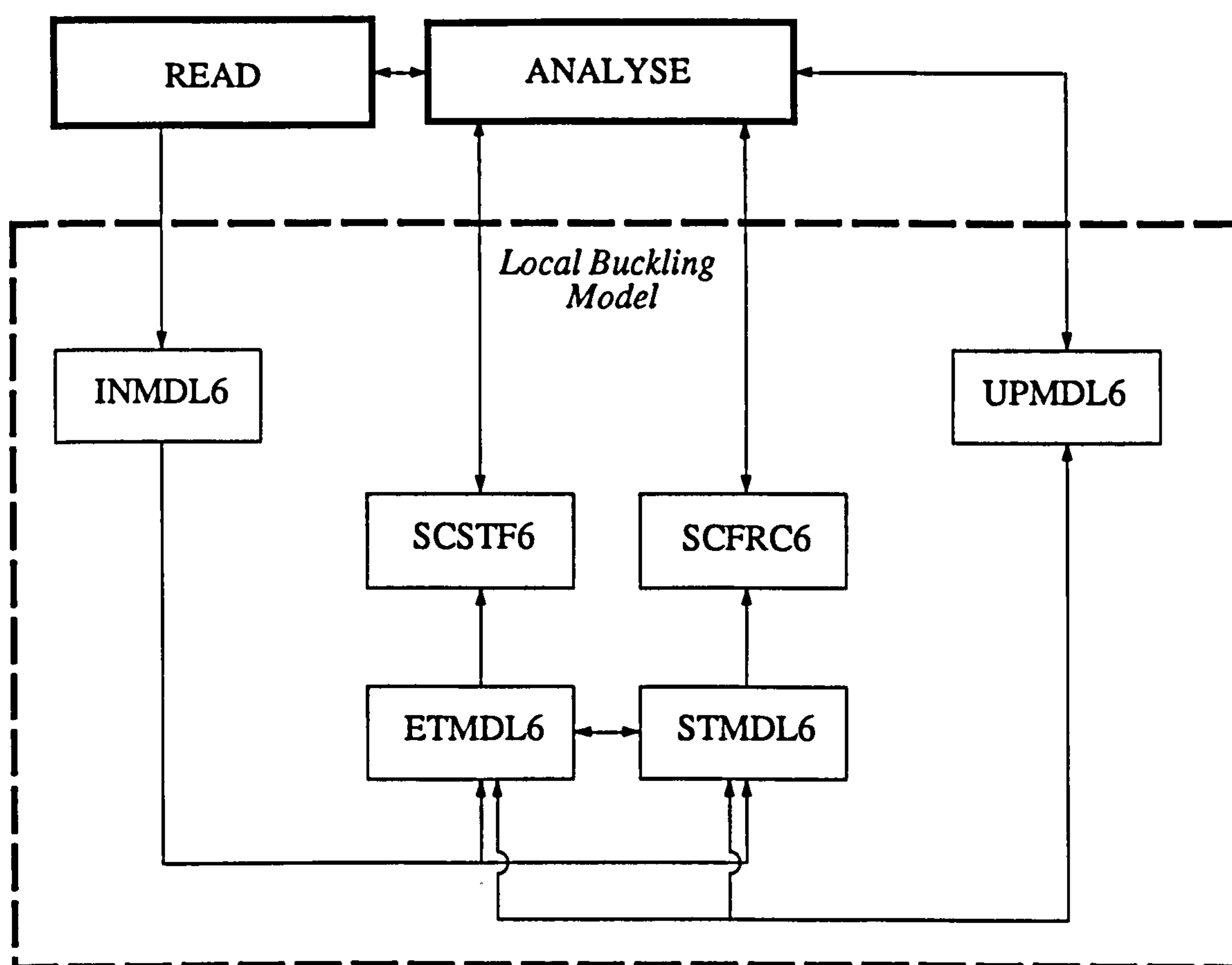


Fig. 7.25 Implementation of the local buckling model within 'ADAPTIC'

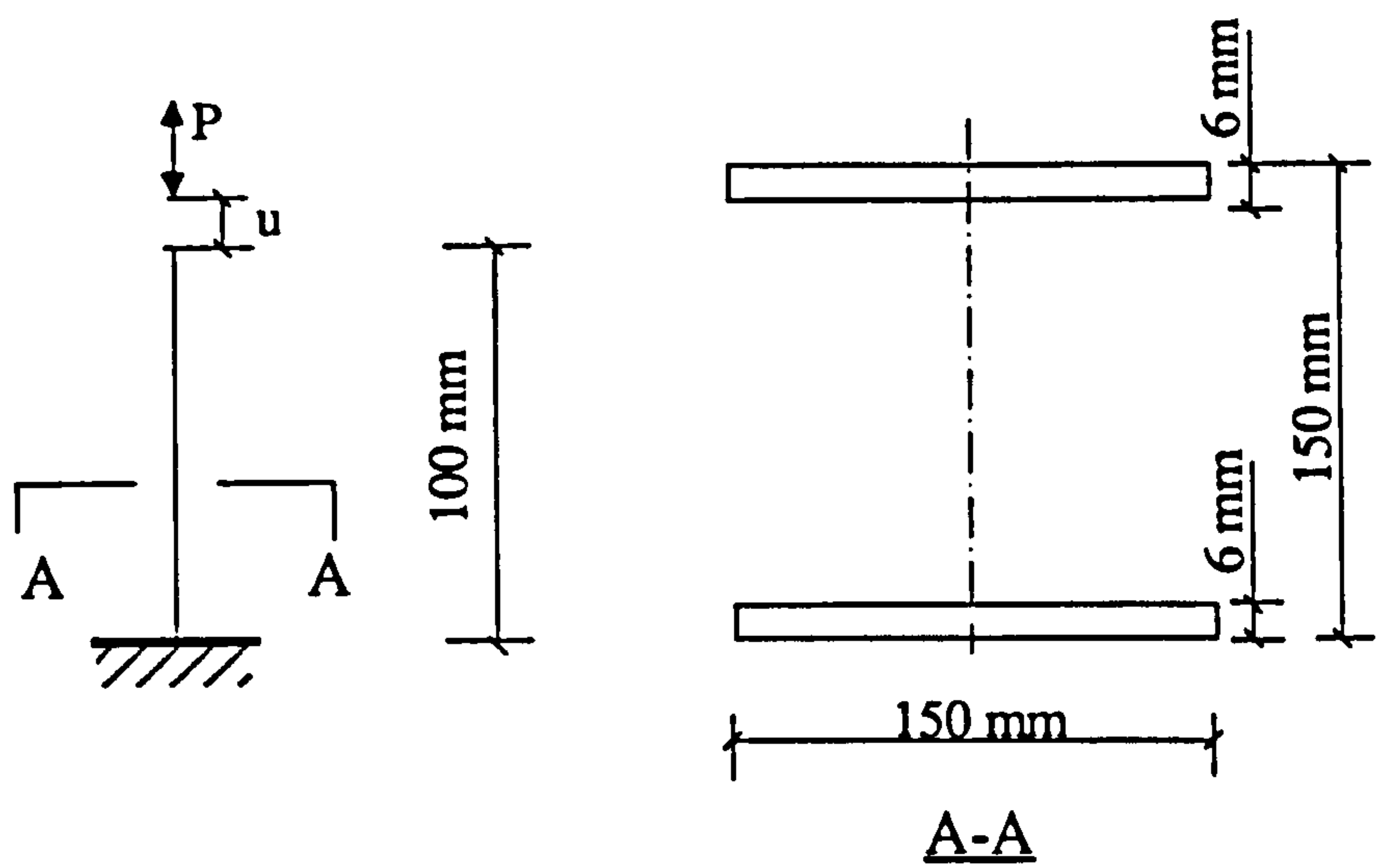


Fig. 7.26 Details of the axially loaded member

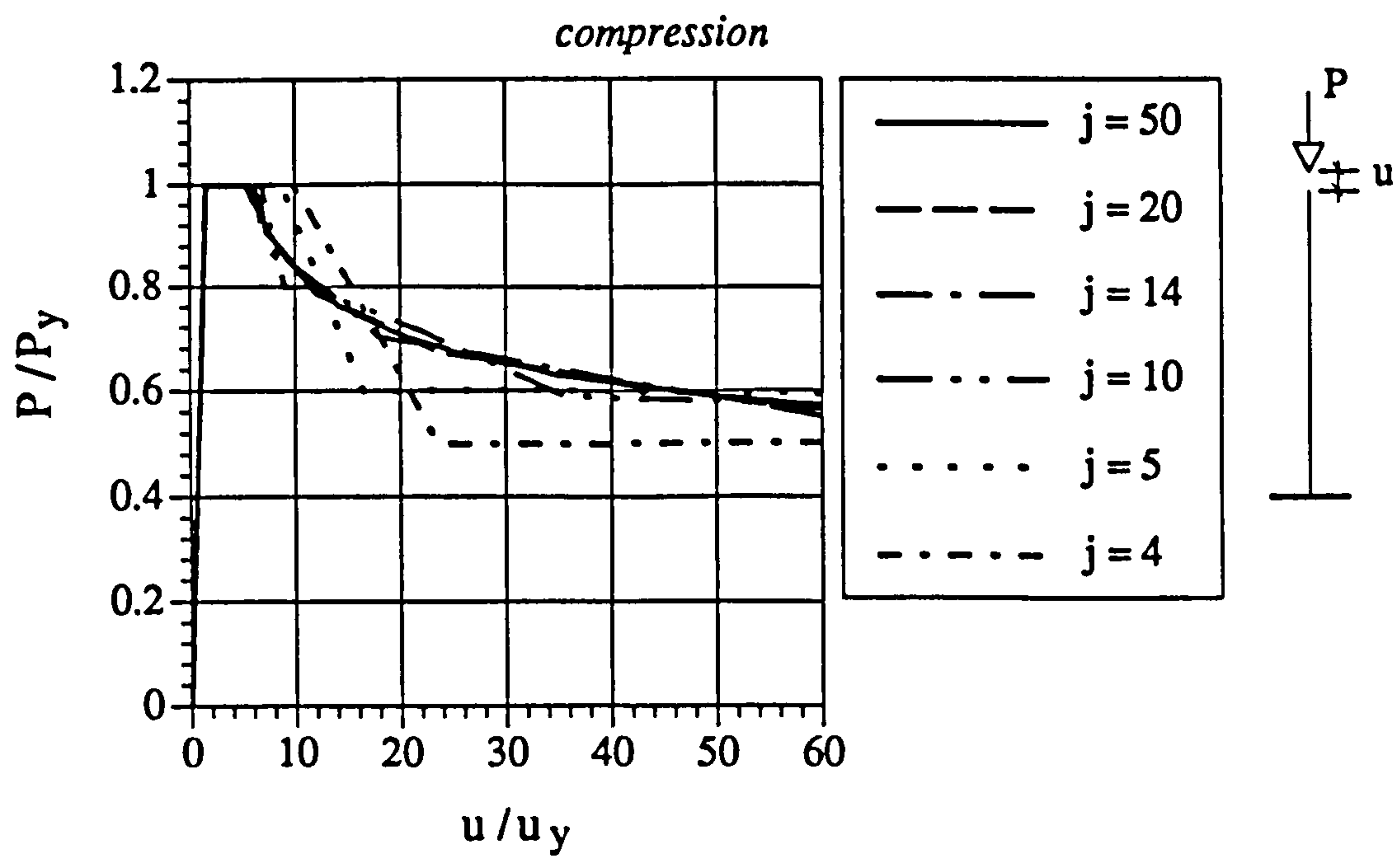


Fig. 7.27 Cyclic response of the flange for different numbers of monitoring points

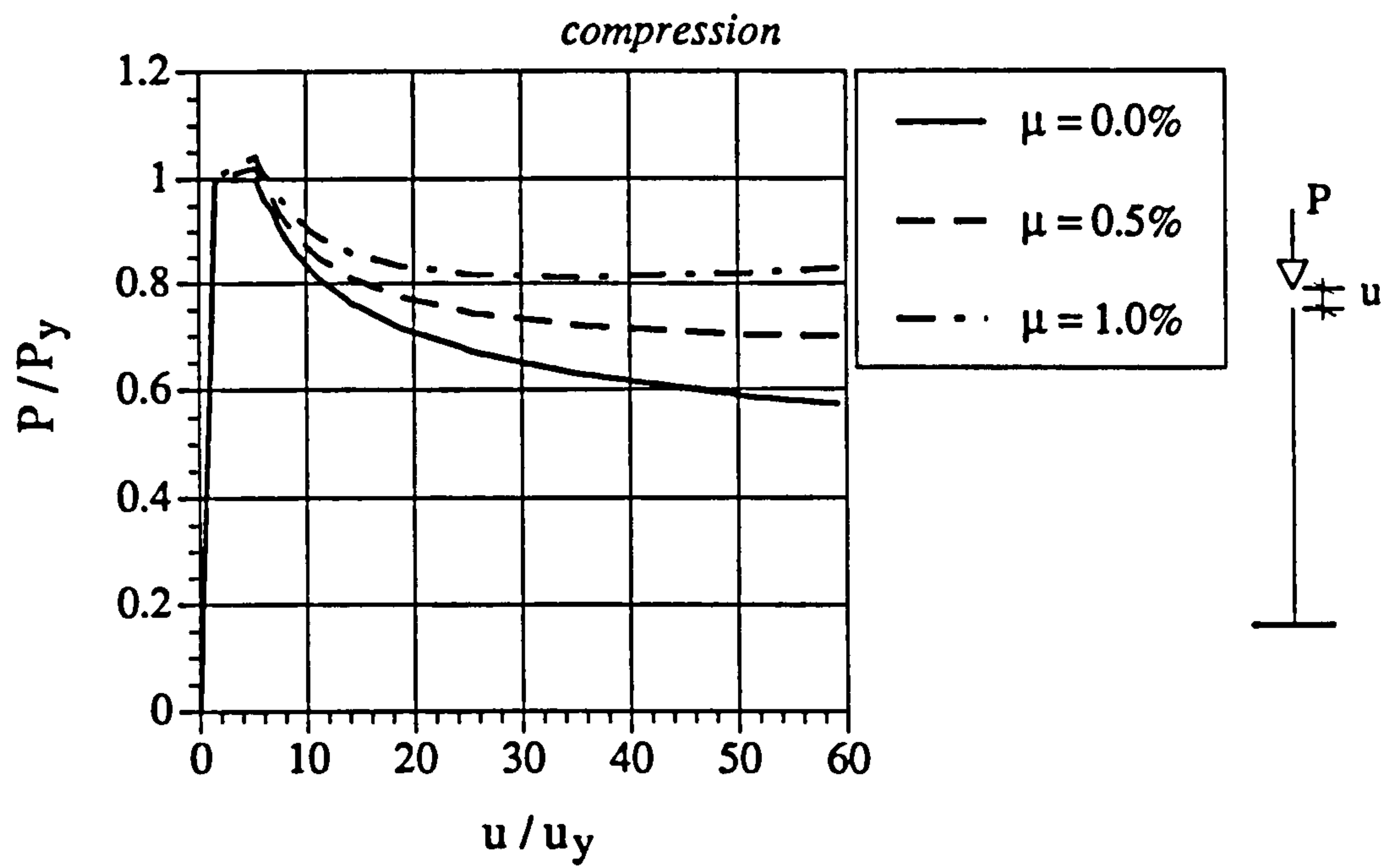


Fig. 7.28 Monotonic response for different values of strain hardening

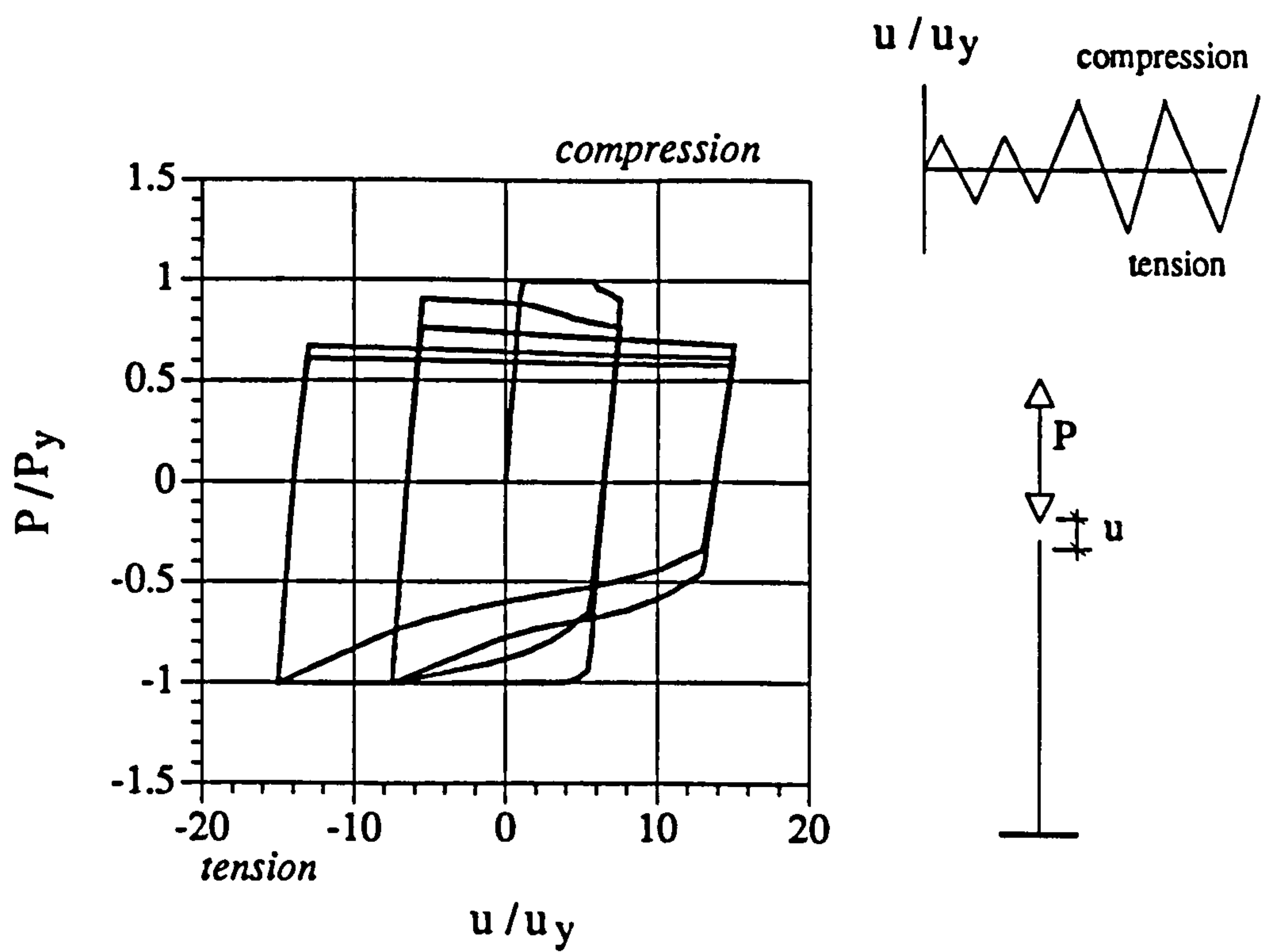


Fig. 7.29 Cyclic response of the flange for zero strain hardening

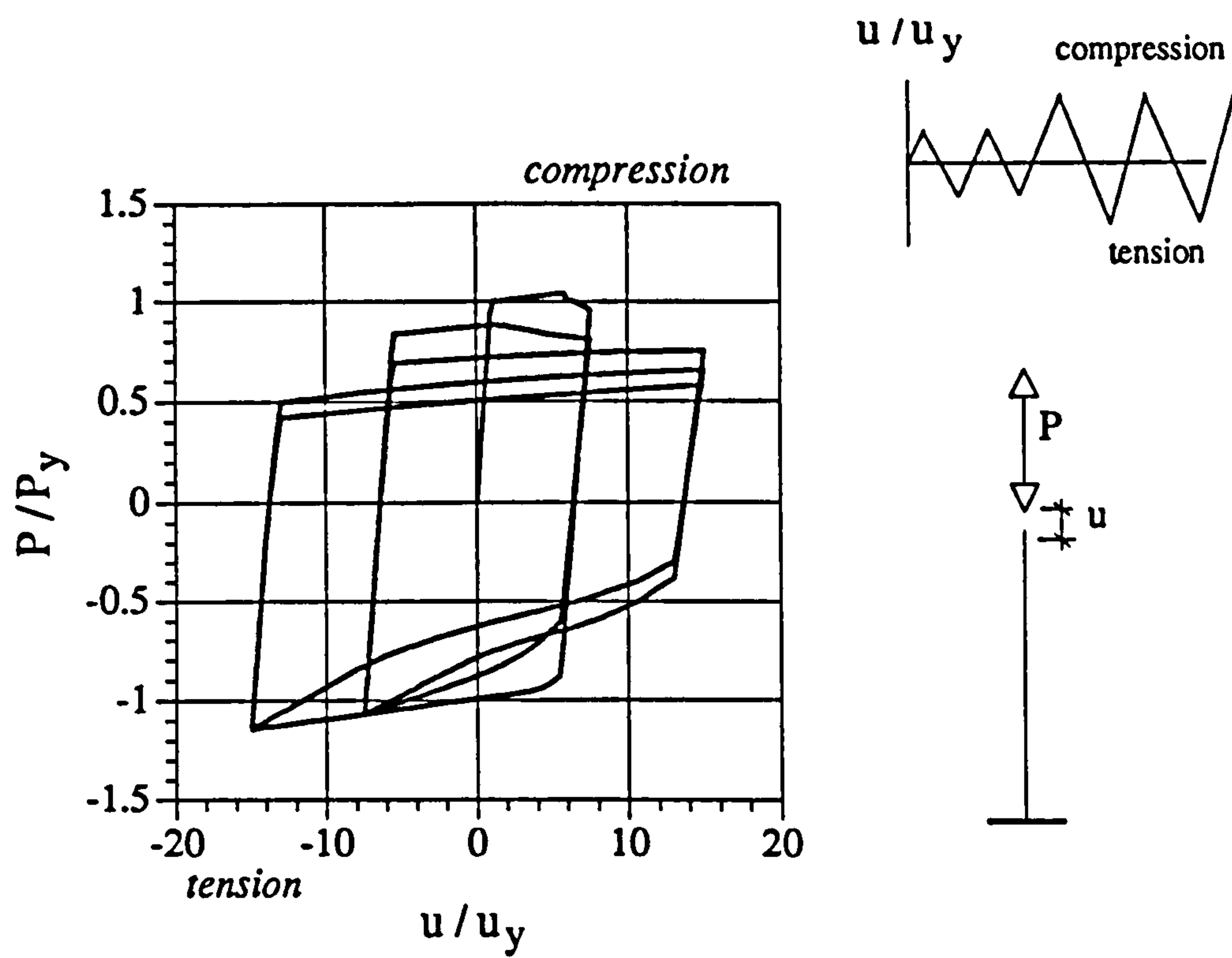


Fig. 7.30 Cyclic reponse of the flange for 1% strain hardening

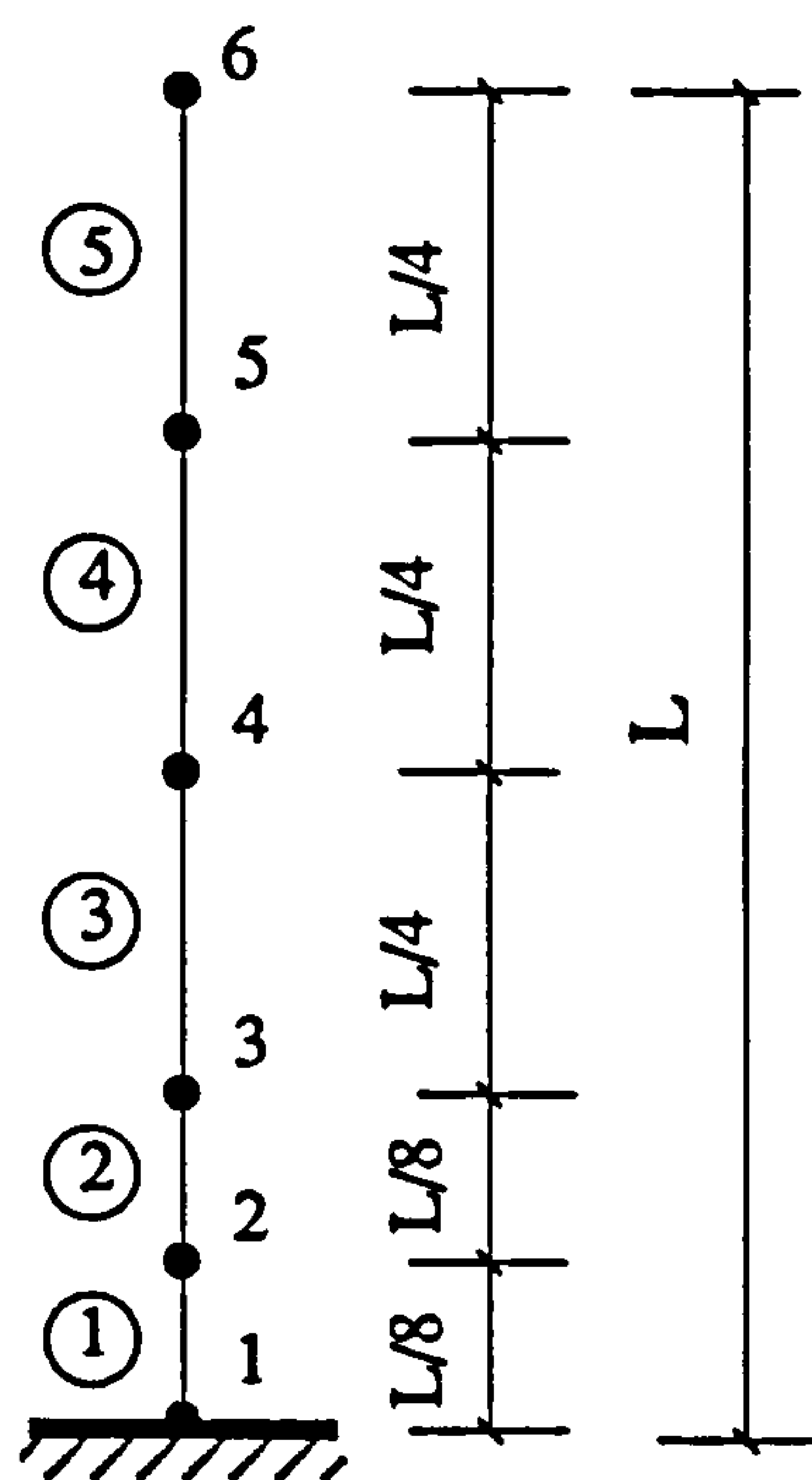
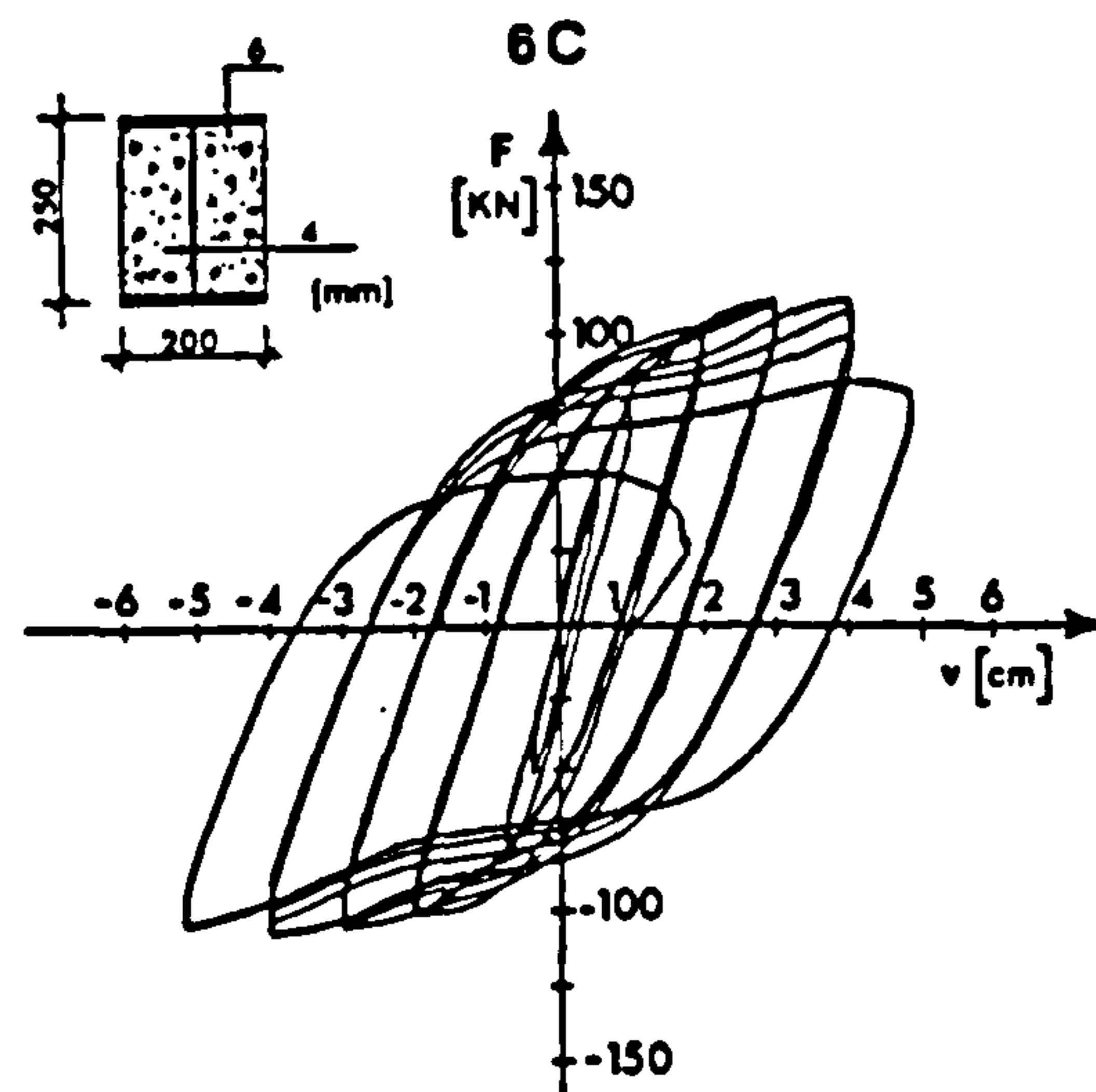
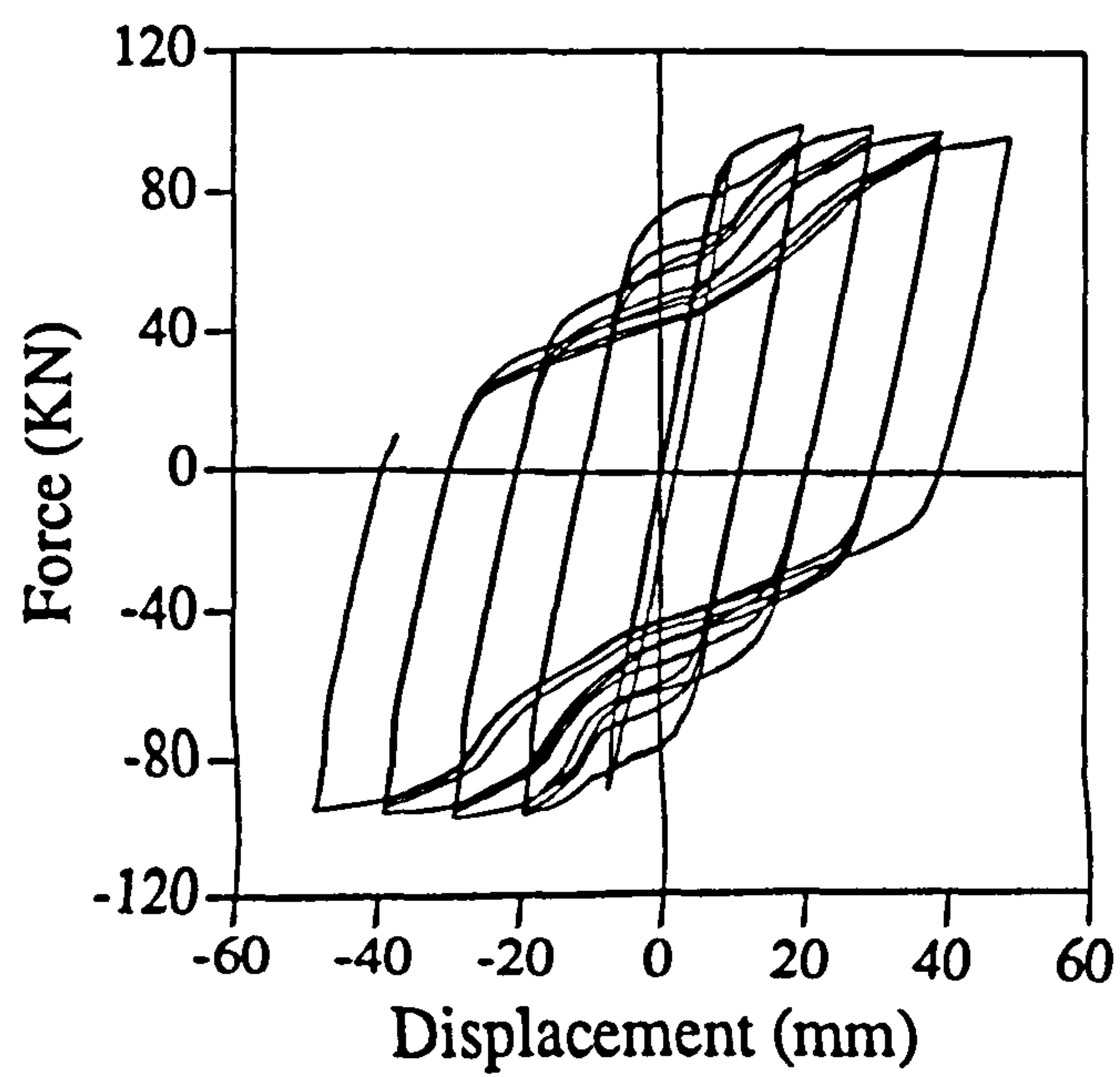


Figure 7.31 ADAPTIC model

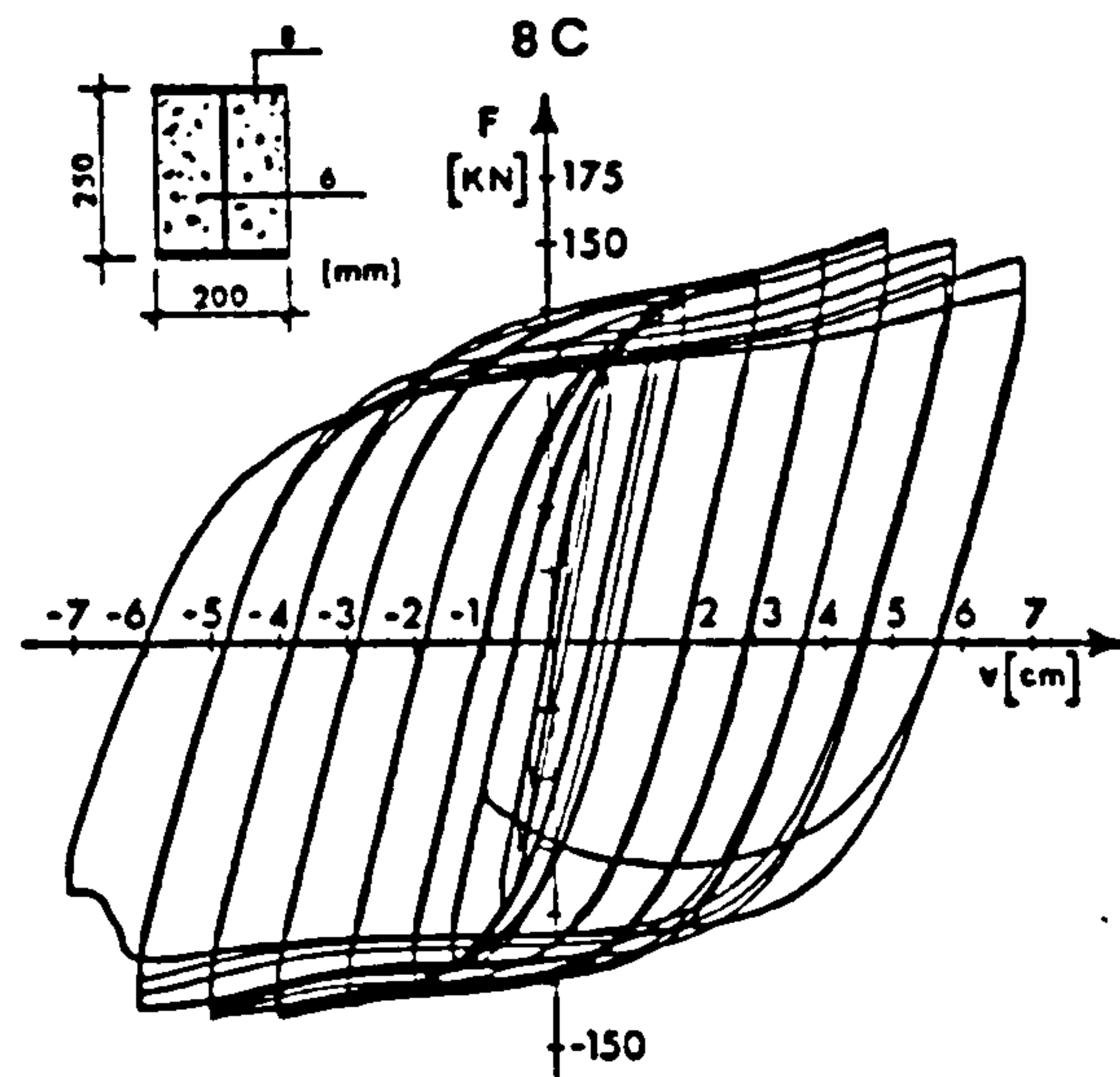


Experiment

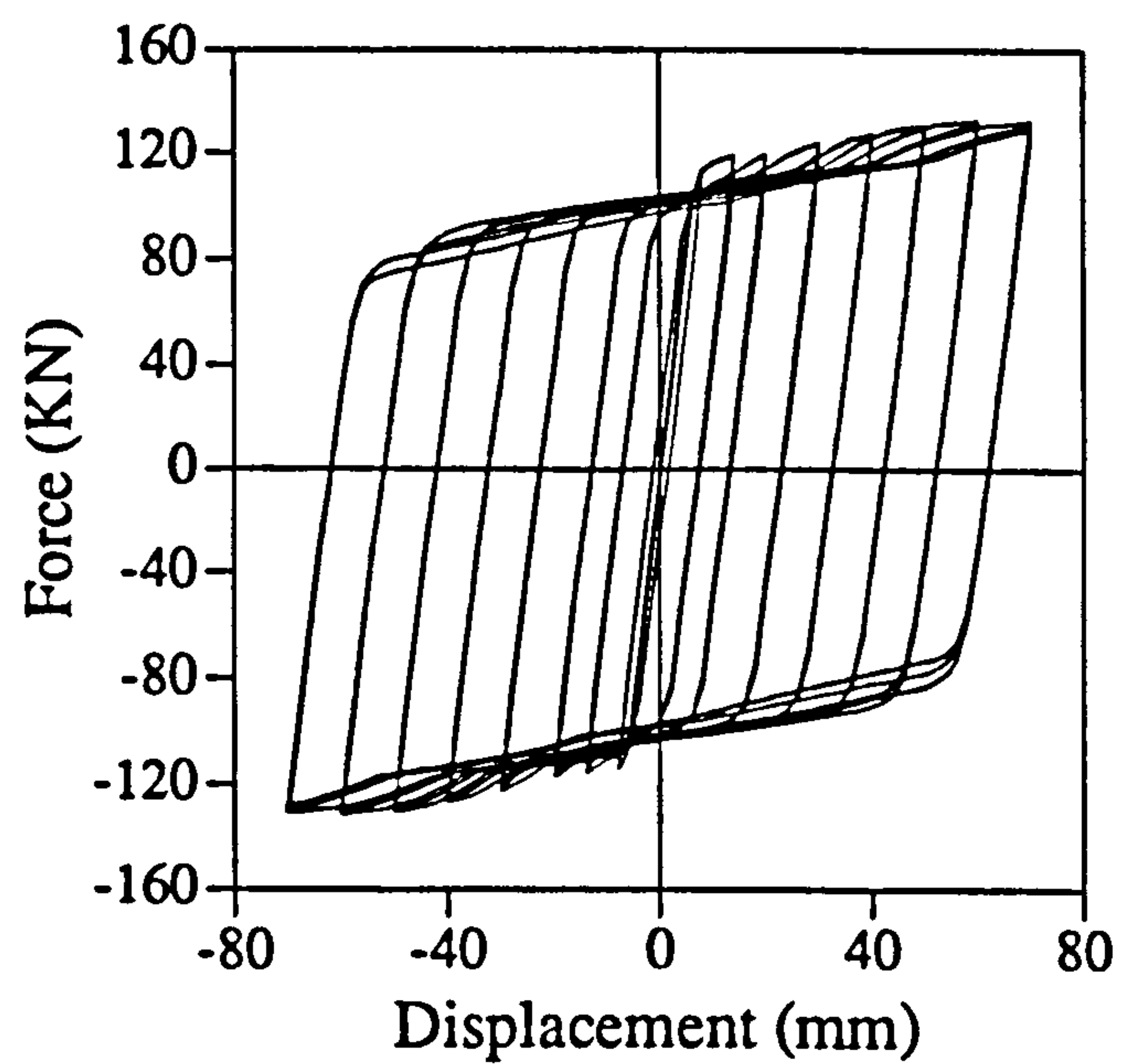


Analysis

Fig. 7.32 Experimental and analytical load-deflection relationships for test 6C conducted by Ballio et al (1987)

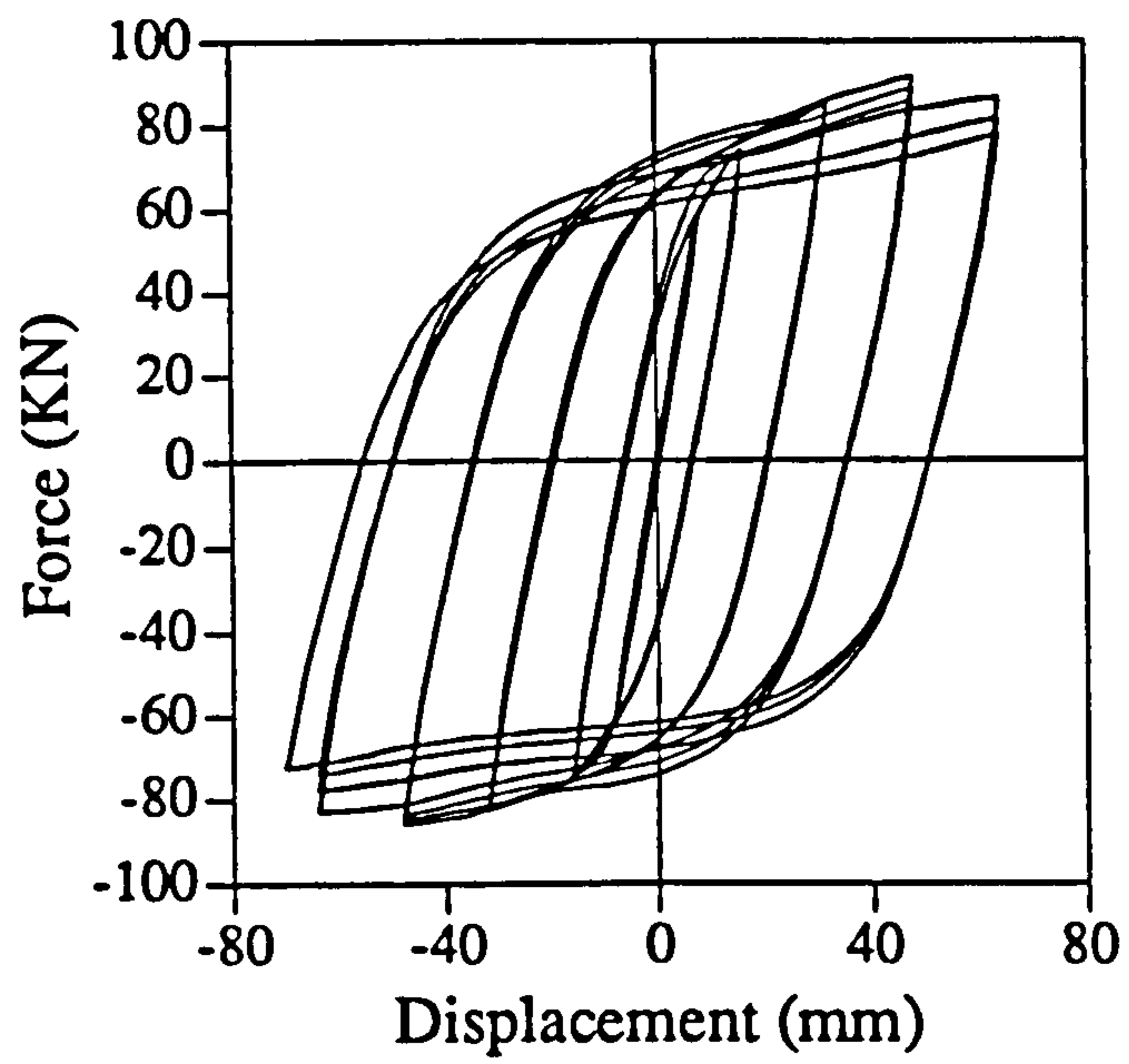


Experiment

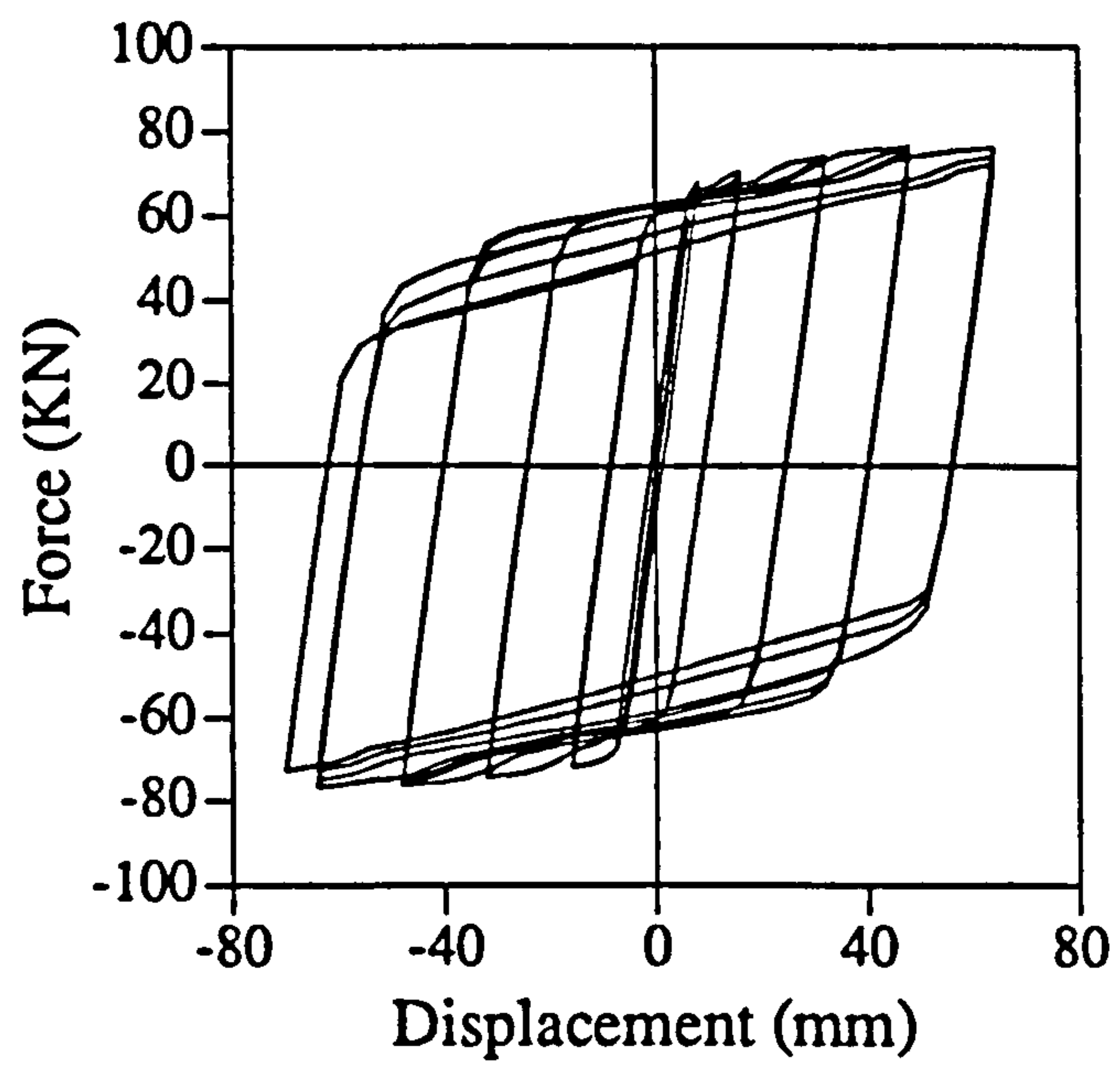


Analysis

Fig. 7.33 Experimental and analytical load-deflection relationships for test 8C conducted by Ballio et al (1987)

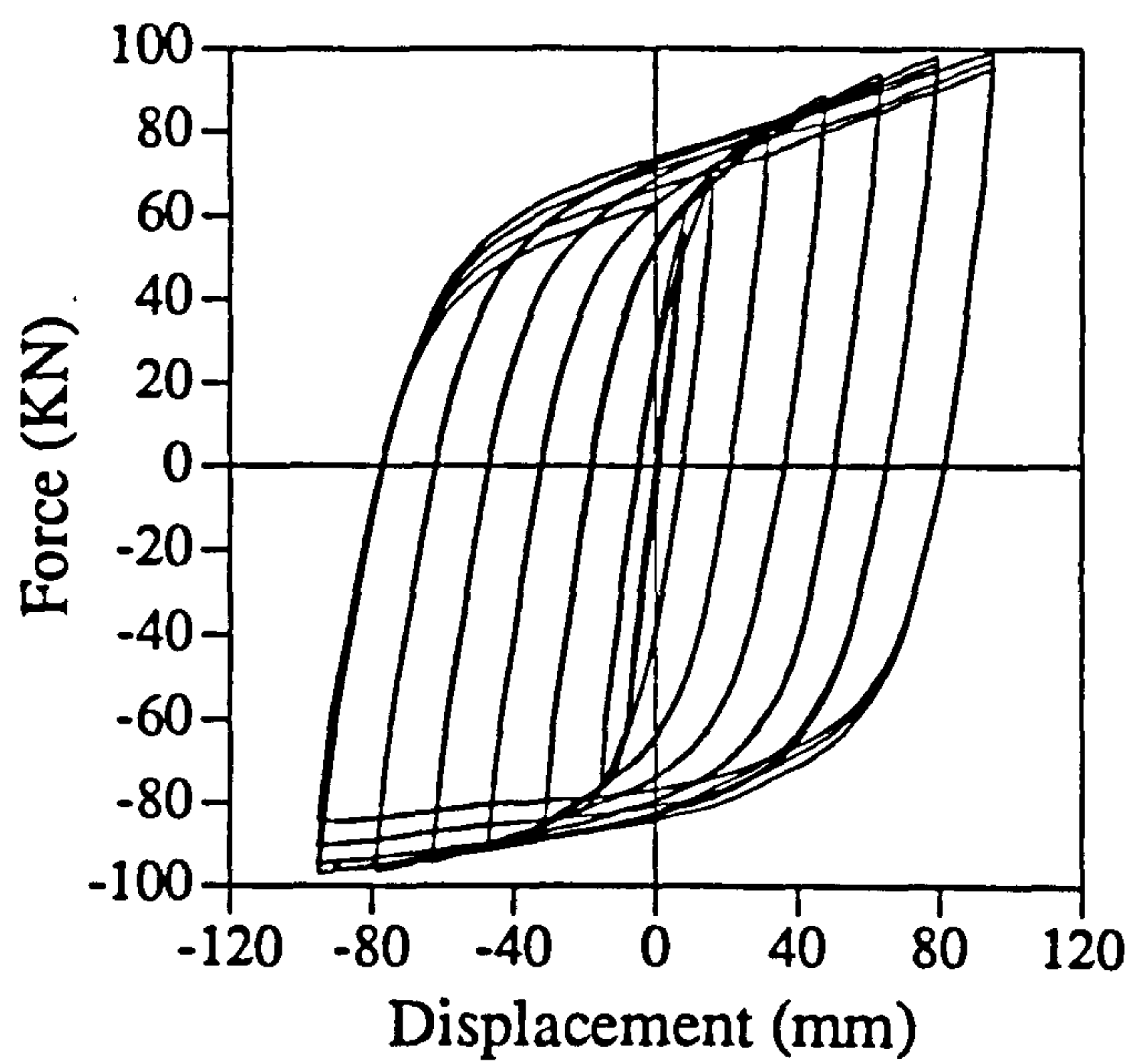


Experiment

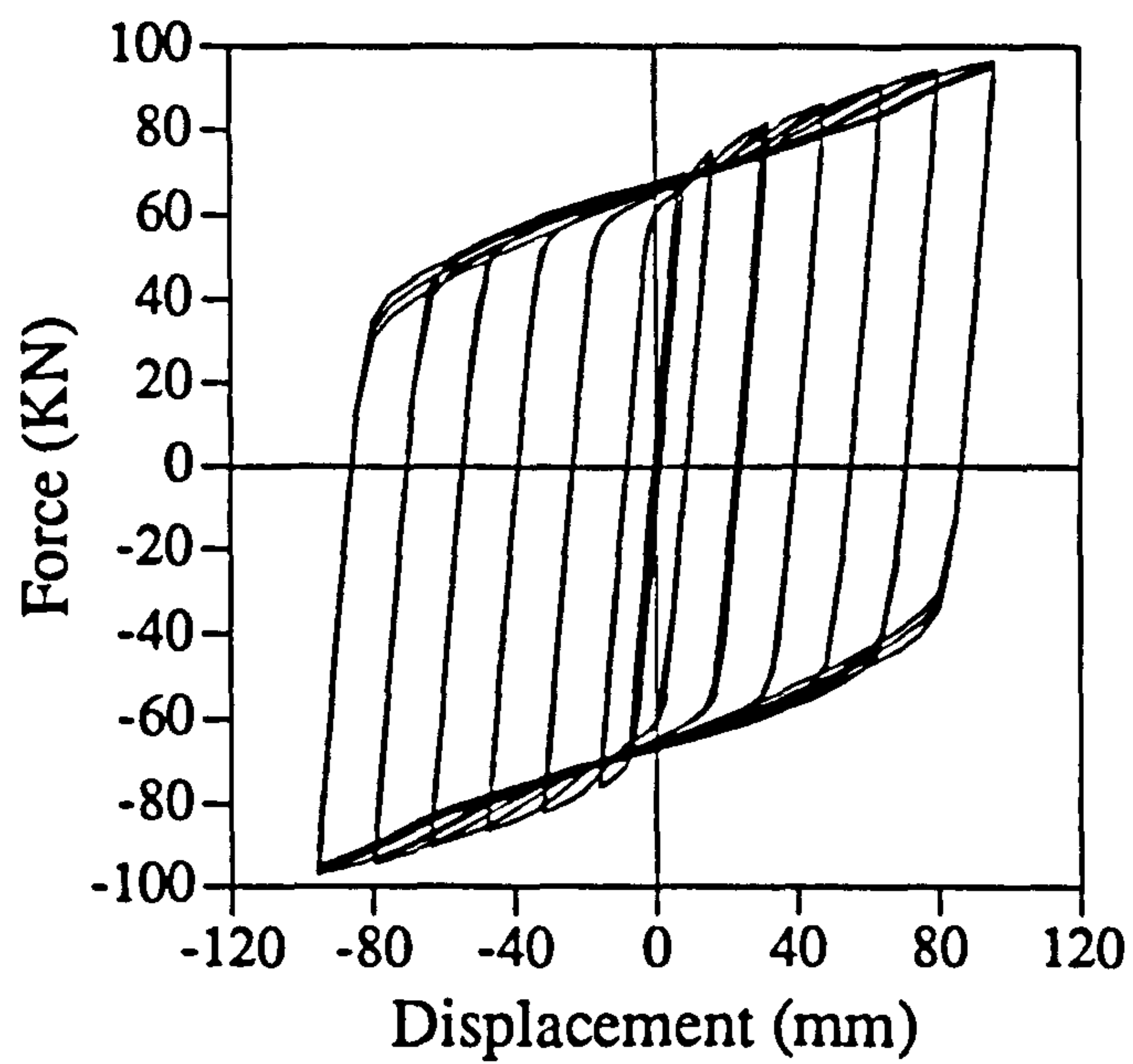


Analysis

Fig. 7.34 Experimental and analytical load-deflection relationships for EM04

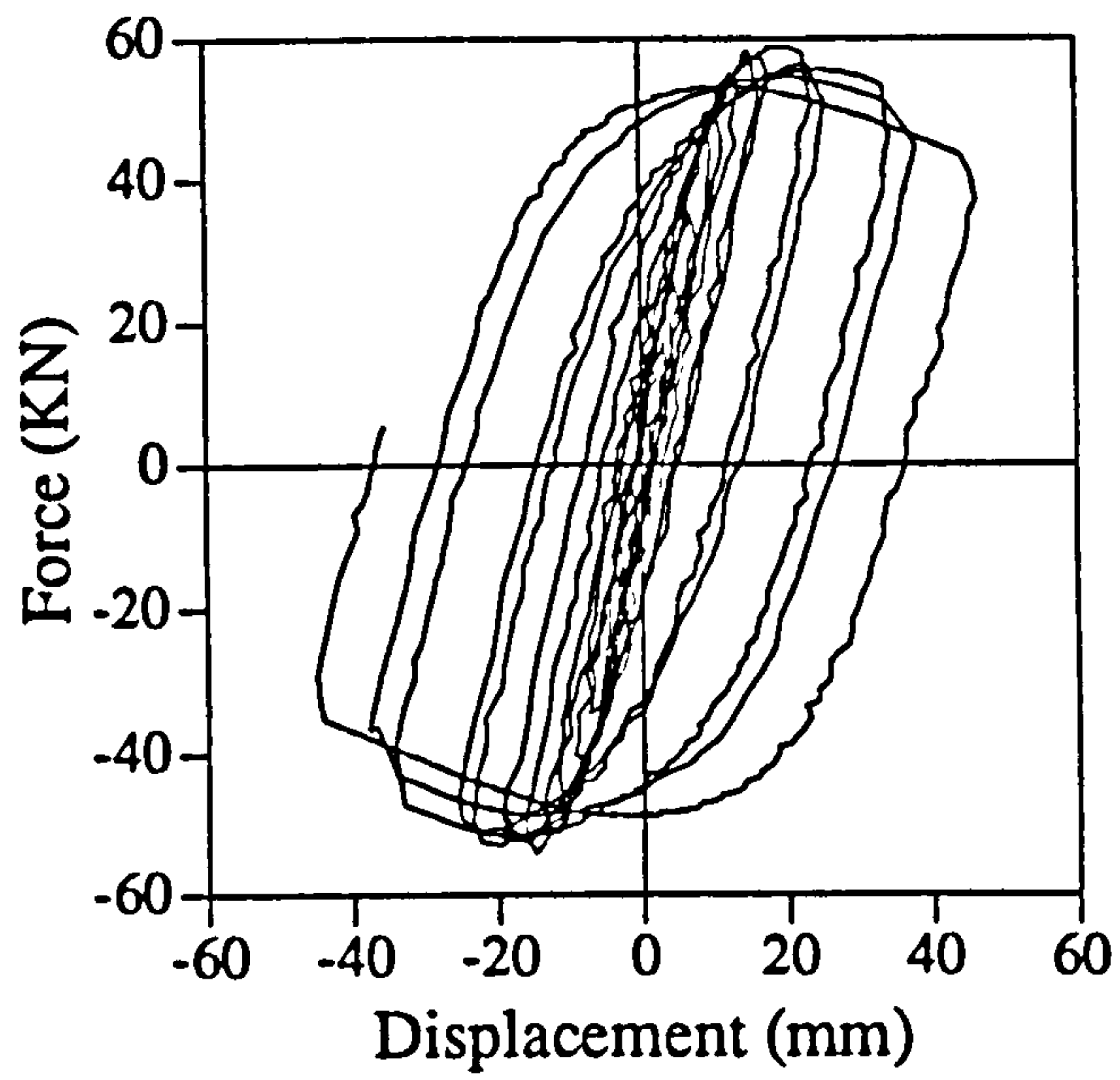


Experiment

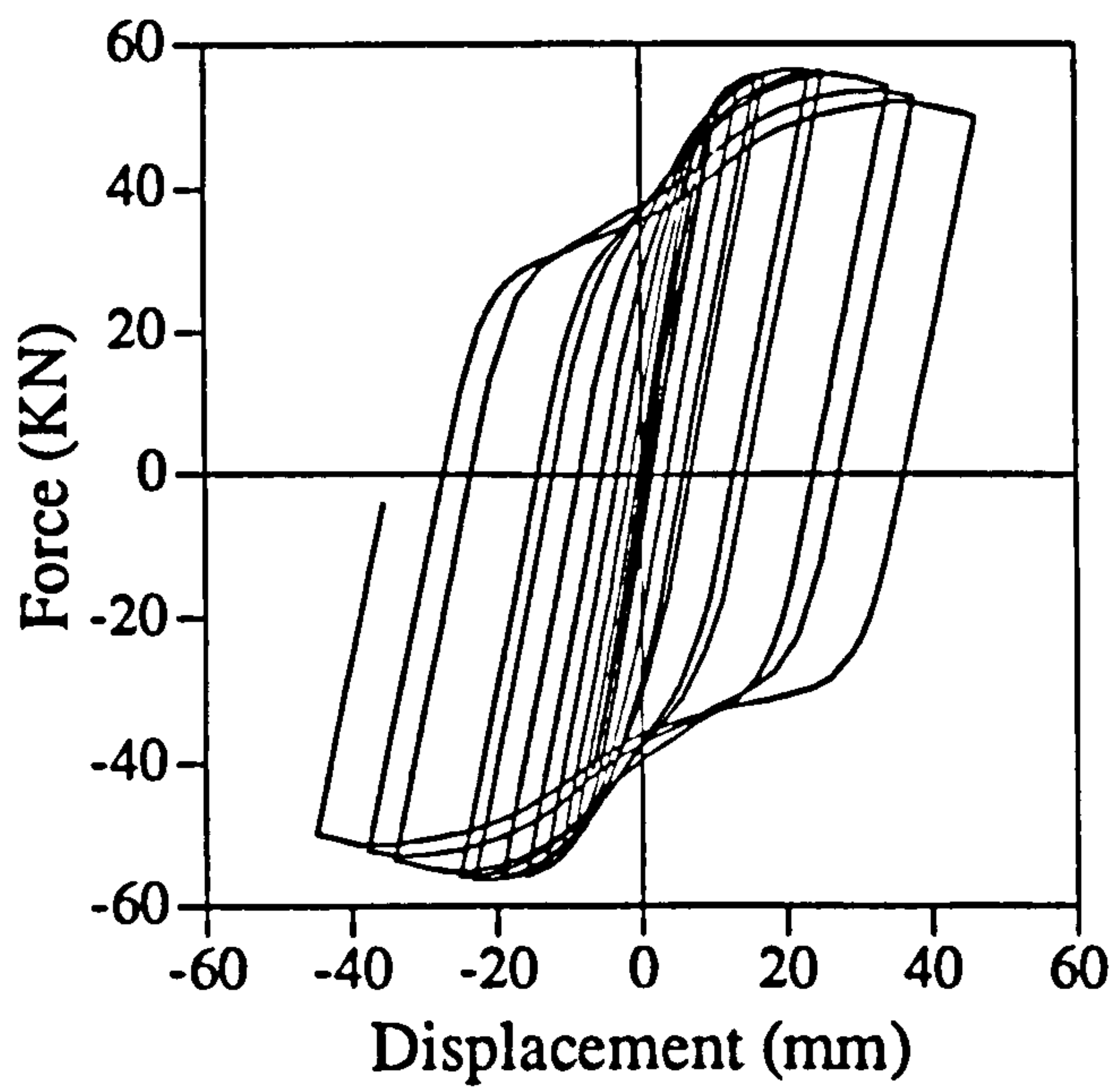


Analysis

Fig. 7.35 Experimental and analytical load-deflection relationships for IC07

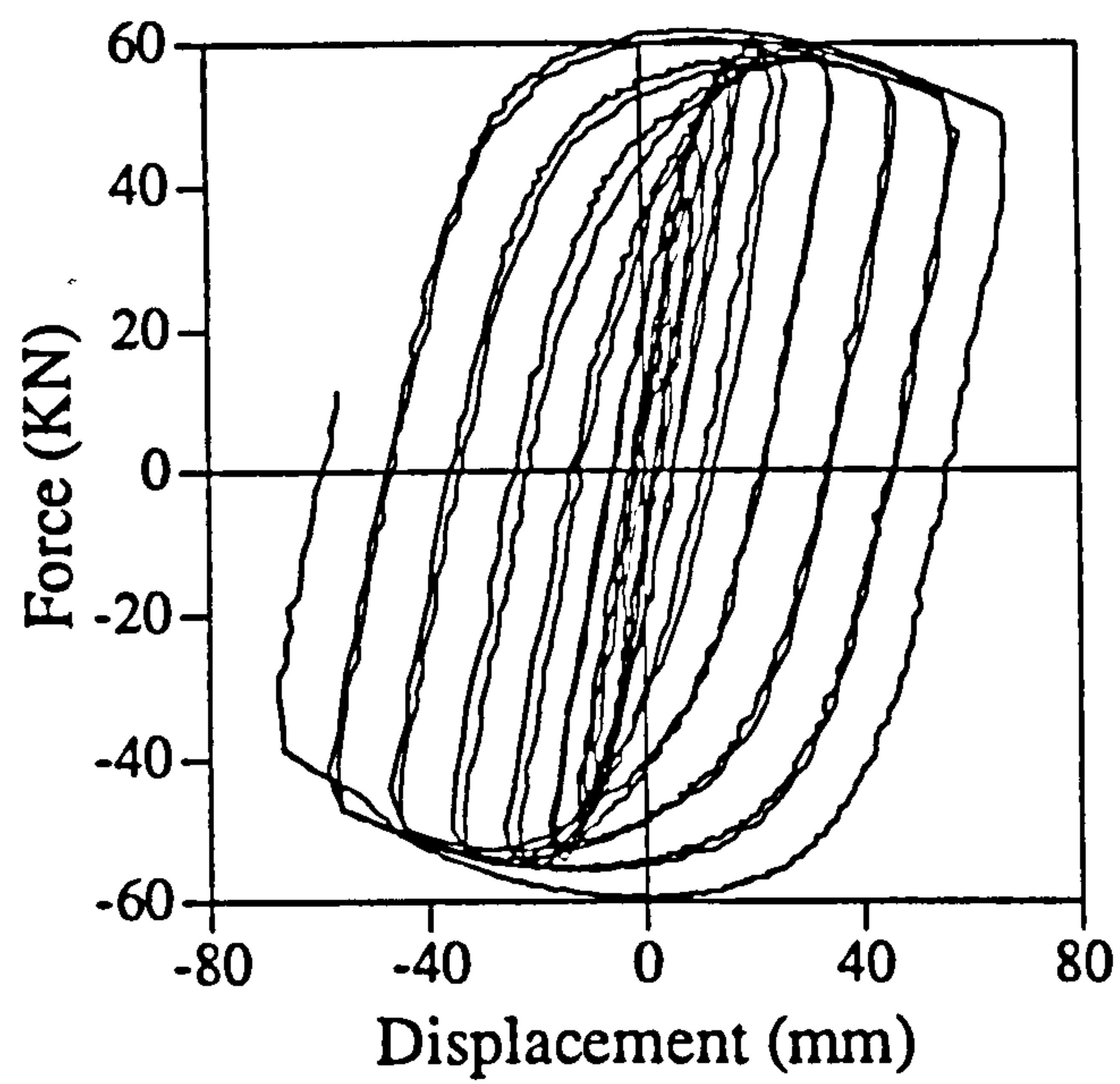


Experiment

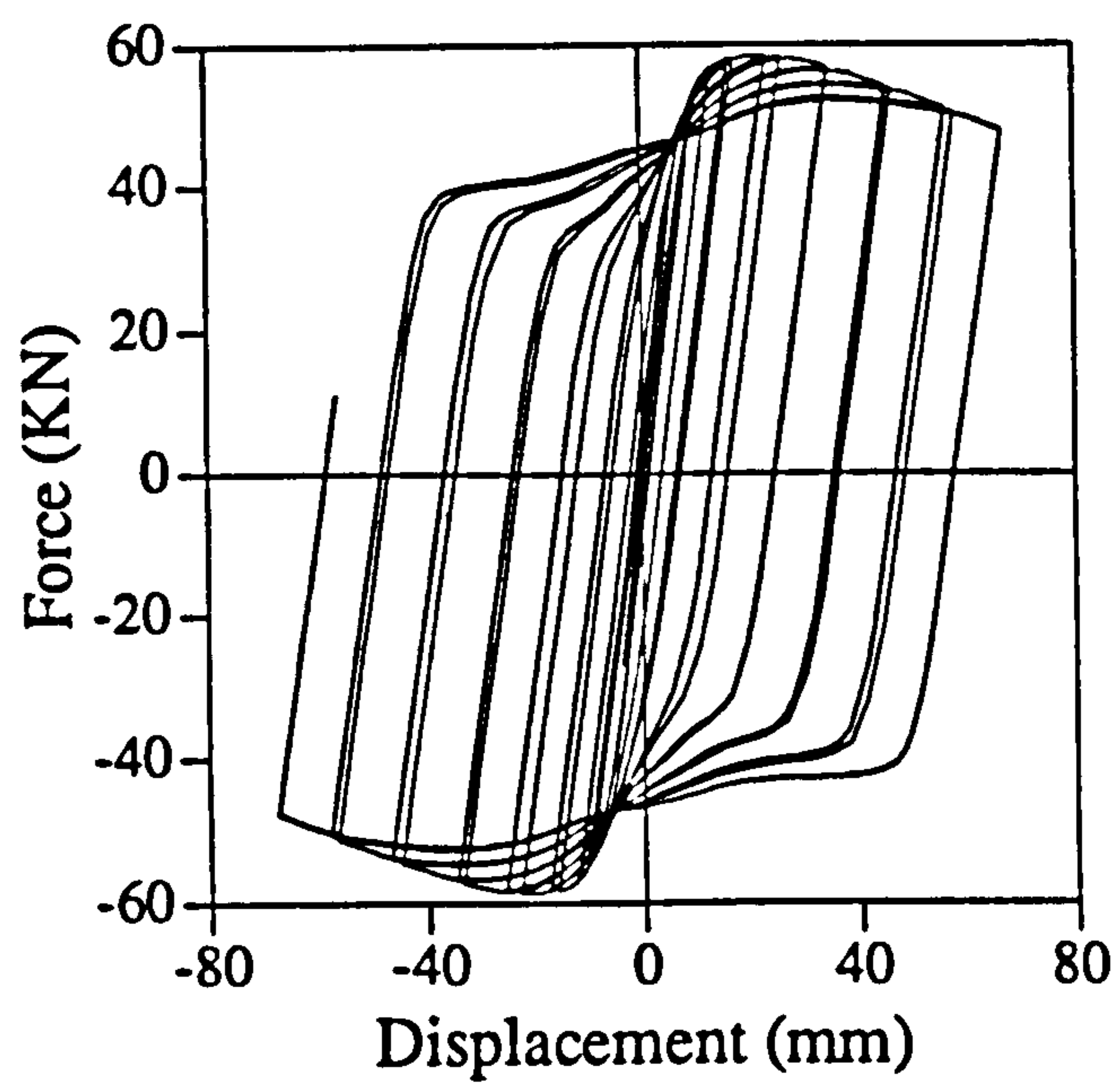


Analysis

Fig. 7.36 Experimental and analytical load-deflection relationships for EM02

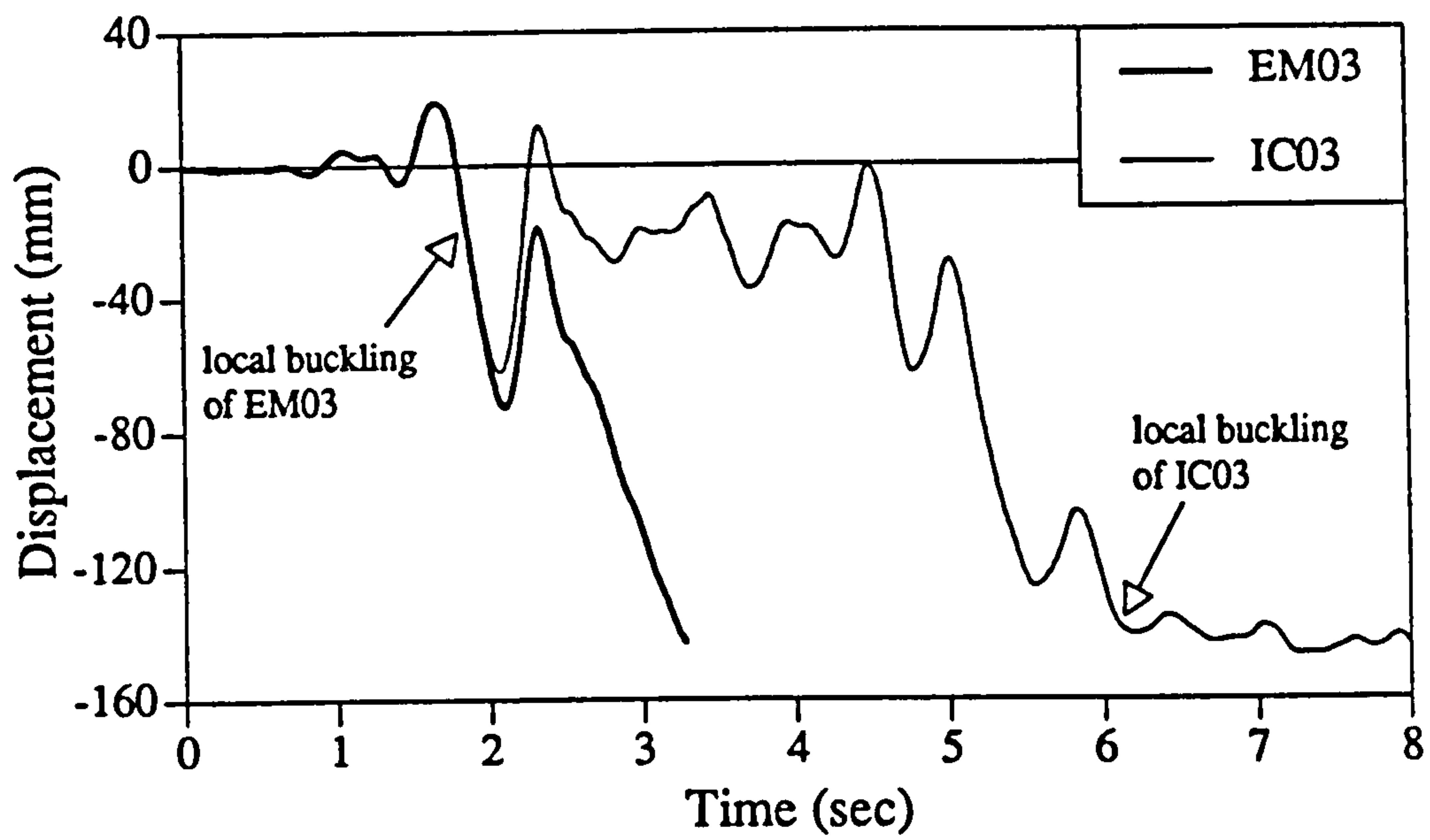


Experiment

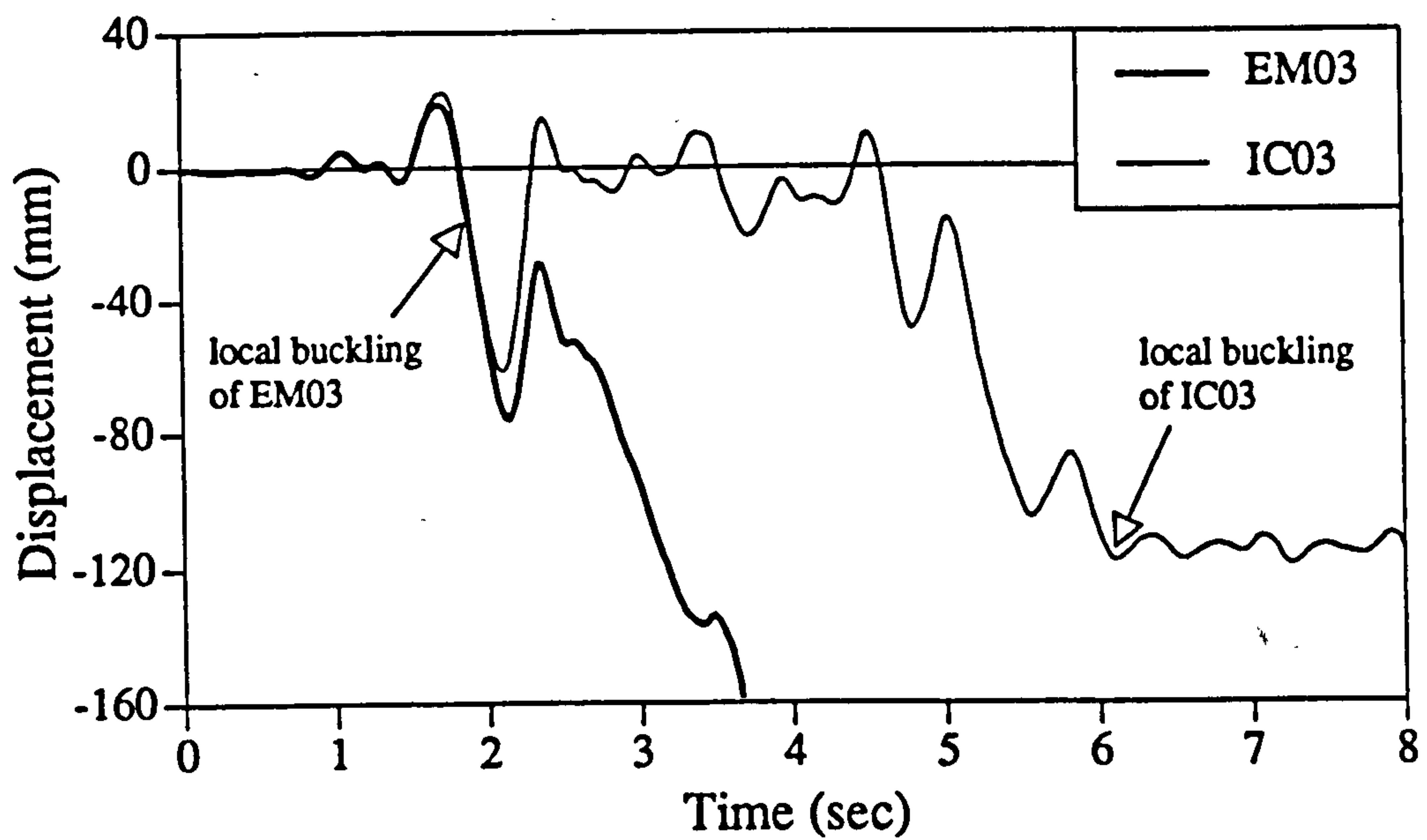


Analysis

Fig. 7.37 Experimental and analytical load-deflection relationships for IC02

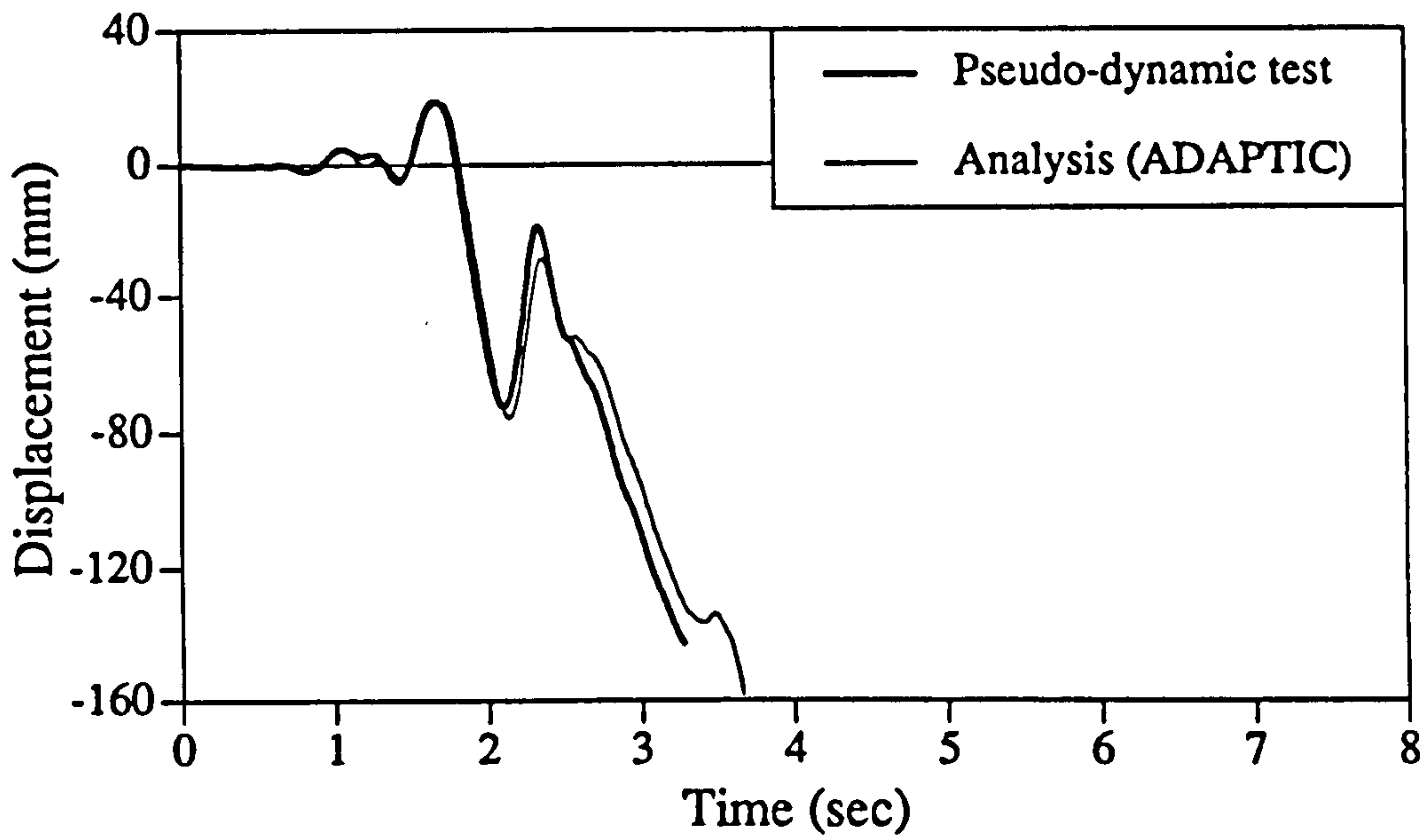


Experiment

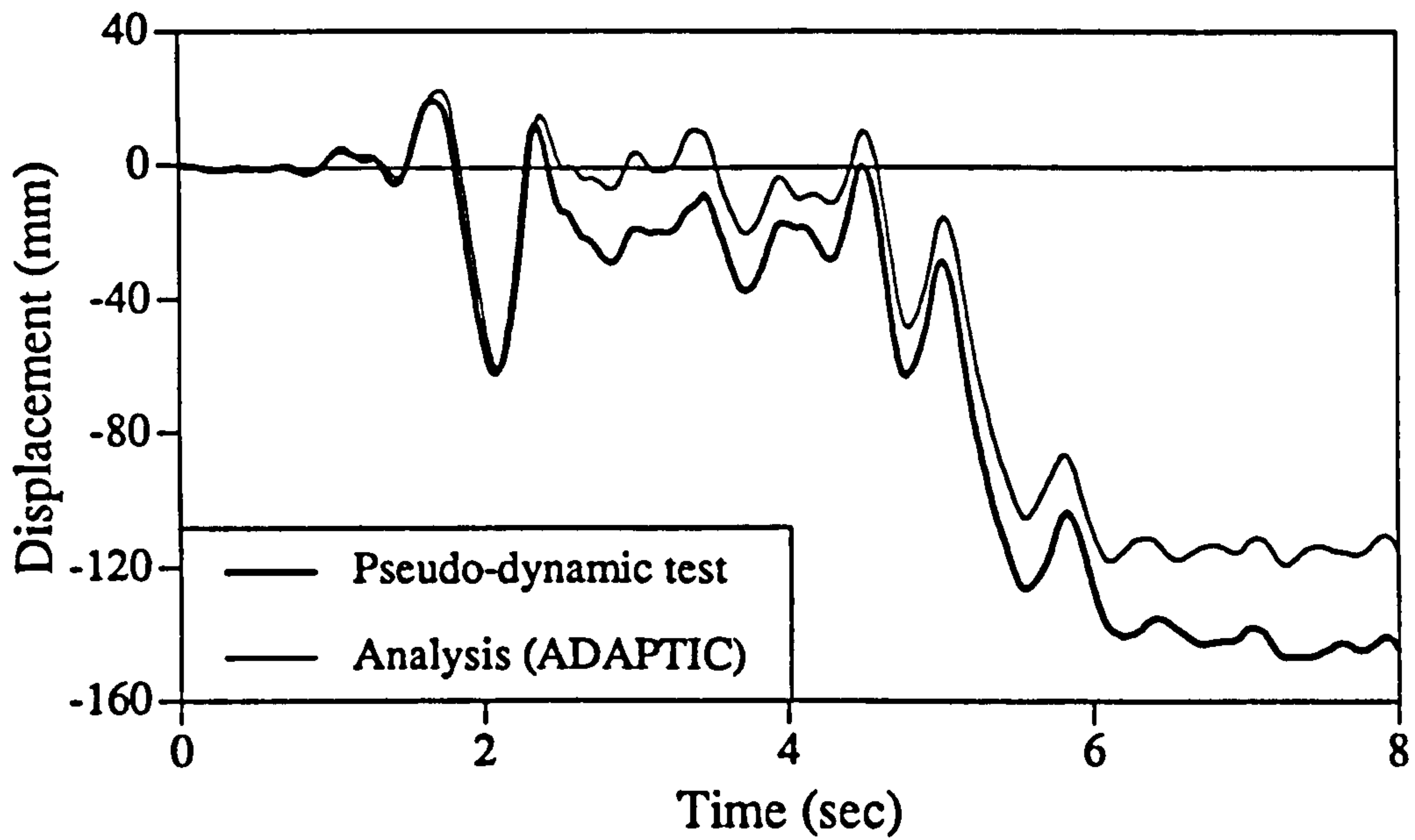


Analysis

Fig. 7.38 Experimental and analytical displacement response histories for EM03 and IC03

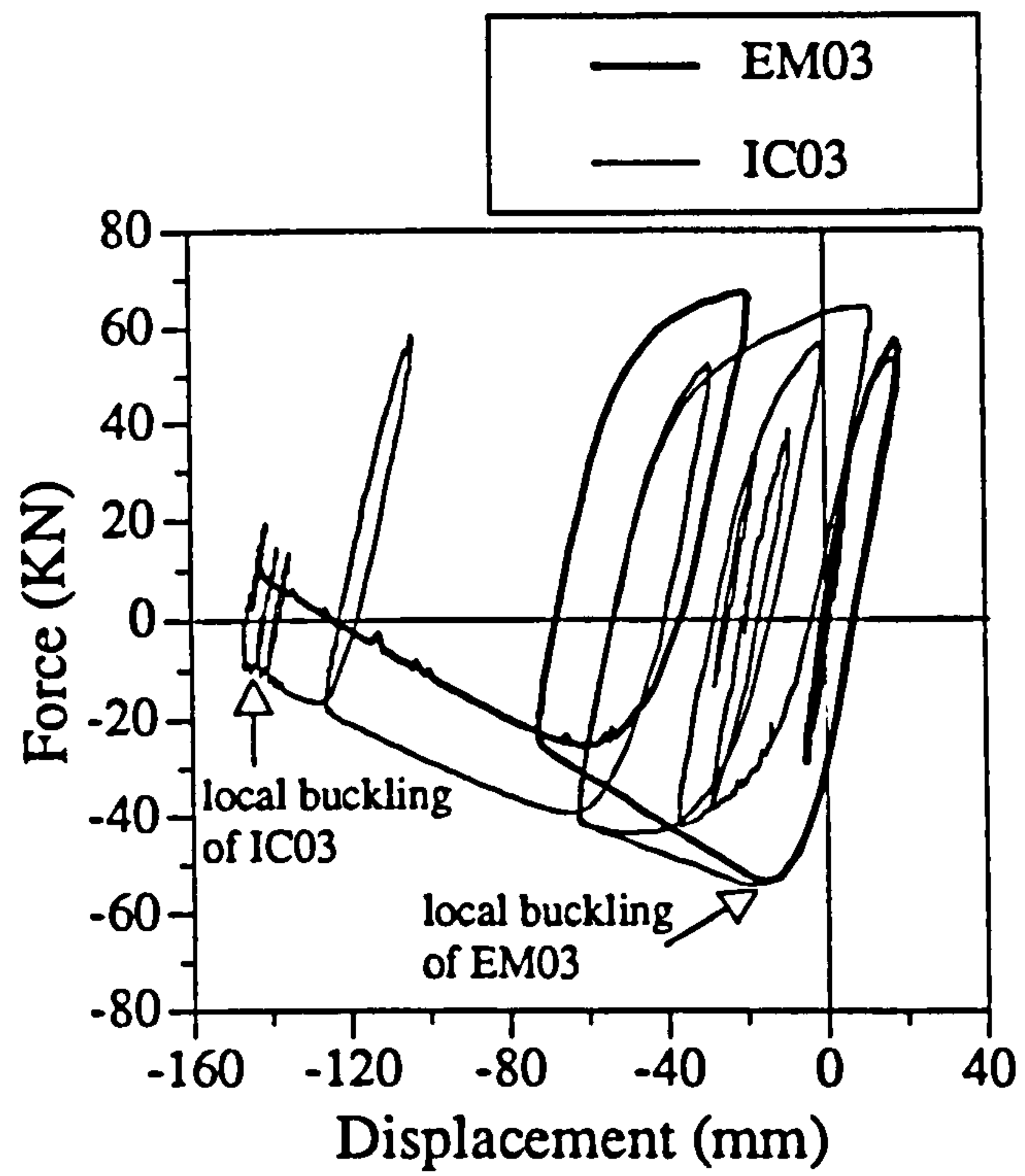


EM03

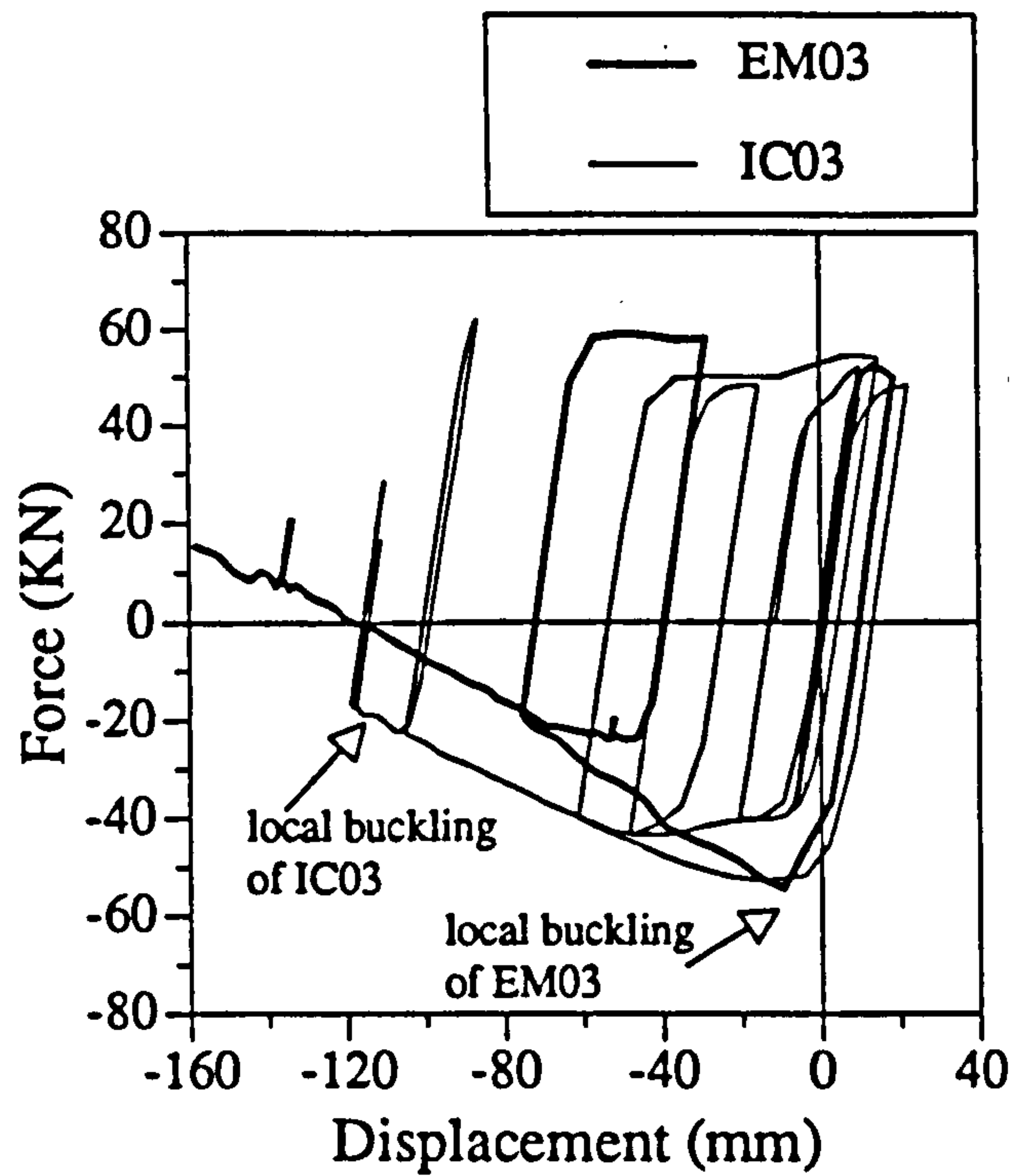


IC03

Fig. 7.39 Comparison of experimental and analytical displacement response for models EM03 and IC03



Experiment



Analysis

Fig. 7.40 Experimental and analytical load-deflection relationships for EM03 and IC03

CHAPTER 8

8. ANALYTICAL PARAMETRIC STUDY

8.1 INTRODUCTION

The main objective of the experimental programme was to examine the difference in behaviour between the EM and IC models. Therefore, the parameters studied experimentally were limited primarily to the applied axial forces and the lateral loading histories. Nevertheless, the behaviour is influenced by many parameters which may be categorized under material characteristics, geometric properties and loading conditions.

It was shown in Chapter 7 that the computer program ADAPTIC, including the new developments discussed in section 7.5, can predict with accuracy the nonlinear behaviour of the composite members under any combination of loading. It is, therefore, possible to use this advanced tool in conducting accurate dynamic analyses. This is required by modern codes of practice for structures of special importance or those classified as irregular. For regular structures, however, simplified approaches are used, whereby idealized elastic response spectra are appropriately scaled using a structural behaviour factor to account for inelastic response. This requires not only an evaluation of the available local ductility in critical members but also the relationship between the local member ductilities and the overall structural behaviour factors.

After establishing confidence through the correlation between the analytical and experimental results, this chapter describes the details of a parametric study undertaken using ADAPTIC. The main purpose of this study is to assess the local ductility of partially encased members and its sensitivity to a number of parameters that are considered to be of foremost importance. These include the effect axial load, steel yield, steel strain hardening, concrete confinement, flange slenderness and member slenderness. The study is limited to flexural members subjected to uniaxial bending and axial loads. Other important parameters such as steel yield ratio, stress softening and the effect of strain gradient on local buckling were not included because of the limitations of the steel material model. Also, to limit the extent of the study, the concrete and steel contributions and the concrete cylinder strength were not varied. The choice and range of parameters are discussed and the results, normalized whenever possible, are subsequently presented in graphical form. Control models were chosen to represent

members similar to the ones used in the experimental investigation. A general discussion of the results and their design implications is given in Chapter 9.

8.2 PRELIMINARIES

8.2.1 Geometry and Loading

For analytical purposes, the actual scale of the model is not expected to influence the results qualitatively, but only quantitatively. It was, therefore, decided to use dimensions similar to that of the experimental models. It was also decided to retain the geometry of the member as a cantilever since the constituent members of a frame subjected to lateral loads undergo double curvature bending which can be simulated by an assembly of cantilevers. Details of the chosen control model is given in Table 8.1. Vertical reinforcement bars were not considered. The finite element model used is as shown in Figure 7.31. The local buckling model described in Chapter 7 was used in all the parametric studies.

TABLE 8.1
Details of the Control Model

| | |
|--|-------------|
| Overall flange dimensions $b_f \times t_f$ (mm) | 150.0 x 6.0 |
| Web dimensions $b_w \times t_w$ (mm) | 138.0 x 6.0 |
| Steel yield stress σ_y (N/mm ²) | 300.0 |
| Strain hardening μ | 1.0 % |
| Concrete cylinder strength (N/mm ²) | 40.0 |
| Confinement factor k_σ | 2.0 |
| Flange slenderness (b/t) | 12.5 |
| Spacing of welded bars s(mm) | 40.0 |
| Axial Load | -- |
| Cantilever height L(mm) | 1200.0 |

The value of axial load applied on the composite section is one of the important parameters that can affect the attained ductility. It was demonstrated in the experimental investigation and in previous work by other researchers that ductility decreases significantly with the increase of compressive axial loads. In addition, axial loads cause second-order effects which may also impair the lateral load carrying capacity and in turn the overall ductility of the member and, consequently, that of the structure.

Because of its relative importance, the value of the axial load was considered as a variable in all the parametric studies. Representative values for the axial compression were chosen as 0, 15, 30, 45 and 60 % of the axial section capacity, referred to as C0, C15, C30, C45 and C60, respectively. Values higher than 60% are not included as they are considered to be beyond the practical range. In some cases, however, members may be subjected to tensile axial loads, especially when significant vertical ground accelerations are experienced. Consequently, a tensile axial load representing 15% of the squash capacity, referred to as T15, was also considered.

It should be noted that in calculating the squash load, the exact material properties and the dimensions of the cross section was used, except that the concrete confinement was ignored. All analyses were carried out by applying a constant vertical load, referred to as axial load, and a monotonically increasing lateral displacement at the tip of the cantilever.

8.2.2 Definition of Yield

In the comparison of code provisions presented in Chapter 3, it was shown that different approaches are used to estimate the capacity of an encased section. Whereas concrete codes, such as that of the ACI, impose a strain limit on the concrete, steel codes consider the full plastic moment of the steel section and the unconfined strength of concrete. In both cases, there are underlying assumptions that can affect the accuracy of the calculated capacity.

In order to obtain a rational estimate for ductility, a reference point for the formation of the plastic hinge must be defined. For reinforced concrete sections, it is customary to consider the point of yielding of one of the main reinforcement bars as the yield point. On the other hand, for steel members, first yield is usually not accompanied by significant curvature increase, hence the yield point is related to the full plastic moment of the section. Whereas using the first yield approach would grossly overestimate the ductility and underestimate the yield moment, an estimate of the plastic moment based on

any of the code approaches would give an unreliable reference for comparison. Also, a graphical estimation of the yield point was found to be an inaccurate alternative.

TABLE 8.2
Effect of Yield Point Definition on Analytical Results

| Axial Load | Parameter | First Yield | Chosen approach |
|------------|----------------|-------------|-----------------|
| C0 | M/My | 0.84 | 1.0 |
| | D _φ | 36.37 | 20.8 |
| | R _ψ | 16.88 | 12.08 |
| | τ | 0.42 | 0.31 |
| C15 | M/My | 1.0 | 1.0 |
| | D _φ | 20.88 | 20.88 |
| | R _ψ | 8.33 | 8.33 |
| | τ | 0.29 | 0.29 |
| C30 | M/My | 0.70 | 1.0 |
| | D _φ | 23.5 | 11.78 |
| | R _ψ | 7.85 | 4.24 |
| | τ | 0.46 | 0.22 |
| C45 | M/My | 0.52 | 1.0 |
| | D _φ | 26.2 | 6.88 |
| | R _ψ | 9.12 | 2.56 |
| | τ | 0.57 | 0.17 |
| C60 | M/My | 0.38 | 1.0 |
| | D _φ | 28.6 | 2.94 |
| | R _ψ | 13.04 | 1.43 |
| | τ | 0.65 | 0.10 |
| T15 | M/My | 0.67 | 1.0 |
| | D _φ | 66.99 | 8.06 |
| | R _ψ | 35.41 | 8.62 |
| | τ | 0.60 | 0.41 |

D_φ curvature ductility
R_ψ rotational ductility
τ normalised plastic hinge length

In the current study, the plastic hinge is assumed to be initiated when the two extreme steel fibres reach yield. This was found to be a reasonable assumption compared to either using the first yield or the full plastic capacity approach as the moment curvature diagram starts deviating noticeably from linearity upon yielding of the two flanges. In order to demonstrate this point, the relationships between the cantilever deflection angle (ψ), defined in section 8.3, and the moment at the critical section for different values of axial load, are presented in Figure 8.1. The control model described in Table 8.1 was used and the bilinear steel model was employed for simplicity. The moment values are normalized to the yield moment, M_y , at which the two extreme points reach yield.

Table 8.2 shows the effect of the definition of the yield point on the yield moment, curvature ductility (D_ϕ), rotational ductility (R_ψ) and normalised plastic hinge length (τ). The value of M/M_y is normalised to that of the chosen approach. The definitions of ductilities and plastic hinge length are given in section 8.3. It is clear that the yield moment is generally underestimated using the first yield approach with the result of obtaining very large ductility values. Also, the plastic hinge length decreases monotonically for the chosen approach, whilst that obtained from first yield is erratic. However, it should be noted that for the case of tensile axial loads, ductility is penalized by the chosen definition of yield. This is a consequence of this particular choice and has to be appreciated in the interpretation of the results of this parametric study.

Figure 8.2 shows the difference in the yield capacity calculated according to the approach adopted in this study and that calculated from the full plastic capacity of the section. As expected, the capacity estimated using the full plastic moment of steel and the unconfined concrete strength would generally give lower values than the yield capacity, whereas using the confined concrete strength would result in a higher strength, especially for high compressive axial loads.

8.2.3 Failure Criteria

In the experimental investigation, it was shown that the capacity of the section starts reducing after local buckling. This is due to the degradation in the steel section and the sudden release of concrete confinement. Although the drop in moment capacity is not significant when low axial forces are imposed, it was shown that a gradual decrease in capacity at the same displacement is to be expected if the specimen is subjected to cyclic loading.

It was, therefore, decided to define the ultimate state as coincident with the onset of local buckling of the compression flange. Nevertheless, in cases of tensile axial loads, another failure criterion is checked, whereby the tensile strains in the extreme fibres are not to exceed a value of 12%. It should also be realised that other failure criteria are needed in case of slender columns. In this case both the drift and the drop in lateral load carrying capacity must be checked. This is discussed further in Chapter 9 of this thesis.

8.3 PRESENTATION OF RESULTS

A large amount of data was obtained from the computer analyses comprising the parametric studies; only the results of most pertinence to this research programme are presented. Simple charts are used, whenever necessary, not only to convey the information concisely, but also to facilitate comparison of results and identification of general trends in behaviour, which is the main aim of this study. Also, the analysis reference and the range of parameters are presented in tabular form for each study. The main parameters used to present the results are described hereafter.

8.3.1 Capacity

The definitions of the parameters used in the parametric studies are given in Figure 8.3. Two moment values are presented for the sections. The first is the yield moment, M_y , as defined in section 8.2. The second is the ultimate moment, M_u , as shown in Figure 8.3. The results are normalised to that of the control model whenever applicable.

8.3.2 Neutral Axis Depth

The depth of the neutral axis is defined as the distance from the most strained compressive fibre to the neutral axis position normalised by the depth of section, D . The normalised neutral axis depth is denoted ξ .

8.3.3 Ductility

Figure 8.3 shows the cantilever member subjected to a lateral displacement, δ , and a constant axial load, N . The moment diagram at ultimate strength and the idealised curvature diagram at failure are also given in the figure. The curvature ductility is defined as:

$$D_{\phi} = \frac{\phi_p}{\phi_y} = \frac{\phi_u}{\phi_y} - 1 \quad (8.1)$$

where ϕ_y , ϕ_p and ϕ_u are the curvature at yield, plastic curvature and curvature at failure, respectively.

The rotational ductility, also referred to as rotation capacity, can be defined either by using the deflection angle, ψ , or the slope angle, θ_s , shown in Figure 8.3. The deflection angle is used in the presentation of the results of the current study. The rotational ductility, R_{ψ} , is hence defined as:

$$R_{\psi} = \frac{\psi_p}{\psi_y} = \frac{\psi_u}{\psi_y} - 1 \quad (8.2)$$

As shown in Figure 8.3, ψ_y , ψ_p and ψ_u are the deflection angles at yield, plastic deflection angle and the deflection angle at failure, respectively.

8.3.4 Plastic Hinge Length

An estimate of the length of the plastic hinge can be obtained from the values of the ultimate and yield moments. From Figure 8.3, the length of the plastic hinge zone normalised to the cantilever height is given by:

$$\tau = 1 - \frac{M_y}{M_u} \quad (8.3)$$

Other parameters are defined as they appear in the body of the study.

8.4 STRAIN HARDENING STUDY

The value of steel strain hardening, μ , of 1.0% was chosen for the control case since it represents the average value obtained in the experimental results. Another value of 0.0% is also considered in this study to investigate the effect of changing this parameter on the behaviour. Table 8.3 gives the range of parameters and identifies the analyses carried out.

TABLE 8.3
Variation of Strain Hardening of Steel

| Axial Load | Strain Hardening | |
|------------|------------------|---------------|
| | $\mu = 0.0\%$ | $\mu = 1.0\%$ |
| T15 | T15H0 | T15H1 |
| C0 | C0H0 | C0H1* |
| C15 | C15H0 | C15H1 |
| C30 | C30H0 | C30H1 |
| C45 | C45H0 | C45H1 |
| C60 | C60H0 | C60H1 |

**Control analysis*

The results are presented in Figures 8.4 to 8.9. No significant difference is observed for the yield moment and the neutral axis depth. The ultimate moment increases considerably with the increase of strain hardening, especially at low values of axial compression. The curvature ductility is not affected by the strain hardening except for C0 and T15. The difference in the ultimate moment is reflected also in plastic hinge length and the rotational ductility. As pointed out previously, the case of T15 shows lower ductility than expected as a consequence of the adopted definition of yield point.

8.5 YIELD STRESS OF STEEL

Variation in nominal yield strength as well as unintentional differences can be investigated by varying the yield stress, σ_y , of the steel. The range considered in this study is 250 to 550 N/mm², as shown in Table 8.4. The axial load was calculated using the corresponding yield stress for each case.

Other steel characteristics such as the steel yield ratio and stress degradation are of great significance to the behaviour. However, these parameters could not be assessed for the purpose of this parametric study. This highlights some of the limitations of the steel material model used.

TABLE 8.4
Variation of Yield Stress of Steel

| Axial Load | Yield Stress σ_y (N/mm ²) | | | |
|------------|--|---------|---------|---------|
| | 250 | 300 | 400 | 550 |
| T15 | T15Y250 | T15Y300 | T15Y400 | T15Y550 |
| C0 | C0Y250 | C0Y300* | C0Y400 | C0Y550 |
| C15 | C15Y250 | C15Y300 | C15Y400 | C15Y550 |
| C30 | C30Y250 | C30Y300 | C30Y400 | C30Y550 |
| C45 | C45Y250 | C45Y300 | C45Y400 | C45Y550 |
| C60 | C60Y250 | C60Y300 | C60Y400 | C60Y550 |

**Control analysis*

The results of this study are presented in Figures 8.10 to 8.15. Both the yield and ultimate moments show a linear increase with the increase in yield stress. The effect on the neutral axis depth increases with the increase of axial compression. It is also clear that curvature and rotational ductilities are inversely related to the yield stress.

8.6 CONCRETE CONFINEMENT

As discussed in Chapter 7, the confinement factor, k_G , is the ratio between the confined and the unconfined concrete strength. An increase in this factor is also accompanied by an increase in the ultimate strain as given in equation (7.6). Although confinement in encased sections is ignored in design codes, it was realised from the experimental results that the concrete confinement can significantly affect the behaviour.

To limit the extent of this study, only the confinement factor is varied. The concrete strength is kept as a constant value of 40 N/mm². An upper limit on the confinement factor of 4.0 is used as values higher than that are difficult to achieve. Table 8.5 gives the ranges of parameters and the reference codes for the analyses used in this study.

TABLE 8.5
Variation of Concrete Confinement

| Axial Load | Confinement Factor (k_{σ}) | | | | |
|------------|-------------------------------------|--------|--------|--------|--------|
| | 1.0 | 1.5 | 2.0 | 3.0 | 4.0 |
| T15 | T15F10 | T15F15 | T15F20 | T15F30 | T15F40 |
| C0 | C0F10 | C0F15 | C0F20* | C0F30 | C0F40 |
| C15 | C15F10 | C15F15 | C15F20 | C15F30 | C15F40 |
| C30 | C30F10 | C30F15 | C30F20 | C30F30 | C30F40 |
| C45 | C45F10 | C45F15 | C45F20 | C45F30 | C45F40 |
| C60 | C60F10 | C60F15 | C60F20 | C60F30 | C60F40 |

**Control analysis*

Figures 8.16 to 8.21 summarize the results of this parametric study. As expected, the confinement factor has no effect on the yield moment for T15, C0 and C15. The yield moment increases with confinement factor for the cases of large axial loads. The ultimate moment also shows a gradual increase with the increase of k_{σ} for all axial load values. Because of the higher concrete strength at ultimate state, the normalised neutral axis depth ξ decreases with respect to k_{σ} . Except for T15, D_{ϕ} , R_{ψ} and τ show a monotonic increase with the increase of k_{σ} .

8.7 MEMBER SLENDERNESS

In order to demonstrate the effect of the member slenderness on the behaviour, the overall height of the cantilever, with respect to the breadth of the section, i.e. L/B , is varied. As shown in Table 8.6, the slenderness is varied between 2.0 and 12.0

The results for curvature and rotational ductilities are not presented since no significant difference was noticed except for the the case of C45 and C60 for L/B of 12 due to geometric effects.

TABLE 8.6
Variation of Member Slenderness

| Axial Load | Slenderness (L/B) | | | | |
|------------|-------------------|-------|-------|--------|--------|
| | 2.0 | 5.0 | 8.0 | 10.0 | 12.0 |
| T15 | T15S2 | T15S5 | T15S8 | T15S10 | T15S12 |
| C0 | C0S2 | C0S5 | C0S8* | C0S10 | C0S12 |
| C15 | C15S2 | C15S5 | C15S8 | C15S10 | C15S12 |
| C30 | C30S2 | C30S5 | C30S8 | C30S10 | C30S12 |
| C45 | C45S2 | C45S5 | C45S8 | C45S10 | C45S12 |
| C60 | C60S2 | C60S5 | C60S8 | C60S10 | C60S12 |

**Control analysis*

Figure 8.22 shows the percentage reduction in the peak lateral load at ultimate state. Whereas the drop in load is less than 20% for slendernesses up to 6, it increases rapidly due to the P- Δ effect as the slenderness increases, particularly for compressive loads higher than C15. Consequently, if another failure criterion is imposed on the reduction in lateral load the values for rotational ductility would be greatly reduced for cases of high axial loads on slender members.

Most codes of practice specify a drift limitation for inter-storey and overall deflection in frame structures. This is discussed in more detail in Chapter 9. Figure 8.23 depicts the relationship between the tip cantilever displacement at ultimate state normalised by the height. The drift is almost directly proportional to the slenderness, with an increased slope for the cases of C0 and C15. If a drift limitation is imposed, the values of rotational ductility obtained from other studies can be proportionally reduced to account for this criterion.

8.8 FLANGE SLENDERNESS

The flange slenderness, represented by half the flange width divided by the flange thickness (b/t) is probably the most important parameter in determining the ductility of the member. It was shown in the experimental investigation that whereas the difference in capacity of the IC models compared with the EM specimens was insignificant, the ductility was substantially increased due to the provision of the bars inhibiting local buckling. Therefore, this section is dedicated to the investigation of the effect of

changing b/t ratios, the spacing of the local buckling inhibitors and the axial load on ductility.

TABLE 8.7
 Flange Slenderness Study

| Axial | Load | T15 | C0 | C15 | C30 | C45 | C60 |
|-------|------|----------|----------|----------|----------|----------|----------|
| b/t | s/b | | | | | | |
| 7.5 | 1.00 | T15B75D | C0B75D | C15B75D | C30B75D | C45B75D | C60B75D |
| | 1.60 | T15B75E | C0B75E | C15B75E | C30B75E | C45B75E | C60B75E |
| 10.0 | 0.53 | T15B100C | C0B100C | C15B100C | C30B100C | C45B100C | C60B100C |
| | 1.00 | T15B100D | C0B100D | C15B100D | C30B100D | C45B100D | C60B100D |
| | 1.60 | T15B100E | C0B100E | C15B100E | C30B100E | C45B100E | C60B100E |
| 12.5 | 0.30 | T15B125B | C0B125B | C15B125B | C30B125B | C45B125B | C60B125B |
| | 0.53 | T15B125C | C0B125C* | C15B125C | C30B125C | C45B125C | C60B125C |
| | 1.00 | T15B125D | C0B125D | C15B125D | C30B125D | C45B125D | C60B125D |
| | 1.60 | T15B125E | C0B125E | C15B125E | C30B125E | C45B125E | C60B125E |
| 17.5 | 0.20 | T15B175A | C0B175A | C15B175A | C30B175A | C45B175A | C60B175A |
| | 0.30 | T15B175B | C0B175B | C15B175B | C30B175B | C45B175B | C60B175B |
| | 0.53 | T15B175C | C0B175C | C15B175C | C30B175C | C45B175C | C60B175C |
| | 1.00 | T15B175D | C0B175D | C15B175D | C30B175D | C45B175D | C60B175D |
| | 1.60 | T15B175E | C0B175E | C15B175E | C30B175E | C45B175E | C60B175E |
| 25.0 | 0.20 | T15B250A | C0B250A | C15B250A | C30B250A | C45B250A | C60B250A |
| | 0.30 | T15B250B | C0B250B | C15B250B | C30B250B | C45B250B | C60B250B |
| | 0.53 | T15B250C | C0B250C | C15B250C | C30B250C | C45B250C | C60B250C |
| | 1.00 | T15B250D | C0B250D | C15B250D | C30B250D | C45B250D | C60B250D |
| | 1.60 | T15B250E | C0B250E | C15B250E | C30B250E | C45B250E | C60B250E |
| 30 | 0.20 | T15B300A | C0B300A | C15B300A | C30B300A | C45B300A | C60B300A |
| | 0.30 | T15B300B | C0B300B | C15B300A | C30B300B | C45B300B | C45B300B |
| | 0.53 | T15B300C | C0B300C | C15B300A | C30B300C | C45B300C | C45B300C |
| 35 | 0.20 | T15B350A | C0B350A | C15B350A | C30B350A | C45B350A | C60B350A |
| | 0.30 | T15B350B | C0B350B | C15B350B | C30B350B | V45B350B | C60B350B |
| 40 | 0.20 | T15B400A | C0B400A | C15B400A | C30B400A | C45B400A | C60B400A |

**Control analysis*

In order to vary the b/t ratios, a variation in the width of the section, B , has to be imposed. This, however, is not expected to have a significant effect on the results. The axial load was appropriately estimated based on the corresponding section dimensions. The spacing of the local buckling inhibitors, s , is presented normalised to half the flange width, i.e. s/b . The flange slenderness, b/t , is varied between 7.5 and 40, whilst the control model has a value of 12.5. The spacing of the bars is varied between 0.2 and 1.6. According to the assumptions made in Chapter 7, the latter value of 1.6 corresponds to the EM specimens and a value of 0.53 would refer to the IC models. Table 8.7 gives the range of parameters and the analyses reference for this study.

The curvature and rotational ductilities and the plastic hinge length for the control case are presented in Figures 8.24, 8.25 and 8.26. The attained ductility shows a consistent parabolic decrease with the increase in b/t ratios. Also, an almost inversely proportional linear relationship is shown for the plastic hinge length. Figures 8.27 to 8.44 give the values of D_ϕ , R_ψ and τ versus b/t ratios for different values of s/b for each case of axial load. The results indicate very clearly the improvement in ductility achieved by using closely spaced bars. The ductility is dramatically enhanced for the same b/t ratio. Also, the same ductility can be achieved using considerably larger b/t ratios.

This study highlights the substantial improvement in behaviour of the IC models over the conventional partially encased composite members currently in use in Europe. A more general discussion of the results and their implication for design is provided in Chapter 9 of this thesis.

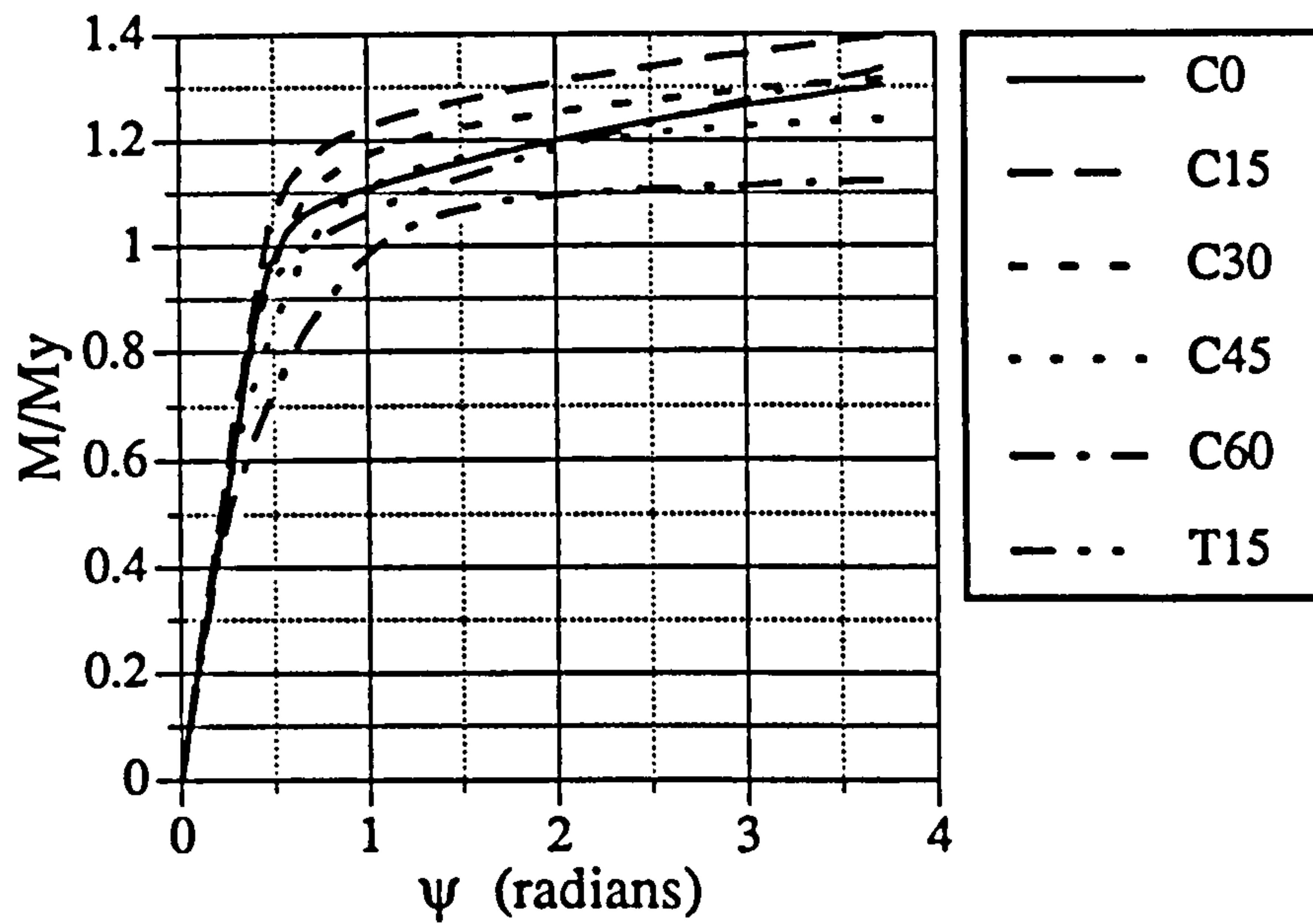


Fig. 8.1 Relationship between the normalised moment and the deflection angle for different values of axial load

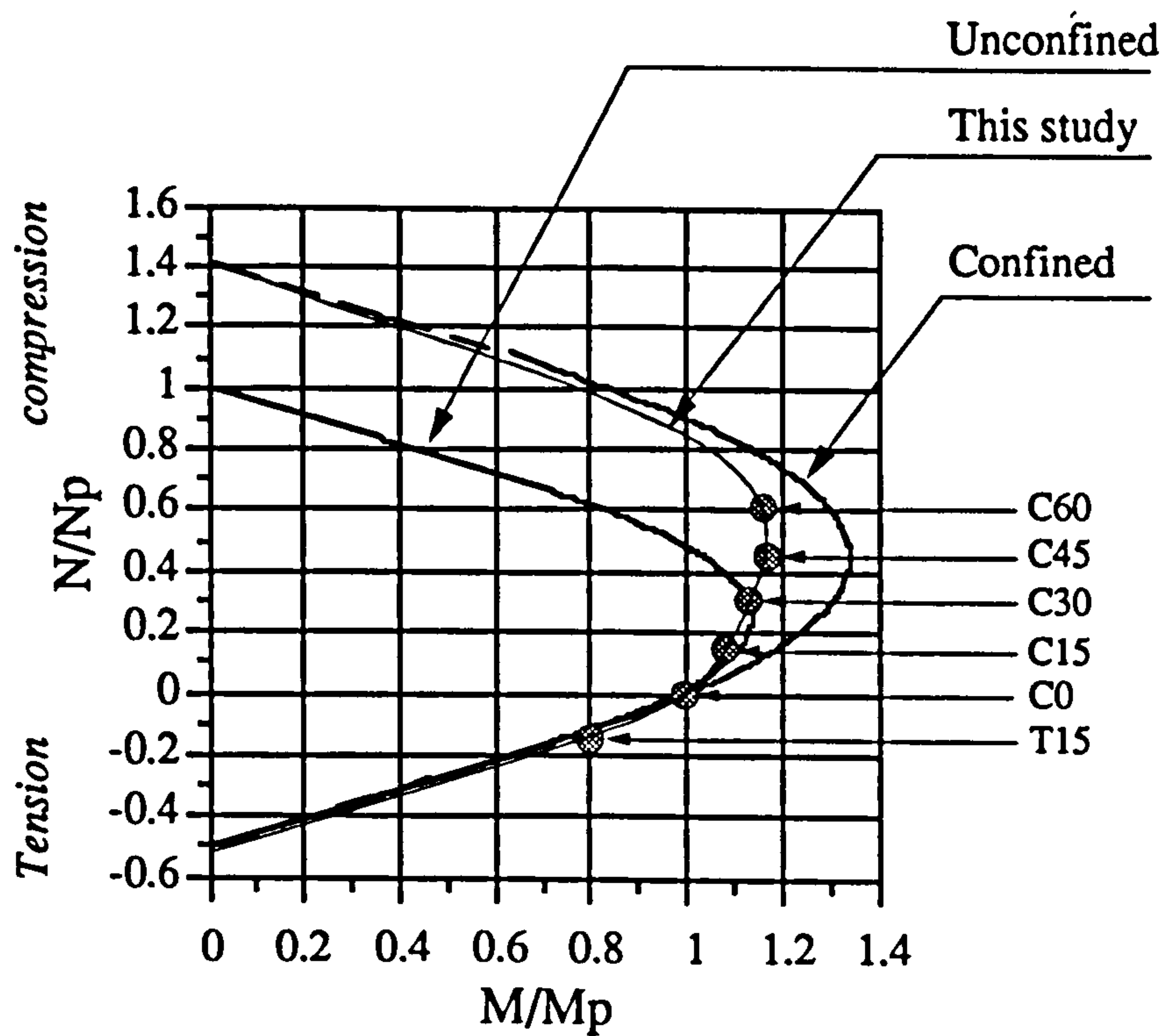


Fig. 8.2 Interaction curves for the control model

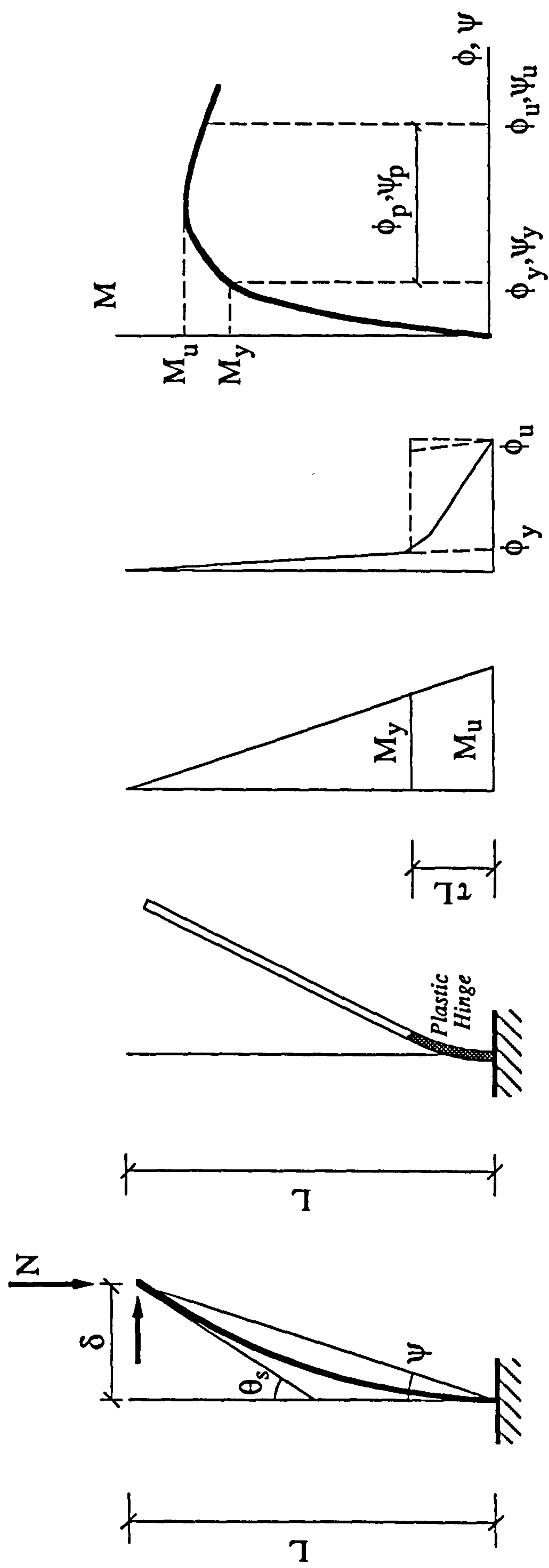


Fig. 8.3 Definition of different parameters used in the study

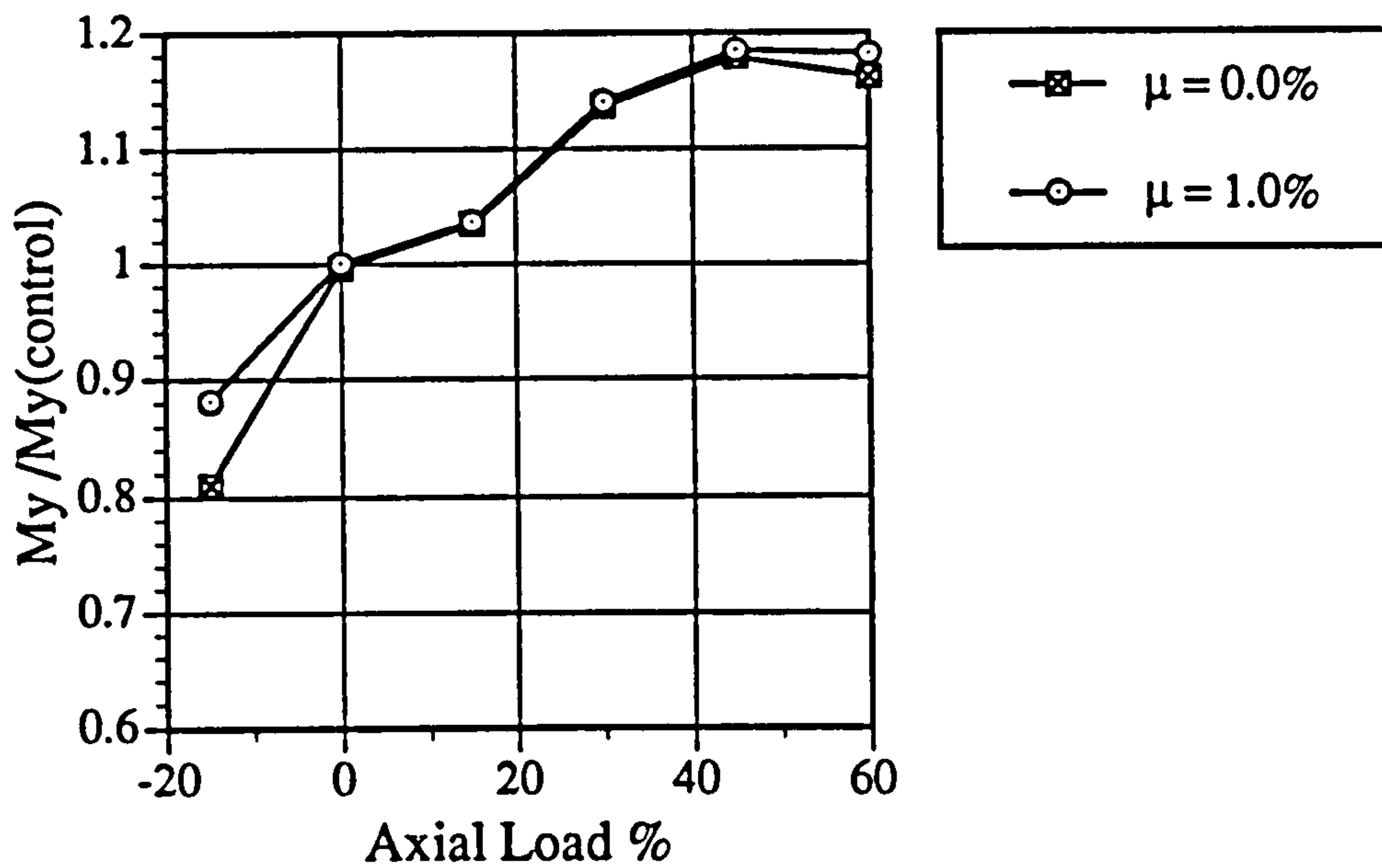


Fig. 8.4 Normalised yield moment versus axial load for 0% and 1% strain hardening

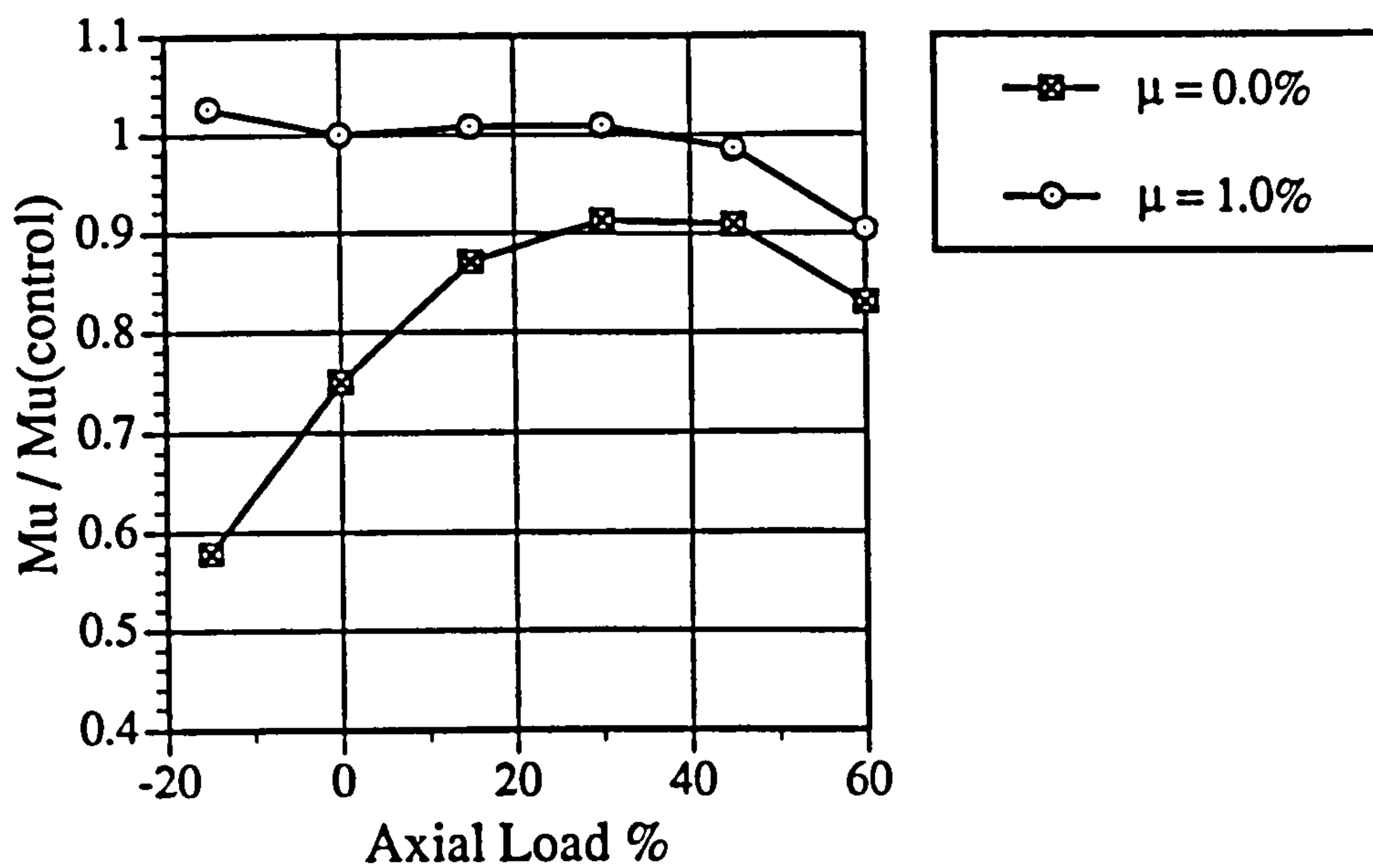


Fig. 8.5 Normalised ultimate moment versus axial load for 0% and 1% strain hardening

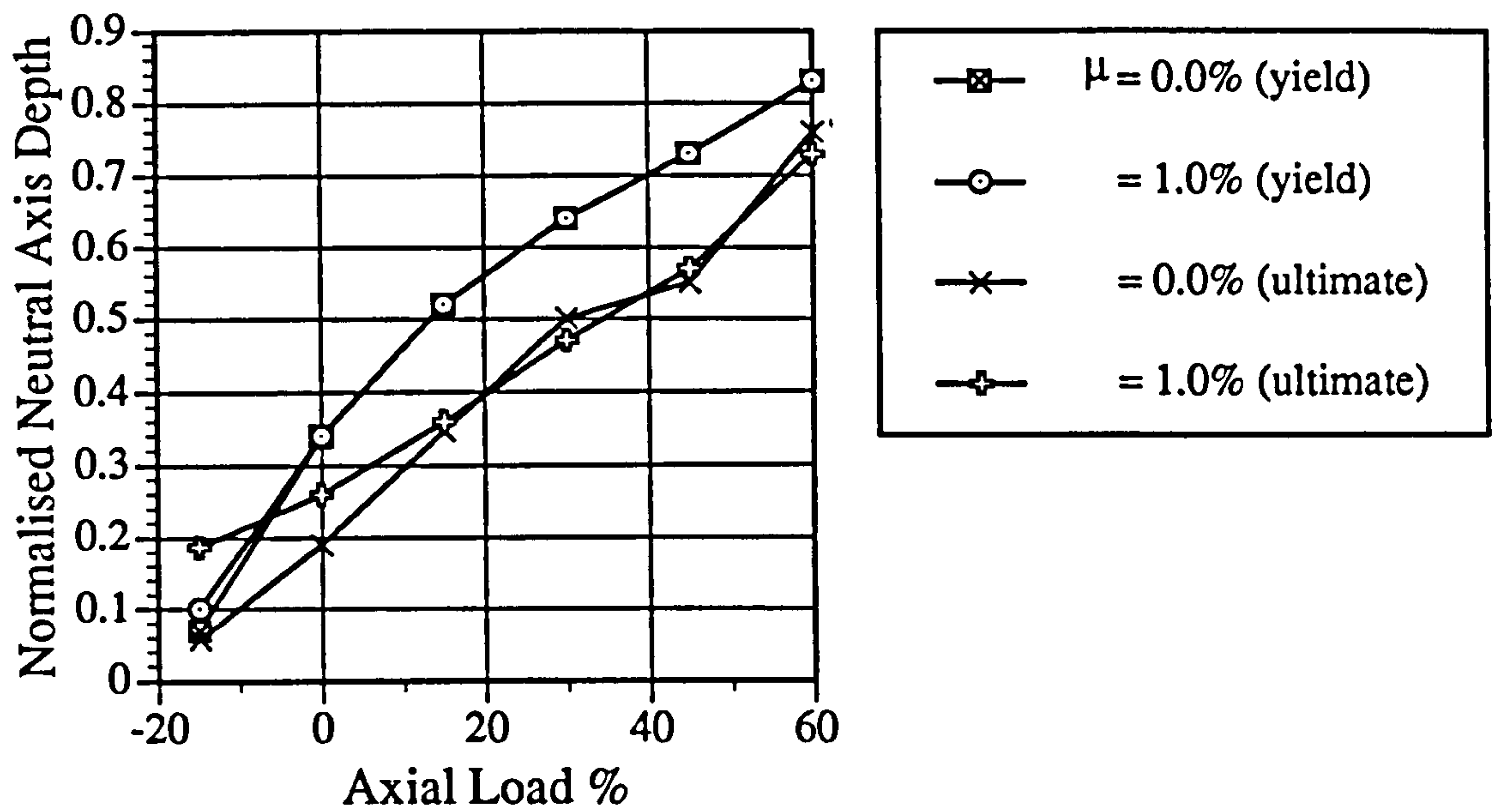


Fig. 8.6 Normalised neutral axis depth at yield and at ultimate versus axial load for 0% and 1% strain hardening

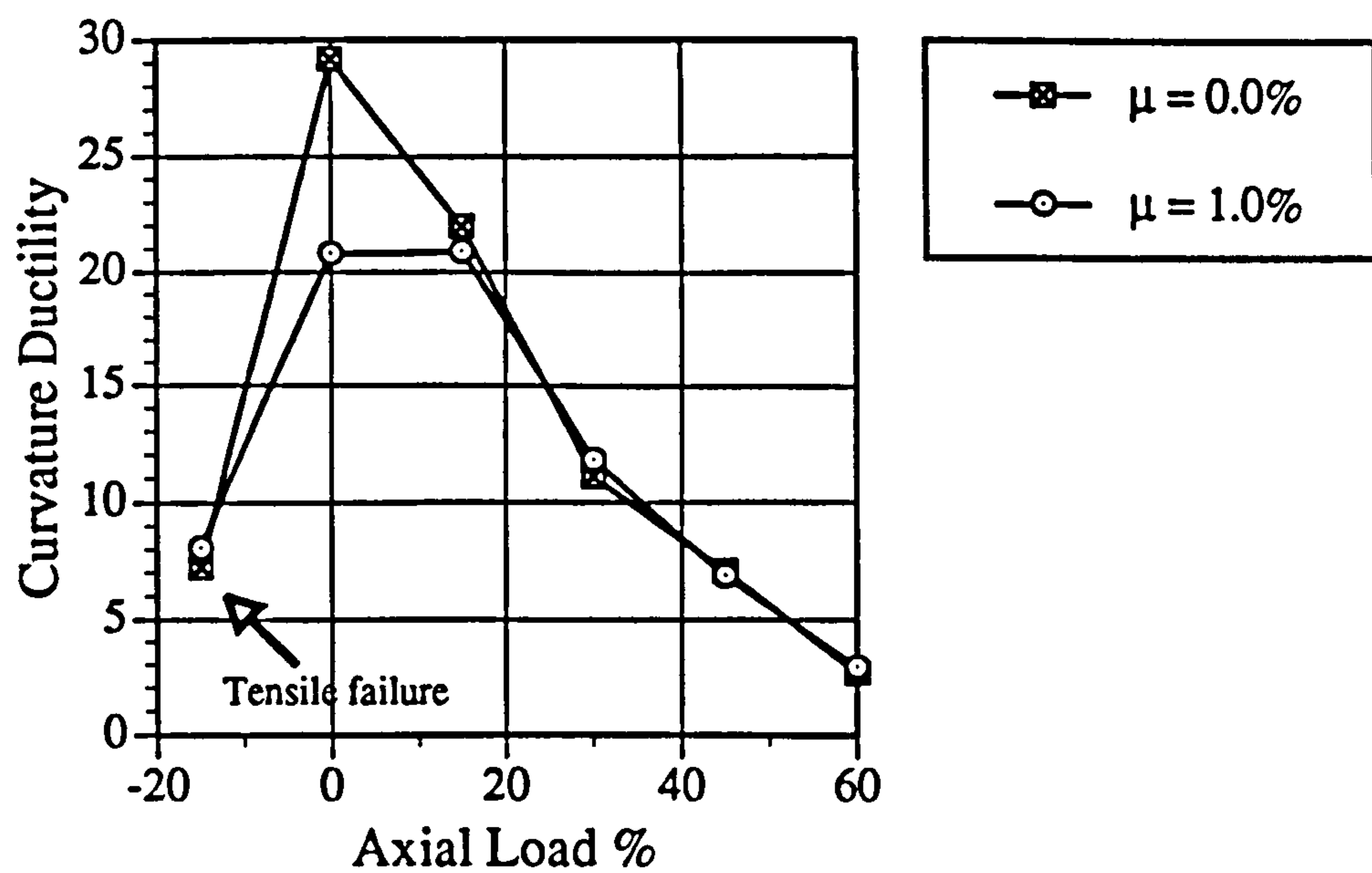


Fig. 8.7 Curvature ductility versus axial load for 0% and 1% strain hardening

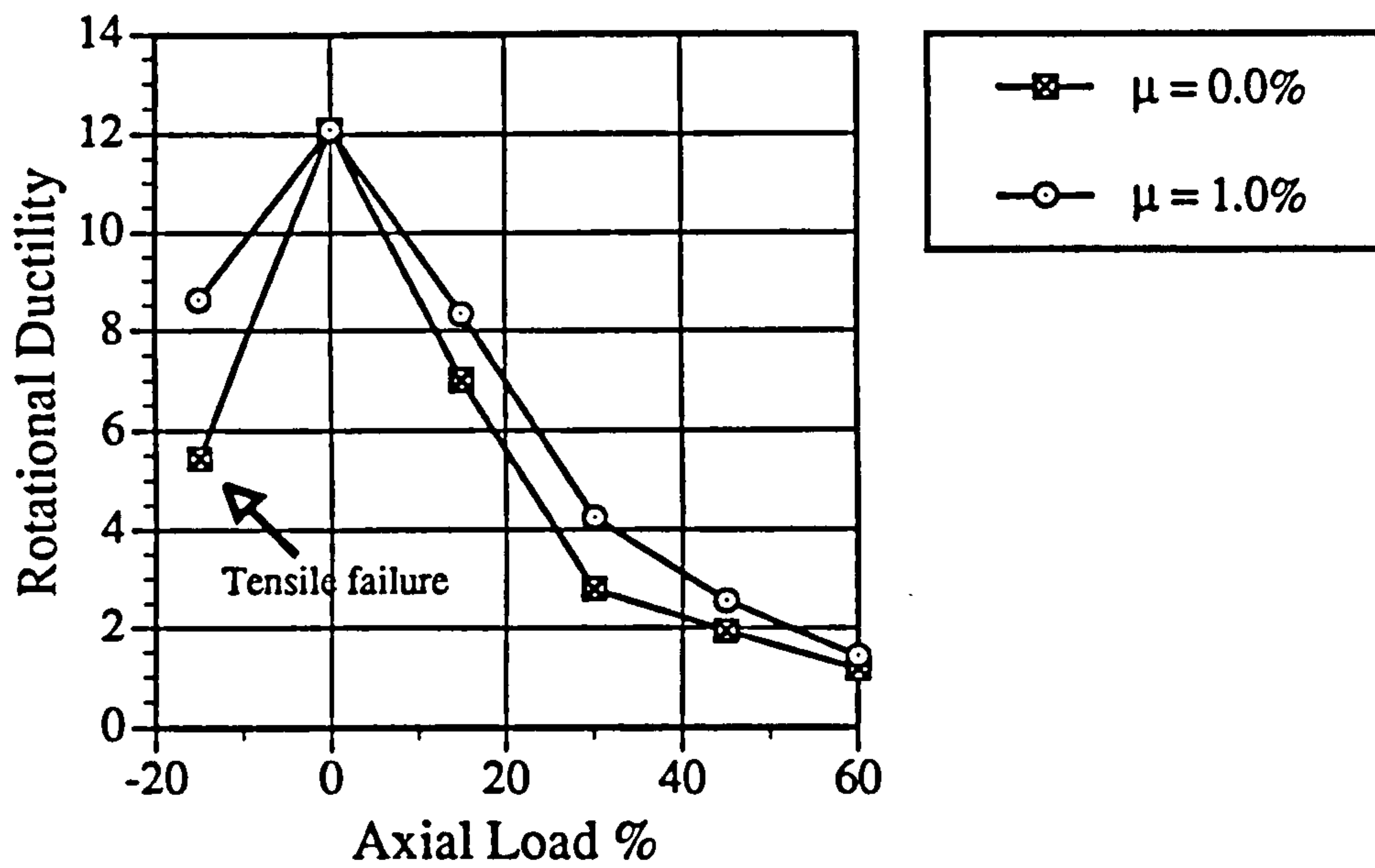


Fig. 8.8 Rotational ductility versus axial load for 0% and 1% strain hardening

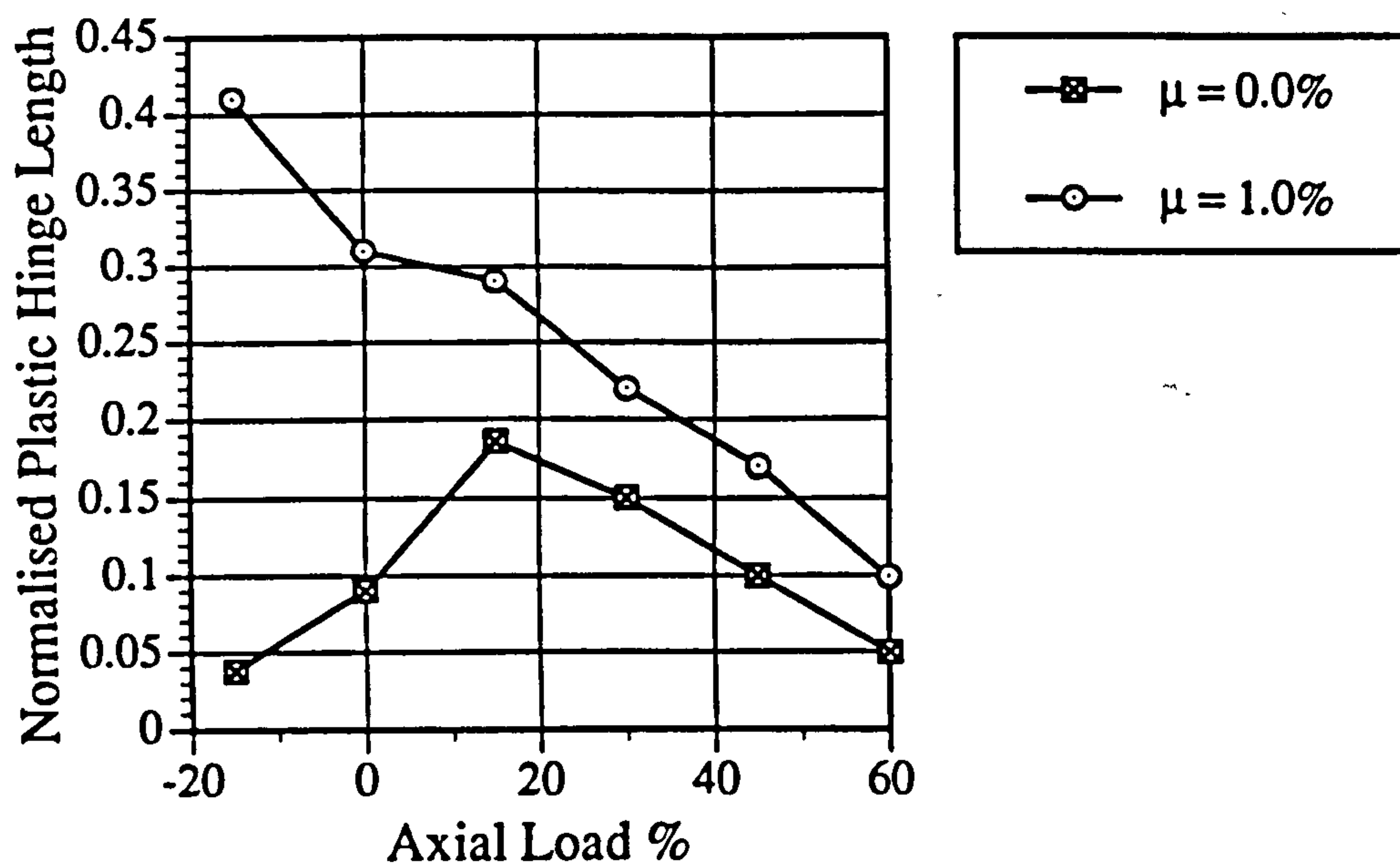


Fig. 8.9 Normalised plastic hinge length versus axial load for 0% and 1% strain hardening

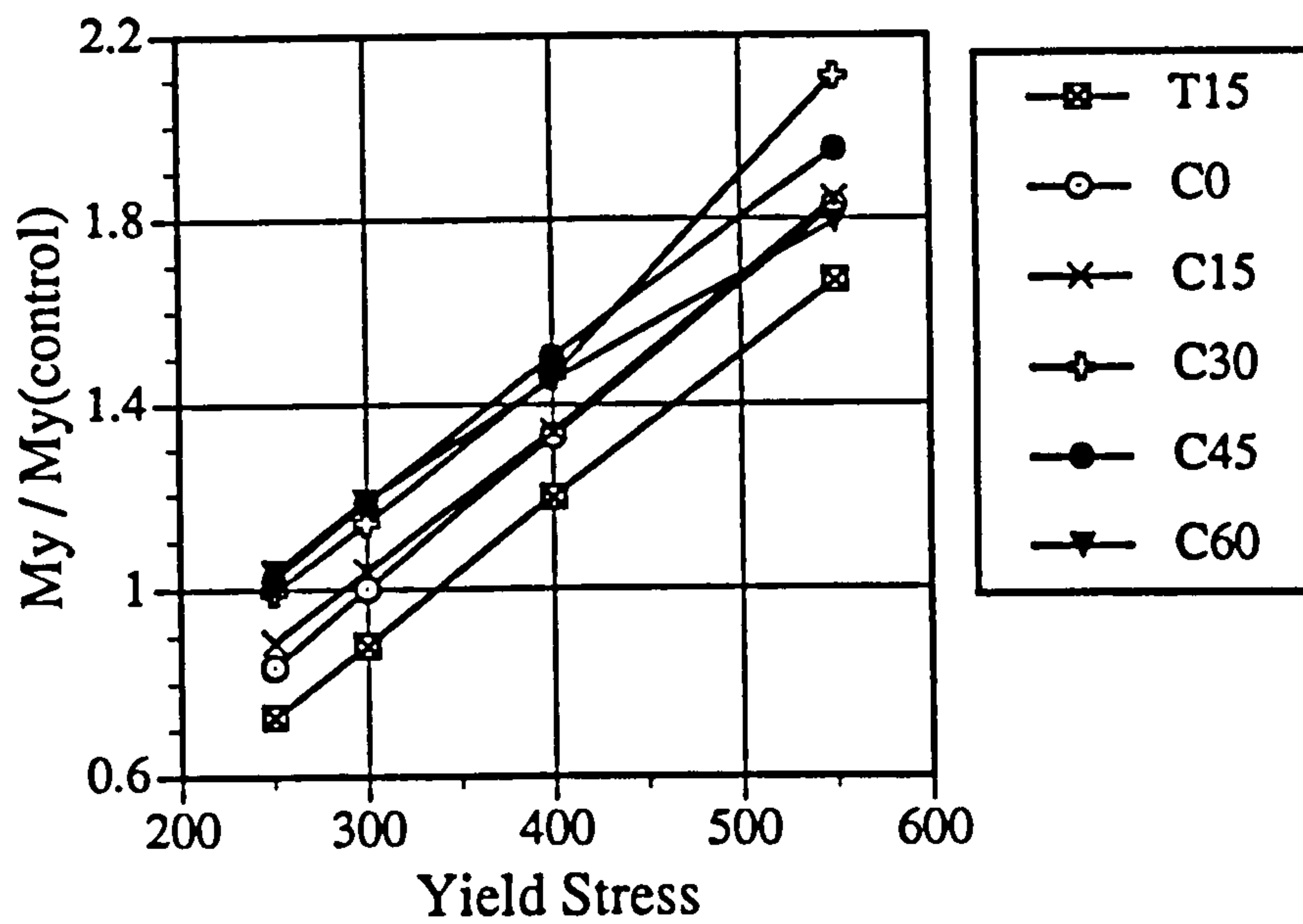


Fig. 8.10 Normalised yield moment versus yield stress for different values of axial load

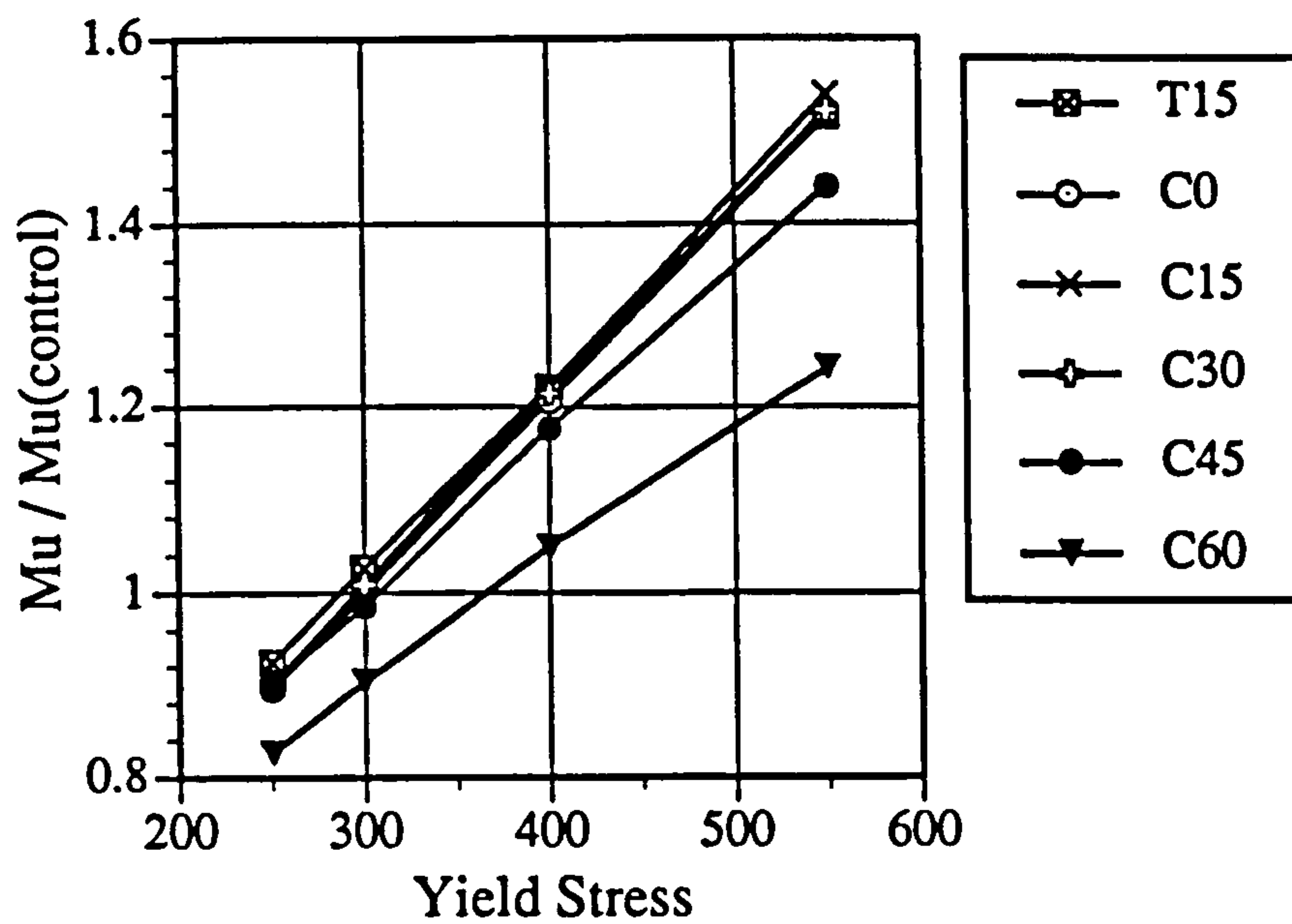


Fig. 8.11 Normalised ultimate moment versus yield stress for different values of axial load

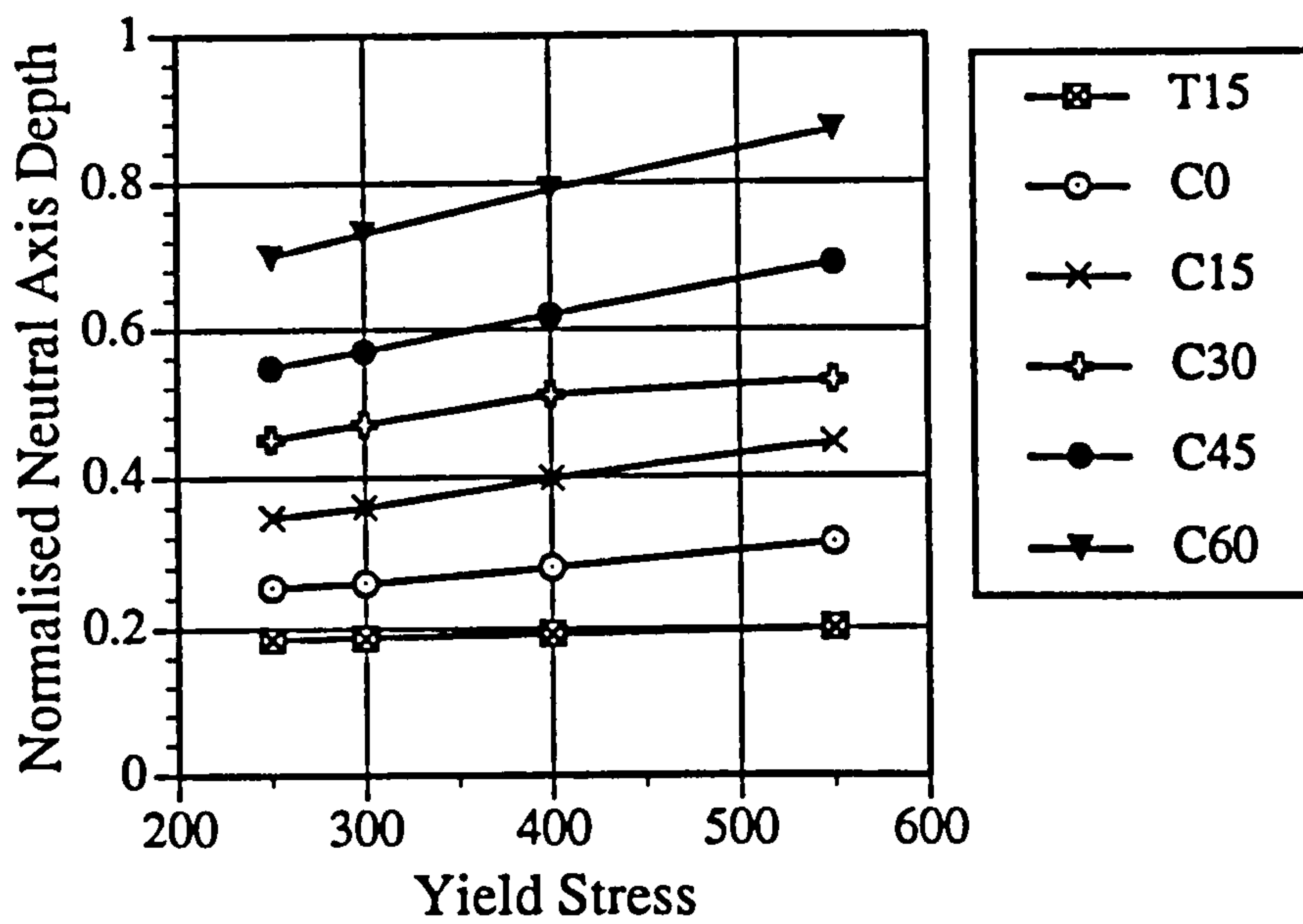


Fig. 8.12 Normalised neutral axis depth at ultimate versus yield stress for different values of axial load

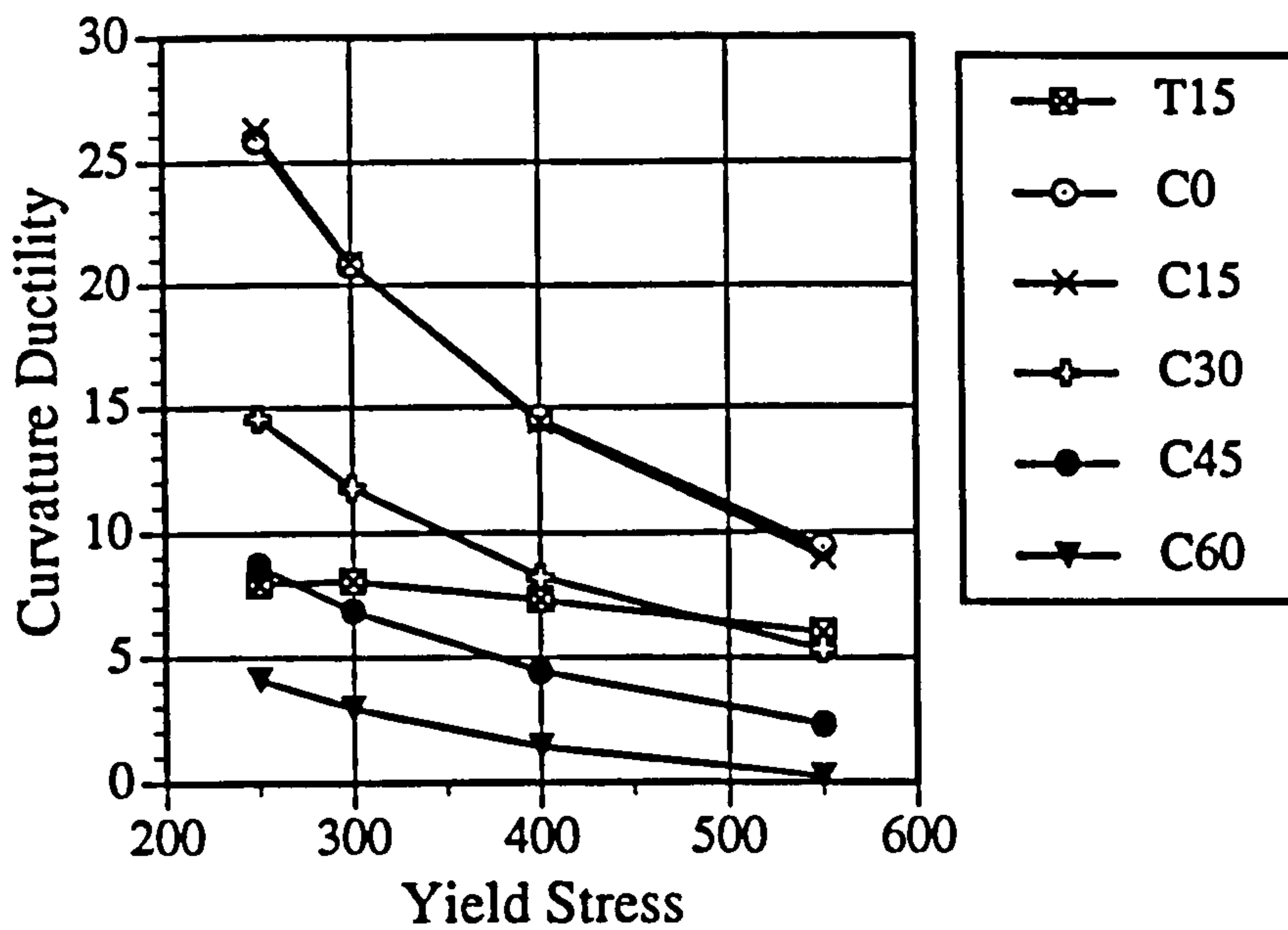


Fig. 8.13 Curvature ductility versus yield stress for different values of axial load

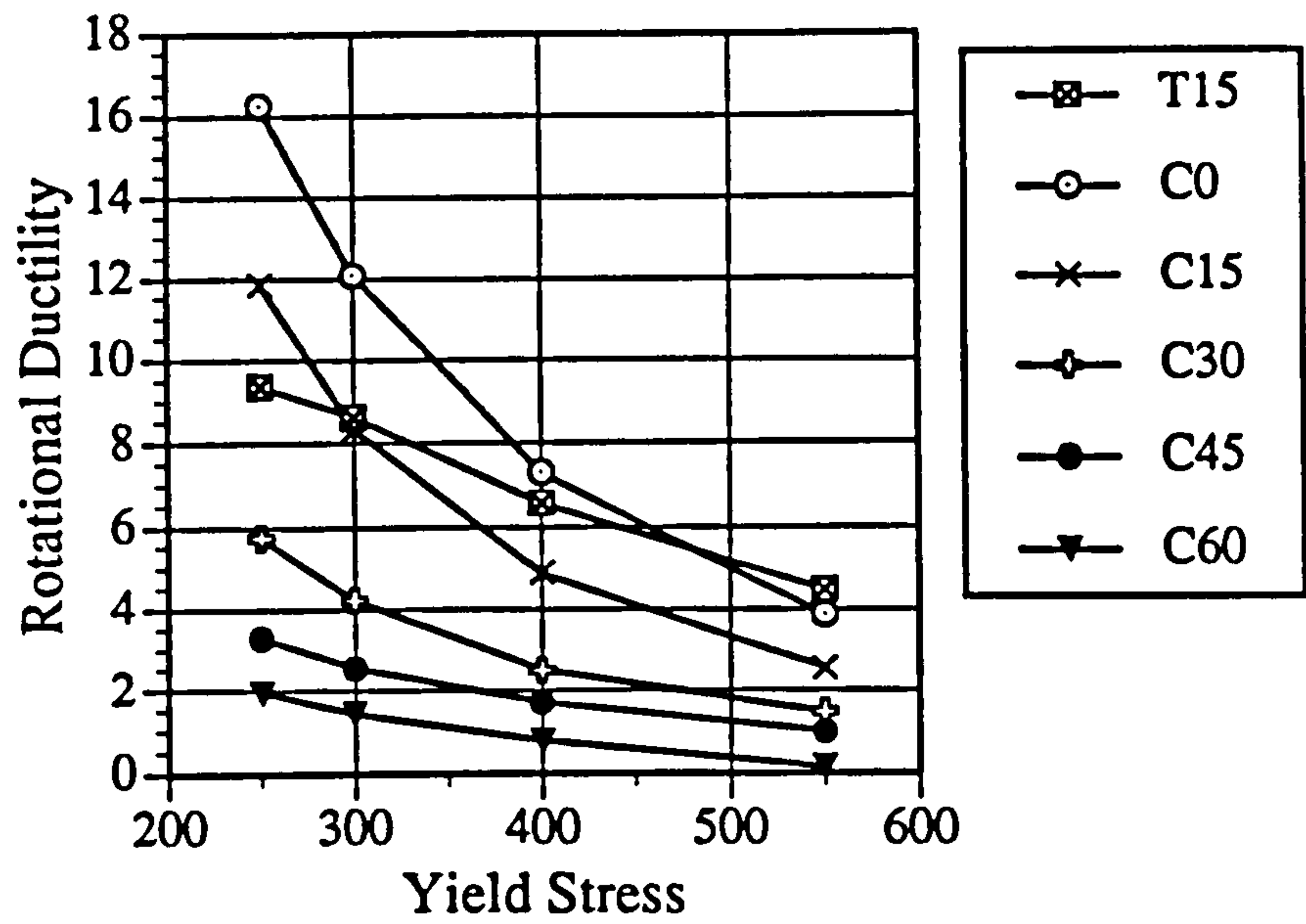


Fig. 8.14 Rotational ductility versus yield stress for different values of axial load

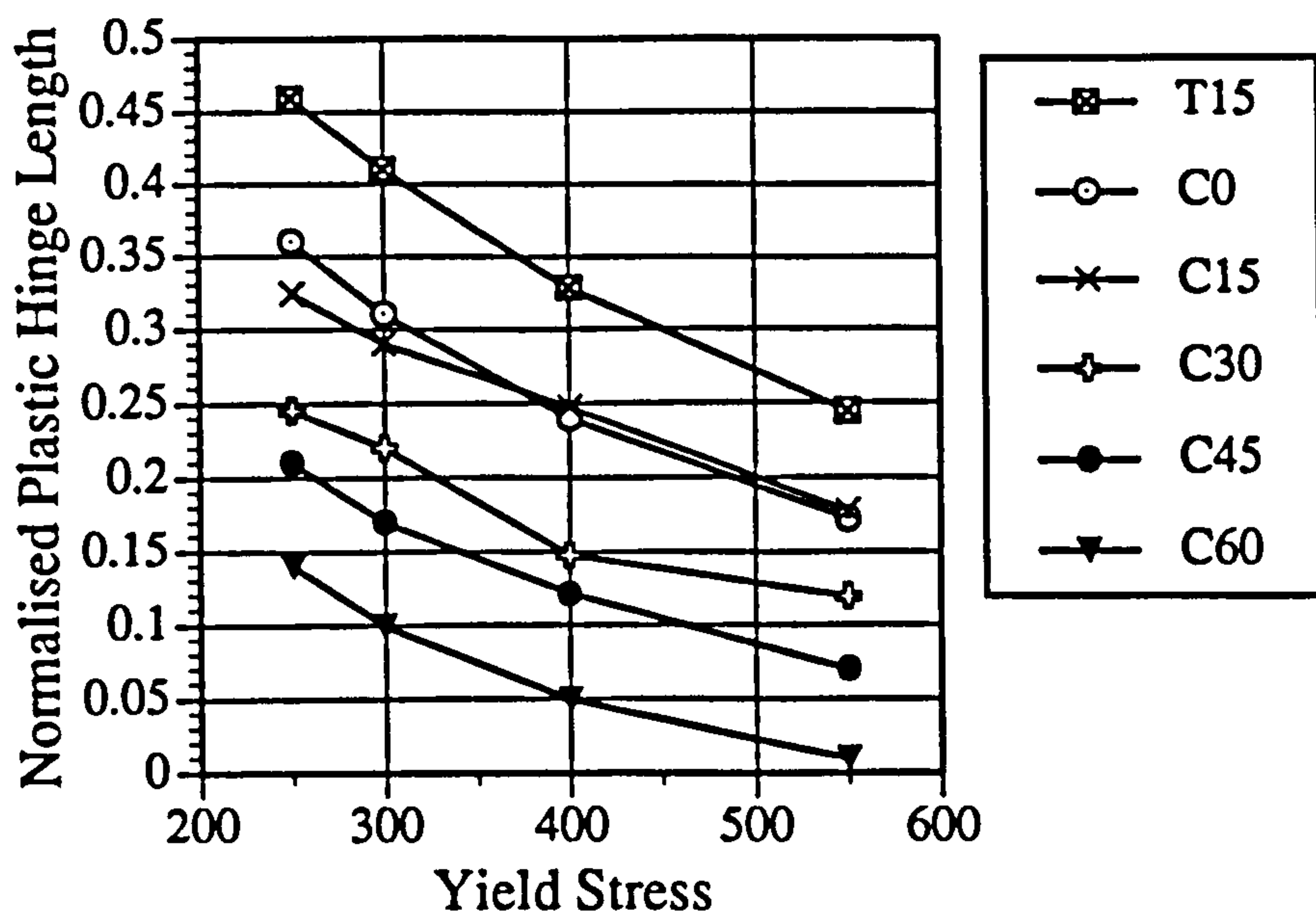


Fig. 8.15 Normalised plastic hinge length versus yield stress for different values of axial load

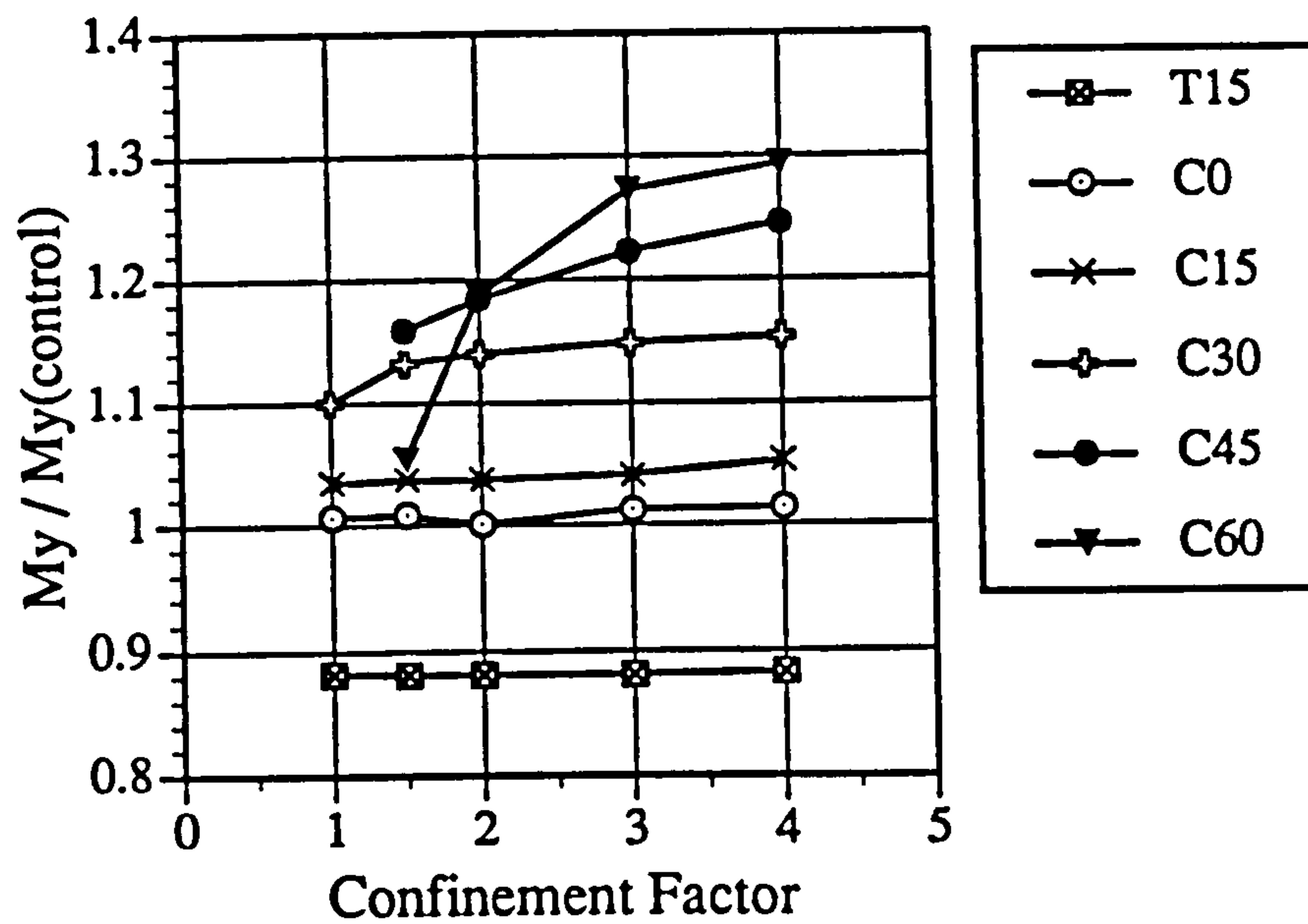


Fig. 8.16 Normalised yield moment versus confinement factor for different values of axial load

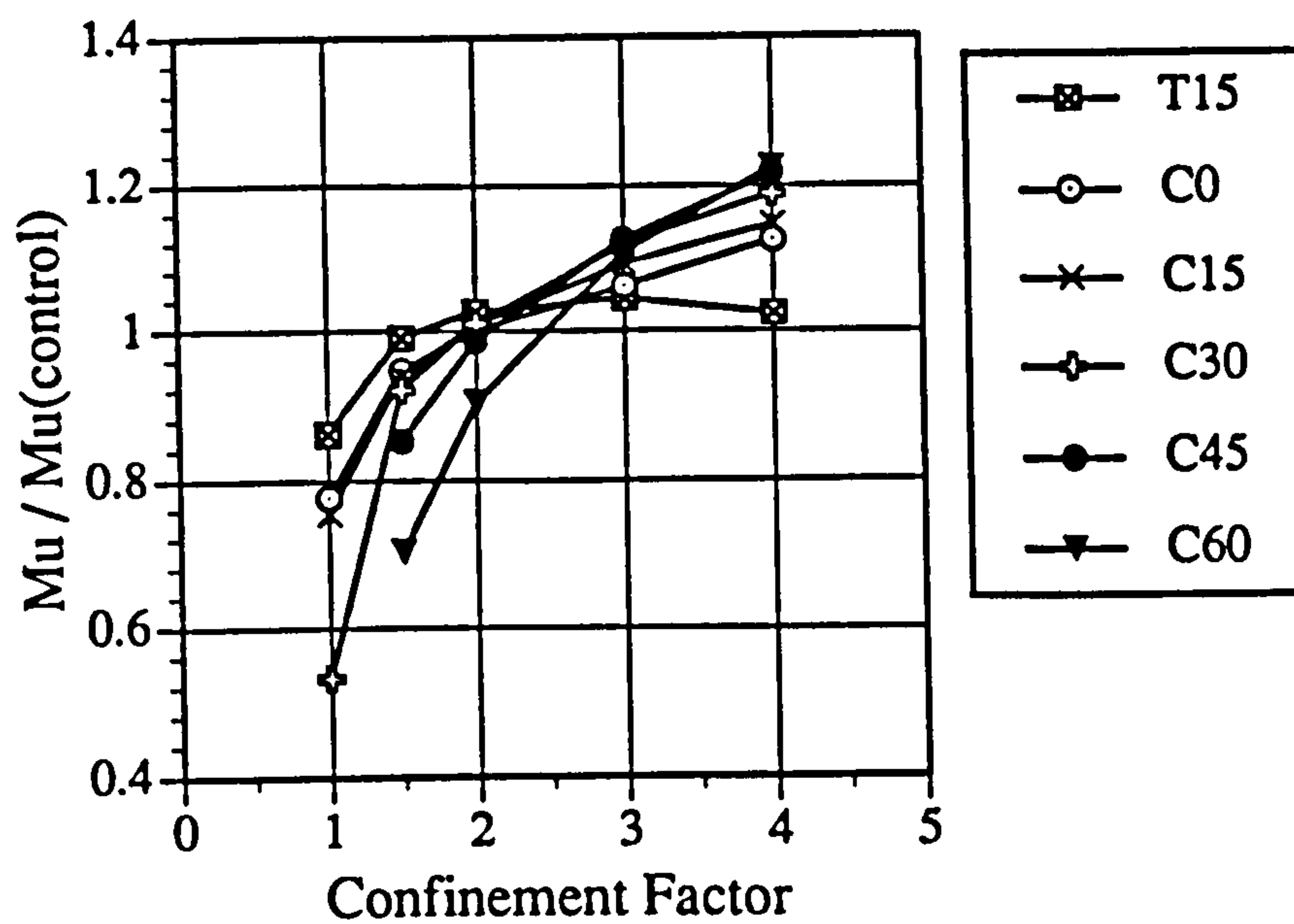


Fig. 8.17 Normalised ultimate moment versus confinement factor for different values of axial load

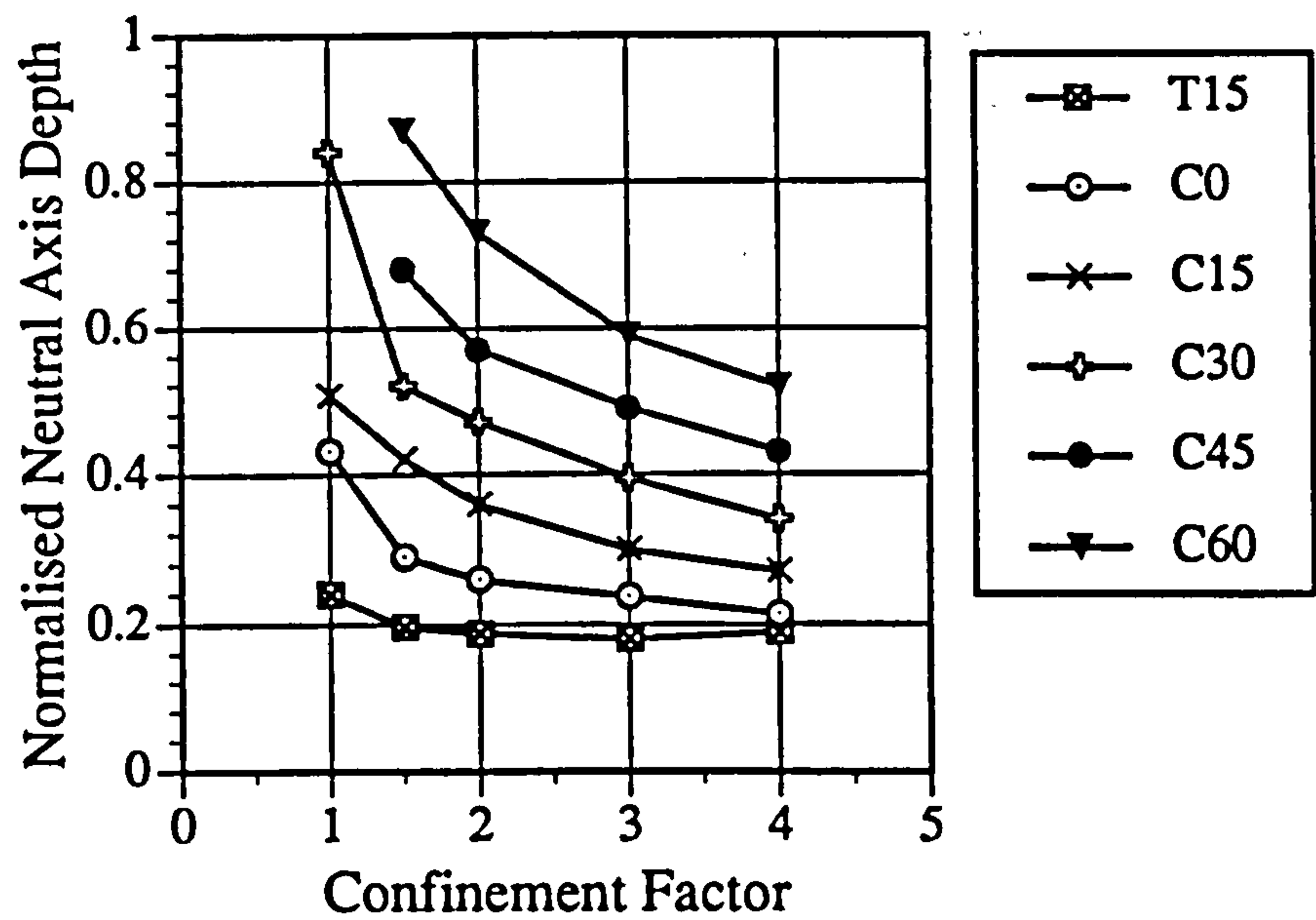


Fig. 8.18 Normalised neutral axis depth at ultimate versus confinement factor for different values of axial load

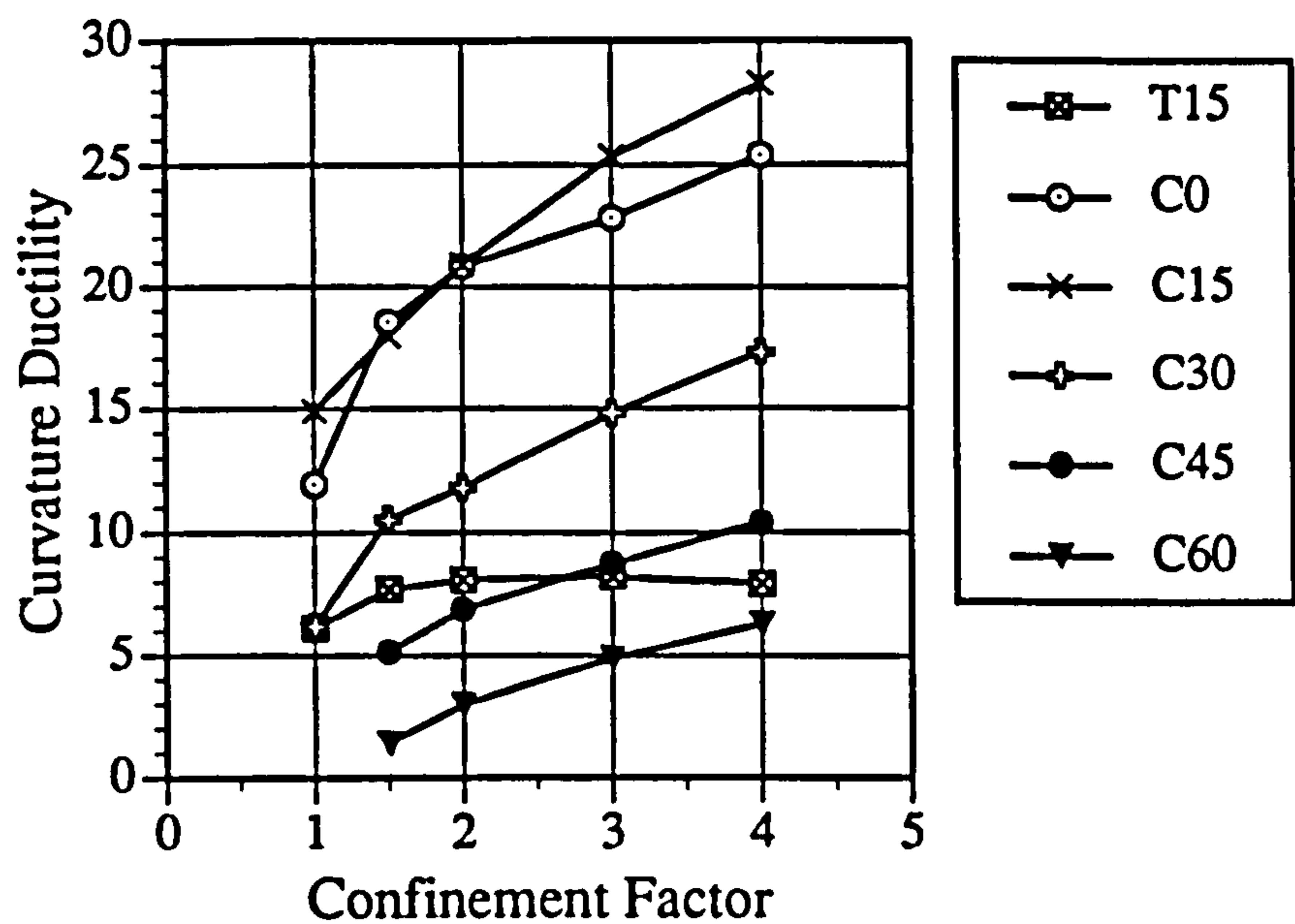


Fig. 8.19 Curvature ductility versus confinement factor for different values of axial load

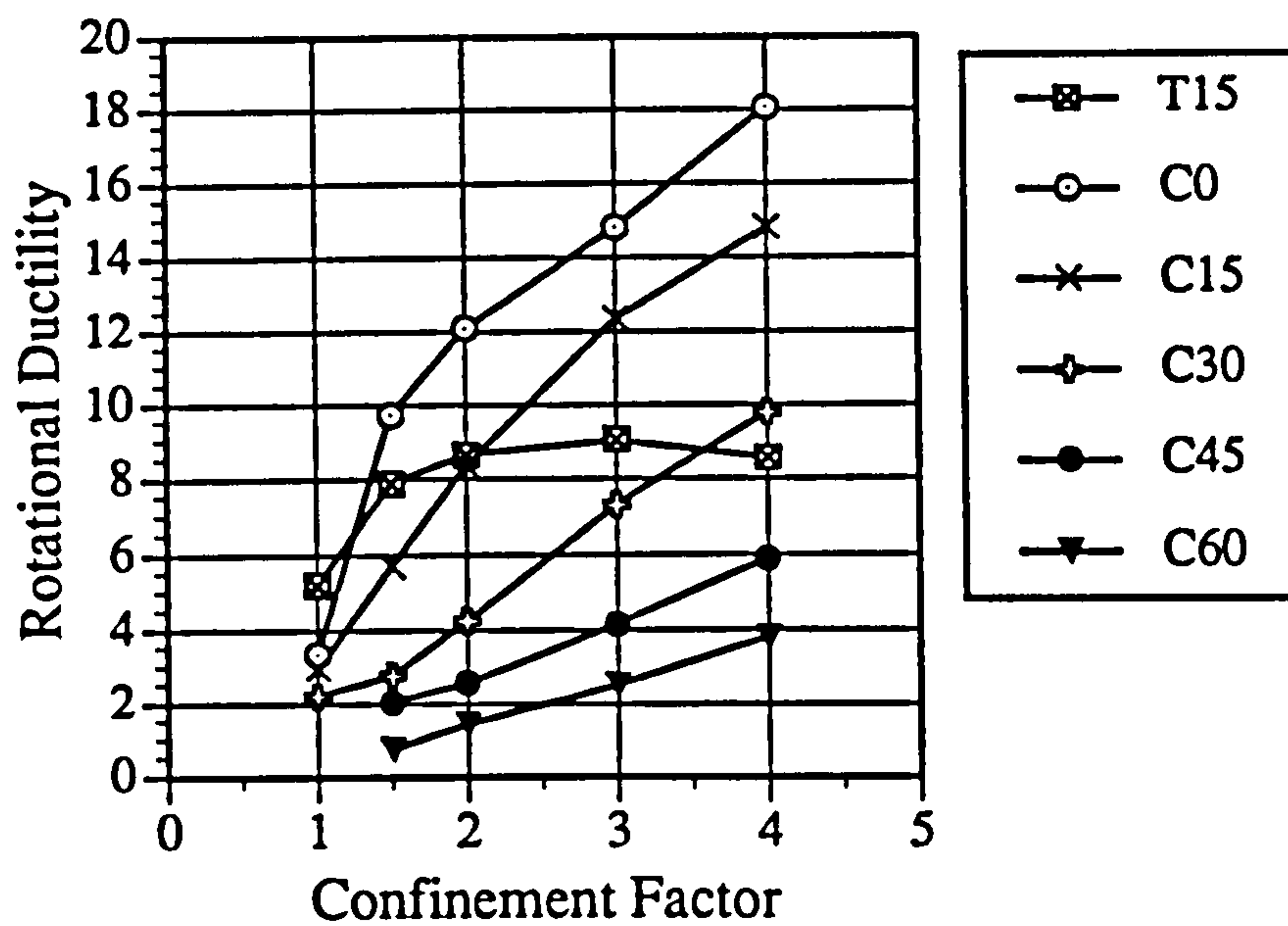


Fig. 8.20 Rotational ductility versus confinement factor for different values of axial load

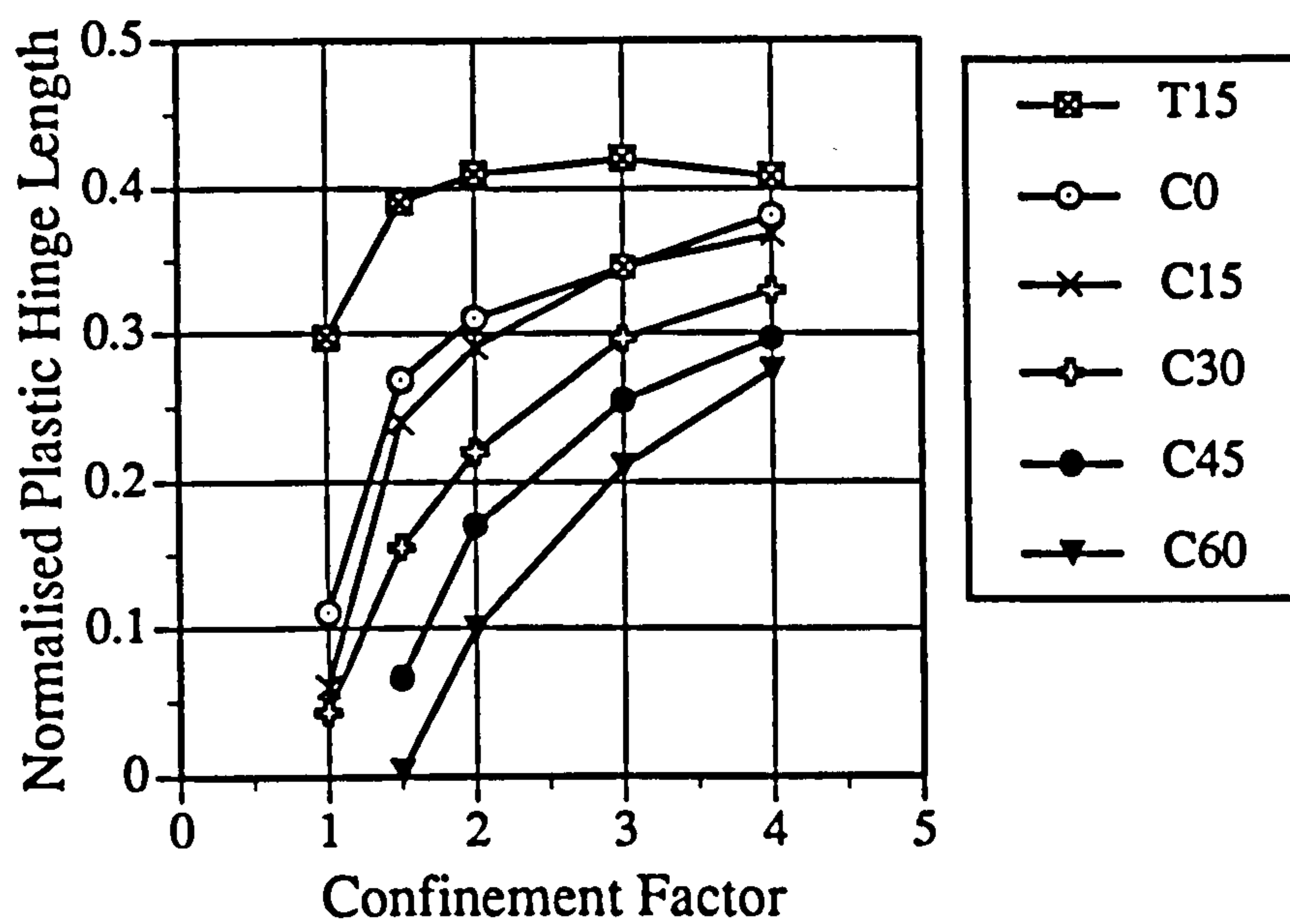


Fig. 8.21 Normalised plastic hinge length versus confinement factor for different values of axial load

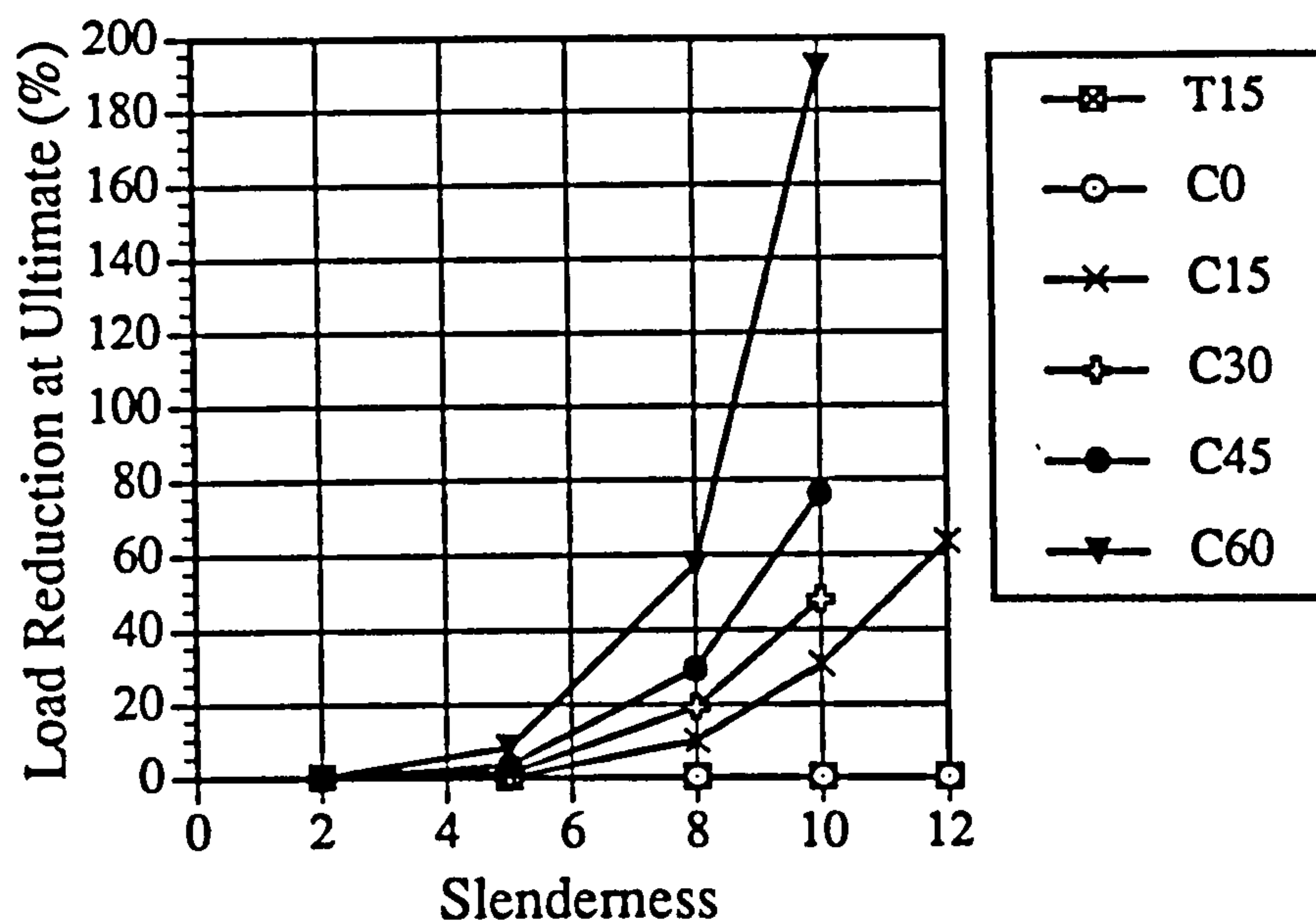


Fig. 8.22 Percentage reduction in lateral load at ultimate displacement versus member slenderness for different values of axial load

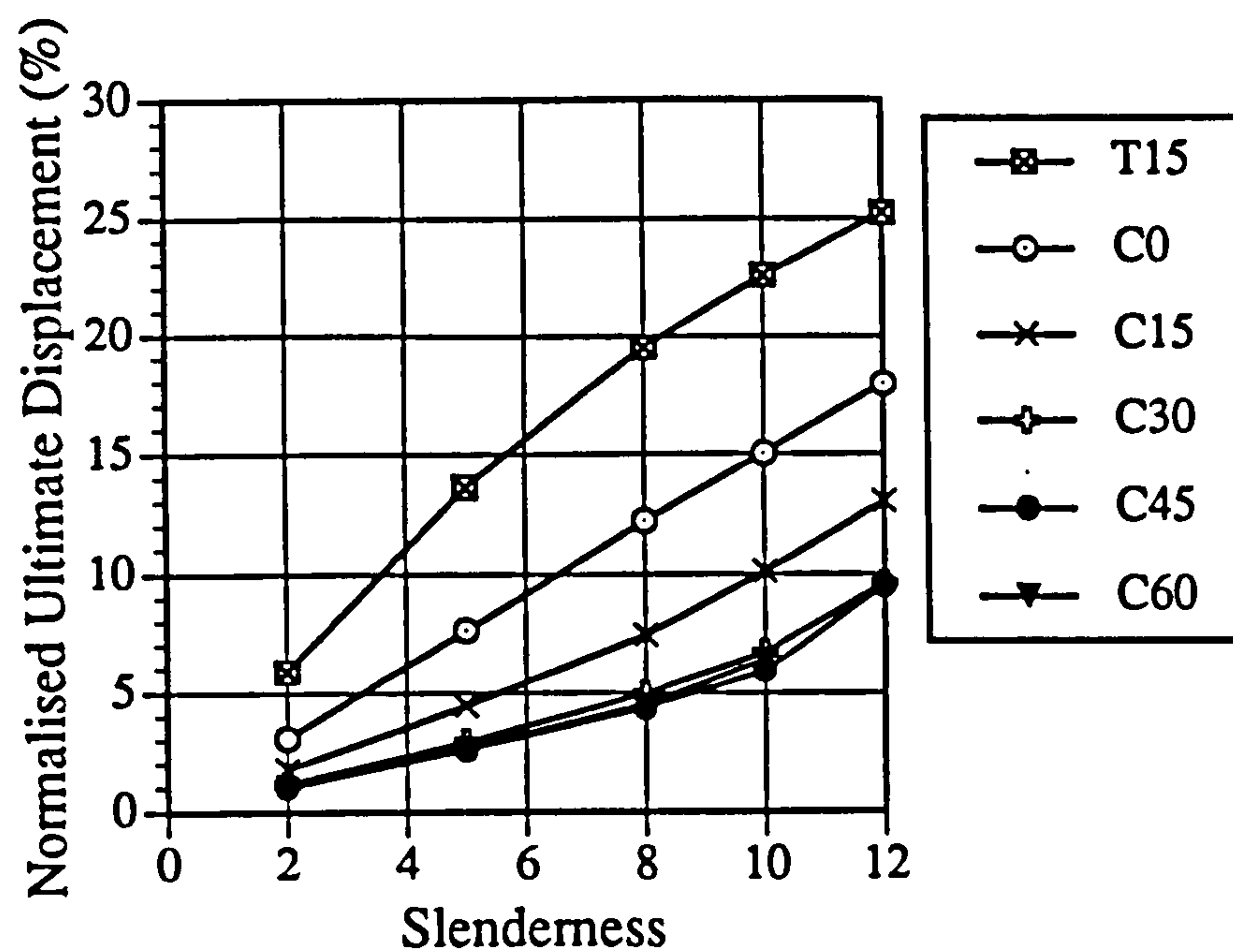


Fig. 8.23 Normalised ultimate displacement (%) versus member slenderness for different values of axial load

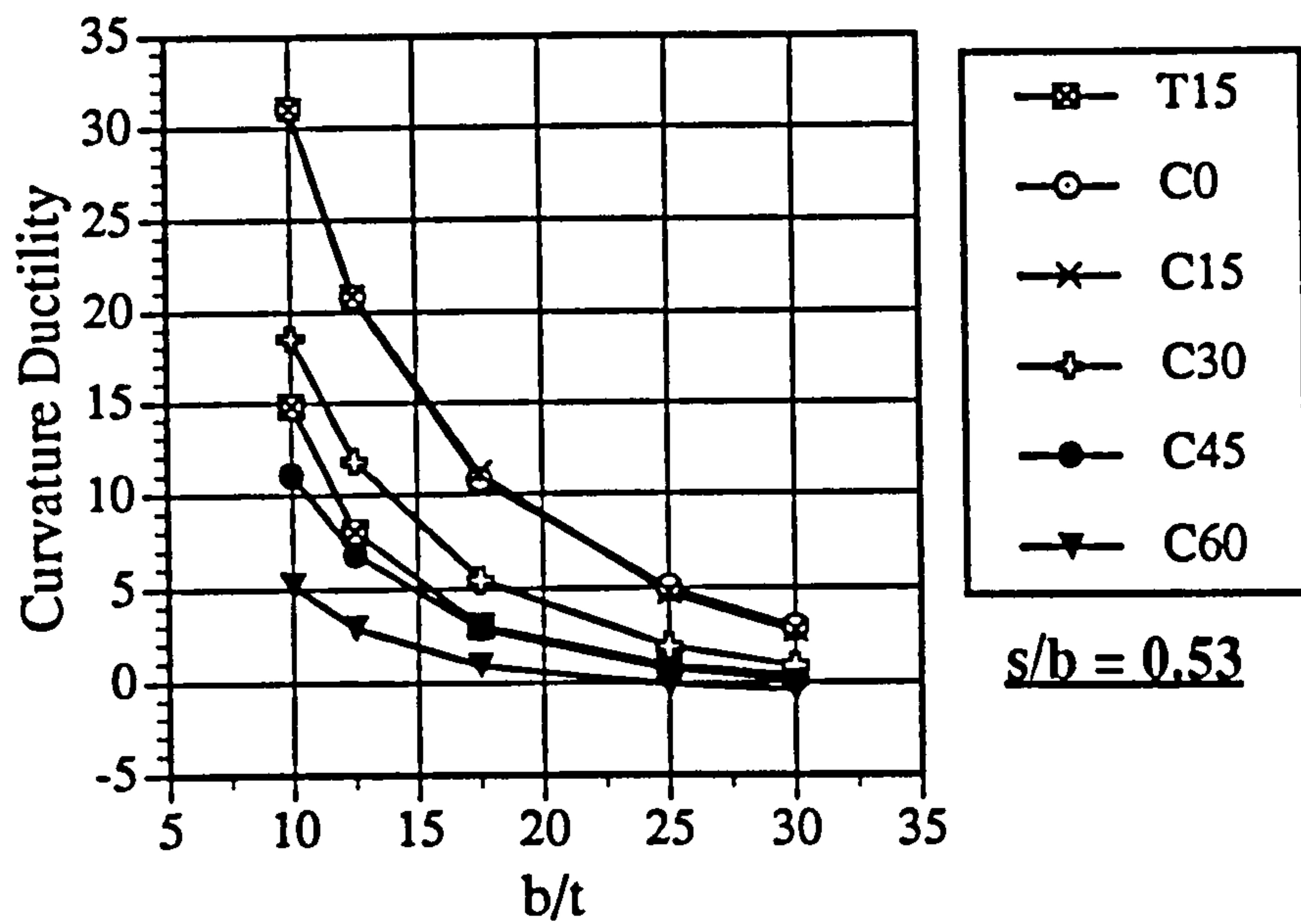


Fig. 8.24 Curvature ductility versus b/t ratio for different values of axial load for s/b of 0.53

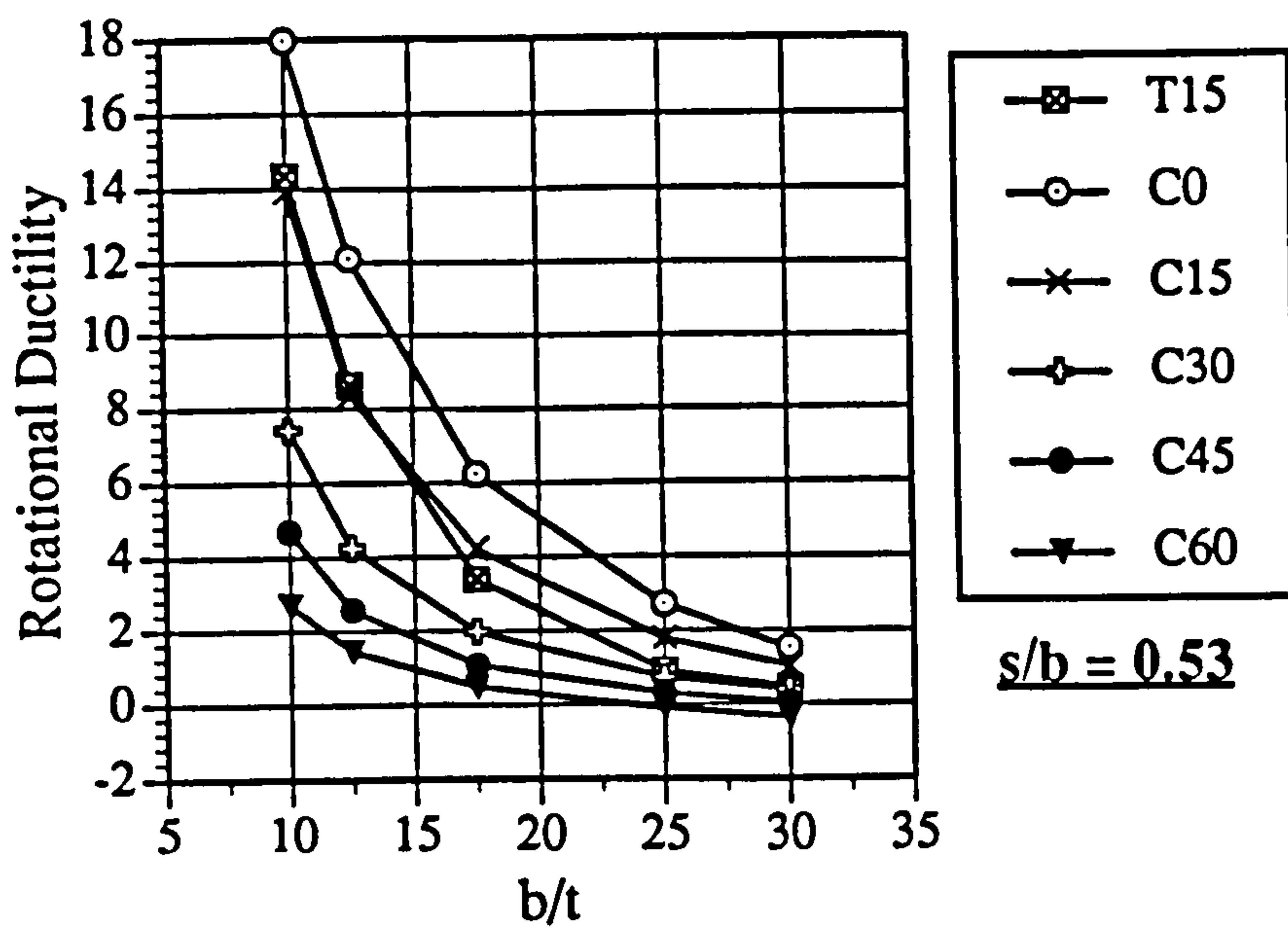


Fig. 8.25 Rotational ductility versus b/t ratio for different values of axial load for s/b of 0.53

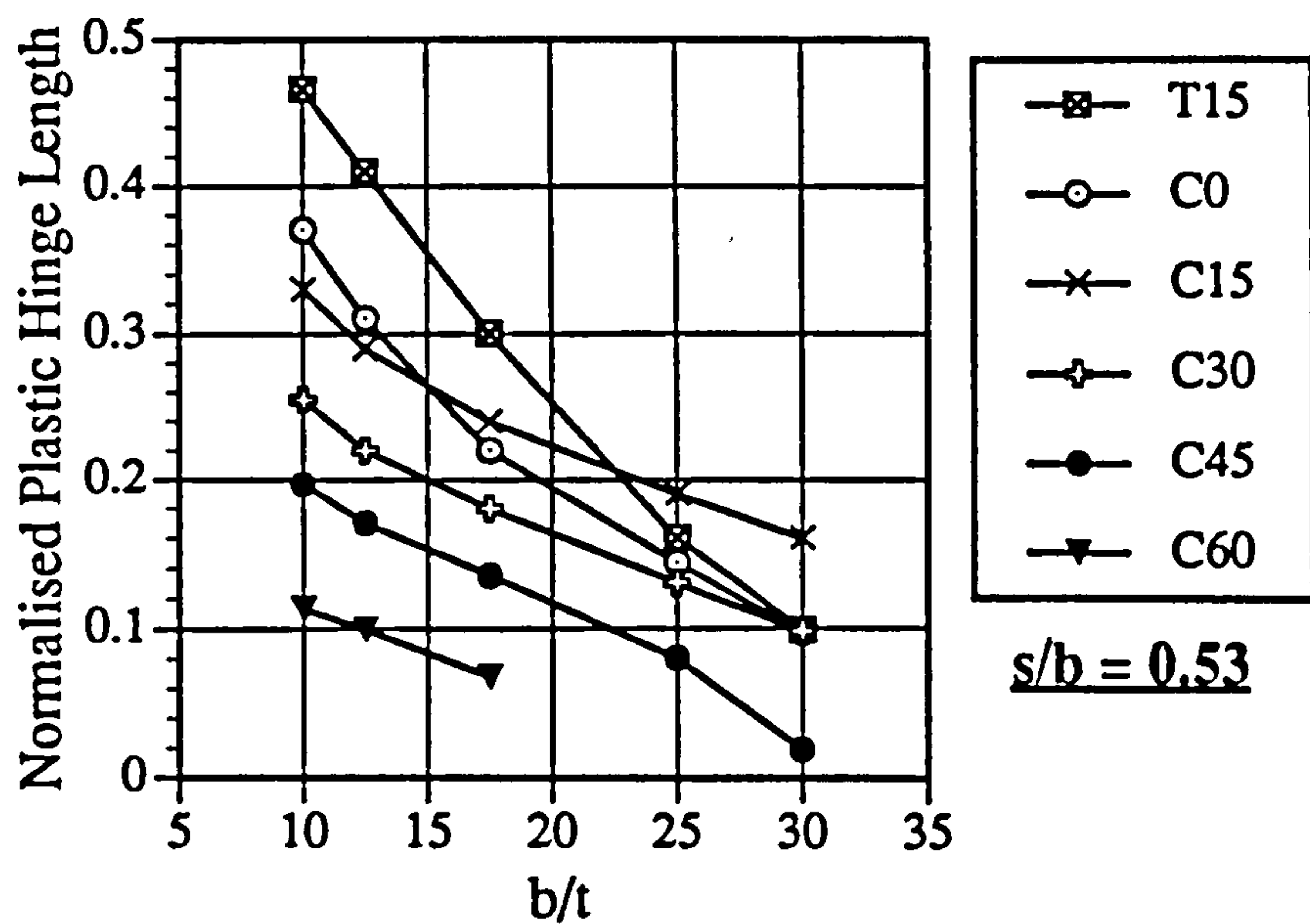


Fig. 8.26 Normalised plastic hinge height versus b/t ratio for different values of axial load for s/b of 0.53

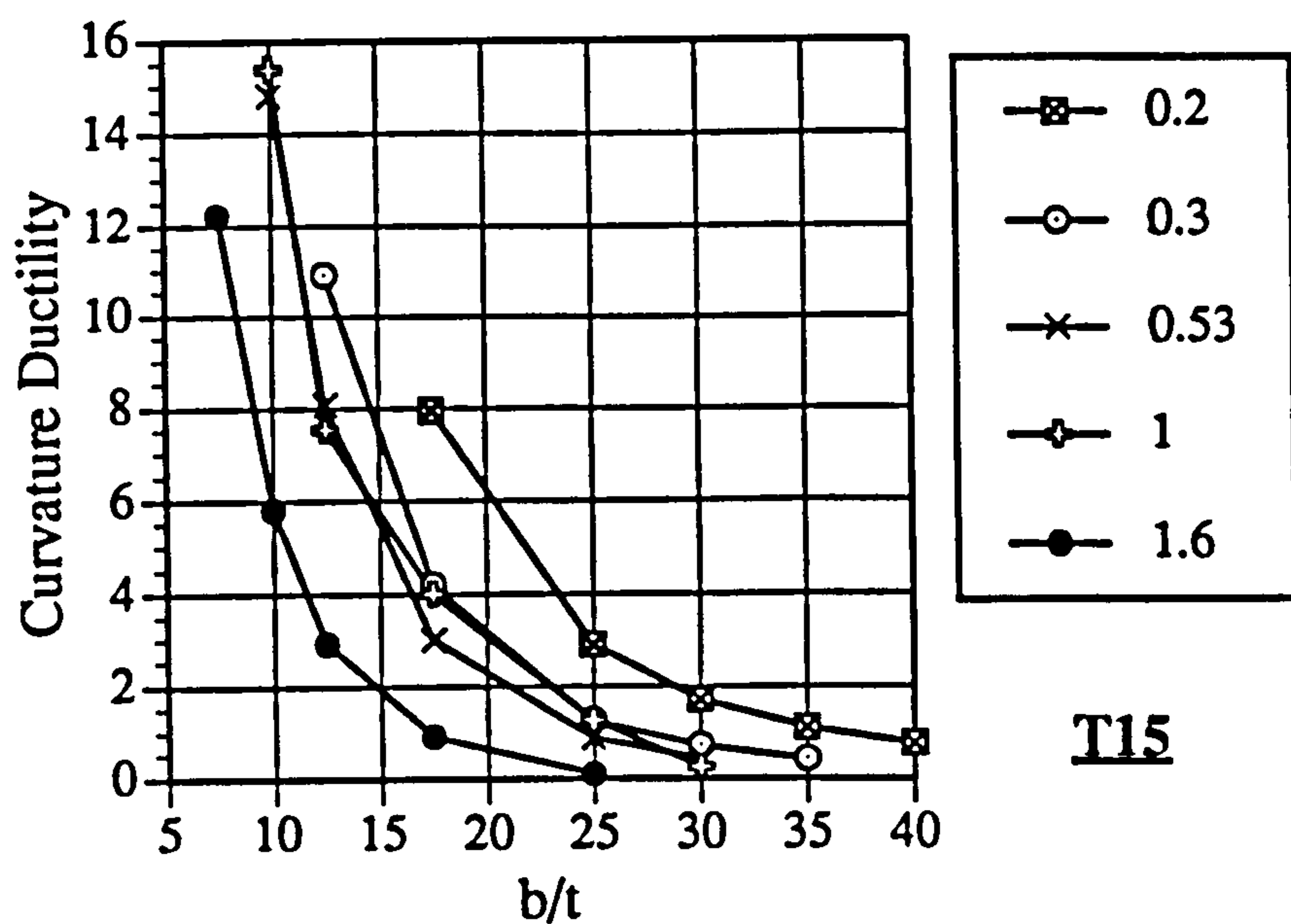


Fig. 8.27 Curvature ductility versus b/t ratio under T15 for different values of s/b

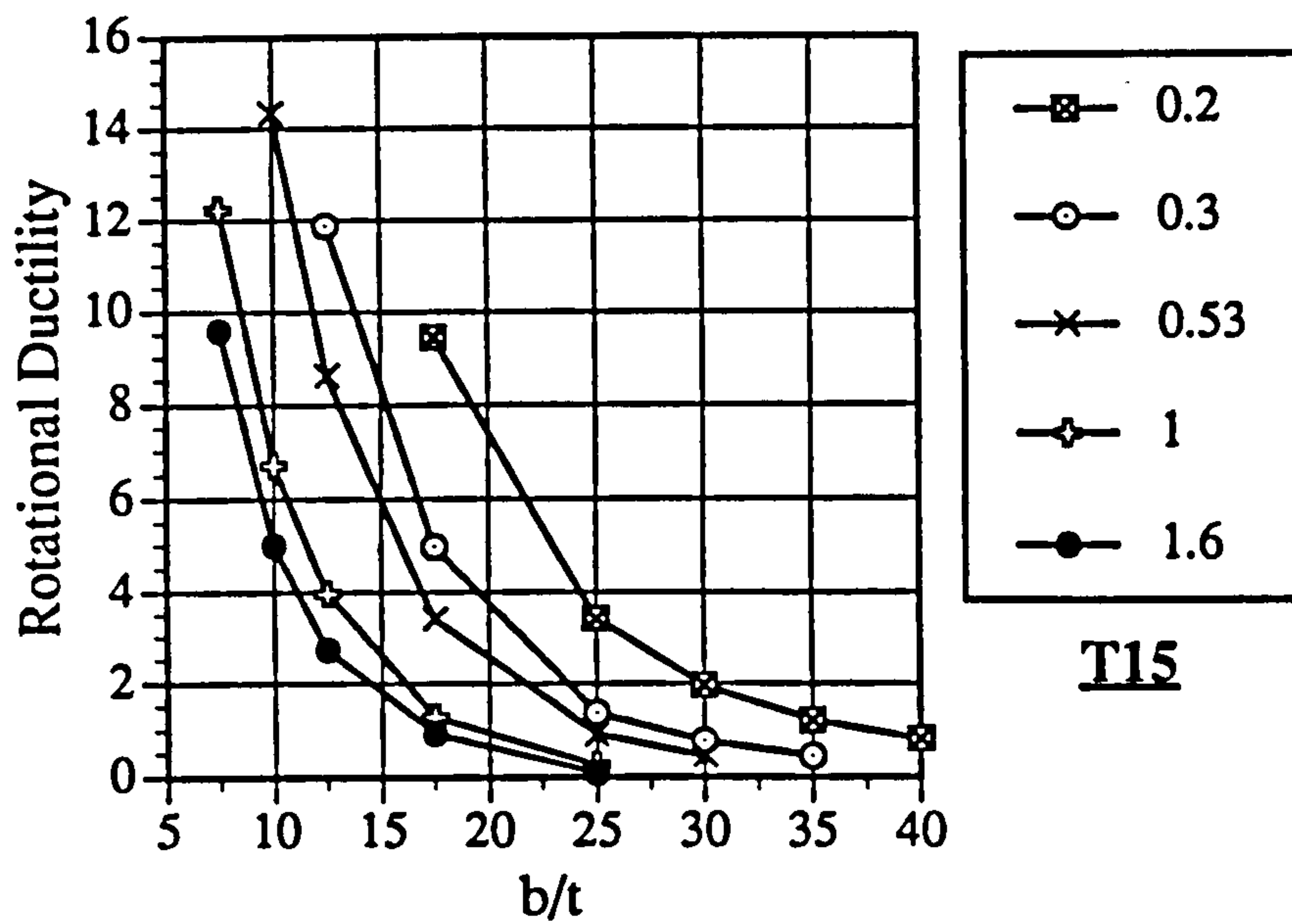


Fig. 8.28 Rotational ductility versus b/t ratio under T15 for different values of s/b

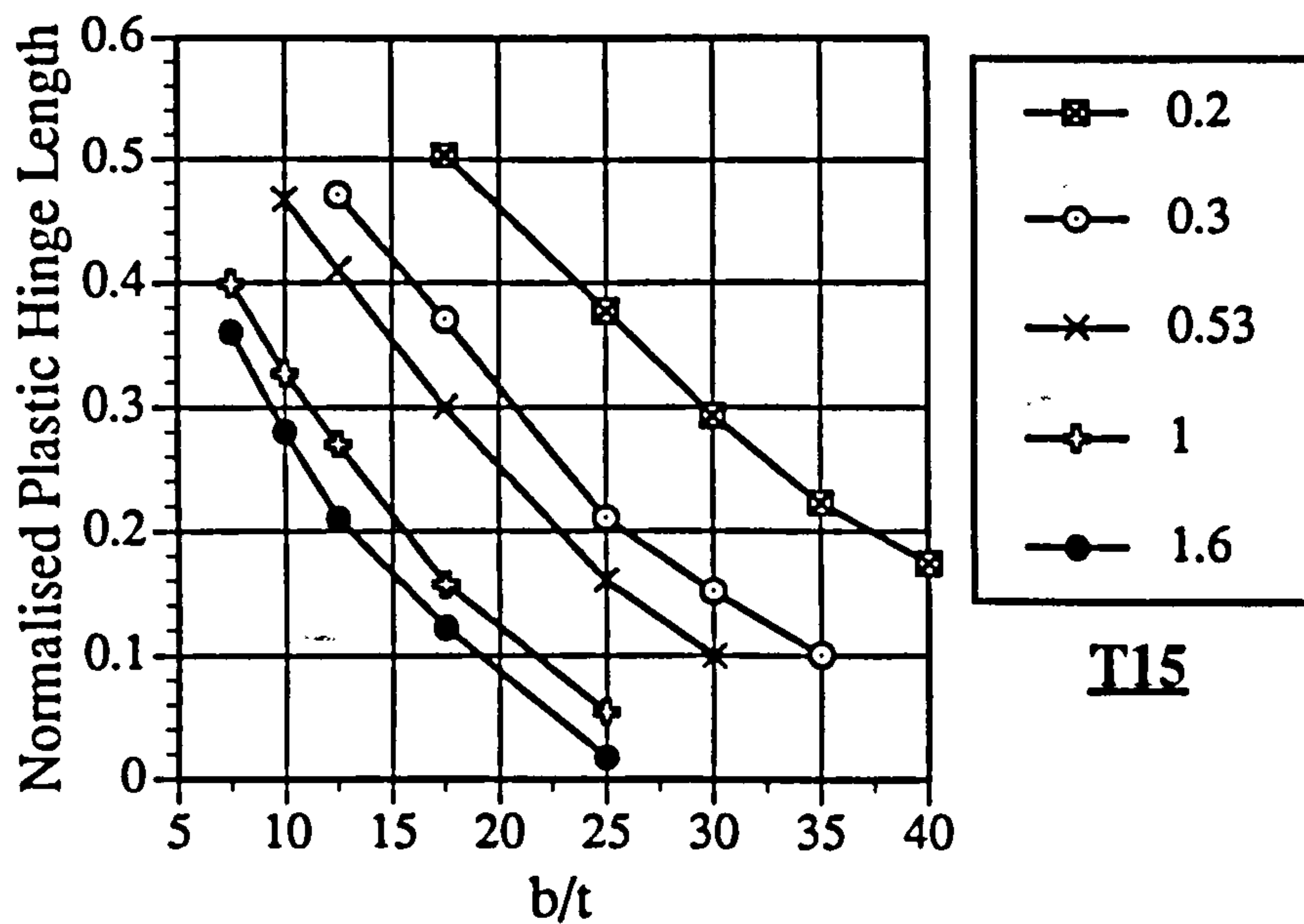


Fig. 8.29 Normalised plastic hinge length versus b/t ratio under T15 for different values of s/b

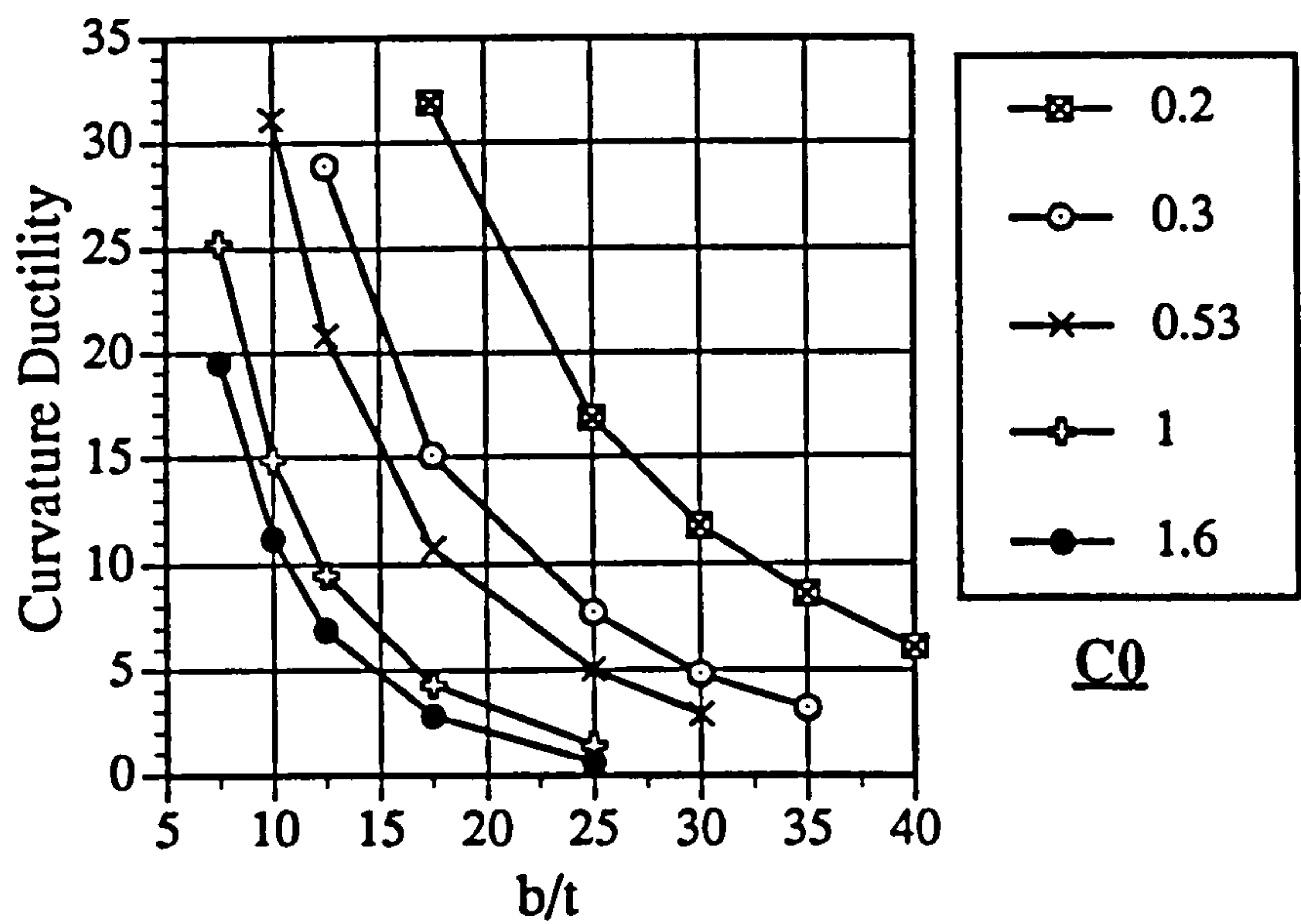


Fig. 8.30 Curvature ductility versus b/t ratio under C0% for different values of s/b

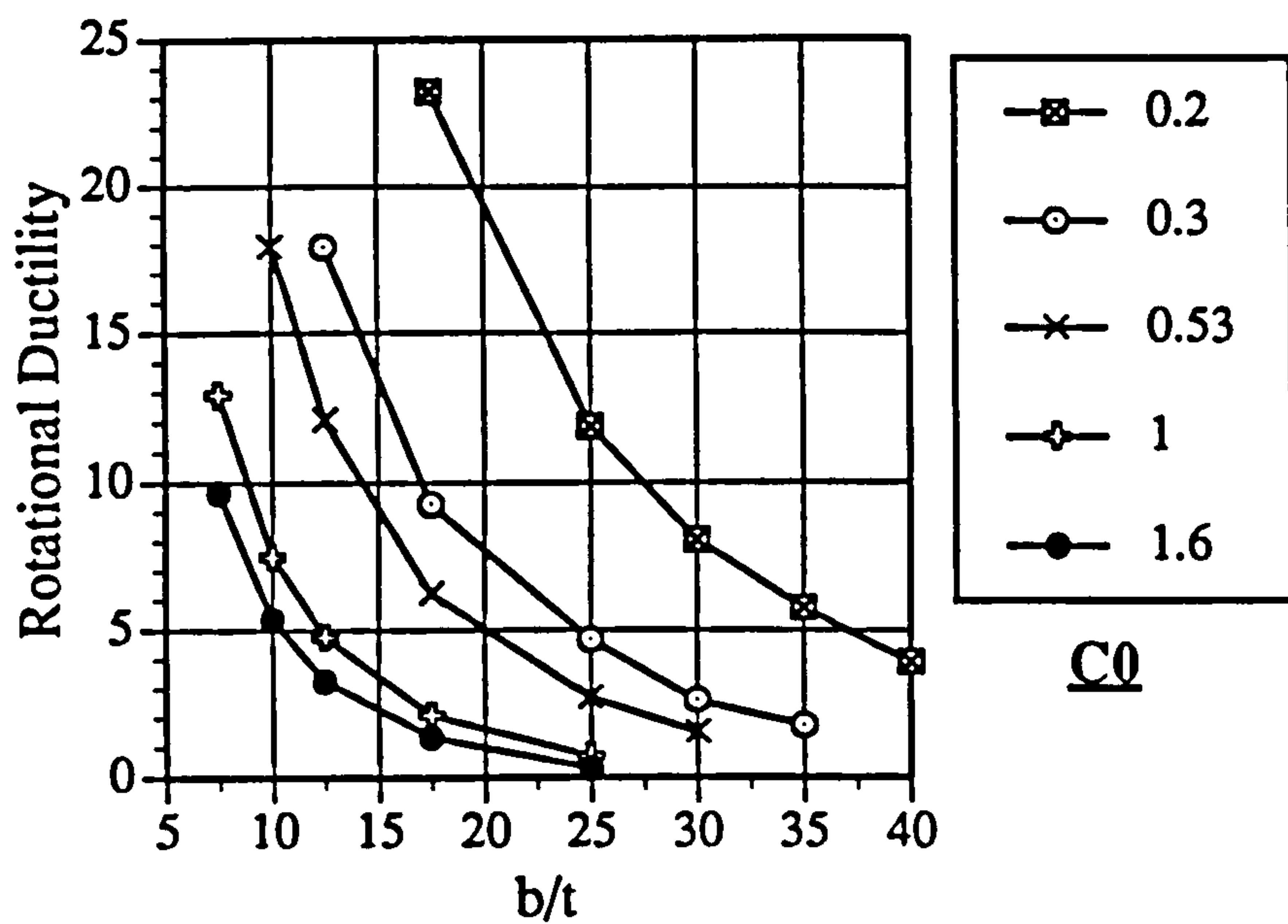


Fig. 8.31 Rotational ductility versus b/t ratio under C0 for different values of s/b

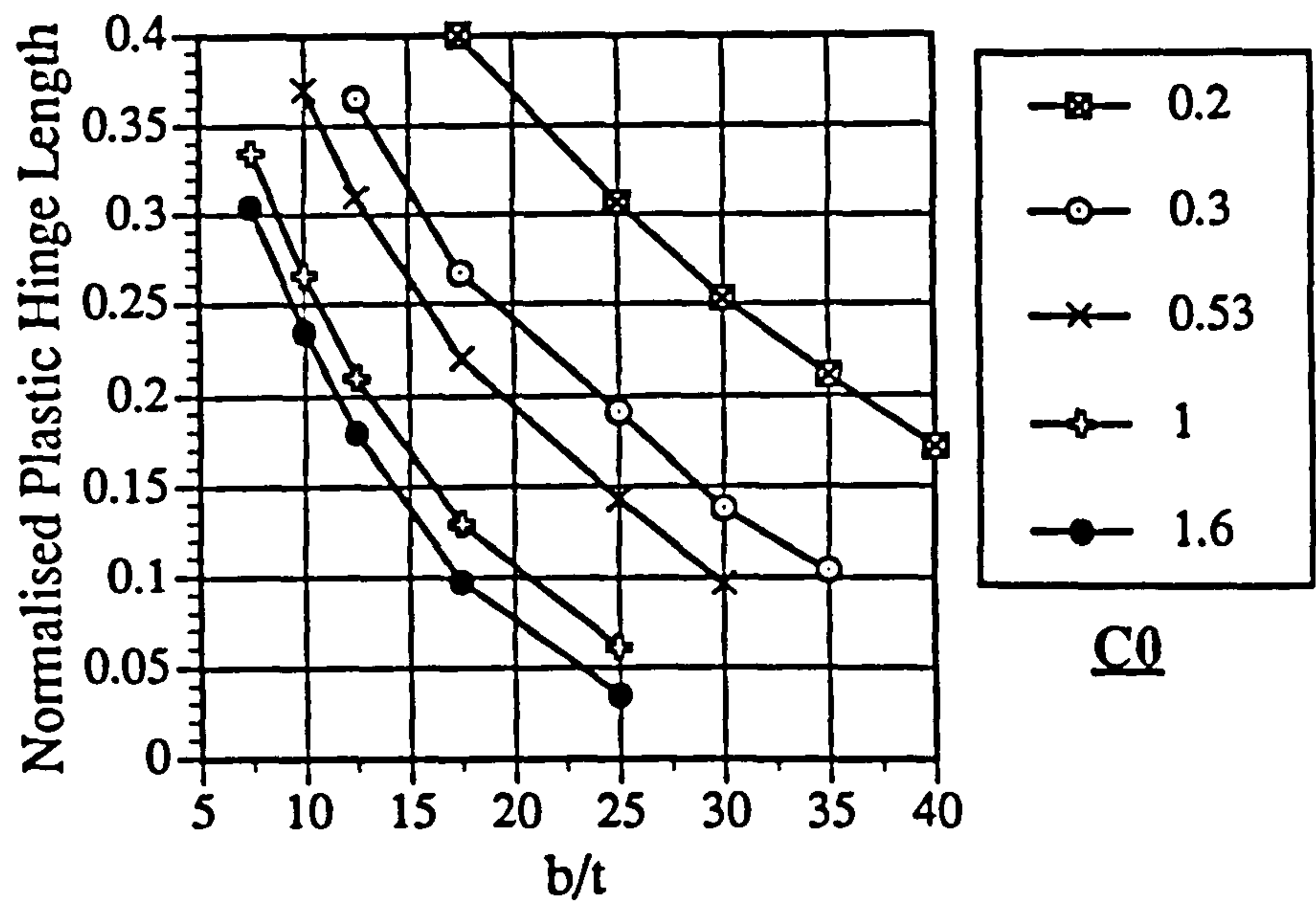


Fig. 8.32 Normalised plastic hinge length versus b/t ratio under C0 for different values of s/b

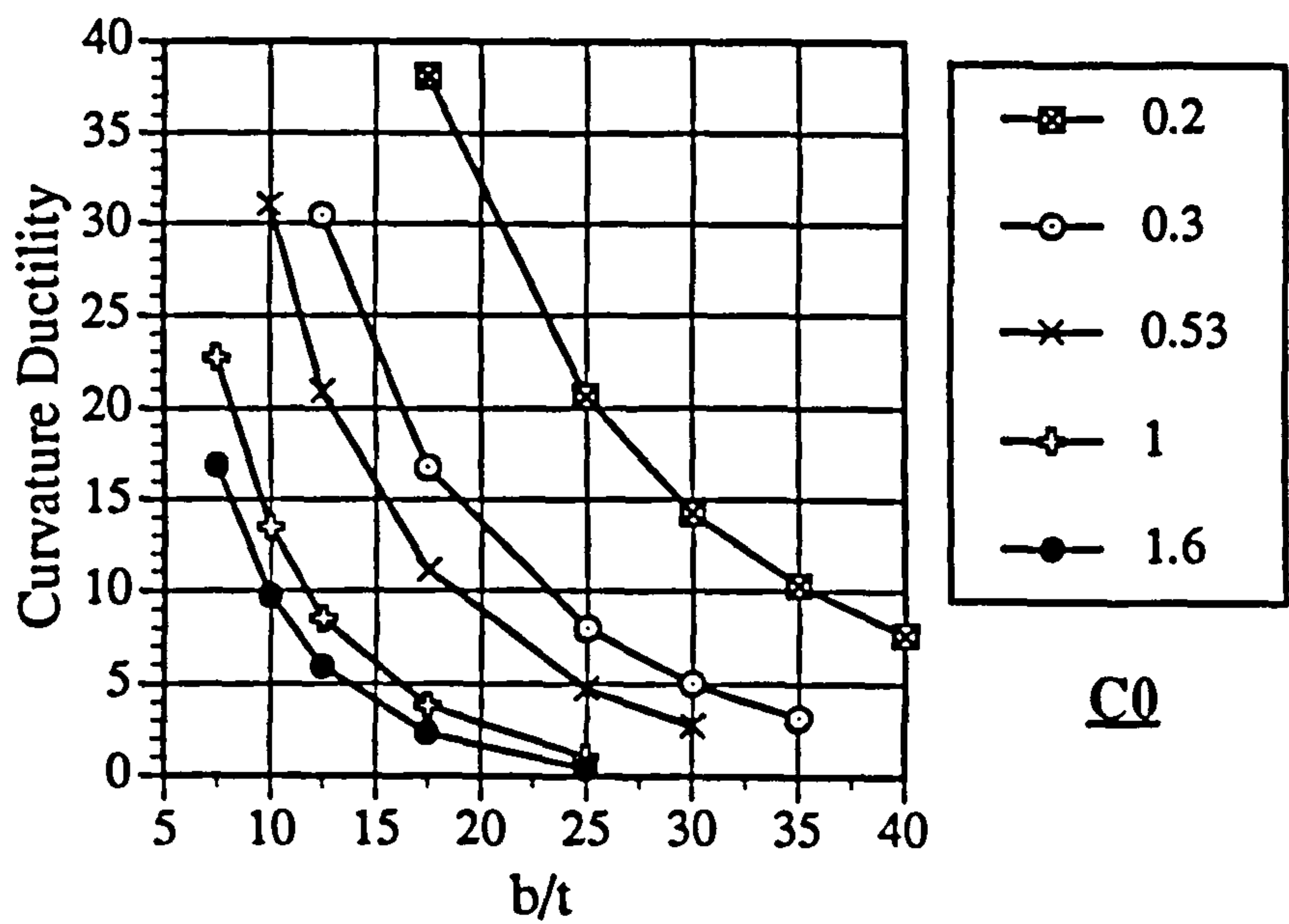


Fig. 8.33 Curvature ductility versus b/t ratio under C15 for different values of s/b

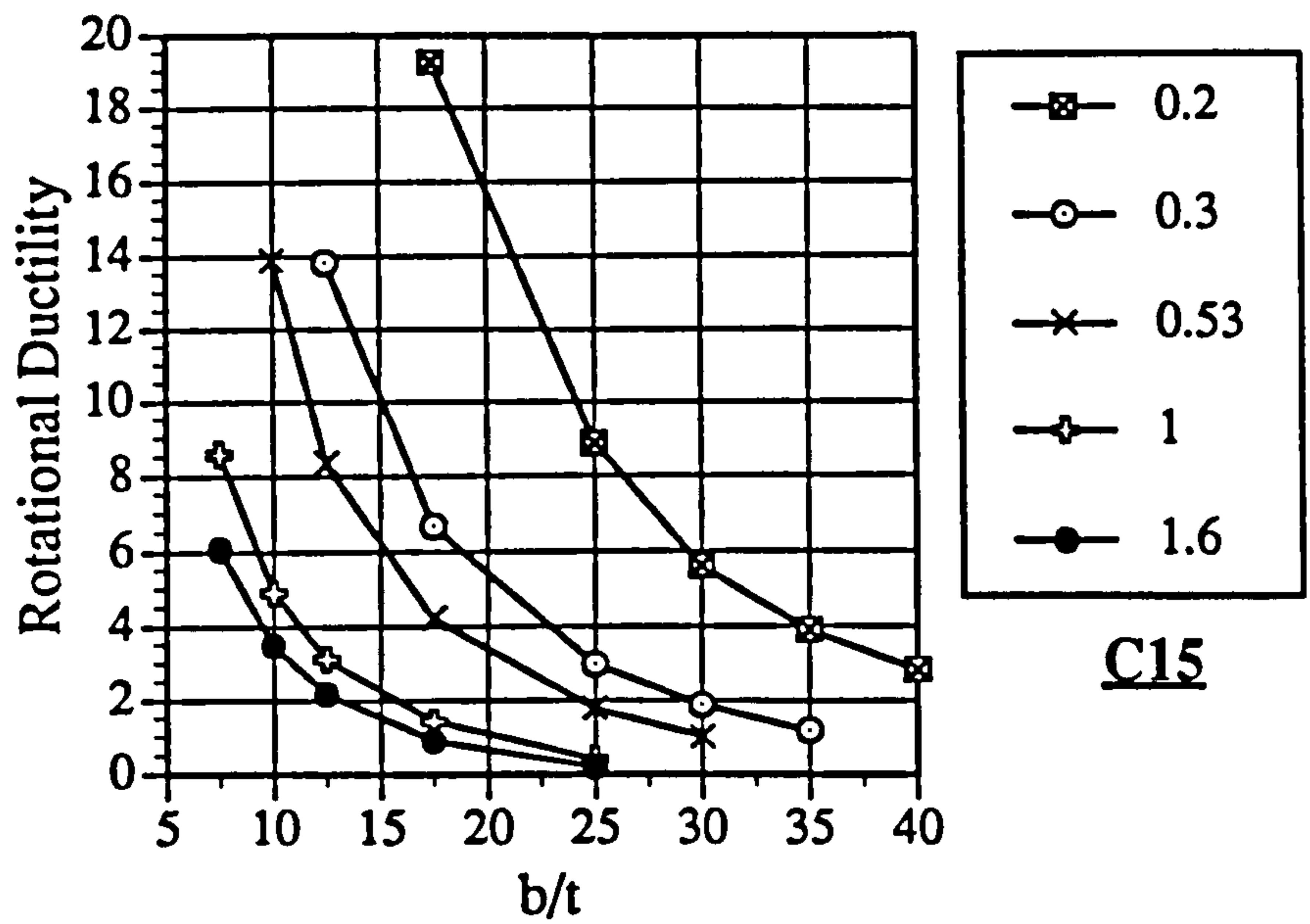


Fig. 8.34 Rotational ductility versus b/t ratio under C15 for different values of s/b

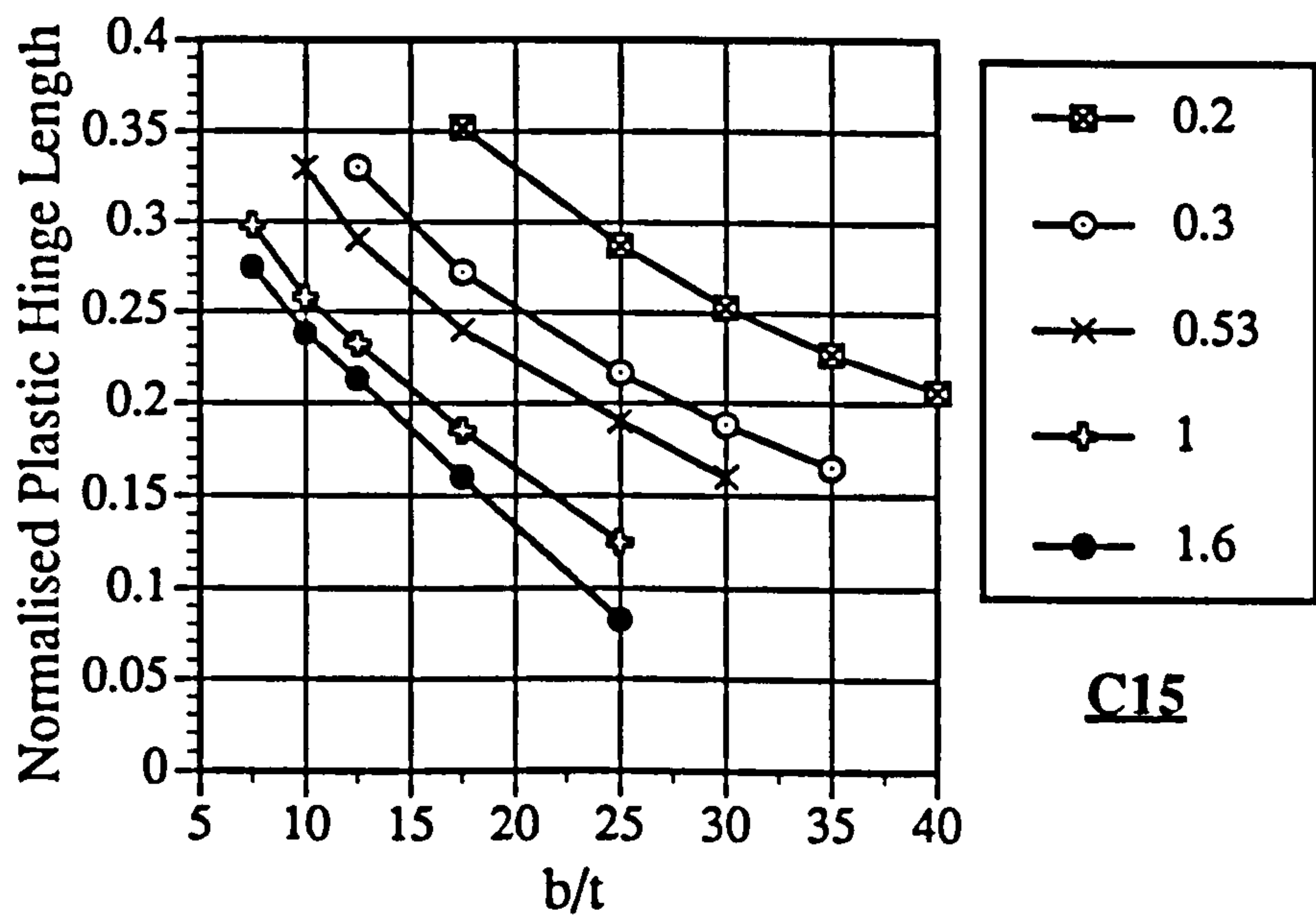


Fig. 8.35 Normalised plastic hinge length versus b/t ratio under C15 for different values of s/b

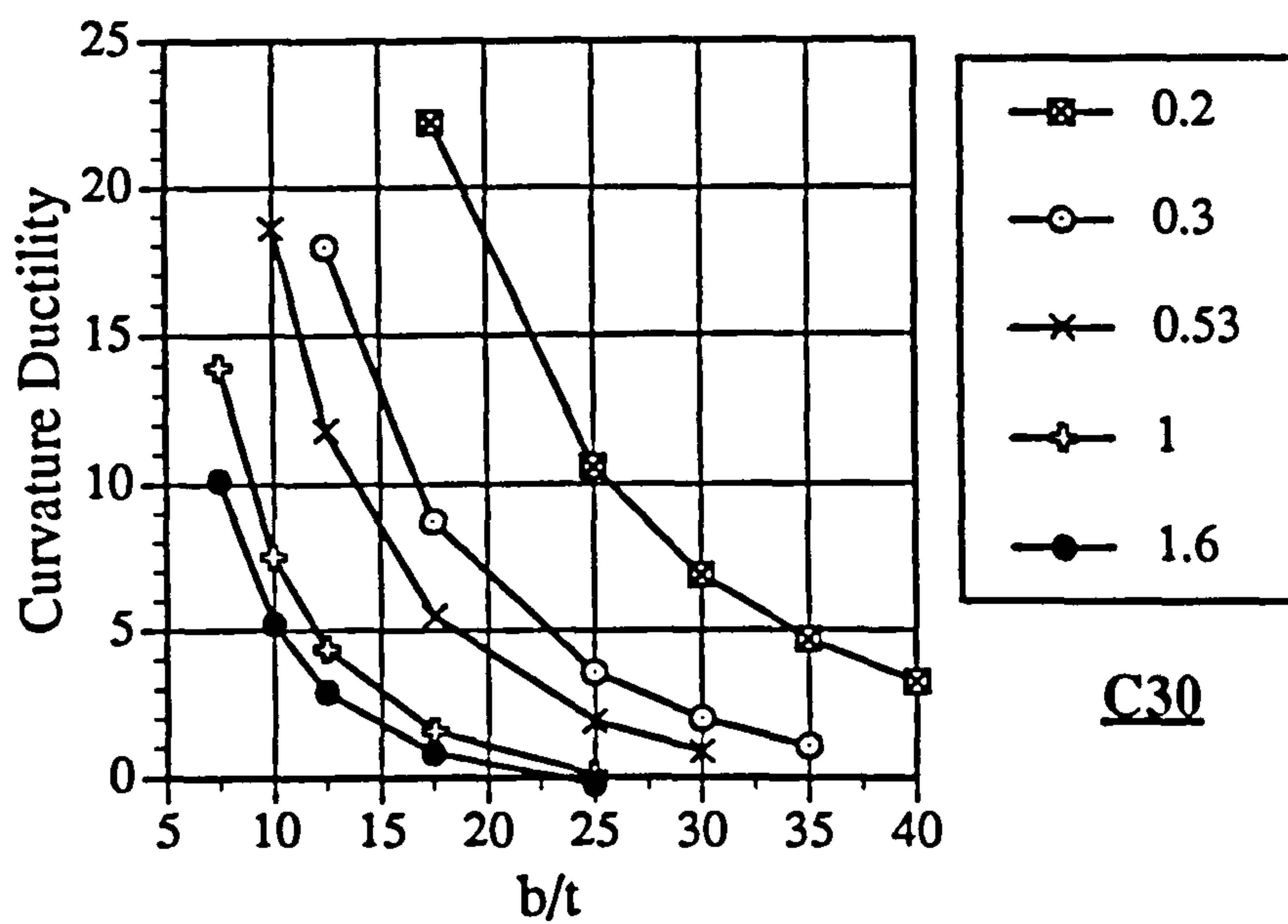


Fig. 8.36 Curvature ductility versus b/t ratio under C30 for different values of s/b

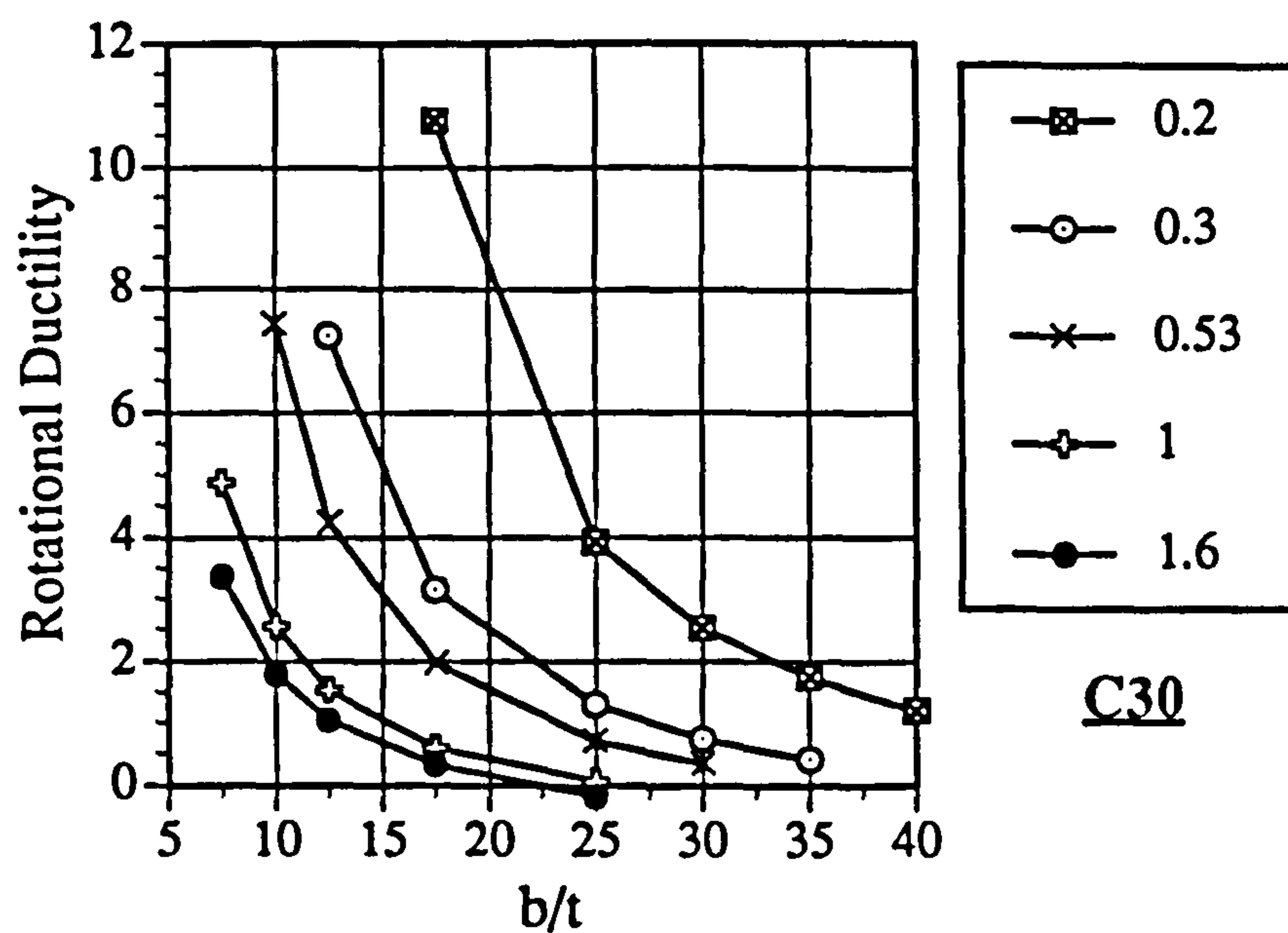


Fig. 8.37 Rotational ductility versus b/t ratio under C30 for different values of s/b

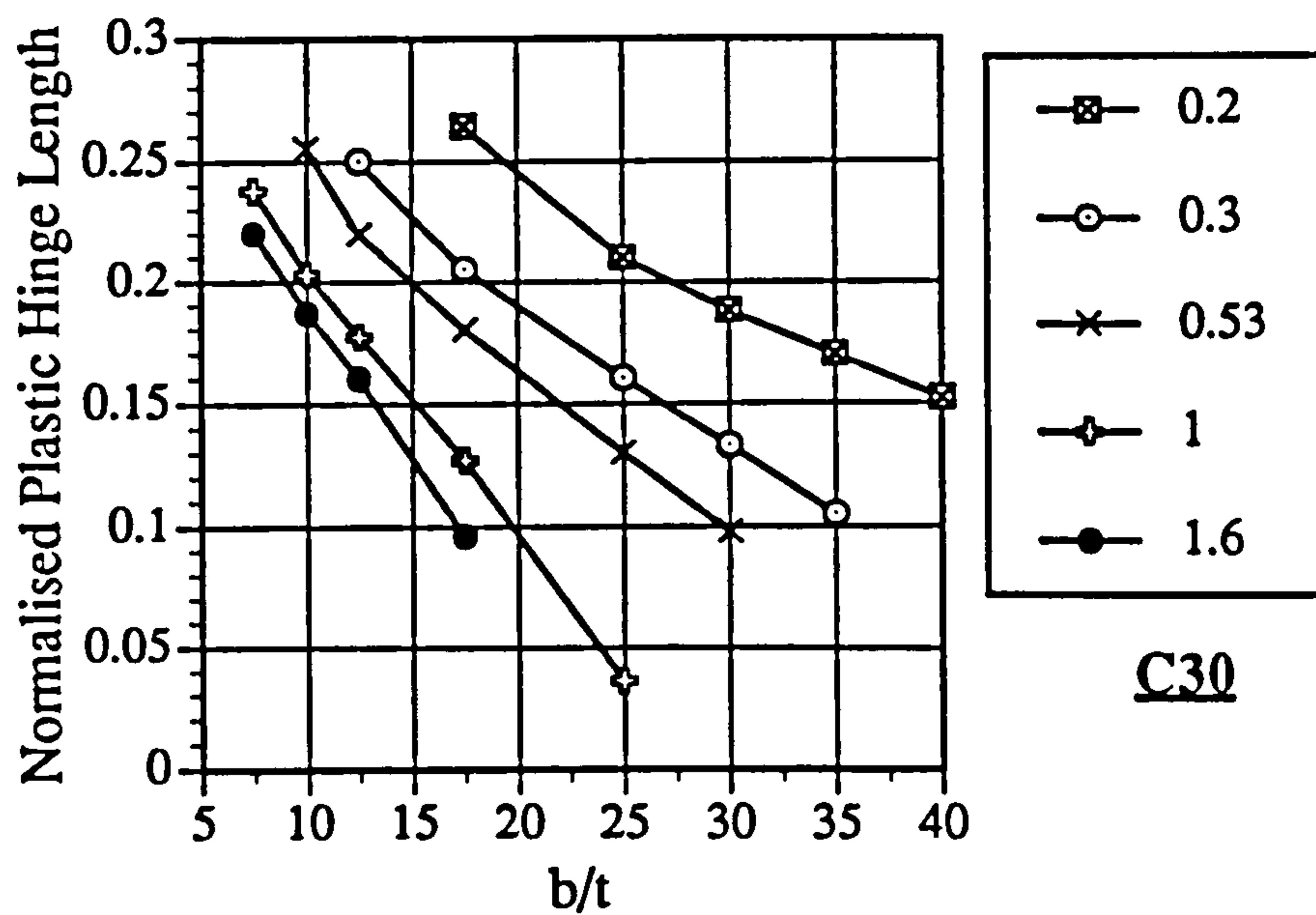


Fig. 8.38 Normalised plastic hinge length versus b/t ratio under C30 for different values of s/b

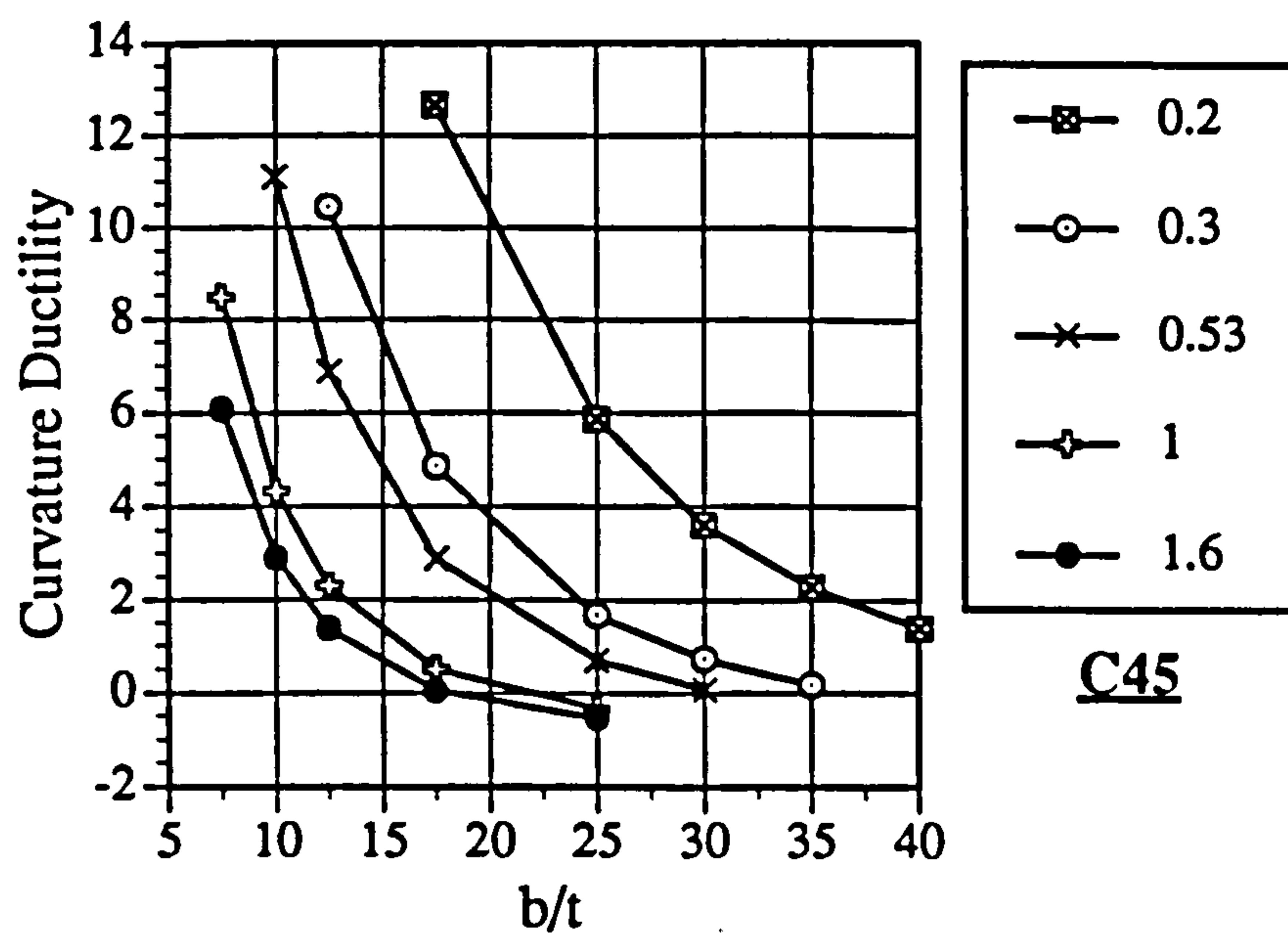


Fig. 8.39 Curvature ductility versus b/t ratio under C45 for different values of s/b

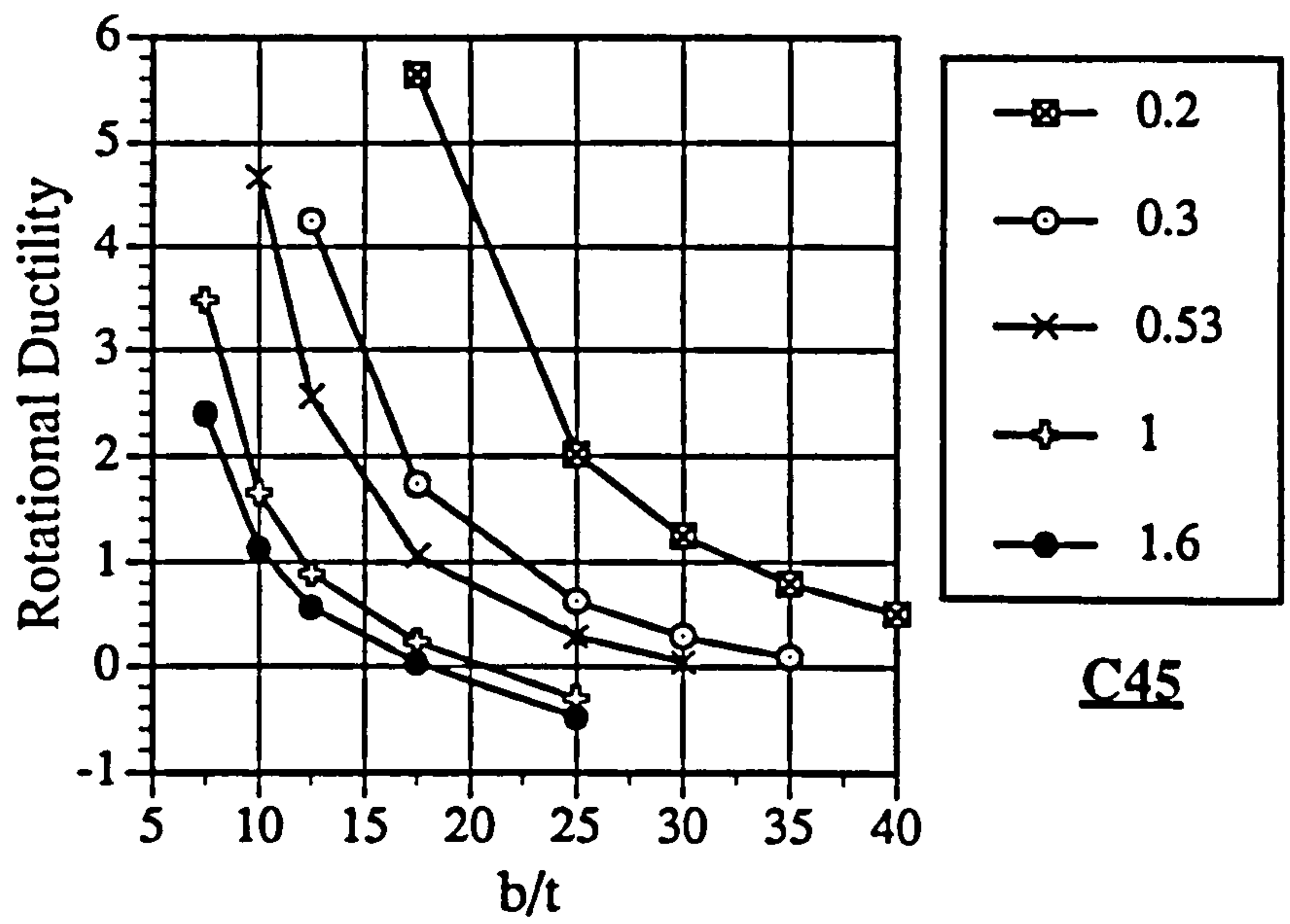


Fig. 8.40 Rotational ductility versus b/t ratio under C45 for different values of s/b

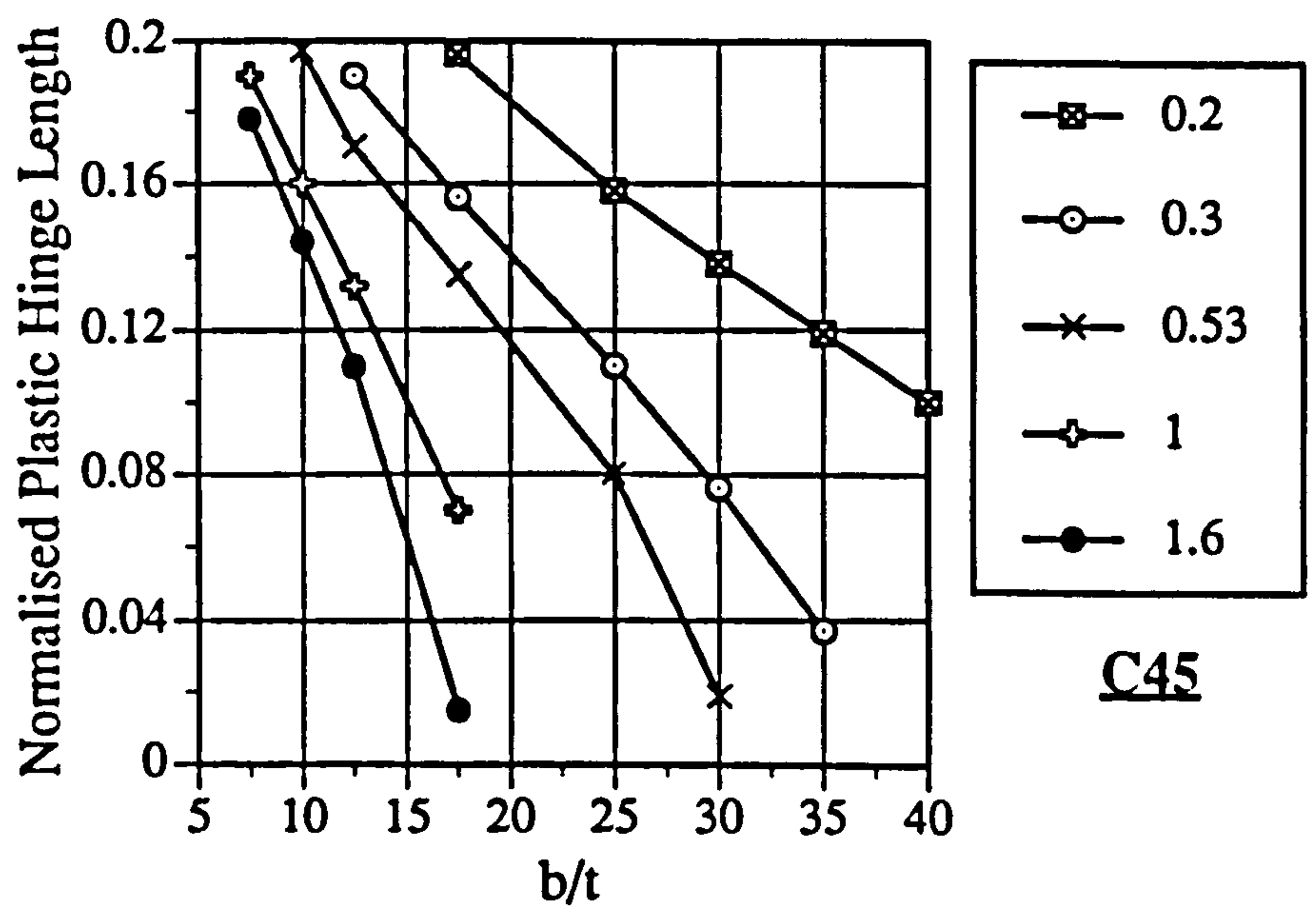


Fig. 8.41 Normalised plastic hinge length versus b/t ratio under C45 for different values of s/b

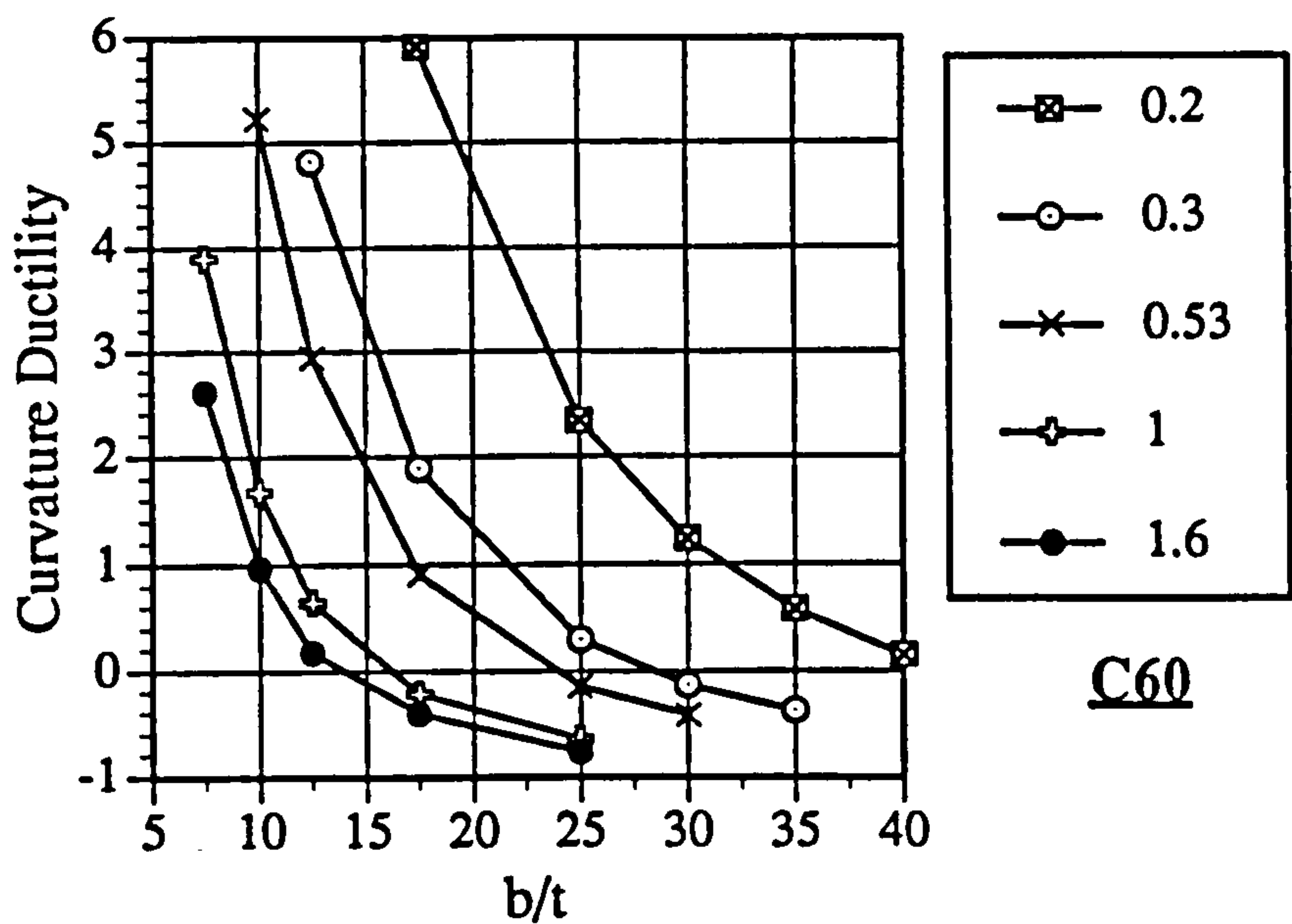


Fig. 8.42 Curvature ductility versus b/t ratio under C60 for different values of s/b

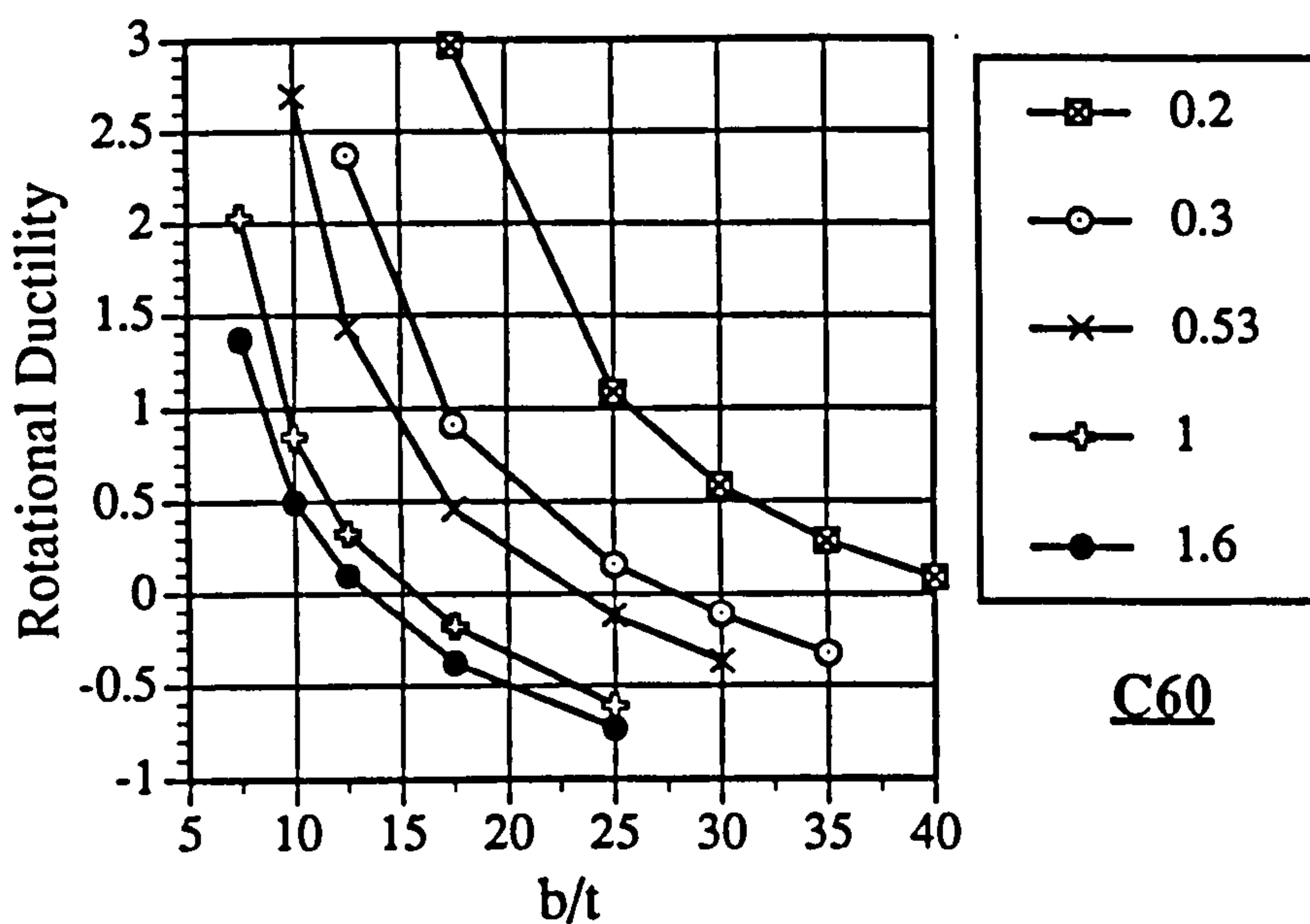


Fig. 8.43 Rotational ductility versus b/t ratio under C60 for different values of s/b

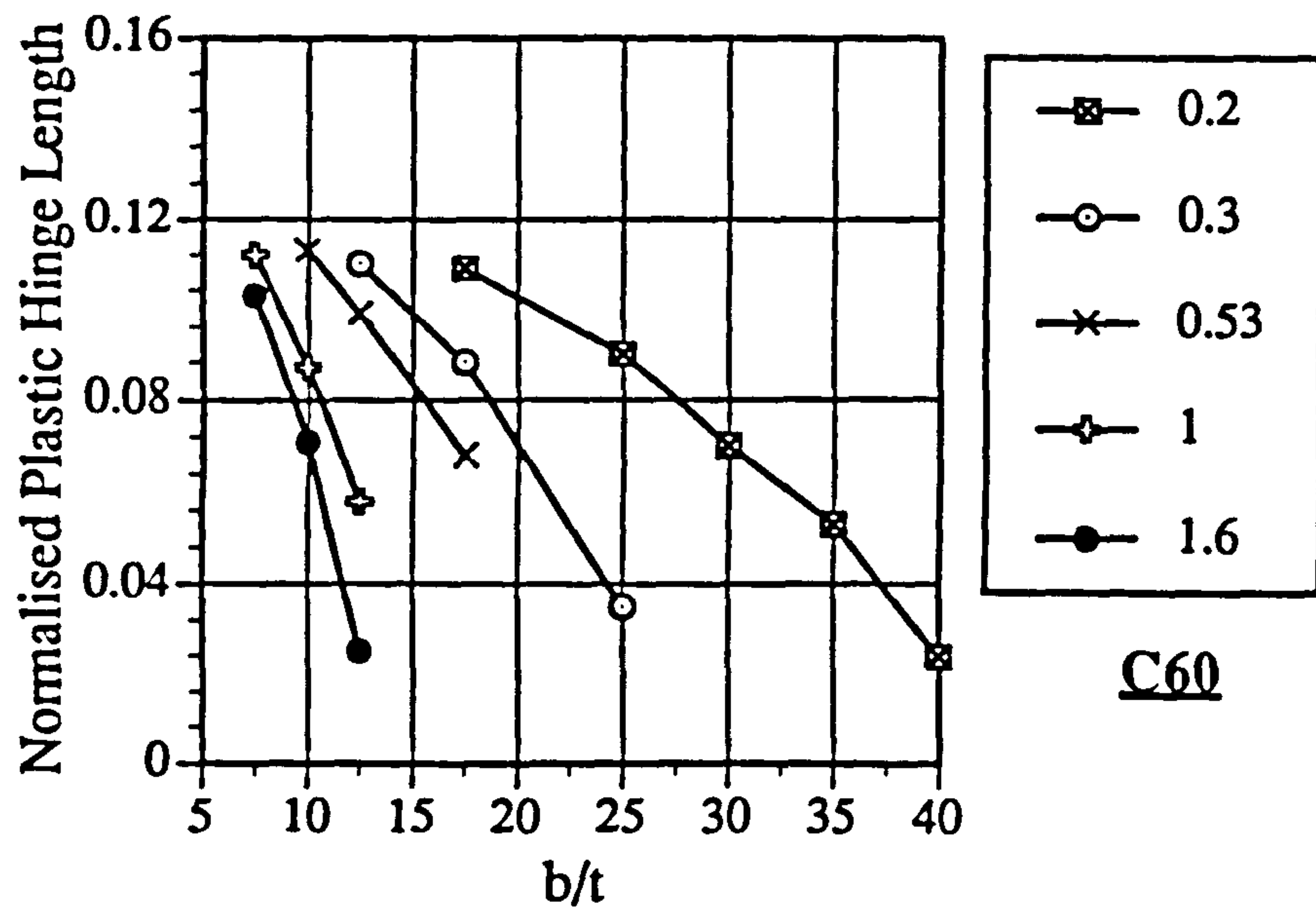


Fig. 8.44 Normalised plastic hinge length versus b/t ratio under C60 for different values of s/b

CHAPTER 9

9. DISCUSSION AND DESIGN IMPLICATIONS

9.1 INTRODUCTION

Modern codes of practice adopt a philosophy by which the ability of a structural system to resist severe seismic loads is represented in terms of specific behaviour factors. This role is assumed in Eurocode 8 by the parameter 'q' which is used to modify the elastic design spectrum. It implicitly accounts for inelastic behaviour and other force-reduction effects. This factor can be derived as the average ratio between the seismic forces inducing an ultimate limit state in the structure taking into account its actual nonlinear behaviour, and the design seismic loads obtained by conventional linear analysis.

The evaluation of the behaviour factor depends on the structural configuration, global collapse mechanism, geometric nonlinearities and types of connections, amongst other effects. It is, most significantly, directly related to the ability of critical members to undergo inelastic deformations. Consequently, sufficient local ductility must be provided by these members and simple methods should be furnished to assess this ductility.

It was shown in preceding parts of this thesis that substantial ductility can be attained from partially encased members particularly those including the proposed modifications. In this chapter, a general discussion of the experimental and analytical results is presented. Their implication on the design process is appraised, where relevant, with particular emphasis given to the recommendations included in Eurocode 8, 1988 draft.

9.2 STIFFNESS CHARACTERISTICS

A reliable estimate of the equivalent stiffness of the composite member is required for the evaluation of seismic design forces, for use in linear dynamic analyses and for deflection calculations. As discussed in Chapter 3, design codes assign different values depending on the assumptions related to the concrete stiffness. In this section, the experimental stiffness of the specimens is extracted and compared with the elastic stiffness using both an uncracked and a cracked concrete section.

The secant stiffness of the specimens during cyclic loading is variable even before reaching the yield displacement. This is due to the deterioration in concrete stiffness and also due to possible early yielding of steel extreme fibres, especially when high axial loads are applied. Due to the consistency in the loading regimes employed, the secant stiffness at each displacement level can be used to monitor the overall stiffness deterioration.

Figure 9.1 depicts the secant stiffness of models EM04, IC04 and IC07, versus the maximum displacement amplitude in each cycle. In these tests, no axial load was applied on the specimens. The secant stiffness for models EM01, IC01, EM02 and IC02 is also shown in Figure 9.2. The values of uncracked and cracked stiffness of the members are indicated on the figures. In calculating this stiffness, the exact material properties were used and a value of $30,000 \text{ N/mm}^2$ was assumed for the concrete modulus of elasticity. Only one fifth of the concrete stiffness was considered to contribute to the total stiffness in the case of the cracked section. For models where axial loads were applied, the effect of this load on reducing the stiffness can be accounted for by deducting the geometric stiffness, N/L , from the overall stiffness of the member.

As shown in Figure 9.1, the stiffness of all models drops significantly below the uncracked stiffness at early stages of loading. At the assumed yield displacement, all three specimens exhibit a secant stiffness which is slightly lower than the cracked one. IC07 initially shows a slightly lower secant stiffness than the other two models, whilst the stiffness of IC05 is marginally higher than that of EM04. At a displacement of 48 mm, where local buckling occurred in model EM04, the secant stiffness shows a gradual deterioration thereafter.

Similar conclusions can be drawn from Figure 9.2. Again, the stiffness falls below the cracked value well before the assumed yield displacement. The deterioration in secant stiffness of EM02 is clear after a displacement of 20 mm, where local buckling and concrete crushing was initiated. This is also observed for EM01 as compared to IC01 after a displacement of 33 mm. From comparison of Figures 9.1 and 9.2 at the estimated yield level and with due consideration to the geometric stiffness, it appears that the deterioration in stiffness under cyclic loading is more significant when axial loads are applied. Although a larger concrete area is effective, some accumulation of plastic strain due to early yielding in steel may have larger influence on the stiffness as compared to the influence of concrete.

Since the stiffness prior to yield is an important design parameter, Table 9.1 depicts the estimated secant stiffness for all models at approximately one quarter, half and at the yield level, respectively. The values are also compared to the calculated uncracked and cracked stiffness. Approximate values extracted from the pseudo-dynamic tests are also presented for general comparison. In the case of models subjected to an axial load, the geometric stiffness is appropriately accounted for.

TABLE 9.1
Initial Stiffness of Specimens

| Model Reference | $K_{\text{uncracked}}$ (KN/mm ²) | K^*_{cracked} (KN/mm ²) | K at $1/4 \delta_y$ (KN/mm ²) | K at $1/2 \delta_y$ (KN/mm ²) | K at $3/4 \delta_y$ (KN/mm ²) | K at δ_y (KN/mm ²) |
|-----------------|---|---|--|--|--|--|
| EM04 | 9.34 | 7.90 | 8.22 | 8.05 | 7.70 | 7.35 |
| IC04 | 9.34 | 7.90 | 8.44 | 8.13 | 7.94 | 7.59 |
| IC07 | 9.34 | 7.90 | 7.82 | 7.48 | 7.39 | 7.16 |
| EM05 | 9.34 | 7.90 | 8.34 | 7.74 | 7.56 | 6.96 |
| IC05 | 9.34 | 7.90 | 8.38 | 7.81 | 7.54 | 6.91 |
| IC06 | 9.34 | 7.90 | 7.94 | 7.62 | 7.44 | 6.88 |
| EM01 | 6.38 | 5.27 | 5.32 | 4.82 | 4.55 | 3.54 |
| IC01 | 6.38 | 5.27 | 5.39 | 4.88 | 4.57 | 3.59 |
| EM02 | 6.15 | 5.04 | 5.26 | 4.71 | 4.50 | 3.58 |
| IC02 | 6.15 | 5.04 | 5.69 | 4.93 | 4.63 | 3.71 |
| EM03 | 6.15 | 5.04 | 5.61 | 5.43 | 4.52 | 3.94 |
| IC03 | 6.15 | 5.04 | 5.69 | 5.56 | 4.57 | 3.96 |

* 20% of elastic EI

It is noticed that the values shown for models EM03 and IC03 are higher than the corresponding cyclic tests EM02 and IC02 since a lower number of cycles was applied prior to yield. This, however, is not the case for EM05, IC05 and IC06 for which the number of cycles was relatively larger.

In general, the deviation from the elastic stiffness depends on the material characteristics, dimensions and to a lesser extent on the loading history. It is obvious from the above discussion that the cracked stiffness, at 20% of the elastic EI , represents more closely the overall stiffness at the yield level. It is, therefore, recommended to use the cracked stiffness rather than the uncracked one, not only for load and displacement calculation in

equivalent static methods, but also in linear elastic dynamic analysis. After yield, both the stiffness deterioration and displacement may be estimated from the expected rotational or displacement ductility. The stiffness deterioration after yield should also be taken into account since the shift in the response frequency may result in variation in design forces.

9.3 CAPACITY

9.3.1 Yield Moment

The yield level is an important design parameter that is used to predict the capacity of the section, the extent of the plastic hinge zone and the ductility of the member. The yield and ultimate moments estimated for all the experimental models are given in Table 9.2. The yield values are based on an assessment of the strain gauge readings at the critical sections. This is also compatible with noticeable deviation from linearity in the hysteresis curves presented in Chapter 6.

TABLE 9.2
Yield and Ultimate Moments of the Experimental Models

| Model Reference | $M_y \times 10^4$ (KN.mm) | $M_u \times 10^4$ (KN.mm) |
|--------------------|------------------------------|------------------------------|
| EM01 | 5.95 | 7.95 |
| IC01 | 5.98 | 8.97 |
| EM02 | 6.06 | 7.75 |
| IC02 | 6.11 | 8.83 |
| EM04 | 6.82 | 9.08 |
| IC04 | 6.91 | 10.40 |
| IC07 | 6.62 | 9.80 |
| EM03 | 6.15 | 7.23 |
| IC03 | 6.18 | 8.49 |
| EM05 | 6.84 | 9.38 |
| IC05 | 6.88 | 9.51 |
| IC06 | 6.69 | 8.58 |

It is generally observed that the difference in the yield moment between each pair of EM and IC models is insignificant, within approximately 2.0%. A similar conclusion was also drawn regarding the stiffness of the models. Consequently, almost the same seismic forces would be initially attracted by both configurations, yet with a much higher ductility achieved by the IC configuration.

It was shown in the parametric study of Chapter 8 that several factors can influence the yield moment of the member. Figure 8.4 indicates that the steel strain hardening has no effect on the yield moment except for C60 and T15. This is due to early yielding of one side of the section. On the other hand, the yield moment shows a linear increase with the increase of the yield stress of steel, as shown in Figure 8.10. Increased concrete confinement has almost no effect on the yield moment at low axial loads. However, as shown in Figure 8.16, for axial loads higher than 30%, higher yield moments are achieved with increased confinement because of the high concrete strength achieved at early levels. For confinement factors less than 1.5, considerably lower yield moments are noticed for C45 and C60 due to early concrete deterioration.

For design purposes, the yield moment can be accurately estimated using section analysis. The unconfined concrete properties can be used since confinement has virtually no effect at the yield level, especially for axial loads lower than C45. Using a simple iterative procedure, the neutral axis position corresponding to the strain distribution at yield can be easily established, for which equilibrium under the applied axial load is attained. Alternatively, from the results of the parametric study, the normalised neutral axis depth at yield, shown in Figure 9.3, can be estimated from the following relationship:

$$\xi = -0.84 \left(\frac{N}{N_p} \right)^2 + 1.32 \left(\frac{N}{N_p} \right) + 0.33 \quad (9.1)$$

The above equation gives the exact position of the neutral axis from Figure 8.6 of the parametric study. It includes implicitly the effect of yield stress of steel. Except for C0 and T15, equation (9.1) is expected to be also valid for sections with different concrete unconfined strength and concrete contribution factors. However, this needs further verification through a wider investigation.

9.3.2 Ultimate Moment

The ultimate moment capacity would be required if an estimation of the height of the plastic hinge is necessary. As presented in Table 9.2, the experimental results indicate a significantly higher ultimate moment for the case of the IC configuration, up to 20% higher than the corresponding EM models. This is a consequence of the early deterioration in the EM section following local buckling. When low axial loads are applied on well-confined sections, the ultimate moment corresponds to the onset of local buckling of the flanges. However, a decrease in confinement or a relative increase in the compressive axial load may cause deterioration of concrete strength and hence an early attainment of the ultimate moment.

In Chapter 8, several parameters were shown to have an effect on the ultimate moment. As indicated in Figure 8.5, lower ultimate moments are attained if no strain hardening is assumed, particularly at low values of axial load. Whereas the difference for C60 is only 7%, it increases to about 25% for C0. The effect of yield stress is shown in Figure 8.11. As in the case of yield moment, there is a direct proportionality with the yield stress, but lower ultimate moments are attained for C45 and C60. As shown in Figure 8.17, the ultimate moment generally increases with the increase of confinement. Particularly low moments are noticed for confinement factors less than 1.5, where the concrete may deteriorate before or close to steel yield.

For use in design, the ultimate capacity can also be calculated using section analysis. However, proper account should be taken of the confinement effects in concrete and post-yield steel characteristics. For low confinement factors and/or at high compressive axial loads, the ultimate moment may be induced before the failure criterion is satisfied. Otherwise, the ultimate moment is reached at ultimate curvature, whereby the strain in the compression flange reaches the critical buckling strain, as indicated in Figure 9.3. Consequently, the estimation of the ultimate moment has to be carried out in conjunction with curvature ductility calculation.

Computer programs can be easily developed for such purpose. However, this is not a simple design procedure since the results would be sensitive to the assumptions and material models used. An alternative is the use of equations or charts developed from an extension of the parametric study presented in Chapter 8.

9.4 PLASTIC HINGE LENGTH

The plastic hinge zone is the part of the member in which most of the deformation takes place. An accurate evaluation of ductility is preceded by an assessment of the plastic hinge length. Also, if special details are included to enhance the ductility of critical sections, such as local buckling inhibitors or closely spaced confinement reinforcement, it should be provided within the entire length of this zone.

The extent of the plastic hinge zone can be calculated from the experimental results by assuming that the section will yield at a given level when the applied moment exceeds the yield moment, M_y , as obtained at the base. It is also assumed that the deterioration of the section in the remaining part of the member is insignificant. Based on these assumptions, equation (8.3) can be used to estimate the length of the plastic hinge. Table 9.3 gives the normalised plastic hinge length, τ , estimated for all the experimental models.

TABLE 9.3
Normalised Plastic Hinge Length of the Experimental Models

| Model Reference | Normalised Length (τ) | Model Reference | Normalised Length (τ) |
|-----------------|------------------------------|-----------------|------------------------------|
| EM01 | 0.25 | IC01 | 0.33 |
| EM02 | 0.22 | IC02 | 0.31 |
| EM03 | 0.15 | IC03 | 0.27 |
| EM04 | 0.24 | IC04 | 0.35 |
| EM05 | 0.25 | IC05 | 0.25 |
| IC06 | 0.21 | IC07 | 0.34 |

Due to early deterioration in the critical sections of the EM models, lower plastic hinge heights are observed compared to the IC models. It is also observed that the extent of the plastic zone decreases when compressive axial loads are applied. The above assessment seems to be in general agreement with the strain gauge results. For example, in model EM01, gauges G23 and G24 located at 30% of the cantilever height indicate yielding at this level, whereas it is not observed in gauges at higher levels. For model EM02, yield is exceeded in gauges G1 to G4 , G21 and G22 located at 18.3% of the height, but is not reached in gauges located above this level. Also, from gauges G22 to G26 in IC02, yield is reached up to a normalised height of approximately 35%. Examining gauges G1 to G6 in models EM03 and IC03 suggest heights of about 19% and 30%, respectively.

In the parametric study of Chapter 8, the plastic hinge length was plotted against all the variables. In general, the length of the plastic hinge zone will decrease with the increase in the compressive axial loads. In Figure 8.9, for an assumed strain hardening of 1%, there is a linear decrease of the extent of the plastic hinge with increased axial load. This is also the case for zero strain hardening under axial loads higher than 15%. Analytical predictions using a steel elastoplastic model ignoring strain hardening will underestimate the extent of the plastic hinge zone.

The plastic hinge length shows a monotonic decrease with the increase in yield stress since it has a more significant effect in increasing the yield moment. On the other hand, an increase in the concrete confinement causes an increase in the length of the hinge since it has a considerable effect on the ultimate moment. However, the plastic hinge length has a tendency to stabilise at higher confinement and for lower axial loads, since the ultimate moment occurs close to the failure level.

The flange slenderness has a significant effect on the extent of the plastic hinge zone. From Figures 8.26 to 8.44, it is clear that the plastic hinge length decreases substantially with the increase in b/t ratios. The relationship between the plastic hinge length and the flange slenderness is inversely proportional with a reduced effect at higher compressive axial loads. It is also observed that reducing the spacing of the local buckling inhibitors is accompanied by an increase in the extent of the plastic hinge zone for the same flange slenderness.

From both the results of the analytical parametric study and from experimental observations, certain detailing requirements need to be satisfied within the plastic zone. If local buckling inhibitors are used, the size and strength of both the bars and the welds must satisfy minimum requirements. Unless verified experimentally and until further investigations are available, these requirements may be conservatively estimated according to section 5.3.

Sufficient confinement should be provided, by using closely spaced stirrups, to ensure the integrity of concrete within the cross-section. At very low confinement factors, both the capacity and the ductility of the section drops substantially, especially under significant compressive axial loads. Based on the results of the parametric study, it is recommended to ensure, by detailing, a minimum confinement factor of 1.5. Until more investigations are available, the EC8 approach to calculate confinement, modified in section 7.4 of this thesis, may be used. It is proposed to limit the spacing of the stirrups

to $d_w/2$ or 100 mm, whichever is smaller, and the diameter of bars to a minimum of 6 mm. The guidelines given in EC8 for reinforced concrete columns may be generally applied for composite members. The spacing of confinement stirrups should also be relaxed gradually outside the plastic hinge zone to cover any uncertainties in determining the plastic hinge length and location.

For detailing purposes, reliable calculations for the yield and ultimate moments should be carried out to determine the length of the plastic hinge. Otherwise, it seems that 40% of the height from the base of the member to the point of contraflexure can be considered as a safe upper bound for most practical cases. Further treatment of the length of the plastic zone is carried out in section 9.5.

9.5 DUCTILITY

9.5.1 Ductility of the Experimental Models

To demonstrate the substantial increase in ductility of the IC cross-section configuration, Figures 9.4 and 9.5 show the moment versus curvature relationships from the cyclic tests on models EM02 and IC02, respectively. The curvatures for both models are calculated from gauges G6 and G9 which should be representative of the behaviour in the plastic hinge area. Also, Figures 9.6 and 9.7 show the same relationships for models EM03 and IC03 as calculated from gauges G8 and G11. Based on the results of the strain gauges, the curvature ductility of IC02 is about four-fold that of EM02, which is in line with the results of the parametric study. In the pseudo-dynamic tests, where a small number of cycles was applied, significantly higher curvatures are attained in the IC configuration.

Table 9.4 depicts the rotational ductilities obtained from the experimental results. It is clear that the rotational ductilities of the IC models are substantially higher than the corresponding EM configurations. This is due to the significant enhancement of curvature ductility of the section, and also due to the spread of plasticity through a longer plastic hinge length, as discussed in section 9.4.

TABLE 9.4
Rotational Ductilities of the Experimental Models

| Model Reference | Rotational Ductility R_{ψ} |
|-----------------|---------------------------------|
| EM01 | 2.84 |
| IC01 | 6.71 |
| EM02 | 1.31 |
| IC02 | 4.23 |
| EM03 | 1.08 |
| IC03 | 8.61 |
| EM04 | 3.80 |
| IC04 | 8.60* |
| EM05 | 3.09 |
| IC05 | 8.55* |
| IC06 | 11.20 |
| IC07 | 9.60 |

**Tests aborted before failure hence higher values are expected*

The relationship between the attained rotational ductility and the applied axial load is implicit in the above table. For models EM02, IC02, EM03 and IC03, where 30% axial load was applied, the ductility is significantly lower than that of other models. The same observation also applies to EM01 and IC01 compared to the other specimens. It is also noticed that the ductility of EM03 is lower than that of EM02, whereas the opposite is observed for IC03 and IC02. This seems to be due to the lower buckling strain of the flanges in EM03. Because of the small number of cycles applied in the pseudo-dynamic test, it was akin to a monotonic test and hence significant stress softening was avoided.

9.5.2 Parameters Influencing Ductility

The results of the parametric study highlight the main factors influencing ductility. From Figure 8.8, it is clear that rotational ductility is substantially reduced with the increase of the axial load. Very low values are achieved for C45 and C60, and even lower ductility is attained if strain hardening is ignored. Within the practical range of parameters studied, consistently low rotational ductility values are obtained for axial loads higher than C30.

Both the curvature and rotational ductilities decrease significantly with the increase of yield stress of steel, as shown in Figures 8.13 and 8.14, due to the increase of the moment and curvature at yield. In Figure 8.19 and 8.20, an increase in confinement is shown to have a positive influence on ductility with a reduced effect for high axial loads. Particularly low ductility is observed for confinement factors less than 1.5.

The flange slenderness is of prime importance in determining the ductility of partially encased members. As demonstrated in Figures 8.33 and 8.34, large ductilities are attained for low slenderness values. Ductility decreases monotonically with the increase in b/t ratios. Moreover, significantly higher ductility is achieved for the same flange slenderness, when smaller s/b values are used and when lower axial loads are applied.

9.5.3 Relationship between Curvature and Rotational Ductilities

Whilst the curvature ductility represents only the section properties, the rotational ductility is related to the member properties, and implicitly accounts for the length of the plastic hinge zone. In order to use simple section analysis for assessing the ductility of a member, a relationship between the curvature ductility and the rotational ductility must first be established. Such a relationship depends mainly on the boundary conditions and the length of plastic hinges, which in turn depends on many parameters. A cantilever is considered here to represent the portion of the member from the point of contraflexure to the point of fixity.

Figure 9.8 shows the actual curvature distribution for a cantilever member. In the rules for concrete structures given in EC8, a constant curvature distribution is assumed. This approximation would tend to overestimate the rotational ductility of reinforced concrete flexural members (Pilakoutas, 1990; Pilakoutas and Elnashai, 1991). Using the distribution proposed in EC8 and assuming that the deflection angles are relatively small, the rotational ductility can be calculated as:

$$R_{\psi} = \frac{\psi_u - \psi_y}{\psi_y} = \frac{(\phi_u - \phi_y) \tau L^2 \left(1 - \frac{\tau}{2}\right)}{\frac{L^2}{3} \phi_y} = \frac{(\phi_u - \phi_y) 3\tau \left(1 - \frac{\tau}{2}\right)}{\phi_y} \quad (9.2)$$

from which the relationship between the curvature and rotational ductility is given by:

$$R_{\psi} = 3\tau \left(1 - \frac{\tau}{2}\right) D_{\phi} \quad (9.3)$$

On the other hand, if a linear distribution of curvature in the plastic hinge zone is assumed, equations (9.2) and (9.3) would be modified as follows:

$$R_{\psi} = \frac{\psi_u - \psi_y}{\psi_y} = \frac{(\phi_u - \phi_y) \frac{\tau L^2}{2} \left(1 - \frac{\tau}{3}\right)}{\frac{L^2}{3} \phi_y} = \frac{(\phi_u - \phi_y) \frac{\tau}{2} (3 - \tau)}{\phi_y} \quad (9.4)$$

from which:

$$R_{\psi} = \frac{\tau}{2} (3 - \tau) D_{\phi} \quad (9.5)$$

Figure 9.9 depicts the relationship between the actual rotational ductility obtained in the parametric study and that obtained using equations (9.3) and (9.5) above. It is clear that the linear approximation is much closer to the actual results than the constant curvature assumption. Moreover, the rotational ductilities calculated using (9.5) are consistently on the lower side of the actual results, and hence conservative values are always estimated. This condition, however, is not satisfied by using (9.3) and the rotational ductility may be significantly overestimated.

As mentioned before, the plastic hinge length is sensitive to many factors. Consequently, an accurate calculation of this length from section analysis would be difficult. For simplicity, a conservative value of τ is assumed to be 0.2. By substituting this value in (9.3), the rotational ductility for the case of constant curvature approximation becomes:

$$R_{\psi} = 0.54 D_{\phi} \quad (9.6)$$

and for the case of linear distribution of curvature, the rotational ductility from (9.5) is given by:

$$R_{\psi} = 0.28 D_{\phi} \quad (9.7)$$

In Figure 9.10, the rotational ductility from the parametric studies is shown versus the curvature ductility. The rotational ductilities estimated from (9.6) and (9.7) are also indicated. Whereas the values given by (9.6) are unconservative, (9.7) represent a lower bound for the actual rotational ductility, except for very few cases where the confinement factor is close to unity. However, such low confinement factors should not be allowed for design since the concrete may deteriorate before yielding of steel.

9.5.4 Design for Ductility

In seismic design of structures, ductile behaviour is achieved through the development of plastic hinge areas. Most codes of practice, either for steel or concrete structures, impose dimensional limitations or include provisions for hoop reinforcement, respectively. However, these codes do not quantify the ductility achieved by the prescribed detailing. Only recently, the Architectural Institute of Japan provided recommendations (AIJ-LSD, 1990) relating the dimensions of steel sections to the available rotational ductility, based on the work of Kato (1989). Also, the specific rules for reinforced concrete structures in the draft EC8 suggest an elaborate procedure for designing critical members to achieve the required structural behaviour.

The ductility of partially encased section is discussed hereafter from the design point of view. Approaches used by several codes are briefly introduced, and methods for assessing ductility are outlined.

9.5.4.1 Steel and Composite Structures in ECCS and EC8

The recommendations for design of steel structures in seismic zones given by the European Convention for Constructional Steelwork (ECCS, 1991) are also introduced in the rules for design of steel structures in the draft of EC8. In this approach sufficient local ductility is ensured by limiting the b/t ratios. Three ductility classes are proposed depending on the estimated behaviour factor 'q' of the structure; Class A for $q < 6$, class B for $q < 4$ and class C for $q < 2$. Class A corresponds to class 1 (plastic sections) of Eurocode 3 (1984), class B corresponds to class 2 (compact sections) and class C is intermediate between classes 2 and 3 of EC3. The b/t ratios of class A can be used for $q \geq 6$ but should be reduced depending on the axial load applied.

In order to examine the ductility provided by the above limitations when applied to partially encased sections, Table 9.5 is constructed. It depicts the rotational ductility extracted from the parametric study for the specified b/t ratios. The limitations given in Eurocode 4 (composite structures, 1984) for partially encased sections are also included for comparison. The value of Φ is equal to $(235/\sigma_y)^{1/2}$, where σ_y is in N/mm². The ductility is given for different axial loads and for two values of s/b. All values are given for a yield stress of 300 N/mm² and a confinement factor of 2.0.

TABLE 9.5
Rotational Ductilities for Different b/t Limitations

| CODE | | EC8 (steel) Class A | EC8 (steel) Class B | EC8 (steel) Class C | EC4 (composite) |
|--------------------------|-----|------------------------|------------------------|------------------------|--------------------|
| b/t Limit | | 9Φ | 10Φ | 12Φ | 22Φ |
| R_{ψ} (s/b=1.6) | C0 | 8.5 | 6.5 | 5.0 | 1.0 |
| | C15 | 5.5 | 4.5 | 3.0 | 0.5 |
| | C30 | 2.5 | 2.0 | 1.5 | 0.1 |
| | C45 | 1.5 | 1.20 | 1.0 | 0.0 |
| R_{ψ} (s/b=0.53) | C0 | 22.5 | 19.0 | 17.5 | 5.0 |
| | C15 | 18.0 | 15.5 | 13.0 | 3.5 |
| | C30 | 8.5 | 7.5 | 7.0 | 1.5 |
| | C45 | 5.0 | 4.7 | 4.5 | 0.7 |

Values of R_{ψ} are based on a yield stress of 300 N/mm² and a confinement factor of 2.0

For the case of s/b of 1.6 and C0, considerable ductility is provided by the three classes of EC8, which decreases gradually with the increase in axial loads. Substantially higher ductilities are obtained for the case of s/b of 0.53. As expected, the limits of EC4 provide little or no ductility, since these were based on tests on axially loaded members for static design purposes. Nevertheless, the same b/t ratios provide higher ductility values for the case of s/b of 0.53 at low axial loads.

The effect of yield stress on b/t limitations is implicitly accounted for in the different classes by means of the factor Φ . In Table 9.6, the rotational ductility is given for yield stresses of 300 and 550 N/mm², respectively, as obtained in the parametric study for the control model. An equivalent value of b/t estimated through the factor Φ to account for the change in yield stress would be 17.0. It appears from the table that the latter approach is unconservative in estimating the rotational ductility.

TABLE 9.6
Effect of Yield Stress on Ductility

| | | | |
|---------------------------------|------|------|------|
| b/t | 12.5 | 12.5 | 17.0 |
| σ_y (N/mm ²) | 300 | 550 | 300 |
| R_ψ (C0) | 12.0 | 4.0 | 6.5 |
| R_ψ (C15) | 8.2 | 2.5 | 4.5 |
| R_ψ (C30) | 4.2 | 1.5 | 2.5 |
| R_ψ (C45) | 2.5 | 1.0 | 1.2 |

Although the flange b/t ratio is the most important parameter influencing the ductility of partially encased members, it was shown in the parametric study that the applied axial load, the yield stress of steel and concrete confinement are also of importance. In the steel codes approach, only the yield stress of steel is accounted for through the factor Φ . Even if a conservative estimate of confinement is assumed, the yield stress changes the balance of concrete contribution to ductility. This contribution is also affected by the applied axial load.

It should be noted that the specific rules for composite structures in Eurocode 8 do not include any particular recommendations for estimating local ductility. Two approaches are mentioned for design of dissipative zones. In the first, the strength and ductility of the reinforced concrete component is ignored assuming that it fails before yield of steel. For steel sections fully encased in concrete, a release in b/t ratios is allowed by using class C limitations of the steel rules. The second approach considers the concrete component, but failure of concrete before yielding of steel is avoided. Design and detailing of both steel and concrete parts refer to the steel and concrete rules, respectively. Also, behaviour factors similar to that of steel structures are proposed.

9.5.4.2 Assessment of Local Ductility

According to the general procedure adopted in EC8 rules for concrete structures, the behaviour factor is first estimated on the overall structural level. This is followed by an estimation of the displacement or rotational ductility demand of critical members. In the third stage, this rotational ductility is converted into a curvature ductility demand. The final step involves providing adequate member detailing to achieve this requirement or to check the existing curvature ductility.

The current research deals with the last two stages of the above-mentioned procedure. Using the information presented in section 9.5.3, a similar approach can be outlined by which the available rotational ductility of a partially encased member can be assessed or, more importantly, the required curvature ductility is ensured for a given rotational ductility demand.

As discussed in section 9.3, the moment and curvature at yield can be easily calculated from simple equations. The ultimate moment can also be estimated using detailed section analysis programs or elaborate relationships including accurate material characteristics. The values of both moments would be needed if the extent of the plastic hinge zone is to be precisely calculated.

If an accurate assessment of the plastic hinge length can be obtained from a detailed section analysis program, equation (9.5) may be used to establish the relationship between the rotational and curvature ductilities. Otherwise, equation (9.7) can be used for this purpose. In the rules of concrete structures of EC8, columns are considered to be fixed at both ends. In this case, the relationships of (9.5) and (9.7) would be valid for a column of height $2L$. Usually columns are not perfectly fixed at the storey level and hence a higher value for the rotational ductility would be required. Nevertheless, this approximation might be acceptable if the grossly conservative assumption that the ductility is provided by the columns of the first level is adopted.

The final stage of relating the curvature ductility to the section properties is a more arduous task. As shown in the parametric study of Chapter 8, many parameters can influence the attained curvature ductility. The most important of which are the extent of axial load, b/t and s/b ratios, the yield stress of steel and concrete confinement. Using an accurate section analysis program incorporating concrete confinement effects, the curvature at ultimate can be calculated. With reference to Figure 9.3, this is achieved by prescribing the critical strain at the extreme fibre of the compression flange.

In order to simplify the design procedure, the parametric study of Chapter 8 may be extended to cover sections with different concrete contributions. Relationships or design charts can then be derived between the curvature ductility and the section properties. This may be used to determine the required section details or to assess the existing configuration. For example, the combination of b/t and s/b ratios required to satisfy a certain curvature ductility demand for a given yield stress and confinement factor may be defined. Also, since the change of s/b ratio will have virtually no effect on neither the

stiffness nor the yield capacity, it might be possible to choose a ratio of s/b that satisfies the curvature ductility demand while retaining the originally assumed flange slenderness.

9.6 SLENDERNESS EFFECTS

In relatively slender members, the lateral load-carrying capacity may be significantly reduced due to the second-order effects caused by vertical loads. As shown in Figure 8.22, the load reduction increases substantially with the increase of slenderness and with the increase of the applied compressive axial load. In cases of very high axial loads (C45 and C60) and for slender members, the lateral load may even change direction to sustain the applied deformations.

In equivalent static methods, most codes of practice neglect $P-\Delta$ effects if a specific stability coefficient is not exceeded. This coefficient relates the moment caused by the vertical loads at the design storey drift to the moment induced by the seismic design shear force acting across the storey under consideration. If such a value is exceeded, the second order moments have to be accounted for in calculating the seismic actions on members.

However, since the overall stiffness of the structure in resisting lateral seismic loads is reduced both prior to and after yield, this leads to a change in the response of the structure. From the design point of view, this should be considered on the behaviour factor level. Considerable work has been carried out on this effect in steel frames by several researchers in Europe. A summary of this work is given in the ECCS seismic design document (1991), in which the geometric effects are introduced by modifying the 'q' factors by means of specific reduction coefficients.

In general, unless rigorous analysis and design methods are applied, it seems reasonable to limit the axial compressive loads applied on vertical members to 30% of the plastic capacity. This should apply, not only to the force from static weight, but also from the overturning moment and possible vertical excitation effects. It was shown that for most practical cases, very low values of local ductility is attained when higher axial loads are applied. This low ductility will even decrease further when the reduction in the lateral load in members within the practical range of slenderness is considered. Also, the geometric effects of significantly high axial loads on both the local ductility and the behaviour factors would generally be difficult to assess.

Figure 8.23 shows the normalised lateral displacement at failure for different slenderness ratios. As expected, the drift increases with increased slenderness and for lower axial loads. If a drift criterion is applied, the limiting rotational ductility can be easily calculated. For slender members, drift limitations imposed on the overall structural level for the collapse limit state must be considered in estimating the rotational ductility demand of the member. Consequently, a provision of unrealistically high member ductility, that may not be utilised due to violation of overall structural considerations, would be avoided.

To sum-up, for design purposes, it would be ideal if recommended behaviour factors could implicitly account for both the geometric nonlinearities and the drift effects. Until such accurate assessment of behaviour factors is available, individual consideration of these effects must be accounted for.

9.7 ENERGY DISSIPATION

Satisfactory performance of a structure under severe earthquake loading is directly related to the ability of critical members to absorb and dissipate energy. For comparison purposes, the energy dissipated can be conveniently calculated as the area under the lateral load versus displacement plot, ignoring the work done by the axial loads. The area under the curves is calculated using the trapezoidal rule for numerical integration.

Figure 9.11 depicts the relationship between the loading step and the cumulative energy dissipation for the cyclic tests on models EM02 and IC02. Since the displacement steps applied in both tests were almost identical, comparison of those two particular models is possible. The following observations are noteworthy:

- a. Before yield, i.e. up to a loading step number 300, a small amount of energy is dissipated.
- b. The intermediate drop in energy at each unloading point is due to the recovery of the elastic displacements at this level.
- c. After yield, due to deterioration of EM02, IC02 dissipates more energy with the increase in the displacement level. However, the cumulative energy is not an accurate comparative measure of the behaviour of the two models since it depends on the imposed loading regime. In other words, an increase in the number of applied

cycles at each displacement level after local buckling would correspond to a larger difference in the cumulative energy.

The cumulative energy dissipated in the pseudo-dynamic tests on models EM03 and IC03 is also shown in Figure 9.12. With reference to the experimental results of Chapter 6, prior to yield, i.e up to 1.5 seconds, almost no energy is dissipated in both models. The energy dissipated in the two models continues to be of the same order up to failure of EM03. However, for model EM03 to sustain this level of energy dissipation, it had to be accompanied by a much larger displacement compared to IC03. After 3 seconds, the energy dissipation of the two models was similar, but the displacement of EM03 was 120 mm and was gradually increasing, compared to a displacement of 20 mm for IC03.

Similar conclusions can be drawn for the pseudo-dynamic tests on models EM05 and IC05 where the displacement after 10 seconds progressively increased beyond 120 mm for EM05 whereas IC05 continued to carry load throughout the full 16 seconds duration with considerably less deformations.

The above discussion highlights the fact that a relatively small degradation in the capacity under displacement-controlled cyclic loading will cause an inferior behaviour under earthquake loading. Whereas the same energy can be dissipated up to a certain level, it is accompanied by excessive deformations and increased second-order effects. This also emphasizes the importance of using realistic earthquake tests to investigate and verify the structural seismic performance.

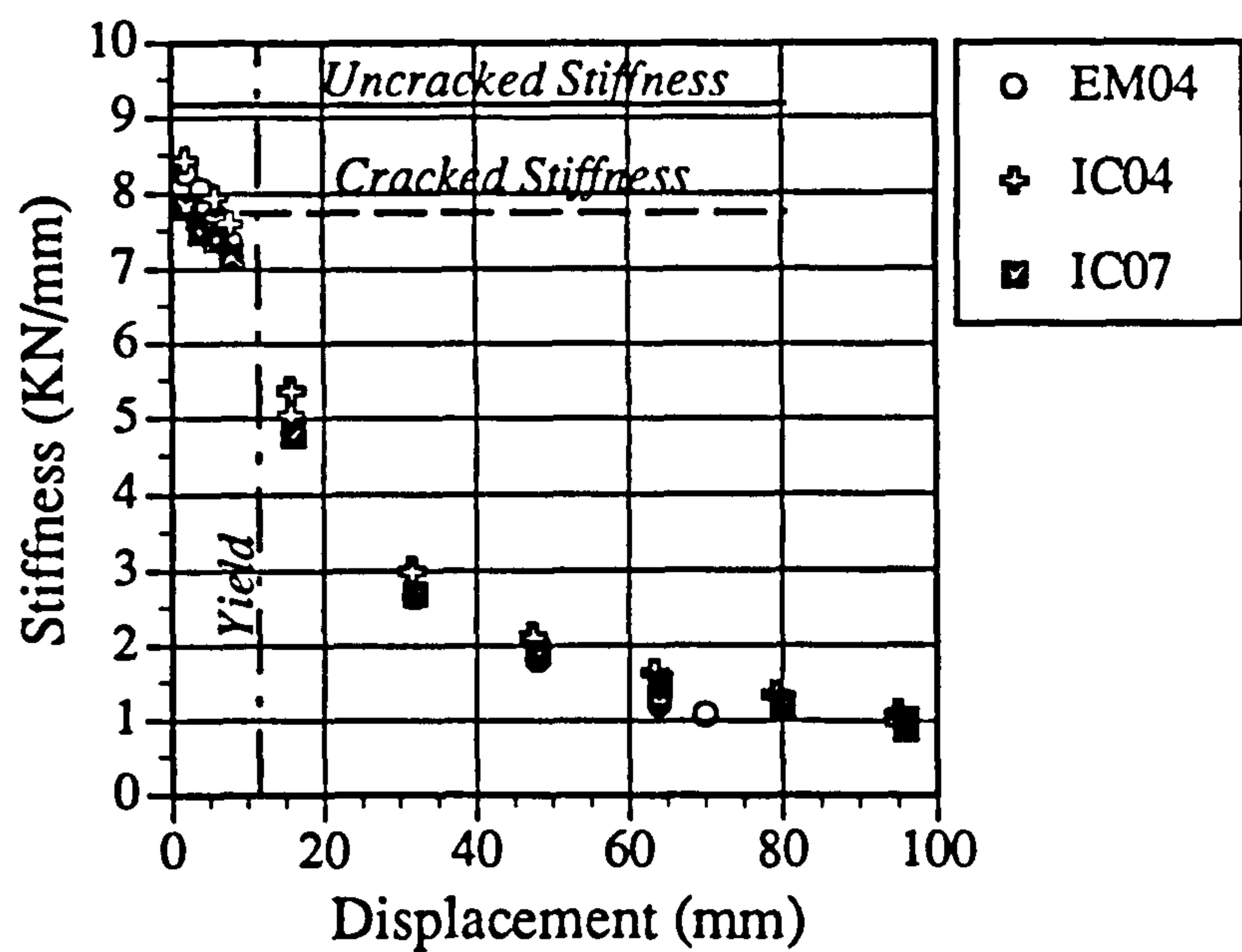


Fig. 9.1 Experimental secant stiffness of EM04, IC04 and IC07

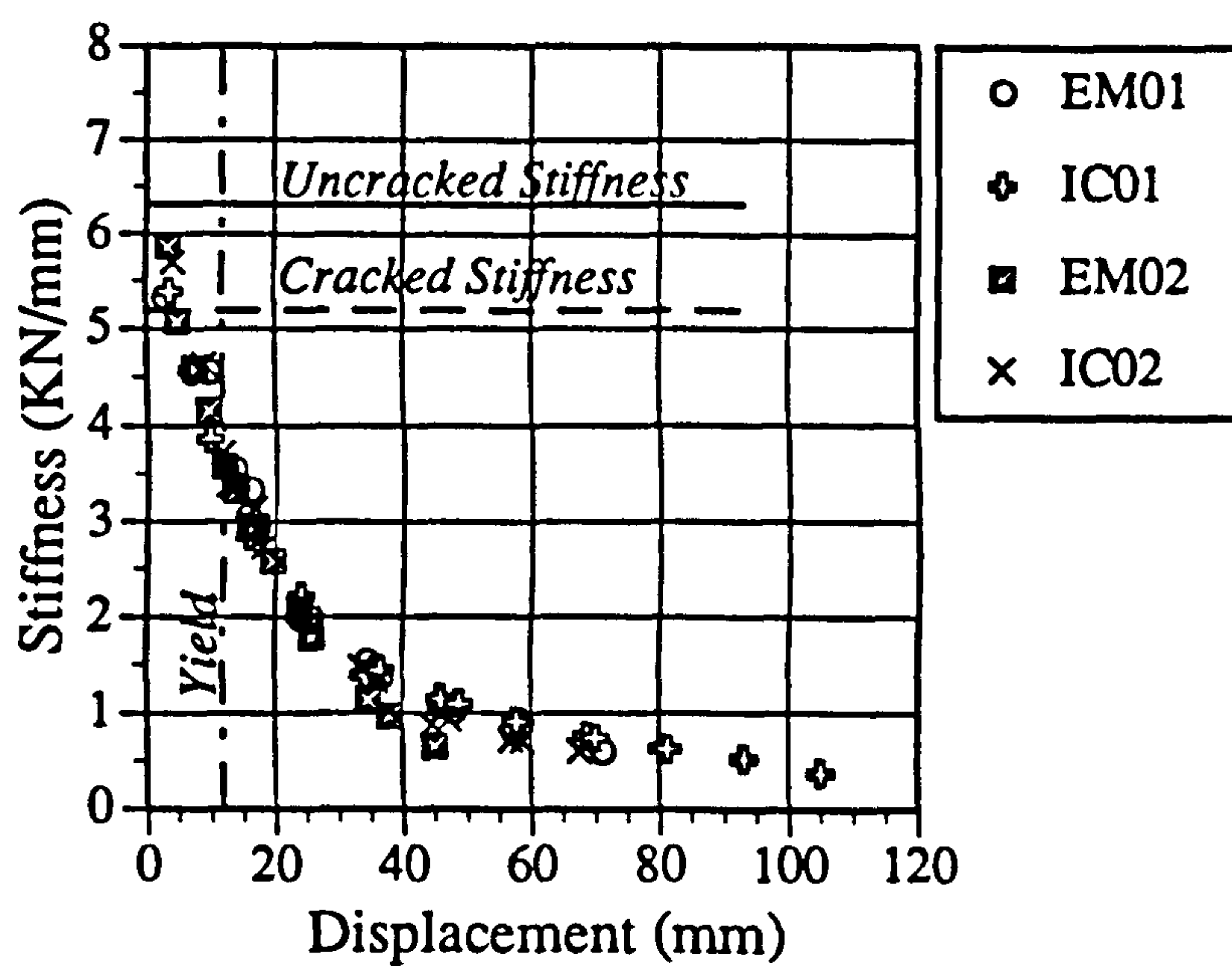


Fig. 9.2 Experimental secant stiffness of EM01, EM02, IC01 and IC02

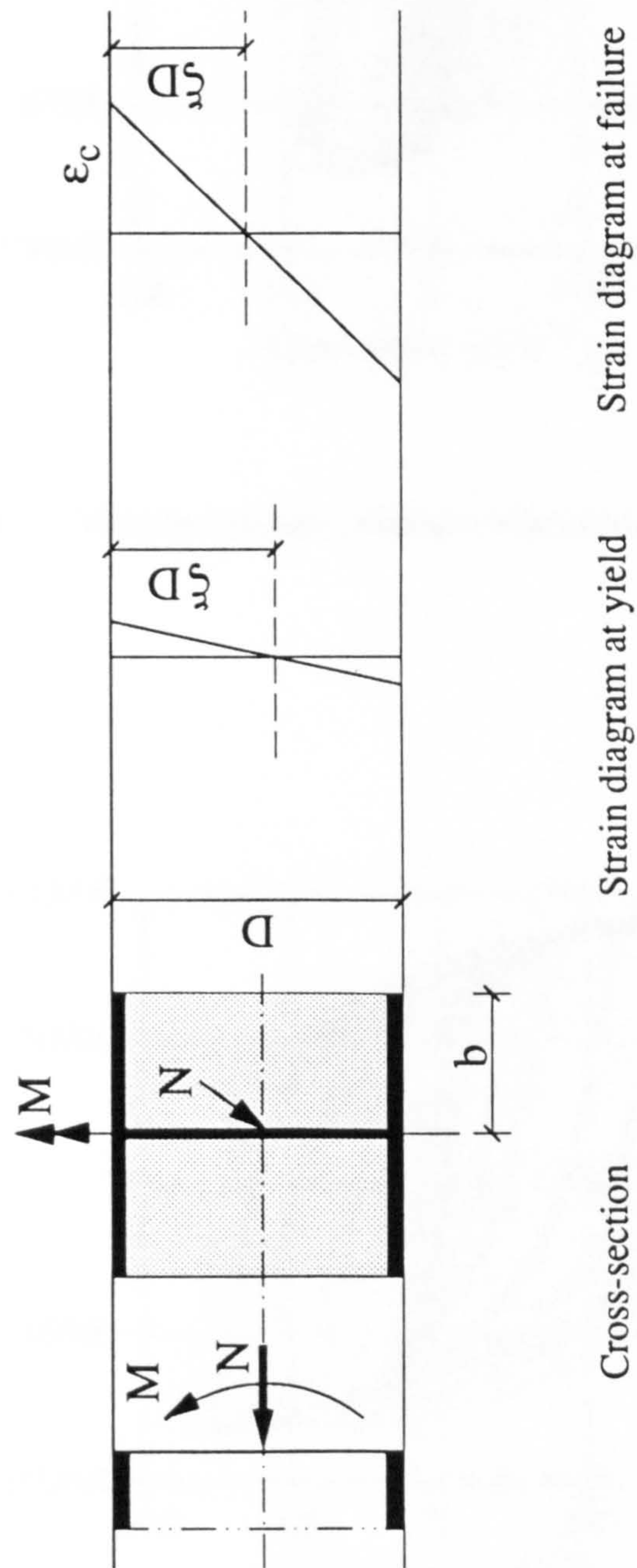


Fig. 9.3 Strain diagrams at yield and failure

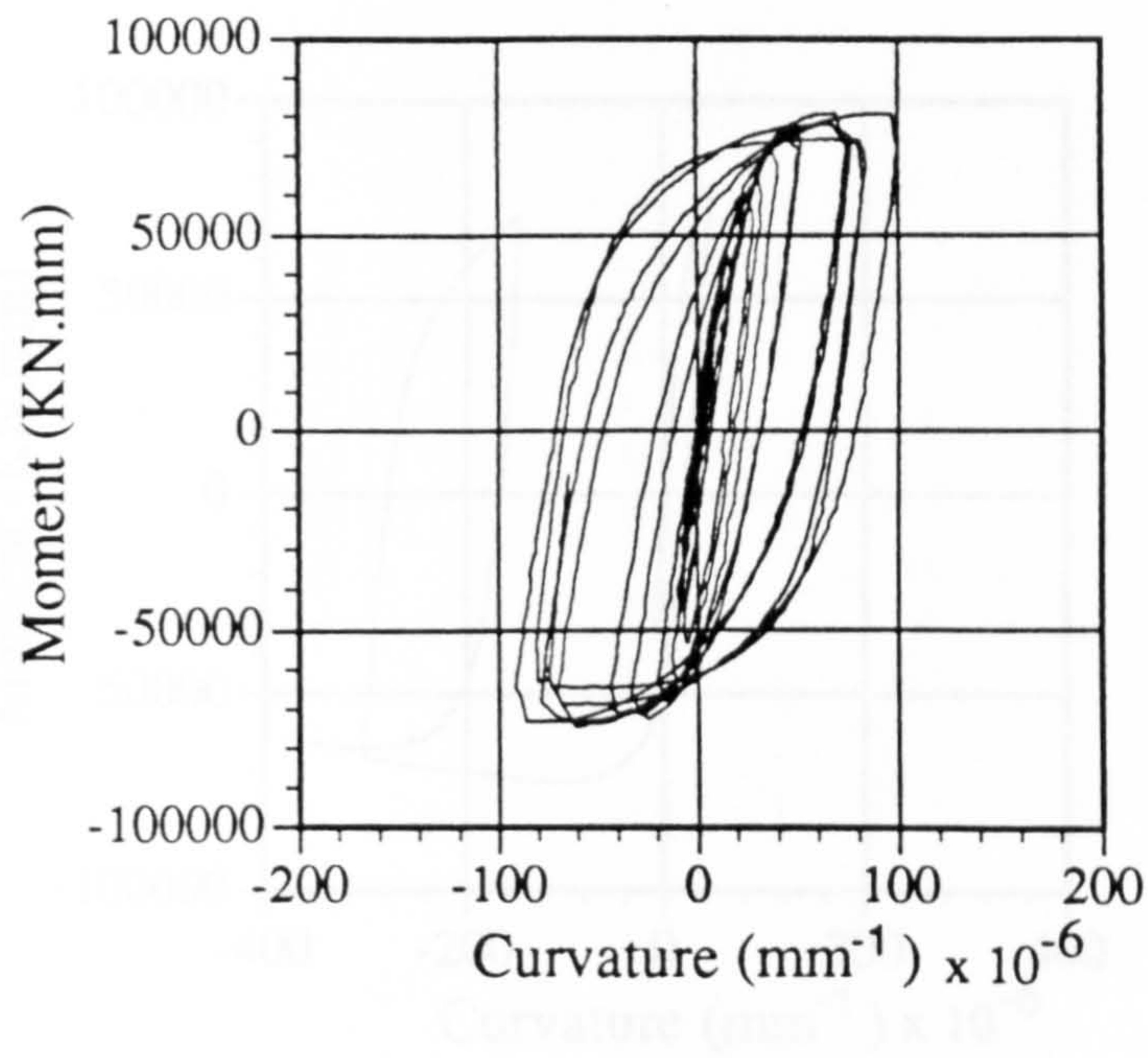


Fig. 9.4 Moment versus curvature relationship for EM02

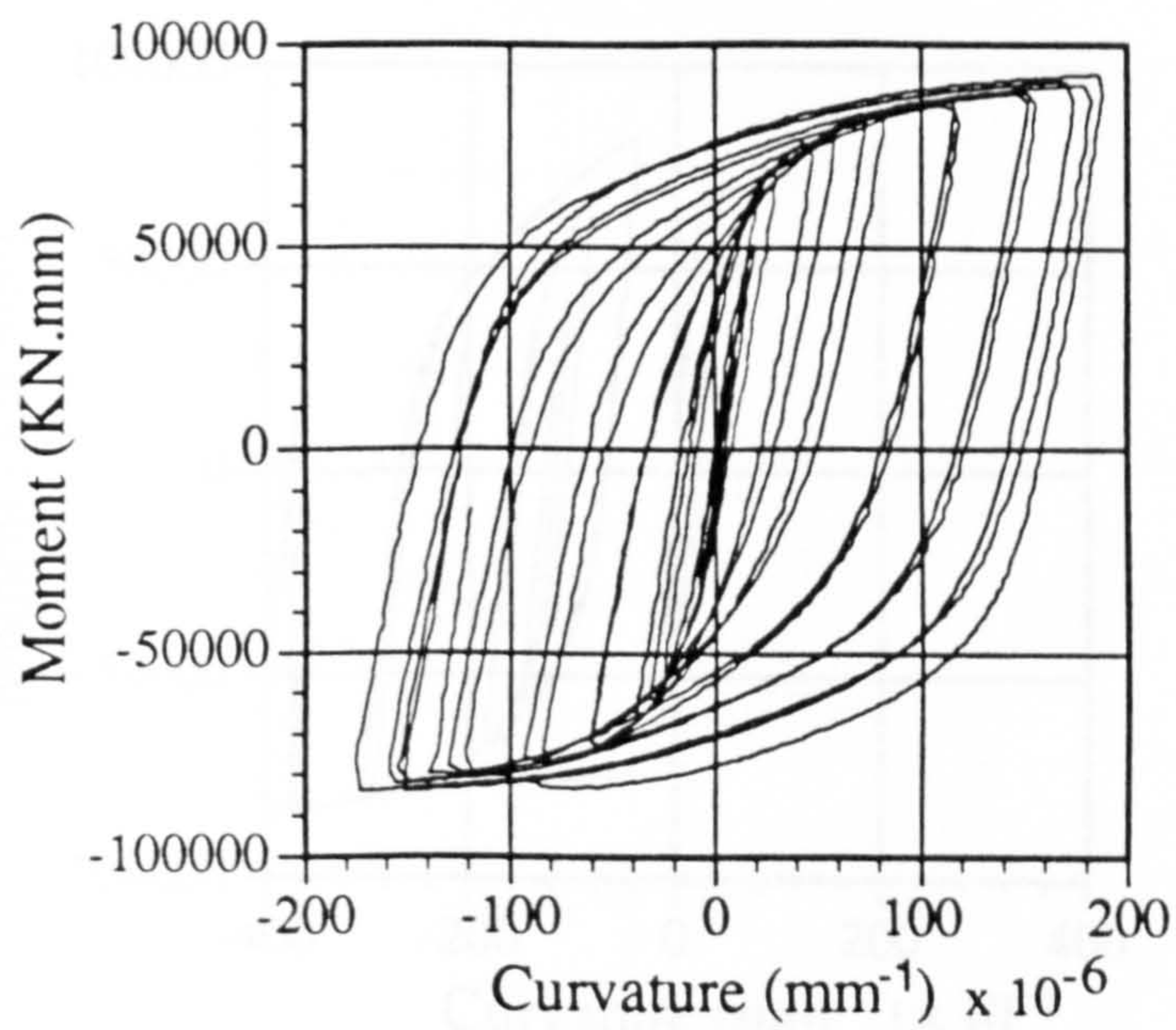


Fig. 9.5 Moment versus curvature relationship for IC02

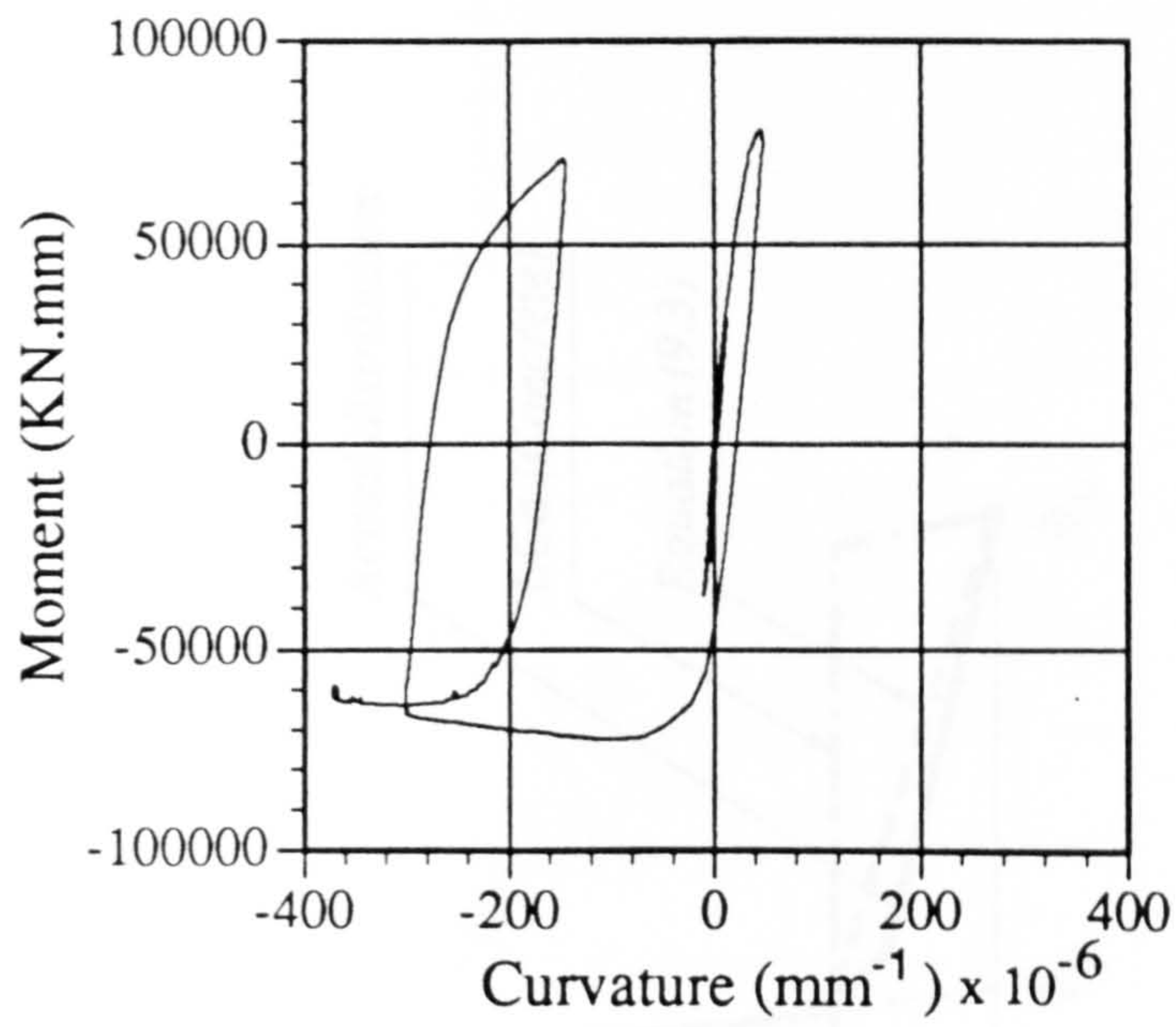


Fig. 9.6 Moment versus curvature relationship for EM03

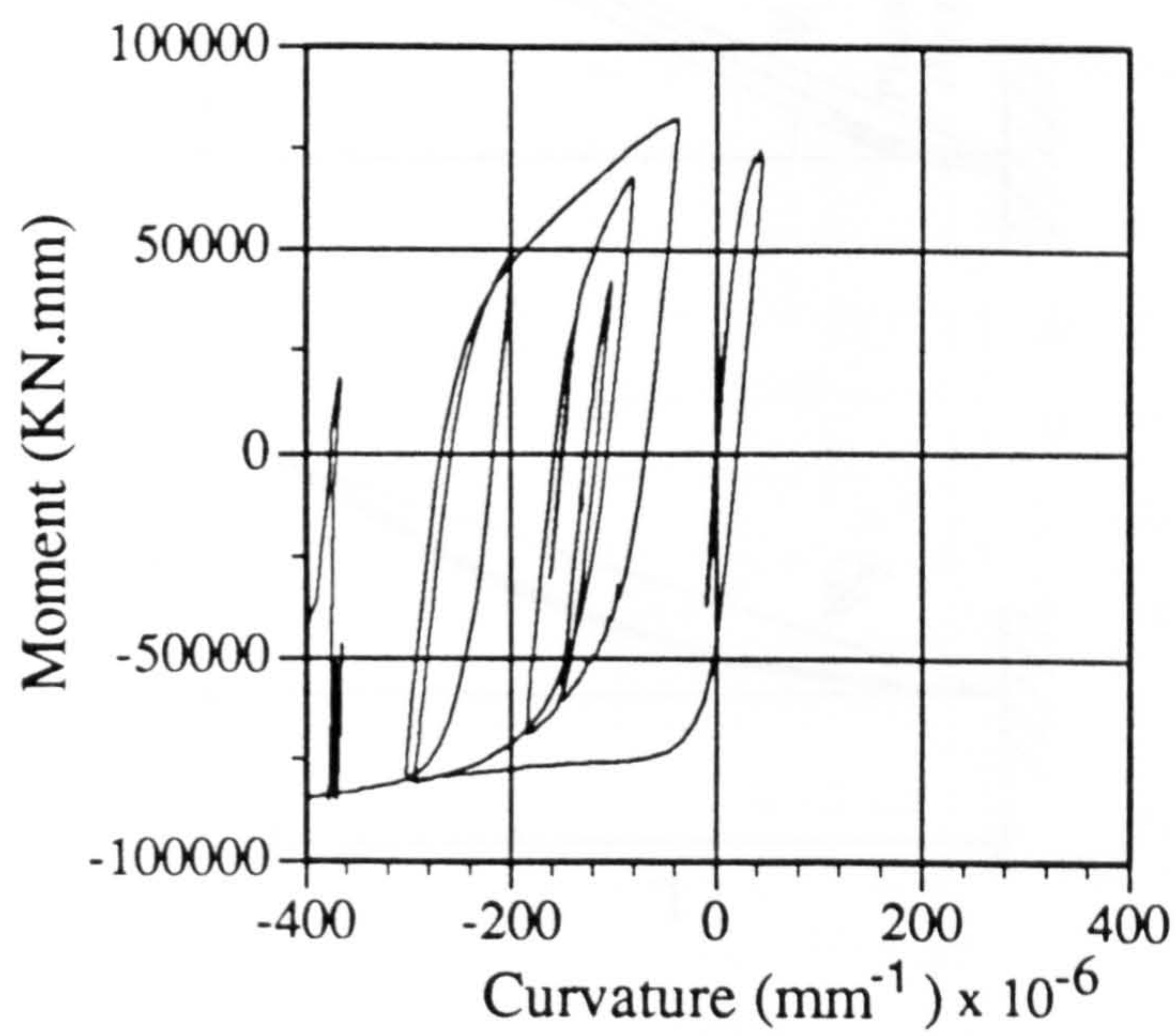


Fig. 9.7 Moment versus curvature relationship for IC03

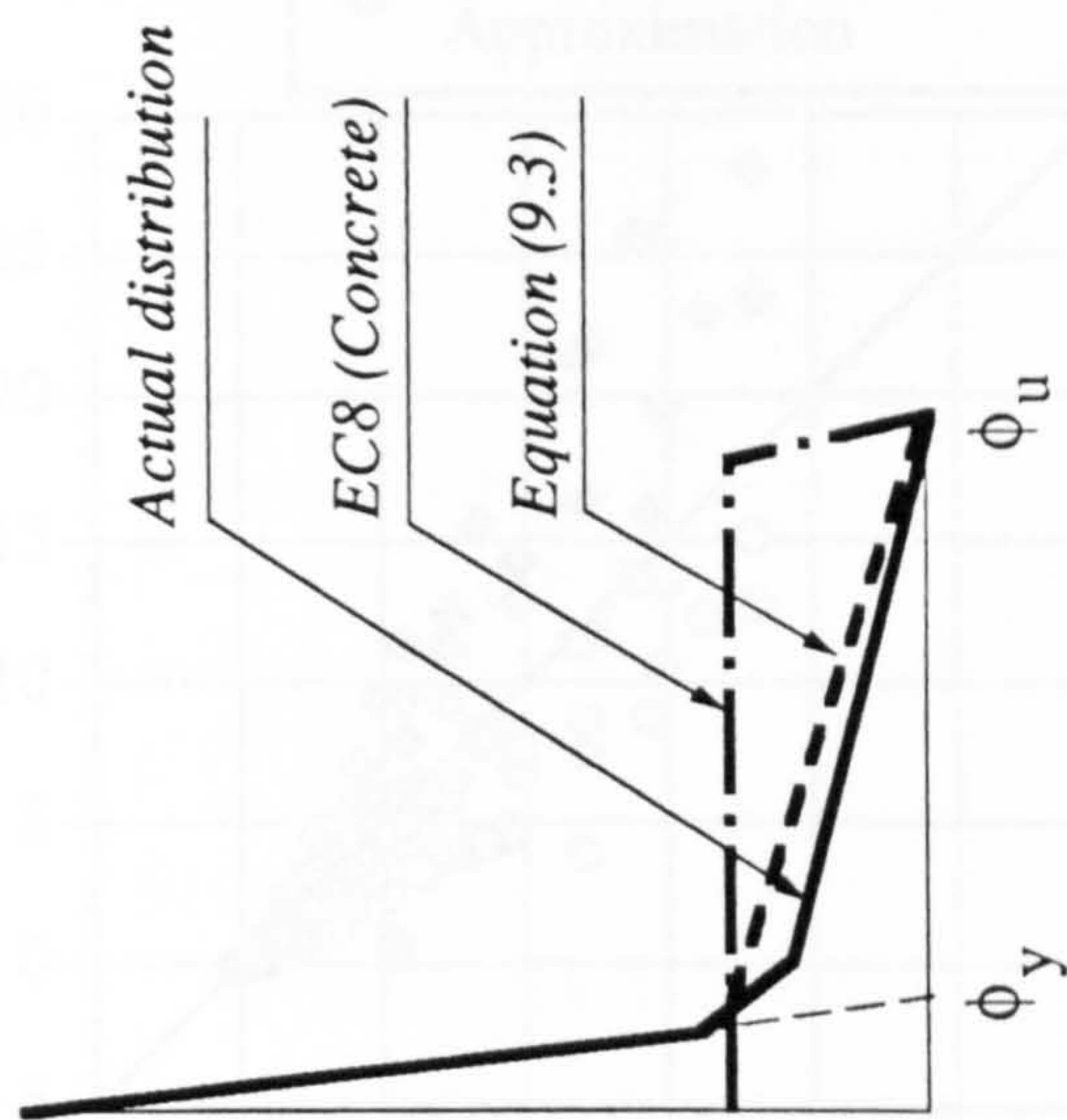
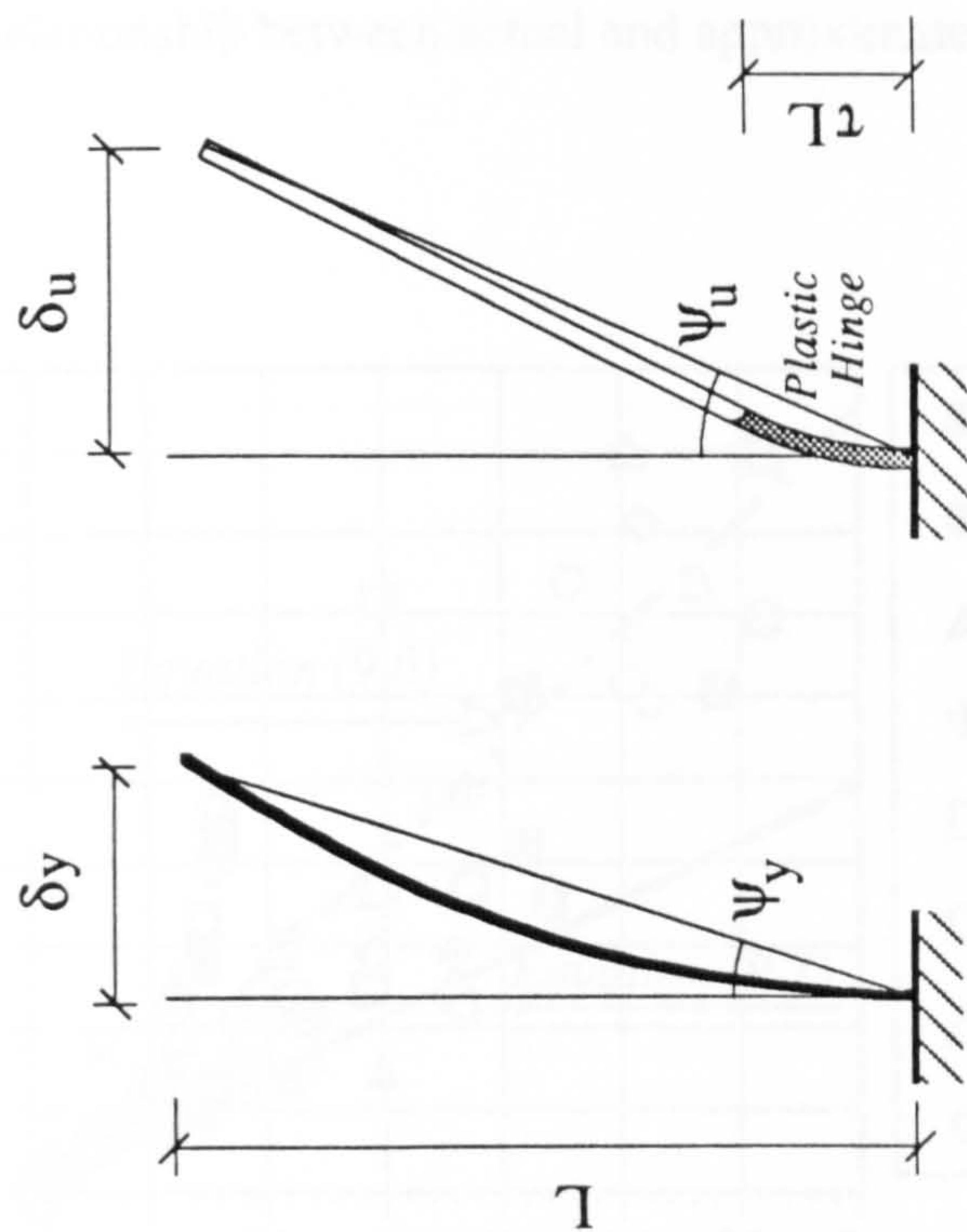


Fig. 9.8 Curvature distribution in the plastic hinge zone

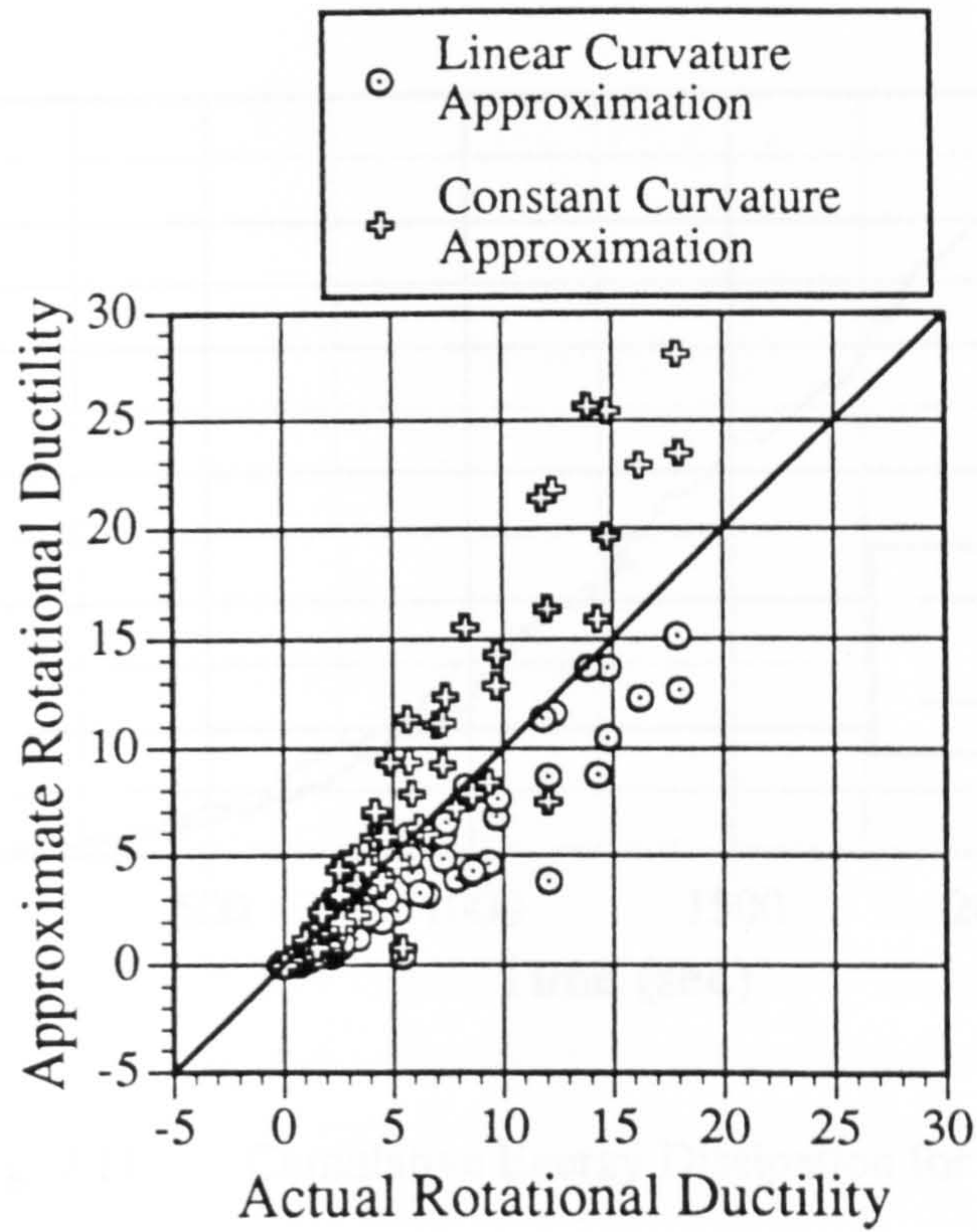


Fig. 9.9 Relationship between actual and approximate rotational ductilities

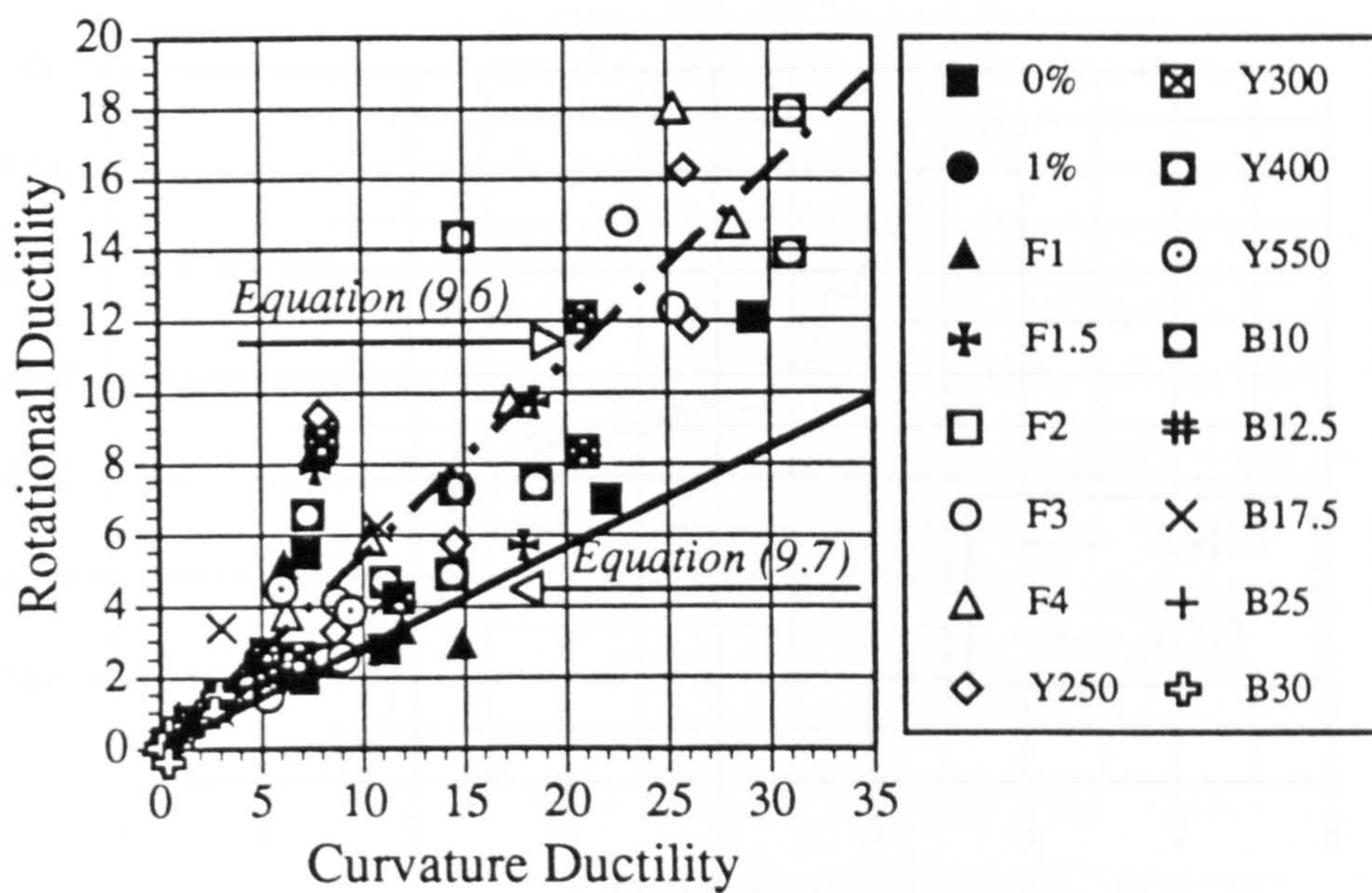


Fig. 9.10 Rotational versus displacement ductility for from the parametric study

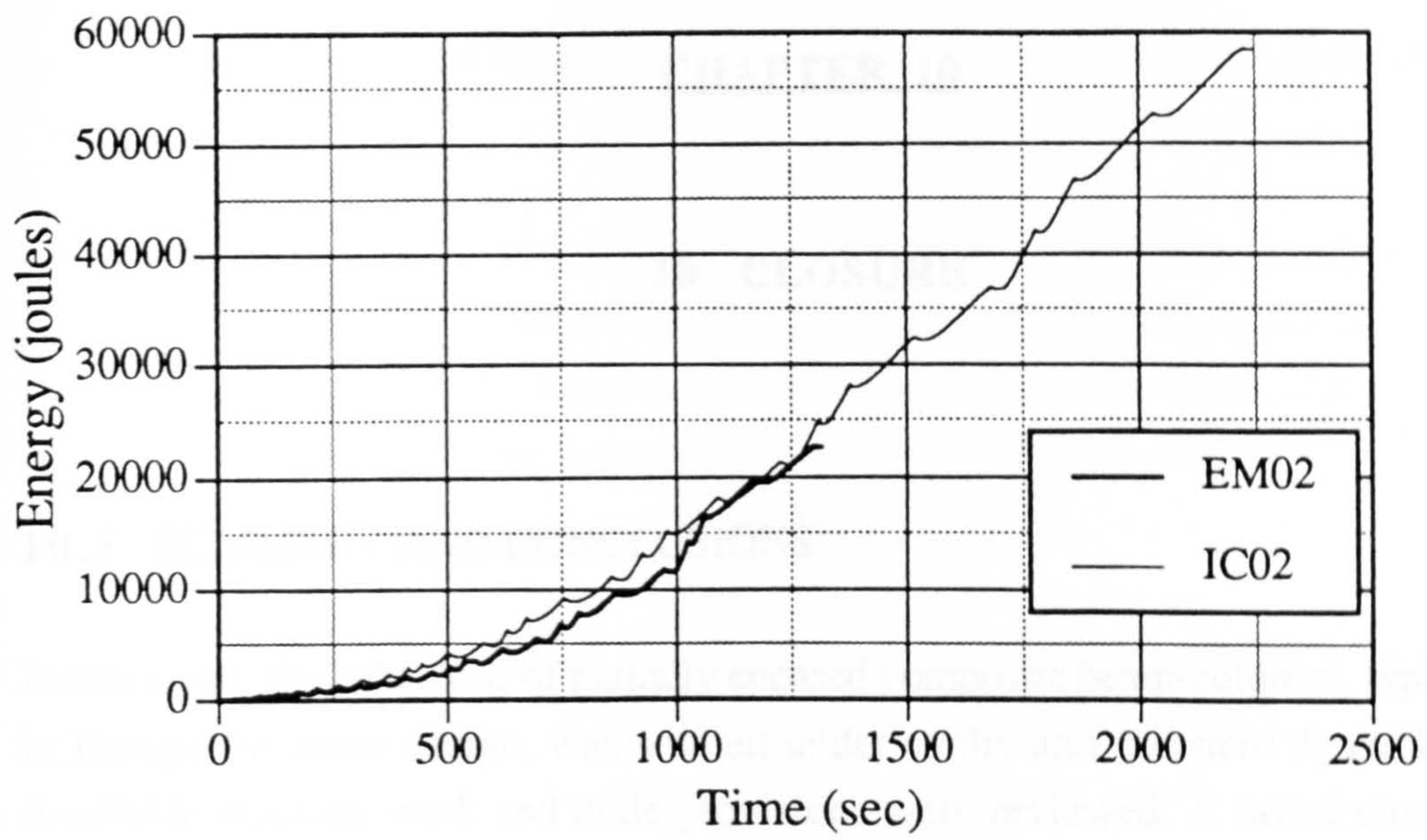


Fig. 9.11 Cumulative Energy Dissipation for EM02 and IC02

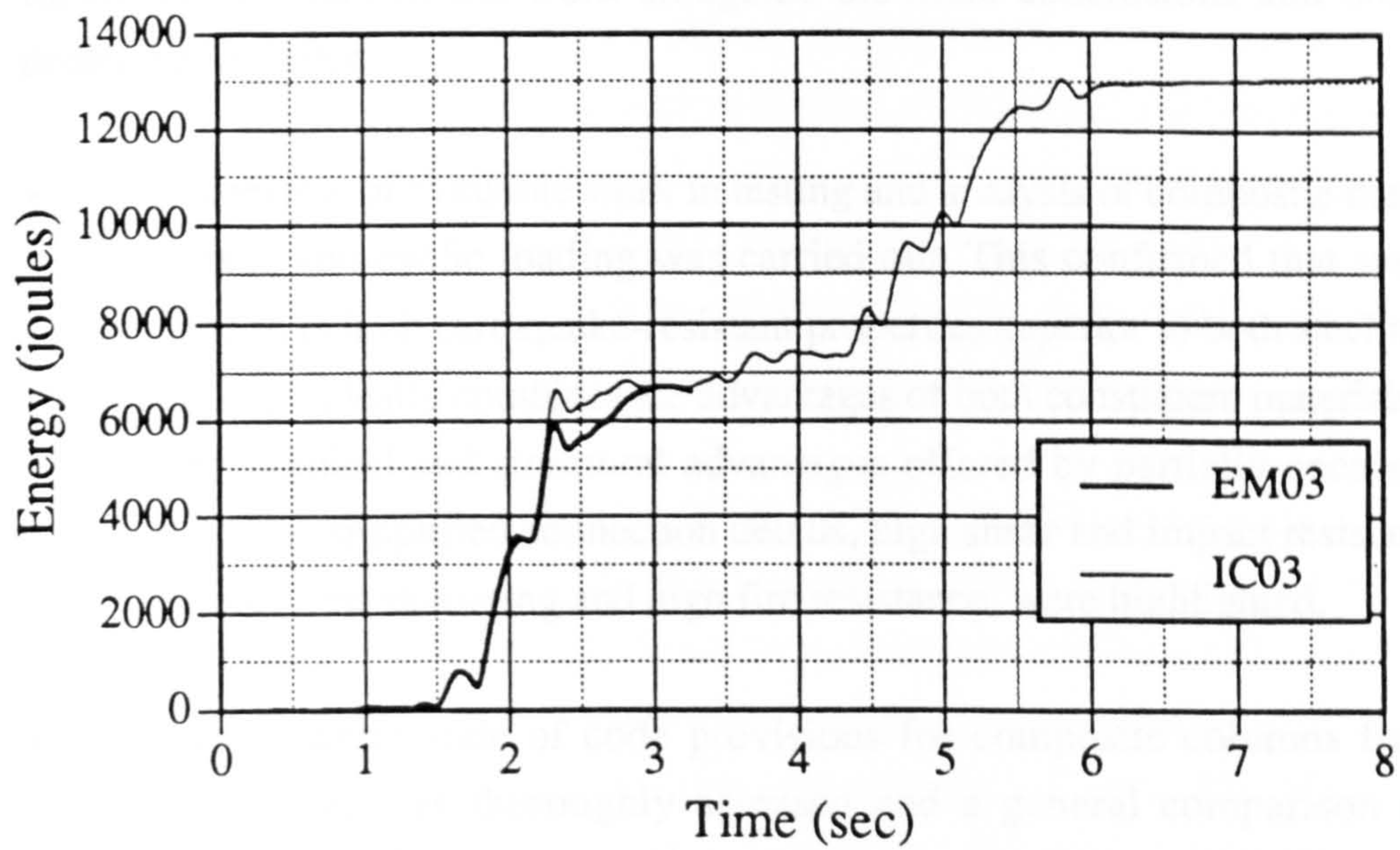


Fig. 9.12 Cumulative Energy Dissipation for EM02 and IC02

CHAPTER 10

10. CLOSURE

10.1 SUMMARY AND CONCLUSIONS

In this thesis, the behaviour of partially encased composite beam-columns, typically used in Europe for static design, was studied under cyclic and transient dynamic loading. Available research work and code provisions were reviewed. A novel configuration, designed to provide improved seismic performance, was proposed. The behaviour of both existing and proposed forms was examined experimentally through a number of cyclic and seismic tests, for which a new refined pseudo-dynamic testing facility was developed. Analytical studies were undertaken using advanced nonlinear analysis methods. Finally, implications of the main findings from the experimental and analytical investigations on the design process were presented.

Specific conclusions pertinent to each section have been given within the body of the thesis. A summary of the work alongside the main conclusions and observations is presented hereafter:

- A review of available work in testing and analysis of composite members under static and cyclic loading was carried out. This confirmed that such structural forms exhibit earthquake-resistant properties superior to both steel and concrete, since it ideally combines the advantages of both constituent materials. Additional economical and structural advantages offered by partially encased members, such as simplified connection details, high shear and impact resistance, reduced or omitted shuttering and high fire resistance, were highlighted.
- The current state of code provisions for composite columns from different countries was thoroughly assessed and a general comparison of the main recommendations was undertaken. Also, quantitative comparisons of capacity calculation for a specific cross-section was carried out. It was concluded that large discrepancies exist between various codes. This was not only due to the difference in design philosophies, but also due to differences in the definition of

important geometric and strength parameters, even when the same design basis was adopted.

- Notwithstanding the differences in capacity of composite members calculated from different codes, it was observed that there was a virtual lack of specific code provisions for composite members subjected to earthquake loading. With the exception of the Japanese code, a composite member is treated either as a steel or a reinforced concrete member.
- The relative merits of various testing procedures for seismic performance evaluation were investigated in terms of their applicability, reliability and economy. Pseudo-dynamic testing was shown to be ideal for research on the behaviour of members and structural assemblies since the method is as realistic as shake table testing, yet retains the versatility and economy of quasi-static testing; it allows for detailed observation of the actual structural behaviour during seismic tests on unscaled or large scale models.
- A new on-line computer-controlled experimental facility was developed. The theoretical basis of the pseudo-dynamic technique was introduced. Possible application of different numerical algorithms to on-line testing was assessed, and the accuracy and stability of basic explicit and implicit step-by-step integration methods were discussed. The details of the software developed for controlling the system were presented. A description of the components of the developed on-line facility was given. The fundamental operation and performance of each unit was briefly described, the main sources of error from each element was indicated and the reliability of each component in relation to the accuracy of pseudo-dynamic testing was discussed.
- Probable sources of error arising from structural idealisation in on-line tests were identified and discussed. Discrete parameter modelling through lumped and consistent mass formulations and geometric effects caused by gravity loads were addressed. The significance of strain rate in pseudo-dynamic testing of steel and concrete structures was assessed. It was also shown that in the inelastic range, the energy dissipation becomes dominated by hysteretic damping, which is implicitly accounted for in the test. Consequently, a discrepancy in the value of viscous damping, which is analytically prescribed, becomes insignificant.

- The accuracy and reliability of the on-line system was verified through a number of tests on two steel cantilevers. An impulse excitation was first applied simulating a free-vibration response, from which the mechanical energy dissipation of the system was examined. This was followed by an earthquake test in the elastic range, for which excellent correlation was obtained with linear elastic dynamic analysis using an equivalent viscous damping value corresponding to the inherent friction of the system. Two tests were also conducted under earthquake loading in the inelastic range. Very good agreement between the pseudo-dynamic results and the analytical simulations was achieved. Although the on-line test is significantly more reliable in the inelastic range, slight discrepancies in the results were observed due to the inaccuracies in the inelastic material modelling.
- Evaluation of the experimental errors in the pseudo-dynamic verification tests was undertaken. The results substantiated the accuracy of the developed system. The significance of displacement and force feedback errors and displacement control errors was discussed. It was shown that by proper control of the feedback errors, through both limiting the discrepancy between measured and computed displacement and ensuring reasonably accurate force measurements, very accurate results were obtained. It was also shown that the experimental accuracy increased with the increase of inelastic displacements.
- It was indicated that to examine the reliability of the integrated system, linear elastic tests should first be carried out, which should then be compared to accurate linear analysis. Any discrepancy would indicate the presence of errors that should be reduced by appropriate modification of testing equipment and techniques.
- A new configuration of partially encased beam-column, designed to provide improved earthquake performance, was introduced. Two unconventional features were incorporated. The first was the provision of additional transverse bars intended to inhibit or delay local flange buckling at post-yield strain levels. The second was using variable pitch confining stirrups.
- The experimental programme comprised a total of twelve composite members. Seven models were tested under lateral displacement cycles and constant axial loads representing various percentages of the axial plastic capacity. Also, to investigate the behaviour under earthquake loading, five models were tested

using the pseudo-dynamic testing technique. Two cross-section details were tested; one typical of European practice and the second includes an additional modification for delaying local flange buckling. In both cases, reduced stirrup spacing was used within the potential plastic hinge zone. The details of test rigs used was described and the choice of loading regimes was discussed.

- Definitive results were achieved from the experimental investigation. The effects of loading history, flange slenderness, axial load and concrete confinement on the behaviour of partially encased members were clearly indicated. Moreover, the expected enhancement in seismic performance of the IC models compared to conventional members was fully verified. Whereas the variation in stiffness and yield capacity was generally insignificant, the ductility of the members including the proposed modifications was substantially enhanced.
- The existing nonlinear dynamic analysis program 'ADAPTIC' was used for the analytical investigations. The available cyclic material models for steel and concrete were briefly described. Expressions for assessing confinement in reinforced concrete members were introduced and simple modifications were suggested for use with composite sections. Also, the problem of local flange buckling in the inelastic range was discussed. In order to account for this effect in partially encased members, a simplified model suitable for frame analysis programs was suggested. The model was calibrated with the results extracted from the experiments, and implemented within 'ADAPTIC'.
- Analytical simulations using 'ADAPTIC', including the new developments, were compared to the experimental results. Very good correlation was achieved. The stiffness, capacity and ductility were well predicted by the analysis. However, the slight discrepancy in the shape of the hysteresis loops observed was attributable to the inaccuracy of the concrete model in representing the imperfect closure of cracks during cyclic loading. The local buckling model was shown to be conservative when a significant number of loading cycles was applied close to the yield region, whilst the accuracy significantly increased for earthquake loading. Discrepancies were also observed in the post-local buckling response due to inaccuracies in the local buckling model, particularly in relating the extent of buckling to the drop in concrete confinement.
- An analytical parametric study was carried out to investigate the effects of significant parameters on the capacity and ductility of partially encased

members. This comprised the level of axial load, steel characteristics, concrete confinement and flange slenderness, including the spacing of local buckling inhibitors, and slenderness of the member. It was shown that ductility can be enhanced by decreasing the axial load, yield stress of steel and flange slenderness, and by increasing the concrete confinement.

- The initial stiffness of all models was lower than that predicted from elasticity. The cracked stiffness was found to represent more closely the overall stiffness at the yield level. It was, therefore, recommended to use this stiffness both in equivalent static design methods and in elastic dynamic analysis.
- Concrete confinement was shown to have no effect on the yield moment, particularly for practical values of axial load. The yield capacity can be accurately calculated using simple section analysis. Based on the results of the parametric study, a simple equation was proposed for determining the position of the neutral axis for the range of parameters studied.
- The moment capacity enhancement under axial loads was shown to be accompanied by a significant drop in ductility. Geometric effects caused by high axial loads further impair the overall ductility and may also change the dynamic characteristics of the structure. Moreover, uncertainties related to the vertical ground accelerations may lead to an underestimation of the level of axial loads. It was, therefore, recommended to limit the extent of the compressive axial force to 30% of the plastic capacity.
- Analytical estimation of the length of the plastic hinge zone was shown to yield good agreement with the experimental results. The relationship between the curvature and rotational ductility was examined and compared with the results of the parametric study. Unlike the constant curvature approximation, linear curvature distribution in the plastic hinge zone was found to give conservative results. Therefore, the equations based on linear distribution were recommended, for which an approximate conservative value of the plastic hinge length was suggested.
- It was shown, both experimentally and analytically, that a safe upper bound for the extent of the plastic hinge, for detailing purposes, can be taken as 40% of the length from the base to the point of contraflexure. The parametric study

indicated the general validity of this assumption for the practical range of parameters studied.

- The experimental results indicated a difference in the attained ductility between the cyclic and the pseudo-dynamic tests. This was due to the higher degree of stress softening and the accumulation of plastic strain when more cycles were applied. The analytical results were calibrated to give a conservative estimate of these effects.
- Methods of assessing local ductility in modern steel and reinforced concrete codes were discussed. The ductility corresponding to the limitations on flange slenderness given in European codes for steel and composite structures was quantified based on the results of the parametric study. In this respect, the approach adopted in the rules for concrete in Eurocode 8 was shown to be a viable basis for design procedures for specific levels of ductility.
- A procedure was outlined by which the details of critical zones of the member may be determined for a required level of ductility using simple section analysis or design charts. For instance, the combination of flange slenderness and spacing of local buckling inhibitors required to satisfy a certain curvature ductility for a given yield stress and confinement factor may be defined.

The overall conclusion of this work is that properly detailed partially encased members, particularly those including the proposed modifications, provide high ductility and energy absorption capacity under seismic loading. Use of this new configuration is highly recommended and will result in economic and reliable solutions to a number earthquake-resistant design problems.

10.2 SUGGESTIONS FOR FUTURE RESEARCH

The current research work has contributed to the understanding of the behaviour of partially encased members under earthquake loading. New developments were introduced and design procedures were recommended. However, a number of interesting issues were not examined, several topics have been opened for investigation and some propositions require further validation. Several suggestions are given hereafter:

- Additional work is required before the newly-developed on-line computer-controlled facility can be used in reliable testing of multi-degree-of-freedom systems, for which achieving high accuracy and reliability becomes an even more difficult task. Due consideration should be given to improvements in experimental equipment such as use of digital instrumentation and electro-mechanical actuators. Also, rapid testing techniques and the employment of unconditionally stable numerical methods must be studied.
- The confinement effects in partially encased members need to be quantified by more experimental and analytical investigations. The suggested expressions based on reinforced concrete work require further modification. Also, although the analytical quantification of the effect of local buckling inhibitors was verifiably conservative for this experimental investigation, few additional tests should be conducted at a different scale before it can be confidently used for design.
- For further accuracy in nonlinear dynamic analysis simulations, improvements are needed in the developed local buckling model. In particular, more effort is required to account for stress softening and loss of concrete confinement at the onset of local buckling.
- Based on the results of this work, simplified equations or charts could be produced for ductility-based seismic design. Through further parametric studies, the structural behaviour factors may also be directly related to the local ductility of the members.
- Considerable research is still needed to extend the scope of the current research for studying the behaviour under minor axis and biaxial bending. Both experimental and analytical investigations are required as well as design recommendations to resist bi-directional earthquake loading.

Some of the above-mentioned topics are currently under investigation at Imperial College. The pseudo-dynamic testing facility is being extended to allow testing of individual members from a multi-storey structure, using on-line sub-structuring techniques. Further work is also underway on the effect of confinement on the earthquake performance of composite members and assemblages.

REFERENCES

ACI 318-83, Building Code Requirements for Reinforced Concrete, American Concrete Institute, Detroit, MI, 1983.

Ahmad, S.H. and Shah, S.P., "Stress-Strain Curves of Concrete Confined by Spiral Reinforcement", J. of the American Concrete Institute, ACI, November, 1982, pp. 484-490.

AII-LSD, Standard for Limit State Design of Steel Structures, Architectural Institute of Japan, First Draft, 1990.

AISC-LRFD, Specifications for the Design, Fabrication and Erection of Structural Steel for Buildings, American Institute of Steel Construction, Chicago, IL, 1986.

Aktan, H.M., "Pseudo-dynamic Testing of Structures", J. of Structural Eng., ASCE, Vol. 112, No. 2, 1986, pp. 183-197.

Ambraseys, N.N., Basili, M., Martinetti, S. and Mohammadioun, B., "CEC Strong-motion Databank and Dissemination Centre", European Earthquake Eng., Vol. II, No. 3, 1989, pp. 51-52.

Ballio, G. and Perotti, F., "Cyclic Behaviour of Axially Loaded Members; Numerical Simulation and Experimental Verification", J. of Constructional Steel Research, Vol. 7, 1987, pp. 3-41.

Ballio, G., Calado, L., Iori, I. and Mirabella Roberti, G., "I Problemi Delle Grandi Costruzioni in Zona Sismica", aicap, Roma, April, 1987, pp. 31-44.

Basu, A.K. and Sommerville, W., "Derivation of Formulae for the Design of Rectangular Composite Columns", Supplement V, Proc. ICE, paper 7206S, 1969, pp. 233-280.

Basu, A.K., "Computation of Failure Loads of Composite Columns", Proc. ICE, Vol. 36, 1967, pp. 557-578.

Bathe, K.J., "Finite Element Procedures in Engineering Analysis", Prentice Hall Inc., New Jersey, 1982.

Bleich, F., "Buckling Strength of Metal Structures", Mc Graw Hill, First Edition, 1952.

Bondale, D.S., "Column Theory with Special Reference to Composite Columns", Consulting Engineer, London, Vol. 30, September, 1966, pp. 68-80.

Bondale, D.S., "The Effect of Concrete Encasement on Eccentrically Loaded Steel Columns", PhD Thesis, Imperial College, University of London, June, 1962.

Bresler, B., "Design Criteria for Reinforced Concrete Columns under Axial Load and Biaxial Bending", J. of American Concrete Institute, ACI, Vol. 57, November, 1960, pp. 481-490.

Bridge, R.Q. and Roderick, W.J., "Behaviour of Built-up Composite Columns", J. of Structural Div., ASCE, Vol. 104, ST7, July, 1978, pp. 1141-1155.

Bridge, R.Q., Ansourian, P., Rotter, J.M., Patrick, M. and Pham, L., "Australian Standards for Composite Constructions in Steel and Concrete", Composite Construction in Steel and Concrete, Proc. of Eng. Foundation Conf., ASCE, Henniker, New Hampshire, 1987, pp. 71-83.

Bridge, R.Q., "Composite Columns under Sustained Load", J. of Structural Div., ASCE, Vol. 105, ST3, 1979, pp. 563-576.

Bridge, R.Q., "The Long-Term Behaviour of Composite Columns", Composite Construction in Steel and Concrete, Proc. of Eng. Foundation Conf., ASCE, Henniker, New Hampshire, 1987, pp. 460-471.

BS 449, British Standard Specification for Structural Steel in Buildings, British Standards Institution, 1959.

BS 5400, British Standard for the Use of Structural Steel in Buildings, Part 3, Composite Construction, Draft, British Standards Institution, London, 1979.

Burr, W.H., "Composite Columns of Concrete and Steel", Proc. ICE, Vol. 188, 1912, pp. 114-126.

Chang, K.C. and Lee, G.C., "Strain Rate Effect on Structural Steel under Cyclic Loading", J. of Eng. Mech., ASCE, Vol. 113, No. 9, 1987, pp. 1292-1301.

Cooling, J.E., "Real-Time Interfacing, Engineering Aspects of Microprocessor Peripheral Systems", Van Nostrand Reinhold, UK, 1986.

EC3, Eurocode No 3, "Common Unified Rules for Steel Structures", Commission of the European Communities, Draft, 1984.

EC4, Eurocode No 4, "Composite Steel and Concrete Structures", Commission of the European Communities, Draft, 1984.

EC8, Eurocode No 8, "Structures in Seismic Regions", Commission of the European Communities, Report EUR 12266 EN, Draft, 1988.

ECCS, European Convention for Constructional Steelwork, "Design of Seismic Resistant Steel Structures", Doc.N.TC13.05.91, TC13, Seismic Design, First Draft, 1991.

ECCS, European Convention for Constructional Steelwork, "Recommended Testing Procedure for Assessing the Behaviour of Structural Steel Elements under Cyclic Loading", Technical Working Group 1.3- Seismic Design, First Edition, 1986.

Elghazouli, A.Y., "Concrete Encased Steel Columns for Earthquake-Resistant Design", MSc Dissertation, Imperial College, University of London, September, 1988, 159 pp.

Elghazouli, A.Y., Elnashai, A.S. and Dowling P.J., "Experimental Behaviour of Ductile Partially Encased Composite Beam-Columns", Measurements and Effects of Vibration Conf., Manchester, Society for Earthquake and Civil Eng. Dynamics, September, 1991, pp. 211-220.

Elnashai, A.S., Elghazouli, A.Y. and Dowling P.J., "Verification of Pseudo-Dynamic Testing of Steel Members", J. of Constructional Steel Research, Vol. 16, 1990, pp. 153-161.

Elnashai, A.S., Izzuddin, B.A. and Dowling, P.J., "Efficient Large Displacement Elastoplastic Dynamic Analysis of Structures", J. of European Earthquake Eng., No. 3, 1989, pp. 32-41.

Faber, O., "Savings to be affected by the More Rational Design of Encased Stanchions as a Result of Recent Full Size Tests", The Structural Engineer, Vol. 34, March, 1956, pp. 88-109.

Fukumoto, Y. and Itoh, Y., "Basic Compressive Strength of Steel Plates from Test Data", Proc. of Japan Society of Civil Eng., JSCE, No. 344/I-1, Structural Eng./Earthquake Eng., April, 1984, pp. 129-139.

Furlong, R.W., "Steel-Concrete Composite Columns", Handbook of Composite Construction Engineering, Van Nostrand Reinhold, Chapter 6, pp. 211-229.

Furlong, R.W., "Binding and Bonding Concrete to Composite Columns", Composite and Mixed Construction, Proc. of the US/Japan Joint Seminar, Seattle, Washington, ASCE, 1984, pp. 330-336.

Furlong, R.W., "Design of Steel-Encased Concrete Beam-Columns", J. of Structural Div., ASCE, Vol. 93, ST5, 1967, pp. 113-124.

Haaijer, G. and Thürlimann, B., "Inelastic Buckling in Steel", Transactions, ASCE, Vol. 125, 1960, pp. 308-344.

Hahn, J. and Jungbluth, O., "Untersuchungen zum Beulverhalten von H-Profilen mit ausbetonierten Kammern", Report N0. 98/83, ARBED Research Centre, Luxembourg, 1983.

Hanson, R.D. and McClamrock, N.H., "Pseudo-dynamic Test Method for Inelastic Building Response", Proc. of the Eighth World Conf. on Earthquake Eng., San Francisco, California, Vol. 6, 1984, pp. 127-134.

Hanson, R.D., "Comparison of Static and Dynamic Hysteresis Curves", J. of Eng. Mech., ASCE, Vol. 92, EM5, 1966, pp. 87-113.

Iemura, H., Yamada, Y. and Tanzo, W., "Testing R/C Specimens by a Substructure-Based Hybrid Earthquake Loading System", Proc. of the Ninth World Conf. on Earthquake Eng, Tokyo, Japan, Vol. IV, 1988, pp. 35-40.

Izzuddin, B.A. and Elnashai, A.S., "ADAPTIC, A Program for Adaptive Large Displacement Elastoplastic Dynamic Analysis of Steel, Concrete and Composite Frames", Eng. Seismology and Earthquake Eng., Imperial College, Research Report No. ESEE 89/7, 1989.

Izzuddin, B.A., "Nonlinear Dynamic Analysis of Framed Structures", PhD Thesis, Imperial College, University of London, December, 1990.

Jones, R. and Rizk, A., "An Investigation on the Behaviour of Encased Steel Columns under Load", The Structural Engineer, Vol. 41, January, 1963, pp. 21-33.

Kato, B., "Rotation Capacity of H-Section Members as Determined by Local Buckling", J. of Constructional Steel Research, Vol. 13, 1989, pp. 95-109.

Klingsh, W., "KSTTR, Computer Program for Load Bearing Analysis of Steel, Reinforced Concrete and Composite Columns in Fire Case", SFB 148, Technical University, Braunschweig, 1975.

Lapos, J. & Streleckij, N., East European Draft Recommendations. In Introductory Document, Stability of Metal Structures, A World View, Chapter 12, Composite members, Structural Stability Research Council, Bethlehem, Pennsylvania, USA, 1989, pp.12/9-12/13.

Madas, P. and Elnashai, A. S., "A New Passive Confinement Model for Concrete Subjected to Variable Amplitude Cyclic Loading", Imperial College, Eng. Seismology and Earthquake Eng., Research Report No. ESEE 91/2, 1991.

Madas, P. and Elnashai, A. S., "A Theoretical Model for Composite Beam-Columns under Cyclic Loading", Imperial College, Eng. Seismology and Earthquake Eng., ESEE Research Report No. 89/10, 1989.

Mahin, S. A., Shing, P. B., Thewalt, C.R. and Hanson R.D., "Pseudodynamic Test Method: Current Status and Future Directions", J. of Structural Eng., ASCE, Vol. 115, No. 8, 1989, pp. 2113-2128.

Mahin, S.A. and Bertero, V.V., "Rate of Loading Effects on Uncracked and Repaired Reinforced Concrete Members", Report No. UCB/EERC-72/09, Earthquake Eng. Research Center, College of Eng., University of California, Berkeley, California, 1972.

Mahin, S.A. and Shing, P. B., "Pseudo-dynamic Method for Seismic Testing", J. of Structural Eng., ASCE, Vol. 111, No. 7, 1984, pp. 1482-1503.

Mander, J.B., Priestley, M.J.N. and Park, R., "Theoretical Stress-Strain Model for Confined Concrete", J. of Structural Eng., Vol. 114, No. 8, August, 1988, pp. 1804-1826.

Manjoine, M.J., "Influence of Rate of Strain and Temperature on Yield Stresses of Mild Steel", ASME, Vol. 66, 1944, pp. A211-A218.

May, R.M. and Johnson, R.P., "Inelastic Analysis of Biaxially Restrained Columns", Proc. ICE, Vol. 65, June, 1978, pp. 323-337.

McClamroch, N.H., Serakos, J. and Hanson, R.D., "Design and Analysis of the Pseudo-dynamic Test Method", UMEE/81/R3, University of Michigan, Ann Arbor, 1981.

Mirza, S.A., "Parametric Study of Composite Column Strength Variability", J. of Constructional Steel Research, Vol. 14, 1989, pp. 121-137.

Mizuno, E., Kato M., and Fukumoto, Y., "Multi-Surface Model Application to Beam-Columns Subjected to Cyclic Loads", J. of Constructional Steel Research, Vol. 7, 1987, pp. 253-277.

Morino, S., Matsui, C. and Watanabe, H., "Strength of Biaxially Loaded SRC Columns", Composite and Mixed Construction, Proc. of the US/Japan Joint Seminar, Seattle, Washington, ASCE, 1984, pp. 185-194.

Morino, S., Matsui, C. and Yoshikai S., "Local Buckling of Steel Elements in Concrete Encased Columns", Proc. of the Pacific Structural Steel Conf. (PSSC), August, 1986, Auckland, New Zealand, pp. 319-335.

Morino, S., Uchida, Y. and Ozaki, M., "Experimental Study of the Behaviour of SRC Beam-Columns Subjected to Biaxial Bending", Composite Construction in Steel and Concrete, Proc. of Eng. Foundation Conf., ASCE, Henniker, New Hampshire, 1987, pp. 753-772.

Naka, T., Wakabayashi, M. and Murata, J., "Steel-Reinforced Concrete Construction", Proc. of the Ninth Conference of IABSE, Amsterdam, The Netherlands, Theme IIa, May, 1972.

Nakashima, K. and Kato, H., "Experimental Error Growth Behavior and Error Growth Control in Pseudo Dynamic Test", Proc. of the Ninth World Conf. on Earthquake Eng., Tokyo, Japan, Vol. IV, 1988, pp. 53-58.

Nakashima, M., Ishii, K., Kamagata, S., Tsutsumi, H. and Ando K., "Feasibility of Pseudo Dynamic Test using Substructuring Techniques", Proc. of the Ninth World Conf. on Earthquake Eng., Tokyo, Japan, Vol. IV, 1988, pp. 47-52.

Ohi, K. and Takanashi, K., "An Improvement of On-line Computer Test Control Method", Proc. of the Ninth World Conf. on Earthquake Eng., Tokyo, Japan, Vol. IV, 1988, pp. 17-22.

Pilakoutas, K. and Elnashai, A.S., "Experimental Behaviour of Ductile Partially Encased Composite Beam-Columns", Measurements and Effects of Vibration Conf., Manchester, Society for Earthquake and Civil Eng. Dynamics, September, 1991, pp. 510-219.

Pilakoutas, K., "Earthquake Resistant Design of Reinforced Concrete Walls", PhD Thesis, Imperial College, University of London, May, 1990.

Popov, E. and Maison, B., "Cyclic Response Prediction for Braced Steel Frames", J. of Structural Div., ASCE, Vol. 106, ST7, 1980, pp. 1401-1416.

Popov, E.P. and Petersson, H., "Cyclic Metal Plasticity: Experiments and Theory", J. Eng. Mech., ASCE, EM6, 1978, pp. 1371-1388.

Procter, A.N., "Full Tests Facilitate Derivation of Reliable Design Methods", Consulting Engineer, London, Vol. 31, August, 1967, pp. 54-60.

Roderick, J.W. and Rogers, D.F., "Load Carrying Capacity of Simple Composite Columns", J. of Structural Div., ASCE, Vol. 95, ST2, February, 1969, pp. 209-228.

Roeder, C.W., "Bond Stress of Embedded Steel Shapes in Concrete", Composite and Mixed Construction, Proc. of the US/Japan Joint Seminar, Seattle, Washington, ASCE, 1984, pp. 227-240.

Roik, K. and Bergmann, R., DIN 18806 Part 1. In Introductory Document, Stability of Metal Structures, A World View, Chapter 12, Composite members, Structural Stability Research Council, Bethlehem, Pennsylvania, USA, 1989, pp.12/38-12/44.

Roik, K. and Bergmann, R., "Composite Beam-Columns, Design and Examples for Construction", In Composite and Mixed Construction, Proc. US-Japan Joint Seminar, ASCE, Seattle, University of Washington, 1984, pp. 267-278.

Roik, K., Bergmann, R. and Mangerig, I., "The German Design Method for Composite Columns with regard to Creep and Shrinkage of Concrete", Composite Construction in Steel and Concrete, Proc. of Eng. Foundation Conf., ASCE, Henniker, New Hampshire, 1987, pp. 561-565.

Salmon, C.G. and Johnson, J.E., "Steel Structures, Design and Behaviour", Harper and Row Publishers, Second Edition, 1980.

Schleich, J.B., "Fire Safety, Design of Composite Columns", Report presented at the Int. Conf. on Fire Safe Steel Construction: Practical Design, Luxembourg, 1984.

Schleich, J.B., Lahoda, E. and Lickes, J.P., "A New Technology in Fireproof Steel Construction", Int. Seminar, Economic Commission for Europe, United Nations, Italy, 1982.

Schleich, J.B., "Fire Eng. Design of Steel Structures", Steel Construction Today, No. 2, 1988, pp. 39-52.

Sharples, B.P.H., "The Structural Behaviour of Composite Columns", PhD thesis, University of Cambridge, England, 1970.

Shing P.B., Mahin S.A. and Dermitzakis, S.N., "Evaluation of On-line Computer Control Methods for Seismic Performance Testing", Proc. of the Eighth World Conf. on Earthquake Eng., San Francisco, California, 1984, Vol. 6, pp. 135-142.

Shing, P. B. and Mahin, S. A., "Rate-of-Loading Effects on Pseudodynamic Tests", J. of Structural Eng., ASCE, 1988, Vol. 114, No. 11, pp. 2403-2420.

Shing, P.B. and Mahin, S. A., "Experimental Error Propagation in Pseudodynamic Testing", Report No. UCB/EERC-83/12, Earthquake Eng. Research Center, College of Eng., University of California, Berkeley, California, June, 1983.

Shing, P.B. and Mahin, S. A., "Pseudodynamic Test Method for Seismic Performance Evaluation: Theory and Implementation", Report No. UCB/EERC-84/01, Earthquake Eng. Research Center, College of Eng., University of California, Berkeley, California, January, 1984.

Shirai, N., Kanda, M., Sato, T., Ishimuru, S., Adachi, H. and Nakanishi, M., "Error Propagation Properties and It's Compensation Method in Pseudo-Dynamic Testing", Proc. of the Ninth World Conf. on Earthquake Eng., Tokyo, Japan, Vol. IV, 1988, pp. 59-64.

Smith, D.G.E. and Johnson, R.P., "Commentary on the 1985 Draft of Eurocode 4, Composite Steel and Concrete Structures", Building Research Establishment Report, 1986, pp. 91-108.

Stevens, R.F., "Encased Stanchions", The Structural Engineer, Vol. 43, No.2, 1965, pp. 59-66.

Takanashi, K. and Nakashima, M., "Japanese Activities on On-line Testing", J. of Eng. Mech., ASCE, 1986, Vol. 111, EM7, pp. 1014-1032.

Takanashi, K. and Nakashima, M., "On-line Computer Test Control Method and its Application to Earthquake Response Simulation of Steel Structural Models", J. of Constructional Steel Research, Vol. 11, 1988, pp. 27-40.

Takanashi, K. and Ohi, K., "A Correlation Study in Pseudo-dynamic On-line Tests vs Shaking Table Tests", Structural Stability Research Council, Annual Session and Meeting, San Francisco, California, 1984, pp. 291-301.

Takanashi, K., "Nonlinear Earthquake Response Analysis of Structures by a Computer-Actuator On-Line System", Bull. of Earthquake Resistant Structure Research Centre, Institute of Industrial Science, University of Tokyo, No. 8, 1975.

Takanashi, K., Udagawa, K. and Tanaka, H., "Pseudo-dynamic Tests on a 2-storey Steel Frame by a Computer-Load Test Apparatus Hybrid System", Proc. of the Seventh World Conf. on Earthquake Eng., Istanbul, Turkey, 1980, Vol. 7, pp. 225-232.

Thewalt, C.R. and Mahin S.A., "Hybrid Solution Techniques for Generalized Pseudodynamic Testing", Report No. UCB/EERC-87/09, Earthquake Eng. Research Center, College of Eng., University of California, Berkeley, California, July, 1987.

Thewalt, C.R. and Mahin, S.A., "Hybrid Analysis Techniques for Seismic Performance Testing", Proc. of the Ninth World Conf. on Earthquake Eng., Tokyo, Japan, Vol.IV, 1988, pp. 29-34.

Timoshenko, S.P. and Gere, J.M., "Theory of Elastic Stability", Mc Graw Hill, Second Edition, 1963.

Tsutsumi, H. and Higashiura A., "Pseudodynamic Testing Method using the Newmark Implicit Integration Method", Proc. of the Ninth World Conf. on Earthquake Eng., Tokyo, Japan, Vol. IV, 1988, pp. 41-46.

Virdi, K.S. and Dowling, P.J., "A Unified Design Method for Composite Columns", IABSE Memoirs, Vol. 36-II, 1976a.

Virdi, K.S. and Dowling, P.J., "The Ultimate Strength of Biaxially Restrained Columns", Proc. ICE, Vol. 61, Part 2, 1976b, pp. 41-58.

Virdi, K.S. and Dowling, P.J., "The Ultimate Strength of Composite Columns in Biaxial Bending", Proc. ICE, Vol. 55, Part 2, 1973, pp. 251-272.

Wakabayashi, M. and Minami, K., "Experimental Study of the Hysteretic Characteristics of Composite Beam-Columns", US-Japan Seminar on Composite Structures, Gihodo Shuppan, Japan, 1980, pp. 197-211.

Wakabayashi, M. and Minami, K., "Experimental Studies on Hysteretic Characteristics of Steel Reinforced Concrete Columns and Frames", Int. Symposium on Earthquake Structural Engineering, St. Louis, Missouri, August, 1976, pp. 467-480.

Wakabayashi, M. and Tsuboi, Y., Transactions of The Architectural Institute of Japan, AIJ, Part 1, No. 48, 1954, pp. 44-49.

Wakabayashi, M. and Tsuboi, Y., Transactions of The Architectural Institute of Japan, AIJ, Part 5, No. 56, 1957, pp. 245-252.

Wakabayashi, M., "A Historical Study of Research on Composite Construction in Japan", Composite Construction in Steel and Concrete, Proc. of Eng. Foundation Conf., ASCE, Henniker, New Hampshire, 1987, pp. 400-427.

Wakabayashi, M., "A New Design Method of Long Composite Beam-Columns", Second Int. Colloquium on Stability of Structures under Static and Dynamic Loads, Washington, May 1977, pp. 742-756.

Wakabayashi, M., AIJ Standards for Steel-Reinforced Concrete Structures. In Introductory Document, Stability of Metal Structures, A World View, Chapter 12, Composite members, Structural Stability Research Council, Bethlehem, Pennsylvania, USA, 1989, pp.12/15-12/26.

Wakabayashi, M., Shibata, M., Matsui, C. and Minami, K., "A Study on the Behaviour of Steel-Reinforced Concrete Columns and Frames", IABSE Symposium, Quebec, Canada, 1974, pp. 53-60.

Yamaouchi, H., Okamoto, S., Hiraishi, H. and Kominosono, T., "Feasibility Study of Pseudo-Dynamic Test Method by a Full-Scale Simple Structure", Proc. of the Eighth World Conf. on Earthquake Eng., San Francisco, California, 1984, Vol. 6, pp. 119-126.

Yamazaki, Y., Nakashima, M. and Kominosono, T., "Correlation Between Shaking Table Test and Pseudo Dynamic Test on Steel Structures", Proc. of the Eighth World Conf. on Earthquake Eng., San Francisco, California, 1984, Vol. 6, pp. 111-118.

APPENDIX A

STRAIN GAUGE RESULTS

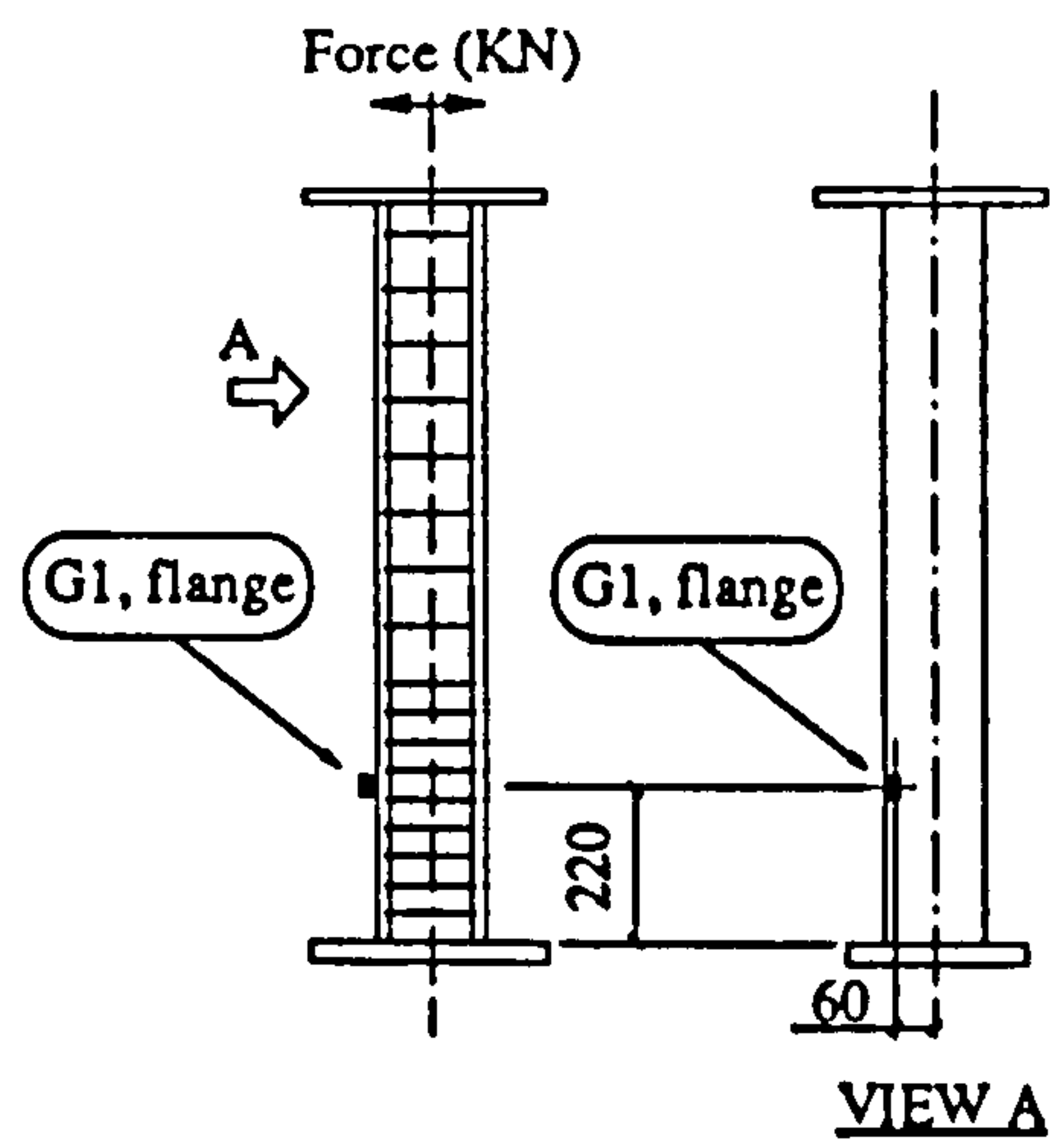
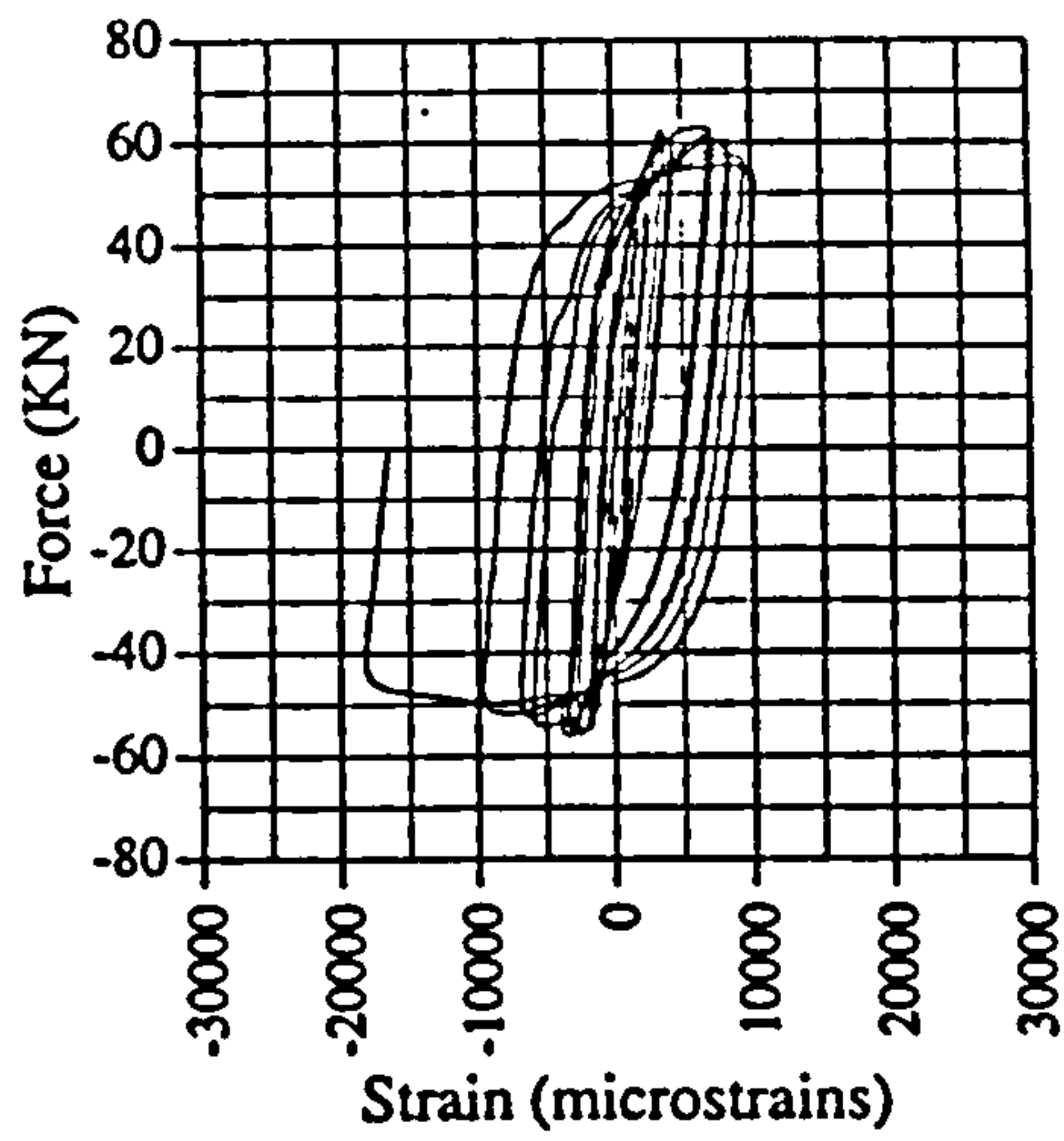


Fig. A.1 Force vs strain, EM01, G1

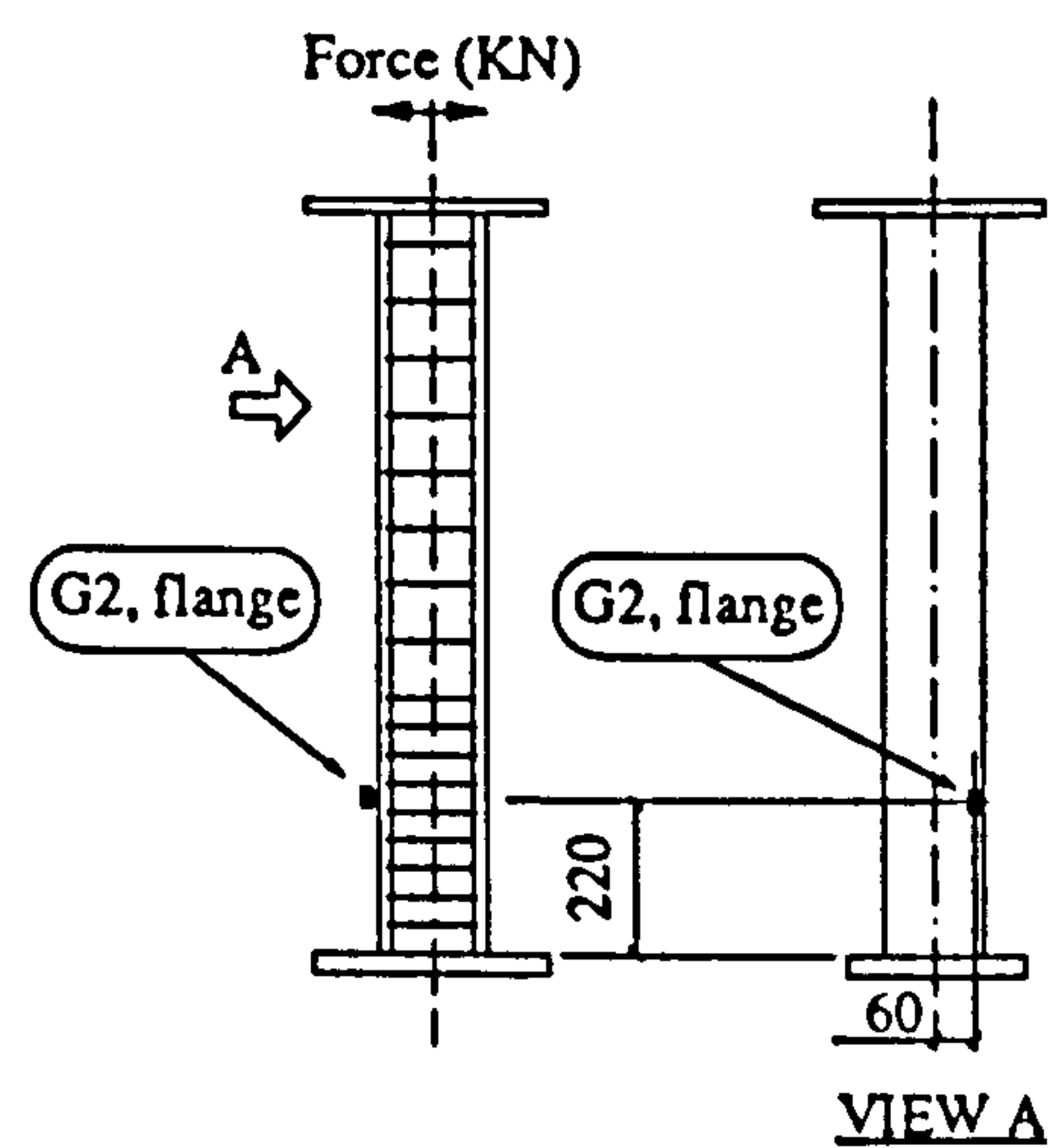
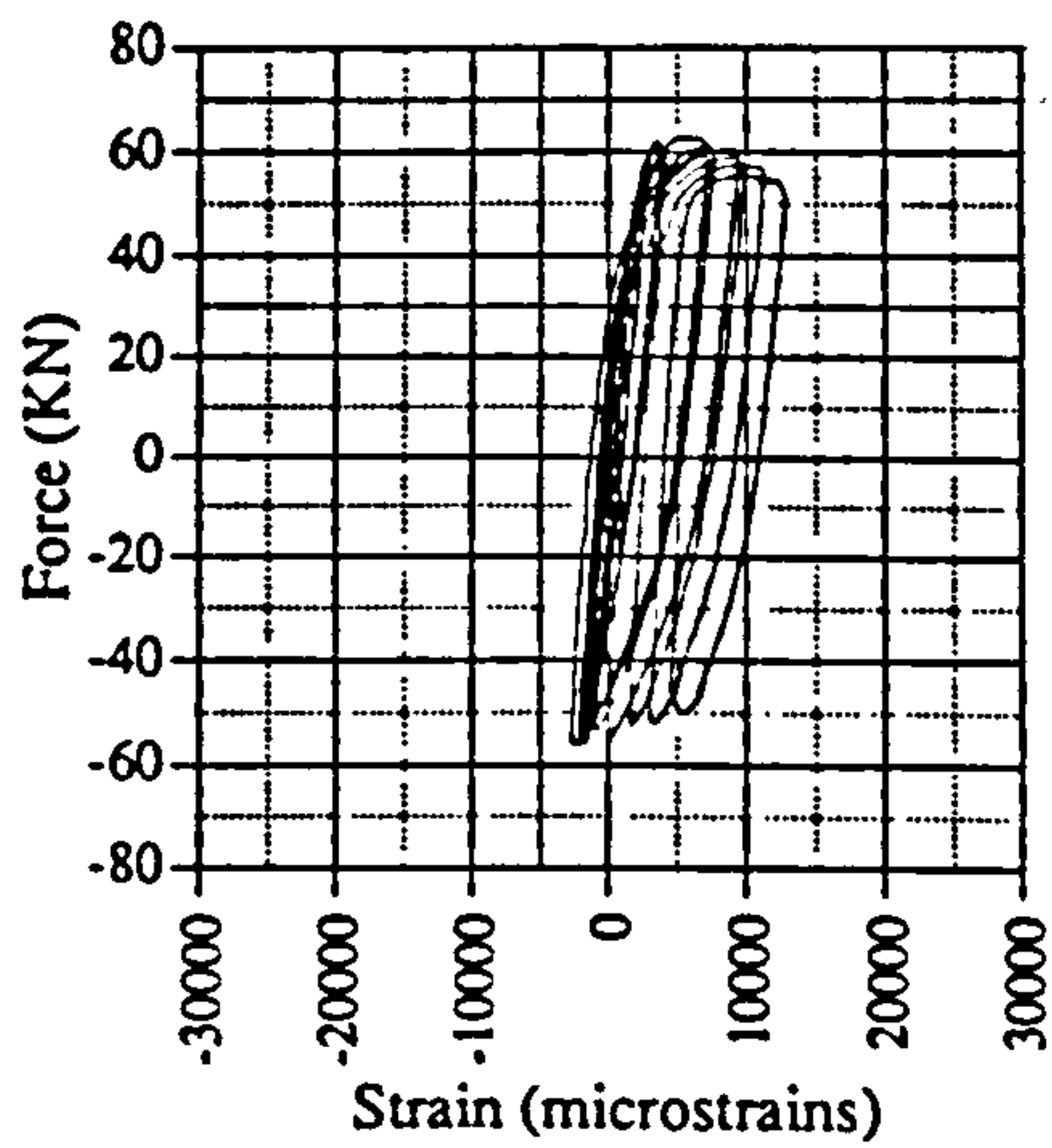


Fig. A.2 Force vs strain, EM01, G2

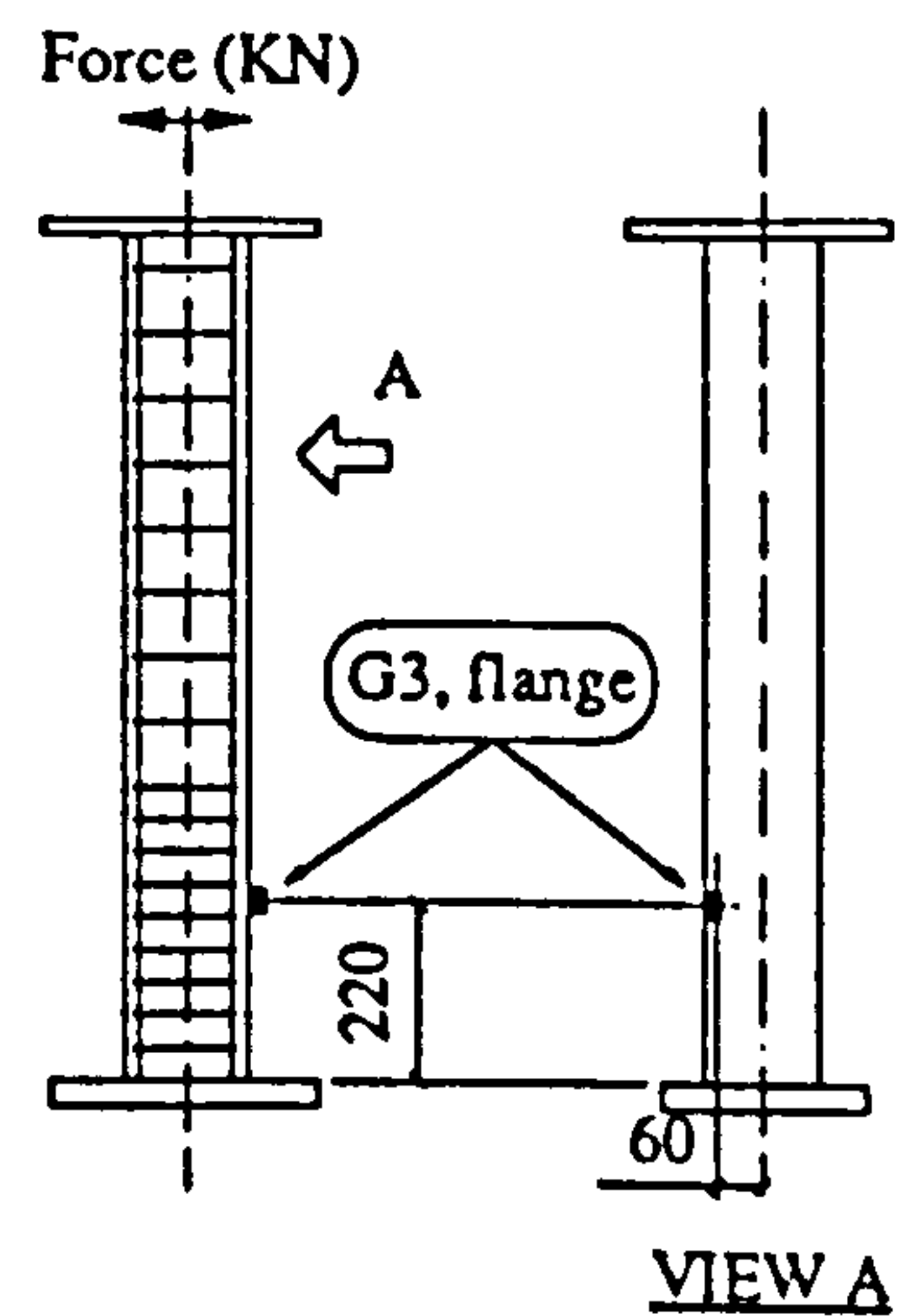
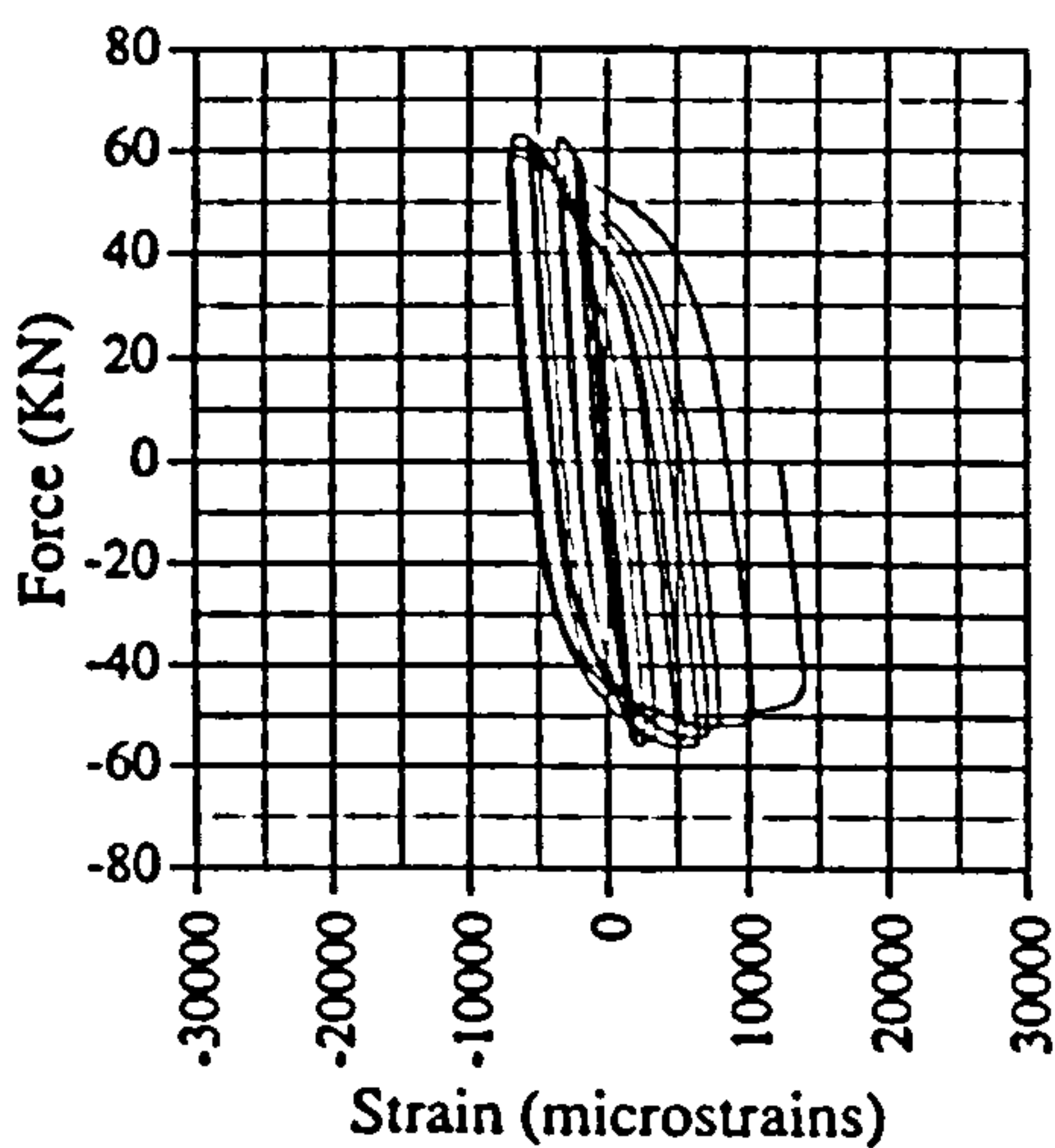


Fig. A.3 Force vs strain, EM01, G3

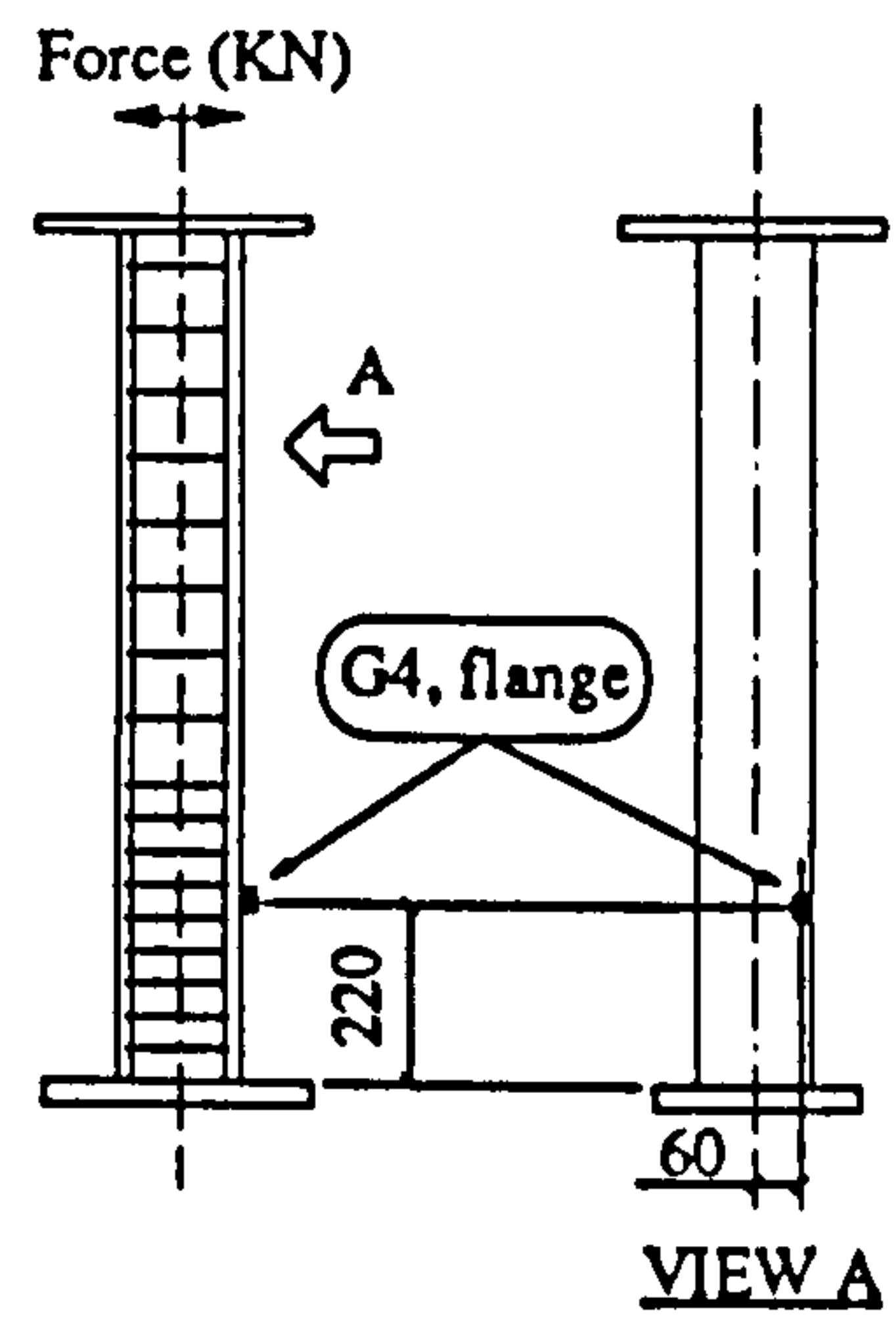
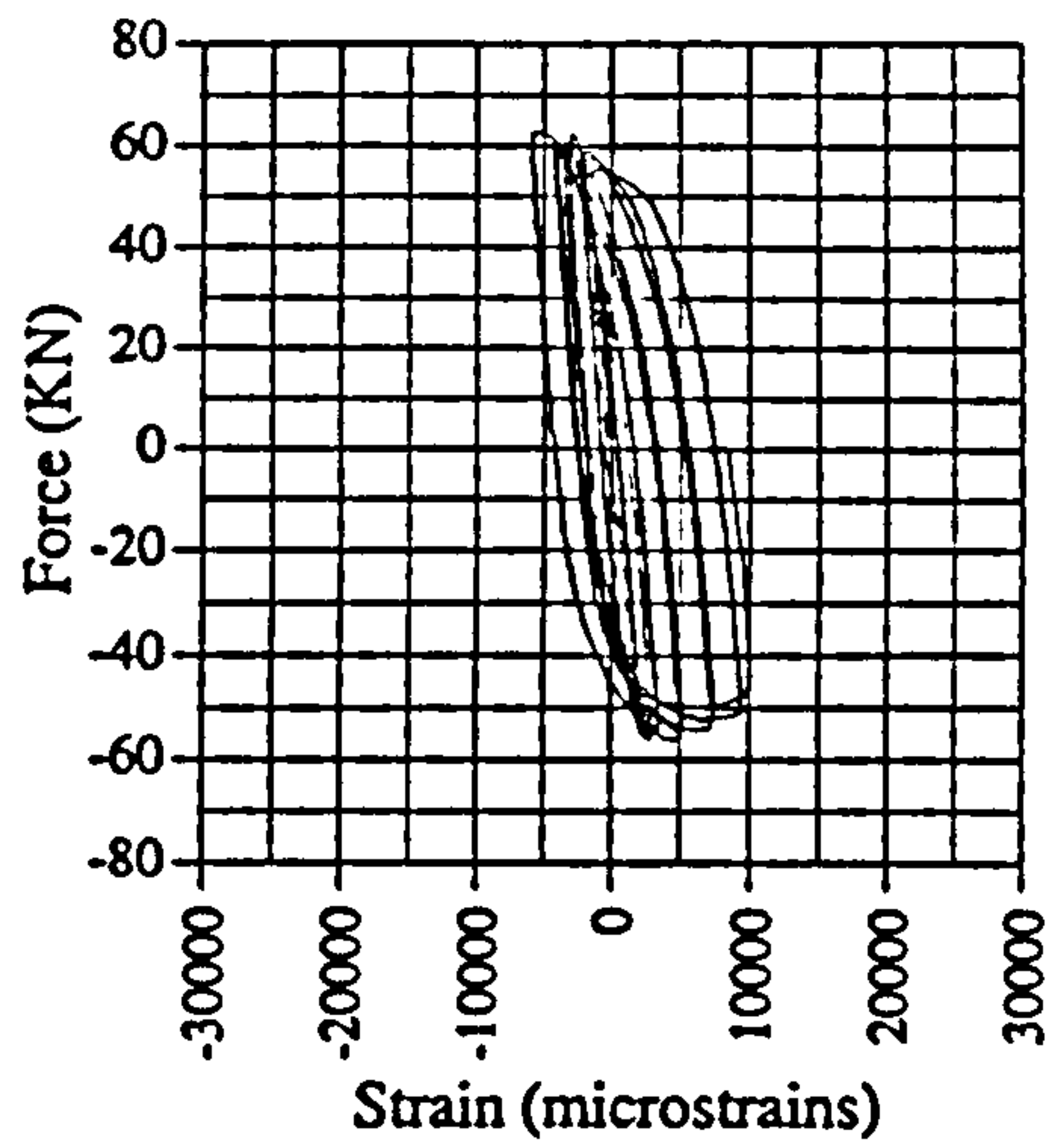


Fig. A.4 Force vs strain, EM01, G4

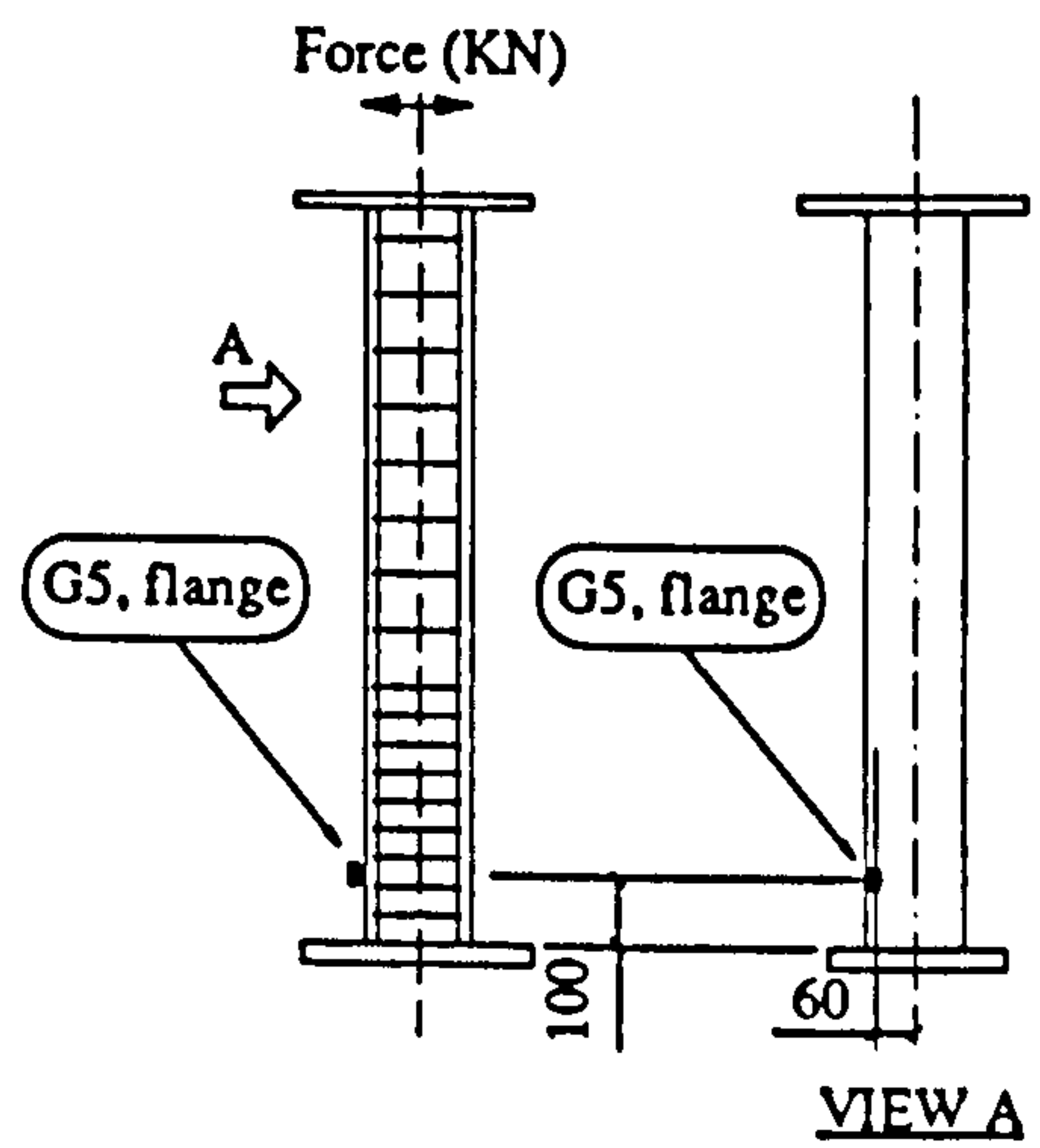
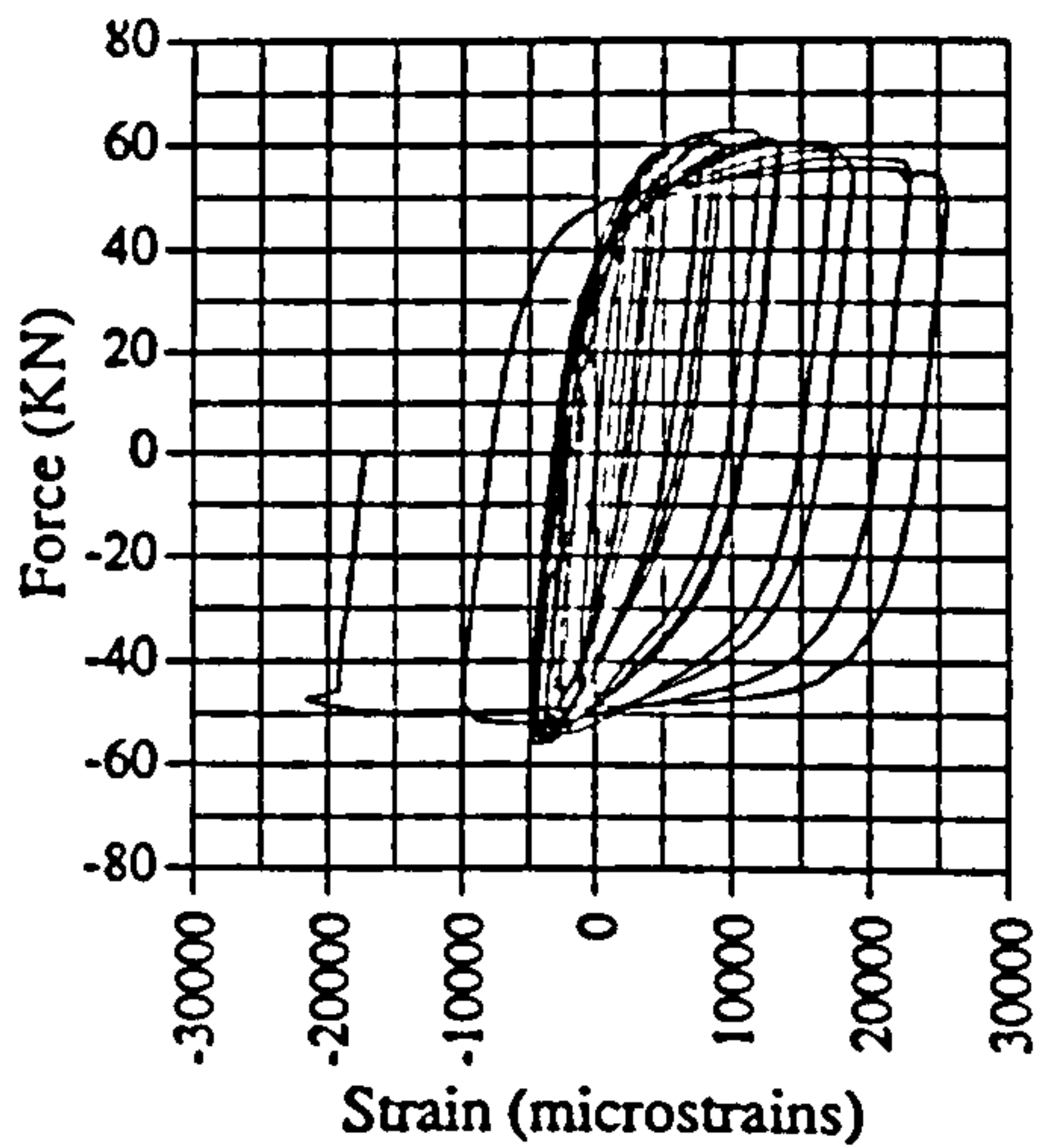


Fig. A.5 Force vs strain, EM01, G5

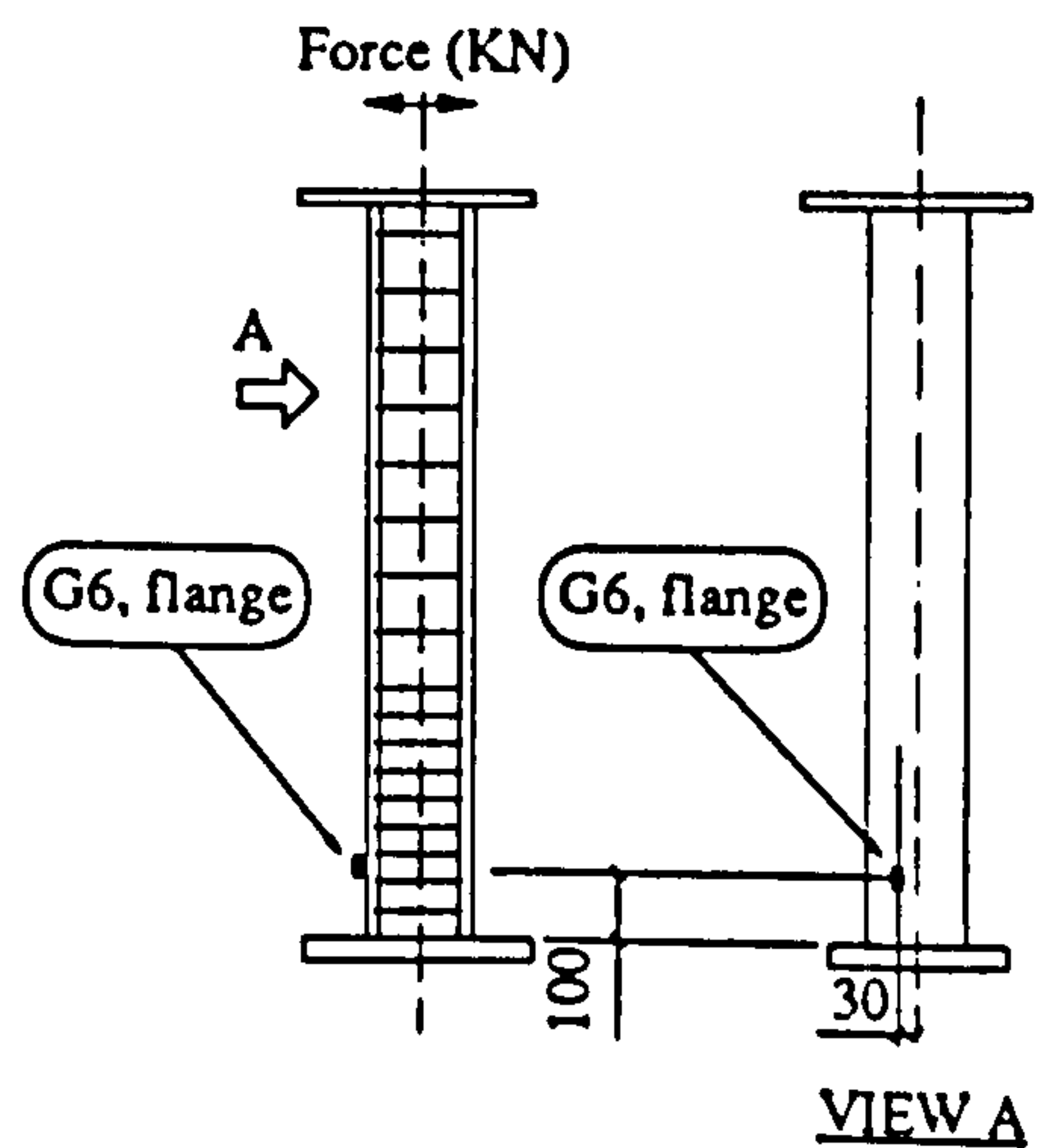
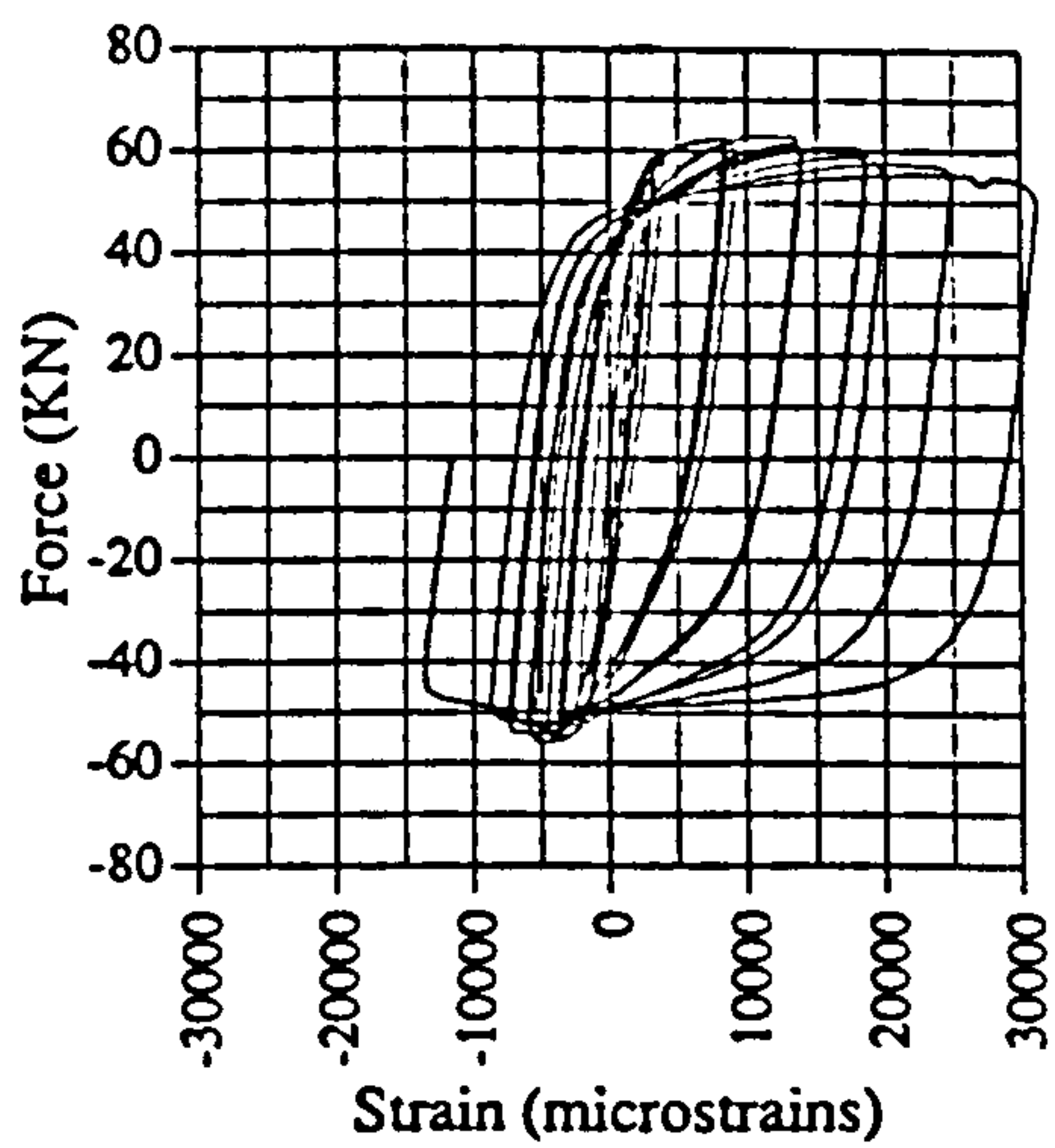
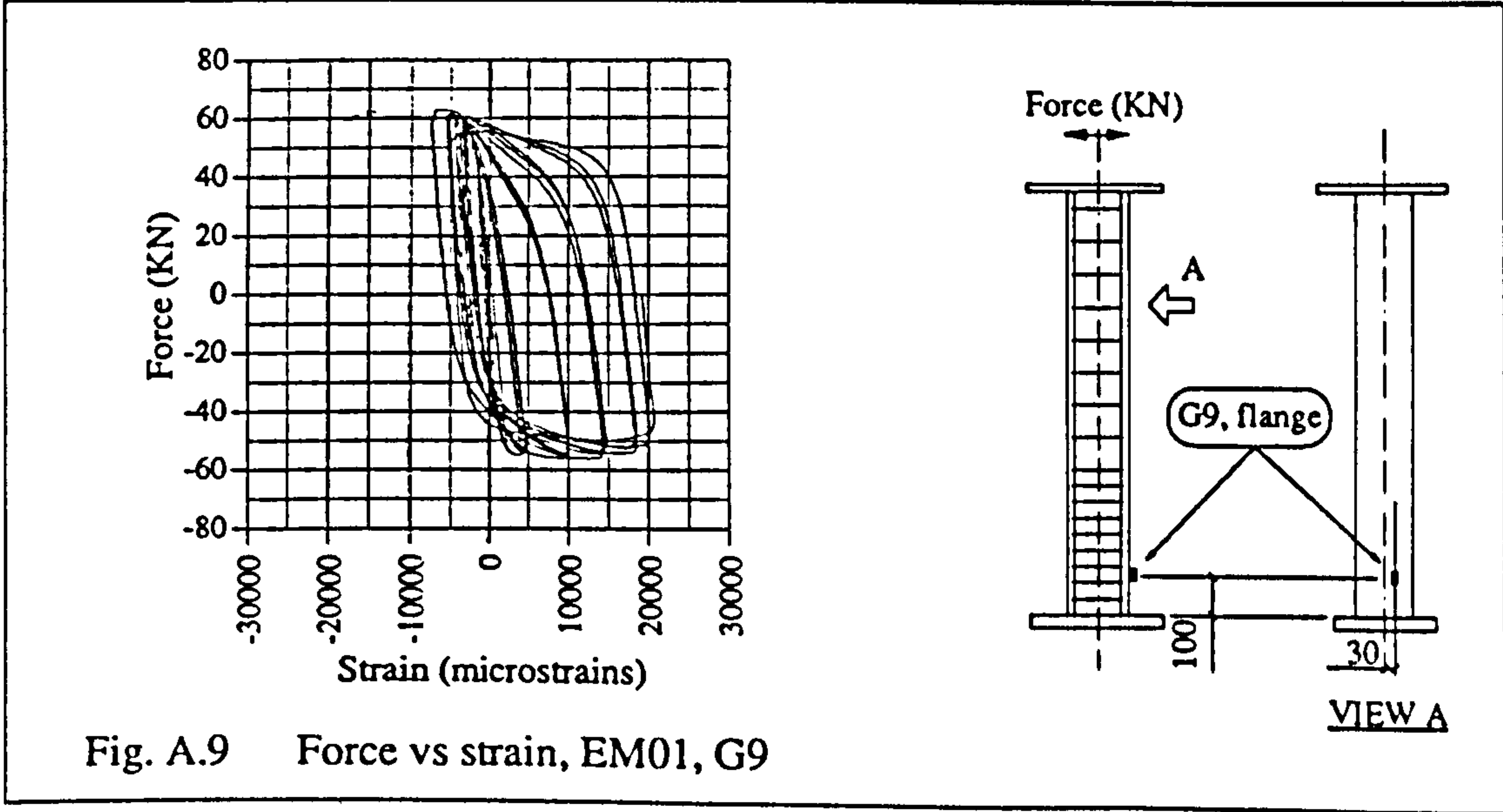
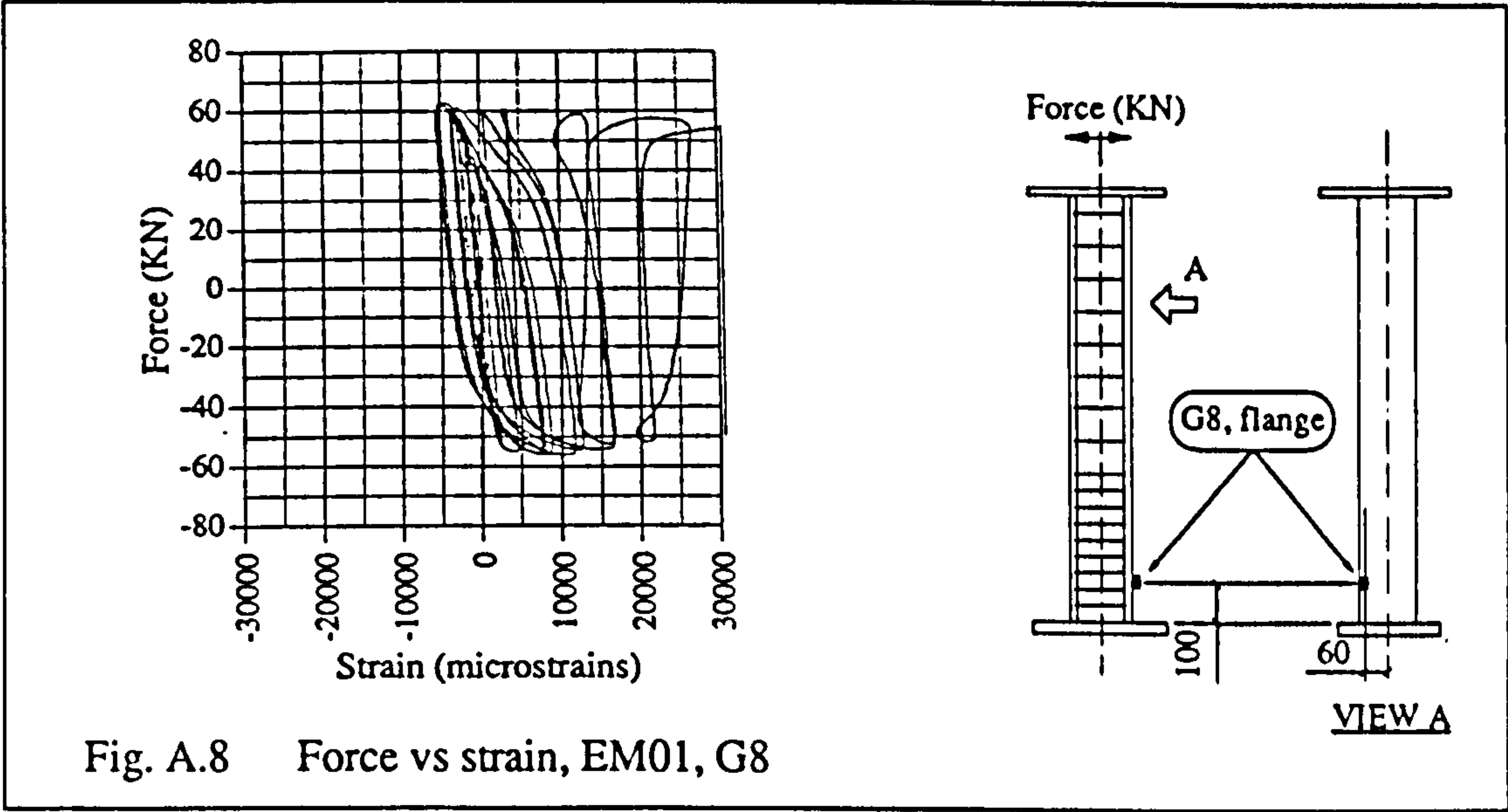
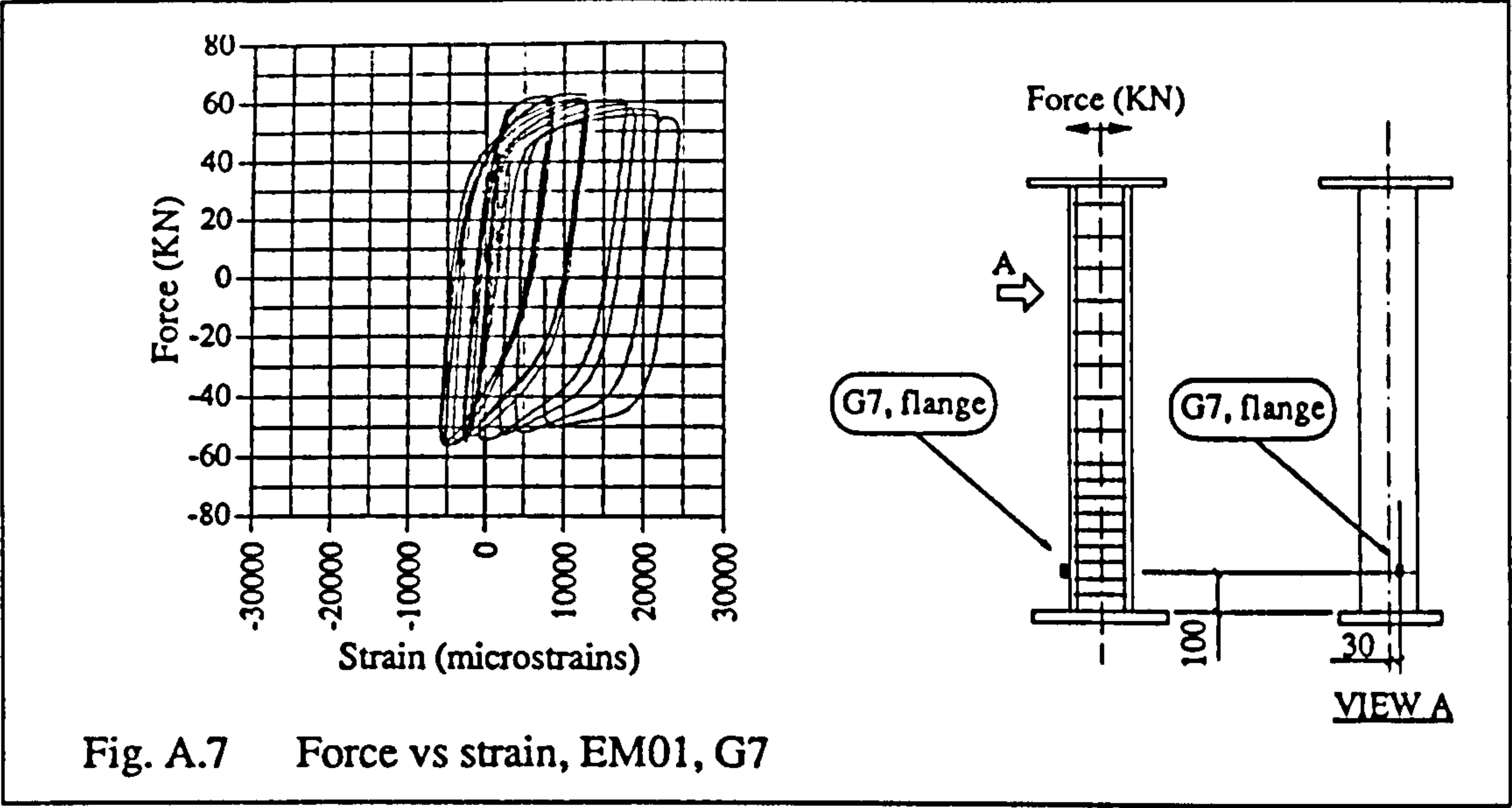


Fig. A.6 Force vs strain, EM01, G6



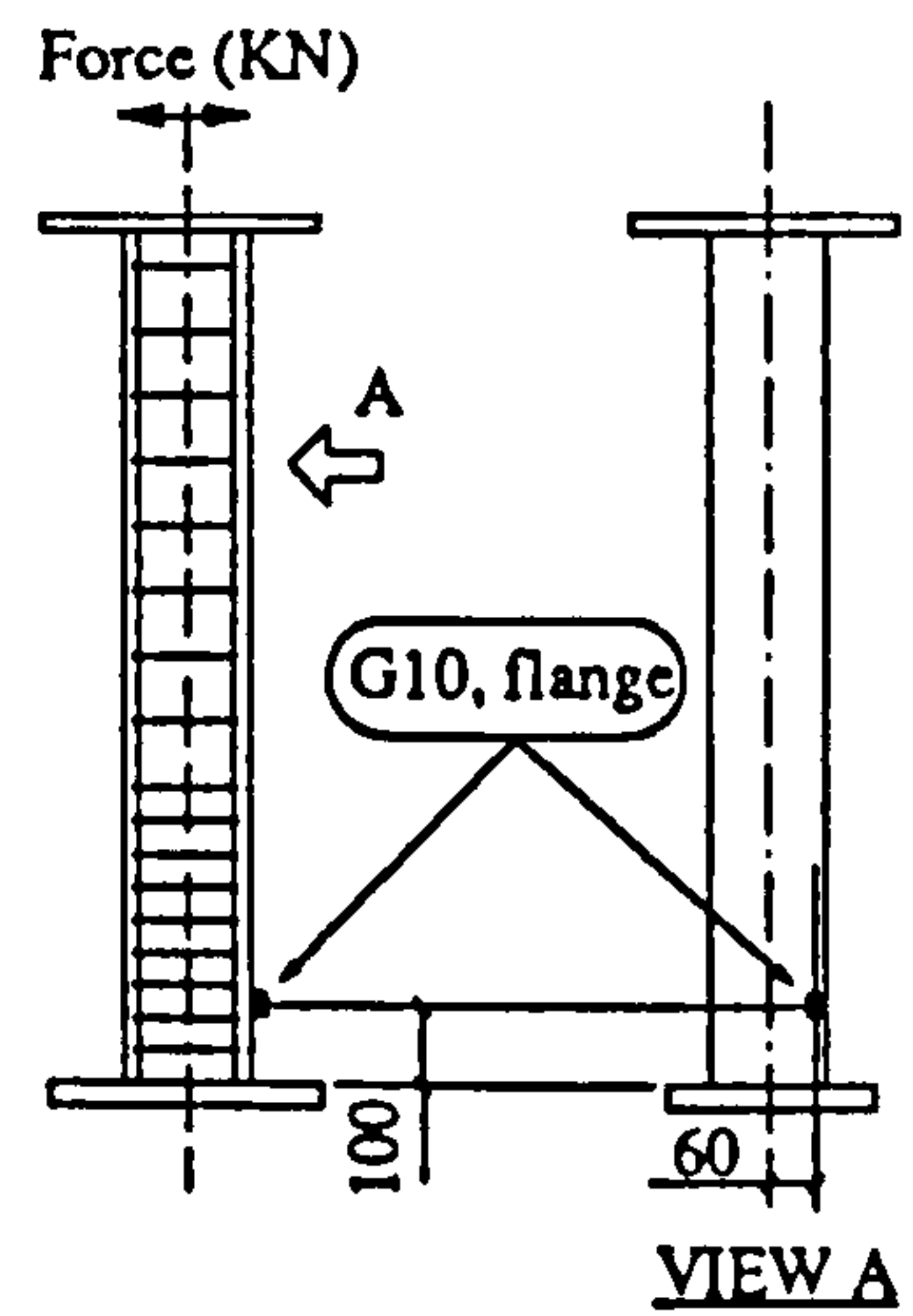
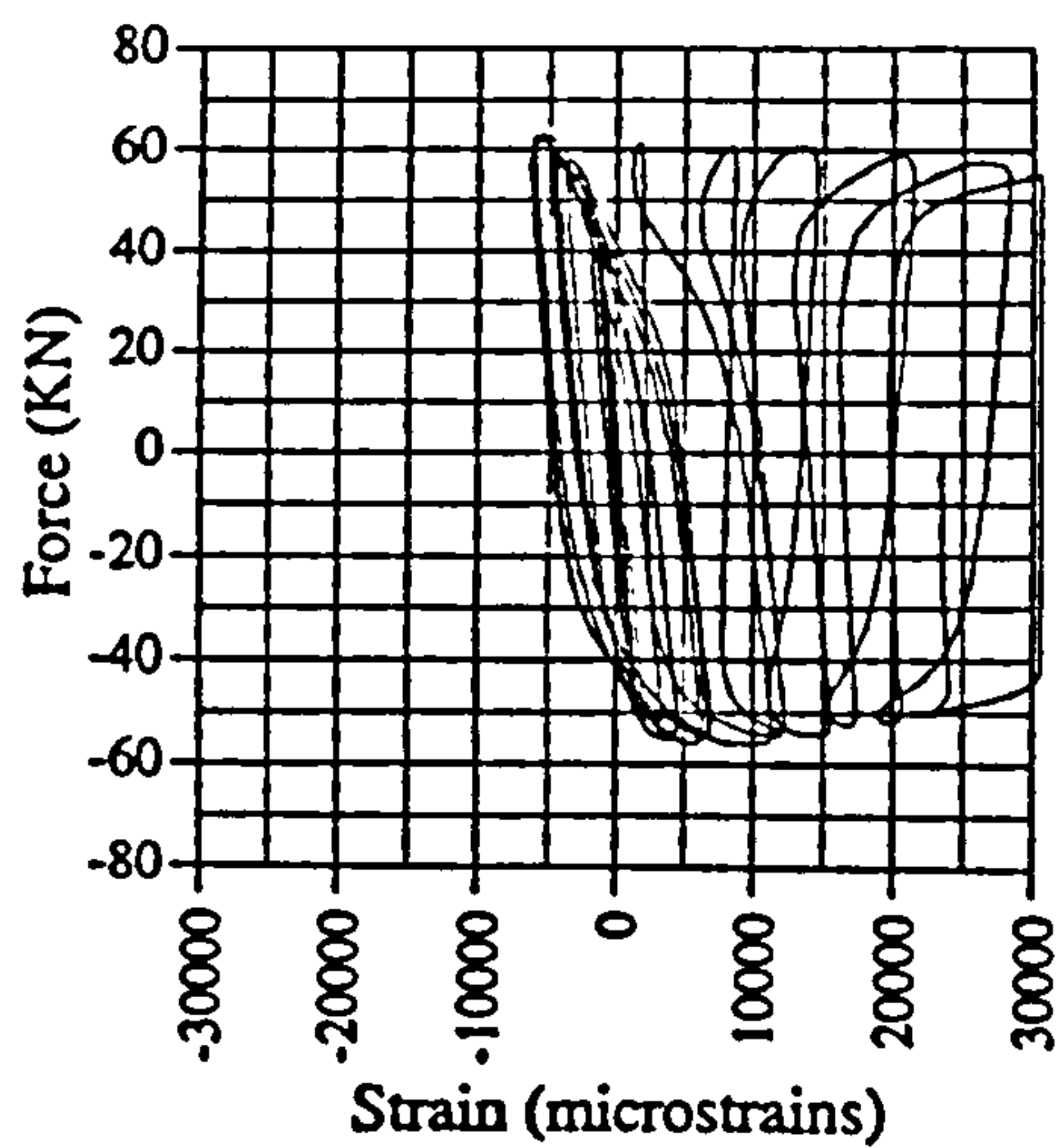


Fig. A.10 Force vs strain, EM01, G10

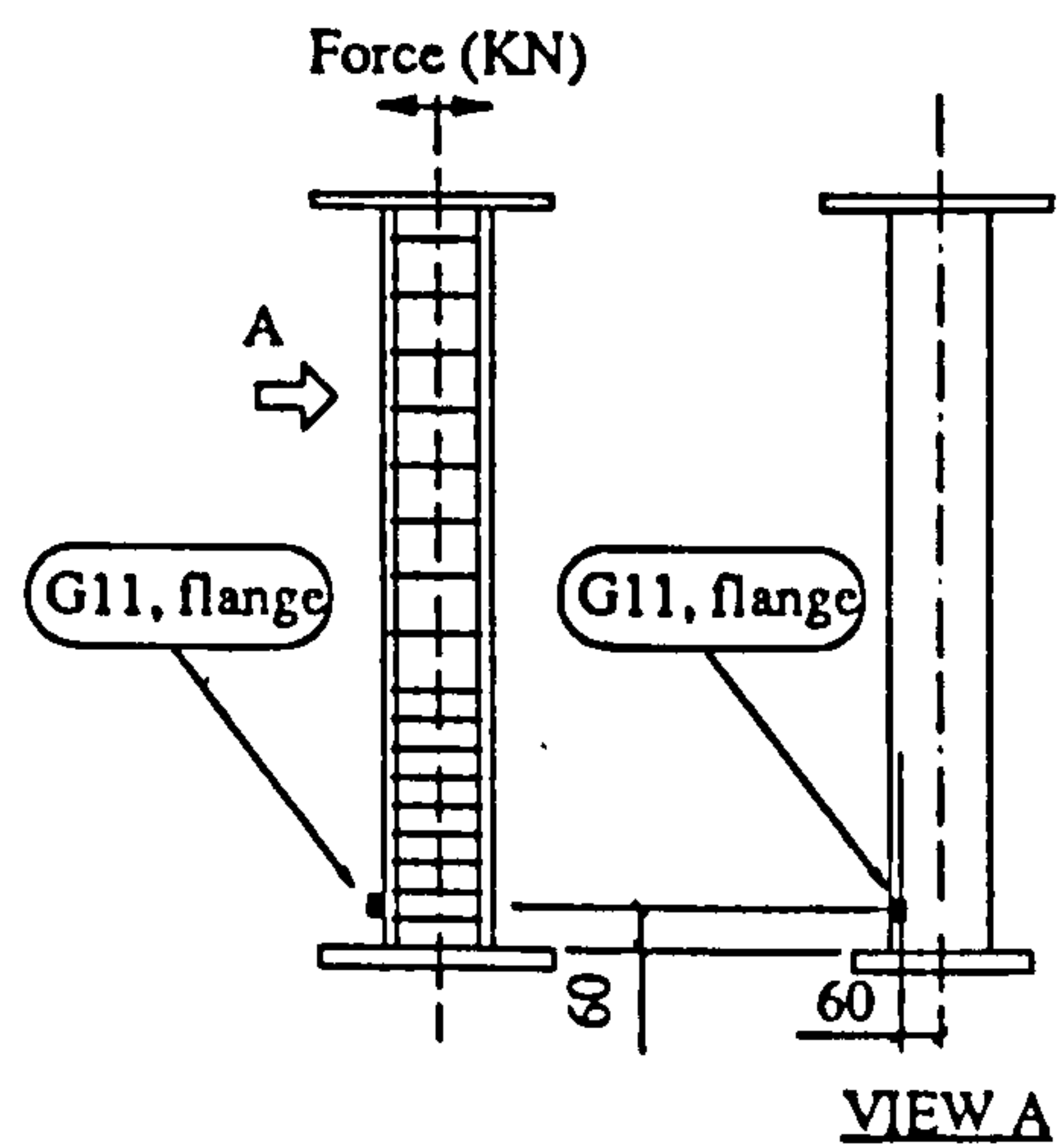
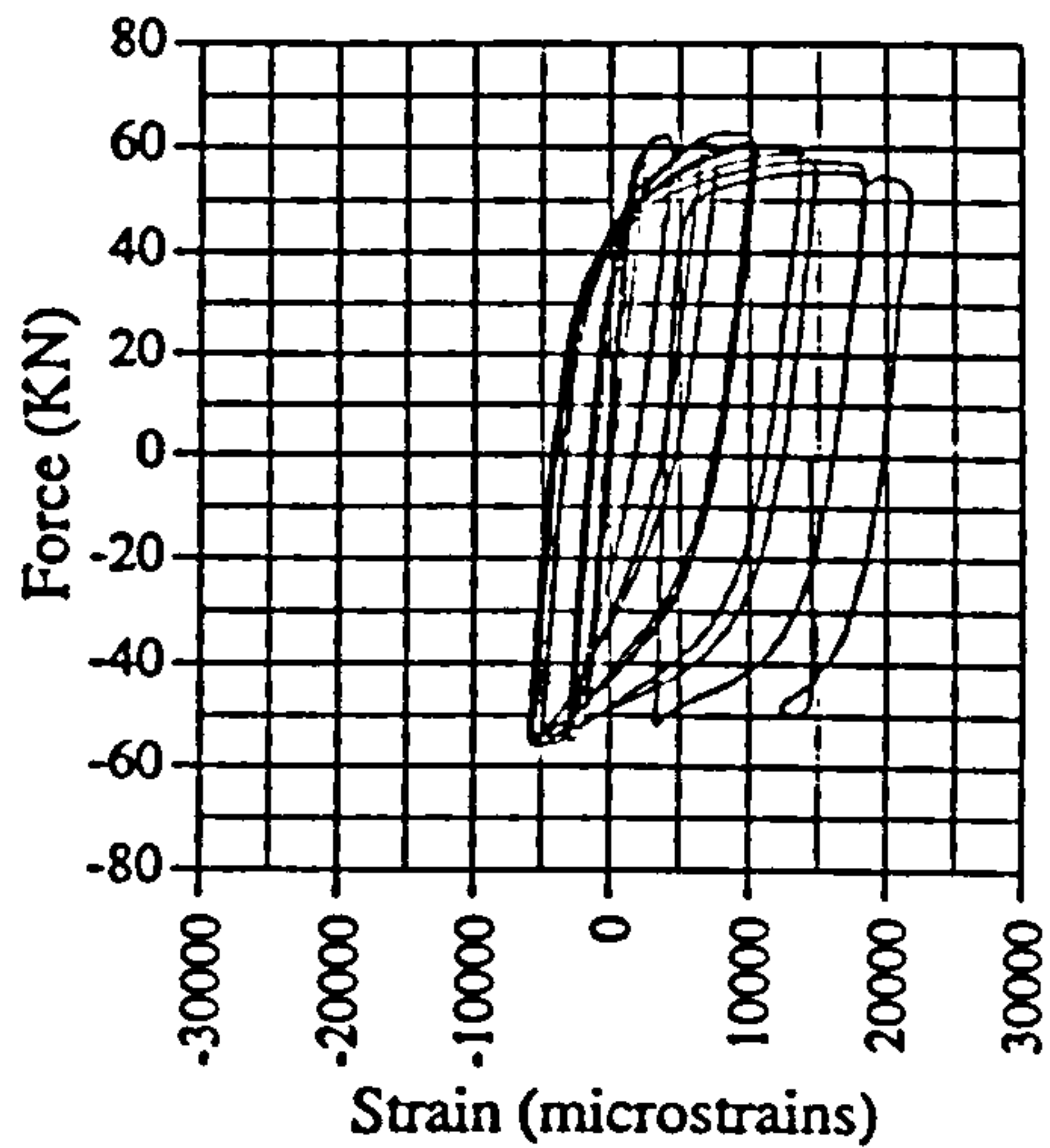


Fig. A.11 Force vs strain, EM01, G11

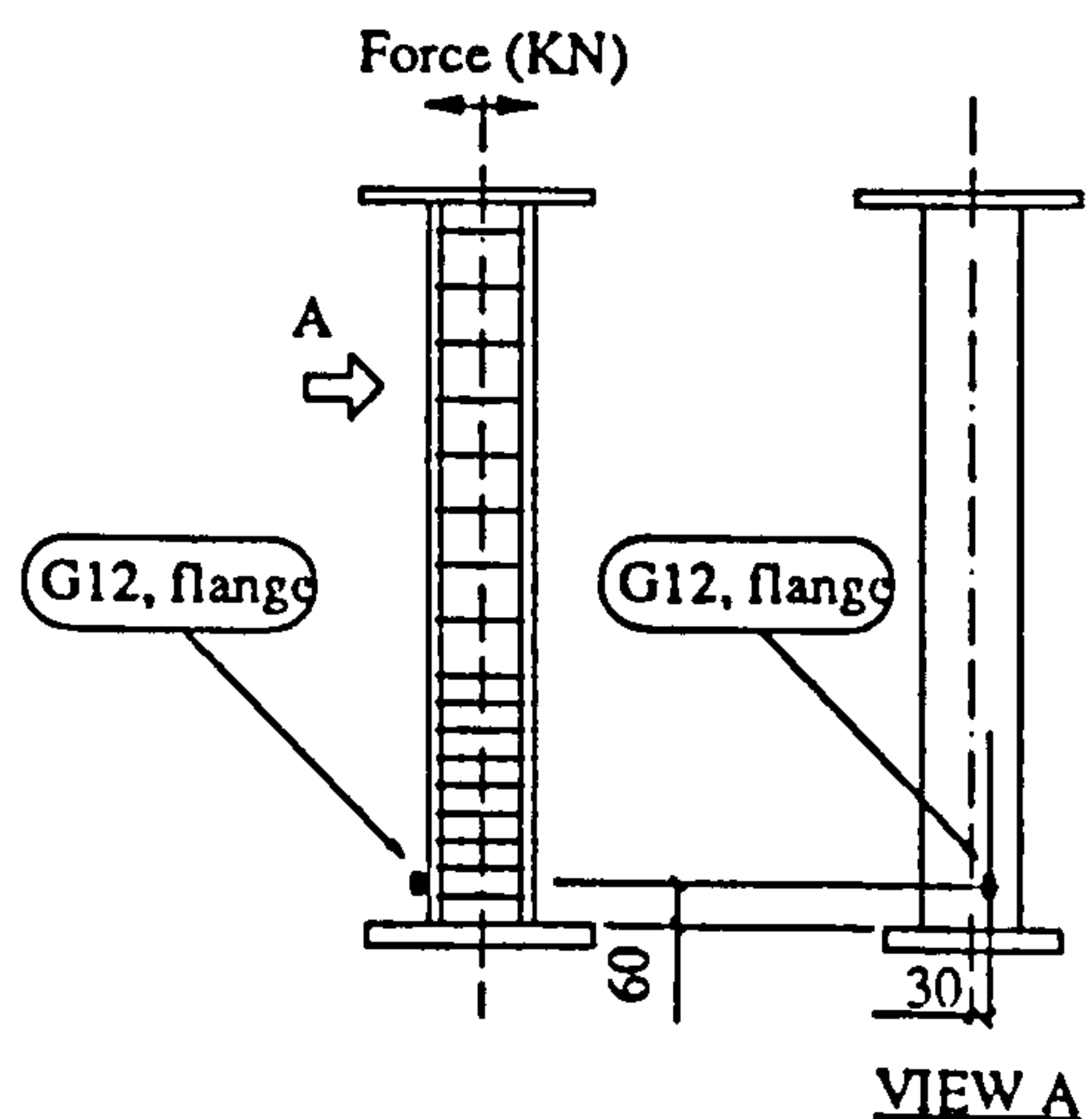
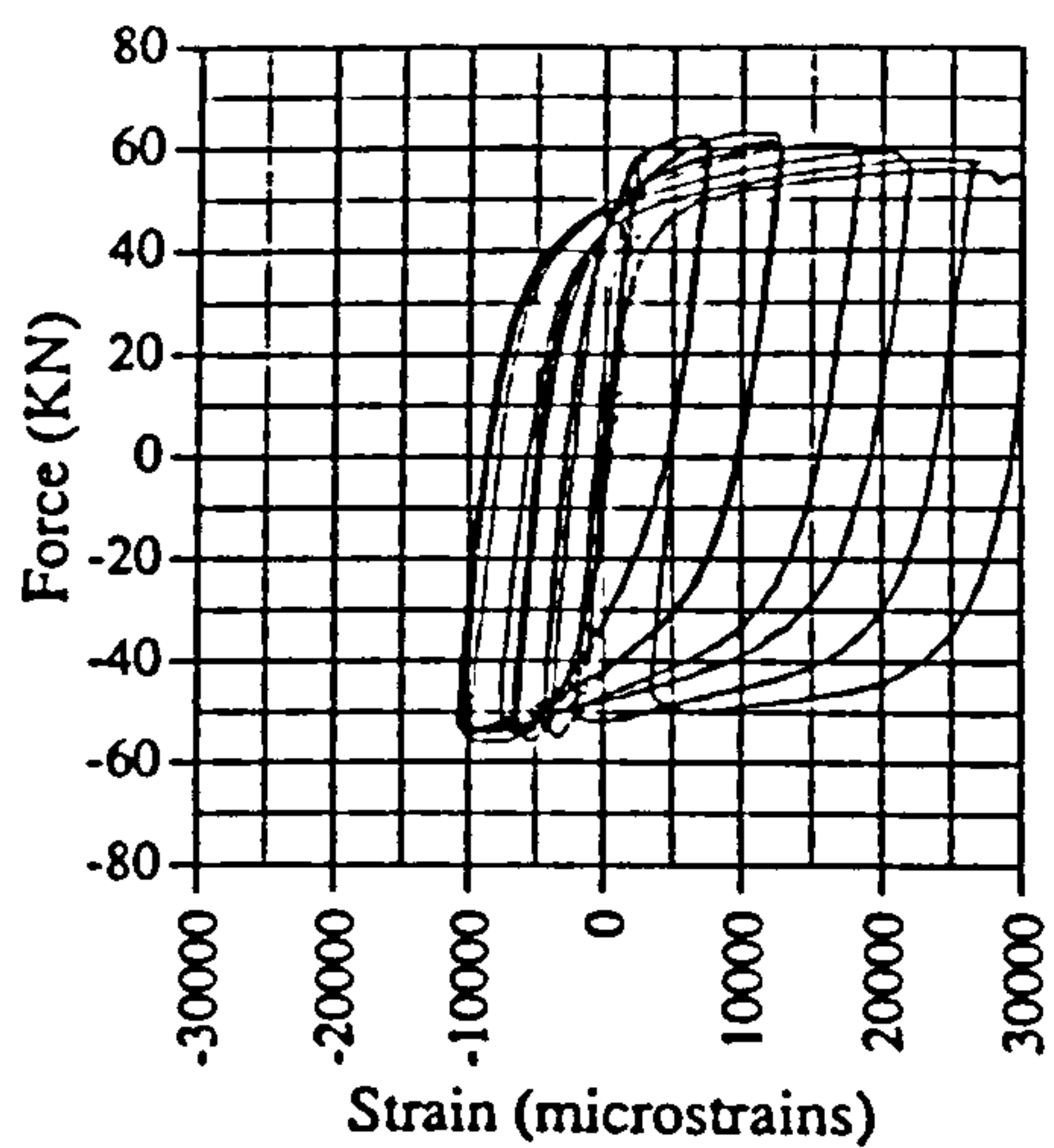
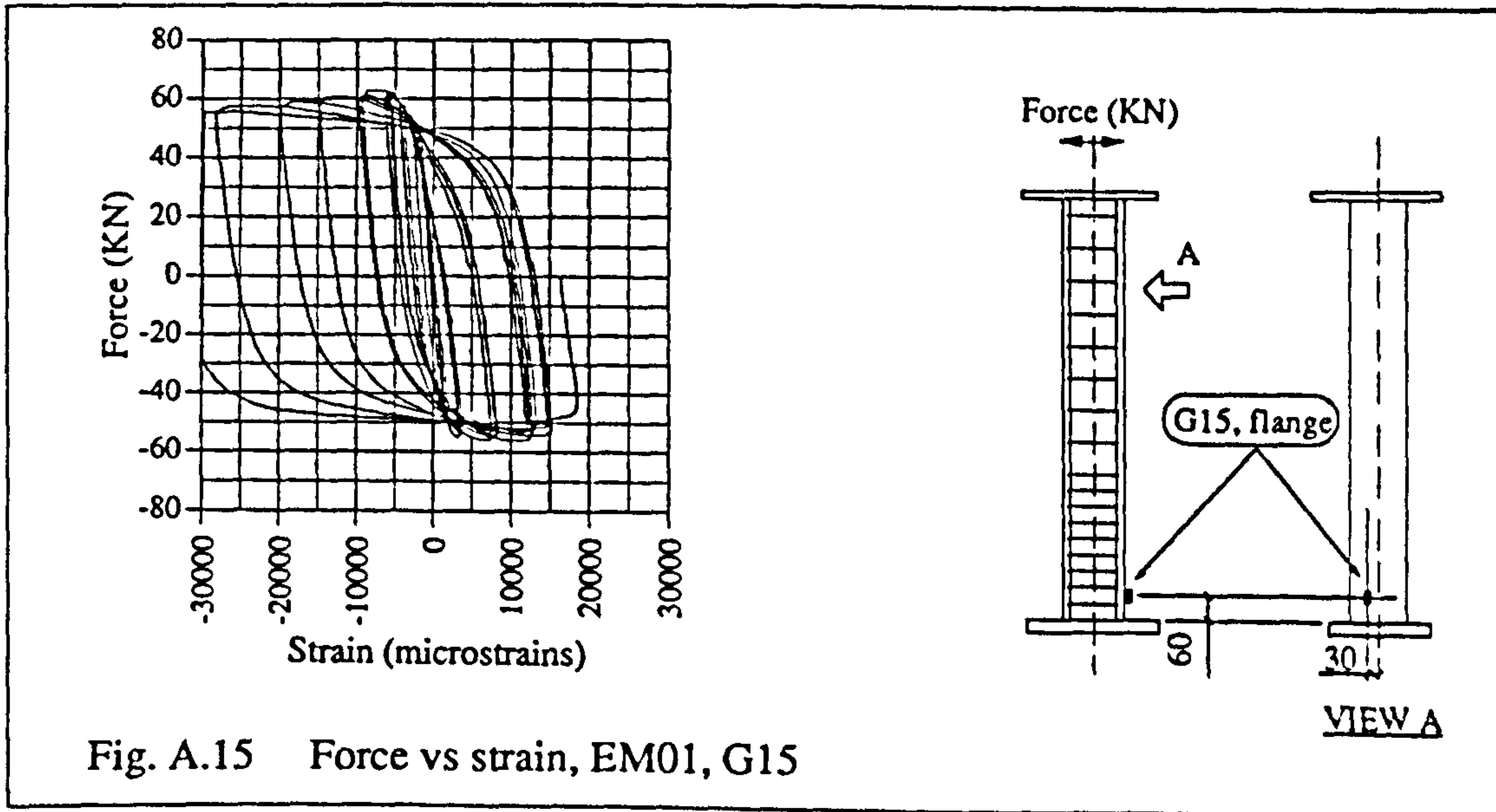
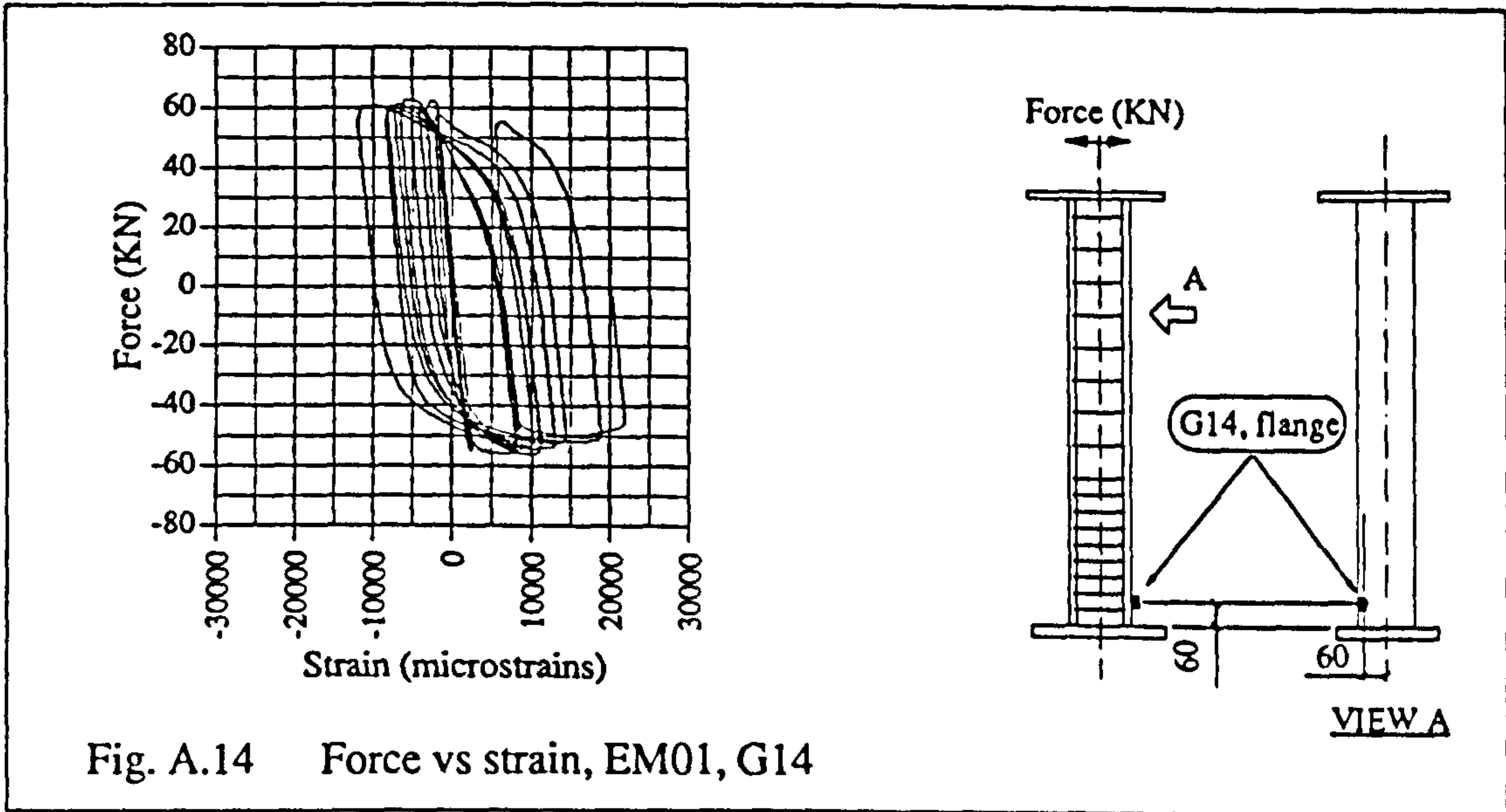
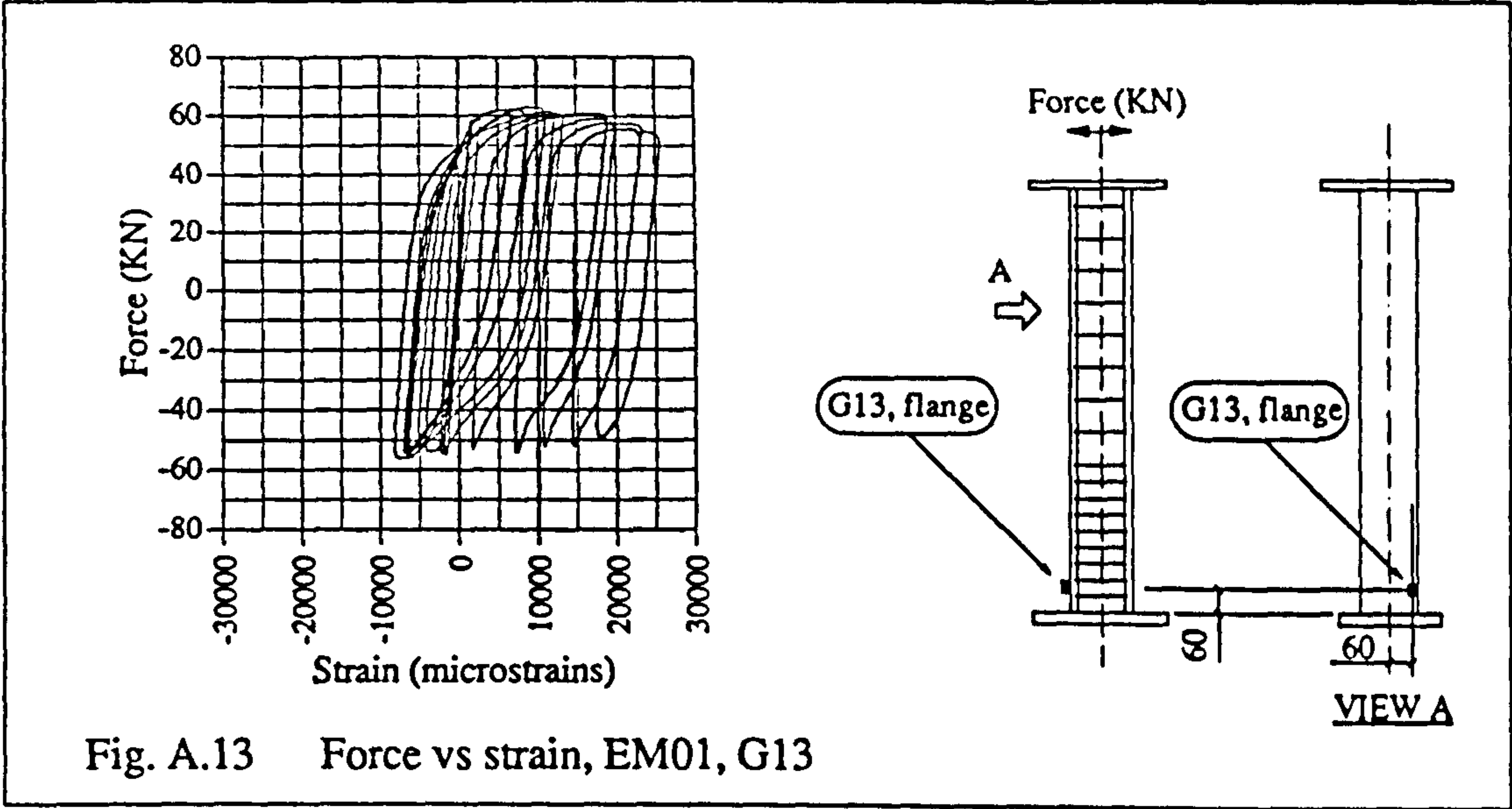


Fig. A.12 Force vs strain, EM01, G12



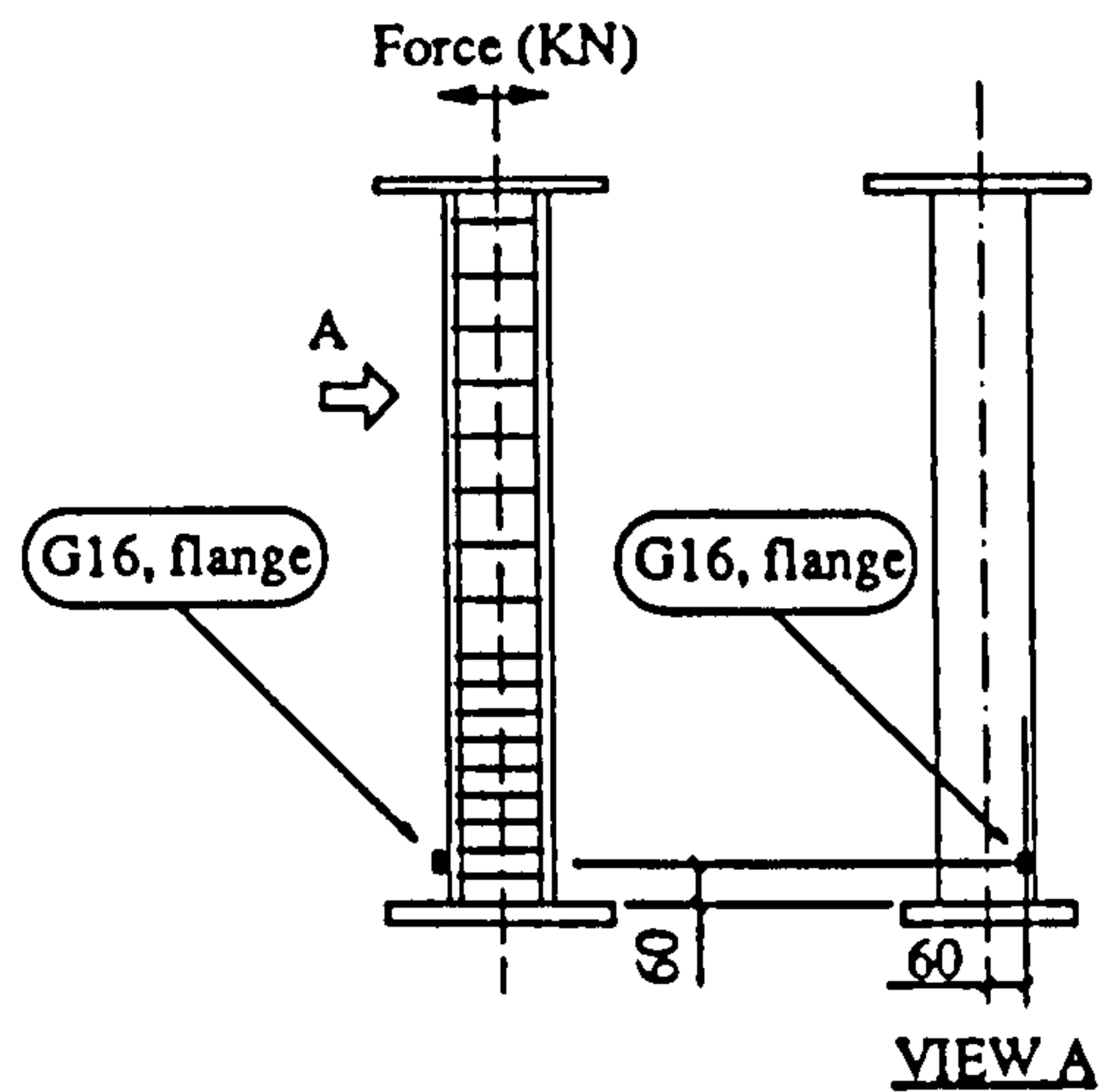
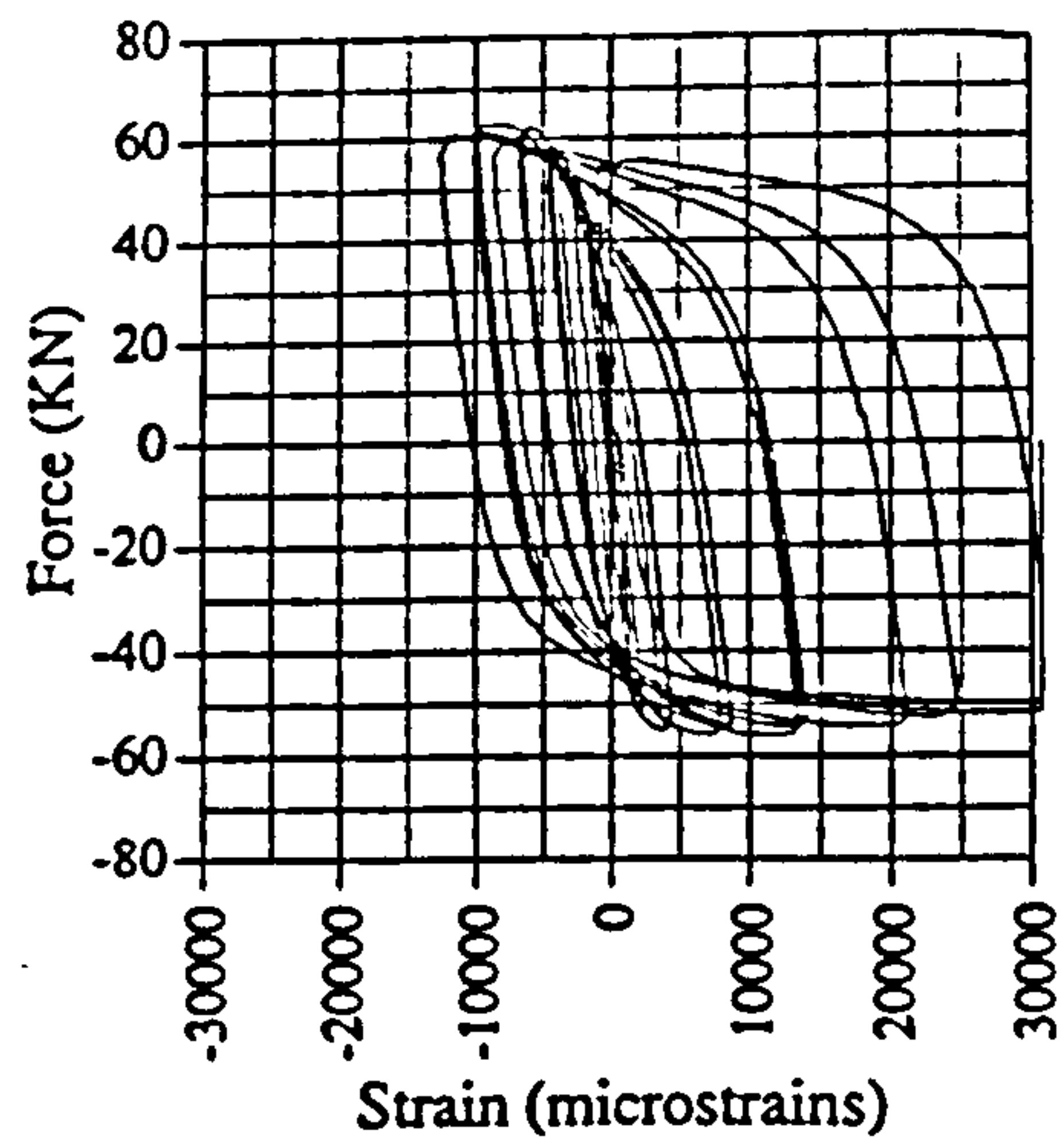


Fig. A.16 Force vs strain, EM01, G16

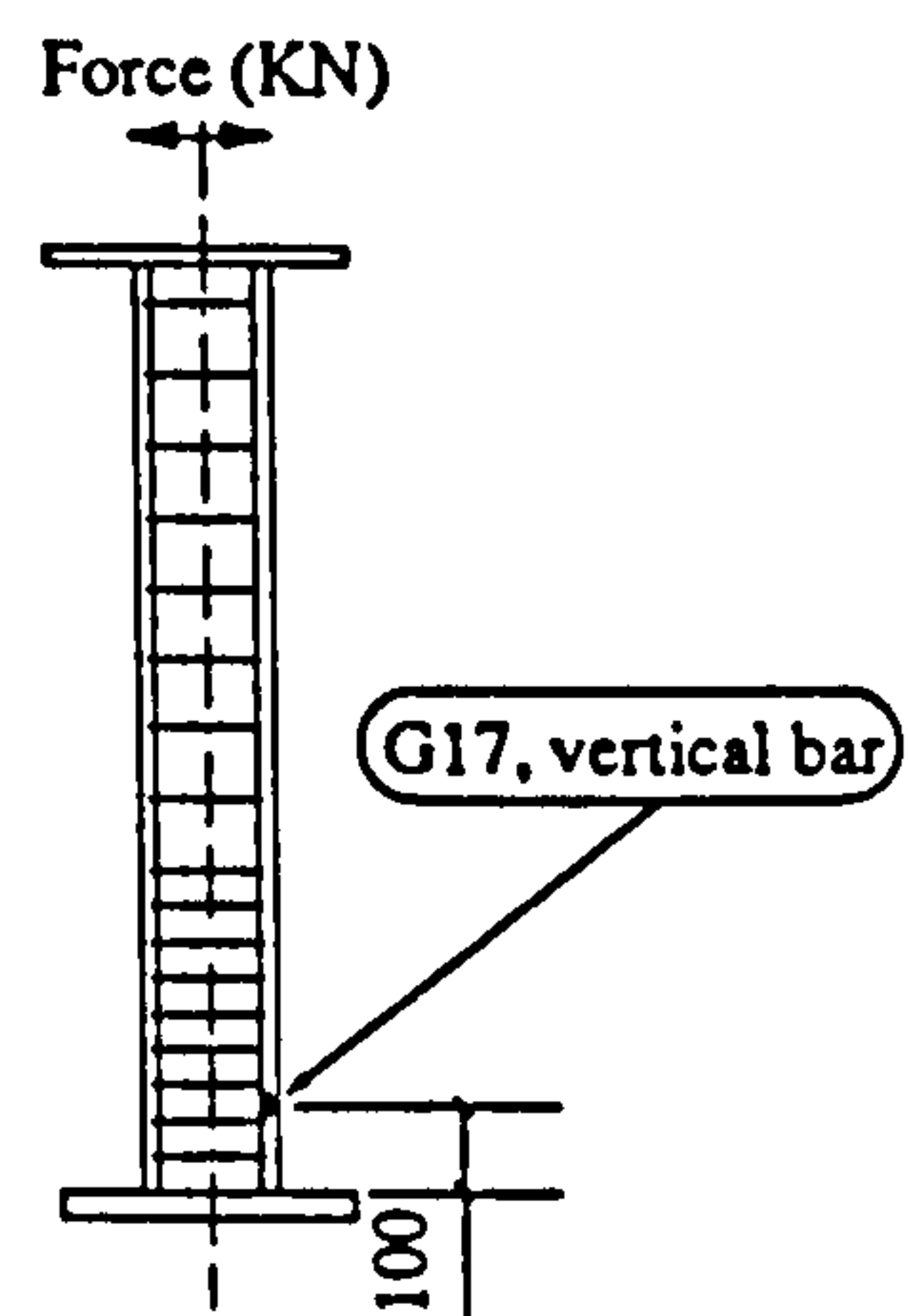
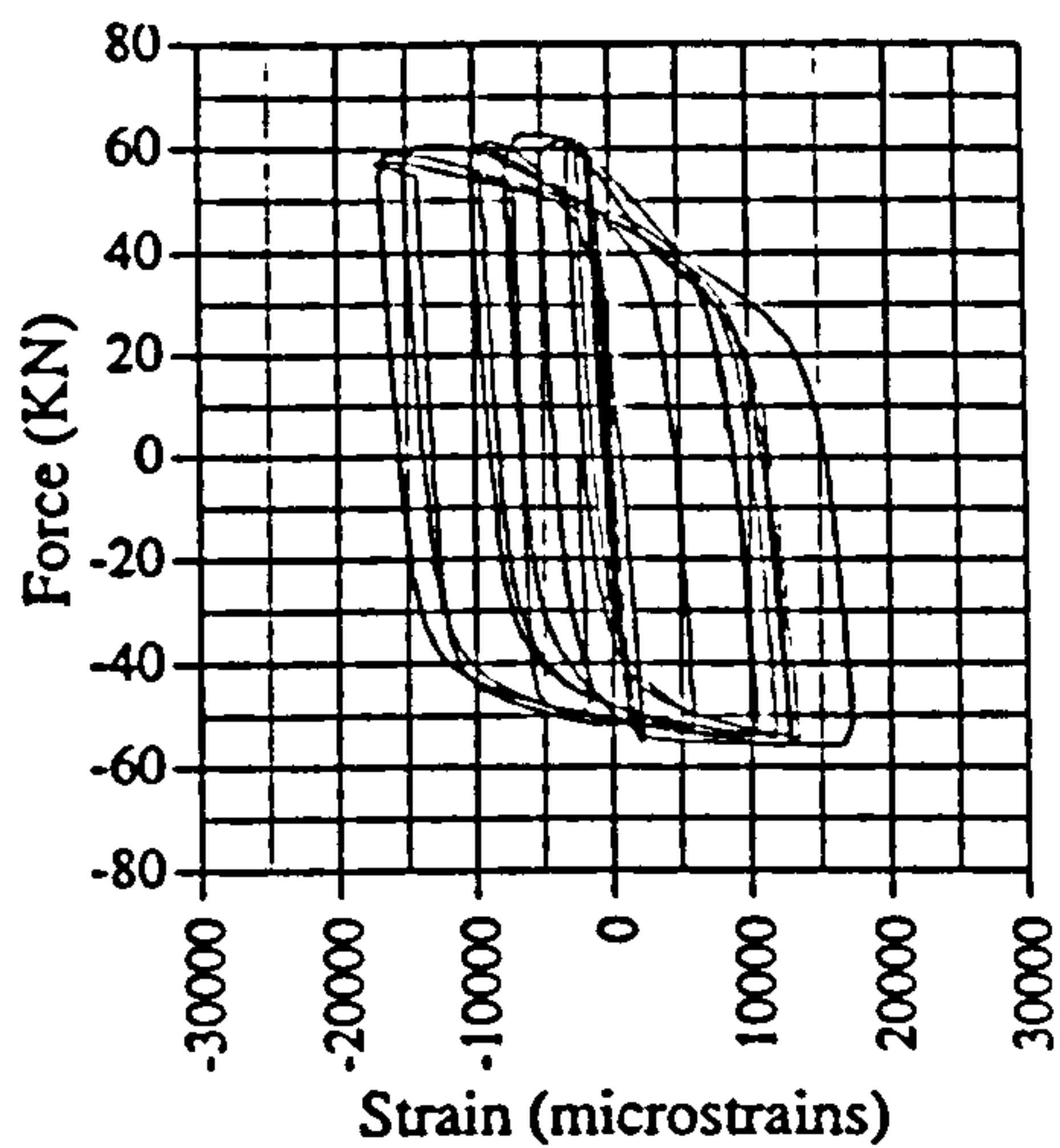


Fig. A.17 Force vs strain, EM01, G17

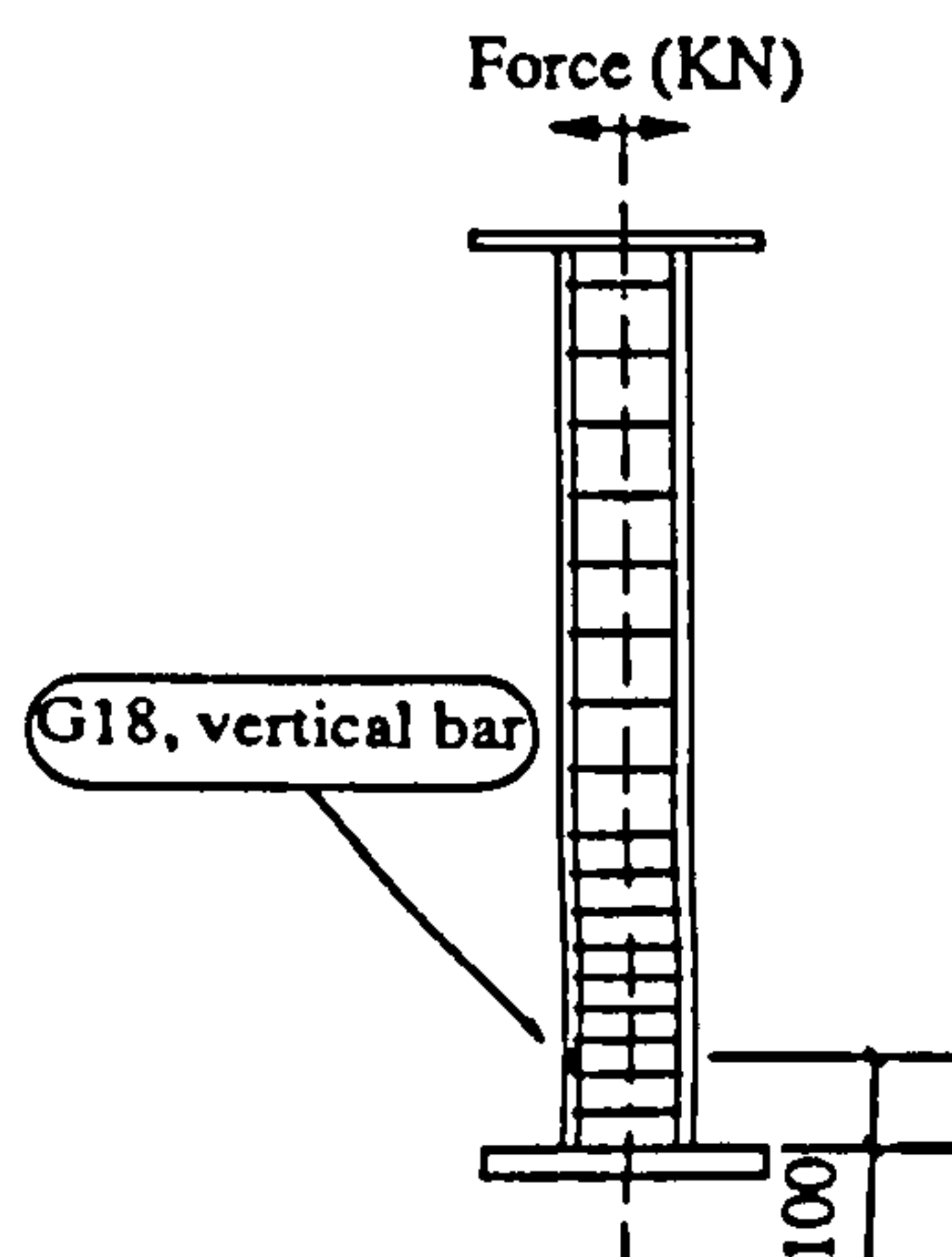
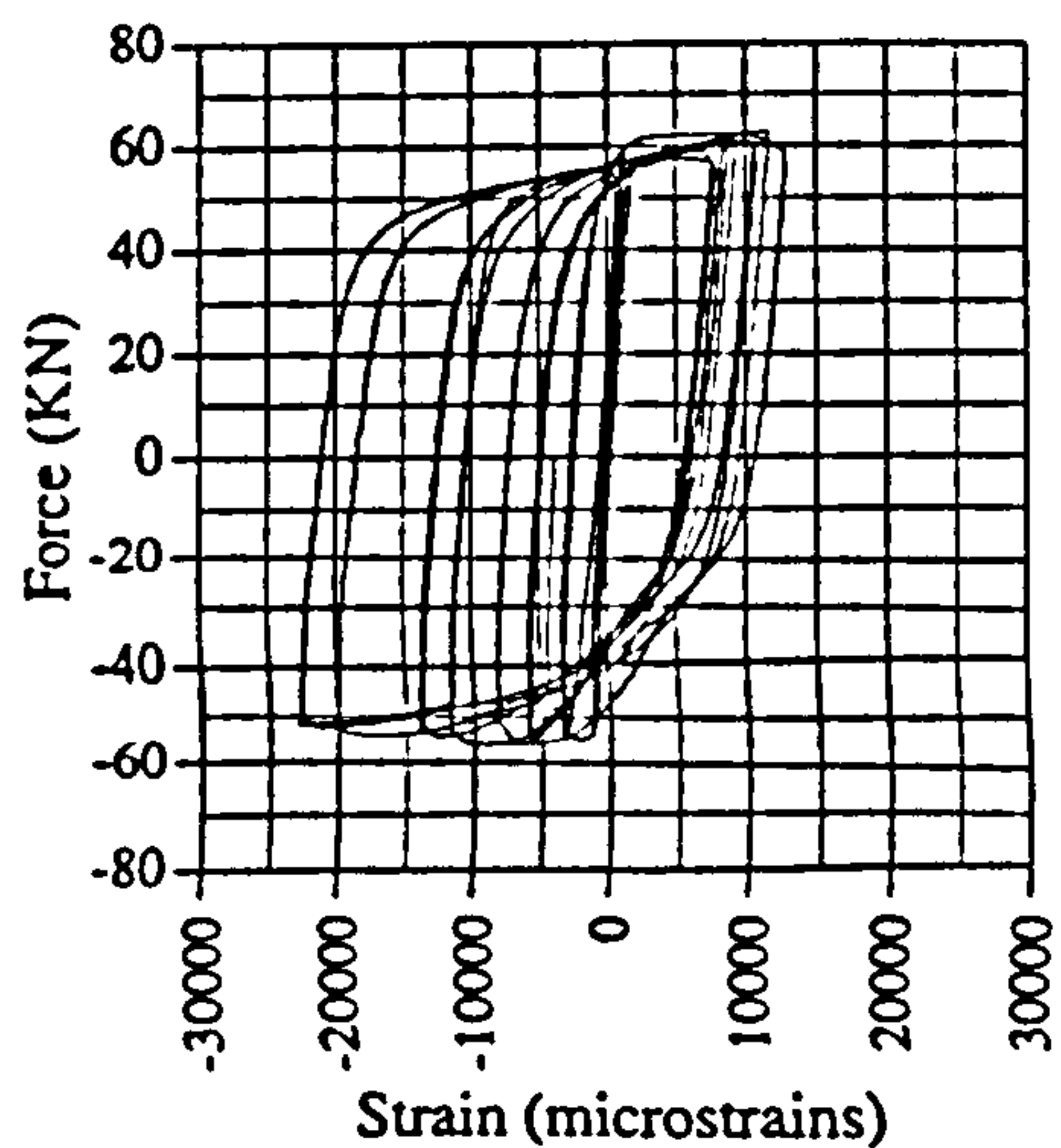


Fig. A.18 Force vs strain, EM01, G18

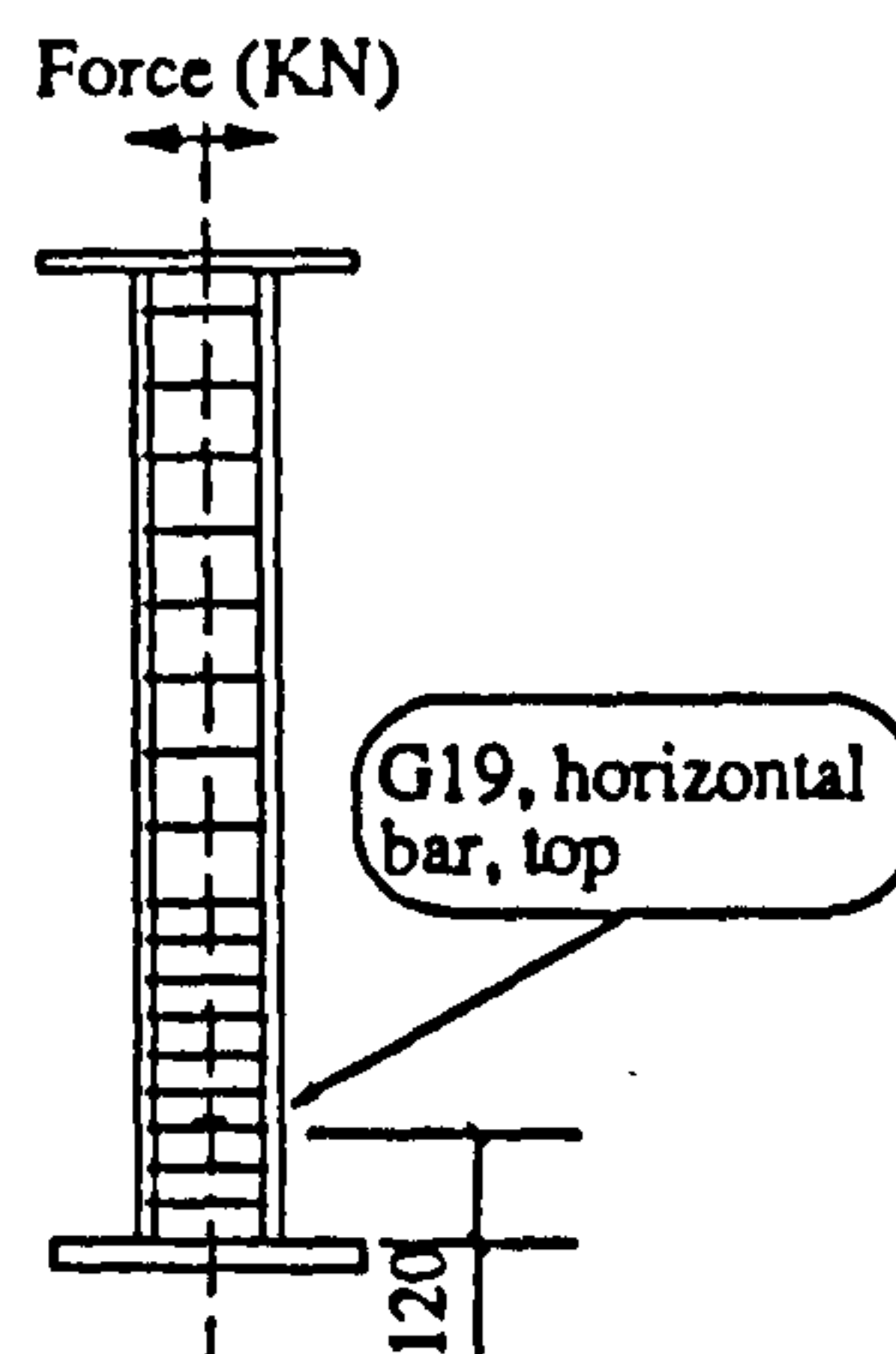
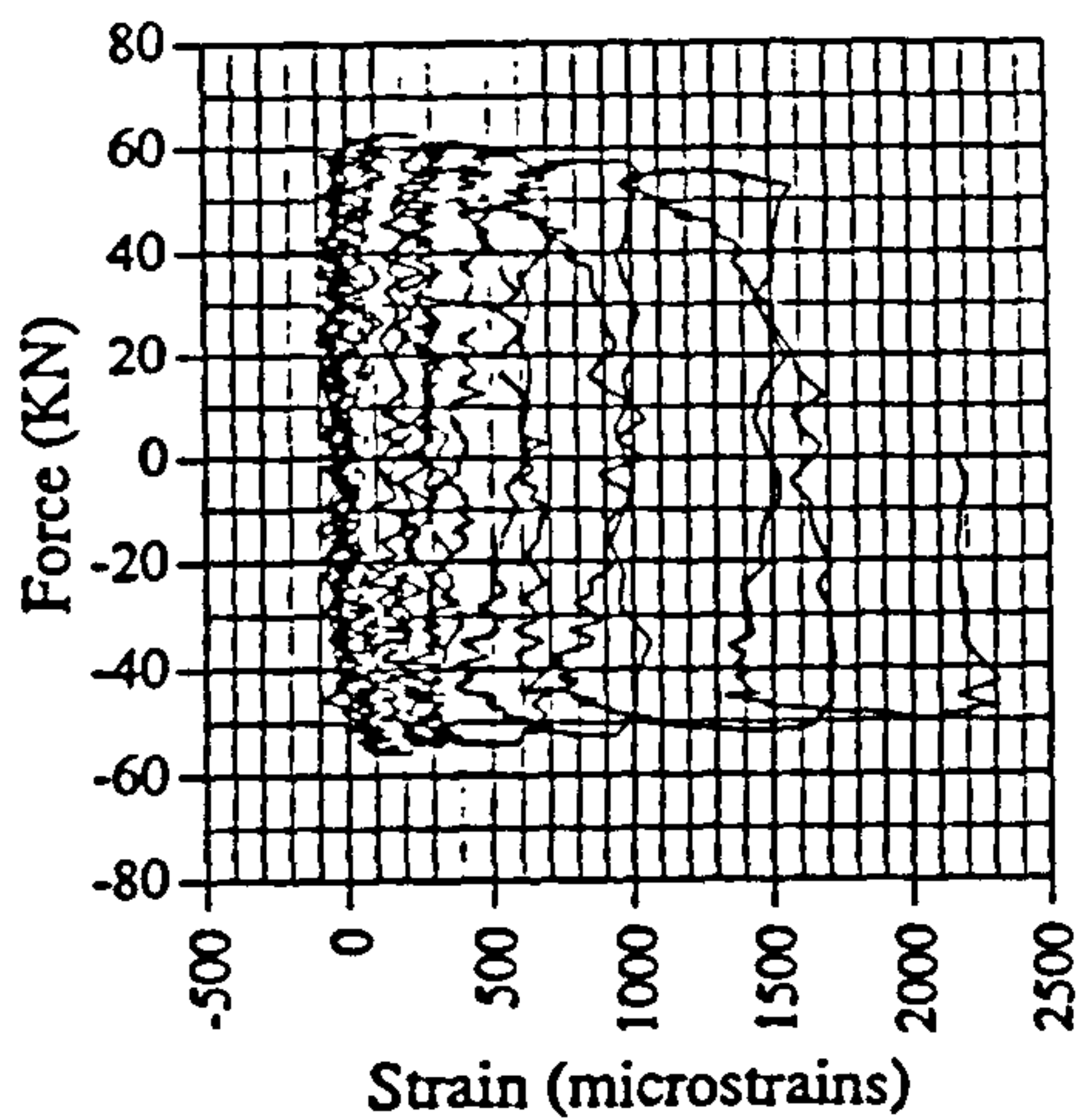


Fig. A.19 Force vs strain, EM01, G19

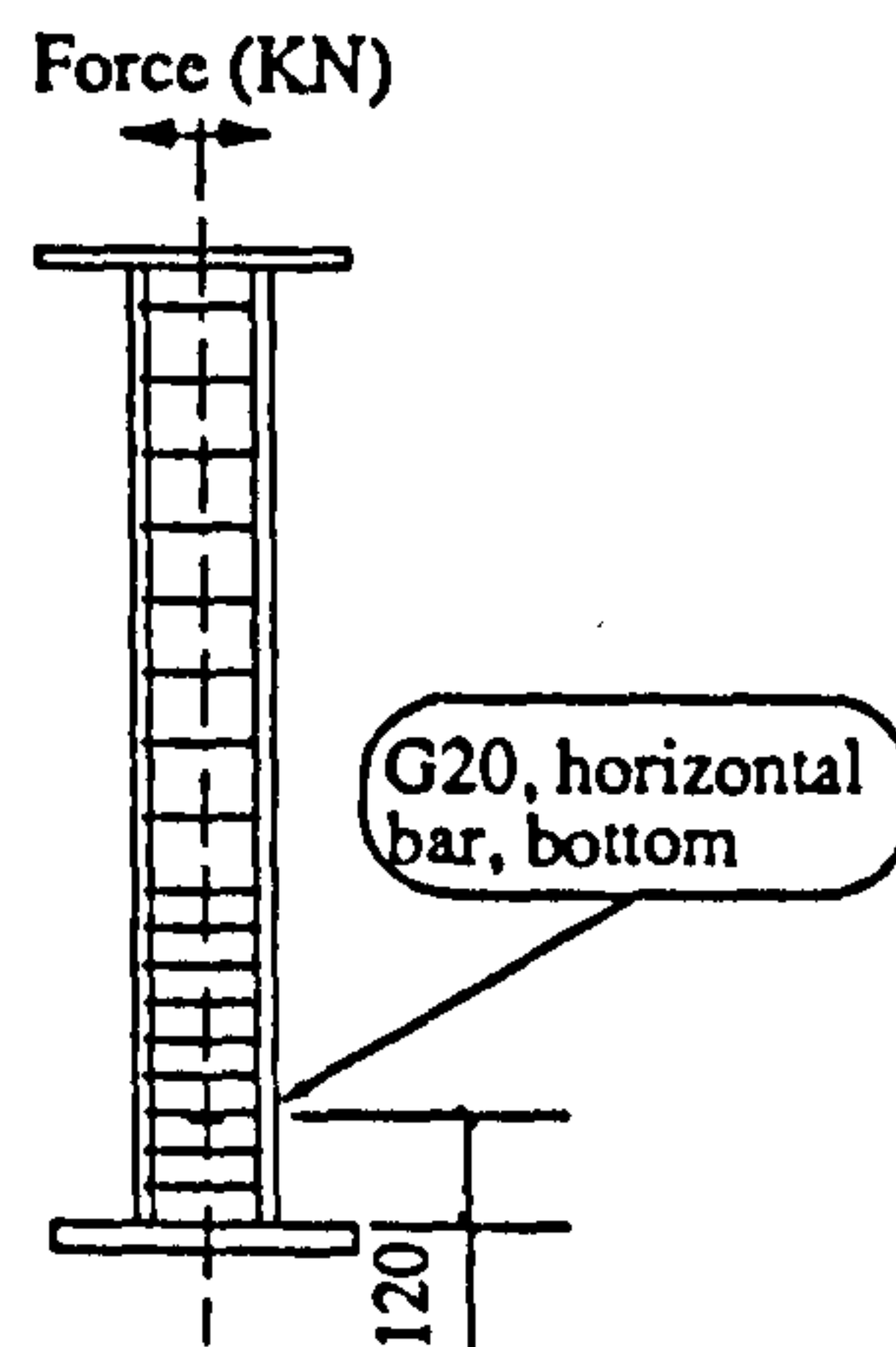
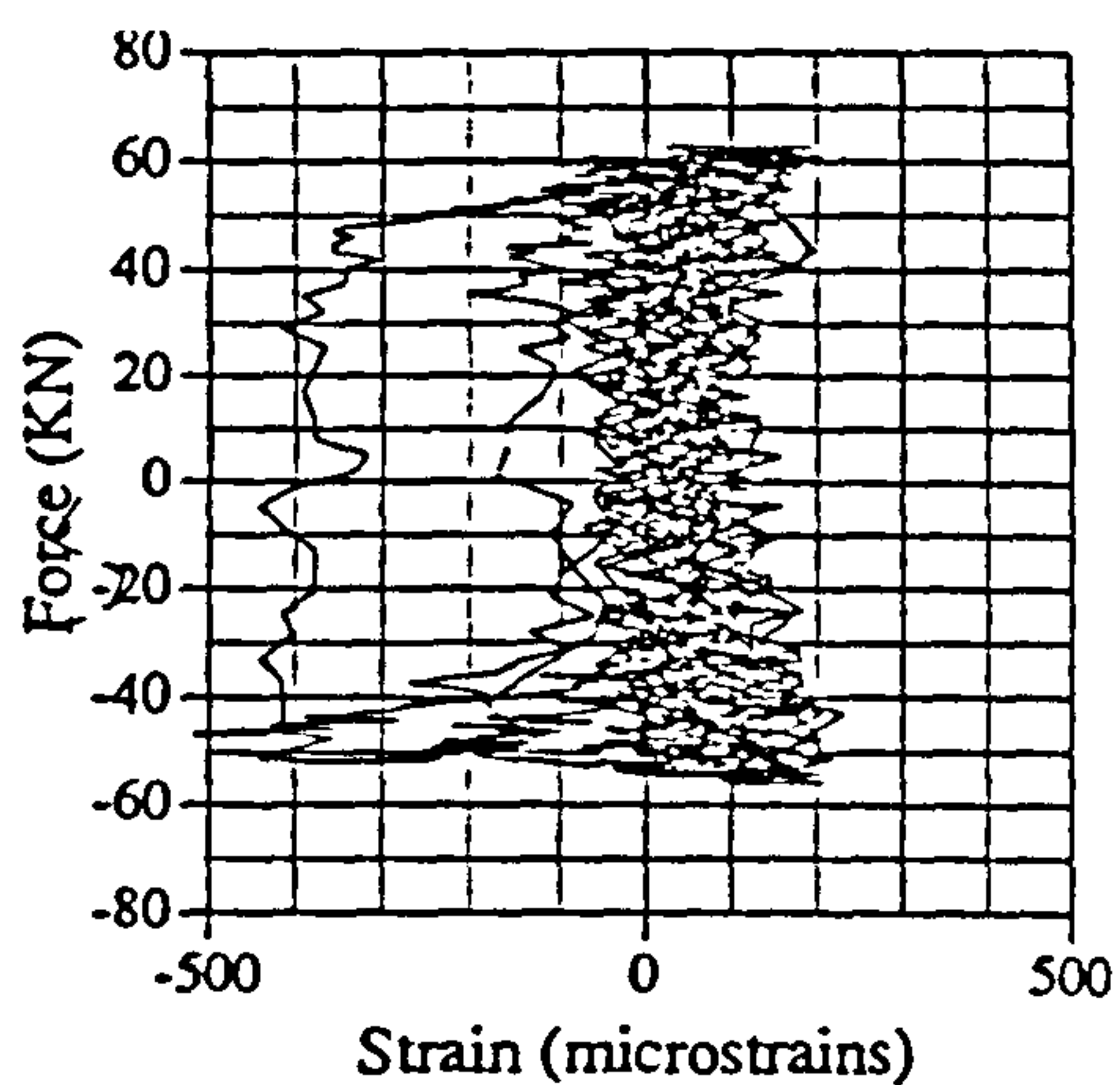


Fig. A.20 Force vs strain, EM01, G20

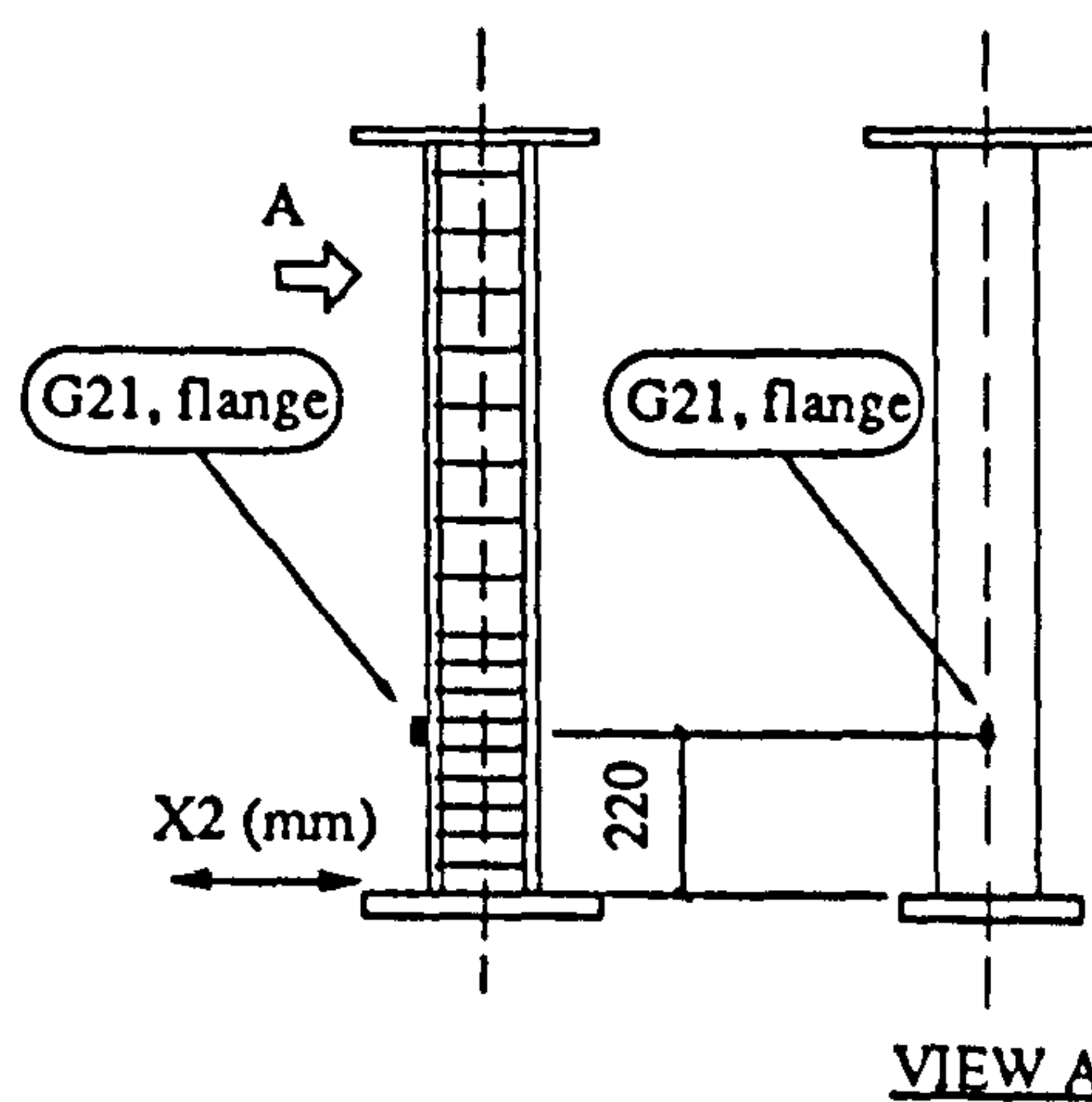
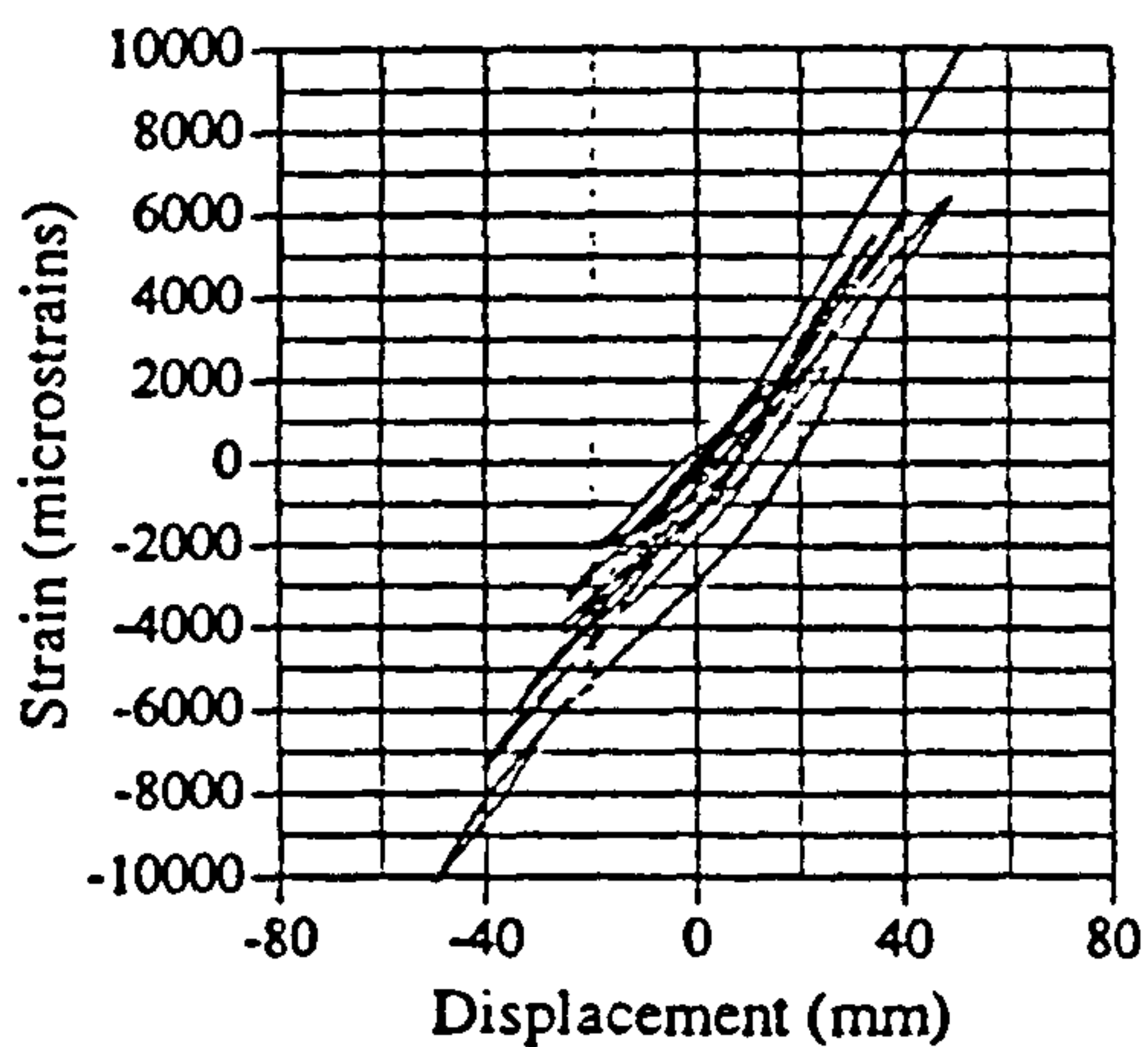


Fig. A.21 Strain vs displacement, EM01, G21

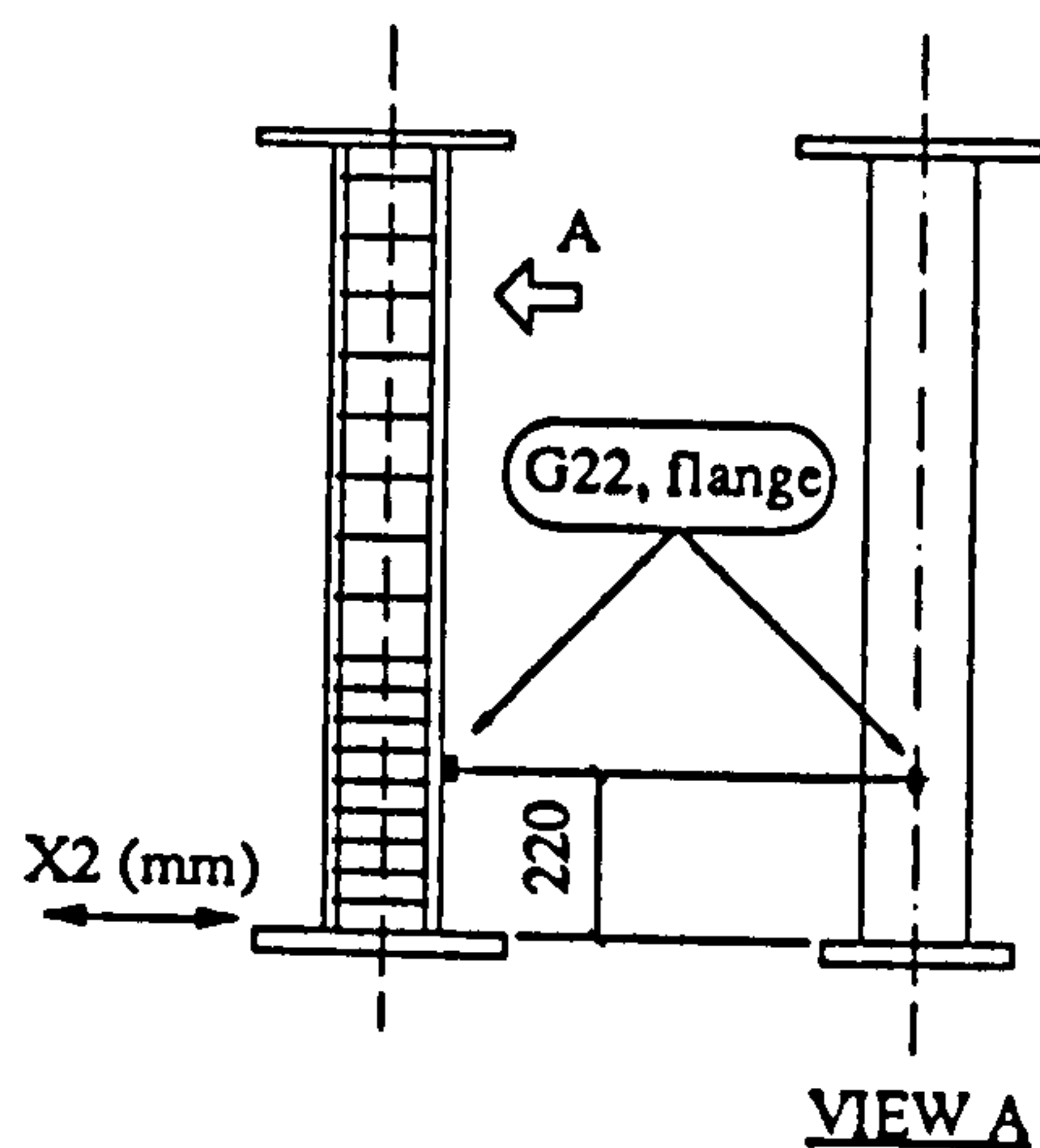
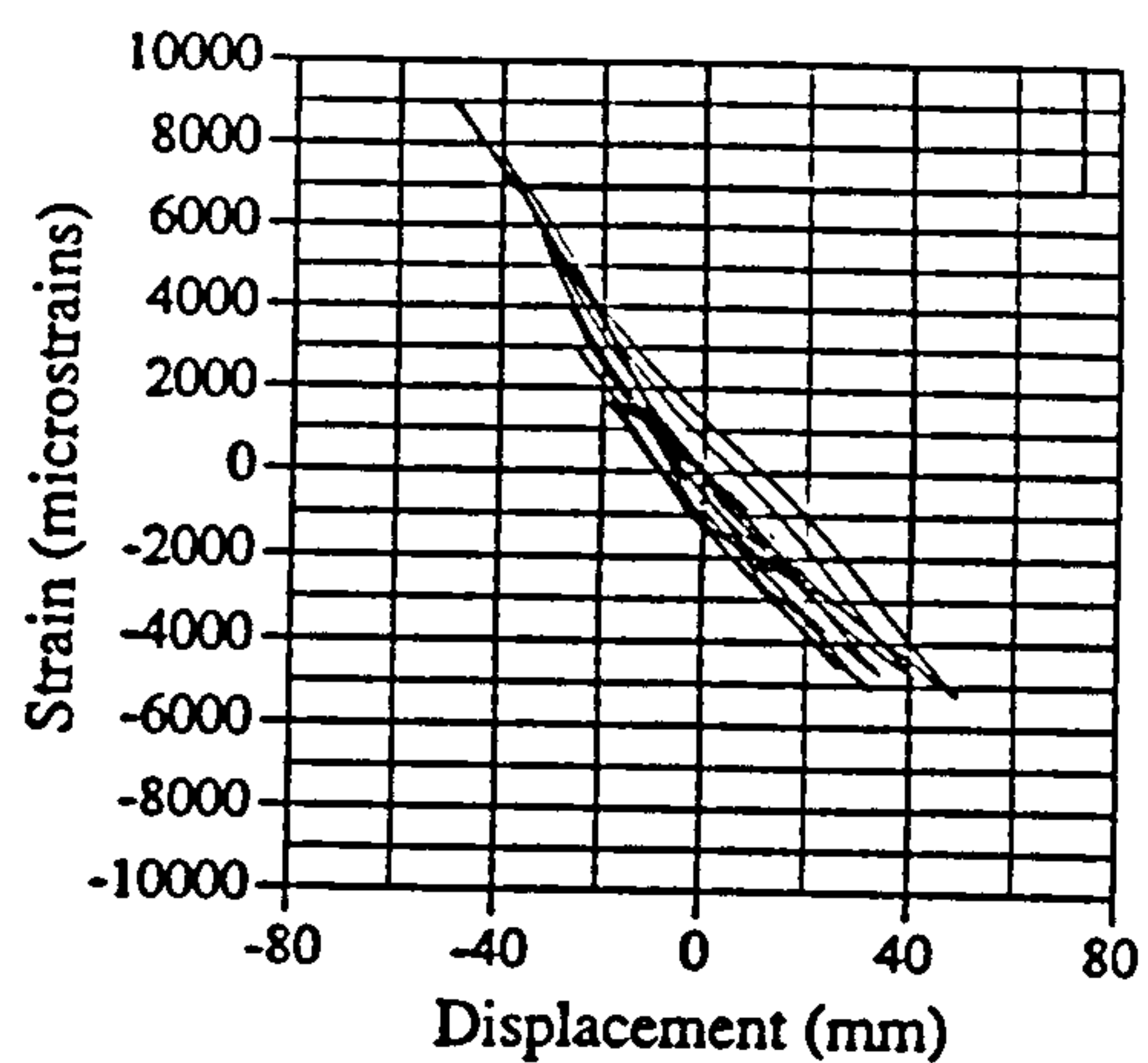


Fig. A.22 Strain vs displacement, EM01, G22

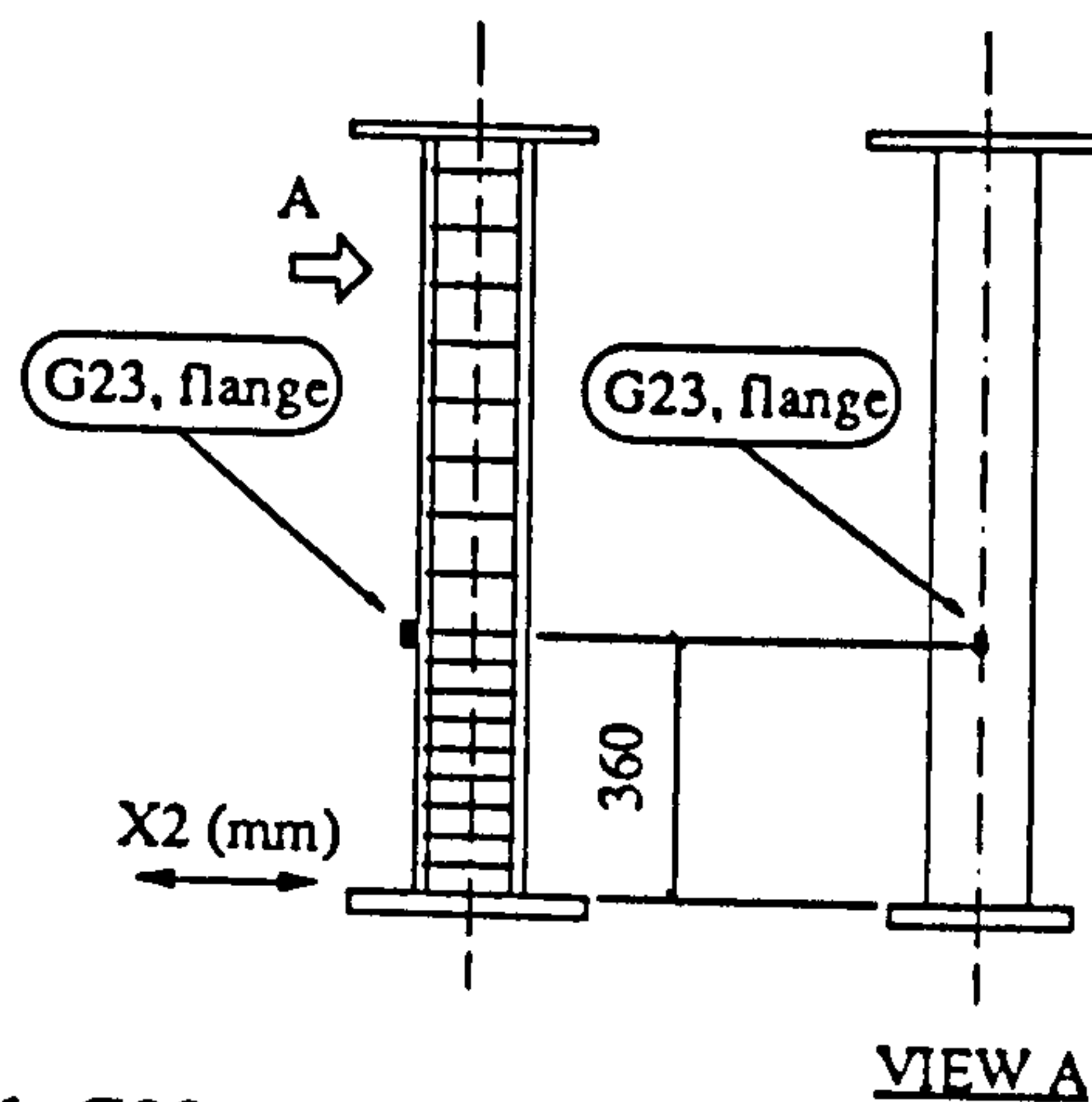
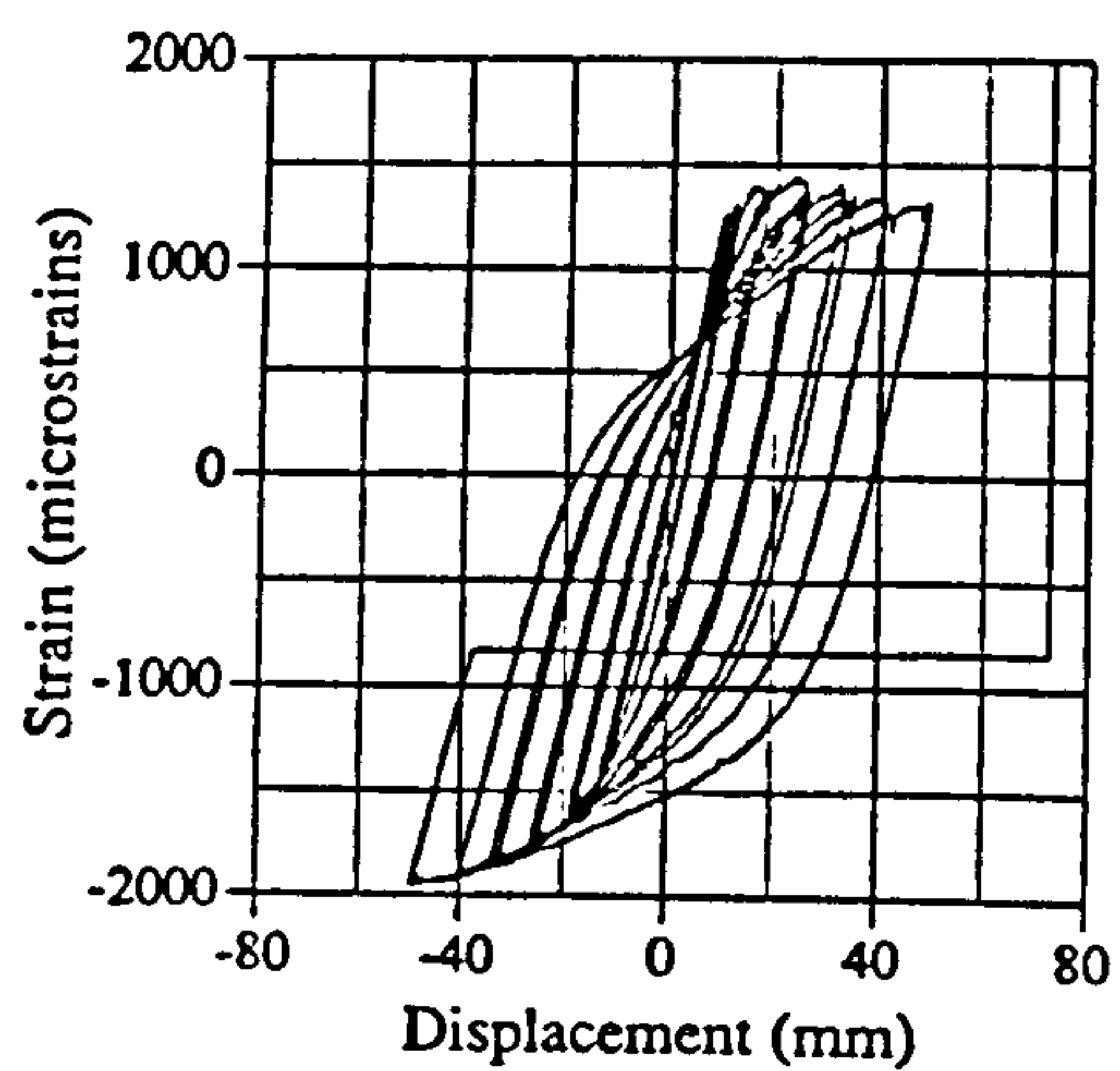


Fig. A.23 Strain vs displacement, EM01, G23

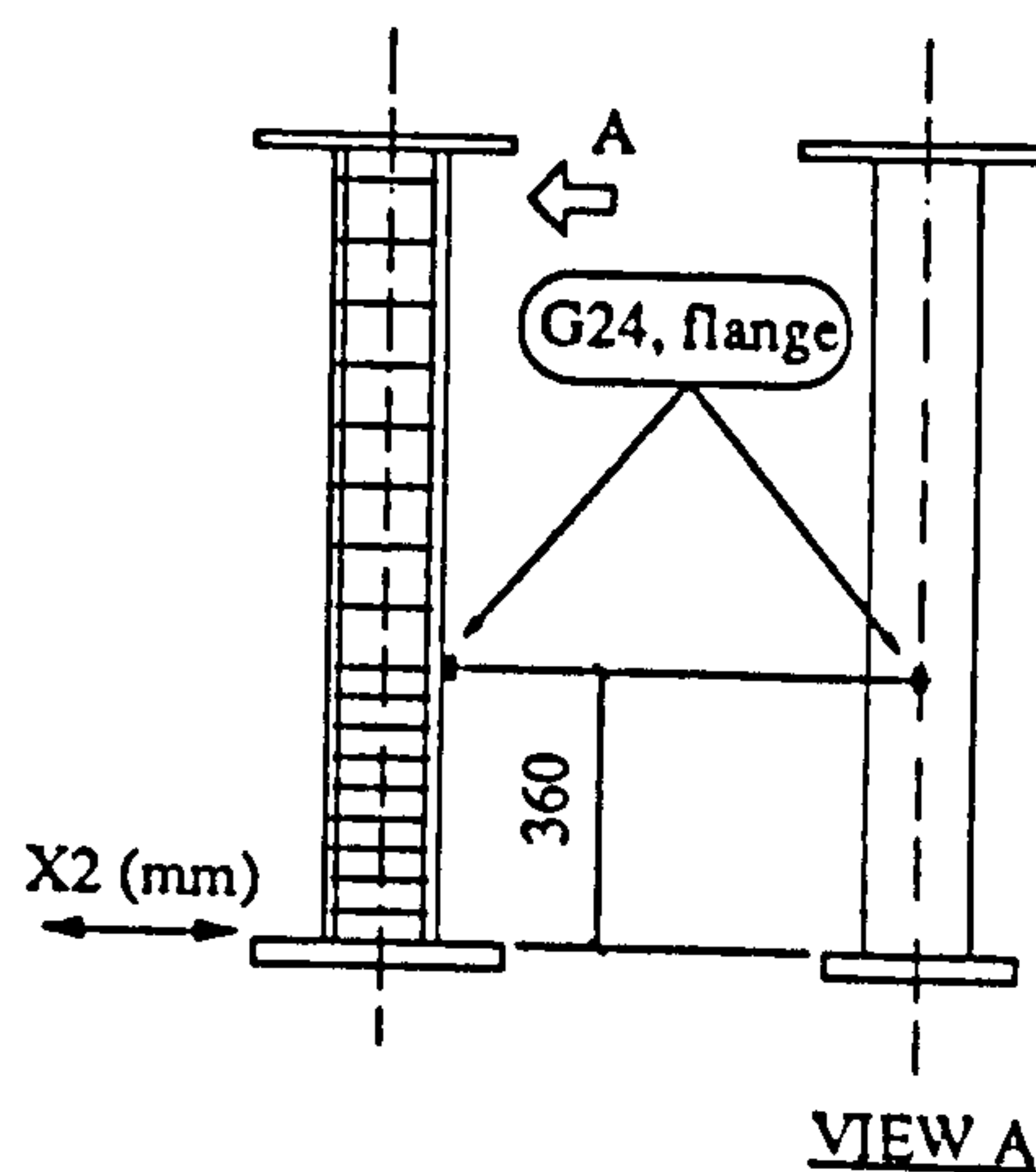
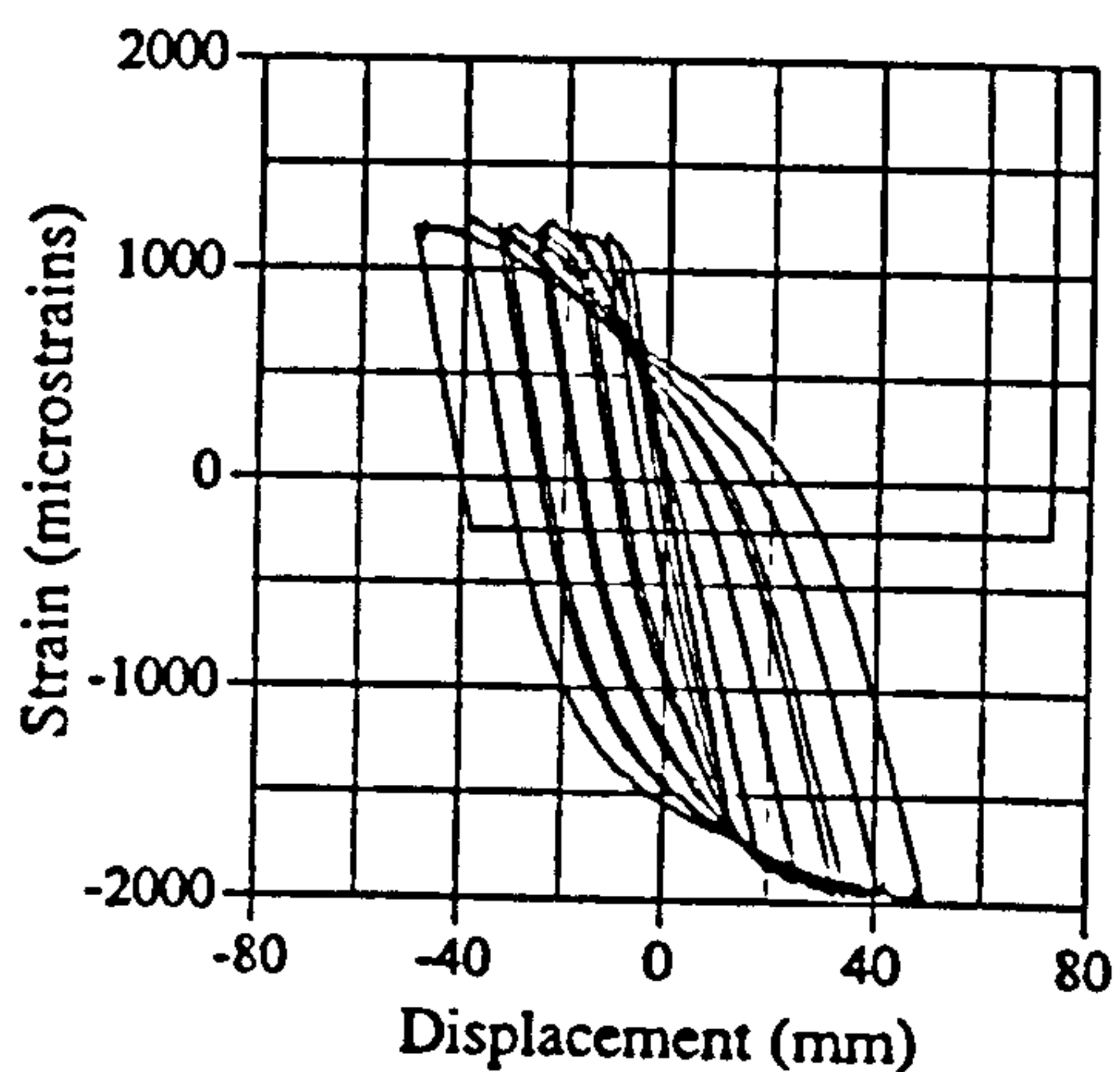


Fig. A.24 Strain vs displacement, EM01, G24

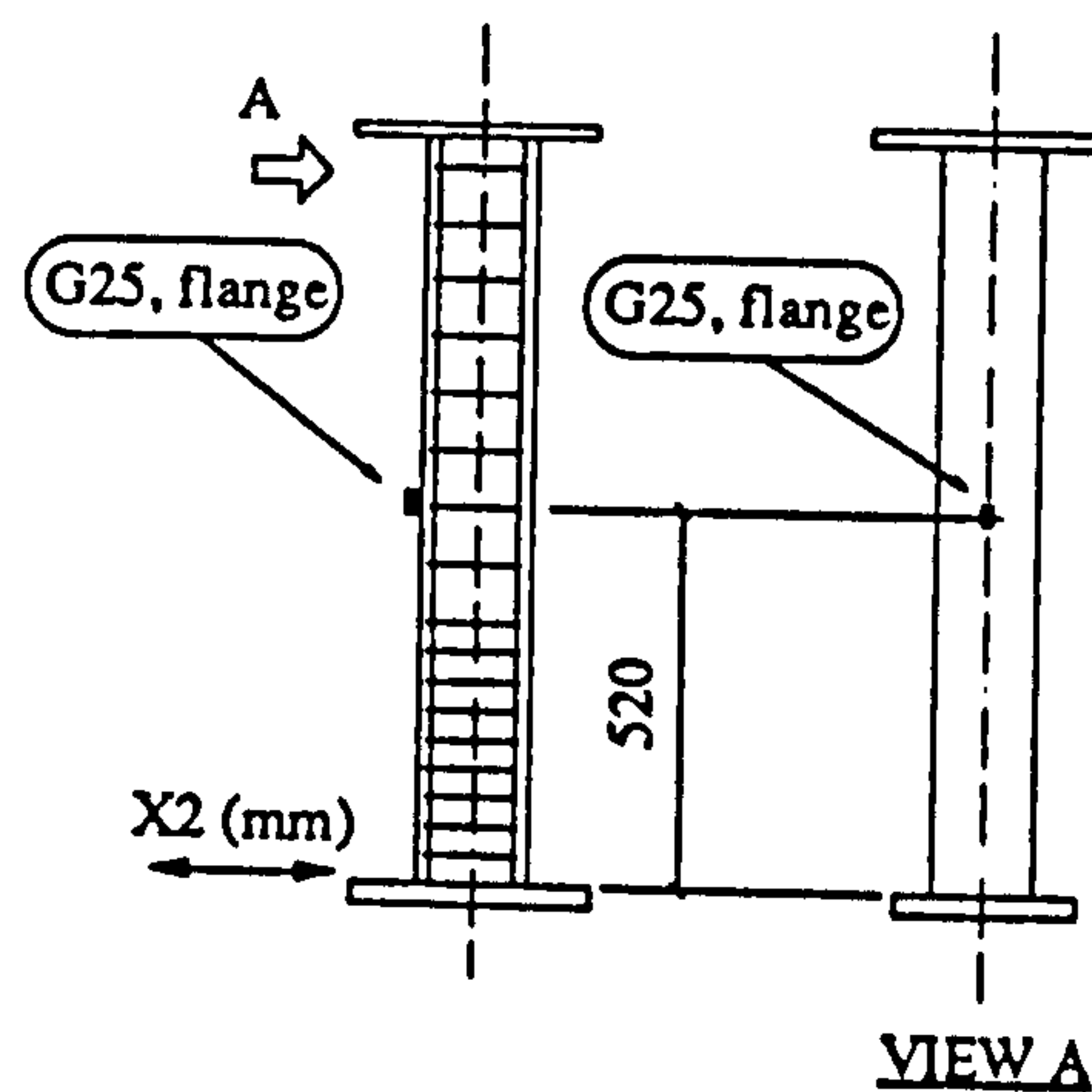
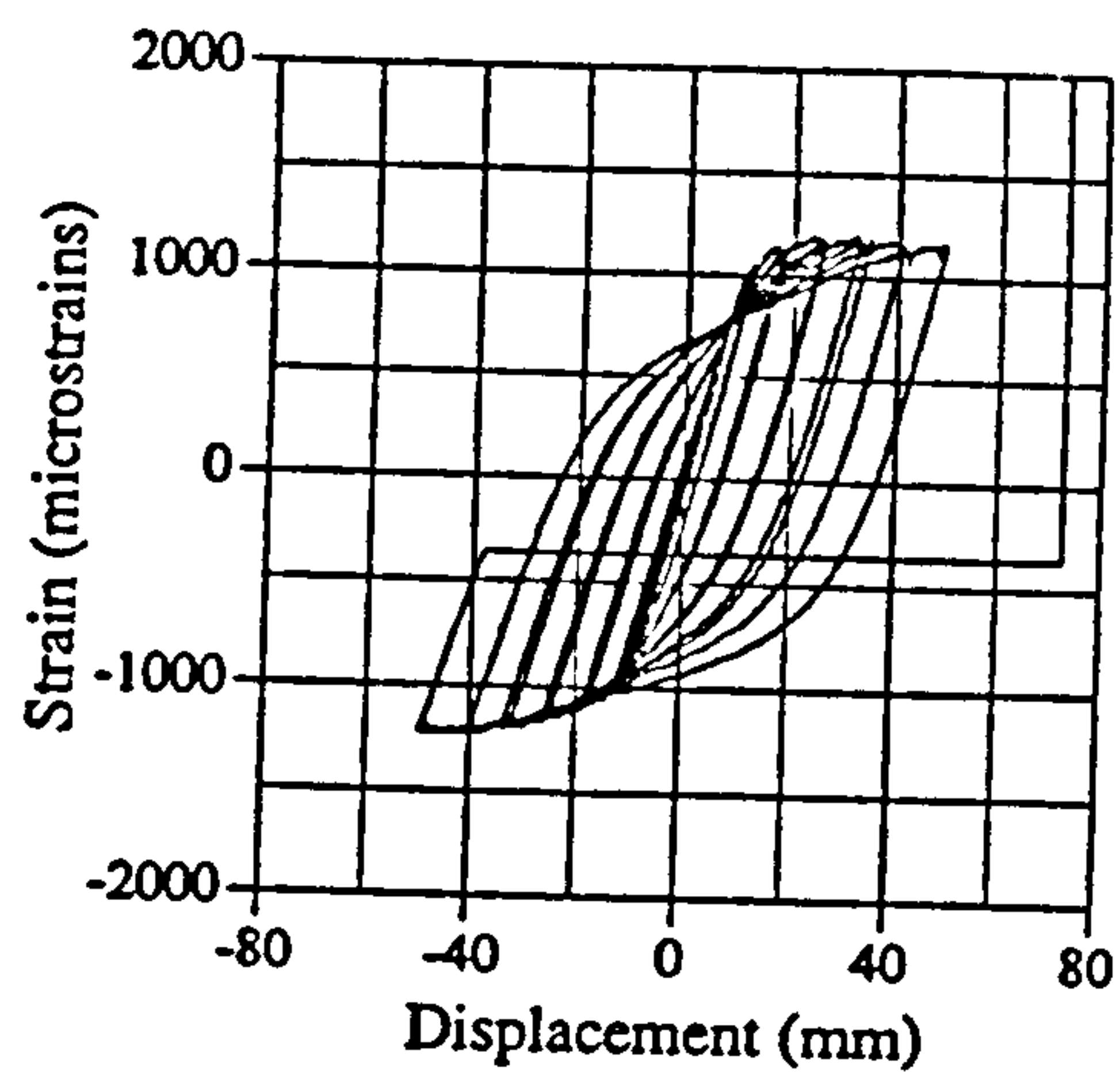


Fig. A.25 Strain vs displacement, EM01, G25

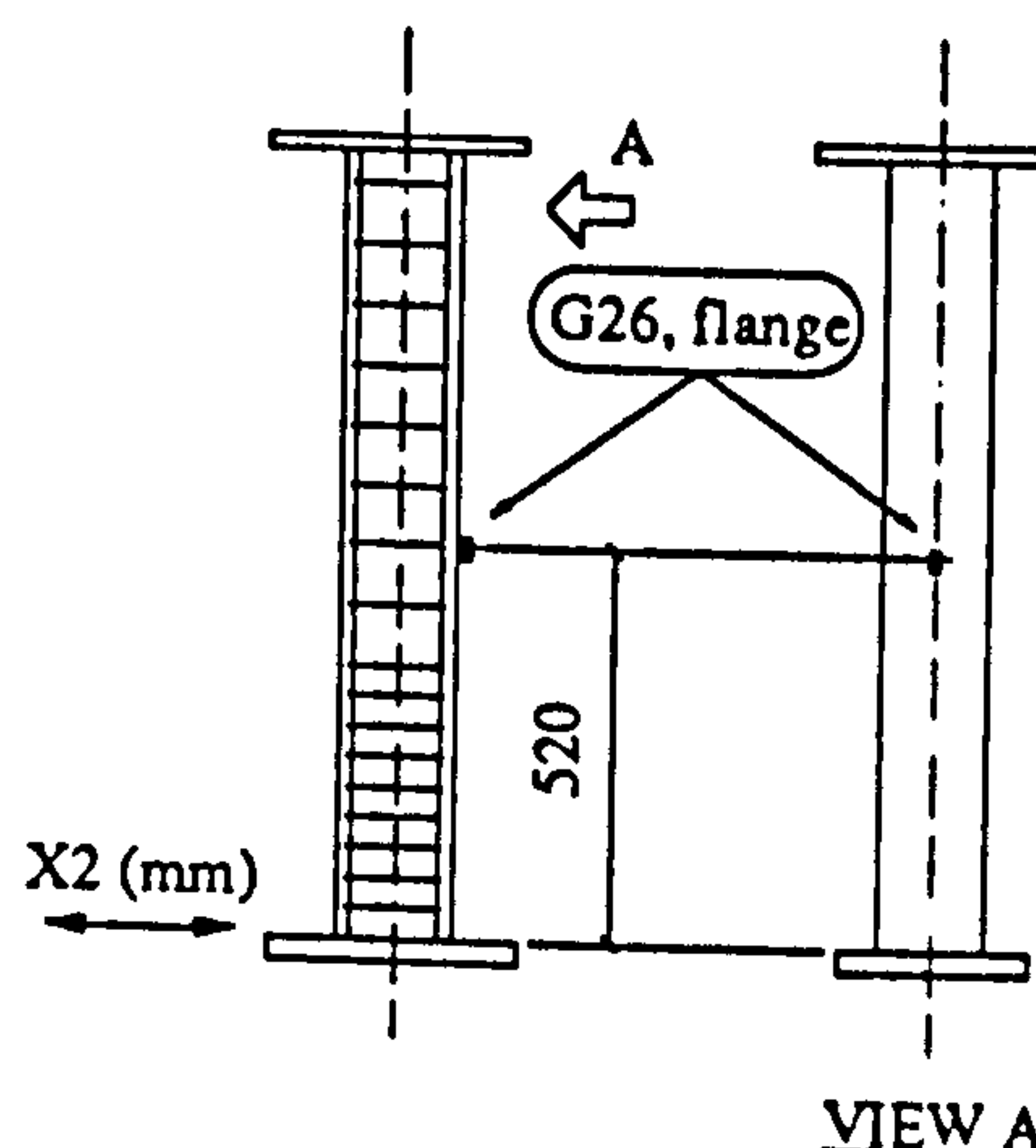
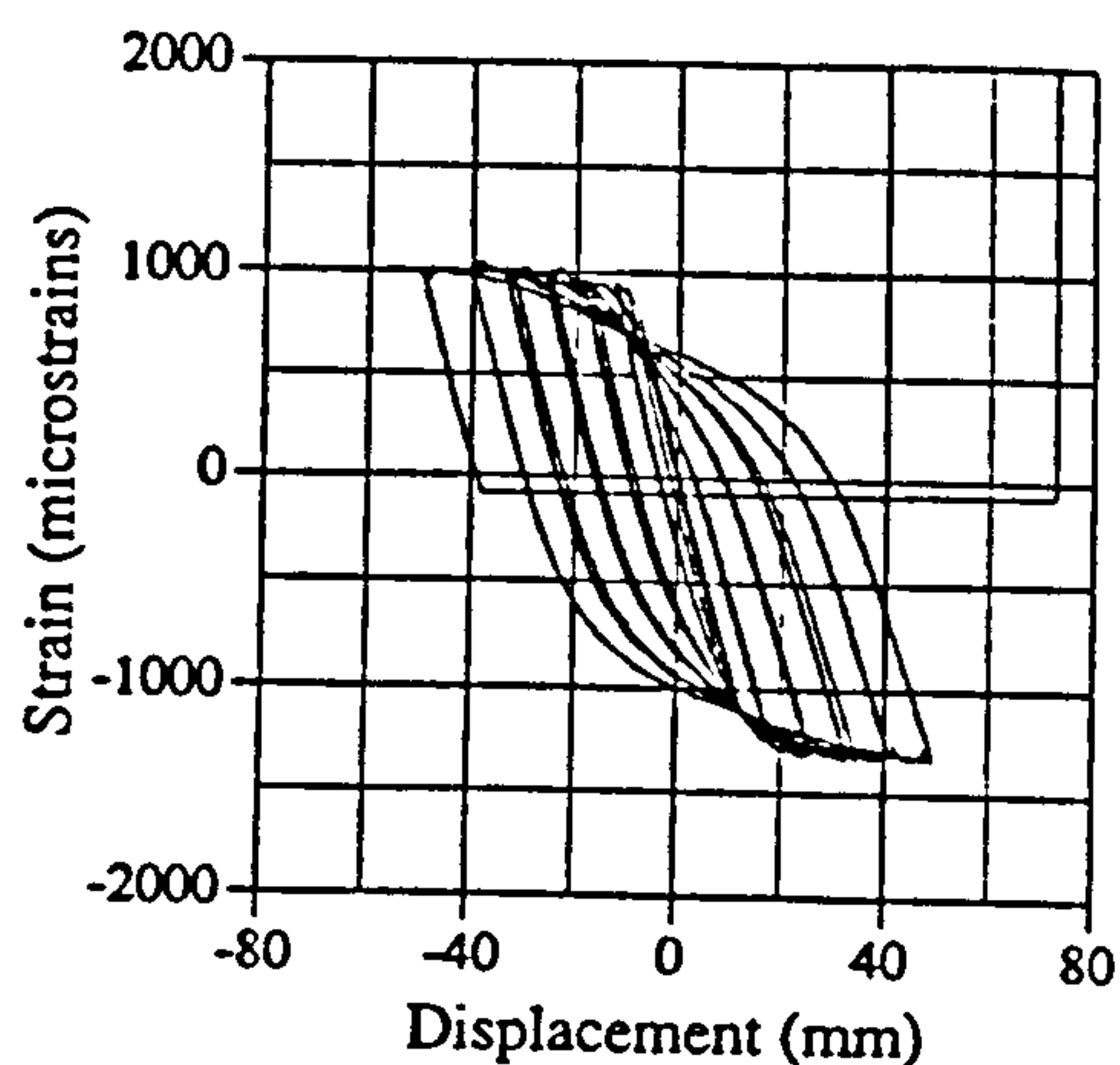


Fig. A.26 Strain vs displacement, EM01, G26

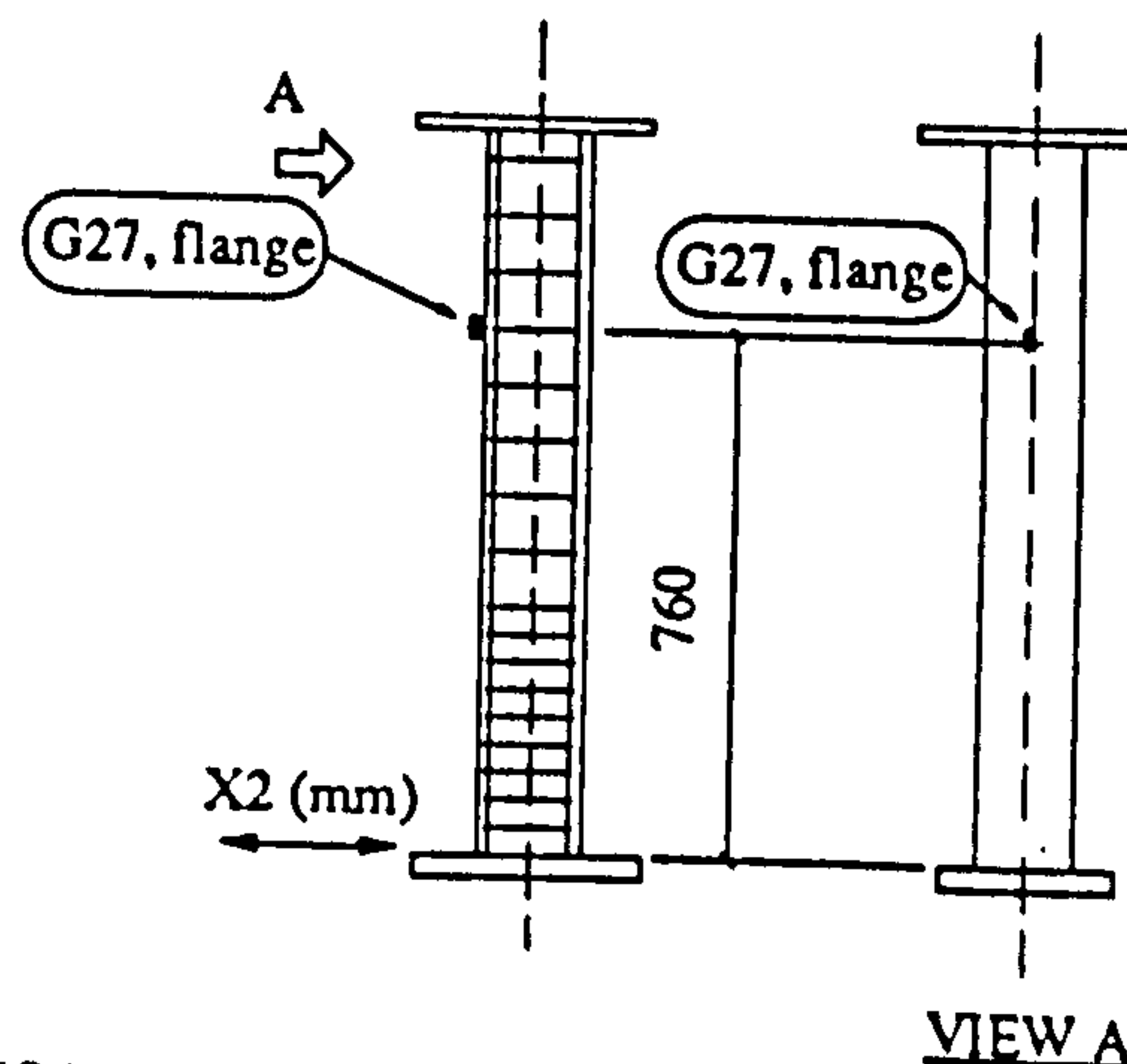
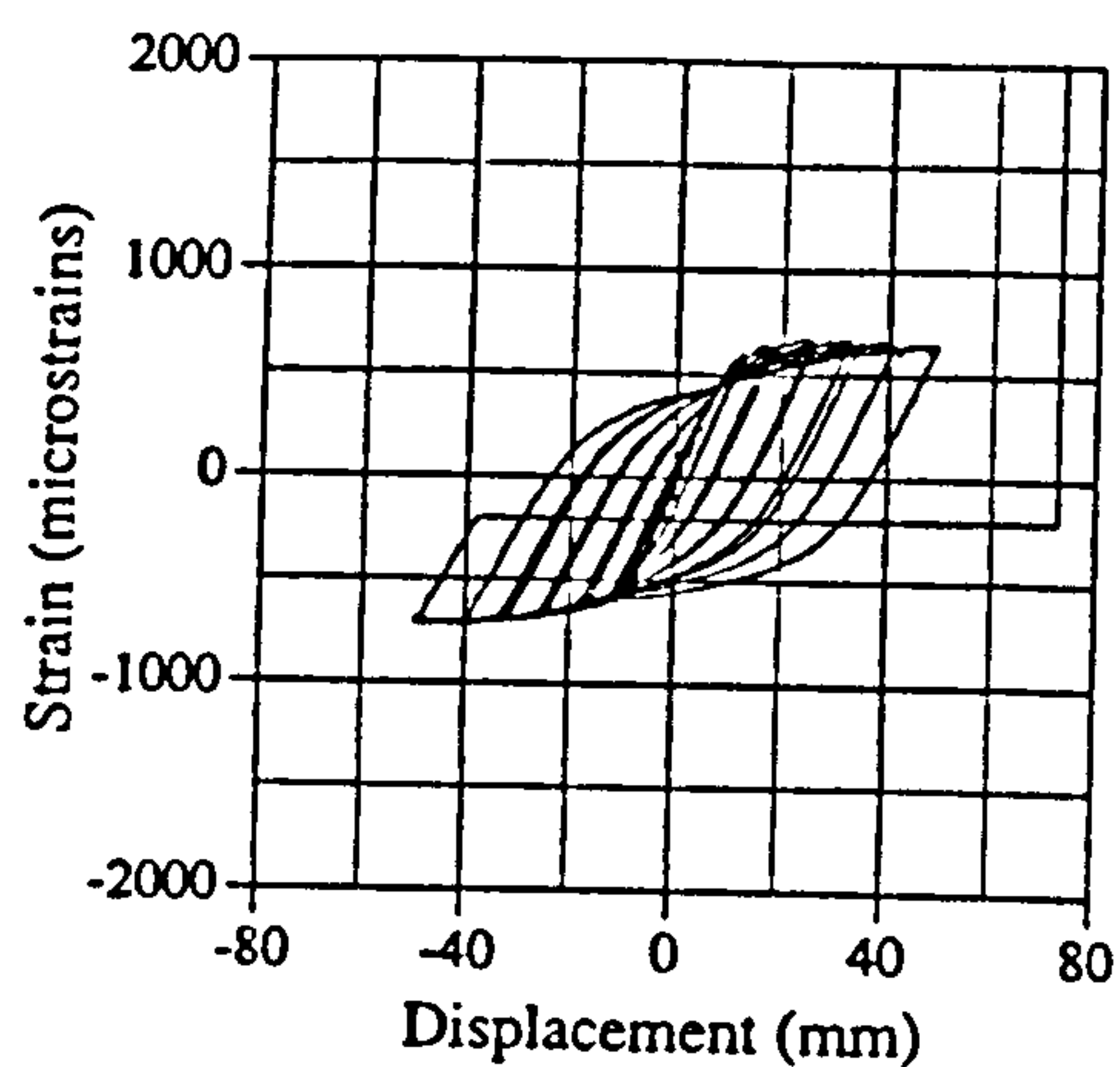


Fig. A.27 Strain vs displacement, EM01, G27

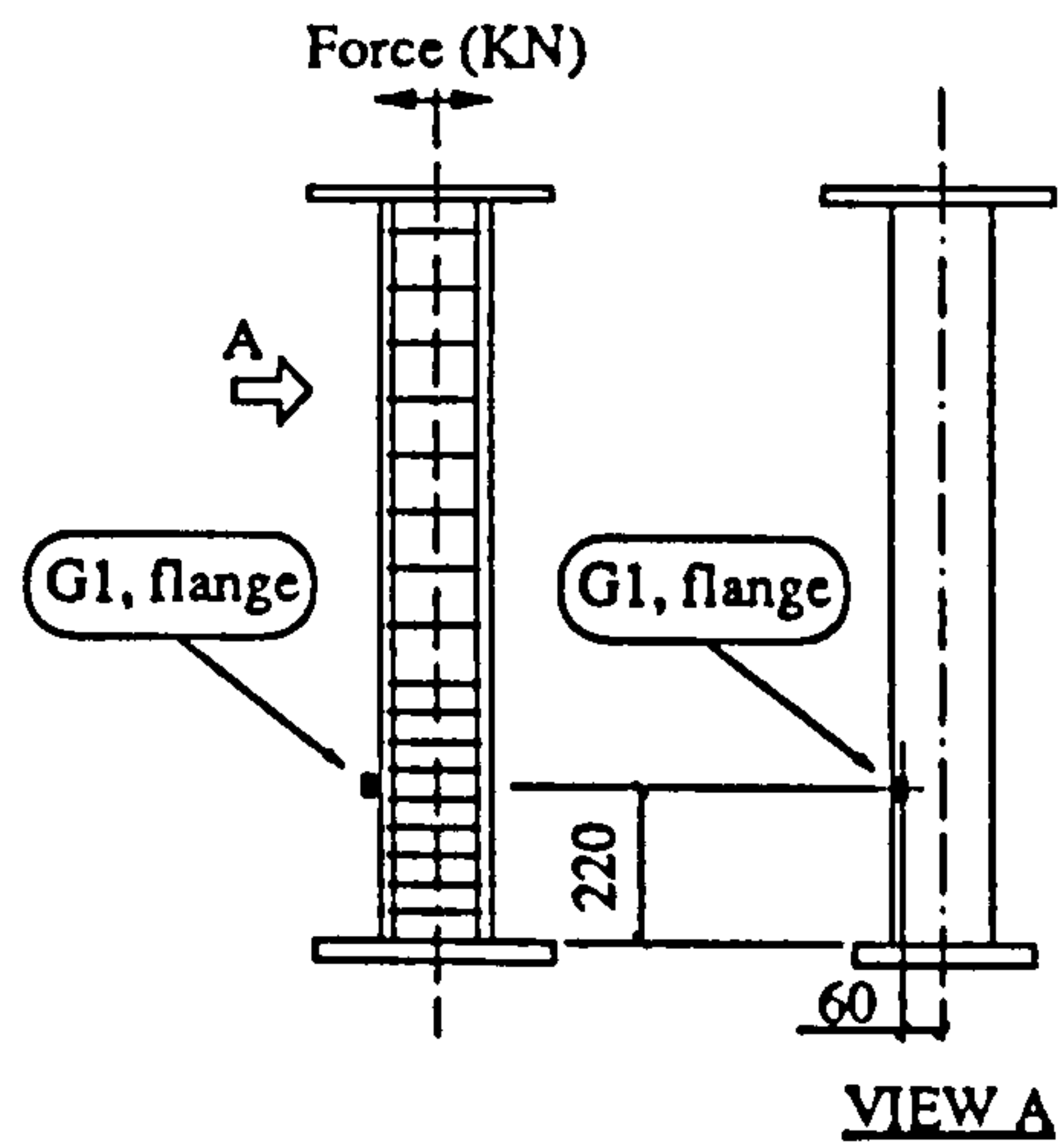
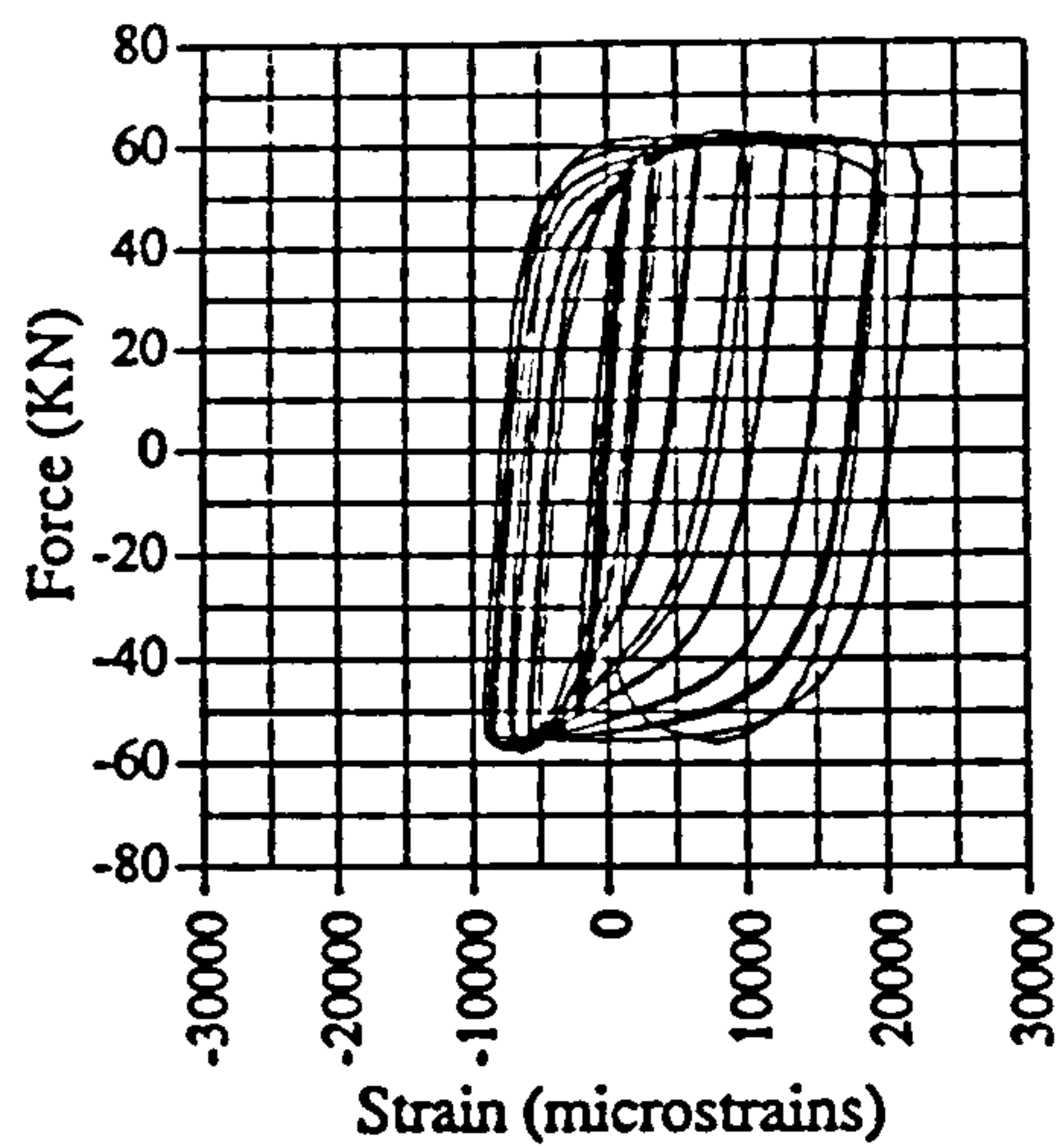


Fig. A.28 Force vs strain, IC01, G1

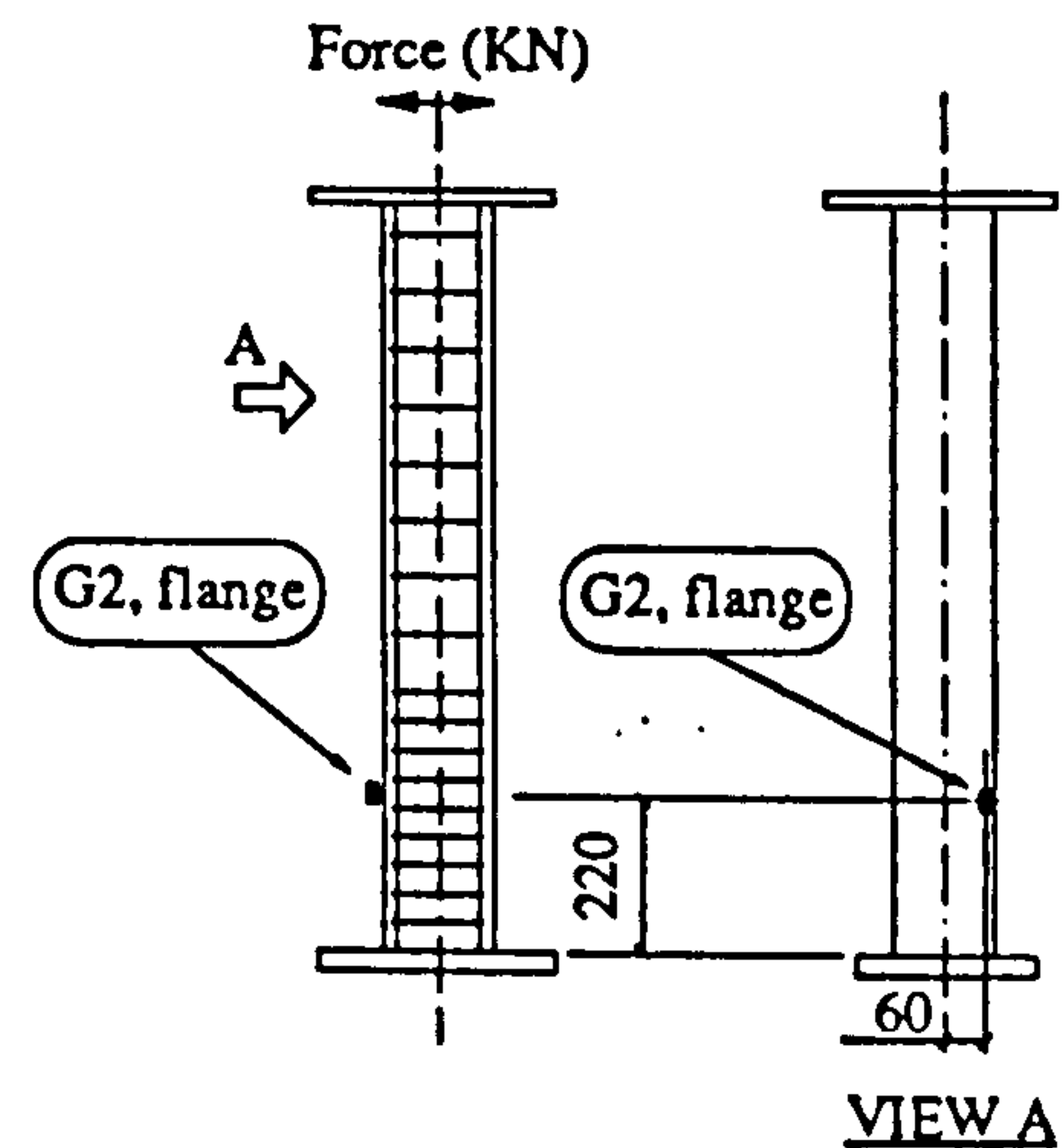
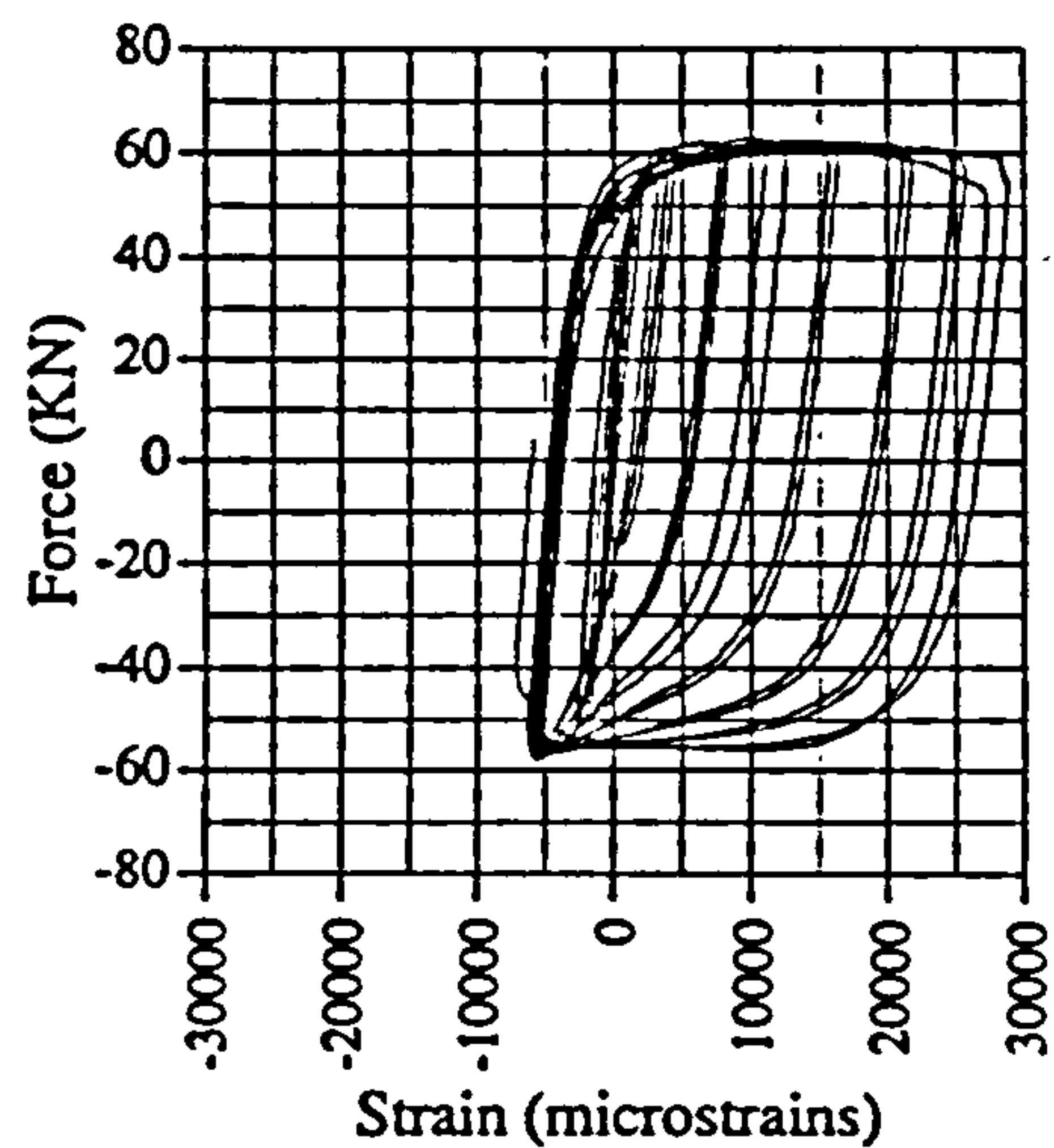


Fig. A.29 Force vs strain, IC01, G2

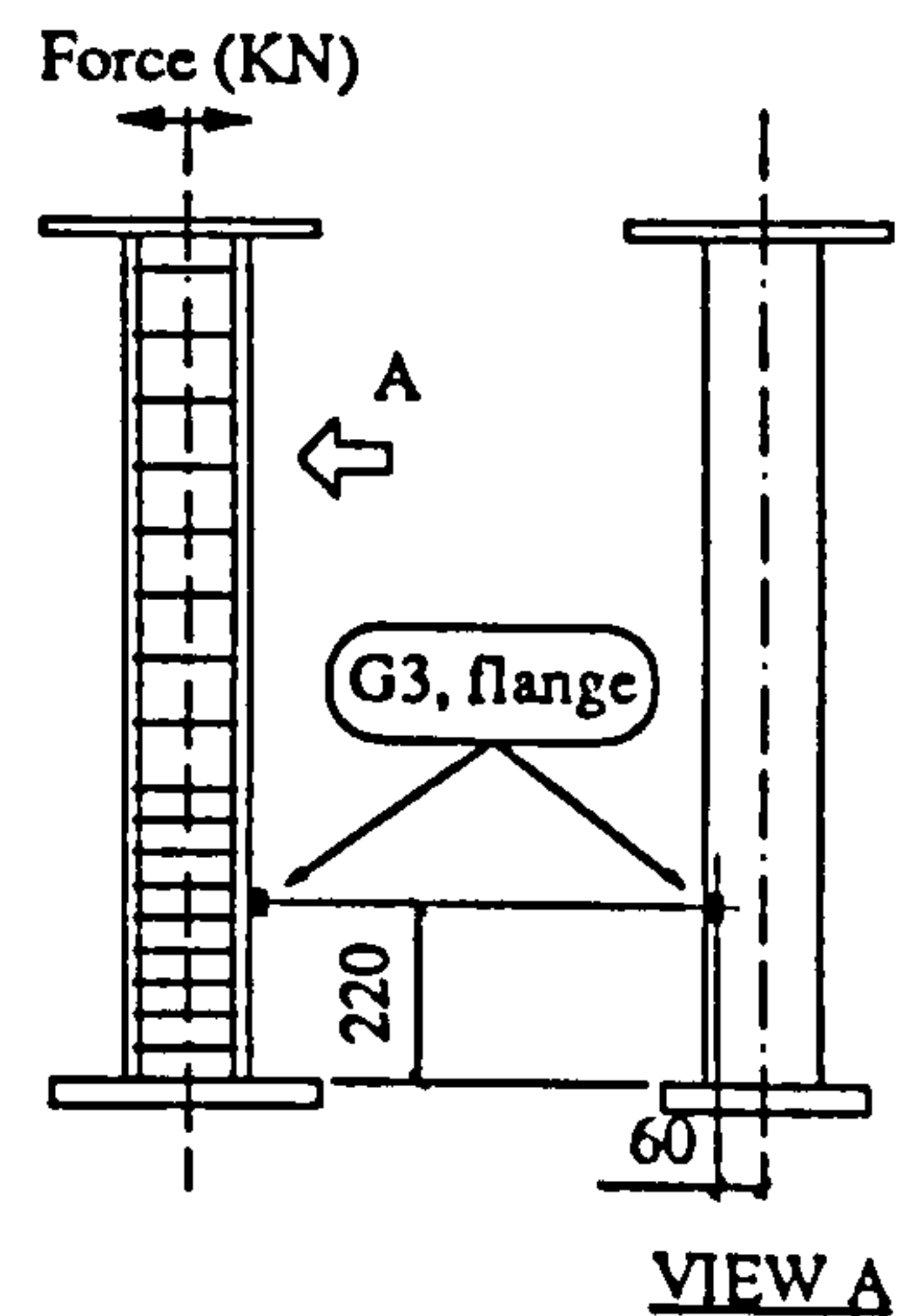
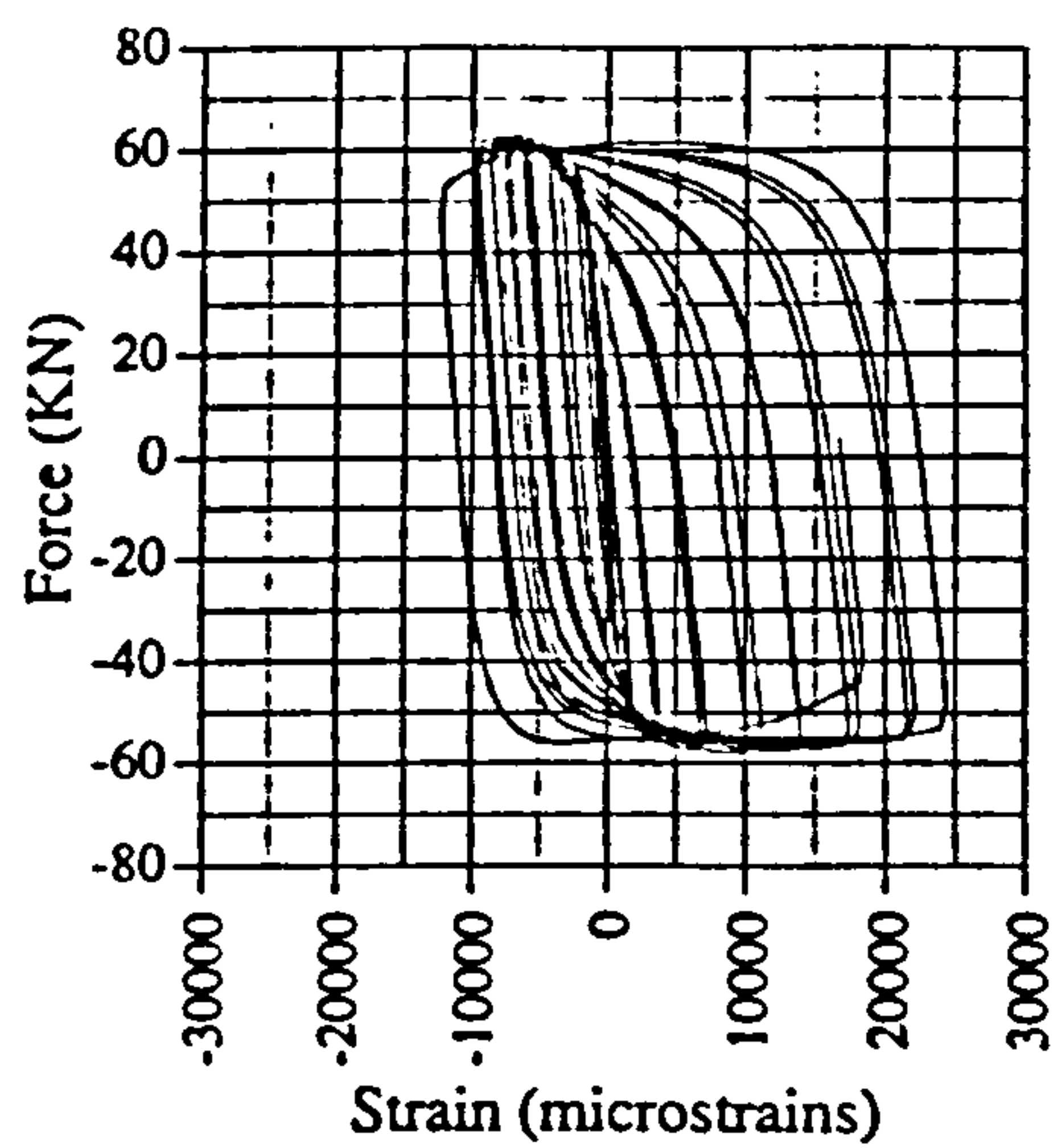


Fig. A.30 Force vs strain, IC01, G3

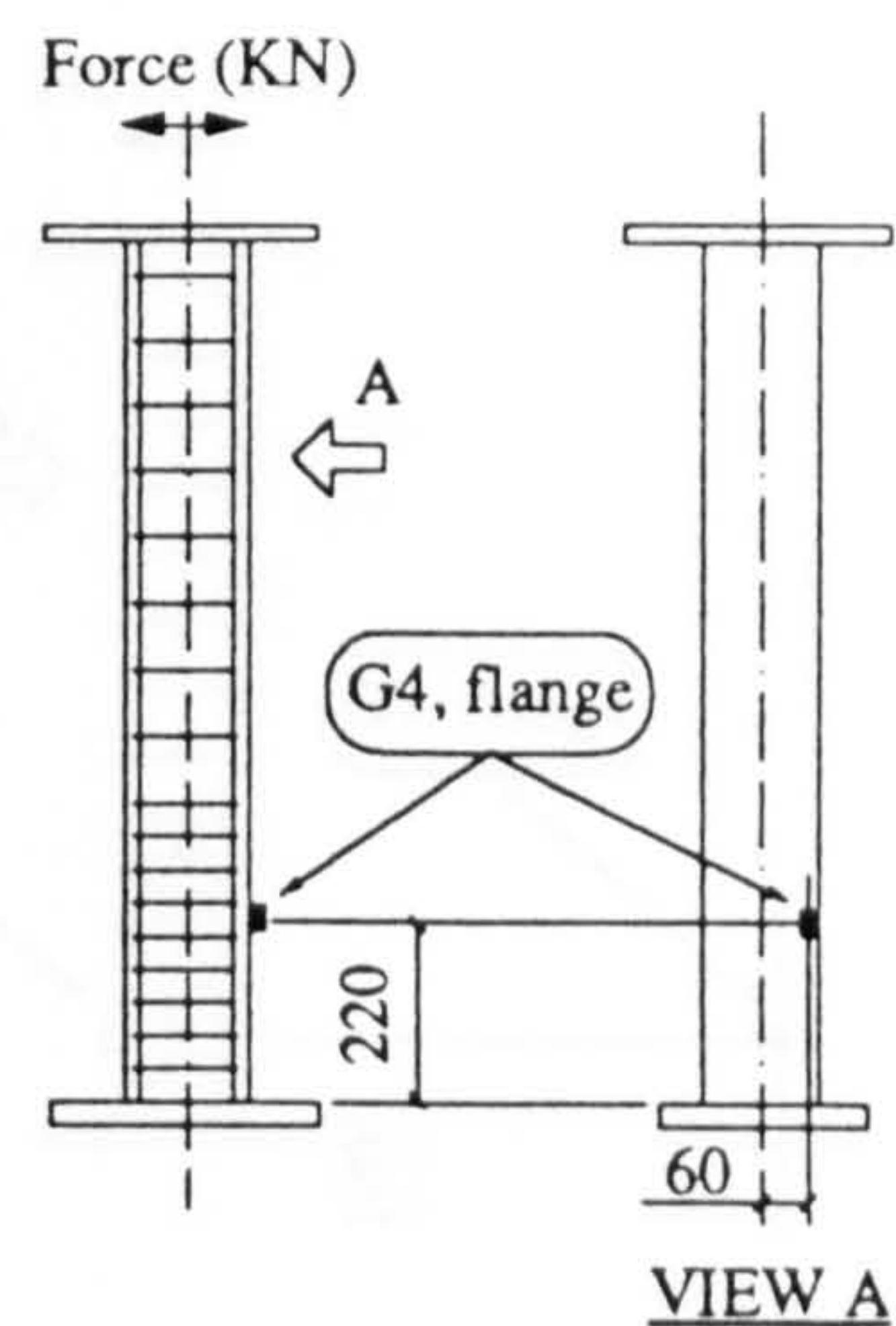
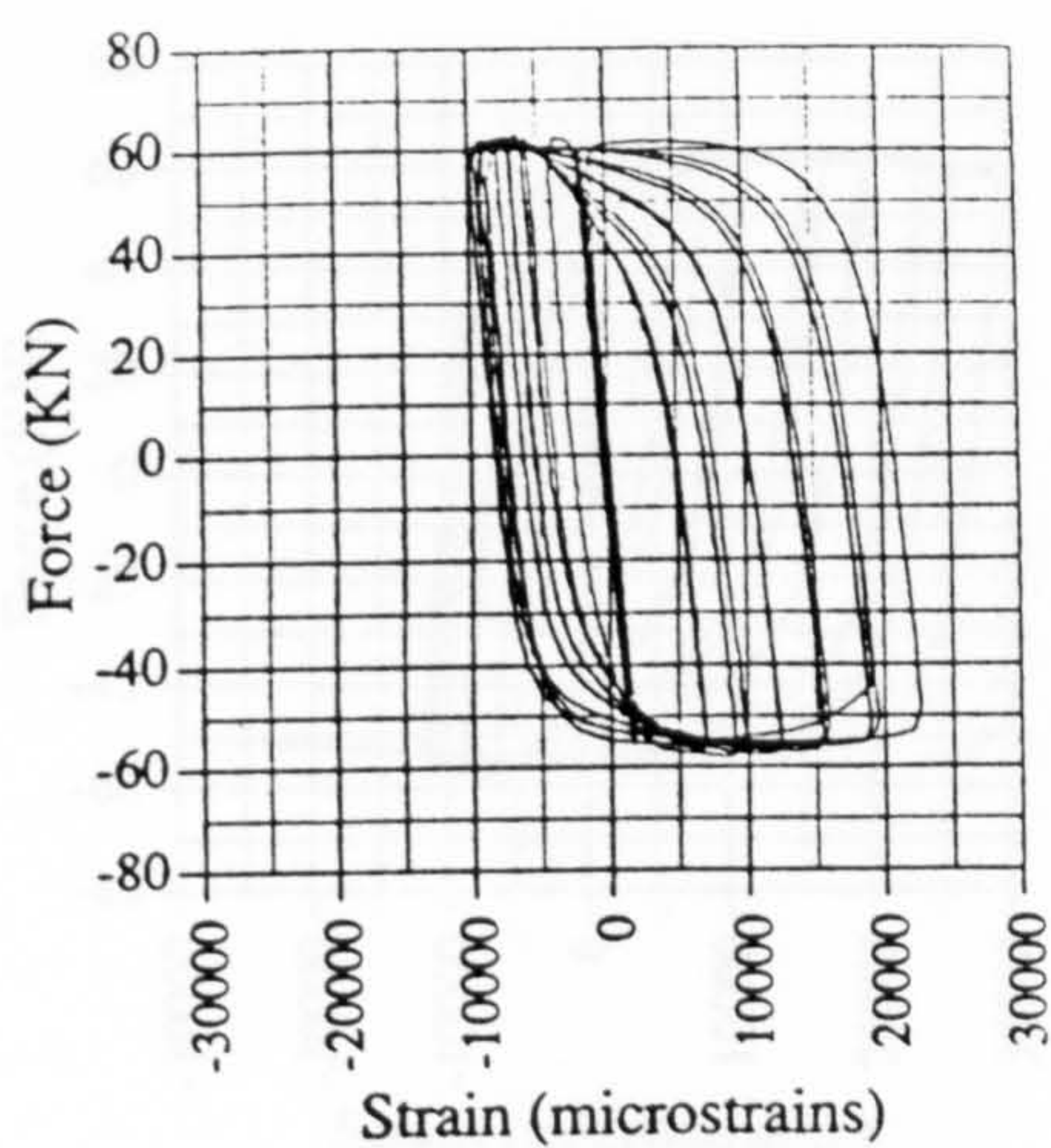


Fig. A.31 Force vs strain, IC01, G4

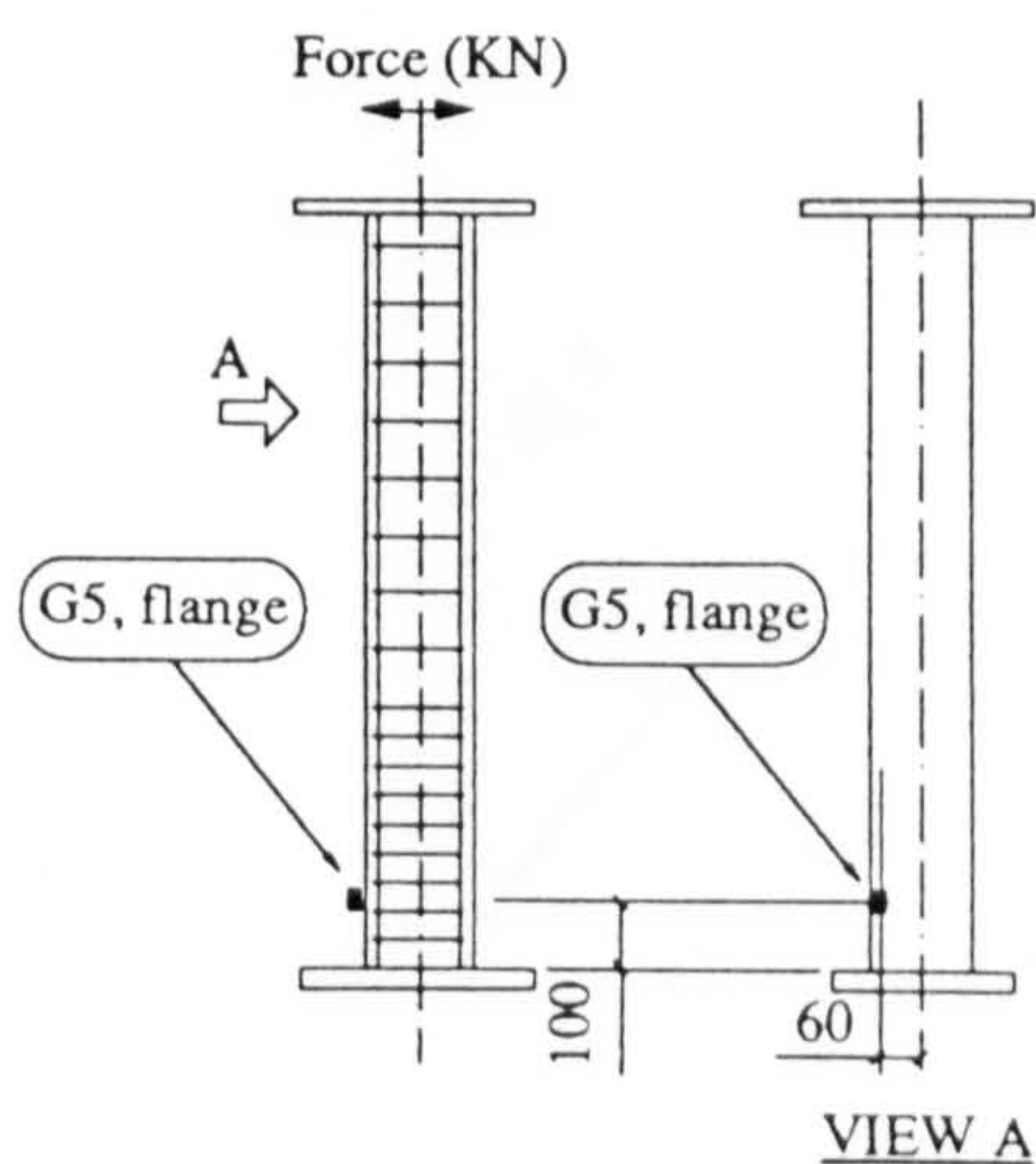
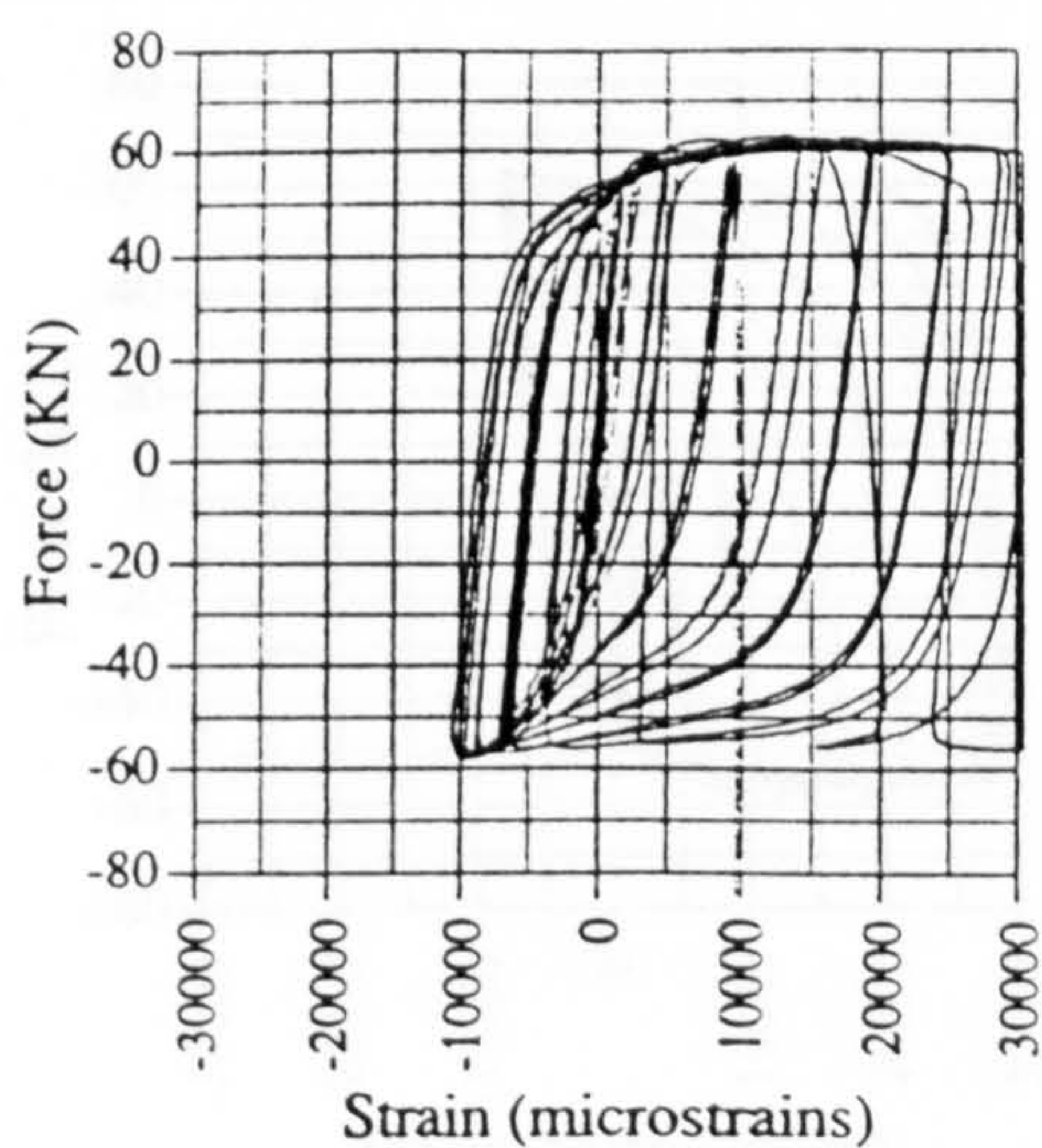


Fig. A.32 Force vs strain, IC01, G5

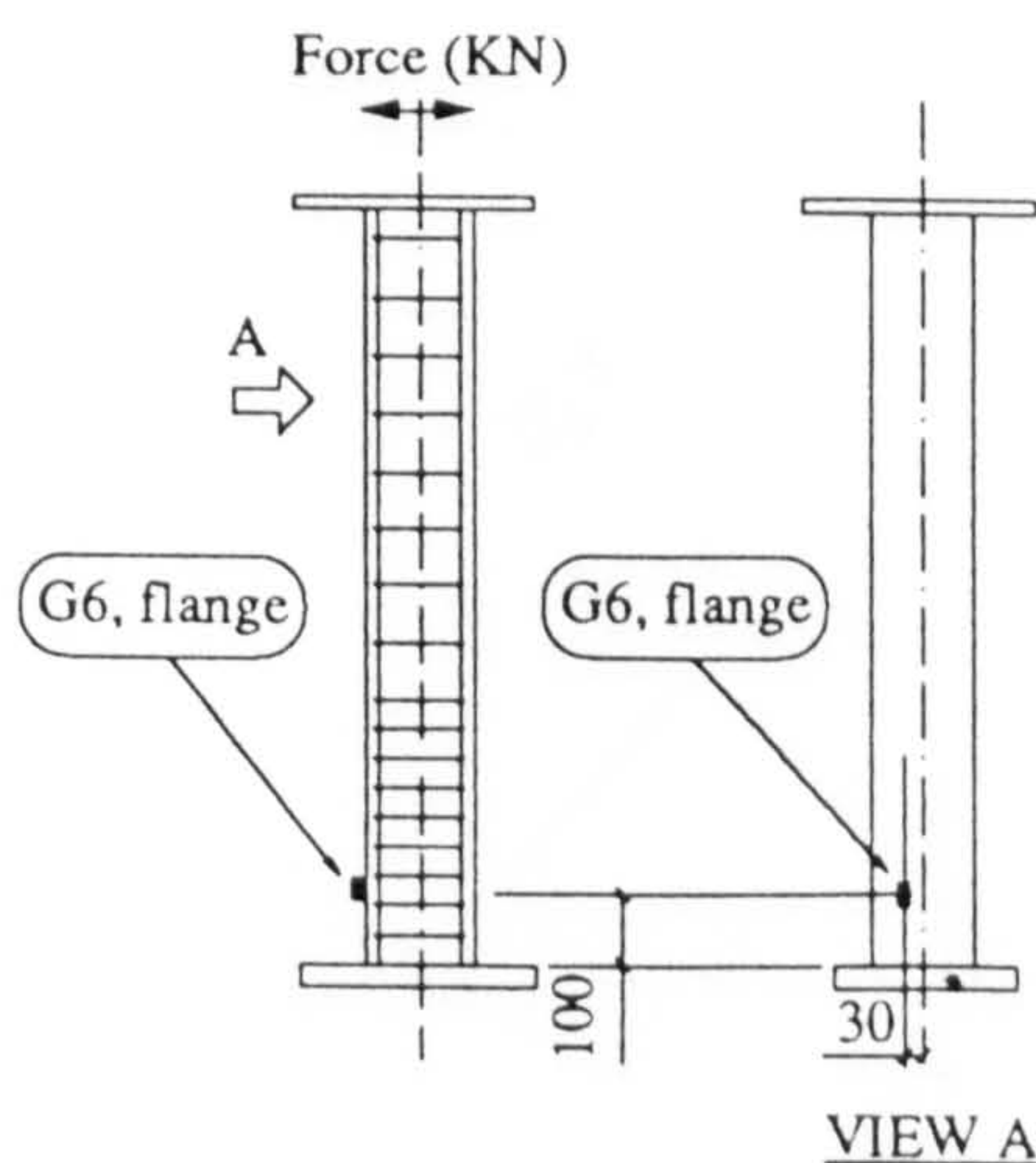
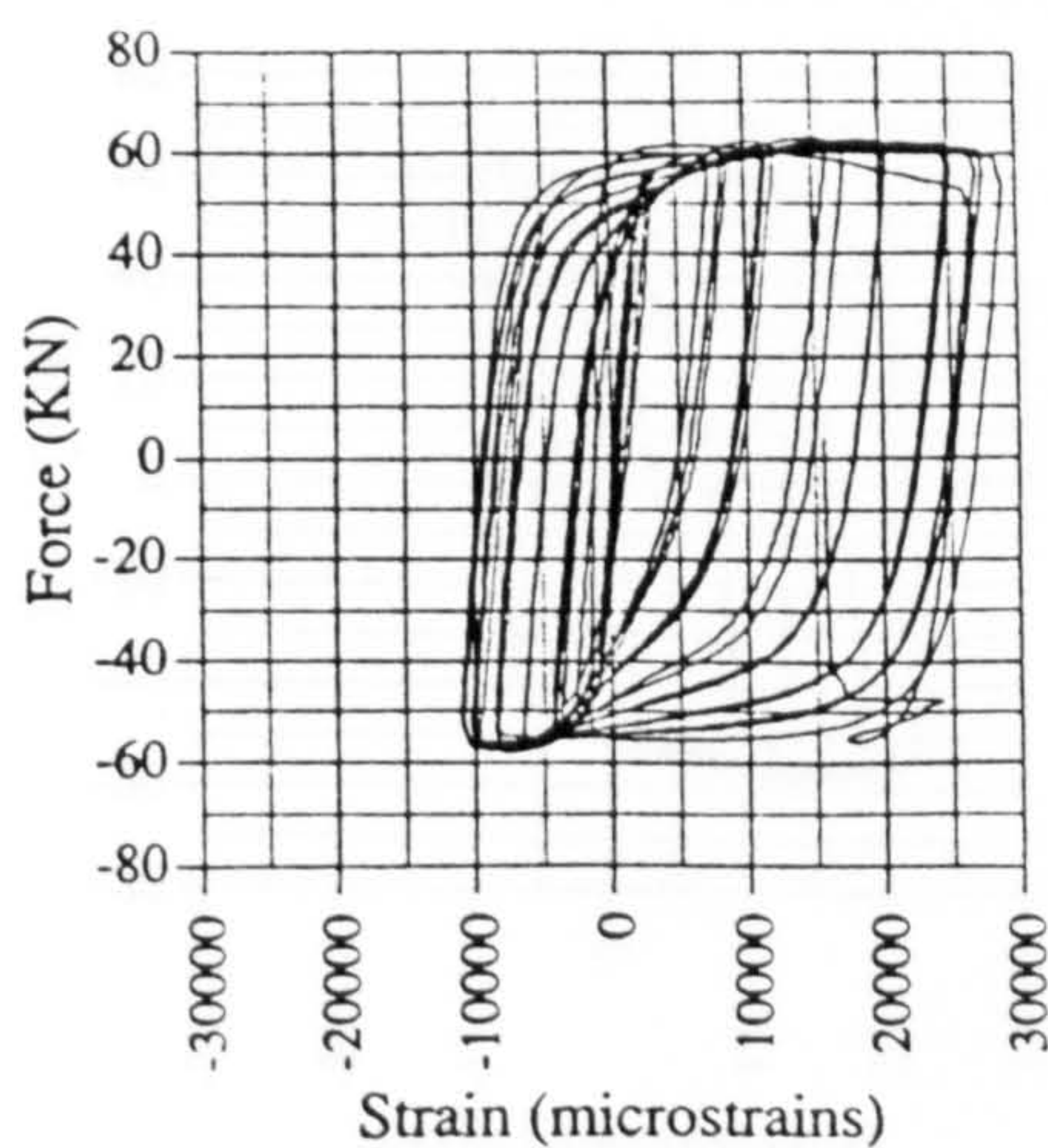


Fig. A.33 Force vs strain, IC01, G6

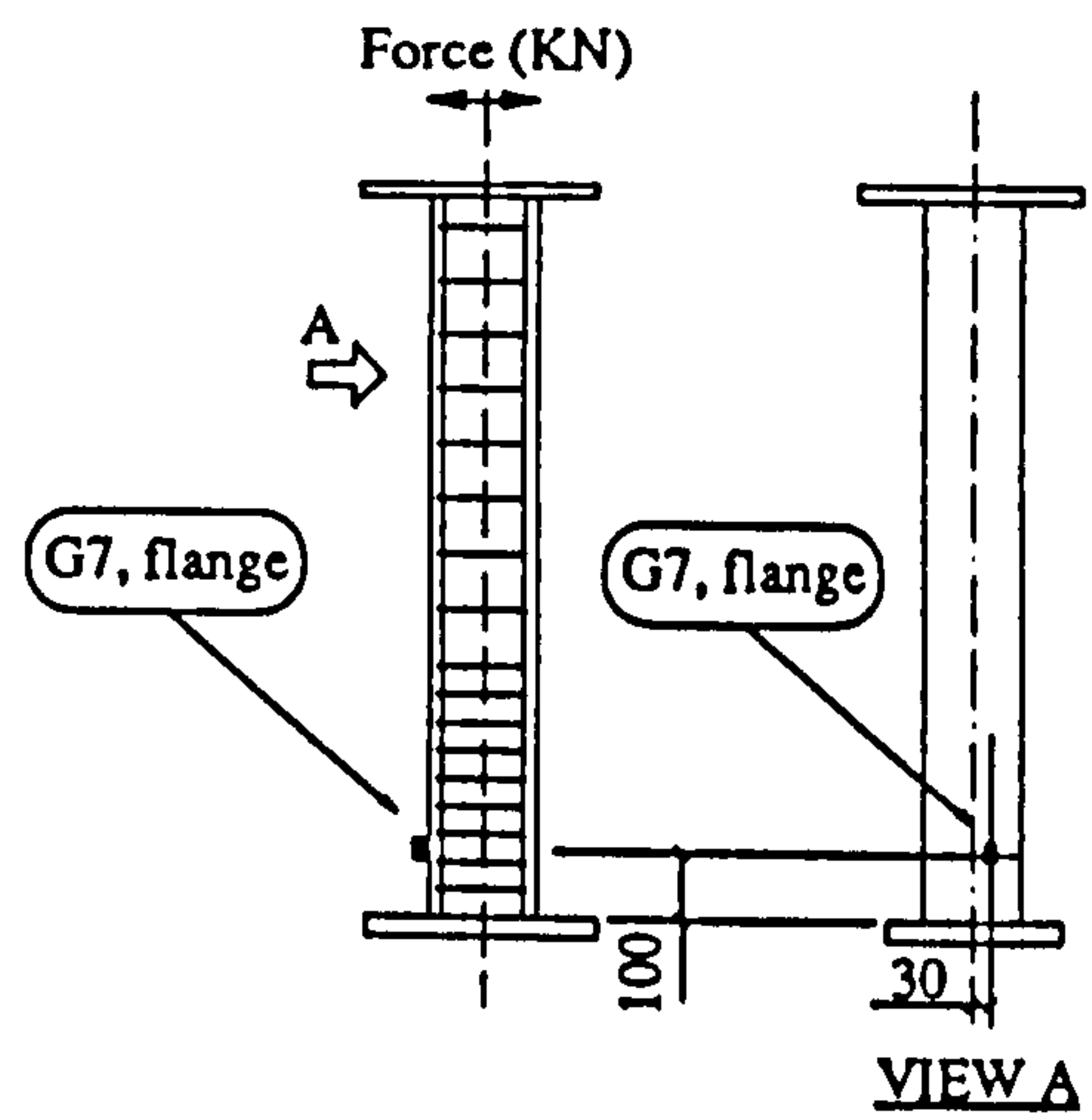
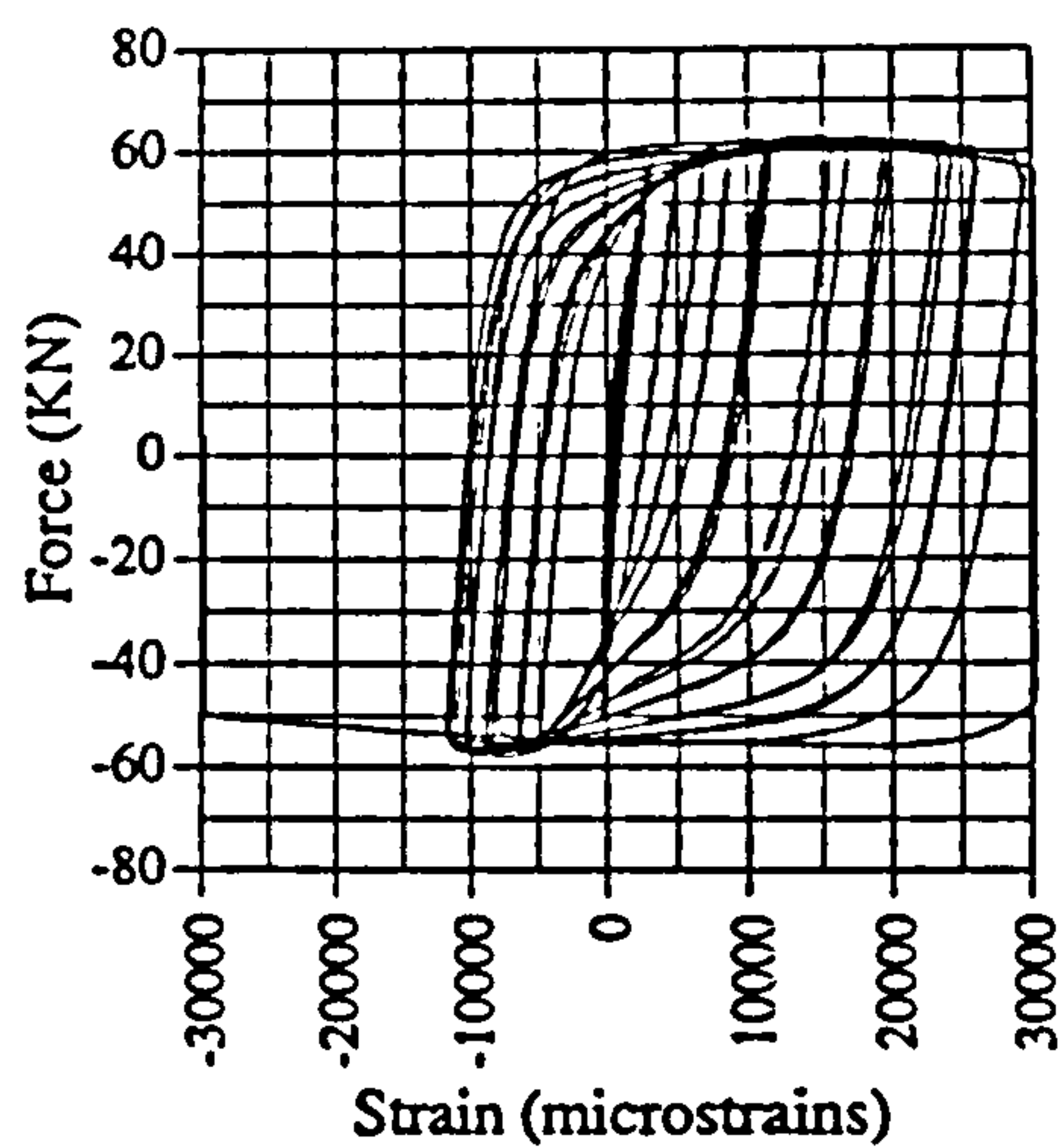


Fig. A.34 Force vs strain, IC01, G7

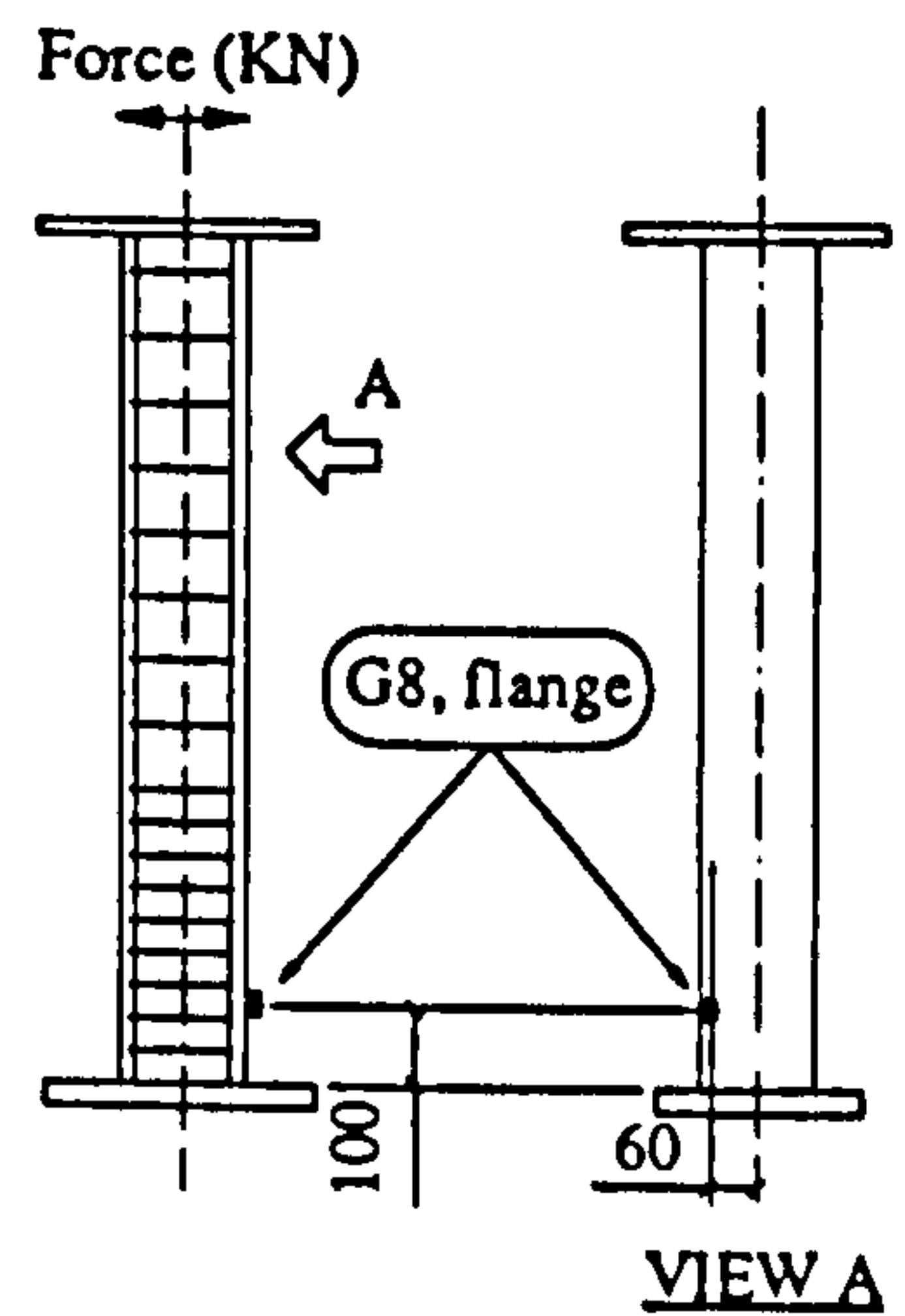
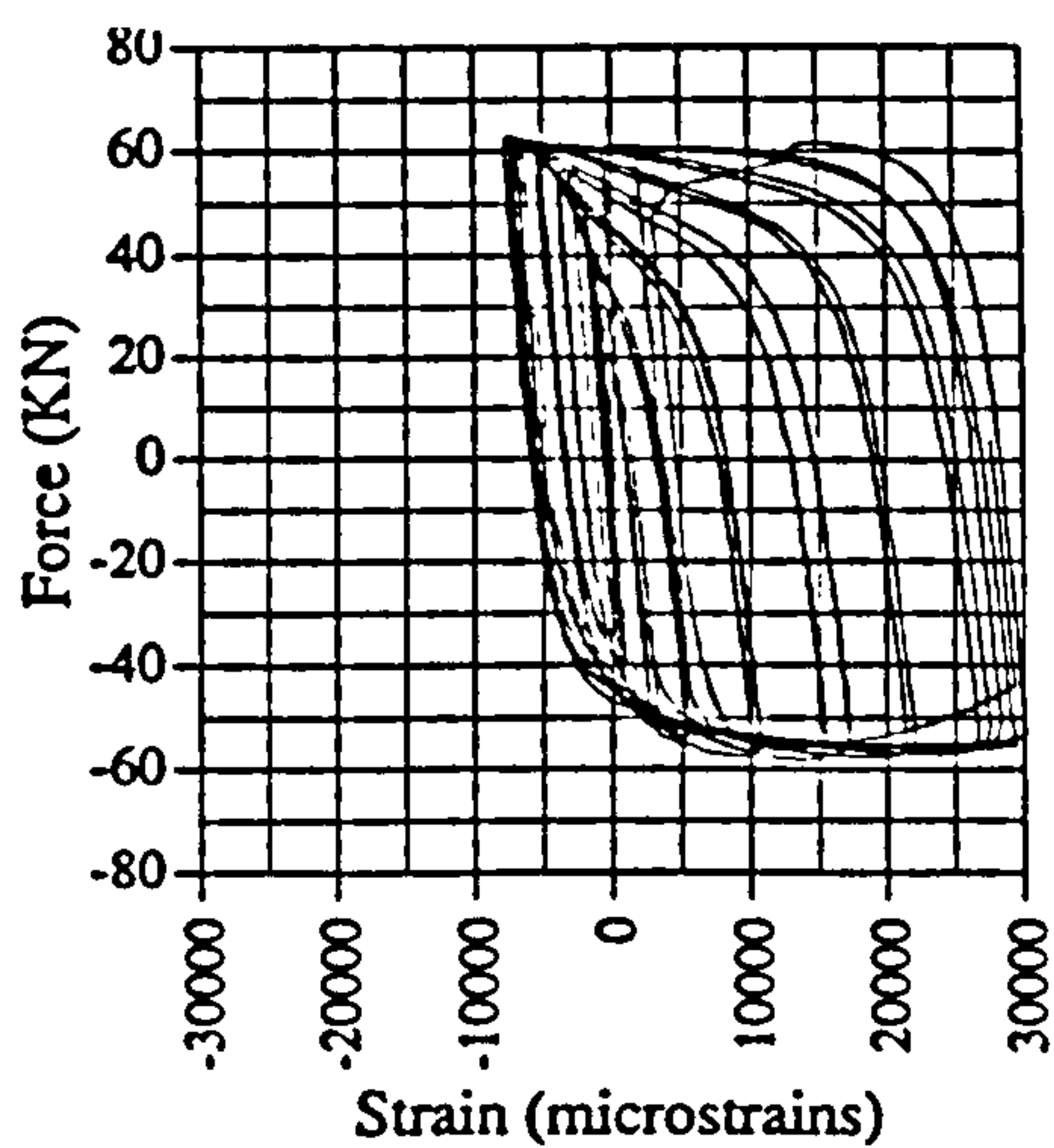


Fig. A.35 Force vs strain, IC01, G8

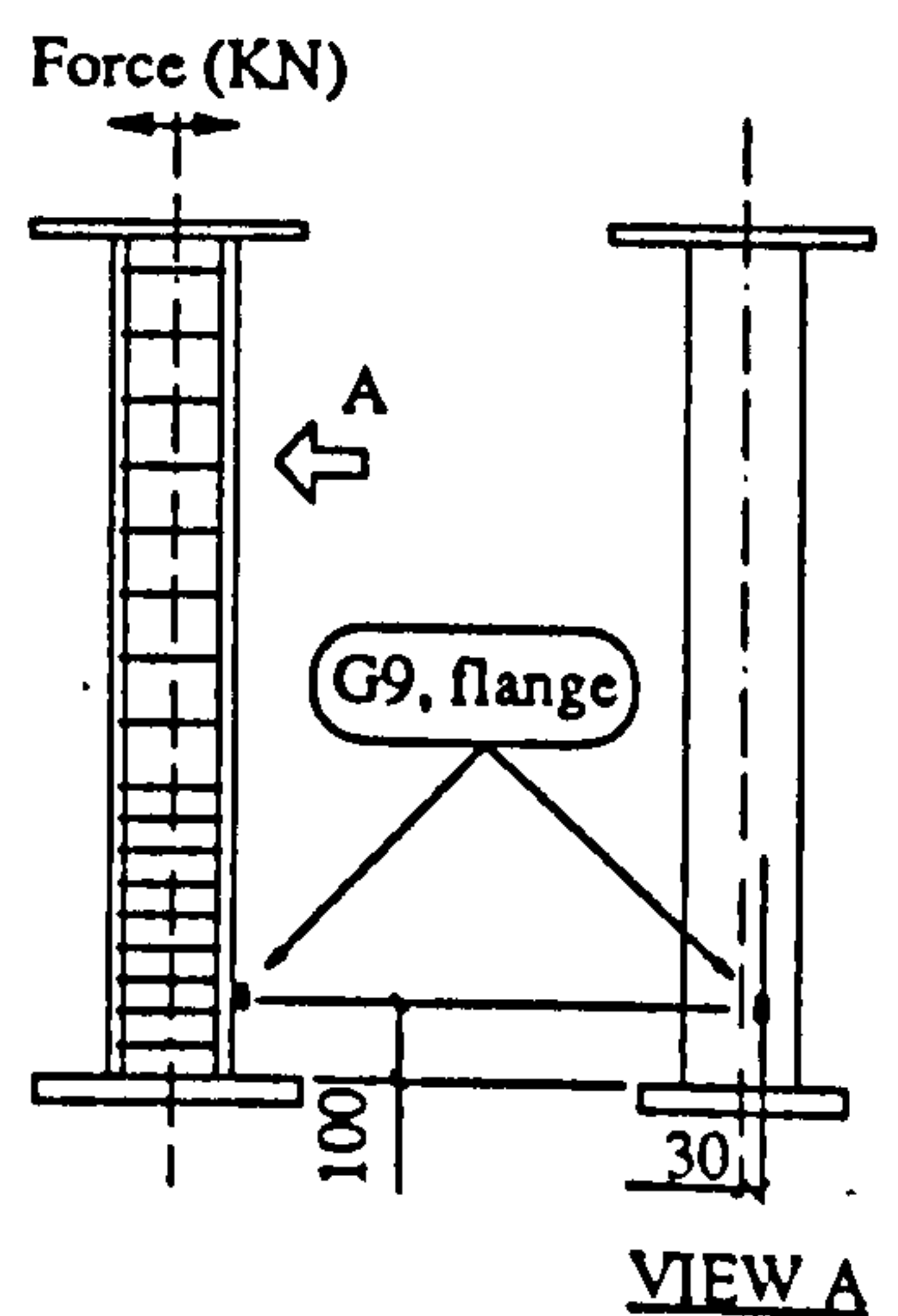
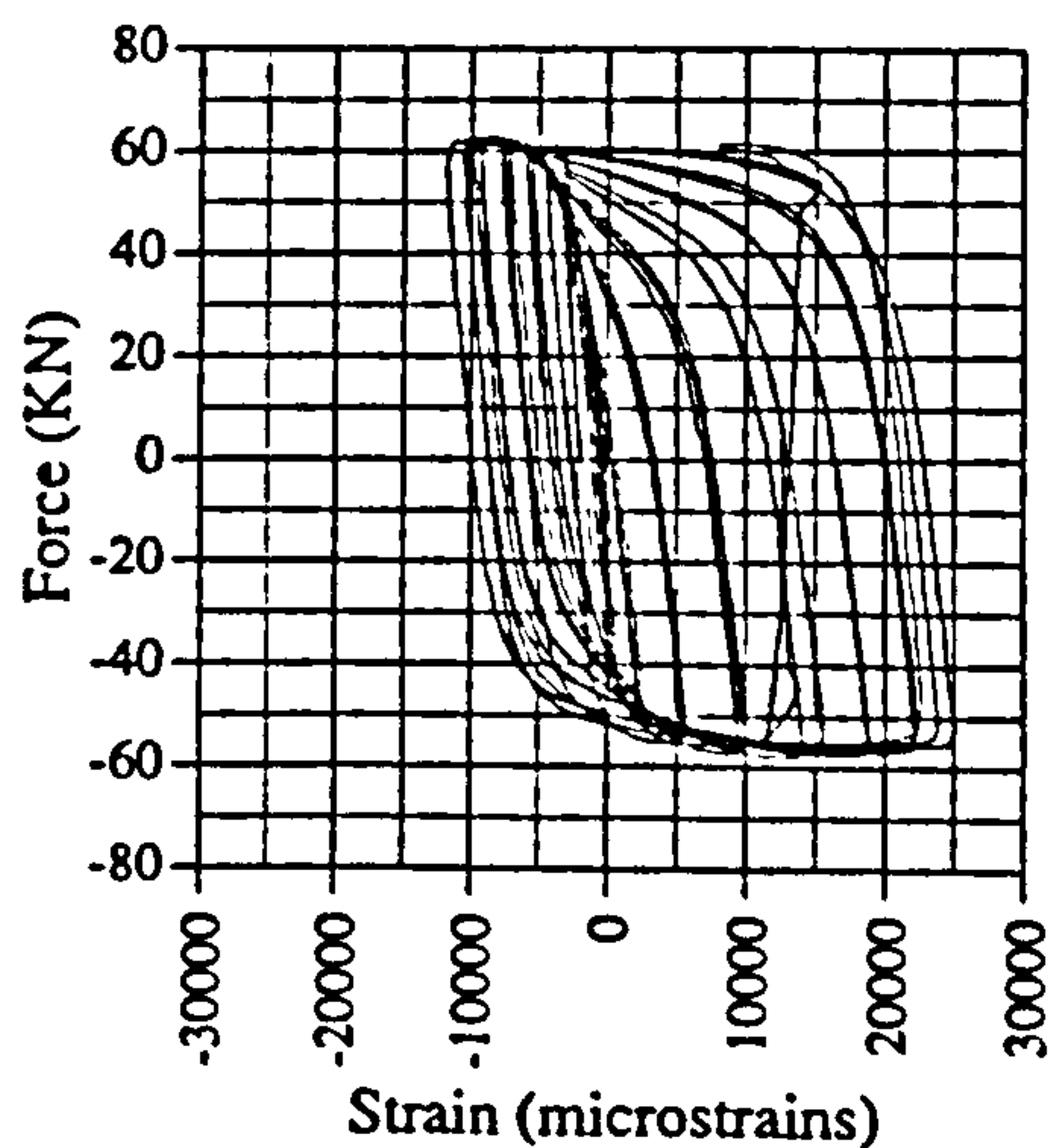
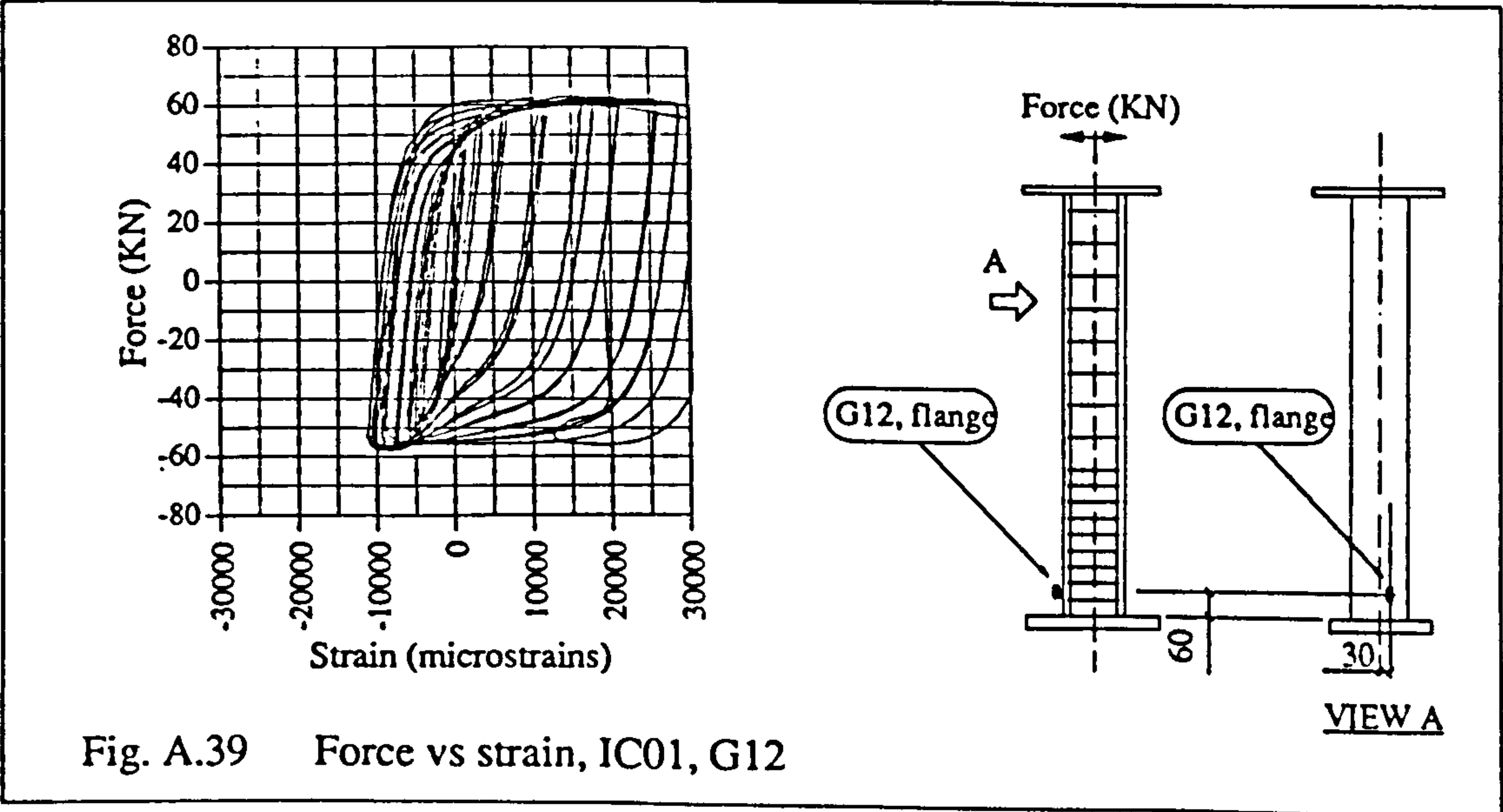
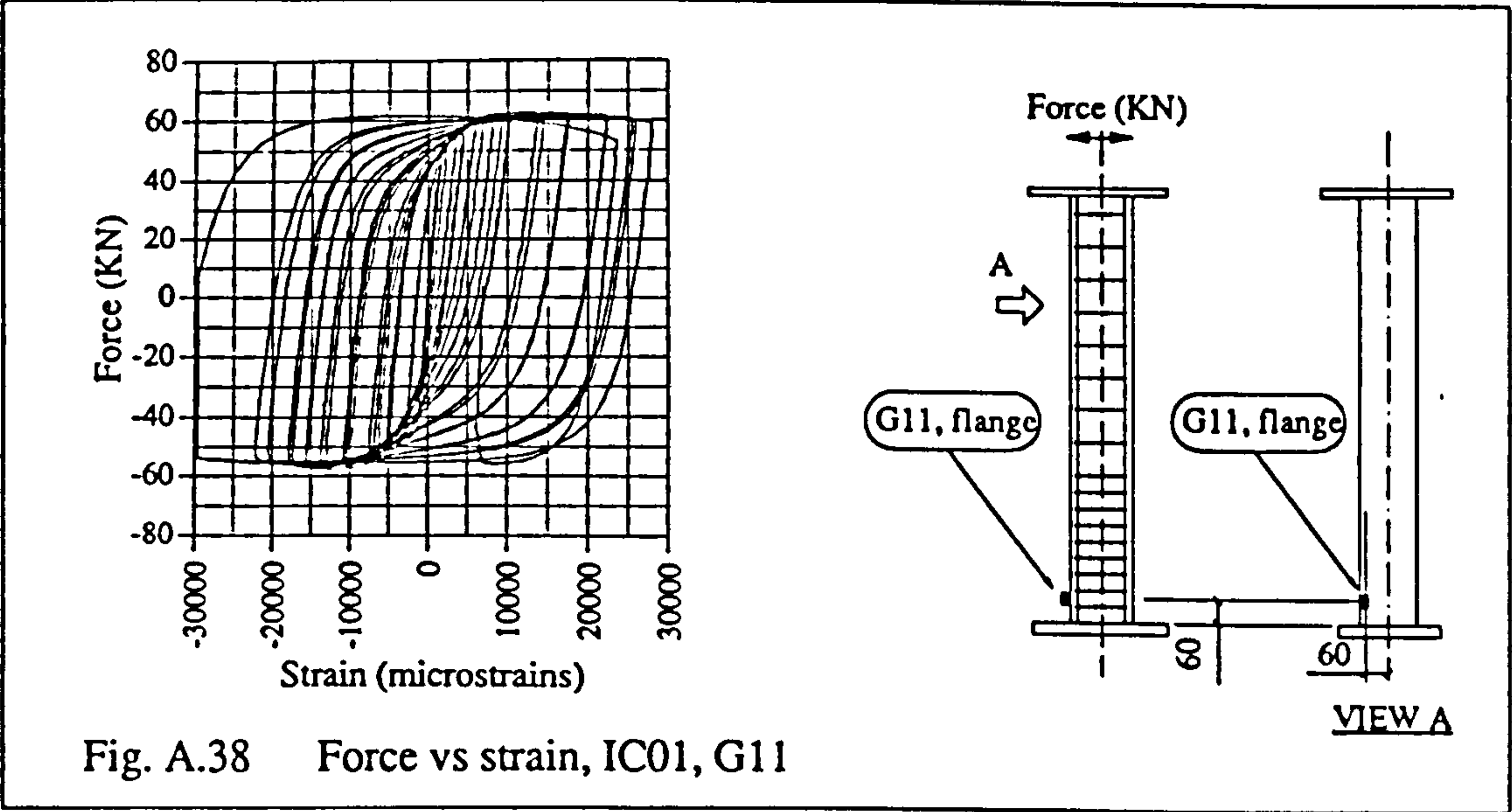
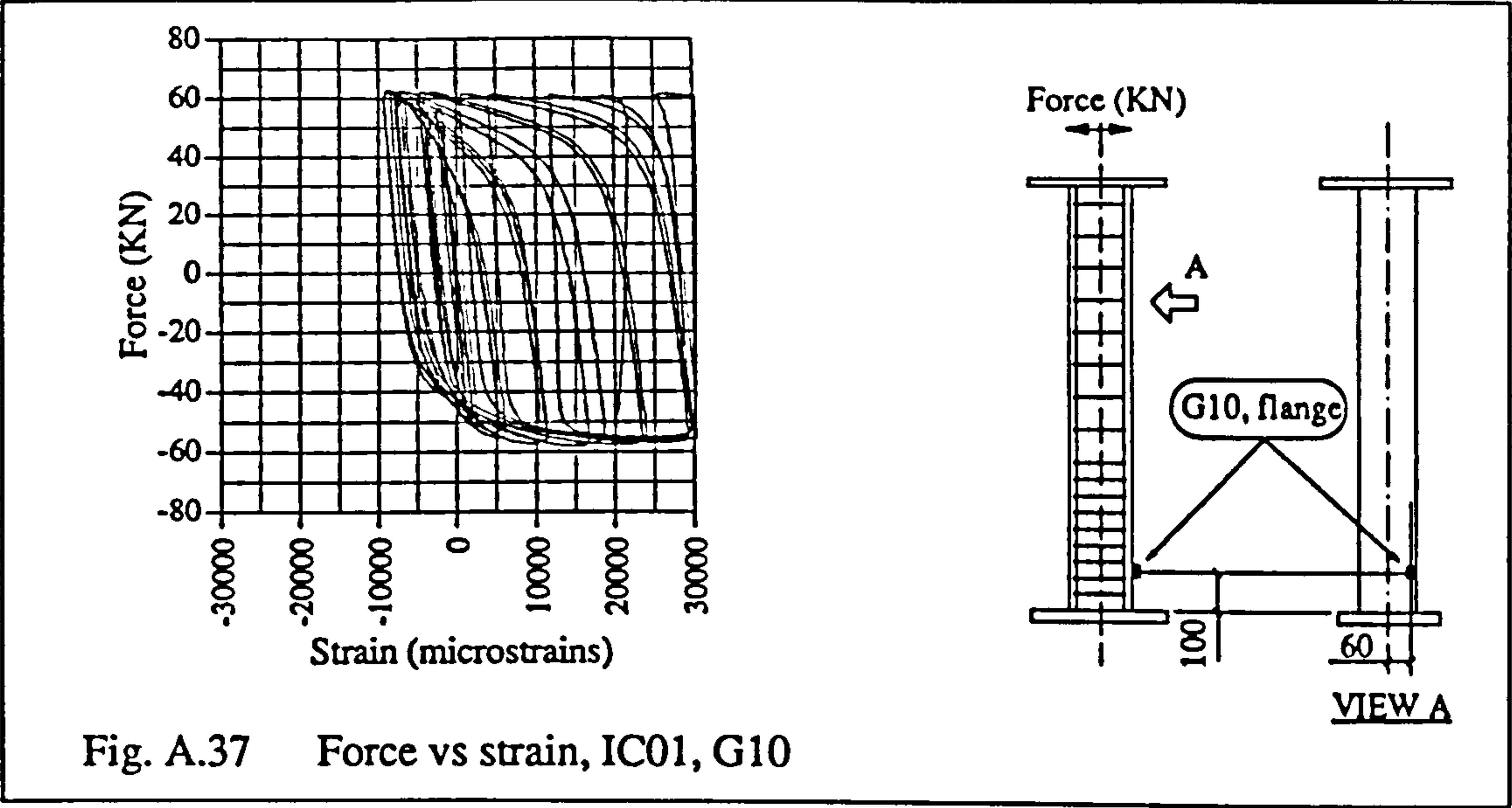
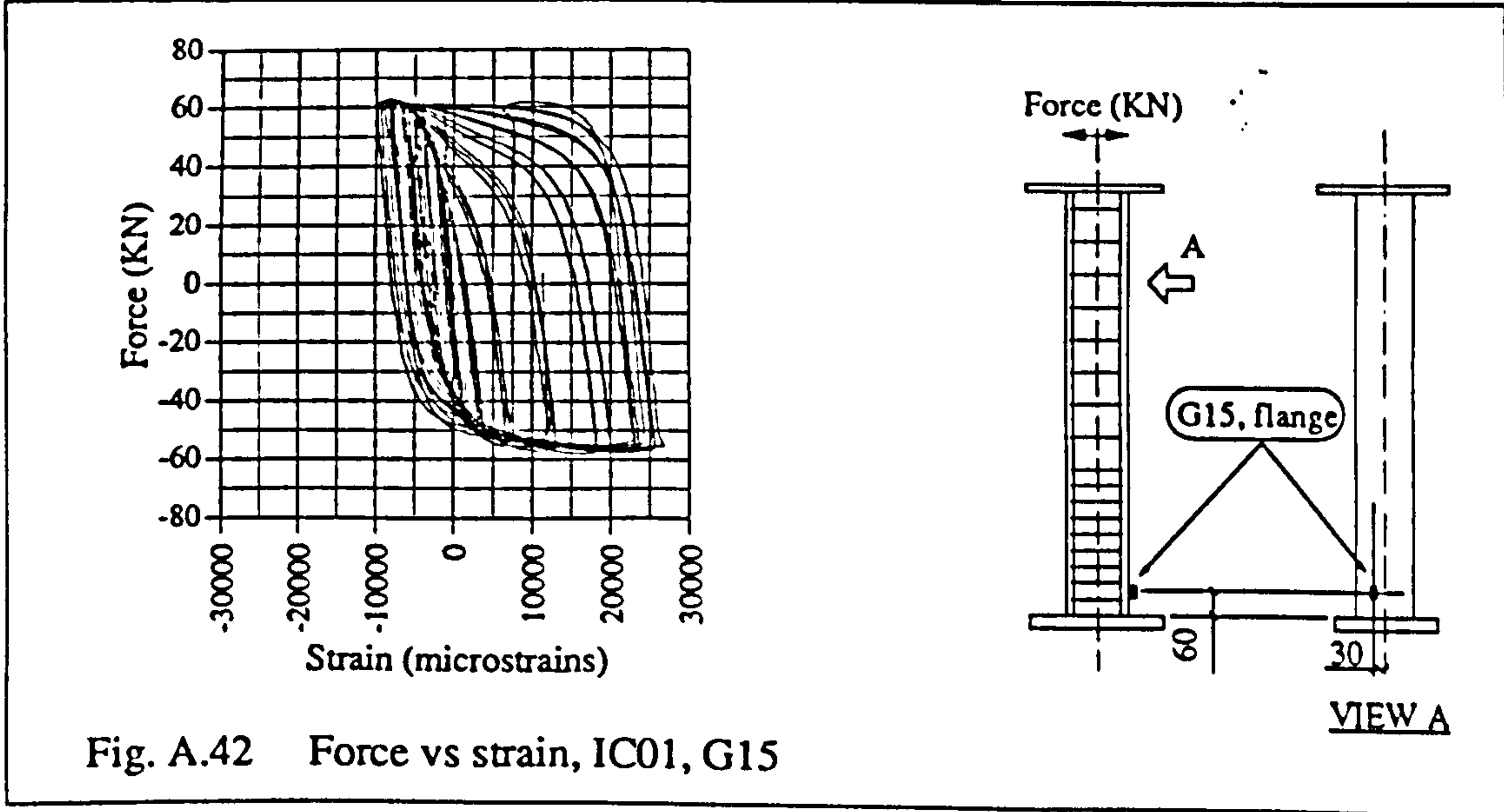
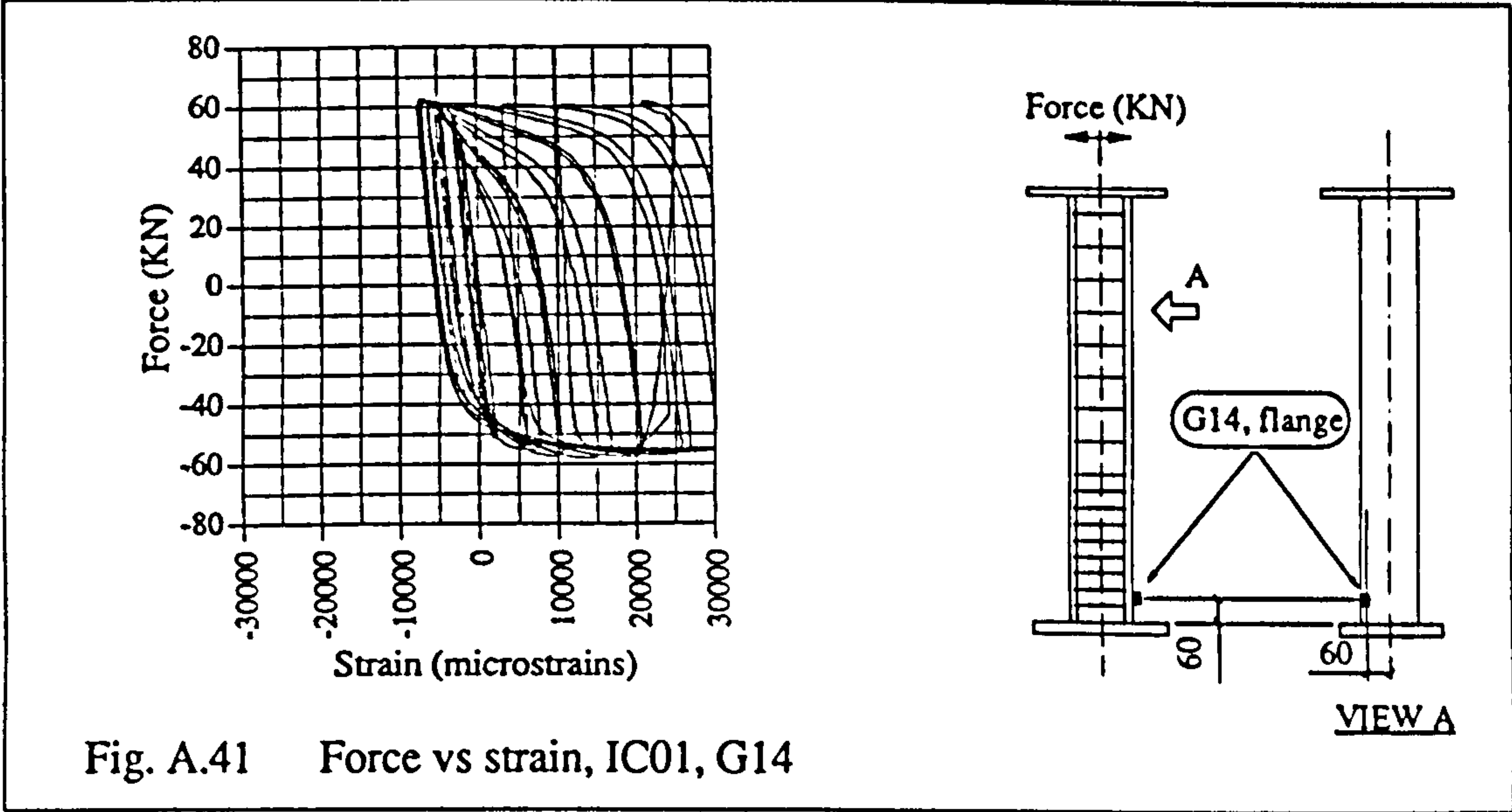
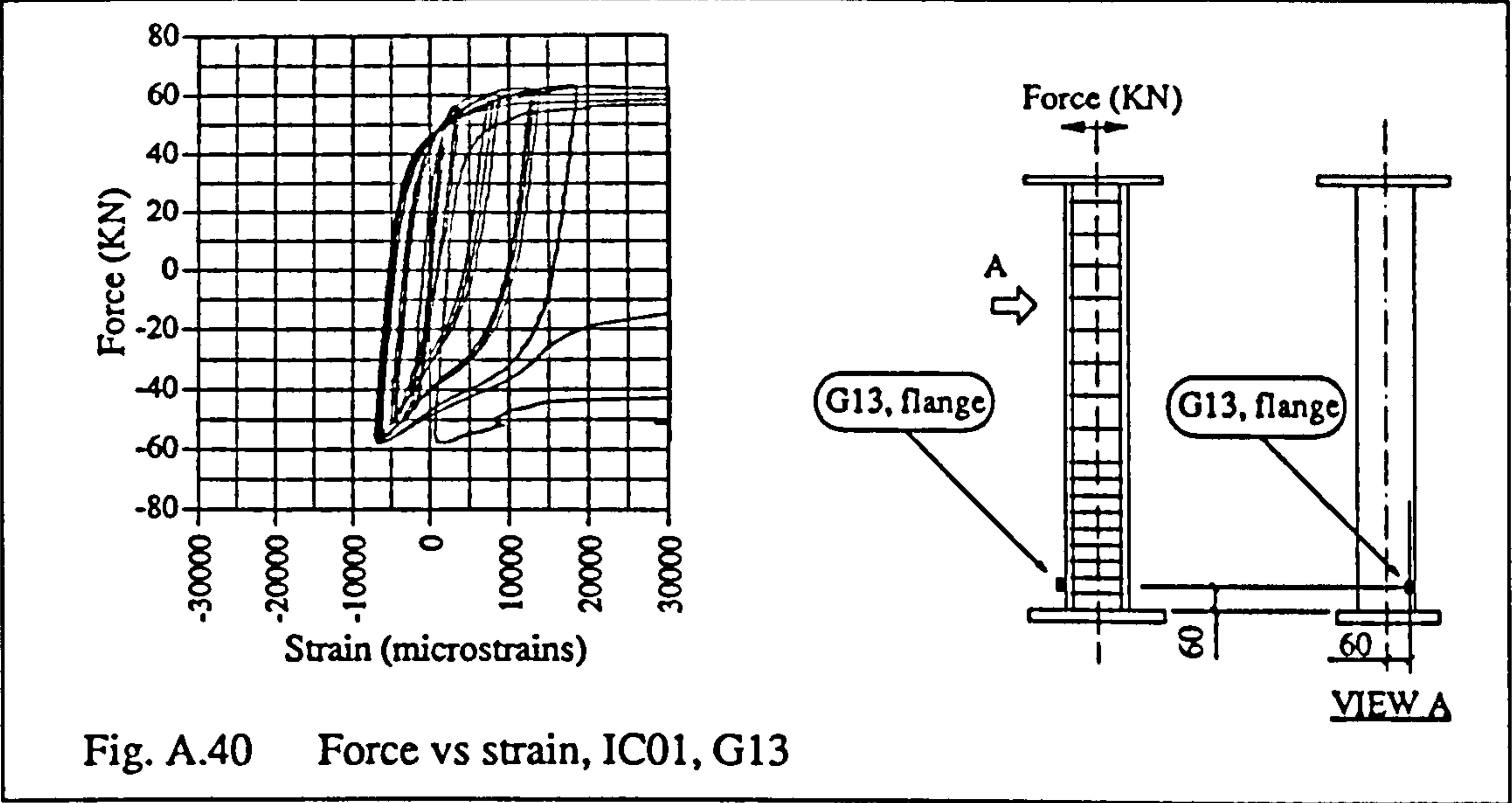


Fig. A.36 Force vs strain, IC01, G9





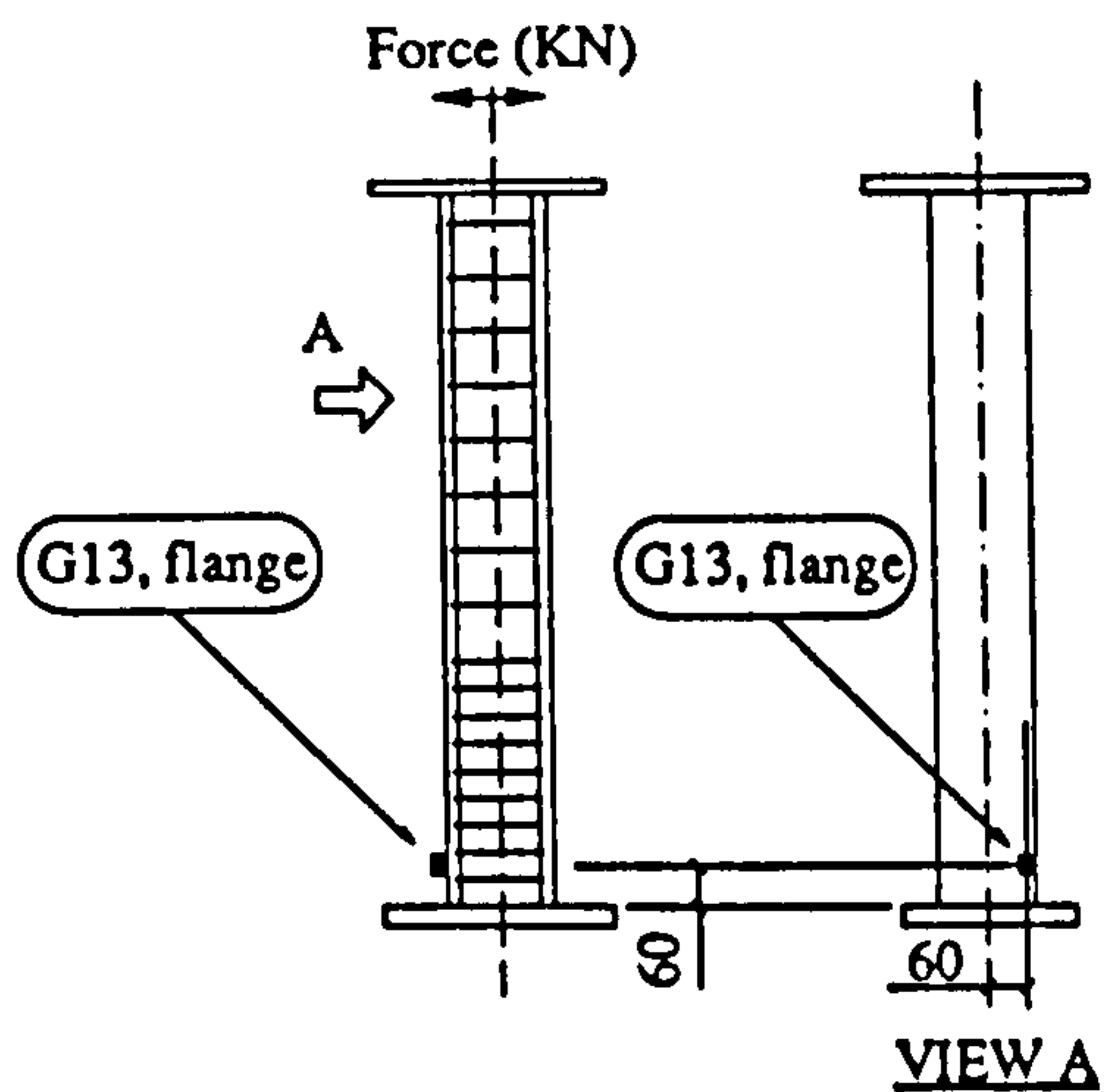
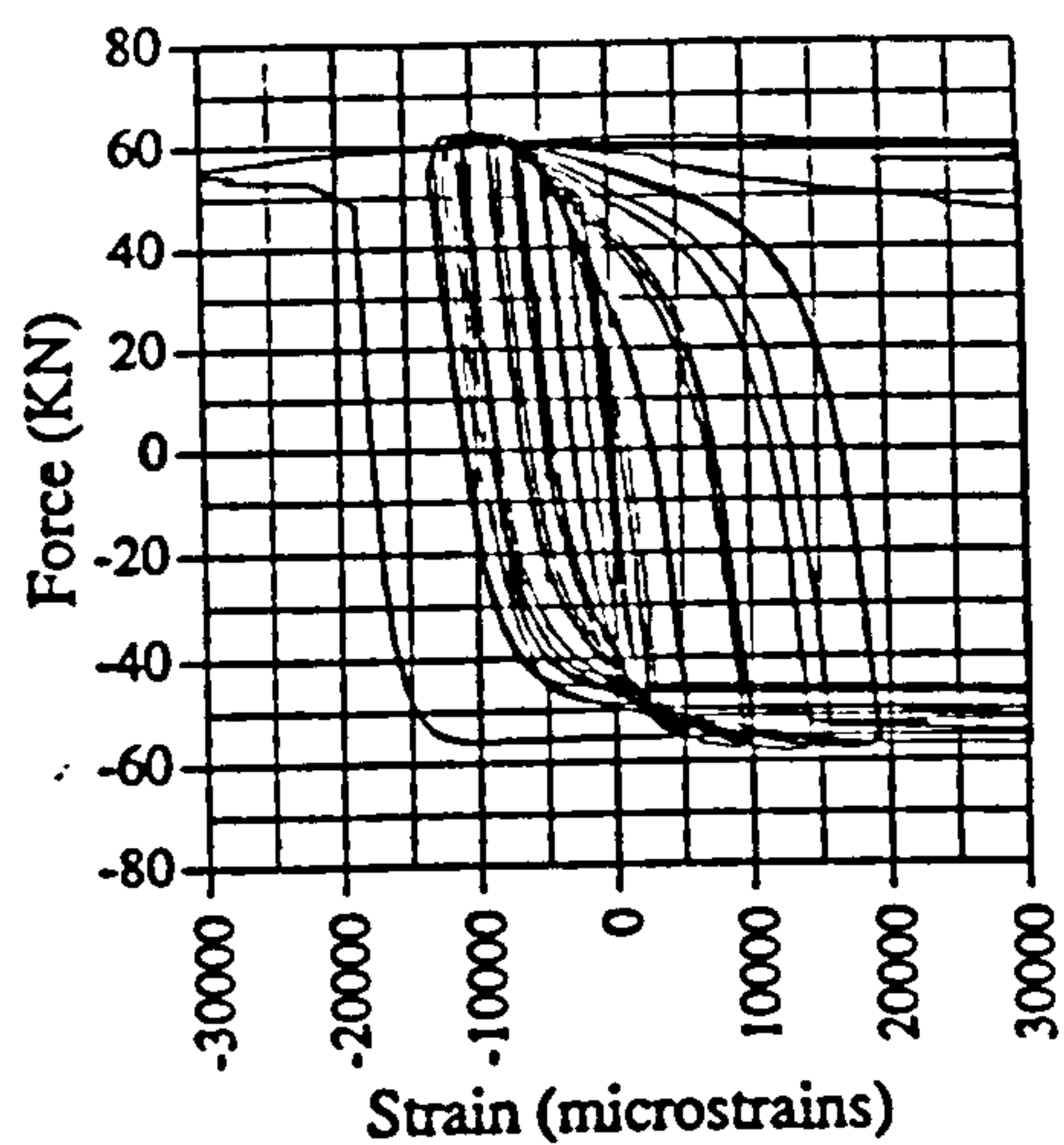


Fig. A.43 Force vs strain, IC01, G16

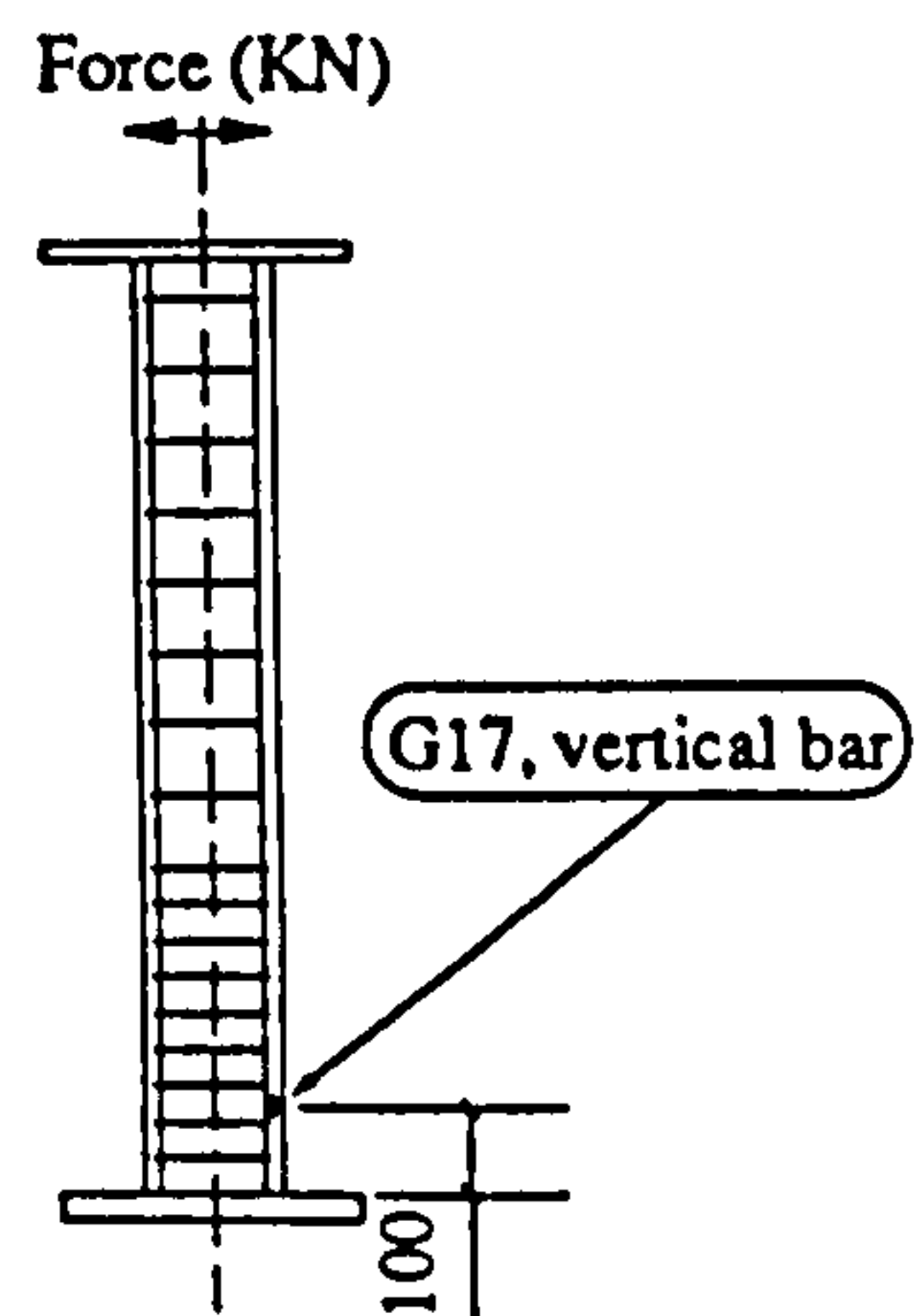
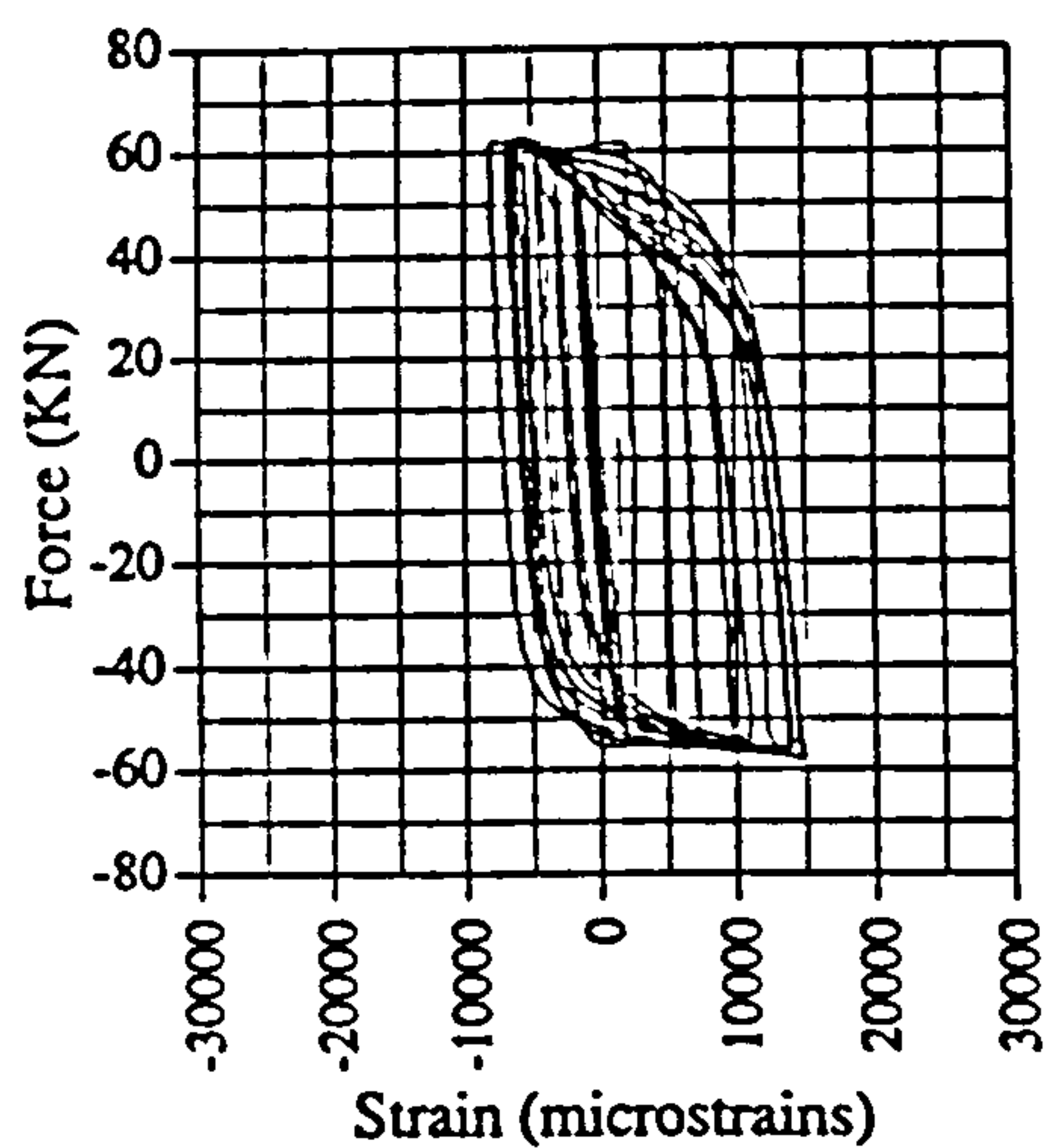


Fig. A.44 Force vs strain, IC01, G17

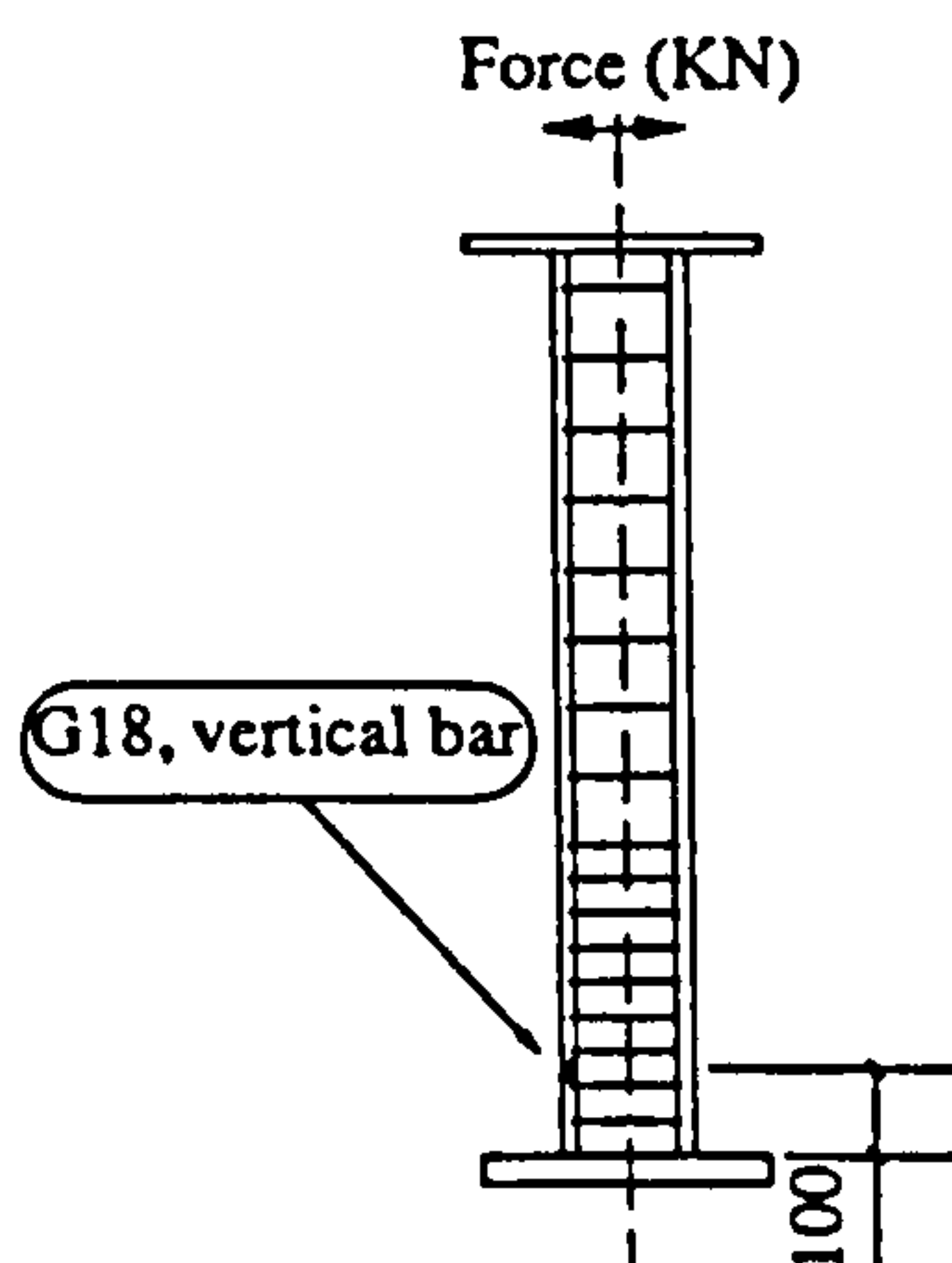
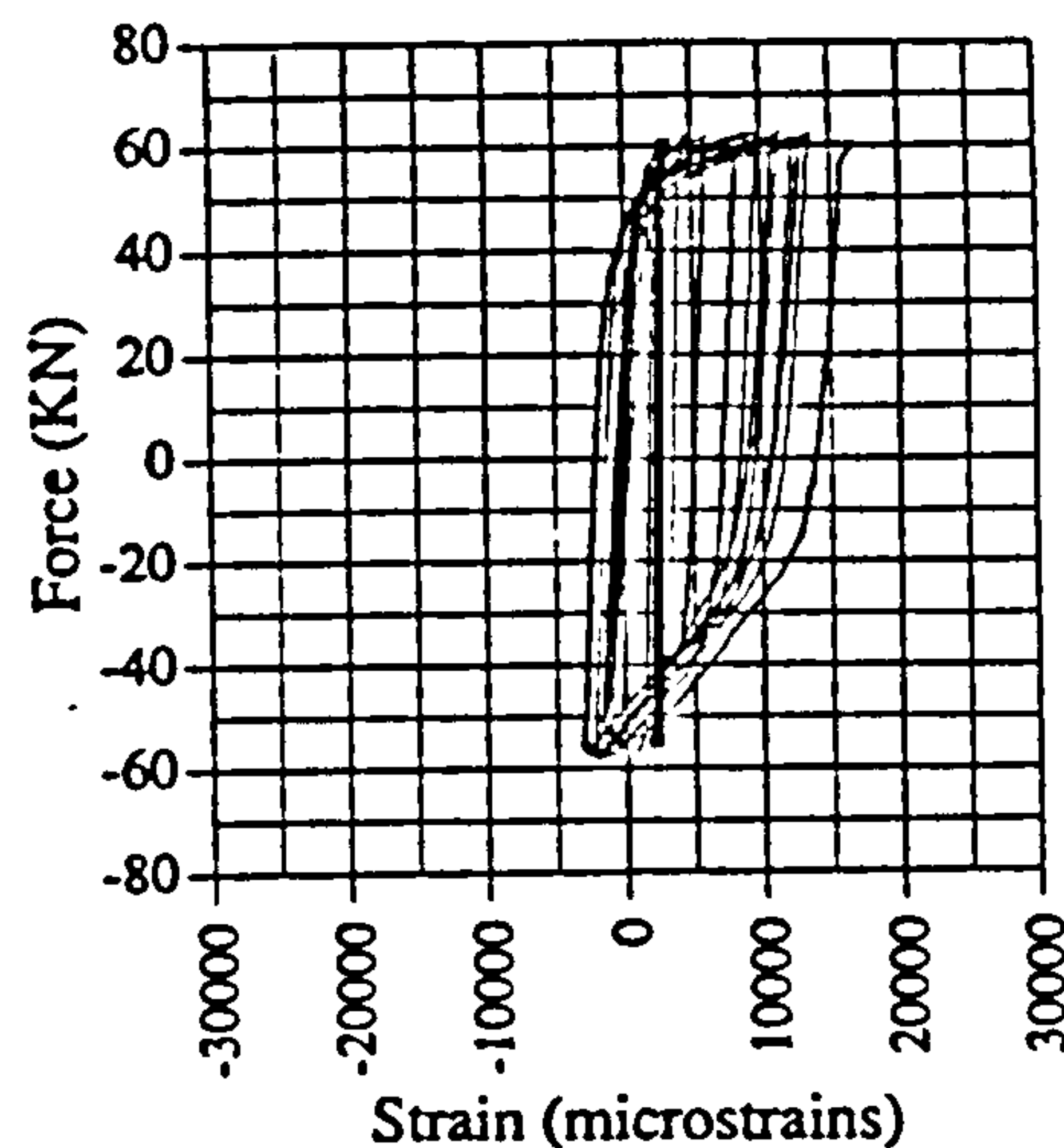


Fig. A.45 Force vs strain, IC01, G18

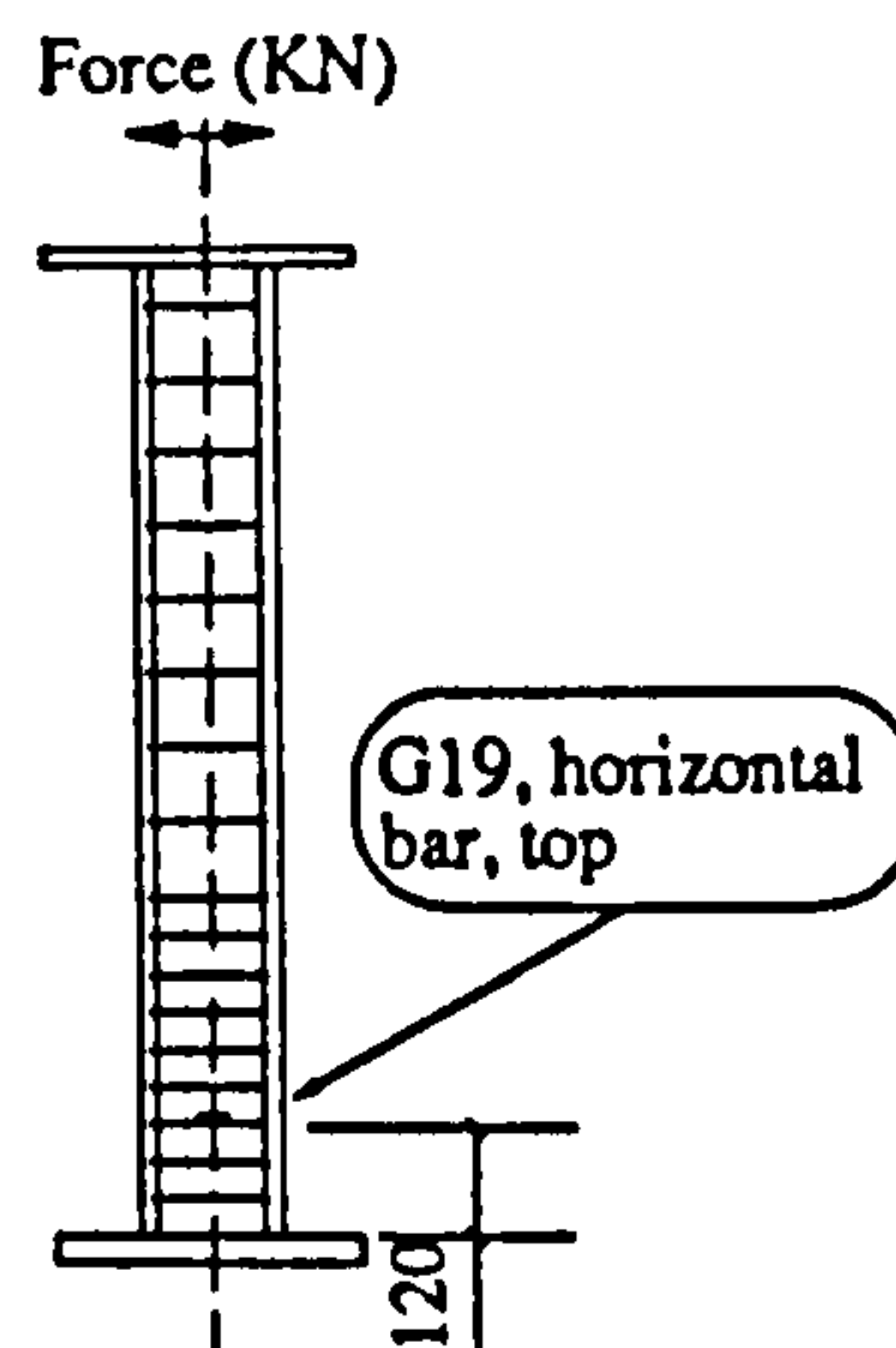
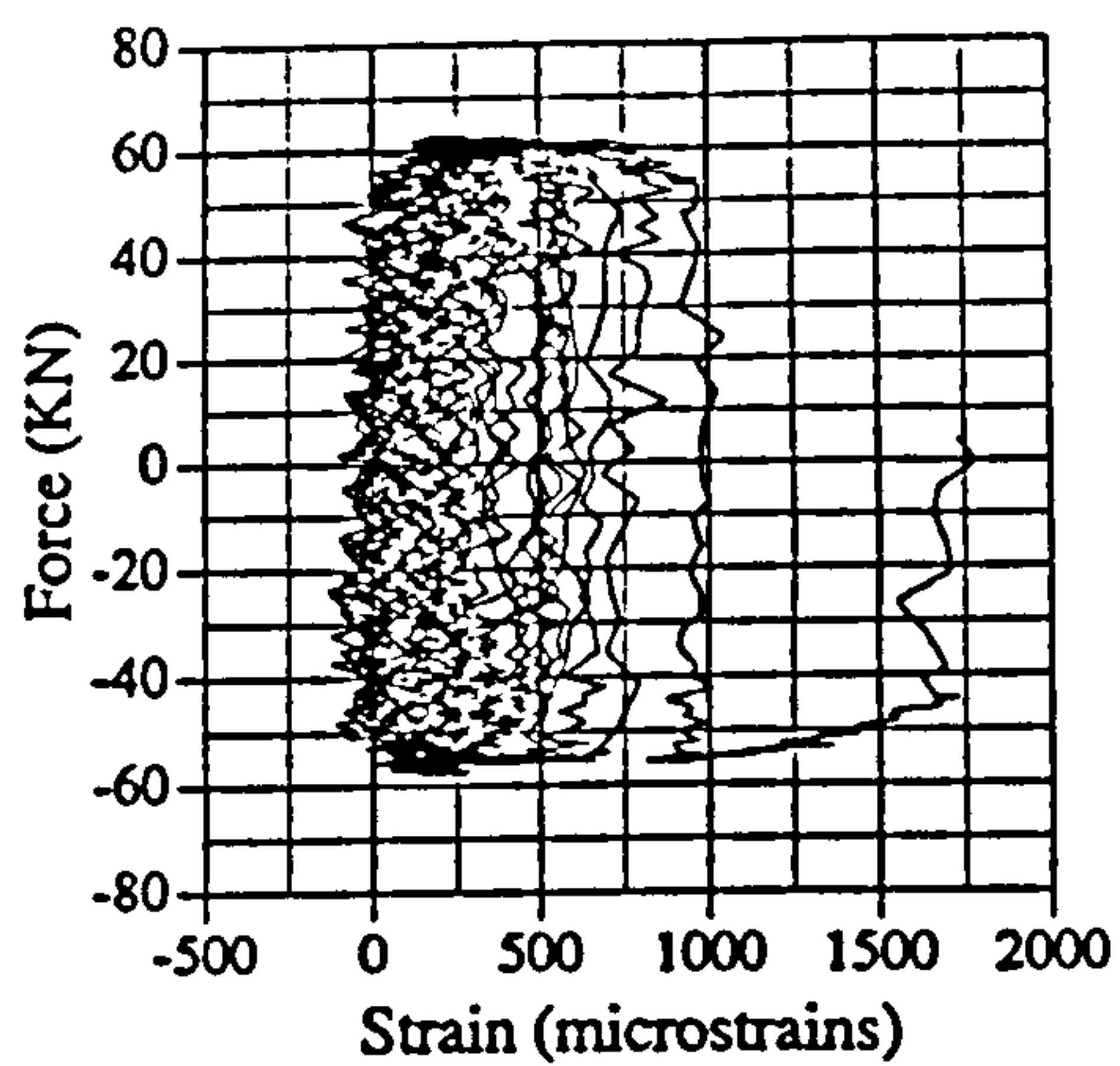


Fig. A.46 Force vs strain, IC01, G19

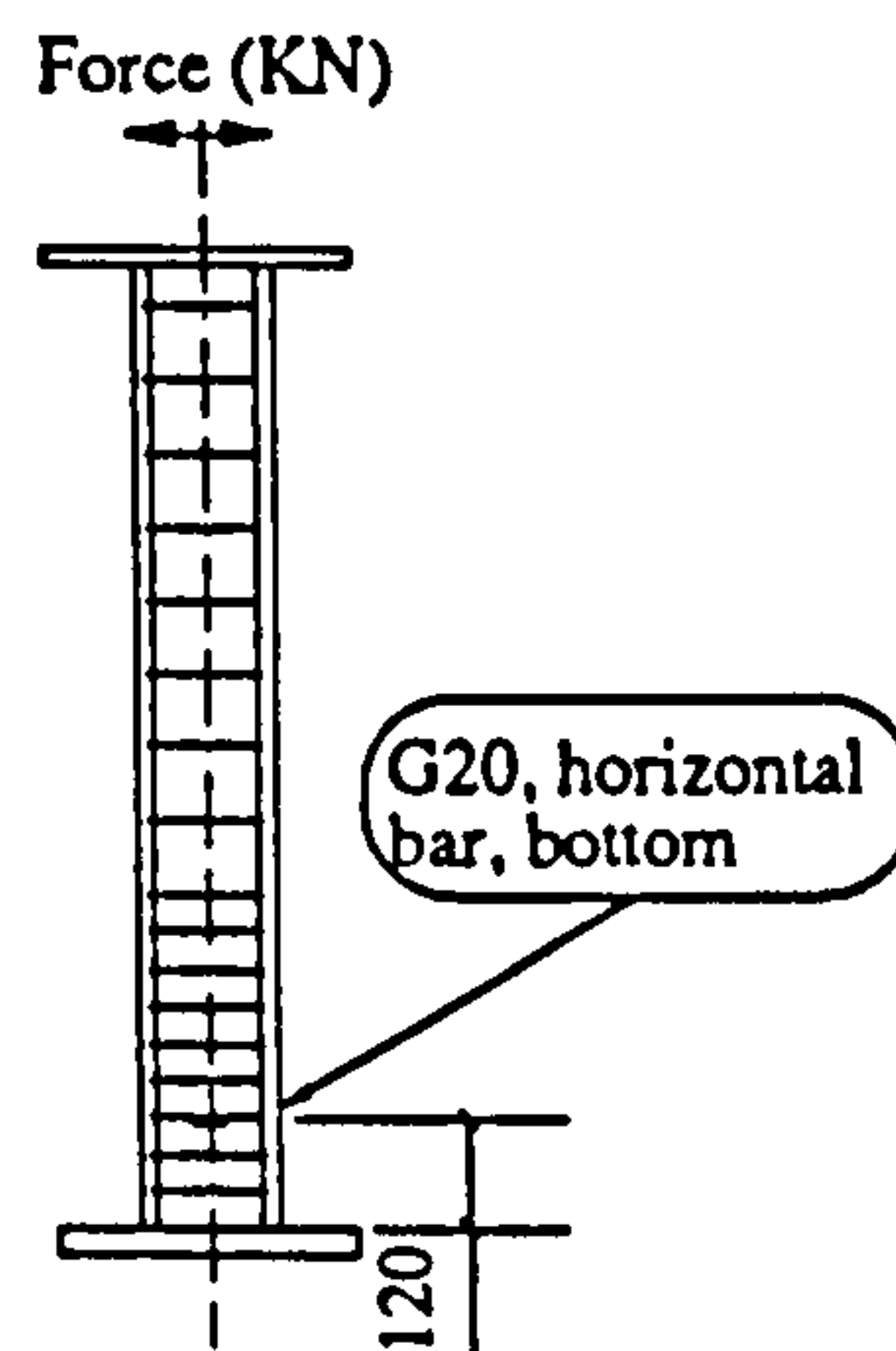
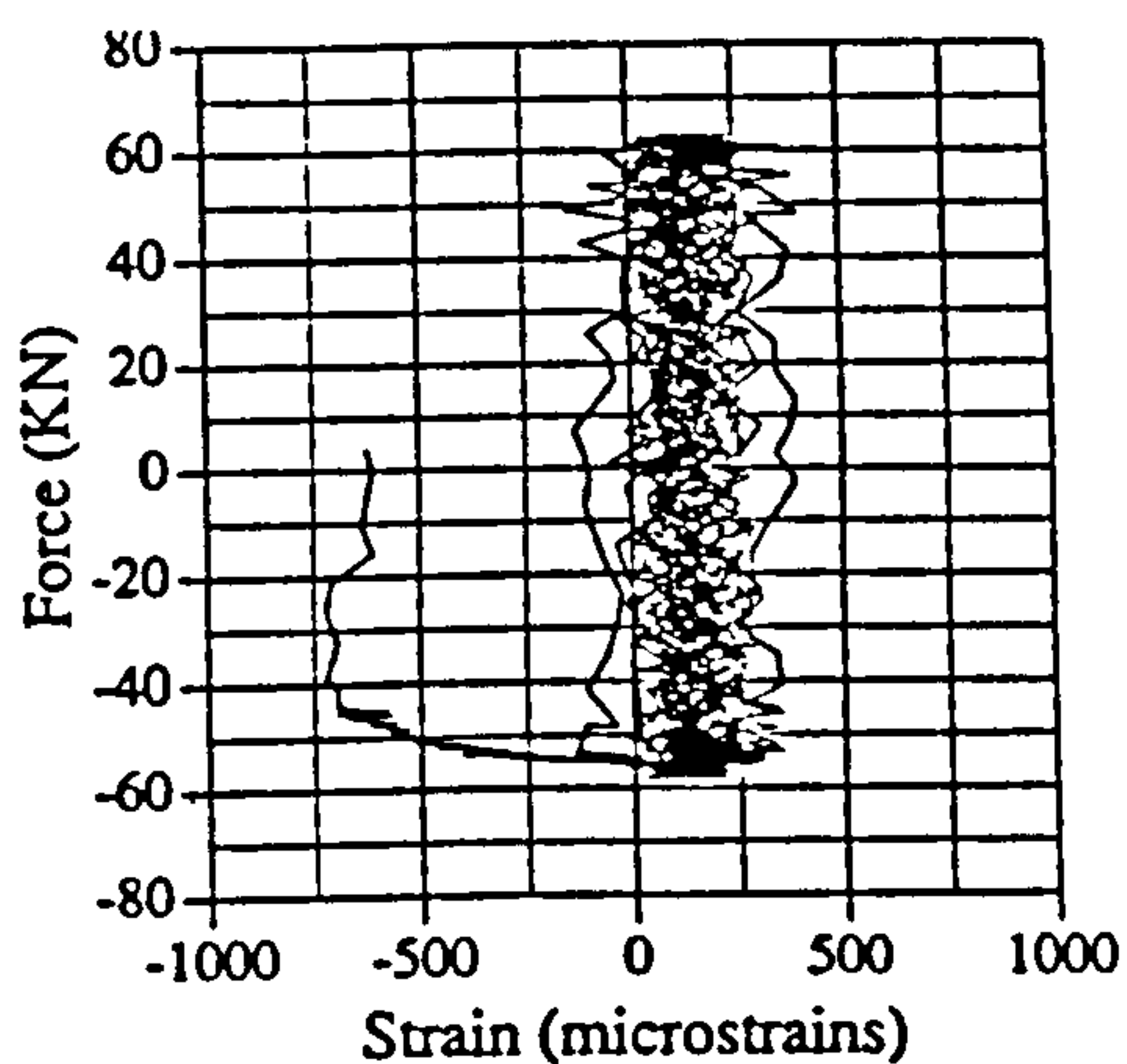


Fig. A.47 Force vs strain, IC01, G20

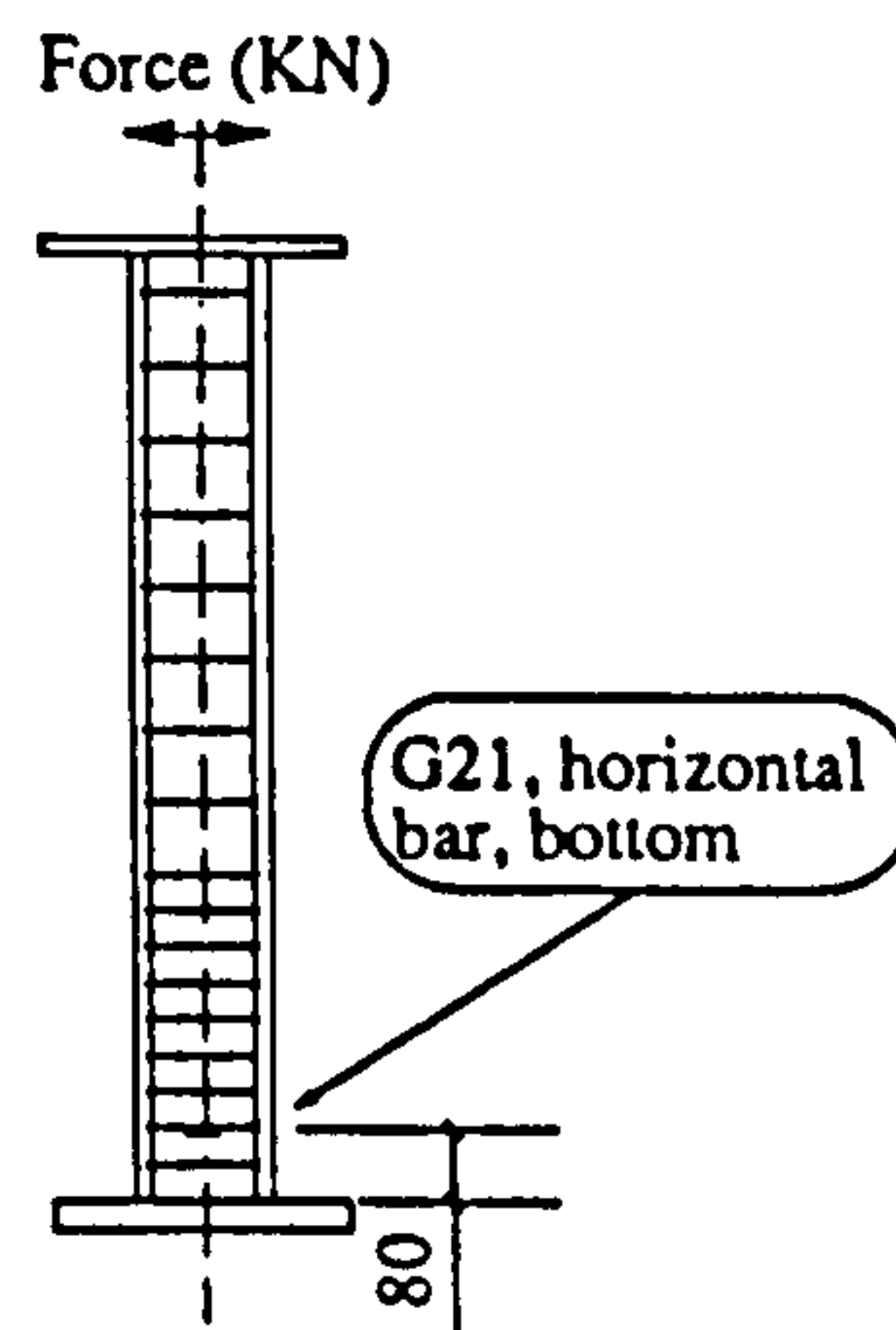
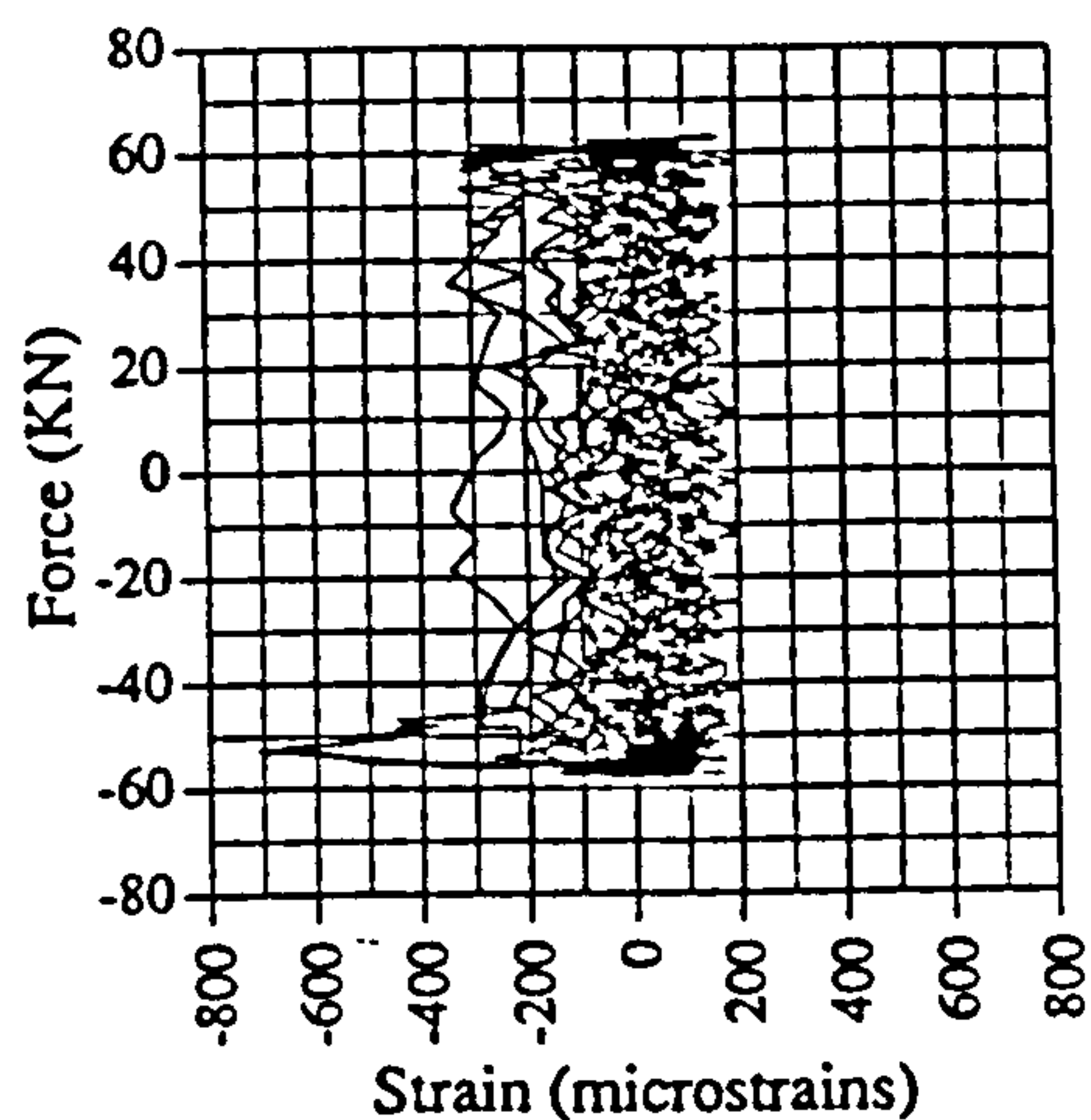


Fig. A.48 Force vs strain, IC01, G21

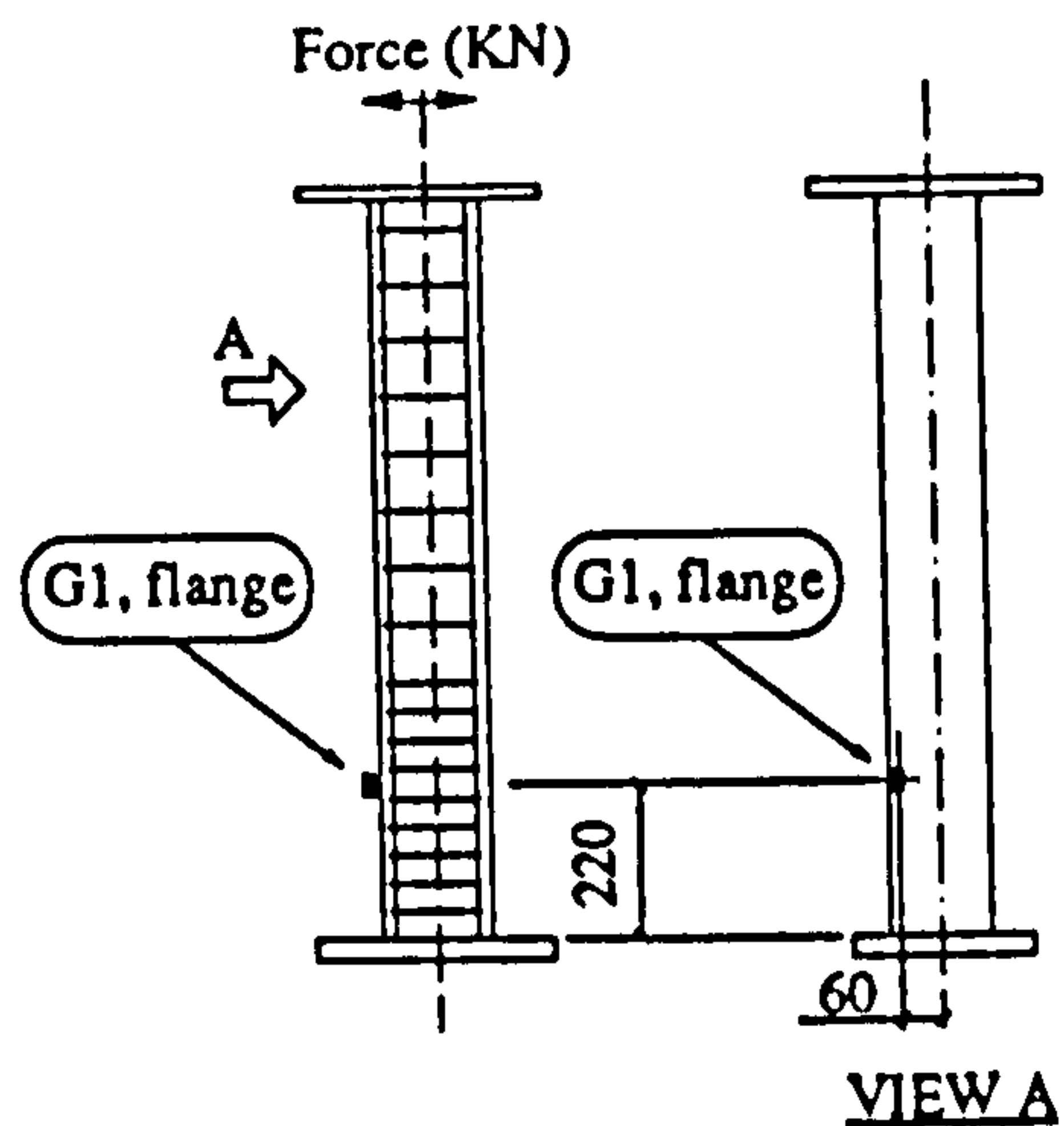
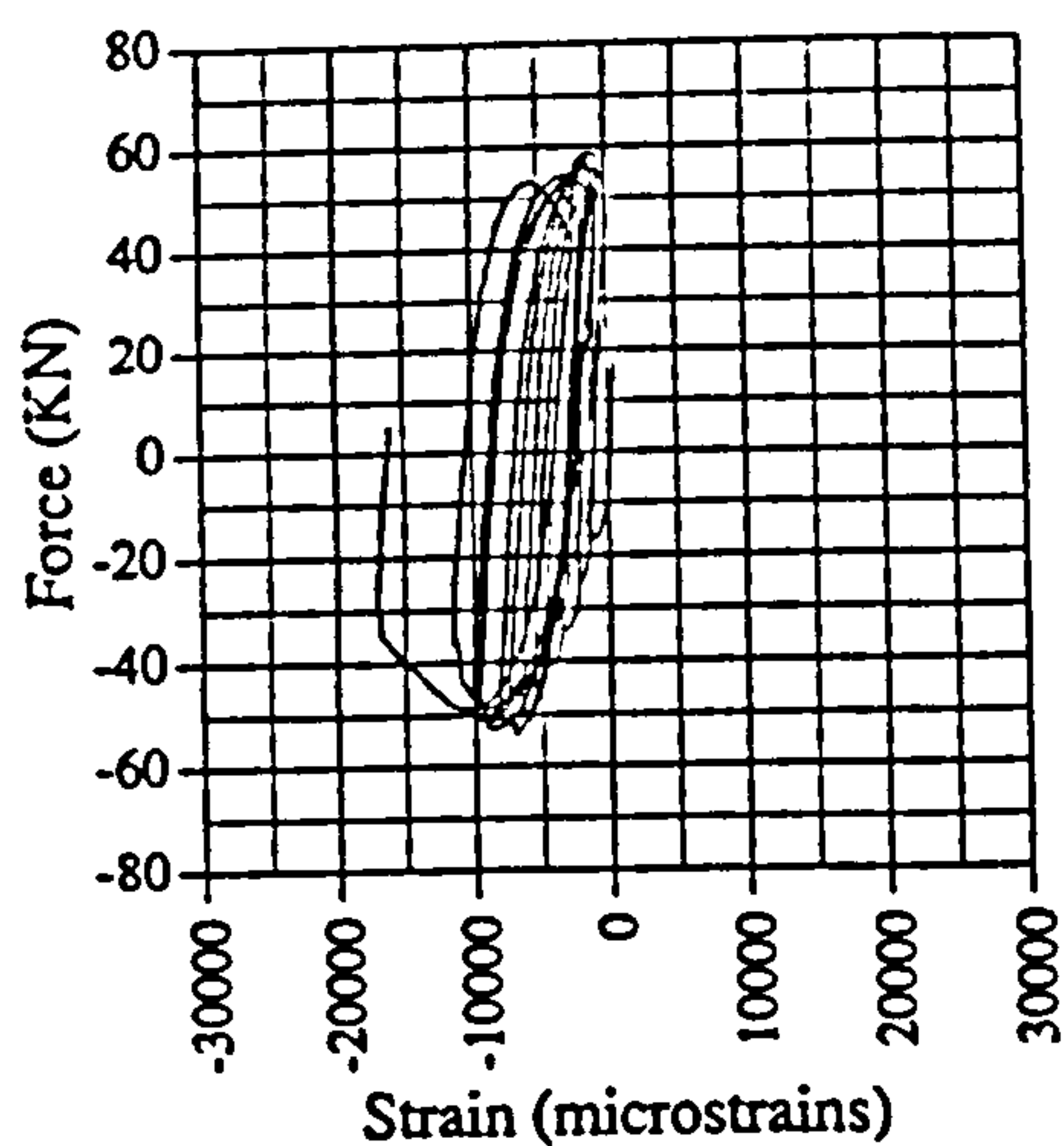


Fig. A.49 Force vs strain, EM02, G1

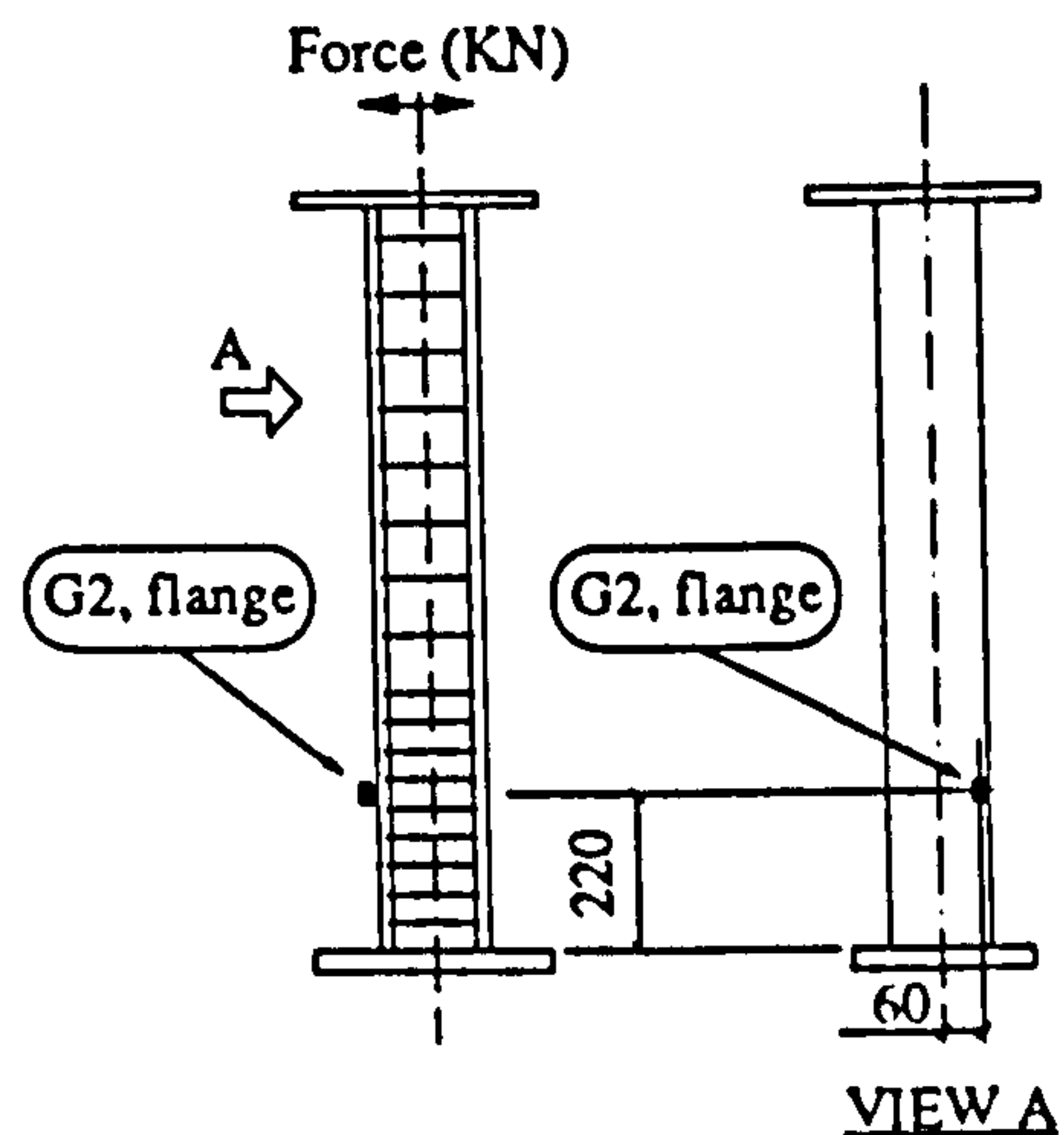
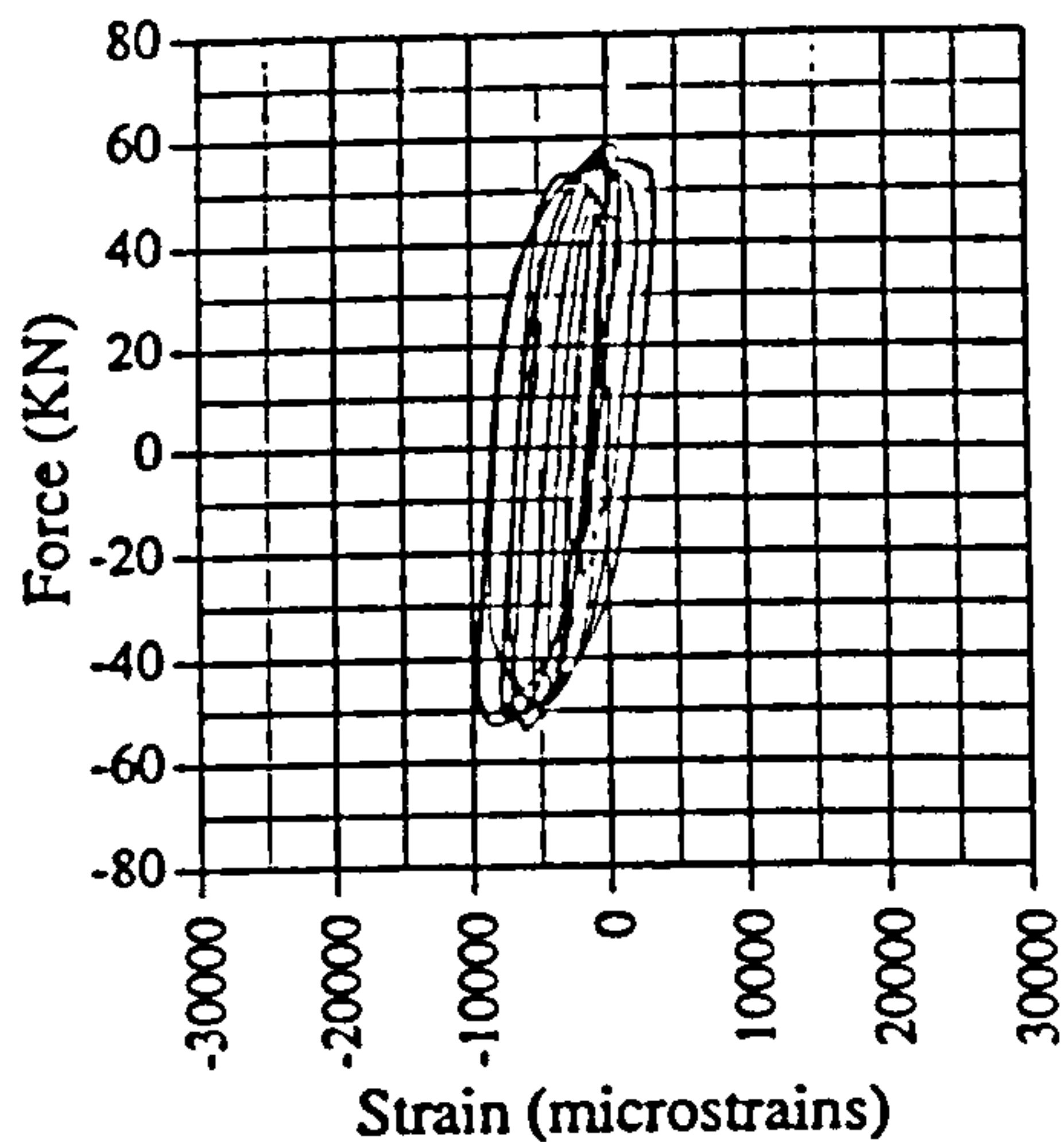


Fig. A.50 Force vs strain, EM02, G2

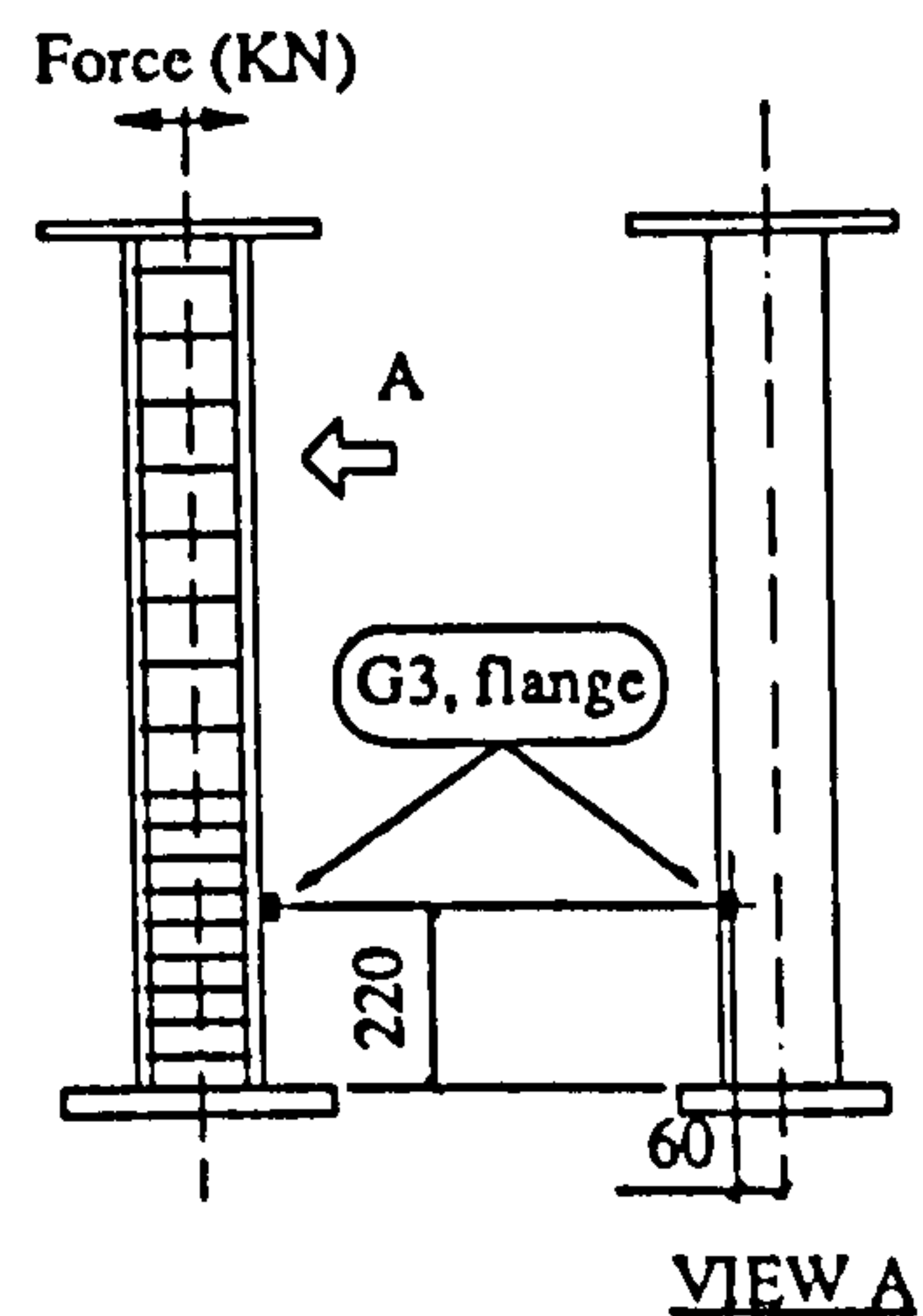
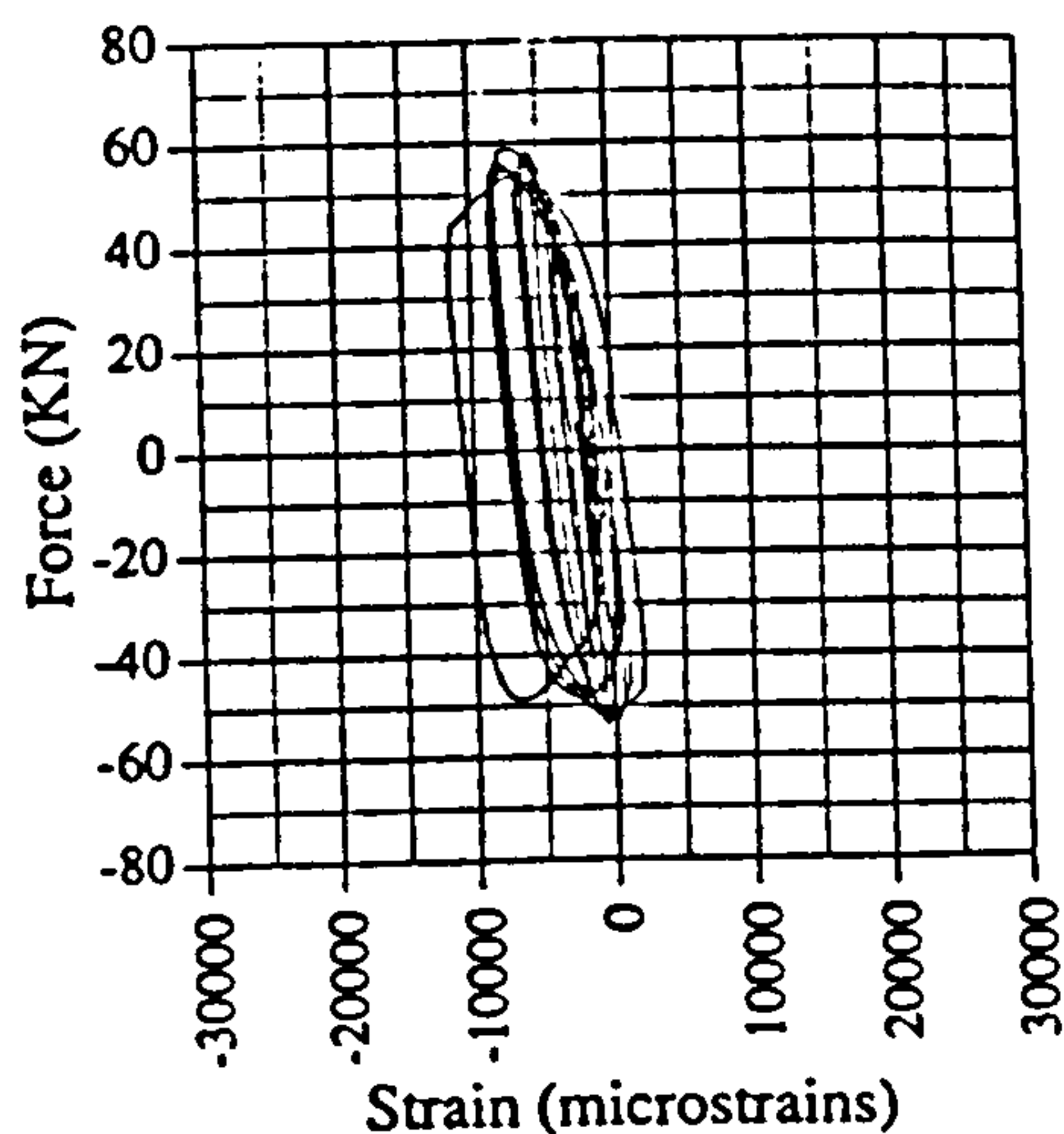


Fig. A.51 Force vs strain, EM02, G3

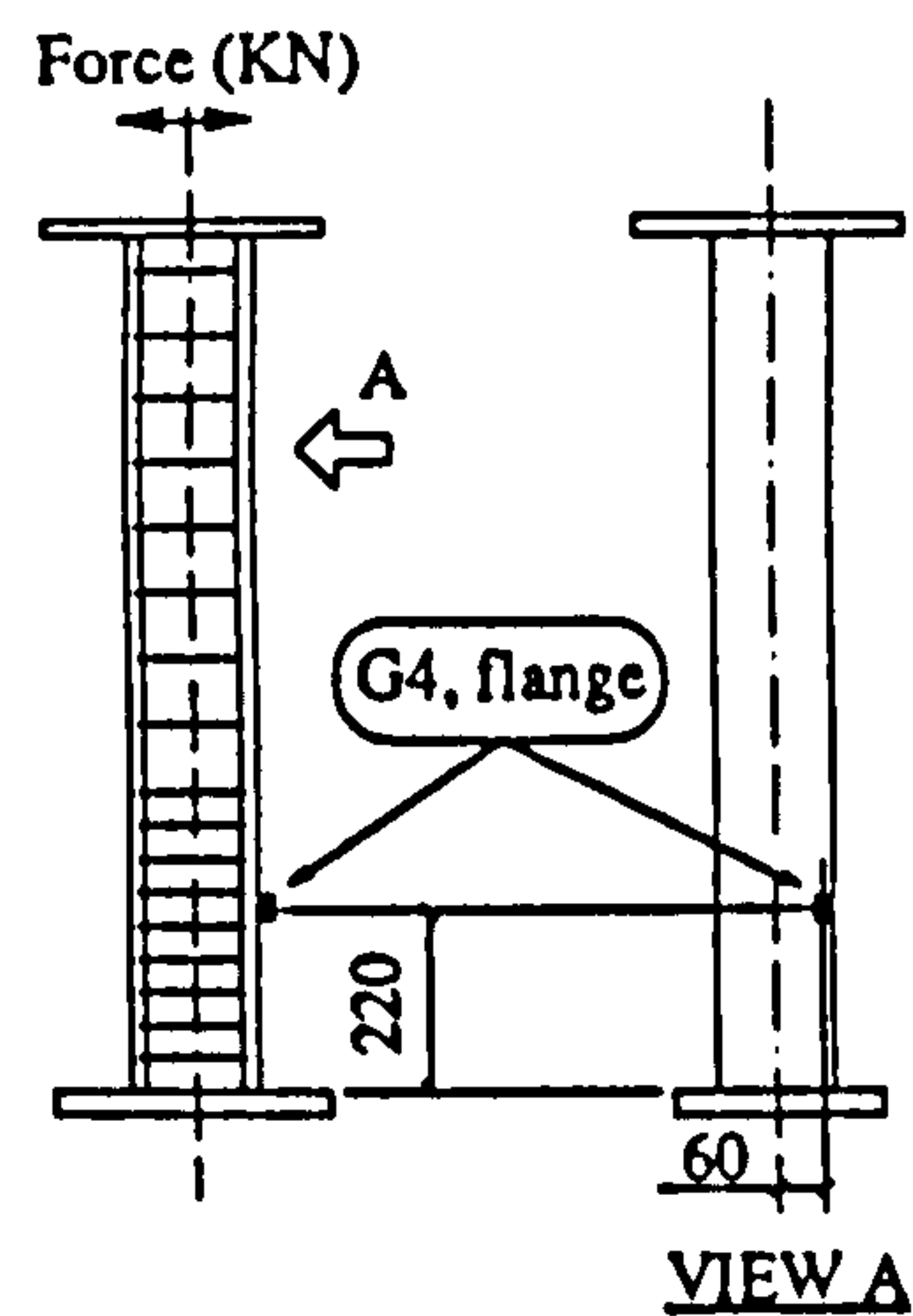
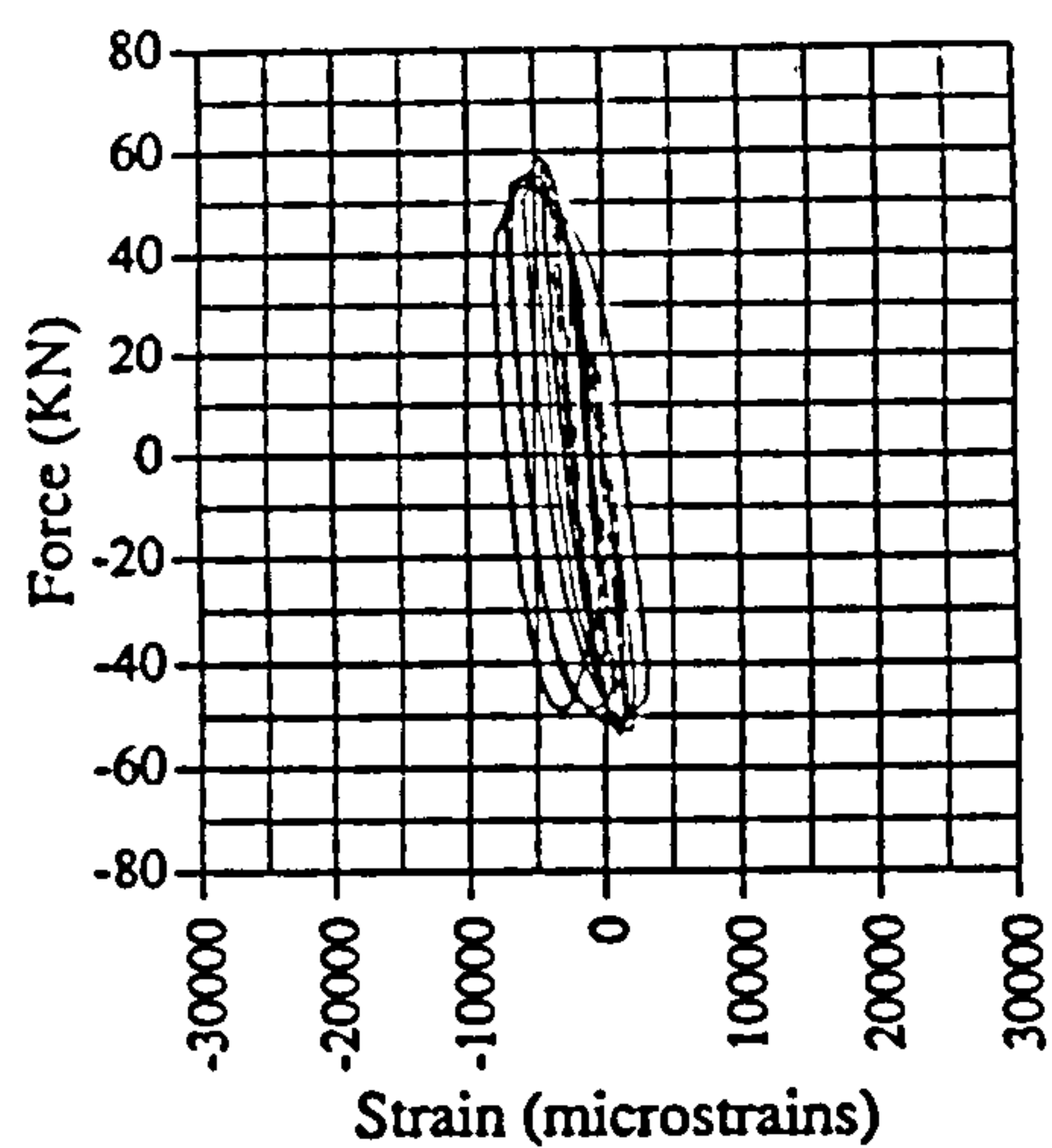


Fig. A.52 Force vs strain, EM02, G4

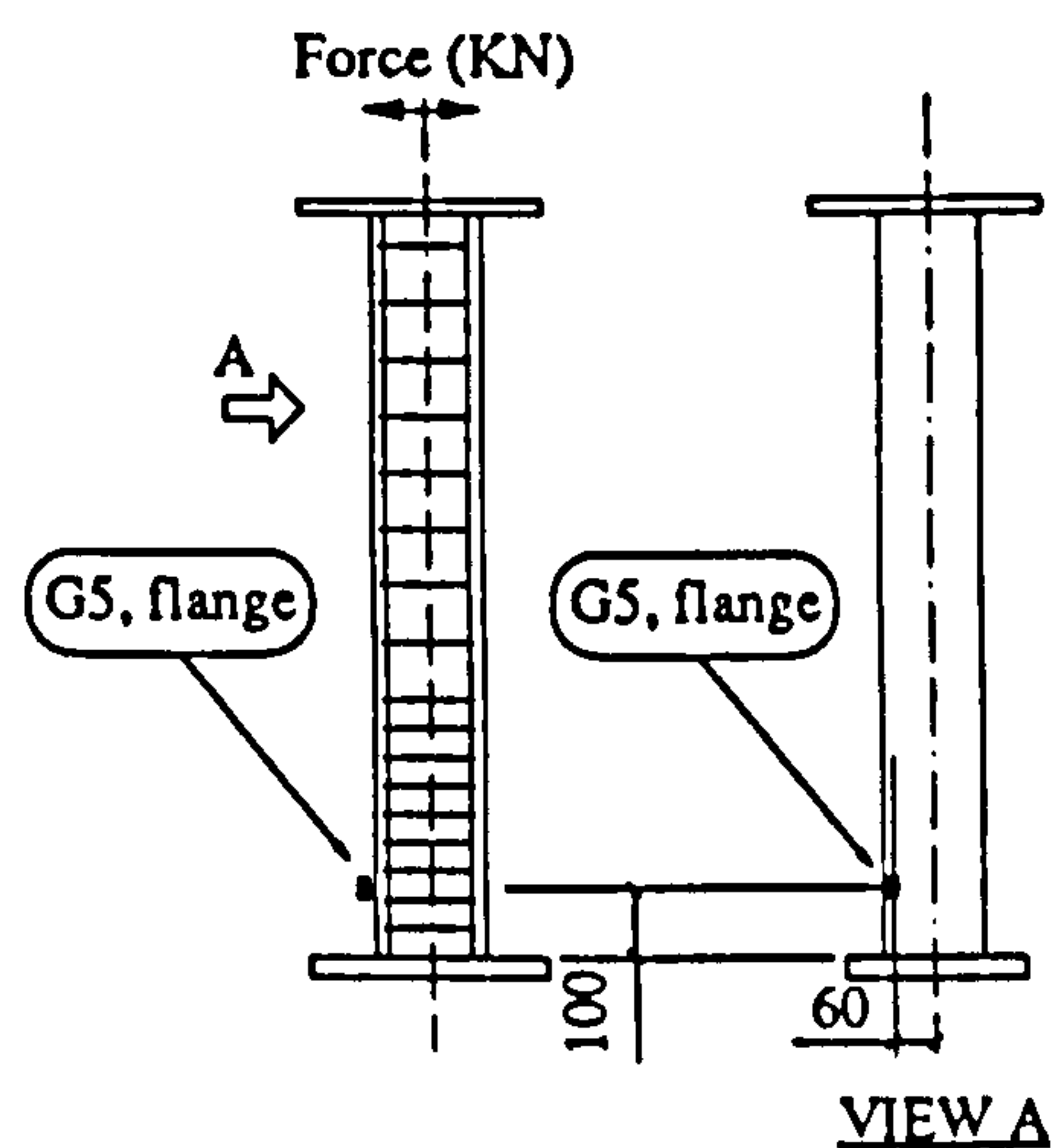
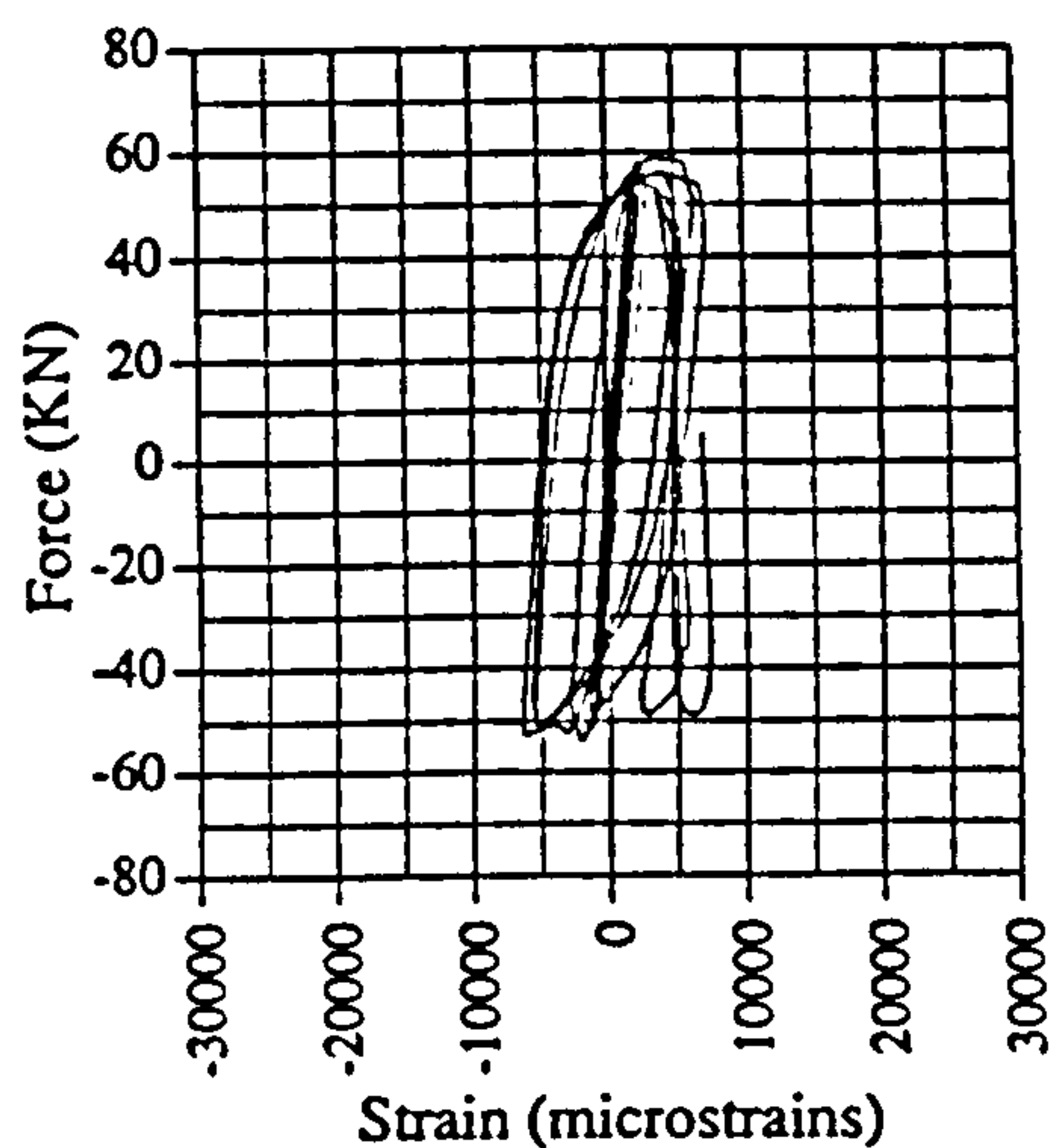


Fig. A.53 Force vs strain, EM02, G5

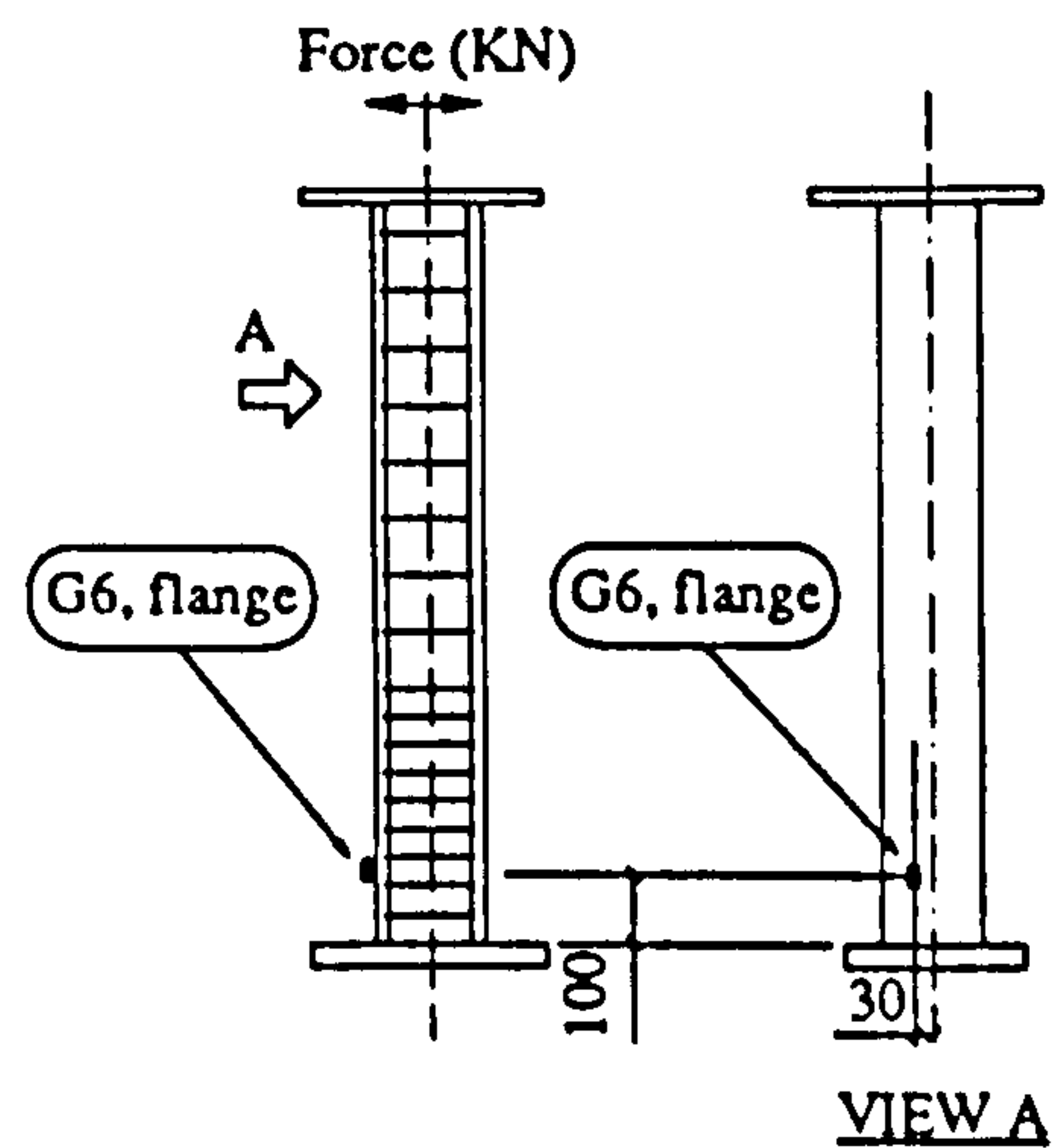
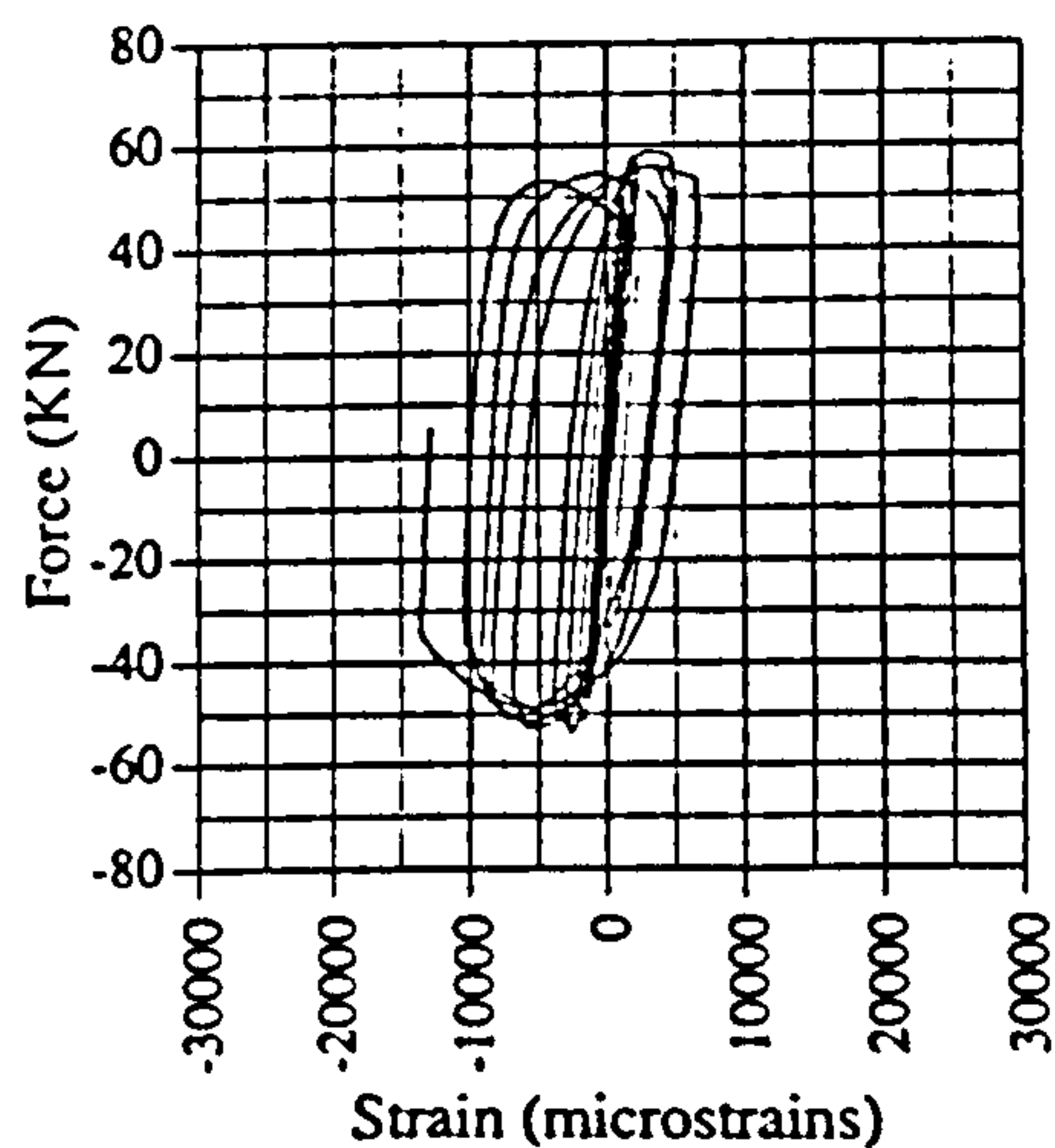


Fig. A.54 Force vs strain, EM02, G6

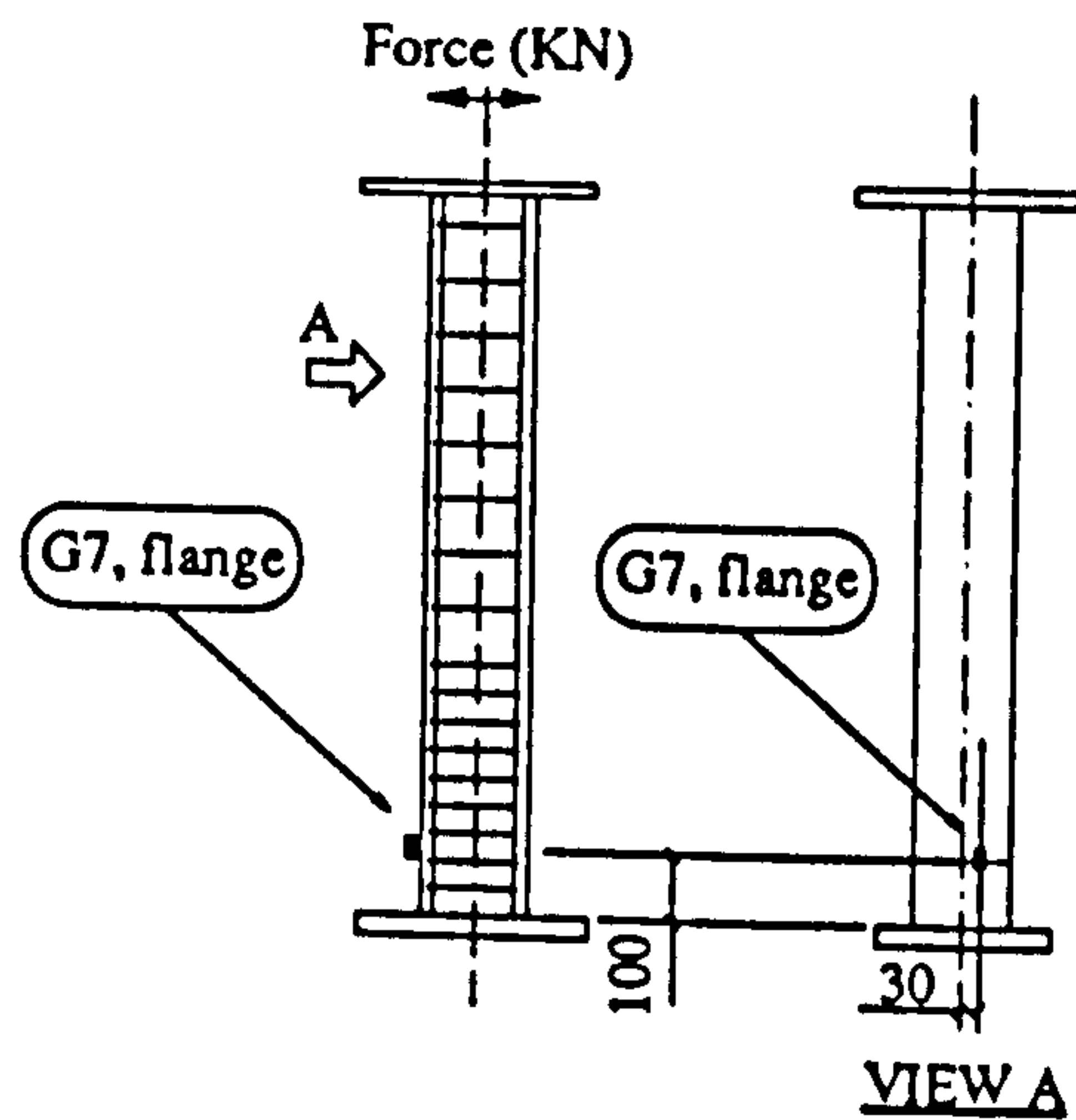
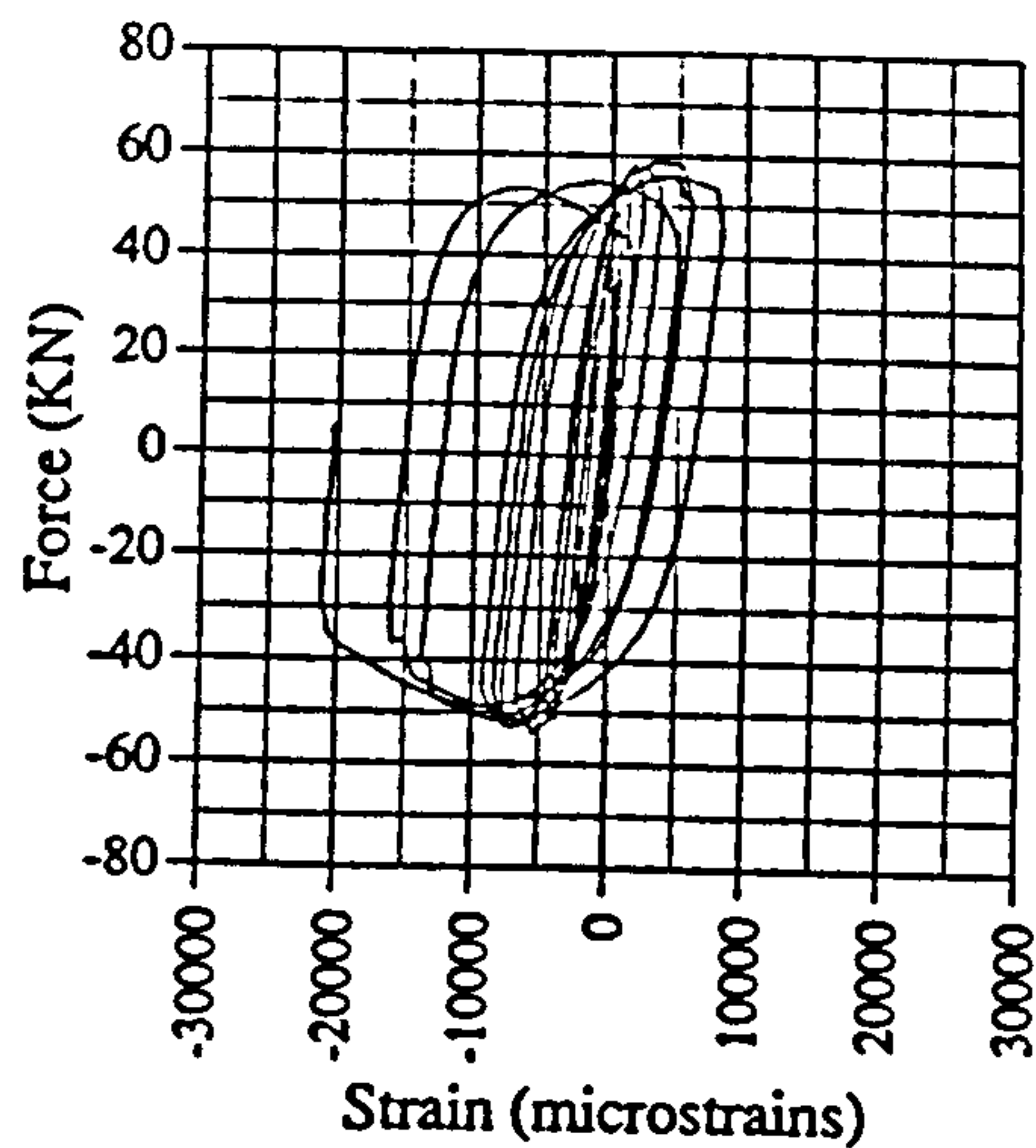


Fig. A.55 Force vs strain, EM02, G7

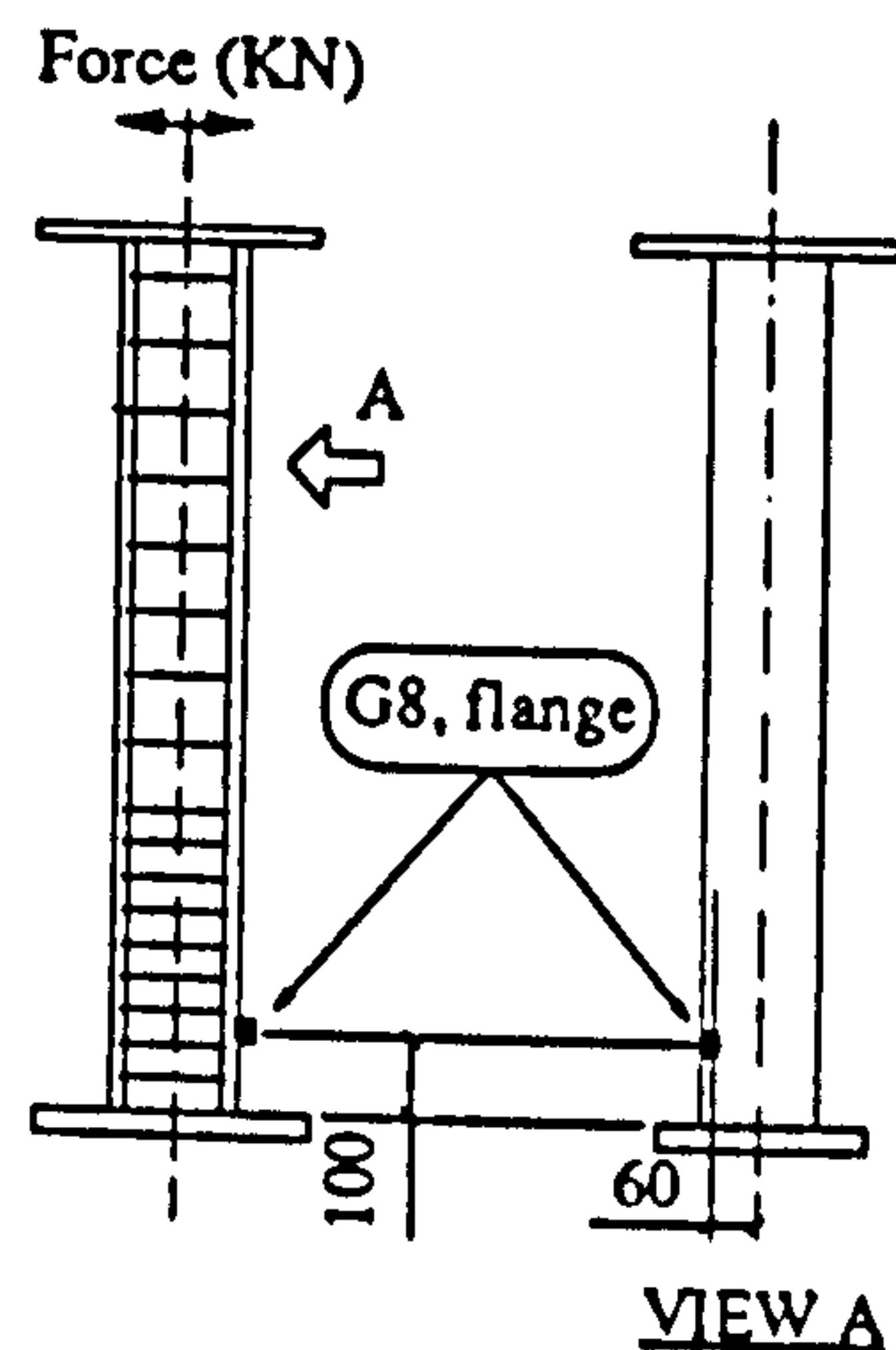
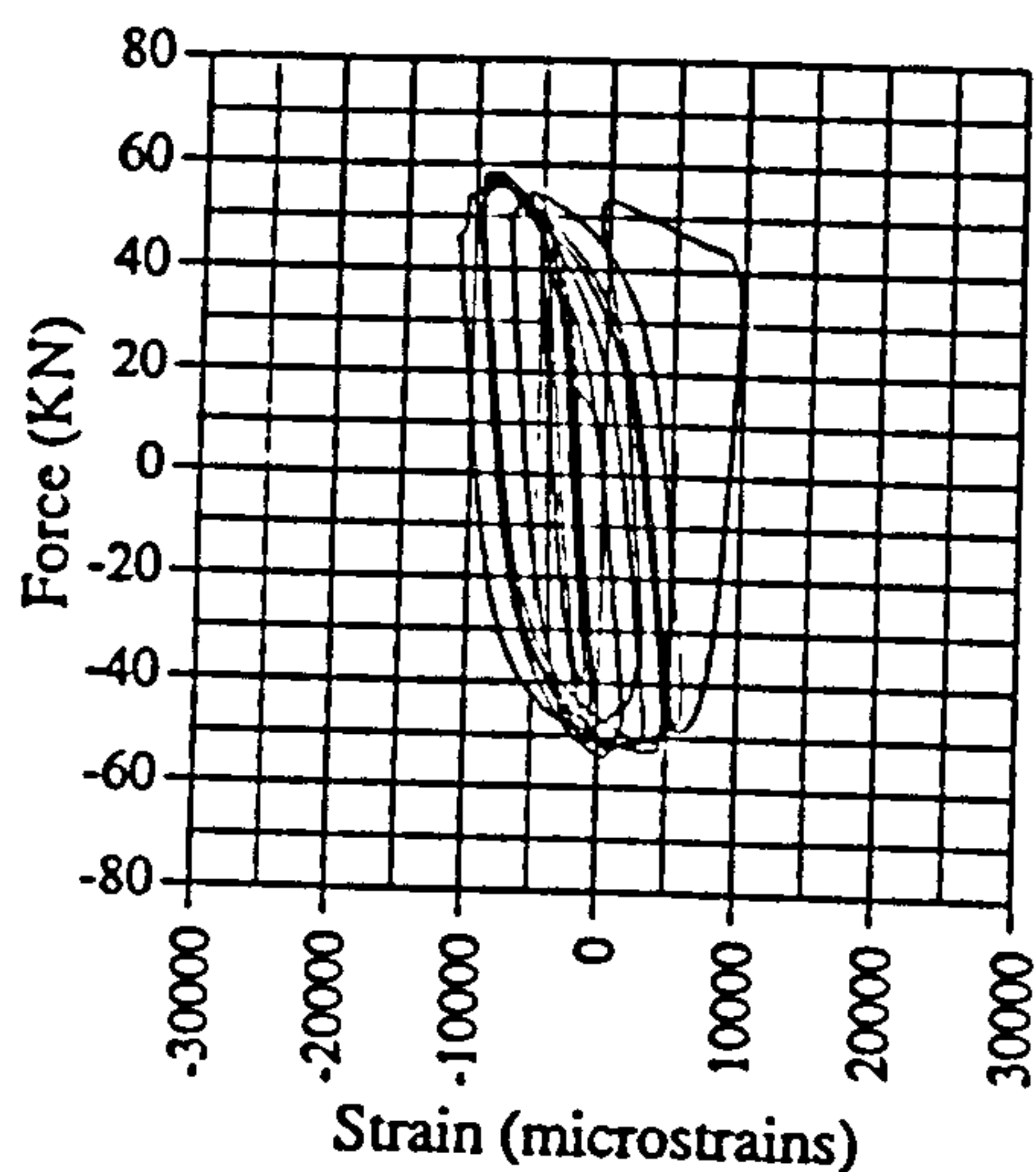


Fig. A.56 Force vs strain, EM02, G8

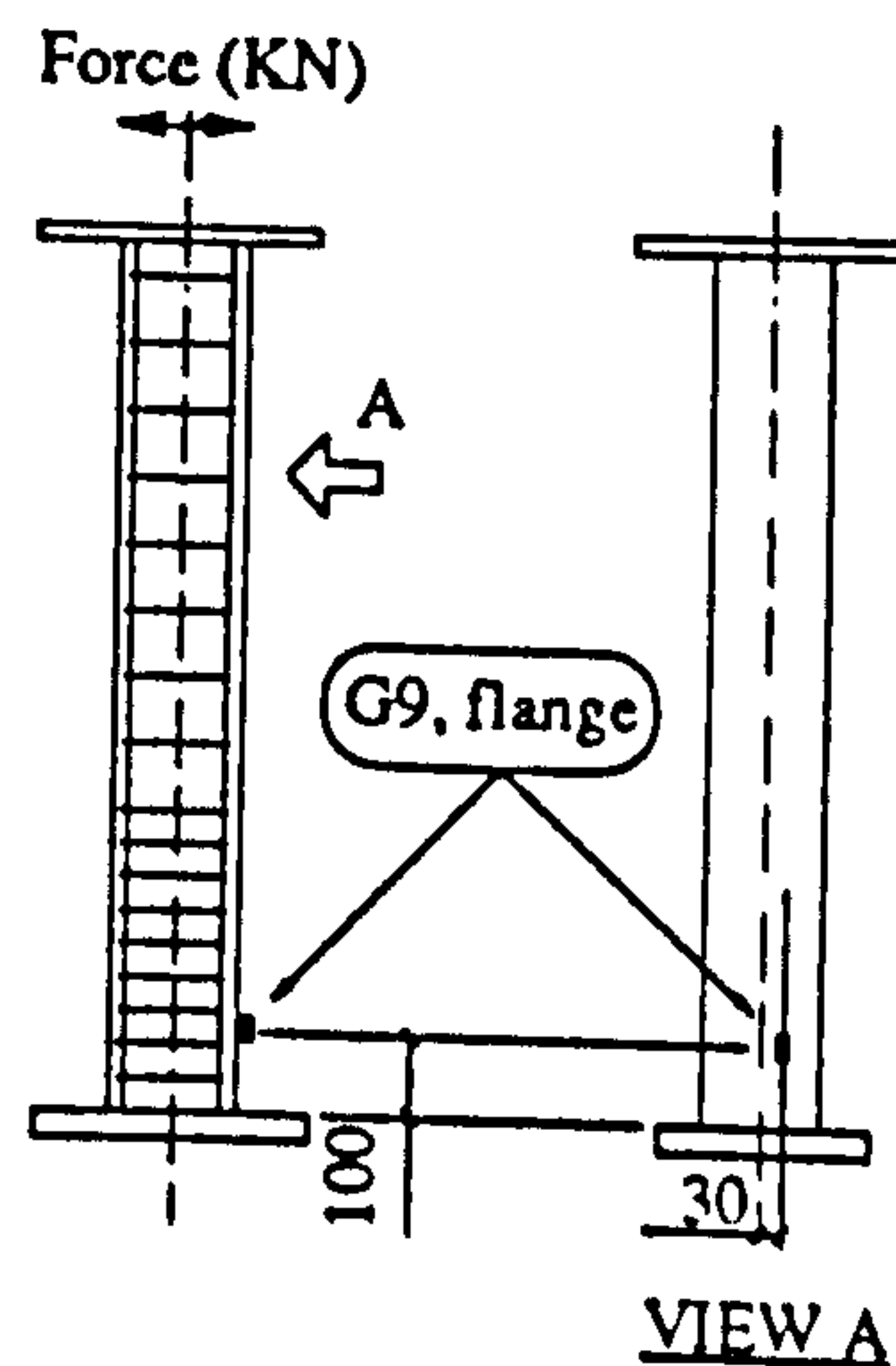
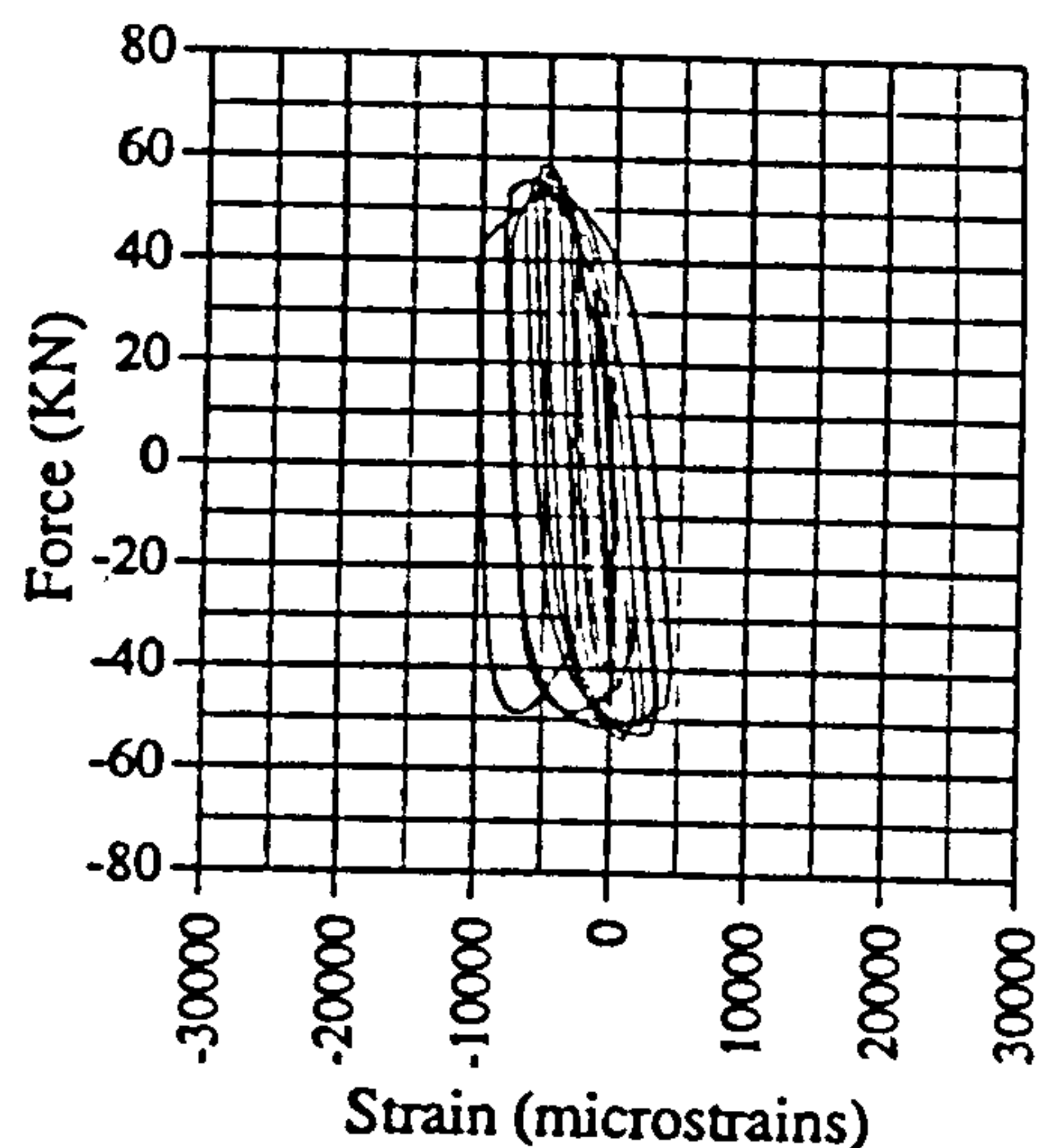


Fig. A.57 Force vs strain, EM02, G9

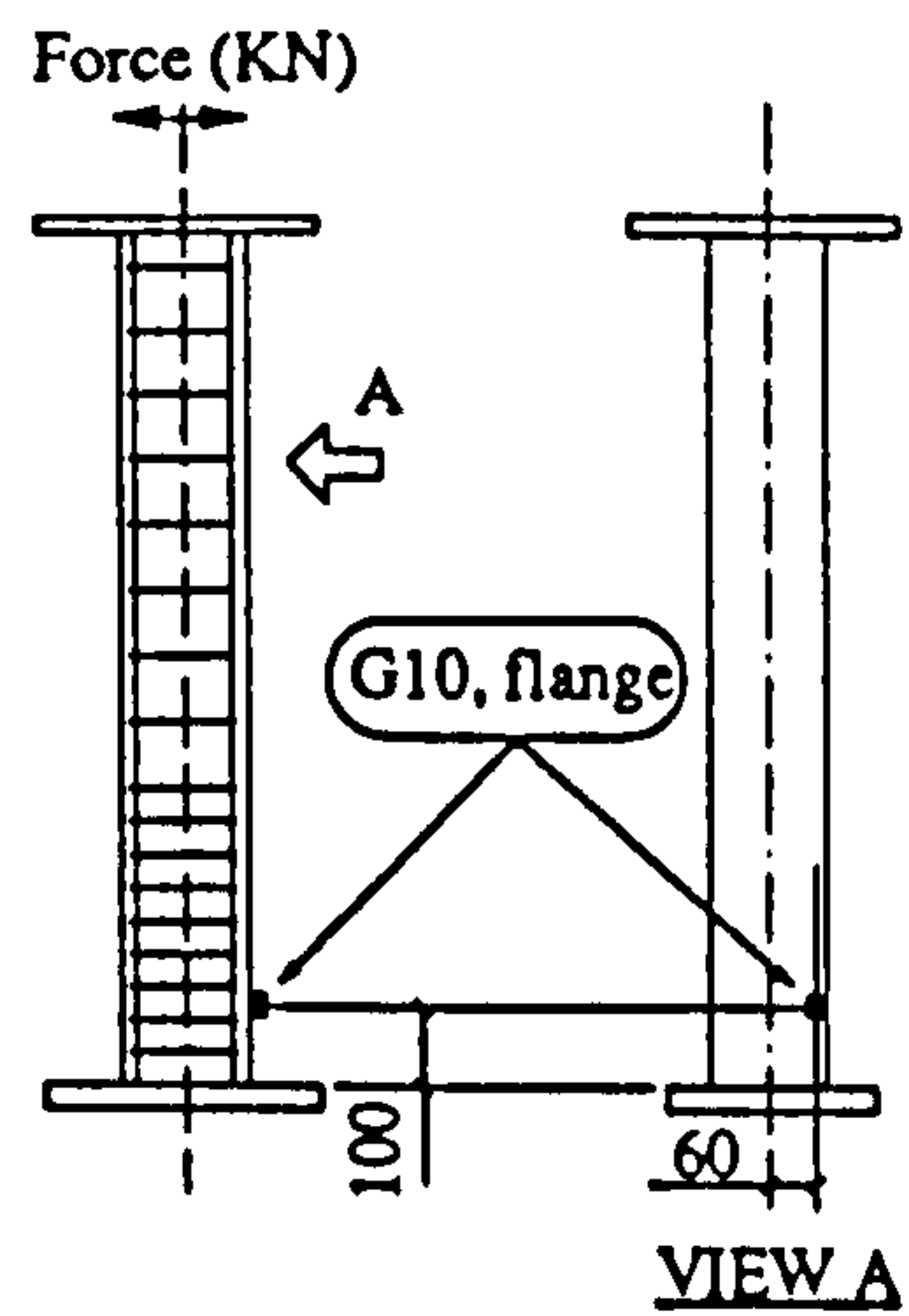
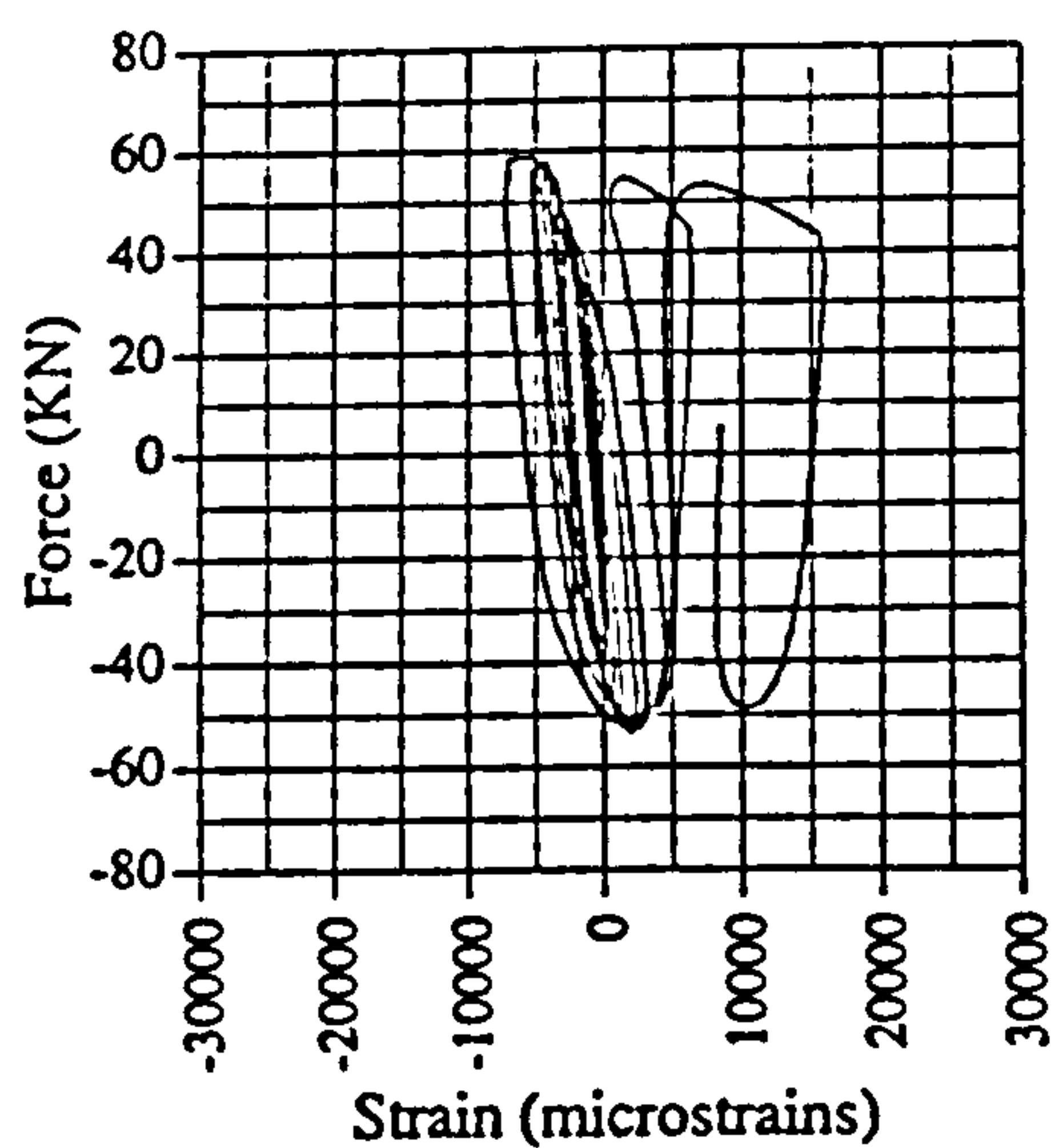


Fig. A.58 Force vs strain, EM02, G10

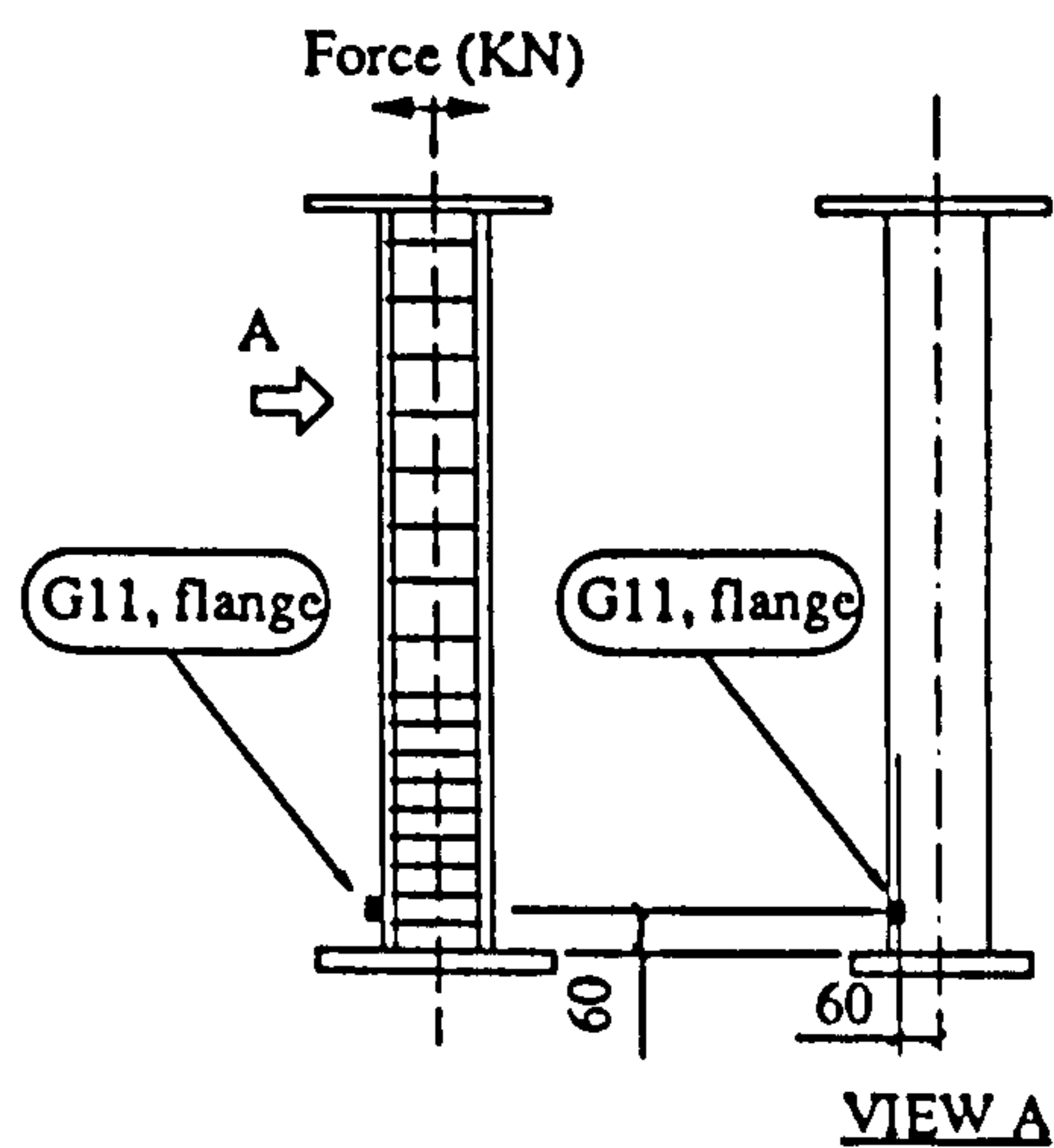
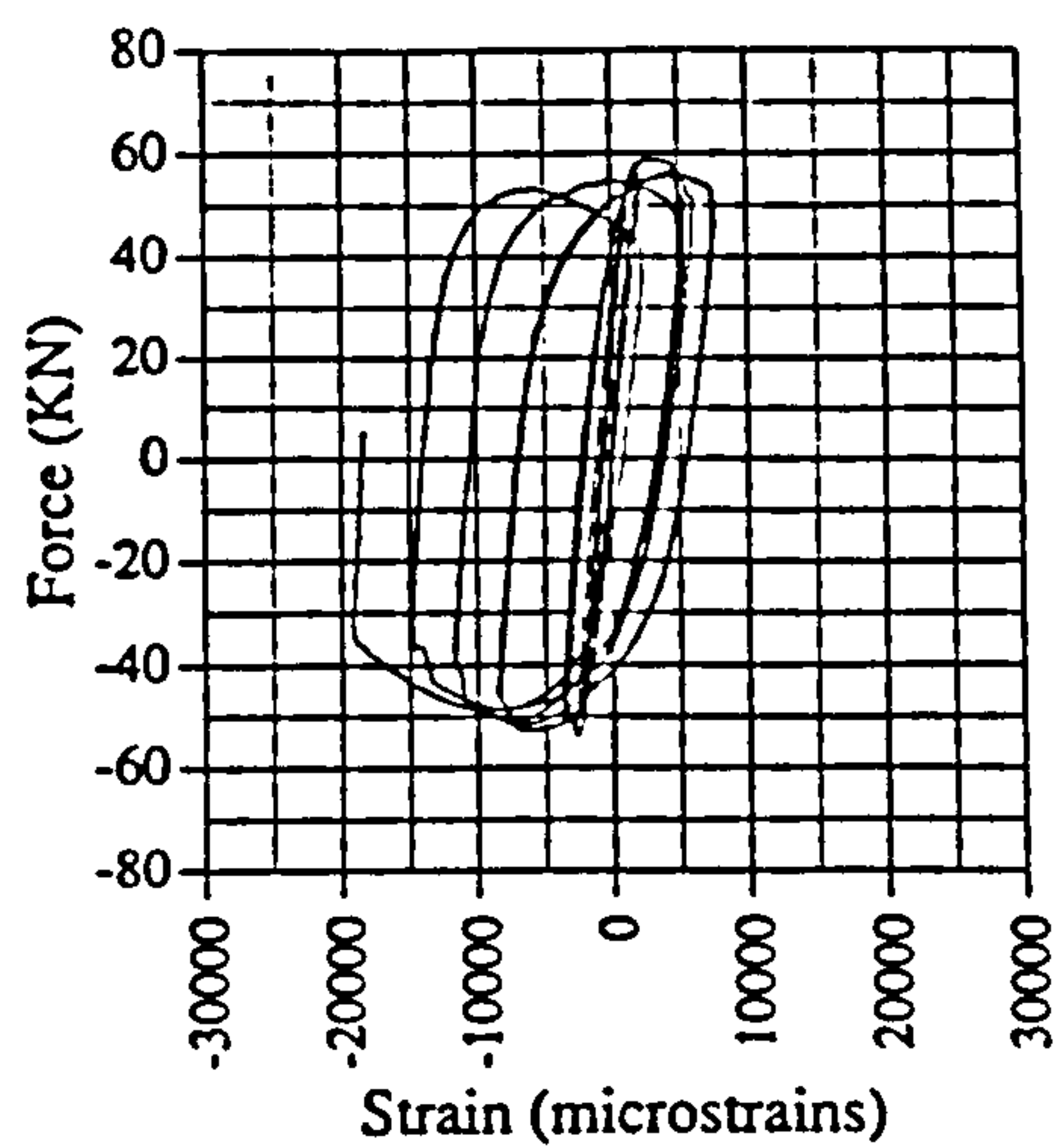


Fig. A.59 Force vs strain, EM02, G11

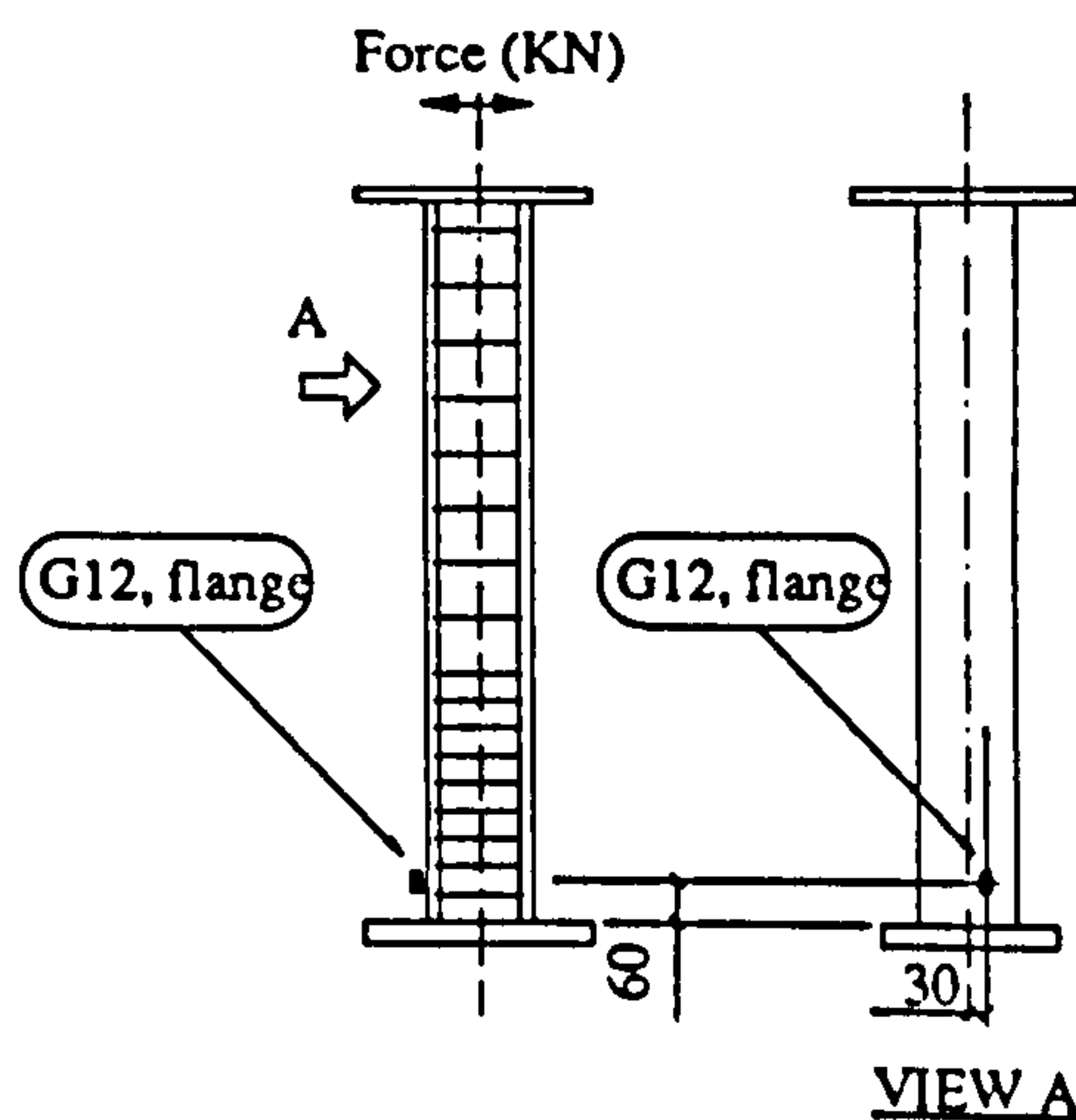
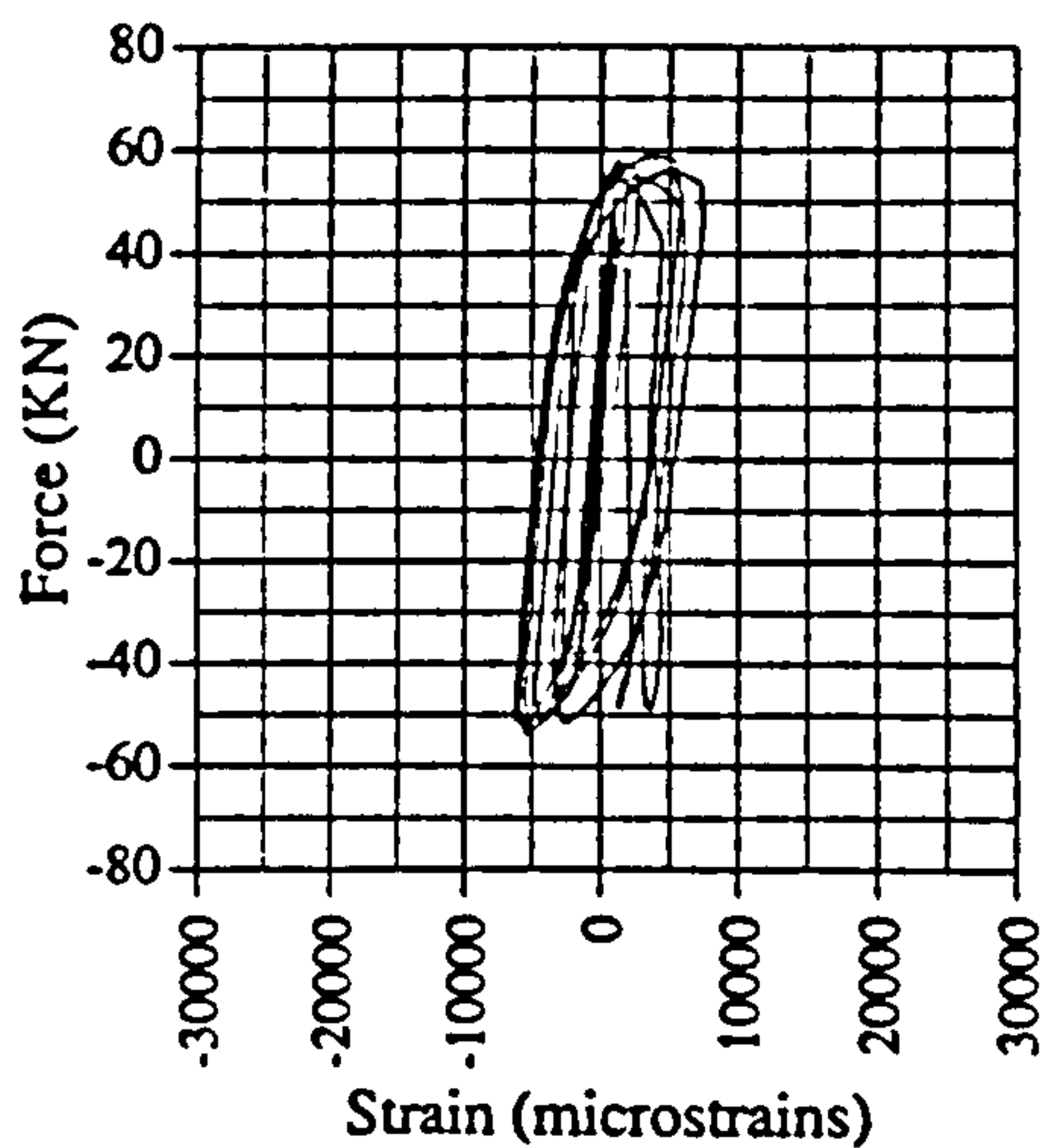


Fig. A.60 Force vs strain, EM02, G12

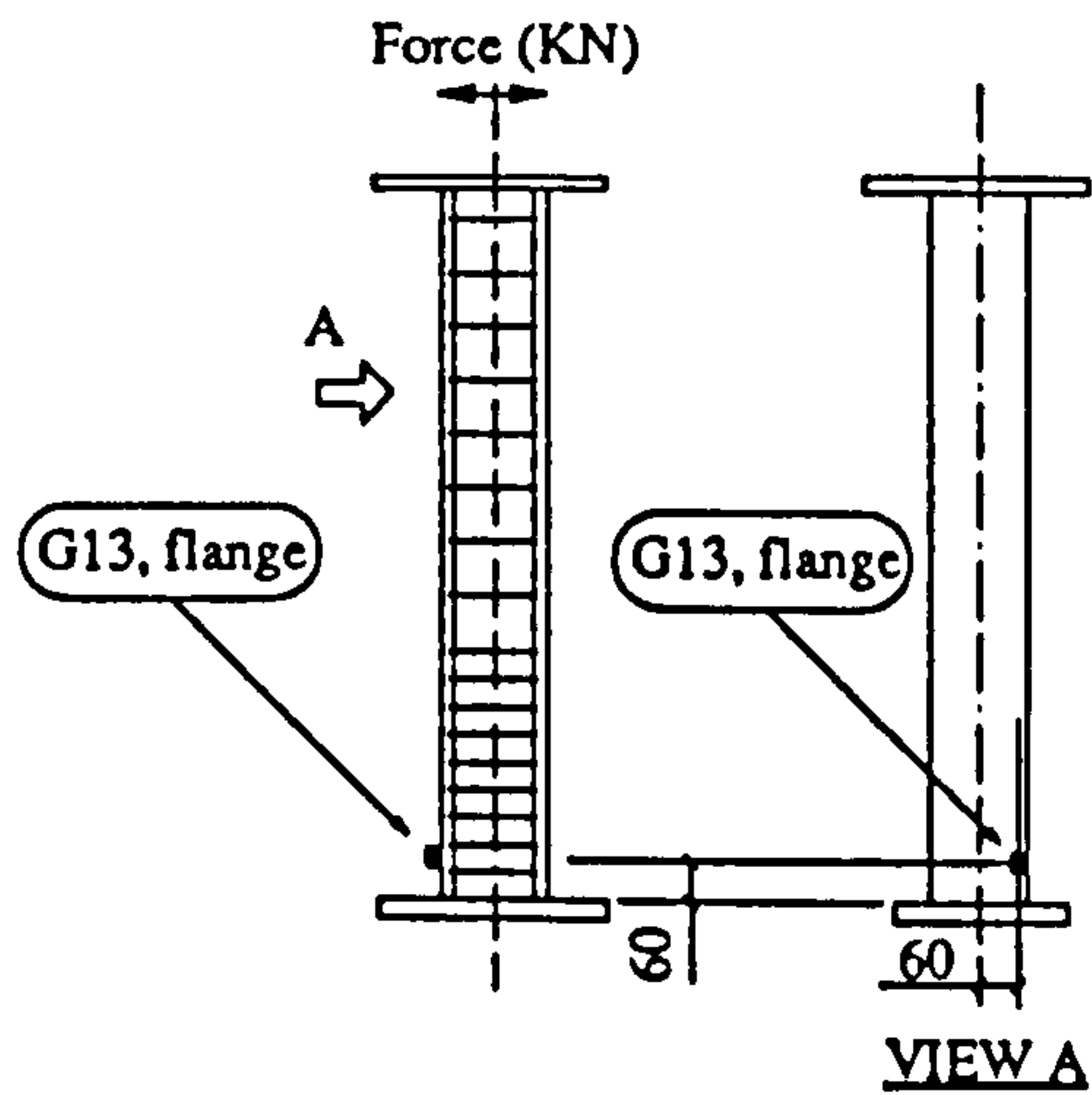
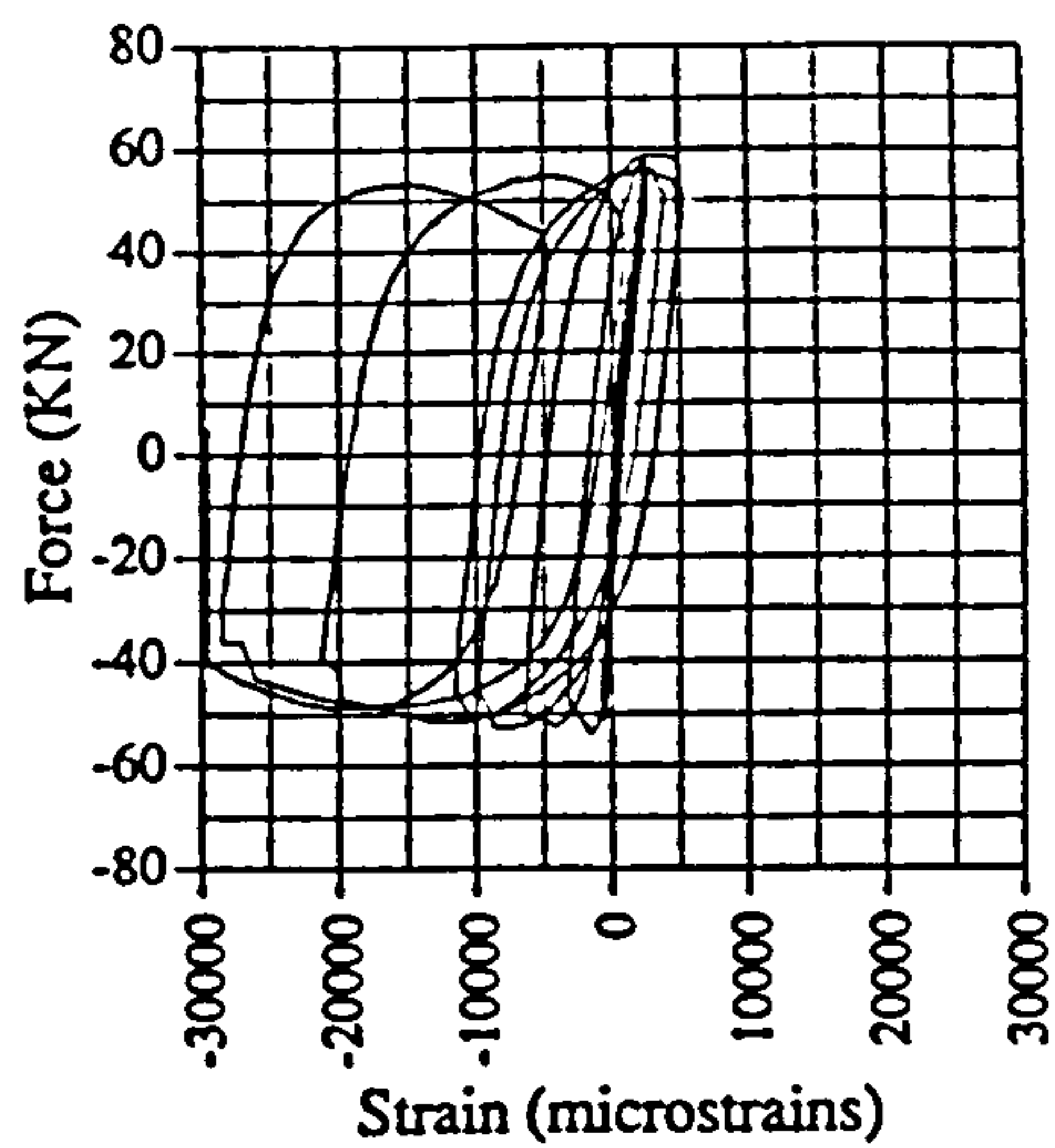


Fig. A.61 Force vs strain, EM02, G13

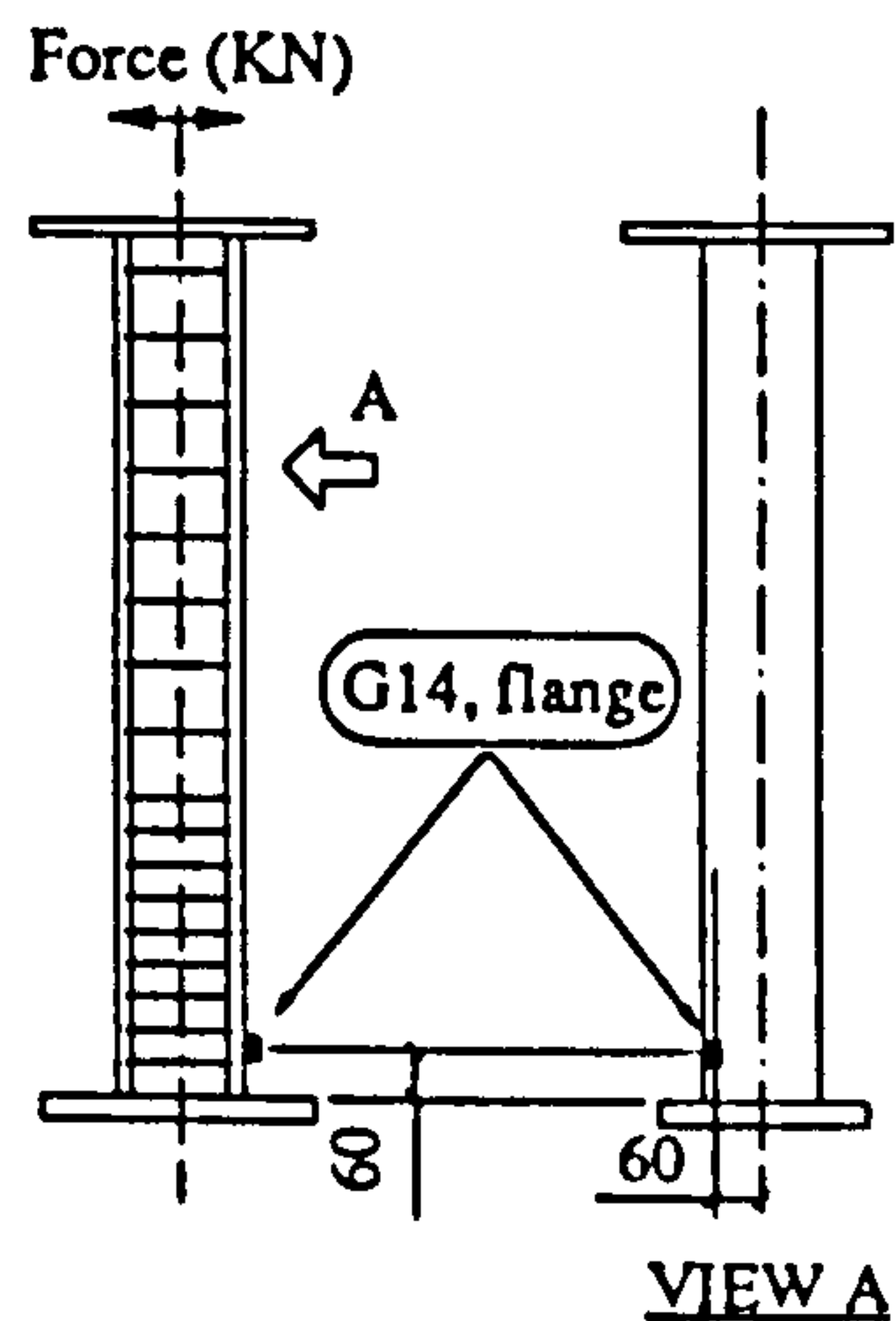
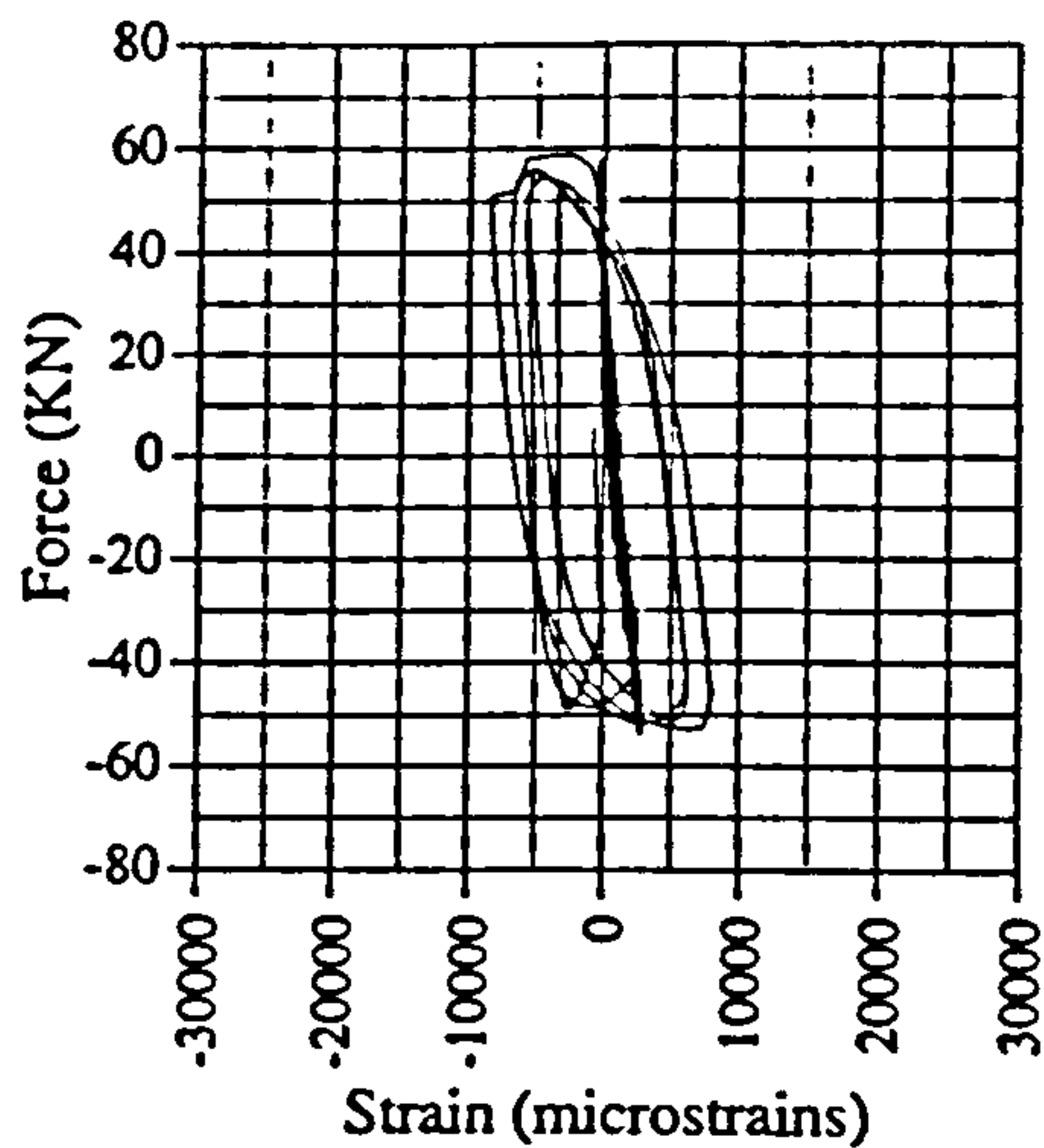


Fig. A.62 Force vs strain, EM02, G14

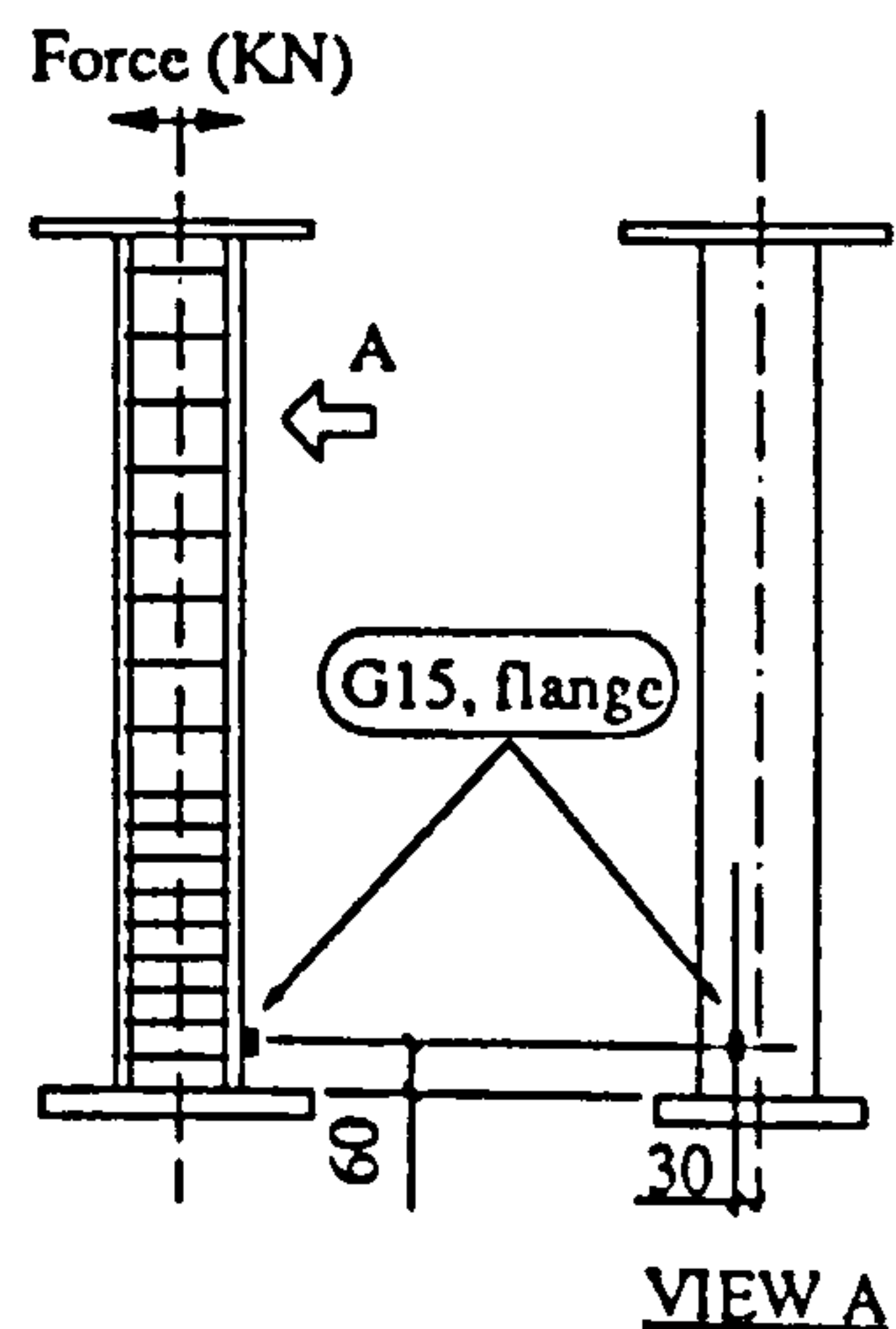
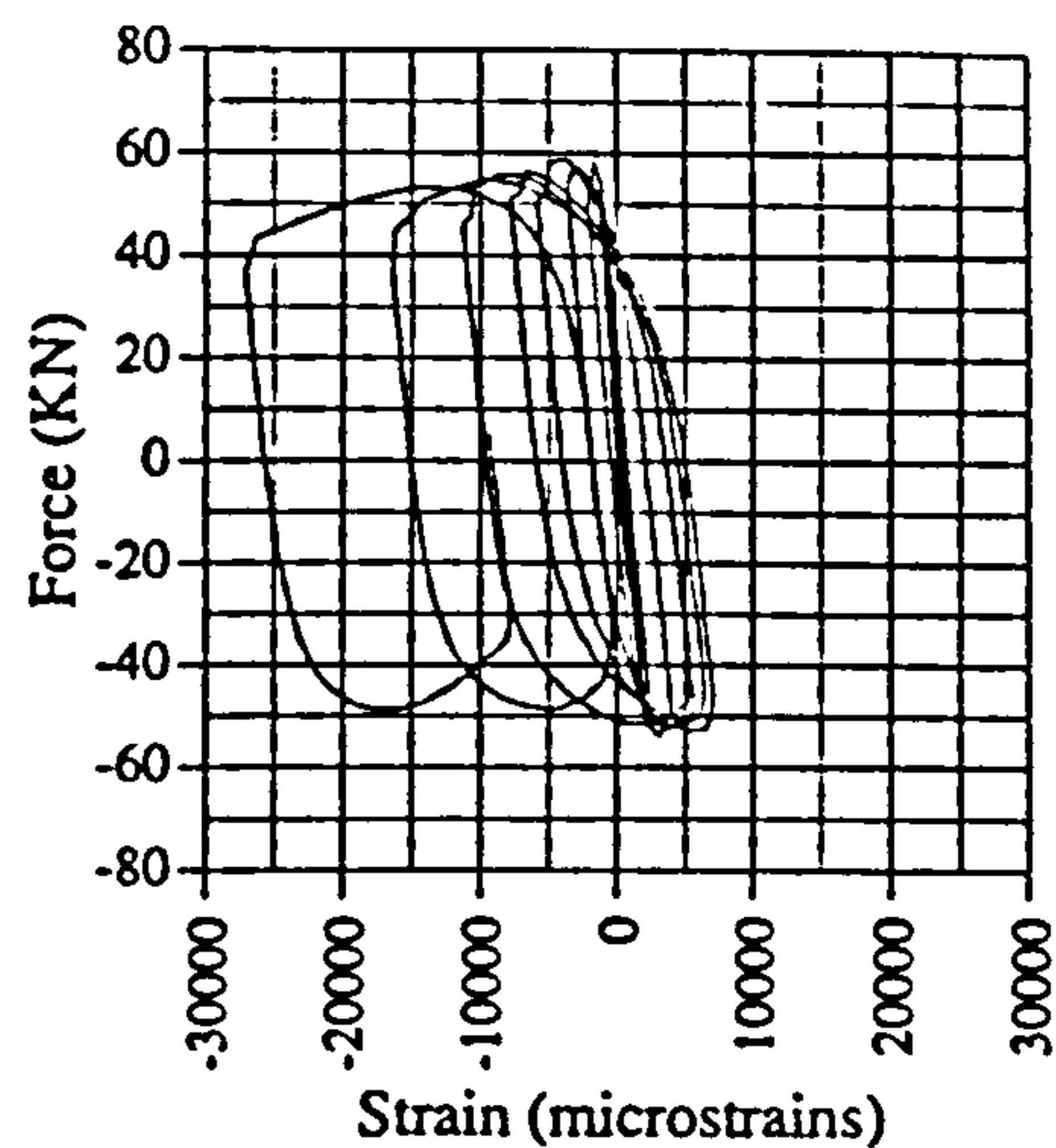


Fig. A.63 Force vs strain, EM02, G15

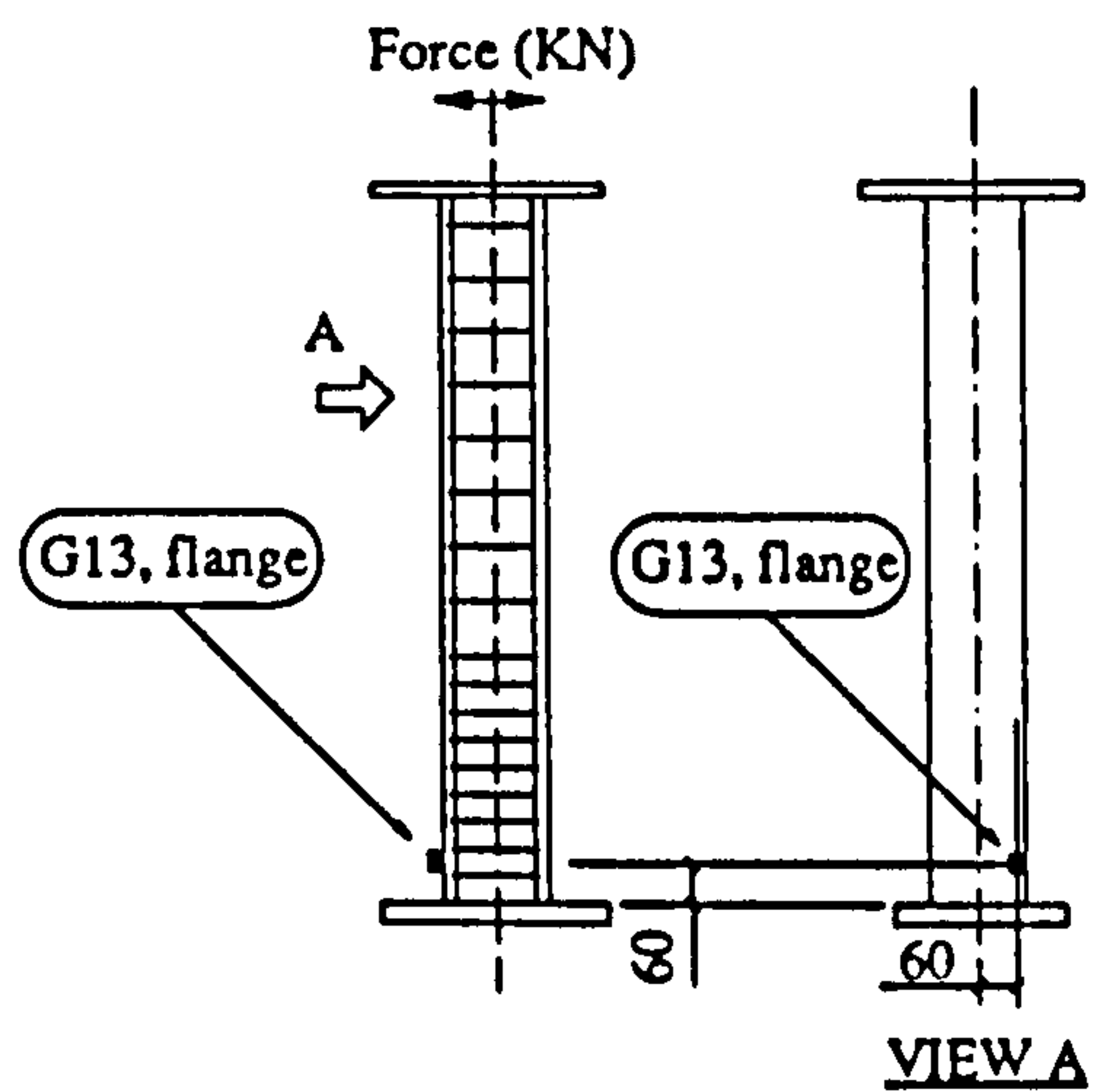
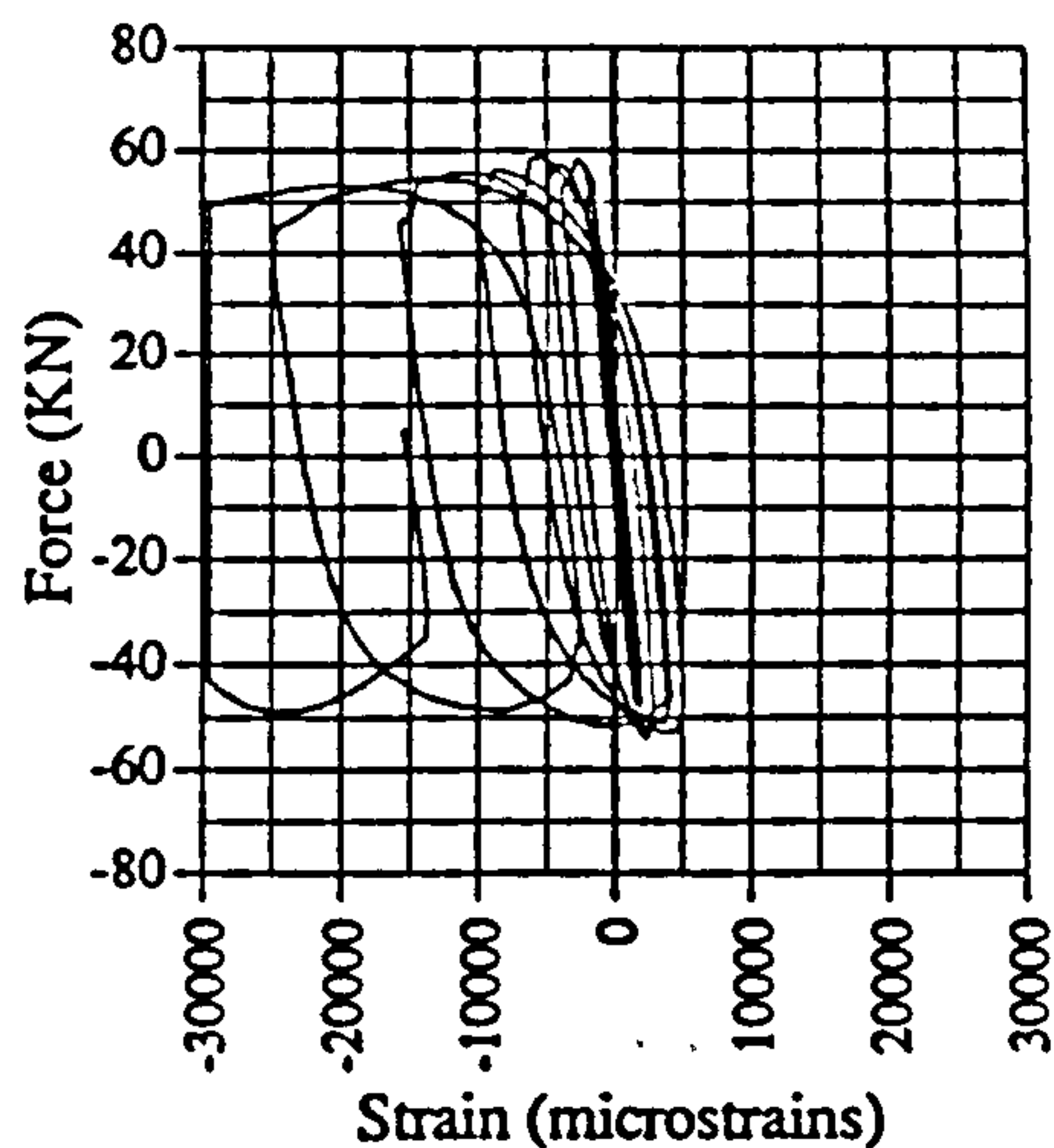


Fig. A.64 Force vs strain, EM02, G16

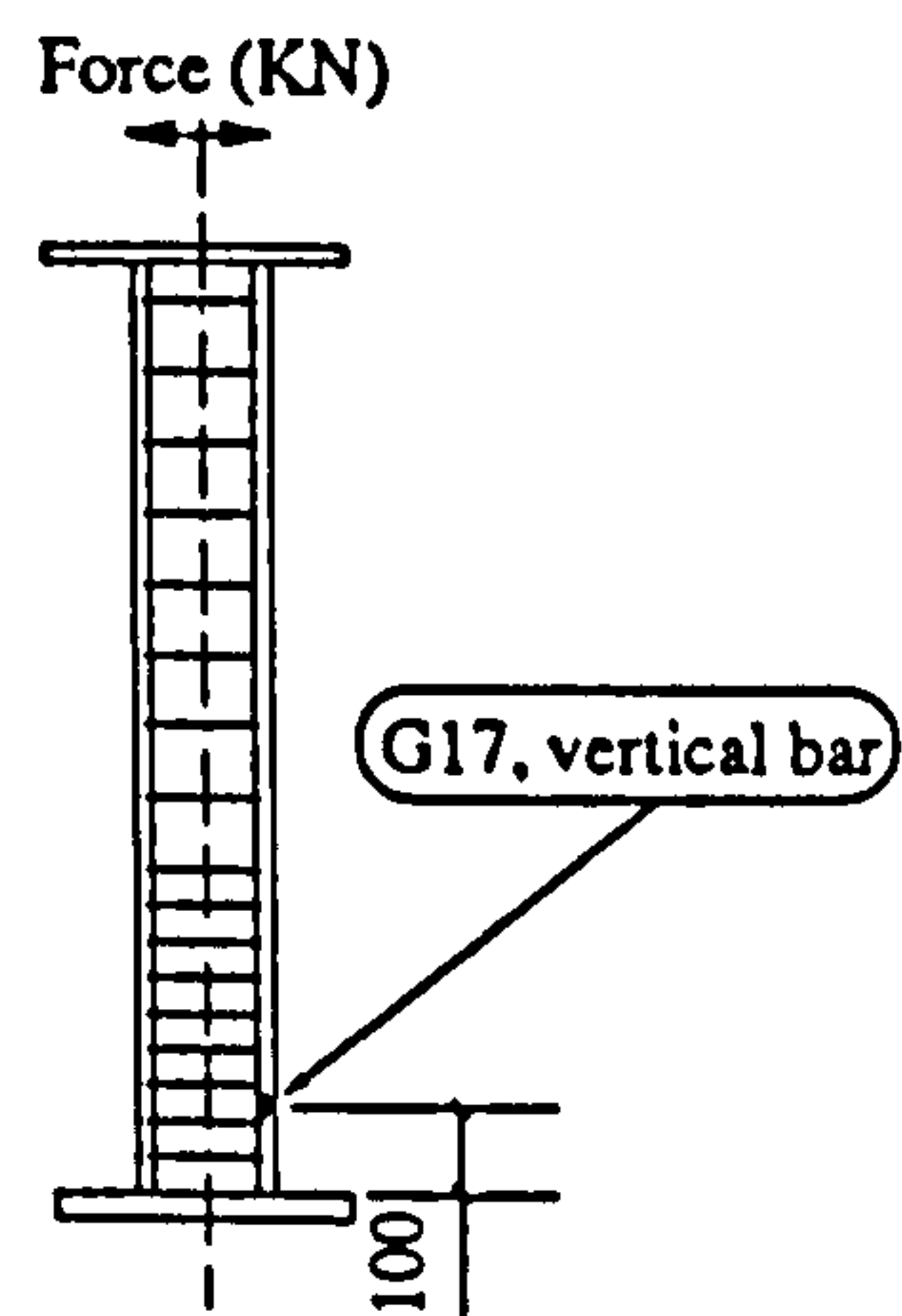
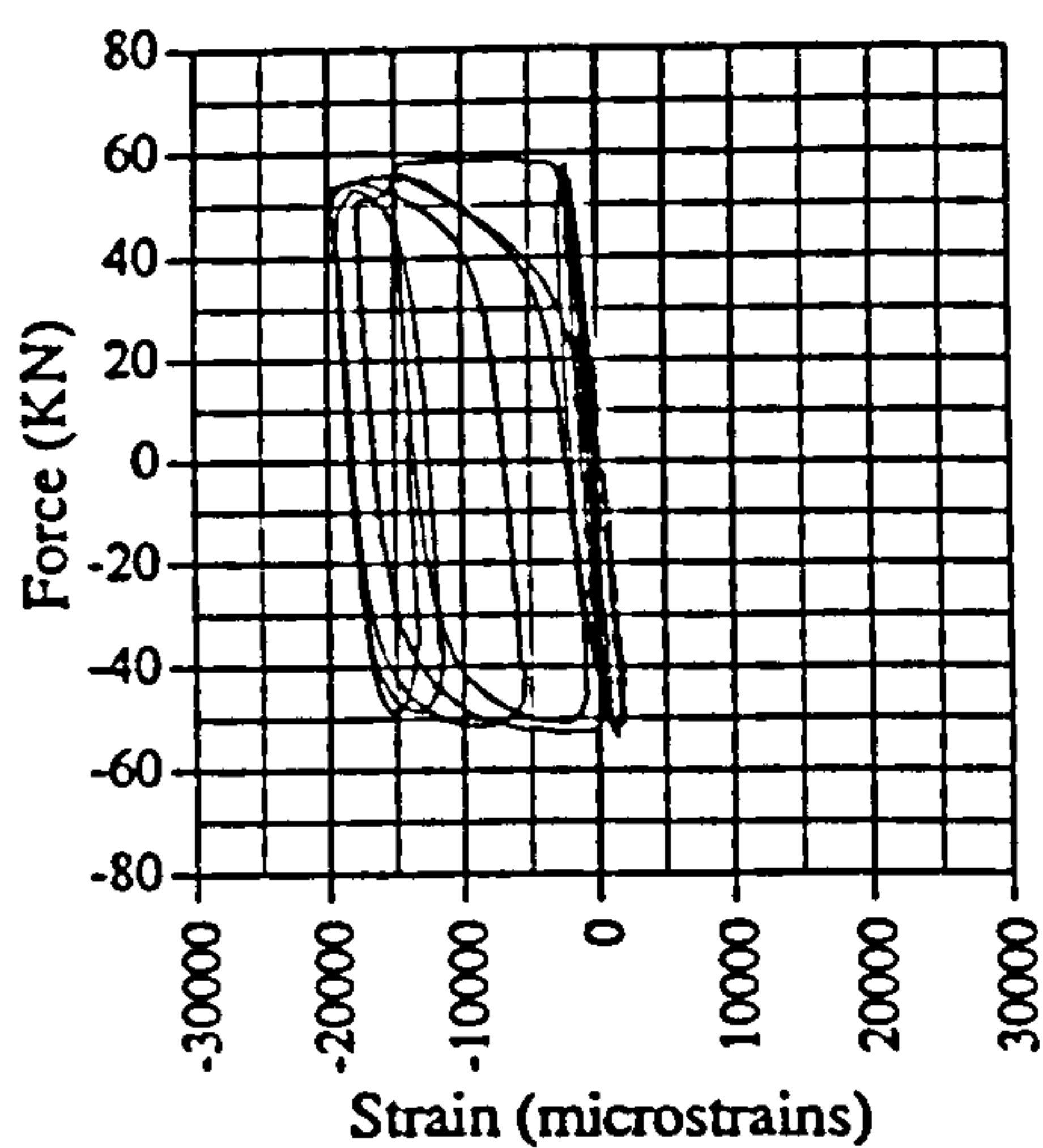


Fig. A.65 Force vs strain, EM02, G17

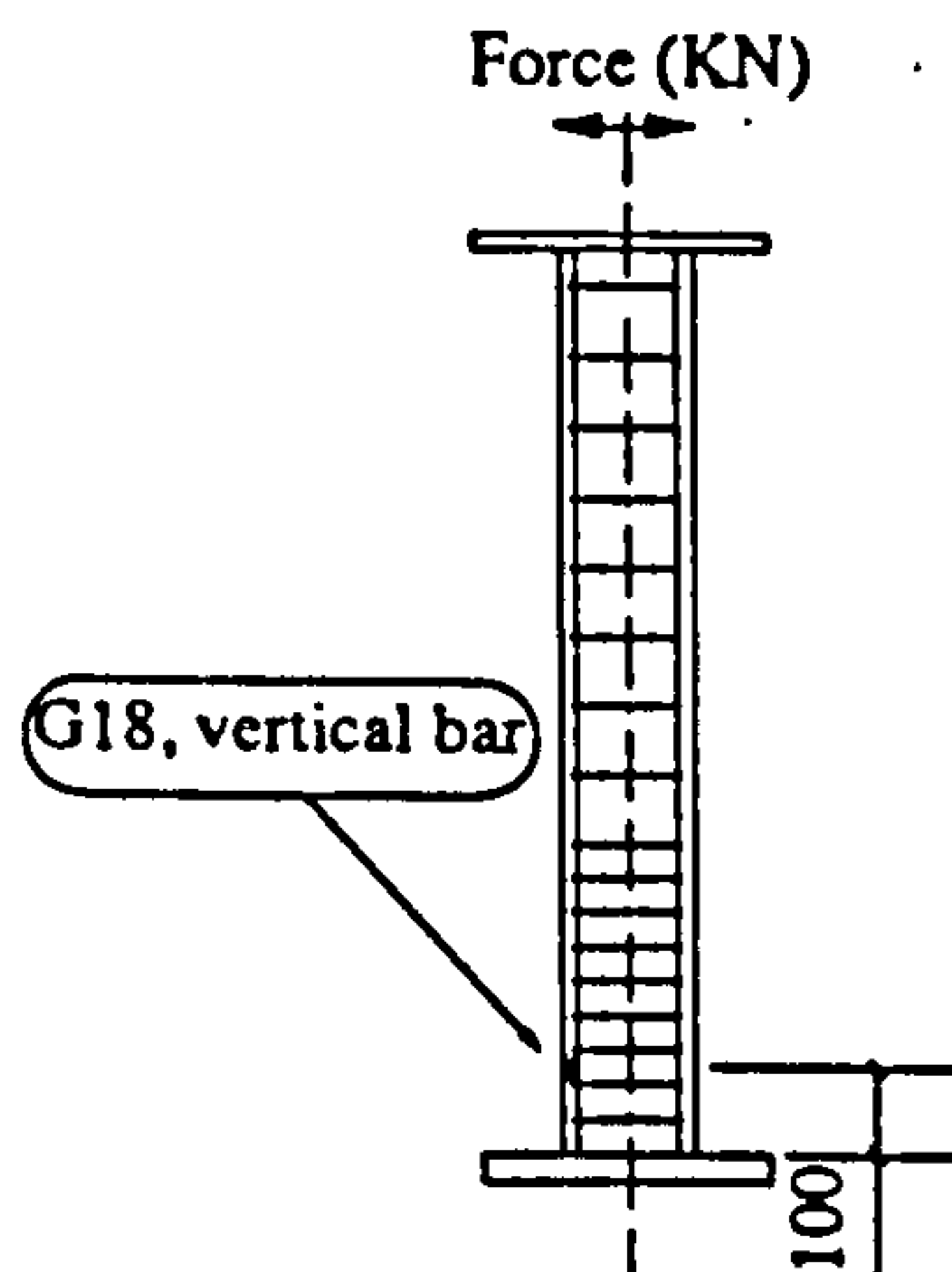
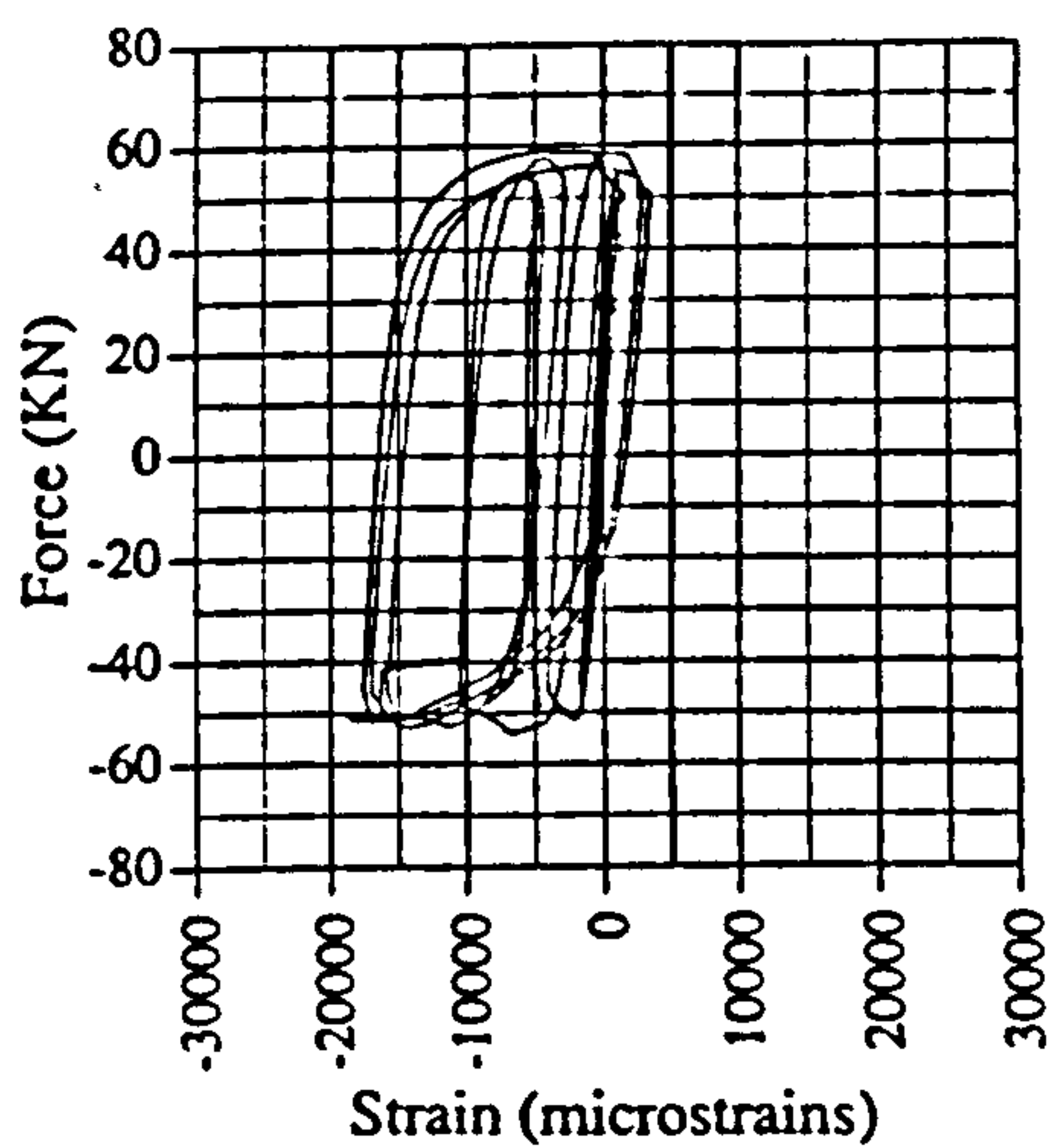


Fig. A.66 Force vs strain, EM02, G18

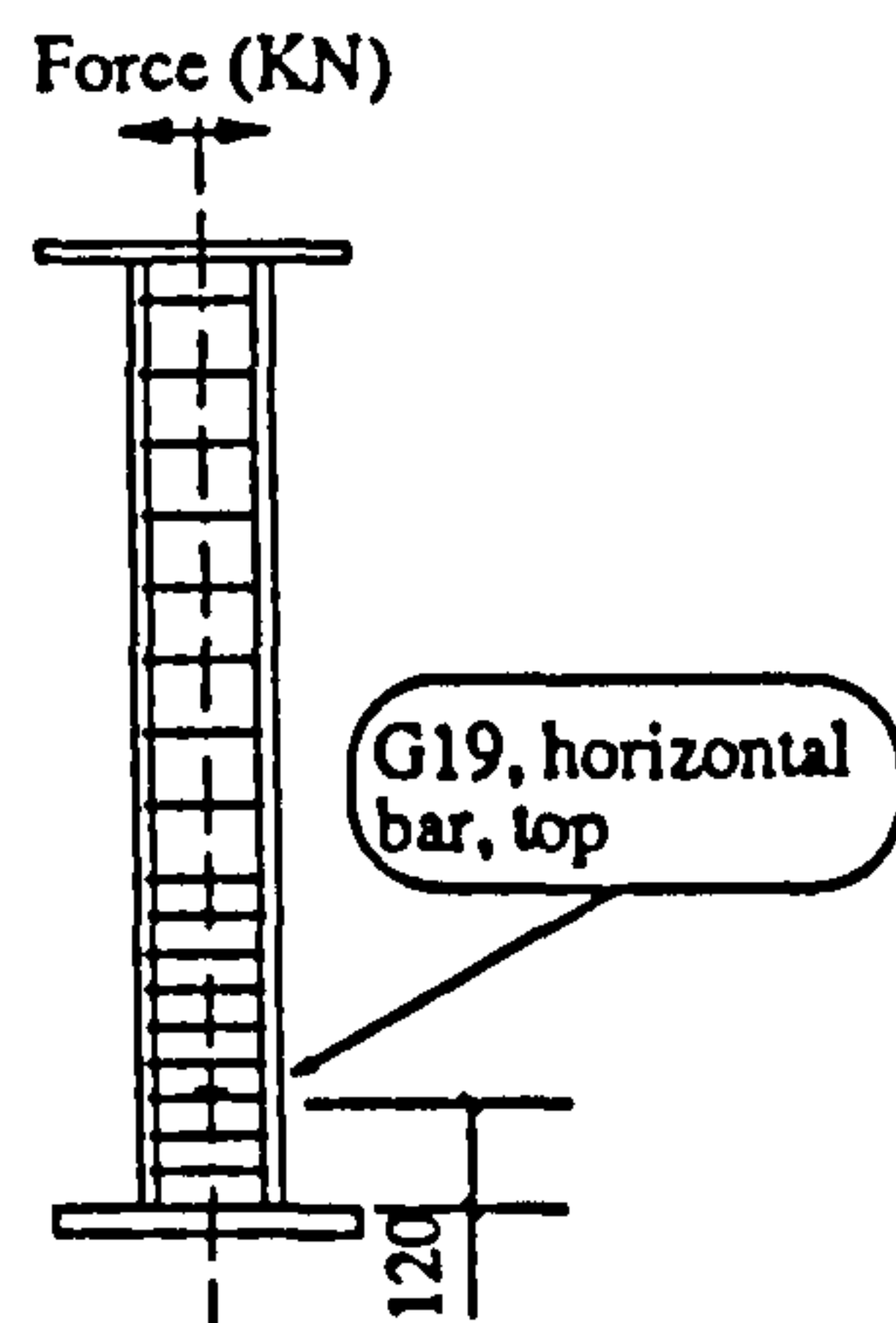
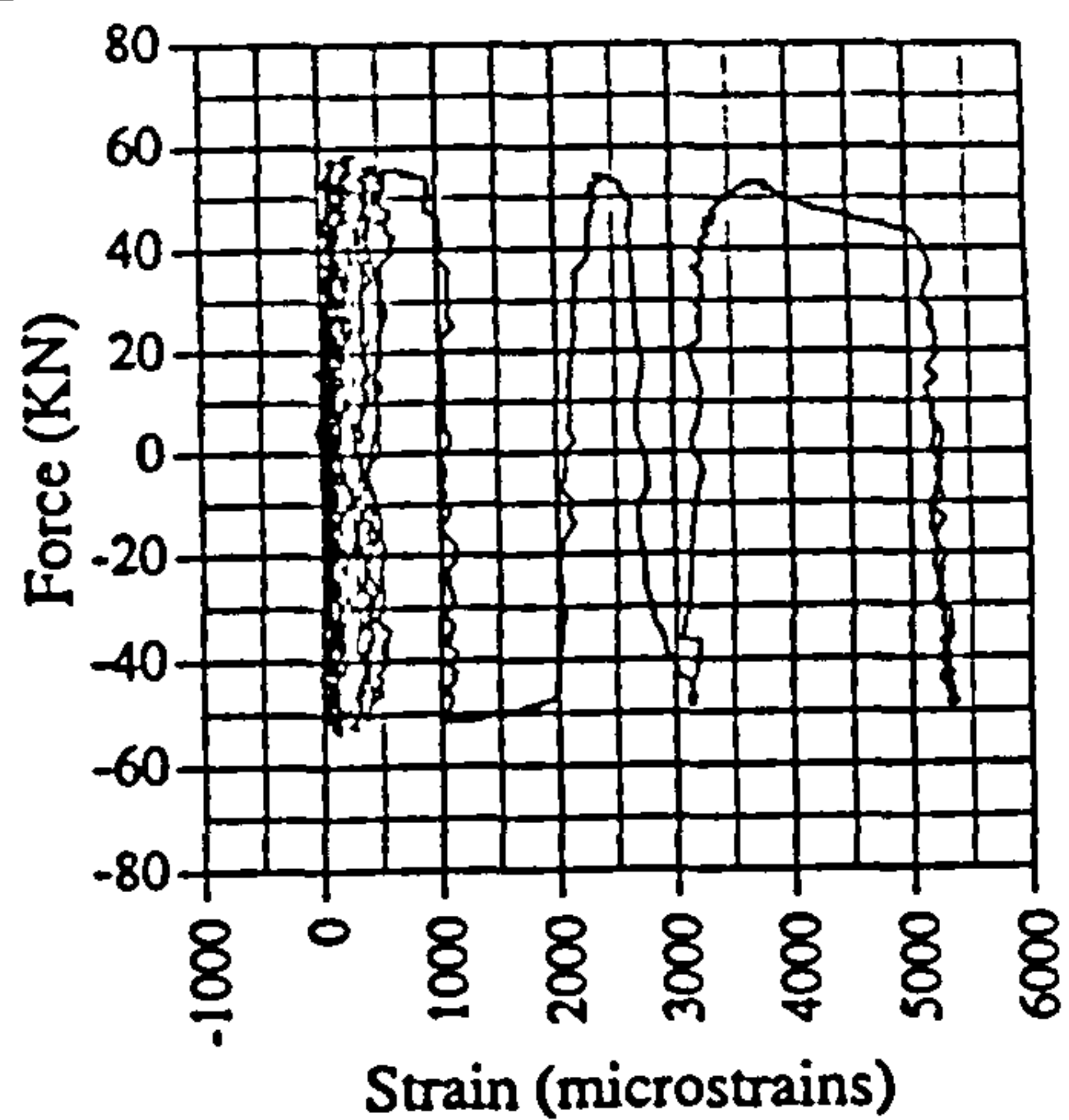


Fig. A.67 Force vs strain, EM02, G19

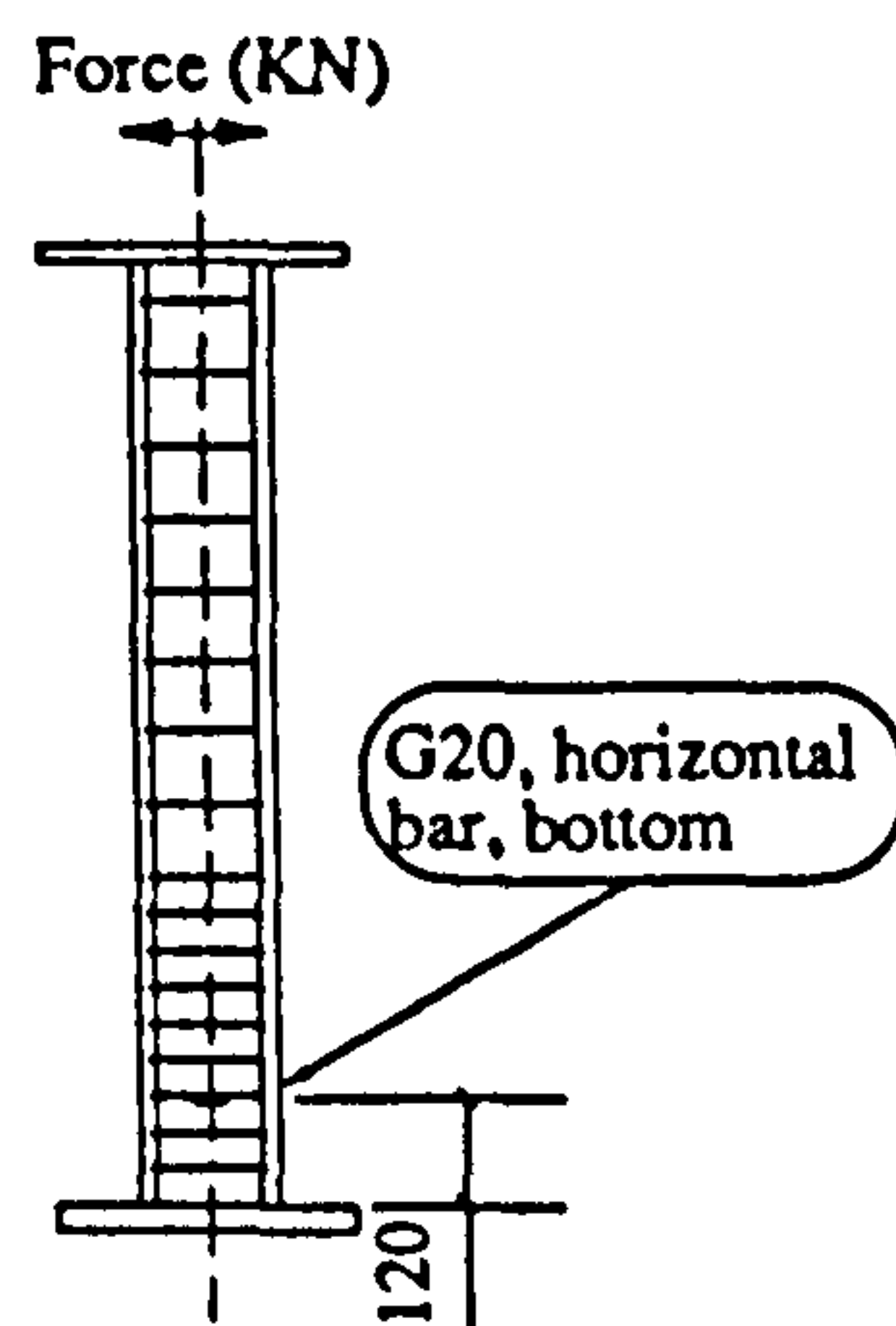
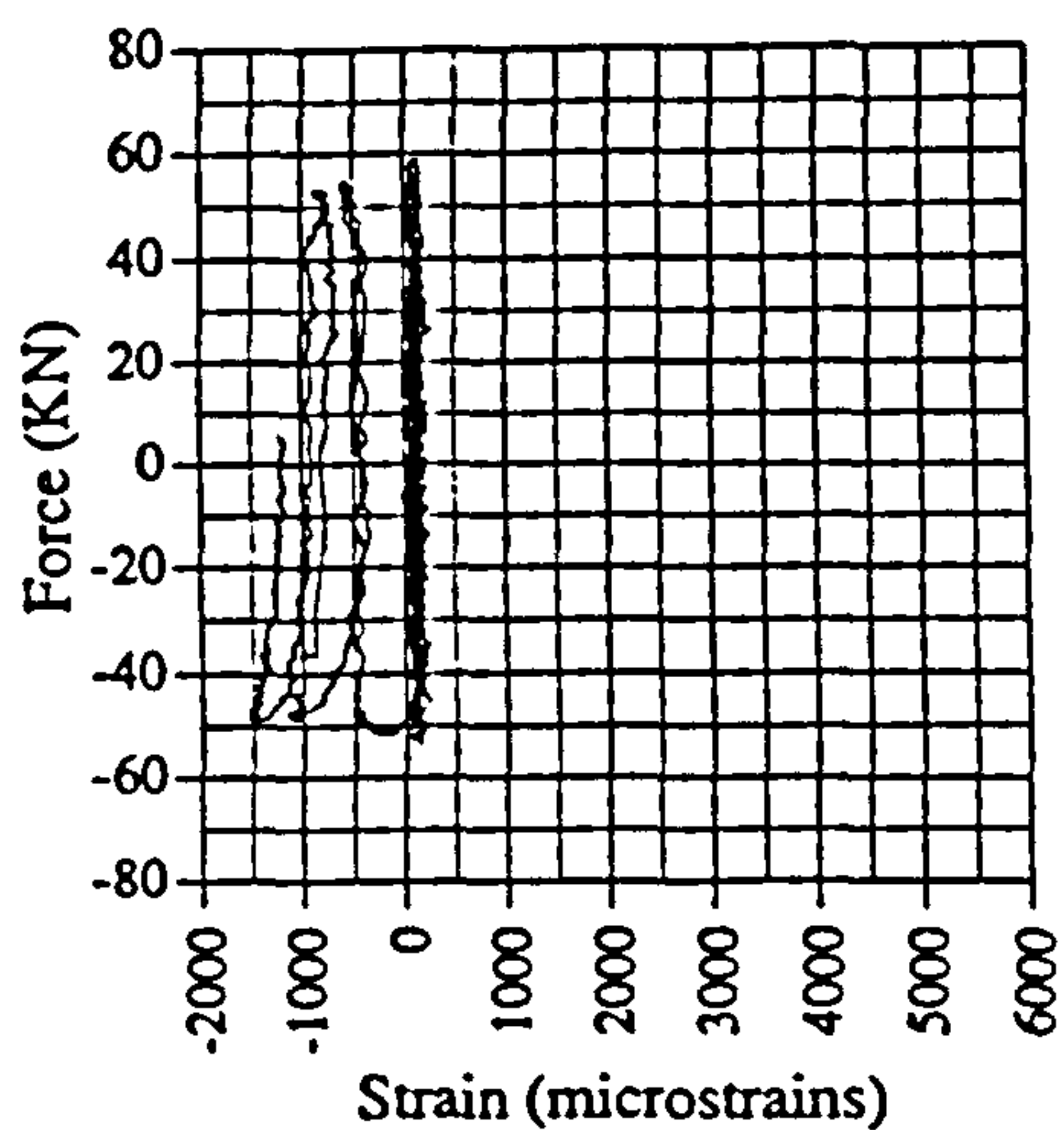


Fig. A.68 Force vs strain, EM02, G20

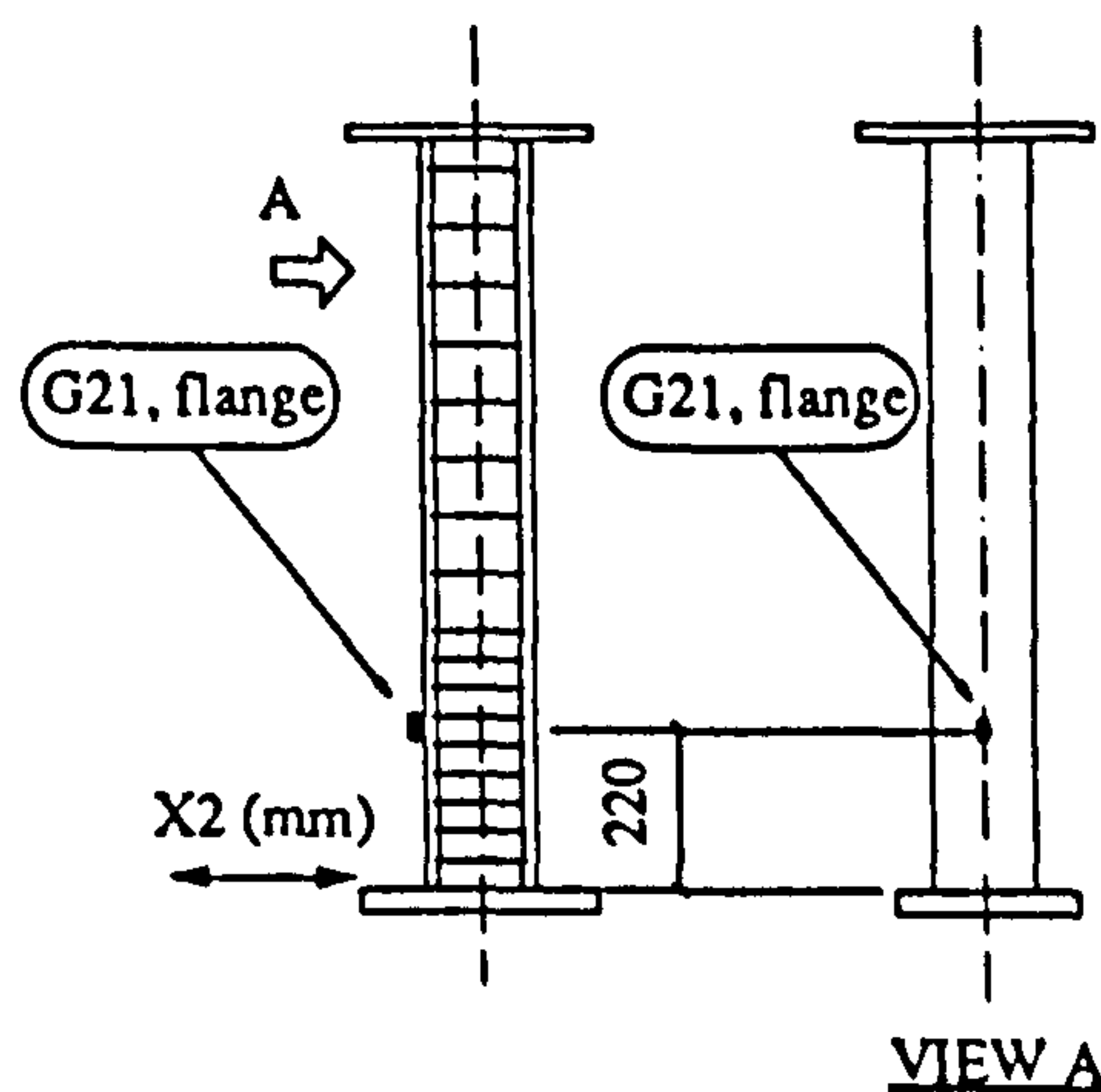
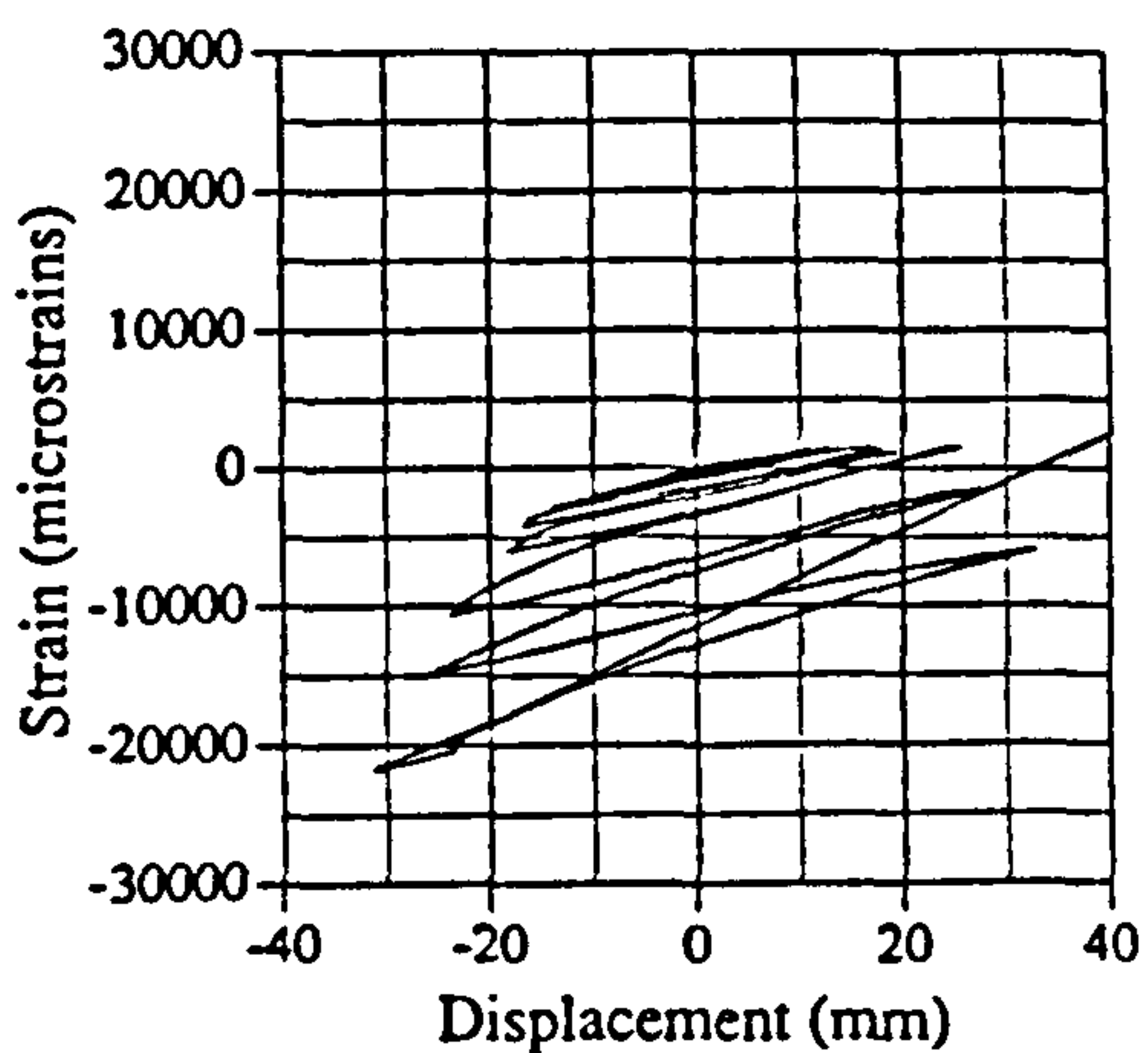


Fig. A.69 Strain vs displacement, EM02, G21

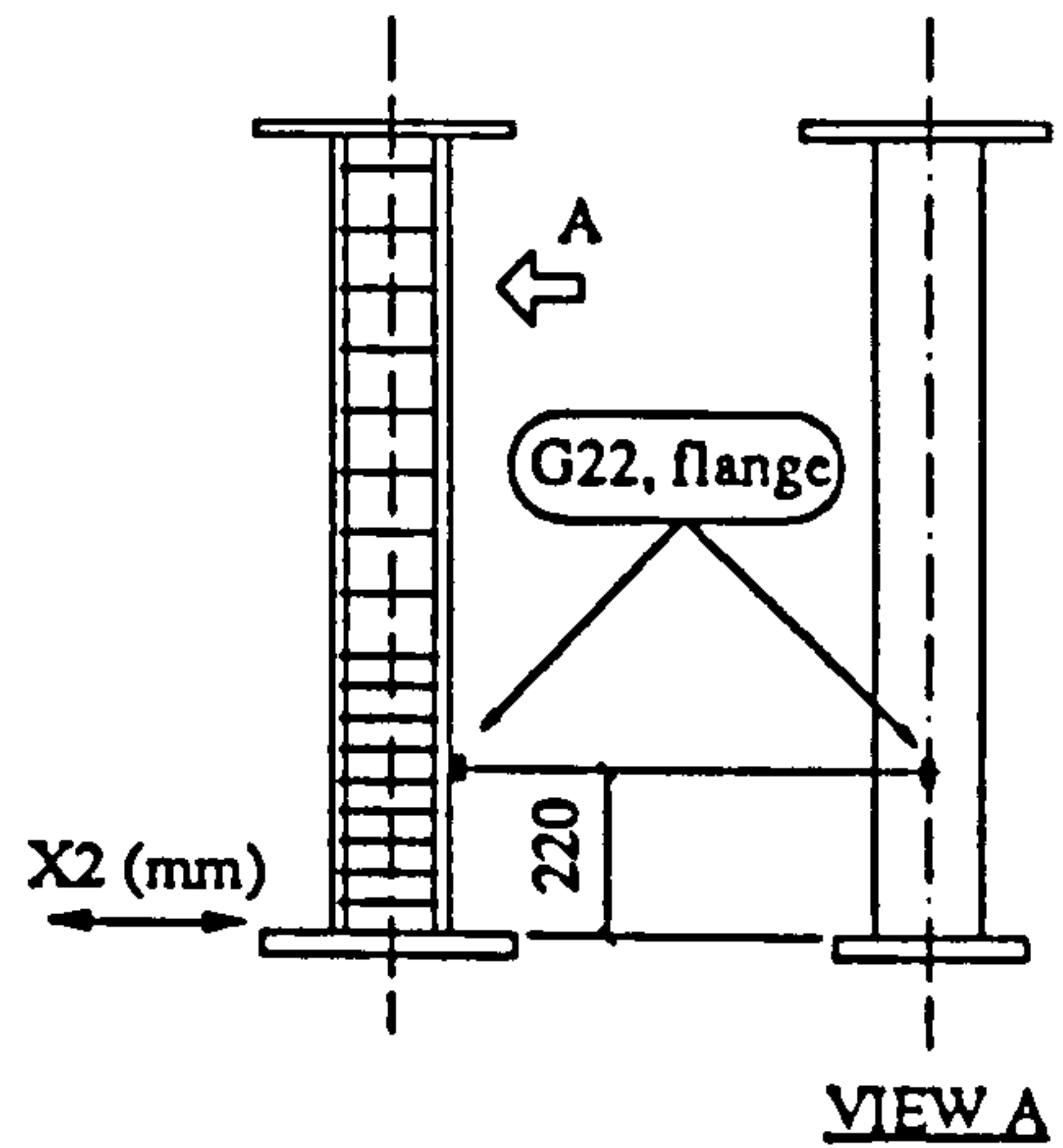
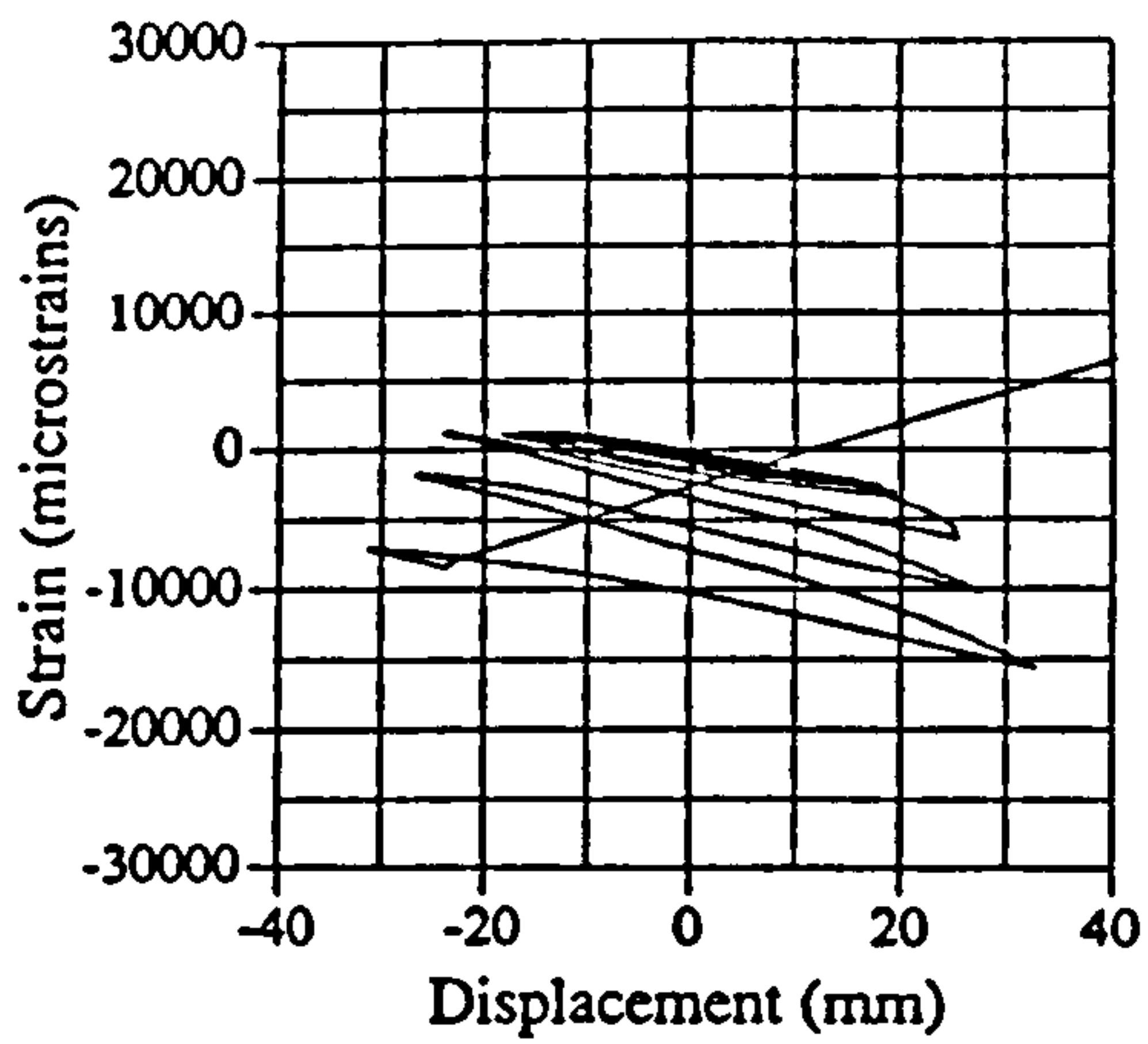


Fig. A.70 Strain vs displacement, EM02, G22

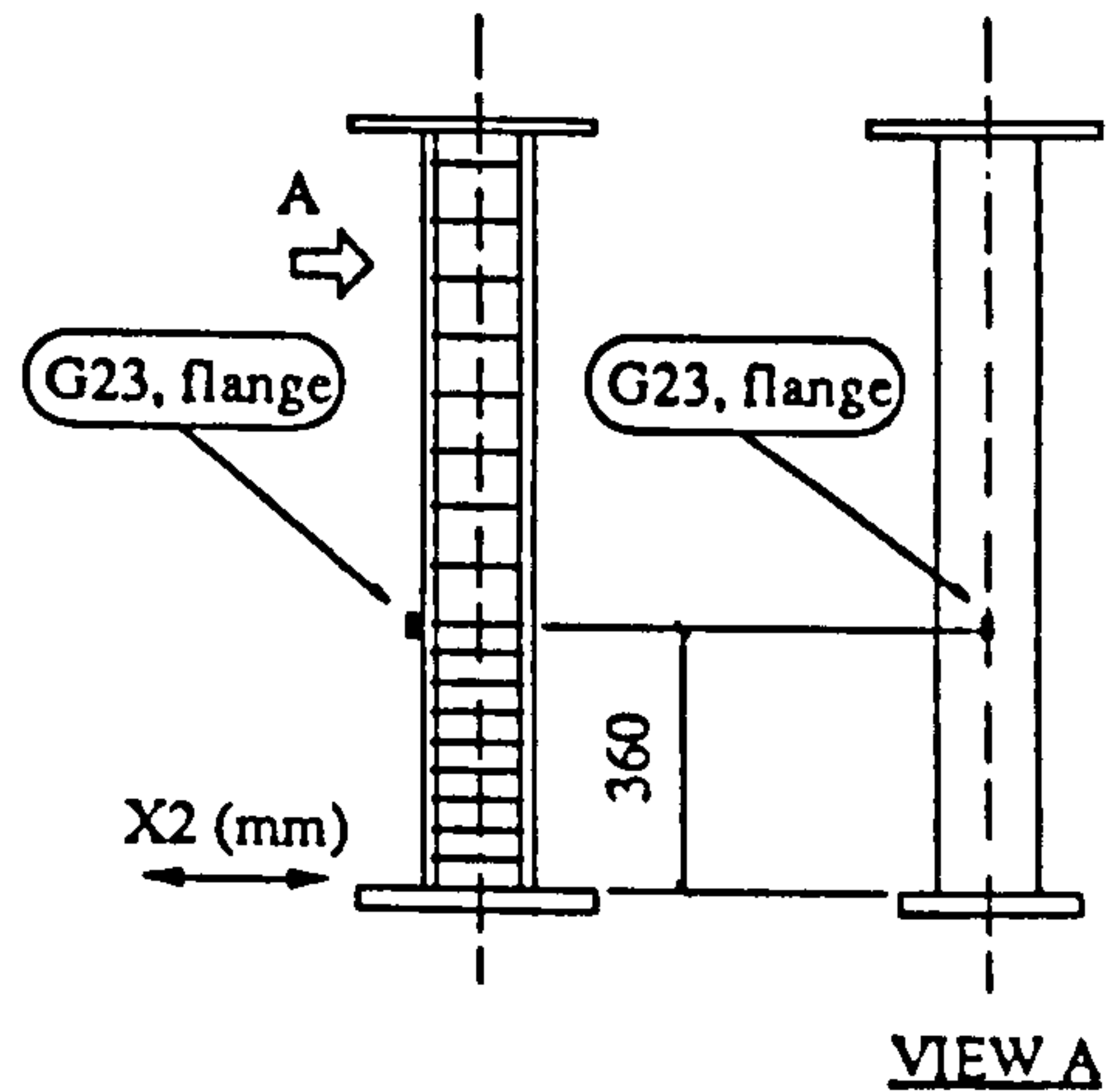
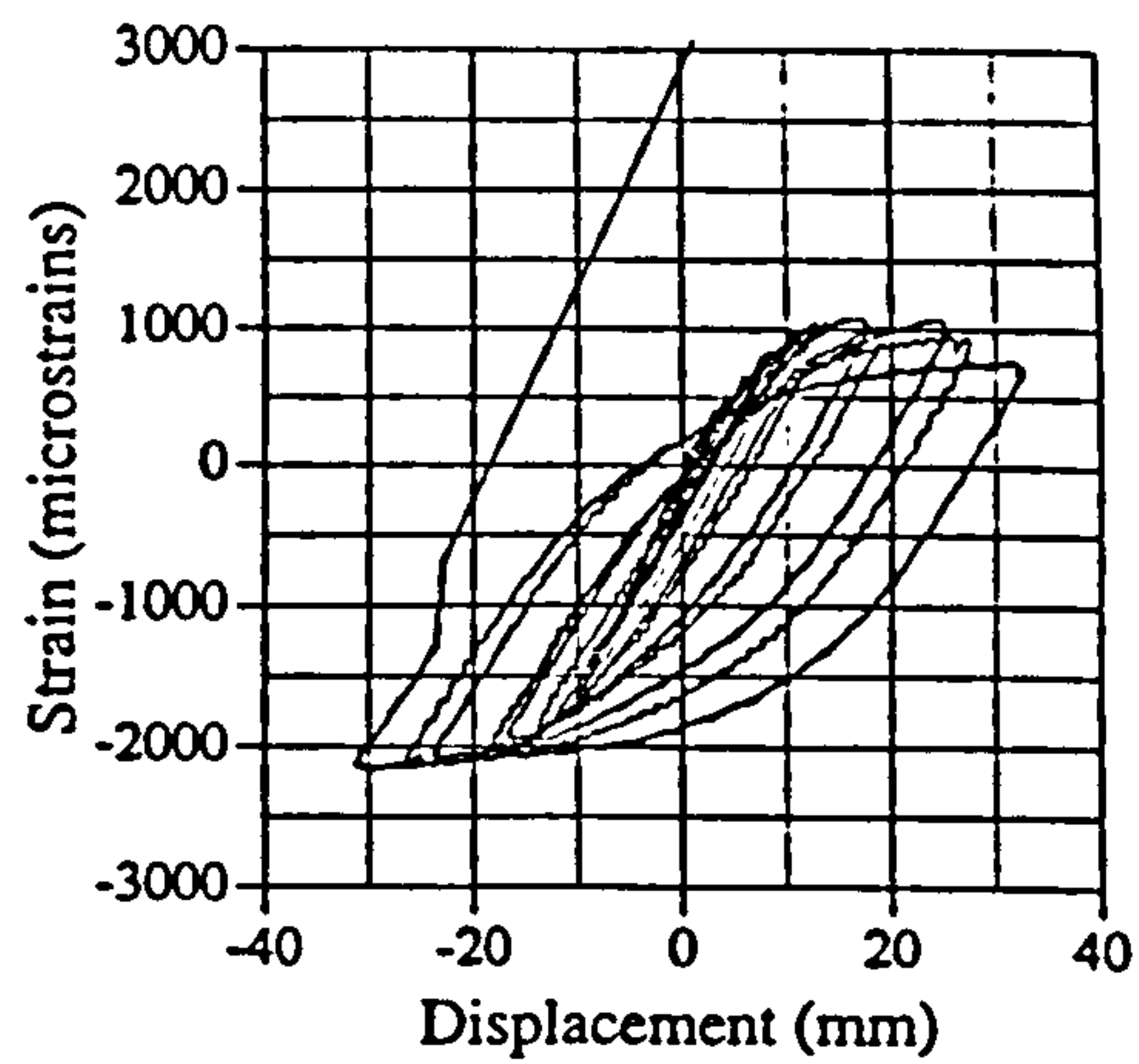


Fig. A.71 Strain vs displacement, EM02, G23

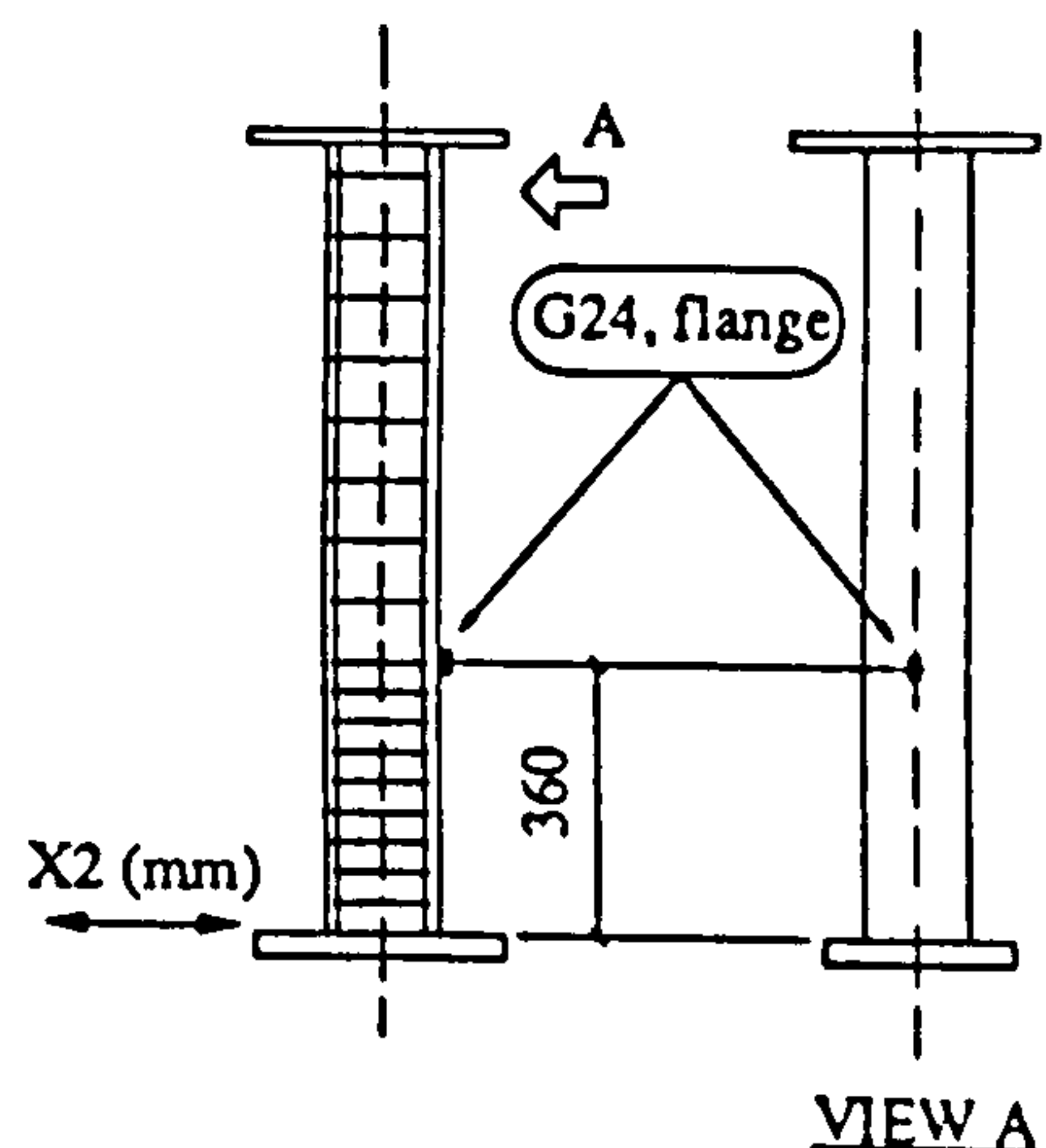
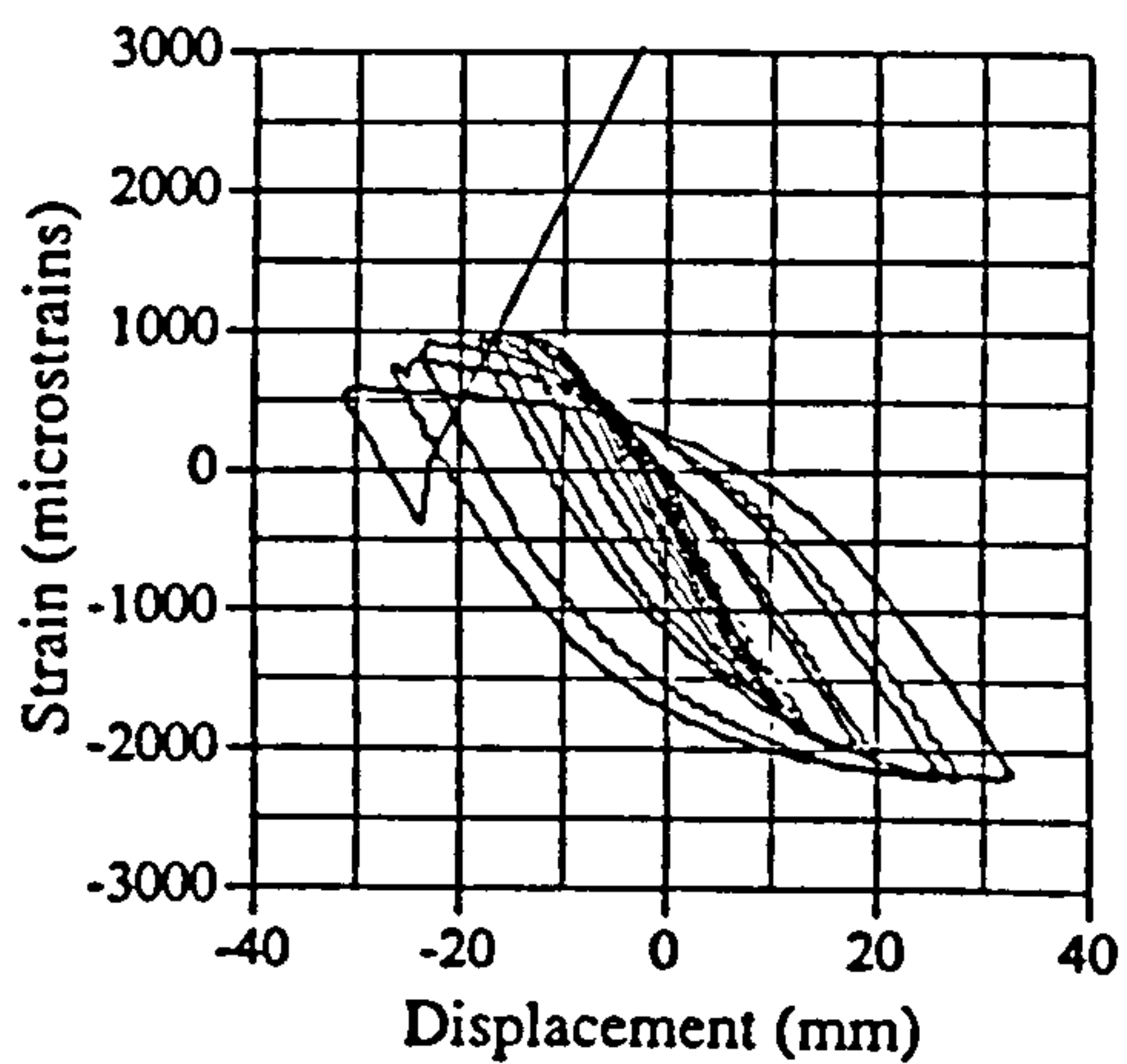


Fig. A.72 Strain vs displacement, EM02, G24

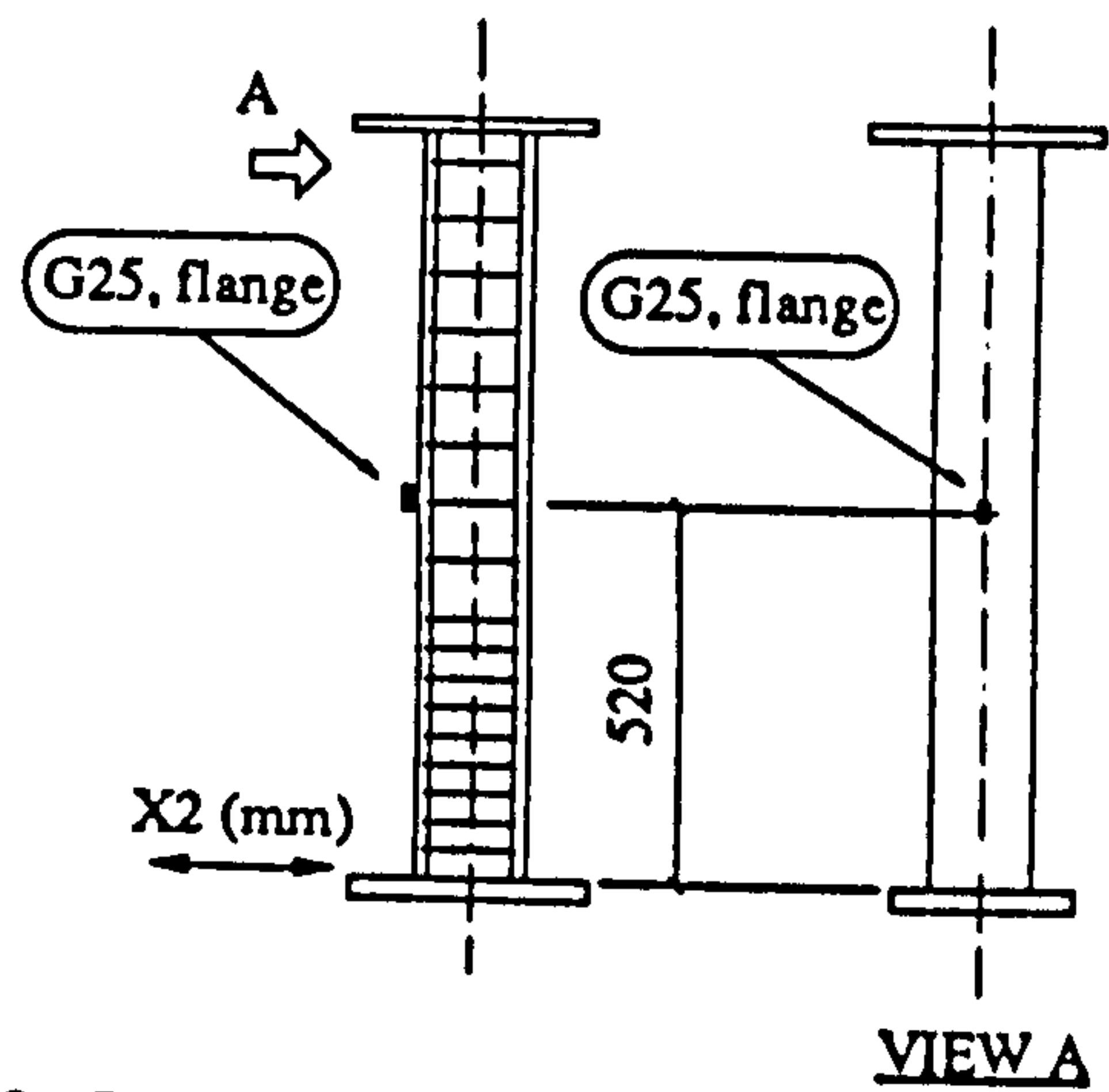
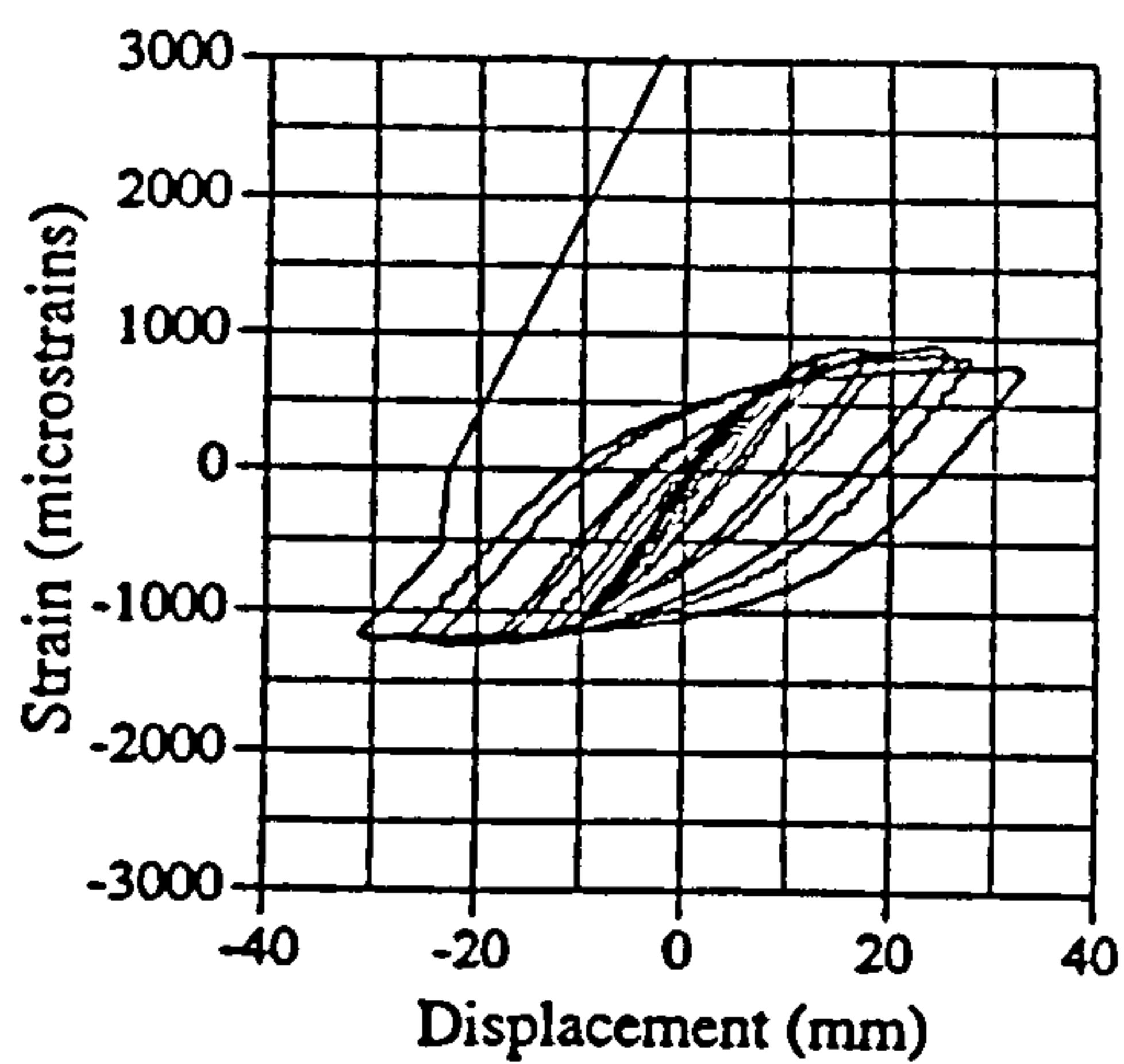


Fig. A.73 Strain vs displacement, EM02, G25

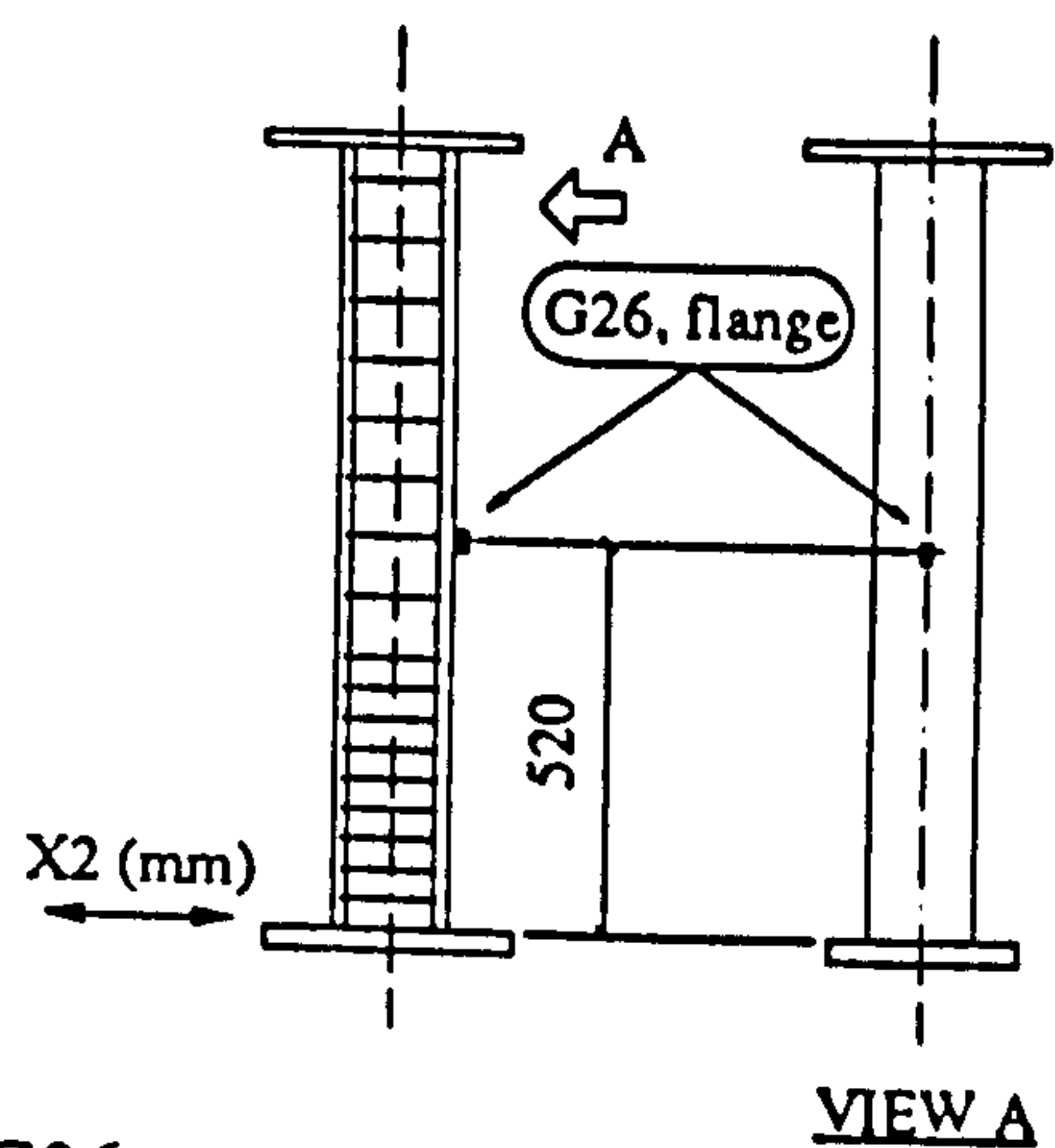
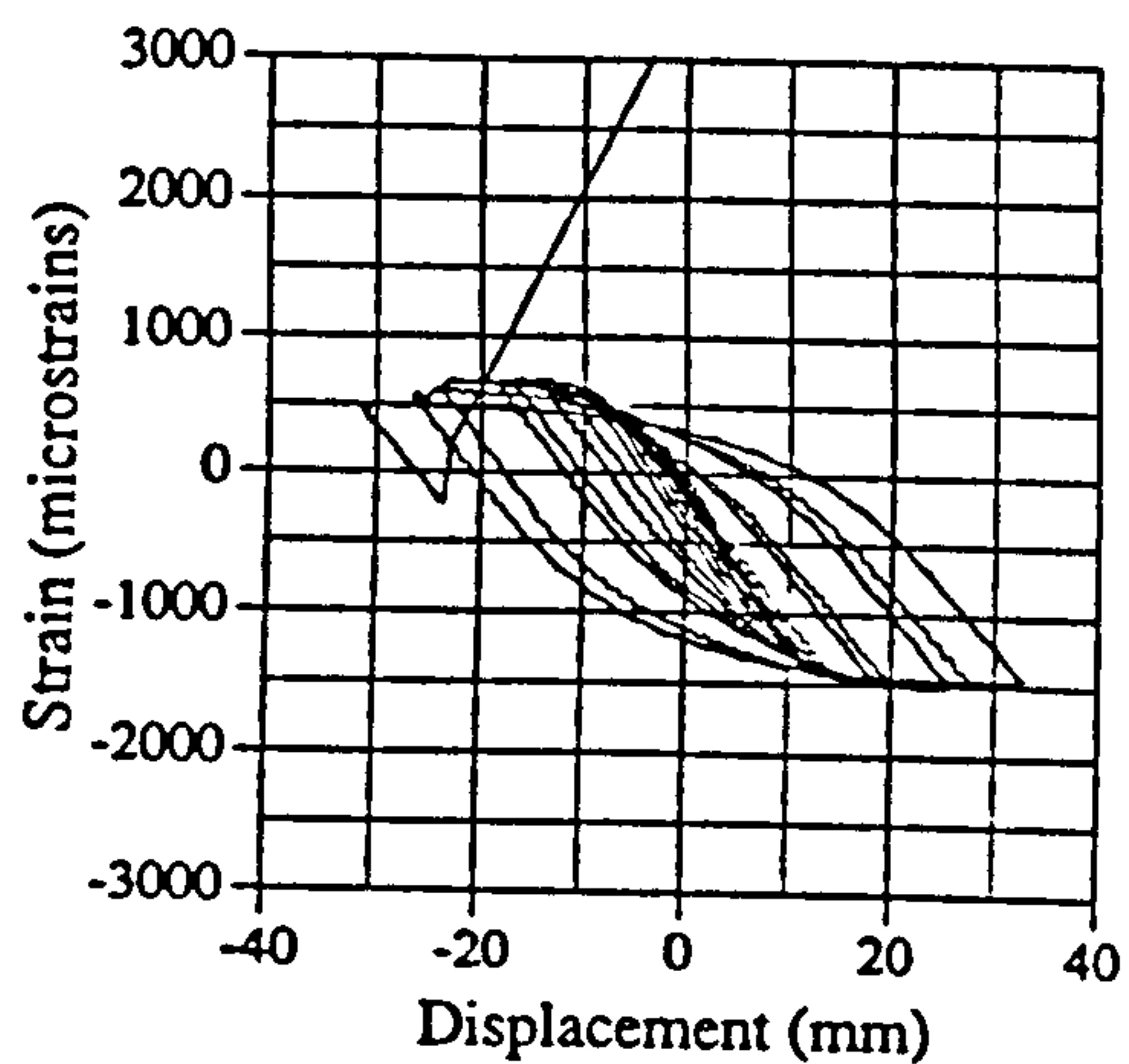


Fig. A.74 Strain vs displacement, EM02, G26

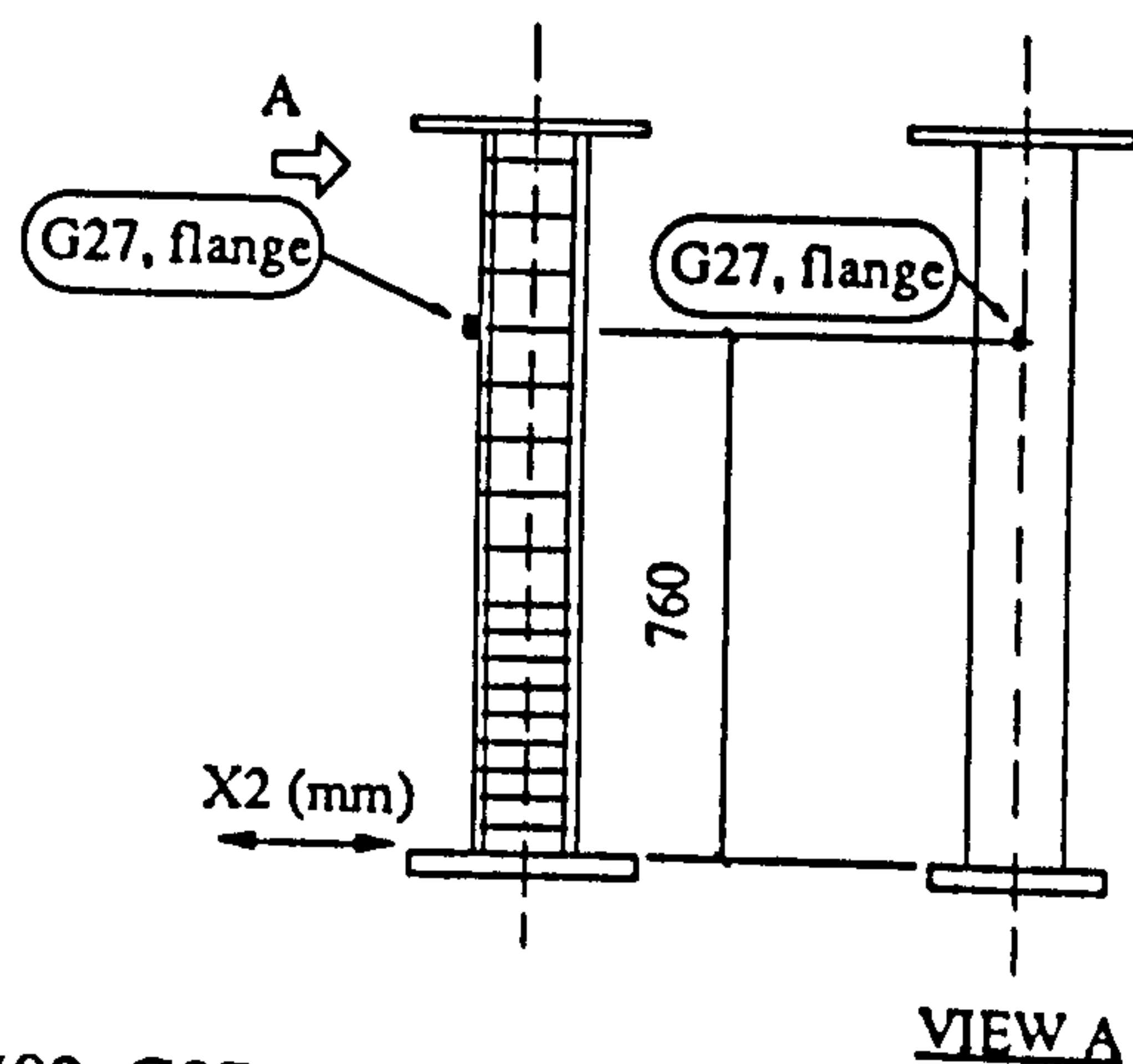
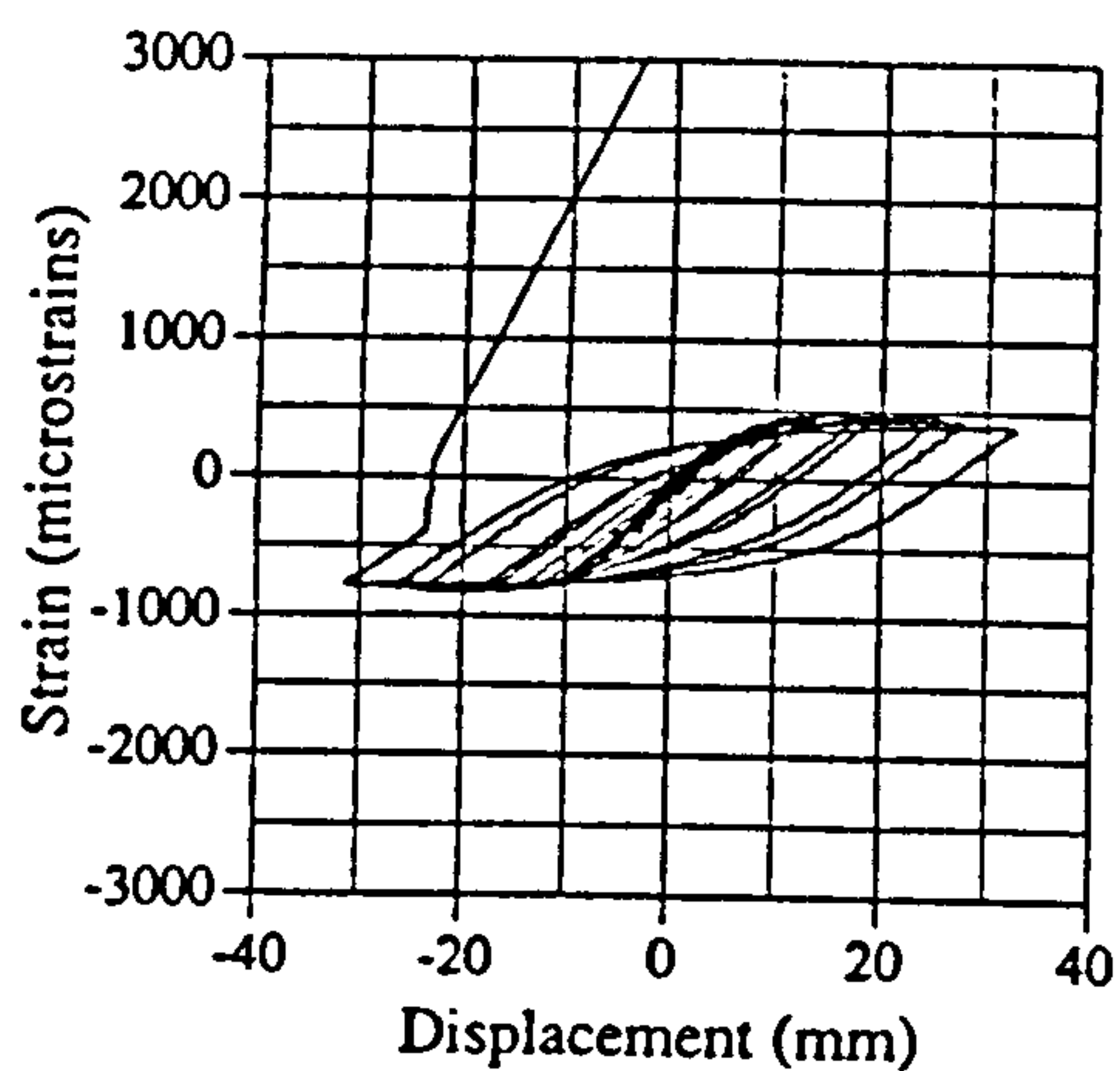


Fig. A.75 Strain vs displacement, EM02, G27

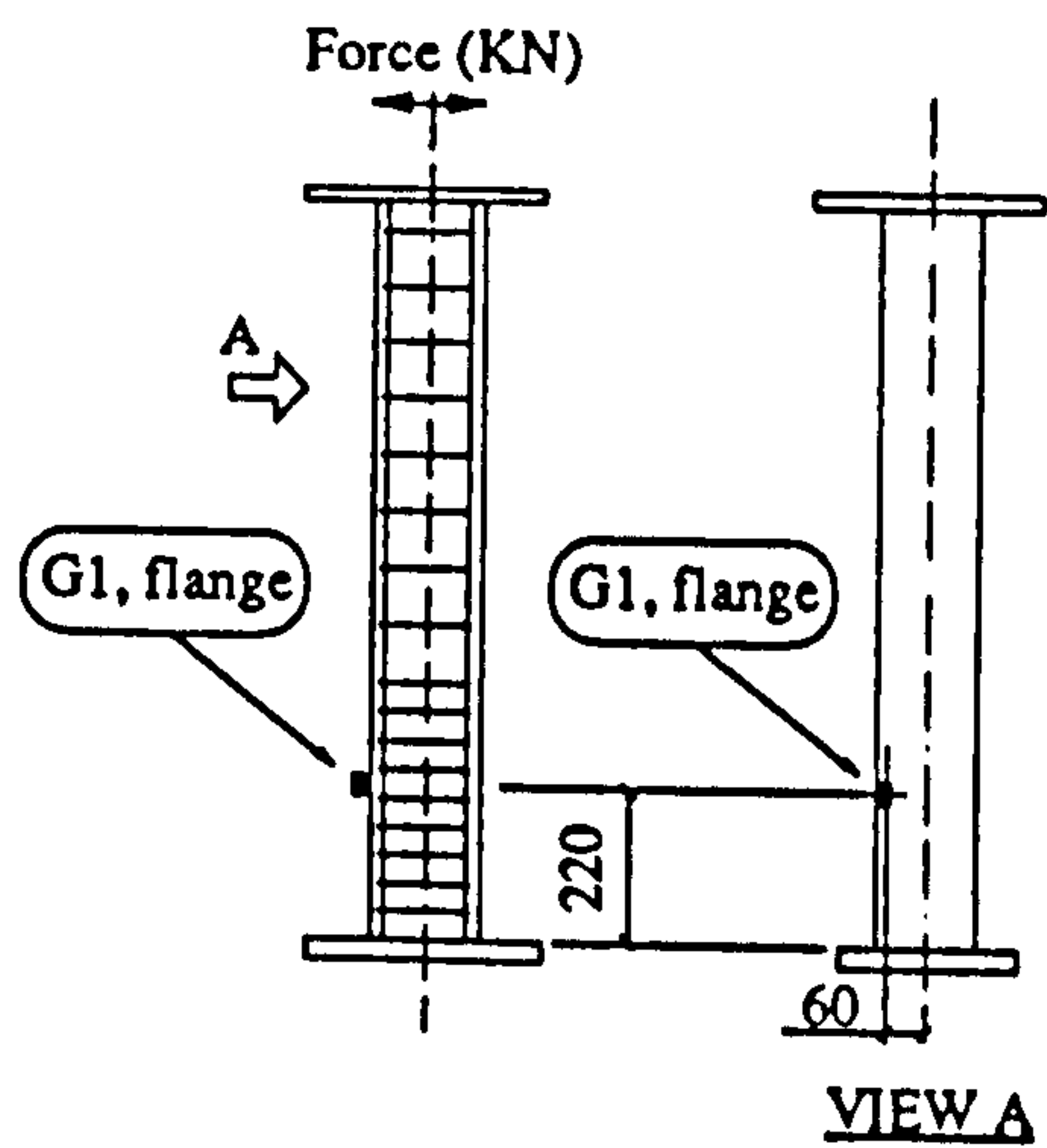
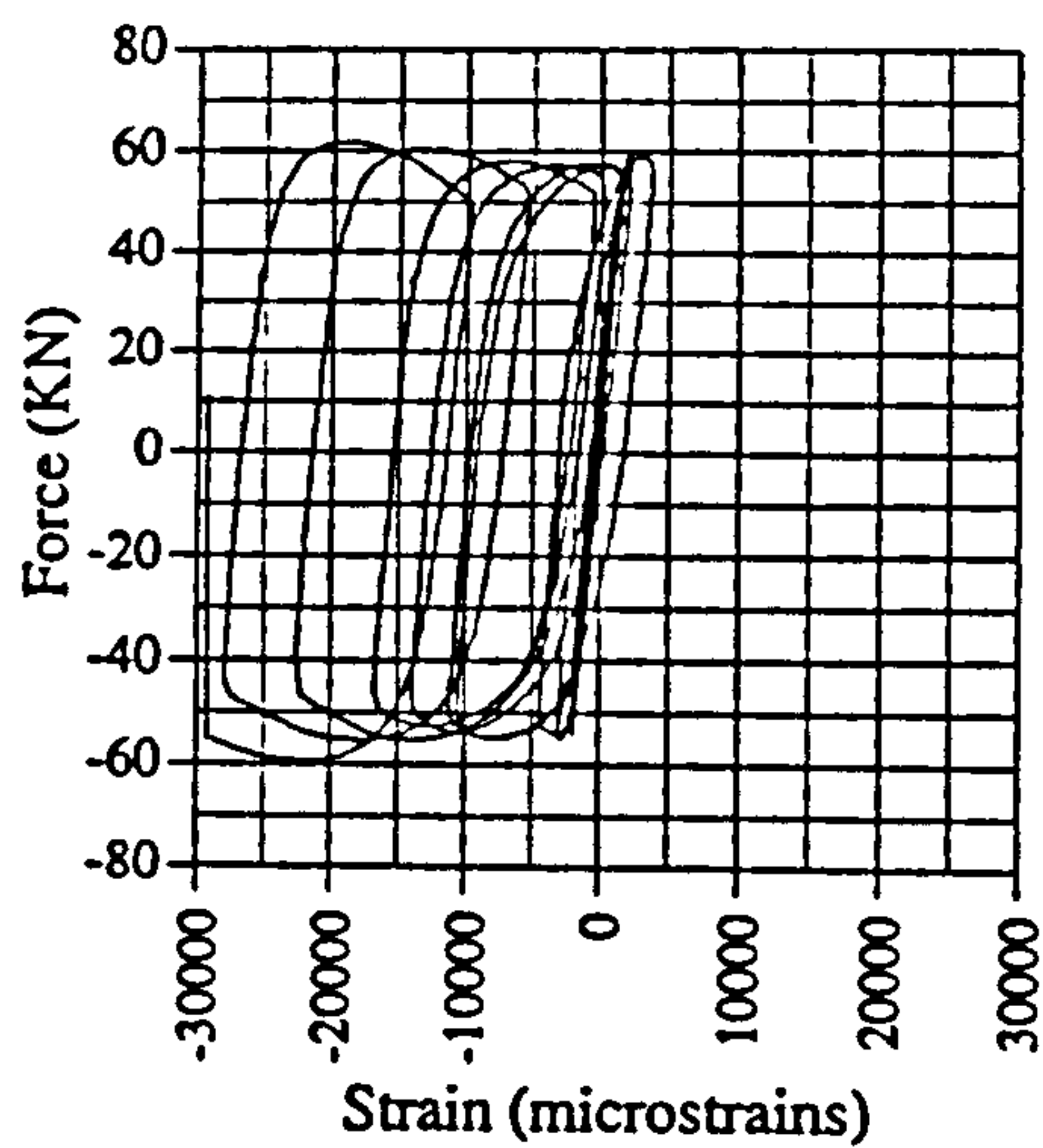


Fig. A.76 Force vs strain, IC02, G1

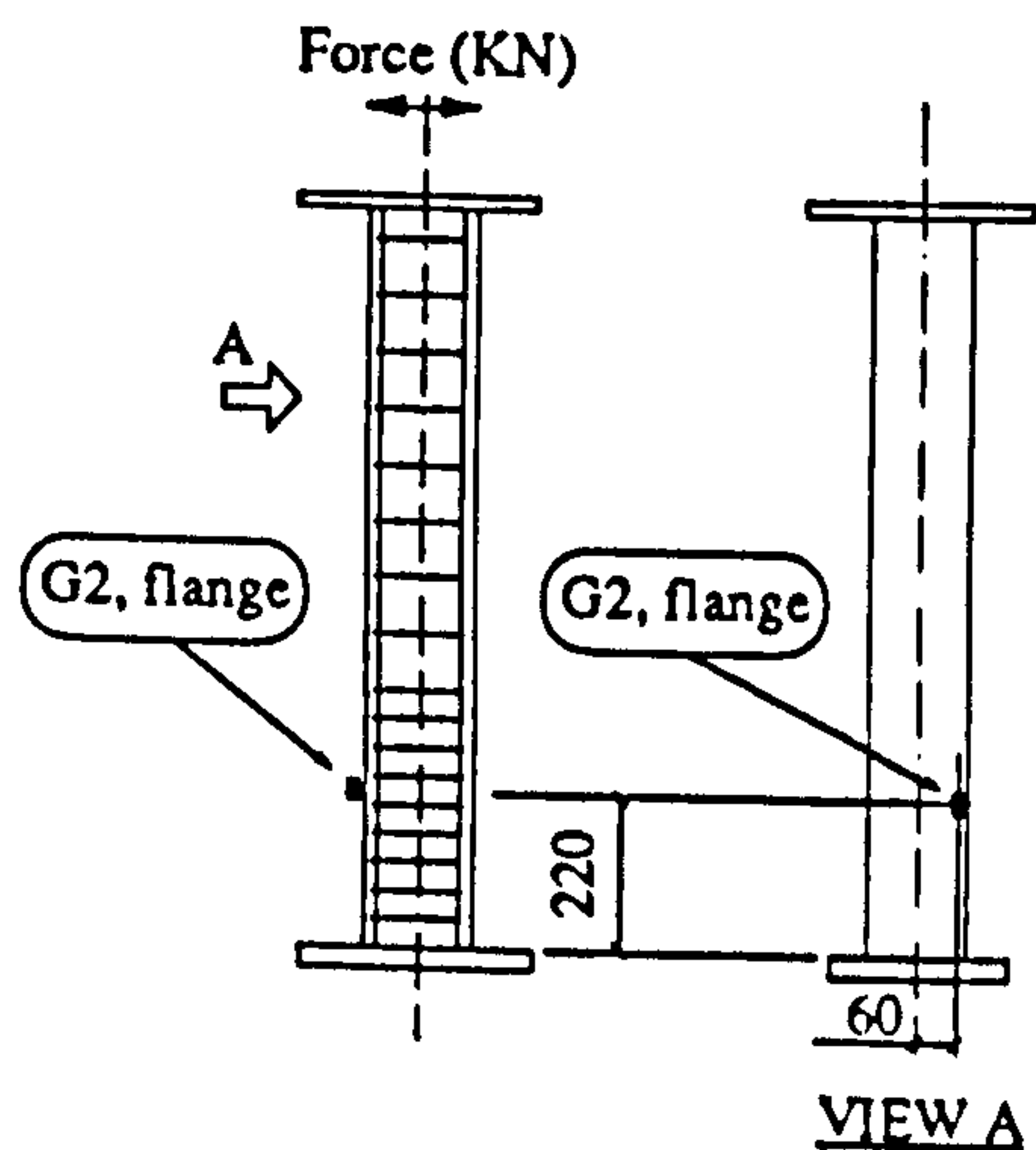
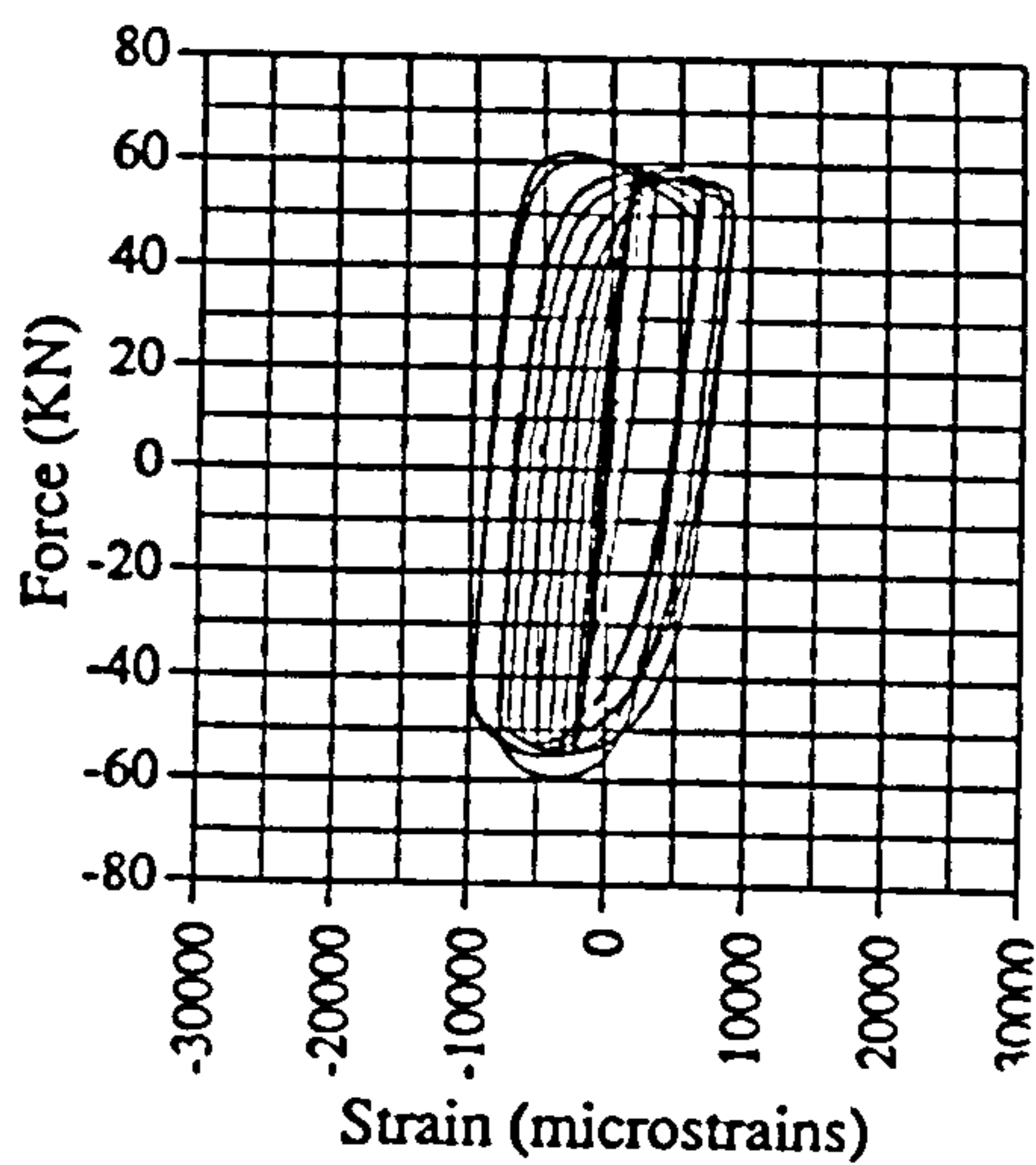


Fig. A.77 Force vs strain, IC02, G2

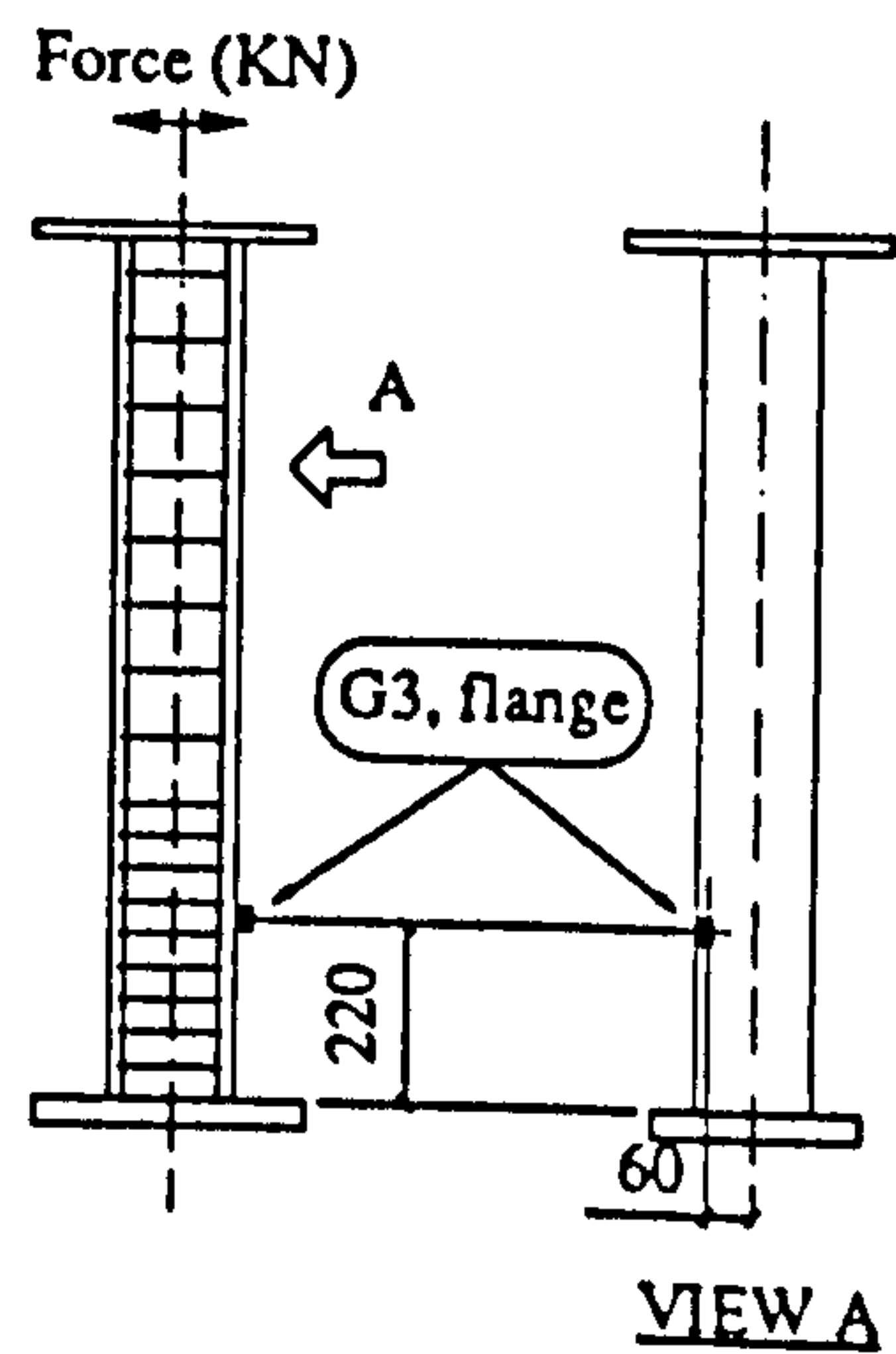
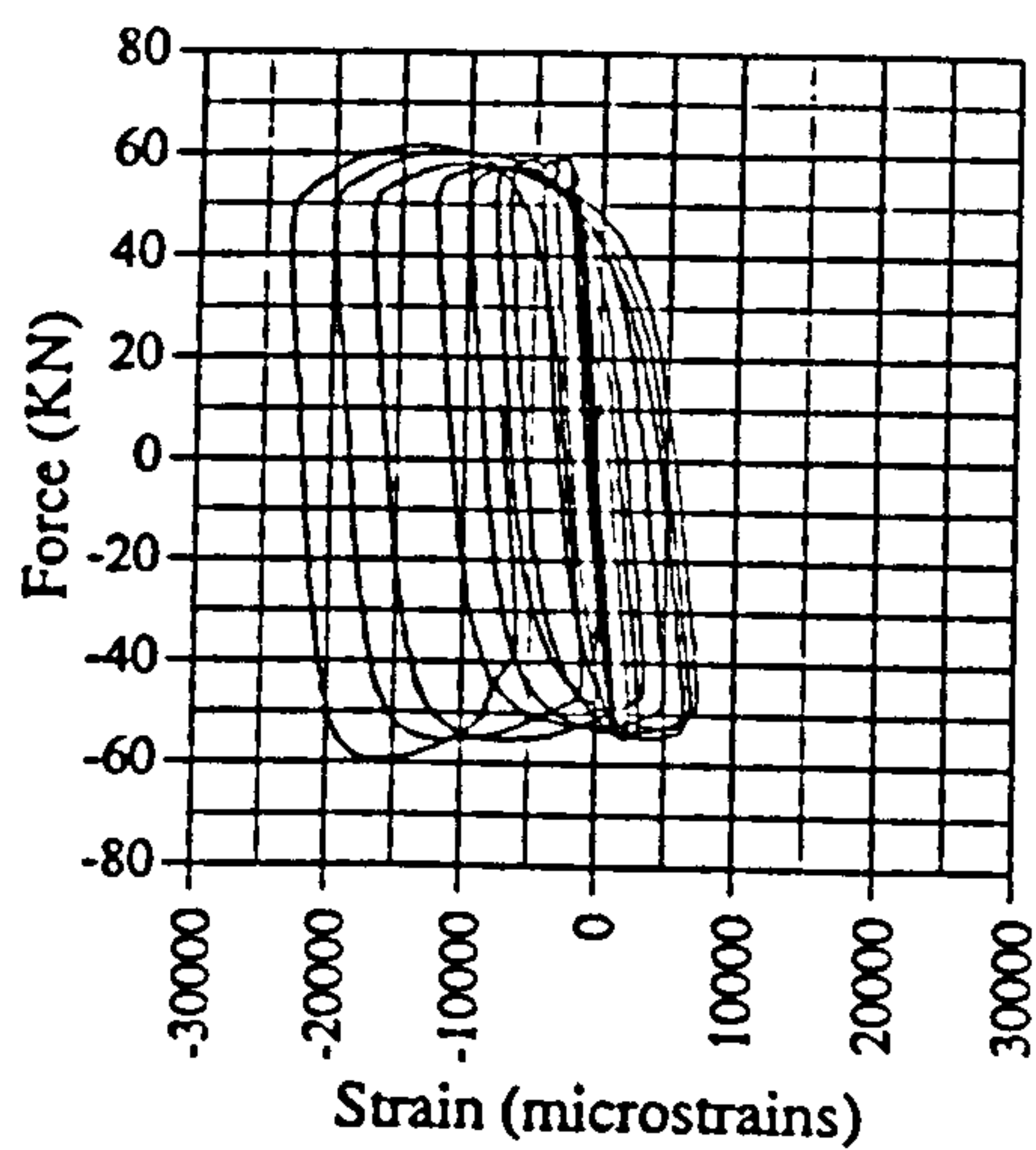


Fig. A.78 Force vs strain, IC02, G3

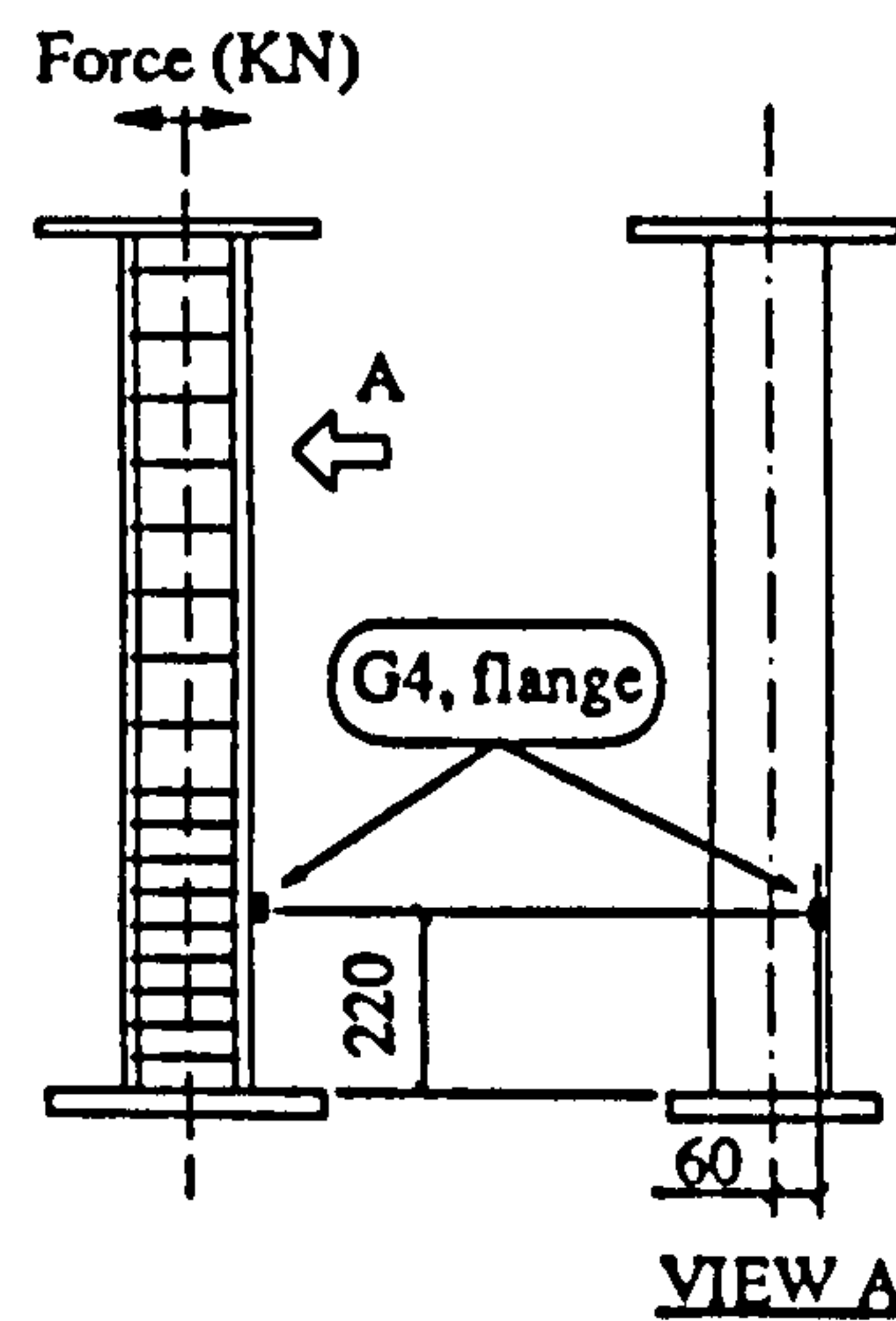
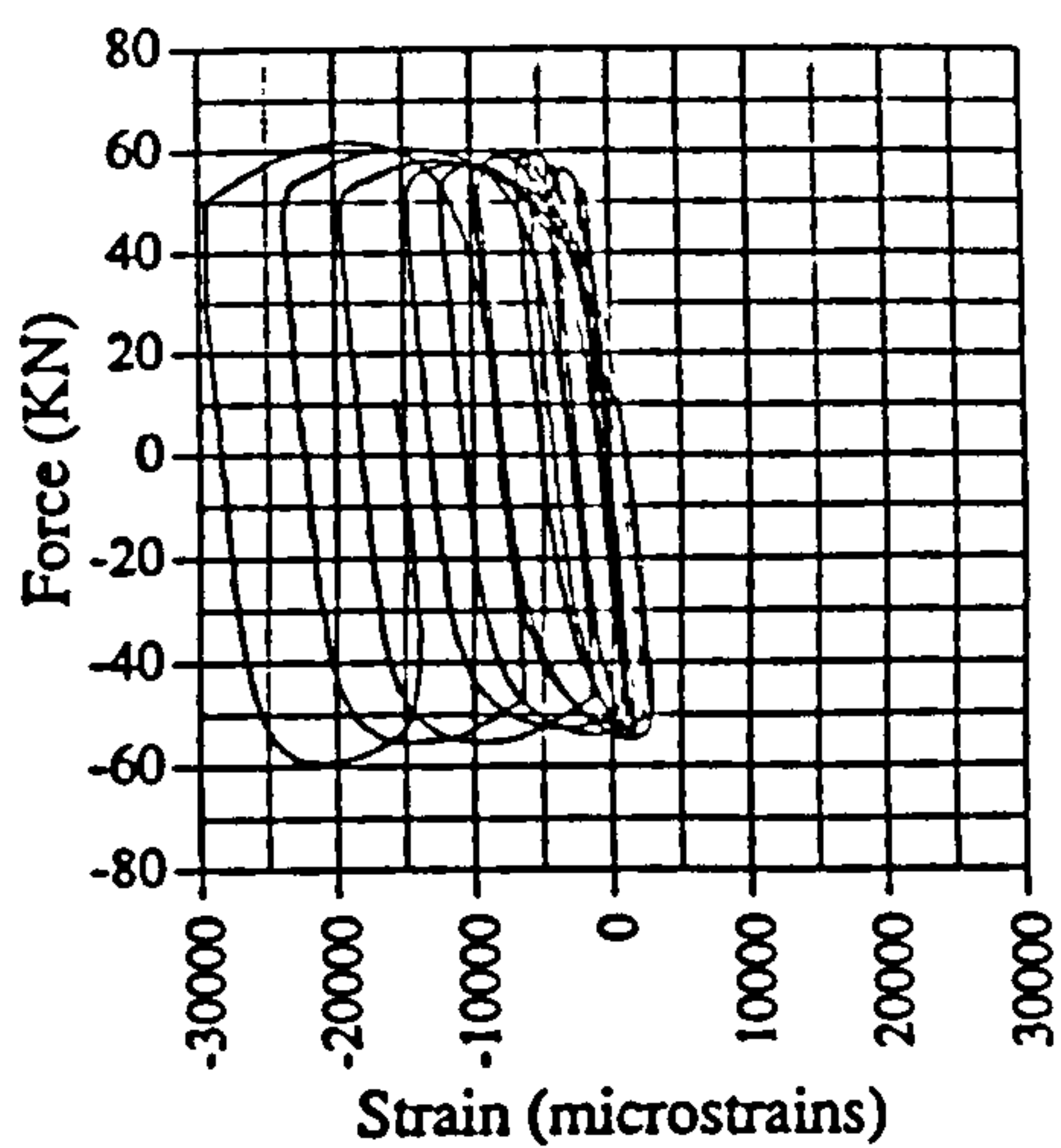


Fig. A.79 Force vs strain, IC02, G4

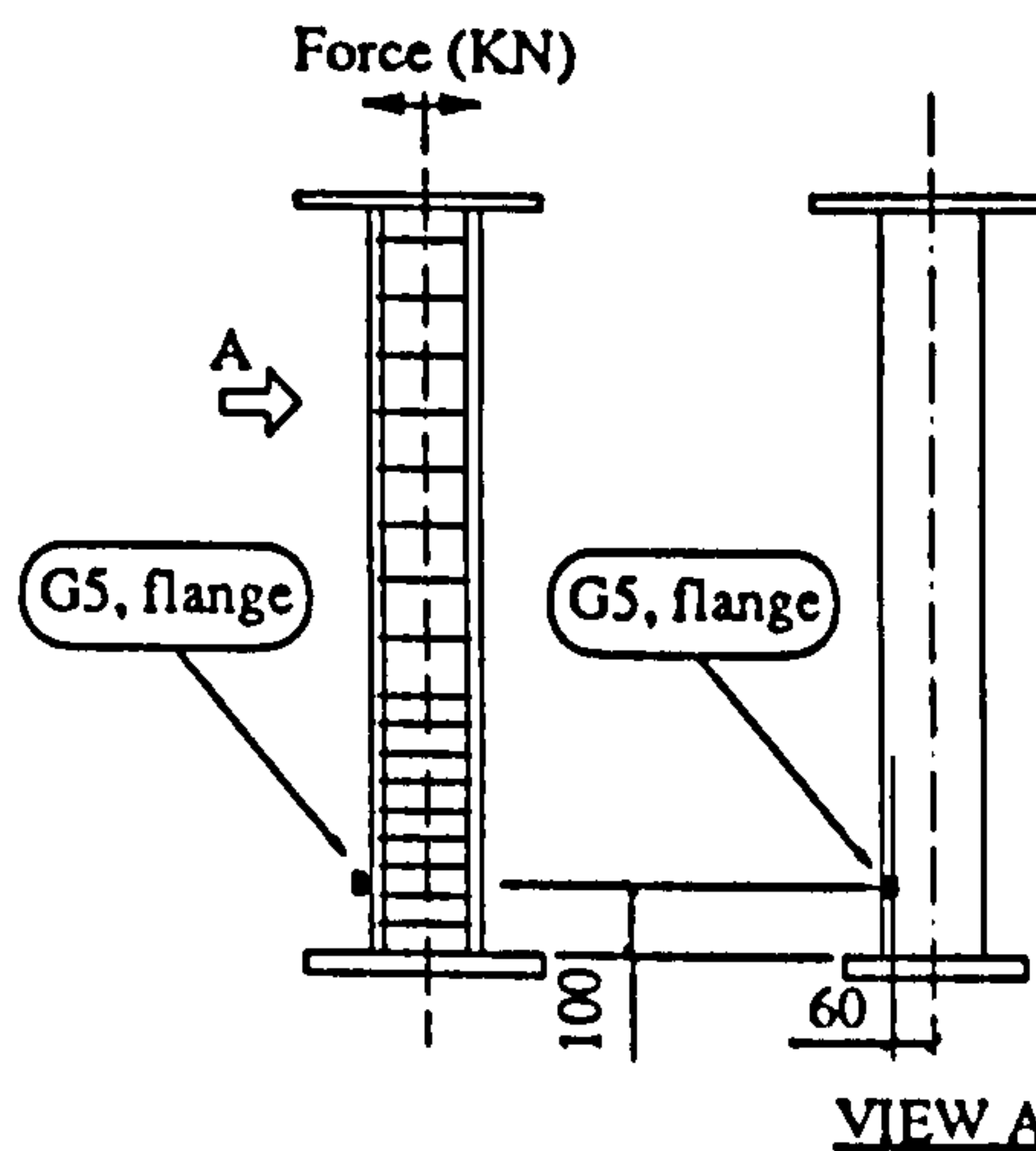
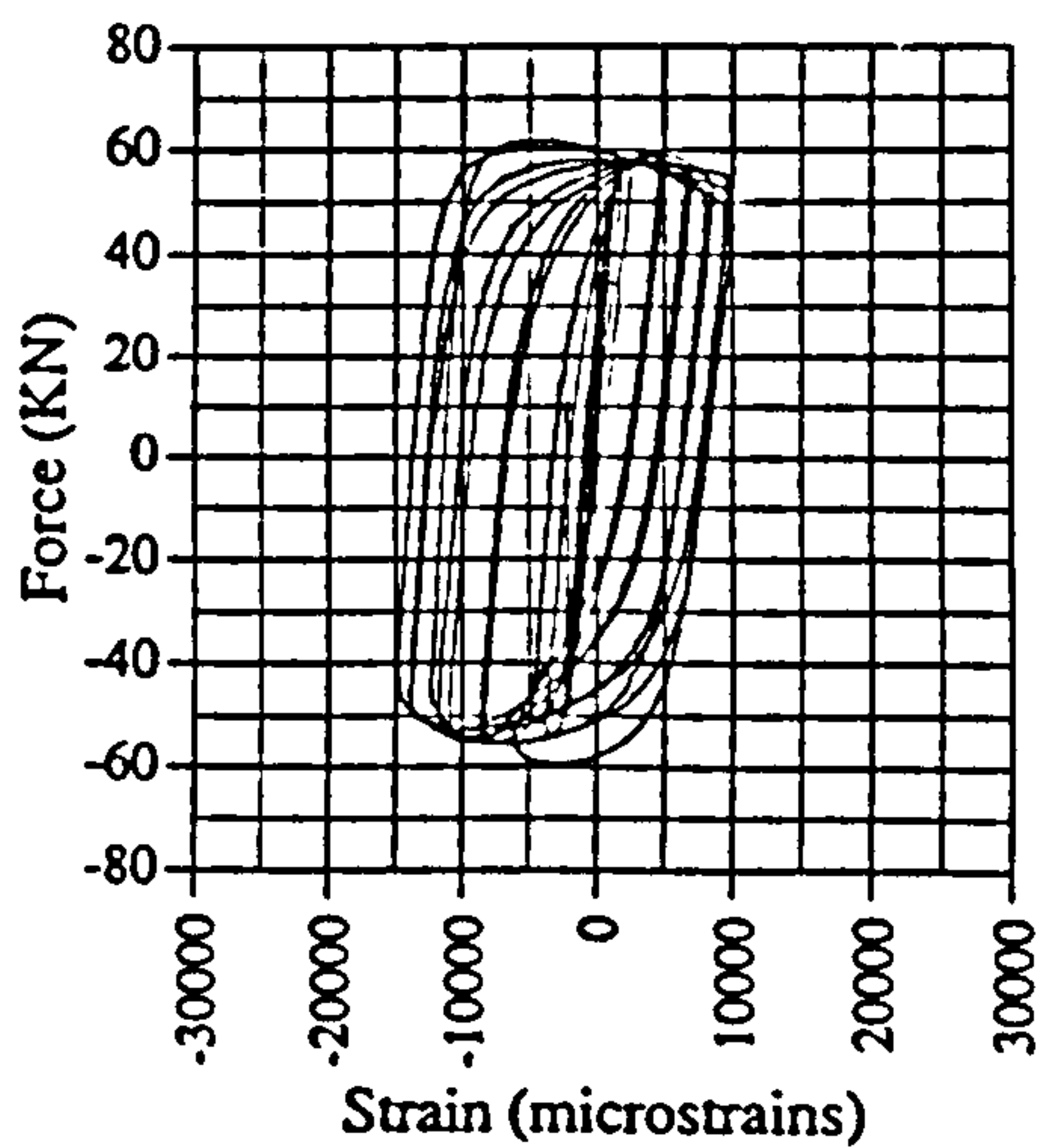


Fig. A.80 Force vs strain, IC02, G5

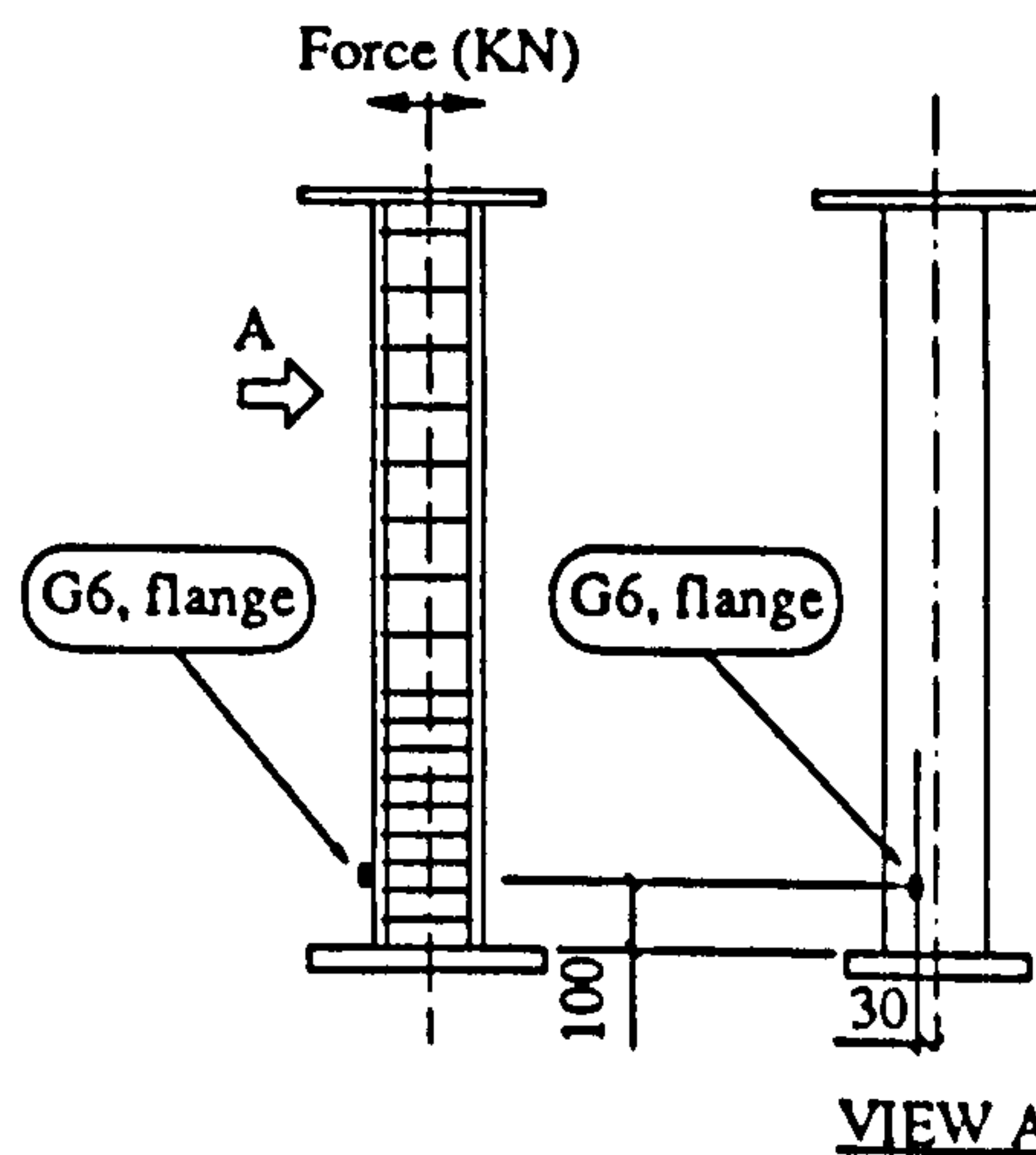
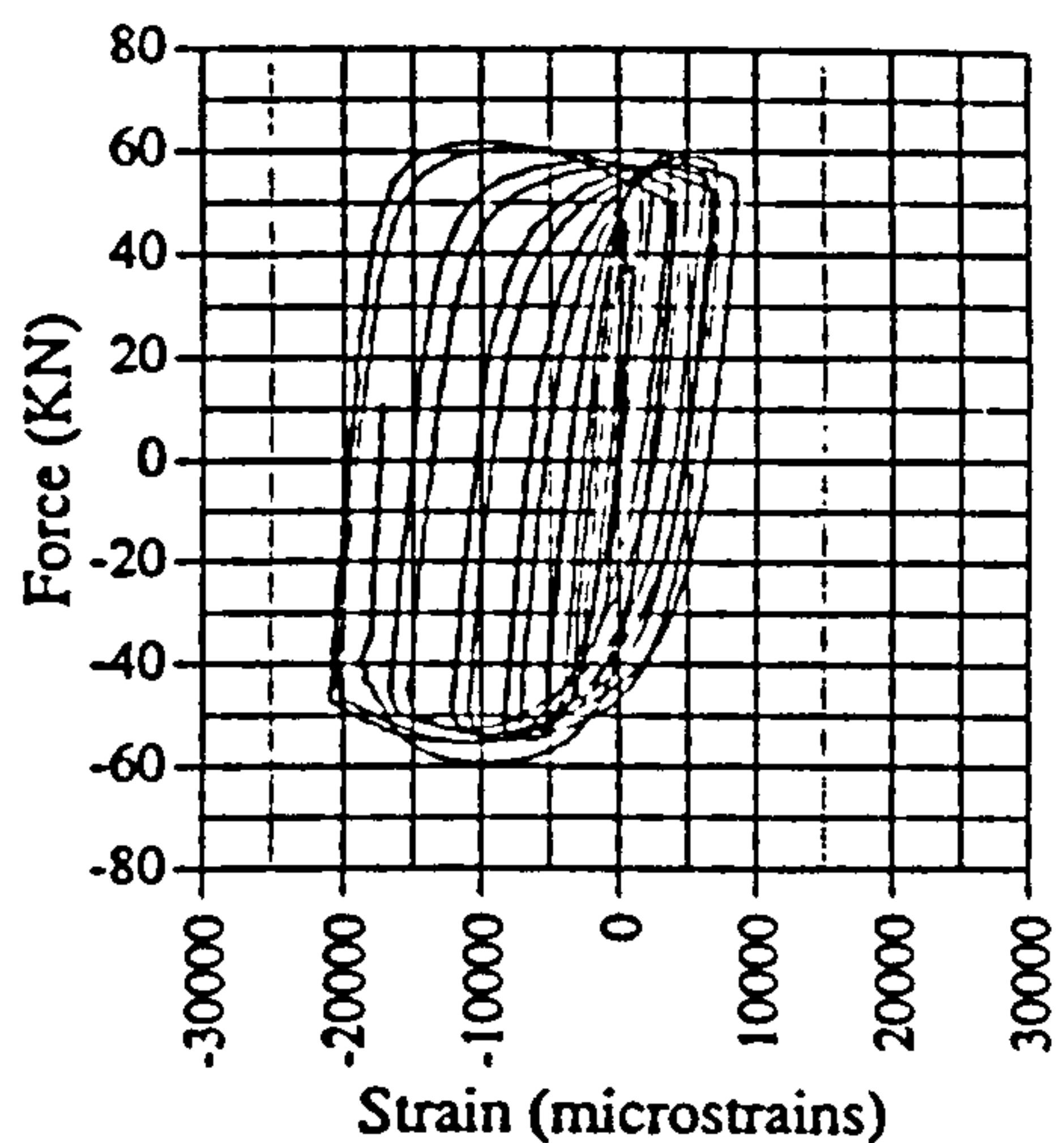


Fig. A.81 Force vs strain, IC02, G6

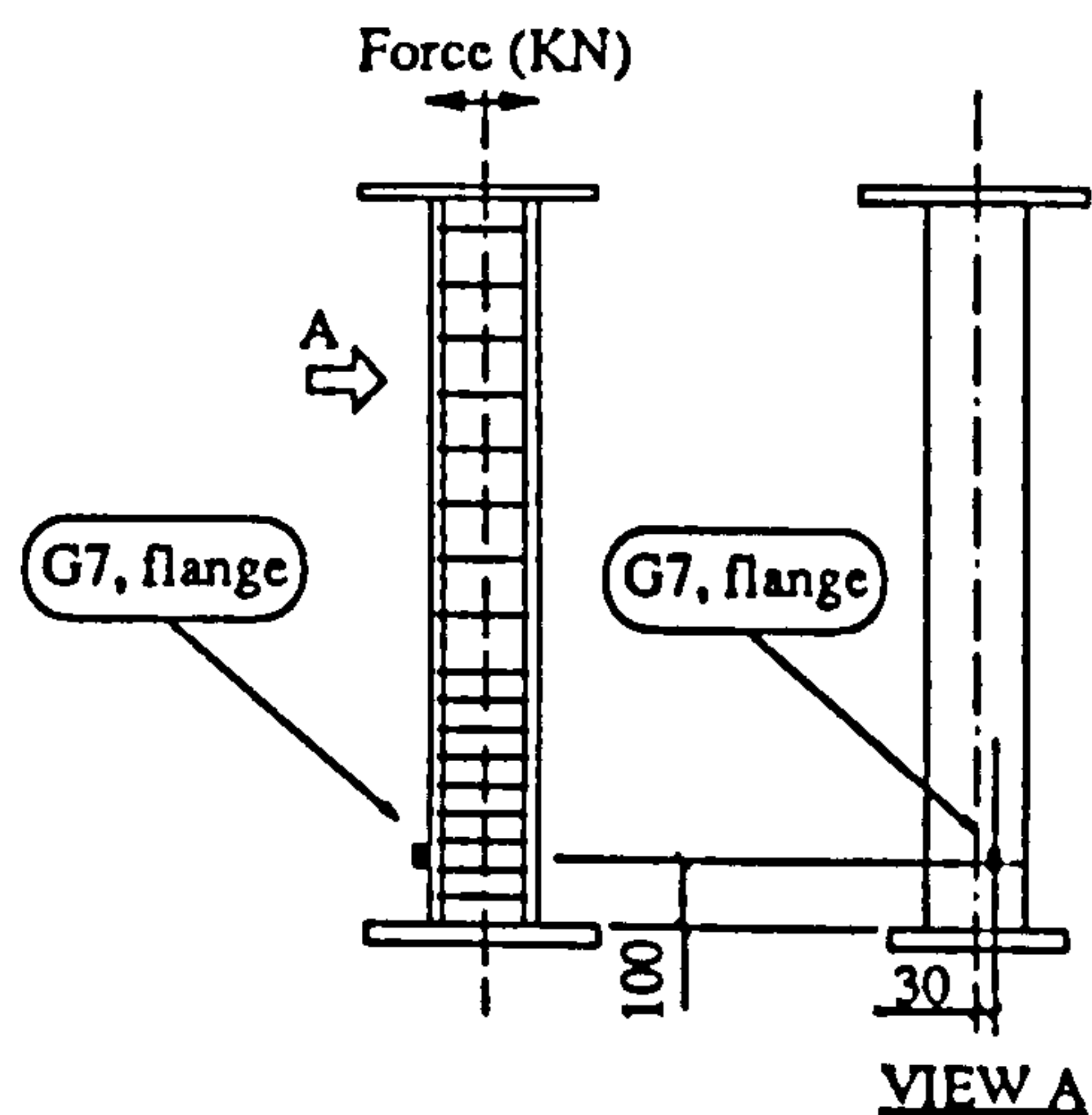
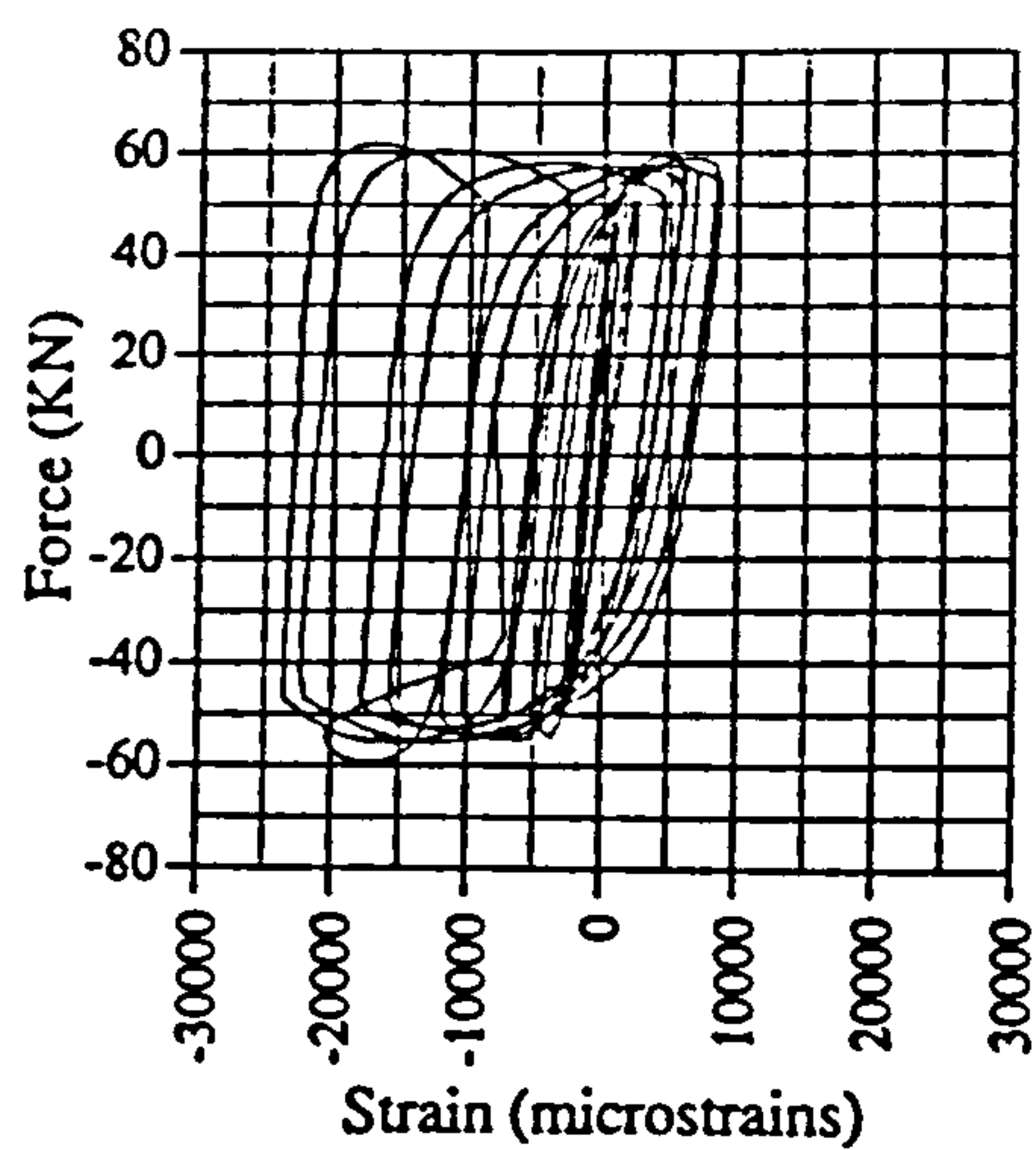


Fig. A.82 Force vs strain, IC02, G7

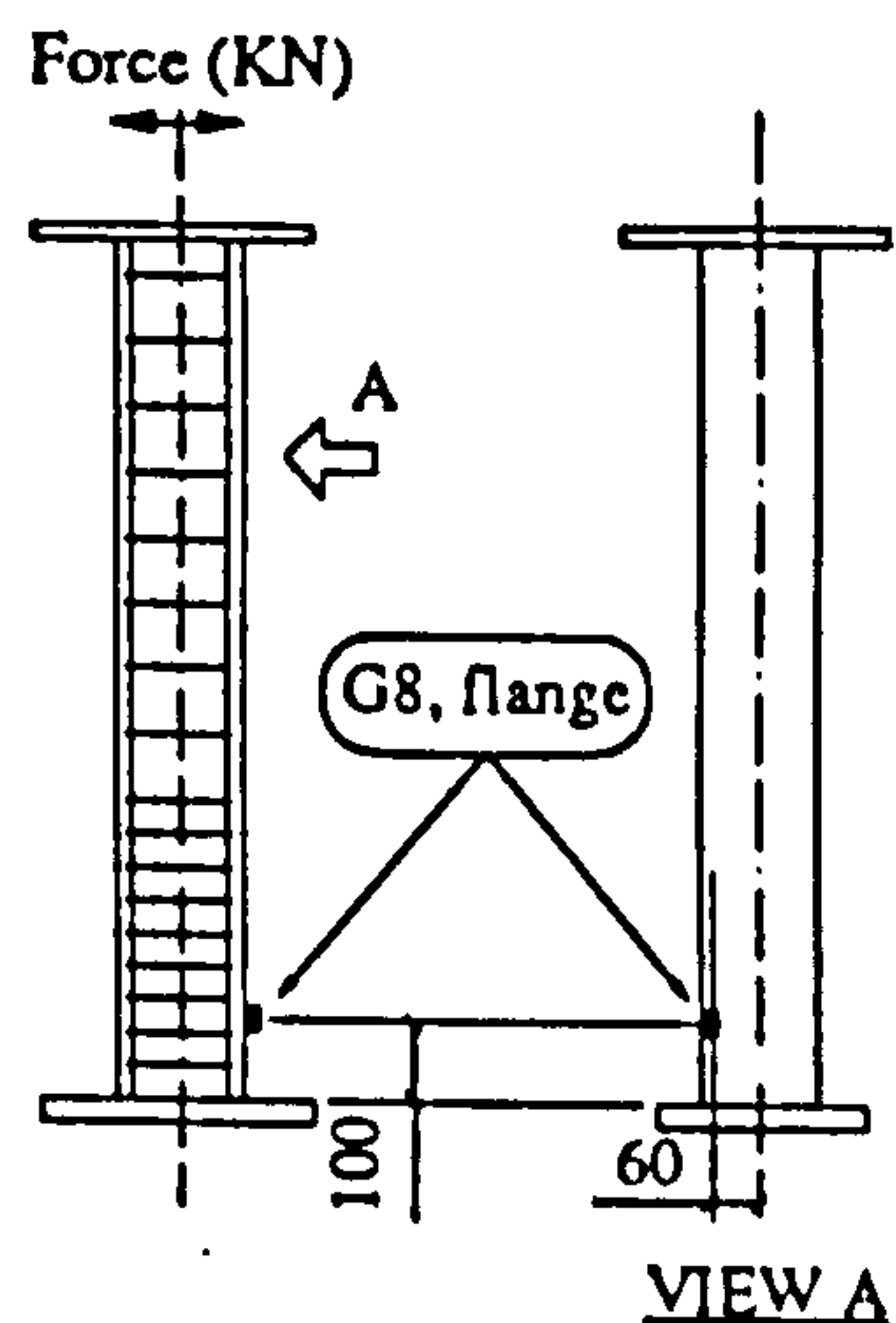
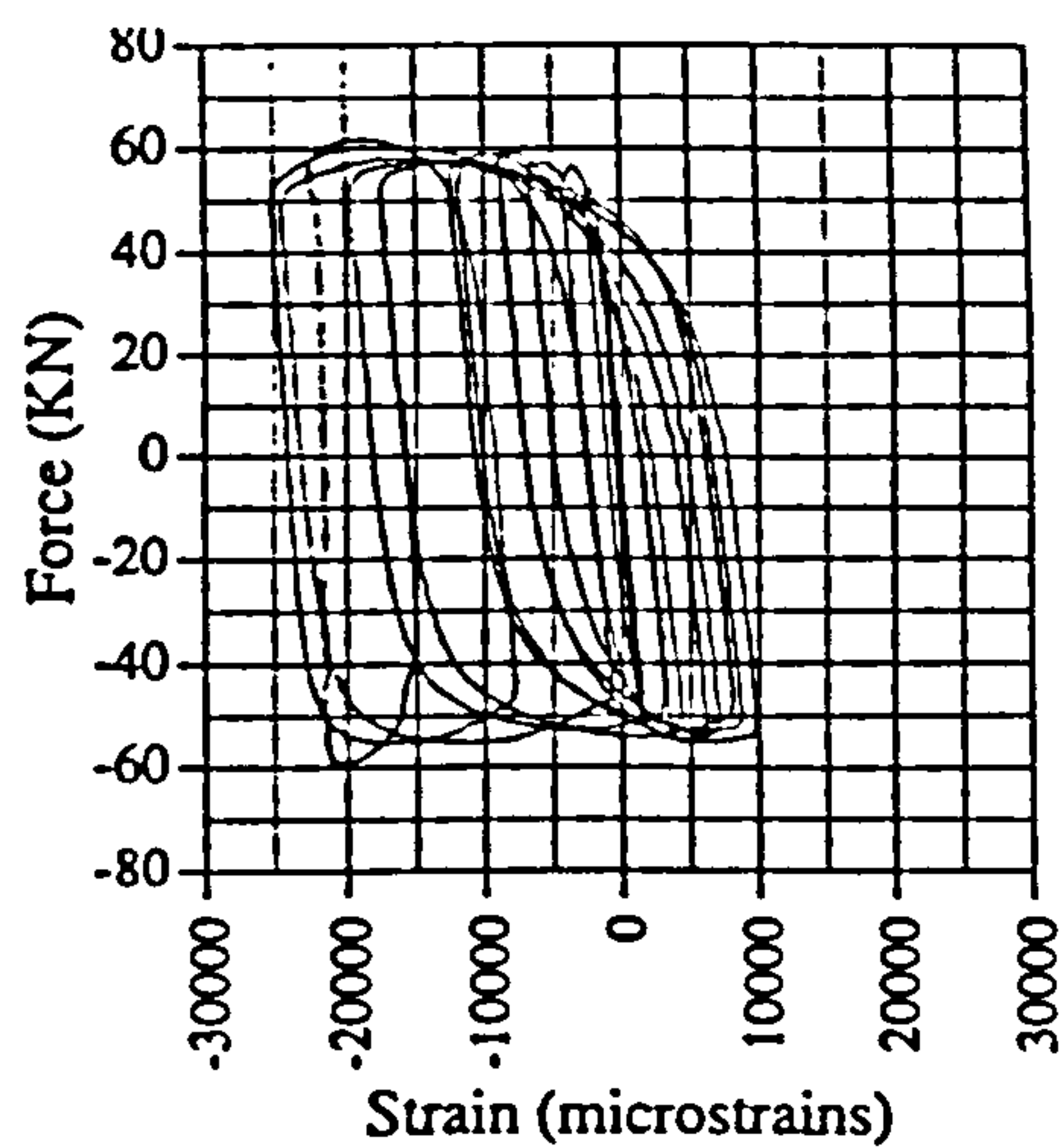


Fig. A.83 Force vs strain, IC02, G8

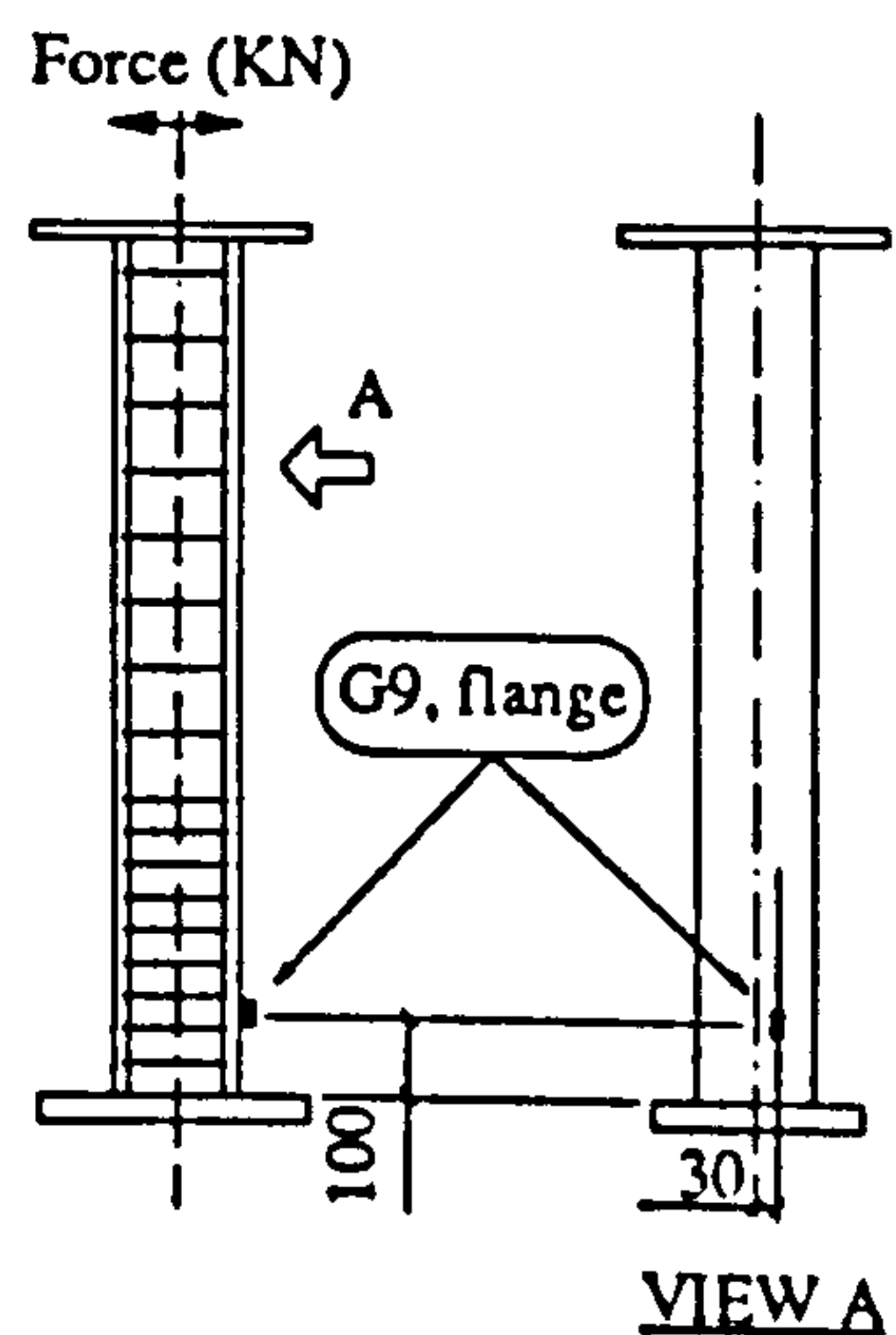
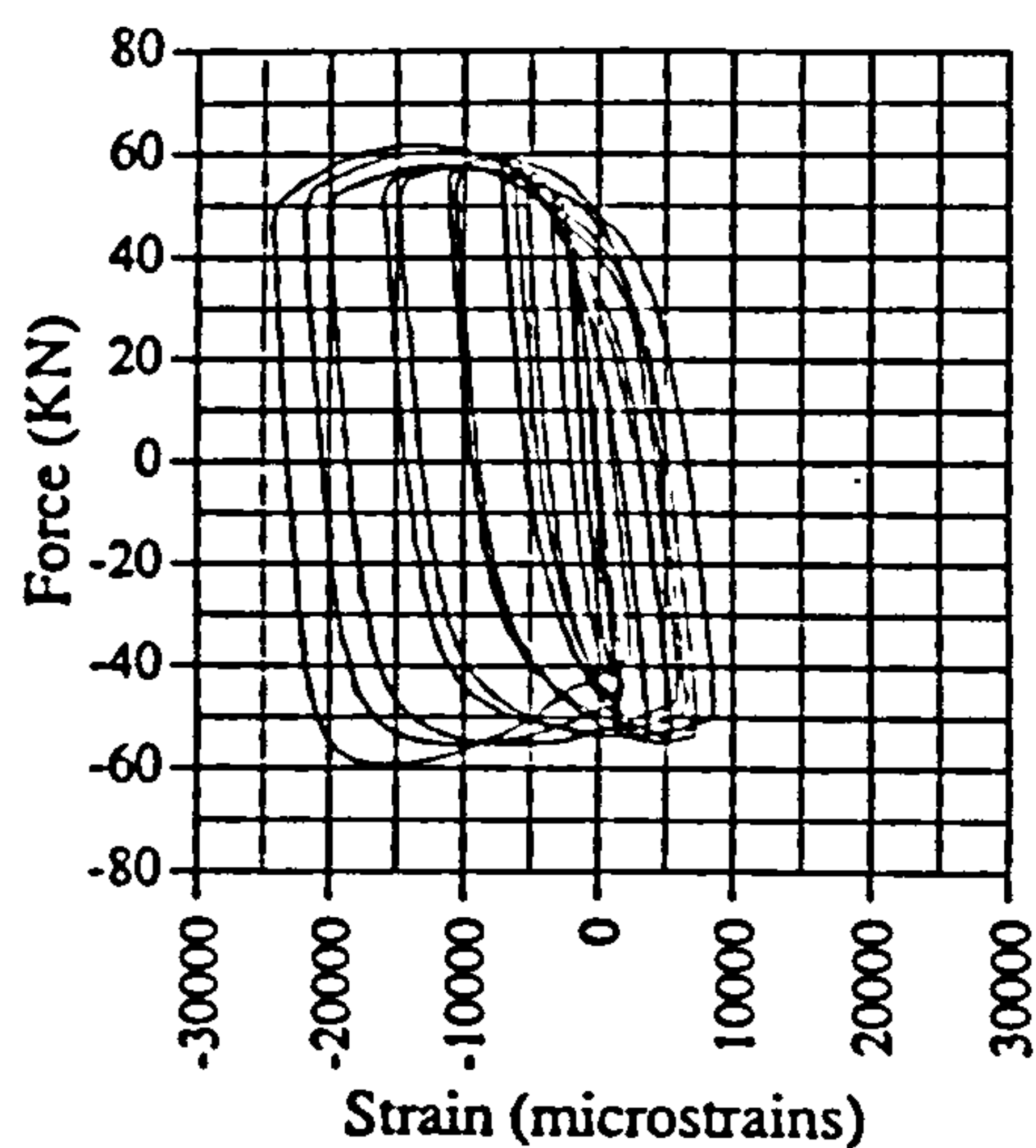


Fig. A.84 Force vs strain, IC02, G9

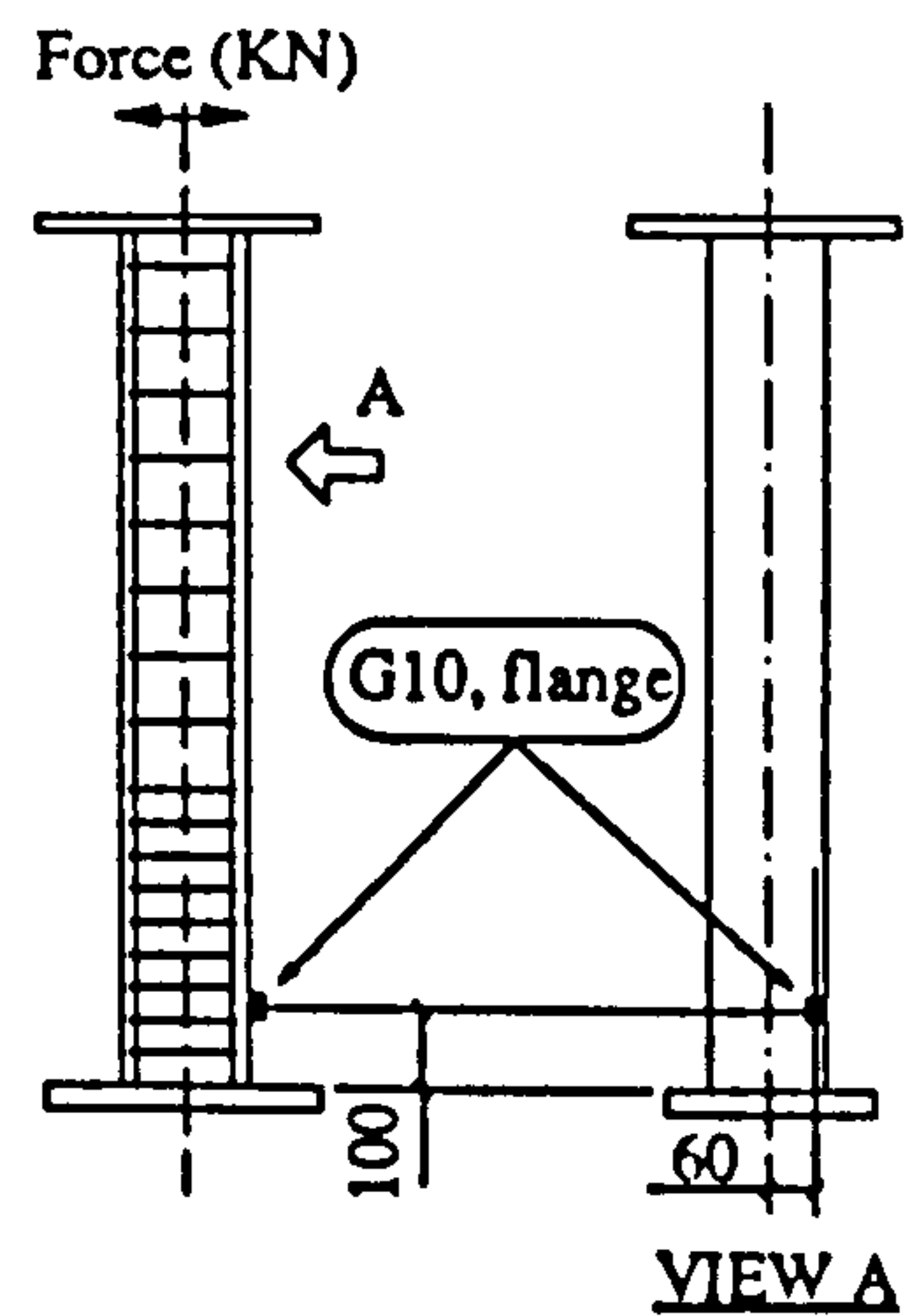
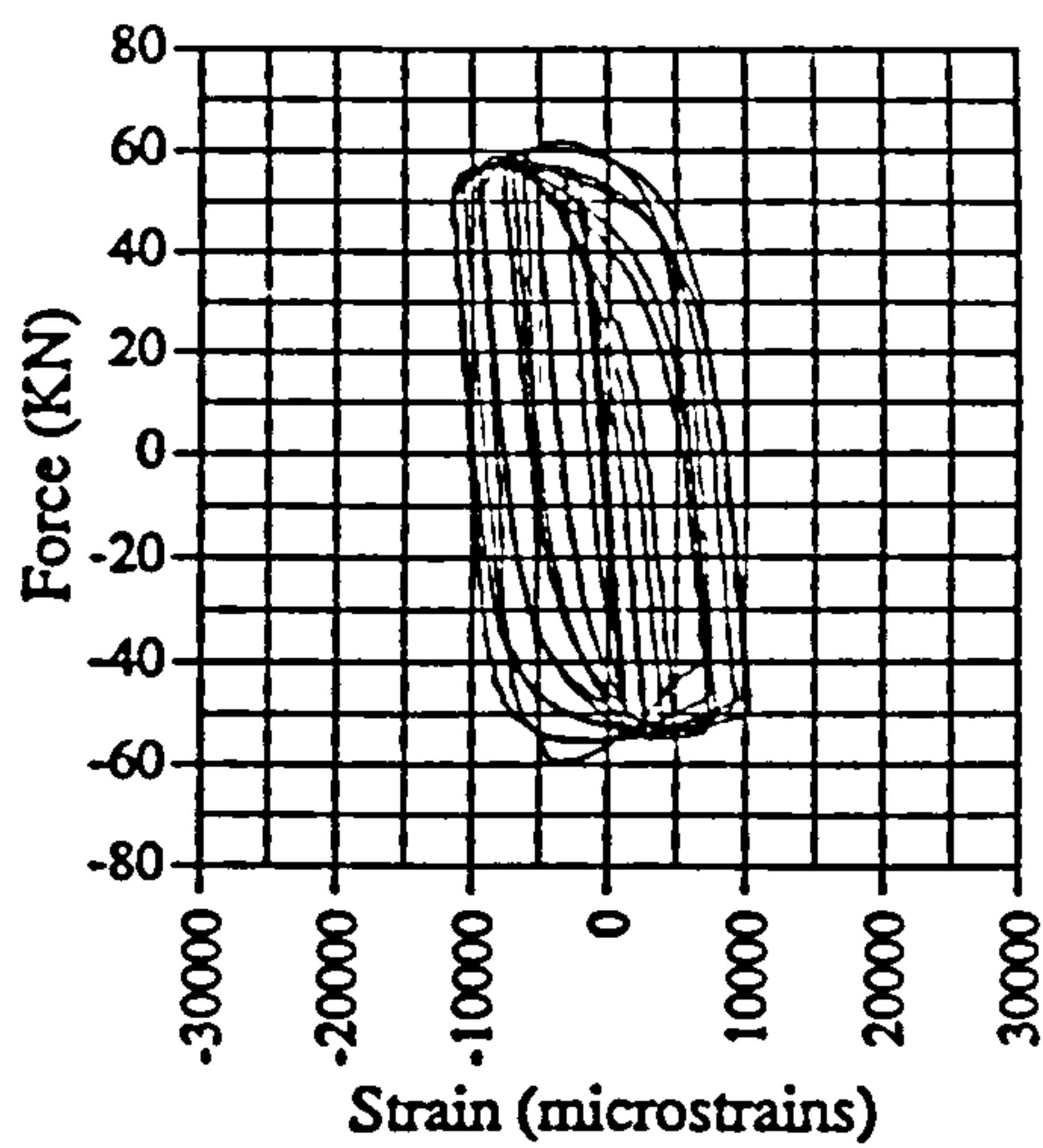


Fig. A.85 Force vs strain, IC02, G10

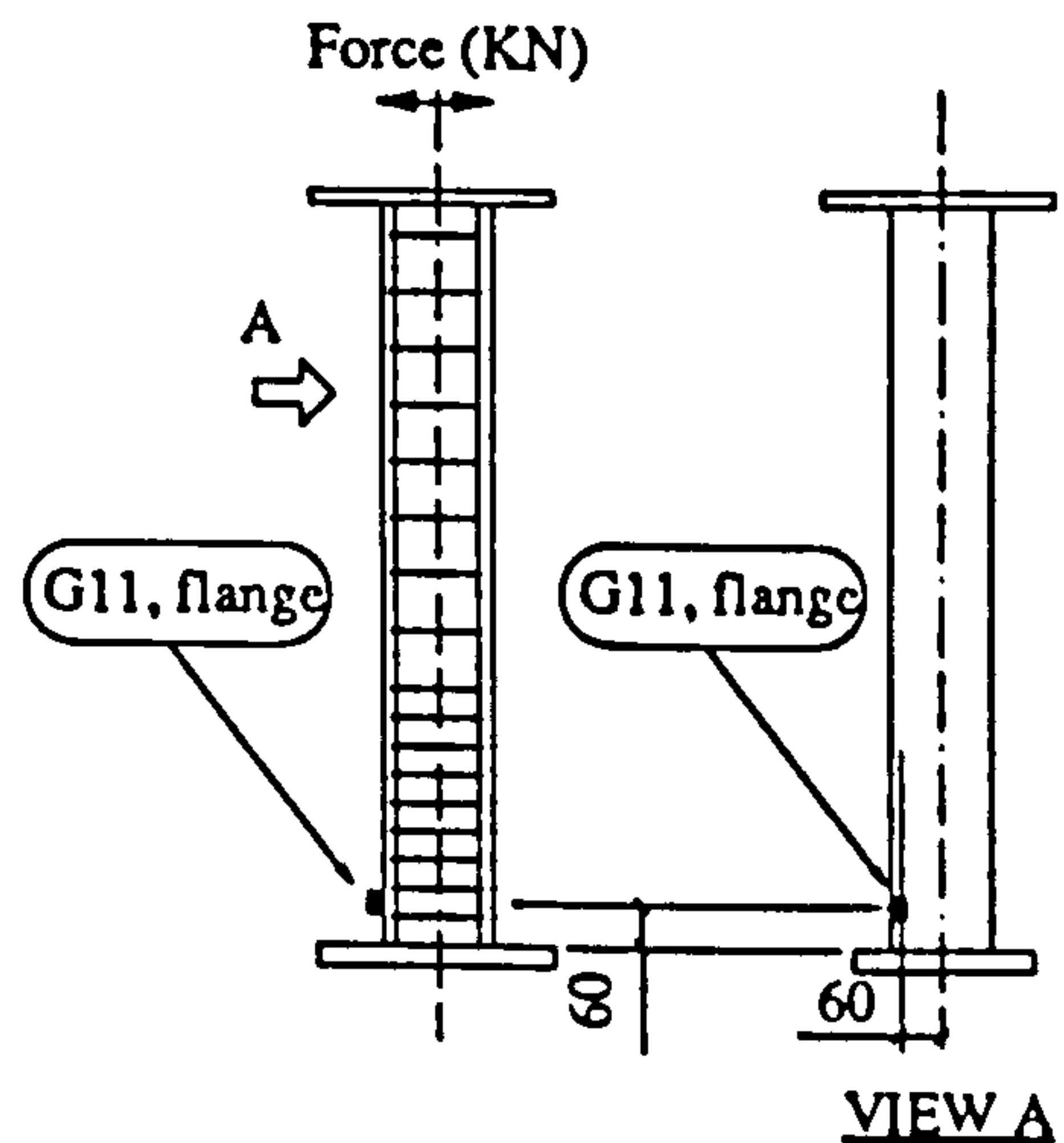
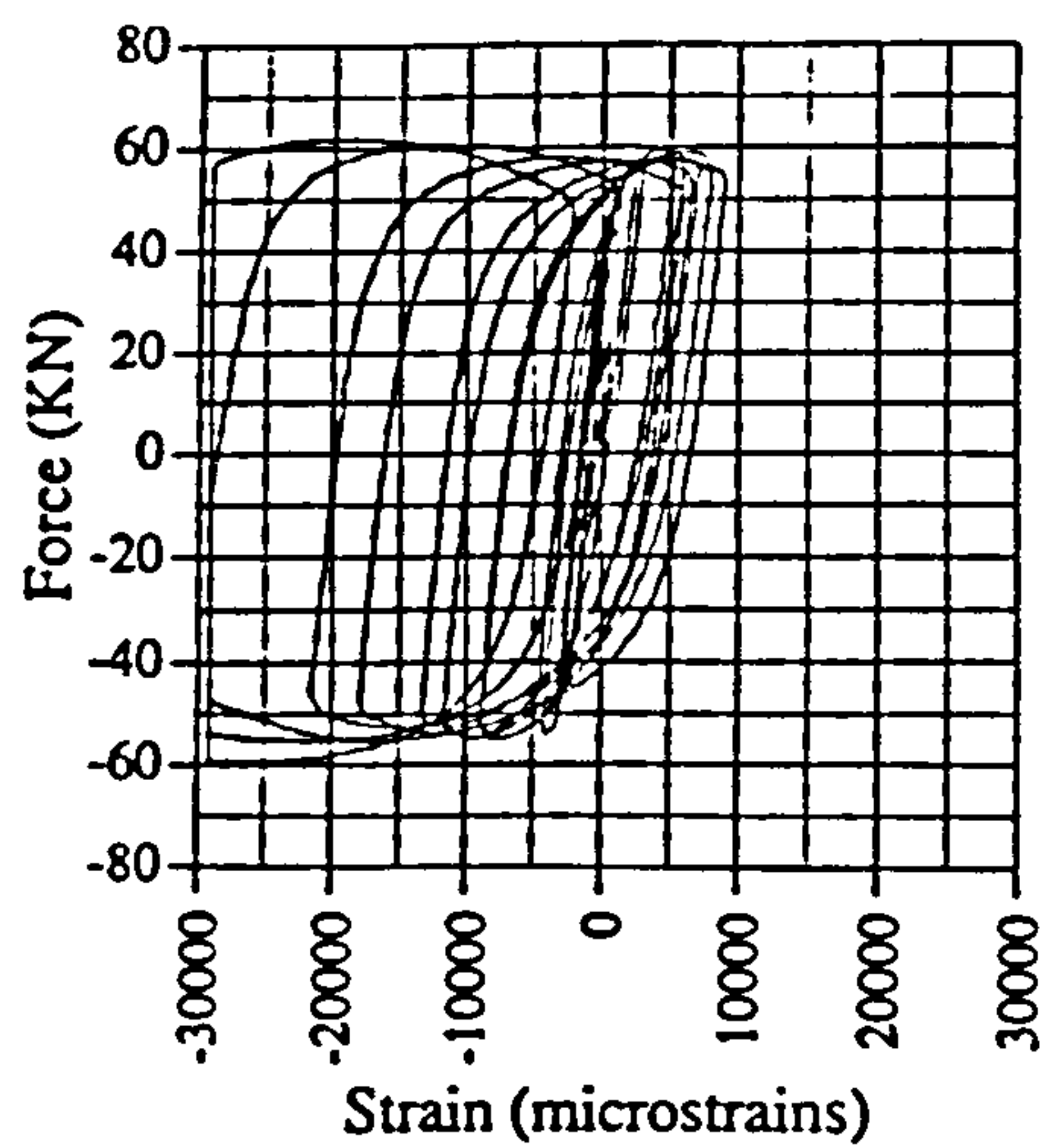


Fig. A.86 Force vs strain, IC02, G11

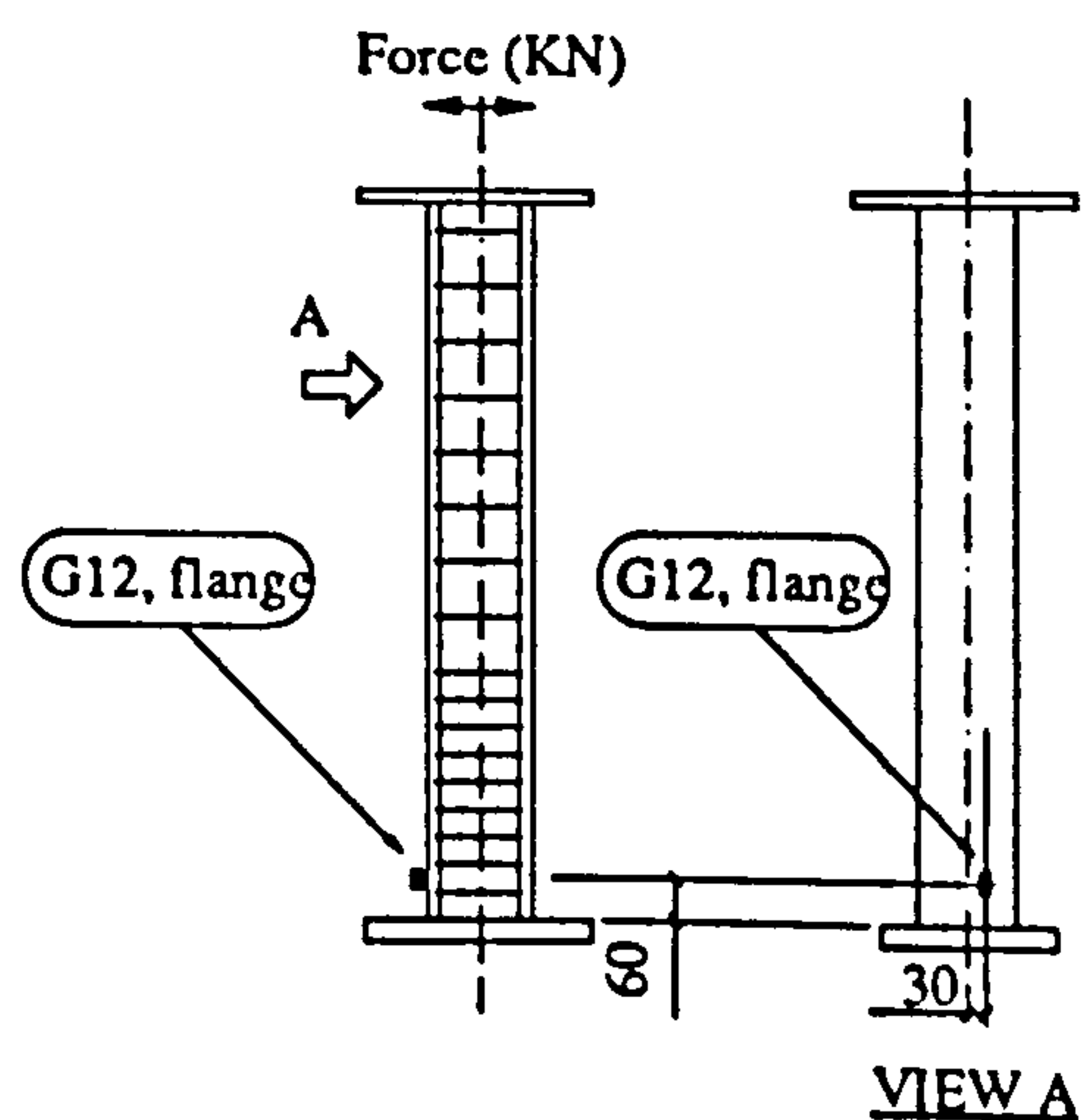
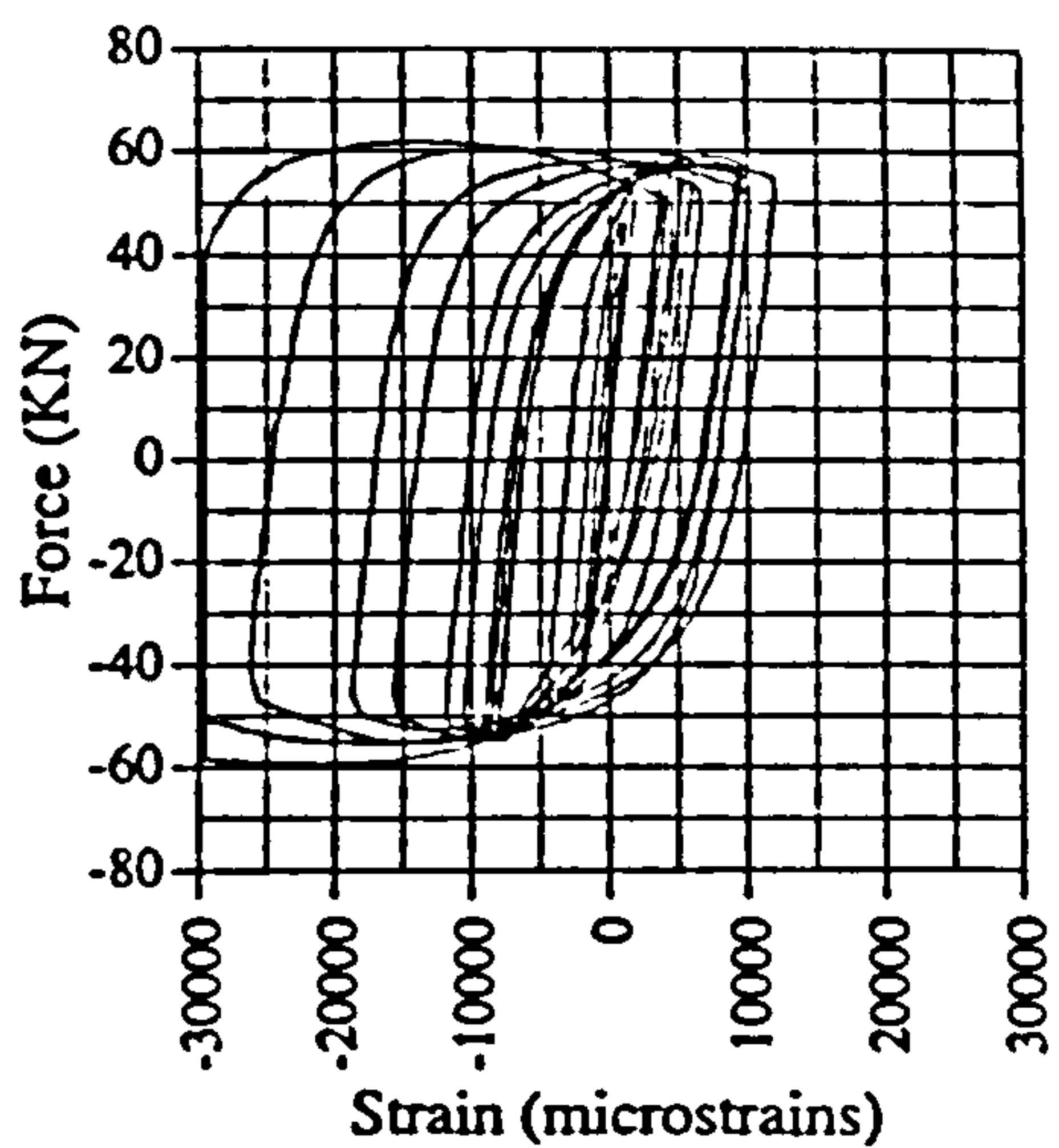


Fig. A.87 Force vs strain, IC02, G12

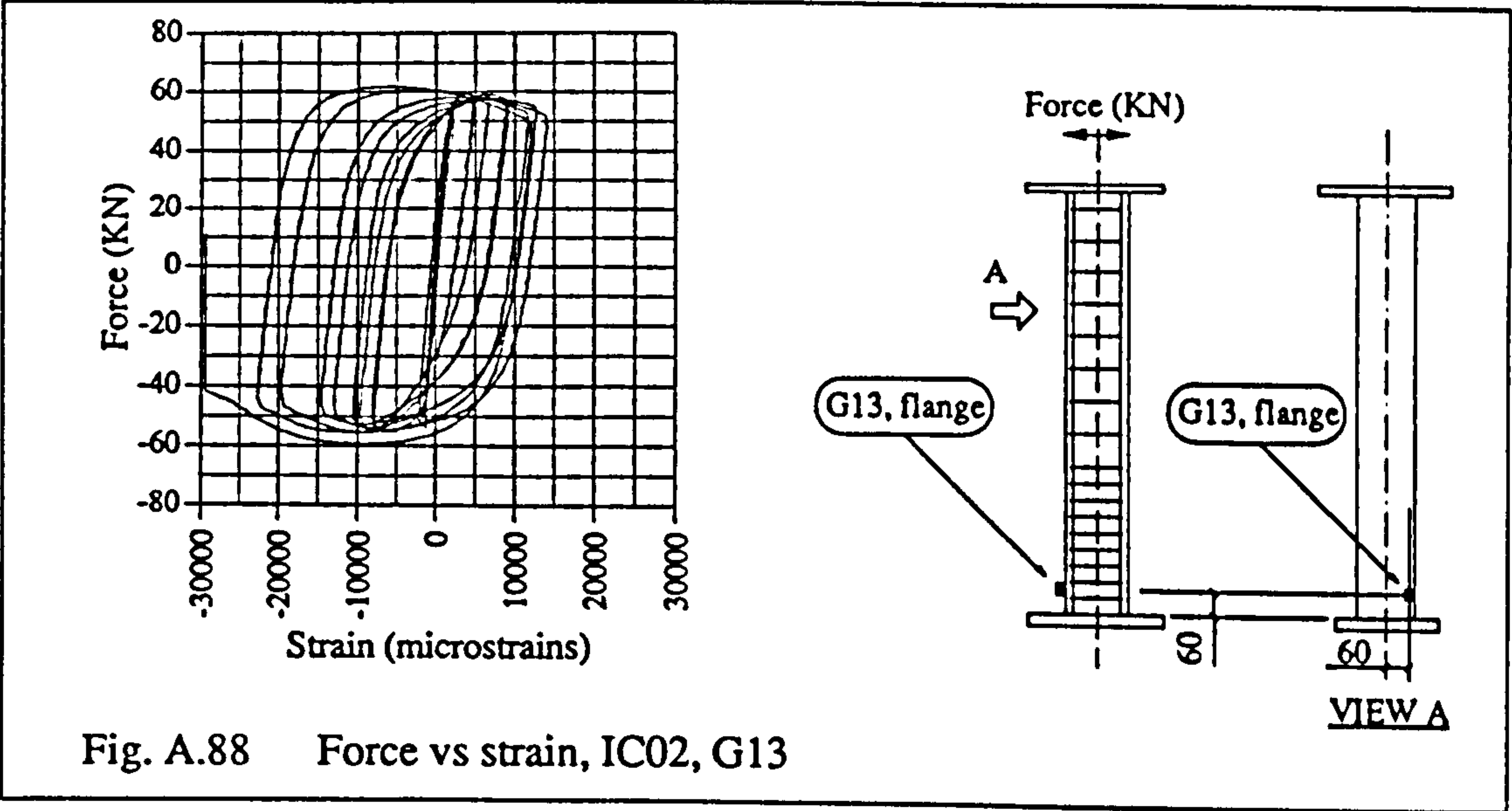


Fig. A.88 Force vs strain, IC02, G13

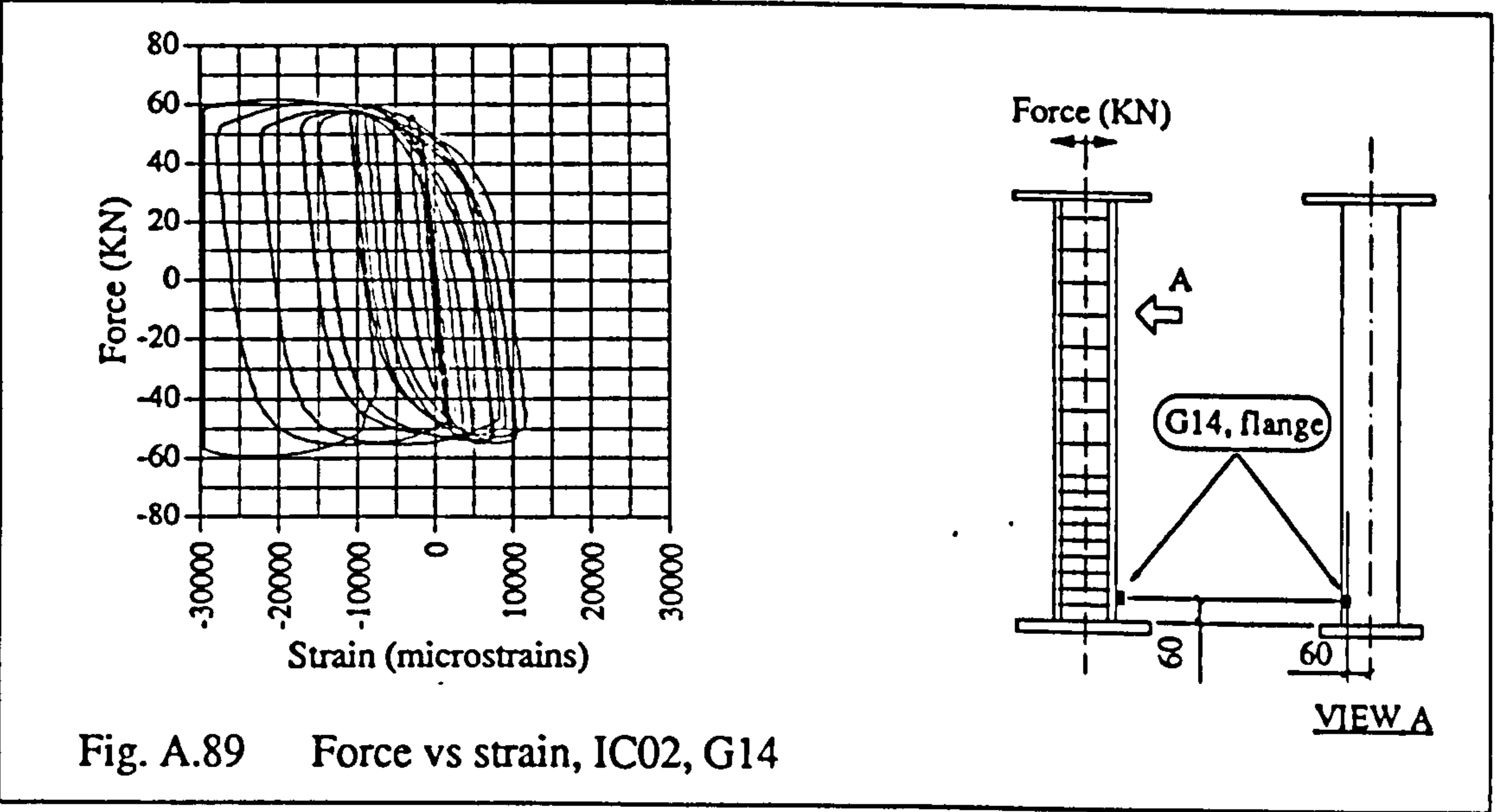


Fig. A.89 Force vs strain, IC02, G14

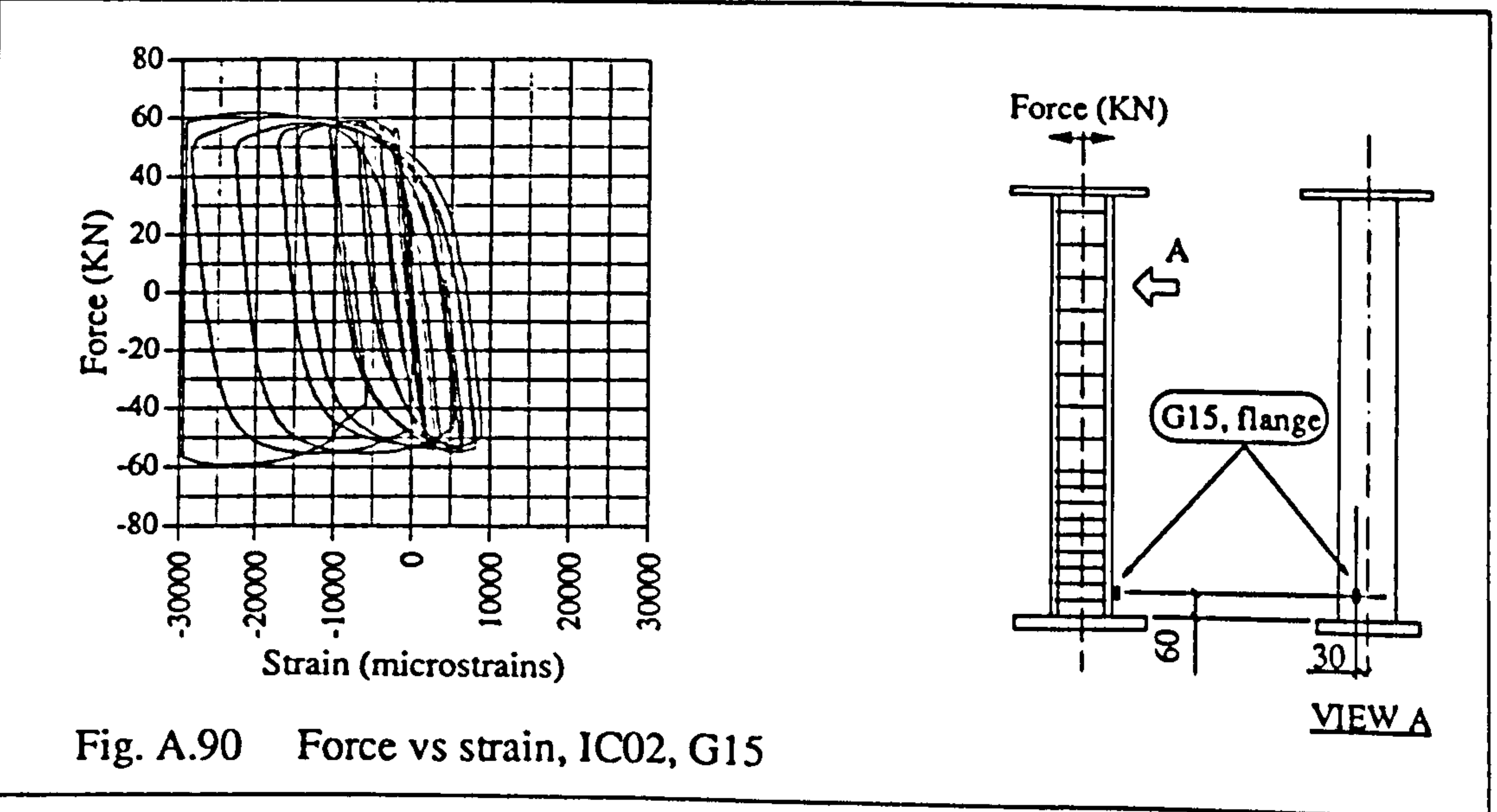


Fig. A.90 Force vs strain, IC02, G15

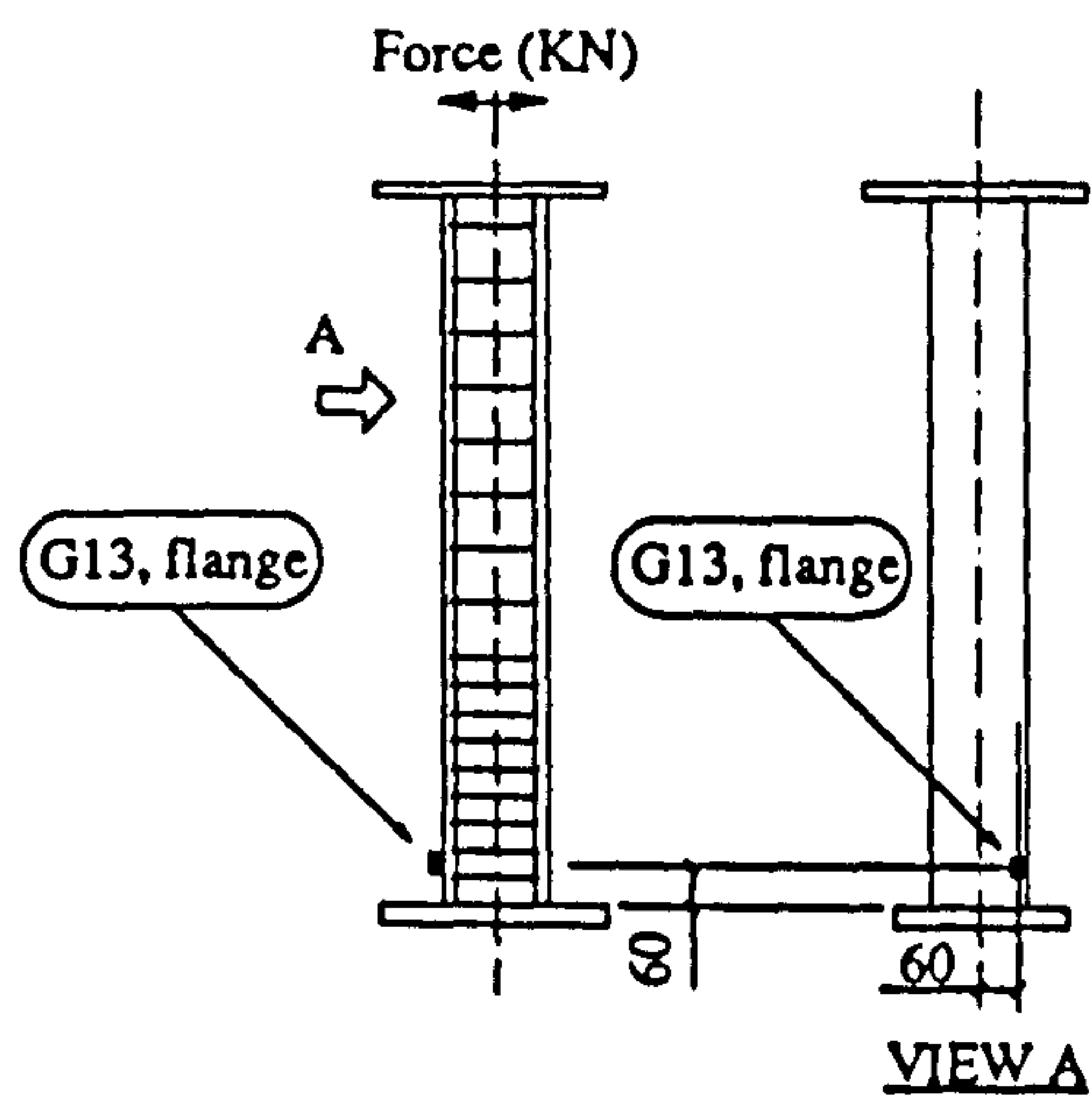
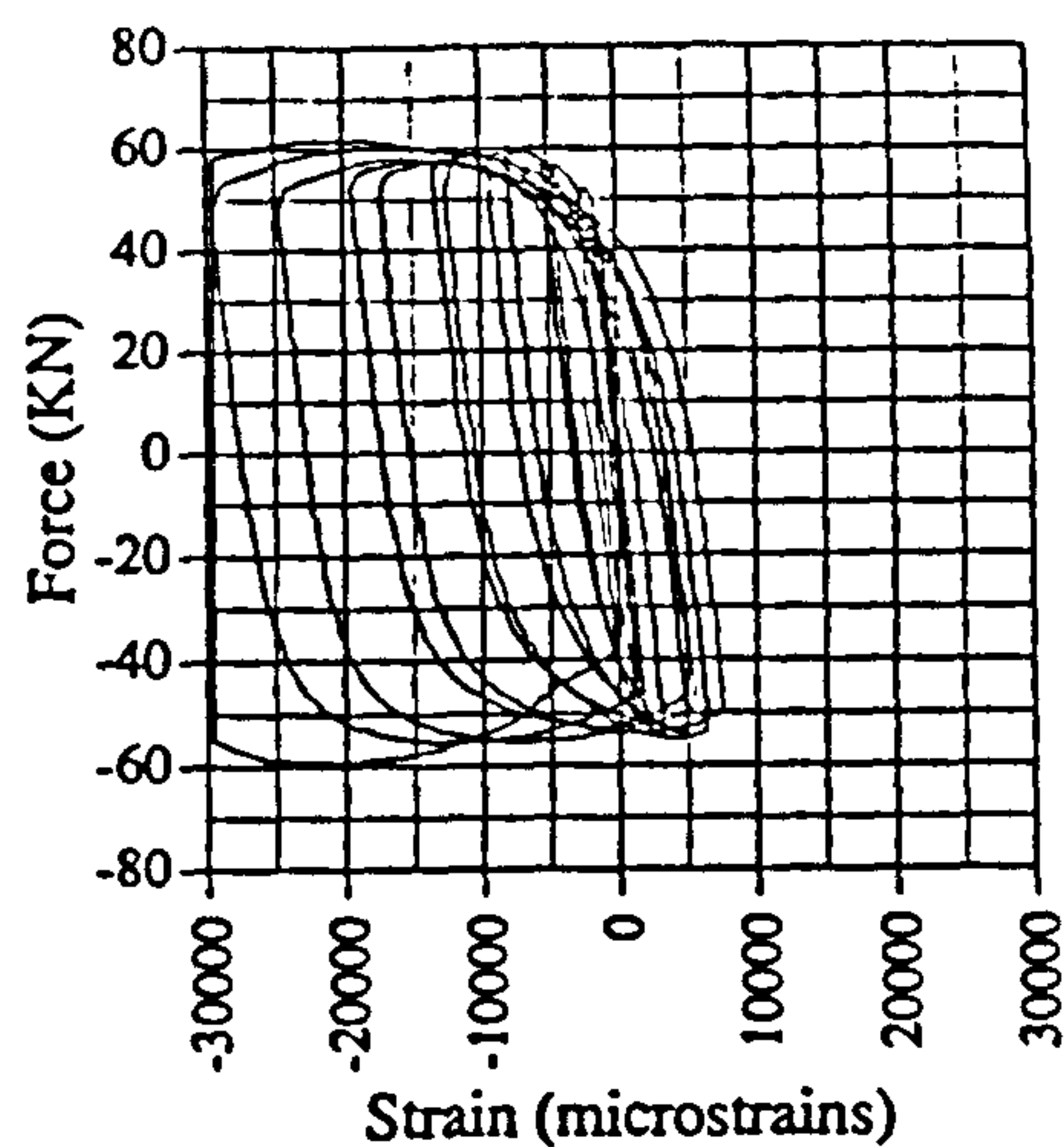


Fig. A.91 Force vs strain, IC02, G16

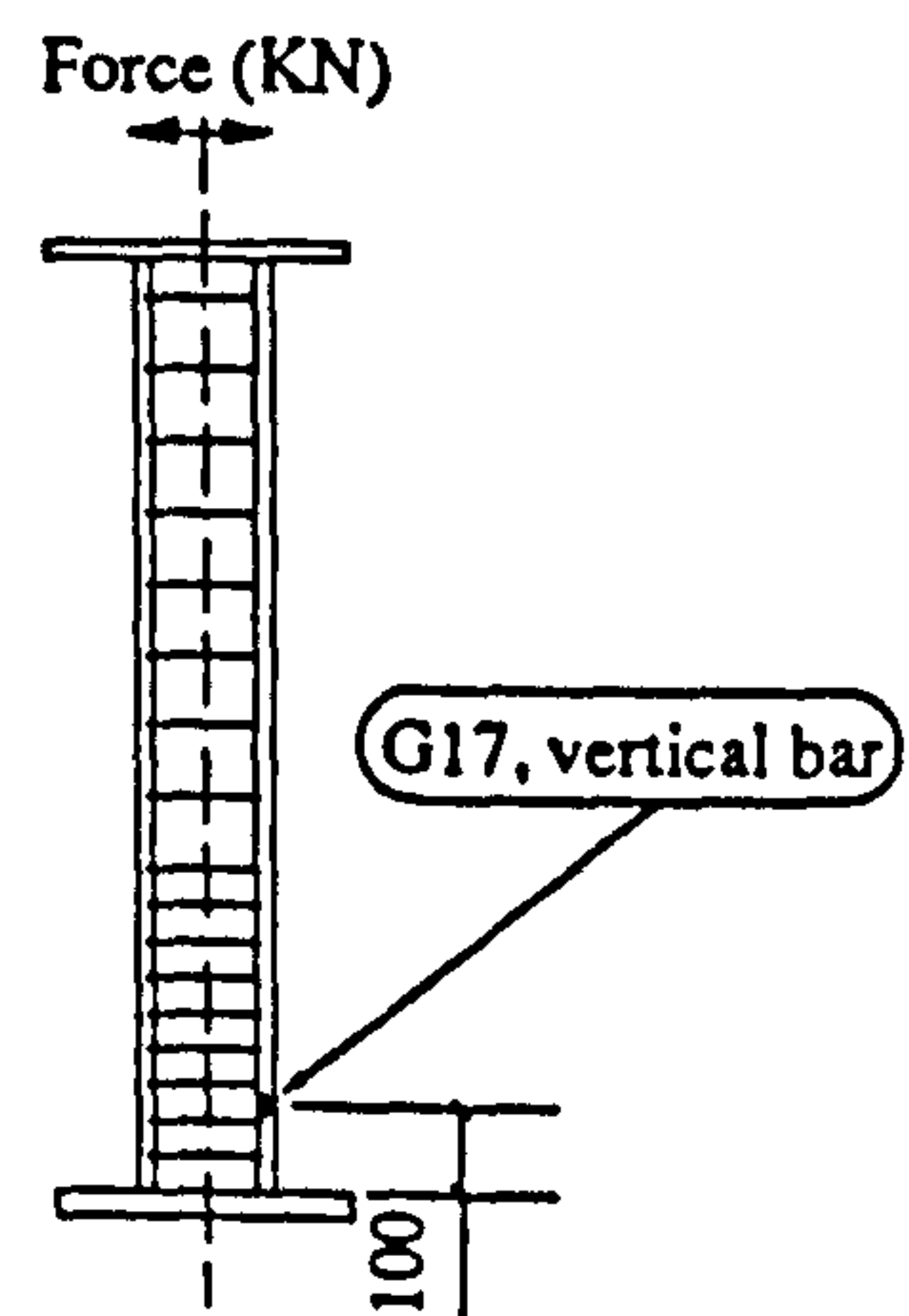
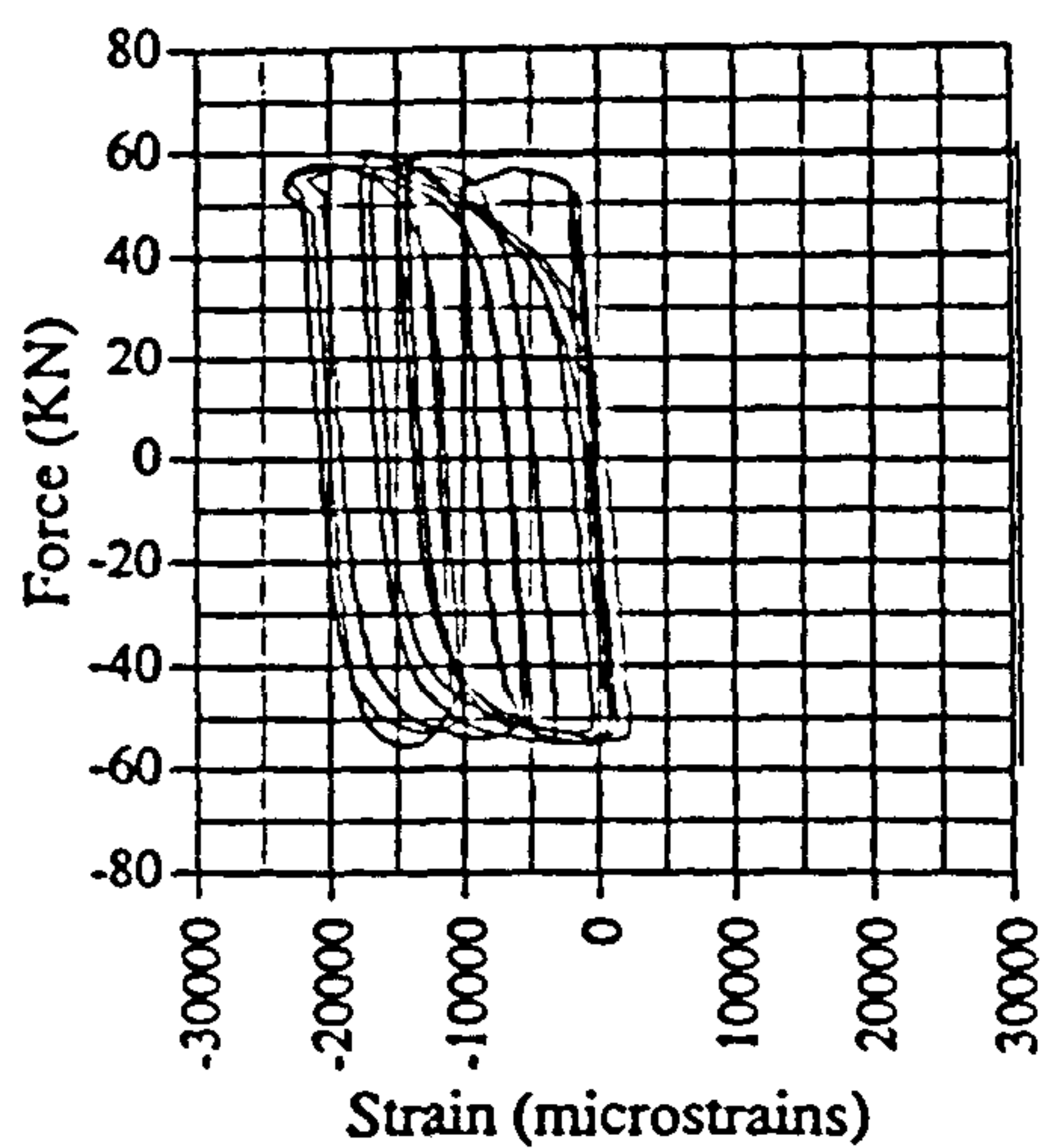


Fig. A.92 Force vs strain, IC02, G17

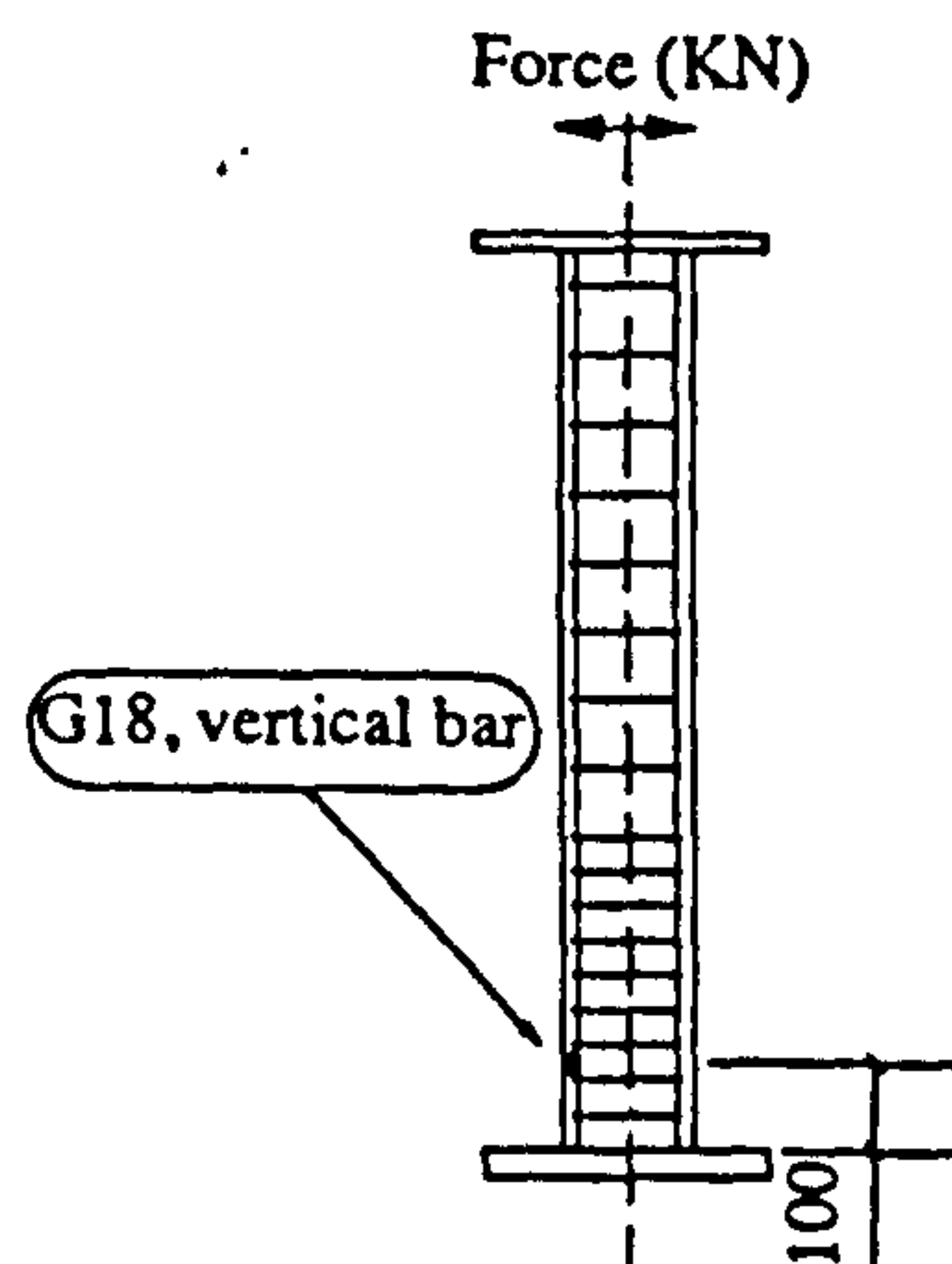
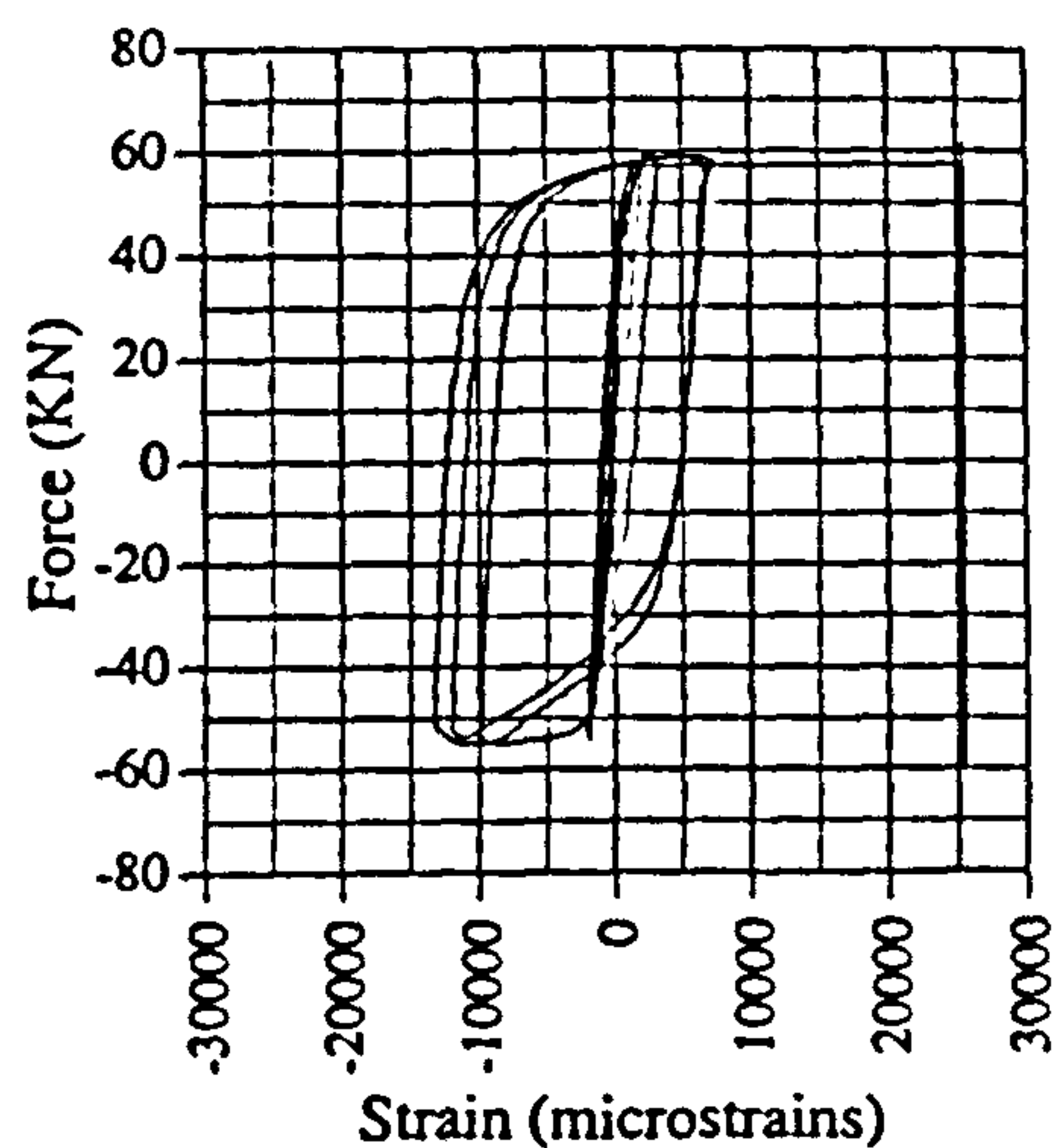


Fig. A.93 Force vs strain, IC02, G18

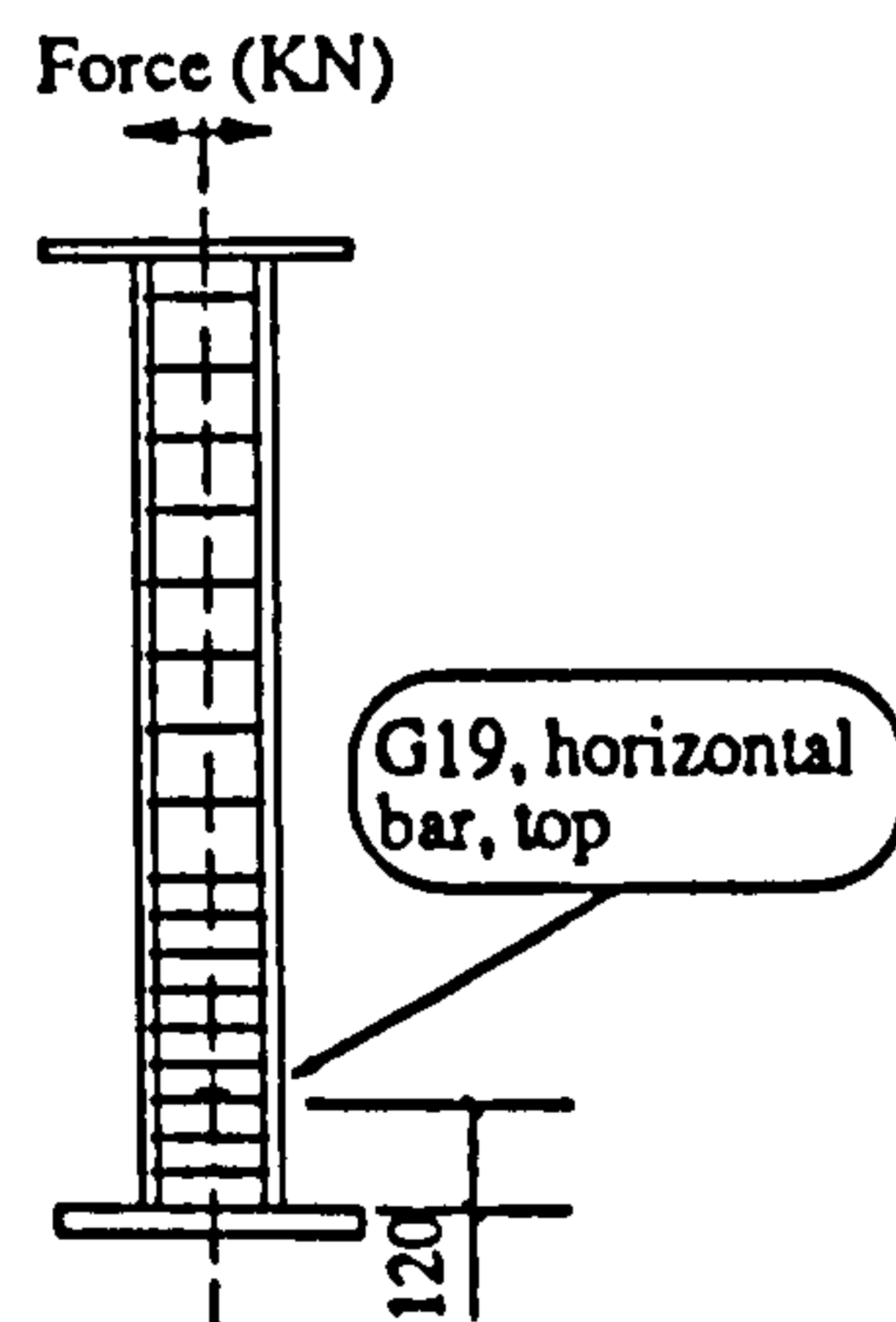
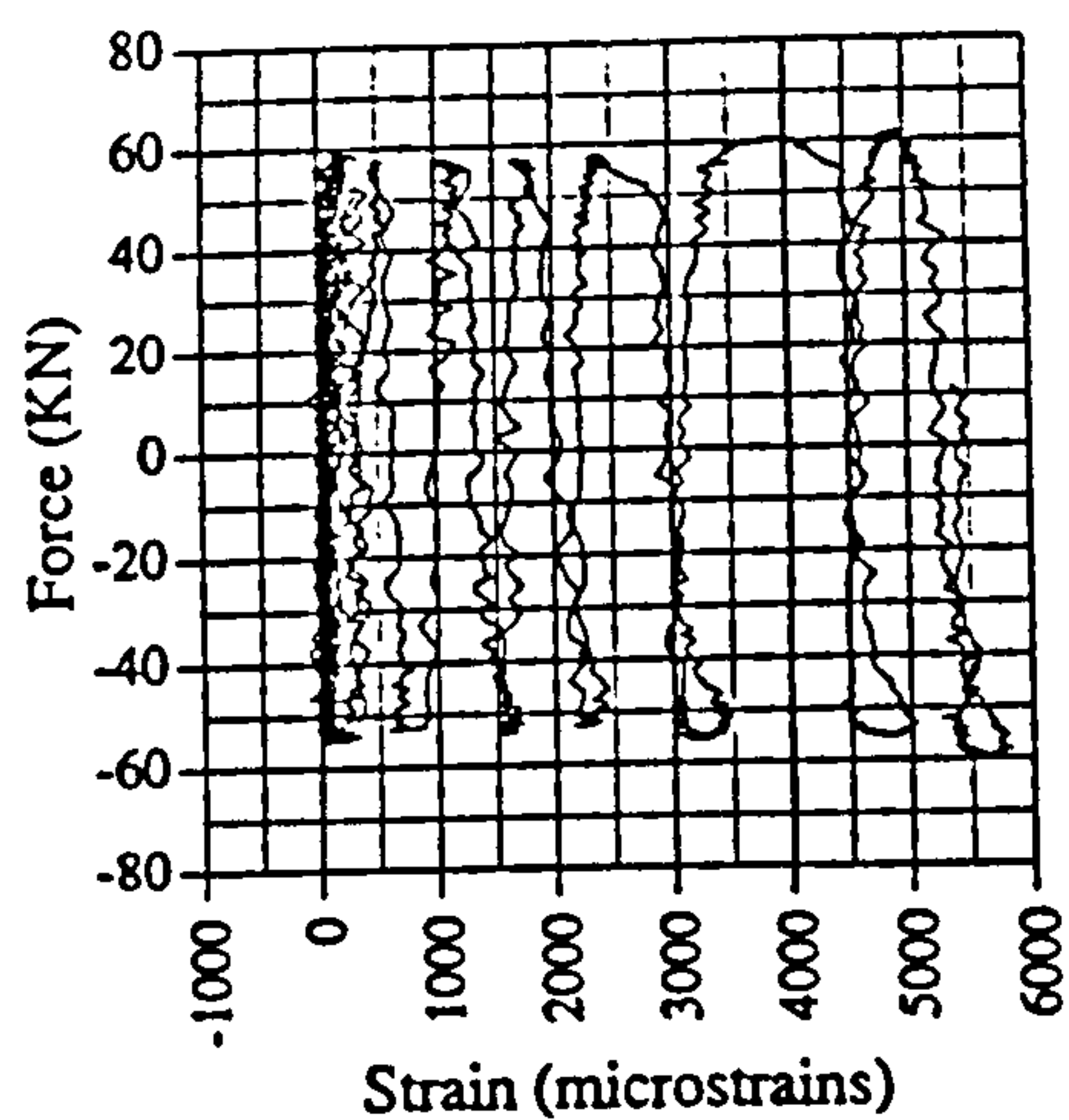


Fig. A.94 Force vs strain, IC02, G19

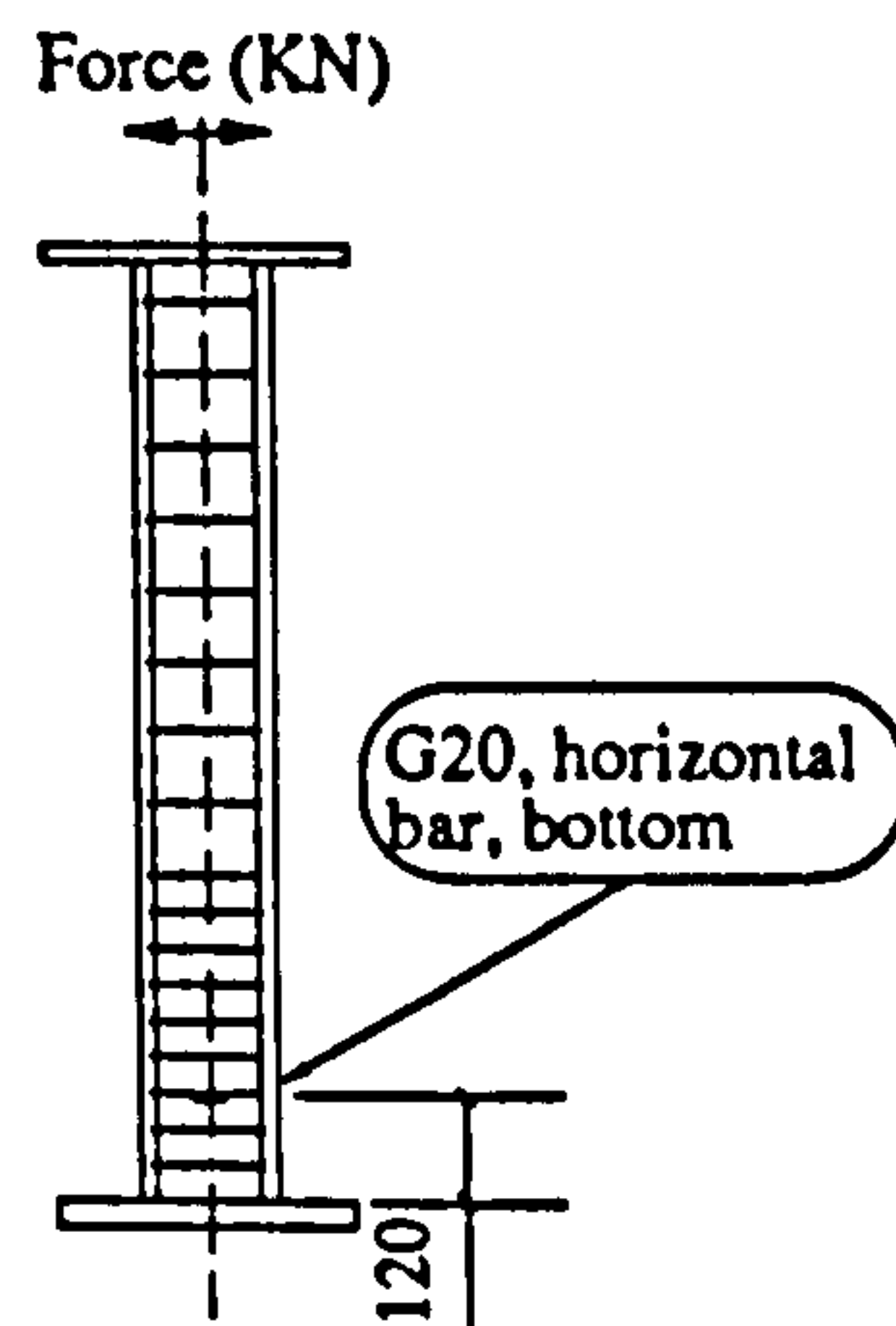
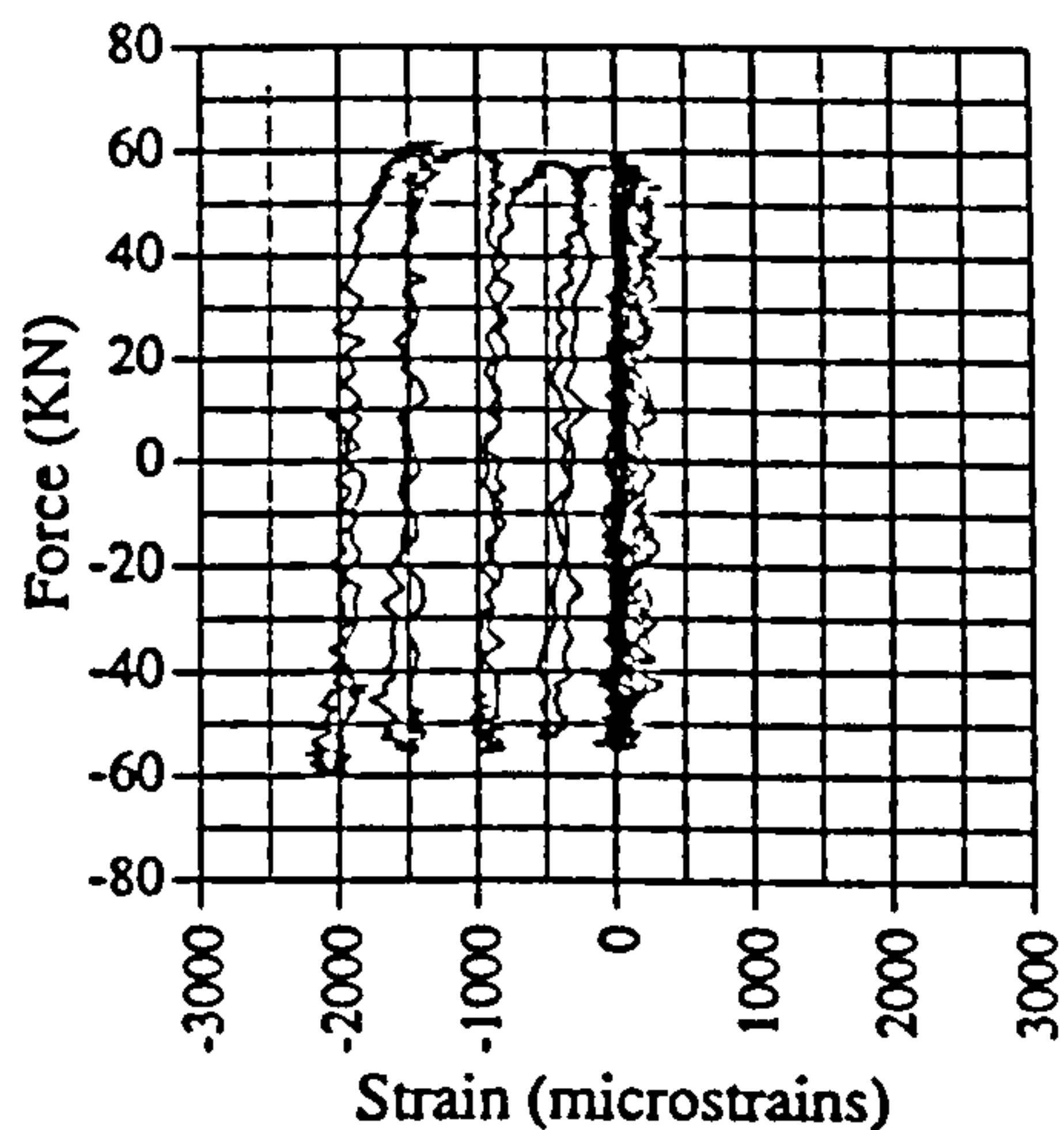


Fig. A.95 Force vs strain, IC02, G20

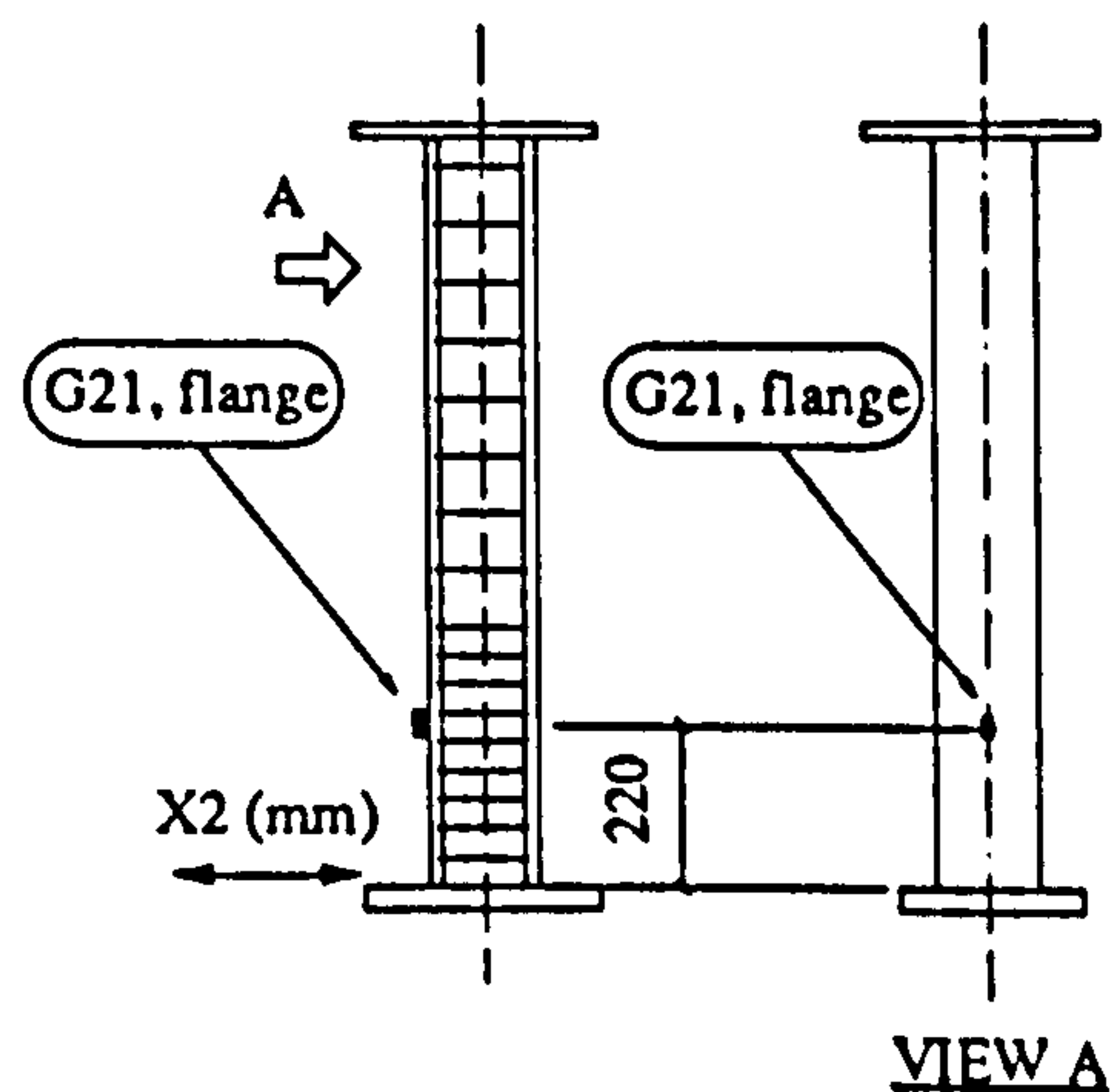
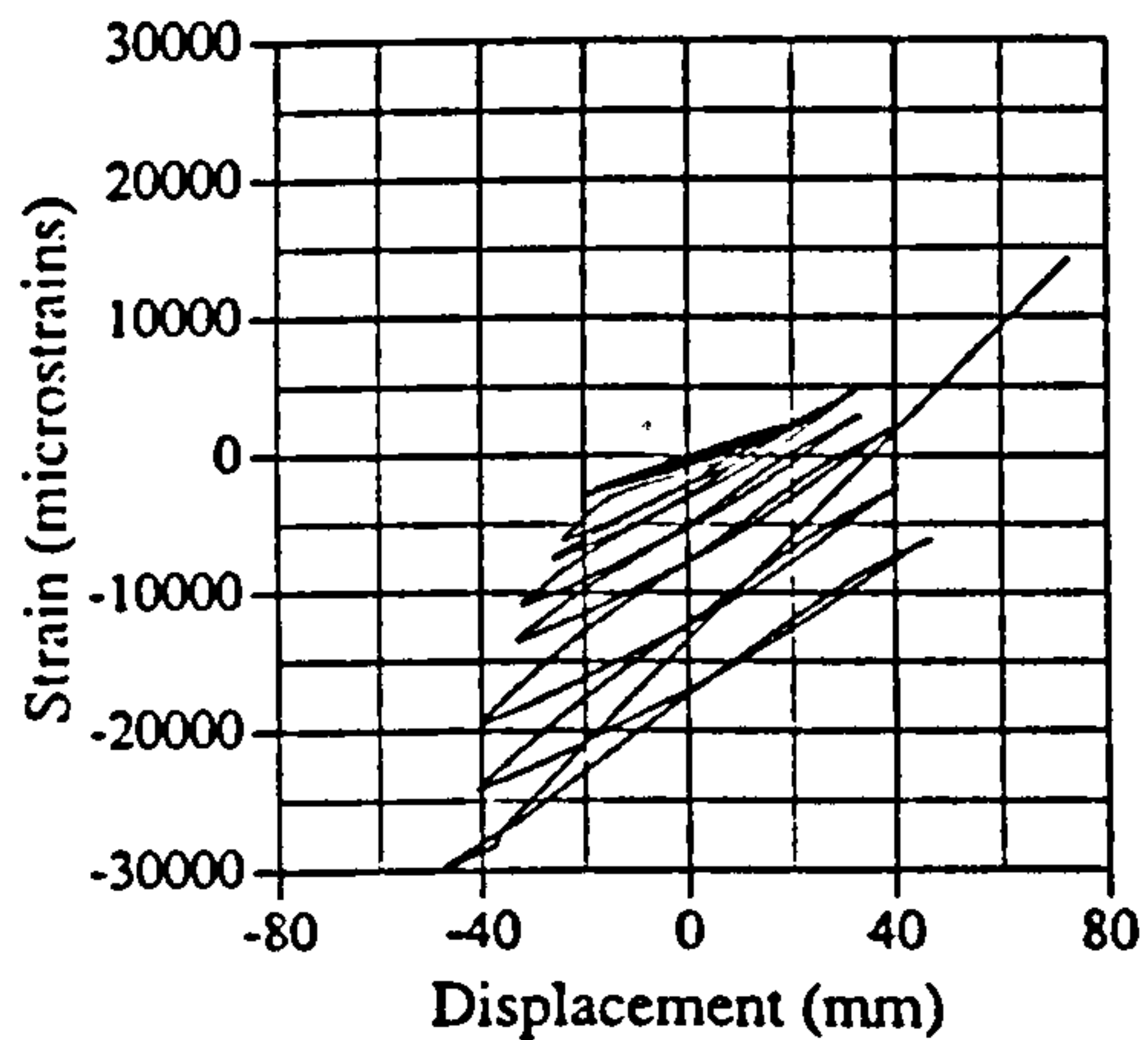


Fig. A.96 Strain vs displacement, IC02, G21

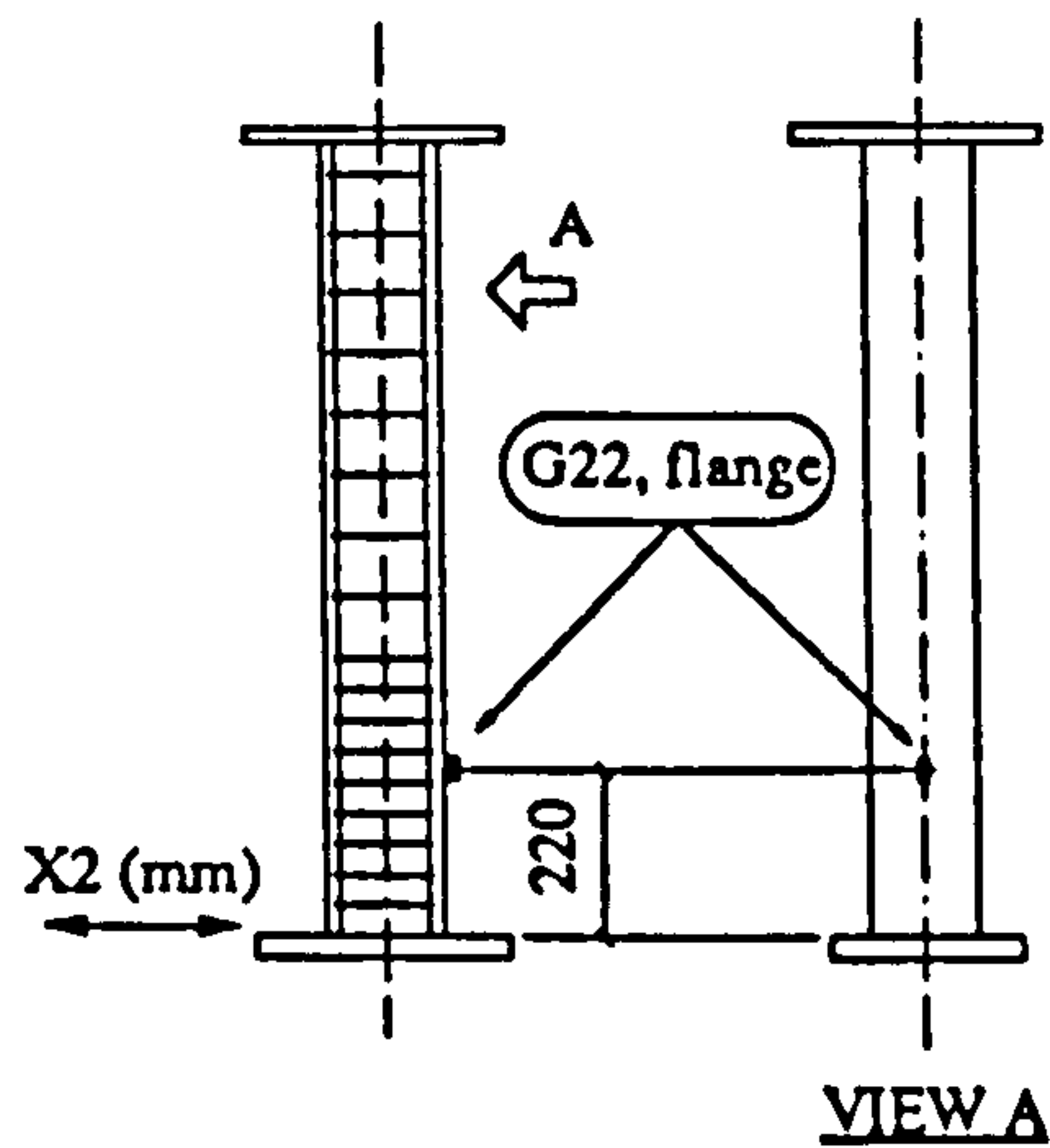
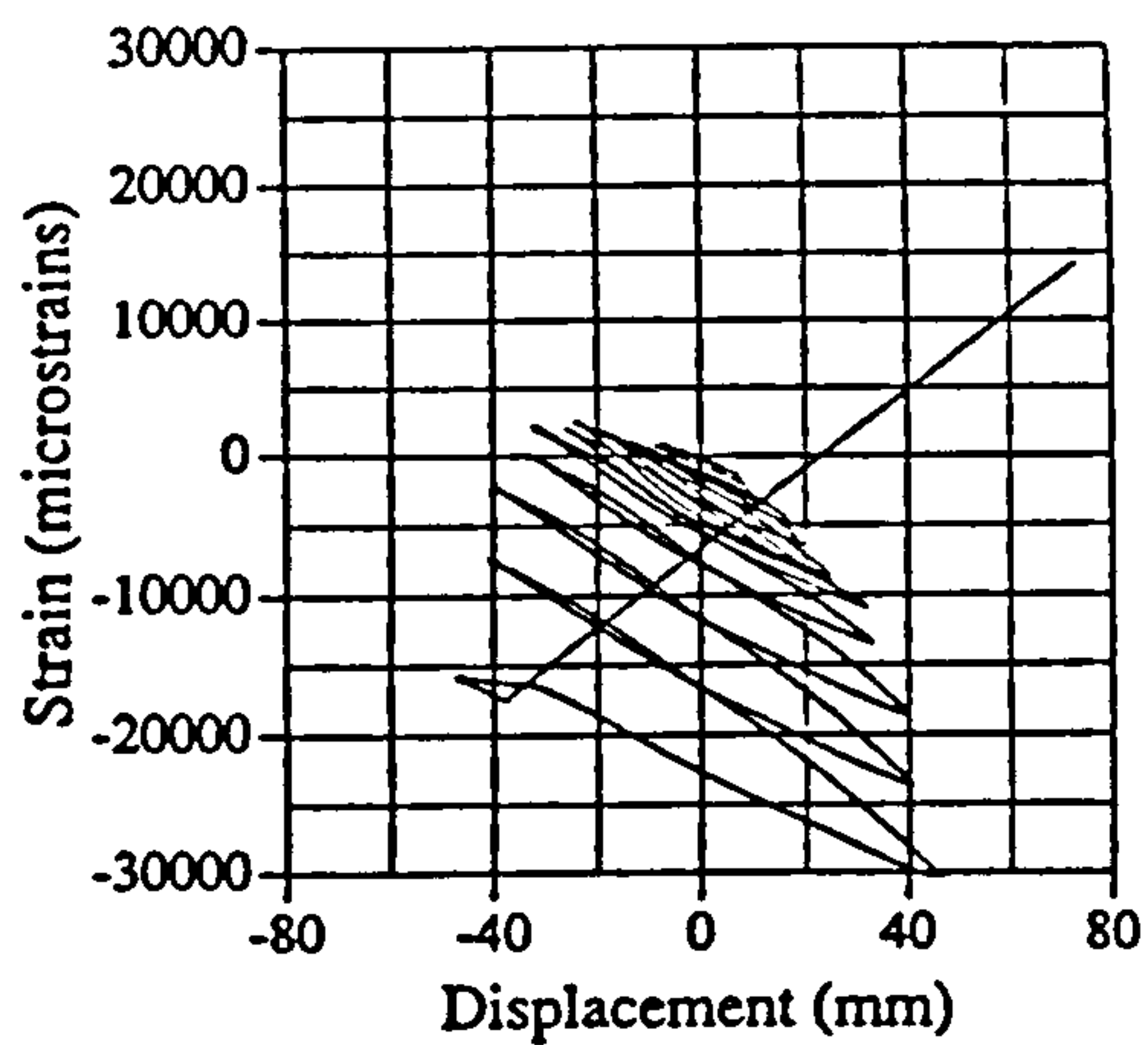


Fig. A.97 Strain vs displacement, IC02, G22

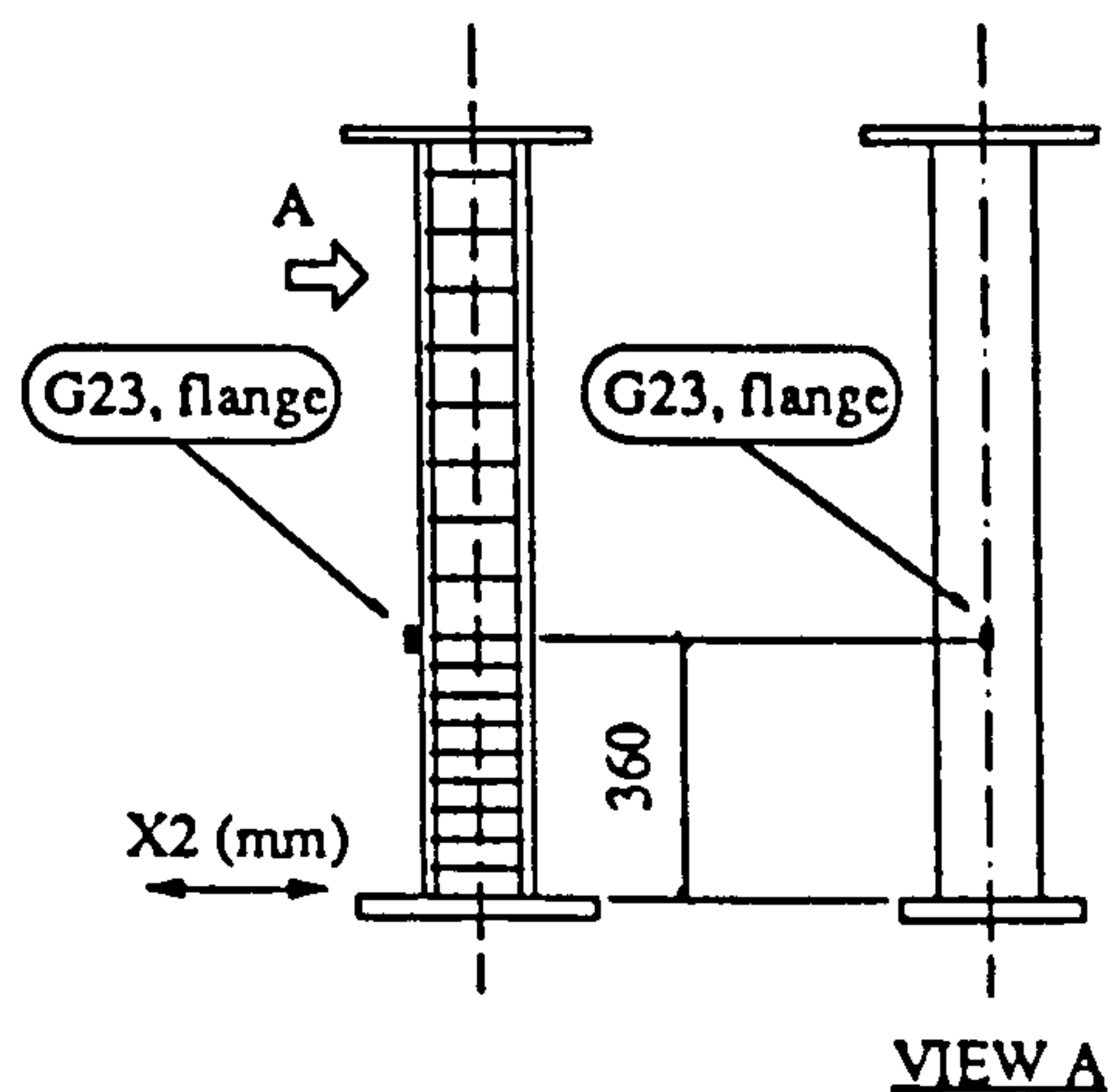
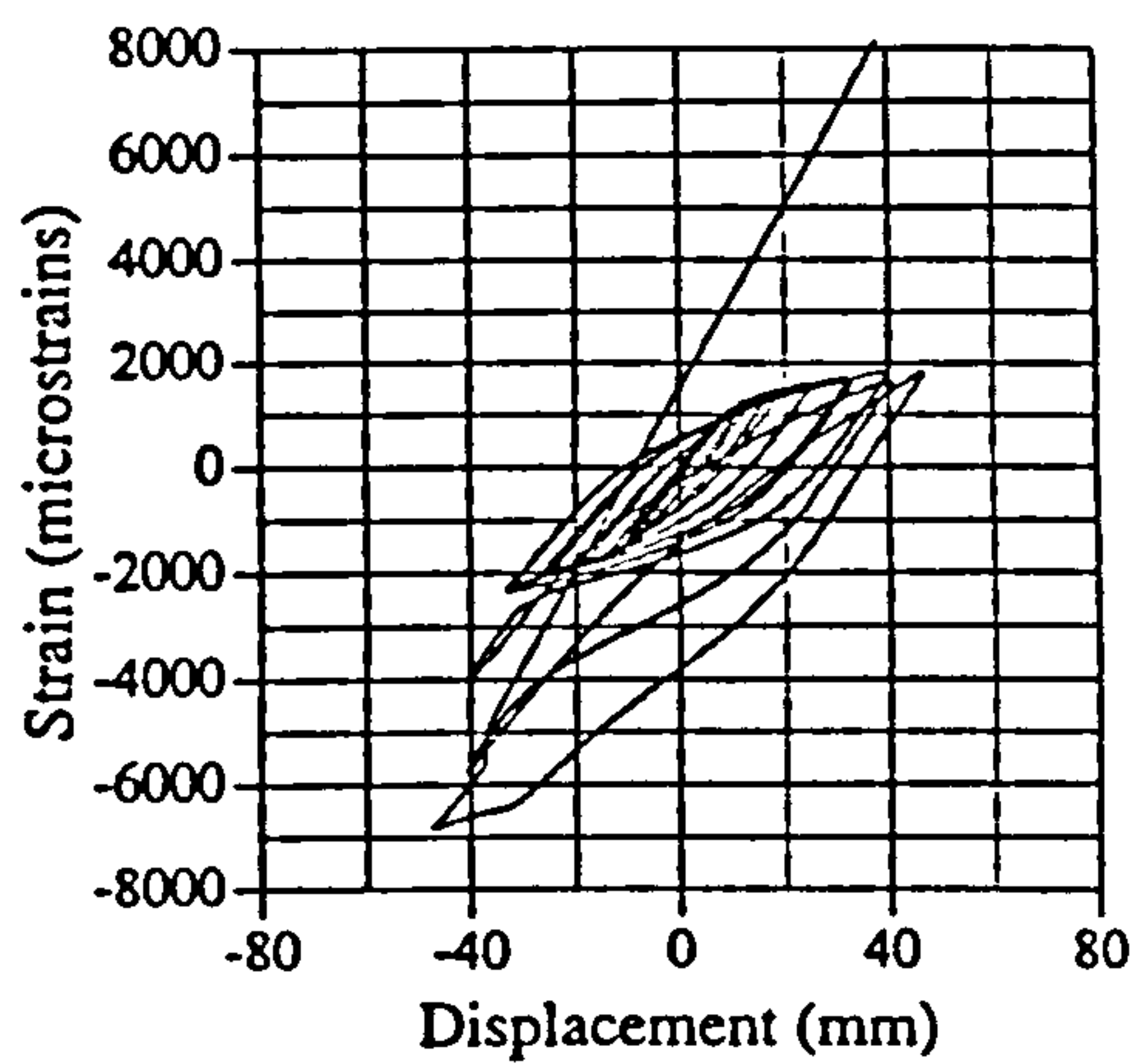


Fig. A.98 Strain vs displacement, IC02, G23

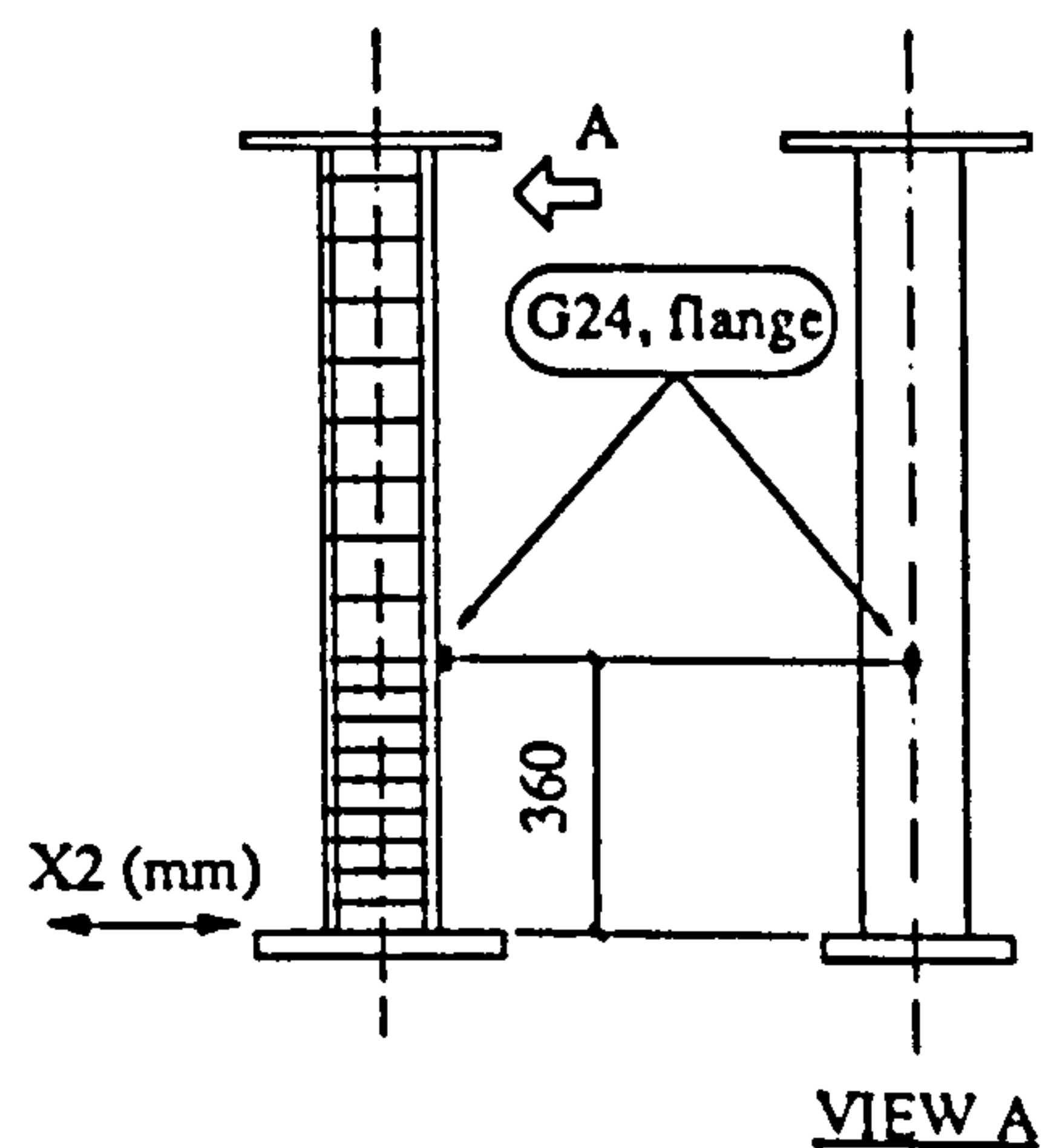
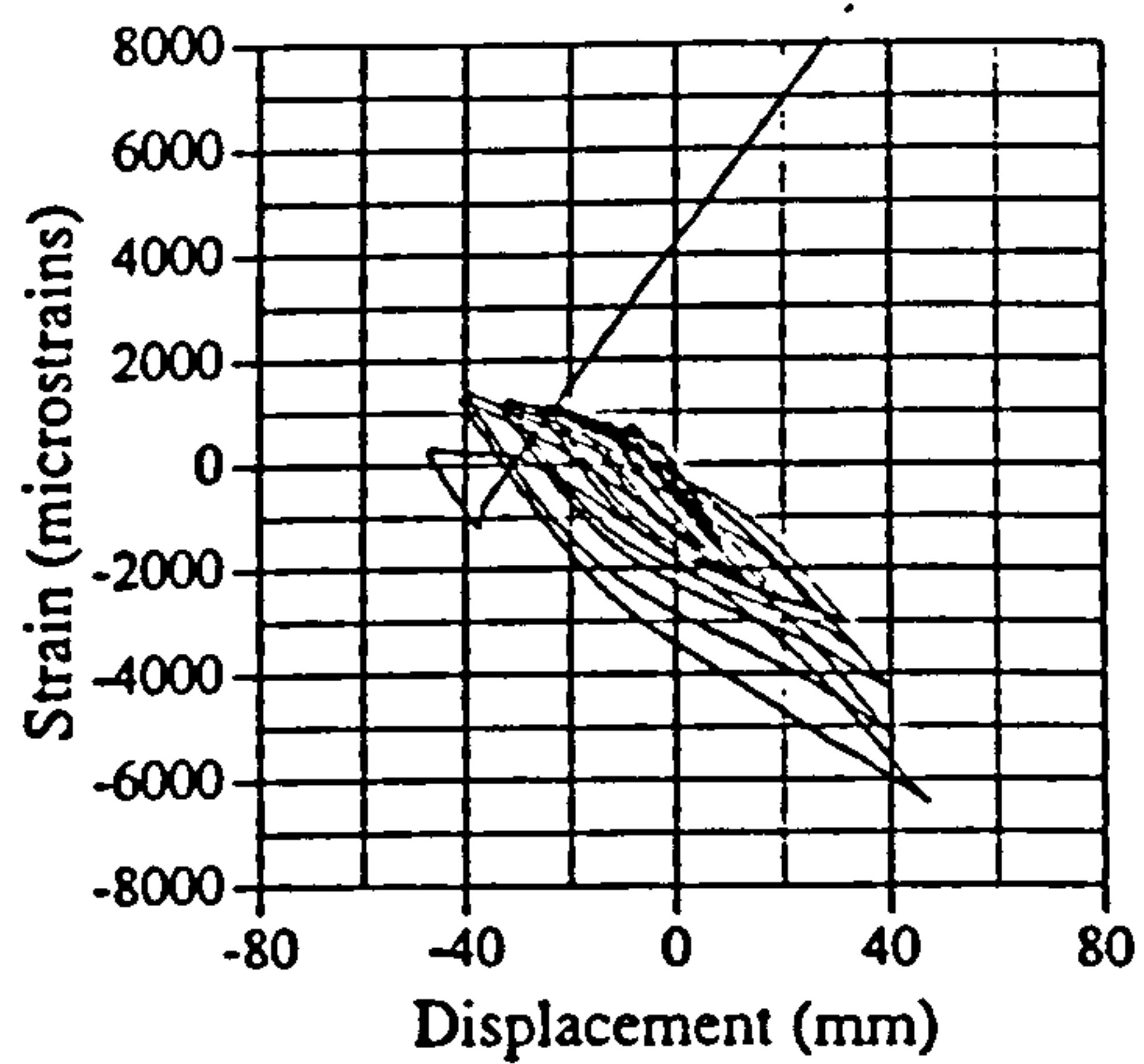


Fig. A.99 Strain vs displacement, IC02, G24

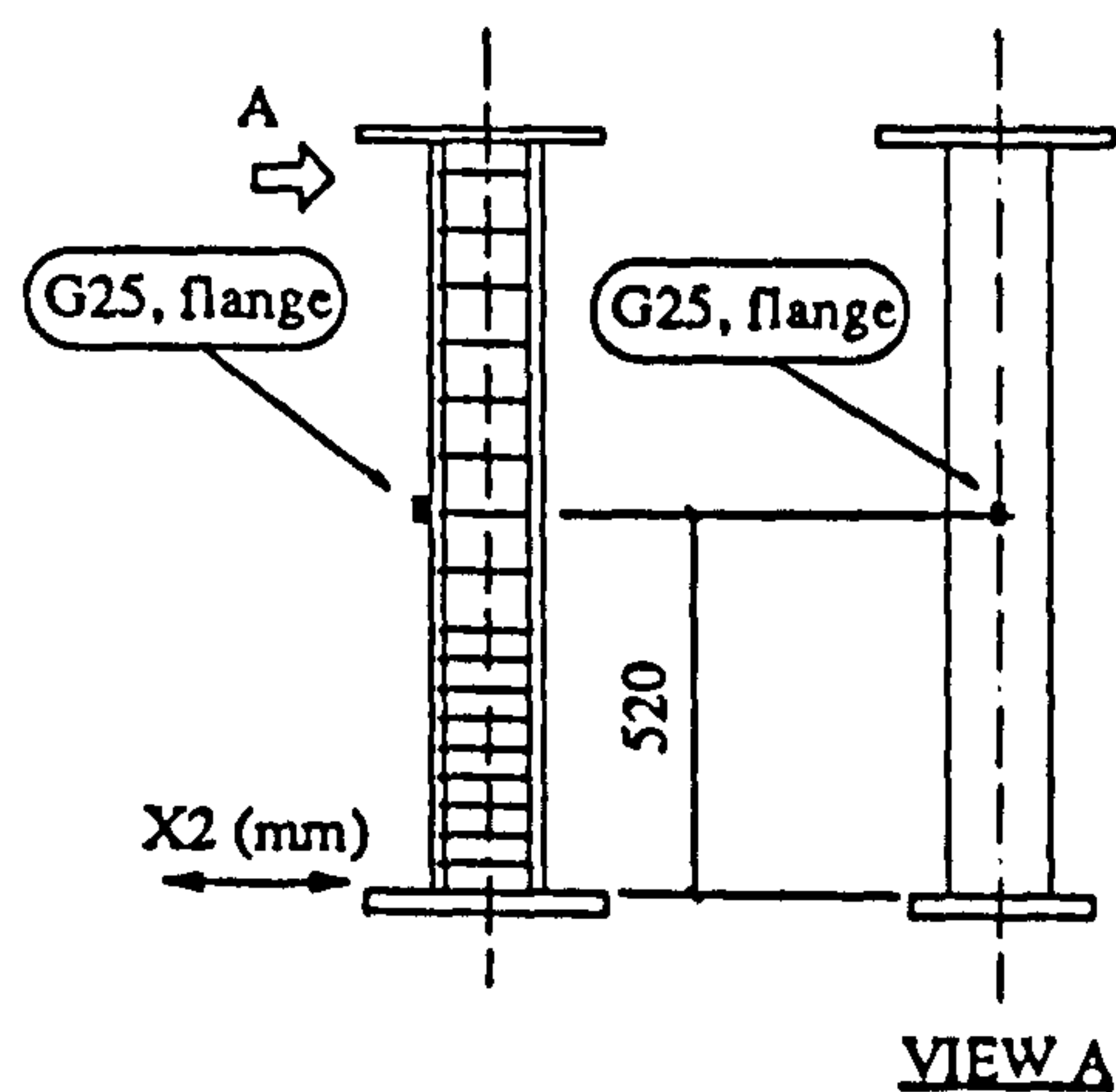
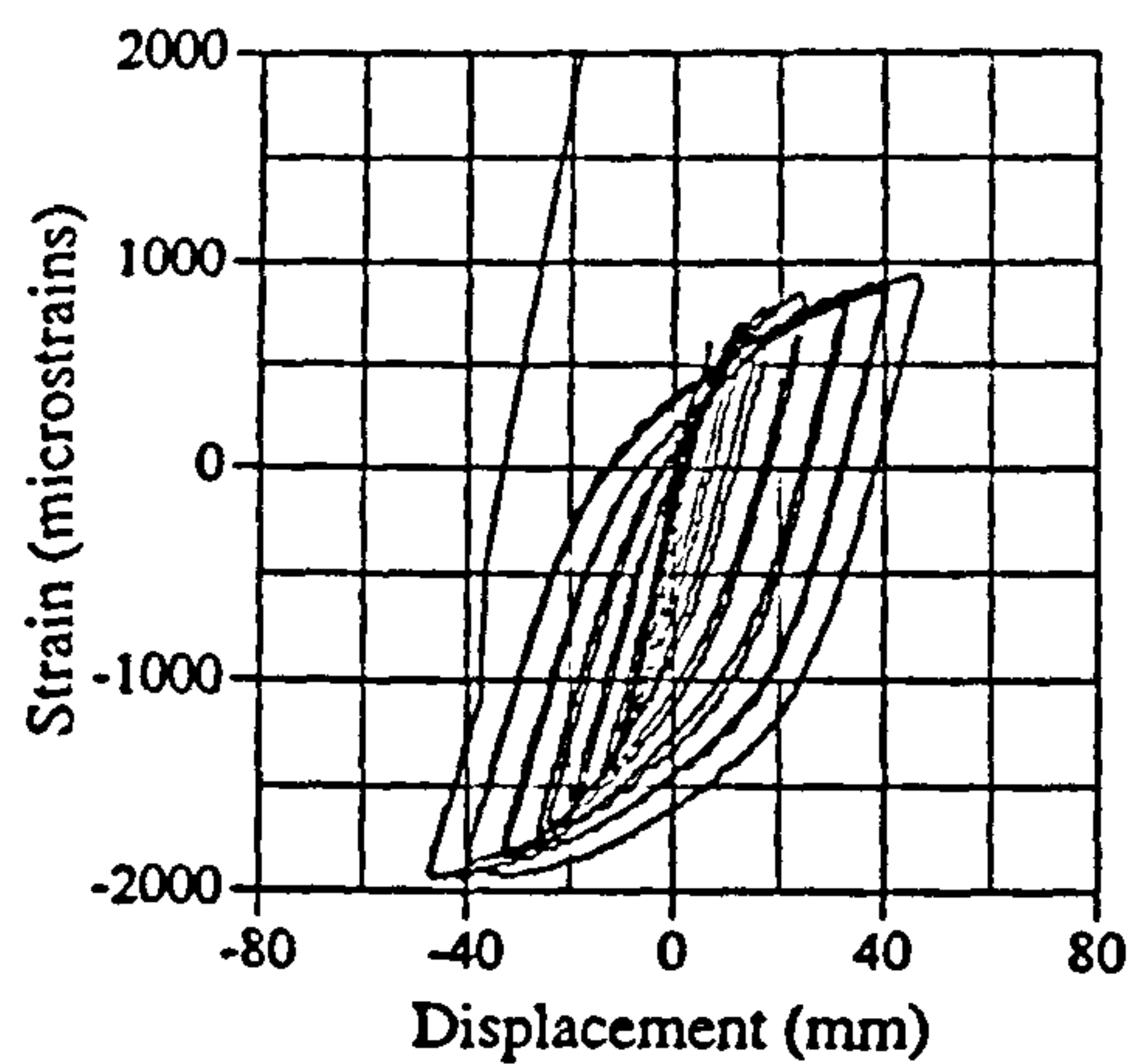


Fig. A.100 Strain vs displacement, IC02, G25

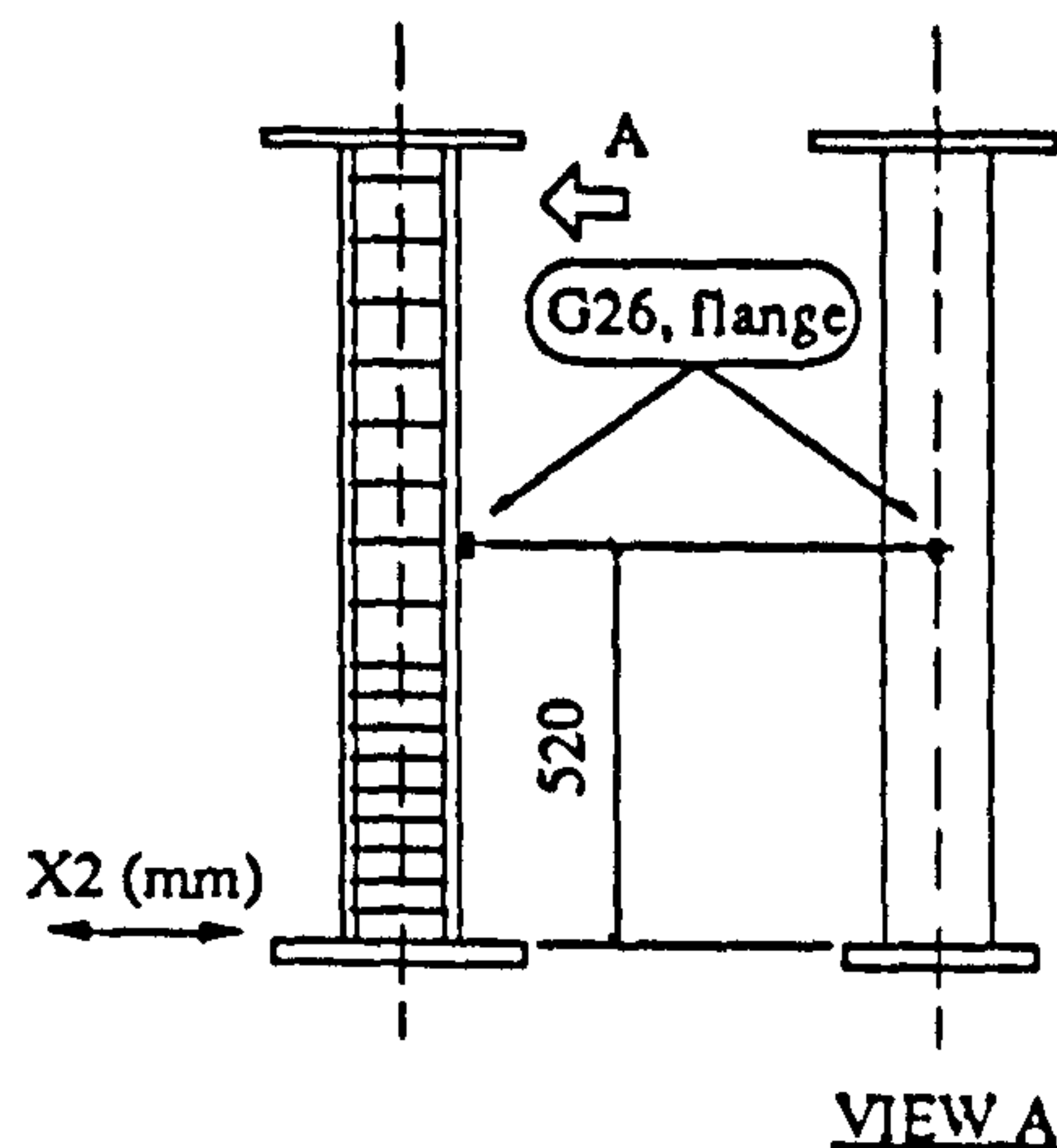
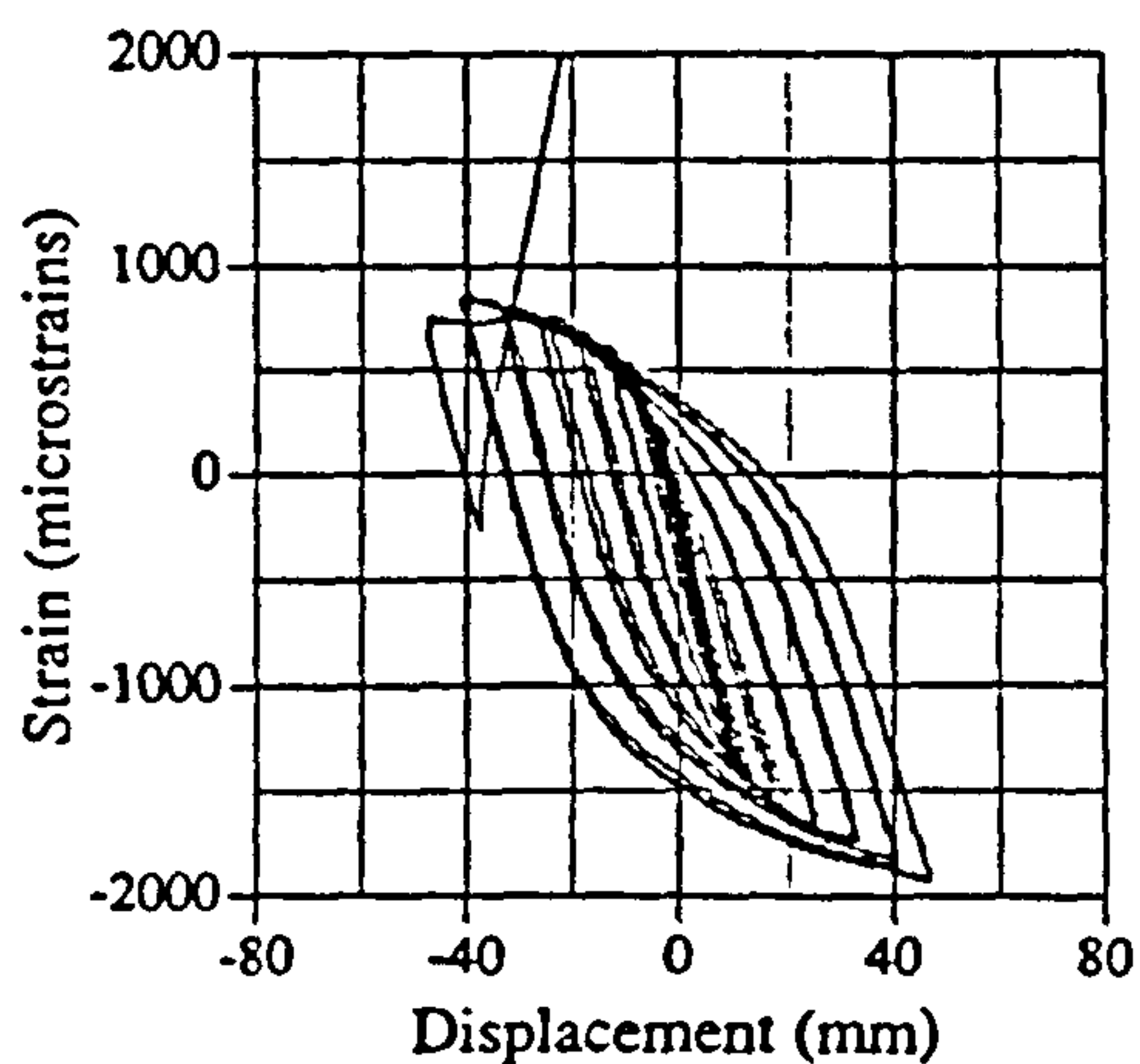


Fig. A.101 Strain vs displacement, IC02, G26

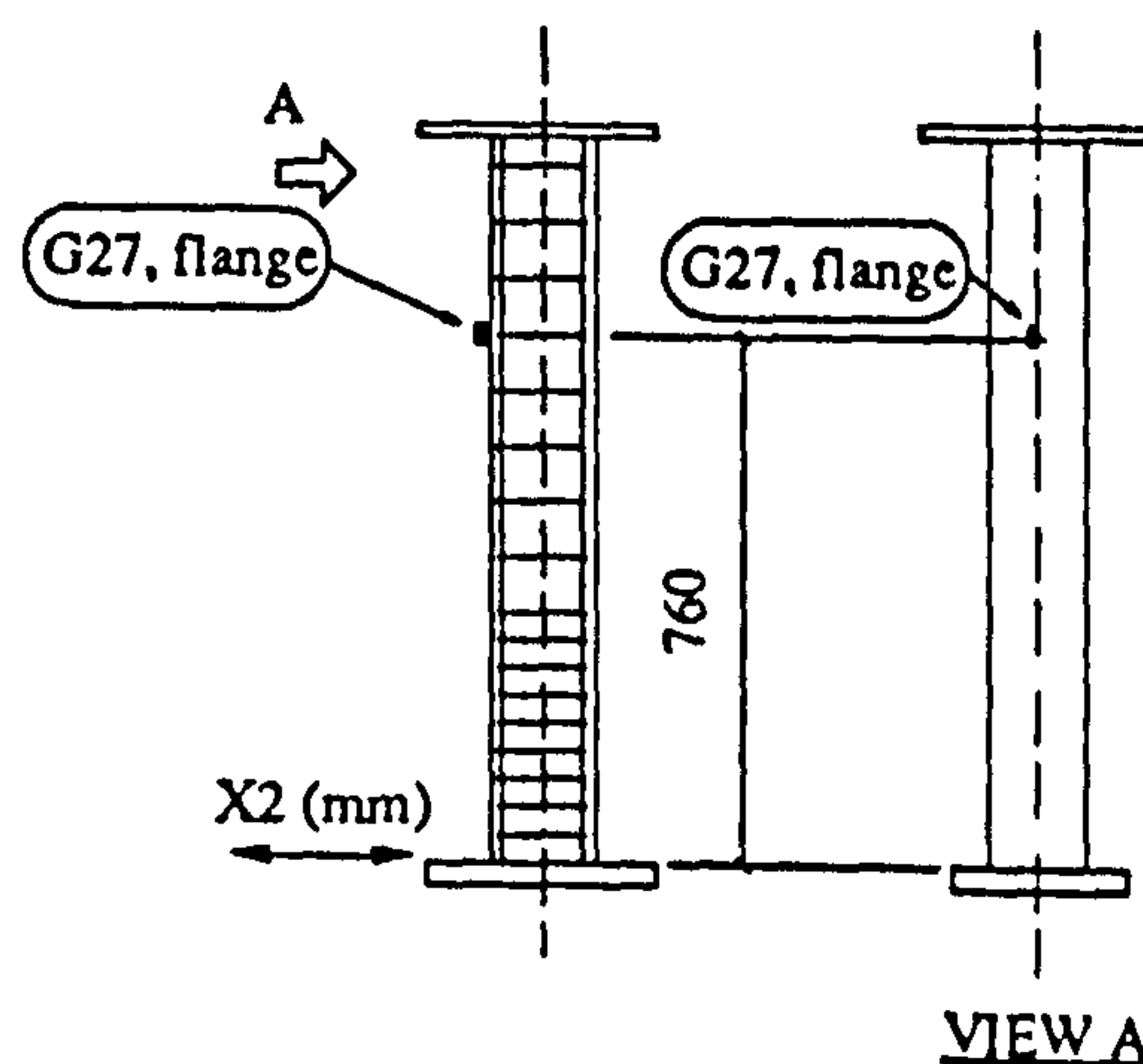
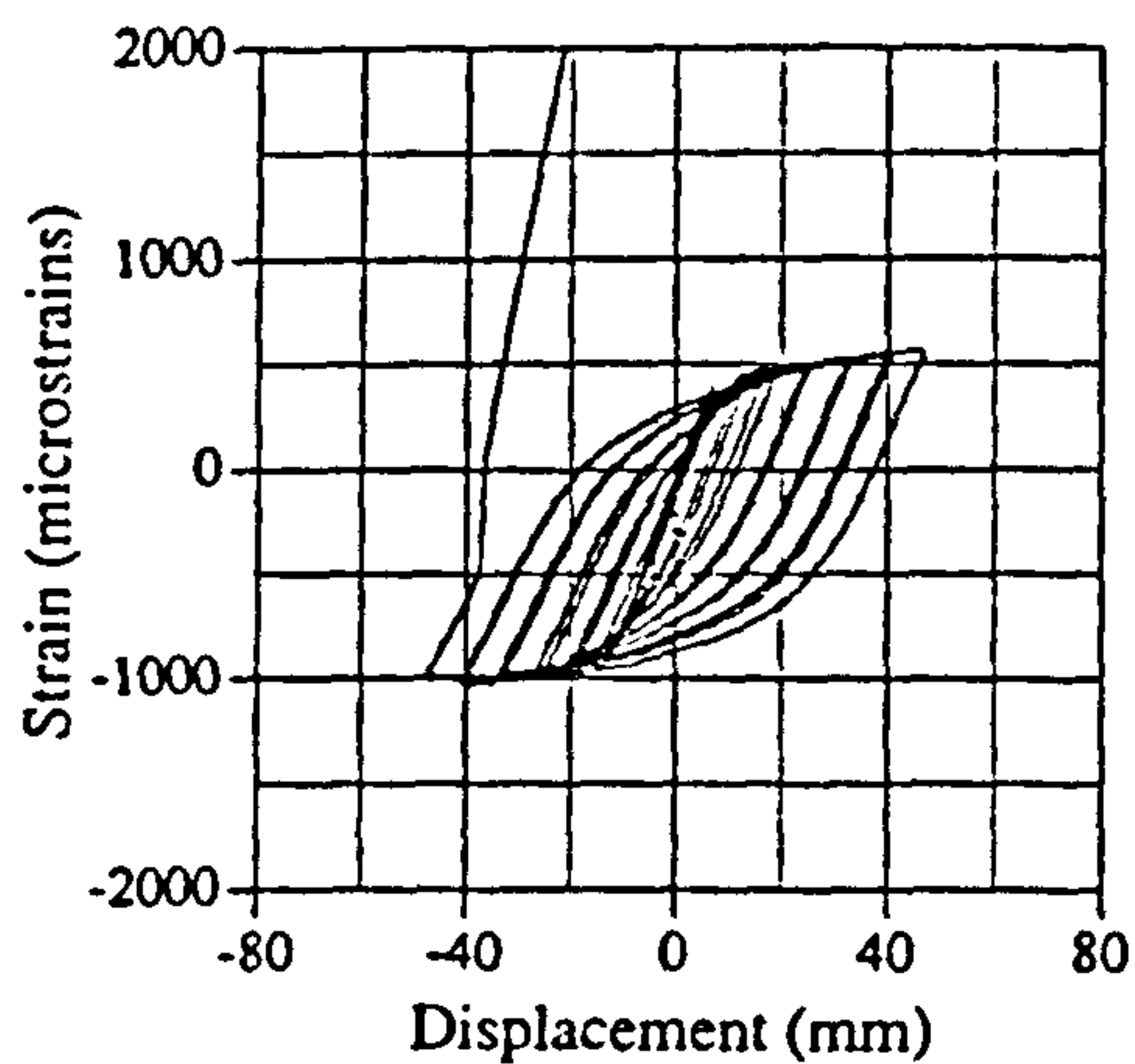


Fig. A.102 Strain vs displacement, IC02, G27

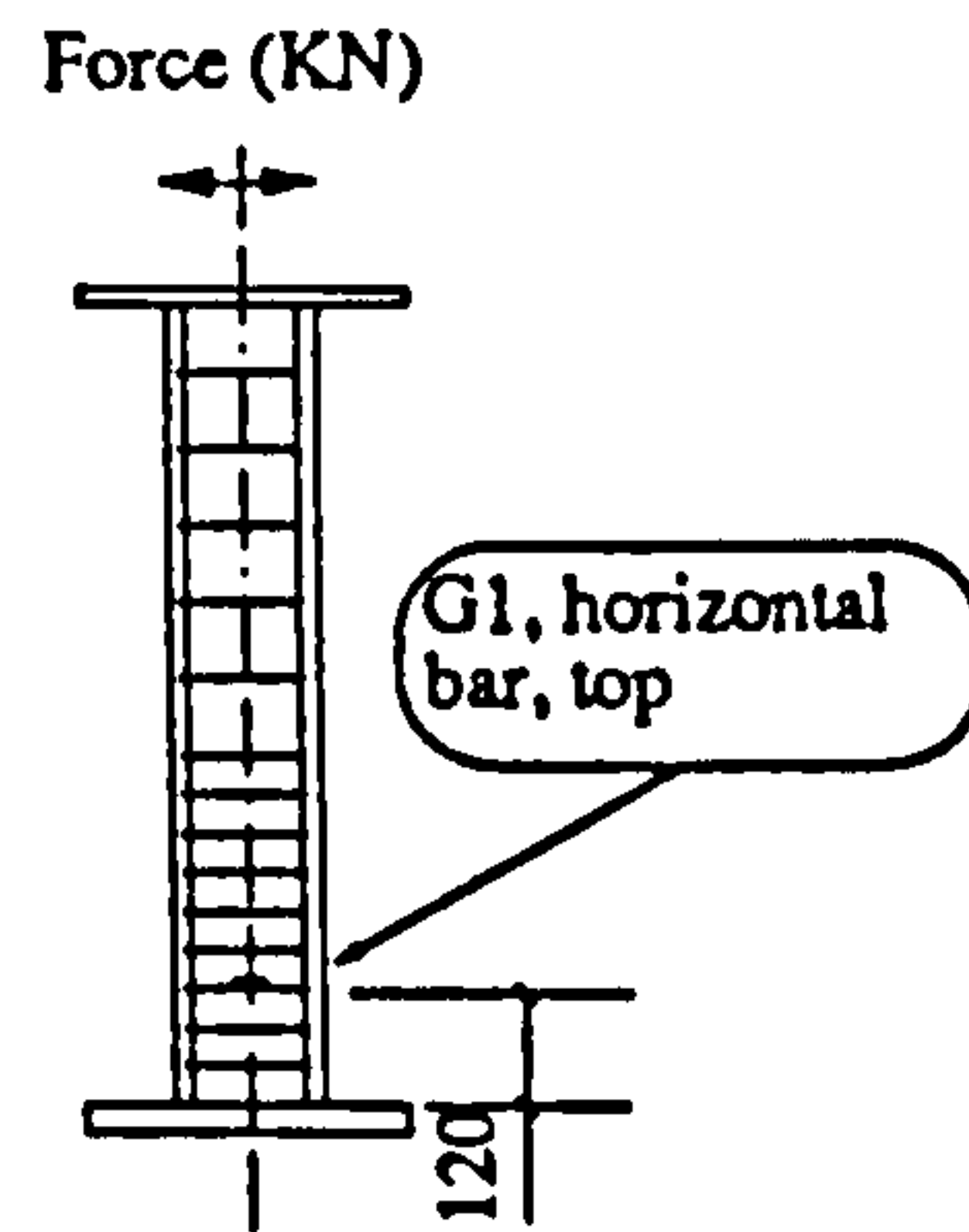
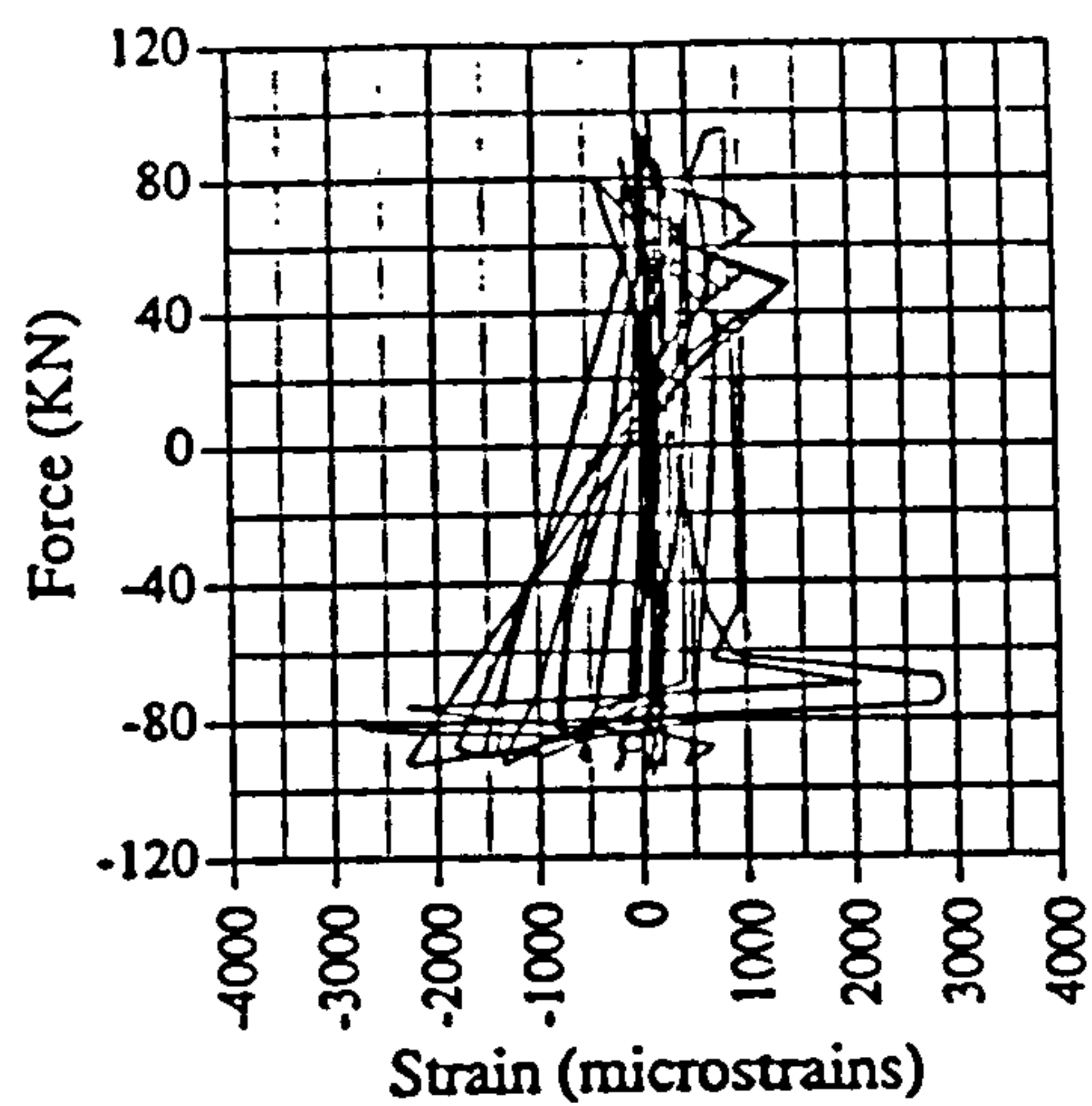


Fig. A.103 Force vs strain, IC07, G1

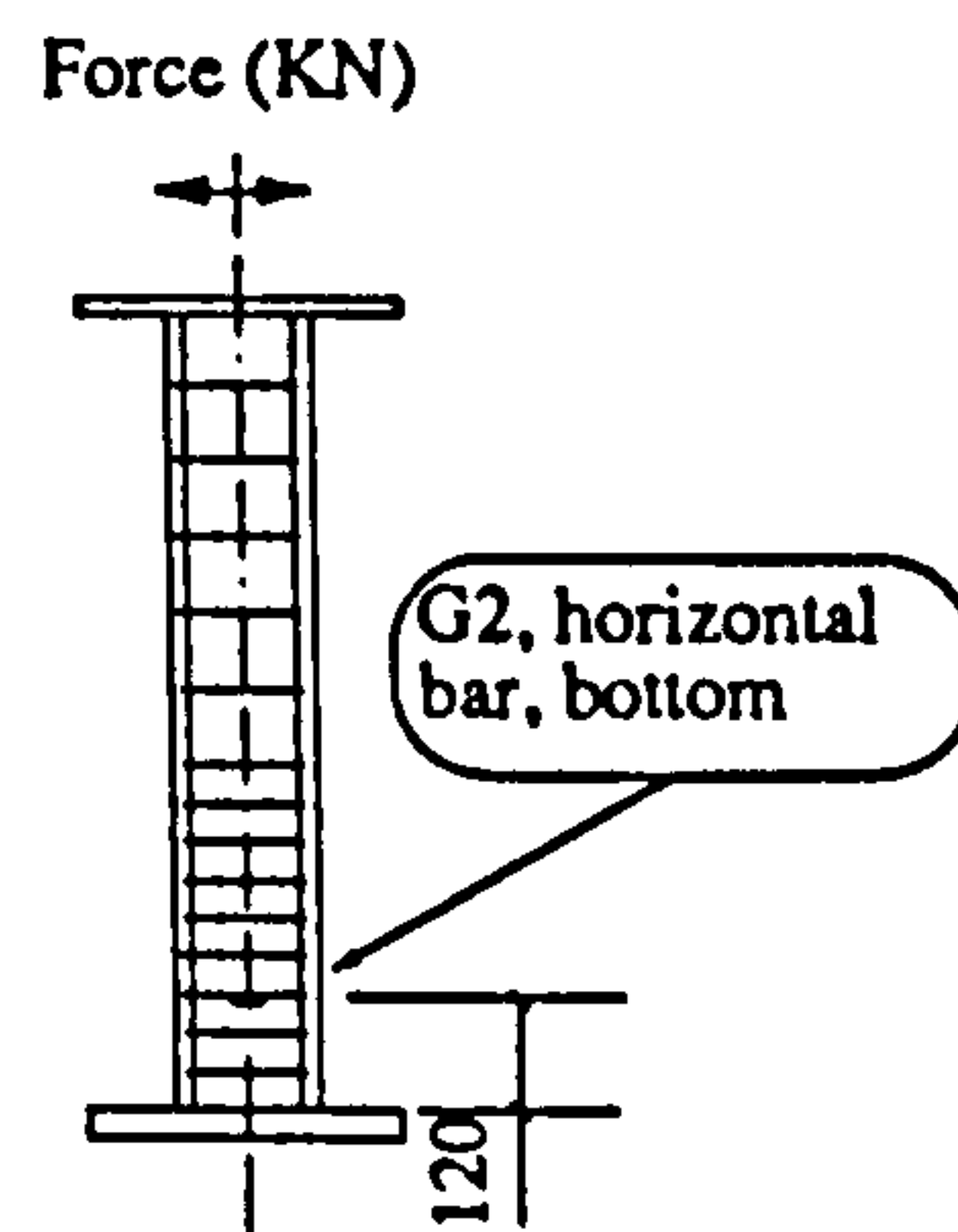
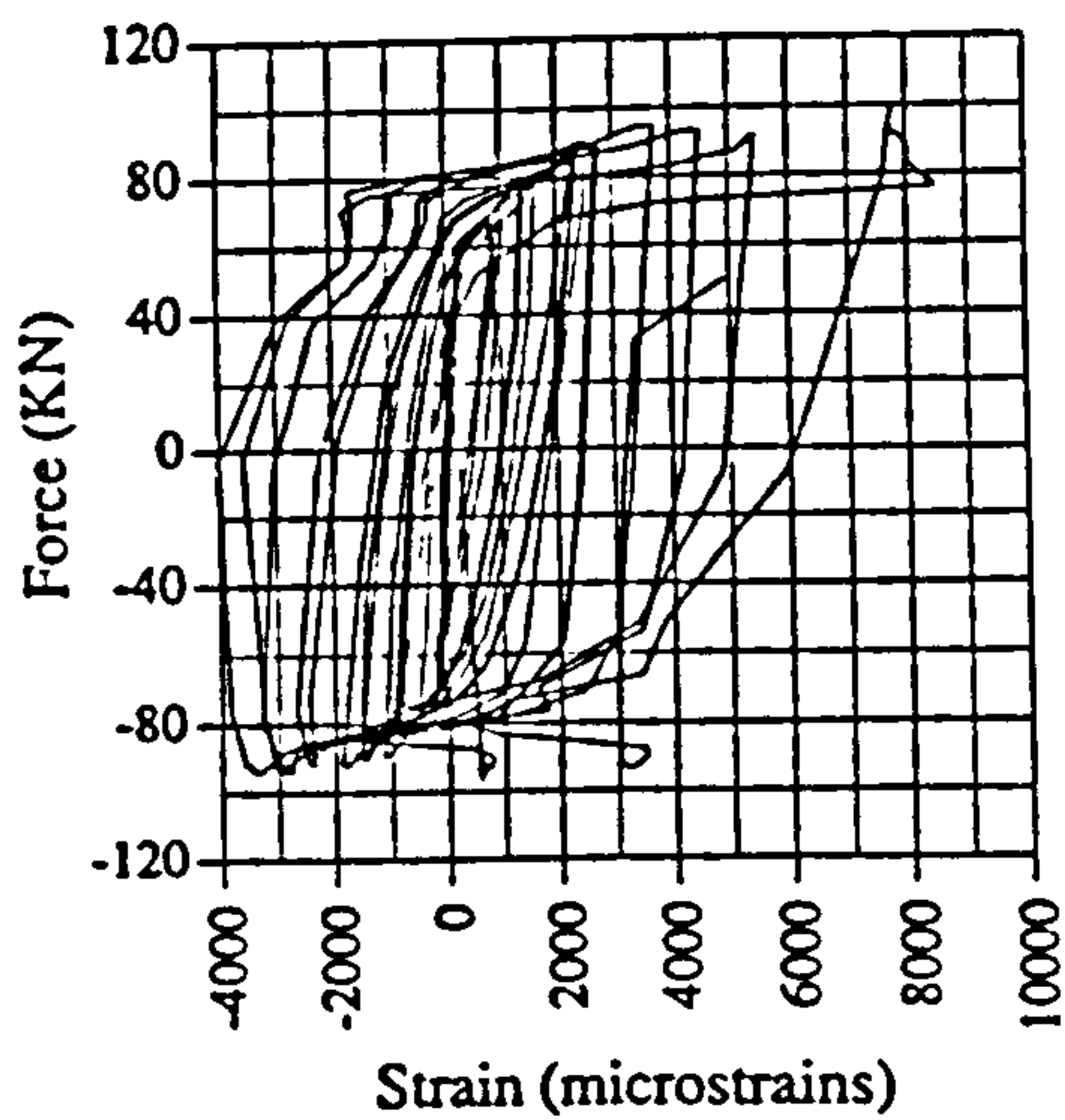


Fig. A.104 Force vs strain, IC07, G2

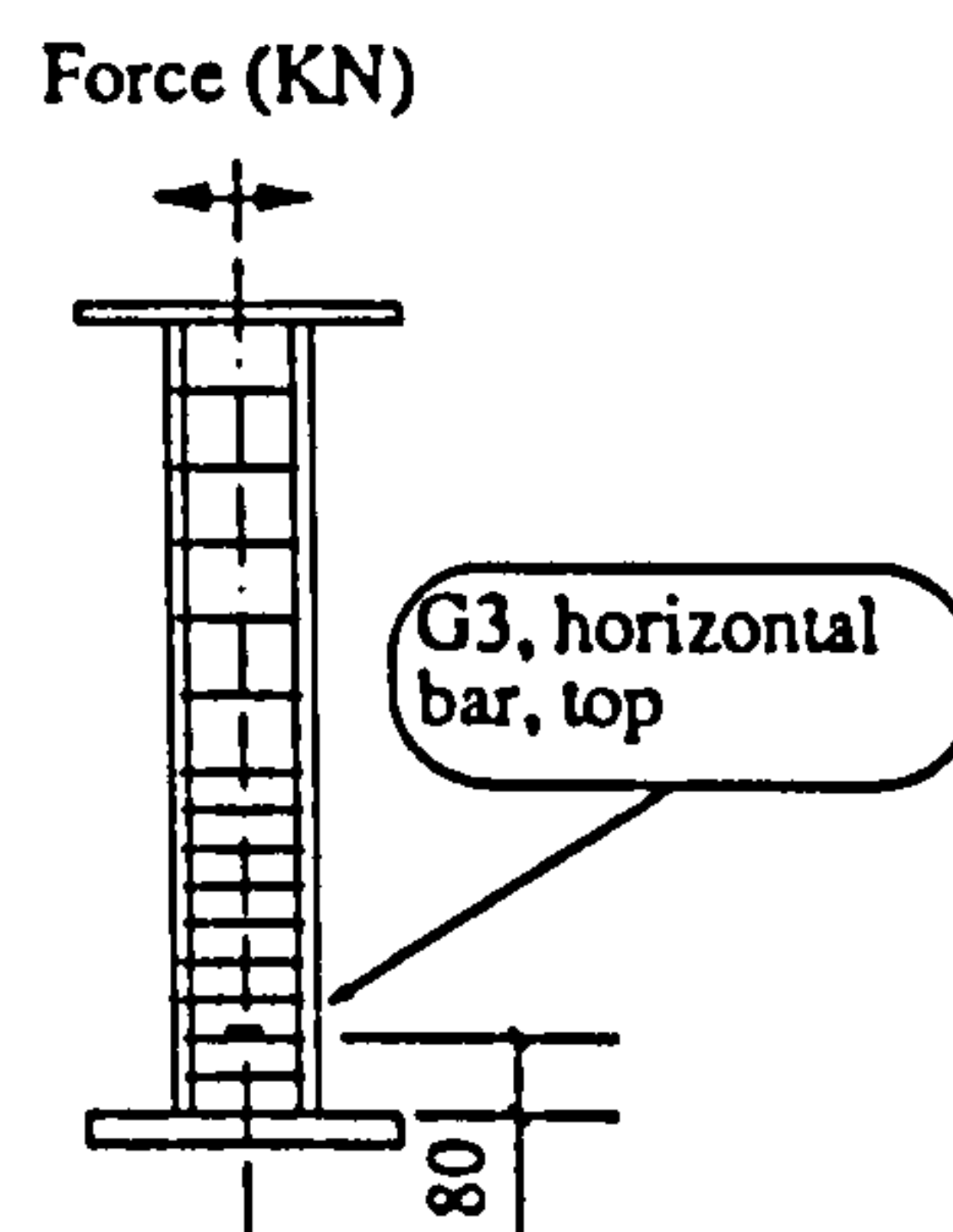
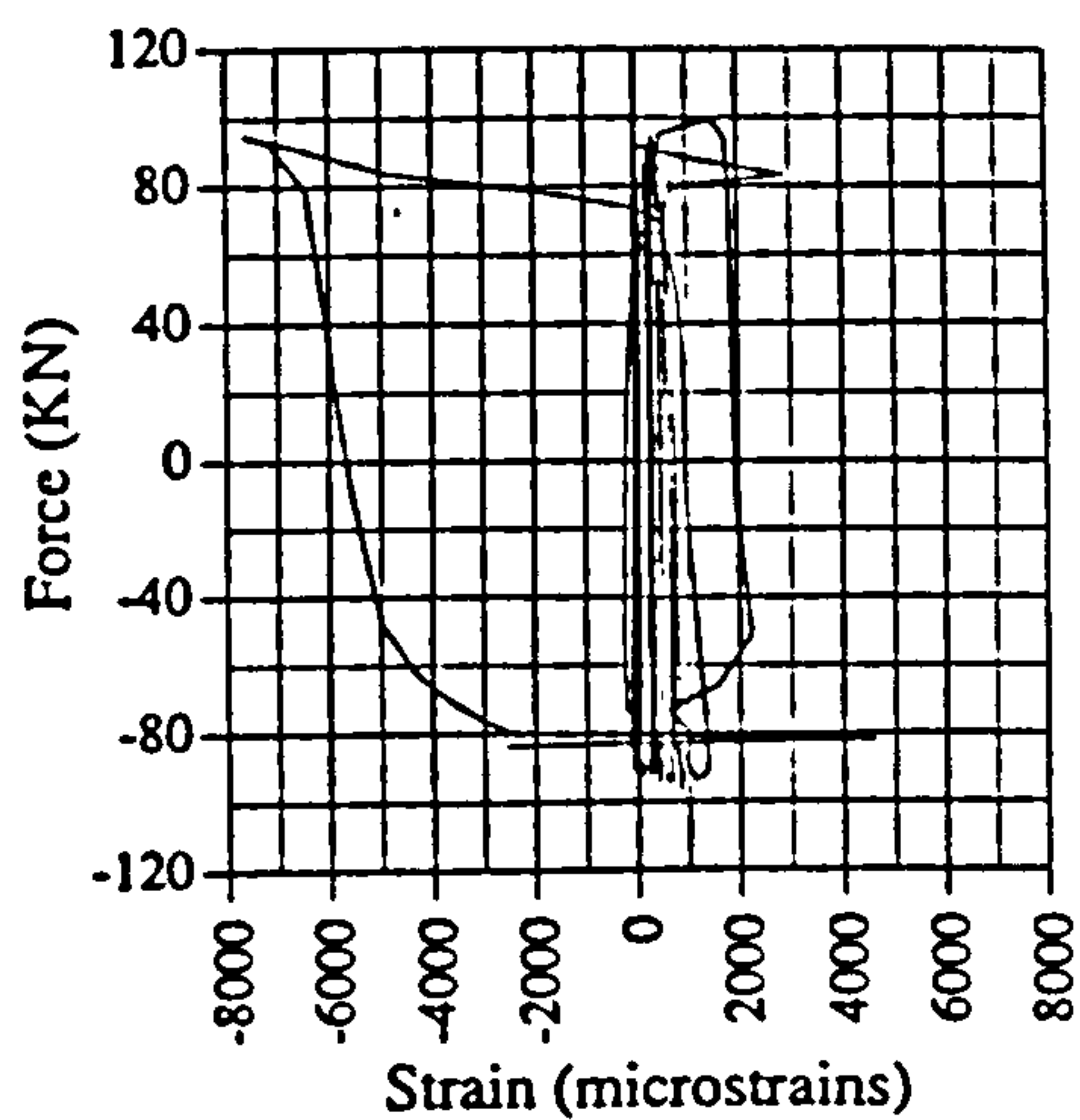


Fig. A.105 Strain vs displacement, IC07, G3

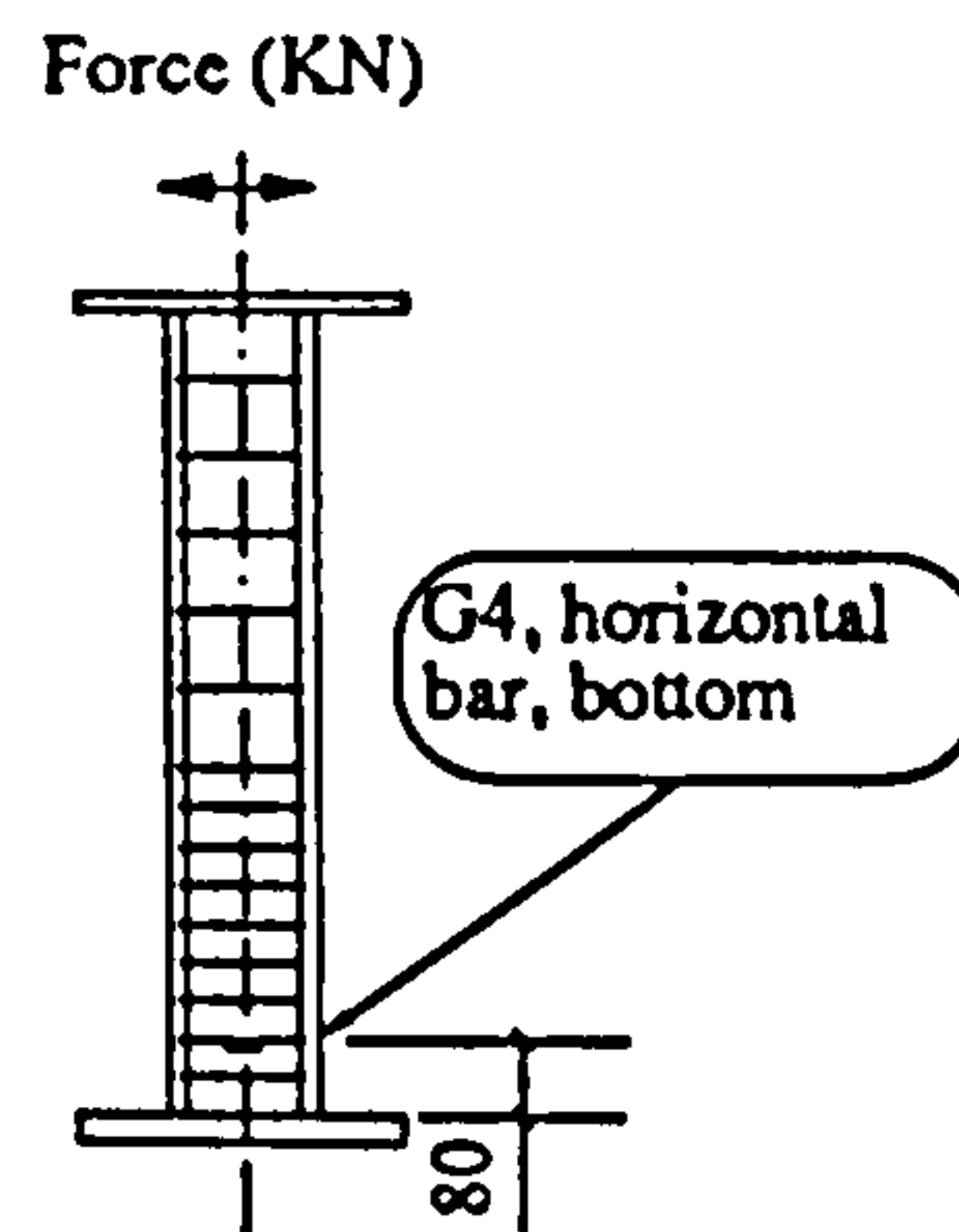
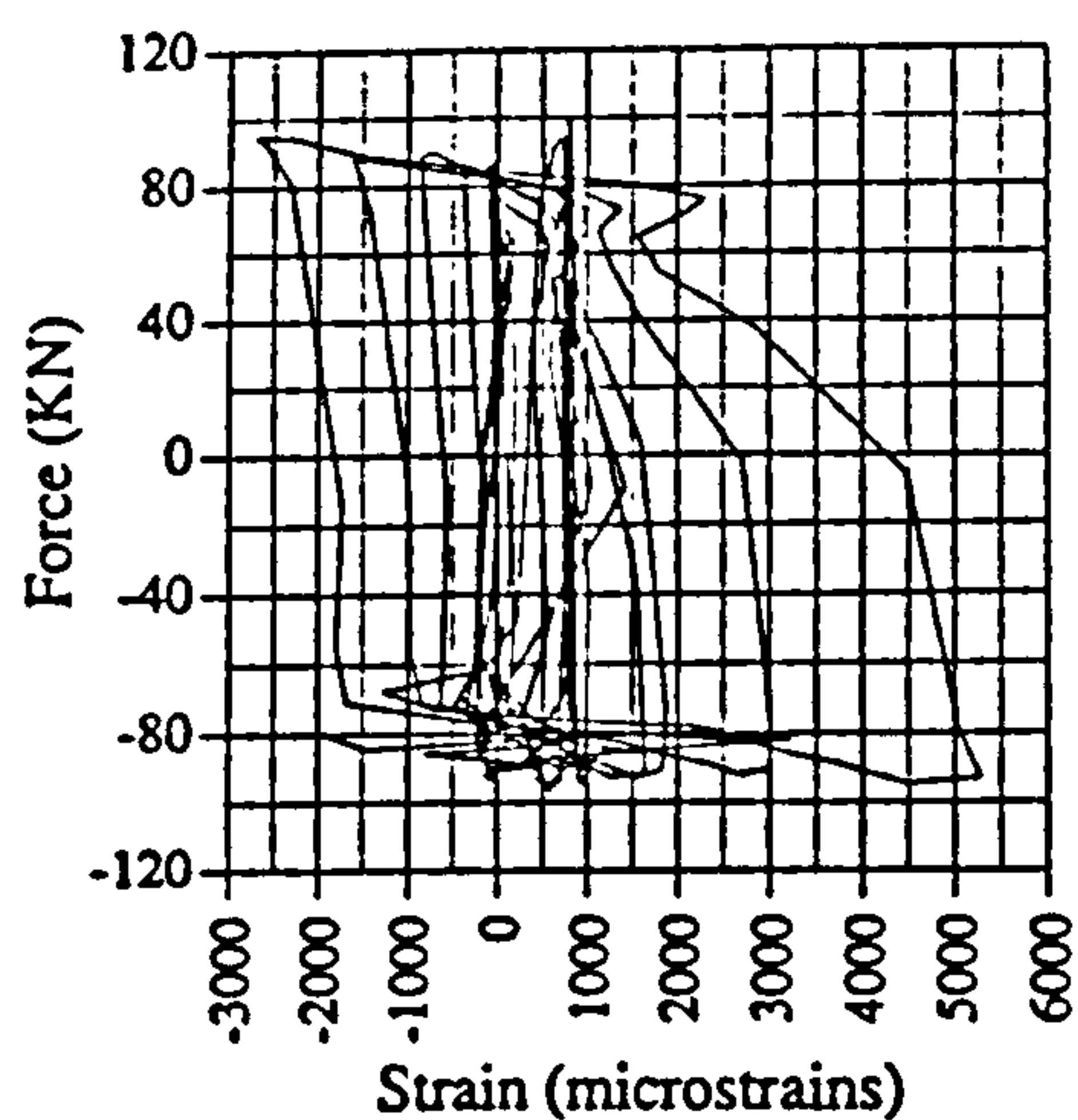


Fig. A.106 Force vs strain, IC07, G4

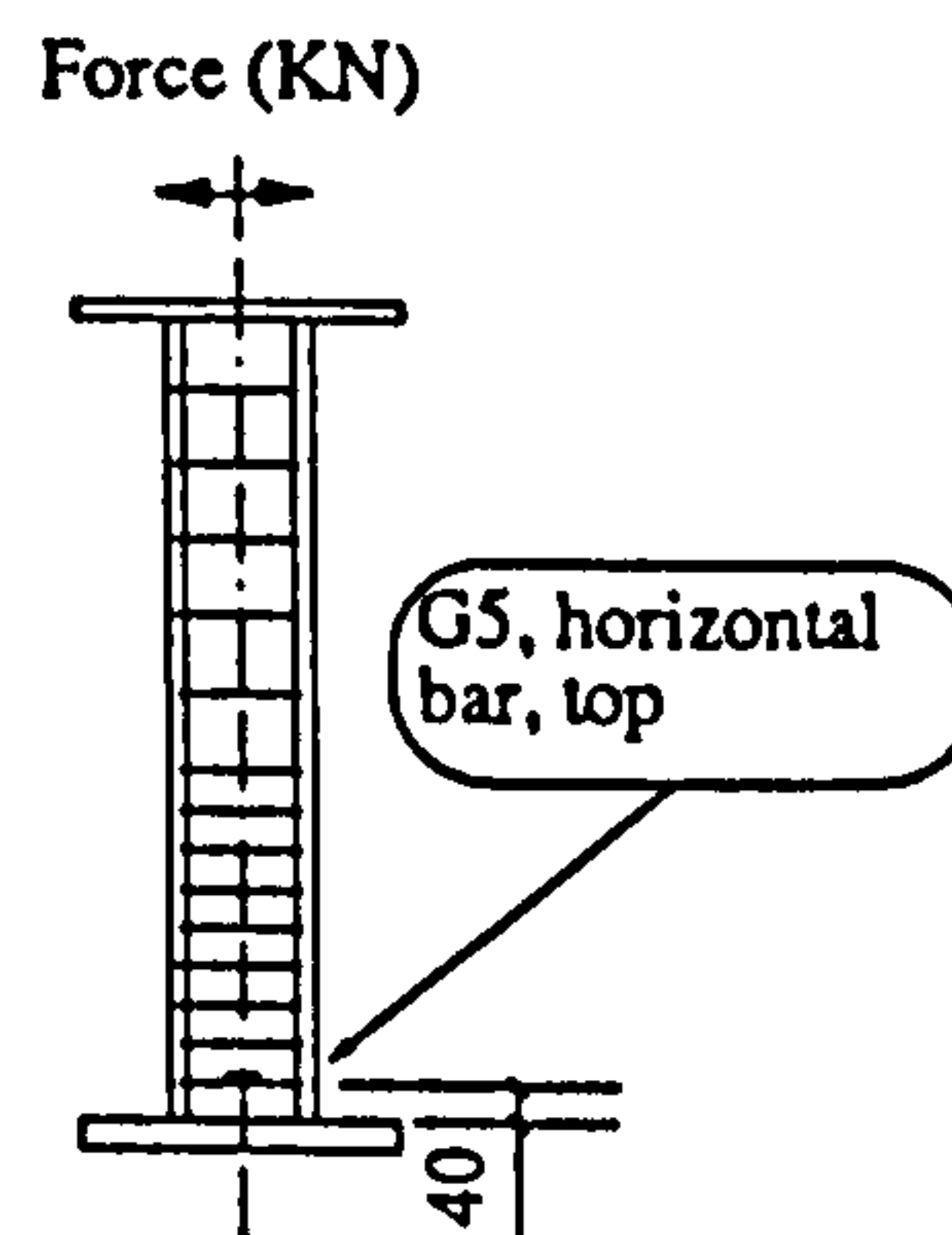
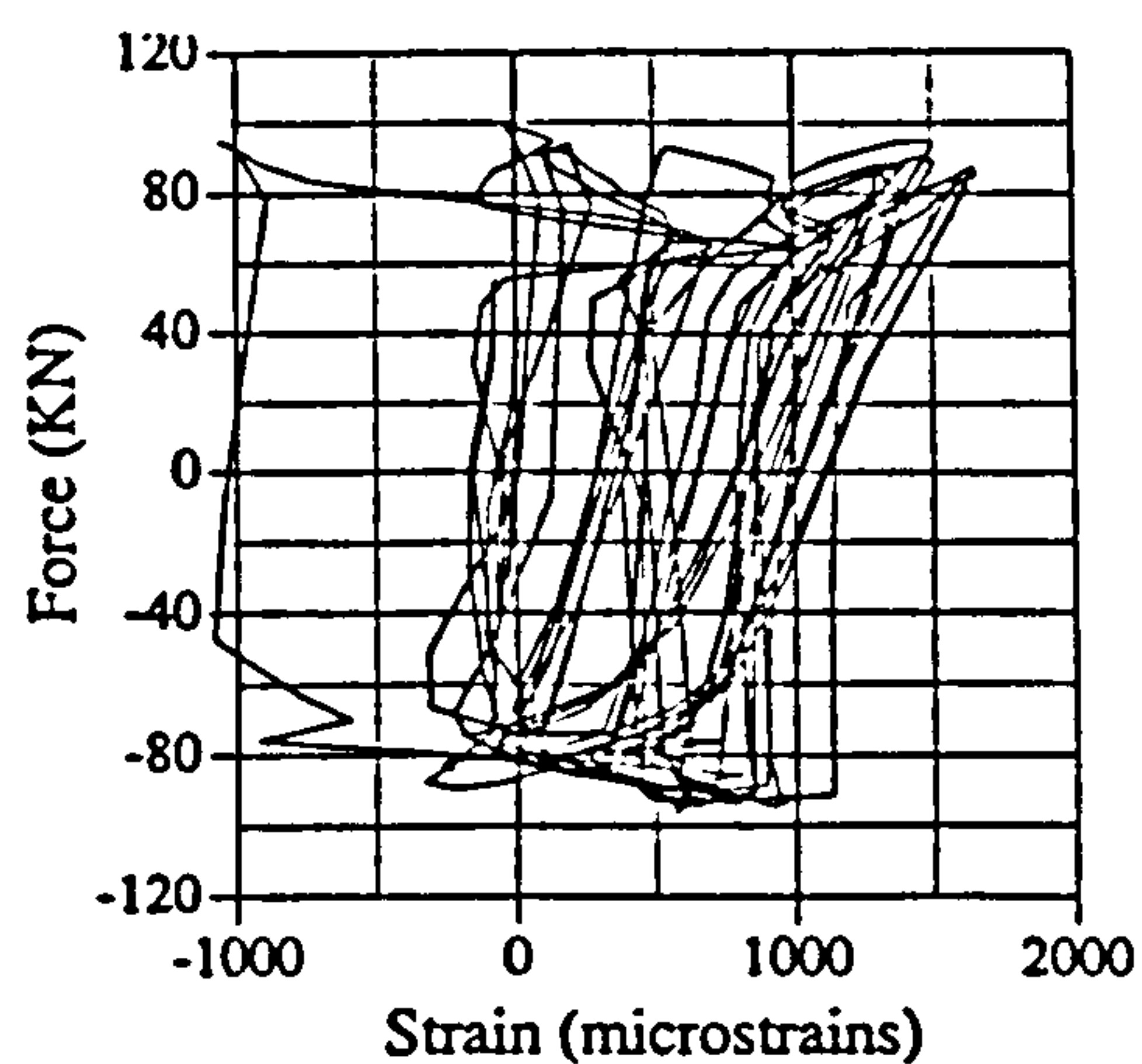


Fig. A.107 Force vs strain, IC07, G5

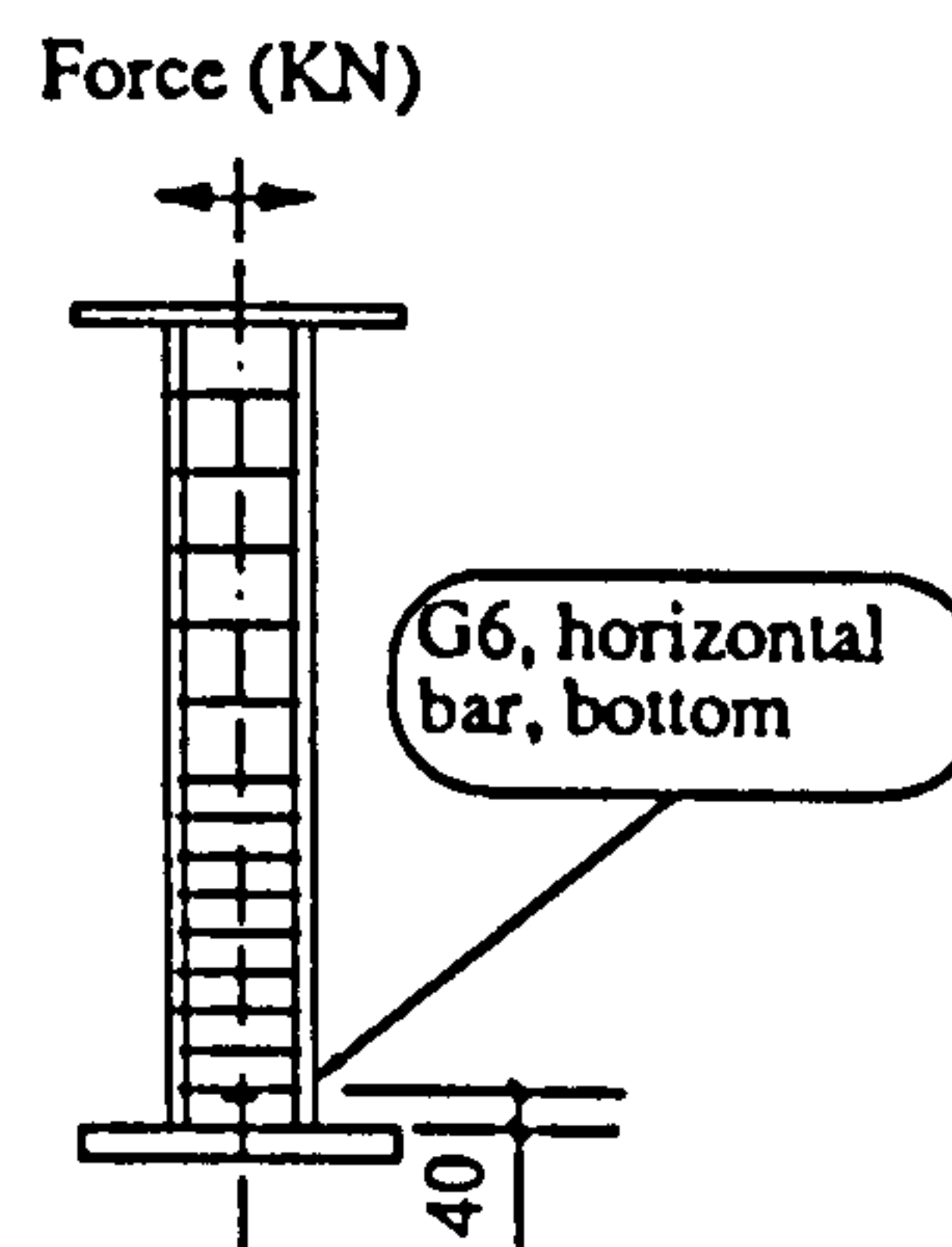
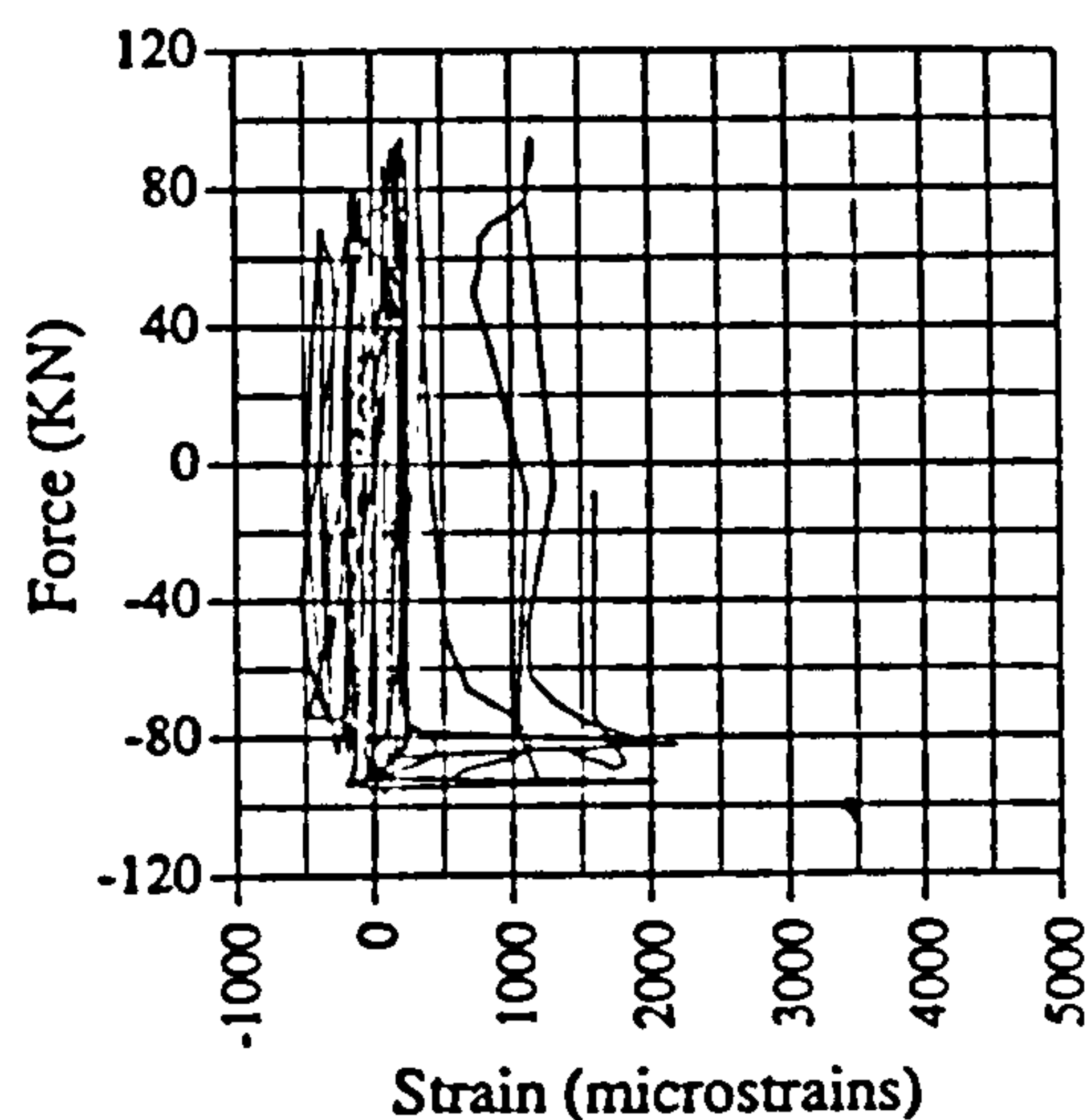


Fig. A.108 Force vs strain, IC07, G6

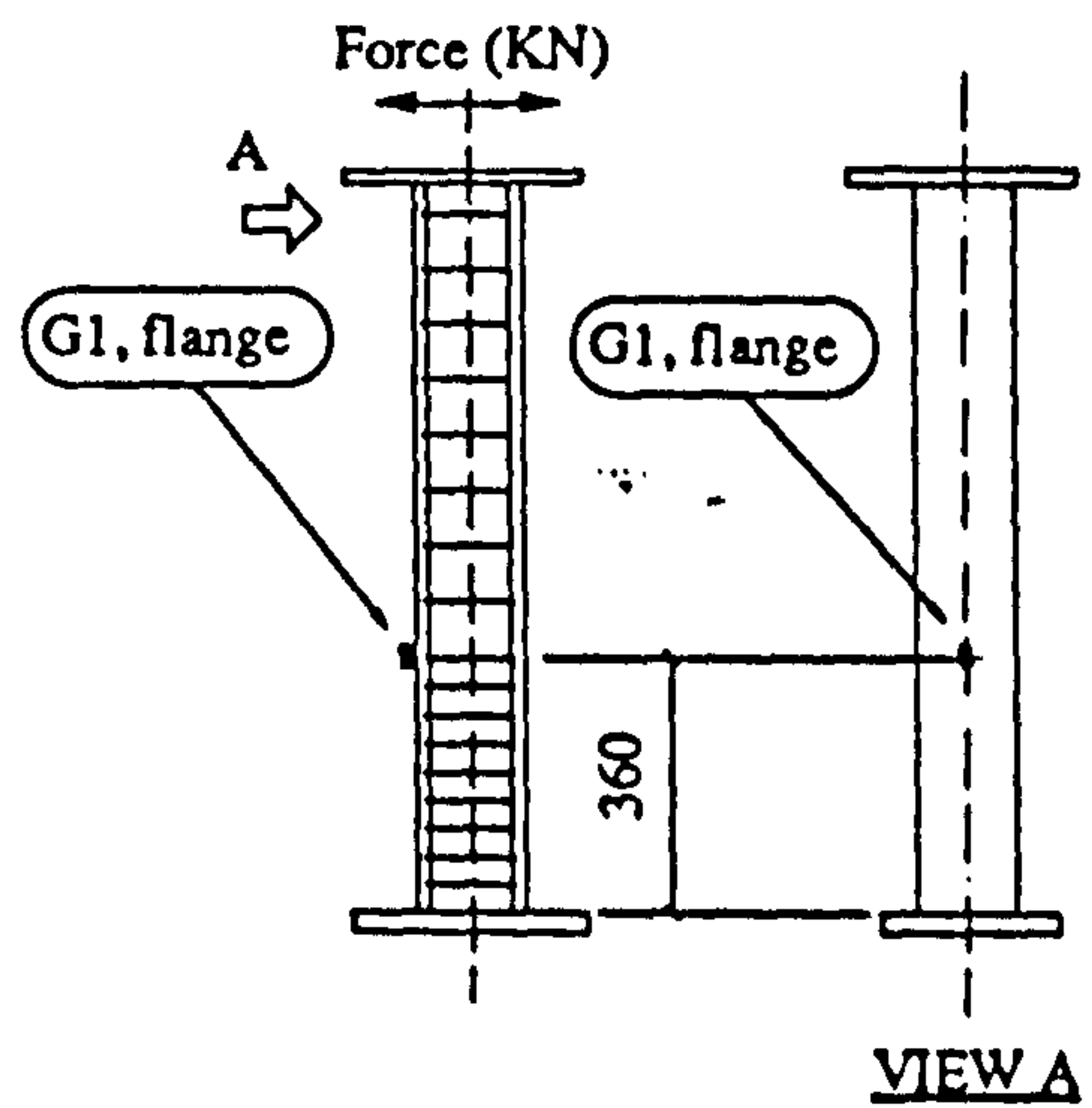
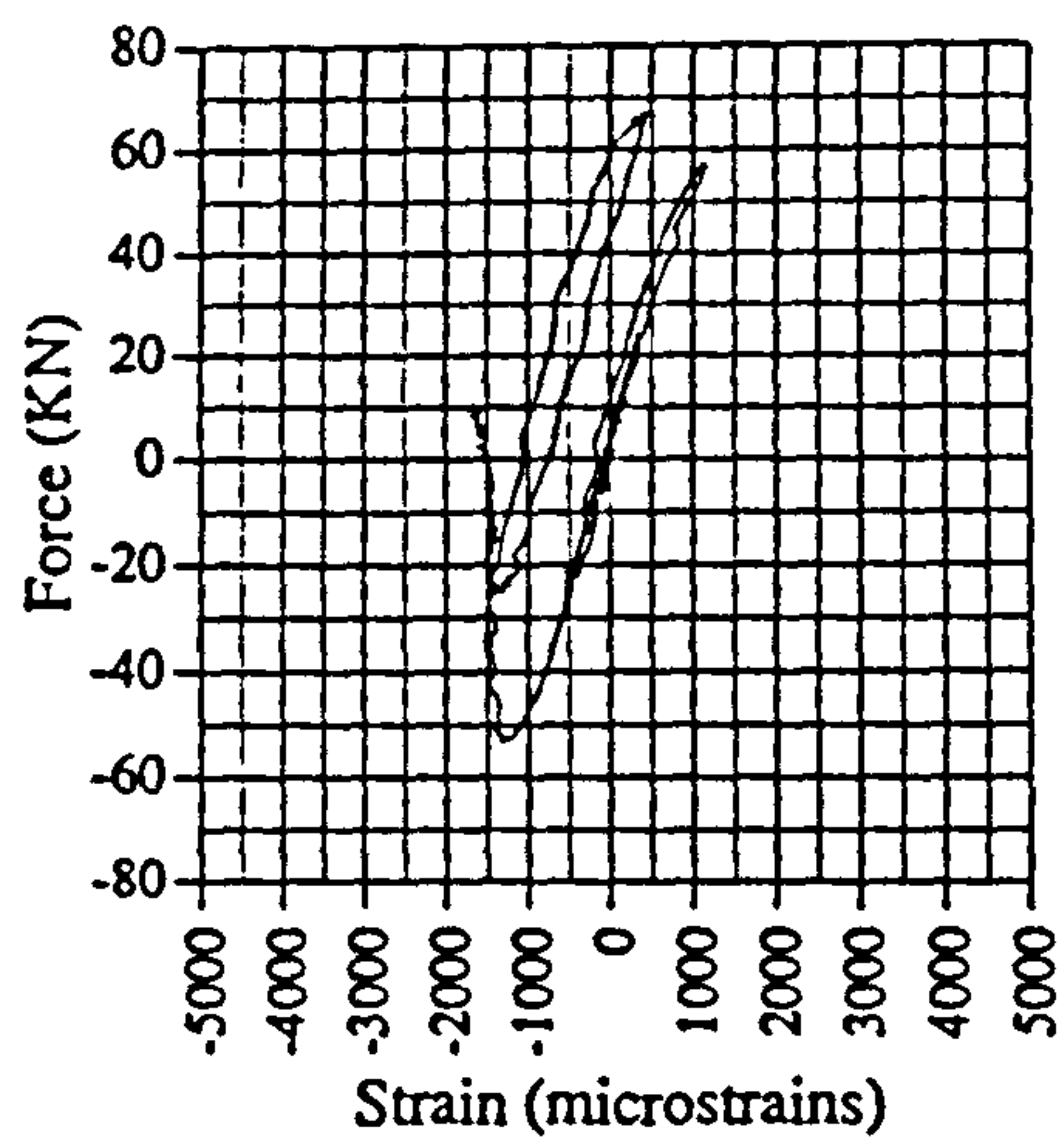


Fig. A.109 Force vs strain, EM03, G1

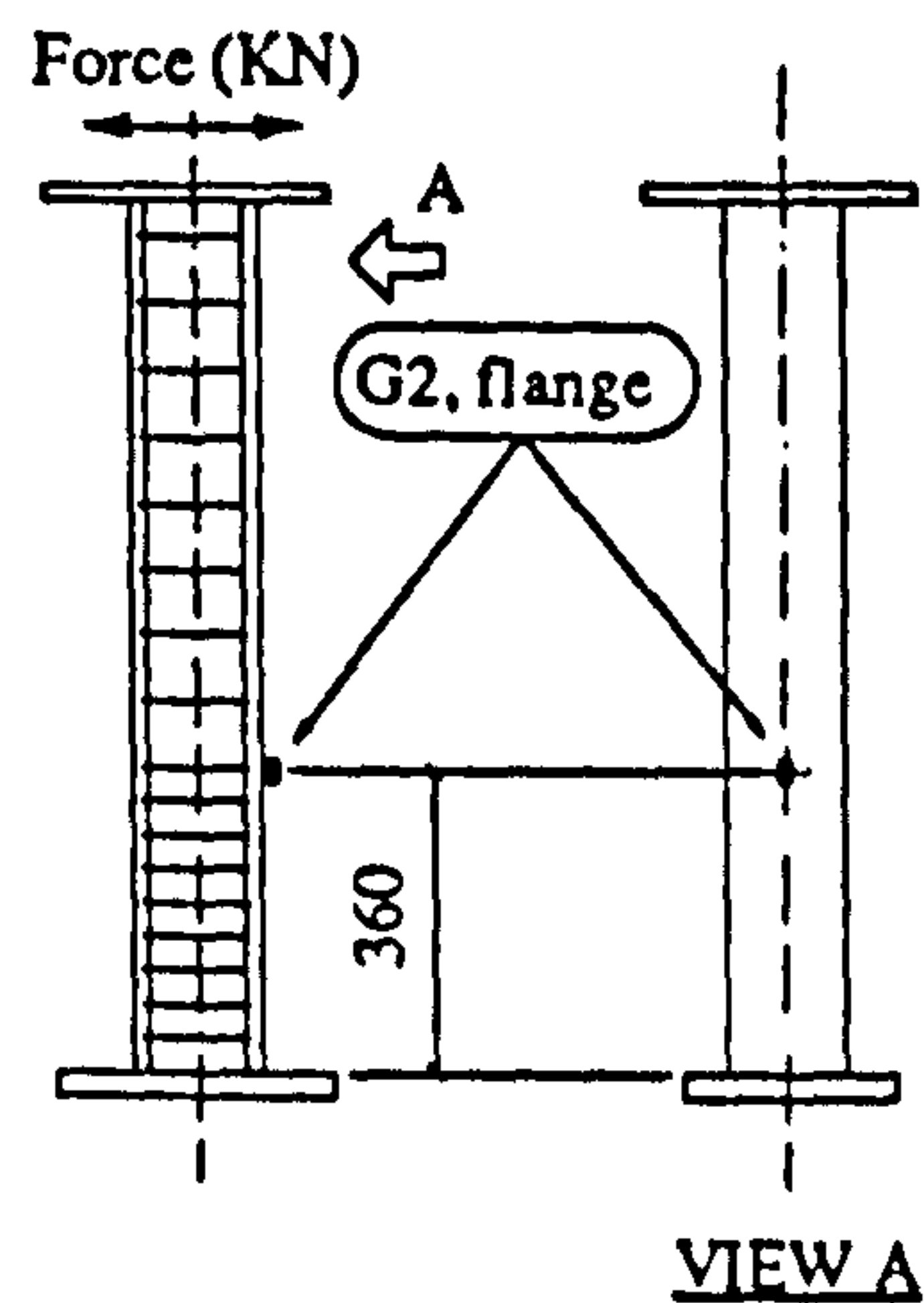
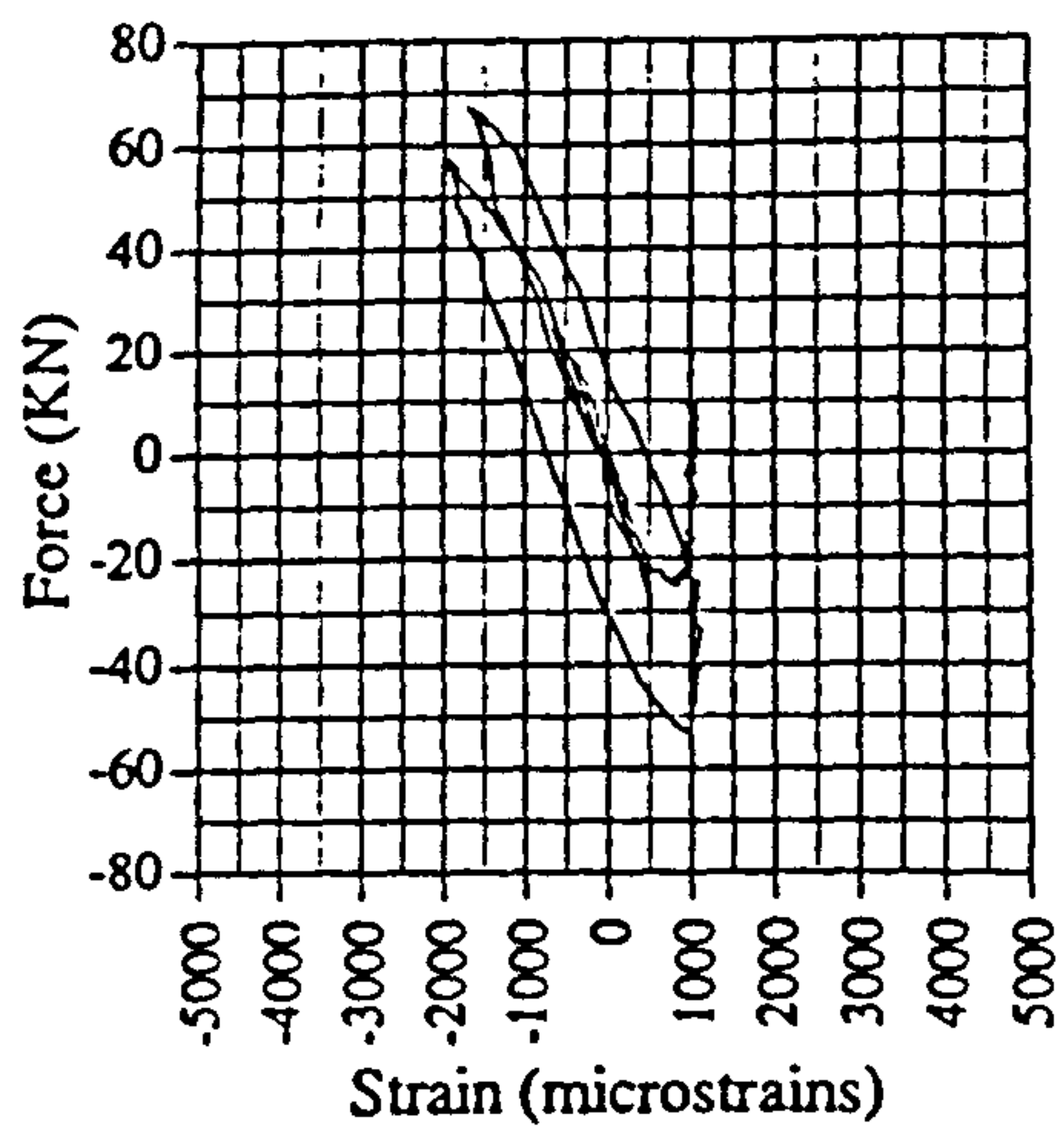


Fig. A.110 Strain vs displacement, EM03, G2

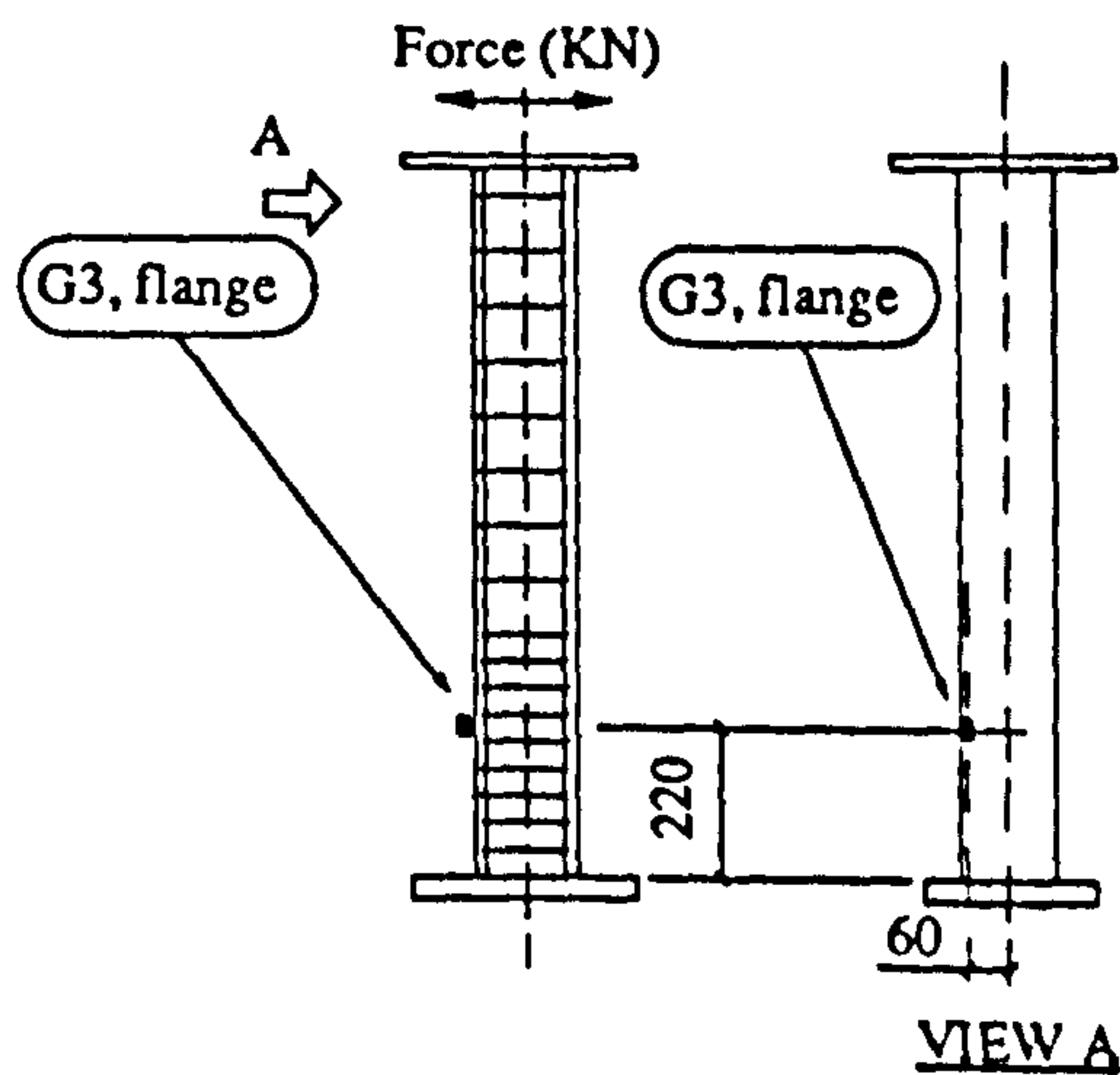
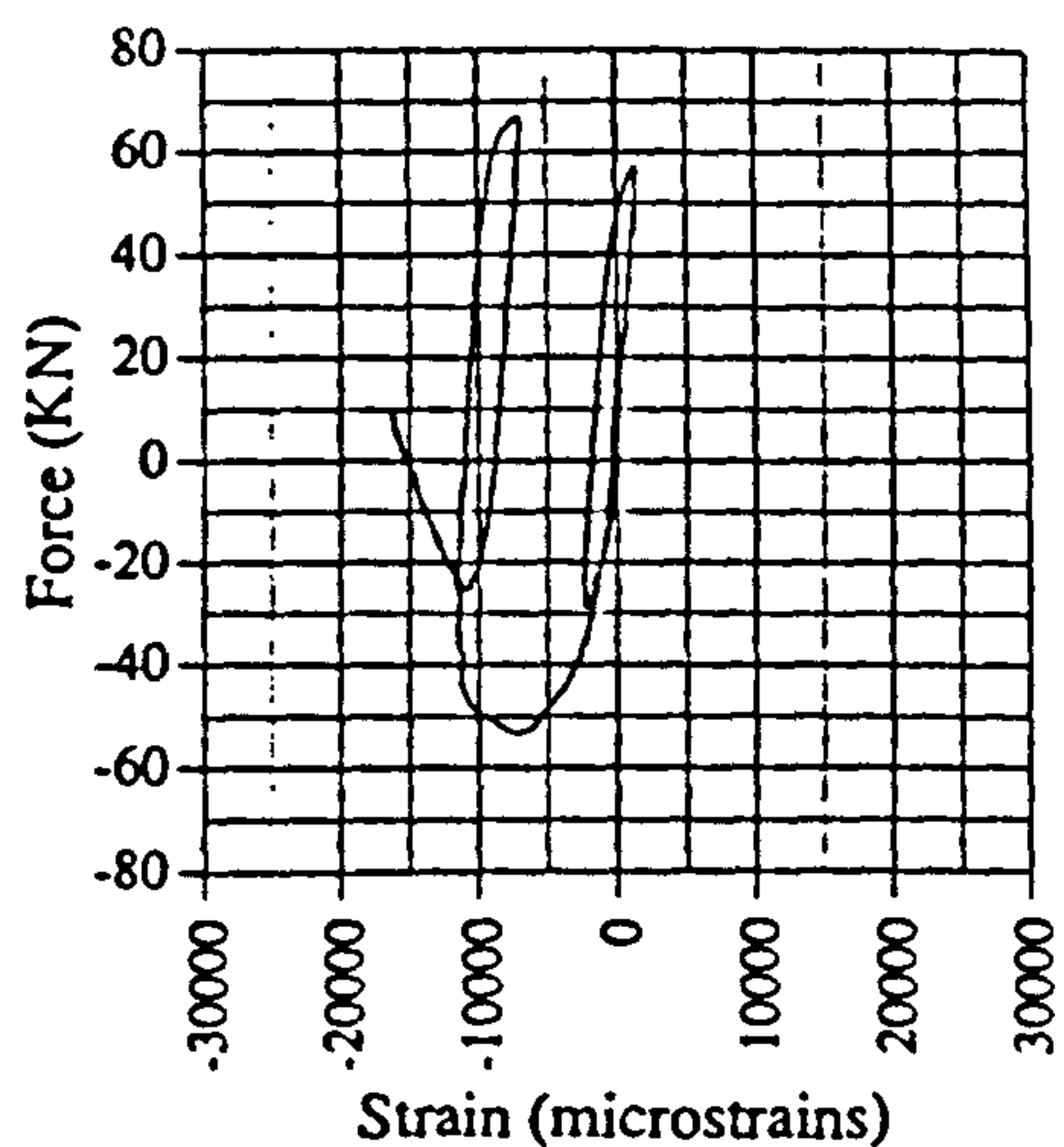


Fig. A.111 Strain vs displacement, EM03, G3

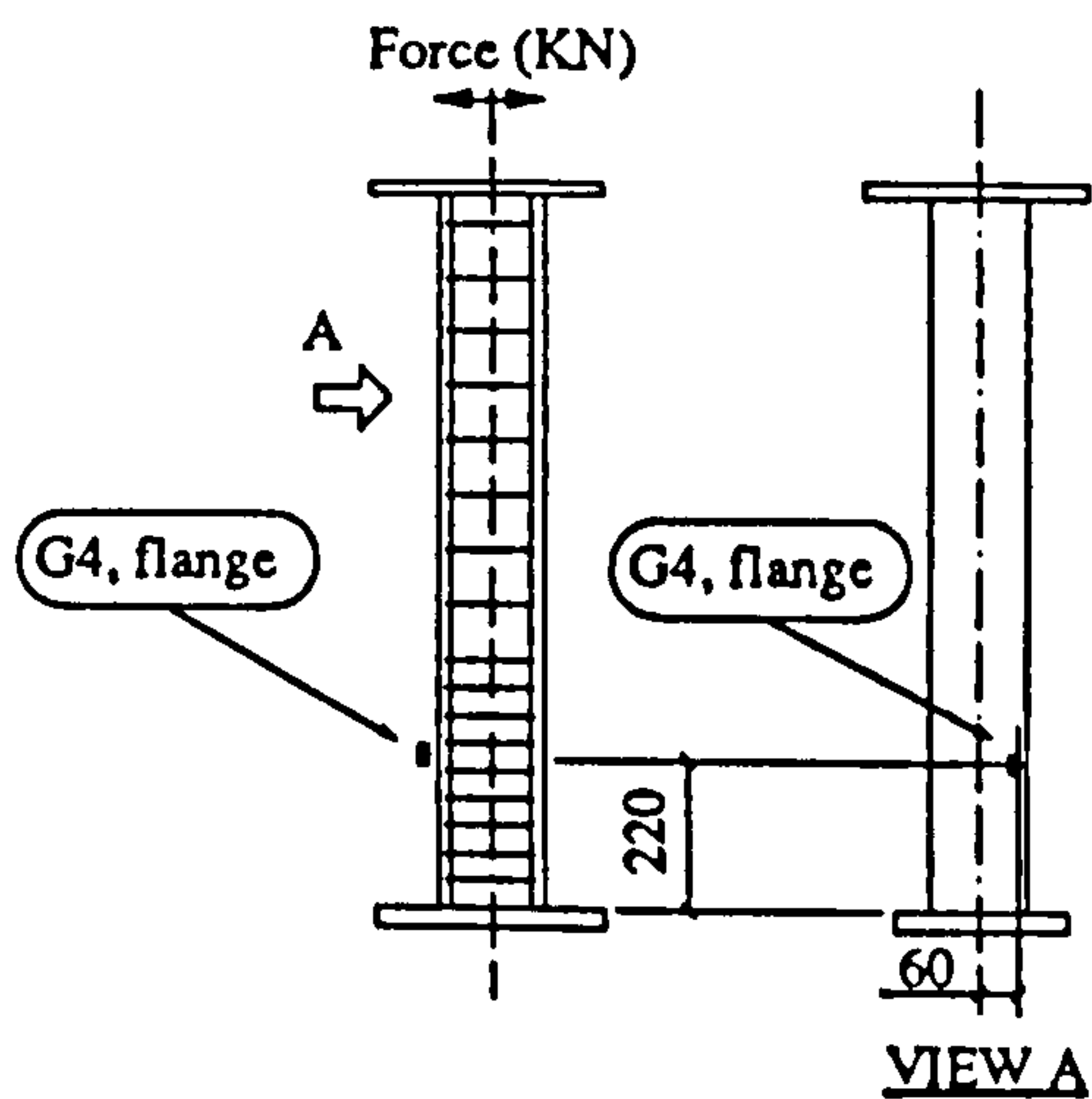
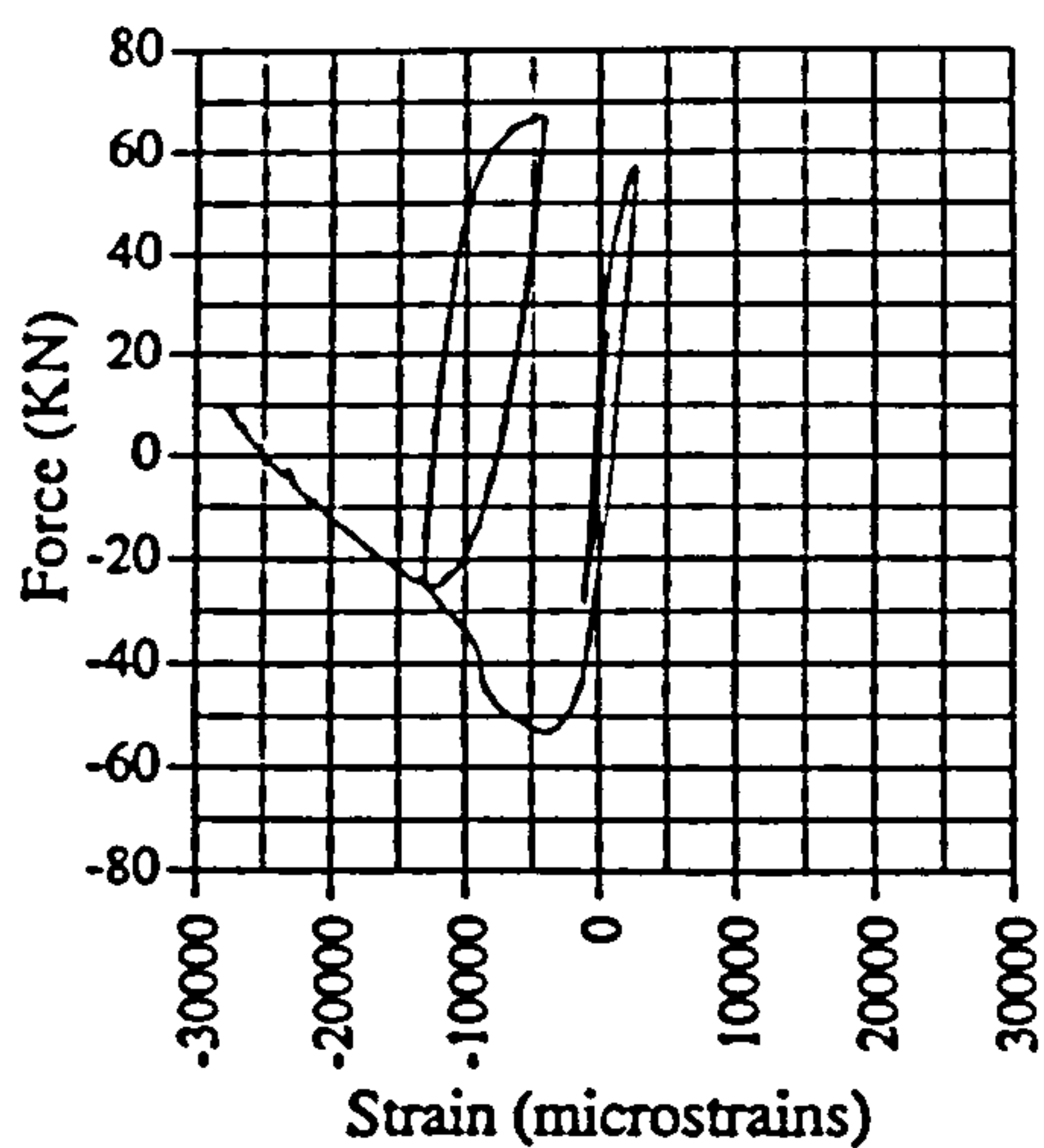


Fig. A.112 Force vs strain, EM03, G4

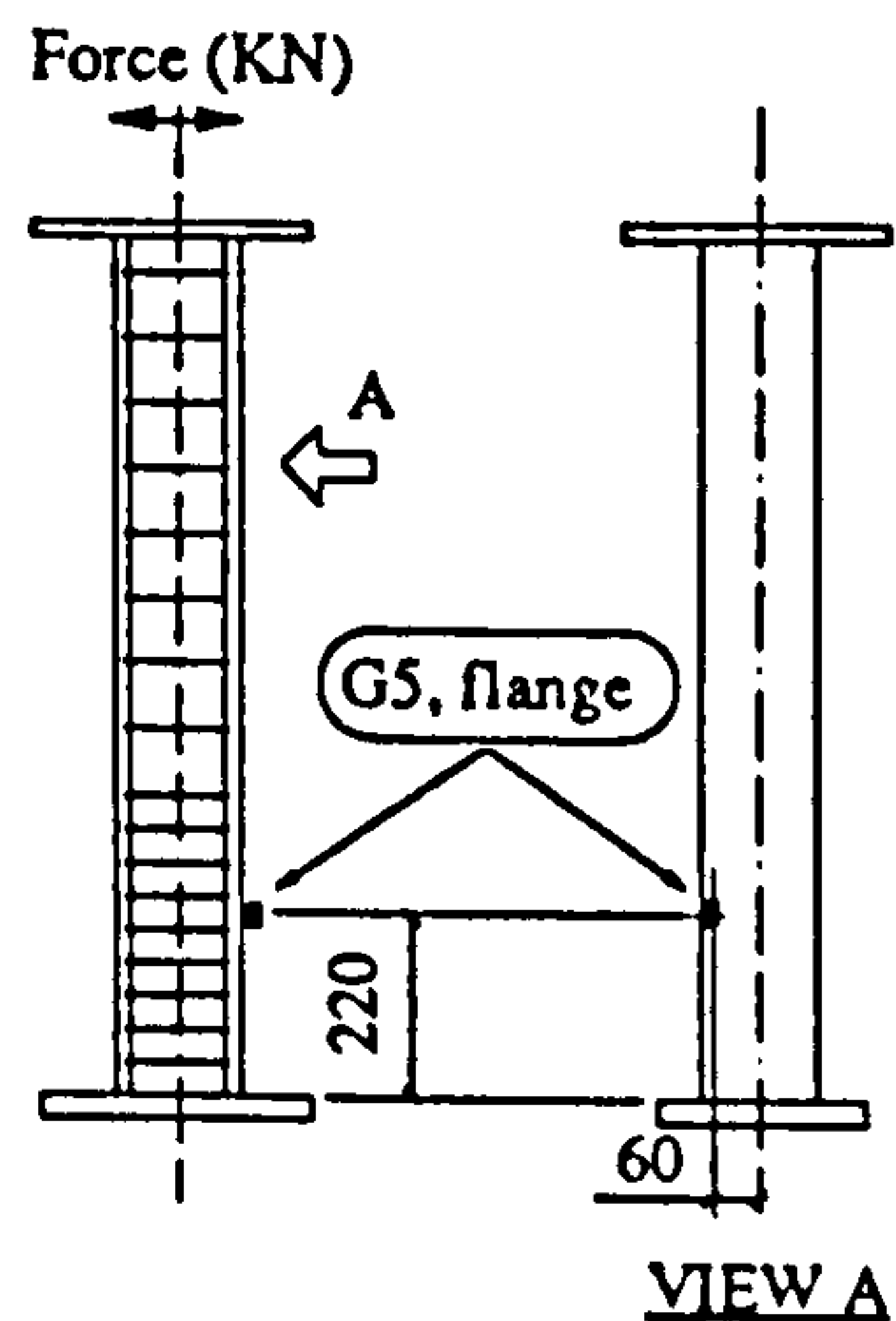
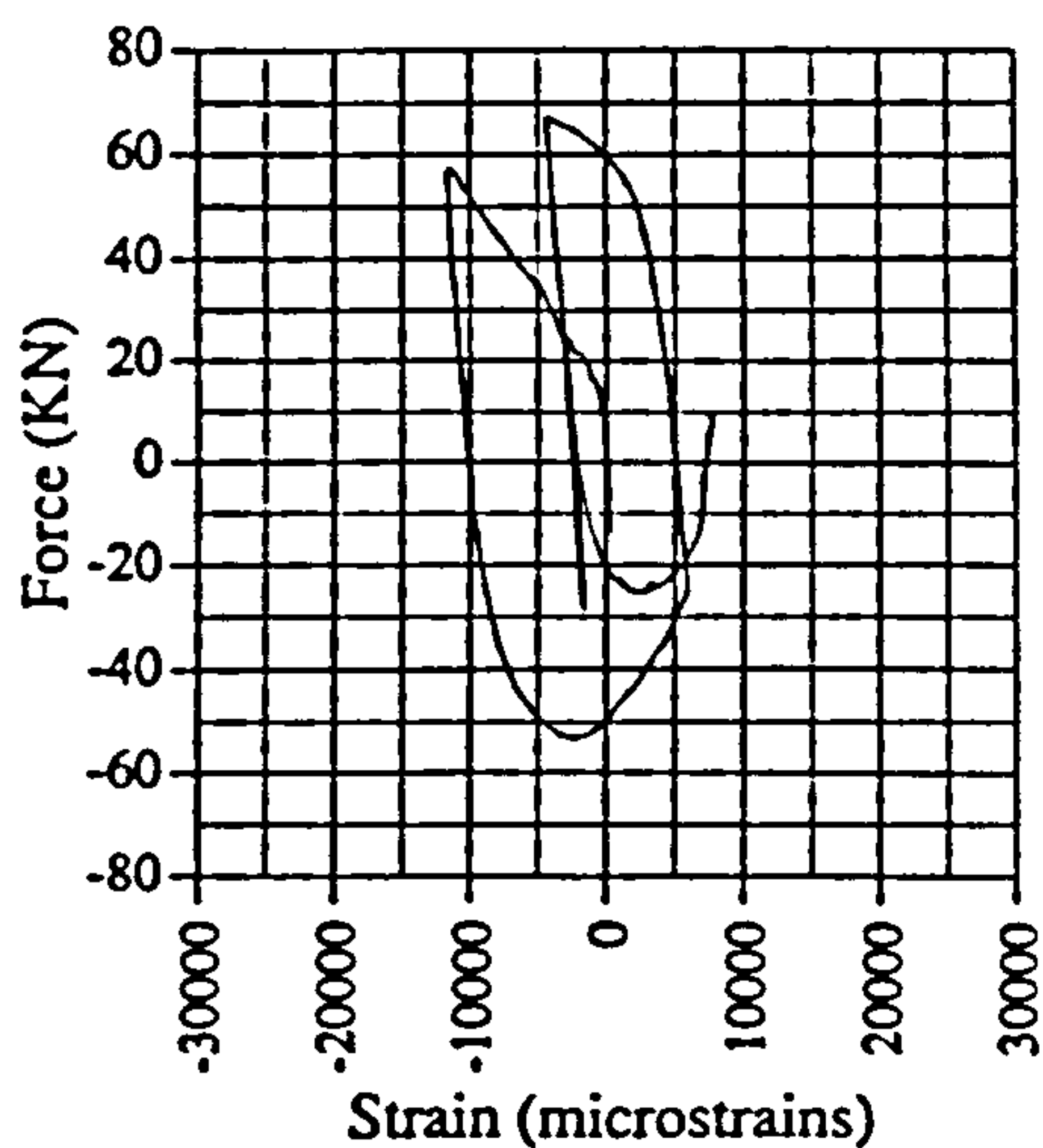


Fig. A.113 Force vs strain, EM03, G5

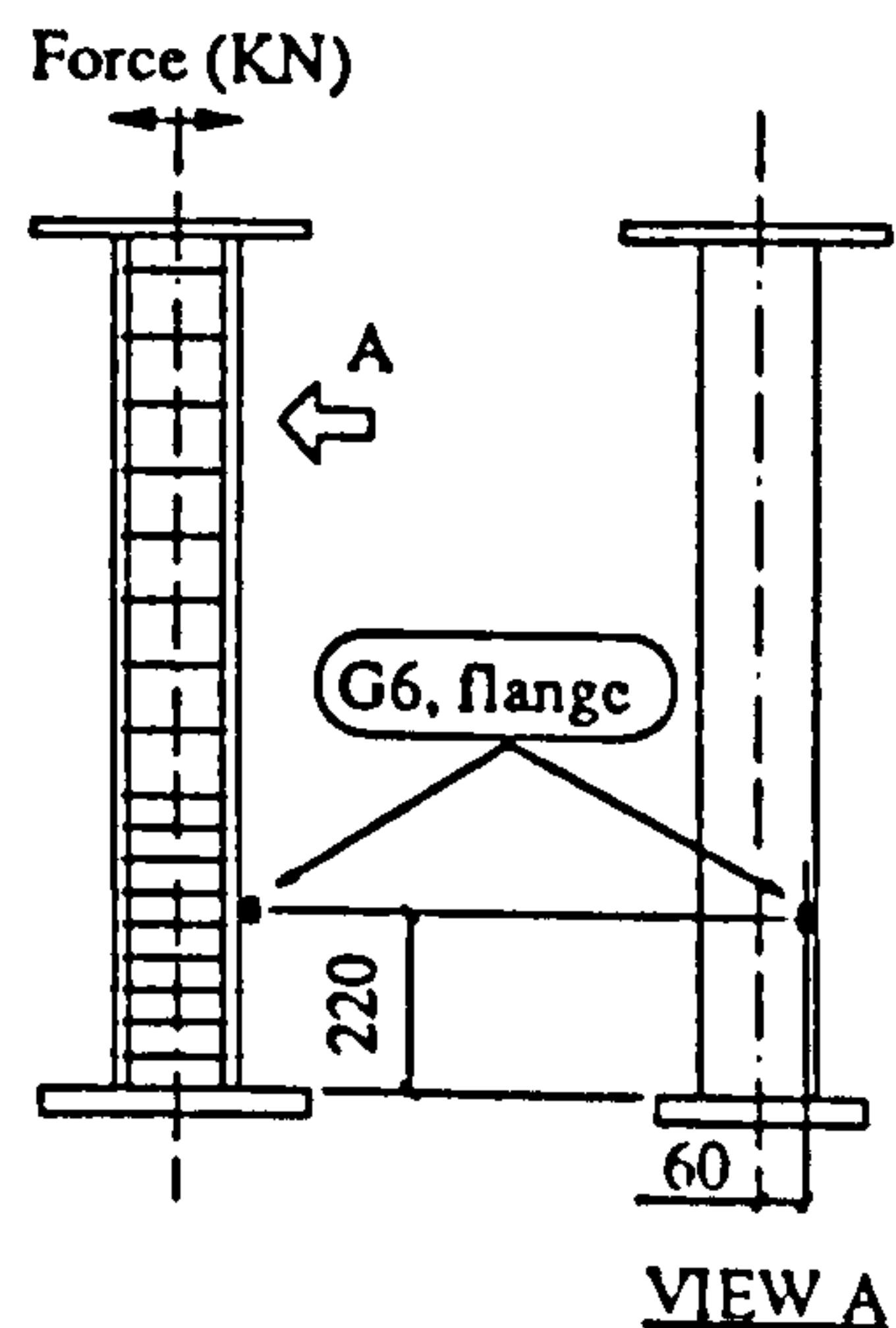
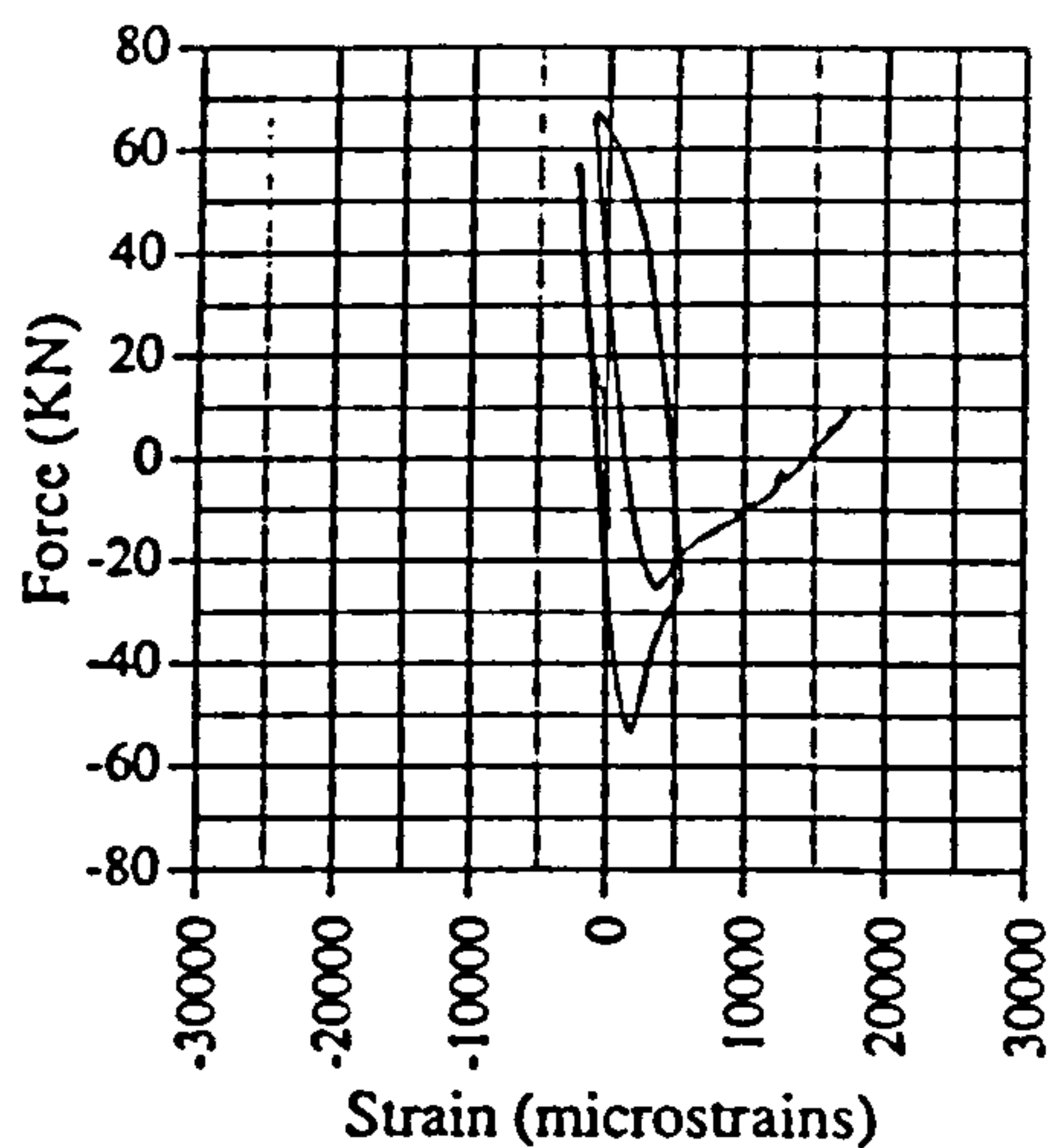


Fig. A.114 Force vs strain, EM03, G6

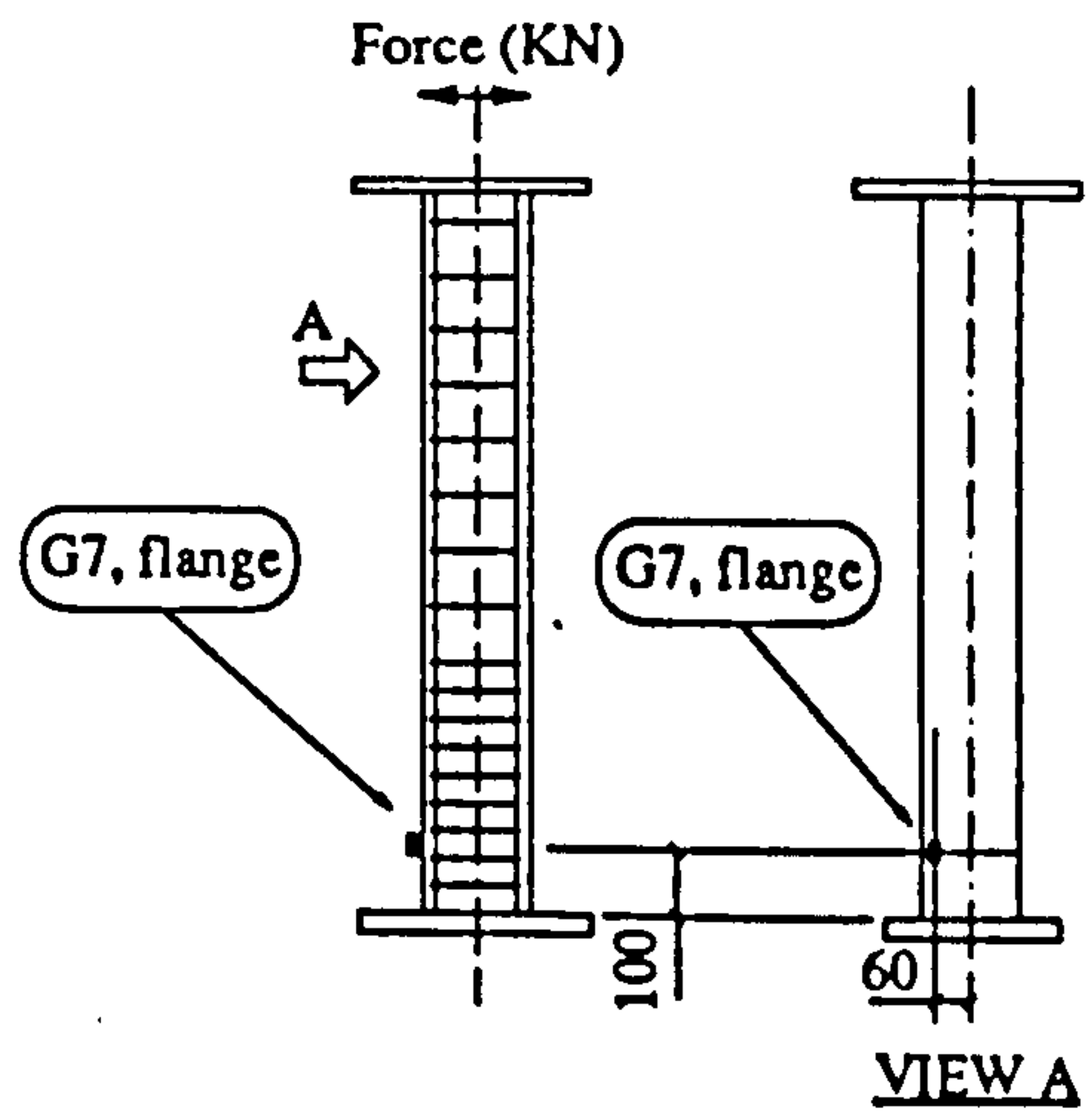
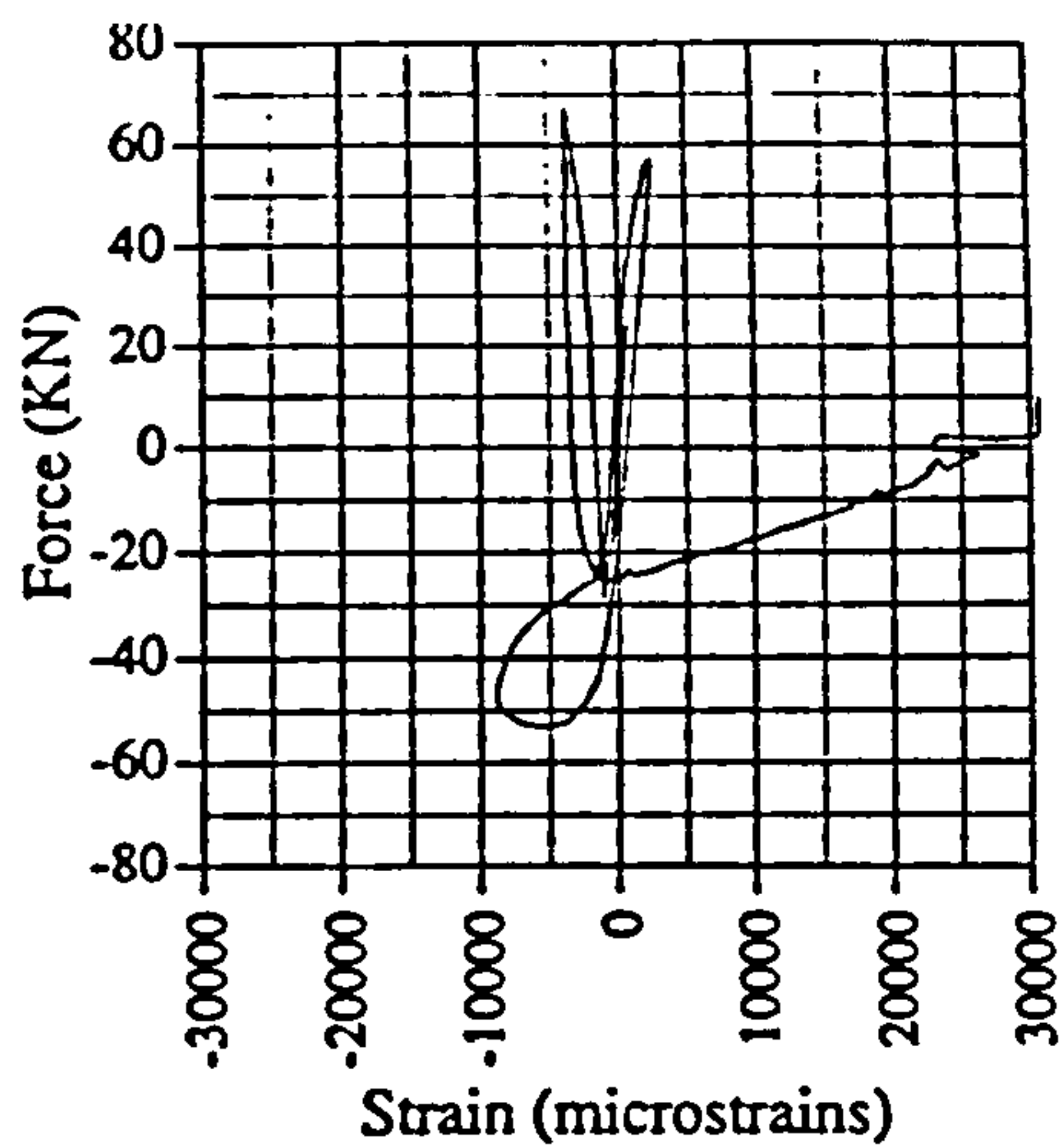


Fig. A.115 Force vs strain, EM03, G7

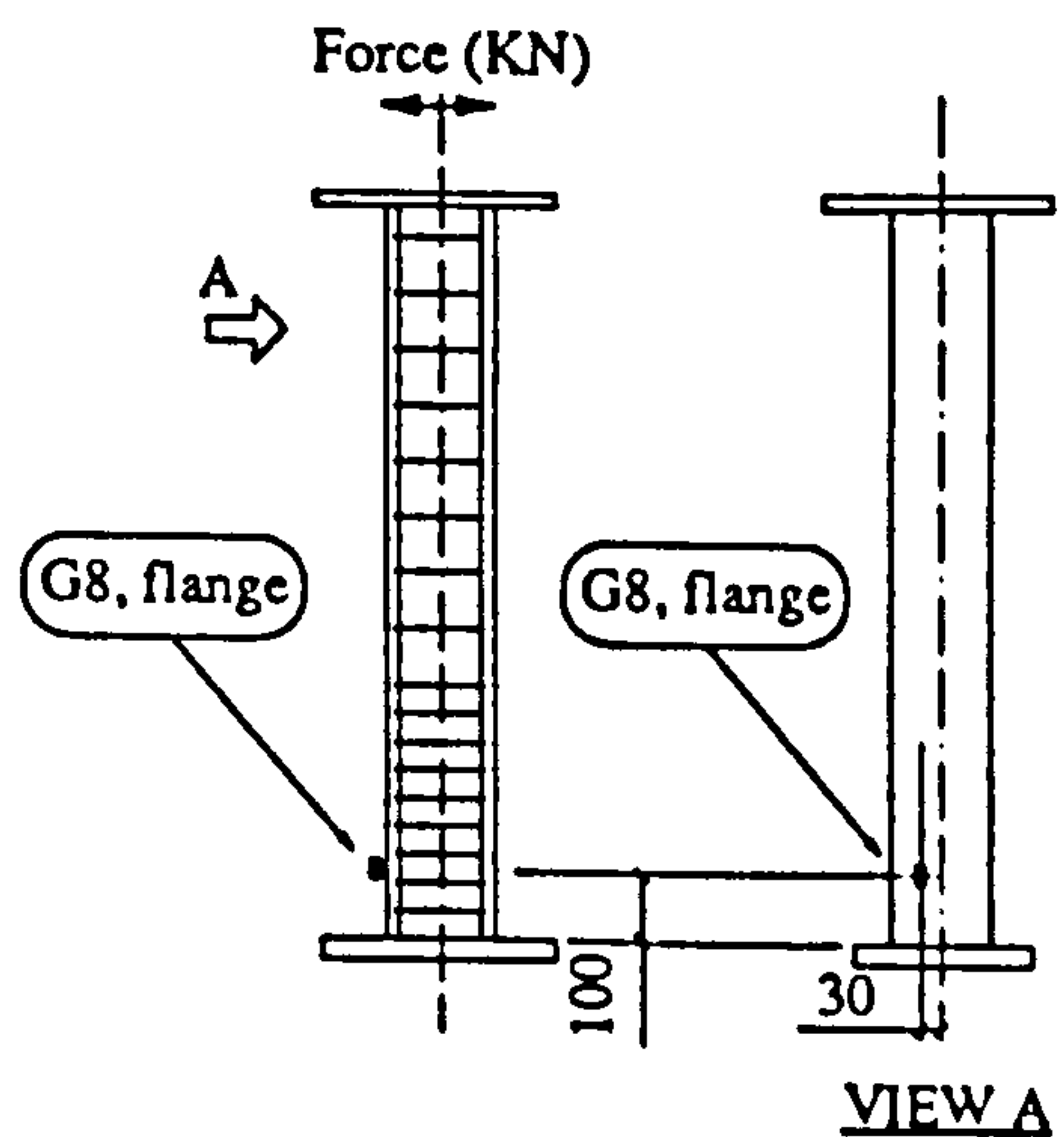
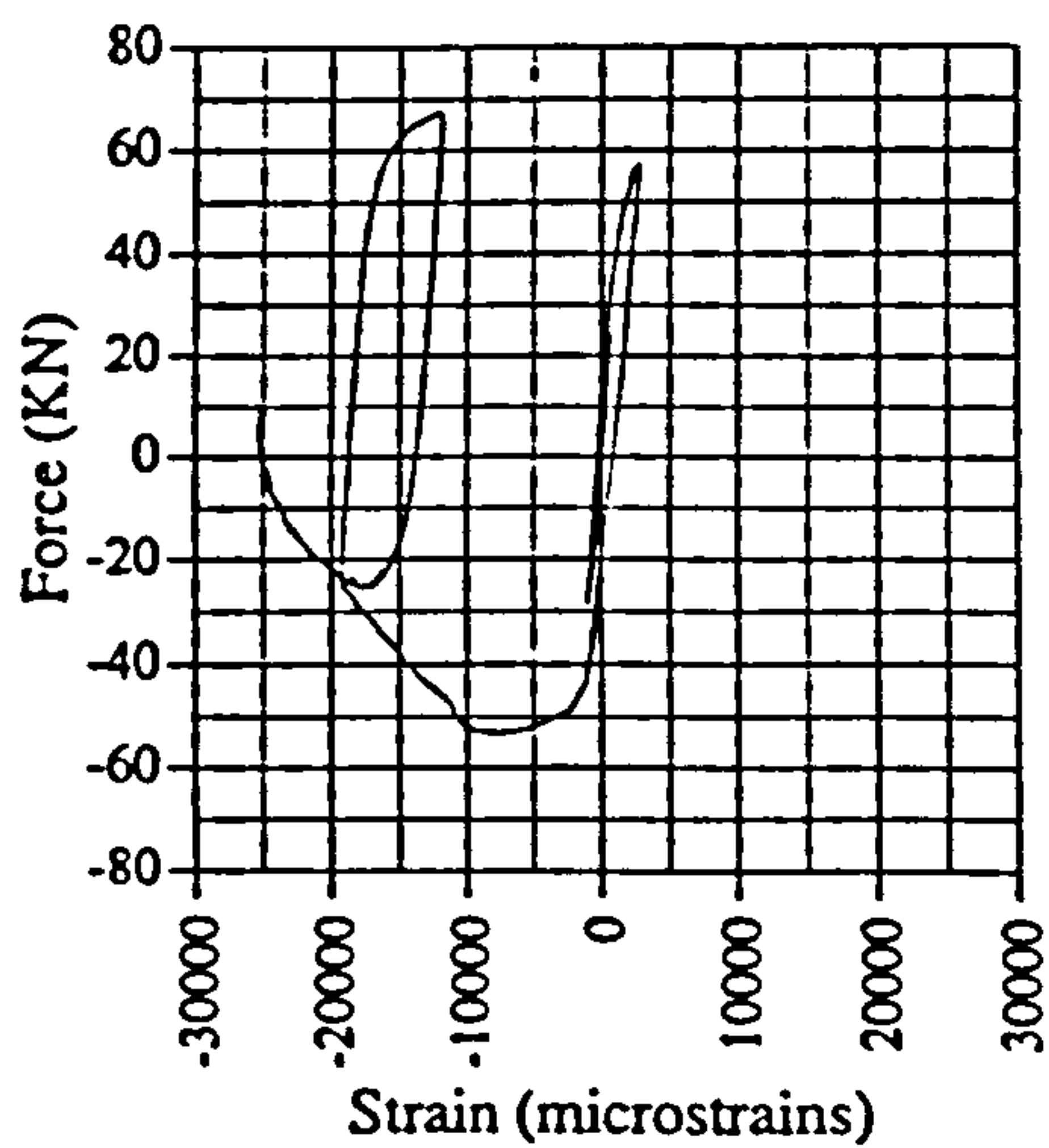


Fig. A.116 Force vs strain, EM03, G8

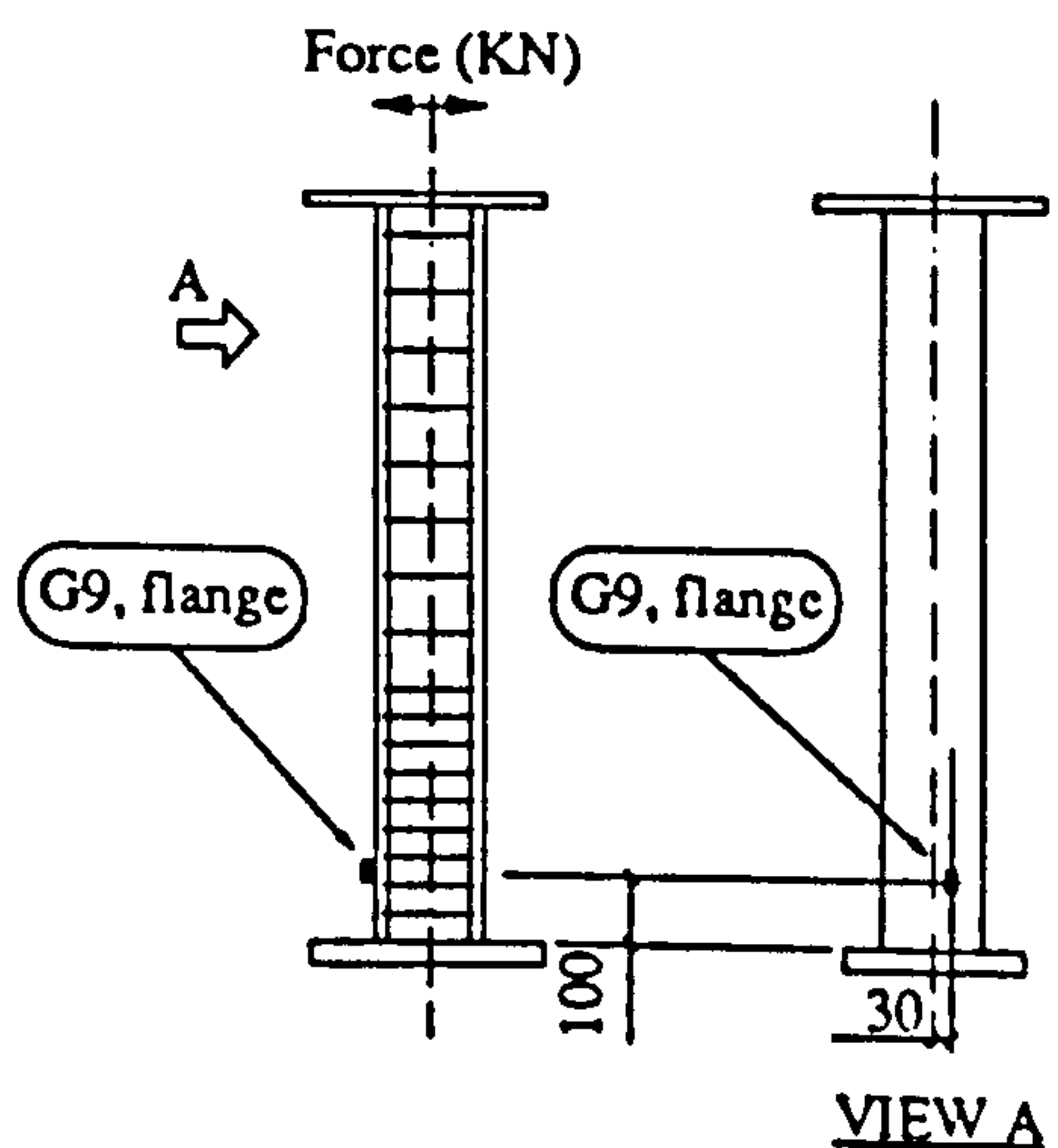
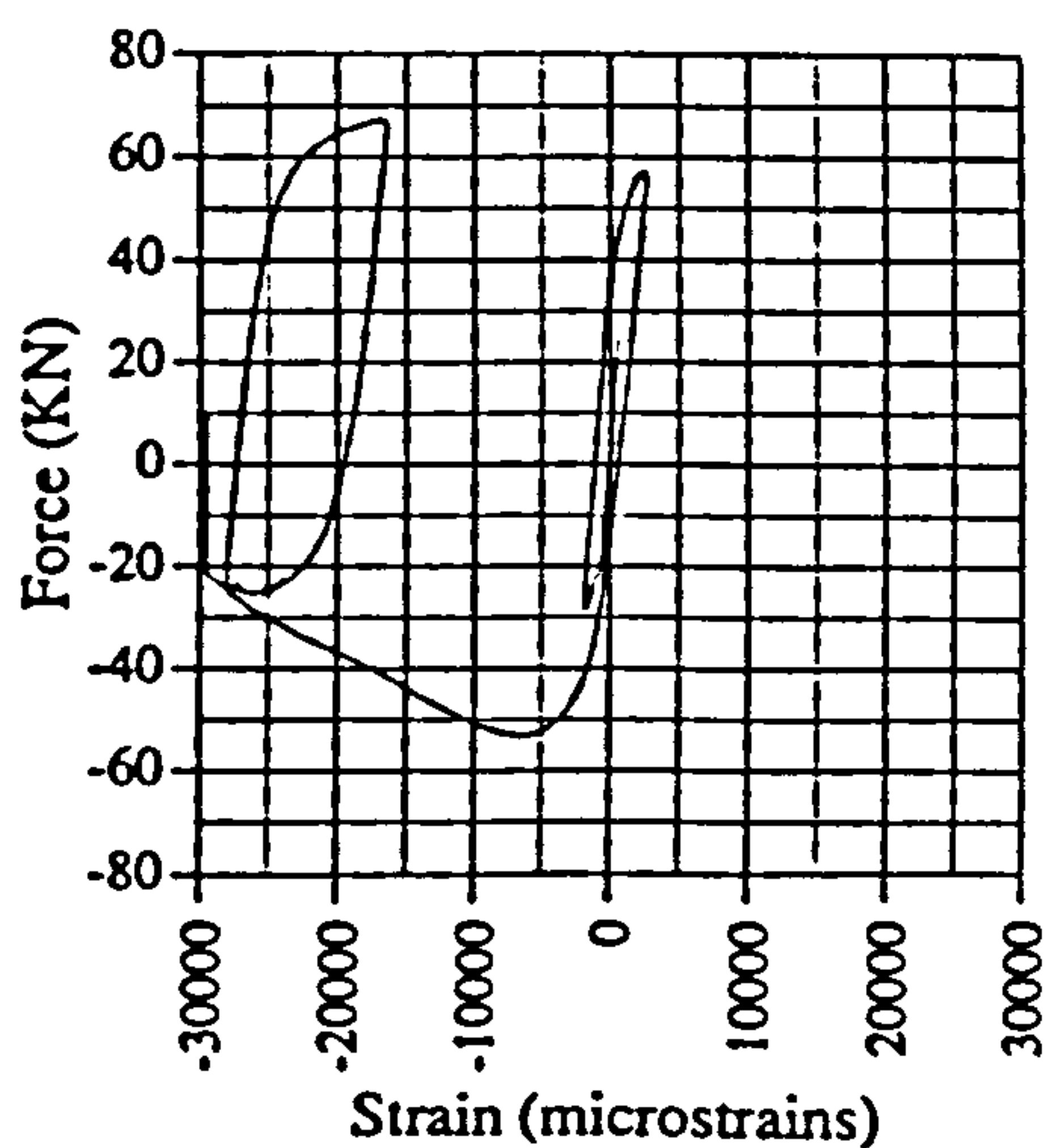


Fig. A.117 Force vs strain, EM03, G9

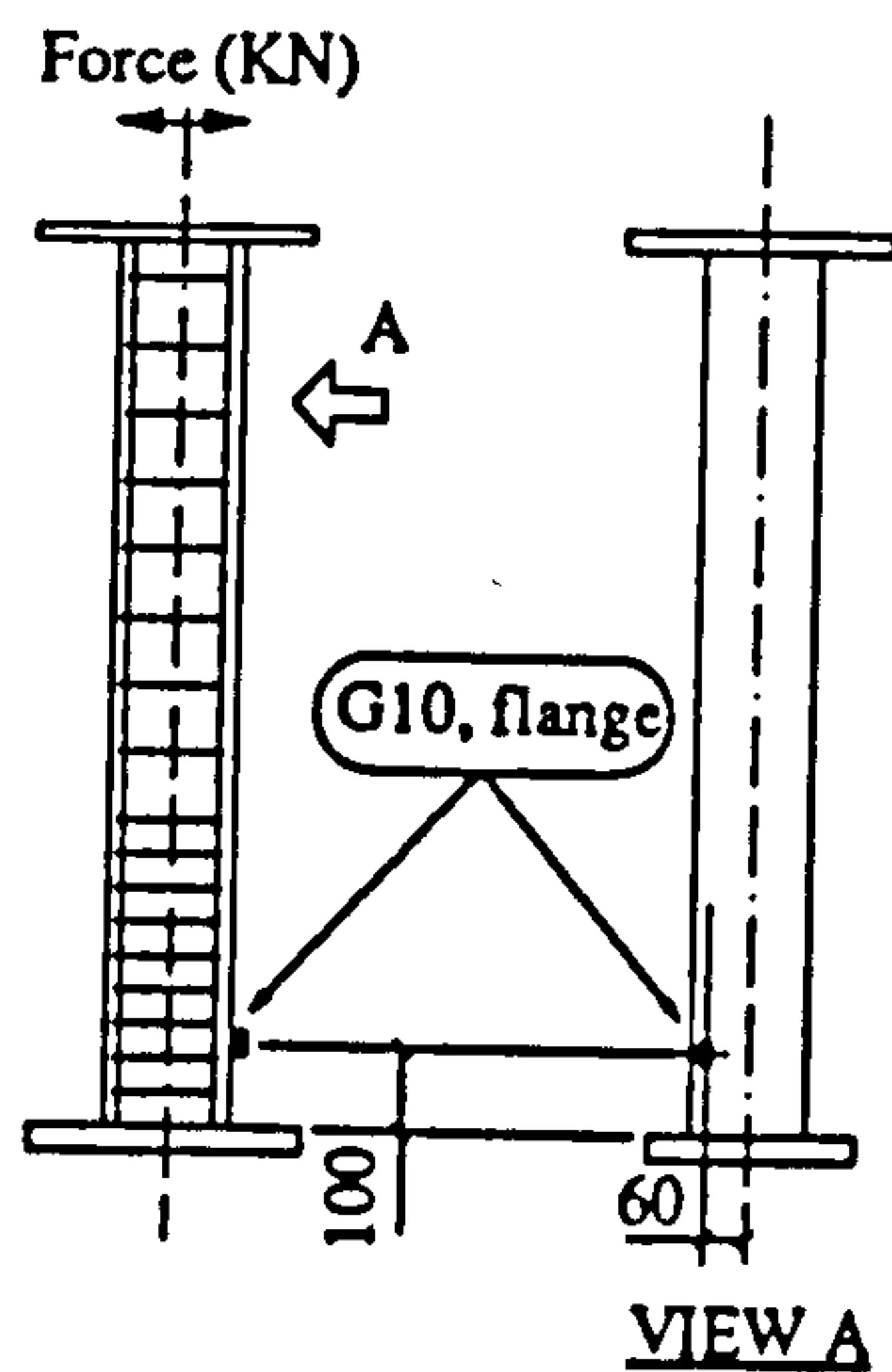
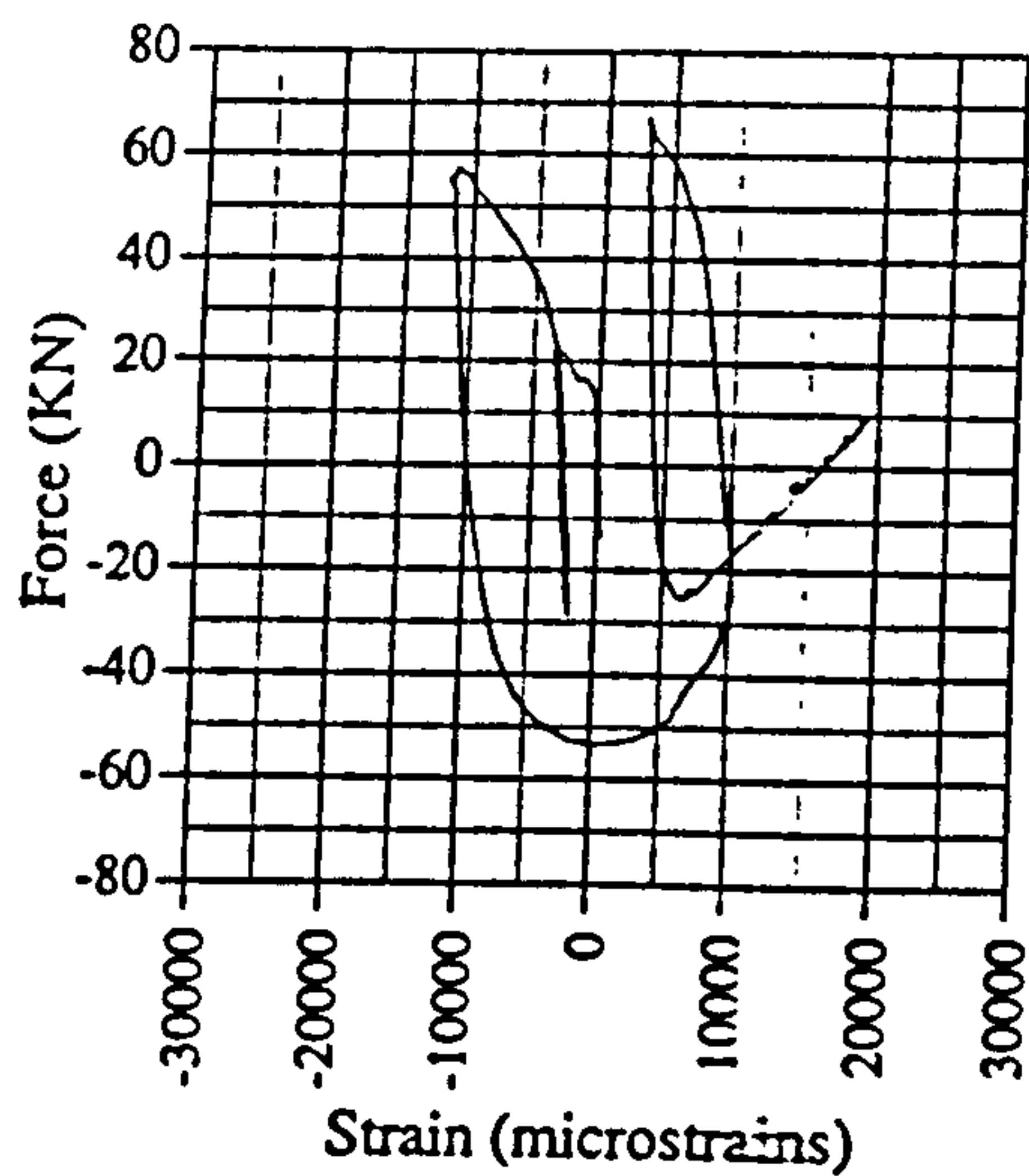


Fig. A.118 Force vs strain, EM03, G10

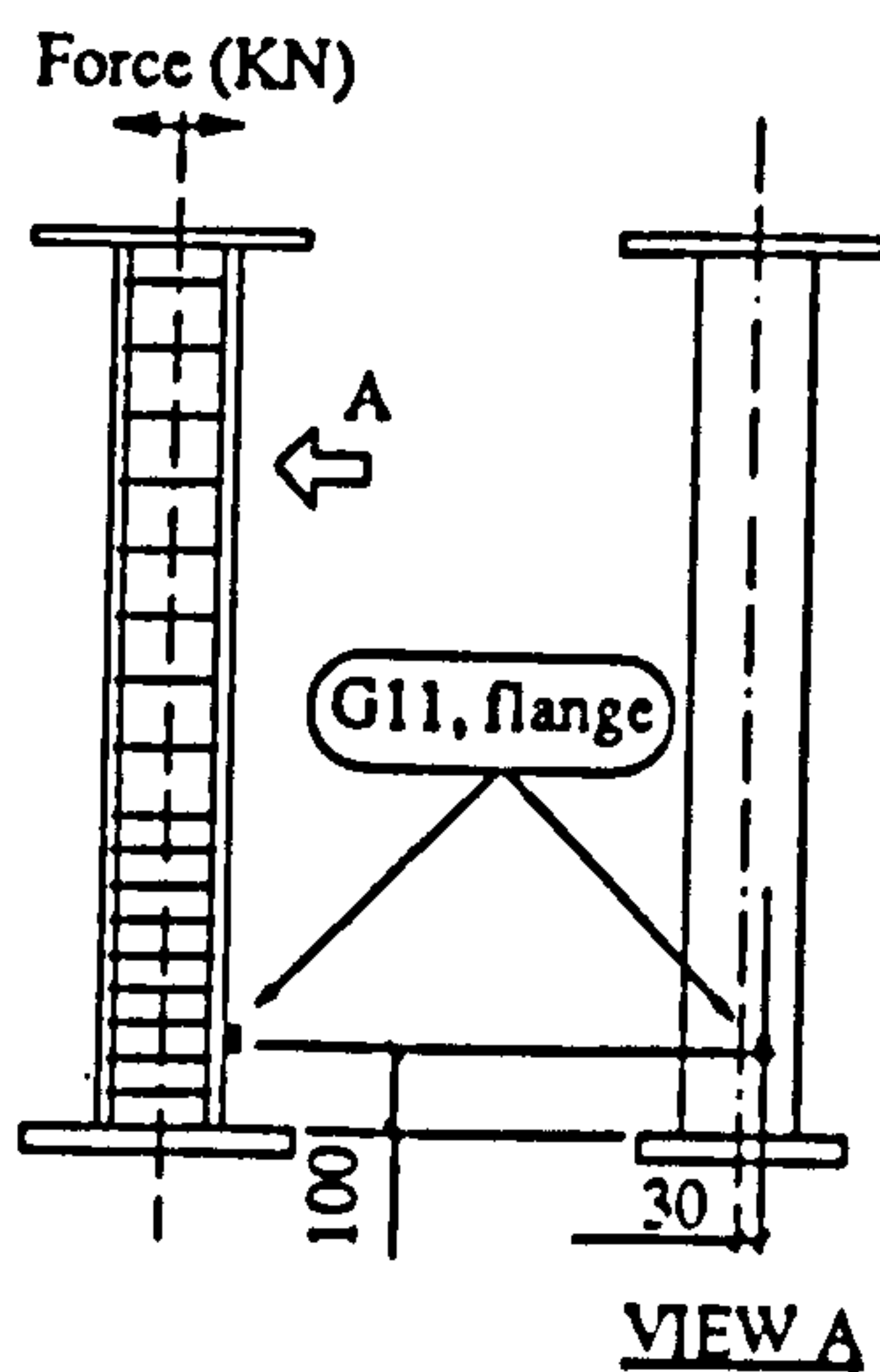
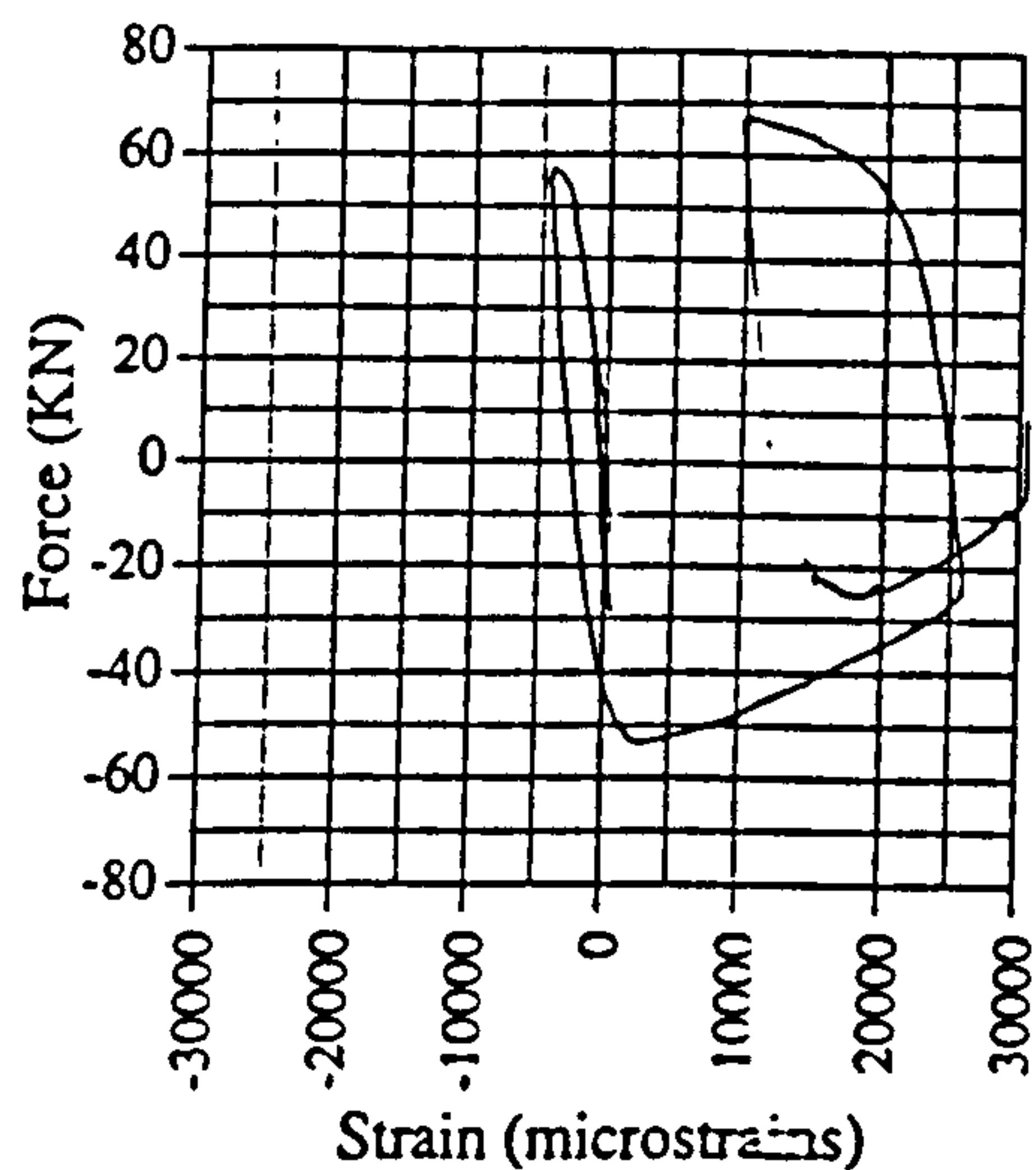


Fig. A.119 Force vs strain, EM03, G11

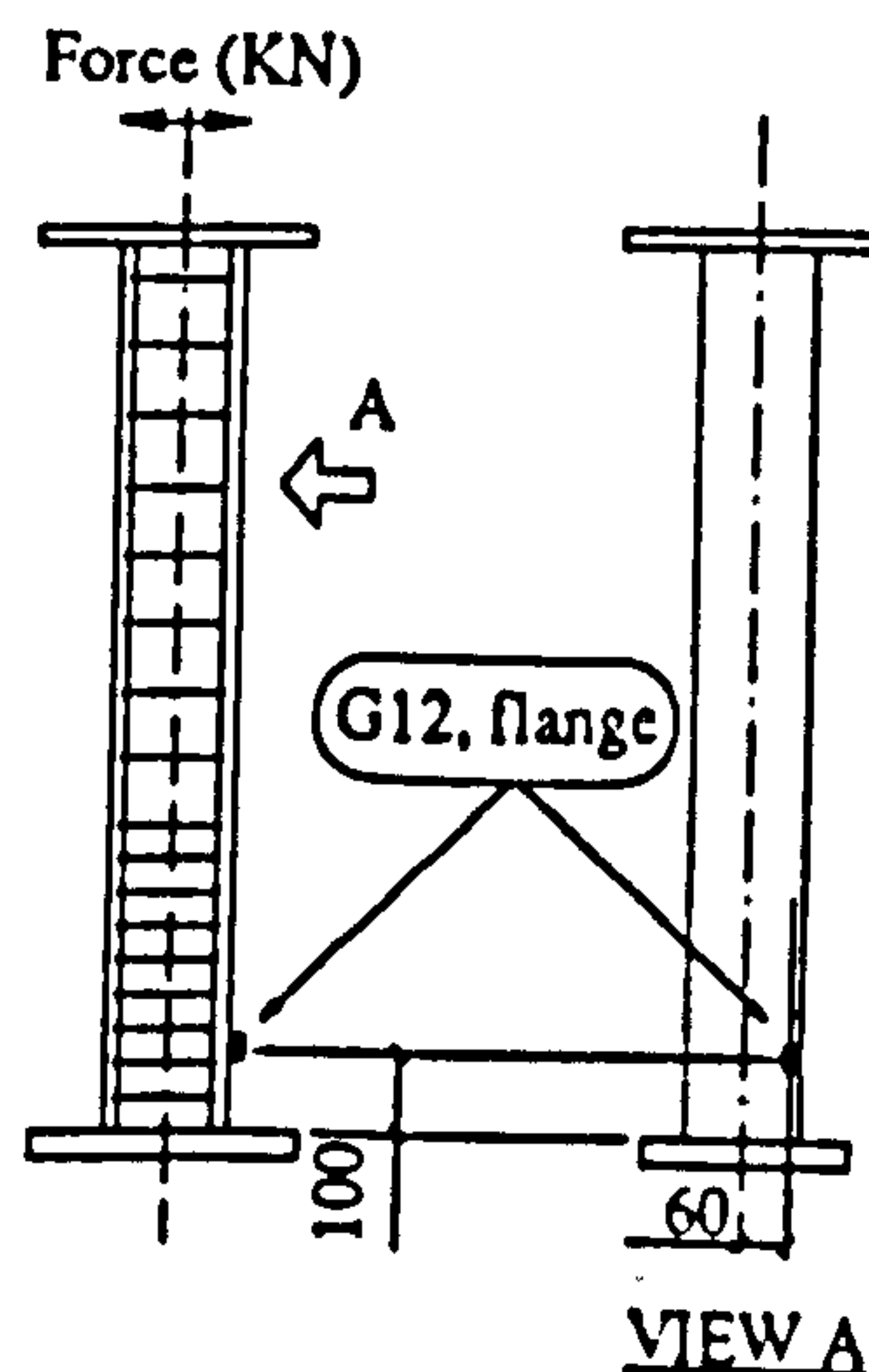
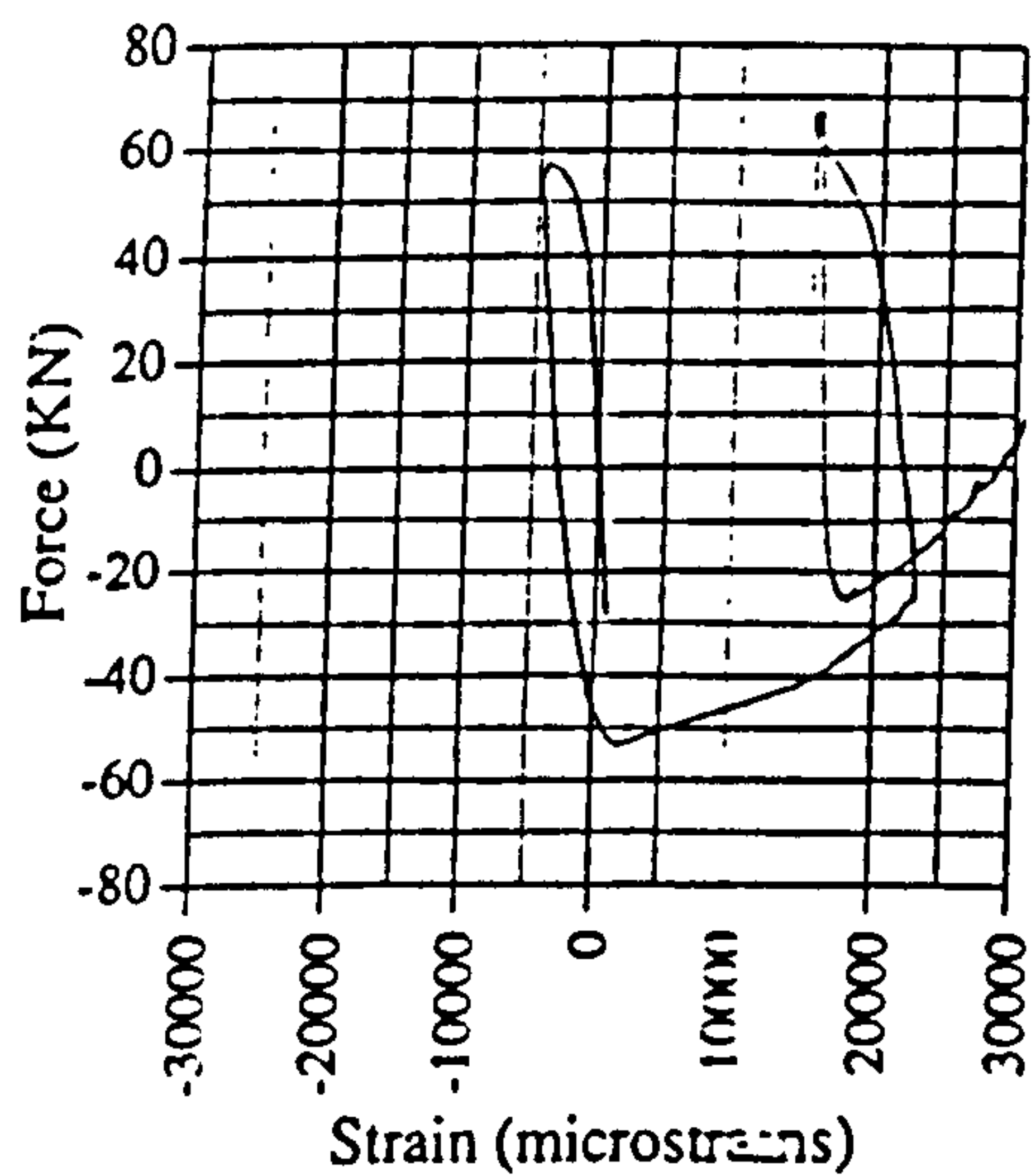


Fig. A.120 Force vs strain, EM03, G12

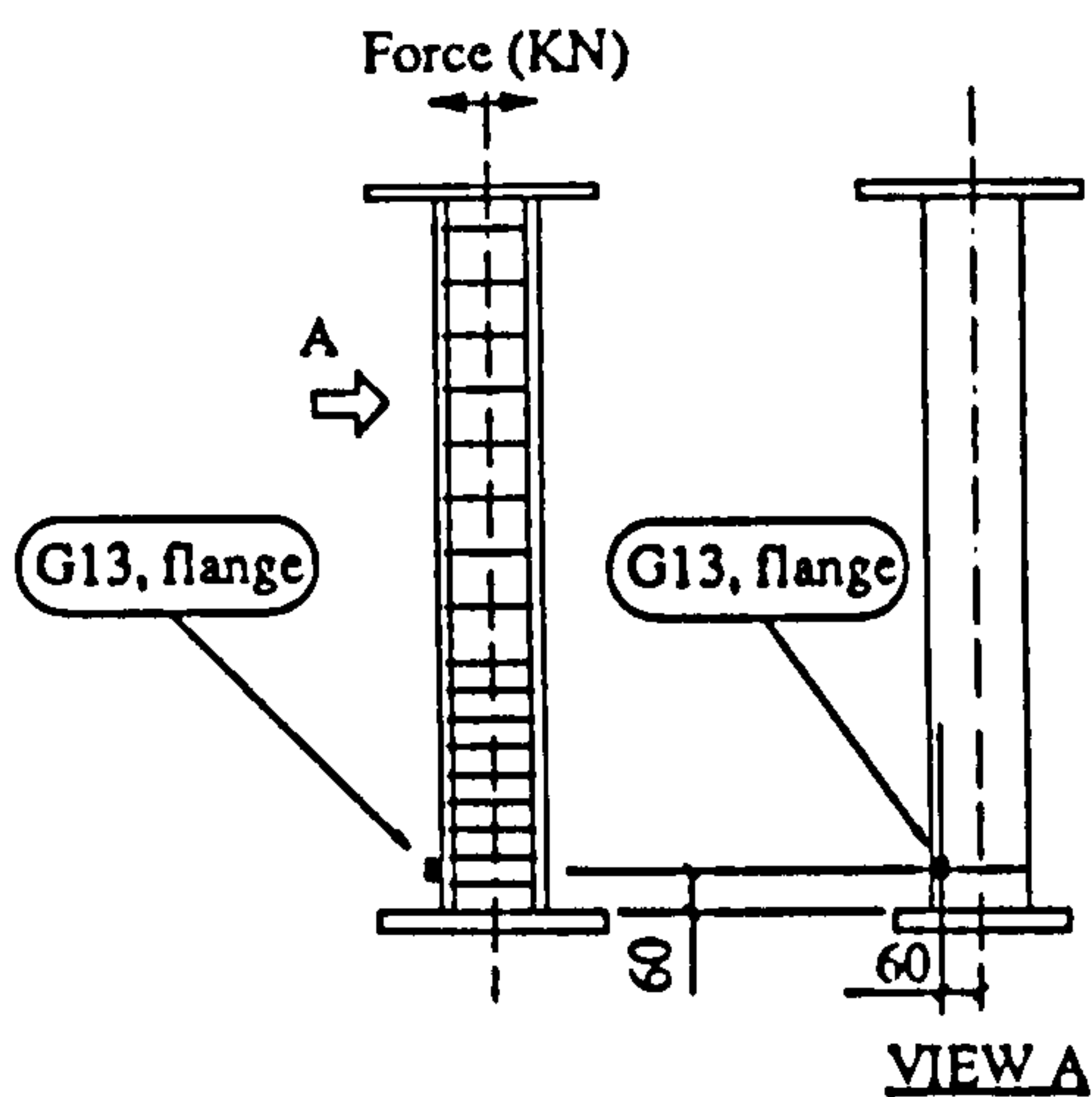
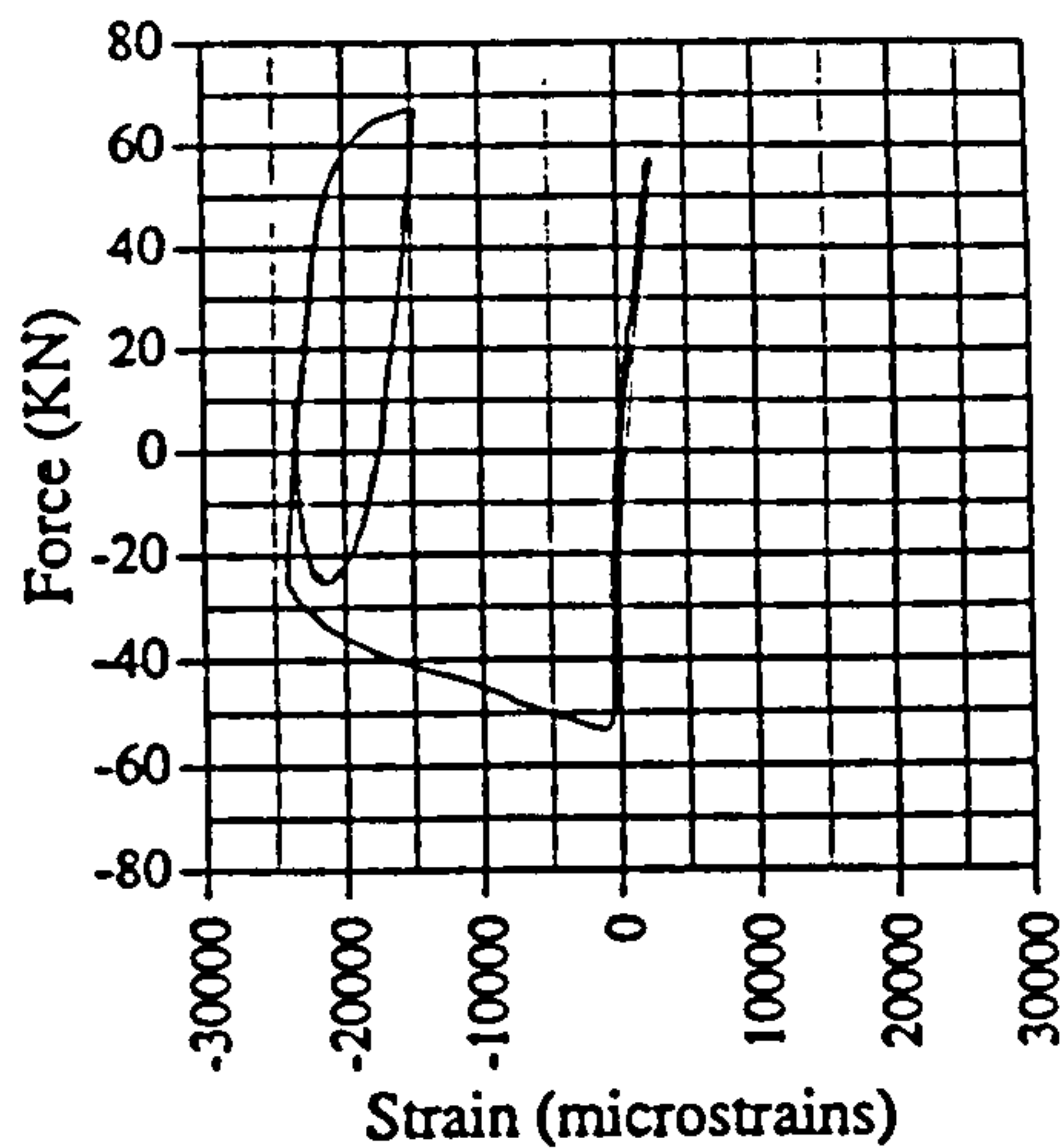


Fig. A.121 Force vs strain, EM03, G13

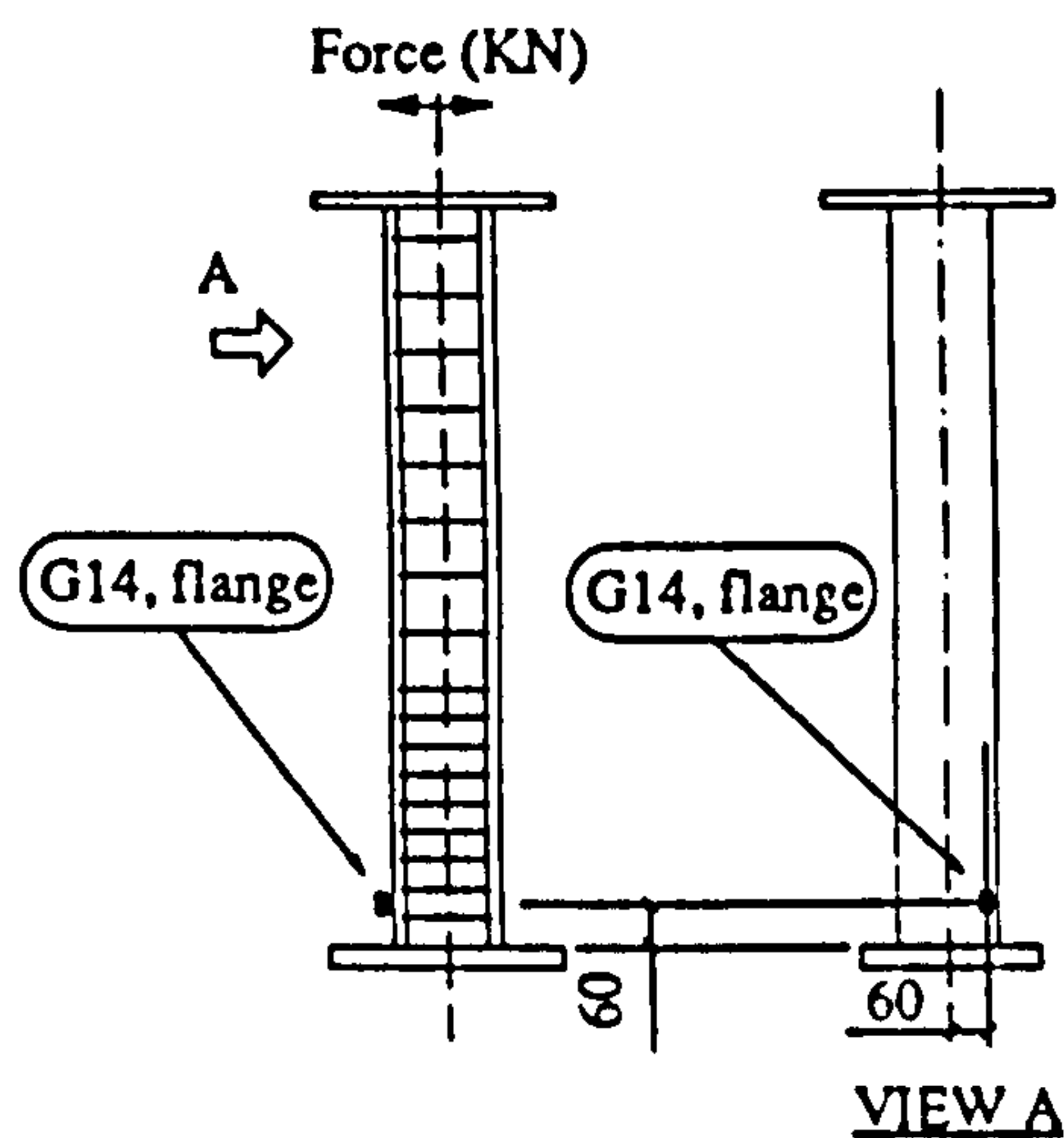
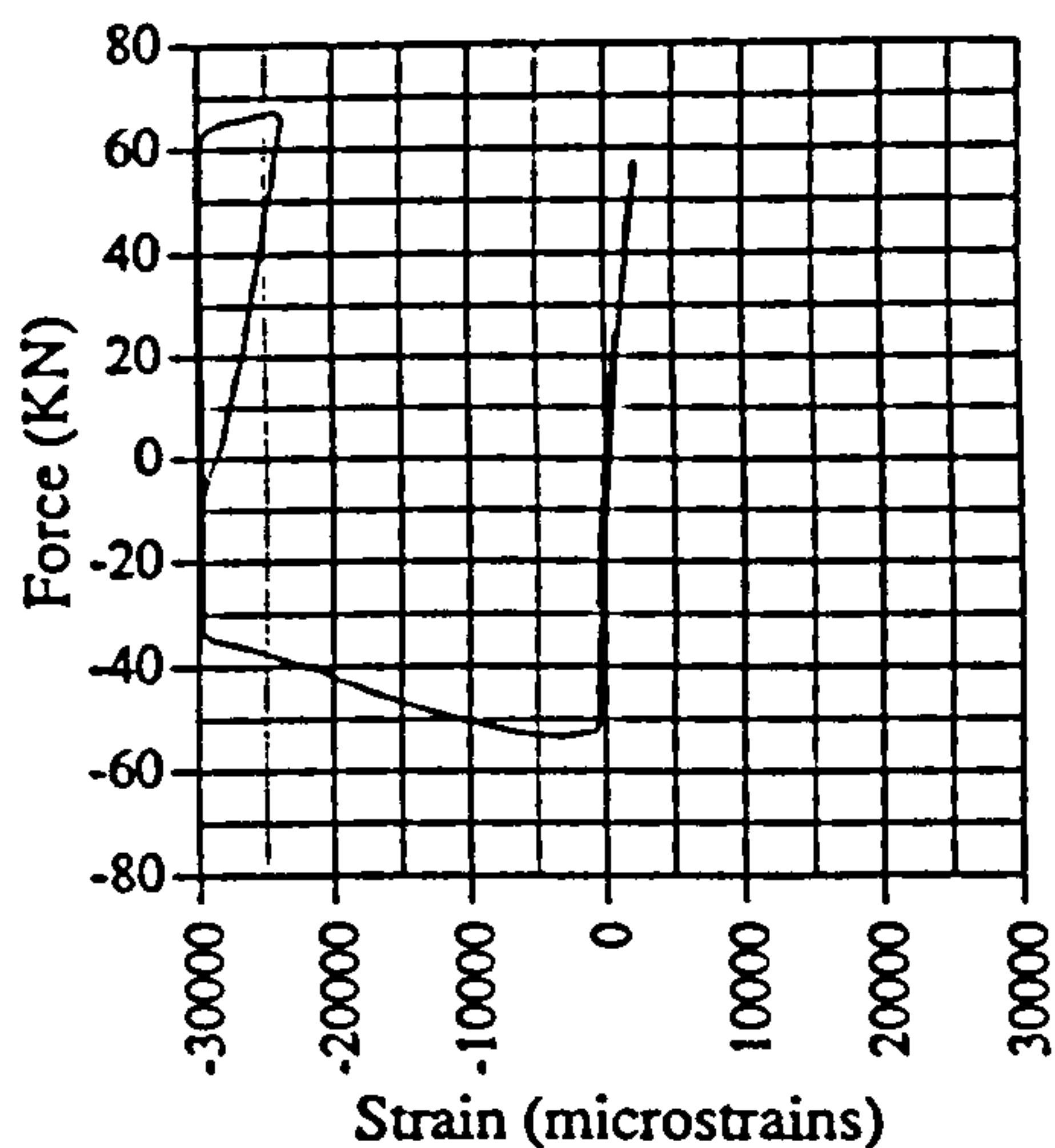


Fig. A.122 Force vs strain, EM03, G14

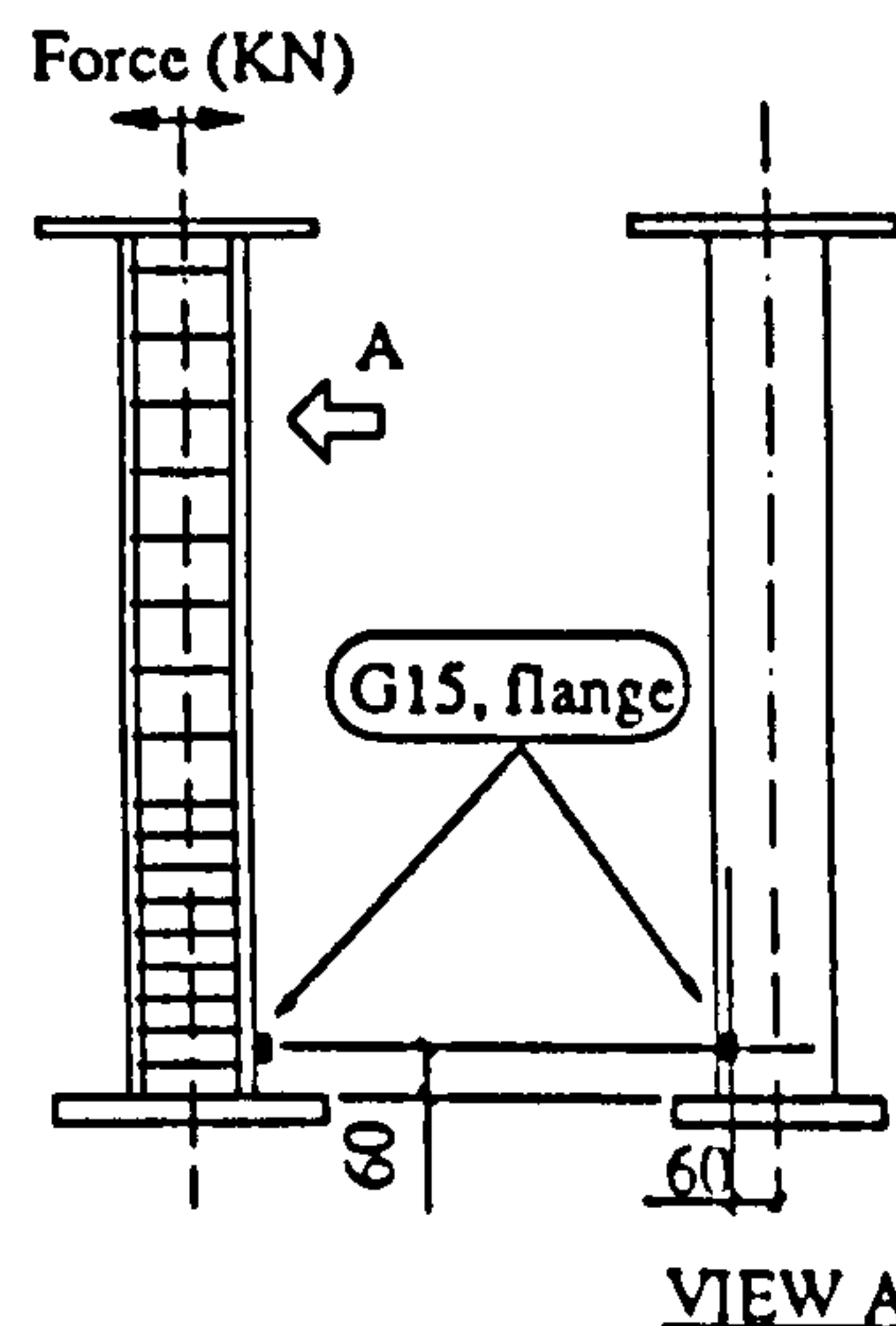
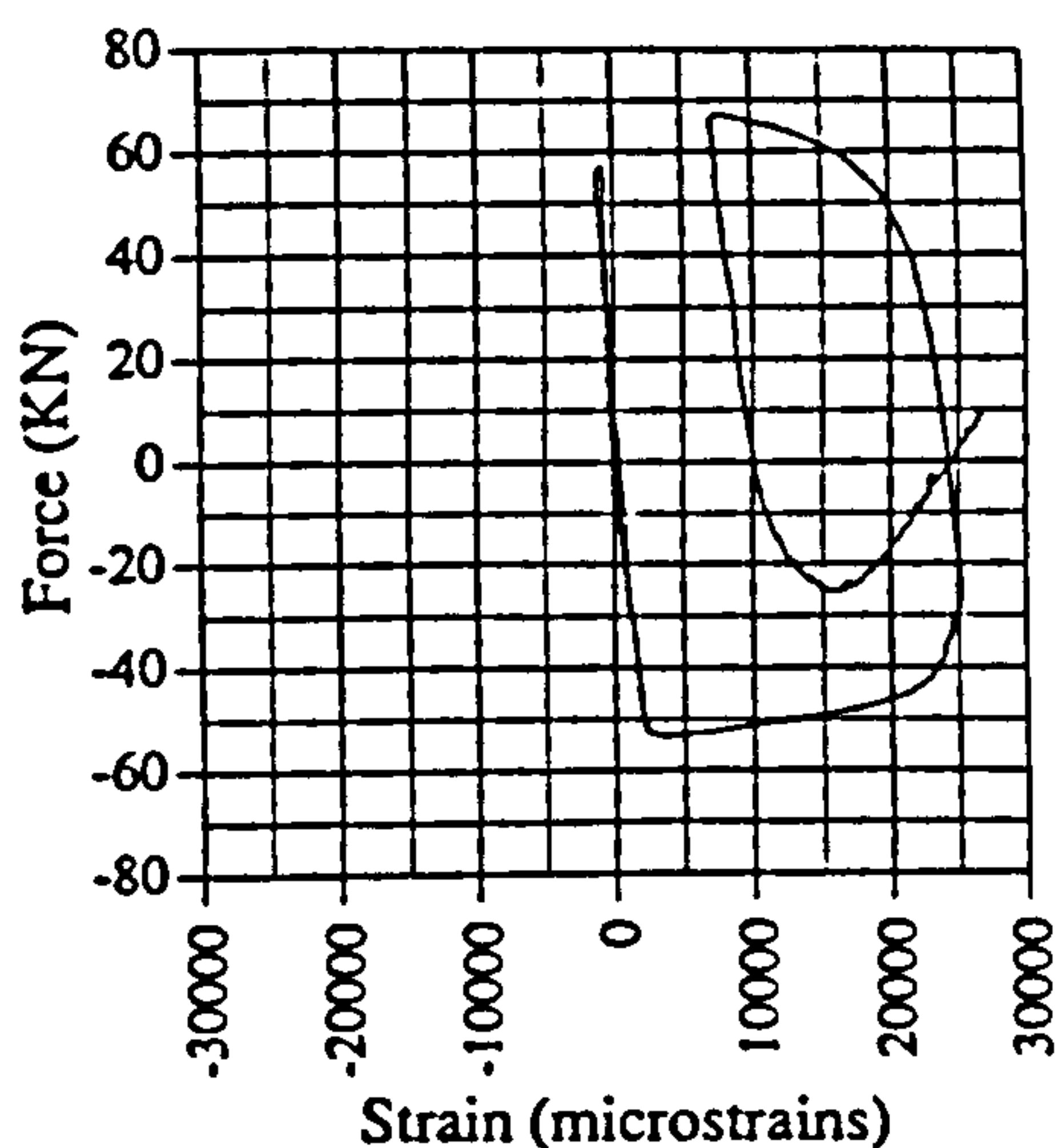


Fig. A.123 Force vs strain, EM03, G15

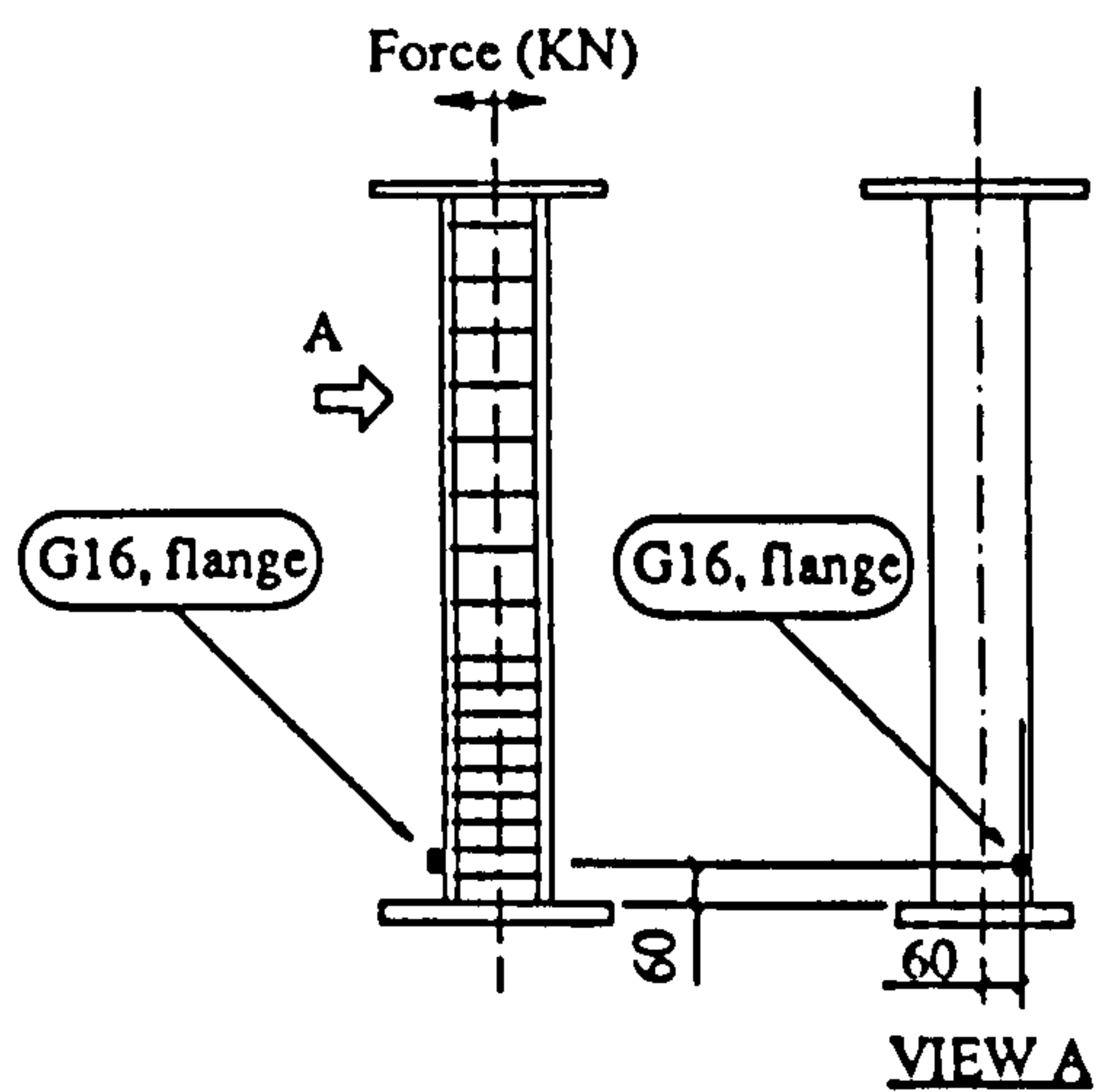
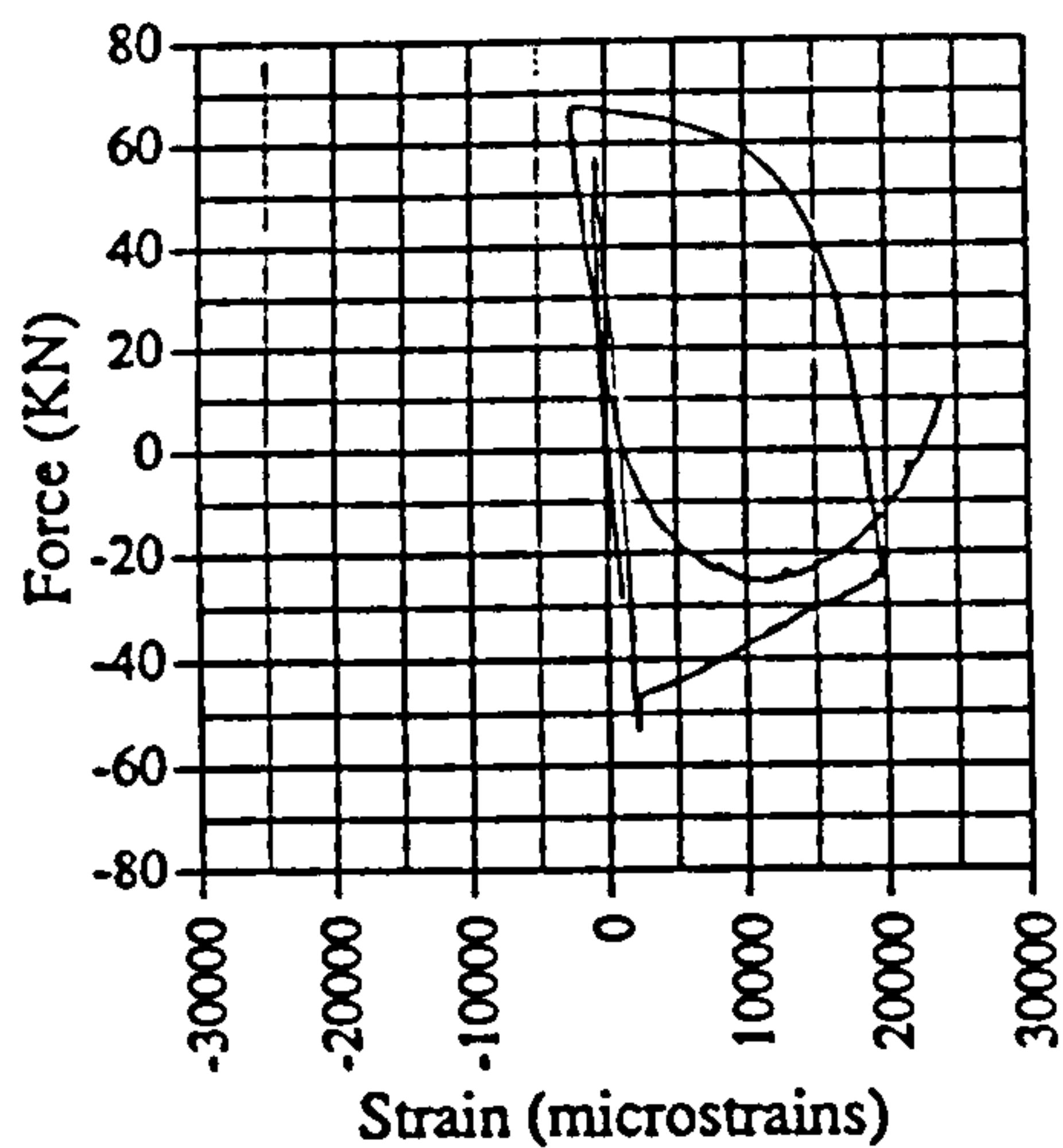


Fig. A.124 Force vs strain, EM03, G16

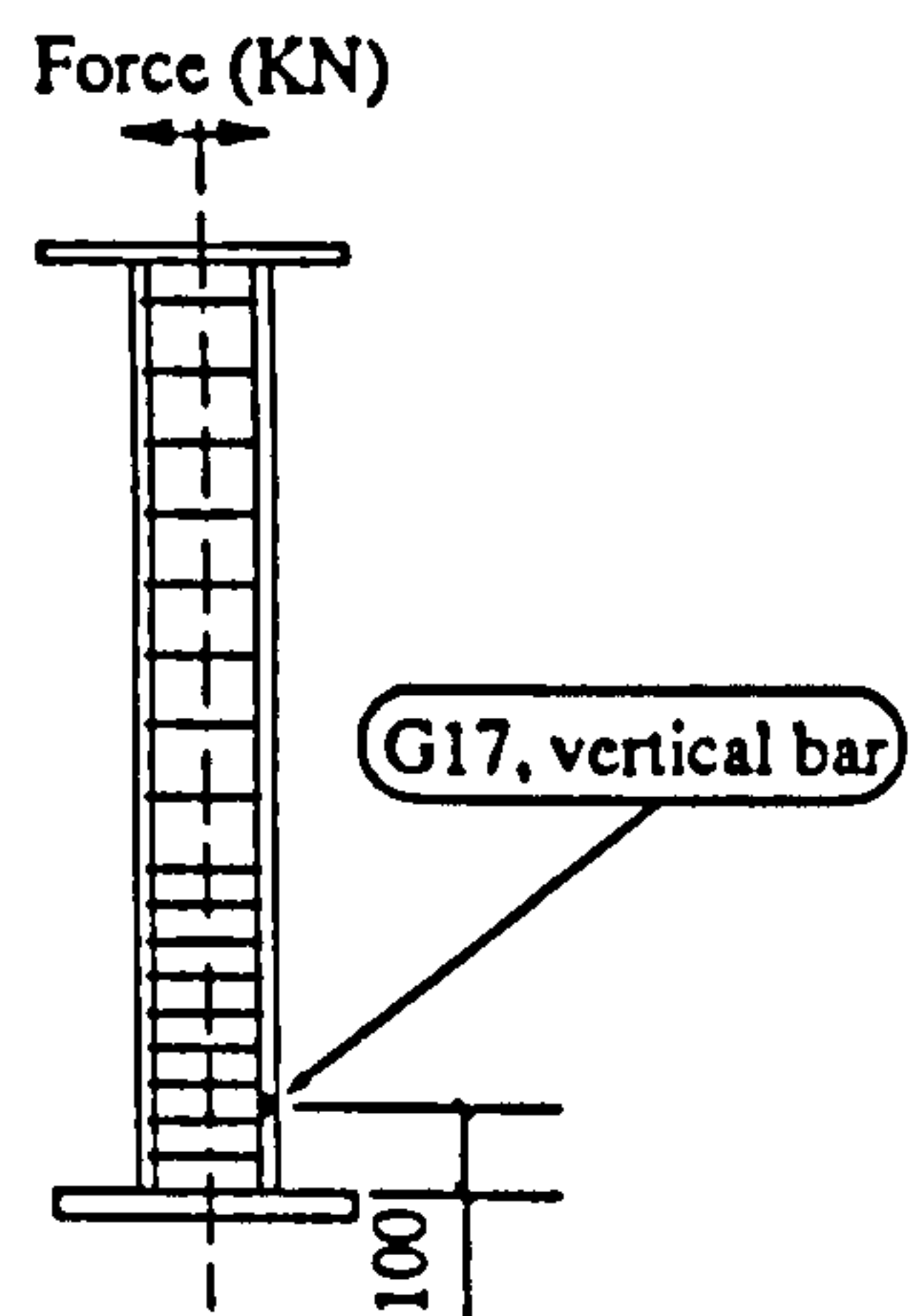
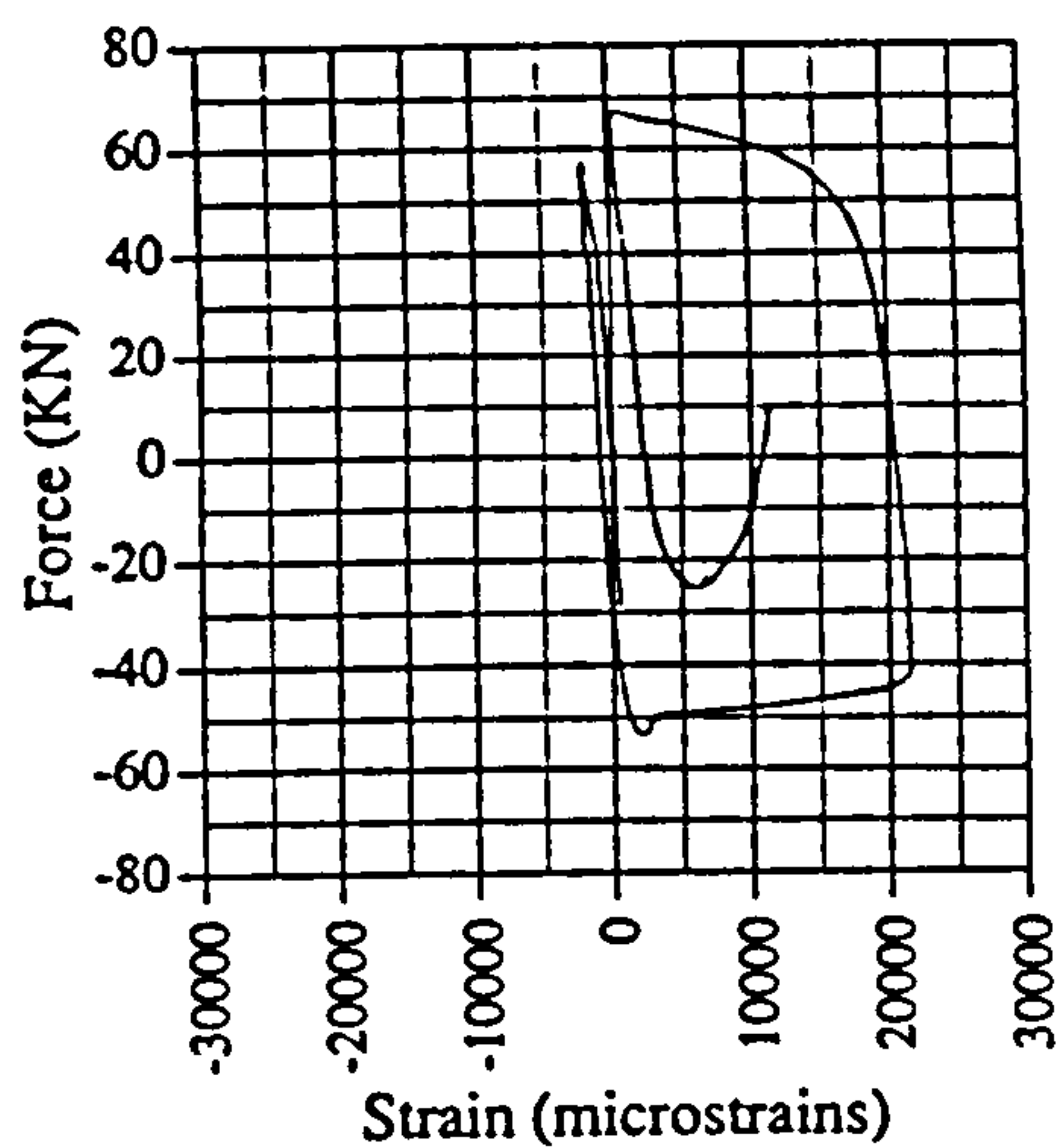


Fig. A.125 Force vs strain, EM03, G17

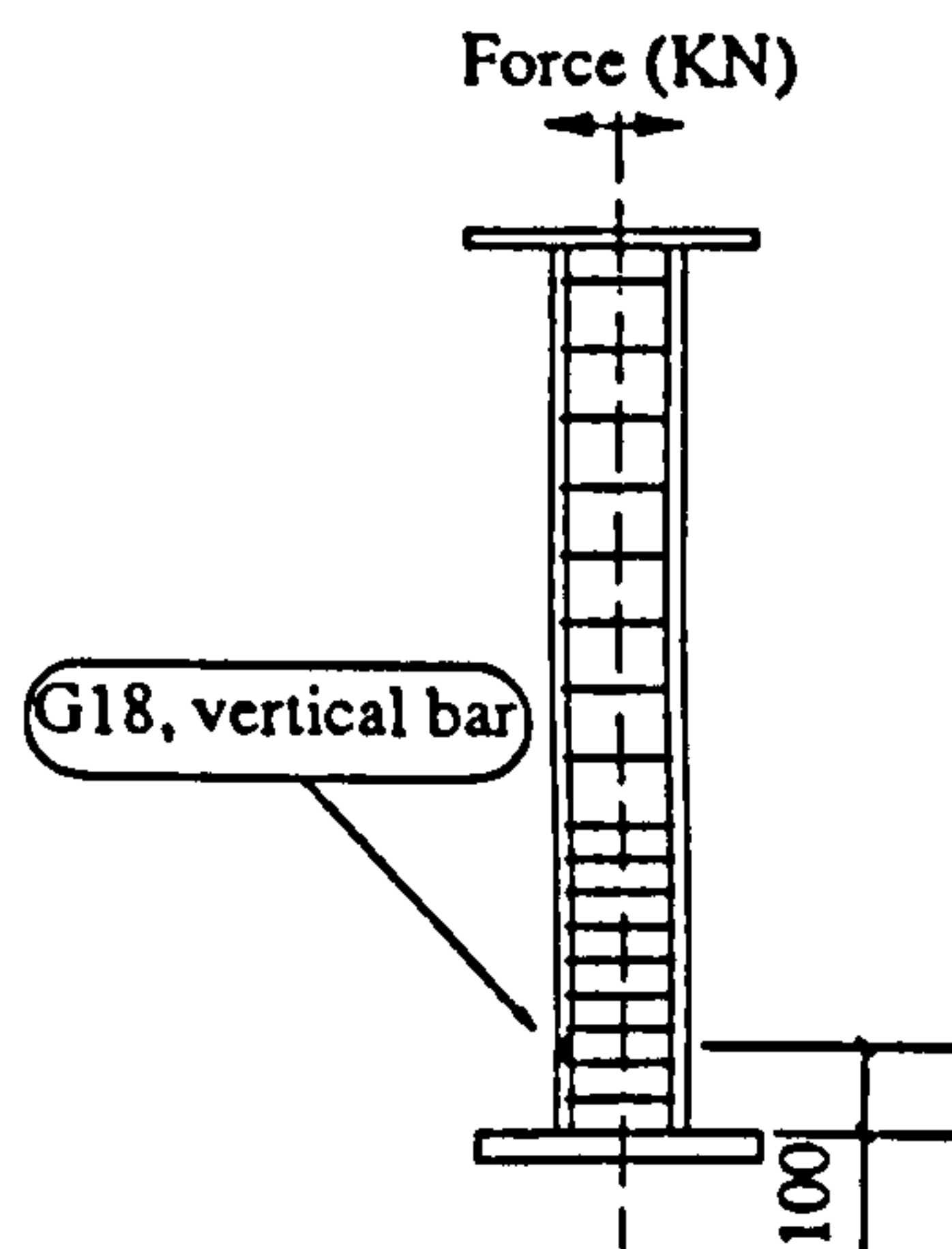
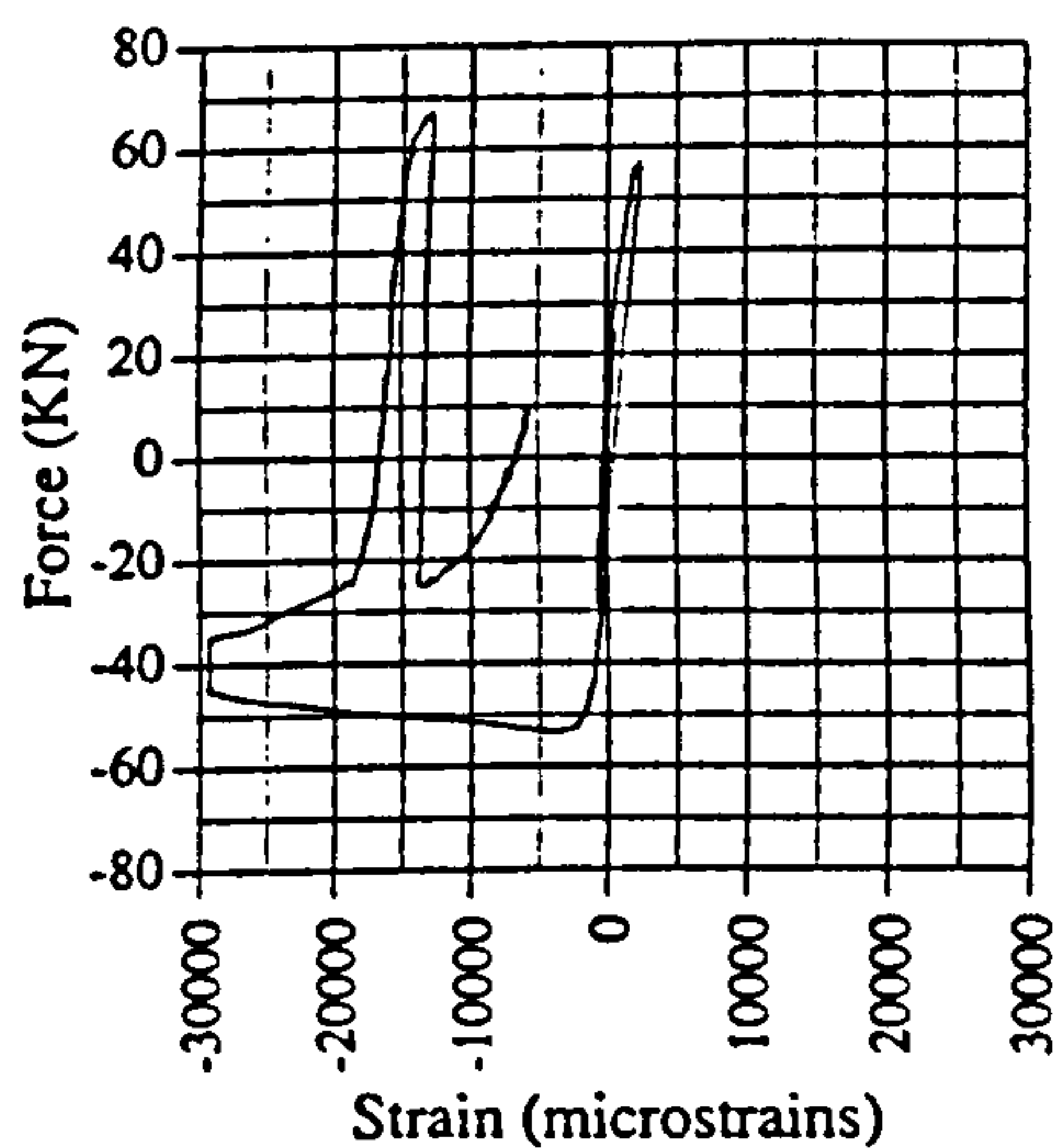


Fig. A.126 Force vs strain, EM03, G18

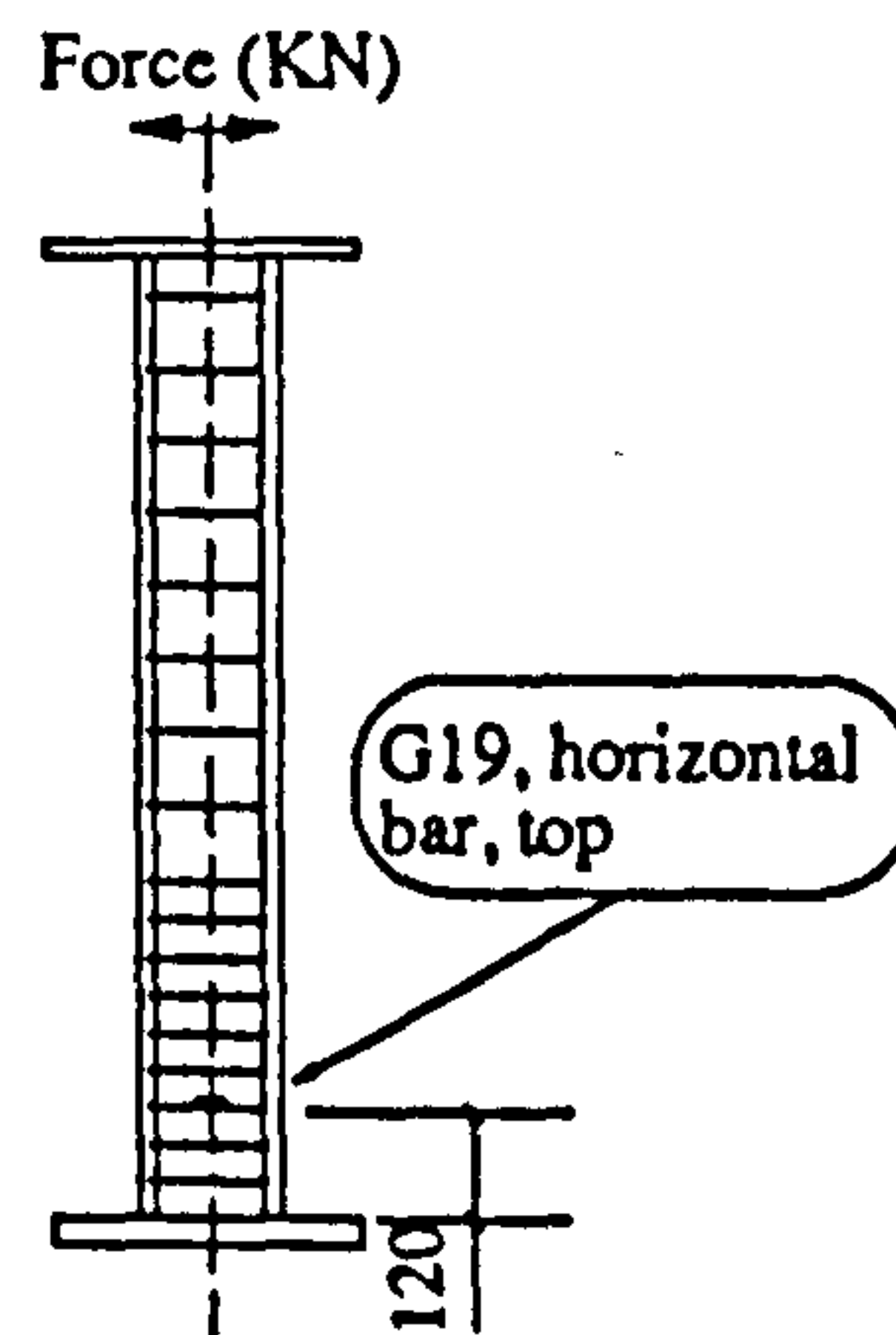
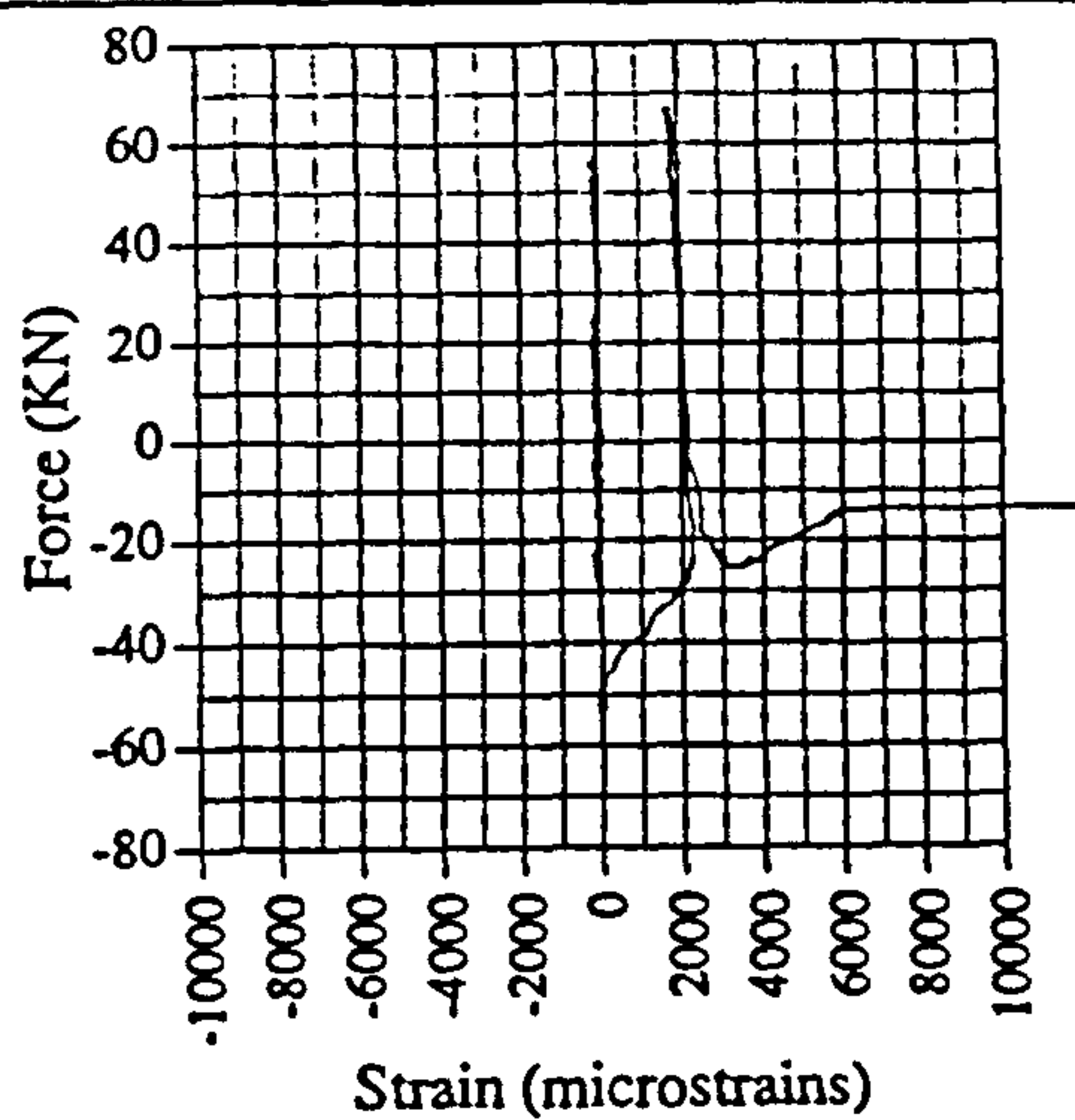


Fig. A.127 Force vs strain, EM03, G19

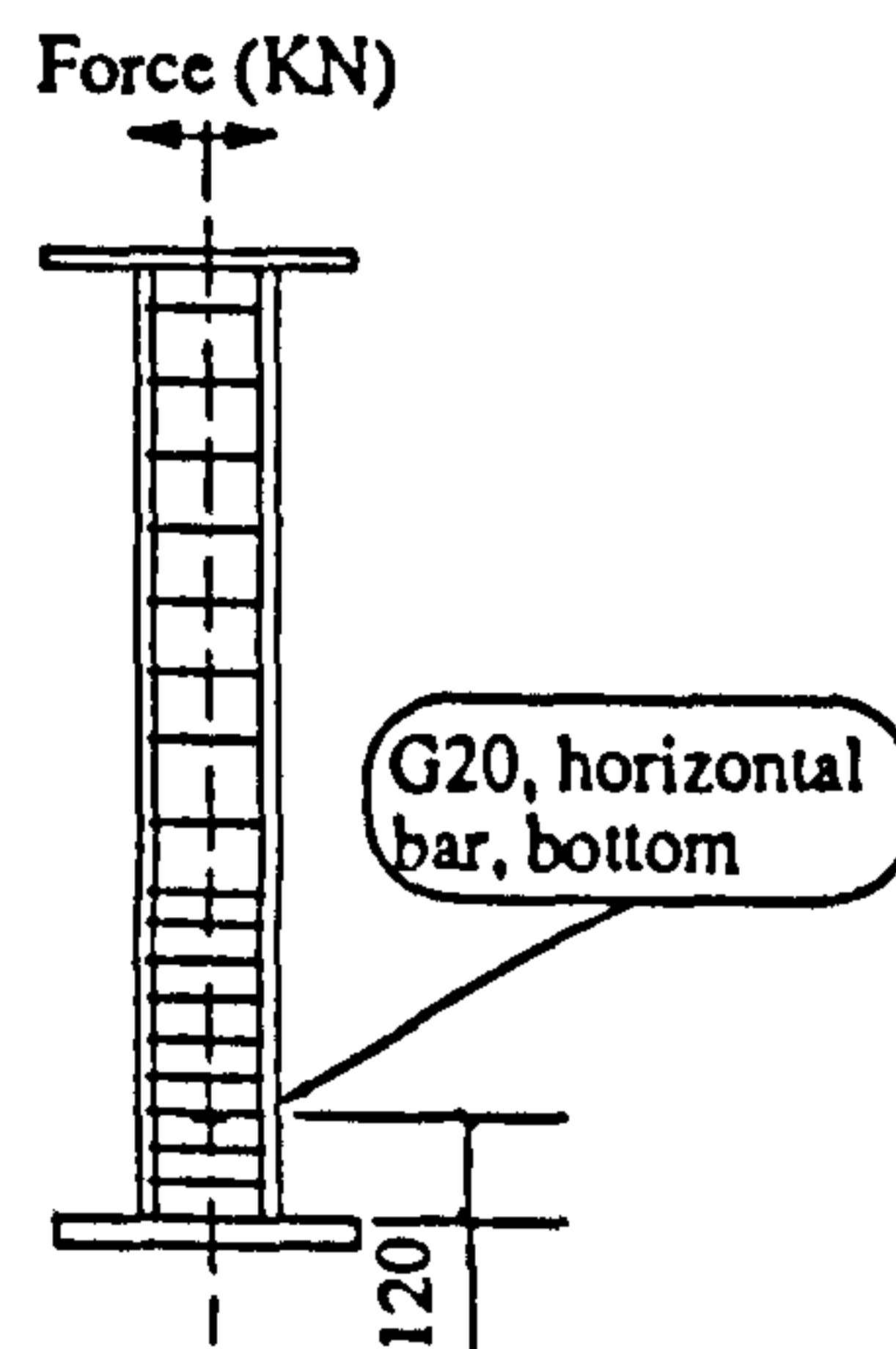
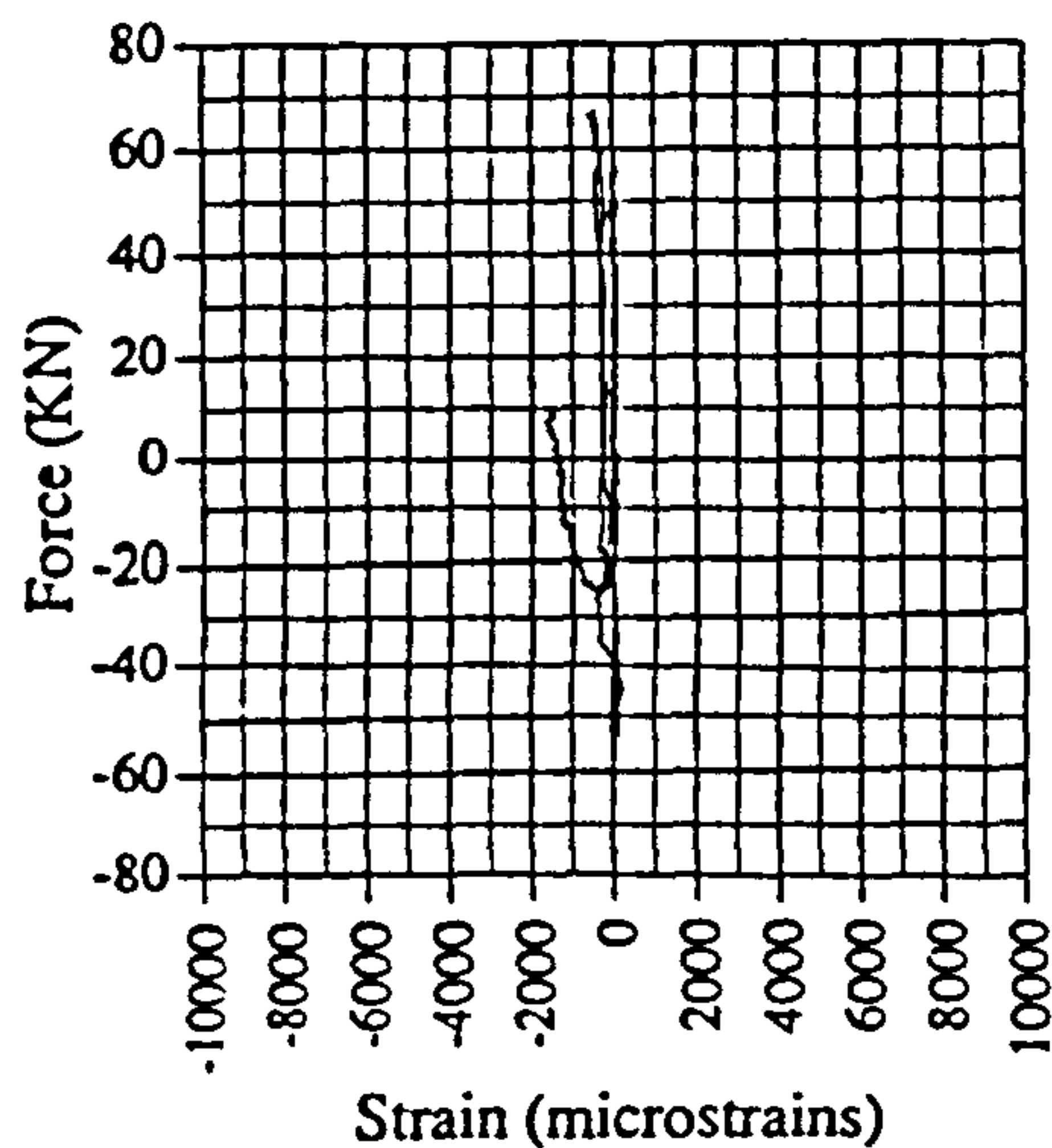


Fig. A.128 Force vs strain, EM03, G20

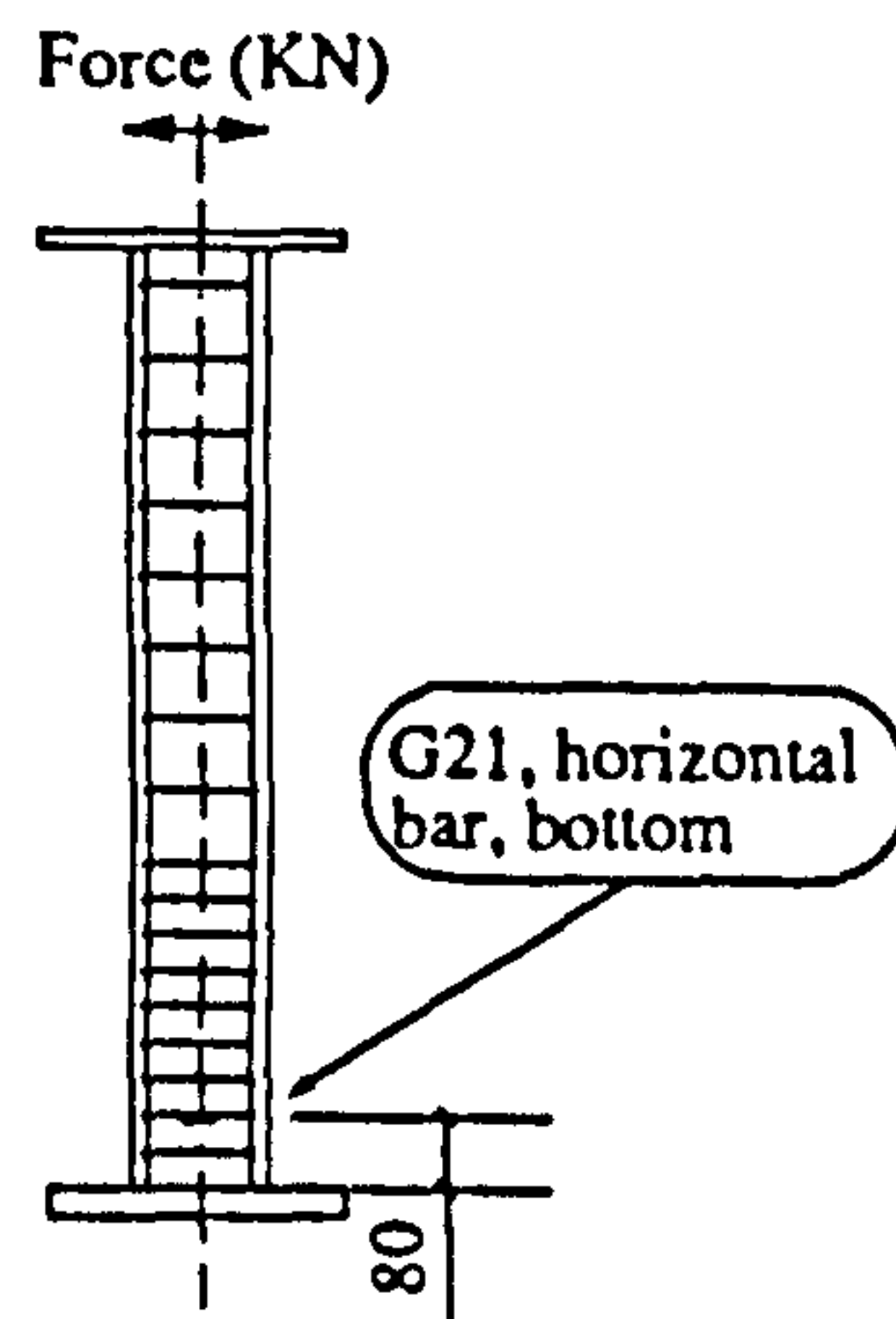
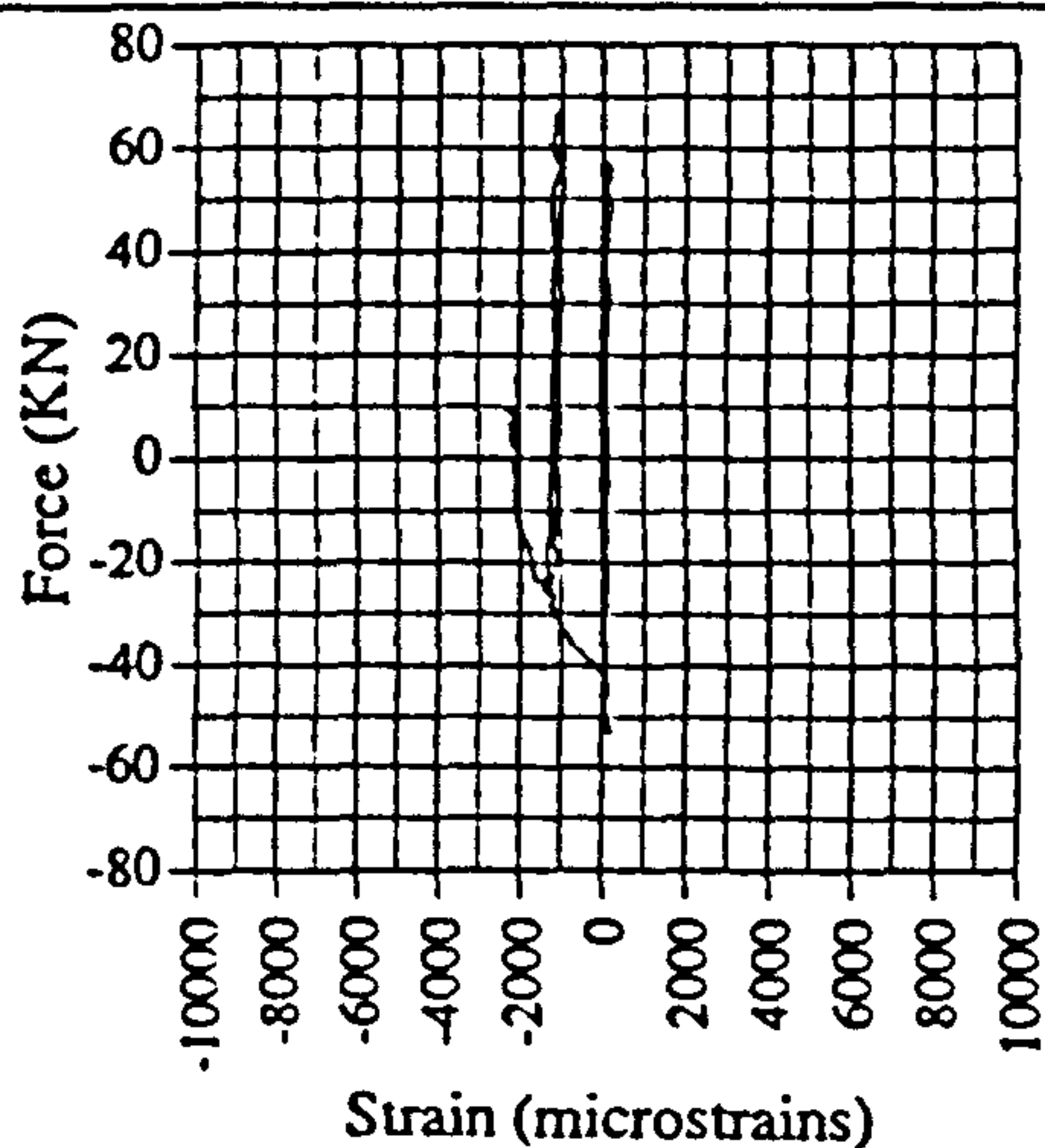


Fig. A.129 Force vs strain, EM03, G21

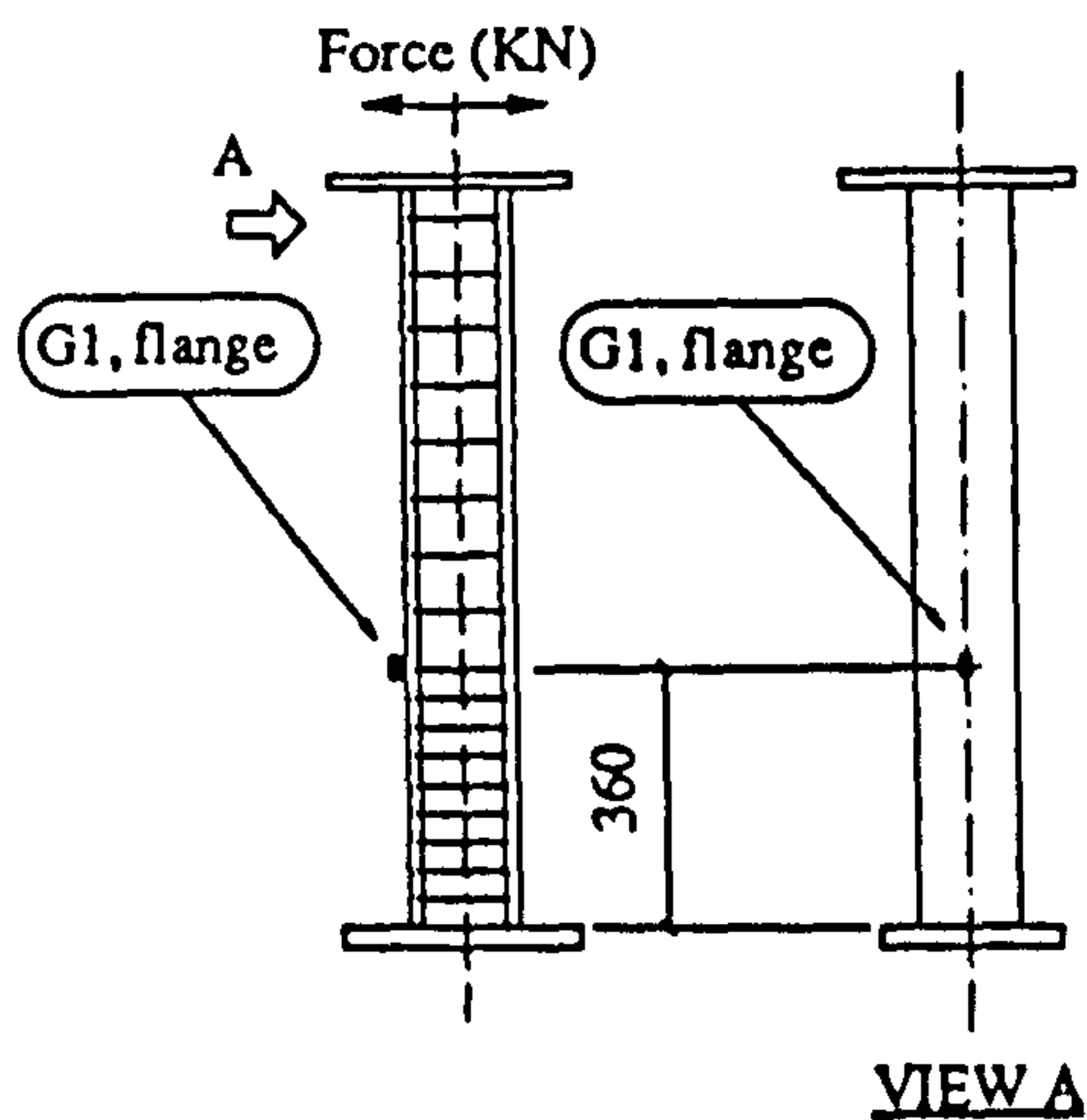
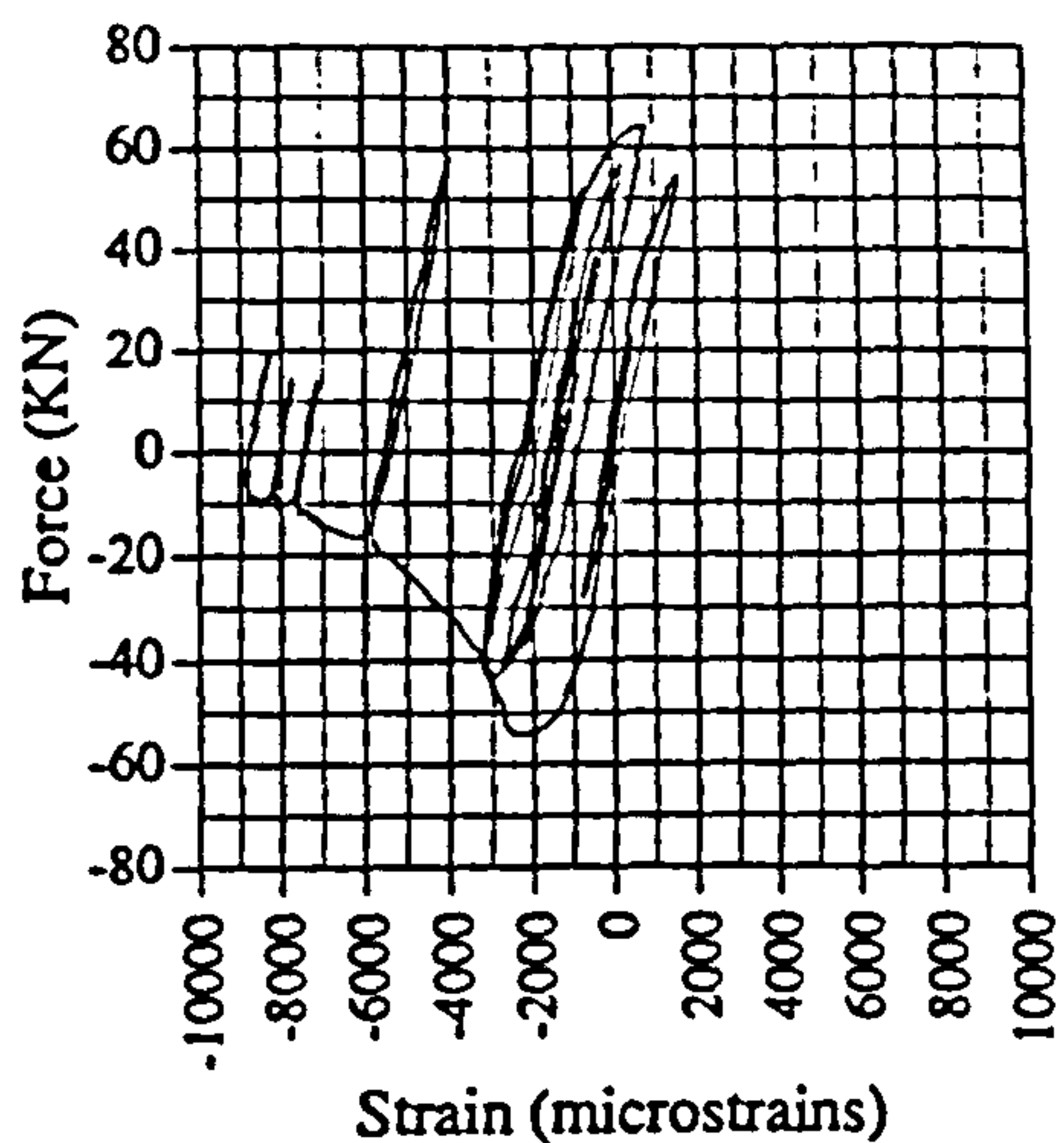


Fig. A.130 Force vs strain, IC03, G1

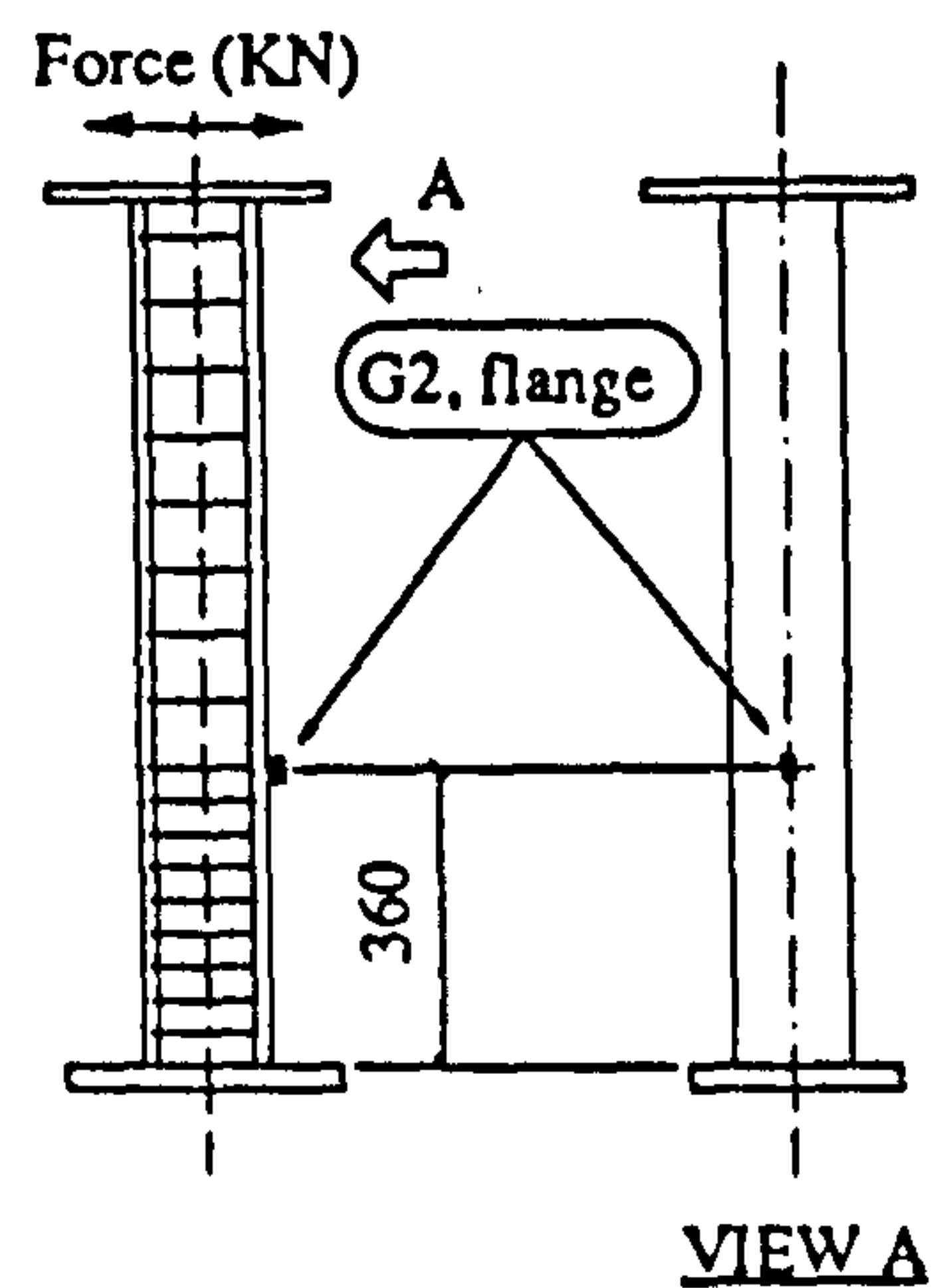
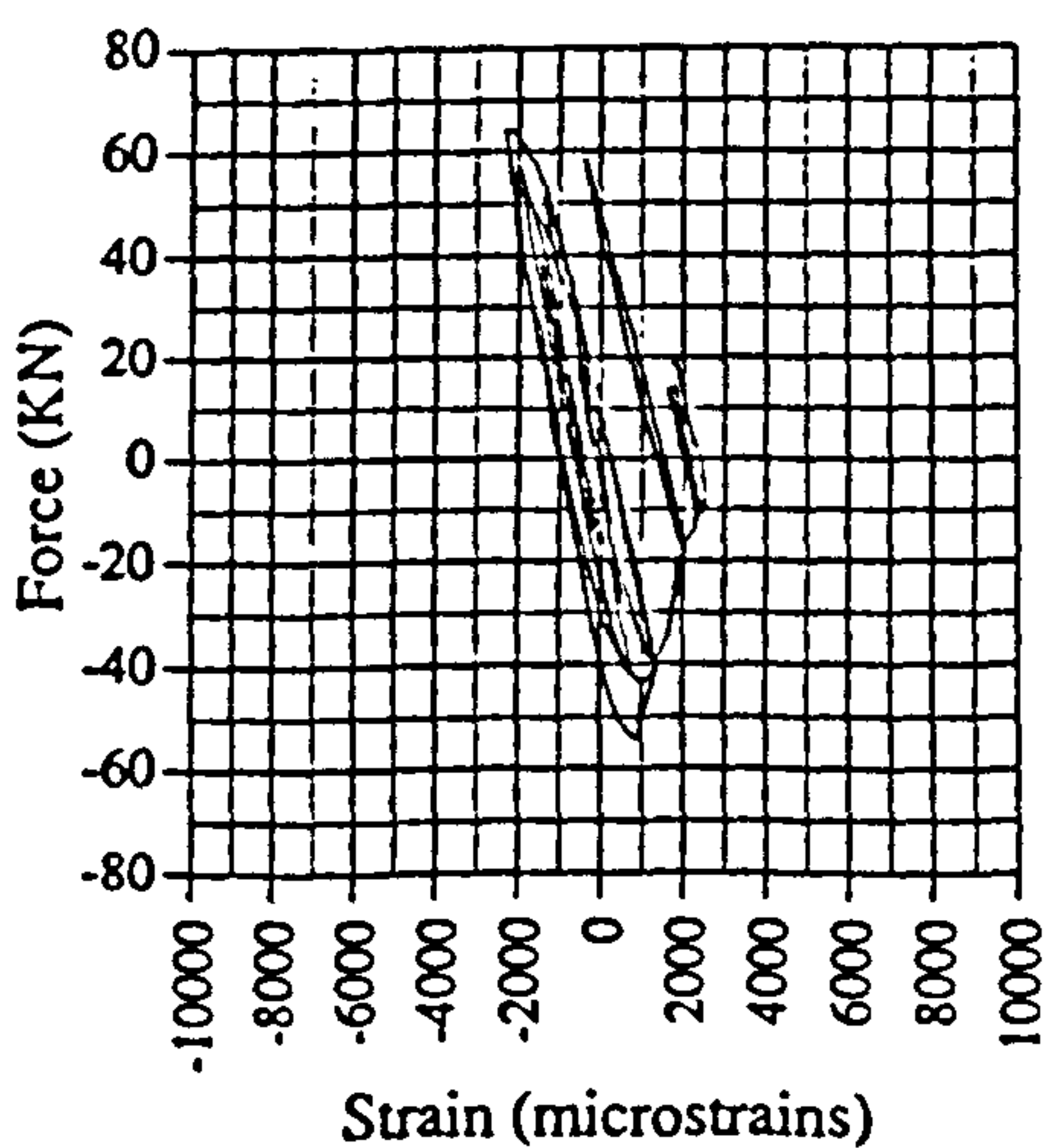


Fig. A.131 Strain vs displacement, IC03, G2

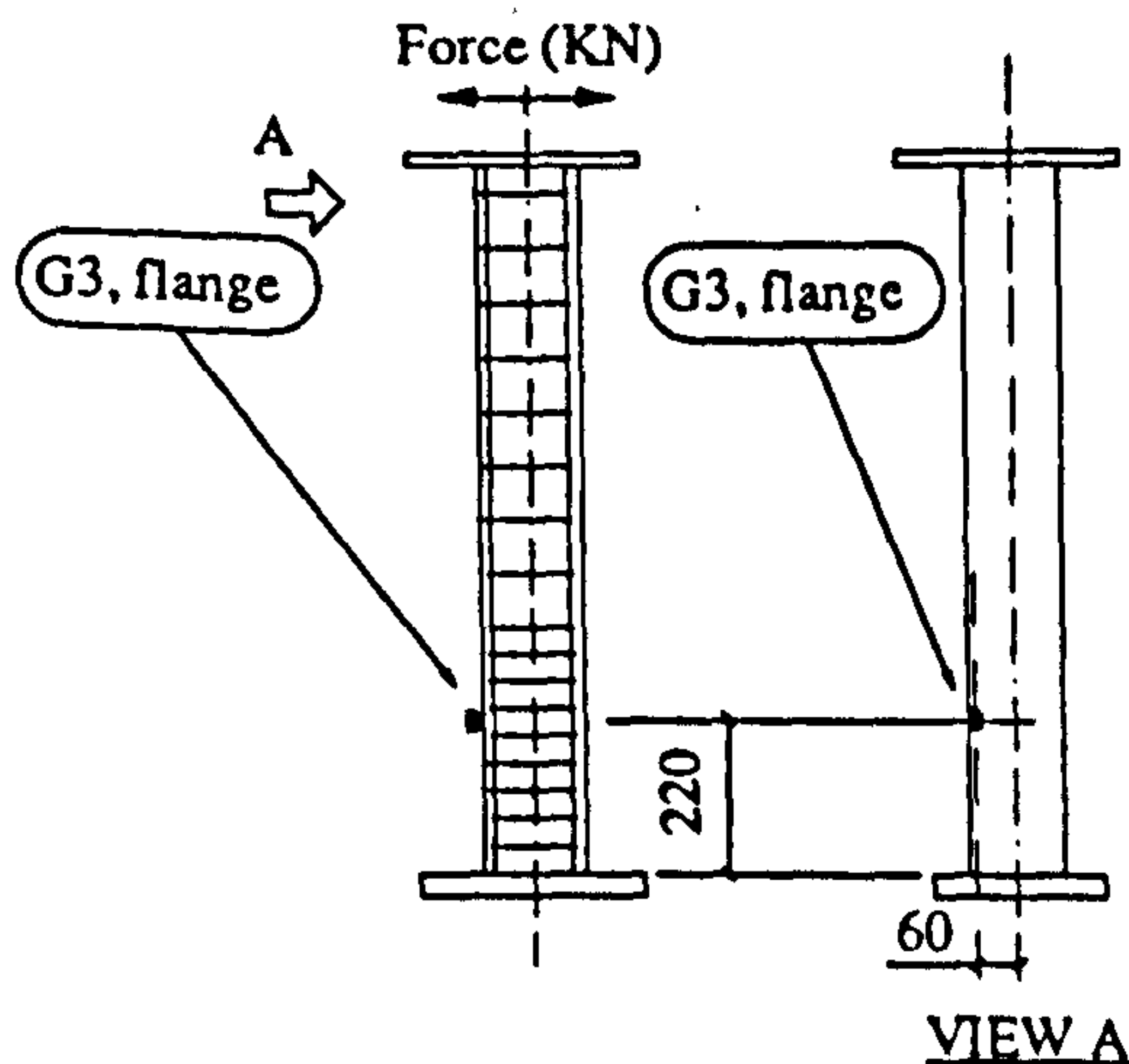
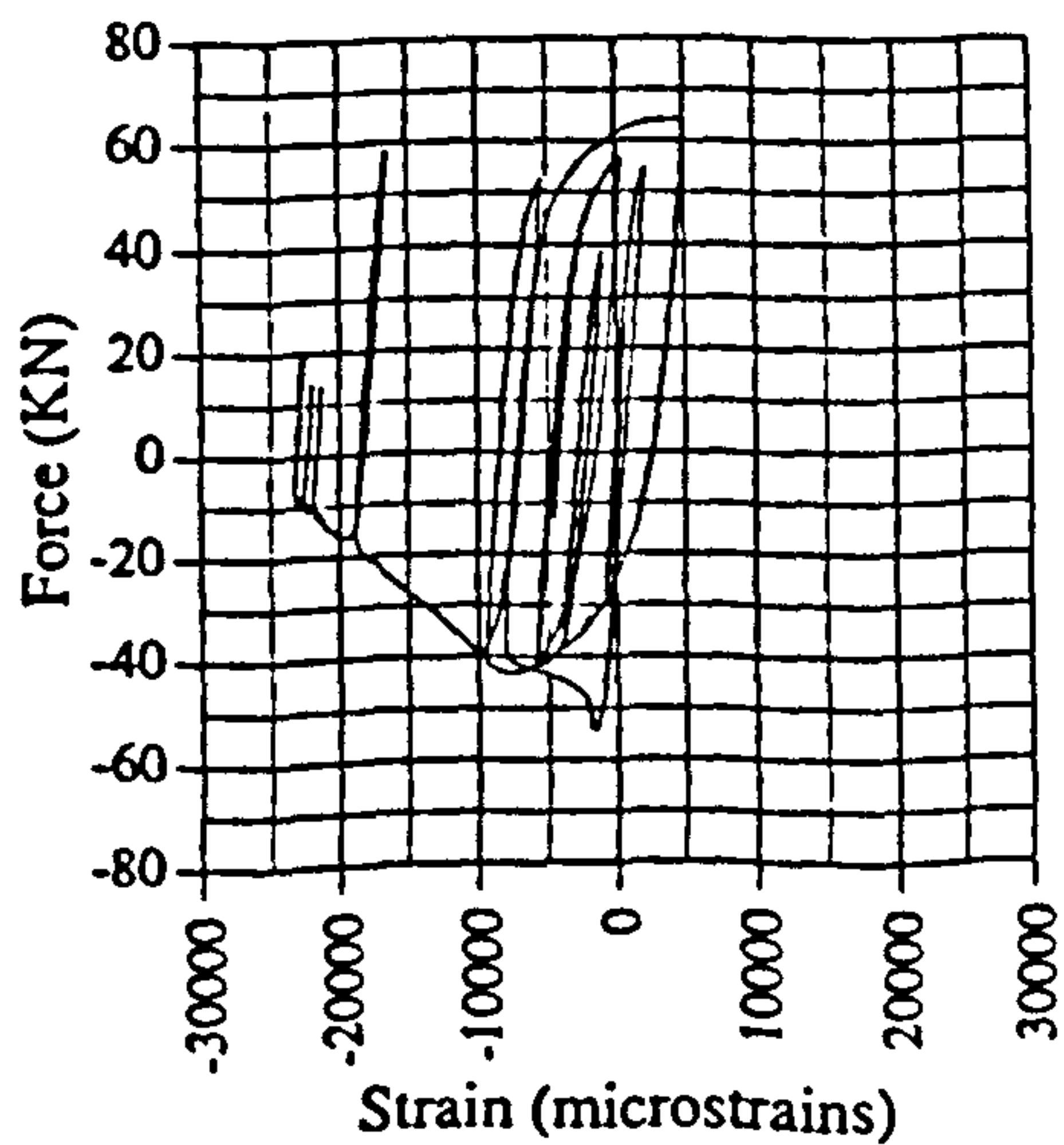


Fig. A.132 Strain vs displacement, IC03, G3

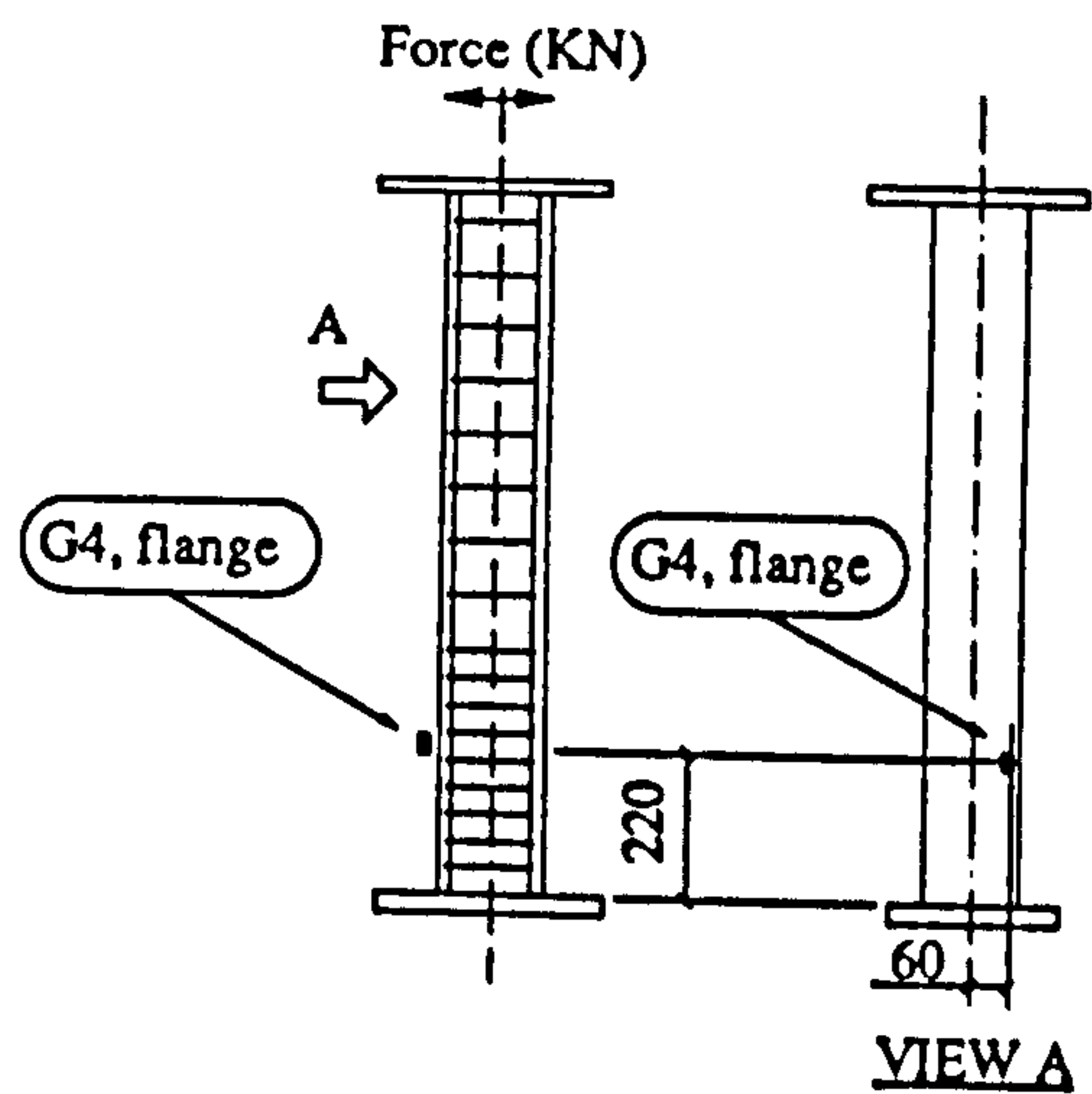
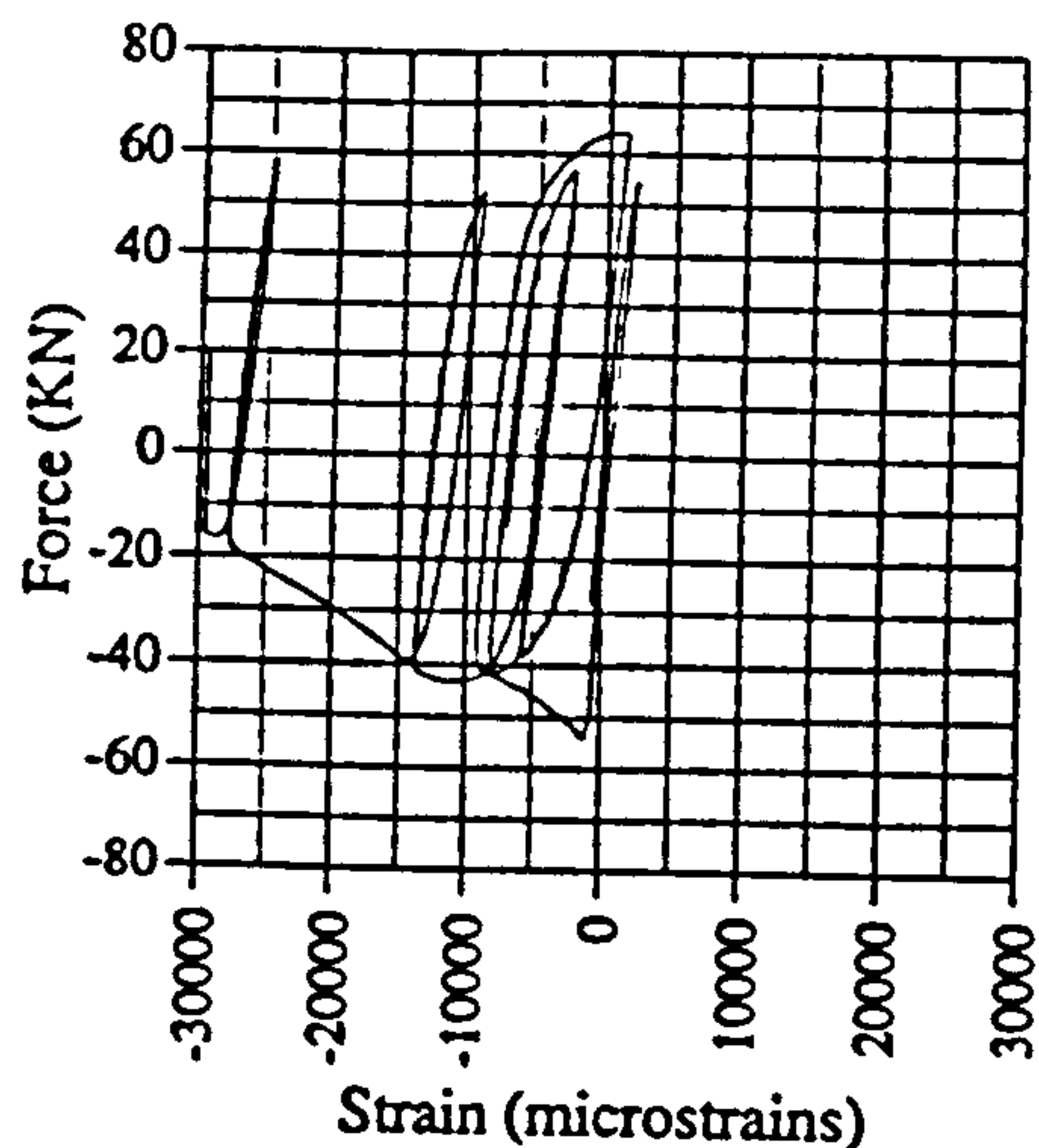


Fig. A.133 Force vs strain, IC03, G4

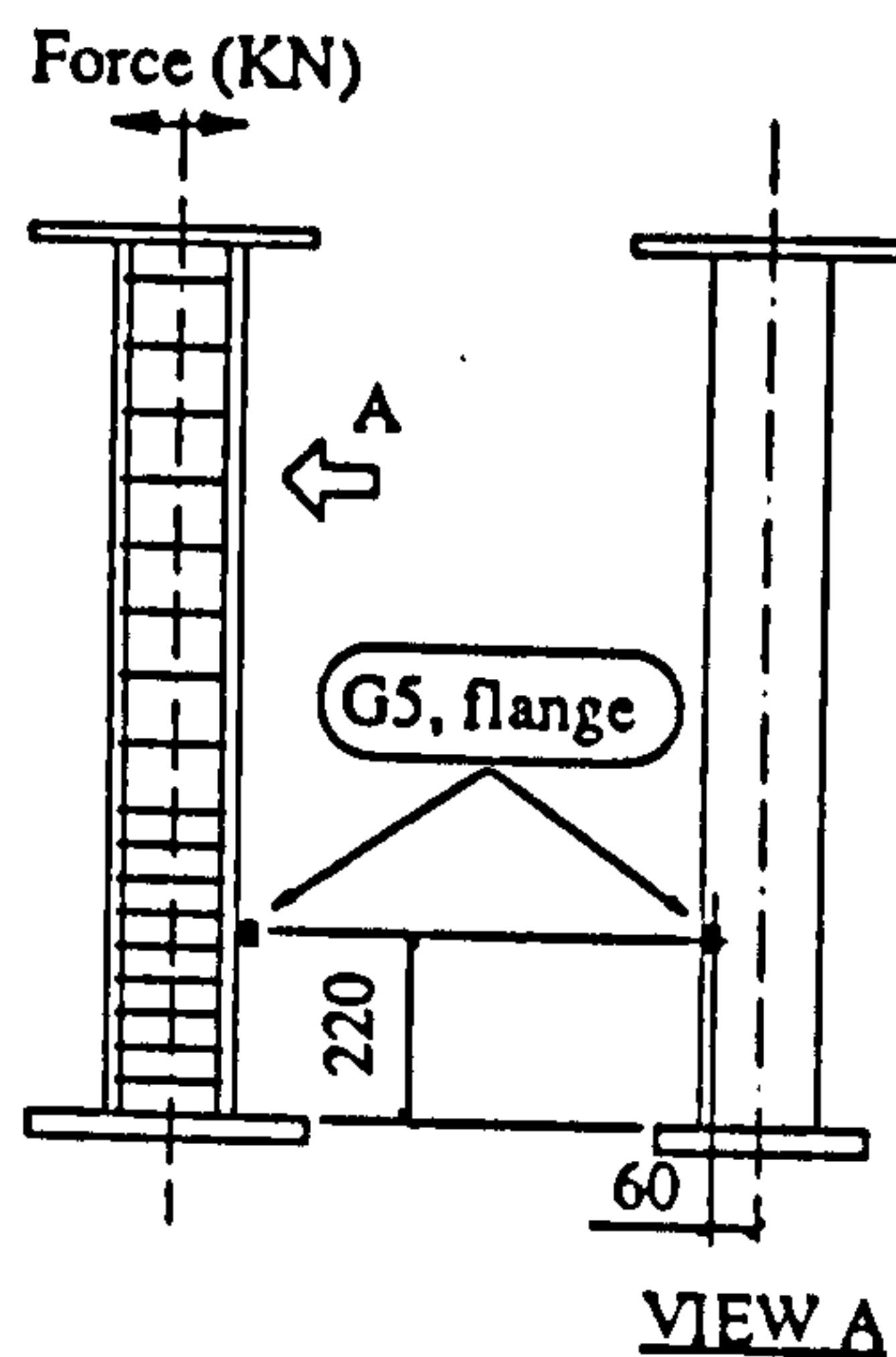
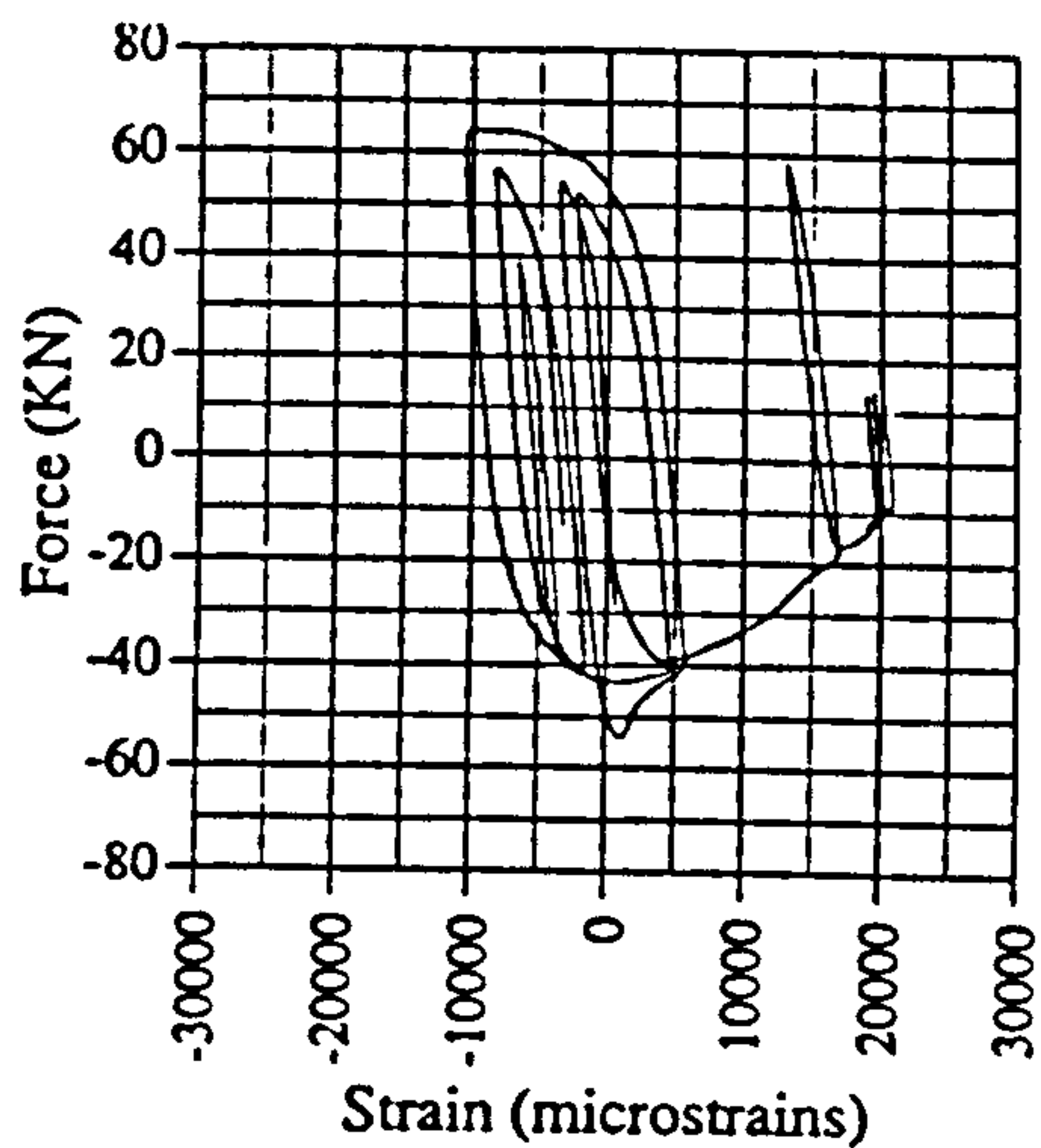


Fig. A.134 Force vs strain, IC03, G5

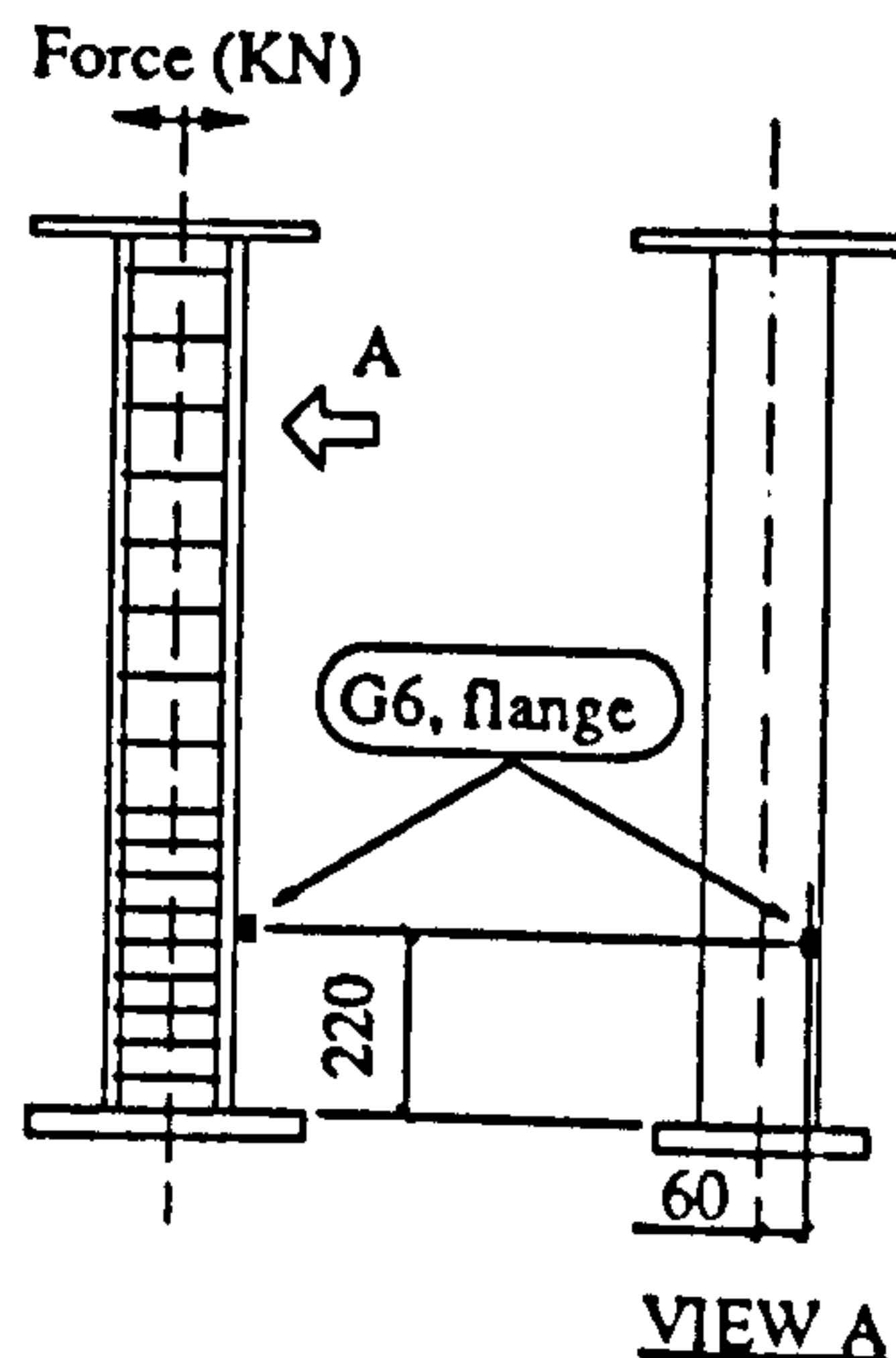
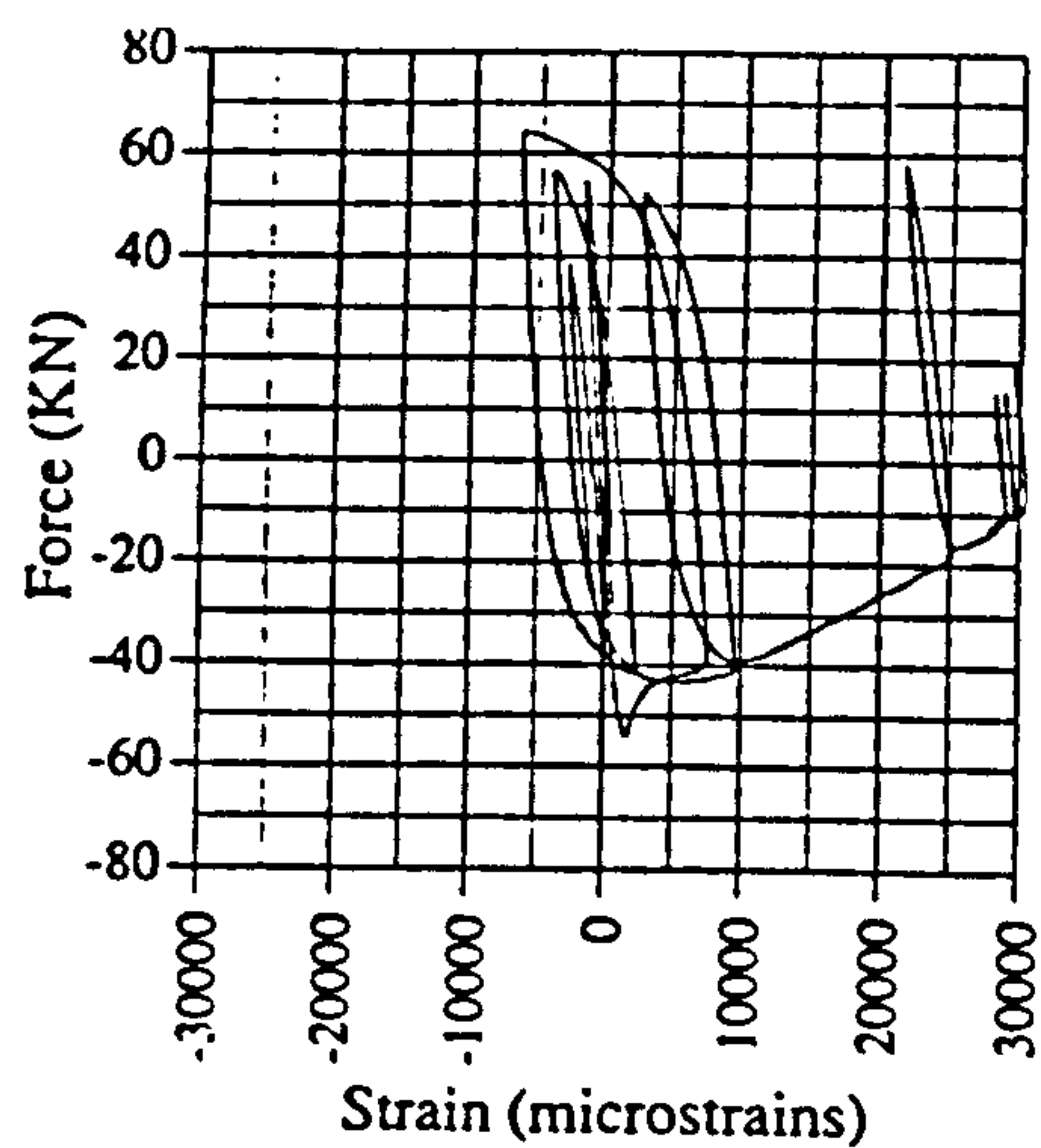


Fig. A.135 Force vs strain, IC03, G6

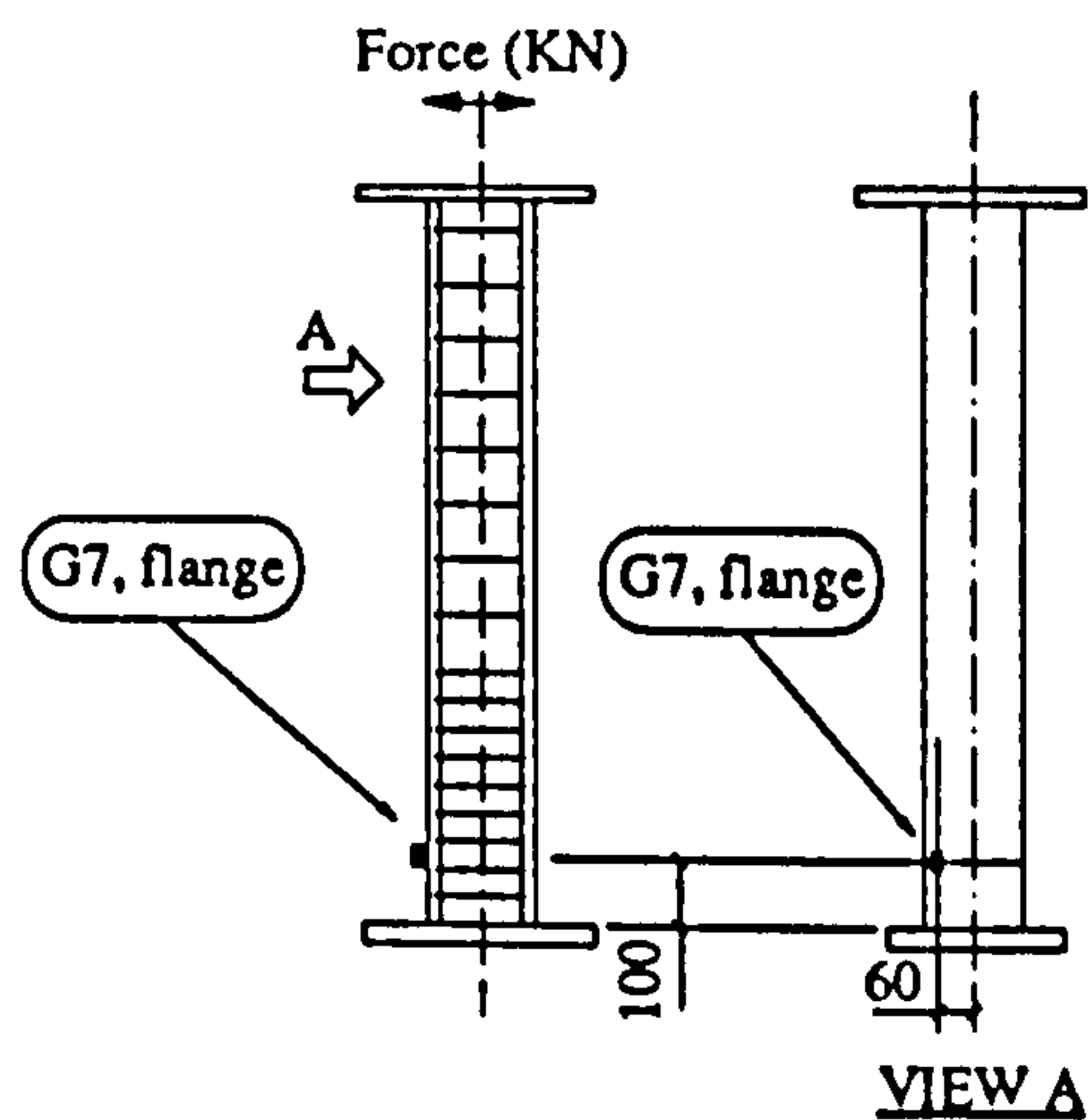
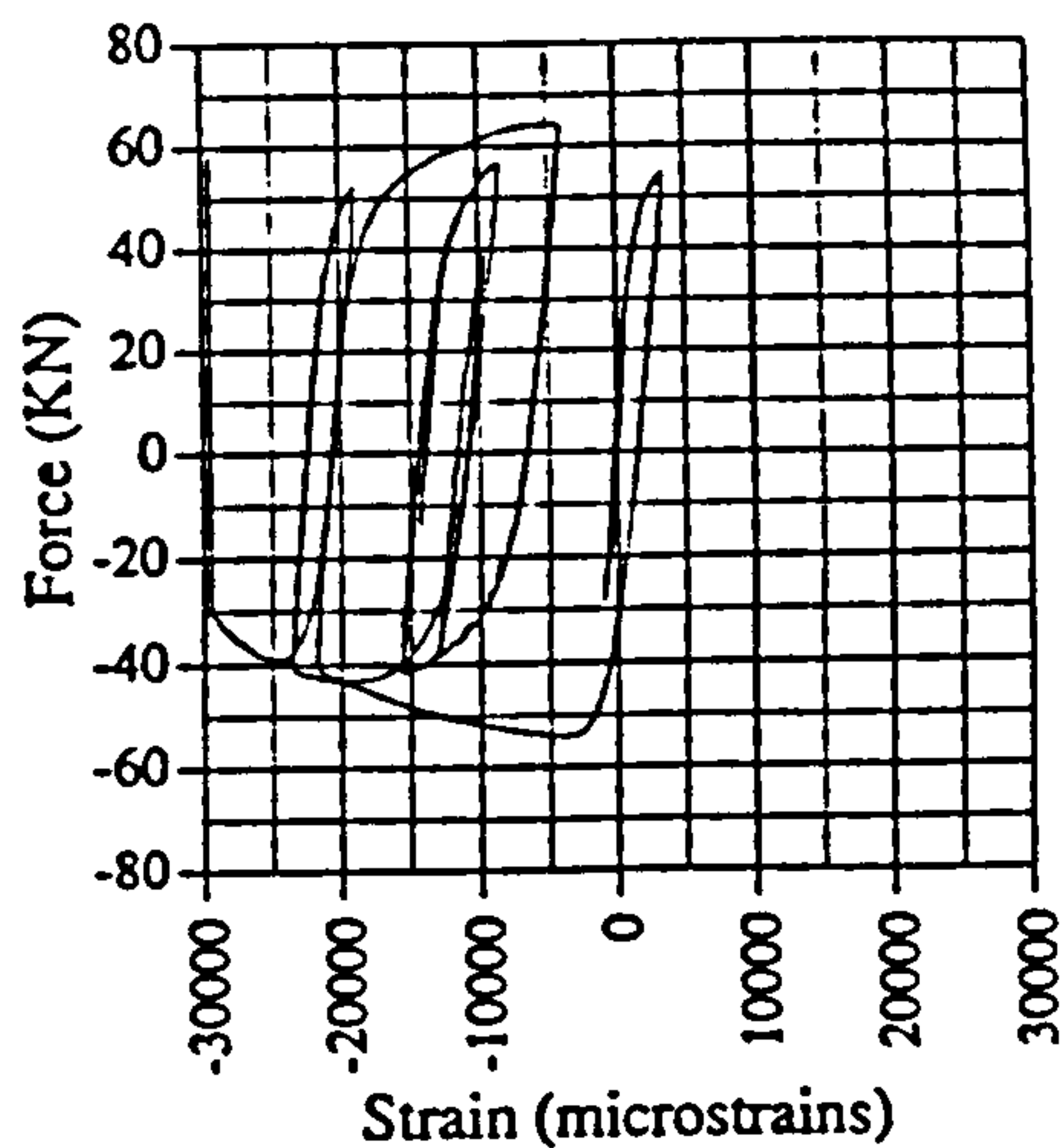


Fig. A.136 Force vs strain, IC03, G7

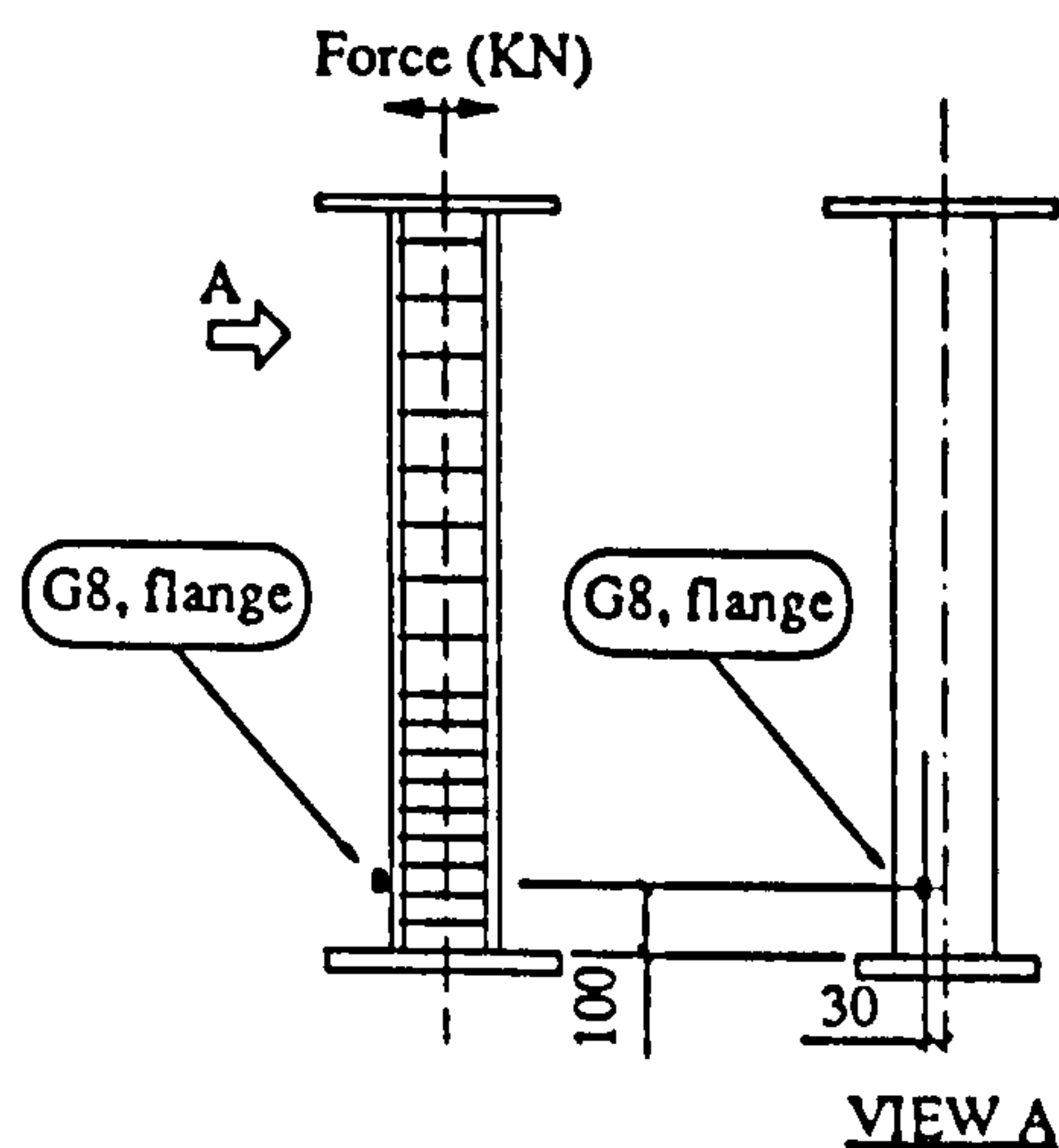
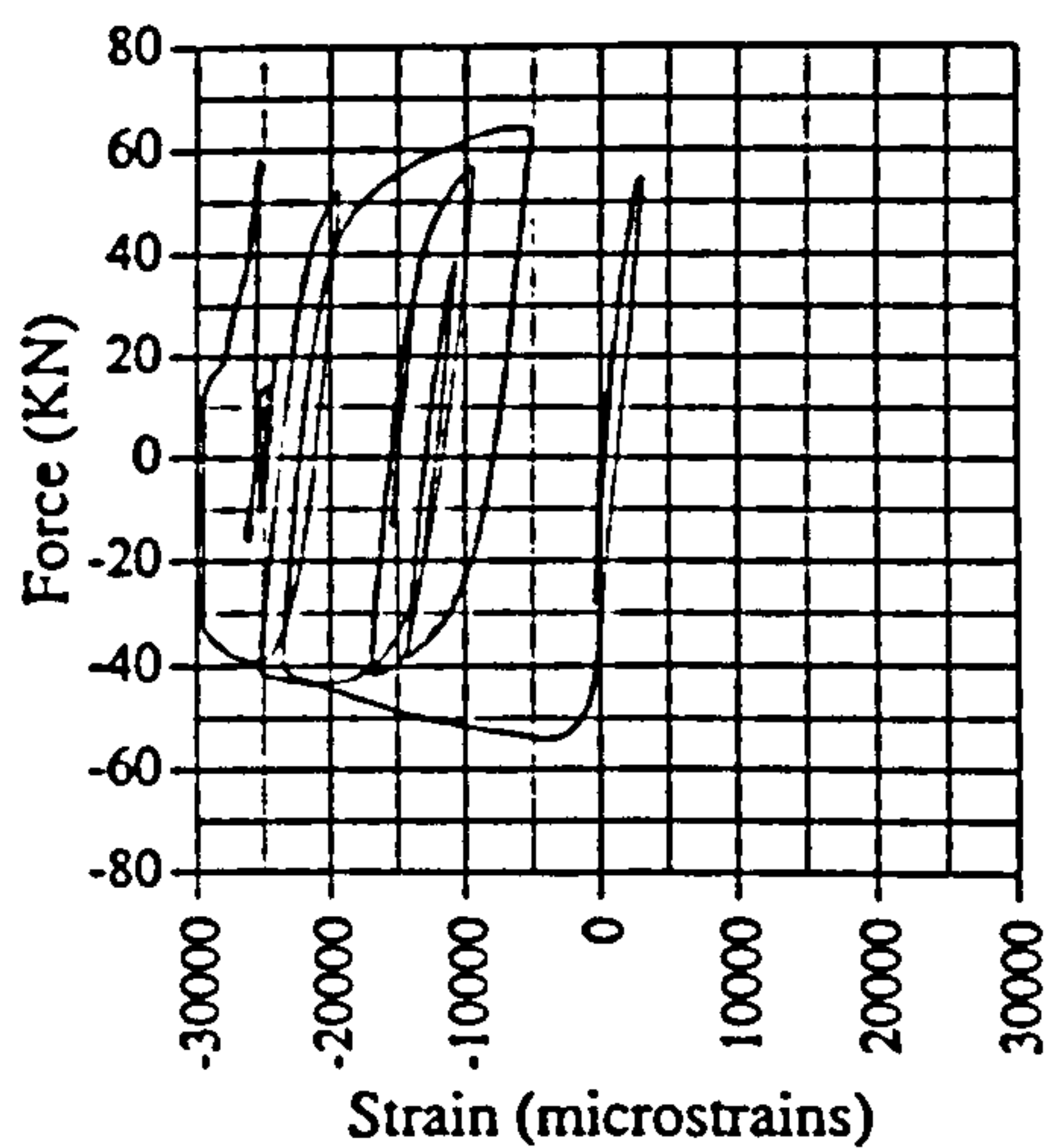


Fig. A.137 Force vs strain, IC03, G8

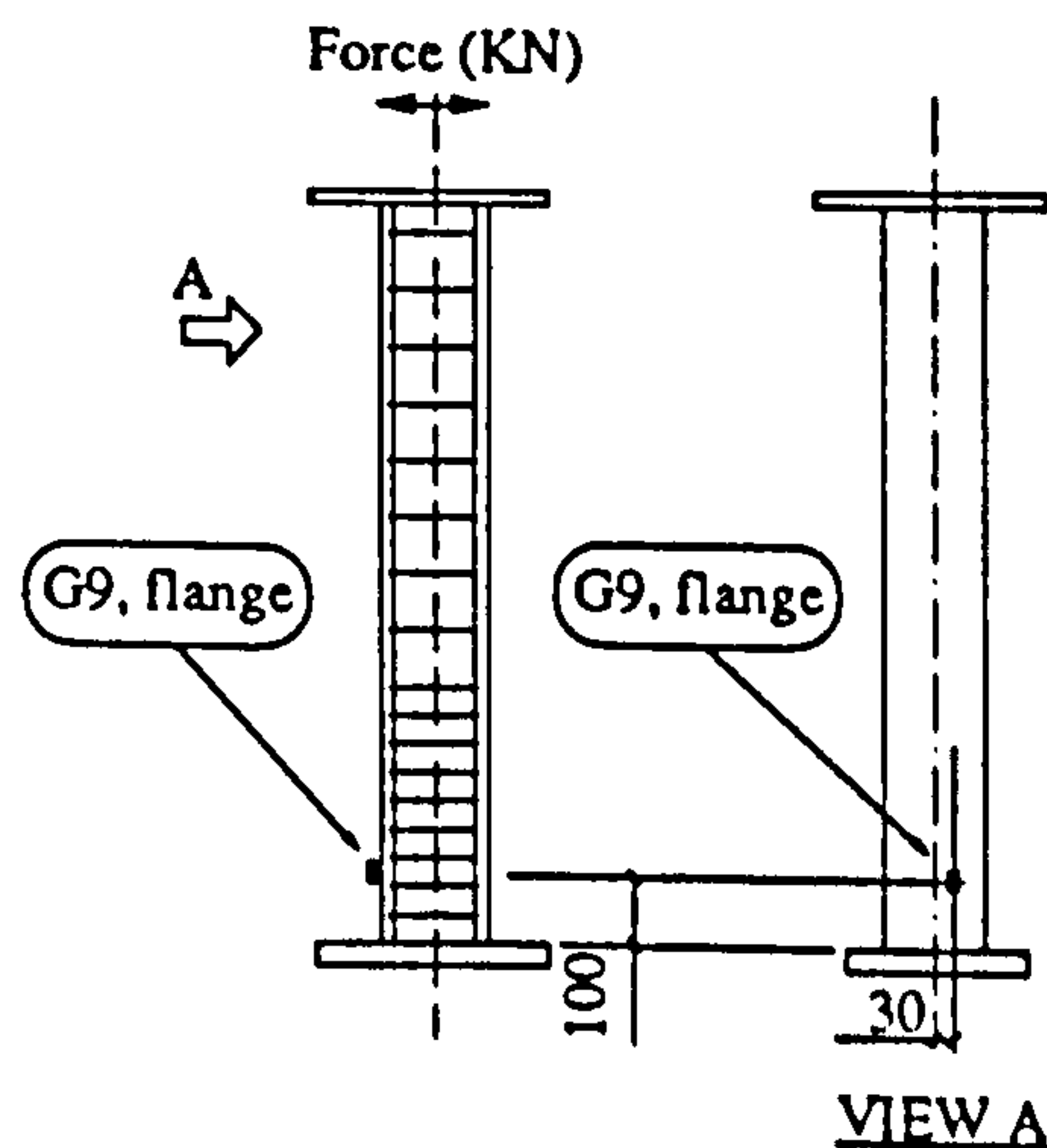
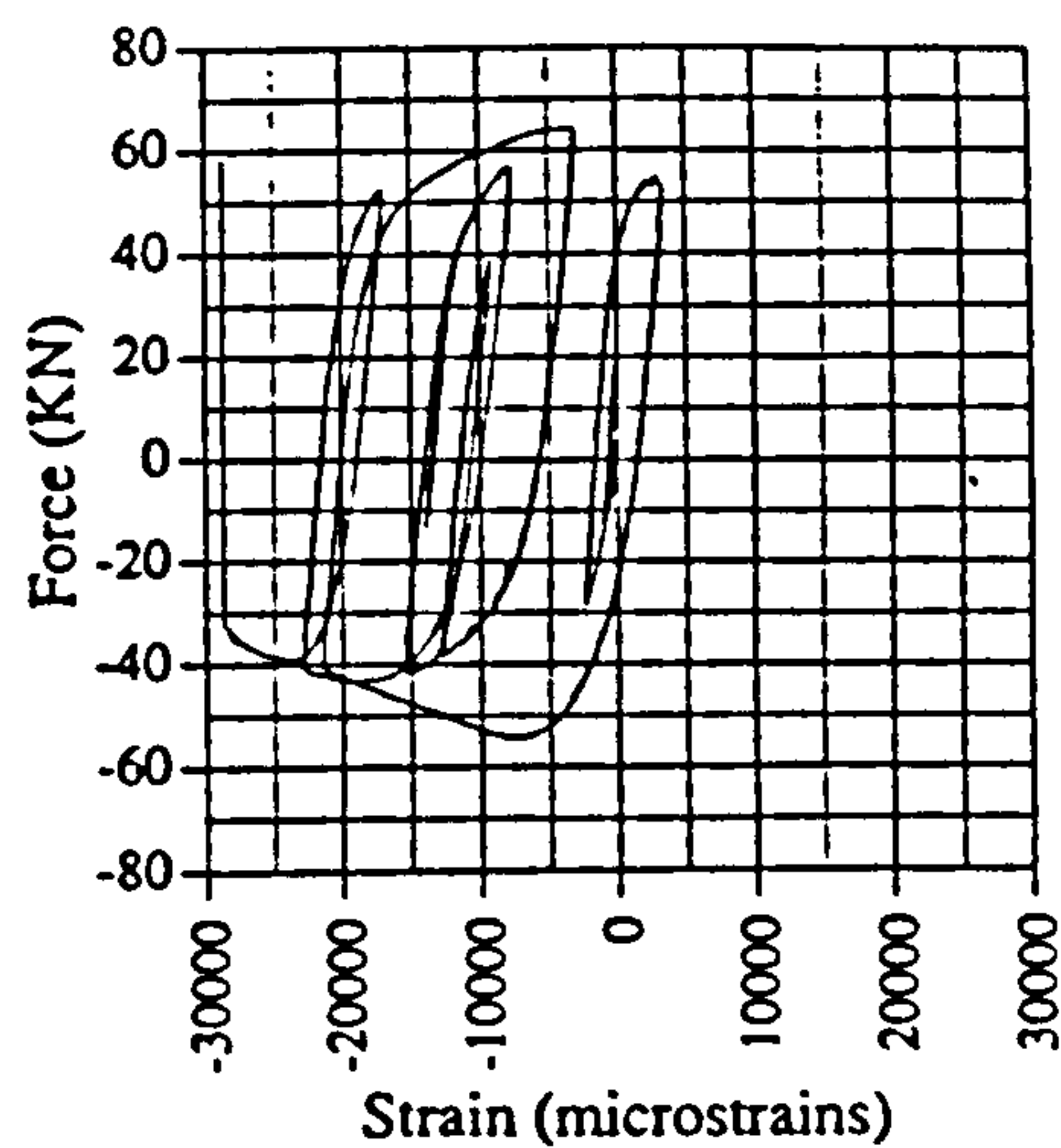


Fig. A.138 Force vs strain, IC03, G9

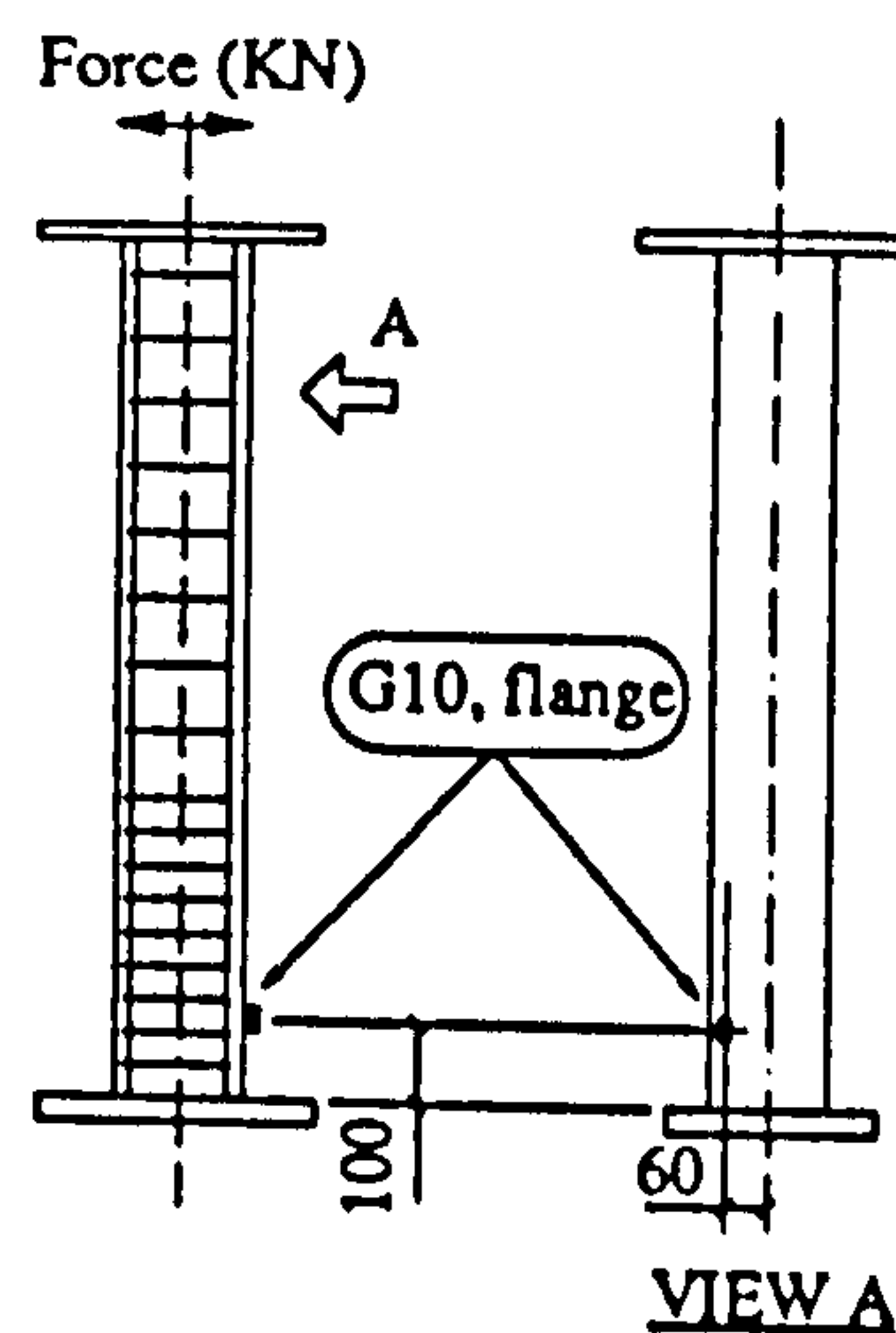
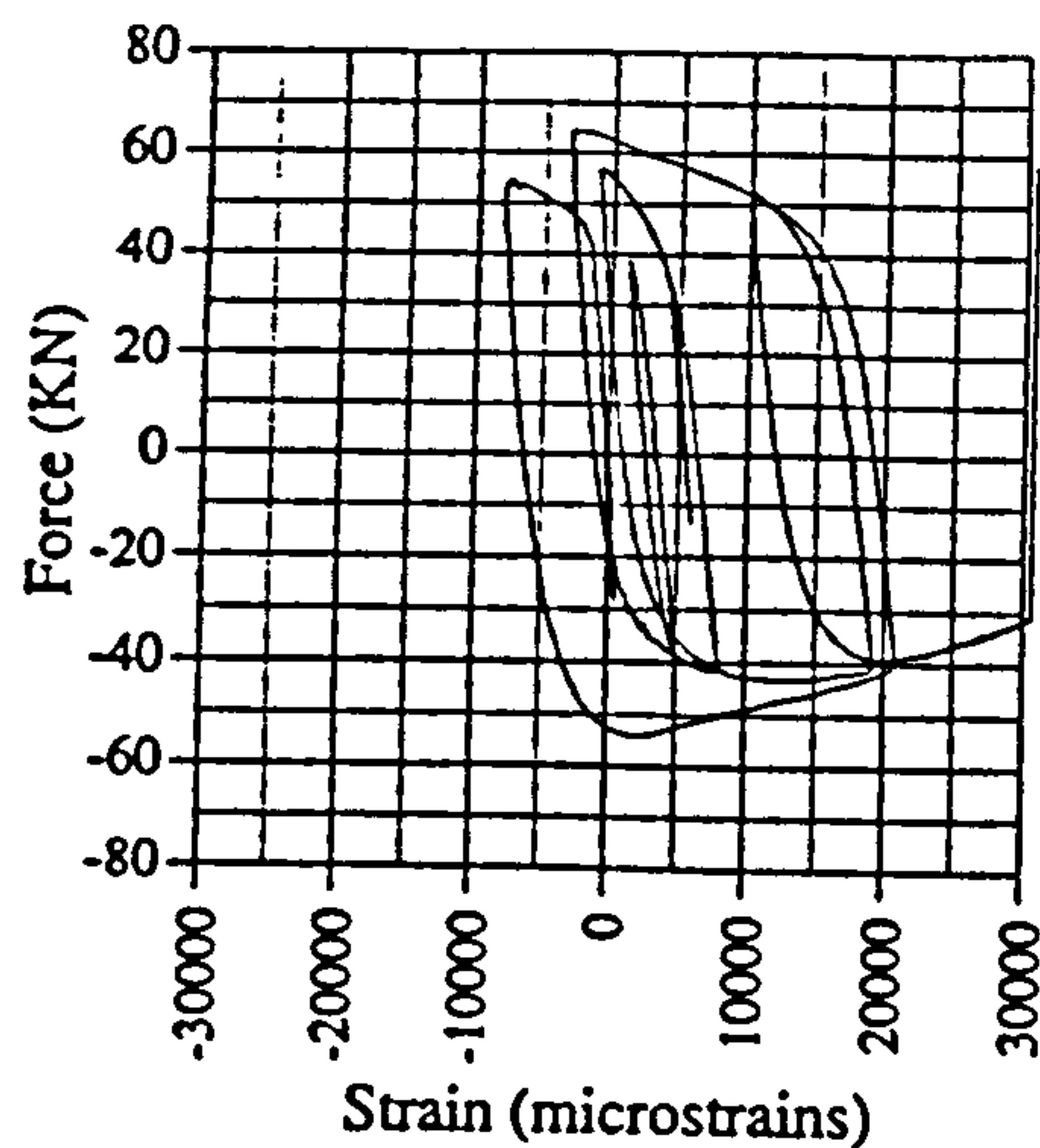


Fig. A.139 Force vs strain, IC03, G10

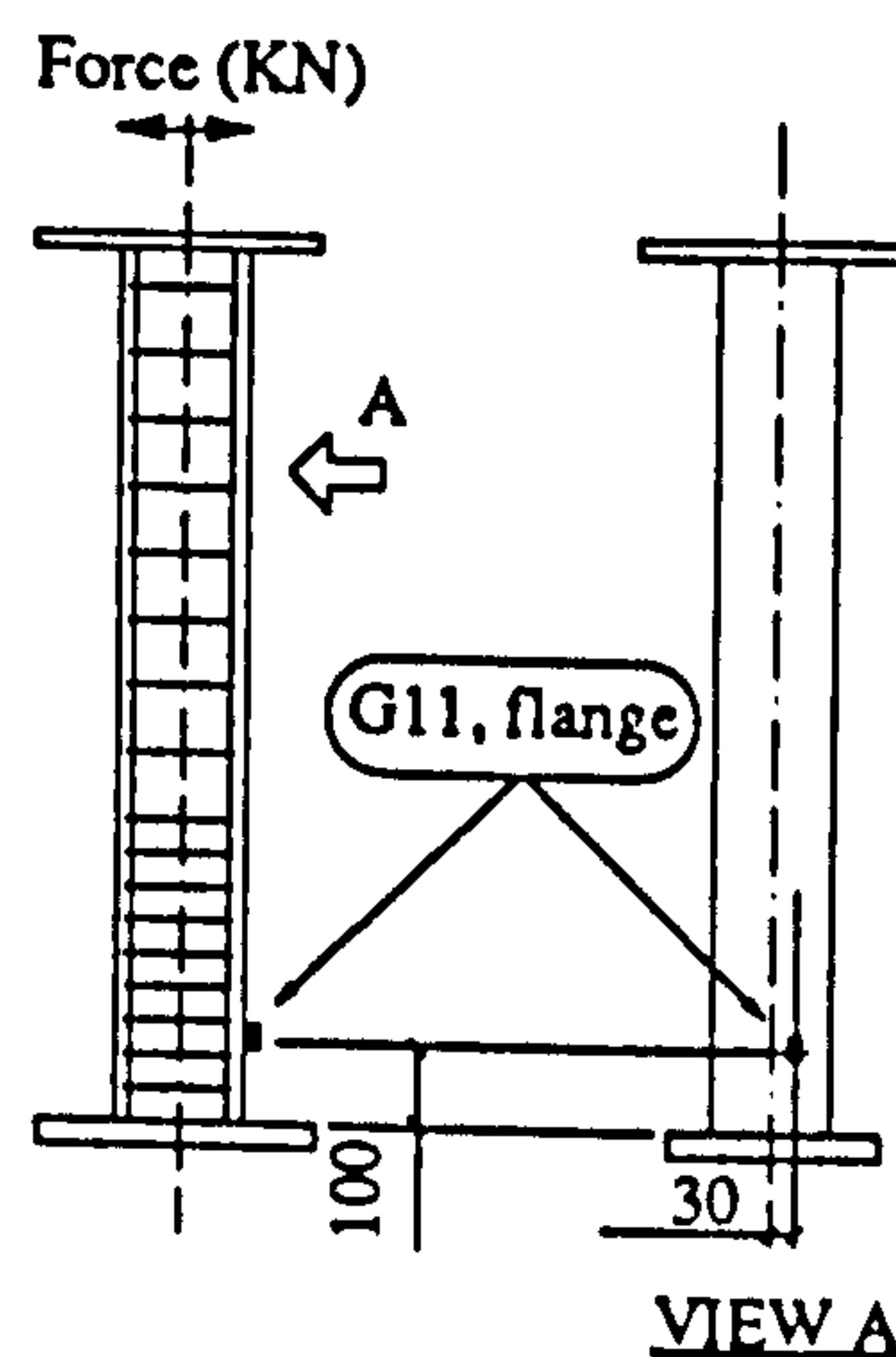
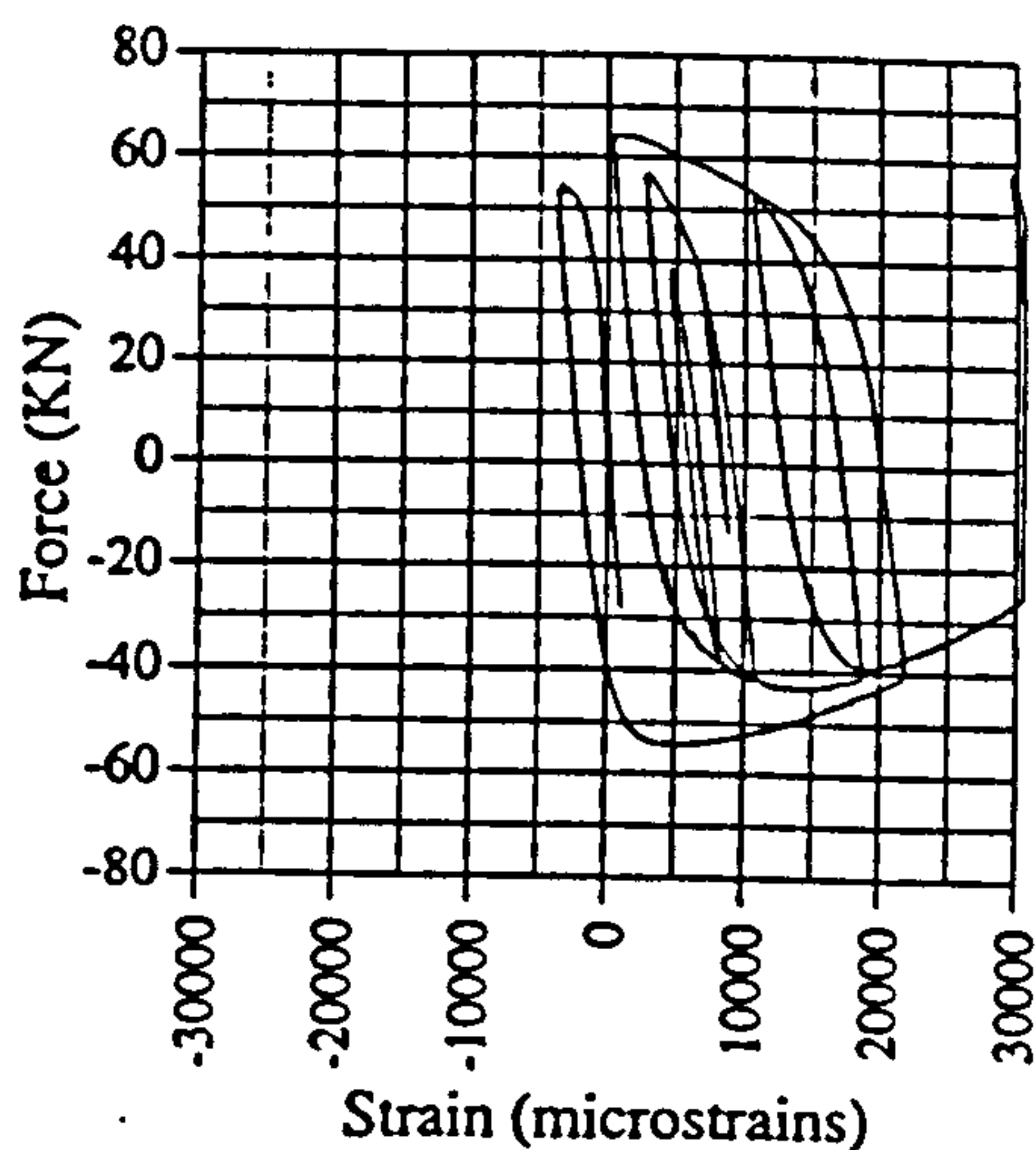


Fig. A.140 Force vs strain, IC03, G11

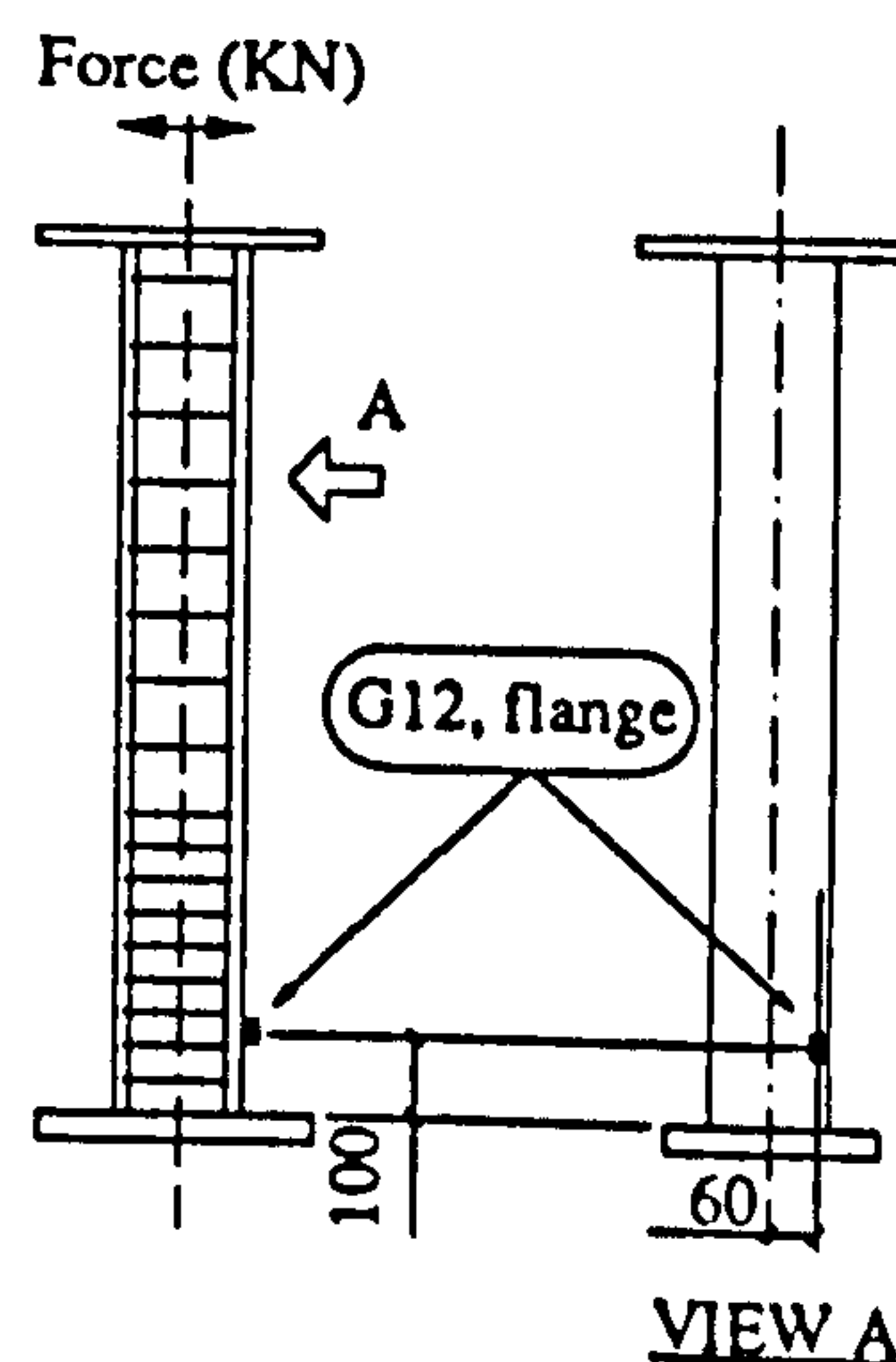
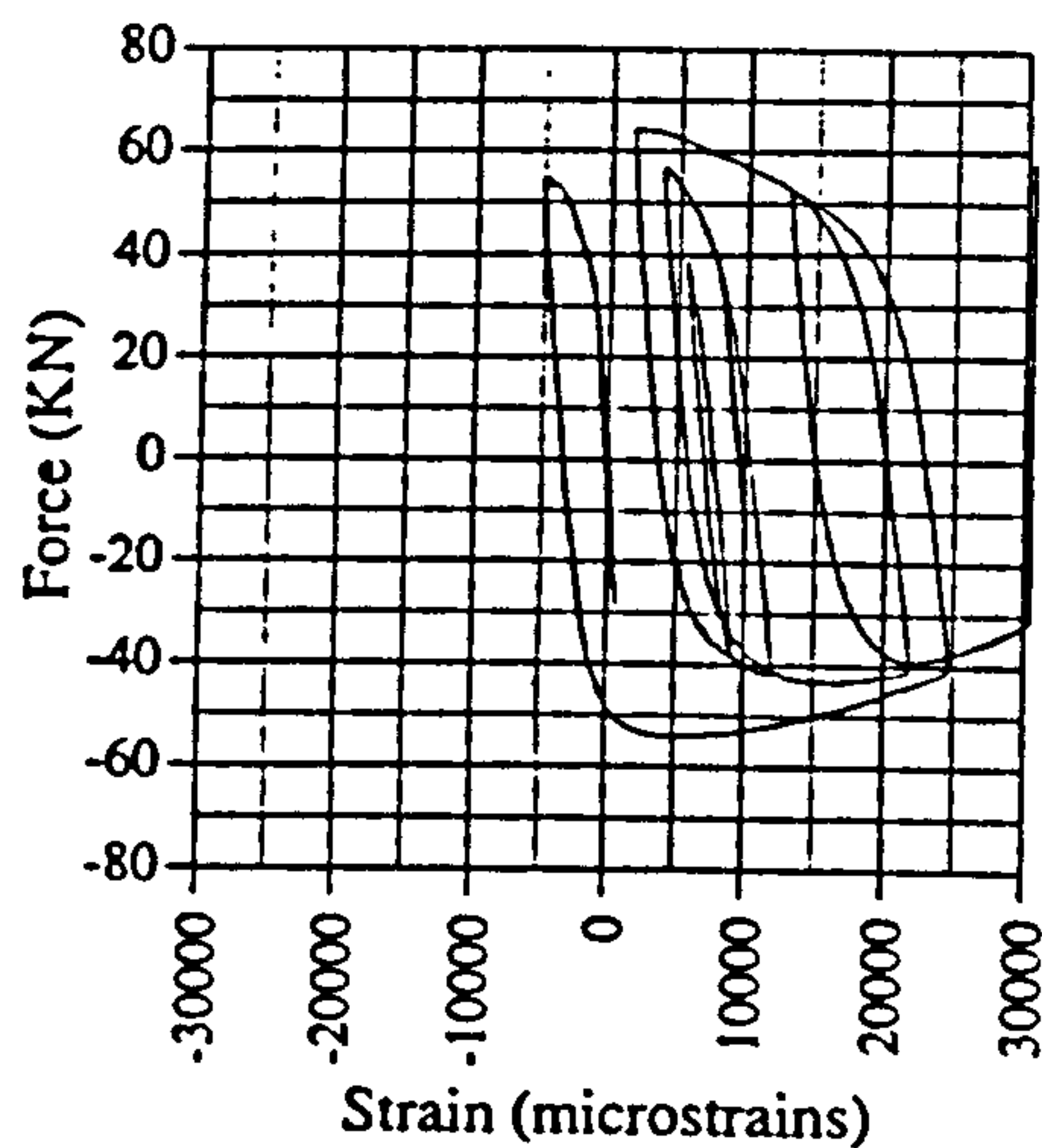


Fig. A.141 Force vs strain, IC03, G12

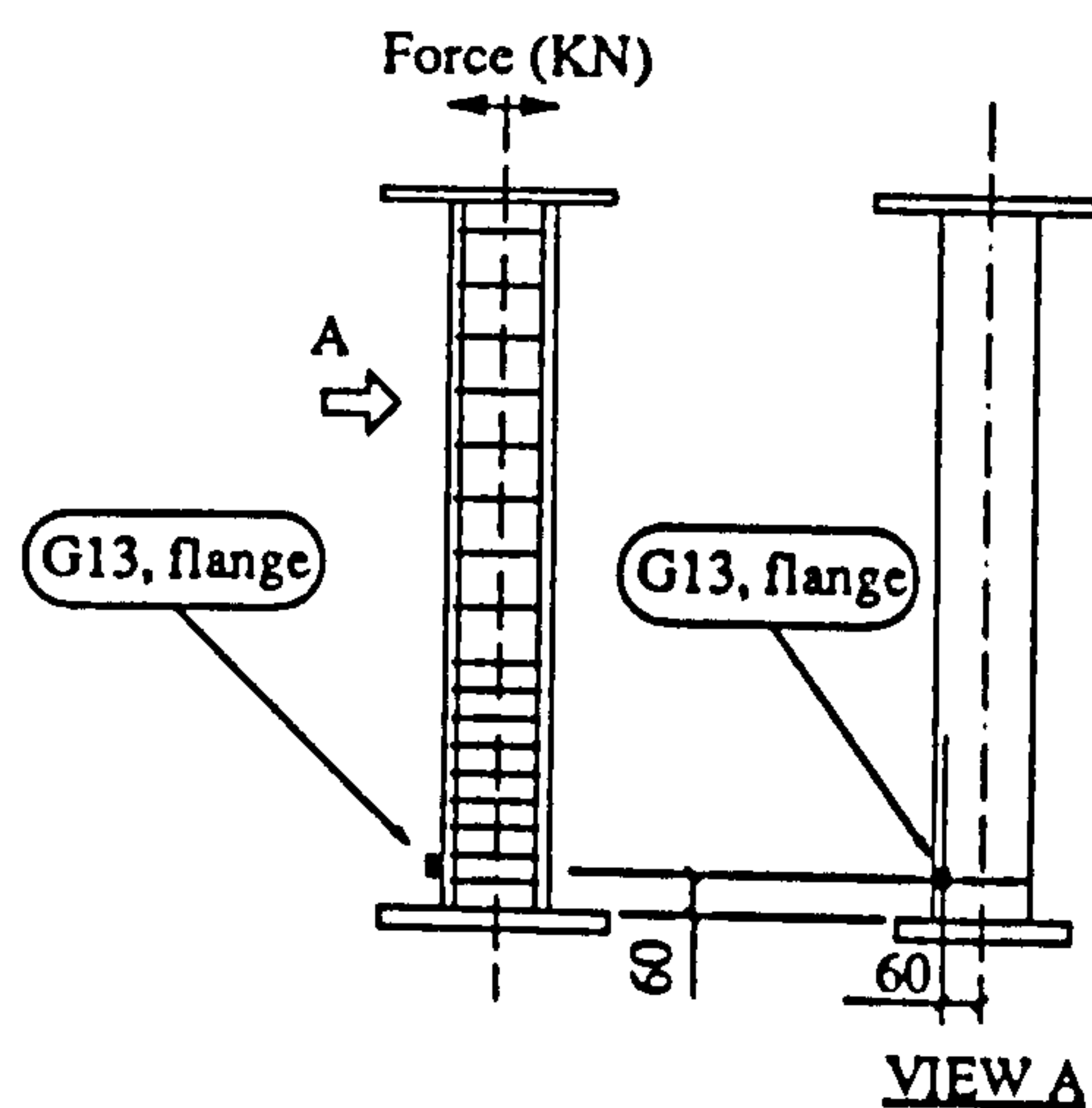
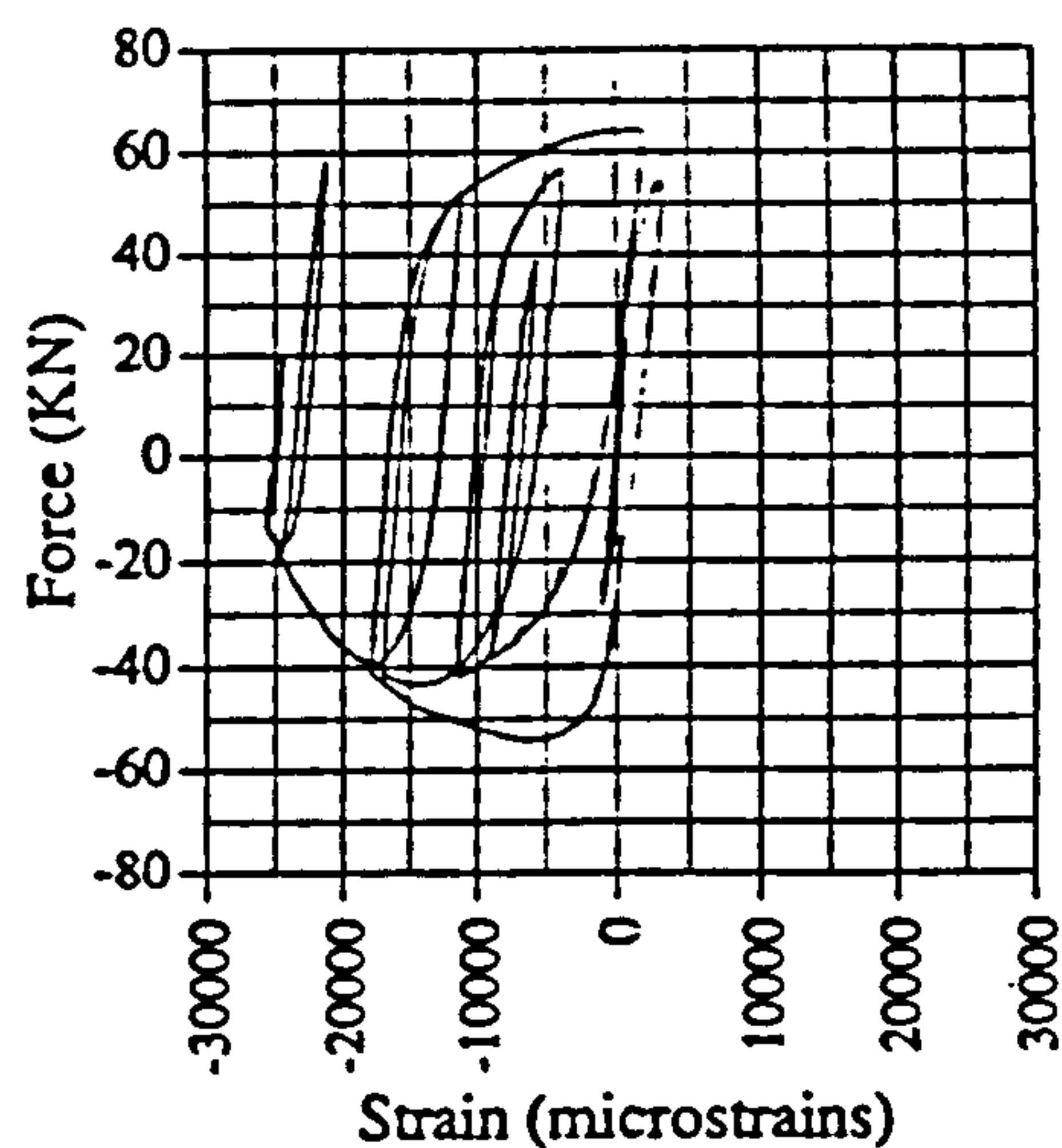


Fig. A.142 Force vs strain, IC03, G13

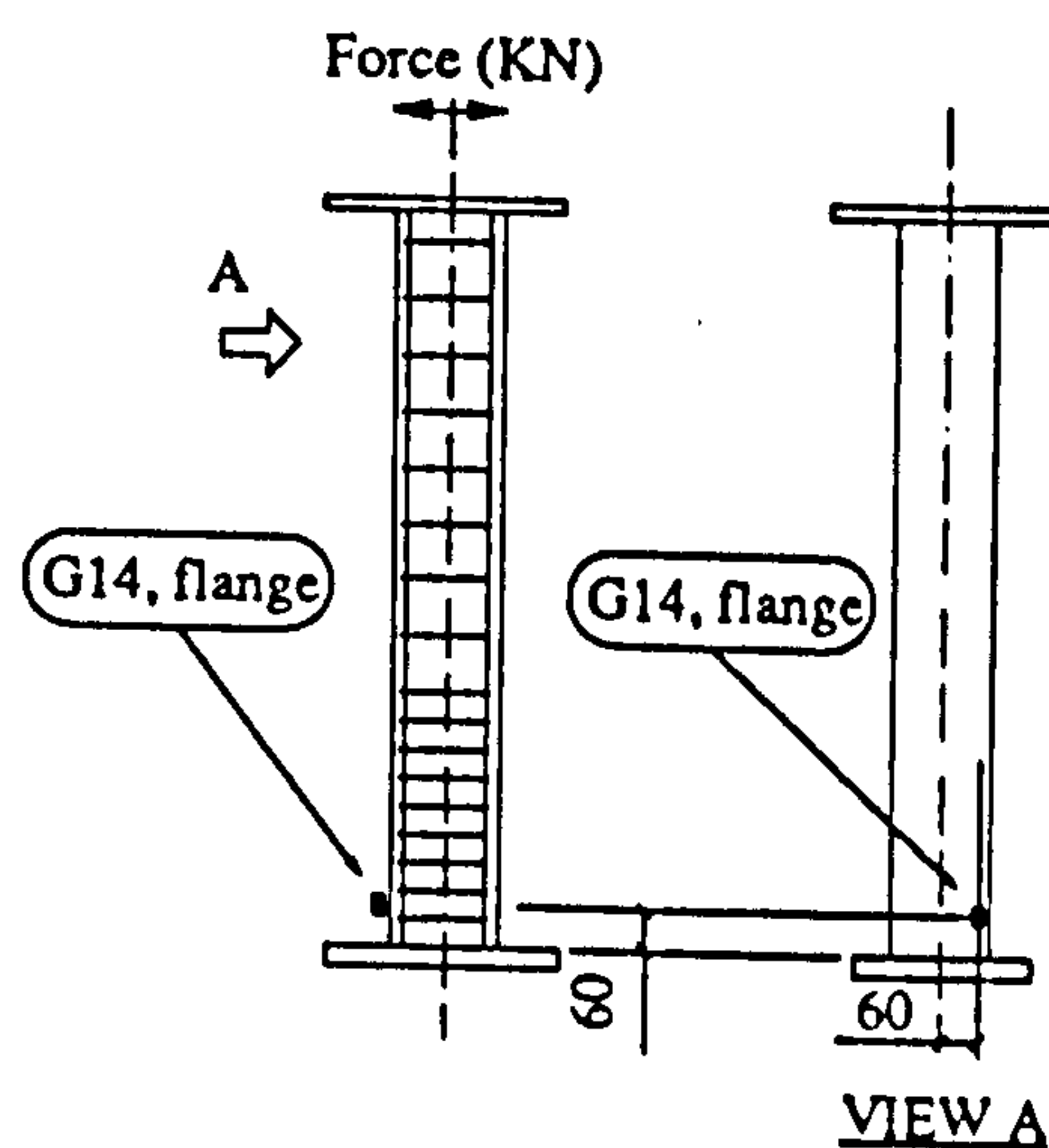
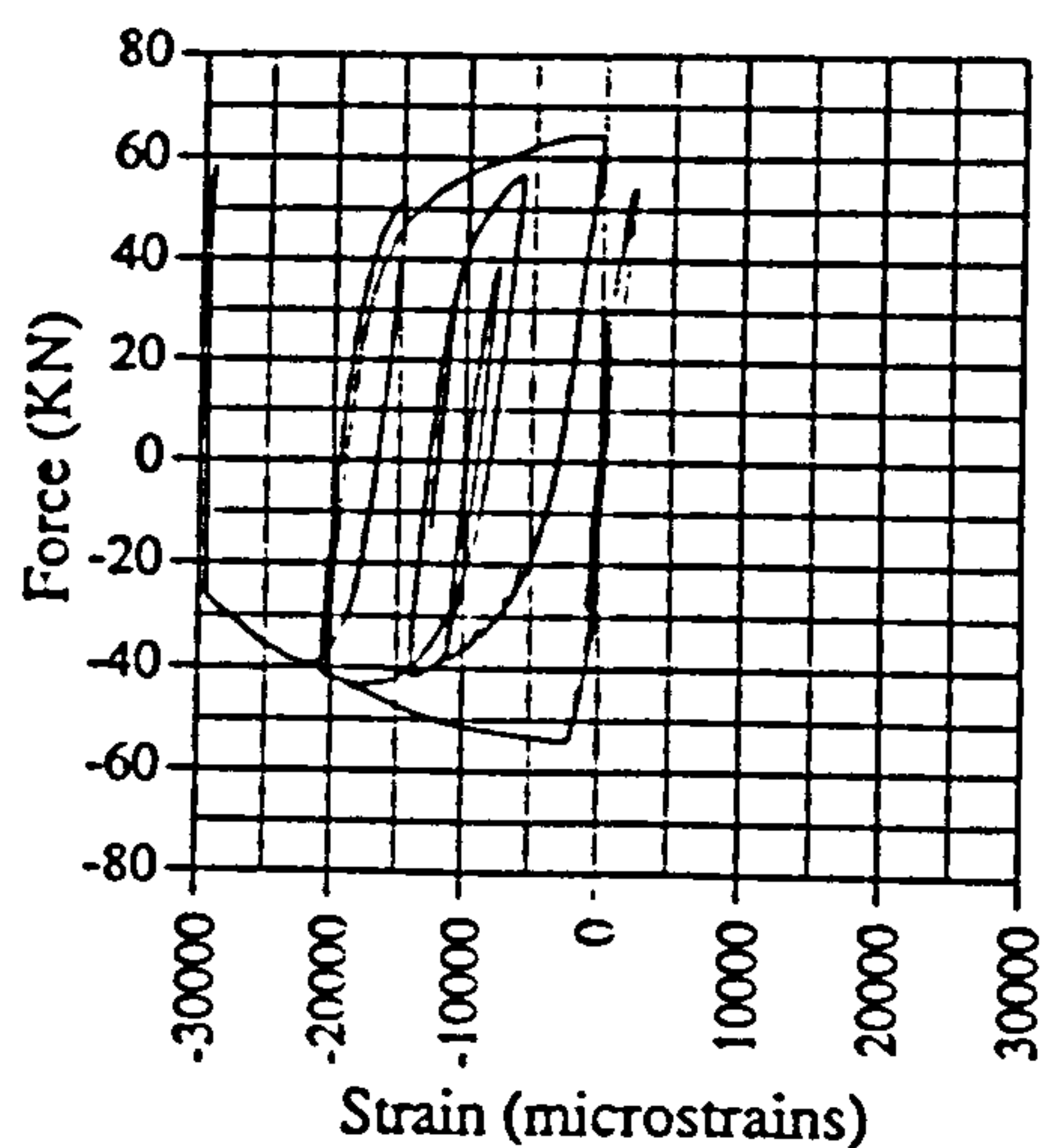


Fig. A.143 Force vs strain, IC03, G14

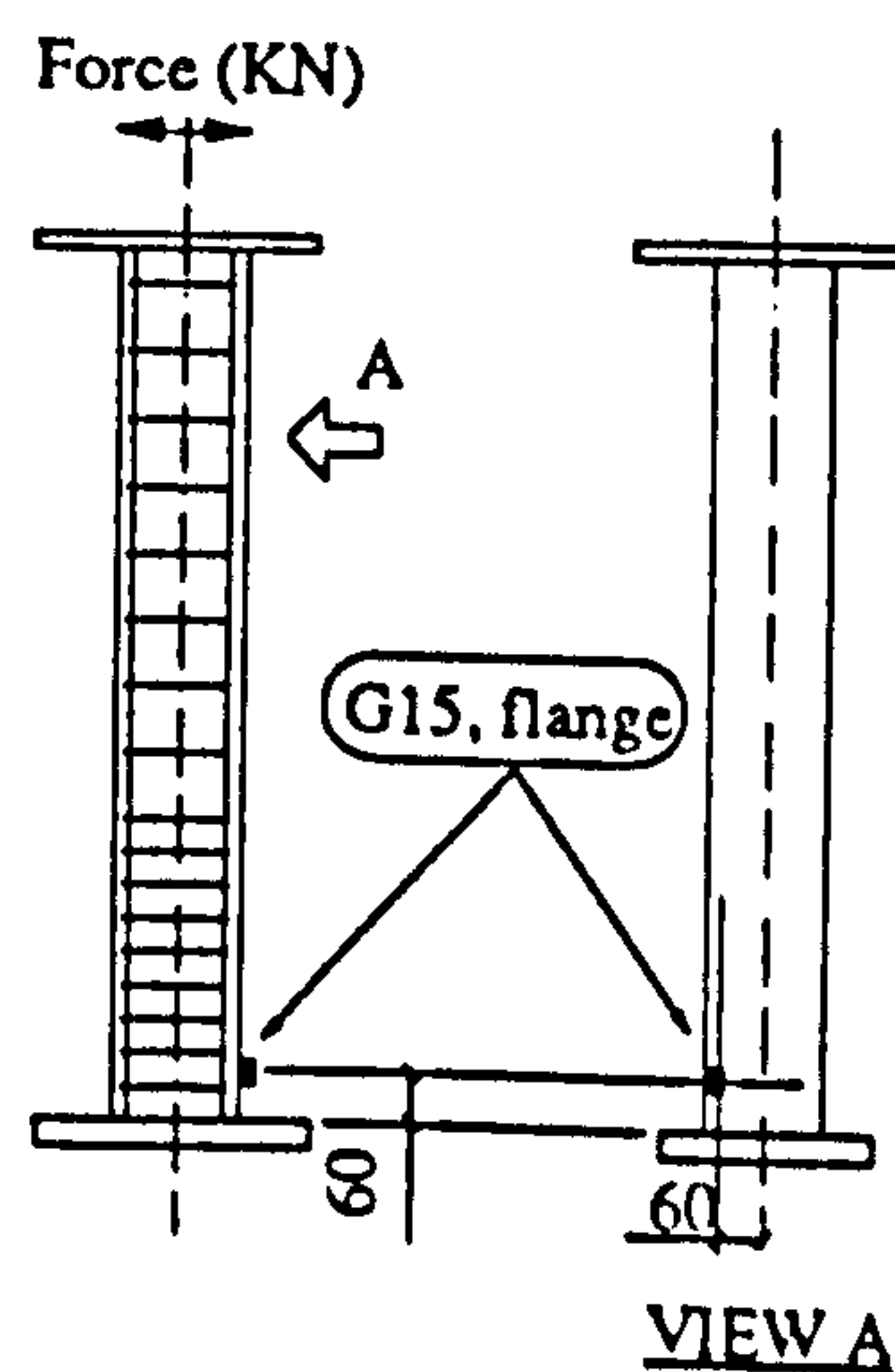
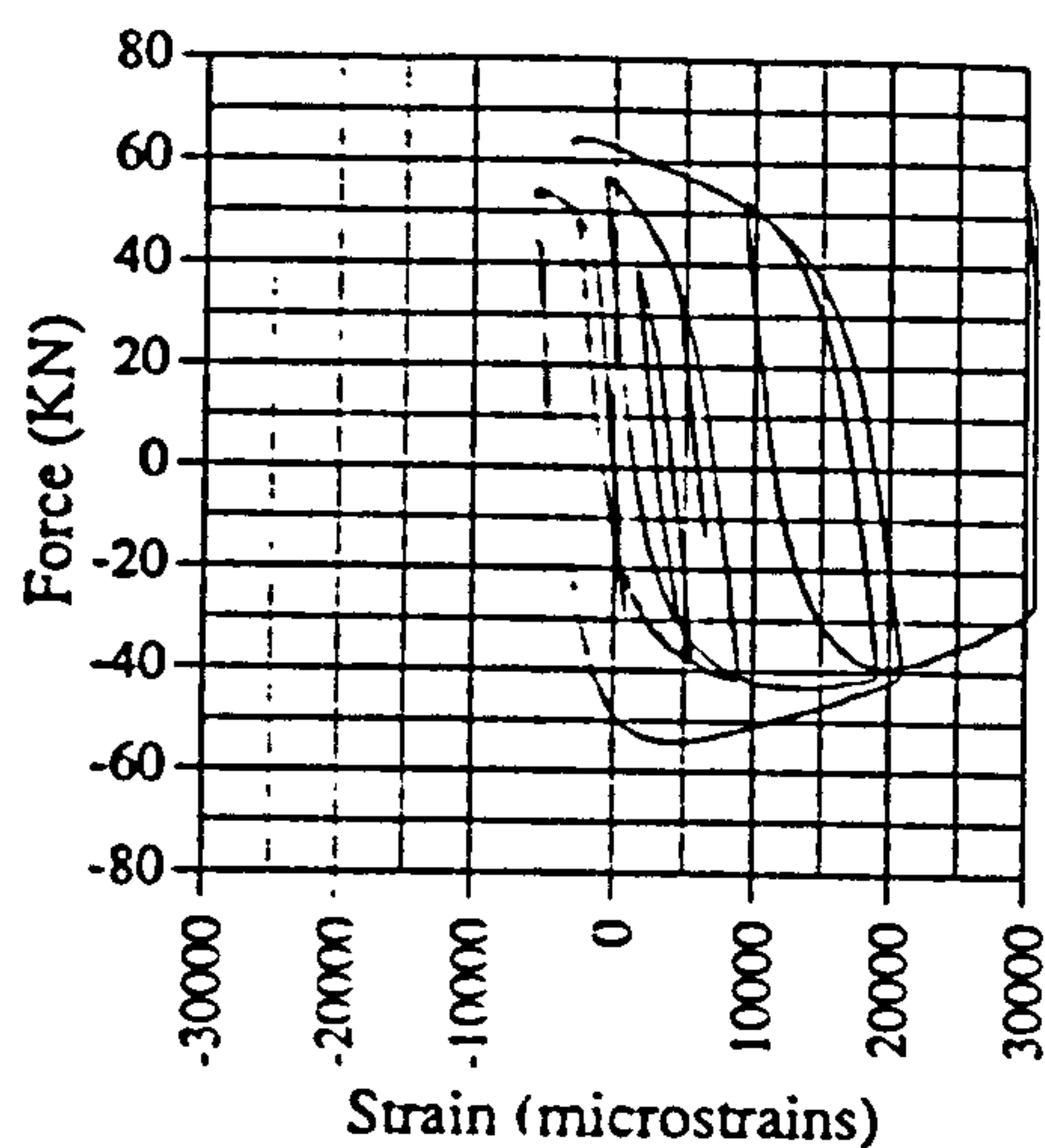


Fig. A.144 Force vs strain, IC03, G15

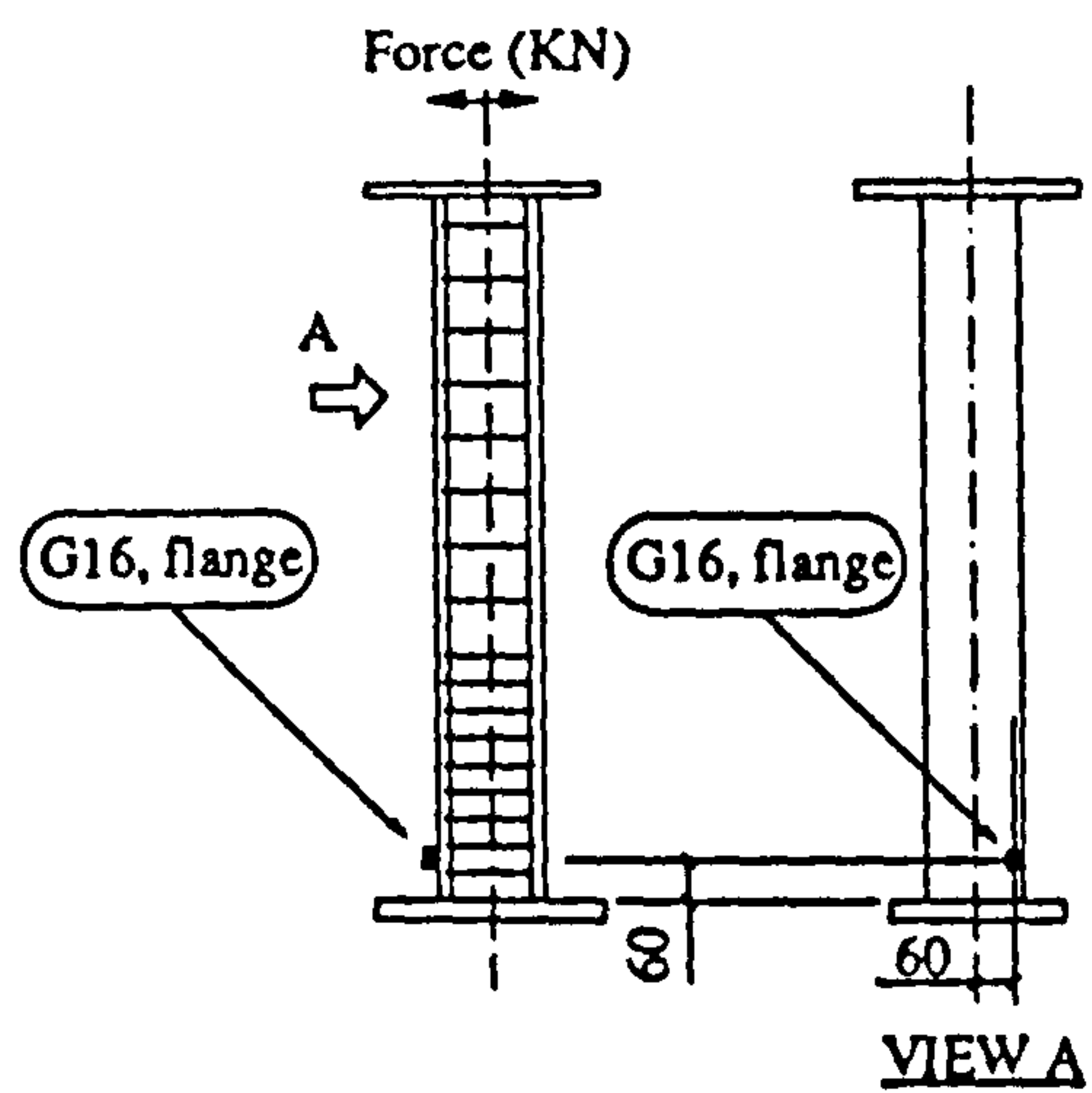
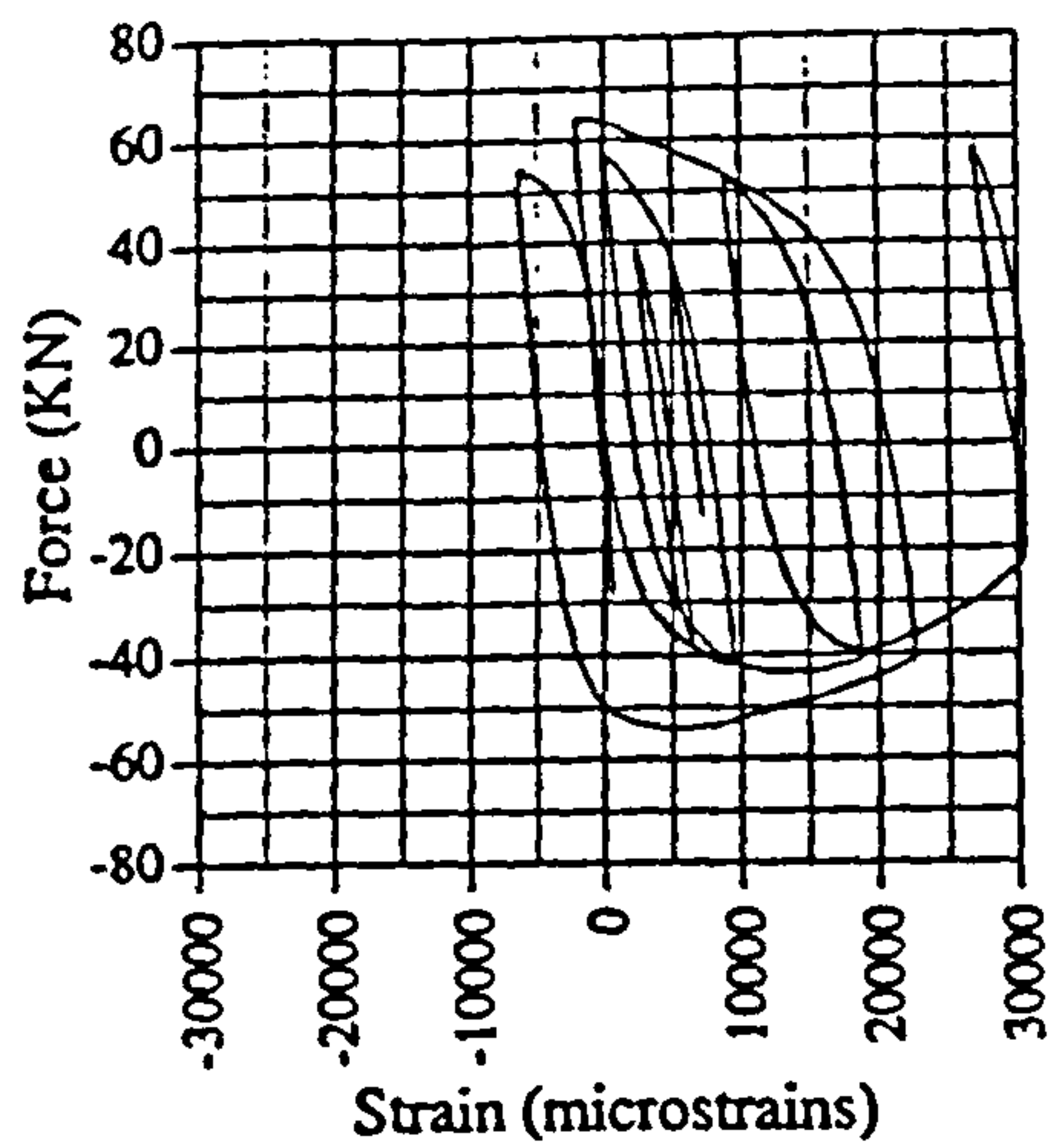


Fig. A.145 Force vs strain, IC03, G16

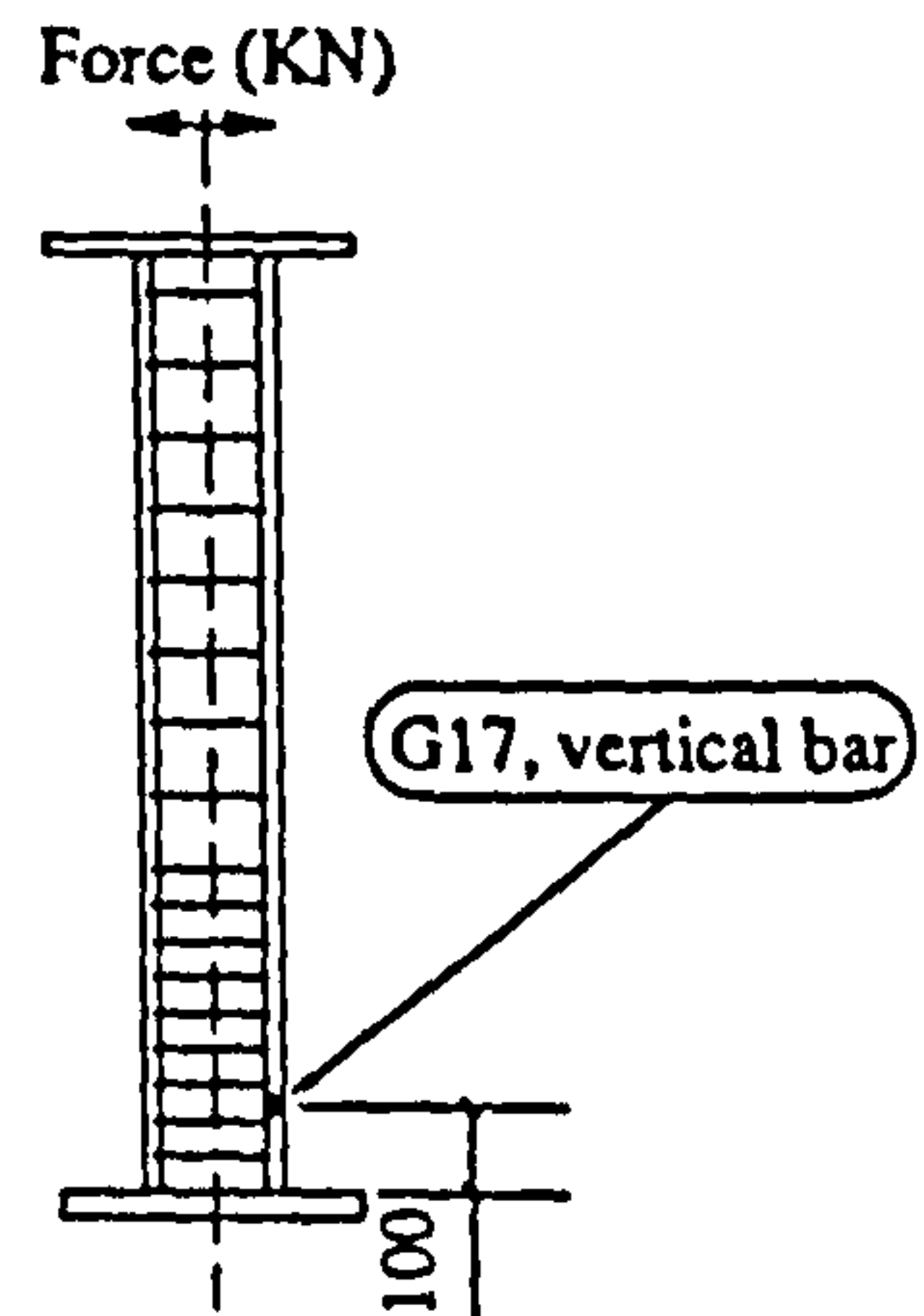
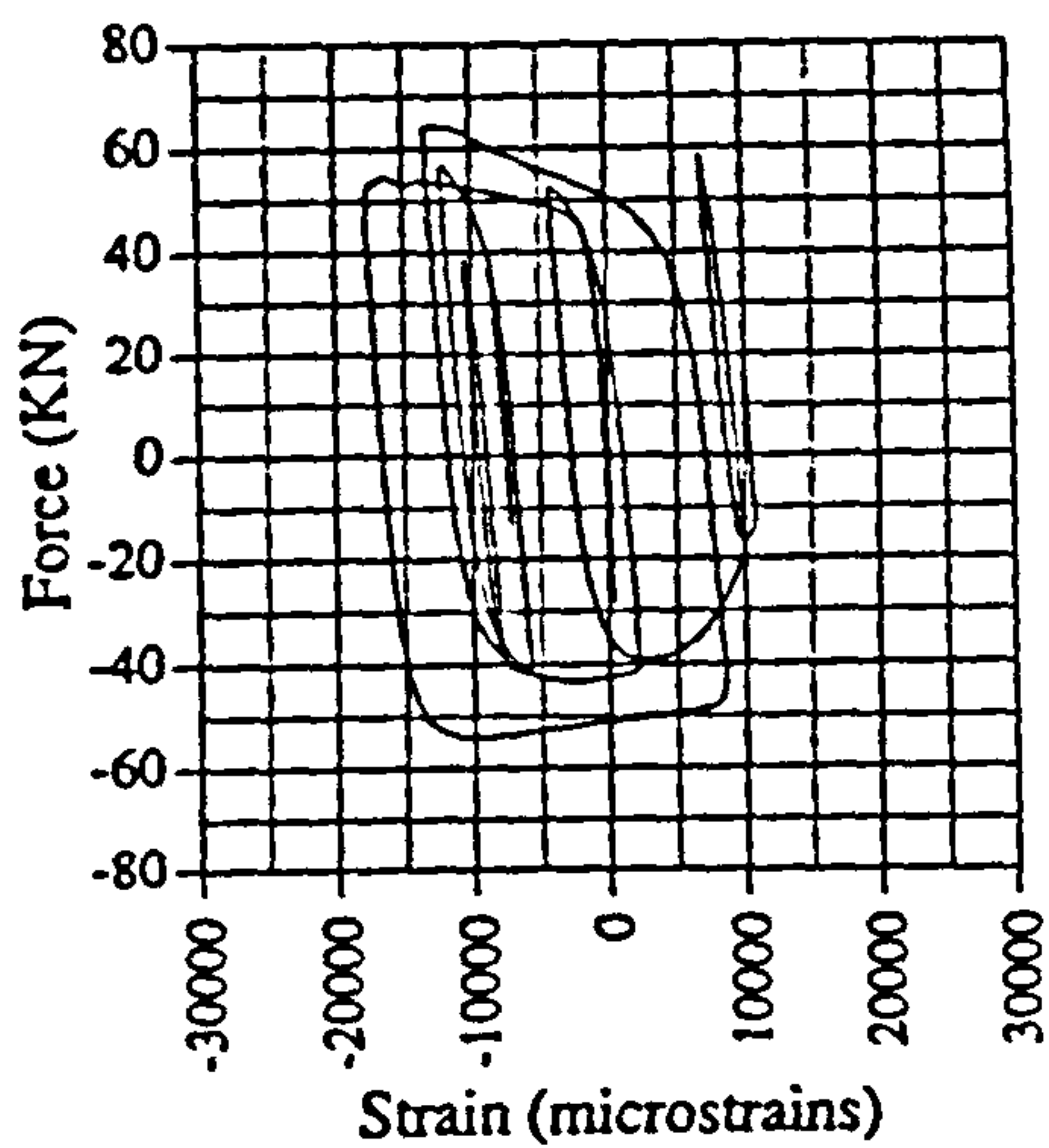


Fig. A.146 Force vs strain, IC03, G17

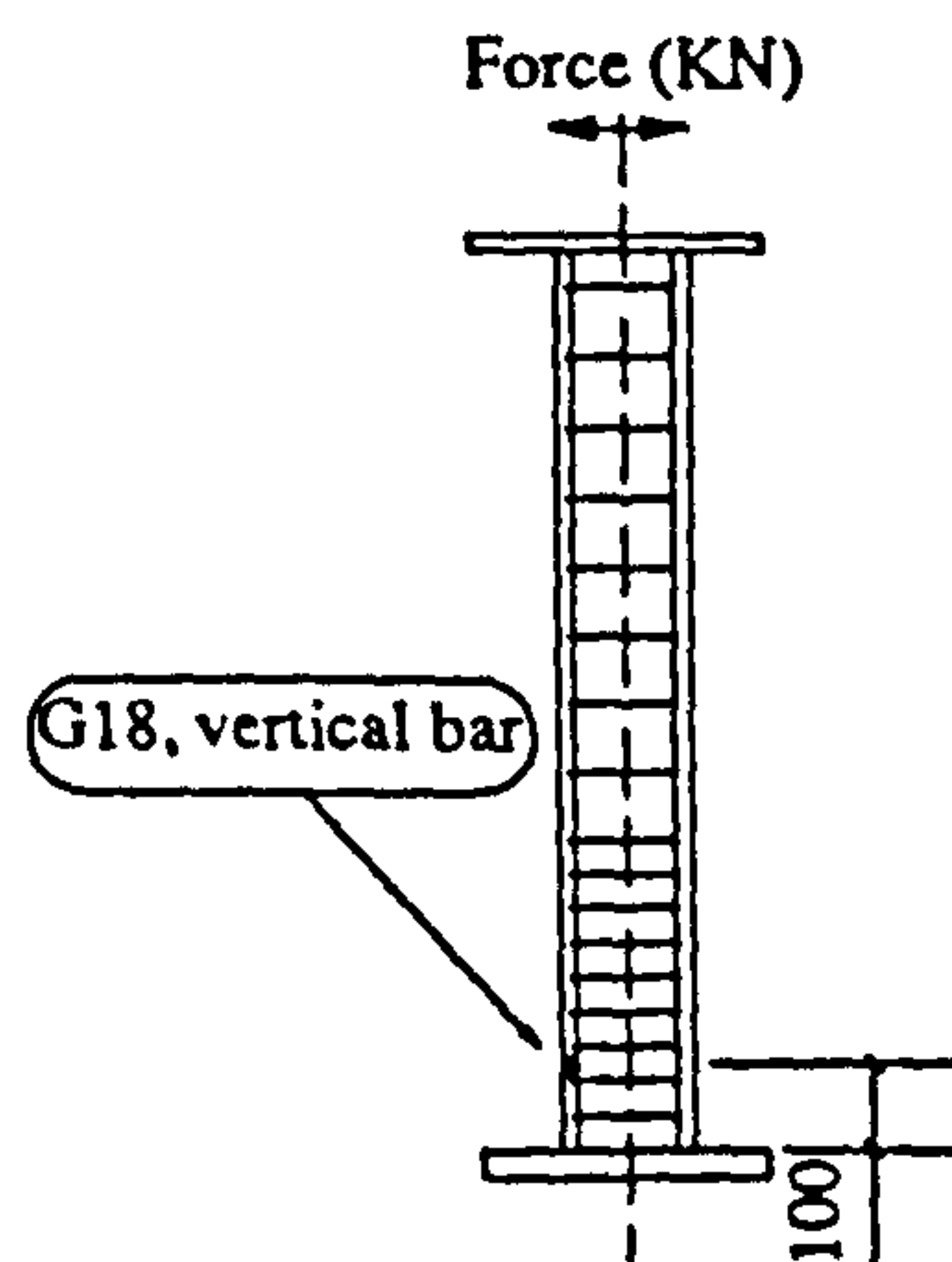
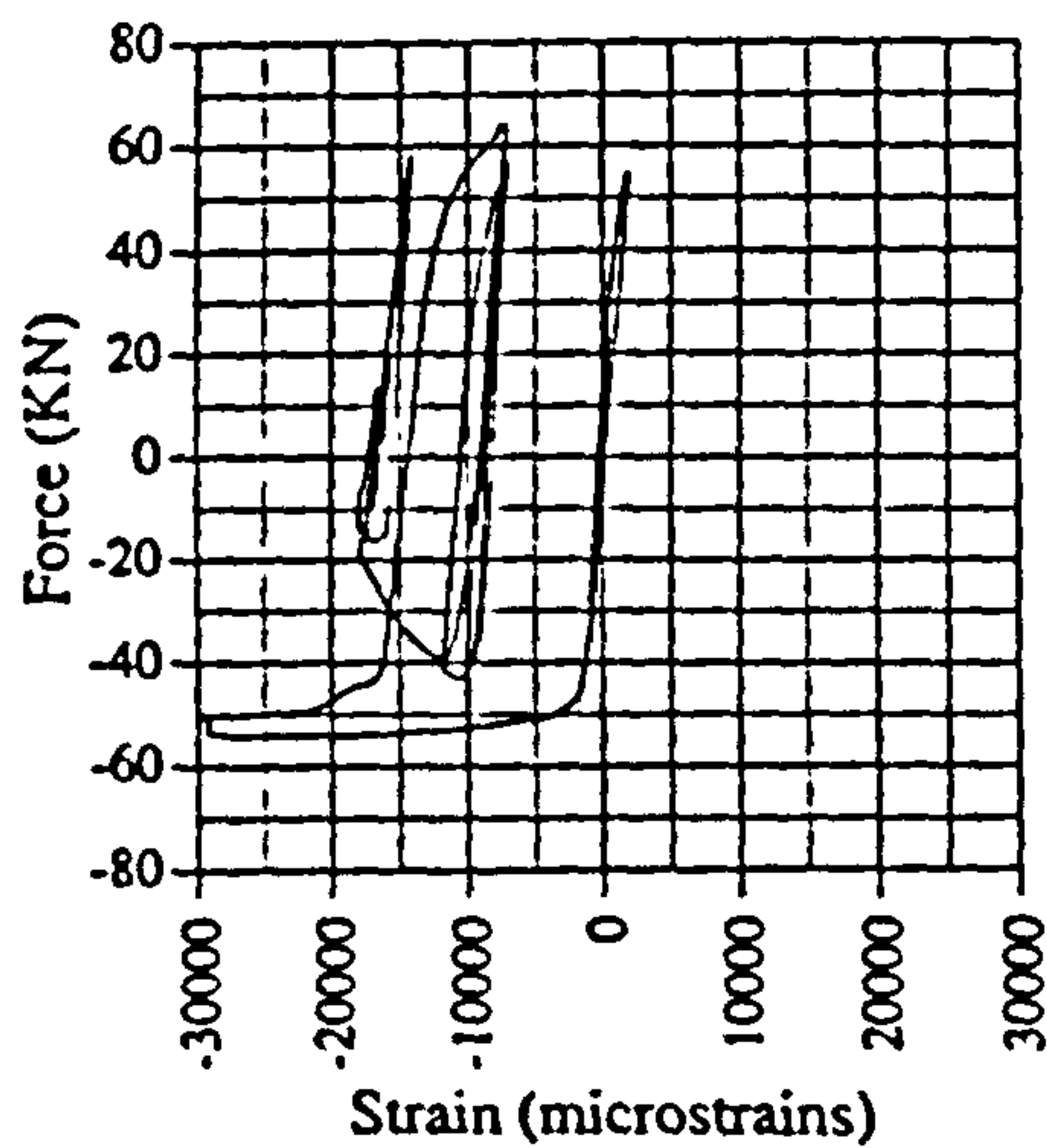


Fig. A.147 Force vs strain, IC03, G18

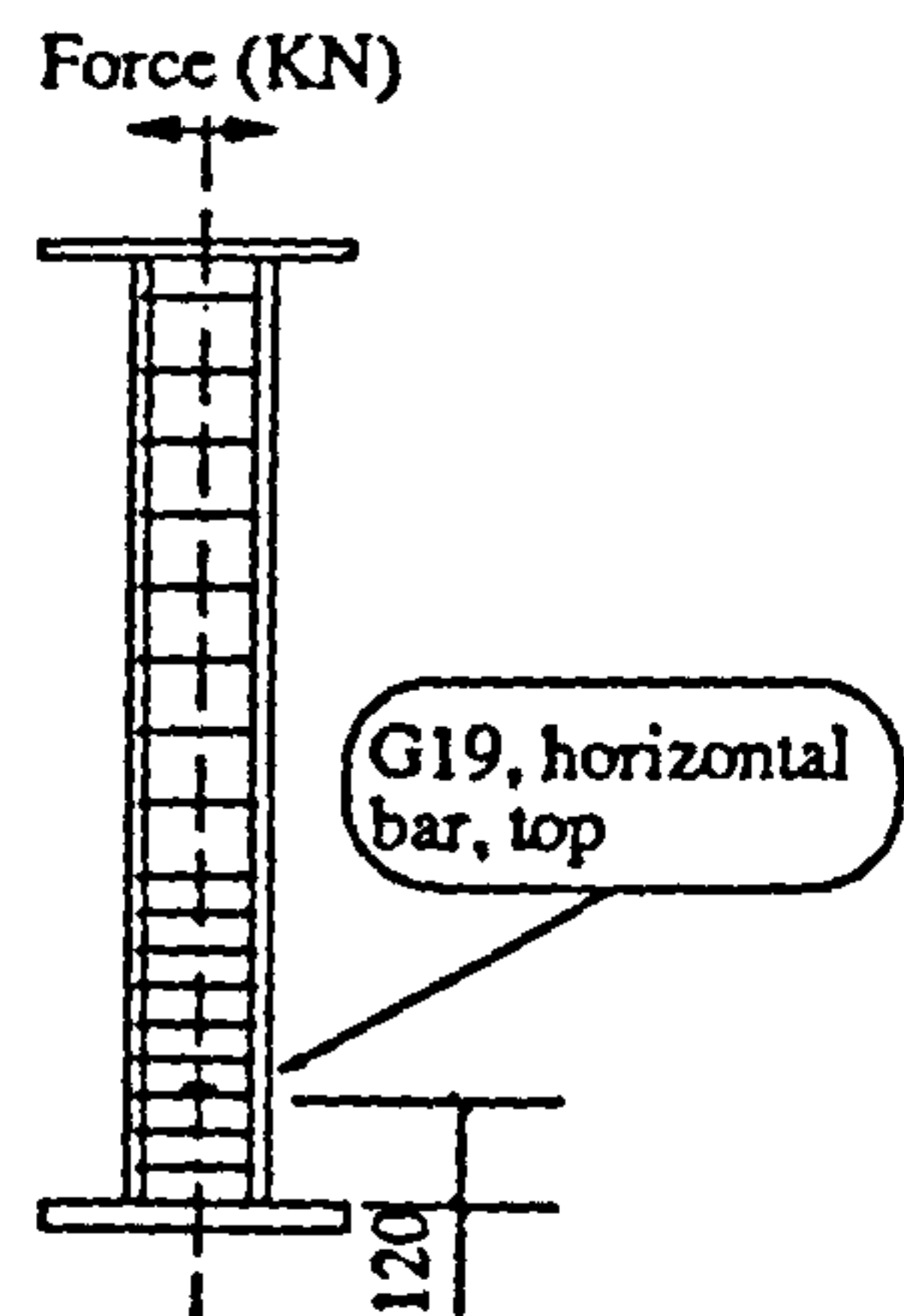
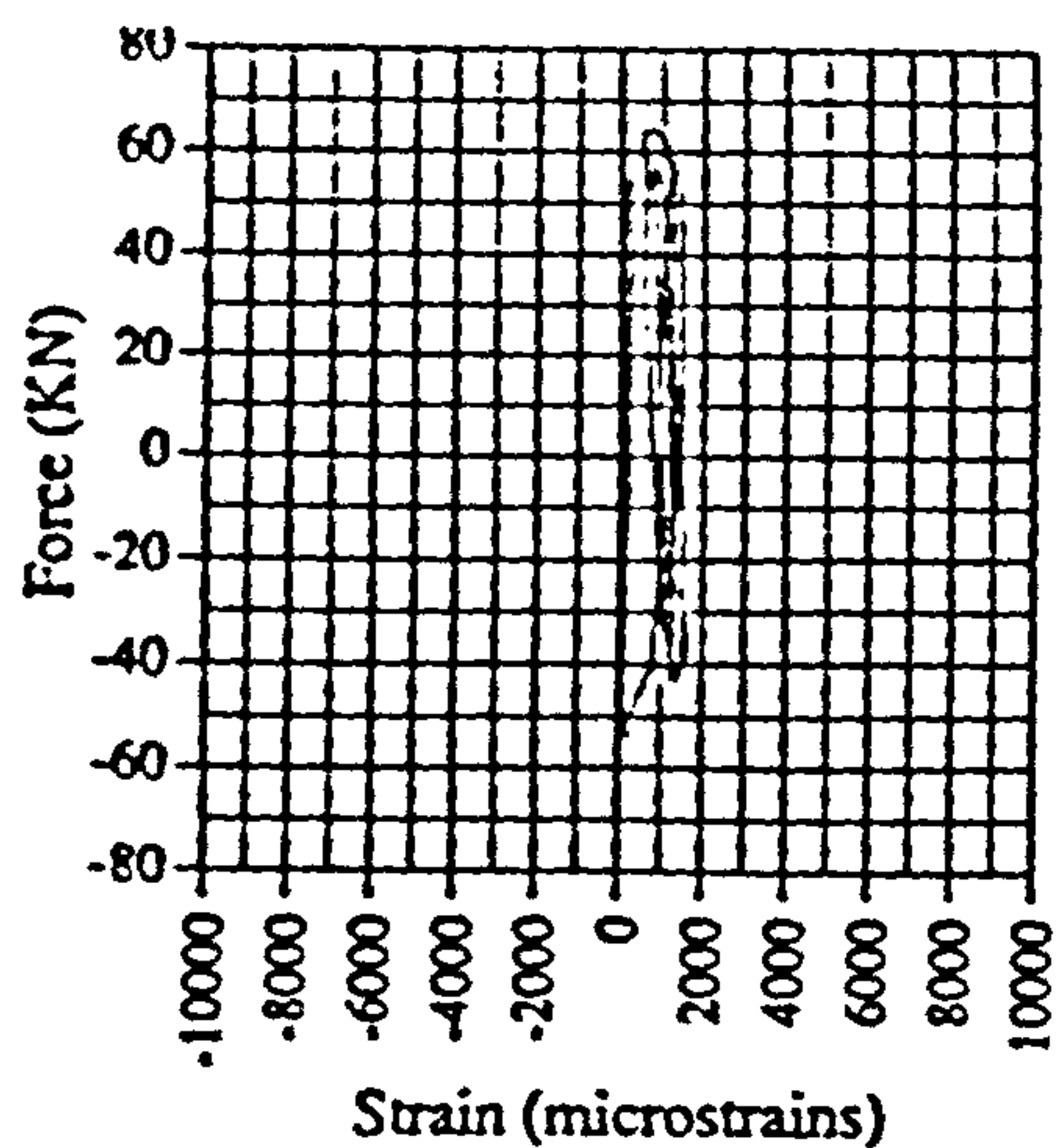


Fig. A.148 Force vs strain, IC03, G19

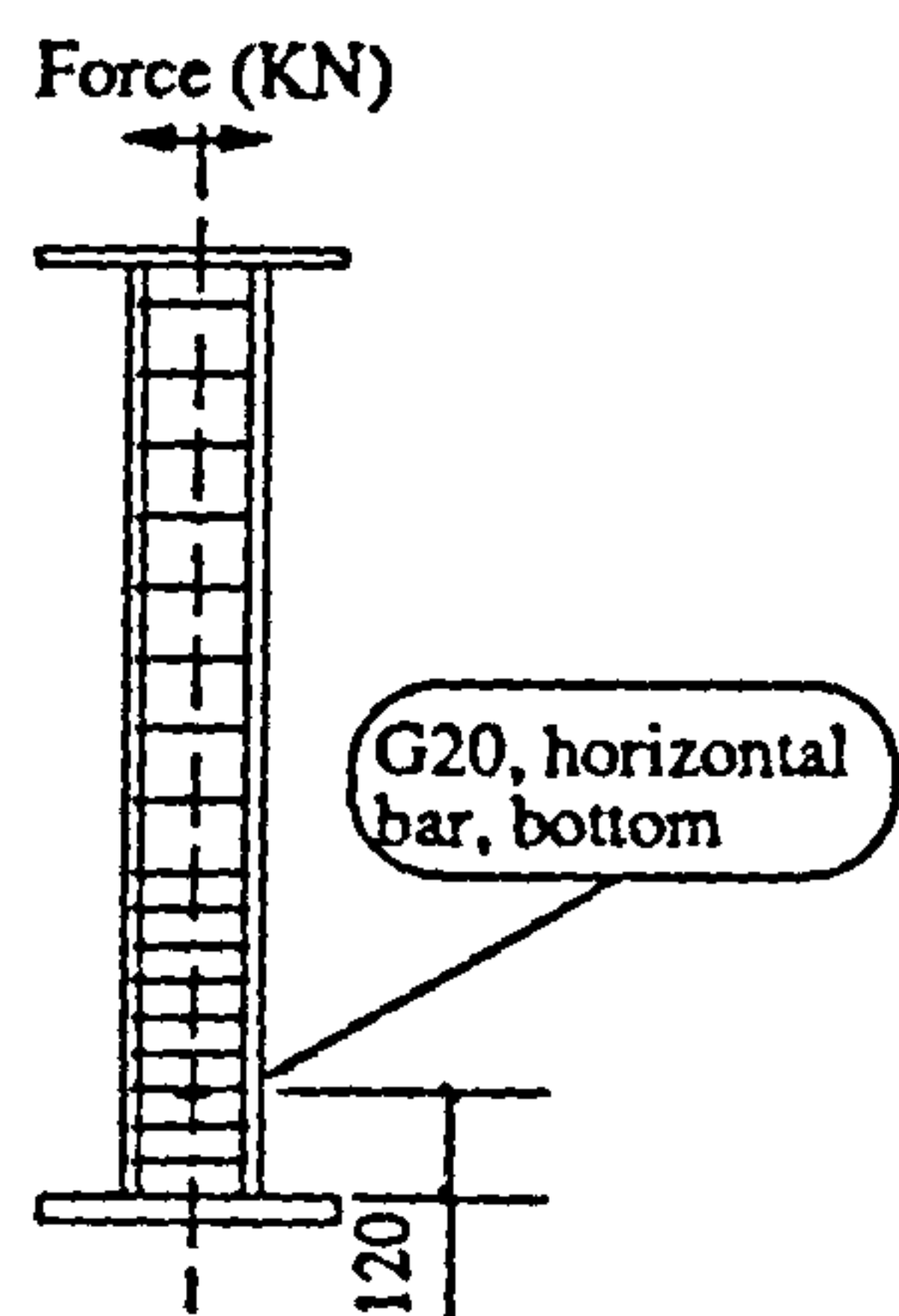
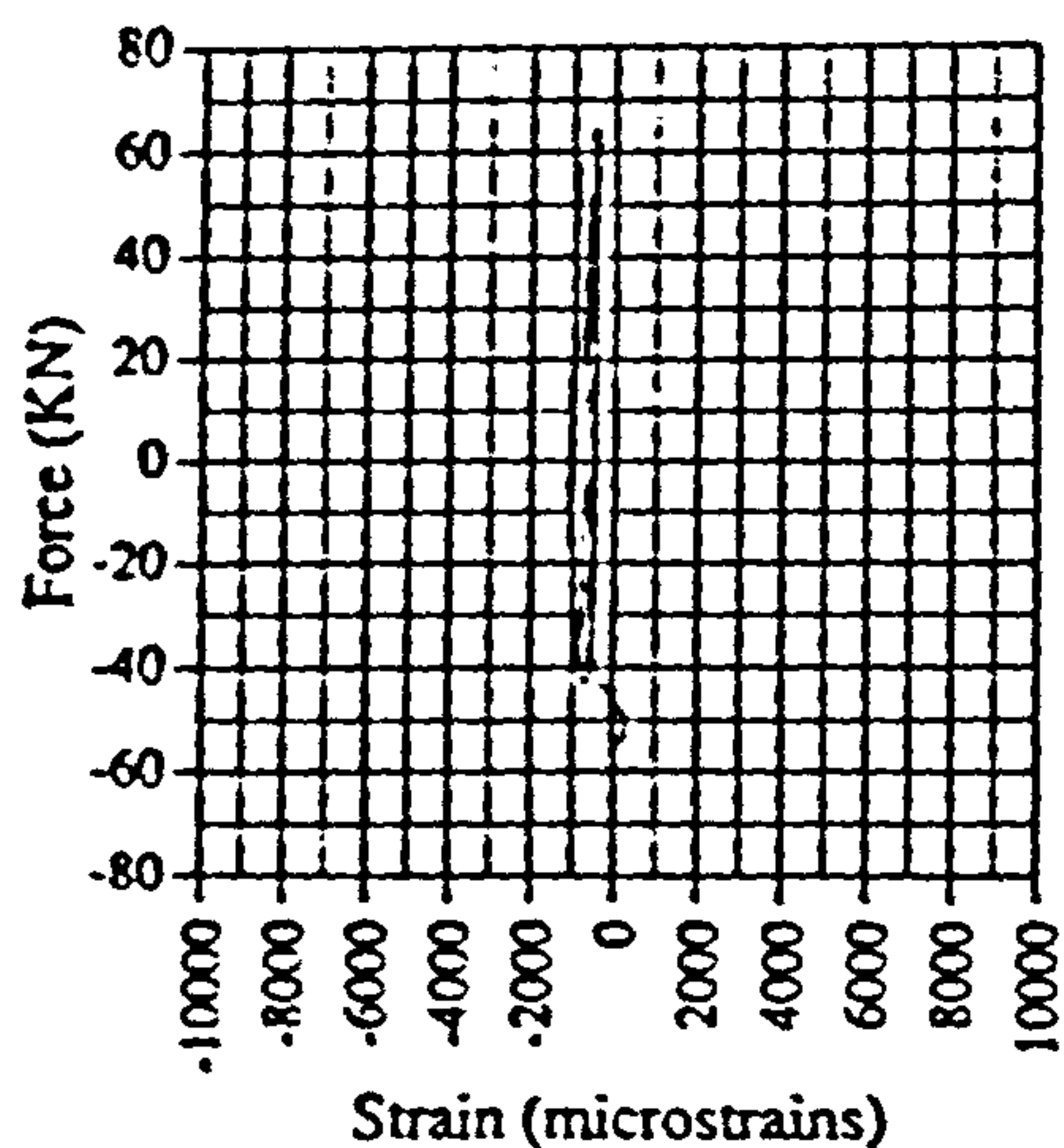


Fig. A.149 Force vs strain, IC03, G20

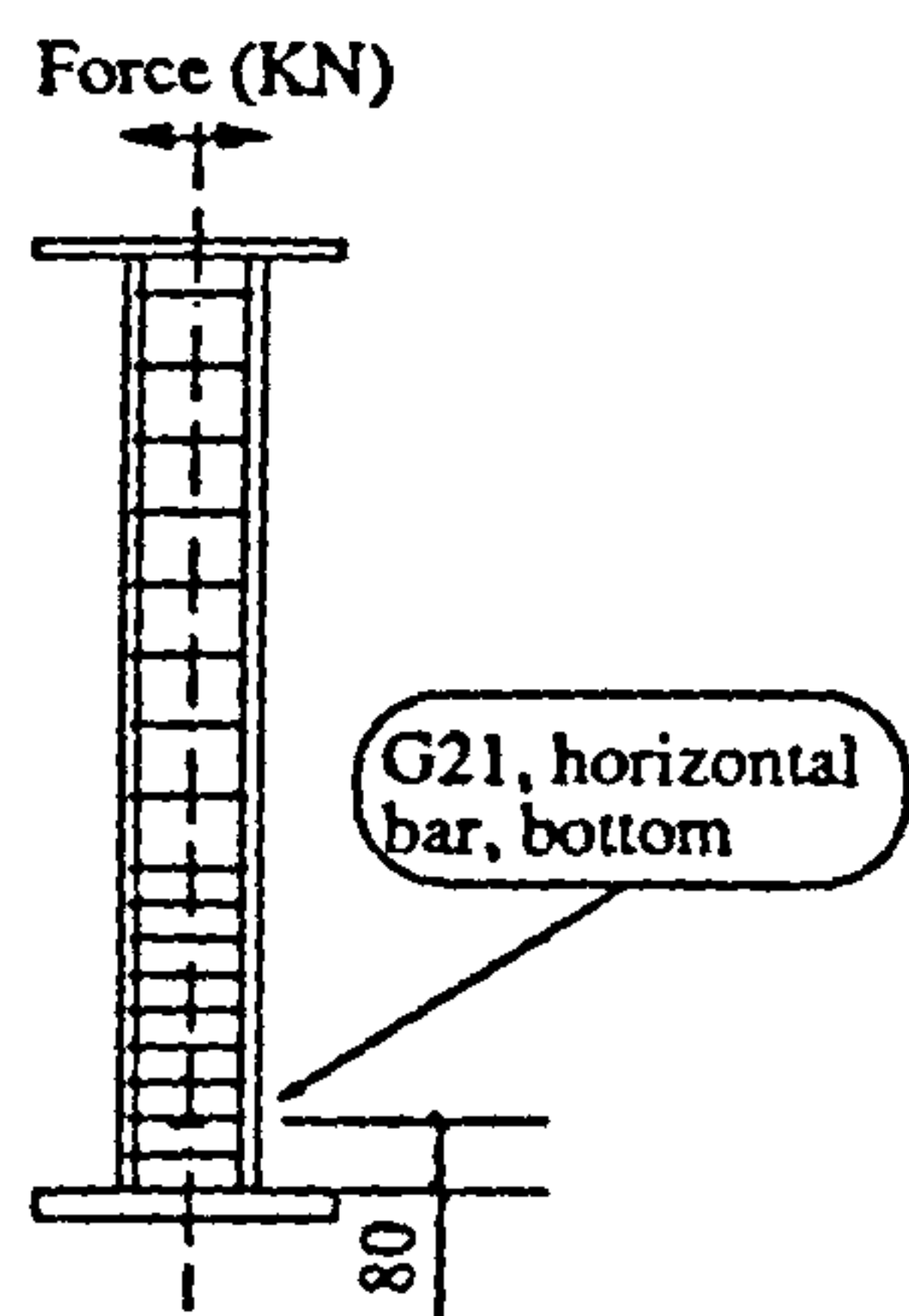
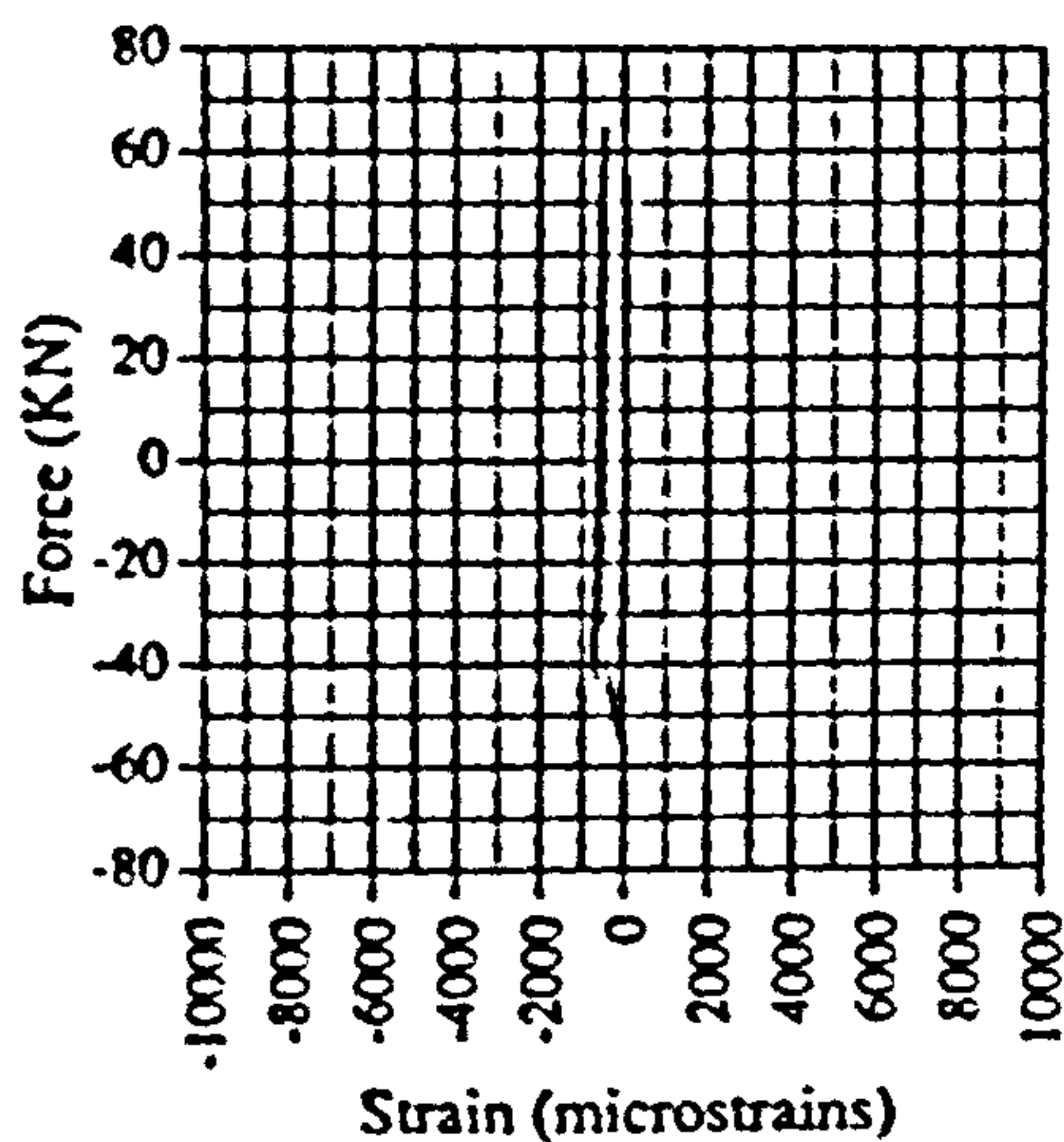


Fig. A.150 Force vs strain, IC03, G21

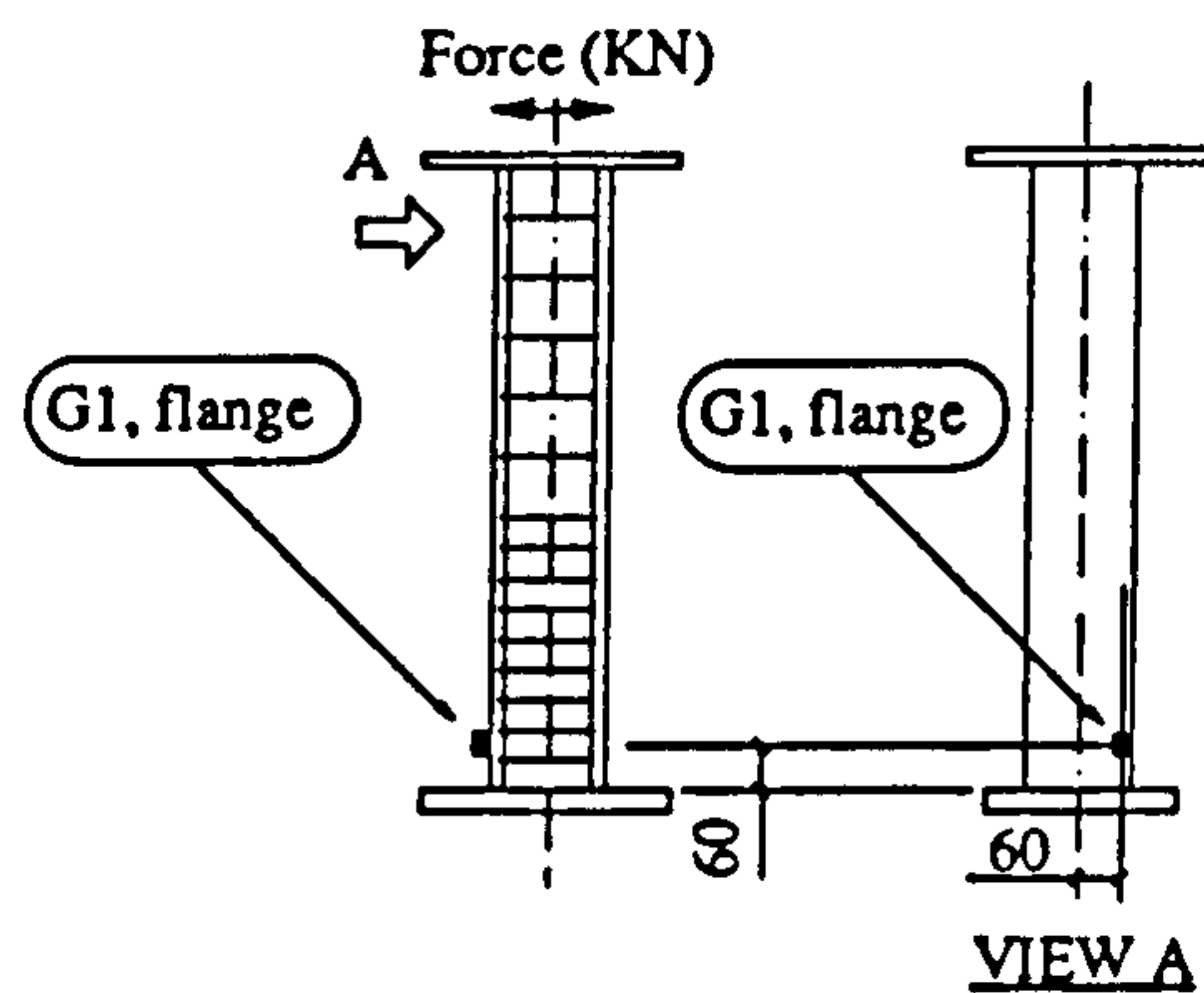
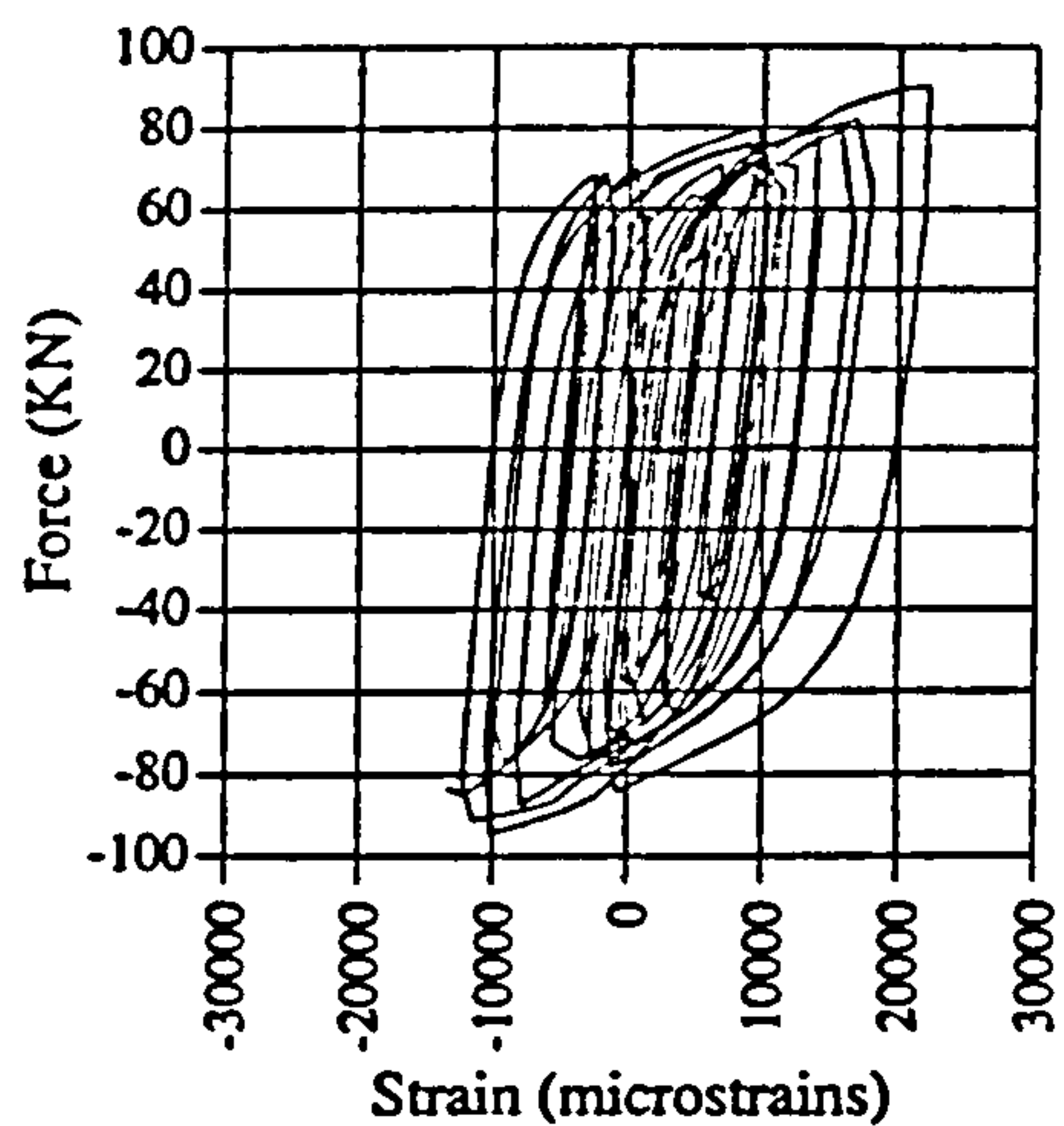


Fig. A.151 Force vs strain, EM05, G1

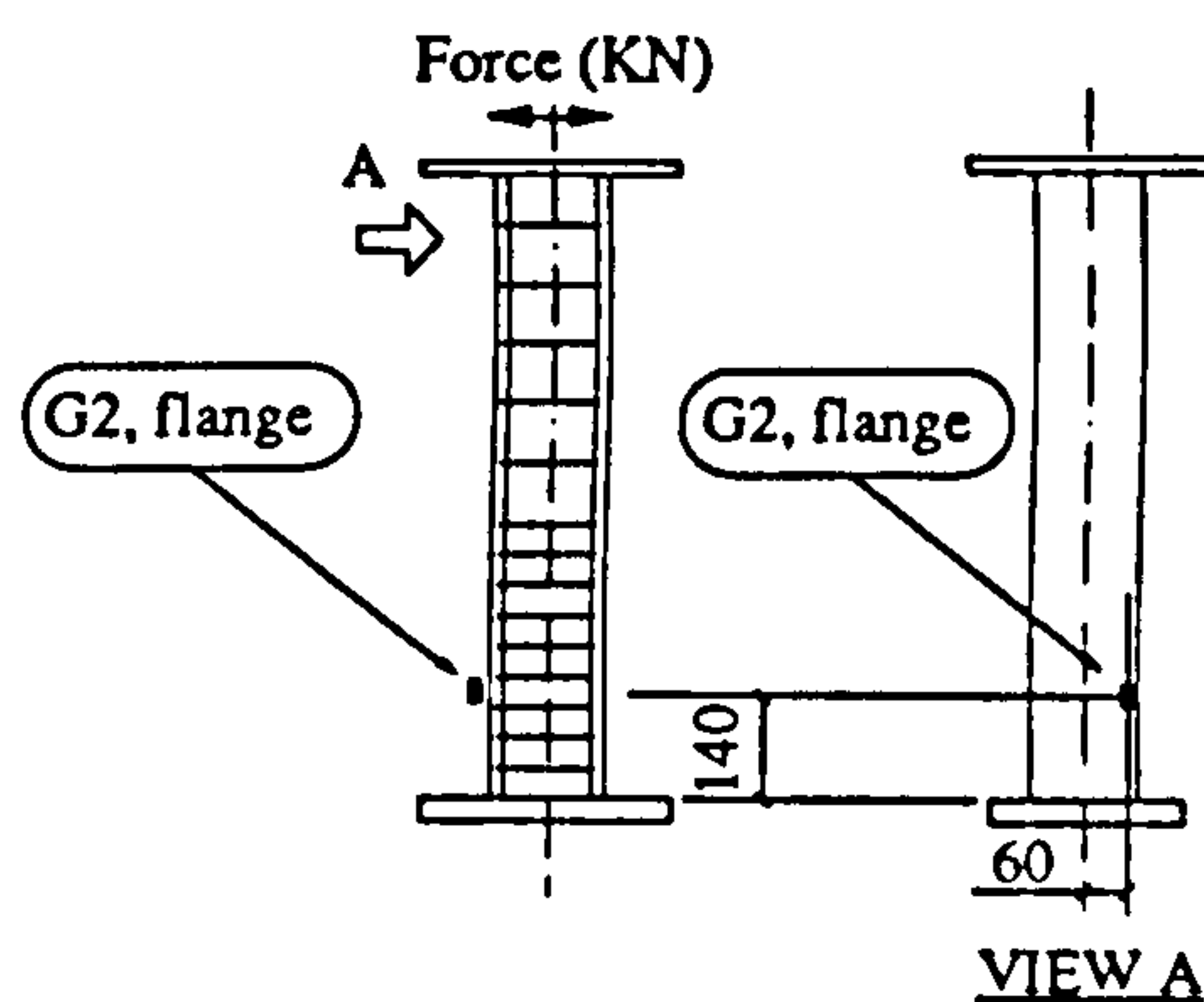
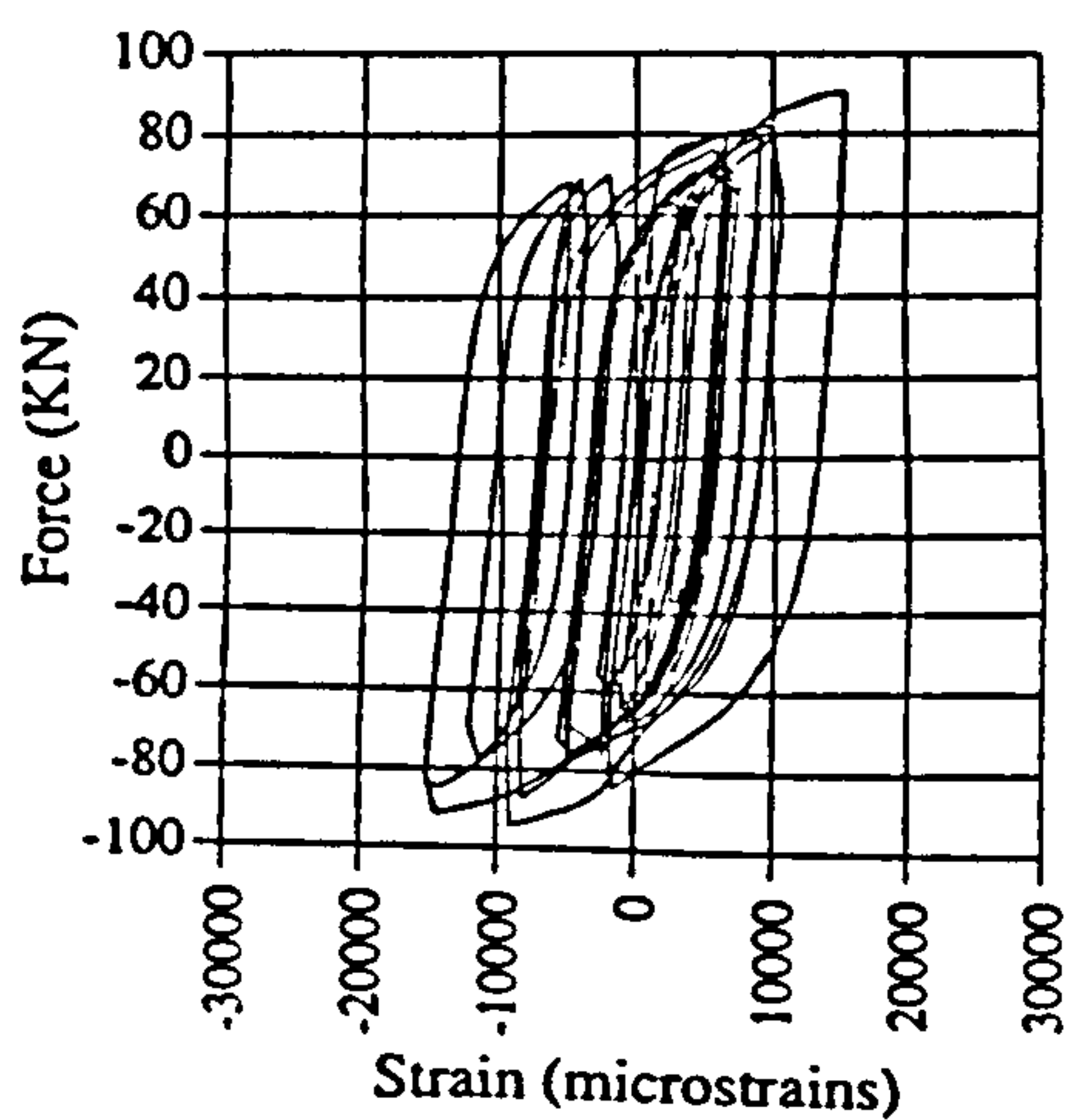


Fig. A.152 Force vs strain, EM05, G2

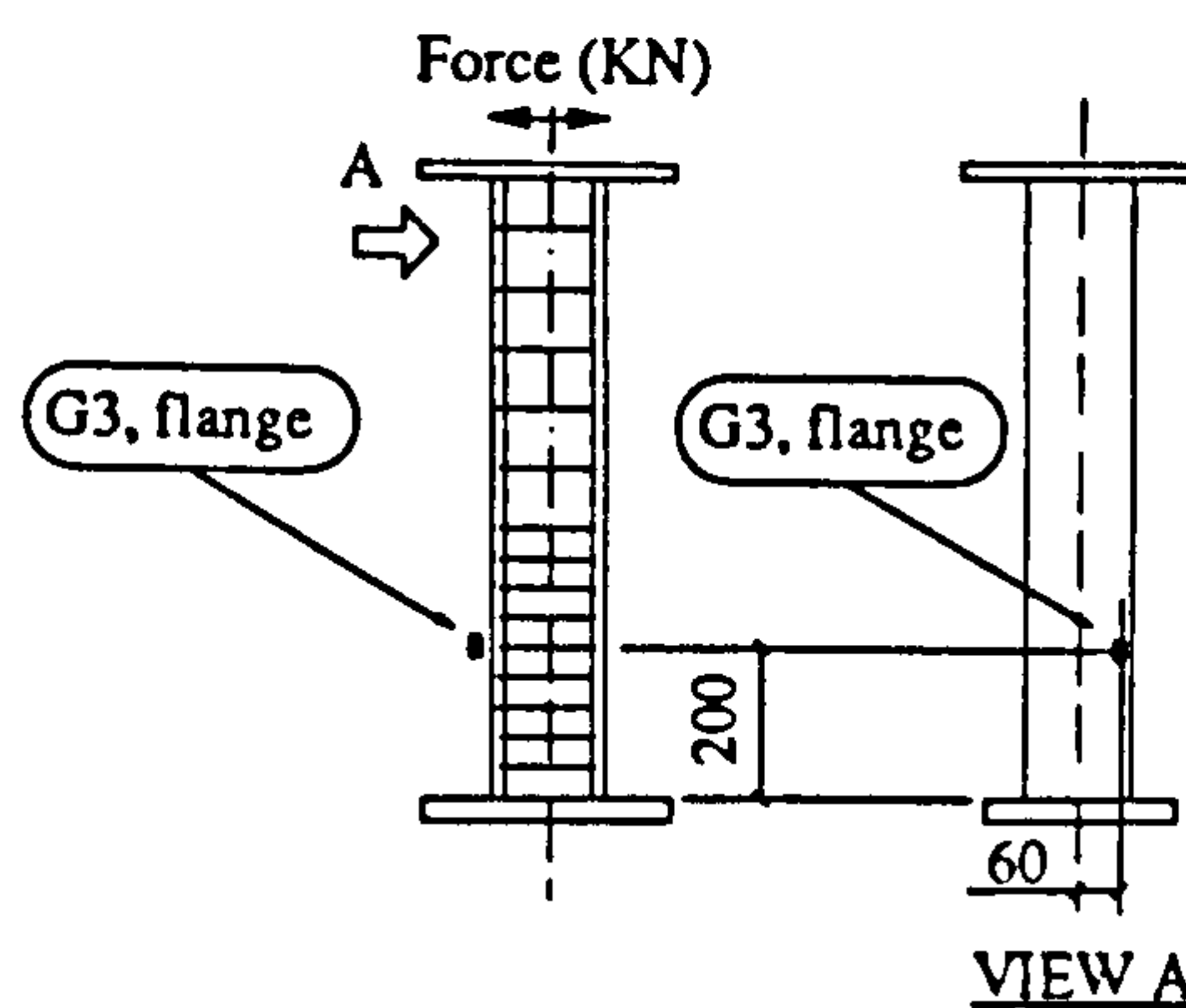
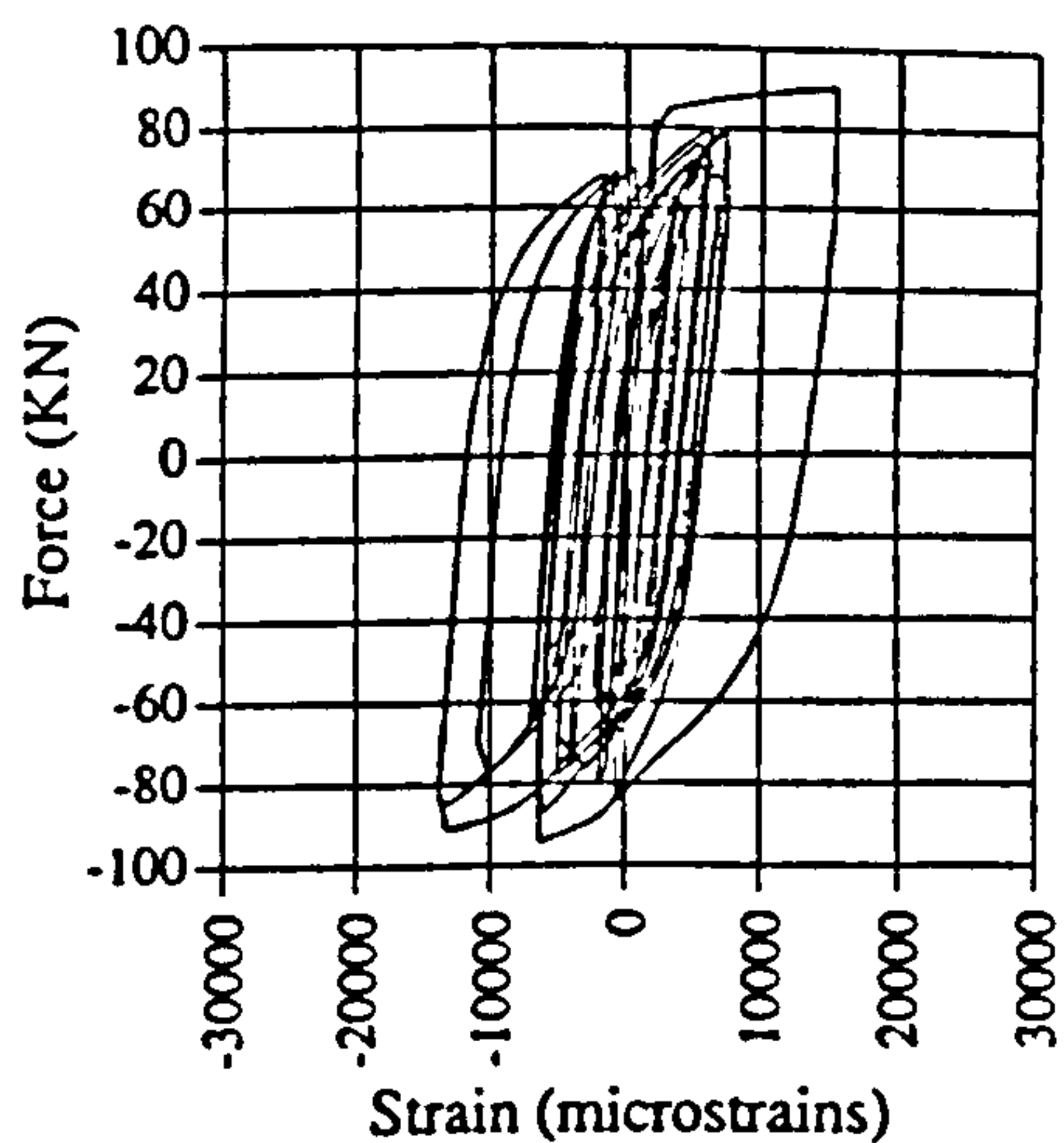


Fig. A.153 Force vs strain, EM05, G3

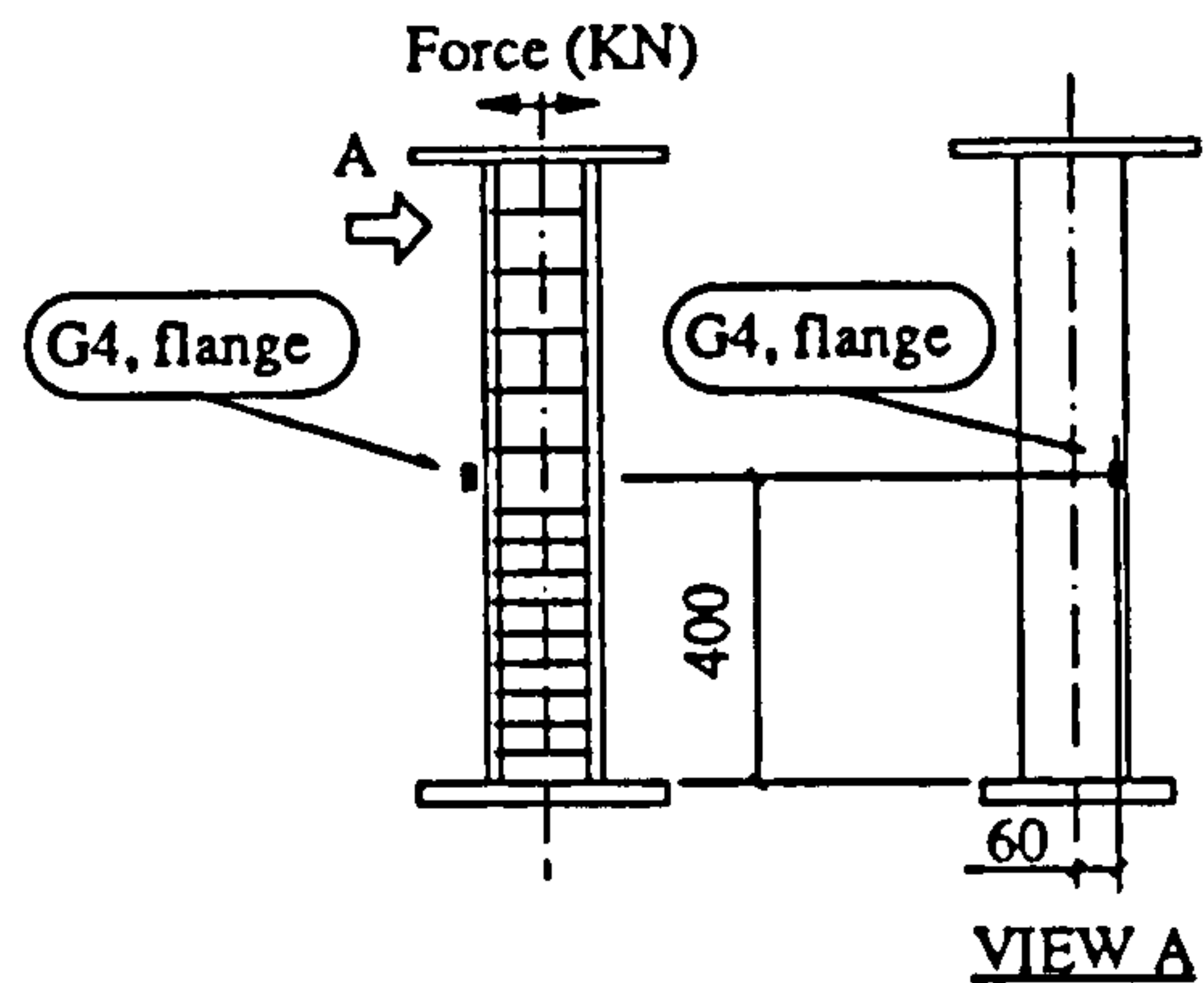
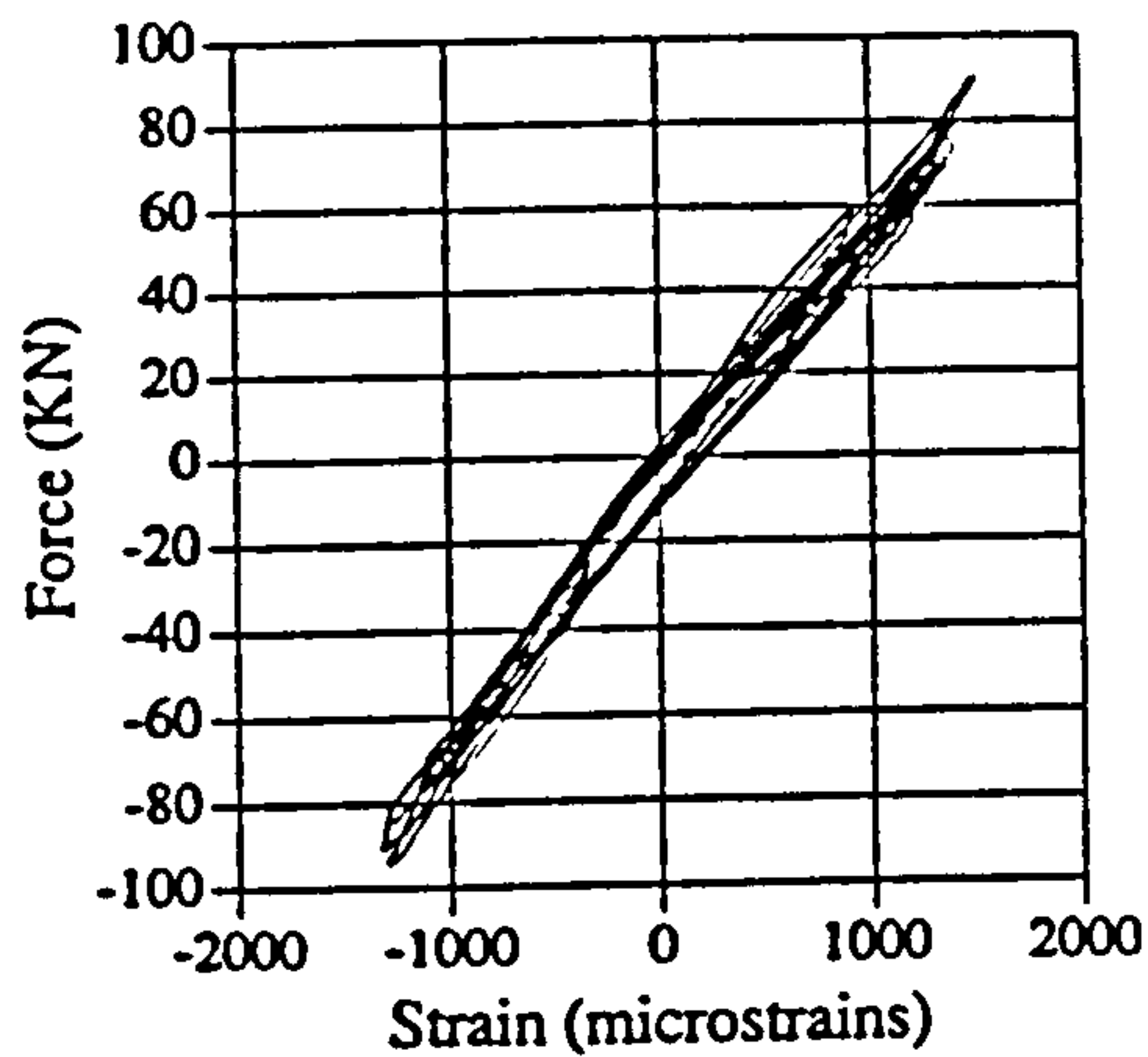


Fig. A.154 Force vs strain, EM05, G4

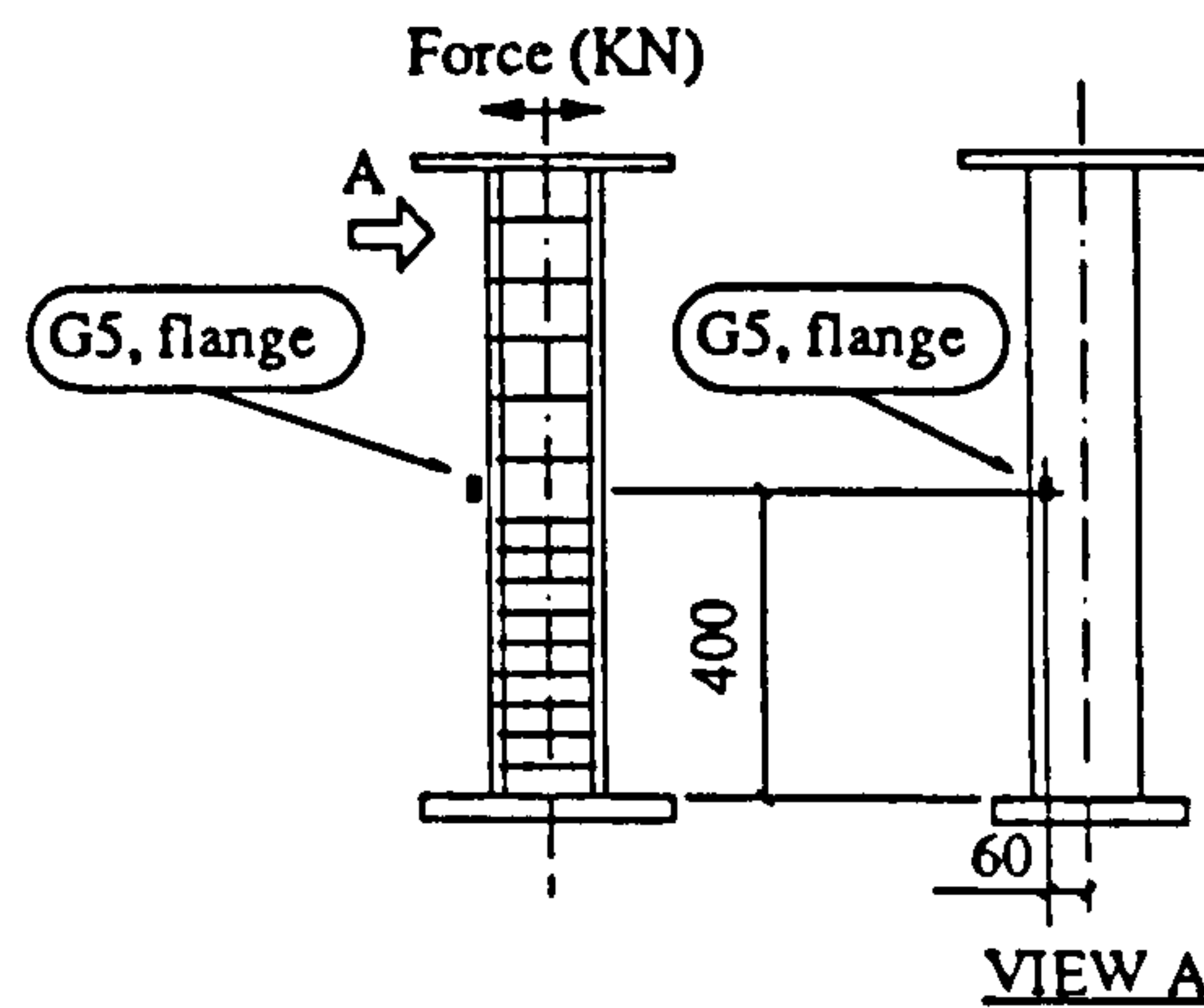
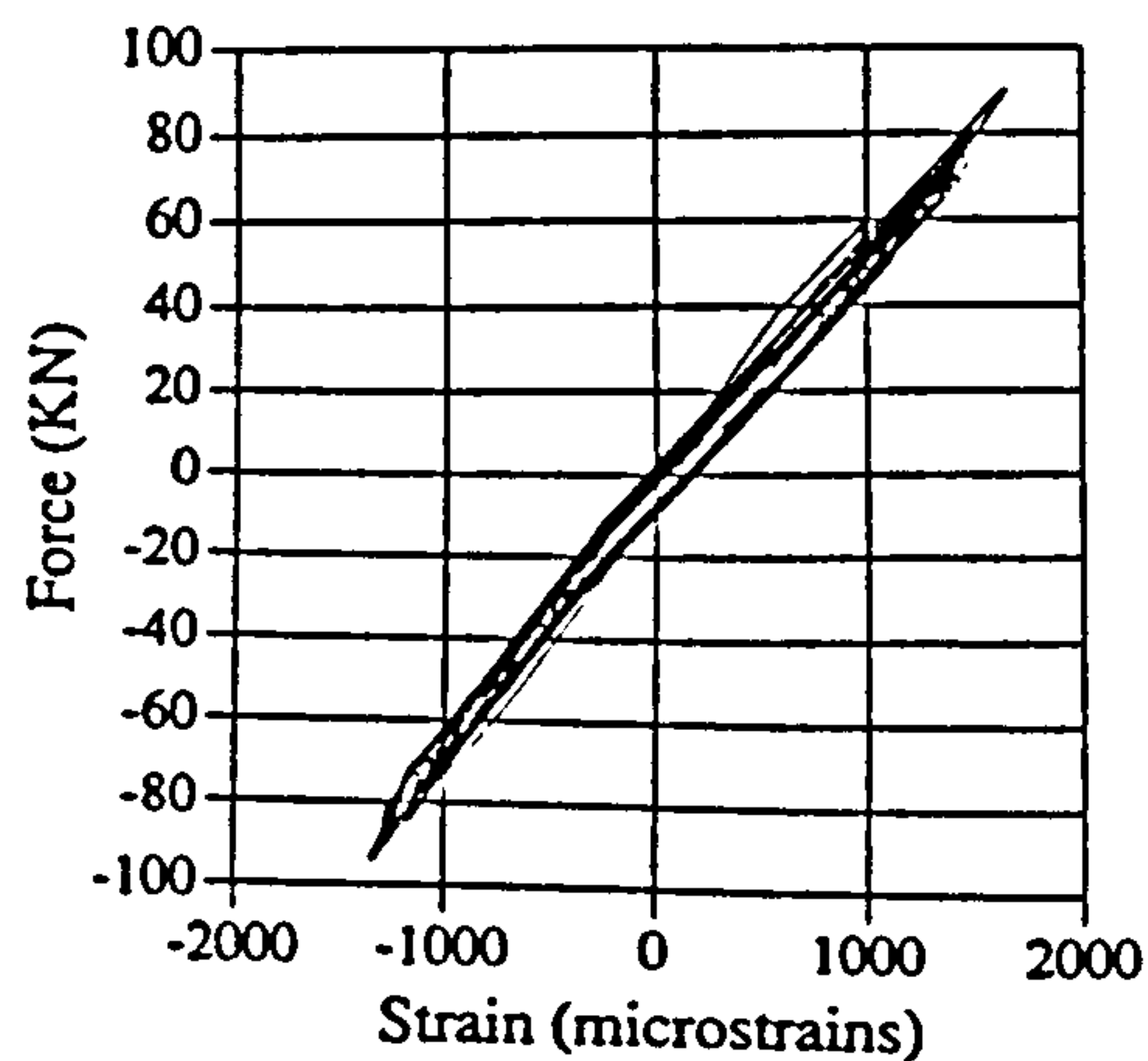


Fig. A.155 Force vs strain, EM05, G5

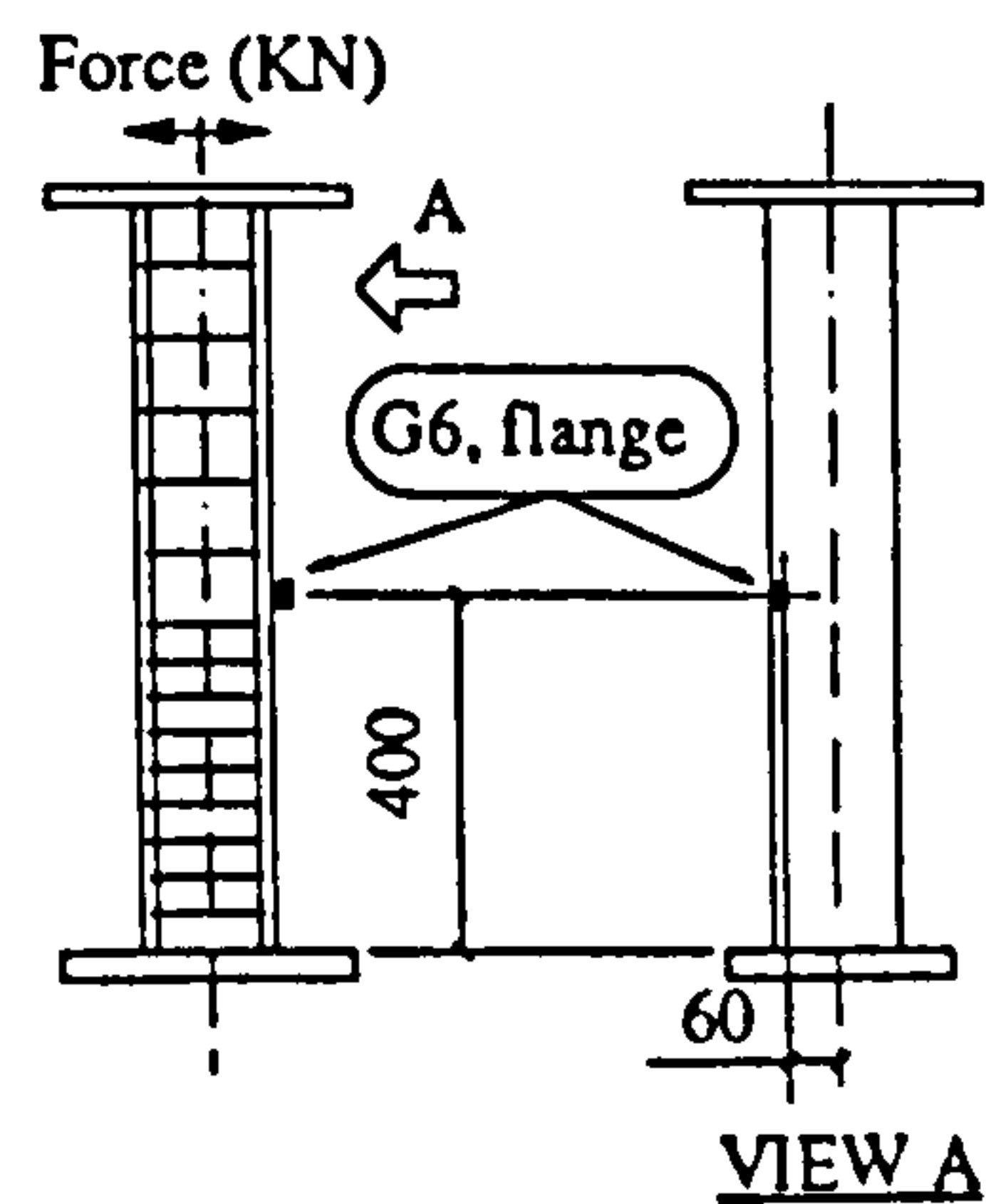
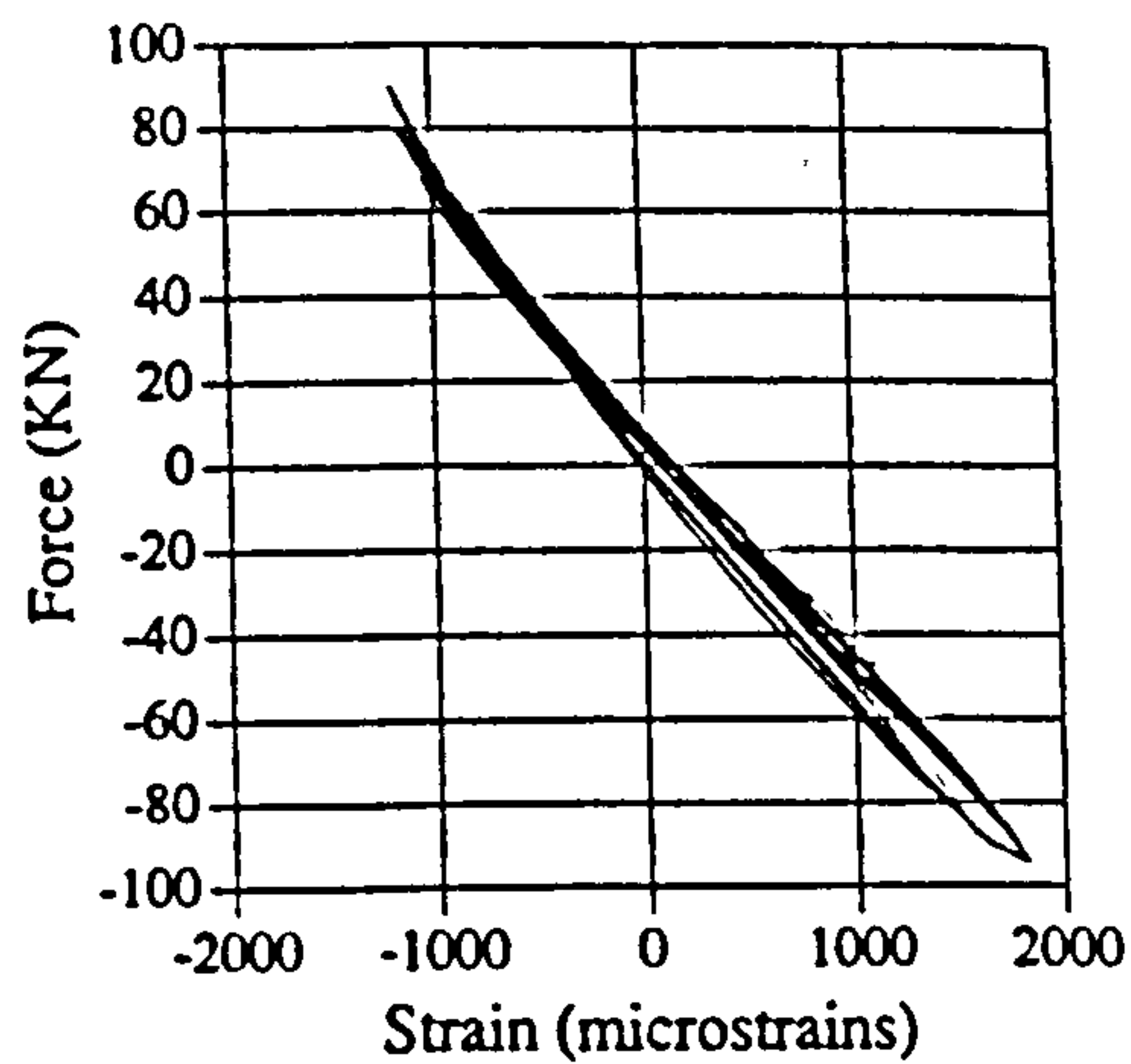


Fig. A.156 Force vs strain, EM05, G6

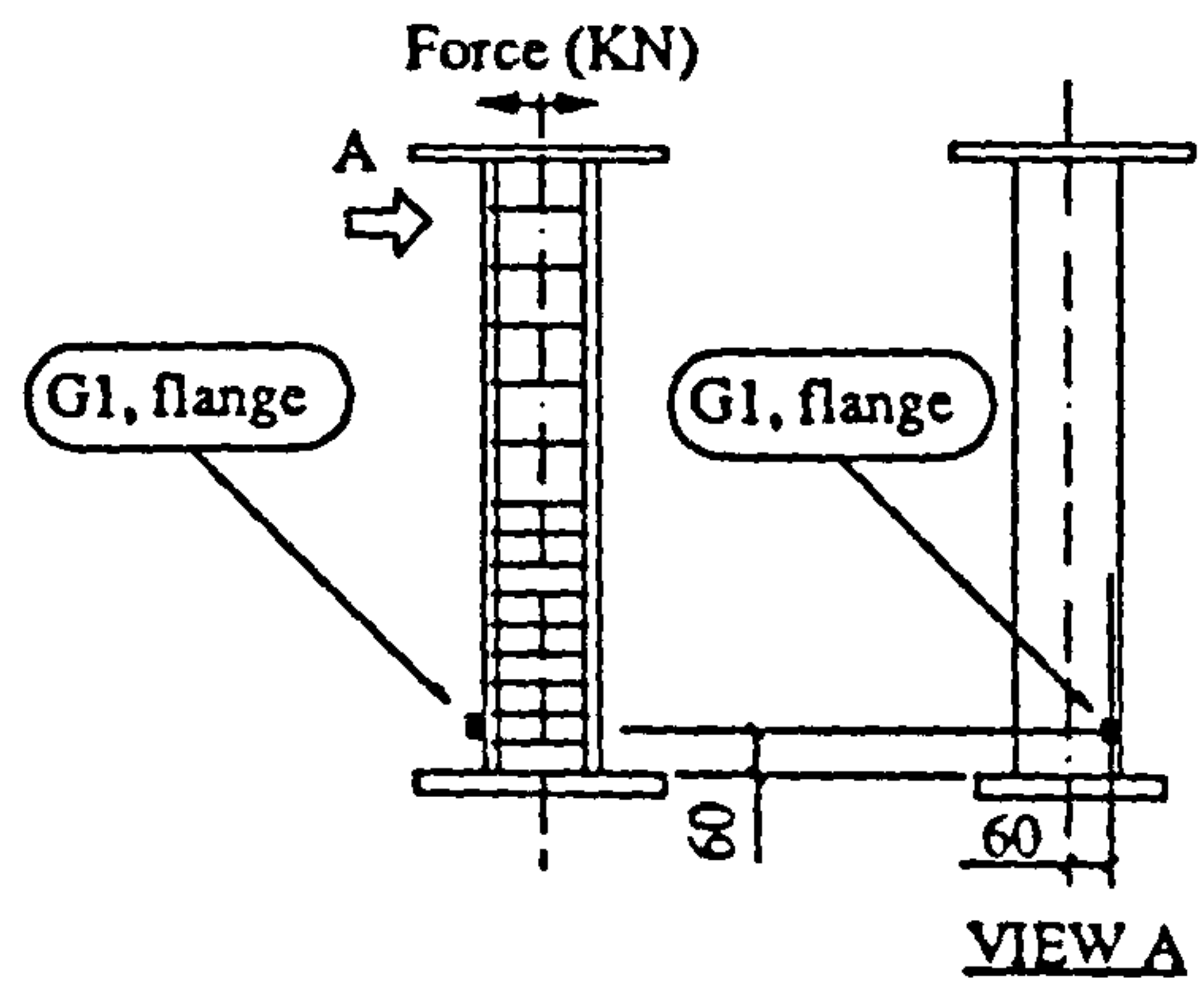
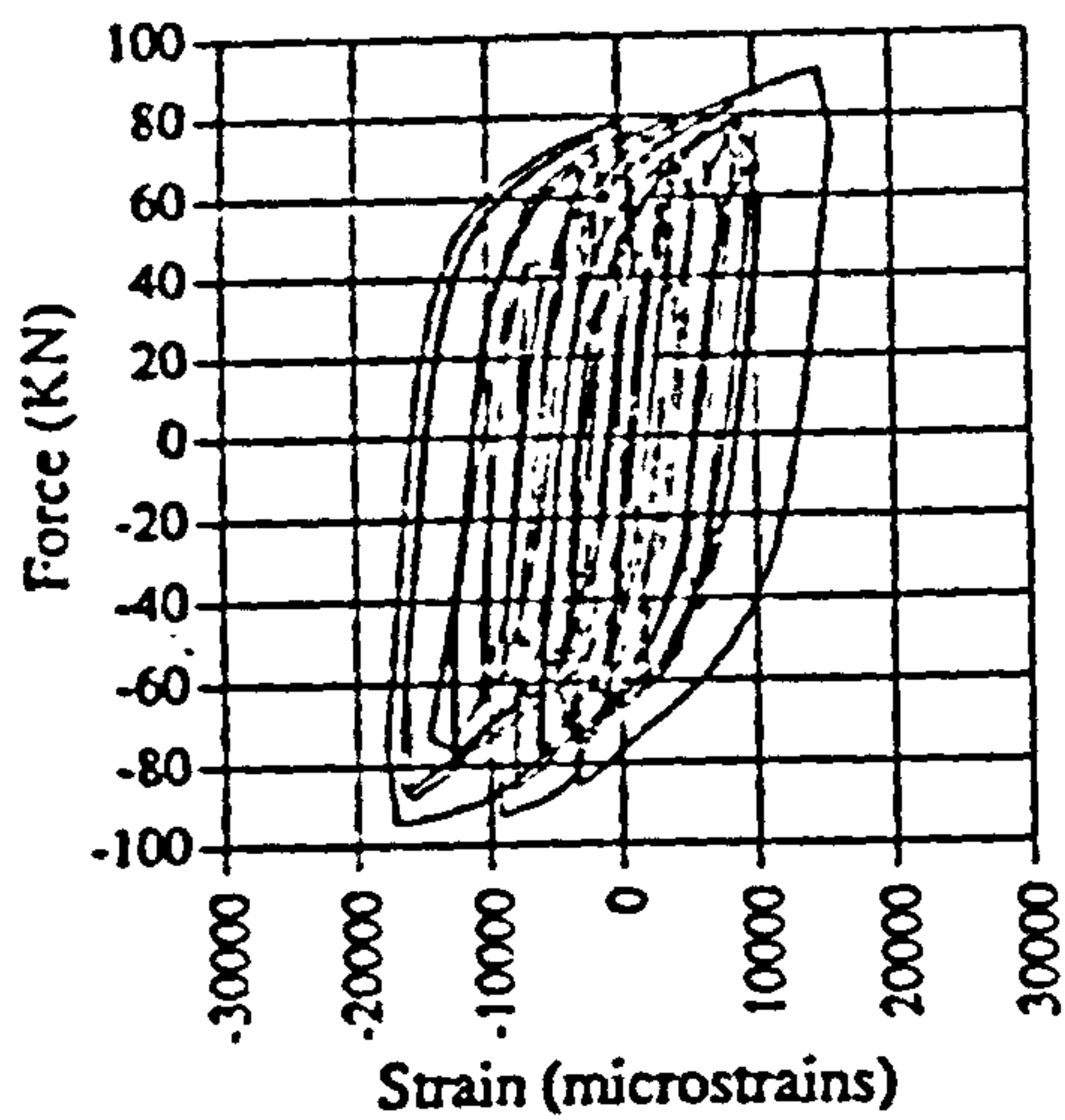


Fig. A.157 Force vs strain, IC05, G1

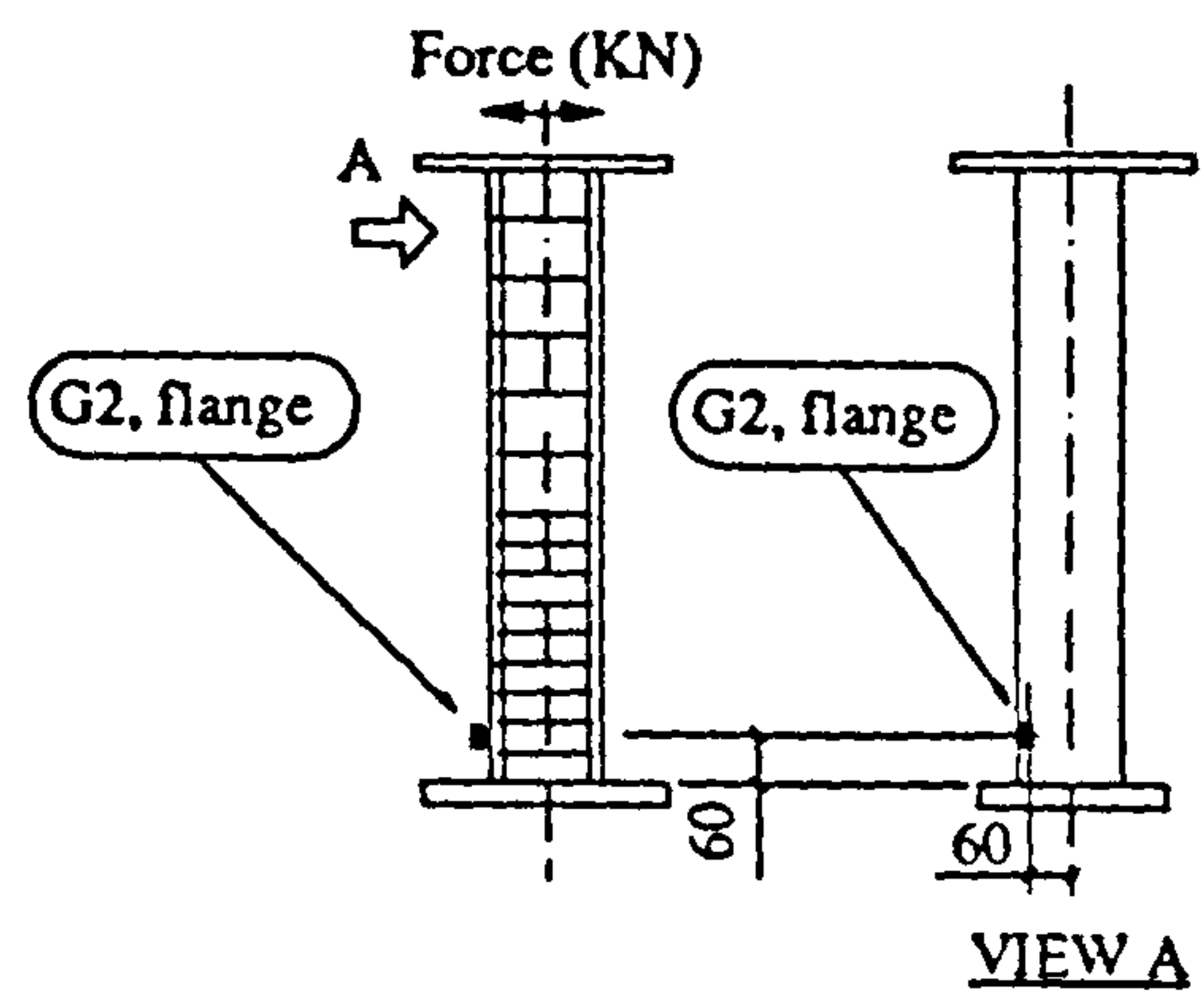
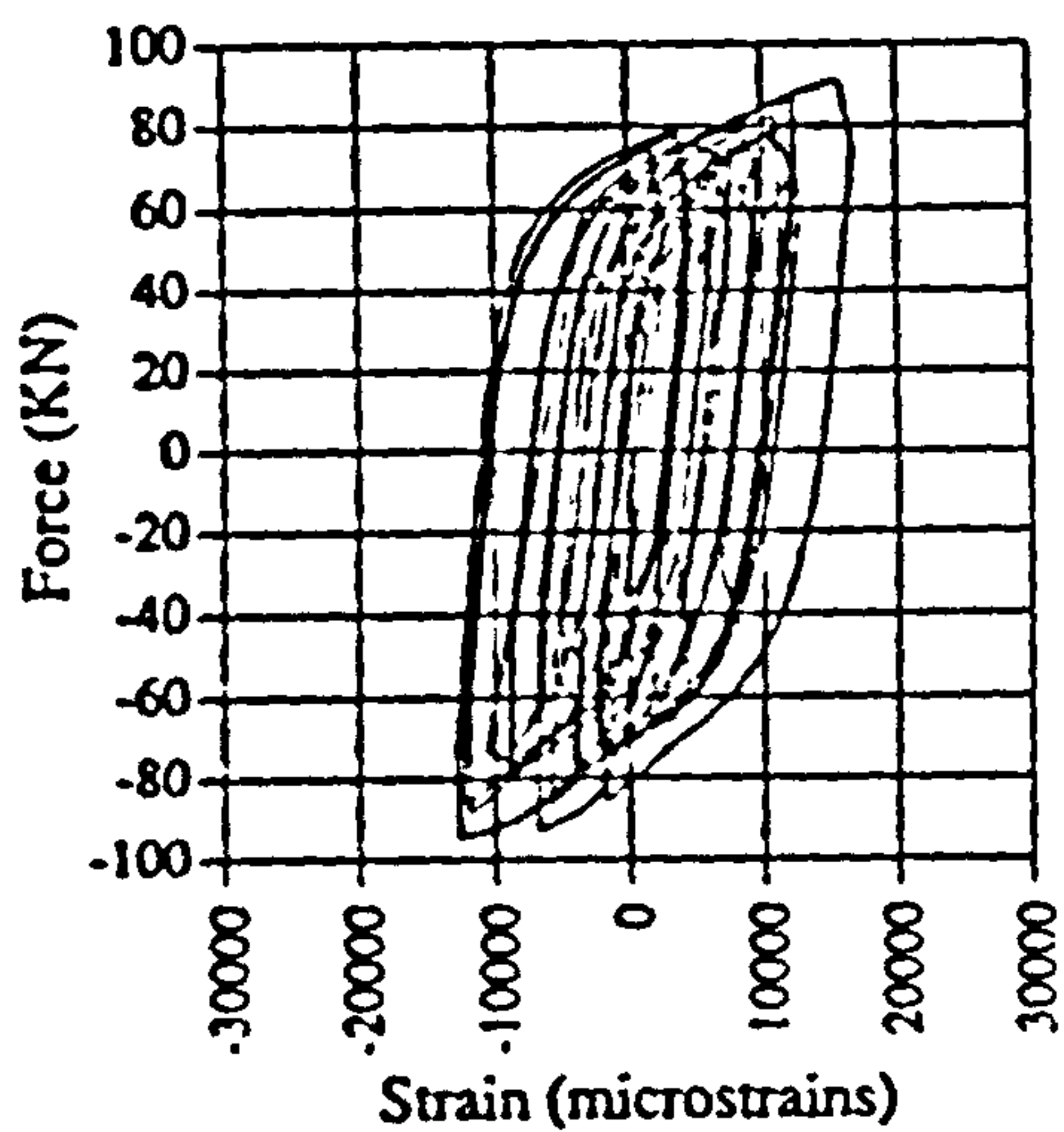


Fig. A.158 Force vs strain, IC05, G2

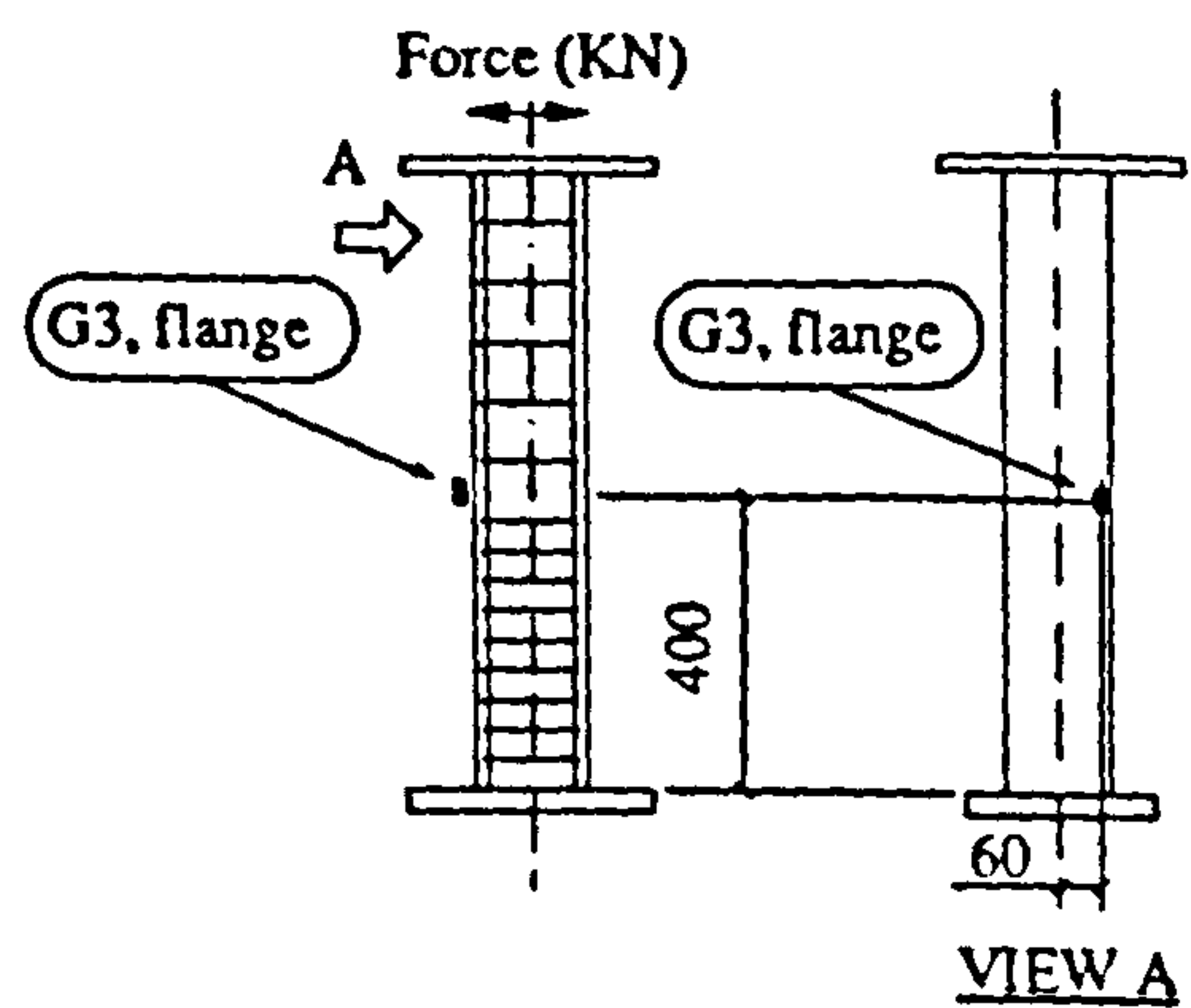
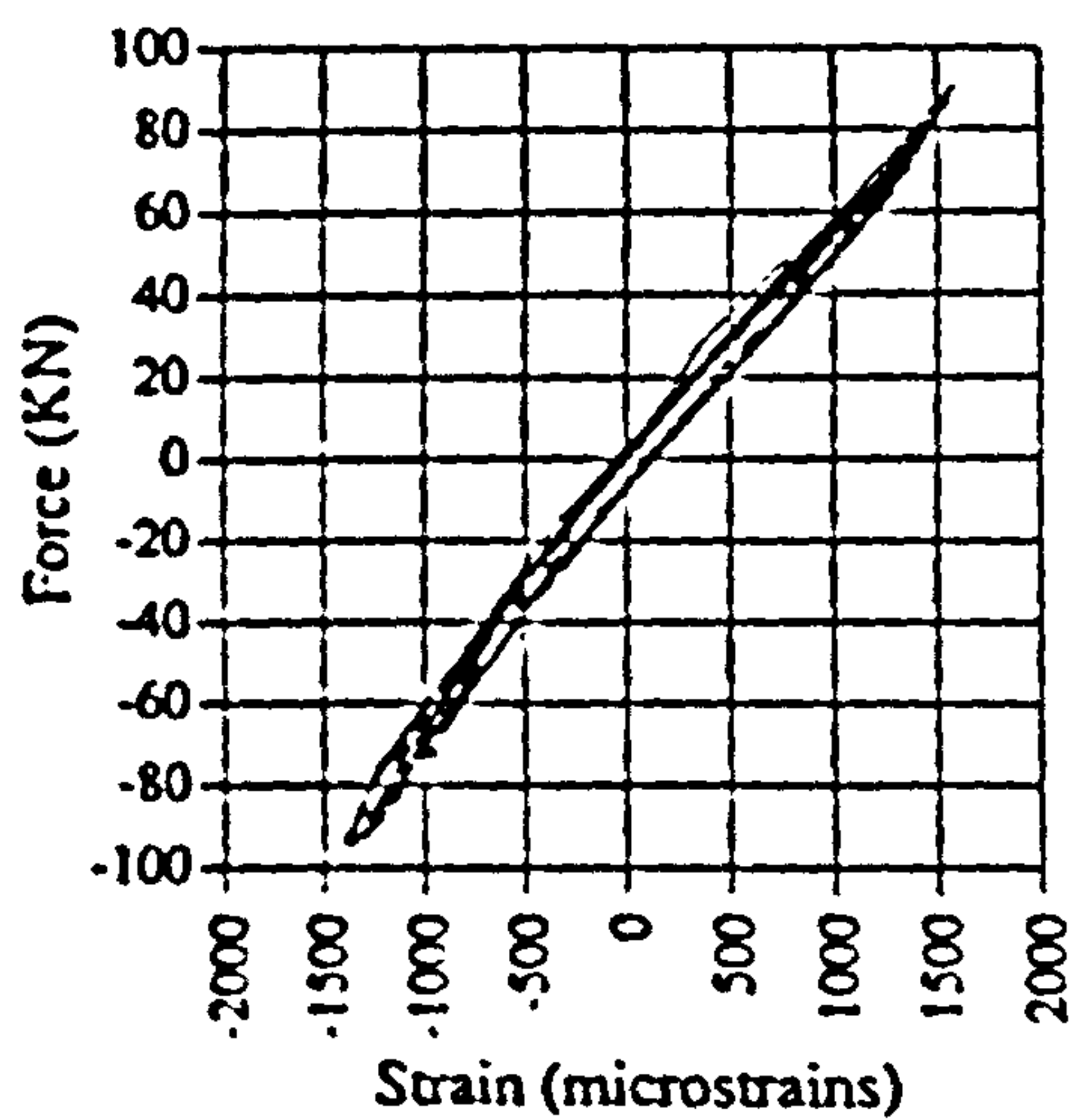


Fig. A.159 Force vs strain, IC05, G3

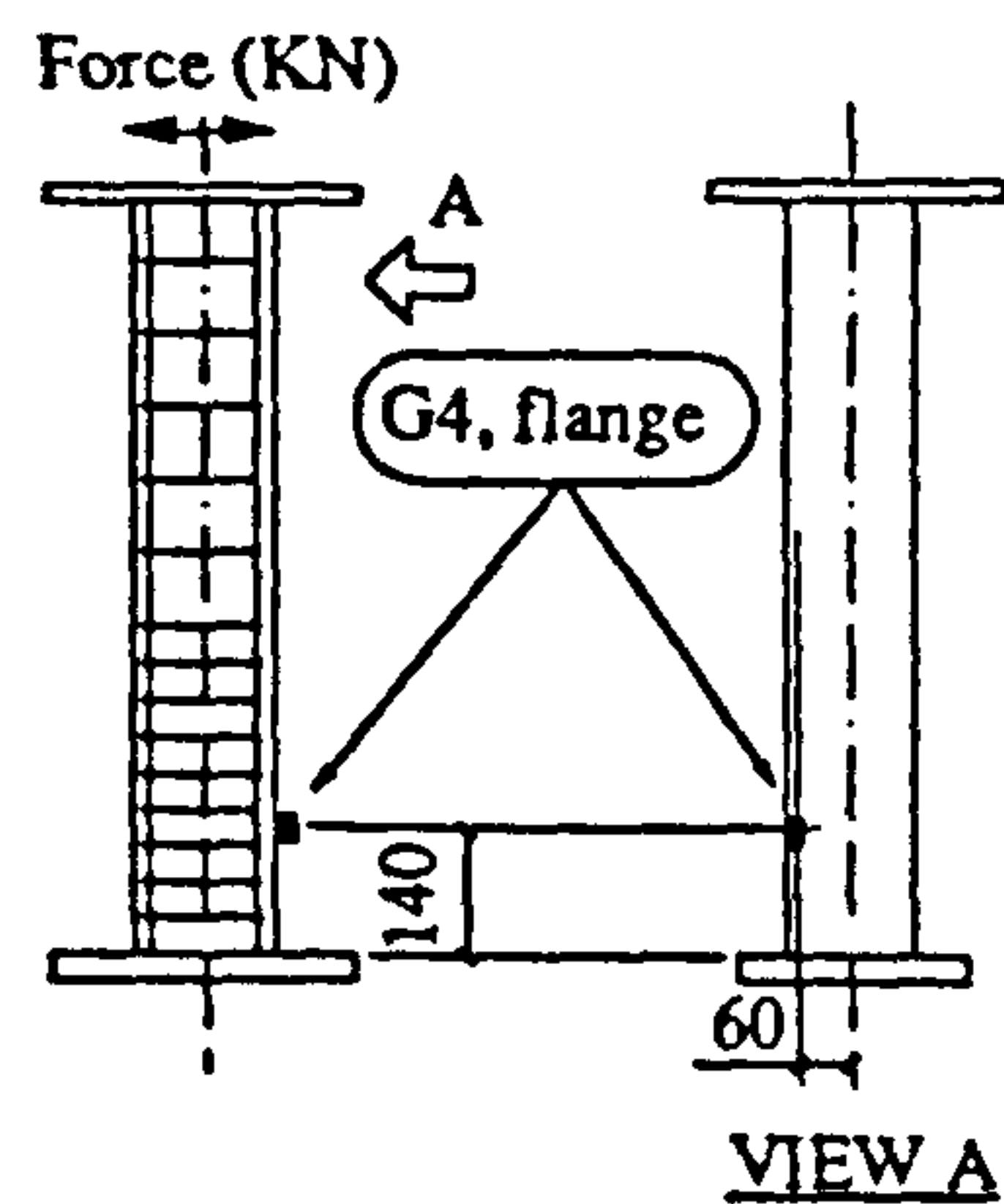
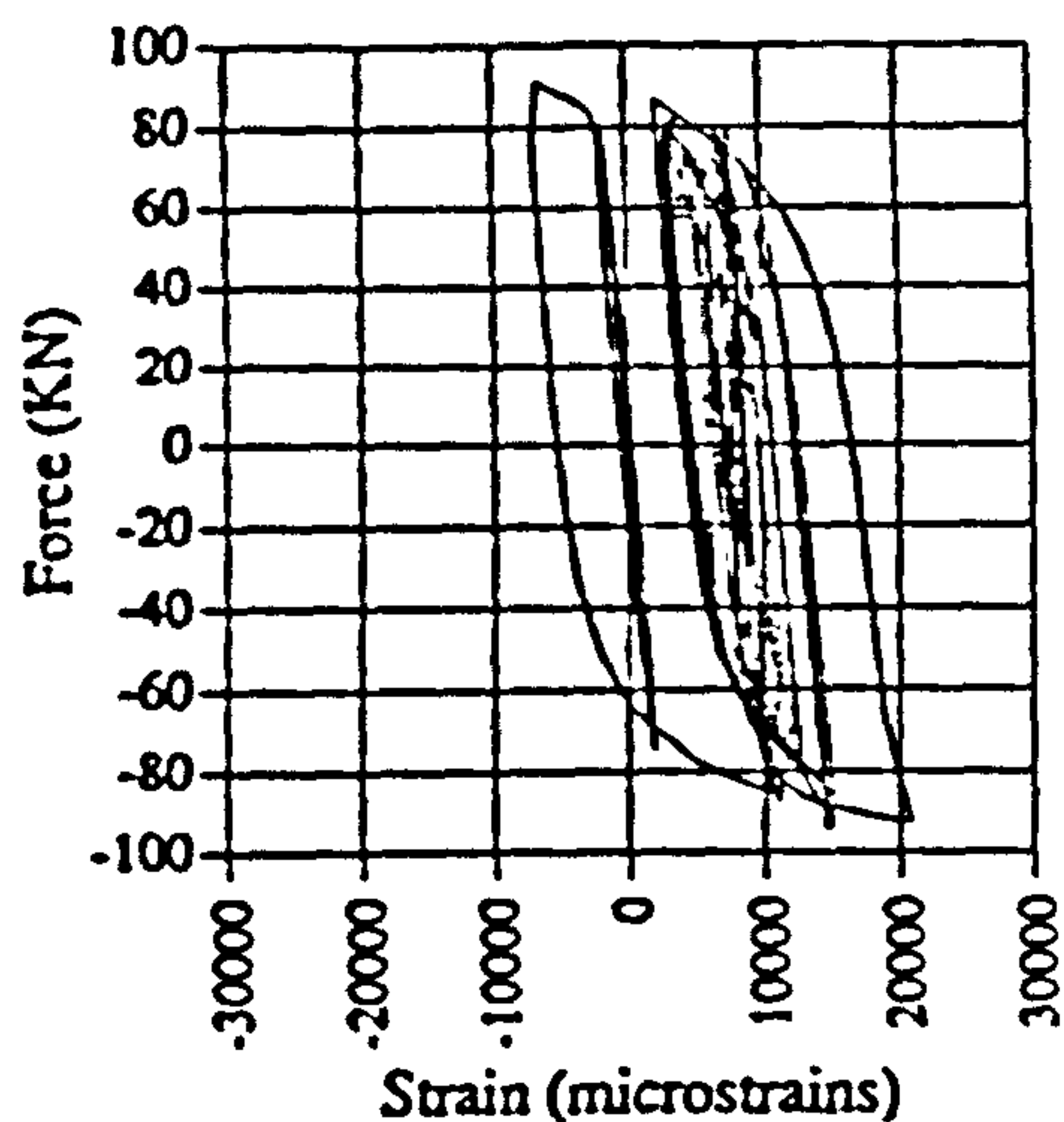


Fig. A.160 Force vs strain, IC05, G4

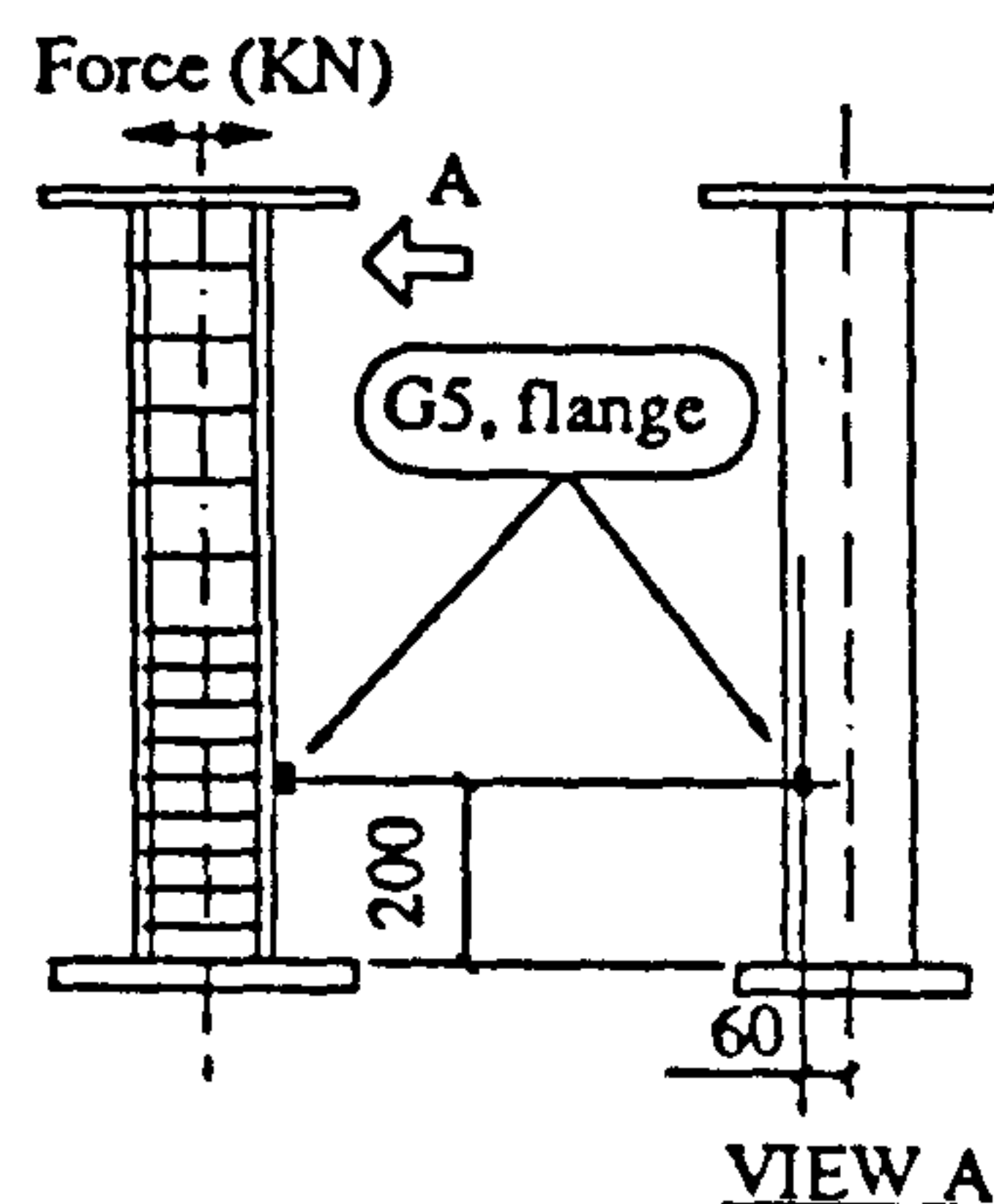
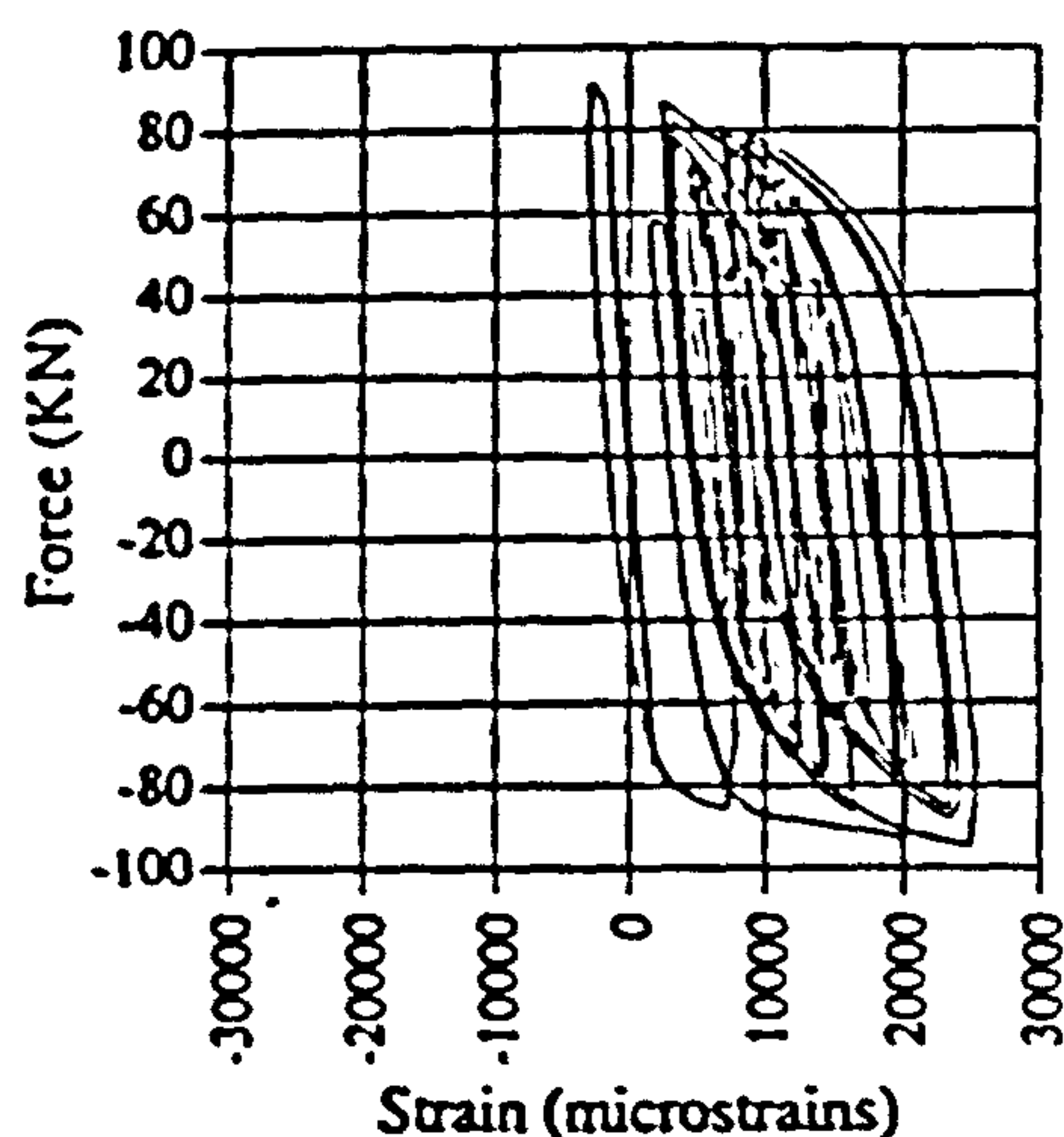


Fig. A.161 Force vs strain, IC05, G5

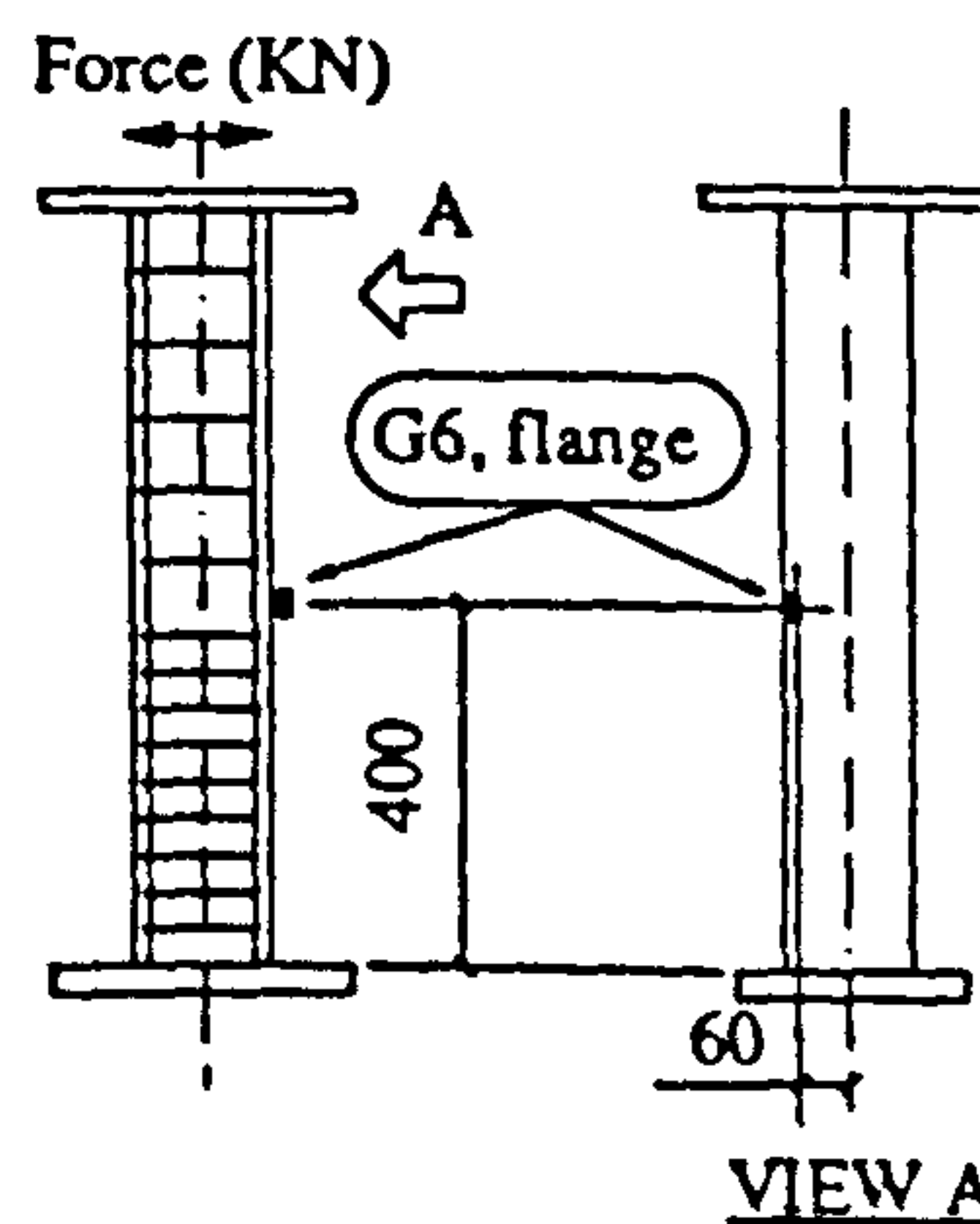
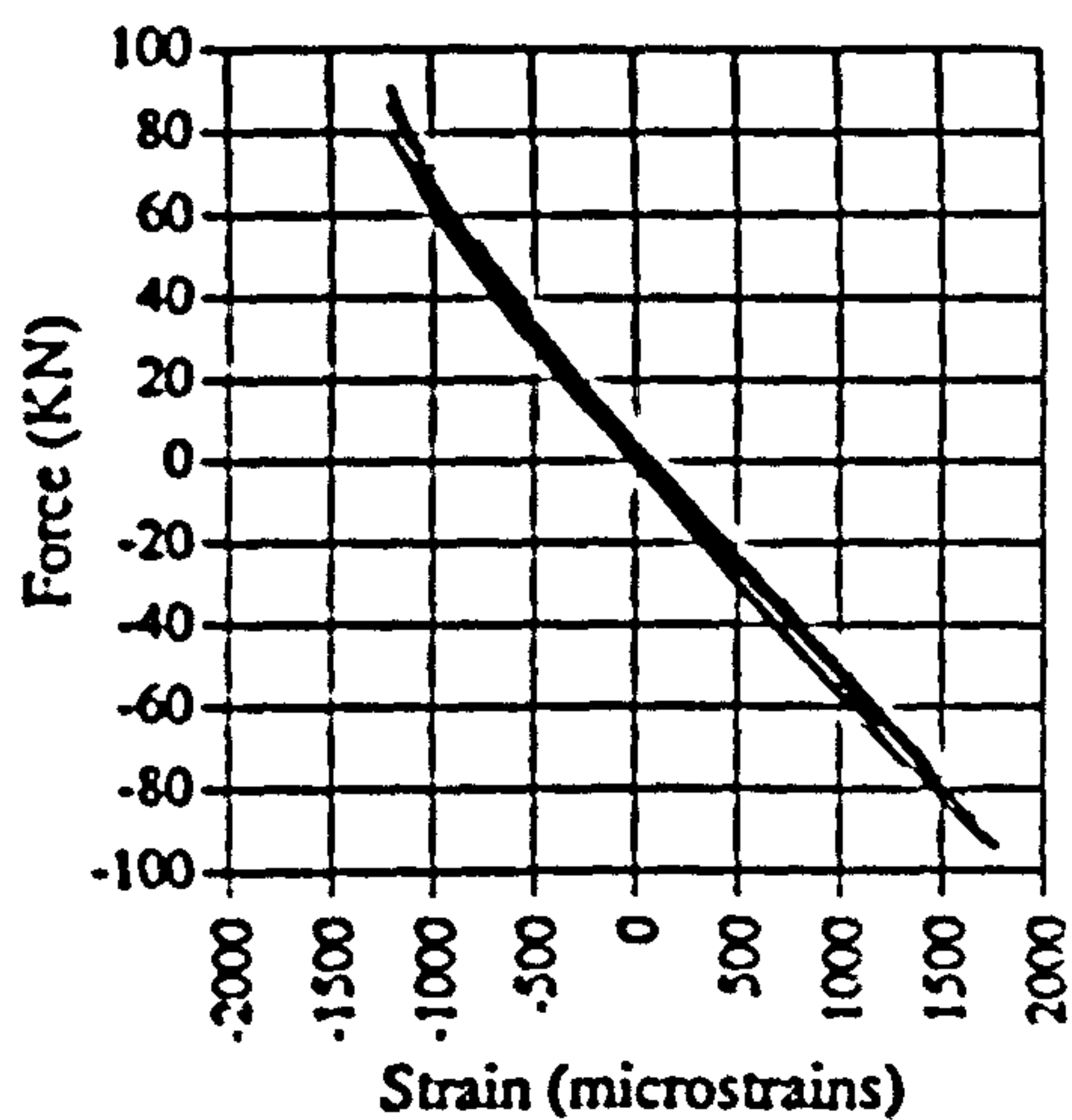


Fig. A.162 Force vs strain, IC05, G6